Proceedings of the TOUGH Symposium 2015

September 28–30, 2015

Lawrence Berkeley National Laboratory
Berkeley, California

Editors

Laura Blanco-Martin, Christine Doughty, Stefan Finsterle, Matthew Reagan, Jonny Rutqvist, Carol Valladao, and Liange Zheng

Lawrence Berkeley National Laboratory
Earth Sciences Division
1 Cyclotron Road, Mail Stop 74R316C
Berkeley, CA 94720

This work was supported by the U.S. Department of Energy under Contract No. DE-AC02-05CH11231

Foreword

This volume contains more than 80 papers presented at the TOUGH Symposium 2015 in both oral and poster formats. The full papers are also available as pdfs linked from the program posted on the TOUGH Symposium 2015 website at

http://esd1.lbl.gov/research/projects/tough/events/symposia/toughsymposium15/program.html

The papers cover a wide range of application areas and generally reflect the continuing trend toward increasing capabilities and broader application of the TOUGH codes to critical problems in Earth sciences and engineering. The two largest-growing areas this year involve coupling fluid flow to geomechanics and to reactive geochemistry.

The Organizing Committee wishes to thank the session chairs, presenters, key note speaker, and participants for their ongoing interest in the TOUGH codes. The support from various agencies and offices in the U.S. and around the world for the development and application of the TOUGH codes is greatly appreciated. We also are grateful to Calpine Corporation, Geofirma Engineering, John Wiley & Sons, Ltd., and Thunderhead Engineering for financial support of the Welcome Reception, Poster Session, Symposium Banquet and related Short Courses.

The papers are grouped by topic and within a topic ordered alphabetically by the last name of the first author. The topical sections start at the following page numbers:

The Organizing Committee

Christine Doughty (Chair)
Laura Blanco-Martin
Matthew Reagan
Jonny Rutqvist
Carol Valladao
Liange Zheng

Berkeley, September 28, 2015

AGENDA

Sunday, September 27, 2015	
Icebreaker	
6:00 PM	**Welcome Reception, DoubleTree by Hilton, Berkeley Marina**
Monday, September 28, 2015 Morning Sessions	
7:30 AM	**Registration, Building 50 Auditorium,** Lawrence Berkeley National Laboratory, Berkeley, CA
Welcome and Opening Remarks	
8:30	**Welcome** **Horst Simon**, Deputy Director, Lawrence Berkeley National Laboratory (LBNL)
8:40	**Opening Remarks** **Christine Doughty**, TOUGH Symposium Organizing Committee Chair
8:50	**Announcements** **TOUGH Symposium Organizing Committee**
Session I: Carbon Dioxide Storage	
Session Chairs: Alfredo Battistelli and Curtis M. Oldenburg	
9:00	**Thermodynamics related processes during the migration of acid gases and methane in deep sedimentary formations** **Alfredo Battistelli** (Saipem SpA), Paolo Berry, Stefano Bonduà, Villiam Bortolotti (Bologna University), Alberto Consonni (eni SpA), Carlo Cormio (Bologna University), Claudio Geloni (eni SpA), Ester Maria Vasini (Bologna University)
9:20	**A new TOUGH2-module: ECO2MG** **Daniel Loeve**, J.G. Maas, A. Obdam (TNO)
9:40	**Geologic carbon dioxide sequestration in natural gas reservoirs: Pressure rise due to CO_2-CH_4 mixing** **Curtis M. Oldenburg**, Kyung Jae Lee, Jonny Rutqvist (LBNL)
10:00	**Thermal perturbations induced by CO_2 production from the Kevin Dome CO_2 reservoir** **Quanlin Zhou**, Curtis M. Oldenburg, Jonathan Ajo-Franklin (LBNL), Stacey Fairweather, Lee H. Spangler (Montana State University, Bozeman)
10:20	***Break***
10:50	**Impacts of formation heterogeneity, injection procedure and hysteresis effect on the reservoir performance in CO_2 geological storage in the Ordos Basin in China** **Cai Li** (University of Sydney, Beijing Normal University, China Institute of Geo-environmental Monitoring), Chaobin Guo (Tongji University), Keni Zhang (Beijing Normal University), Federico Maggi (University of Sydney)
11:10	**Effect of boundary openness, domain size and relative permeability on pressure and CO_2 saturation predictions by numerical simulation under geologic carbon storage conditions** **Liwei Zhang**, Robert Dilmore, Grant Bromhal (National Energy Technology Laboratory)
11:30	**Impact of relative permeability on CO_2 phase behavior, phase distribution, and trapping mechanisms** **Nathan Moodie**, Brian McPherson, Feng Pan (University of Utah)
11:50	***Lunch***

Monday, September 28, 2015 Afternoon Sessions

Session II: Geothermal

Session Chairs: Andrea Borgia and Grimur Bjornsson

1:10	**Managing large geothermal reservoir models under the iTOUGH2 platform** **Grimur Bjornsson** (Warm Arctic ehf) and Andri Arnaldsson (Vatnaskil Consulting Engineers)
1:30	**TOUGH2-EOS1 modeling of the long term exploitation of the Paratunsky Geothermal Field, Kamchatka** **Alexey V. Kiryukhin** (Institute of Volcanology & Seismology), N.P. Asaulova, L.A. Vorozheikina, N.V. Obora (SUE KamchatskBurGeoTermia), A.I. Rozhenko (United Institute of Computer Science SB RAS), N.B. Zhuravlev (Institute of Volcanology & Seismology), P.A. Kiryukhin (Exigen Services Ltd.), A.Y. Polyakov, P.O. Voronin, E.V. Kartasheva (Institute of Volcanology & Seismology)
1:50	**3D dual porosity modeling of tracer transport in Palinpinon 1 Geothermal Field, Philippines** **Anthony E. Ciriaco** and Michael O'Sullivan (Energy Development Corporation)
2:10	**Description of explicit surface features using updated field data of Rotorua Geothermal Field** **Thomas M.P. Ratouis**, Michael J. O'Sullivan, John P. O'Sullivan (The University of Auckland)
2:30	**Interpretation of production tests in geothermal wells with T2Well-EWASG** **Ester Maria Vasini** (Bologna University), Alfredo Battistelli (Saipem SpA), Paolo Berry, Stefano Bonduà, Villiam Bortolotti, Carlo Cormio (Bologna University), Lehua Pan (LBNL)
2:50	***Break***
3:20	**Simulating supercritical water in magmatic geothermal reservoirs** **Lilja Magnusdottir** and Stefan Finsterle (LBNL)
3:40	**A numerical code to incorporate gravity data into geothermal reservoir models** **Sophie C.P. Pearson-Grant** (GNS Science Wairakei Research Center)
4:00	**Simulations of CO_2 push-pull in fractures to enhance geophysical contrast for characterizing EGS sites** **Andrea Borgia**, Curtis M. Oldenburg (LBNL), Rui Zhang (University of Louisiana at Lafayette), Lehua Pan, Stefan Finsterle (LBNL), T.S. Ramakrishnan (Schlumberger-Doll Research)
4:20	**Modeling a CO_2 thermosiphon in a partially saturated reservoir using T2Well with EOS7CMA** **Lehua Pan**, Christine Doughty, Barry Freifeld, Curtis M. Oldenburg (LBNL)
4:40	**Geochemical modeling of Tourmaline formation at Elba Island** **Giordano Montegrossi**, Giovanni Ruggieri (CNR-IGG), Barbara Cantucci (INGV)

Evening Poster Session and Reception (agenda separate)

5:30 – 8:00	***LBNL Cafeteria***
8:00	**Shuttle bus leaving for DoubleTree, Berkeley Marina & Downtown Berkeley BART**

Tuesday, September 29, 2015 Morning Session	
Session III: Numerical Methods	
Session Chairs: Ronald Falta and George Pau	
8:30	**TOUGH3: A new base version of the TOUGH suite of codes** **Yoojin Jung**, George Pau, Stefan Finsterle (LBNL)
8:50	**Implementation of a simple well-bore model in iTOUGH2 for high enthalpy wells** **Jean-Claude Berthet**, Andri Arnaldsson, Snorri Kjaran (Vatnaskil Consulting Engineers)
9:10	**Development of numerical approaches for simulation of slurry flow in fracture/porous media** Xiaoyu Wang (Beijing Normal University), **Keni Zhang** (Beijing Normal University, LBNL), Lehua Pan (LBNL), Chaobin Guo (Tongji University)
9:30	**Fast method to predict oil production from fractured reservoir** **George Shu Heng Pau**, Stefan Finsterle, Kyung Jae Lee (LBNL), Rishi Parashar (Desert Research Institute), Yingqi Zhang (LBNL)
9:50	***Break***
10:20	**Quality assurance for the TOUGH2 family of codes using the code SITA** **Martin Navarro**, Holger Seher, Stephan Hotzel, Jens Eckel (Gesellschaft für Anlagen- und Reaktorsicherheit (GRS) gGmbH)
10:40	**MeshMaker V2.0S and V2.0P: New grid generators for complex heterogeneous domains in TOUGH2/TOUGH+ simulations** **George J. Moridis** and Noel Keen (LBNL)
11:00	**Unstructured 3D mesh generation for geological applications using LaGriT** **Carl W. Gable** (Los Alamos National Laboratory) and Manuel Sentís (ENSI)
11:20	**3D Voronoi pre- and post-processing tools for the modeling of deep sedimentary formations with the TOUGH2 family of codes** **Stefano Bonduà** (Bologna University), Alfredo Battistelli (Saipem SpA), Paolo Berry, Villiam Bortolotti (Bologna University), Alberto Consonni (eni SpA), Carlo Cormio (Bologna University), Claudio Geloni (eni SpA), Ester Maria Vasini (Bologna University)
11:40	**Generating one-column grids with fractal flow dimension** **Christine Doughty** (LBNL)
Awards	
12:00	**Student Award Ceremony** **TOUGH Symposium Organizing Committee**
12:05	***Lunch***

Tuesday, September 29, 2015 Afternoon Sessions

Session IV: Coupled Fluid Flow and Geomechanics

Session Chairs: Rainer Senger and Robert Walsh

1:20	**An overview of TOUGH-based geomechanics models** **Jonny Rutqvist** (LBNL)
1:40	**Extension of the TOUGH-FLAC simulator to account for finite strains** **Laura Blanco-Martin**, Jonny Rutqvist, Jens T. Birkholzer (LBNL)
2:00	**Development of a hydro-geomechanical model to simulate coupled fluid flow and reservoir geomechanics** **Mamun Miah** (University of Mississippi), Laura Blanco-Martín, William Foxall, Jonny Rutqvist, (LBNL), Antonio P. Rinaldi (ETH Zürich), Christopher Mullen (University of Mississippi, LBNL)
2:20	**Simulations of fluid-driven fracturing within discrete fracture networks using TOUGH-RBSN** **Kunhwi Kim**, Jonny Rutqvist, Seiji Nakagawa, James Houseworth, Jens Birkholzer (LBNL)
2:40	**TOUGH2-SEED: A coupled fluid flow mechanical-statistical model for the study of injection-induced seismicity** **Massimo Nespoli** (Istituto Nazionale di Geofisica e Vulcanologia - Sezione di Bologna, Università di Bologna), Antonio P. Rinaldi, Stefan Wiemer (Swiss Seismological Service, ETH Zurich)
3:00	***Break***

Session V: Nuclear Energy and Waste

Session Chairs: Jens Birkholzer and Nicolas Spycher

3:30	**Preliminary analyses and numerical modeling of the Gas Permeable Seal Test (GAST) at the Grimsel Test Site, Switzerland** **Thomas Spillmann** (Nagra), Rainer Senger (Intera Incorporated), George W. Lanyon (Fracture Systems), Niels Giroud, Paul Marschall (Nagra)
3:50	**Modeling of gas migration through low-permeability clay using information on pressure and deformation from fast air injection tests** **Rainer Senger** (Intera Incorporated), Enrique Romero (UPC), Paul Marschall (Nagra)
4:10	**Coupled THMC models for bentonite in clay repository for nuclear waste using TOUGHREACT-FLAC3D** **Liange Zheng**, Jonny Rutqvist, Jens T. Birkholzer (LBNL)
4:30	**Application of 1D hydromechanical coupling in TOUGH2 to a deep geological repository glaciation scenario** **Nicola Calder**, John Avis (Geofirma Engineering Ltd.), Erik Kremer (Nuclear Waste Management Organization), Robert Walsh (Geofirma Engineering Ltd.)

Banquet Dinner

6:00	**Shuttle bus pick-up at the Guest House and DoubleTree, Berkeley Marina**
6:30	**Banquet, *Mira Vista Golf & Country Club*** **7901 Cutting Blvd, El Cerrito**
8:00	**Computational modeling of induced seismicity: A sequential iterative approach to coupled flow and geomechanics** **Ruben Juanes** (Massachusetts Institute of Technology)
9:00	**Shuttle bus leaving for the Guest House, DoubleTree, Berkeley Marina & Downtown Berkeley BART**

Wednesday, September 30, 2015 Morning Sessions	
Session VI: Hydrocarbon Recovery and Reservoir Processes	
Session Chairs: Laura Blanco-Martin and Matthew Reagan	
8:30	**Numerical simulation of transport between fractured tight/shale gas reservoirs and near-surface groundwater** **Matthew T. Reagan**, George J. Moridis, Noel D. Keen (LBNL)
8:50	**Joint inversion of hydrological and geophysical data for enhanced reservoir characterization during enhanced oil recovery** **Michael Commer**, Stefan Finsterle, Yingqi Zhang (LBNL), Michael Hoversten (Chevron Energy Technology Company)
9:10	**A new simulation model of kerogen pyrolysis for the *in-situ* upgrading of oil shales** **Kyung Jae Lee** and George J. Moridis (LBNL)
9:30	**Combining TOUGH2 and FLAC3D to solve problems in underground natural gas storage** **Robert Walsh**, Othman Nasir, Nicola Calder, Sean Sterling, John Avis (Geofirma Engineering Ltd.)
9:50	***Break***
Session VII: Environmental Engineering and Vadose Zone	
Session Chairs: Stefan Finsterle and Karsten Pruess	
10:20	**A semi-analytic approach for modeling matrix diffusion effects in TOUGH2 and other groundwater transport models** **Ronald W. Falta** (Clemson University)
10.40	**Comparison between equivalent continuum and discrete crack models of transient radon transport at the soil-building foundation crack interface using the TOUGH2/EOS7Rn** **Zakaria Saâdi** and Jérôme Guillevic (Institut de Radioprotection et de Sûreté Nucléaire (IRSN))
11.00	**Determining *in situ* heating temperature for optimizing return on investment in DNAPL source zone remediation** **Amy Y. Fu** (Ellis & Associates, Inc., University of Florida), Stefan Finsterle, Yingqi Zhang (LBNL), Michael D. Annable (University of Florida)
Session VIII: Tips & Tricks	
Session Chair: Stefan Finsterle	
11:20	**Short pop-ups with TOUGH tips and tricks** **All Participants – sign up**
12:00	***Lunch***

Wednesday, September 30, 2015 Afternoon Sessions

Session IX: Reactive Transport

Session Chairs: Eric Sonnenthal and Dorothee Rebscher

1:00	**Development of syn-depositional models of carbonate diagenesis: An application of PyTOUGH to complex geological processes** **Miles Frazer** (Chevron Energy Technology Company, University of Bristol), Fiona Whitaker (University of Bristol), Cathy Hollis (University of Manchester)
1:20	**A reactive transport model of sulfur cycling and isotope fractionation during microbial reservoir souring and remediation** **Yiwei Cheng** (LBNL), Li Li (Pennsylvania State University), Nicholas Bouskill, Christopher G. Hubbard, Sergi Molins, Liange Zhang, Eric Sonnenthal (LBNL), Anna Engelbrektson (University of California, Berkeley), Mark E. Conrad (LBNL), John D. Coates (University of California, Berkeley), Jonathan Ajo-Franklin (LBNL)
1:40	**Carbon saturation affects soil C dynamics?** **Dipankar Dwivedi**, William J. Riley, Jinyun Tang (LBNL)
2:00	**Use of reactive transport modelling to study well integrity in a natural analogue for the geological CO_2 storage** **Ana Hernández-Rodriguez** (West Systems s.r.l., Università di Firenze), Giordano Montegrossi (CNR-IGG), Giorgio Virgili (West Systems s.r.l.), Orlando Vaselli (Università di Firenze), Bruno Huet (Lafarge Research Center), Luigi Marini (West Systems s.r.l.)
2:20	**Simulating CO_2-brine-rock interactions including mercury and H_2S impurities in the context of CO_2 geologic storage** **Nicolas F. Spycher** and Curtis M. Oldenburg (LBNL)
2:40	***Break***

Session X: Optimization, Parameter Estimation, Data-Worth Analysis

Session Chairs: Yingqi Zhang and Liange Zheng

3:10	**What's new in iTOUGH2?** **Stefan Finsterle** (LBNL)
3:30	**Fast large-scale inversion for deep aquifer characterization** **Jonghyun Harry Lee**, Amalia Kokkinaki, Judith Yue Li, Peter K. Kitanidis (Stanford University)
3:50	**Bayesian parameter inversion with implicit sampling for a vadose zone hydrological model** **Yaning Liu**, George Shu Heng Pau, Stefan Finsterle (LBNL)
4:10	**Determining optimal monitoring strategies for managing risk of cyclic steam injection using data-worth analysis** **Yingqi Zhang**, Laura Blanco-Martín, Christine Doughty, Stefan Finsterle, Quanlin Zhou, Curtis M. Oldenburg (LBNL)
4:30	**Closing Remarks/Adjourn** **TOUGH Symposium Organizing Committee**

POSTER SESSION

Monday, September 28, 5:30–8:00 PM
LBNL Cafeteria

BOARD	TITLE / AUTHOR
Carbon Dioxide Storage	
Board 1	**Pressure management during geological CO_2 sequestration: Optimal well placement and brine extraction in a heterogeneous reservoir** **Abdullah Cihan**, Jens Birkholzer (Lawrence Berkeley National Laboratory (LBNL)), Marco Bianchi (British Geological Survey)
Board 2	**Risk scenario analysis for heterogeneous geological model in a carbon sequestration application in Taiwan** Chi-Wen Yu and **Shih-Chang Lei** (Sinotech Engineering Consultants Inc.)
Board 3	**ECO2N V2.0: Enhancements for modeling CO_2-H_2O-NaCl system in TOUGH2** **Lehua Pan**, Nicolas Spycher, Christine Doughty, Karsten Pruess (LBNL)
Board 4	**The effect of natural groundwater flow on CO_2 migration and trapping: The case of the Jurassic saline aquifer of the Negev (Israel)** **Ravid Rosenzweig** and Ran Calvo (Geological Survey of Israel)
Geothermal	
Board 5	**Experimental study on flow friction and heat transfer performance of a single rough fracture in granitic rock under confining pressure** **Xiaoxue Huang**, Jialing Zhu, Jun Li (Tianjin University)
Board 6	**Stress field respond to massive injection of cold water into a geothermal reservoir: TOUGH-FLAC simulation** **Pierre Jeanne** and Jonny Rutqvist (LBNL)
Board 7	**Modeling laboratory experiments of fluid flow and heat transfer in supercritical-CO_2-saturated cores with ECO2N V2.0** **Mario Magliocco** (University of California, Berkeley), Christine Doughty, Tim Kneafsey (LBNL), Steve Glaser (University of California, Berkeley, LBNL)
Board 8	**Geothermal exploration through numerical modeling of cold CO_2 soil fluxes** Loic Peiffer (Universidad Nacional Autónoma de México), Christoph Wanner (University of Bern), Lehua Pan (LBNL)
Numerical Methods	
Board 9	**pTOUGH+: Status of re-engineering parallel TOUGH+** **Noel Keen**, Jeff Johnson, George Moridis, Matt Reagan (LBNL)
Board 10	**iMatTOUGH: An open-source Matlab-based graphical user interface for pre- and post-processing of TOUGH2 and iTOUGH2 models** **Anh Phuong Tran**, Baptiste Dafflon, Susan Hubbard (LBNL)
Board 11	**Using GMS as a pre- and post-processor for TOUGH2** **Andrea Borgia** (LBNL)
Coupled Fluid Flow and Geomechanics	
Board 12	**Inverse modeling of coupled fluid flow and geomechanics with iTOUGH2-PEST and TOUGH-FLAC: Application to In Salah CO_2 storage site** **Antonio P. Rinaldi** (LBNL, Swiss Seismological Service), Jonny Rutqvist, Stefan Finsterle (LBNL), H.H. Liu (Aramco Research Center)

BOARD	TITLE / AUTHOR
Coupled Fluid Flow and Geomechanics (cont.)	
Board 13	**Modelling fault reactivation and velocity dependent friction with TOUGH-FLAC** **Luca Urpi** (Utrecht University), Antonio P. Rinaldi (Swiss Seismological Service, LBNL), Brecht Wassing (TNO Geo Energy)
Board 14	**A coupled flow and geomechanics simulator for CO_2 storage in fractured reservoirs** **Philip H. Winterfeld** and Yu-Shu Wu (Colorado School of Mines)
Hydrocarbon Recovery and Reservoir Processes	
Board 15	**iTOUGH2-FLAC modeling of thermal-hydraulic-mechanical processes related to steam-assisted heavy oil recovery from diatomite** **Laura Blanco-Martin**, Jonny Rutqvist, Christine Doughty, Yingqi Zhang, Stefan Finsterle, Curtis M. Oldenburg (LBNL)
Board 16	**Modeling steam, water, and oil flow overlying a heavy oil reservoir undergoing cyclic steaming** **Christine Doughty**, Laura Blanco-Martin, Yingqi Zhang, Curtis M. Oldenburg (LBNL)
Board 17	**Water injection close to fault risk analysis, field application** **Julia Diessl**, Vahid Serajian, Mike S. Bruno (GeoMechanics Technologies)
Board 18	**Methane diffusion and adsorption in shale rocks – A numerical study using the Dusty Gas Model in TOUGH2/EOS7C-ECBM** **Weijun Shen** (Chinese Academy of Sciences, University of Chinese Academy of Sciences), Liange Zheng, Curtis M. Oldenburg, Abdullah Cihan, Jiamin Wan, Tetsu K. Tokunaga (LBNL)
Environmental Engineering and Vadose Zone	
Board 19	**Multiphase flow and transport of methane in soil under varying subsurface and atmospheric conditions: Bench-scale experimental and numerical study** **Chamindu Deepagoda**, Kathleen. Smits, Tissa llangasekare (Colorado School of Mines), Curtis M. Oldenburg, Abdullah Cihan (LBNL)
Board 20	**TOUGH2 application for an assessment of open pit slope stability using saturated/unsaturated groundwater flow modeling to estimate hydraulic forces, Arkhangelsk kimberlite pipe, Russia** **Ivan Leonidovich Kharkhordin** (Geostroyproekt Ltd), V.V. Nazima, A.N. Gurin (VNIMI Institute), I.E. Shkil (Severalmaz Co.)
Board 21	**Influence of permeability on the initial gas bubble evolution in compressed air energy storage in aquifers** **Chaobin Guo** (Tongji University), Keni Zhang (Tongji University, Beijing Normal University), Cai Li (University of Sydney)
Board 22	**Simulating water flow through a layered snowpack** Ryan W. Webb (Colorado State University) and **Stephen W. Webb** (Canyon Ridge Consulting, LLC)
Reactive Transport	
Board 23	**Modeling processes affecting carbon dynamics at a biogeochemical hotspot in a floodplain aquifer** **Bhavna Arora**, Dipankar Dwivedi, Nicolas Spycher, Carl Steefel (LBNL)
Board 24	**TOUGHREACT wrapping using Python towards code intercomparison** **Alain Dimier**, Roman Zorn (Karlsruhe, EIFER Institute), Fabrizio Gherardi (Istituto di Geoscienze e Georisorse, Pisa)
Board 25	**Analysis of fault "self-sealing" associated with CO_2-leakage in geologic carbon sequestration** Vivek V. Patil, Brian J. McPherson (University of Utah), Alexandra Priewisch (University of New Mexico), Joseph Moore, **Nathan Moodie** (University of Utah)
Board 26	**Numerical simulations of the chemical impact of impurities on geological CO_2 storage – Comparison between TOUGHREACT V2.0 and TOUGHREACT V3.0-OMP** **Dorothee Rebscher**, Jan Lennard Wolf (Bundesanstalt für Geowissenschaften und Rohstoffe, BGR), Jacob Bensabat (Environmental and Water Resources Engineering, EWRE Ltd.), Auli Niemi (Uppsala Universitet)

BOARD	TITLE / AUTHOR
Reactive Transport (cont.)	
Board 27	**Potential chemical impacts of CO_2 leakage on underground sources of drinking water (USDWs) assessed by quantitative risk analysis** **Ting Xiao**, Brian McPherson, Feng Pan, Rich Esser (The University of Utah)
Optimization, Parameter Estimation, Data-Worth Analysis	
Board 28	**Effect of anisotropy on multi-directional pressure-pulse-decay experiments** **Michael J. Hannon, Jr**. (The University of Alabama at Birmingham) and Stefan Finsterle (LBNL)
Board 29	**fKF-TOUGH: A software package for data assimilation in TOUGH2 using Fast Kalman Filters methods** **Amalia Kokkinaki**, J.Y. Li, H. Ghorbanidehno, E.F. Darve, P.K. Kitanidis (Stanford University)
Board 30	**Smoothing-based compressed state Kalman Filter (sCSKF) for real-time data assimilation: Applications in CO_2 reservoir monitoring and characterization** **Judith Yue Li**, Amalia Kokkinaki, Eric F. Darve, Peter K. Kitanidis (Stanford University)
Board 31	**Global sensitivity and data-worth analyses in iTOUGH2** **Haruko Wainwright** and Stefan Finsterle (LBNL)

Carbon Dioxide Storage

THERMODYNAMICS RELATED PROCESSES DURING THE MIGRATION OF ACID GASES AND METHANE IN DEEP SEDIMENTARY FORMATIONS

Alfredo Battistelli[(1)], Paolo Berry[(2)], Stefano Bonduà[(2)],Villiam Bortolotti[(2)], Alberto Consonni[(3)], Carlo Cormio[(2)], Claudio Geloni[(3)], Ester Maria Vasini[(2)]

[(1)]AMBEN Dept., Saipem SpA, 61032 Fano (PU), Italy
[(2)]DICAM Dept., Bologna University,40131 Bologna, Italy
[(3)]GEOLAB Dept., eni SpA, 20097 San Donato Milanese (MI), Italy

alfredo.battistelli@saipem.com, paolo.berry@unibo.it, stefano.bondua@unibo.it, villiam.bortolotti@unibo.it
alberto.consonni@eni.com, carlo.cormio3@unibo.it, claudio.geloni@eni.com, estermaria.vasini2@unibo.it

ABSTRACT

TMGAS, an EOS module of TOUGH2 V.2.0, was used to simulate the migration of CO_2, H_2S and CH_4 in a deep sedimentary formation. The scope is the improvement of the description of non-condensable gas (NCG) migration within modelling studies of sedimentary basins evolution. Different scenarios have been simulated with NCG migration taking place in a large sedimentary formation discretized with a full 3D Voronoi approach by using specifically improved versions of the pre- and post-processing tools developed for TOUGH2 by the University of Bologna. Simulated reference scenarios are related to the migration of CO_2, H_2S, and CH_4 injected at constant rate for 1 Myr in a fresh water aquifer. Additional scenarios are simulated with NCG migration taking place in the same formation but saturated with brine. The effects of Pressure-Temperature-Composition (PTX) conditions on thermodynamic equilibria, phase composition, and phase thermophysical properties and, consequently, on the migration features of different NCGs are described and discussed.

INTRODUCTION

Modeling of sedimentary basins evolution is conventionally performed to support the exploration activities of the Oil & Gas (O&G) industry using both commercial and proprietary numerical codes. Burial history, with sedimentation, compaction and fluid expulsion processes, is simulated at basin scale and for geological times. While brine and heat flow are modeled with approaches similar to those of reservoir simulators, migration of liquid hydrocarbons and gases (here referred to as NCG) towards sedimentary and structural traps is routinely performed at Eni SpA using ray-tracing and percolation theory approaches.

The present study is performed within a wider R&D program aimed to improve the modeling of NCG migration in sedimentary basins. The specific goal is to improve the capability to evaluate the exploration risk associated to the presence of acid gases (CO_2 and H_2S) in G&O reservoirs. The TMGAS EOS module (Battistelli and Marcolini, 2009) of TOUGH2 V.2.0 (Pruess et al., 1999) is then used to simulate the migration of CO_2, H_2S and CH_4 in a large and deep sedimentary formation in order to verify the reliability of TMGAS thermodynamic approach and anticipate the needs for code improvements. The accuracy of TMGAS in reproducing phase equilibria and estimating phase properties of NaCl brine – NCG mixtures has been evaluated within the range of PTX values of interest, with temperatures up to 250°C and pressures up to 1000 bar. The sedimentary formation occupies an area of 25,000 km^2 and extends at depths from 6800 to 2000 m. To reproduce the geometry of the sedimentary formation and preserve the integral finite difference method (IFDM) requirements, the discretization grid has been built with a full 3D Voronoi approach by using specifically improved versions (Bounduà et al., 2015) of the pre- and post-processing tools developed for the TOUGH2 simulator (Berry et al., 2014; Bonduà et al., 2012). Reference scenarios related to the migration of NCG injected at constant rate for 1 Myr into selected zones of the sedimentary formation saturated with fresh water were studied. Additional scenarios were simulated with NCG injected in the same zones, but in the presence of a saline aquifer. Sensitivity simulations related to grid spacing, heterogeneous rock property distribu-

tions and boundary conditions have also been performed. In order to better focus on the effects of PTX conditions on thermodynamic equilibria, phase composition, and phase thermophysical properties and, consequently, on the migration features of different simulated NCGs, only the reference scenarios are described and discussed here.

TMGAS PHASE EQUILIBRIA AND PROPERTIES

TMGAS uses the IAPWS-IF97 formulation for water properties (IAPWS, 1997) with relevant subroutines kindly supplied by Michael O'Sullivan (Croucher and O'Sullivan, 2008). Dynamic viscosity of water and steam is computed with the IAPWS (2008) correlations, which are more accurate at high T. For the properties of NaCl brine and halite, TMGAS uses slightly modified versions of the correlations given by Driesner and Heinrich (2007) (D&H) and Driesner (2007) for H_2O-NaCl system up to 1000°C and 2200 bar, and for mixtures ranging from pure water to pure salt. In implementing the D&H approach into TOUGH2, the IAPWS-IF97 correlations have been used to evaluate pure water properties. Thus, the H_2O-NaCl EOS implemented into TMGAS is limited to T up to 350°C (with minor errors up to 370°C), pressures up to 1000 bar and NaCl concentrations from 0 up to 1 (Battistelli, 2012). The correct reproduction of D&H correlations is documented in Figures 1 and 2 with respect to vapor-saturated brine density and enthalpy, respectively.

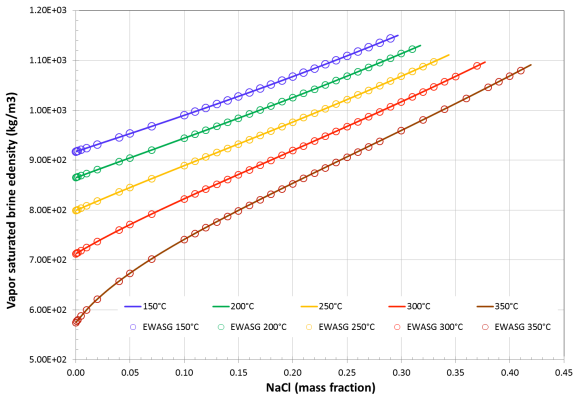

Figure 1. Vapor-saturated brine density: lines = SOWAT code (Driesner, 2007); circles = TMGAS.

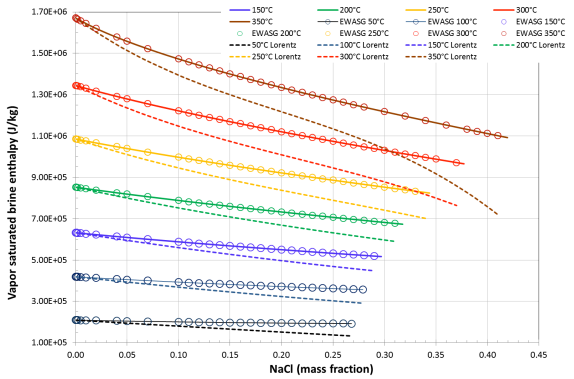

Figure 2. Vapor-saturated brine enthalpy: lines = SOWAT code (Driesner, 2007); circles = TMGAS Driesner's model; dotted lines = TMGAS Lorenz's model.

The calculation of thermodynamic equilibrium of non-aqueous (NA) phase and brine, and the NA phase properties in TMGAS, as well as the ability of TMGAS to reproduce published NCG solubilities in water and brines are described in Battistelli and Marcolini (2009). Examples of TMGAS capability to reproduce pure CO_2 properties from 50 to 350°C and P up to 1000 bar are shown in Figures 3, 4 and 5. Similar results are obtained for pure H_2S and CH_4.

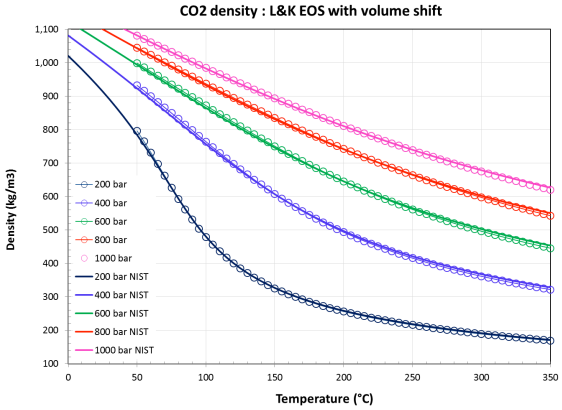

Figure 3. CO_2 density: lines= REFROP8 code (Lemmon et al., 2007) from NIST; circles= TMGAS with LK EOS (Lee and Kesler, 1975) and the volume shift (Peneloux et al., 1982).

A further check is presented (Figure 6) related to the CO_2-H_2O system at 250°C and up to 600 bar. TMGAS results are compared with published mutual solubilities and with values computed using ECO2H (Spycher and Pruess, 2010). Additional comparisons up to 300°C suggest the need to improve the CO_2-H_2O phase equilibria calculation at T higher than 250°C, which was the upper limit of TMGAS calibration.

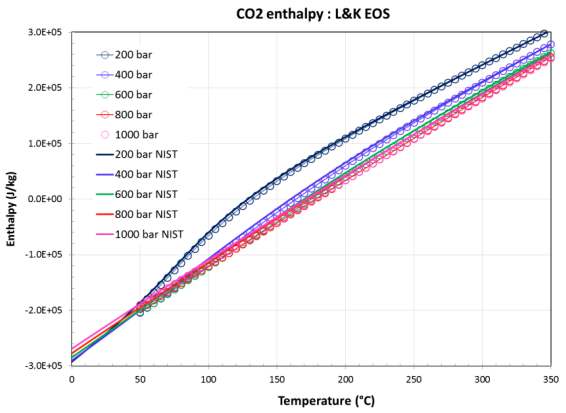

Figure 4. CO_2 enthalpy: lines = REFROP8 code from NIST; circles = TMGAS with LK EOS.

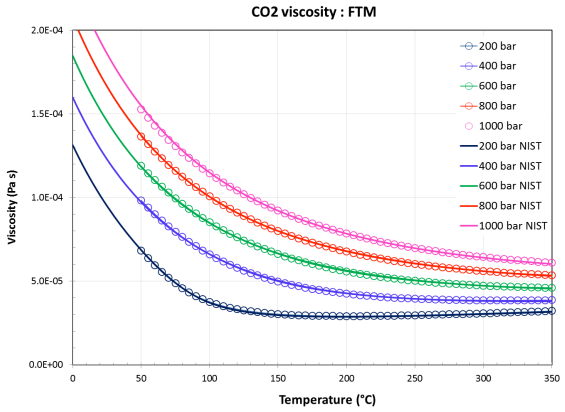

Figure 5. CO_2 dynamic viscosity: lines = REFROP8 code from NIST; circles = TMGAS with FTM (Quiṇones-Cisneros et al., 2001).

The reproduction of H_2S-H_2O phase equilibrium at T from 171 to 315°C and P up to 230 bar is shown in Figure 7 by comparison of TMGAS results with experimental data by Zezin et al. (2014). Despite the good reproduction of Zezin's experimental data, further tests suggested that the TMGAS parameters involved in the H_2S-H_2O phase equilibrium need to be better calibrated using experimental data at high pressure which were not available at the time TMGAS was coded. In fact, TMGAS was initially developed for applications related to geological sequestration of greenhouse gases (GHG) and underground disposal of sour and acid gas mixtures, therefore the phase equilibria algorithms were optimized for T lower than those reached in the present application. Thus, the improvement of equilibrium algorithms to better reproduce the experimental data and enhance the convergence speed is possible and will be the subject of further code development.

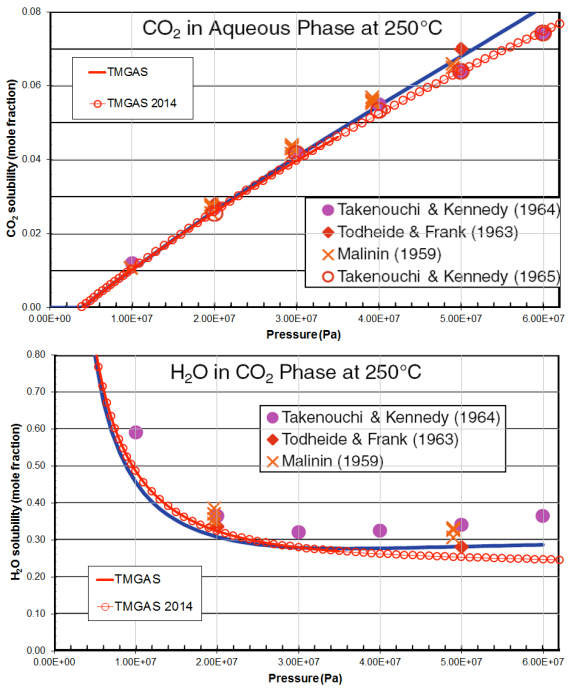

Figure 6. CO_2-H_2O system: (a) CO_2 solubility in aqueous (Aq) phase, and (b) H_2O solubility in NA phase (bottom) at 250°C. Comparison of TMGAS results (red) with experimental data and values computed by ECO2H (Spycher and Pruess, 2010, blue line).

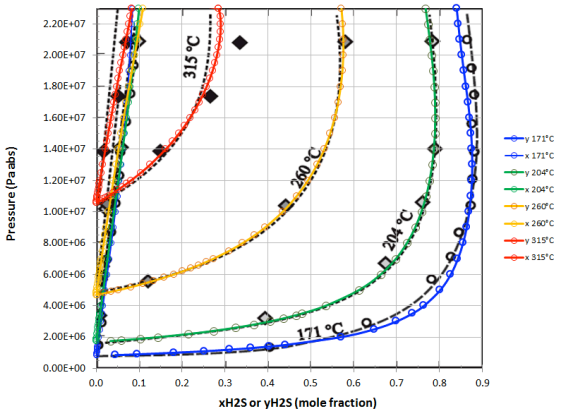

Figure 7. Phase composition of H_2S-H_2O system: TMGAS (color) vs experimental data by Zezin et al. (2014) (black).

3D NUMERICAL MODEL

The modeled domain, which occupies an area of about 25,000 km^2 and depths from 6800 to 2000 m, is part of a larger sedimentary formation. In order to reproduce the geometry of the formation and preserve the IFDM requirements, the discretization grid has been built with a full 3D

Voronoi approach by using specifically improved versions (Bonduà et al., 2015) of the pre- and post-processing tools developed for the TOUGH2 simulator (Berry et al., 2014; Bonduà et al., 2012). This approach avoids the approximations introduced when using 3D discretization grids with node connections not perfectly orthogonal to the elements interface area.

The 3D grid, composed by 11293 elements, is shown in Figure 8, while Figure 9 shows the location of NCG injection elements located at the bottom on the S boundary of the model. The domain is closed except at a single element hold at constant conditions and located at the top on the NW corner at a depth of 2579 m.

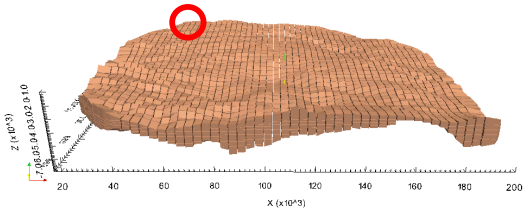

Figure 8. South view of 3D discretization grid. Red circle= spill point location.

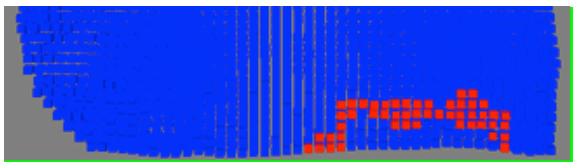

Figure 9. Portion of bottom grid layer, showing location of NCG injection elements near the S boundary.

The reference scenarios are related to the isothermal migration of one NCG at the time (CO_2, H_2S, and CH_4) injected at a global constant rate of 7 kg/s for 1 Myr in a fresh water aquifer. Additional scenarios are simulated with NCG migration taking place in the same formation but in the presence of a NaCl brine aquifer with NaCl content of 50 g/l (48517 ppm).

The initial P conditions, shown in Figure 10, are obtained by fixing the P at the depth of the spill point and running the system to steady state, with a linear T profile having a gradient of 3°C/100 m and 20°C at the ground surface. Constant rock properties have been used, with porosity of 0.15, and permeability of 5E-13 m^2. Relative permeabilities and capillary pressure curves are shown in Figures 11 and 12, respectively. The Brooks and Corey (1966) model has been used for the capillary pressure introducing a finite NA phase entry pressure.

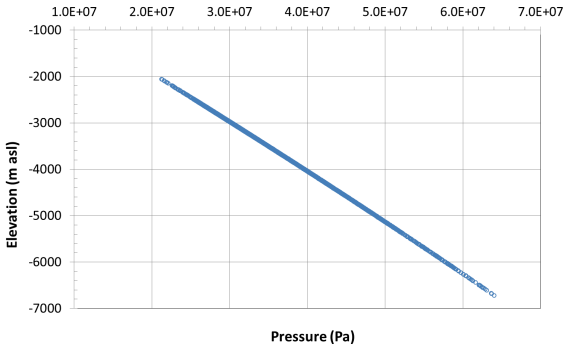

Figure 10. Steady-state pressure distribution in the fresh water aquifer.

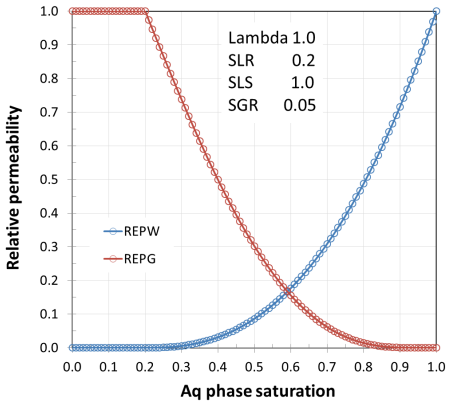

Figure 11. Relative permeability functions: Aq phase = VG; NA phase = Corey.

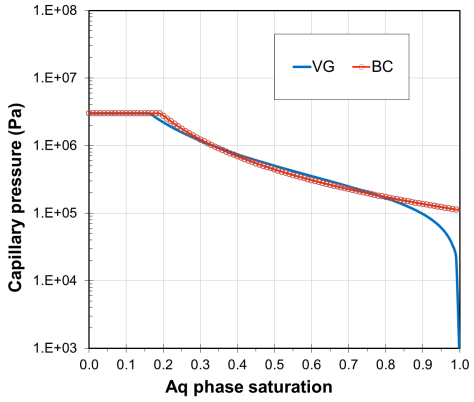

Figure 12. Capillary pressure function: BC model compared with the initial VG model.

NCG MIGRATION IN A FRESH WATER AQUIFER

Results obtained after 1 Myr CO_2 injection are presented in detail in Figures 13 to 16. The CO_2-rich NA phase, lighter than the Aq phase, migrates upwards and accumulates at the top of the formation. The Aq phase with dissolved CO_2 is denser than fresh water and migrates down to the deepest part of the formation.

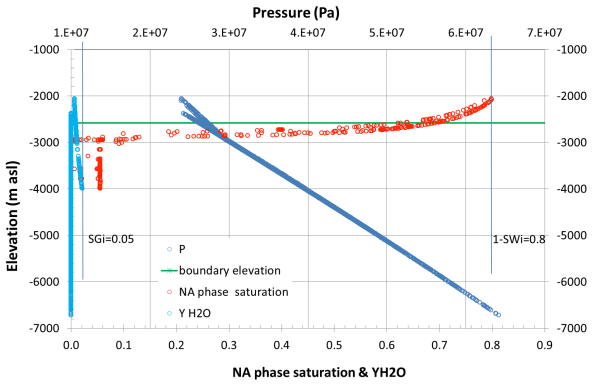

Figure 13. Vertical distribution of P, SNA and water content in NA phase after 1 Myr CO_2 injection.

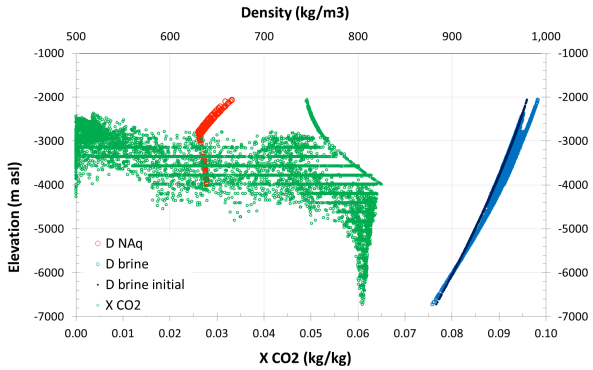

Figure 14. Vertical distribution of Aq and NA phase density and CO_2 content in Aq phase after 1 Myr CO_2 injection.

Due to its high density, the cumulative volume of NA phase is limited. The NA phase appears at the top of the formation only in the S sector of the model (Figure 15, top). On the other hand, dissolved CO_2 is transported by convective Aq phase flow towards the spill point on the NE and is more widely spread over the formation top (Figure 15, bottom). Figure 16 shows the cumulative mass of Aq phase and of total CO_2 vs time contained in the model grid. Most of the CO_2 remains confined within the model, while a fraction of Aq phase is discharged through the spill point as it is displaced by the NA phase.
The distribution of P and NA phase, the distribution of NA phase density and H_2S content in the Aq phase when injecting H_2S are shown in Figures 17 and 18, respectively.

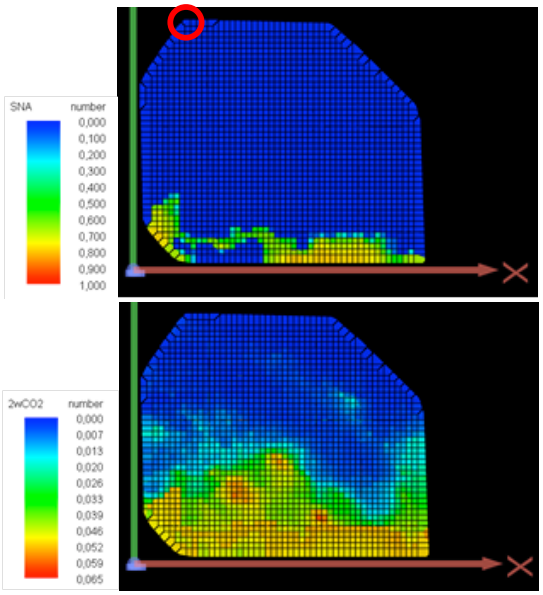

Figure 15. Spatial distribution of S_{NA} (top) and CO_2 content in Aq phase (bottom) in the top grid layer after 1 Myr CO_2 injection.

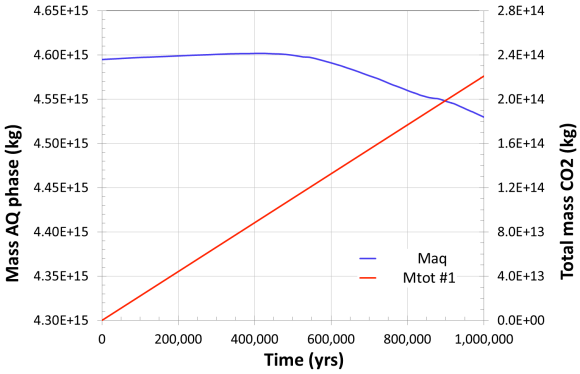

Figure 16. Mass of Aq phase and mass of total CO_2 within the model vs time during 1 Myr CO_2 injection.

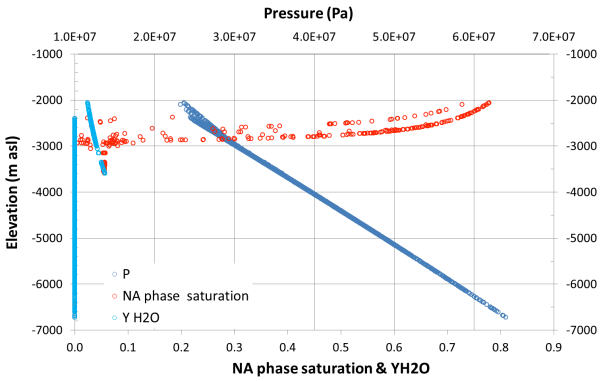

Figure 17. Vertical distribution of P, SNA and water content in NA phase after 1 Myr H_2S injection.

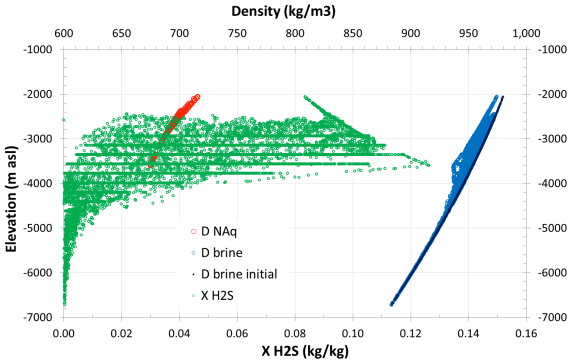

Figure 18. Vertical distribution of Aq and NA phase density and H_2S content in Aq phase after 1 Myr H_2S injection.

The H_2S-rich NA phase is denser than the CO_2-rich NA phase, while the dissolution of H_2S makes the Aq phase lighter than fresh water. H_2S is also more soluble than CO_2 in water. This results in a slightly smaller NA phase migration at the top layer than CO_2, but in a much wider spreading of dissolved H_2S (Figure 19), which migrates also because of upward Aq phase density-driven flow. As for CO_2, most of H_2S remains within the model grid after 1 Myr injection.

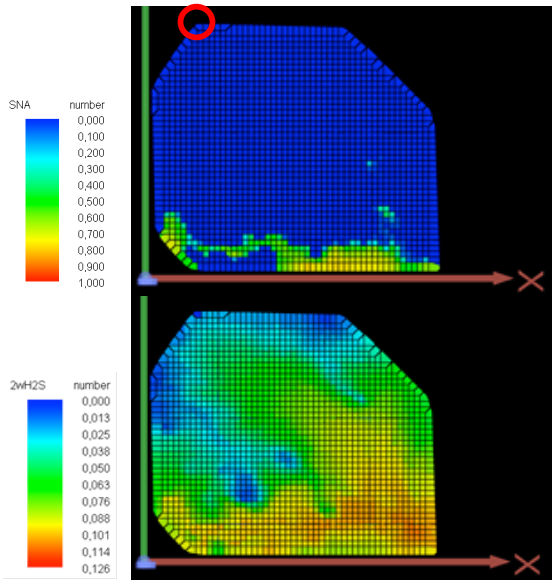

Figure 19. Spatial distribution of S_{NA} (top) and H_2S content in Aq phase (bottom) in the top grid layer after 1 Myr H_2S injection.

Injection of CH_4 produces quite different migration patterns as the NA phase has low density and CH_4 has low solubility in water.

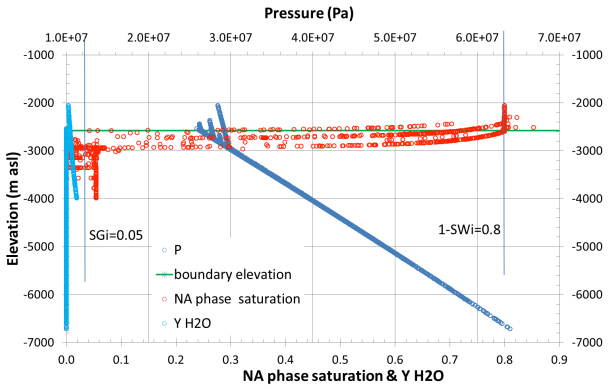

Figure 20. Vertical distribution of P, SNA and water content in NA phase after 1 Myr CH_4 injection.

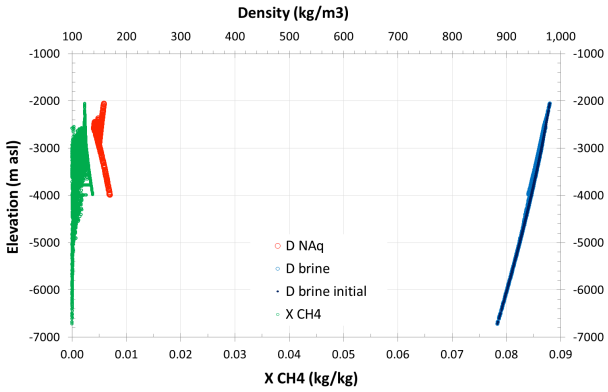

Figure 21. Vertical distribution of Aq and NA phase density and CH_4 content in Aq phase after 1 Myr CH_4 injection.

Thus, the volume of CH_4-rich NA phase is much higher than for the acid gases (Figures 20 and 21) and this results in a more widespread migration of NA phase which in this case reaches the spill point on the NW corner after about 150,000 yrs of injection (Figure 22). This is clearly shown in Figure 23 where the total mass of Aq phase and that of CH_4 plotted vs time almost stabilize, suggesting that conditions close to steady-state are reached.

NCG MIGRATION IN A SALINE BRINE AQUIFER

The initial P distribution in the saline aquifer differs slightly from that of the fresh one: P is equal at the spill point and is 15 bar higher at the grid deepest element. Figures 24 and 25 show the vertical distribution of main parameters after 1 Myr CO_2 injection. Figure 26 shows the spatial distribution of S_{NA} at the top grid layer.

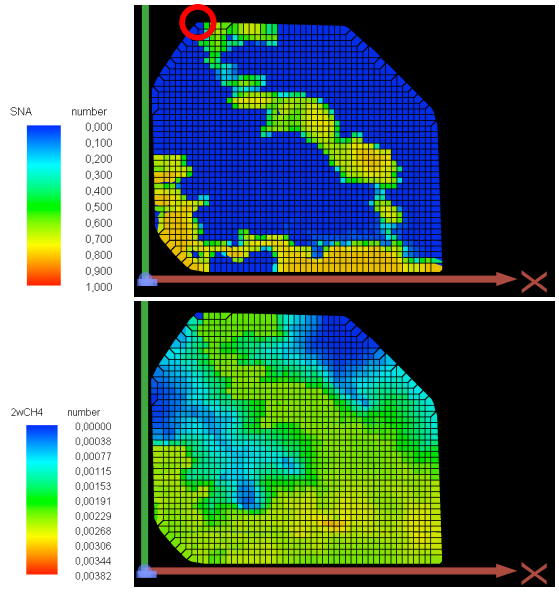

Figure 22. Spatial distribution of S_{NA} (top) and CH_4 content in Aq phase (bottom) in the top grid layer after 1 Myr CH_4 injection.

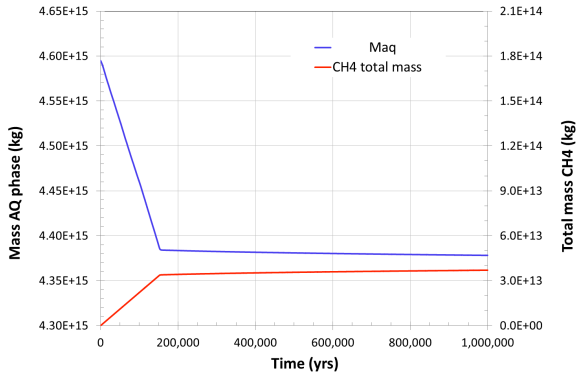

Figure 23. Mass of Aq phase and mass of total CH_4 within the model vs time during 1 Myr CH_4 injection.

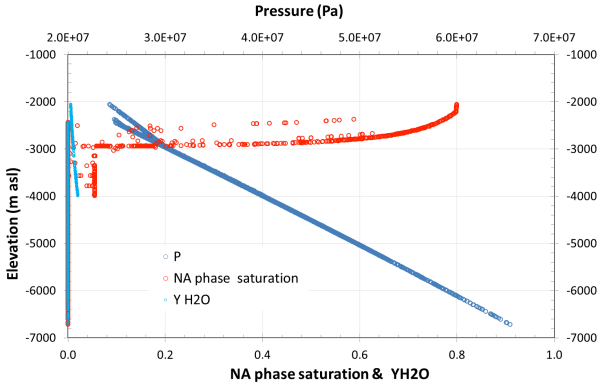

Figure 24. Vertical distribution of P, NA saturation and water content in NA phase after 1 Myr CO_2 injection in saline aquifer.

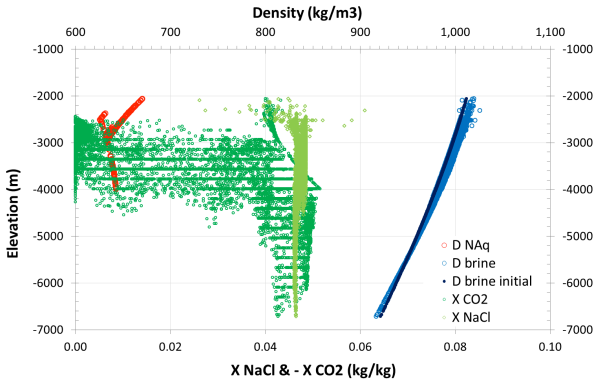

Figure 25. Vertical distribution of brine and NA phase density, and CO_2 and NaCl content in Aq phase after 1 Myr CO_2 injection in saline aquifer.

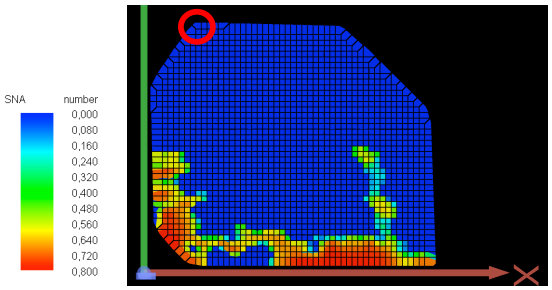

Figure 26. Spatial distribution of S_{NA} (top) in the top grid layer after 1 Myr CO_2 injection.

NaCl reduces the solubility of CO_2 in brine inducing a slightly enhanced migration of NA phase which advances a bit more towards the spill point. The NaCl content in Aq phase changes in response to evaporation/condensation processes, whose are more pronounced where the S_{NA} reaches the maximum value. Similar effects are obtained for the injection of H_2S and CH_4 in saline aquifer.

CONCLUSIONS

TOUGH2-TMGAS has been successfully applied to model the migration of CO_2, H_2S, and CH_4 in a deep sedimentary formation at high-P and high-T and at basin scale. The need for improvements of present algorithms for phase equilibria calculations at high T has been identified. Simulations of different NCG injection for 1 Myr allowed to verify how the NCG properties affect the migration of the NA phase through their impact on thermodynamic equilibrium, phase composition and phase transport properties. In particular, at the high P encountered, the NA has a high density (600-700 kg/m^3) in the case of CO_2 and H_2S compared to CH_4 (130-170 kg/m^3). Thus, the

CH_4-rich NA phase occupies a much larger volume, migrating upward and eventually reaching the spill point. When migration takes place in a saline aquifer, the changes in water solubility drive the concentration/dilution of NaCl in the brine with consequences on NCG solubility in the Aq phase and with additional density driven flows due to salinity gradients.

ACKNOWLEDGMENTS

The management of eni SpA is acknowledged for the permission to publish the present work, which was performed within the R&D project "Gas Systems" financed and coordinated by eni SpA.

REFERENCES

Battistelli, A., Calore C., and Pruess, K., The simulator TOUGH2/EWASG for modelling geothermal reservoirs with brines and a non-condensible gas. *Geothermics*, 26, 4, 437-464, 1997.

Battistelli, A., Marcolini, M., TMGAS: a new TOUGH2 EOS module for the numerical simulation of gas mixtures injection in geological structures. *Intl. J. Greenhouse Gas Control*, 3, 481-493, 2009.

Battistelli, A., Improving the treatment of saline brines in EWASG for the simulation of hydrothermal systems. TOUGH Symposium 2012, Sept. 17-19, 2012, Berkeley (USA).

Bonduà, S., Battistelli, A., Berry, P., Bortolotti, V., Consonni, A., Cormio, C., Geloni, C., Vasini, E.M., Voronoi 3D pre- and post- processing tools for the modeling of deep sedimentary formations with the TOUGH2 family of codes. TOUGH Symposium 2015, Sept. 28-30, 2015, Berkeley (USA).

Brooks, R.H., Corey, A.T., Properties of Porous Media Affecting Fluid Flow. *J. Irrig. Drain. Div.*, 6, 61, 1966.

Croucher, A.E., O'Sullivan, M.J., Application of the computer code TOUGH2 to the simulation of supercritical conditions in geothermal systems. *Geoth.*, 37, 622–634, 2008.

Driesner, T., Heinrich, C.H., The system H_2O–NaCl. Part I: Correlation formulae for phase relations in temperature–pressure–composition space from 0 to 1000°C, 0 to 5000 bar, and 0 to 1 XNaCl. *Geoch.Cosm.A.*, 71, 4880–4901, 2007.

Driesner, T., The system H_2O–NaCl. Part II: Correlations for molar volume, enthalpy, and isobaric heat capacity from 0 to 1000°C, 1 to 5000 bar, and 0 to 1 XNaCl. *Geoc. Cosm. Acta*, 71, 4902–4919, 2007.

International Association for the Properties of Water and Steam, *Release on the IAPWS Formulation 2008 for the Viscosity of Ordinary Water Substance*. Berlin, Germany, 2008.

International Association for the Properties of Water and Steam, *Release on the IAPWS Industrial Formulation 1997 for the Thermodynamic Properties of Water and Steam*. Erlangen, Germany, 1997.

Lee, B.I., Kesler, M.G., A generalized thermodynamic correlation based on three-parameter corresponding states, *AIChE Journal*, 21,3,510-527,1975.

Lemmon, E.W., Huber, M.L., McLinden, M.O., Reference fluid thermodynamic and transport properties, NIST Standard Reference Database 23, Version 8.0, 2007.

Lorenz, S., Maric, D., Rirschl, C., Eine analytische Funktion zur Bestimmung der Enthalpie wässriger NaCl-Lösungen. Report ISTec - A – 447, 2000.

Peneloux, A., Rauzy, E., Freze, R., A consistent correction for Redlich-Kwong-Soave volumes. *Fluid Phase Equilibria*. 8, 1, 55-73, 1982.

Peng, D.-Y., Robinson, D.B., A new two-constant equation of state. *Industrial &Engineering Chem. Fund.* 15, 59 – 64, 1976.

Pruess, K., Oldenburg, C., Moridis, G., *TOUGH2 User's Guide, Version 2.0*. Report LBNL-43134. Lawrence Berkeley National Laboratory, Berkeley, Calif., 1999.

Quiņones-Cisneros, S.E., Zéberg-Mikkelsen, C.K., Stenby E. H., The friction theory for viscosity modeling: extension to crude oil systems, *Chem. Eng. Sci.,* 56, 7007–7015, 2001.

Spycher, N., Pruess, K., A phase-partitioning model for CO_2–brine mixtures at elevated temperatures and pressures: Application to CO_2-enhanced geothermal systems. *Transport in Porous Media*, 82, 1, 173-196, 2010.

van Genuchten, M.Th., A closed-form equation for predicting the hydraulic conductivity of unsaturated soils. *Soil Sci. Soc. Am. J.*, 44, 892 – 898, 1980.

Zezin, D.Y., Migdisov, A.A., Williams-Jones, A.E., PVTx properties of H_2O–H_2S fluid mixtures at elevated temperature and pressure based on new experimental data. *Geoch. Cosm. Acta*, 75, 5483–5495, 2011.

PRESSURE MANAGEMENT DURING GEOLOGICAL CO_2 SEQUESTRATION: OPTIMAL WELL PLACEMENT AND BRINE EXTRACTION

Abdullah Cihan[a], Jens Birkholzer[b], and Marco Bianchi[c]

[a] Earth Sciences Division, Lawrence Berkeley National Laboratory, Email: acihan@lbl.gov
[b] Earth Sciences Division, Lawrence Berkeley National Laboratory, Email: jtbirkholzer@lbl.gov
[c] Environmental Modelling Department, British Geological Survey, Email: marcob@bgs.ac.uk

ABSTRACT

Pressure management involving the extraction of native fluids from storage formations can be used to minimize large-scale pressure increases resulting from carbon dioxide (CO_2) injection while maximizing CO_2 storage. However, dealing with a large volume of extracted brine can be technically challenging and expensive. This extended abstract summarizes applications of a recently developed global optimization method, a constrained differential evolution (CDE) algorithm, for optimal well placement and brine extraction under realistic field situations with reservoirs of complex geometry and heterogeneity. The material presented is based on a recent paper by the authors submitted to International Journal of Green House Gas Control. We present example application of the developed method for a hypothetical CO_2 injection scenario in a heterogeneous reservoir containing critically stressed faults. Multiple realizations of the reservoir permeability field were created to understand the impact of reservoir heterogeneity on optimization results. High variability in the calculated optimal extraction ratios among different permeability realizations indicates the importance of detailed site characterization and understanding of heterogeneity. Although the focus here is on optimization of brine, the CDE optimization methodology can be used to solve other complex optimization problems related to geological CO_2 sequestration.

INTRODUCTION

Large-scale pressure increases during geologic carbon sequestration (GCS) may impact caprock integrity, induce fault slippage, and cause leakage of brine and/or CO_2 into shallow fresh groundwater resources. Extraction of native brine during GCS operations is a pressure management approach for controlling pressure buildup to reduce risk of environmental impacts and increase storage capacity (Bergmo et al., 2011). However, pumping, transportation, treatment and disposal of extracted brine can be challenging and costly (Harto and Veil, 2011). Therefore, minimizing the volume of extracted brine, while maximizing CO_2 storage and meeting other constraints needed for safe and efficient GCS operations, is an essential objective of pressure management with brine extraction schemes.

The results from the earlier studies (e.g., Birkholzer et al., 2012) suggest that optimization can allow for a significant reduction in the brine extraction volumes needed to keep pressure increase in the storage formation below a given critical value. However, placing of injection and extraction wells is not intuitive in real cases because of heterogeneity in reservoir properties and complex reservoir geometry. Computerized algorithms combining reservoir models and optimization methods are needed to make proper decisions on well locations and control parameters.

This extended abstract, based on a recent paper by Cihan et al. (2015), summarizes an application of the global optimization methodology, a constrained differential evolution (CDE) algorithm, for solving constrained global optimization problems involving well placement and brine extraction to control pressure increases during GCS. The application of the CDE optimization methodology is presented for hypothetical CO_2 storage scenarios in the Vedder Formation in the Southern San Joaquin Basin in California, USA. Industrial-scale storage of CO_2 would generate significant pressure buildup in this formation, which in turn would raise concerns about induced seismicity due to the presence of multiple faults surrounding the injection zone. Optimal placements of wells and selection of injection and extraction rates are

evaluated under the constraints that the maximum pressure buildup does not exceed critical pressure changes for fault activation, and that no CO_2 is to be pulled into extraction wells.

PROBLEM DESCRIPTION

The optimization problem involving the objective function and the constraints for controlling pressure locally (e.g., for fault protection, preventing caprock damage) can be formally expressed as

$$\text{Minimize} \quad f(\boldsymbol{p}) = V_{ext}/V_{inj} \tag{1}$$

$$\text{Subject to} \quad g_1(\boldsymbol{p}) = V_{ext,CO_2} = 0 \tag{2a}$$

$$g_2(\boldsymbol{p}) = \Delta P_{crt} - \max\left\{\Delta P(\boldsymbol{x}_{obs}, \boldsymbol{y}_{obs}, t)\right\} \quad 0 \tag{2b}$$

where V_{inj} denotes the total volume of injected CO_2, and V_{ext} denotes the total volume of extracted fluid. The objective is to minimize the extraction ratio denoted by V_{ext}/V_{inj}. $\boldsymbol{p}$ is the parameter vector that may involve locations of injection wells (x_{inj}, y_{inj}) and extraction wells (x_{ext}, y_{ext}), and constant or time-dependent function parameters for controlling injection and extraction. Specific costs associated with the pumping per volume of injected or produced fluid and treatment of extracted brine are assumed to be proportional to the extraction ratio defined in Eq. (1). Other costs related to drilling of wells are not considered. The first constraint in Eq. (2) assures that no CO_2 breakthrough occurs at the extraction wells. The second constraint represents the pressure management goal of keeping reservoir pressure increases in defined impact zones below one (or more) critical pressure buildup values (ΔP_{crt}) (with respect to the pressure prior to the injection). We may assume that an environmental impact can be expected if the pressure buildup at any location in the impact zones exceeds ΔP_{crt}. Pressure buildup at impact zones is recorded through a vector of observation points (x_{obs}, y_{obs}) as many as required. The optimization problem may also involve additional constraints, such as parameter bounds, which are not included in Eq. (2).

GLOBAL OPTIMIZATION METHOD

For solving the constrained optimization problems, we implemented the CDE algorithm by modifying an existing FORTRAN90 code built into Itough2 (Finsterle, 2007) for the Differential Evolution (DE) algorithm developed by Dr. Feng-Sheng Wang and his students.

The DE algorithm is a parallel direct search method that was originally developed by Storn and Price (1995) and has been shown to be a powerful evolutionary algorithm (e.g., Storn and Price, 1996), but the original method is in general applicable to unconstrained optimization problems. In this work, we have modified the DE algorithm based on Deb (2000) to solve constrained global optimization problems relevant to GCS projects. The basic strategies of the DE algorithm and modifications to obtain a CDE algorithm for treatment of constraints are described in more detail in Cihan et al. (2015). Cihan et al. (2015) also presents testing of the CDE algorithm for a simple optimization problem whose solution can be partially obtained with a gradient-based optimization methodology, the sequential quadratic programming (SQP) algorithm.

APPLICATION TO A HYPOTHETICAL CO_2 STORAGE SCENARIO

We demonstrate the applicability of the CDE algorithm for a CO_2 injection scenario in the Vedder Formation in the Southern San Joaquin Basin in California, USA. Hydrogeological properties are identified based on site characterization data available from oil and gas exploration and groundwater development in the area (USGS, 2007). The Vedder formation has been used in the past to evaluate pressure impacts for a hypothetical storage scenario with injection of 5 Mt CO_2 per year over 50 years (e.g., Birkholzer et al., 2011). Concerns about induced seismicity would almost certainly require pressure management at this site, and pressure management via targeted brine extraction seems particularly suitable because the pressure control needs to be along the faults. On the other hand, well locations and pumping rates need to be carefully designed to minimize extraction volumes and to avoid pulling CO_2 into the extraction wells or even near the faults.

Numerical Reservoir Model

The Vedder formation involves six alternating sand/shale layers. The thickest sand layer (the first Vedder Sand) with a maximum thickness of 197m is located at the top portion underlying the Temblor-Freeman shale. We considered only the

first Vedder Sand to model the hypothetical CO_2 storage and to apply the CDE algorithm for pressure management. The three faults considered (Fig. 1) are assumed to be vertically impermeable and are represented as linear features with two orders of magnitude lower horizontal permeability than the Vedder Sand. Average porosity, permeability, two-phase flow parameters and initial conditions are based on earlier studies (Birkholzer et al. 2011). We considered only horizontal heterogeneity in this study based on the average horizontal permeability data available from existing wells in the vicinity of the site. A sequential Gaussian simulation was utilized to generate five conditional realizations of log(k) (permeability) fields.

The CDE method (or any other evolutionary and stochastic algorithm), requiring a large number of forward model runs to find the global minimum, demands selection of computationally efficient forward models. Therefore, a balance is needed to keep higher computational efficiency while representing the physics of the problem reasonably well by a forward model with sufficient fidelity. Giving more weight on computational efficiency in this application case, we selected to employ an in-house numerical vertically-averaged two-phase flow model instead of TOUGH2, for representing CO_2/brine flow in the first Vedder sand. Such models are based on vertical integration of the 3D two-phase flow equations under the assumption of vertical equilibrium (VE) or hydrostatic pressure distribution in each phase. Once the assumption of vertical equilibrium behavior is appropriate for a particular reservoir, the vertically-averaged models become very advantageous over the full 3D models, especially for large-scale reservoir modeling and optimization studies because they are computationally much more efficient with reduced dimensionality. Readers are referred to Cihan et al. (2015) for further details on the numerical reservoir model.

Optimization for Well Placement and Extraction Control

We initially conducted numerical simulations without optimization via brine extraction to evaluate pressure buildup and CO_2 plume distribution for each realization. The peak value of the maximum pressure buildup along the faults ranges from about 1.5MPa for Realization 3 to about 2.7MPa for Realization 1 (Fig. 2). In contrast, in this study we assumed a threshold value of 1MPa as the maximum pressure buildup that can be sustained without activating the faults. We first conducted basic optimization studies by using the SQP algorithm without brine extraction to calculate the maximum possible constant injection rate for the 1MPa pressure buildup constraint. The maximum allowed constant injection rates without brine extraction appear to be about 35% to 65% less compared to the goal of 5 Mt/yr injection rate (Table 1). Second, we conducted an optimization of brine extraction (well locations and rates) to be able to inject 5 Mt of CO_2 over 50 years with the objective of minimum brine extraction volume subject to the 1 MPa pressure buildup threshold along the faults and no pulling of CO_2 into the extraction wells. Including the locations and parameters of a time-dependent extraction rate function (Cihan et al., 2015), the total number of unknowns for two extraction wells is equal to 14. The CDE algorithm was employed to solve 14-dimensional optimization problems for minimizing the brine extraction ratio in each realization of the reservoir heterogeneity.

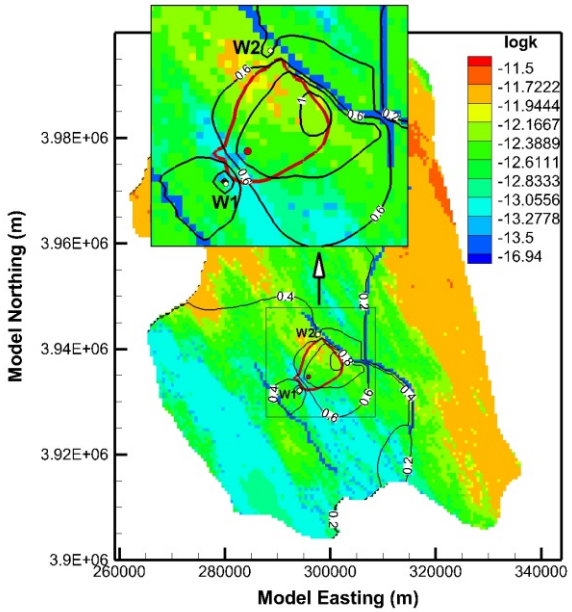

Figure 1. Optimization results for Realization 1: Pressure buildup (black contour lines with values in MPa) and CO_2 plume extent (red line) with optimal well placement and brine extraction (Cihan et al., 2015).

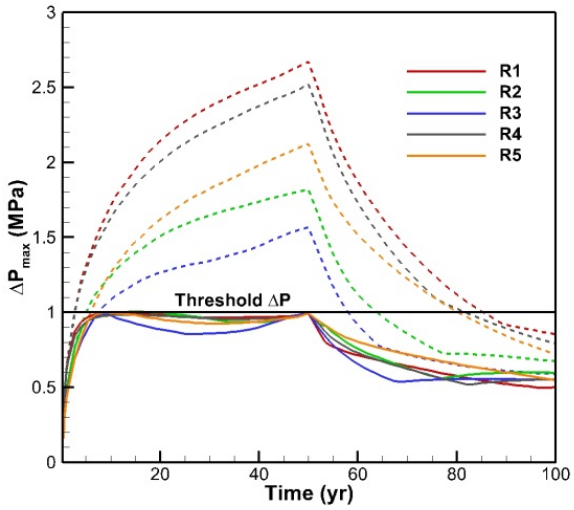

Figure 2. Evolution of maximum pressure buildup as a function of time along the three faults without brine extraction (dashed lines) and with optimal brine extraction (adapted from Cihan et al., 2015)

Fig. 1 demonstrates contour plots of pressure buildup and the maximum extent of the CO_2 plume at 50 years based on the optimization result of Realization 1. The figure also shows the estimated location of the two brine extraction wells. The CDE optimization methodology minimized the extraction ratio and successfully satisfied the constraints for all the realizations (see Fig. 2). Estimated minimum extraction ratios range from 38% to 67% (Table 1). The highest extraction ratio occurs for Realization 1 with the extraction period extending about 5 years beyond the end of injection.

Table 1. Summary of optimization results.

R#	Optimal Injection Rates (Mt/yr) w/o Brine Extraction	Optimal Extraction Ratios for 5Mt/yr - Injection
1	1.968	0.672
2	2.739	0.393
3	3.229	0.380
4	2.061	0.654
5	2.451	0.538

CONCLUSIONS

The results show that heterogeneity, reservoir slope and geometry may have significant effect on the selection of well locations as these change the CO_2 plume migration path and shape. High variability in the extraction ratios among the different realizations (Table 1) indicates the importance of the heterogeneity and its characterization in a real CO_2 storage project. Optimization studies for designing a real injection operation may typically require evaluating optimal conditions for multiple realizations of hydraulic properties, especially if there are very limited data and significant uncertainty about field site hydrogeology. In reality, selection of extraction well locations and rates through optimization would wait until more accurate information about local conditions and heterogeneity are obtained by field tests prior to actual injection and/or by pressure monitoring data obtained during initial or later stages of a storage project. Forward models and optimization calculations should be updated based on continuously collected monitoring data during the project to prevent any environmental impact with optimal control. Although our focus was on brine extraction in this work, the CDE optimization methodology presented in this paper is general enough to handle other optimization objectives related to GCS, such as reducing 'Area of Review', reducing risk of leakage, increasing storage capacity and trapping, and monitoring design. Our future works include optimizations for improved storage and real-time applications of the optimization methodology.

ACKNOWLEDGMENT

The work was funded by the Assistant Secretary for Fossil Energy, Office of Sequestration, Hydrogen, and Clean Coal Fuels of the U.S. Department of Energy under Contract No. DE-AC02-05CH11231.

REFERENCES

Bergmo, P.E., A. Grimstad, and E. Lindeberg, Simultaneous CO_2 injection and water production to optimize aquifer storage capacity, *Int. Journal of Greenhouse Gas Control*, 5, 555-564, 2011.

Birkholzer, J.T, Q. Zhou, A. Cortis and F. Finsterle, A sensitivity study on regional pressure build-up from large-scale CO_2 storage projects, *Energy Procedia*, 4, 4371-4378, 2011.

Birkholzer, J., A. Cihan, and Q. Zhou, Impact-driven pressure management via targeted brine - extraction – Concept studies of CO_2 storage in saline formations with leakage pathways, *Int. Journal of Greenhouse Gas Control*, 7, 168, 2012.

Cihan, A., J.T. Birkholzer, M. Bianchi, Optimal well placement and brine extraction for pressure management during CO_2 sequestration, submitted to *Int. Journal of Greenhouse Gas Control*, 2015.

Deb K., An efficient constraint handling method for genetic algorithms, *Comput. Methods Appl. Mech. Engrg*., 186, 311-338, 2000.

Finsterle, S., iTOUGH2 User's Guide, Report LBNL-40040, Lawrence Berkeley National Laboratory Report, Berkeley, CA, 2007.

Harto, C.B., J.A. Veil, Management of extracted water from carbon sequestration projects, Report ANL/EVS/R-11/1, Argonne National Laboratory, Lemont, IL, 2011.

Price, K., R. Storn, and J. Lampinen, Differential Evolution: A practical approach to global optimization. Berlin, Germany, Springer, 2005.

Storn, R. and K. Price, Minimizing the real functions of the ICEC'96 contest by Differential Evolution, Proceedings of IEEE International Conference on Evolutionary Computation, 842-844, Nagoya, Japan, May 20-22, 1996.

Storn, R. and K. V. Price, Differential evolution: A simple and efficient adaptive scheme for global optimization over continuous spaces, Int. Comput. Sci. Instit., Berkeley, CA, Tech. Rep. TR-95-012, 1995.

USGS, Petroleum systems and geologic assessment of oil and gas in the San Joaquin Basin Province, California. U.S. Geological Survey, Professional Paper 1713, Edited by Allegra Hosford Scheirer, 2007.

IMPACTS OF FORMATION HETEROGENEITY, INJECTION PROCEDURE AND HYSTERESIS EFFECT ON THE RESERVOIR PERFORMANCE IN CO_2 GEOLOGICAL STORAGE IN THE ORDOS BASIN IN CHINA

Cai Li[1,2,4], Chaobin Guo[3], Keni Zhang[2], Federico Maggi[1]

[1] The School of Civil Engineering, the University of Sydney,
Sydney, NSW, 2006, Australia.
e-mail: cali8165@uni.sydney.edu.au
[2] College of Water Sciences, Beijing Normal University,
Beijing, 1000875, China
[3] The School of Mechanical Engineering, Tongji University,
Shanghai, 201804, China
[4] China Institute of Geo-environmental Monitoring
Beijing, 100081, China

ABSTRACT

The reservoir for the Shenhua 100,000 tons/year Carbon Capture and Storage (SHCCS) Demonstration Project, which applied hydraulic fracturing and multi-layer injection to improve the injectivity, showed unique responses to injection over time. The in-situ monitoring data showed that the injectivity of one un-fractured storage layer arose quickly to be dominant, whereas the other layers showed very variable injectivity. Meanwhile, no steep pressure build-up has been observed yet. We firstly investigated the reservoir performance through numerical simulation with a comparison against the 2.5-year recorded data and found that formation heterogeneity and intermittent injection were helpful to explain the changes in injectivity and low pressure build-up. Furthermore, if hysteresis effects were included in the simulation, the resultant cumulative mass would be much higher than for the simulation without hysteresis effects. The finding suggests that more mobile CO_2 in the hysteresis case can facilitate pressure spreading from the well, enable more CO_2 to dissolve in the water, and in turn increase the injectivity. Therefore, during the evaluation of reservoir performance of CO_2 geologic storage on a site-scale, formation heterogeneity and injection procedure, and the possible hysteresis effects accompanying an intermittent injection, should be given deep consideration.

INTRODUCTION

As the first pilot project for carbon geological storage in saline aquifers in China, as well as the first coal-based CCS (carbon capture and storage) demonstration project with an entire chain from capture to storage, Shenhua Carbon Capture and Storage Demonstration Project (SHCCS) is unique with respect to reservoir performance of CO_2 geologic storage in low permeability aquifers. This project was planned to capture 100,000 metric tons/year CO_2 and store it in deep saline aquifers at depths of -1500 to -3000 m under the storage site (Wu, 2014). Hydraulic fracturing and a multi-layer injection scheme were applied to improve the injectivity and reduce the risk of over-pressurization. An injection test has been carried out annually since 2011 when the project started the injection.

In-situ monitoring data showed a very different picture of injectivity changes over time from what was estimated in the pre-assessment. The injectivity of one un-fractured storage layer increased quickly with the injection, showing the potential to accommodate the target rate by itself. Meanwhile, the threshold pressure decreased significantly from 6.19 MPa in May 2011 to 4.81 MPa in September 2013, and no steep pressure build-up was observed around the injection well. Although many recent publications about this project, e.g. Zhang, et al. (2012), Ling, et al. (2013), Liu, et al. (2014), Kuang, et al. (2014), Lei, et al. (2014), Wei, et al. (2014), Jiang, et al. (2014), Liu, et al. (2015), and Xie, et al. (2015), made a great contribution to under-

standing the storage process in the reservoir, this unique pattern of reservoir responses has not been studied in depth yet.

In this paper, we investigated the reservoir performance through numerical simulation with a comparison against 2.5-year histories relating to the cumulative injected CO_2 mass, mass ratios in storage layers, pressures at different depths, and CO_2 plume extent measured by VSP (Vertical Seismic Profile) surveys. Further, we studied the impacts of hysteresis effects on the reservoir performance. We contend that the results could improve the reservoir assessment and injection design for geologic CO_2 storage in a saline reservoir with low to medium permeability and porosity.

SITE CHARACTERATION

The storage site is located on a massive monocline in the sedimentary Ordos Basin, dipping from northeast to southwest with a very gentle slope. 21 sandy layers bearing saline water in seven formations below 1500 m underground were chosen to receive and store CO_2. The pre-injection evaluation showed that none of the promising layers alone would have an injectivity high enough to meet the target rate, and the pressure build-up was highly likely to exceed the safety limit in a short time period (Wang et al., 2010). Thus, the injection occurred in multiple layers simultaneously and hydraulic fracturing was applied in 6 of the layers to increase the injectivity.

MODELLING APPROACH

Simulation Tool

This research only dealt with the multiphase fluid process and the equilibrium of water and CO_2 between phases, and precipitation and dissolution of solid salt in the water. Displacement of the surface and chemical reactions between the fluids and the rock were not considered. As no significant temperature changes were observed at the monitoring well (70 m away from the injection well), the original thermal conditions of the reservoir were assumed unchanged.

Numerical simulations were all run on the parallel version of TOUGH2-ECO2N (Zhang et al., 2008), and a scenario accounting for hysteresis effects was simulated with a hysteresis module developed by Doughty (2013). Governing equations for simulation can be found in the manual of TOUGH2 (Pruess, 2005) and are not repeated here.

Model Setup

The model was 1020 m (long)×1020 m (wide) × 1100 m (thick), centered at the injection well, and discretized almost evenly into 43 layers, in which 16 were storage layers and the rest were confining layers. Hydraulic fractures were involved in 4 of the storage layers and stretched from the injection well along the principle geostress orientation with a half-wing length of 45 m (Fig 1). Horizontal discretization was irregular (Fig 1). The closer to the injection well, the finer the grid was. West of the injection well was a monitoring well, which had 4 monitoring points at different depths (-2424.26 m, -2198.43 m, -1907.45 m, and -1690.45 m).

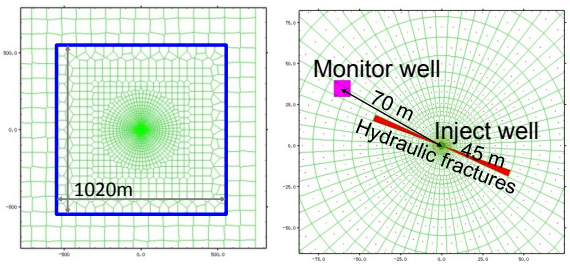

(a) (b)

Figure 1. (a) Simulation domain; (b) mesh configuration around the injection well.

Main Parameters

The model is heterogeneous but isotropic. Permeability and porosity were element-by-element assigned based on the geologic model. The heterogeneous permeability distribution was enabled by assigning a permeability modifier number (PMOD) to the elements in the MESH file. The PMODs were initially determined by dividing the permeability from the geological model by $10^{-15}m^2$, but PMODs for the injection well and the fractures were all set as 1.0. Each element's absolute permeability was the product of its PMOD and the basic absolute permeability assigned to its rock type. Porosity was set directly for each element. Relative permeability and capillary pressure were calculated by van Genuchten functions (Van Genuchten, 1980). In the scenario with hysteresis effects, the effects

were assumed to only happen in the main four storage layers. The main parameters are shown in Table 1.

Table 1. Main parameters in the model

Parameter Name	Value
Storage Layer basic Permeability (m^2)	1×10^{-15}
Seal Layer Basic Permeability (m^2)	1×10^{-20}
Injection Well Permeability (m^2)	3.16×10^{-6}
Fracture Permeability (m^2)	3.0×10^{-13}
Porosity for Injection Well	0.99
Porosity for Fractures	0.30
Liquid saturated saturation(S_{ls})	1.0
Residual liquid saturation (S_{lr})	0.05
Gas saturated saturation (S_{gs})	0.99
Residual gas saturation (S_{gr})	0.05
λ (exponent in van Genuchten functions)	0.457
Pore compressibility (Pa^{-1})	$1.1\text{-}3.5\times10^{-10}$
S_{grmax} (maximum residual gas saturation when accounting hysteresis effects)	0.05
γ (exponent in k_{rg} when accounting hysteresis effects)	0.33
Fitting parameter for k_{rg} extension for $S_l<S_{lr}$)	0
Numerical factor used for k_{rl} extension to $S_l>S_l$*	0.92
S_{lmin} (liquid saturation at which original van Genuchten P_c goes to infinity)	0.03
P_{cmax} (maximum capillary pressure from the original van Genuchten capillary pressure, Pa)	1.0×10^{7}
P_0^d (capillary strength parameter for drainage branch, Pa)	4.90×10^{3}
P_0^w (capillary strength parameter for wetting branch, Pa)	4.90×10^{3}
threshold value of S_{rg}^{Δ} (S_{rg}^{Δ} is wetting-drainage residual gas saturation)	0.03

Boundary Conditions

The volume of the elements on the lateral boundaries was enlarged by 120 times to prevent boundary effects (Li, et al., 2013). The top and the bottom of the model were set as no-flow boundaries. The injection well was set with CO_2 saturation of 1.0 and zero salinity. The pressure and temperature distributions along the injection well over time were used as boundary conditions for the CO_2 input.

Initial Conditions

The reservoir's initial thermal and pressure conditions were calculated, respectively, from the temperature gradient and pressure gradient defined by the monitored data from the points in the monitoring well before injection. The reservoir's elements were zeroed in CO_2 and saturated with saline water with a salinity of 2% (mass fraction). The injection well's elements were saturated with CO_2 (gas saturation > 0.999) and zero salinity.

Model Calibration

Permeability is believed the most sensitive parameter, so model calibration was done through changing the PMODs in the storage layers. As a time-varying pressure boundary was used as the CO_2 input term, simulated cumulative mass must be calibrated with the monitoring (reconstructed) data of cumulative mass.

It was assumed that all the storage layers changed their injectivity at the same time and that happened at the start of a certain injection period between two injection tests. Those elements for which CO_2 had not arrived (S_g<0.01) until the start of the assumed injection period for injectivity change, had PMODs changed. For each time of injectivity change, PMODs of those going-to-change elements in the same layer were modified by the same number. The modifying number of the layer was the ratio of monitored injected mass to the simulated value in the layer during an injection test.

The whole calibration process experienced four steps, which is schematically illustrated in Figure 2. The first step was to match the injected mass monitored in the first injection test. The calibration started with the model directly translated from the geologic model. The initial run of the model generated the simulated cumulative mass at certain durations, which included the injection tests from 2011-2013. By comparing the monitored and the simulated cumulative mass in each storage layer during the 2011 injection test, a set of ratios (the monitored mass / the simulated mass), R1, was obtained. Then PMODs of the elements in a storage layer were multiplied by the layer's ratio in R1. The model with new PMODs was run again, yielding a new set of ratios. The process would be repeated in a

layer until its resultant ratio was between 0.95 ~ 1.05.

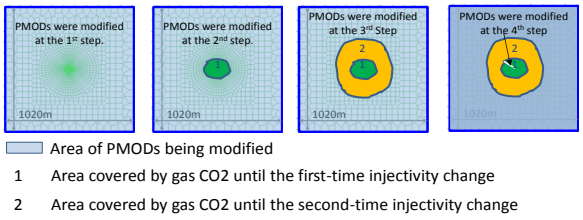

Figure 2. Schematic graph of calibration process.

Then came the second step, in which PMODs of the storage layer were partially further modified to calibrate against the 2012 injection test data. Since the last round simulation for the first step also resulted in the simulated mass during the 2012 injection test, a set of ratios (R2) for the second injection test was obtained too. For those layers that became inactive (mass ratio was zero) in the second injection test, their ratio was reset to 0.001 to prevent permeability from becoming zero in later simulations. The assumption time for injectivity change was made on one of the injection periods between the 2011 and 2012 tests. The elements needing PMODs modification in a layer were multiplied by the layer's ratio in R2. Then the model with further-modified PMODs was run again to see how the simulated cumulative mass over time fit the monitored line. We tried each of the injection periods between the two tests to get the simulated cumulative mass line closest to the monitored line. The third step was to calibrate with the injectivity shown by the 2013 injection test, which was similar to the process done in the second step. Because the injection pressure data in 2014 was not available when the research was being conducted, the model was not calibrated further against the injectivity shown by the 2014 injection test.

The last step was to calibrate against the pressures measured at the four points in the monitoring well. Pressure response in the monitoring well in the injection tests showed that hydraulic connection between the two wells was good. Therefore, the elements connecting the two wells in the 4 pressure-monitored layers were given an identical layer-dependent PMOD.

Scenarios

There were 4 scenarios in the research. Scenario 1 was the calibrated case without considering hysteresis effects, showing how well the simulated results would match the monitored data and serving as a basic case for other scenarios to compare with. Scenario 2 was to investigate the effects of permeability heterogeneity on the reservoir performance, in which a homogeneous permeability model was simulated. Scenario 3 was to look at how injection procedure would affect the reservoir performance, in which a continuous injection procedure was assumed. Scenario 4 was to see how hysteresis effects would affect the performance in the same intermittent injection procedure, but only the four layers active (CO_2 mass ratio is not zero) through all the injection tests were assumed to be affected by hysteresis effects.

RESULTS AND DISCUSSION

History Match

Simulated results vs. monitored data

The history match related to the data in four aspects. Overall, the simulated results had good agreements with the monitored histories, which implied a successful calibration.

The simulated cumulative mass by the calibrated model (Scenario 1) had a fare agreement with the reconstructed history (Figure 3). The simulated masses matched better in the beginning and ending sections than in the middle section, in which the simulated values were overestimated 10% to 30%.

The layers (-1690 ~ -1699 m, -1751 ~ -1756 m, -1909 ~ -1922 m, and -2406 ~ -2407 m) active through all the injection tests were selected to make the mass ratio comparison between the monitored and the simulated. Mass ratio change in a layer indicated the relative injectivity change in the layer. Figure 4 shows the simulated mass ratios in these layers had a good match with the data measured in the injection tests from 2011 to 2013, except the big difference in the first injection layer in the injection test. Simulated results in the layer -1690 ~ -1699 m clearly displayed the significant growth in absorbing performance of this layer, which also shown by the monitored data. The two layers,

from -1751 ~ -1756 m and from -1909 ~ -1922 m, showed a clear decrease in injectivity from 2011's injection test to 2012. It should be noticed that the hydraulic fractures were created in 4 layers including the layer from -1909 ~ -1922 m, but mass ratios in these layers reduced considerably or became zero in later injection tests. Even in the first injection test, the fractured layers did not even take up the majority of the injected mass. It indicated that injectivity improvement by the fractures was limited. The overall injectivity in this project still depends on the reservoir's natural conditions. The artificial fractures can improve the injectivity but in a limited degree and for a short time.

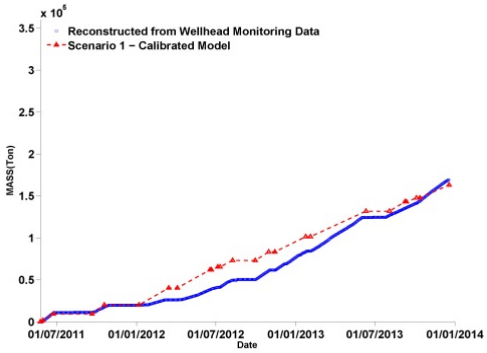

Figure 3. Comparison of cumulative injected CO_2 mass between the reconstructed history and results from the calibrated model.

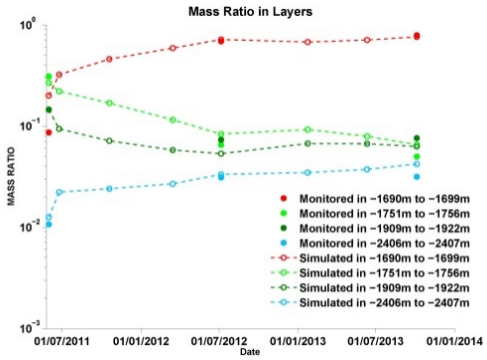

Figure 4. Comparison of mass ratios in the layers active through all the injection tests between the measured data and results from the calibrated model.

Figure 5 shows the pressure response at four depths in the monitoring well. The simulated pressure series in Scenario 1 agreed with the measured histories at these points in varying degree. Simulated pressures at these points were all underestimated at the early time, but they gradually matched the monitored data later during the injection periods; the shallower the monitoring point the earlier the agreement came. However, during the pause periods, most of the simulated pressures were noticeably lower than the monitored data, indicating a quicker drop-down in the model when injection paused. This indicates that the model may not fully capture the dynamic process when the reservoir's status changed suddenly.

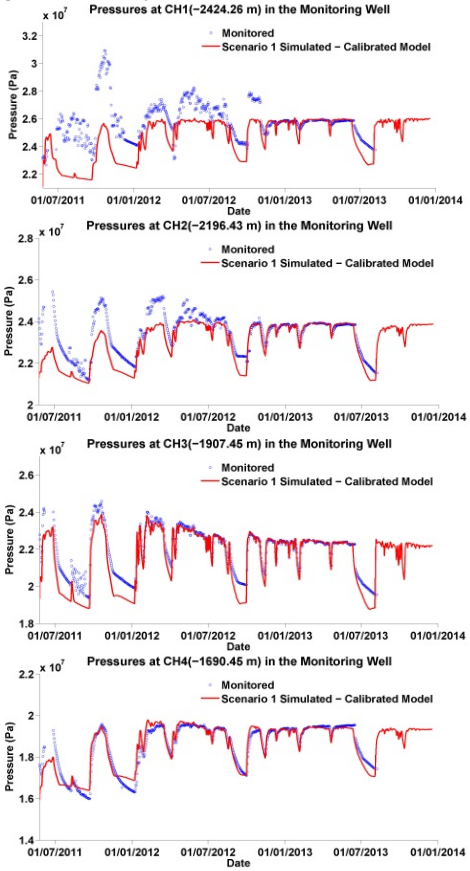

Figure 5. Comparison of pressures at the four monitoring depths in the monitoring well between the measured values and results from the calibrated model.

Figure 6 shows the area of gas CO_2 plume in the first layer in late 2013 simulated by Scenario 1 and detected by VSP surveys. The VSP-detected plume shows that CO_2 the in gas phase moved from the injection well almost radially, but a bit more favorably to west. The travel distance ranged from 250 m to 300 m shown by VSP, while the simulated plume had shorter distances ranging from 200 m to 250 m but with a similar pattern in shape. This means that the calibrated model captured the features of CO_2 expanding pattern in the layer but with some underestimate about the scale.

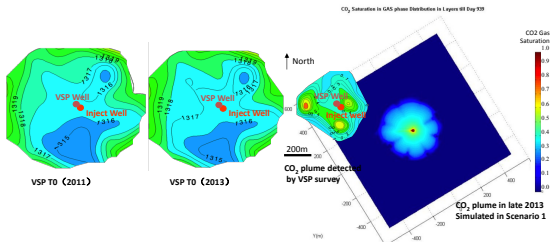

Figure 6. Comparison of gas CO_2 plume in the layer (-1690 ~ -1699 m) in late 2013 between the detected and the simulated.

Permeability distribution comparison

Figure 7 compares the permeability distribution in the dominant layer (-1690 ~ -1699 m) before (GeoModel) and after the calibration. The pattern of the permeability distribution in the layer was not significantly changed by calibration, but the permeability magnitude was one order bigger. Permeability population analysis found that, after calibration, although elements with permeability less than 4 mD still took up over 20% in the layer, elements with permeability from 12 to 32 mD were over 56%, which mainly controlled the performance in the layer (Figure 8) in the simulation. The trend of permeability getting higher as moving away from the injection well in the northwest direction (Figure 7) may offer an explanation to why the injectivity of the layer grew over the injection tests.

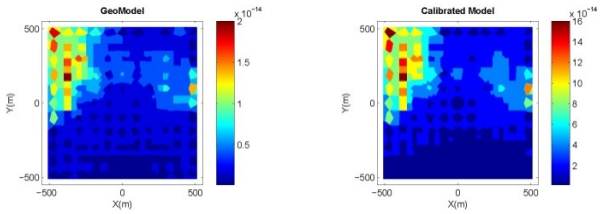

Figure 7. Permeability distribution comparison in the dominant layer between before and after the calibration.

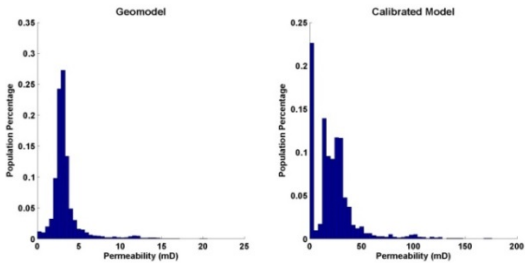

Figure 8. Percentage of permeability population in a range in the dominant layer (-1690 ~ -1699 m) before and after the calibration.

Effects of Permeability Heterogeneity

To investigate the effects of heterogeneity in permeability on the injection layer's performance, a layer-wise homogeneous model was built in Scenario 2 and simulated under the same other conditions as Scenario 1. Each layer's permeability and porosity were the average values of that layer in the geo-model. Figure 9 shows differences of the mass ratios in the selected layers between Scenario 1 and Scenario 2. Mass ratios in the four selected layers in Scenario 2 remained at almost the same level throughout the injection, meaning that the performance in absorbing CO_2 in these layers did not change significantly over time. Based on the results in the calibration, the highly heterogeneous nature of the permeability distribution in the injection layers most likely contributed to the performance variation over time in these layers.

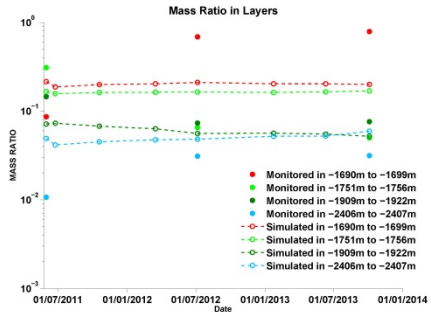

Figure 9. Mass ratios in the selected layers simulated in Scenario 2.

Effects of Injection Procedure

An intermittent injection procedure (an injection period alternating with a pause period) was used in the project. Unlike what was predicted in the pre-assessment, no steep pressure build-up was observed in the reservoir. We speculated that the intermittent injection procedure helped in controlling the pressure build-up and remaining a desired overall injection rate. Therefore, Scenario 3 was the calibrated model simulated under a hypothesized continuous injection (Figure 10 (a)). Fig. 10 (b) indicates the average injection rate during each of the actual injection periods and the overall effective injection rate (total accumulated mass over total injection days) in Scenarios 1 and 3. The injection rate in Scenario 3 decreased over time, while the counterpart in Scenario 1 remained dynamic. The overall effective injection rate in Scenario 1

was 3.20 kg/s, a bit above the target rate (3.17 kg/s), and also higher than in Scenario 3 (3.01 kg/s). Fig. 10 (c) and (d) showed the comparisons of the highest pressure build-up around the injection well and at the lateral boundary in the most absorptive injection layer, respectively. Around the injection well, the difference of the maximum pressure build-up in each actual injection period between the two scenarios is not significant; while during an actual pause period, the pressure build-up in Scenario 1 was much lower than Scenario 3 (Fig. 10 (c)).

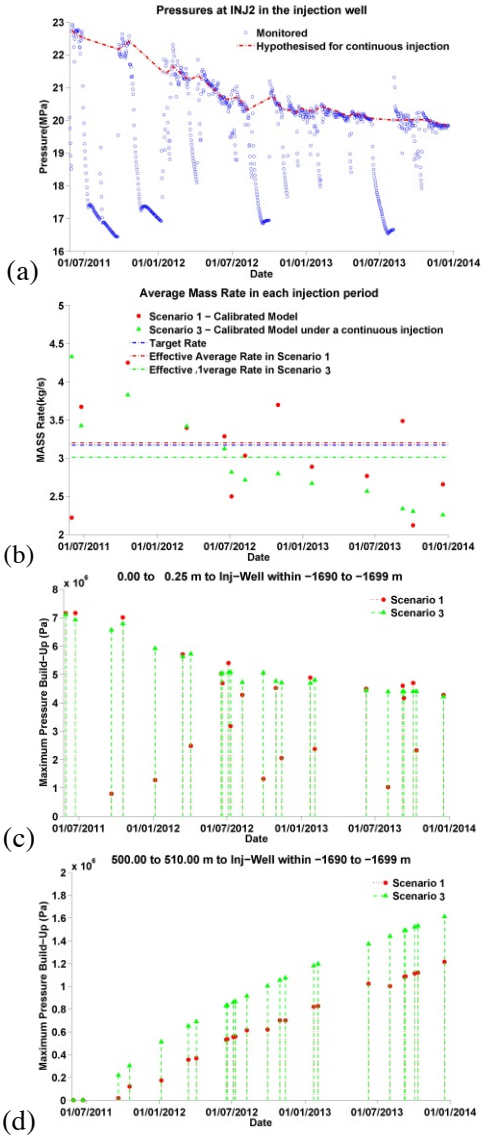

Figure 10. Continuous injection pressure used in Scenario 3 (a) and results from it (b, c, and d).

On the model lateral boundary, a steady increase in the highest pressure build-up was observed in both scenarios, but Scenario 3 had 25% - 300% more than Scenario 1 (Fig. 10 (d)). According to Darcy's law, fluid from the injection well is driven into the reservoir by the pressure difference between the injection well and the reservoir. Theoretically, given that other conditions were the same, the fluid-driving pressure would decrease as the pressure build-up on the lateral boundary increases. So it brings about reducing fluid flux into the reservoir in turn.

Impacts of Hysteresis Effects

Simulated cumulative mass in Scenario 4 was about 56% higher than Scenario 1 (Figure 11). This mass increase mainly comes from the aqueous CO_2 mass growth. Figure 12 indicates that pressure spread out more easily in Scenario 4 than Scenario 1. Within 20-30 m around the injection well, the hysteresis scenario always had lower pressure build-up, while beyond these distances it had higher pressure build-up. Lower pressure build-up around the well means that pressure spreads quickly. This is because hysteresis effects make gaseous CO_2 more mobile (S_{gr} = 0 for drainage and $S_{gr} \leq 0.05$ during imbibition, whereas in the non-hysteretic case $S_{gr} = 0.05$ at all times), and in turn decrease the gas CO_2 pressure in the reservoir, enabling gaseous CO2 to spread more, and increase the opportunity for CO_2 to dissolve in the water. Thus, the injectivity increased and more CO_2 entered into the reservoir in the same time duration.

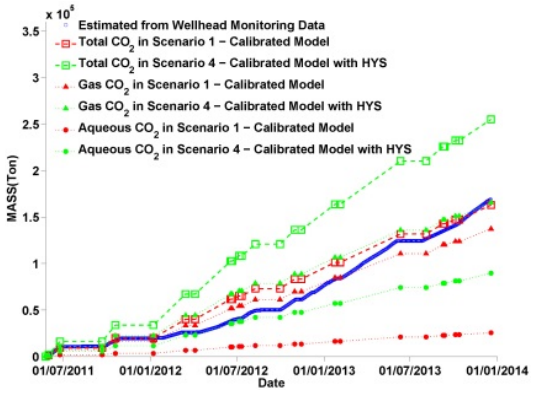

Figure 11. Cumulative mass comparison between Scenarios 1 and 4.

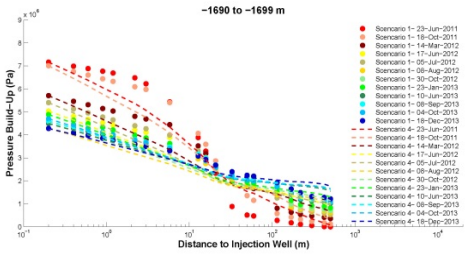

Figure 12. Comparison of pressure build-up over distance to the injection well between Scenarios 1 and 4.

CONCLUDING REMARKS

The highly heterogeneous nature of the reservoir contributes greatly to the highly varying injectivity of the injection layers over time in China's first demonstration project of CO_2 geological storage. The intermittent injection procedure employed in this project helps to reduce the pressure build-up in the reservoir and keeps the overall effective injection rate at the desired level. If hysteresis effects are included in the simulation, the estimated cumulative mass will be much higher than in the non-hysteresis simulation, which is mainly because CO2 is more mobile, which facilitates pressure spreading from the well, and allows a higher percentage of CO_2 to dissolve in the water, which in turn increases the injectivity. For a reservoir pre-assessed as low permeability and low porosity, like the one in this project, reservoir heterogeneity, injection procedure, as well as the accompanying hysteresis effects, should be considered carefully when assessing the performance of the reservoir.

ACKNOWLEDGMENT

This research was granted by the Ministry of Science and Technology of China, under the National Key Technologies R&D Program (Grant No. 2011BAC08B00) and by the National Energy Administration of China under the grant number NY20111102-1 for the National Energy Application Technology Research and Engineering Demonstration Program.

REFERENCES

Doughty, C., *User's guide for hysteretic capillary pressure and relative permeability functions in TOUGH2*, Rep. LBNL-6533E, Lawrence Berkeley National Lab., Berkeley, Calif., 2013.

Jiang, P., X. Li, R. Xu, Y. Wang, M. Chen, H. Wang and B. Ruan. Thermal modeling of CO_2 in the injection well and reservoir at the Ordos CCS demonstration project, China, *I. J. of Greenhouse Gas Control,* 23 135-146, 2014.

Kuang, D.-q., Q. Li, Y.-s. Wang, X.-j. Wang, Q. Lin, X.-c. Wei and R.-r. Song. Numerical simulation of distribution of migration of CO_2 in Shenhua carbon capture and storage demonstration project, *Rock and Soil Mechanics,* 35 (9), 2623-2633, 2014.

Lei, H.-w., G.-r. Jin, Y. Shi, J.-q. Li, F.-g. Wang and T.-f. Xu. Numerical simulation of subsurface coupled thermo-hydro-mechanical (THM) processes: Application to CO_2 geological sequestration, *Rock and Soil Mechanics,* 35 (8), 2415-2425, 2014.

Li, C., N.-C. Tien, K. Zhang, C.-P. Jen, P.-S. Hsieh, S.-Y. Huang and F. Maggi. Assessment of large-scale offshore CO_2 geological storage in Western Taiwan Basin, *I. J. of Greenhouse Gas Control,* 19, 281-298, 2013.

Ling, L.-l., Y.-q. Xu, Y.-s. Wang and K.-n. Zhang. Application of numerical simulation to pilot project of CO_2 geological sequestration, *Rock and Soil Mechanics,* 34 (7), 2017-2022, 2013.

Liu, H., Z. Hou, P. Were, Y. Gou and X. Sun. Simulation of CO_2 plume movement in multilayered saline formations through multilayer injection technology in the Ordos Basin, China, *Environmental Earth Sci.,* 71 (10), 4447-4462, 2014.

Liu, H., Z. Hou, P. Were, Y. Gou, L. Xiong and X. Sun. Modelling CO_2-brine-rock interactions in the Upper Paleozoic formations of Ordos Basin used for CO_2 sequestration, *Environmental Earth Sci.,* 73, 2205-2222, 2015.

Van Genuchten, M. T. A closed-form equation for predicting the hydraulic conductivity of unsaturated soils, *Soil Sci. Soc. of America J.,* 44 (5), 892-898, 1980.

Wei, N., M. Gill, D. Crandall, D. McIntyre, Y. Wang, K. Bruner, X. Li and G. Bromhal. CO_2 flooding properties of Liujiagou sandstone: influence of sub‐core scale structure heterogeneity, *Greenhouse Gases: Sci. and Tech.*, 4 (3), 400-418, 2014.

Wu, X. Shenhua Group's carbon capture and storage (CCS) demonstration, Mining Report, 150 (1‐2), 81-84, 2014.

Xie, J., K. Zhang, L. Hu, Y. Wang and M. Chen. Understanding of the carbon dioxide sequestration in low-permeability saline aquifers in the Ordos Basin with numerical simulations, *Greenhouse Gases: Sci. and Tech.,* 5:1–19 (2015).

Zhang, K., Y.-S. Wu and K. Pruess, *User's guide for TOUGH2-MP-A massively parallel version of the TOUGH2 code*, Rep. LBNL-315E, Lawrence Berkeley National Lab., Berkeley, Calif., 2008.

A NEW TOUGH2-MODULE: ECO2MG

D. Loeve, J.G. Maas, A. Obdam

TNO
Princetonlaan 6
3584 CB Utrecht
e-mail: daniel.loeve@tno.nl

ABSTRACT

This paper presents the new ECO2MG module of TOUGH2, which is able to model the thermal effects of methane and nitrogen in the CO_2 stream. Also the effect of methane and nitrogen initially present in the depleted gas field can be modelled. One of the remaining challenges is to predict the impact of the methane, which is still present in a depleted gas reservoir, on the phase behavior of gas mixtures and the cold zone around the well. Also other effects, like impurities in the CO_2 stream (e.g. N_2, CH_4) will have an influence on the thermal and phase behavior of the gas mixture in the storage location. The existing TOUGH2-ECO2M module only allows CO_2 besides the aqueous phase. We extended this module into ECO2MG with additional components CH_4 or N_2. We used the new module to model the effect of methane present in a depleted gas field (P18) and the effect of nitrogen in the CO_2 stream while injecting in an aquifer (Ketzin). The simulations on P18 showed that the Joule Thomson effect is less pronounced in the presence of methane which is good news for the risks associated with fractures and hydrate forming. The simulations on Ketzin show that the CO_2 containing nitrogen impurity propagates faster into the aquifer. This paper shows that the ECO2MG module is able to model additional components including phase changes for example, from the gas phase to supercritical phase. In short, the best abilities of EOS7C and ECO2M are merged together into the ECO2MG model.

INTRODUCTION

In the Netherlands depleted gas fields are investigated for geological storage of CO_2. The advantage of hydrocarbon fields is that the characteristics, such as storage capacity and proven sealing capacity are known (Oldenburg et al., 2001, 2004b; Hughes, 2009), which is not the case for saline aquifers. One of the uncertainties and risks associated with depleted gas fields is the low initial pressure, which can lead to adiabatic cooling (Joule-Thomson Cooling or JTC) upon injection of the CO_2 (Hofstee et al., 2013). The resulting relatively low temperatures in and around the well can initiate thermal fractures in the reservoir and the sealing caprock. Furthermore at sufficiently low temperatures, CO_2 injection can induce the formation of gas hydrates with the water in the pores. An unwanted effect is that the hydrates hamper the injection due to reduced injectivity resulting from pore neck plugging. CO_2 storage is planned in the P18 depleted gas field, which is located offshore close to the Rotterdam harbor. This project is also known as the ROAD project, which is the Rotterdam capture and storage demonstration project (Vandeweijer et al., 2012).

In order to investigate these effects during injection, we could have used the EOS7C module (Oldenburg et al., 2004a), which can model the behavior of gas mixtures in supercritical and subcritical conditions. However, the EOS7C module is not able to model phase transitions of CO_2. Another option is to use the ECO2M module, which was initially designed for CO_2 behaviour in saline aquifers (i.e., brine-CO_2 mixtures), including all possible phase transitions. Unfortunately this module is not able to model gas mixtures like CO_2-CH_4 and CO_2-N_2.

The choice we made to model gas mixtures including a CO_2 phase change was to extend the ECO2M module (Pruess, 2011) into a new module called ECO2MG. This new module has a new algorithm, which can handle the multi-component and multi-phase behavior of the gas mixture.

In addition, the Netherlands aquifers are a very promising option for geological storage of CO_2. An advantage of aquifers is that the storage capacities generally may be much higher compared to depleted gas fields. The first onshore aquifer pilot site in Europe is the Ketzin project in Germany, located about 25 km west of Berlin (Fischer et al., 2014). From June 2008 to August 2013 about 67 kt of CO_2 were injected (Möller et al., 2014).

One of the experiments carried out at the Ketzin site is the four-week period of N_2-CO_2 injection between July 24th and August 18th 2013, (Fischer et al, 2014). Since commercial CO_2 streams will contain impurities and we would like to see the effect on the reservoir behaviour itself, a volume ratio CO_2:N_2 of 95:5 was used during the co-injection period. In total 32 tons of N_2 and 613 tons of CO_2 were co-injected.

The new ECO2MG module is used to investigate the effects of impurities at the P18 reservoir and the Ketzin aquifer.

In the next section we will focus on the new ECO2MG module and the related improvements. Subsequent sections describe the model setup and results of P18 and Ketzin, followed by the conclusion.

THE ECO2MG MODULE

New description of equation of state

In the ECO2M module, four components are described in the following order, H_2O, NaCl, CO_2, and Energy. In the new ECO2MG module, component 4 is CH_4 or N_2, and energy becomes component 5.

The key in developing the new module was a new implementation of the thermophysical properties (i.e., viscosity, density, specific enthalpy). In the ECO2M module the thermophysical properties of pure CO_2 are based on the Altunin correlations. In the ECO2MG module the thermophysical properties of the mixture are described by 3-dimensional tables based on NIST data (Figure 1). The three axes of the table describe pressure, temperature and composition (fraction CO_2-CH_4 or CO_2-N_2). This new thermophysical table consist of a mixture composition of 0 % CO_2 (which means: 100% CH, or N_2), 20% CO_2, 33% CO_2 and 100% CO_2 (see Figures 2 and 3).

An interpolation scheme can determine the correct phase/component and properties of the gas mixture needed in the simulation (Loeve et al., 2014).

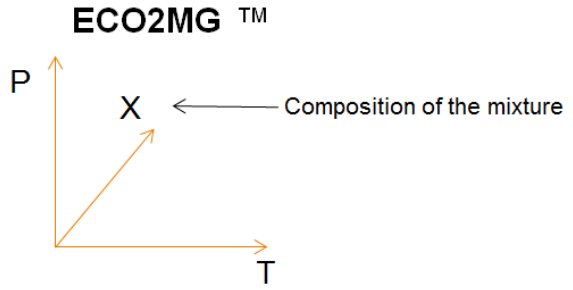

Figure 1. Three-dimensional tables used to describe the thermophysical properties in the ECO2MG module

The original phase envelopes based on the NIST data belonging to the mixtures are not monotonically ascending to the critical point. The set-up of the interpolation algorithm is done in such a way that each pressure has a unique temperature on the dew-point line and bubble-point line.

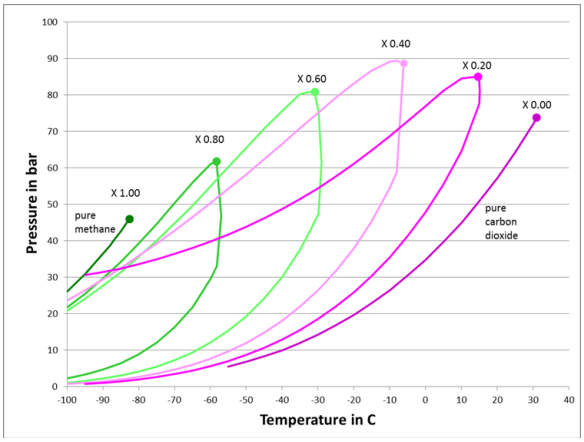

Figure 2. Pressure-temperature diagram of the different phase envelopes of the CO_2-CH_4 mixture.

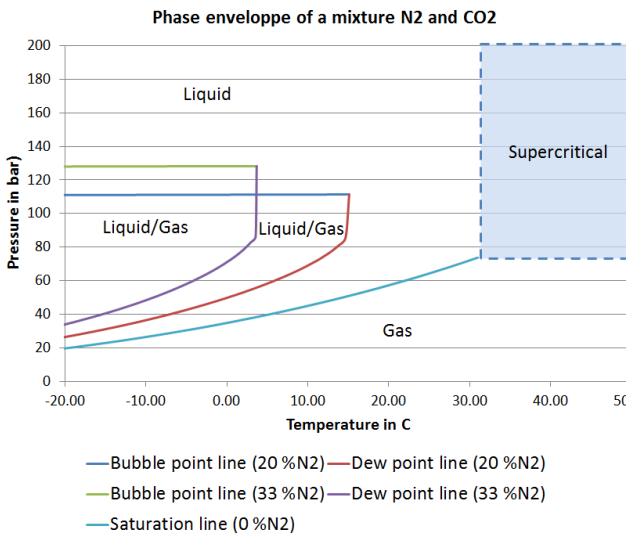

Figure 3. Pressure-temperature diagram of the different phase envelopes of the CO_2-N_2 mixture. The critical point of pure CO_2 is 30.98 °C and 73.77 bar and of pure N_2 is -146.96 °C and 3.60 bar, which is far outside the temperature region of interest.

Therefore we modified the data and defined a pseudo critical point close to the real critical point in such a way that the bubble point line is monotonically increasing until the critical point. With this modification, only one temperature value corresponds to each pressure value. This is obviously important for the simulator as it is designed right now. Although we introduce an error around the critical point by using the modified pressures, the thermophysical behaviour away from the critical point is correct (more information can be found in Loeve et al., 2014).

New description of relative permeability

The simulation stability appeared to be very sensitive on the choice of the relative permeability function. Therefore a new description of the relative permeability with a smoother character was created. In the ECO2MG module the relative permeabilities are only dependent on their own specific phase saturation, as can be seen in equation (1)

$$Kr_i = \left(\frac{(S_i - Sr_i)}{(1 - Sr_i)} \right)^n \qquad (1)$$

where:

i is the particular phase (aqueous, gas or liquid)
Kr_i is the relative permeability of the phase i
Sr_i is the residual saturation of the phase i
S_i is the saturation of the phase i
n is the Corey coefficient

The endpoints in this Corey formulation are assumed to be equal to 1.

Other improvements

During the development of the new ECO2MG module several smaller improvements were also made, which are listed below

1. The maximum number of time steps was limited to 4 digits (9999) and is upgraded to 100000. We observed many small time steps especially during the phase transition of CO_2 and this modification gave us the ability to finish the simulations properly.
2. The TIMES keyword permits the user to obtain printout at specified times. When a regular time step is close (less than one second) to a specified time then the next time step will become very small. The requested information is written to a file; however the following time steps after the printout will remain small and will increase rather slowly, which is impractical. This issue is solved in the ECO2MG version.
3. The diffusion option is not consistent between the ECO2M code and in the TOUGH2 core code. For example, phase 1 is the aqueous phase in the ECO2M code, however in the TOUGH2 core code phase 1 is the gas phase.
4. In the EOS subroutine, improvements were made on the transition between primary variables. These variables were not always correctly (re)set, especially from and to phase index 6 and 7 where primary variables are changing (see Figure 4). In addition the transition from phase index 2 and 3 was improved as well.
5. In subroutine YH20 a correlation is used to calculate the water mole fraction in a

H_2O-CO_2 gas mixture. A small discontinuity in this function was observed and corrected. Newton Rapson procedures are sensitive to these types of discontinuities.

Phase conditions	Phase Index	Primary Variables				
		X1	X2	X3	X4	X5
Aqueous only	1	P	Xsm	X	Z	T
Liquid only	2	P	Xsm	X	Z	T
Gas only	3	P	Xsm	X	Z	T
Aqeous and liquid	4	P	Xsm	Sa	Z	T
Aqeous and gas	5	P	Xsm	Sa	Z	T
Liquid and gas	6	P	Xsm	Sg	Z	Y
Three phase	7	P	Xsm	Sa	Z	Sg

Figure 4. Primary thermodynamic variables used for multiphase mixture of brine and CO_2, where P is pressure, X_{sm} is salt mass fraction, X is CO_2 mass fraction, T is temperature, S_a aqueous phase saturation, S_g is the gas phase saturation, Y water mass fraction and Z the new component mass fraction.

P18-MODEL SETUP

A 20-layered radial model was created to analyze the temperature distribution and the dry out zone around the injector. This radial model is based on the P18 reservoir properties. The two most important formations in the P18 reservoir are the Hardegsen and the Detfurth formation (Figure 5). The 2-D model has 87 grid-cells in the horizontal direction, with grid refinement in the vicinity of the well. The radius of the model is 700 m and with closed boundaries. The injection well, which is situated at the left hand site of the reservoir, is constrained at a CO_2 injection rate of 1.1 Mton/yr for a period of 5 years. The injection temperature is set at 15°C, which is chosen as a lower limit to avoid hydrate formation (Vandeweijer, 2011).

The initial reservoir pressure and temperature are 20 bar and 100°C. Note that the real reservoir temperature is 120°C but the thermodynamic tables in the simulator are limited to a temperature between 0°C of 103°C. Other properties of the P18 reservoir model are given in Table 1 and Table 3 (Appendix A).

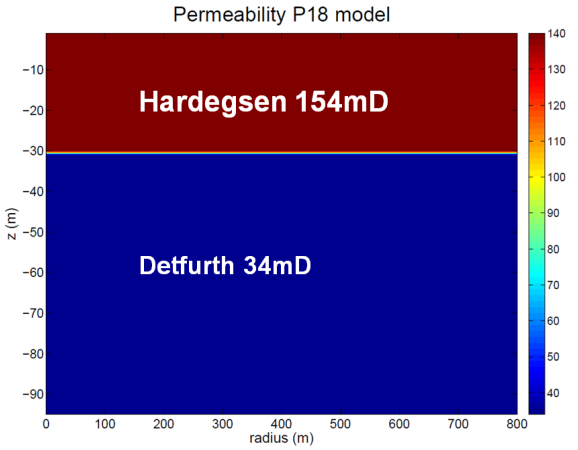

Figure 5: 2D-P18 Reservoir model

Table 1. P18-4 properties.

Property	Value	Unit
Temperature	100	°C
Initial Pressure	20	Bar
K_v/K_h	0.1	
Injection rate	1.1	Mton/yr
K of the Hardegsen	154	mDarcy
Porosity of the Hardegsen	0.11	
Thickness of the Hardegsen	26	m
K of the Dethfurt	34	mDarcy
Porosity of the Dethfurt	0.08	
Thickness of the Dethfurt	72	m

P18-4 is a compartment of a depleted gas field (part of the ROAD project) and was initialized with a brine-methane mixture at 20 bar, which is the expected abandonment pressure of the reservoir.

P18-RESULTS

The predicted thermal effects from the new tool were compared with those from the earlier version (CO_2 only) at several instances during the projected 5 year injection period (Figure 6).

In the ECO2MG module the Joule Thomson cooling is similar compared to the ECO2M module, but is propagating faster in this layer into the reservoir, The injected volumes are in both cases the same, however in the ECO2MG module the reservoir is initialized with methane in contrast to the ECO2M module, which is initialized with CO_2.

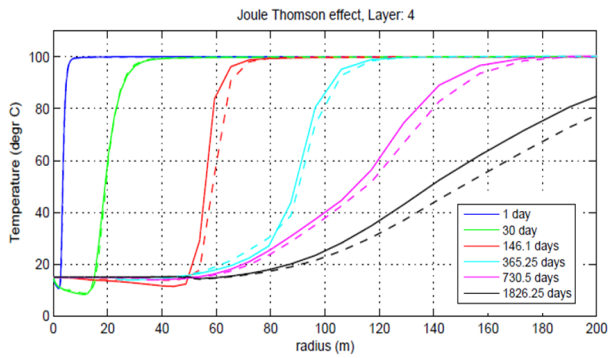

Figure 6. Joule Thomson effect in layer 4 for low temperature injection. The solid line shows the temperature profile, illustrating the Joule Thomson effect with the ECO2M module and the dashed line shows results obtained with the ECO2MG module.

KETZIN-MODEL SETUP

The Ketzin aquifer is modelled as a radial symmetric model like the P18 model described above. However the properties are different and given in Table 2 and Table 3 (Appendix A). Furthermore a shale layer with no transmissibility is included in the model at 33% depth of the aquifer. The Ketzin aquifer is initialized at 80 bar and 40 ºC.

Table 2. Ketzin type properties.

Property	Value	Unit
Temperature	40	ºC
Initial Pressure	80	Bar
K_v/K_h	0.1	
Injection rate	45	ton/day
K of the Hardegsen	154	mDarcy
Porosity of the Hardegsen	0.11	
Thickness of the Hardegsen	26	m
K of the Stuttgart fm	750	mDarcy
Porosity of the Stuttgart fm	0.23	
Thickness of the Stuttgart	210	m

KETZIN-RESULTS

We present the results with ambient temperature injection conditions for pure CO_2, and for CO_2 with 20% N_2 in the CO_2 stream in Figure 7 and Figure 8. The reason we show extreme nitrogen content at ambient injection conditions is so that we can observe a clear effect of the nitrogen on the behavior of the fluid in the reservoir.

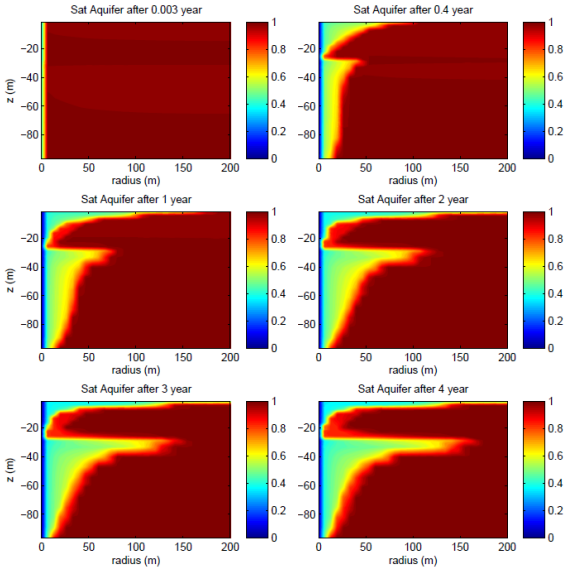

Figure 7. The six panels show the brine saturation at the start and, 1, 2, 3 and 4 years.

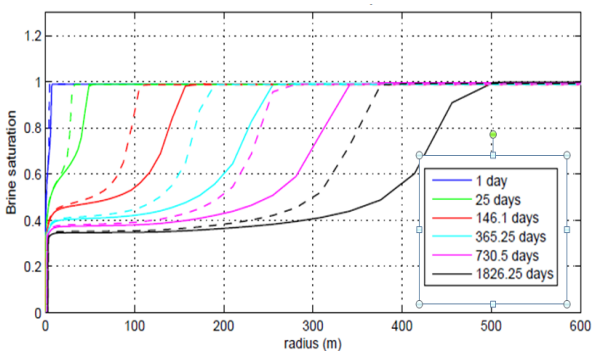

Figure 8. Model results of brine saturation with distance from the well in the first layer below the caprock. The solid lines show the results of a CO_2 stream with 80% CO_2 and 20% N_2, the dashed lines represent the pure CO_2 injection scenario.

A small dry out zone (<5m) around the well is observed (Figure 7) and the brine saturation values are lowered by the lateral CO_2 migration through the aquifer. A clear gravity override can be seen to the caprock and the intermediate shale layer. At ambient temperature injection conditions, the mixture of CO_2 and N_2 propagates faster into the reservoir compared to the pure CO_2 injection (Figure 8). The main reason is that the density of the mixture is lower compared to the pure CO_2. At the conditions of interest (40°C and 80 bar) the density of pure CO_2 is almost 2 times higher compared to the mixture.

CONCLUSION

The developed module has two important upgrades to the existing TOUGH2 modules. First the tool is able to model the phase change of pure CO_2 from gas to liquid and of CO_2 from gas to liquid in the presence of an aqueous phase; these types of simulations appeared not possible in the ECO2M module. Secondly another component is added to the model in such a way it can simulate all phase transitions as well. In short, the best abilities of the EOS7C and ECO2M are merged together in the ECO2MG model.

ACKNOWLEDGMENT

We thank Karsten Pruess for sharing his knowledge and for assistance during the development of the ECO2MG code, which greatly improved the new TOUGH2 module

REFERENCES

Arts, R.J., V.P. Vandeweijer, C. Hofstee, M.P.D. Pluymaekers, D. Loeve, A. Kopp and W.J. Plug, The feasibility of CO_2 storage in the depleted P18-4 gas field offshore the Netherlands (the ROAD project). *Int. J. of Greenhouse Gas Control*, 11S, S10-S20, 2012.

Fischer, S., A. Szizybalski, M. Zimmer, C. Kujawa, B. Plesse, A. Liebscher, F. Moeller, N_2-CO_2 co-injection field test at the Ketzin pilot CO_2 storage site, *Energy Procedia* 63, 2848-2854, 2014.

Hofstee, C., J.G. Maas, D. Loeve, The injection of liquid cool CO_2 in a warm depleted gas reservoir, presented at European Association of Geoscientists and Engineers Second Sustainable Earth Sciences Conference, Pau, France, 30 Sept. – 4 October, 2013.

Hughes D.S., Carbon storage in depleted gas fields: key finding, Greenhouse gas Control Technologies 9 (GHGT9), *Energy Procedia,* 1, 3007-3014, 2009

Loeve D., C. Hofstee,J.G. Maas,Thermal effects in a depleted gas field by cold CO_2 injection in the presence of methane, GHGT12, *Energy Procedia*, 63, 3632-3647, 2014.

Möller F., A. Liebscher, S. Martens, C. Schmidt-Harttenberger, M. Streibel, Injection of CO_2 at ambient temperature conditions - Pressure and temperature results of the cold injection experiment at the Ketzin pilot site, *Energy Procedia* 63, 6289-6297, 2014.

Oldenburg, C.M., G.J. Moridis, N. Spycher, K. Pruess, *EOS7C version 1.0: TOUGH2 module for carbon dioxide or nitrogen in natural gas (methane) reservoirs*. Rep. LBNL-56589 Lawrence Berkeley National Laboratory, Berkeley, Calif., http://www.repositories.cdlib.org/lbnl/LBNL-273E, 2004a.

Oldenburg, C.M., K. Pruess, and S.M. Benson, Economic feasibility carbon sequestration with enhanced gas recovery (CSEGR) *Energy* 29(2-10), 1413-1422, 2004b.

Oldenburg, C.M., Stevens S.H. and Benson S.M., Process modelling of CO2 injection into natural gas reservoirs for carbon sequestration and enhanced gas recovery, *Energy & Fuels*, 15 (2) 293-298, 2001.

Pruess, K., *ECO2M: A TOUGH2 fluid property module for mixtures of water, NaCl, and CO_2, including super- and sub-critical conditions, and phase change between liquid and gaseous CO_2*. Rep. LBNL-4590E, Lawrence Berkeley National Laboratory, Berkeley, Calif., 2011. Vandeweijer, V.P. et al. Feasibility study P18 (final report). CATO2-WP3.01-D06, 2011. (Confidential)

APPENDIX A

Table 3. Relative permeability and capillary pressure properties.

Property	Value
Relative permeability	Corey
Residual water saturation	0.3
Residual gas saturation	0.01
Corey coefficient aqueous, gas and liquid phase	3
Capillary pressure	No capillary pressure

IMPACTS OF RELATIVE PERMEABILITY ON CO_2 PHASE BEHAVIOR, PHASE DISTRIBUTION, AND TRAPPING MECHANISMS

Nathan Moodie, Brian McPherson, Feng Pan

University of Utah
201 Presidents Circle
Salt Lake City, Utah, 84109, USA
e-mail: nathan.moodie@m.cc.utah.edu

ABSTRACT

A critical aspect of geologic carbon storage, a carbon-emissions reduction method under extensive review and testing, is effective multiphase CO_2 flow and transport simulation. Relative permeability is a flow parameter particularly critical for accurate forecasting of multiphase behavior of CO_2 in the subsurface. The relative permeability relationship assumed and especially the irreducible saturation of the gas phase greatly impacts predicted CO_2 trapping mechanisms and long-term plume migration behavior.

A primary goal of this study was to evaluate the impact of relative permeability on efficacy of regional-scale CO_2 sequestration models. To accomplish this we built a 2-D vertical cross-section of the San Rafael Swell area of East-central Utah. This model simulated injection of CO_2 into a brine aquifer for 30 years. The well was then shut-in and the CO_2 plume behavior monitored for another 970 years. We evaluated five different relative permeability relationships to quantify their relative impacts on forecasted flow results of the model, with all other parameters maintained uniform and constant.

Results of this analysis suggest that CO_2 plume movement and behavior are significantly dependent on the specific relative permeability formulation assigned, including the assumed irreducible saturation values of CO_2 and brine. More specifically, different relative permeability relationships translate to significant differences in CO_2 plume behavior and corresponding trapping mechanisms.

INTRODUCTION

Perhaps the most critical tool for designing an effective geologic carbon storage project is multiphase CO_2 flow and transport simulation. Such simulations are essential not only for project design, but also for forecasting storage capacity and quantifying possible risks. Relative permeability is probably the most important multiphase flow parameter for CO_2 migration. Many previous studies focused on the trapping mechanics and CO_2 migration behaviors in geological sequestration (e.g., Han et al., 2010; Tian et al., 2014; Xu et al., 2005; Kumar et al., 2004; Suekane et al., 2008; Macminn et al., 2010). For example they found that the irreducible gas saturation value has a very large impact on the predicted amount of CO_2 that is trapped by residual trapping (Han et al., 2010; Suekane et al., 2008; Kumar et al., 2004). However, studies on the impact of relative permeability on CO_2 phase behaviors and trapping mechanics are rare, especially at regional scale. Therefore, a primary goal of this study was to evaluate the impact of relative permeability on efficacy of regional-scale CO_2 sequestration models. We selected the San Rafael Swell on the Colorado Plateau as a case study site because of its status as a top-tier sequestration candidate based on previous studies. (Morgan and Chidsey, 1991; White et al., 2005).

The area of the Colorado Plateau around the San Rafael Swell offers the potential for sequestering large volumes of CO_2 in natural saline formations, including the Navajo and White Rim sandstones. (Allis et al., 2003; Morgan and Chidsey, 1991) The San Rafael Swell is an anticline structure situated close to the Hunter Power plant and several other large point sources of CO_2 emissions. White et al. (2005) suggested that this area has significant storage potential but the unconfined nature of the primary target reservoirs may likely allow CO_2 to escape back to the atmosphere. Therefore, we elected to revisit this candidate site with a more comprehensive analysis of how different relative permeability models affects CO_2 migration and trapping mechanisms.

For this purpose we developed a 2-D vertical cross-section of the San Rafael Swell area of East-central Utah. The model design included injection into a target formation for 30 years (assumed typical lifespan of a coal-fired power plant) and then simulated plume behavior was tracked for an arbitrary additional 970 years. We evaluated five different relative permeability relationships to quantify their relative impacts on forecasted flow results of the model, with all other parameters maintained uniform and constant.

Results indicate that the relative permeability relationship that is selected and implemented has a large impact on simulated phase behavior and distribution, and that the value of irreducible saturation exerts the greatest effect on residual trapping. No leakage of CO_2 to the surface occurred in any of our simulations over the 1000-year period. We suggest that it is possible to trap CO_2 completely and effectively permanently in an unconfined structure like the San Rafael Swell. But, in the absence of robust relative permeability information, "conservative" formulations may be the best choice to ensure that simulation forecasts are not artificially optimistic.

STUDY SITE

The San Rafael Swell is a Northeast to Southwest trending asymmetrical anticline that consists of sedimentary rock ranging in age from the Cretaceous to the Pennsylvanian in age. (Hawley et al., 1968; Lupe (1976) The sedimentary structures on the Western part of the anticline dip at around 2°-5° to the west. (Hawley et al., 1968) Hood and Patterson (1984) evaluated the hydraulic properties of the sandstone aquifers in the area. They determined a range of permeability and porosity values for the formations, 20-1000 mD and 10%-20% porosity for the sandstone aquifers and 0.03-.1 mD and 2-10% porosity for the limestone and shale formations. (Hood and Patterson (1984))

NUMERICAL MODEL SETUP

Based on the information from White et al. (2005) and a cross-section of the San Rafael Swell under the Hunter Power Plant, a model of the area was constructed. This area was of interest because of near-by large point source CO_2 emitter, the Hunter power plant, and the available storage in the underlying sandstone formations like the Navajo and White Rim. The model was built with an unstructured grid so that the geologic cross-section could be matched as closely as possible. The model was made 87-km wide so that the model boundary would not exert an influence on the injected fluid. The model has a regional groundwater flow from the highlands in the West to an area where many of the shallower formations outcrop in the East. The reservoir has a shallow dip trending upward to the east towards these outcrops. The White Rim Sandstone comes close to surface but doesn't outcrop. Other potential reservoirs that are shallower like the Navajo and the Wingate do outcrop as well as the potential sealing units of the Black Box, Moenkopi and Chinle formations. Under the Hunter Power Plant the White Rim sandstone is deep enough to sequester supercritical CO_2. At the top of the formation, about 800 meters depth, the pressure is above 14 MPa and temperature is 45.5°C.

The area around the well has a refined grid. The cells within 4 km of the injection well are 50 meters wide. The cells then increase to the east in size to 100 meters, than 300 meters, and finally 565 meters and to the west in size to 150 meters, 300 meters, and 500 meters near the edge of the model (Figure 1). This was done to achieve a balance between good resolution of the grid in areas that matter and keeping the number of cells low enough that the model runs with in a reasonable time frame. The vertical cell distribution was defined in each layer, with the number of cells in the z-direction being specified during mesh generation. Figure 1 show the mesh generated by Petrasim with the resolution around the injection well. The model has a total of 27179 cells, of which 26622 are active cells and the 557 inactive cells that represent the boundary cells along the East, West, and top of the model.

A heterogeneous permeability field, random and uncorrelated, was assigned to this model. The field was generated using a random linear permeability coefficient multiplier approach (the SEED option in TOUGH2). Specifically, a base value of 200 mD for reservoir units and 0.02 mD for seal units (based on White et al., 2005) were assigned, and these base values were multiplied by random values of x, with $0 < x < 1.0$ to create

the random distribution for each unit, using the SEED function in TOUGH2. A homogeneous porosity distribution was assumed with values of 20% for the reservoir unit (White Rim sandstone), 10% for the principal seal unit (Black Box Dolomite), and 2% for the secondary seal units (Moenkopi and Chinle formations), respectively. (Harris and Chapman (1995); White et al., 2003)

The top boundary of the model was representative of the ground surface and was set to Dirichlet conditions with atmospheric pressure, 101325 Pa, and a surface temperature of 25°C. The East and West boundaries were also Dirichlet conditions set to a hydrostatic pressure distribution and the bottom of the reservoir was set to a no flow boundary with 60 mW/m^2 heat flux. The initial pressure and temperature values were assigned by layer based on the depth to the center of that layer vertically along the well path. The initial temperature was assigned as a temperature gradient of 20°C/km. Initial pressure was assigned as a hydrostatic gradient. The entire model has a uniform initial salt concentration of 3600 ppm. The model was then run with no injection for 1 million years to get a steady state condition.

Injection of CO_2 into the White Rim Sandstone lasted for 30 years at a mass flow rate of 1 kg/s. The response of the reservoir was then monitored for an additional 970 years. Specific 'monitoring' periods were investigated with the idea that they would represent possible EPA class VI well monitoring programs (EPA, 2013). The first period ended at 30 years, the end of injection period and the start of well shut-in. The next period evaluated was at 50 years post-injection which corresponds to EPA's Post Injection and Site Care (PISC) default monitoring period and would be the worst case scenario for a CCS monitoring program (EPA, 2013). After this point three more temporal points were evaluated in detail, 140 years, 500 years, and 1000 years to get an idea of relative permeability function and parameter selection impact on phase distribution, phase behavior, and trapping mechanisms over much longer time than is required of a CCS monitoring program (Table 1).

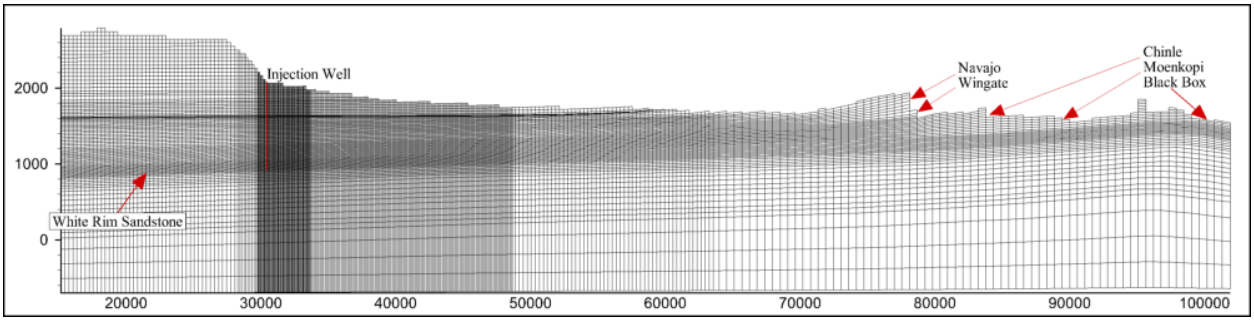

Figure 1. Model domain showing the refined mesh around the injection well and the coarsening of the grid away from the injection well. The principal reservoir, the White Rim Sandstone is indicated. Also shown are the outcrop areas of the overlying dolomite and shale layers of the Black Box, Moenkopi, and the Chinle formations and the much shallower Wingate and Navajo Sandstones.

Table 1. Study Parameters

Relative Permeability Curve Analysis					
Functions/ Curves	van Genuchten	Corey's Curve 1	Corey's Curve 2	Linear 1	Linear 2
Monitoring Periods	30 years Typical lifetime of coal power plant	80 years End of PISC monitoring period	140 years 60 years post monitoring	500 years Midpoint in simulation	1000 years End of simulation
Trapping Mechanisms	Residual Trapping	Solubility Trapping	Mobile CO_2		

RELATIVE PERMEABILITY AND CAPILLARY PRESSURE

Five relative permeability curves were selected for this study, two using the Corey's function (Fig 2), two using the linear function (Fig. 3), and one using the van Genuchten function (Fig. 4). All other input variables were kept constant across all simulations. The goal of curve selection was to use 'default', or commonly utilized relative permeability curves that are often employed when no formation specific relative permeability information is available. Three 'default' curves were evaluated: the Linear 1, Corey 2, and the van Genuchten (Table 2). The van Genuchten curve and the Corey 2 curve used parameters from the TOUGH2 manual (Pruess et al., 1999) and the Linear 1 curve is the default relative permeability relationship used by Petrasim. The remaining two curves, Linear 2 and Corey 1, were created to be different than the three default curves to show how parameter selection can affect simulation outcomes. Table 2 summarizes the parameters used by each of the relative permeability functions.

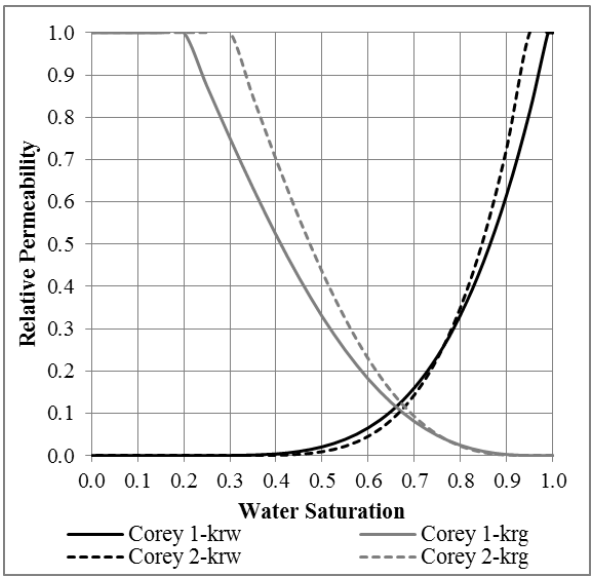

Figure 2. The two relative permeability curves using the Corey's Curves function.

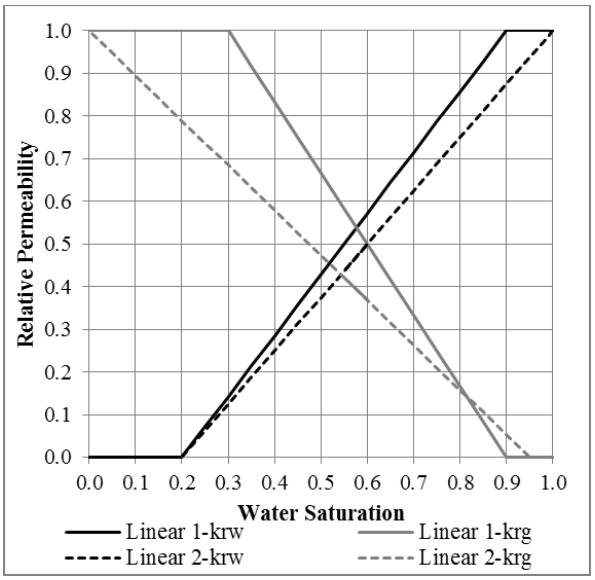

Figure 3. The two relative permeability curves using the linear function.

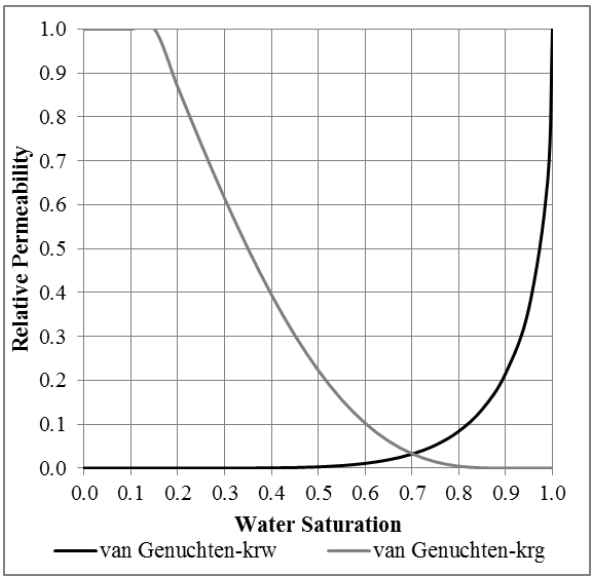

Figure 4. Relative permeability function using the van Genuchten function.

van Genuchten (1980) developed a closed-form analytical expression for predicting the unsaturated hydraulic conductivity in soils. It has been used to describe multi-phase flow in consolidated saturated porous media (Pruess et al., 1999; Pruess et al., 2003; Xu et al., 2005) and that was why it was selected for this study. Corey (1954) developed the relative permeability relationship to describe the flow of oil and gas in saturated sedimentary rocks. This relationship is used in TOUGH2 to describe the

flow of two immiscible fluids, brine and CO_2 in this study. The linear function was chose for this study because simulation run relatively quickly and making it ideal for simulation where specific relative permeability relationships are unknown or not needed. All simulation used a consistent capillary pressure function with a capillary entry pressure tailored to the geologic formation; 19.61 kPa for the reservoir units (sandstone) and 6.2 MPa for seal units (shale). The values for shale and sandstone came from a study done by Xu et al., 2005 of CCS in a sandstone reservoir capped by a shale seal.

RESULTS

Supercritical CO_2 Saturation

The CO_2 saturation profile exhibited in the principal reservoir (White Rim Sandstone) and in the overlying seal layers (Black Box Dolomite, Moenkopi, and Chinle formations) was largely influenced by the relative permeability function and parameter selection. The liner function predicts close to the same saturation profile for both of the curves tested, showing that parameter selecting has little impact on supercritical CO_2 saturation predictions by the linear function. Parameter selection becomes much more important with the Corey's Curve function. The Corey 1 curve is predicting between 0.65 and 0.75 gas saturation with the Corey 2 curve is predicting 18% less supercritical CO_2, between 0.55 and 0.65 gas saturation. The largest difference in saturation predictions was when the difference between the functions was analyzed. There was almost a 43% difference in predicted gas saturation values between the Linear 1 curve and the van Genuchten curve. Both of these curves use similar parameters and the same irreducible gas saturation value. Figure 5 illustrates the variation in plume shape seen between these functions at the end of the first monitoring period (80 years).

Table 2. Relative Permeability Parameters.

	Relative Permeability Parameters				
	Corey 1	Corey 2	Linear 1	Linear 2	van Genuchten
Water i-sat. (S_{lr})	0.2	0.3	0.2	0.2	0.15
Water sat. (S_{ls})	n/a	n/a	0.9	1	1
Gas i-sat. (S_{gr})	0.01	0.05	0.1	0.05	0.1
Gas sat. (S_{gs})	n/a	n/a	0.7	1	n/a
Lambda - λ	n/a	n/a	n/a	n/a	0.457

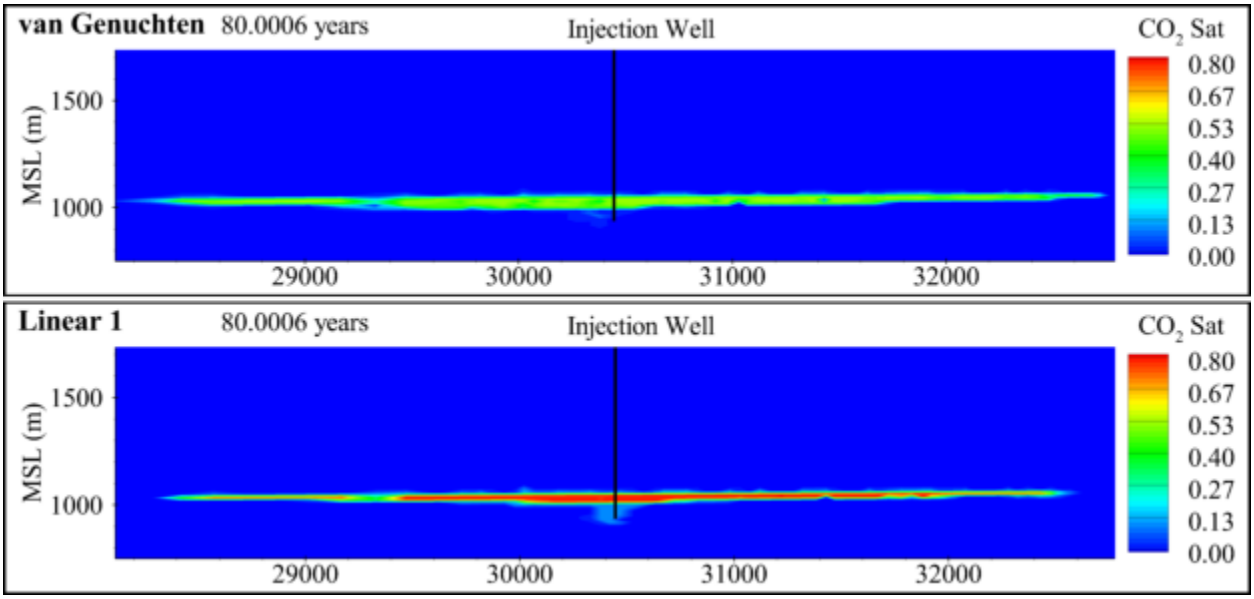

Figure 5. Supercritical CO_2 saturation predicted by the van Genuchten (top) and Linear 1 (bottom) curves at the end of the 50 year PISC monitoring period.

Residual Gas Trapping

Compounding the variation caused by function selection, the assumed irreducible gas saturation value selected for each function has a significant impact on the 'trapped' gas saturation and mass in both the reservoir and seal layers. This behavior was to be expected, as those values were end point saturations on the relative permeability curve and were specified in the relative permeability function (Table 2). This translates into trapped masses that were correlated to the specified irreducible saturation and less so to the relative permeability function itself. Figure 6 shows the impact of the specified irreducible saturation on the mass of residually trapped CO_2. It can also be seen that there was definitely a difference between functions even when they have the same irreducible gas saturation value, as with the Linear 1 and van Genuchten curves and the Corey 2 and Linear 2 curves (Fig 6).

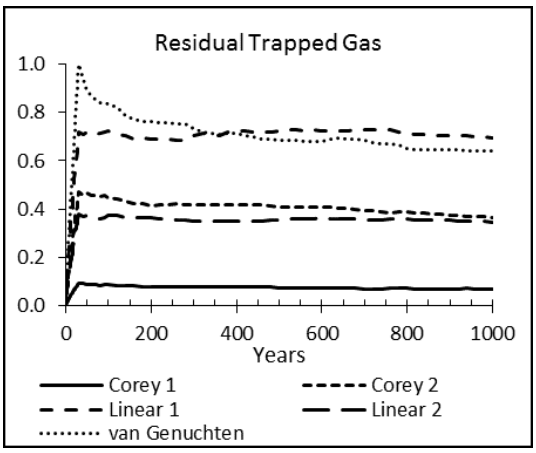

Figure 6. Normalized total mass of CO_2 that is trapped as residual gas.

Mobile Gas

Where the relative permeability function selection has the most influence was in the 'free', or mobile supercritical CO_2. The mobile mass of CO_2 moves up-dip through time due to a regional flow regime and buoyancy forces acting on the supercritical CO_2 plume. This causes the plume to continually move into area free of CO_2, residually trapping gas as the front of the plume advances. At the tail of the plume 'fresh', unsaturated brine imbibes into areas that have residually trapped CO_2 and dissolves this CO_2 as the plume moves away up-dip. This was why in figure 7 the mass of mobile gas continually decreases with time after injection stops.

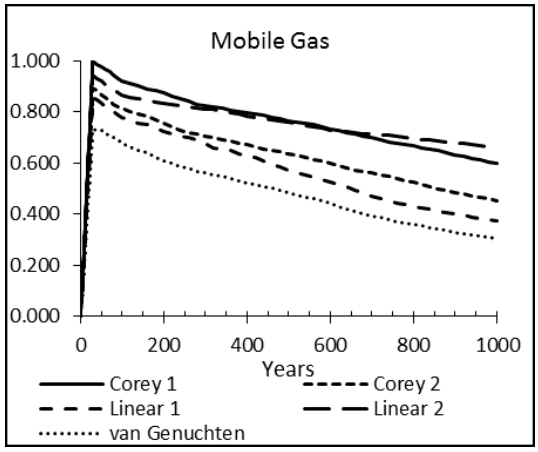

Figure 7. Normalized total mass of CO_2 that is mobile.

Dissolved Gas

The dissolution of CO_2 was coupled to the behavior of the supercritical plume. The impact of the relative permeability curve selection in the principal reservoir was seen principally at the front and tail of the supercritical CO_2 plume. Most of the reservoir unit had similar dissolved phase saturation. Where the relative permeability curves influence becomes more pronounced was in the overlying seal layers, mainly the Black Box Dolomite. After injection has stopped the supercritical plume migrates into the lower portion of the seal formation due to buoyancy and capillary pressure effects. The choice of relative permeability curve affects how much, if any of the CO_2 migrates into and eventually through the seal layers. Only the linear function and its curves allow any of the dissolved phase CO_2 to move through the seal layers and into the overlying Wingate Sandstone aquifer. This phenomenon only starts to manifest itself well after the second monitoring period, around 340 years. Until that point there was almost no difference in dissolved phase CO_2 saturation in the seal layers. So for any realistic monitoring period the risk was pretty low that the simulation will give you the 'wrong answer' if any of these curves are used. As seen in figure 8 for long-term predictions the choice of relative permeability curve becomes important as the differences in gas saturation become more pronounced between the curves post 500 years.

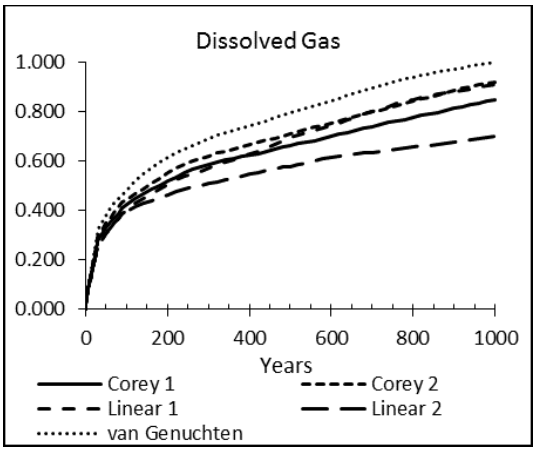

Figure 8. Normalized total mass of CO_2 that is dissolved in the brine.

Total Mass CO_2

Table 3 lists the total amount of CO_2 in the reservoir as trapped mass, mobile mass, and dissolved mass for each of the 5 monitoring periods. It shows, along with figures 6, 7, and 8, that the mass of trapped and mobile CO_2 decreases with time while the mass of dissolved CO_2 continues to increase until the end of the simulation. A combination of the relative permeability function and its specified irreducible saturation were controlling the magnitude of this change. The implication of this was that for predicting the mass of CO_2 that could be sequestered as residually trapped gas the specified irreducible saturation of the CO_2 was as big a factor as choosing the function itself. The two Corey's curves are a good example of this. There was an 80% difference in the mass of residually trapped CO_2, between 11% and 30% difference in mobile gas (values increase with time), and only a 5% difference in dissolved phase CO_2. Similar variation was seen with the linear curves as well, with about a 50% difference in trapped CO_2, between 9% and 45% difference in mobile gas (increasing with time), and between 0.2% to 30% difference in dissolved gas (increases with time).

Table 3. Total mass of CO_2 predicted by each of the relative permeability curves for each of the monitoring periods.

CO_2 Mass Distribution by Relative Permeability Curve					
	Monitoring Periods				
	30 years	80 years	140 years	500 years	1000 years
Residual CO_2	Increases with S_{gr}				
Corey1 (S_{lr} = 0.2, S_{gr}=0.01)	18,765	16,943	16,627	14,823	13,888
Corey2 (S_{lr} = 0.3, S_{gr}=0.05)	95,518	92,059	87,689	83,173	74,254
Linear1 (S_{lr} = 0.2, S_{gr}=0.1)	145,869	144,659	142,651	147,454	141,539
Linear2 (S_{lr} = 0.2, S_{gr}=0.05)	76,384	73,253	74,024	72,007	70,287
van Genuchten (S_{lr} = 0.15, S_{gr}=0.1)	203,101	170,573	159,943	138,950	130,594
Dissolved CO_2	Controlled by plume movement				
Corey1 (S_{lr} = 0.2, S_{gr}=0.01)	176,281	245,717	295,626	419,164	537,367
Corey2 (S_{lr} = 0.3, S_{gr}=0.05)	182,905	261,228	309,120	449,044	582,070
Linear1 (S_{lr} = 0.2, S_{gr}=0.1)	162,000	233,267	284,190	438,986	575,358
Linear2 (S_{lr} = 0.2, S_{gr}=0.05)	161,626	232,440	270,253	366,164	444,340
van Genuchten (S_{lr} = 0.15, S_{gr}=0.1)	201,487	282,536	345,437	504,140	631,674
Free CO_2	Inverse relationship with S_{gr}				
Corey1 (S_{lr} = 0.2, S_{gr}=0.01)	794,344	750,517	715,627	608,516	475,392
Corey2 (S_{lr} = 0.3, S_{gr}=0.05)	710,716	659,055	629,971	505,243	360,476
Linear1 (S_{lr} = 0.2, S_{gr}=0.1)	634,715	634,715	600,770	452,410	298,166
Linear2 (S_{lr} = 0.2, S_{gr}=0.05)	748,755	705,273	677,469	603,909	522,663
van Genuchten (S_{lr} = 0.15, S_{gr}=0.1)	582,464	556,973	517,358	383,919	242,036

CONCLUSION

Taken together not only was the relative permeability function itself a very important factor to consider in multi-phase flow simulation but also the parameters selected for that function, such as the irreducible saturation. For accurate prediction of supercritical CO_2 movement and trapping mechanisms, use of a relative permeability relationship that was suitable for not only the reservoir but also the seal units under consideration was important. This was because the assumed relative permeability relationship controls the saturation of each phase present and in turn the movement and phase behavior of the supercritical CO_2 and brine. Assuming a 'default' relationship may result in forecasts of CO_2 migration into and through 'seal' layers when this may not be the case in a real sequestration site, such as in the simulations that used the Linear 1 and Linear 2 curves. The linear function predicts the highest gas saturation values of all the simulations. This was due to the 'linearity' of the curves, small changes in saturation equal small changes in relative permeability values. Simulations using the Corey's Curve function and the van Genuchten functions exhibit a much larger change in relative permeability for small changes in saturation values, rendering phase behavior and plume movement more sensitive to small shifts in saturation. Only at the end points of the curve, depending on parameter selection, will the van Genuchten or Corey's function have higher relative permeability values. Finally, results of this study suggest that choice of relative permeability function and associated parameters were ultimately critical for designing and forecasting CCS projects, and at the least, it may be best to quantify the uncertainty due to (implementation of) different relative permeability functions and propagate that uncertainty appropriately.

REFERENCES

Allis, R.G., T.C. Chidsey, C. Morgan, J. Moore and S.P.White, *CO2 sequestration potential beneath large power plants in the Colorado Plateau-Southern Rocky Mountains region, USA.,* Alexandria, VA, 2003

Corey, A.T., The interrelation between gas and oil relative permeabilities, *Producers Monthly,* 19 (1), 38-41, 1954

EPA, *Geologic Sequestration of Carbon Dioxide: Draft Underground Injection Control (UIC) Program Guidance on Class VI Well Plugging, Post-Injection Site Care, and Site Closure,* 2013

Han, W.S., B.J. McPherson, P.C. Lightner and F.P. Wang, Evaluation of Trapping Mechanisms in Geologic CO2 Sequestration: Case Study of SACROC Northern Platform, A 35-year CO2 Injection Site, *American Journal of Science,* 310 (April), 282-324, 2010

Harris, R.N. and D.S. Chapman, Climate change on the Colorado Plateau of eastern Utah inferred from borehole temperatures, *Journal of Geophysical Research,* 100 (B4), 6367-6381, 1995

Hawley, C.C., R.C. Robeck and H.B. Dyer, *Geology, altered rocks and ore deposits of the San Rafael Swell Emery County, Utah,* United States Government Printing Office,Washington, D.C., 1968

Hood, J.W. and D.J. Patterson, *Bedrock Aquifers in the Northern San Rafael Swell Area, Utah, with Special Emphasis on the Navajo Sandstone,* United States Geological Survey, Salt Lake City, 1984

Kumar, A., M. Noh, G. Pope, K. Sepehrnoori, S. Bryant and L. Lake, *Reservoir simulation of CO2 storage in deep saline aquifers,* 2004

Lupe, R., *Depositional environments as a guide to uranium mineralization in the Chinle Formation, San Rafael Swell, Utah,* 1976

Macminn, C.W., M.L. Szulczewski and R. Juanes, CO2 migration in saline aquifers. Part 1. Capillary trapping under slope and groundwater flow, *Journal of Fluid Mechanics,* 662 329-351, 2010

Morgan, C.D. and J. Thomas C. Chidsey, Gordon Creek, Farnham Dome, and Woodside Fields, Carbon and Emery Counties, Utah, *Utah Geological Association,* 19 301-310, 1991

Pruess, K., C. Oldenburg and G. Moridis, *TOUGH2 User's Guide, Version 2.0,* Earth Sciencees Division, Lawrence Berkeley National Laboratory,University of California, Berkeley, 1999

Pruess, K., T. Xu, J. Apps and J. Garcia, Numerical modeling of aquifer disposal of CO2, *Spe Journal,* 8 (1), 49-60, 2003

Suekane, T., T. Nobuso, S. Hirai and M. Kiyota, Geological storage of carbon dioxide by residual gas and solubility trapping, *International Journal of Greenhouse Gas Control,* 2 58-64, 2008

Tian, H., F. Pan, T. Xu, B.j. McPherson, G. Yue and P. Mandalaparty, Impacts of hydrological heterogeneities on caprock mineral alteration and containment of CO2 in geological storage sites, *International Journal of Greenhouse Gas Control,* 24 30-42, 2014

van Genuchten, M.T., A closed-form equation for predicting the hydraulic conductivity of unsaturated soils, *Soil Science Society of America,* 44 (5), 892-898, 1980

White, S.P., R.G. Allis, J. Moore, T. Chidsey, C. Morgan, W. Gwynn and M. Adams, *Injection of CO2 into an unconfined aquifer located beneath the Colorado Plateau, Central Utah,* Alexandria, VA, 2003

White, S.P., R.G. Allis, J. Moore, T. Chidsey, C. Morgan, W. Gwynn and M. Adams, Simulation of reactive transport of injected CO2 on the Colorado Plateau, Utah, USA, *Chemical Geology,* 217 387-406, 2005

Xu, T., J.A. Apps and K. Pruess, Mineral sequestration of carbon dioxide in a sandstone–shale system, *Chemical Geology,* 217 (3), 295-318, 2005

GEOLOGIC CARBON DIOXIDE SEQUESTRATION IN NATURAL GAS RESERVOIRS: PRESSURE RISE DUE TO CO_2-CH_4 MIXING

Curtis M. Oldenburg, Kyung Jae Lee, and Jonny Rutqvist

Earth Sciences Division
Lawrence Berkeley National Laboratory
Berkeley CA USA
e-mail: cmoldenburg@lbl.gov

ABSTRACT

Depleted natural gas reservoirs are promising targets for geologic carbon sequestration (GCS) by virtue of their proven capacity to store and produce gas, predominantly methane (CH_4). Upon injection into the reservoir for GCS, carbon dioxide (CO_2) will mix with residual CH_4 by diffusion and dispersion. At pressures larger than the critical pressure of CO_2 (7.4 MPa) in the reservoir, CO_2 density can be 75% that of water. If CH_4 mixes with supercritical CO_2 even in small amounts (e.g., >5% by mass), the mixture density decreases drastically. What this means for GCS is that pressure in the reservoir will tend to rise due to CO_2-CH_4 mixing, even long after injection has stopped. The potential for post-injection pressure rise is critical for assessing the induced seismicity hazard related to GCS in depleted gas reservoirs. In this study, we have used TOUGH2/EOS7C to simulate the CO_2-CH_4 mixing and related pressurization effects in a closed reservoir. The time scale for post-injection CO_2-CH_4 mixing-related pressurization depends on the CO_2-CH_4 mixing time, which is generally controlled by gas-gas molecular diffusion time scales. We present results of sensitivity analyses to constrain CO_2-CH_4 pressure rise as a function of depleted gas-reservoir properties such as thickness and strength of molecular diffusion.

INTRODUCTION

Geologic carbon sequestration (GCS) relies on effective seals for containing the injected CO_2 and high-quality reservoirs for injecting CO_2. Depleted natural gas reservoirs are therefore promising targets for GCS by virtue of their proven capacity to store and produce gas, predominantly methane (CH_4), and because of the possibility of carrying out carbon sequestration with enhanced gas recovery (CSEGR) (Oldenburg et al., 2001).

In contrast to its colloquial meaning which can sometimes imply complete loss or exhaustion of a resource, the term "depleted" does not mean that CH_4 is no longer present in a depleted natural gas reservoir. Rather, gas reservoirs can become depleted because they are no longer economical to operate, and/or if water up-coning prevents gas production. As such, significant CH_4 can remain in depleted natural gas reservoirs. In addition, the pressure in depleted natural gas reservoirs is not necessarily low; pressures above the critical point for CO_2 (7.4 MPa) will be common.

Upon injection of CO_2 into a depleted gas reservoir, CO_2 will mix with residual CH_4 by molecular diffusion and by dispersion where flow rates are high. If CH_4 mixes with supercritical CO_2 even in small amounts (e.g., >5% by mass), the mixture density will decrease drastically. This effect is shown in Figure 1 by the curves of CO_2-CH_4 gas-mixture density calculated by the NIST Chemistry Webbook as a function of pressure at 40 °C. As shown, pure CO_2 undergoes a sharp increase in density as pressure increases from 60 to 120 bars (6-12 MPa). In contrast, the density increases nearly linearly for pure CH_4. As small amounts of CH_4 mix with CO_2 at pressures greater than around 100 bars (10 MPa), gas-mixture density decreases significantly.

What this means for GCS in depleted gas reservoirs is that pressure in the reservoir will tend to rise due to CO_2-CH_4 mixing, even long after injection has stopped. The potential for post-injection pressure rise is critical for assessing induced seismicity hazard related to GCS in depleted gas reservoirs.

In this study, we have used TOUGH2/EOS7C to simulate the CO_2-CH_4 mixing and related pressurization effects in a closed reservoir. The time scale for post-injection CO_2-CH_4 mixing-related pressurization depends on the CO_2-CH_4 mixing time, which is generally controlled by gas-gas molecular diffusion time scales. We present results for two different reservoir aspect ratios and four different values of molecular diffusivity to understand time scales of CO_2-CH_4 pressure rise as a function of typical depleted gas reservoir properties such as thickness and strength of molecular diffusion.

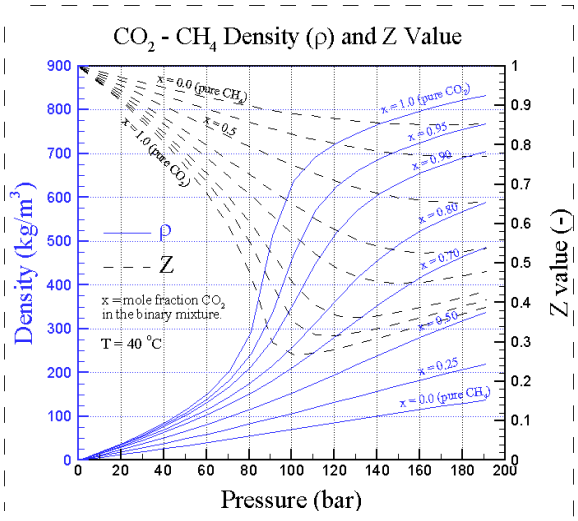

Figure 1. Density and compressibility factor (Z) for CO_2-CH_4 mixtures at 40 °C as a function of pressure.

RESERVOIR TYPE

We note that natural gas reservoirs span a range from water-drive, in which gas production is driven by the hydrostatic pressure of surrounding formation water, to depletion-drive, in which the production of gas is driven by the gas pressure alone with no support provided by surrounding formation water. In the former case, the pressurization due to CO_2-CH_4 mixing would be accommodated by the surrounding aquifers and reservoir pressure would not increase. In the latter case, the pressure in the reservoir would increase due to CO_2-CH_4 mixing. Most natural gas reservoirs are neither purely depletion-drive nor purely water-drive. The current study presents results only for the depletion-drive case as a demonstration of the mixing-induced pressurization effect.

The efficiency with which aquifers supporting water-drive reservoirs will compensate for the volume increase of the CO_2-CH_4 mixing effect can be understood by examination of pressure diffusion (i.e., flow and compressibility) effects. Pressure diffusivity (aka hydraulic diffusivity) is defined as transmissivity (T) over storativity (S) as follows

$$D_P = \frac{T}{S} = \frac{\frac{k\rho g}{\mu} b}{\rho g b(\alpha + \phi\beta)} = \frac{\frac{k}{\mu}}{\alpha + \phi\beta} \quad [=]\, m^2 s^{-1} \quad (1)$$

(Freeze and Cherry, 1976) where k = permeability (m^2), μ = viscosity (Pa s), α = rock compressibility (Pa^{-1}), ϕ = porosity, β = fluid compressibility (Pa^{-1}). A time scale (τ) for pressure diffusion can be estimated from

$$\tau = \frac{L^2}{D_P} \quad (2)$$

Where L is a typical length scale. Assuming permeability of 500 mD, viscosity of CH_4 (160 bar, 60 °C) is 1.7×10^{-5} Pa s, rock compressibility is 1×10^{-8} Pa^{-1}, porosity is 0.2, and fluid compressibility is 1×10^{-7} Pa^{-1}, the pressure diffusivity is 1 m^2/s, which results in a pressure diffusion time scale over 10 m of 100 s. This simple analysis reveals that open reservoirs can very quickly dissipate the mixing-induced pressure change. The results presented here are for a depletion-drive (i.e., closed) reservoir for which pressure-induced mixing is maximized.

MODEL SYSTEM

Potential GCS sites exist throughout the San Francisco Bay Delta region where large accumulations of natural gas have been produced for over 75 years. One example is King Island, near Lodi, CA. The King Island stratigraphy and trace of a stratigraphic characterization well are shown in Figure 2. Our modeling assumes the presence of a hypothetical depleted gas reservoir near the top of the Mokelumne River Sandstone. The reservoir is assumed to be closed on all sides, e.g., by shale rocks at the top and bottom, and by sealing faults along the sides. We show two blow-ups of the discretizations for two idealized radial (R-Z) models for these reservoirs. Case 1 is 10 m thick and Case 2 is 40 m

thick. Both of these reservoirs are closed (depletion-drive reservoirs).

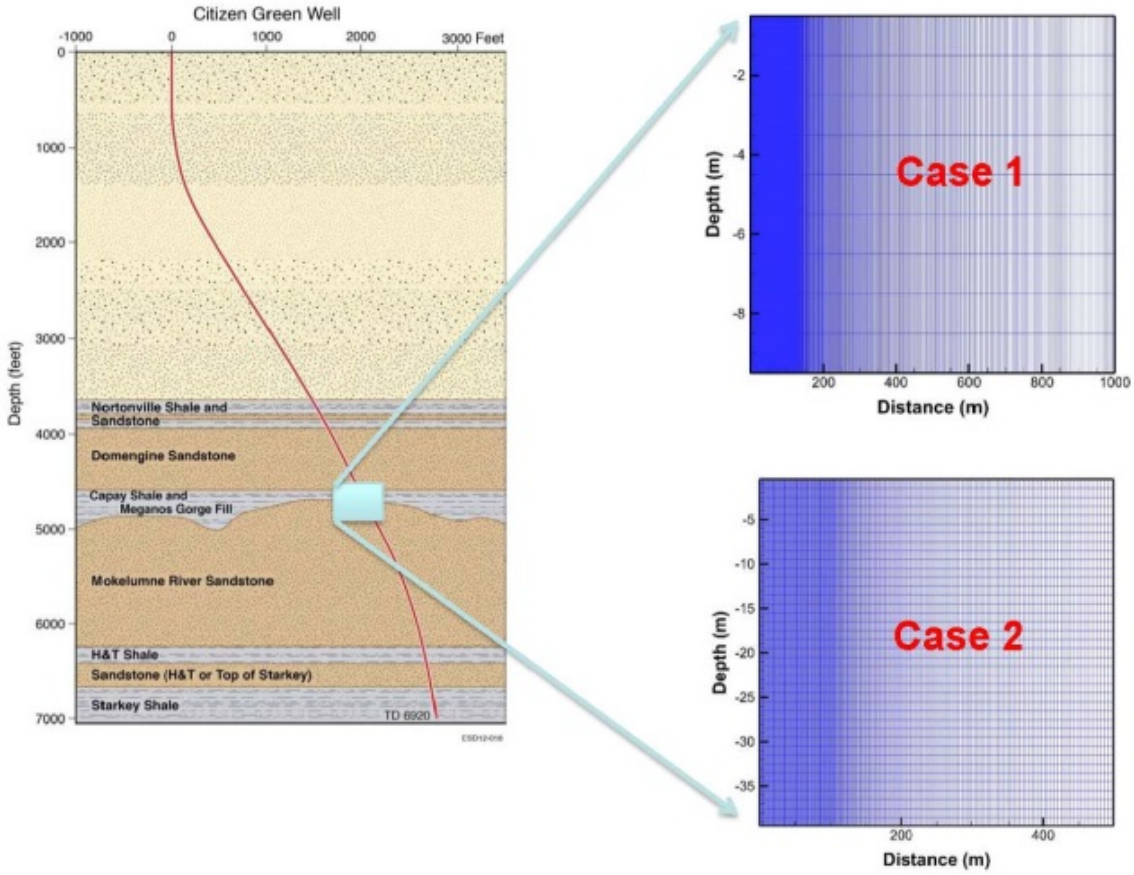

Figure 2. Cross-section showing the King Island well near Lodi, CA. The blow-up shows the radial discretizations for Case 1 (10 m-thick domain) and Case 2 (40 m-thick domain).

We use TOUGH2/EOS7C which models water, brine, CO_2, a gas tracer, and CH_4 (Oldenburg et al, 2004) to simulate CO_2 injection into two idealized radial (RZ) depleted natural gas reservoirs. These model systems are shown in Figure 3. The injection interval is 10 m long in both cases, and both reservoirs are the same volume so that we can compare pressure rise based on CO_2-CH_4 mixing on the same basis without complication by different reservoir volume. Three monitoring points are shown at which pressure and gas composition will be shown as a function of time.

The properties of the porous media are shown in Table 1. Briefly, the properties are chosen to represent a sandstone with good permeability, strong anisotropy, and 30% residual water saturation. The gas in the pore space is initially CH_4 and minor water vapor at 150 bar, 60 °C. The injection rate is chosen as 1 million tonnes CO_2 per year. The simulation is run for 100 years with 10 years of injection and 90 years of shut in.

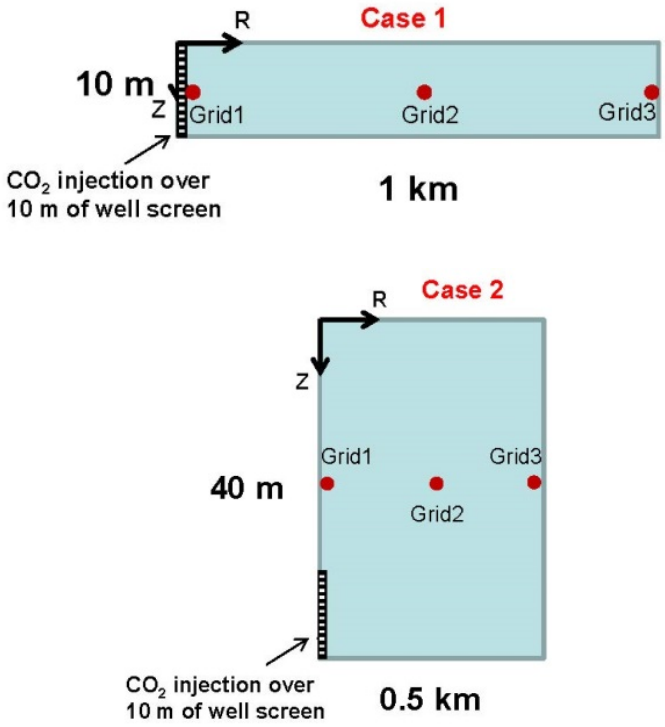

Figure 3. Case 1 domain (upper), and Case 2 domain (lower). The reservoirs are the same volume and show screened interval and three monitoring locations (Grid1, 2, and 3).

Table 1. Properties of the idealized closed reservoirs.

Property	Value	Property	Value
Porosity (ϕ)	0.326	CO_2 injection rate	1.0e5 tonne/year
Permeability (k_h)	430.8 md	Anisotropy (k_h/k_v)	22.32
Molecular diffusivity (D)	1.e-5 m^2 s^{-1} (base case)	Tortuosity (τ)	$\phi^{1/3}S_g^{10/3}$ (Millington-Quirk)
Initial Pressure	1.5e7 Pa (2,175 psi)	Temperature	60 ° C
Initial aqueous phase saturation	0.3	Vertical grid spacing	1 m
Relative permeability	(1) Reservoir van Genuchten k_{rl} $\lambda = 0.457$, $S_{lr} = 0.3$, $S_{ls} = 1$, $S_{gr}=0.01$ $k_{rg} = (1-\hat{S})^2(1-\hat{S}^2)$ where $\hat{S} = (S_l-S_{lr})/(1-S_{lr}-S_{gr})$ (2) Well Linear function $S_{lr} = 0.03$, $S_{ls} = 1$ $S_{lr} = 0.03$, $S_{ls} = 0.003$	Capillary pressure	(1) Reservoir van Genuchten function $\lambda = 0.457$, $S_{lr} = 0$, $1/P_0 = 5.1e-5$, $P_{max} = 1.0e7$, $S_{ls} = 0.999$ (2) Well: 0.0

RESULTS

The pressure fields at 10, 20, 50, and 100 years for Case 1 are shown in Figure 4. (Note the large vertical exaggeration). The pressure fields show that during injection, pressure propagates from the injection well across the reservoir with evidence of gravity effects as dense supercritical CO_2 enters the system. After injection stops at 10 years, the pressure differences decrease both horizontally and vertically in the reservoir because of the large pressure diffusivity in this 430 mD reservoir.

We present in Figure 5 the CO_2 gas mass fraction fields at 10, 20, 50, and 100 years for Case 1. These figures illustrate the injection and subsequent flow and mixing of CO_2 in the reservoir. Specifically, the large density of supercritical CO_2 relative to CH_4 causes the downward flow of CO_2 resulting in CH_4 tending to rise in the reservoir. The Case 1 reservoir is only 10 m thick (note the large vertical exaggeration of the figures) which explains the fast mixing in the vertical direction.

Results for the thicker reservoir (Case 2) are shown in Figure 6. In this 40 m-thick reservoir with injection of CO_2 into the bottom 10 m, we see that the dense CO_2 tends to remain in the lower parts of the reservoir both because of density effects and permeability anisotropy (low vertical permeability). As such, CO_2-CH_4 mixing is much slower than for Case 1.

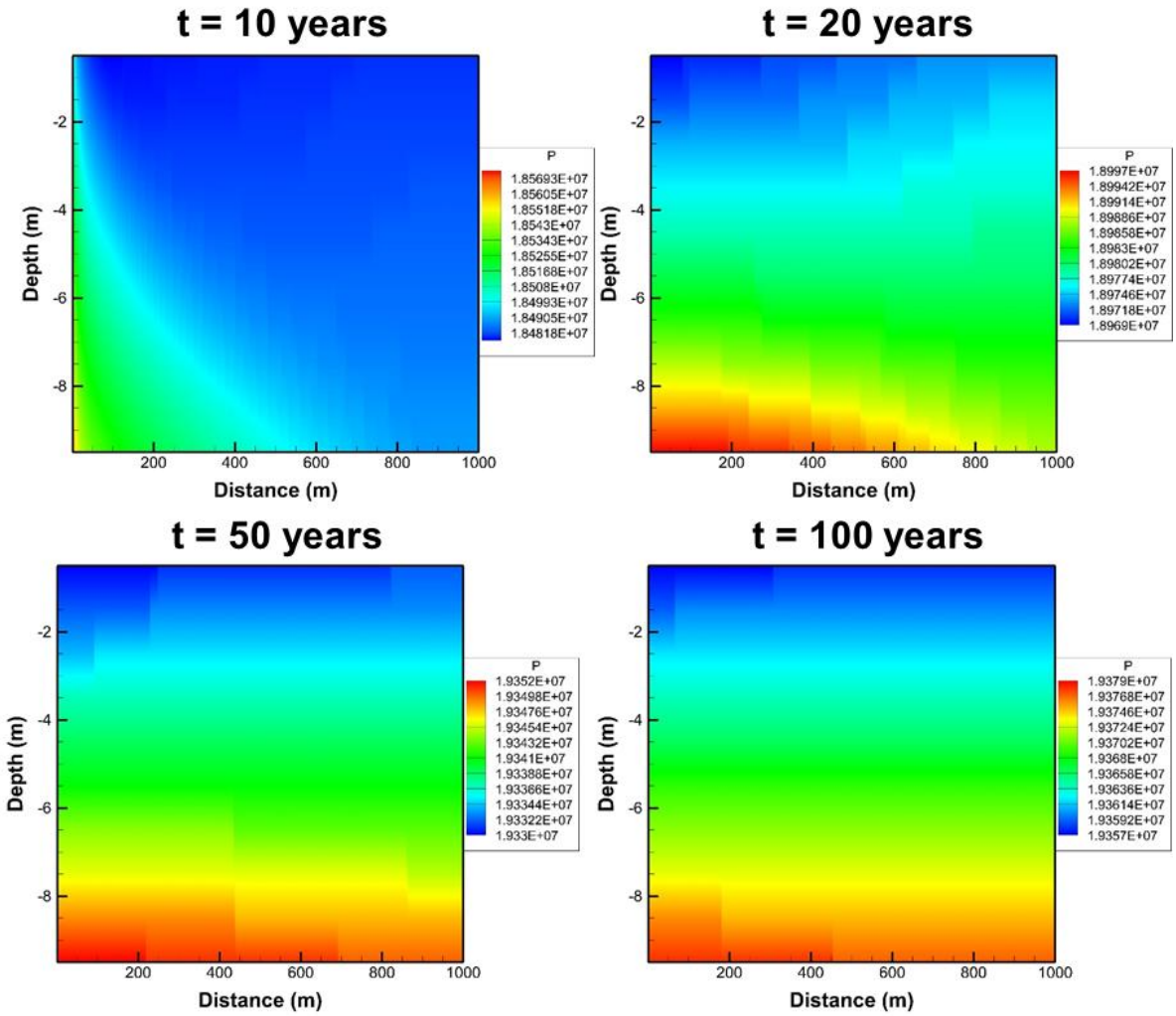

Figure 4. Pressure in the Case 1 domain at 10, 20, 50, and 100 yrs. Note different pressures scales for each frame.

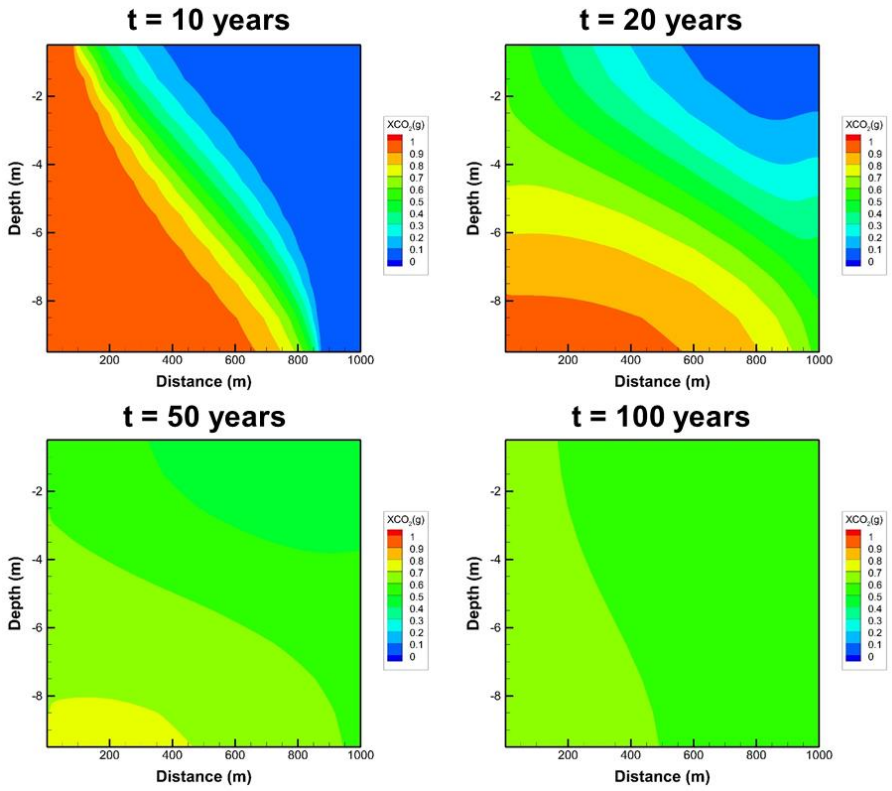

Figure 5. Mass fraction CO_2 in the gas phase at 10, 20, 50, and 100 yrs for Case 1.

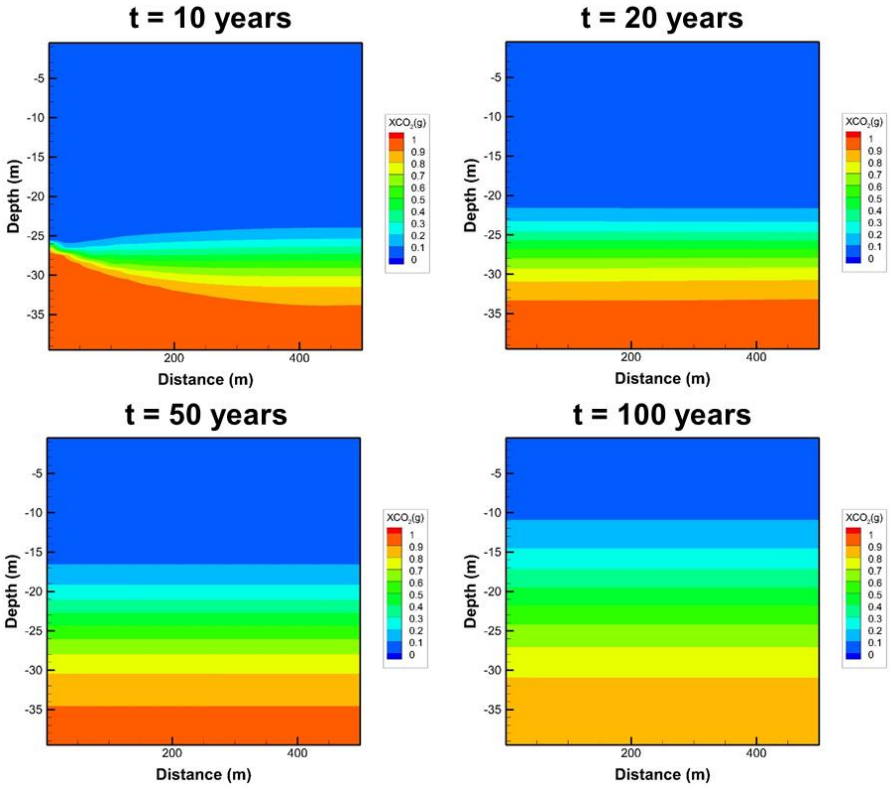

Figure 6. Mass fraction CO_2 in the gas phase at 10, 20, 50, and 100 yrs for Case 2.

In Figures 7 and 8 we show the evolution of pressure and gas composition at specific points in Case 1 and Case 2, respectively. In Case 1 (Figure 7), pressure rises at all three monitoring points almost uniformly because of high horizontal permeability. Pressure rise is linear during the 10-year injection period, and then rises more slowly over the next 40 years as CO_2-CH_4 mixing occurs. The total mixing-related ΔP is about 10 bar (1 MPa). The stair-step pattern of pressure rise represents time-step sizes.

As for the concentration profiles in Figure 7, high concentrations at the point next to the injection well (Grid1) occur from the first time step, and then decline starting after injection stops. The monitoring point mid-way across the domain (Grid2) rises steadily during injection and then more slowly as mixing occurs. The far-right-hand-side monitoring point (Grid3) starts rising at about 15 years. All three monitoring points are converging as mixing occurs, but concentration has not become completely uniform at 100 years.

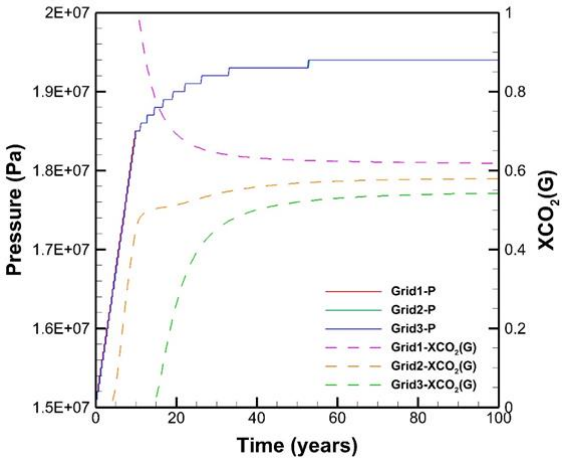

Figure 7. Pressure and mass fraction CO_2 vs. time for Case 1 at the three different monitoring points (Grid1, 2, and 3). Note pressures at Grid1, 2, and 3 overlap.

Figure 8 shows the same curves as Figure 7 for Case 2, the 40 m-thick reservoir. As in Case 1, the three monitoring points have essentially the same pressure over time, but pressure rise post-injection is smaller than for Case 1. As shown, the post-injection mixing-induced pressure rise (ΔP) is approximately 5 bar (0.5 MPa) in Case 2, but it is still increasing at 100 years. Eventually, when complete mixing has occurred, the Case 2 ΔP should equal the Case 1 ΔP.

Concentrations at the three monitoring points are very different for Case 2 relative to Case 1. Specifically, because the injection is into the lower-most part of the reservoir, the large density and small vertical permeability greatly diminish vertical mixing of CO_2 making the monitoring points all move approximately in lock-step after injection stops. Consistent with the pressure still changing at t = 100 yrs, diffusive mixing is still changing the composition of the gas at the monitoring points at 100 yrs.

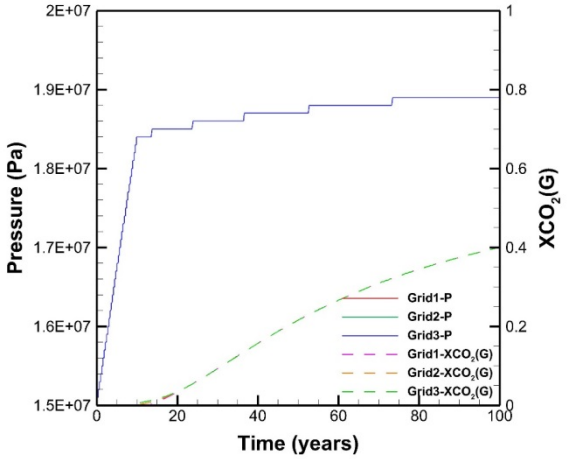

Figure 8. Pressure and mass fraction CO_2 vs. time for Case 2 at the three different monitoring points (Grid1, 2, and 3). Note curves at Grid1, 2, and 3 overlap.

In order to investigate the controls on mixing time of molecular diffusion, we varied the binary molecular diffusion coefficients (i.e., molecular diffusivity) of CO_2 and CH_4 from 1×10^{-4} to 1×10^{-7} m^2/s. Results for the Grid2 monitoring point are shown in Figure 9 for Case 1 (10 m-thick reservoir). As shown, large molecular diffusivity allows a rapid increase in CO_2 concentration during the injection period. For very small values of molecular diffusivity, the CO_2 concentration stays small until about 10 years and then increases sharply before diminishing again. We explain this behavior as a gravity effect; during injection, CO_2 is forced outward to the midpoint of the reservoir, while after injection, CO_2 slumps downward reducing the CO_2 concentration at this monitoring point. Behavior for values of molecular diffusivity in-between show intermediate behavior. We believe the base-case value of 1×10^{-5} m^2/s is probably the most realistic value.

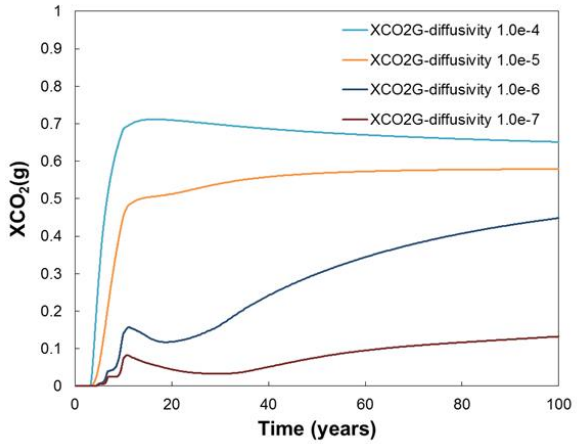

Figure 9. Mass fraction CO_2 vs. time for Case 1 at the central monitoring point.

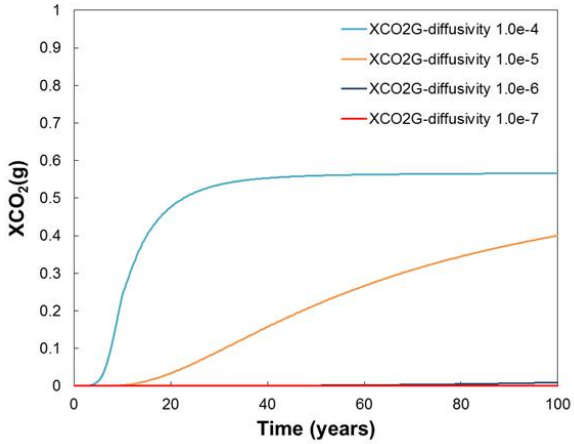

Figure 10. Mass fraction CO_2 vs. time for Case 2 at the central monitoring point.

The same comparison of sensitivity to molecular diffusion is shown for Case 2 in Figure 10. In this thicker reservoir, gravity stratification, injection into the lower region of the reservoir, and low vertical permeability combine to keep the CO_2 concentration at Grid2 low for all cases except the very large 10^{-4} m^2/s value, which is considered unrealistically high.

This simulation suggests that mixing in the vertical direction may be very slow. We show in Figure 11 the Case 1 and Case 2 CO_2 mass fraction fields to emphasize the slow mixing in thick reservoirs. This stratification potential was mentioned as an advantage for CSEGR because it would delay mixing and breakthrough of CO_2 to production wells if the CO_2 were injected deep and the CH_4 were produced high in the reservoir (Oldenburg et al., 2004). In the context of induced seismicity hazard, it may extend the period over which concern for mixing-induced pressure rise occurs. On the other hand, longer time allows for more likelihood of pressure dissipation. We emphasize that results presented here are for a closed system, with no pressure diffusion possible. In actual reservoirs, there would likely be pressure leak off through cap rock and/or surrounding sealing formations.

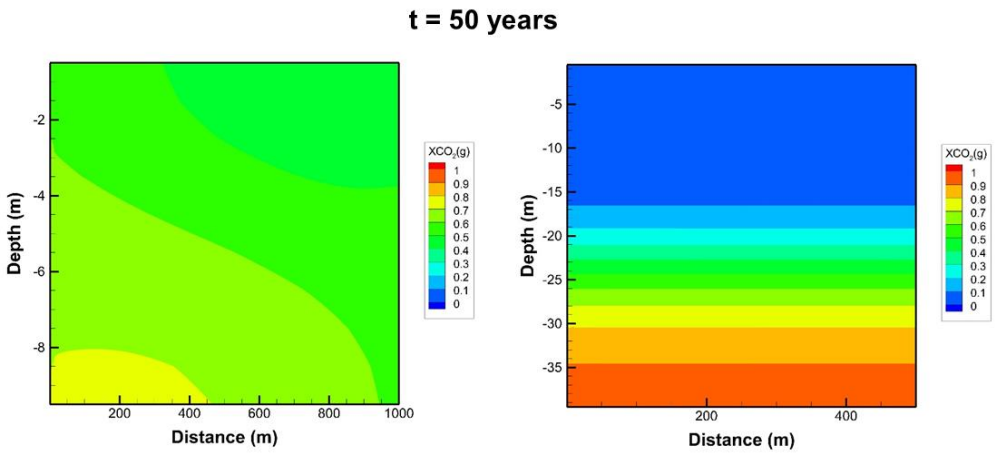

Figure 11. CO_2 mass fraction in the gas phase at t = 50 yrs for Case 1 (10 m-thick reservoir) (left-hand side) and Case 2 (40 m-thick reservoir) (right-hand side). As shown, the thick reservoir maintains concentration differences much longer than the thin reservoir.

DISCUSSION

The differences in mixing time can be understood from scale analysis-based estimates of mixing times due to molecular diffusion. The time scale for molecular diffusion can be estimated in an order of magnitude sense from the equation

$$\tau \sim \frac{L^2}{D} \qquad (3)$$

For a molecular diffusivity, D, of 1×10^{-5} m^2/s, tortuosity by Millington-Quirk of 0.06, porosity of 0.3, and a vertical distance of 10 m as in Case 1, the predicted molecular-diffusion mixing time is 18 yrs ($\tau = 10^2/(0.3 * 0.06 * 1 \times 10^{-5}) = 5.5 \times 10^8$ s), whereas the 40 m length of Case 2 has molecular diffusion mixing time of 290 yrs. The simulation results roughly match these estimates.

CONCLUSIONS

For a depletion-drive (i.e., closed) reservoir, CO_2-CH_4 mixing leads to ~10 bars of pressure change. The time scale for mixing is of order 10-100 yrs. The next step is to couple the effect with geomechanics (e.g., TOUGH-FLAC) to investigate whether the pervasive mixing-induced pressurization can lead to induced seismicity.

We note that if the reservoir is a water-drive reservoir, the surrounding aquifer(s) providing pressure support will prevent significant pressure rise, depending on pressure diffusivity and the degree of connectivity, along with the strength of competing long-term storage processes such as dissolution trapping.

ACKNOWLEDGMENT

This work was supported by the California Energy Commission project on geologic carbon sequestration and induced seismicity, and by the Assistant Secretary for Fossil Energy, Office of Sequestration, Hydrogen, and Clean Coal Fuels, through the National Energy Technology Laboratory of the U.S. Department of Energy, and by Lawrence Berkeley National Laboratory under U.S. Department of Energy Contract No. DE-AC02-05CH11231.

REFERENCES

Freeze, R. Allan, and John A. Cherry. *Groundwater*. Prentice-Hall, 1977.

Oldenburg, C.M., K. Pruess, and S.M. Benson, Process modeling of CO_2 injection into natural gas reservoirs for carbon sequestration and enhanced gas recovery, *Energy & Fuels*, 15, 293–298, 2001. LBNL-45820.

Oldenburg, C.M., S.H. Stevens, and S.M. Benson, Economic feasibility of carbon sequestration with enhanced gas recovery (CSEGR), *Energy*, 29, 1413–1422, 2004. LBNL-49762.

Pruess, K., C. Oldenburg, and G. Moridis, *TOUGH2 User's Guide, Version 2.0*, Report LBNL-43134 (revised), Lawrence Berkeley National Laboratory, Berkeley, Calif., 2012.

ECO2N V2.0: ENHANCEMENTS FOR MODELING CO_2-H_2O-NACL SYSTEM IN TOUGH2

Lehua Pan, Nicolas Spycher, Christine Doughty, and Karsten Pruess

Earth Sciences Division, Lawrence Berkeley National Laboratory
University of California, One Cyclotron Road
Berkeley, CA 94720, USA
e-mail: lpan@lbl.gov

ABSTRACT

We have improved ECO2N, the TOUGH2 fluid property module of the CO_2-H_2O-NaCl system. The major enhancements include: (1) the upper temperature limit is increased from 110 to about 300^oC; (2) the thermophysical properties of the CO_2-rich phase are more accurately calculated as a non-ideal mixture of CO_2 and H_2O; (3) the approach to calculate the specific enthalpy of dissolved CO_2 has been improved to make the code more robust in modeling phase transitions under non-isothermal conditions; and (4) more sophisticated models for effective heat conductivity of formations saturated with supercritical CO_2 have been provided. The new module includes a comprehensive description of the thermodynamic and thermophysical properties of H_2O - NaCl - CO_2 mixtures, that reproduces fluid properties largely within experimental error for the temperature, pressure and salinity conditions 10 °C < T < 300 °C, P < 600 bar, and salinity up to halite saturation. This includes density, viscosity, and specific enthalpy of fluid phases as functions of temperature, pressure, and composition, as well as partitioning of mass components H_2O, NaCl and CO_2 among the different phases. ECO2N with the TOUGH2 reservoir simulator can be applied to a wide range of problems in geologic sequestration of CO_2 in saline aquifers, and in enhanced geothermal reservoirs. ECO2N can describe both sub- and supercritical states of CO_2, but applications that involve sub-critical conditions are limited to systems in which there is no change of phase between liquid and gaseous CO_2, and in which no mixtures of liquid and gaseous CO_2 occur.

INDRODUCTION

ECO2N V2.0 is an enhanced version of ECO2N V1.0 that inherits all the capabilities of ECO2N V1.0 and expands the applicable temperature range up to about 300^oC by incorporating the newly developed mutual solubility correlations for higher temperature of Spycher and Pruess (2010). The fluid property module can be used to model non-isothermal multiphase flow in the system H_2O-NaCl-CO_2. TOUGH2/ECO2N V2.0 represents fluids as consisting of two phases: a water-rich aqueous phase, hereafter referred to as aqueous or "liquid," and a CO_2-rich phase, hereafter referred to as "gas." In addition, solid salt may also be present. The only chemical reactions modeled by ECO2N V2.0 are equilibrium phase partitioning of water and carbon dioxide between the liquid and gas phases, and precipitation and dissolution of solid salt. The partitioning of H_2O and CO_2 between liquid and gas phases is modeled as a function of temperature, pressure, and salinity, using the recently developed correlations of Spycher and Pruess (2005, 2010). Dissolution and precipitation of salt is treated by means of local equilibrium solubility. Associated changes in fluid porosity and permeability may also be modeled. All phases - gas, liquid, solid - may appear or disappear in any grid block during the course of a simulation. Thermodynamic conditions covered include a temperature range from about 10 to 300 °C (approximately), pressures up to 600 bar, and salinity up to NaCl (halite) saturation. Note that ECO2N can describe both sub- and supercritical states of CO_2, but applications that involves sub-critical conditions are limited to system in which there is no change of phase between liquid and gaseous CO_2, and in which no mixtures of liquid and gaseous CO_2 occur. For those cases, the fluid property module ECO2M (Pruess, 2011) may be used instead.

ECO2N V2.0 uses the same framework for describing the thermophysical status of H_2O-NaCl-CO_2 systems as its preceding version (Table 1). This paper will only describe the new enhancements which are not available in V1.0.

Table 1. Summary of ECO2N V2.0 thermophysical capabilities.

Components	# 1: water # 2: NaCl # 3: CO_2
Parameter choices (NK, NEQ, NPH, NB) = (3, 4, 3, 6) water, NaCl, CO_2, nonisothermal (default) = (3, 3, 3, 6) water, NaCl, CO_2, isothermal molecular diffusion can be modeled by setting NB = 8	
Primary Variables single fluid phase (only aqueous, or only gas)# (P, X_{sm}, X3, T) P – pressure (Pa) X_{sm} – NaCl salt mass fraction X_s (on the basis of a two-component, CO_2-free water-salt system), or solid NaCl saturation S_s+10 X3 - CO_2 (true) mass fraction in the aqueous phase, or in the gas phase, in the three-component system water-salt-CO_2 T – temperature (°C) two fluid phases (aqueous and gas)# (P, X_{sm}, S_g+10, T) P – pressure (Pa) X_{sm} – NaCl salt mass fraction X_s (on the basis of a two-component, CO_2-free water-salt system), or solid saturation S_s+10 S_g - gas phase saturation T – temperature (°C)	

When discussing fluid phase conditions, we refer to the potentially mobile (aqueous and gas) phases only; in all cases solid salt may precipitate or dissolve, adding another active phase to the system.

CODE ENHANCEMENTS

Extended CO_2-H_2O solubility model

The temperature range of the H_2O-CO_2 mutual solubility model has been extended from 110°C to about 300°C. In particular, partitioning among co-existing aqueous and gas phases is calculated based on the correlations developed by Spycher and Pruess (2005) for the low temperature range (<99°C) and Spycher and Pruess (2010) for the high temperature range (109 to ~300°C). At temperatures between 99 and 109°C, a cubic function is applied to interpolate both the equilibrium mass fraction of CO_2 in the aqueous phase and the equilibrium mass fraction of H_2O in the gas (CO_2-rich) phase. This approach guarantees a smooth transition between the low temperature and the high temperature ranges such that both the solubility function and its first derivative are continuous (Fig. 1).

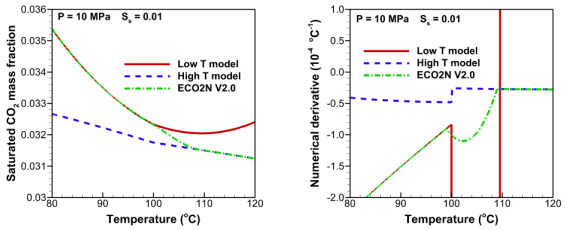

(a) (b)

Figure 1. Transition between low temperature model (<99°C) and high temperature model (>109°C). a) Computed dissolved CO_2 mass fraction (at saturation) as a function of temperature; b) the numerical derivative of the dissolved CO_2 mass fraction with respect to temperature (ΔT = 1E-8 $^oC^{-1}$). "Low T model" indicates the mutual solubility model developed by Spycher and Pruess (2005), whereas "High T model" indicates the mutual solubility model for higher temperatures by Spycher and Pruess (2010). "ECO2N V2.0" indicates the combined model implemented in ECO2N V2.0.

Non-ideal gas (CO_2-rich) phase properties

Unlike V1.0 which approximates the gas phase properties with the properties of pure CO_2, V2.0 calculates the actual properties of non-ideally mixed gas phase of CO_2 and H_2O. In the gas phase, the CO_2 behaves either as a liquid, gas, or supercritical fluid while the water could be considered as water vapor. However, water properties tend to deviate from "vapor-like" and approach "liquid-like" values as the gas phase pressure increases (Spycher and Pruess, 2011). At elevated pressures, the H_2O partial pressure in the gas phase can be well above the saturation pressure of pure H_2O, $P_{sat}(T)$. To properly model the effects of H_2O on the properties of the CO_2-rich phase, two approaches have been implemented in ECO2N V2.0: (1) The use of simple, smooth mixing functions of pure component properties (default option) and (2) the direct use of the cubic EOS implemented for solubility calculations (invoked by setting IE(16)=2 in the input file). The following is a brief description of the first approach (default). The second approach is discussed in detail by Spycher and Pruess (2010 and 2011) and will not be repeated here.

The gas phase density ρ_{gas} is calculated as a sum of the partial densities, ρ_{CO2} and ρ_{H2O}:

$$\rho_{gas} = \rho_{CO2} + \rho_{H2O} \qquad (1a)$$

The partial densities are calculated as follows:

$$\rho_{CO2} = (1 - y_{H2O})\,\rho_a(P, T)$$
$$\rho_{H2O} = \rho_{sv}(P_v, T) + X_L^{1.8}\, y_{H2O}\, \rho_{sL}(P, T) \qquad (1b)$$

where y_{H2O} is the mole fraction of H_2O in the gas phase and X_L is taken as zero if the actual partial pressure of water (P_{H2O}) is equal to, or less than, the saturation pressure of pure water (P^0_{sat}) at the prevailing temperature, or as $(1 - P^0_{sat}/P_{H2O})$ if $P_{H2O} > P^0_{sat}$ (X_L could be viewed as a factor proportional to the fraction of "liquid-like" H_2O within the total H_2O component). ρ_a and ρ_{sL} are the densities of pure CO_2 and H_2O liquid, respectively, at the prevailing temperature and pressure, whereas ρ_{sv} is the density of pure H_2O vapor at the prevailing temperature but corresponding to P_v (= $\min(P_{H2O}, P^0_{sat})$). The calculated densities compare well with the experiment data reported in the literature for various composition, pressure, and temperature (Fig. 2).

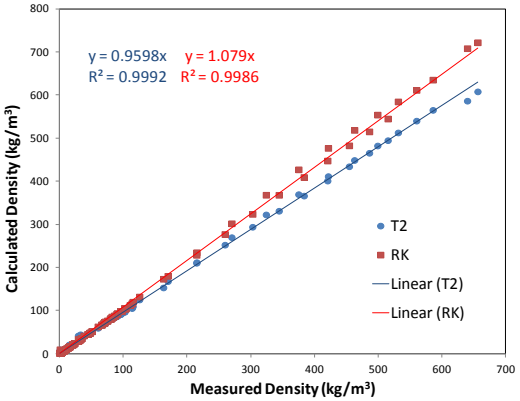

Figure 2. Comparison of computed densities of the gas phase against the experimental data reported in the literature (Fenghour et al., 1996; Patel et al., 1987; Patel and Eubank, 1988; Zawisza and Malesnska, 1981; Zakirov, 1984). "T2" indicates the default model (Eq(1)) while "RK" indicates the alternative model (IE(16)=2).

The gas phase specific enthalpy is also calculated as a sum of contributions from both components plus an empirical mixing heat term:

$$h_{gas} = y_{H2O}\, h_{H2O} + (1 - y_{H2O})\, h_{CO2} + y_{H2O}\left(\frac{P}{\rho_{gas}} - \frac{P_{H2O}}{\rho_{H2O}}\right) \qquad (2)$$

where h_{CO2} is the specific enthalpy of CO_2 component, and h_{H2O} is the specific enthalpy of the H_2O component which is calculated as:

$$h_{H2O} = (1 - X_L)\, u_{sv} + X_L\, u_{sL} + \frac{P_{H2O}}{\rho_{H2O}} \qquad (3)$$

where u_{sv} and u_{sL} are the specific enthalpies of water vapor and liquid water, respectively. The calculated enthalpy values compare well with the experiment data reported in the literature for various composition, pressure, and temperature (Fig. 3). Note that the same reference state (i.e., the internal energy of saturated liquid water equals zero at the triple point of pure water) is used in ECO2N V2.0 for both components. As a result, the enthalpy of CO_2 component in V2.0 is smaller than that in V1.0 by a constant (302192 J/kg) except when IE(16) is set to 1.

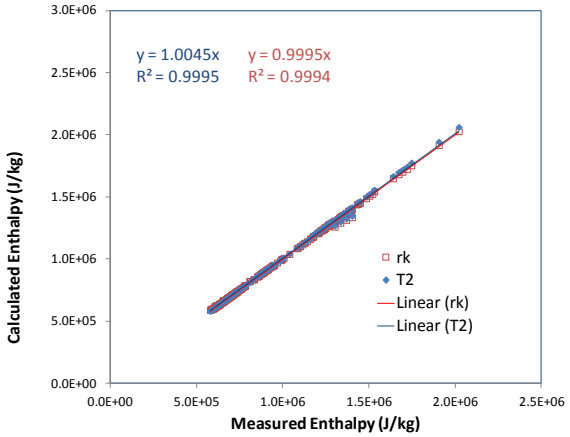

Figure 3. Comparison of computed specific enthalpy of the gas phase against the experimental data reported in the literature (Patel and Eubank, 1988; Bottini and Salville, 1985; Wormald et al. 1986). "T2" indicates the default model while "RK" indicates the alternative model (IE(16)=2).

The viscosity of the gas phase is calculated based on the fluidity method proposed by Davidson (1993).

Non-iterative calculation of specific enthalpy of dissolved CO_2 under single phase aqueous condition

The iterative calculation to obtain the saturation pressure corresponding to the given CO_2 mass

fraction in the aqueous phase, which is required to determine the specific enthalpy of the dissolved CO_2 under single-phase aqueous condition, has been replaced with a non-iterative scaling method. As a result, V2.0 does not suffer the convergence problems caused by the discontinuous first derivatives of the specific enthalpy across the CO_2 saturation line and appears more robust than V1.0 especially for nonisothermal applications, even though the calculated enthalpies of the dissolved CO_2 are practically identical in V2.0 and V1.0 (Fig. 4).

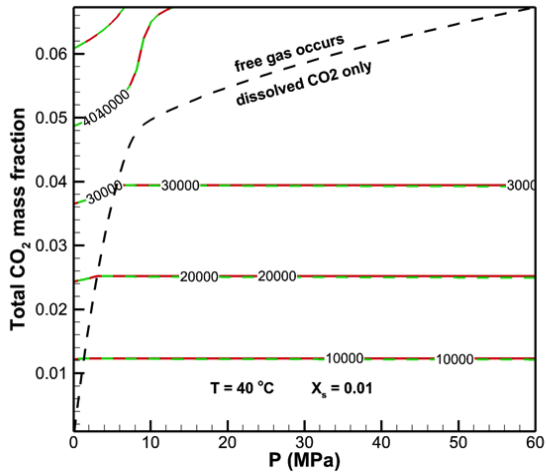

Figure 4. Contours of enthalpy contribution of dissolved CO_2 (= dissolved mass fraction multiplied by specific enthalpy), (J/kg) as a function of total CO_2 mass fraction and pressure at a given temperature (40°C) and salt mass fraction (0.01). V1.0 is the red lines whereas V2.0 is the green dashed lines. The phase partition line (black dashed line) is calculated using the correlations developed by Spycher and Pruess (2005).

Sophisticated models for effective heat conductivity

More sophisticated models for effective heat conductivity of formations containing CO_2 have been provided (optional, require some modifications to the TOUGH2 core code) for further improvement of simulation of CO_2-H_2O-NaCl systems. The new models consider the fact that the thermal conductivity of CO_2 varies greatly depending on its occurrence as a gas, a liquid, or a supercritical fluid (Fig. 5). The details of models are described in the users' guide (Pan et al., 2015).

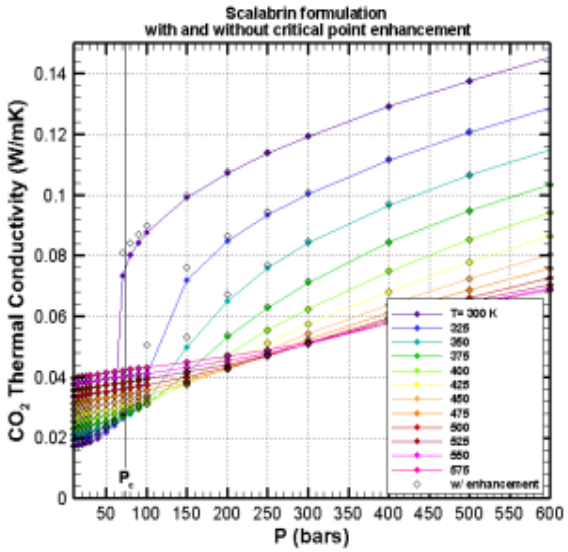

Figure 5. CO_2 thermal conductivity as a function of temperature and pressure.

EXAMPLES

The following two examples are brief summaries of the two nonisothermal problems (problems 5 and 6) in the ECO2N V2.0 users' guide (Pan et al., 2015).

Nonisothermal Radial Flow from a CO_2 Injection Well

A CO_2 injection well fully penetrates a homogeneous, isotropic, infinite-acting aquifer of 100 m thickness (Fig. 6), at conditions of 120 bar pressure, 45 ˚C temperature, and a salinity of 15 % by weight. Colder CO_2 (at 15°C) is injected uniformly at a constant rate of 100 kg/s.

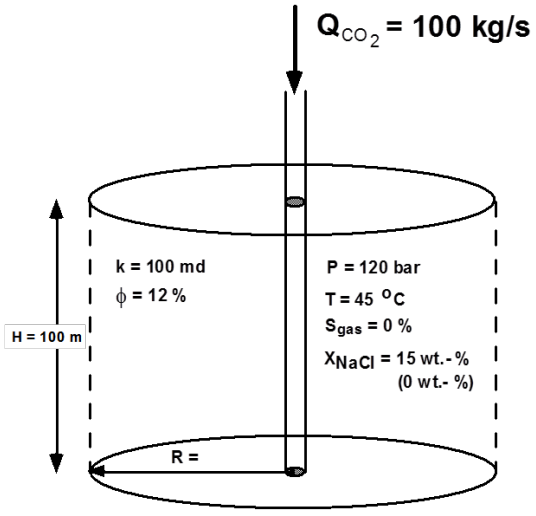

Figure 6. Schematic of radial flow sample problem

As shown in Fig. 7, three distinct regions of gas saturation (Fig. 7b), solid salt saturation (Fig. 7c), CO_2 mass fraction in liquid (Fig. 7d), and NaCl mass fraction in liquid (Fig. 7e), can be found in this nonisothermal CO_2 injection process, namely, dry-out zone, two-phase zone, and single aqueous phase zone. The two-phase zone consists of two sub-regions. In the sub-region near the dry end, the CO_2 mass fraction is higher than that in the sub-region near the wet end. The dividing point corresponds to the temperature front formed during injection of colder CO_2 into a warm aquifer (Fig. 7f). Behind the front, the temperature is low and more CO_2 can be dissolved in water, while higher temperature and less dissolved CO_2 exist ahead of the front. Interestingly, the temperature in the dry sub-region is slightly lower than the injection temperature, implying that the cooling effect due to water evaporation into the flowing CO_2 is dominating behind the temperature front, whereas the temperature in the wet sub-region is slightly higher than the ambient aquifer temperature, implying that the heating effect due to dissolution of CO_2 into water is dominating ahead of the temperature front (Fig.8). Note from the temperature profile (Fig. 7f) that because of accounting for the effects of water in the CO_2-rich phase on the enthalpy calculation, the water-evaporation induced temperature drop predicted by ECO2N V2.0 is smaller than that obtained by the cases using pure CO_2 properties for the gas phase (V1.0 or V2.0 with IE(16)=1). As shown in Fig. 7d, ECO2N V2.0 predicts slightly lower dissolved CO_2 mass fraction than ECO2N V1.0. This is related to slight differences in the implementation of the water-CO_2 solubility model. ECO2N V2.0 offers users an option to use the exact same water-CO_2 solubility model (for low temperature) as ECO2N V1.0 by setting IE(16)=1 in the input file, if 100% consistency with ECO2N V1.0 in the low temperature range is preferable.

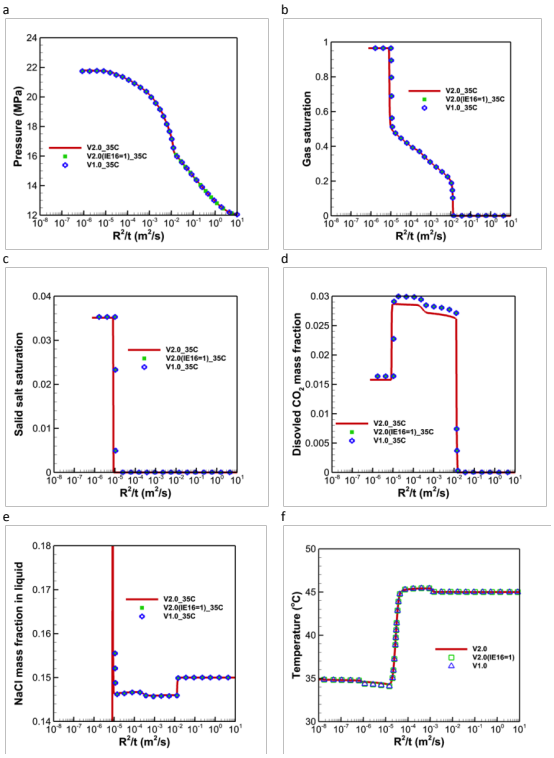

Figure 7. Simulated pressures(a), gas saturation (b), solid salt saturation (c), dissolved CO_2 mass fraction (d), dissolved NaCl mass fraction (e), and temperature (f) as a function of the similarity variable R^2/t, where R is radius from well and t is time. The thick solid red line represents the result simulated by new code (ECO2N V2.0) while the blue symbols represent the result simulated by ECO2N V1.0. The green symbols represent the result simulated by ECO2N V2.0 with IE(16)=1 to enforce using the exact same routine for calculation of mutual solubility as ECO2N V1.0. All results are time series for a grid block at a radial distance of R = 25.25 m.

The agreement between ECO2N V2.0 and ECO2N V1.0 is excellent in terms of pressure (Fig. 7a), gas saturation (Fig. 7b), and temperature (Fig. 7f), except for the differences noted above, based on more complete physics.

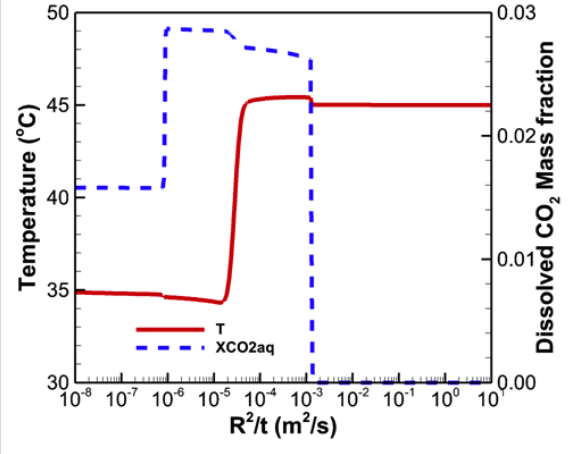

Figure 8. Simulated temperature and dissolved CO_2 mass fraction as a function of the similarity variable (nonisothermal radial flow). The thick solid red line represents temperature while the blue dash line represents the mass fraction of the dissolved CO_2 in aqueous phase. All results are spatial data at time = 8.64E7 seconds (1000 days).

GCS/GHE with a double-porosity reservoir

In this problem, we consider one injection-well/production-well pair (known as a doublet) of the five-spot pattern (Fig. 9a) that makes up a geothermal heat extraction (GHE) system combined with geological carbon sequestration (GCS). The geothermal reservoir we consider here is an idealized 100 m thick, double porosity reservoir whose parameters are shown in Table 2 and Table 3. In the double-porosity model, one continuum represents the mobile (higher permeability) regions and the other represents the immobile (lower permeability) regions. The reservoir is assumed to be initially filled with pure CO_2 in the mobile continuum and pure water in the immobile continuum, under the same hydraulic static pressure (29.15 MPa) and temperature (152.2°C). Because the mobile continuum makes up 20% of the reservoir, this initial condition is equivalent to an initial bulk gas saturation of 20%.

A two-dimensional, irregular, dual-continuum grid was created to represent the reservoir, in which each continuum is represented by a 2D mesh having the same geometry (Fig. 9b) except that the immobile continuum mesh does not have lateral connections. The two overlapping meshes are connected locally by the mobile/immobile interface defined in Table 2. In other words, fluid can flow from the injection well to the production well through the mobile continuum only, whereas the immobile continuum plays a passive role through mass and heat exchange with the mobile continuum. Grid resolution varies from 0.1 m near the wells to 50 m at far field to capture the important details of the flow field. Both the injection and the production wells are fully perforated in the reservoir (connected to the mobile continuum only). The parameters for the double porosity model used in this study are shown in Table 2.

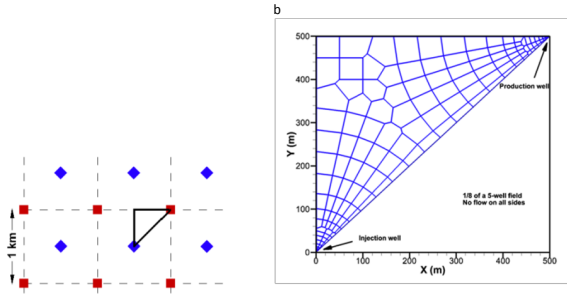

Figure 9. (a) Diagram of five-spot pattern of geothermal wells (blue-injector; red-producer); (b) Map view of the numerical grid used in the simulation. Finer grid resolution is used near the two wells.

Table 2. Parameters of the double porosity model.

Parameter	Value
Percentage of mobile pores (%)	20
Permeability of mobile continuum (m^2)	2E-14
Permeability of immobile continuum (m^2)	2E-17
Percentage of immobile pores (%)	80
Mobile/immobile interface area per unit volume (m^2/m^3)	0.2
Characteristic mobile/immobile distance (m)	5.0

With the exception of capillary strength, the parameters for relative permeability and capillary functions are the same for both continua, as shown in Table 3.

No-flow boundaries are assigned on all sides except for heat flow through the reservoir / basement rock interface, which is calculated using the semianalytical solution implemented in TOUGH2. Injection of CO_2 is simulated as a source term at the injection well cell with a rate of 6.25 kg/s (1/8 of 50 kg/s for the full well) at constant temperature of 75°C. The same flow rate is assigned for the mass produced at the production well cell.

Table 3. Other properties of the reservoir (both continua).

Parameter	Value	Note
Porosity	0.254	Uniform
Thermal conductivity	2.51 W m^{-1} K^{-1}	
Pore compressibility	10^{-10} Pa^{-1}	
Parameters for relative permeability		Liquid relative permeability using van Genuchten-Mualem model (van Genuchten, 1980) and gas relative permeability using Corey (1954) model
Residual gas saturation	0.01	
m_{VG}	0.65	
Residual liquid saturation	0.05	
Saturated liquid saturation	1.0	
Parameters for capillary pressure		Capillary pressure using van Genuchten (1980) model
Residual liquid saturation	0.03	
m_{VG}	0.4118	
α	6.08E-5 Pa^{-1} (mobile continuum) 1.216E-6 Pa^{-1} (immobile continuum)	
Maximum capillary pressure	$6.4x10^{7}$ Pa	
Saturated liquid saturation	1.0	

Fig. 10 shows six snapshots of pressure drop (from the initial pressure) in the mobile continuum during the production. The reservoir pressure drops quickly at early time and then slowly recovers to some degree. As a result, the pressure drop after 1 year is the biggest among the six snapshots. This implies that the reservoir pressure loss is mainly caused by the volume imbalance due to production of hot CO_2 and injection of cold CO_2. Such volume loss is gradually compensated by the expansion of the injected "cold" CO_2 with time. Fig. 11 shows the temperature distribution in both continua at various times. The cold front advances with time from the injection well to the production well. There is a time-delay in the immobile continuum in such propagation, especially at early time.

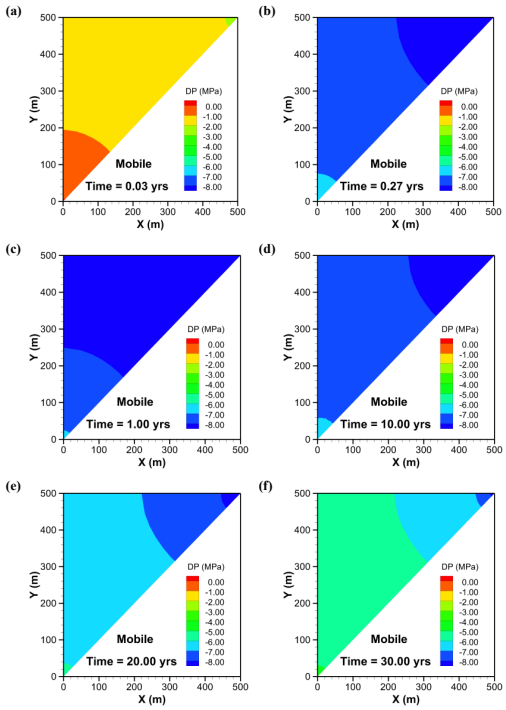

Figure 10. Simulated pressure drop (from the initial reservoir pressure) in the reservoir (a) 10 days, (b) 100 days, (c) 1 yr, (d) 10 yrs, (e) 20 yrs and (f) 30yrs.

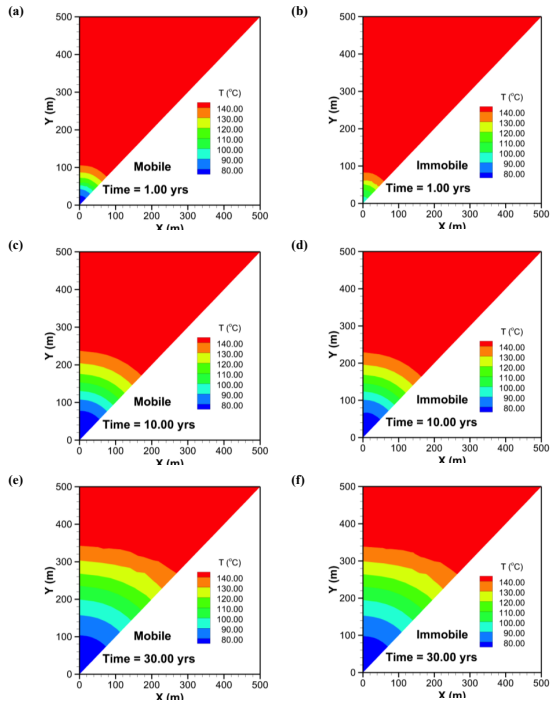

Figure 11. Simulated temperature in the reservoir after 1 year ((a) and (b)), 10 years ((c) and (d)), and 30 years ((e) and (f)) in the two continua.

Fig. 12 shows three snapshots of gas saturation in each continuum during production. The gas saturation in the immobile continuum slowly

increases with time as CO_2 enters from the mobile continuum. The gas saturation in the mobile continuum first drops over the entire domain and then increases near the injection well as injection continues, forming a significant gradient from the injection well to the production well. Water accumulates in the region close to the production well (Fig. 12e). However, the liquid phase production rate is small for most times (Fig. 13a), and the CO_2 component in the total production is larger than 97% (Fig. 13b).

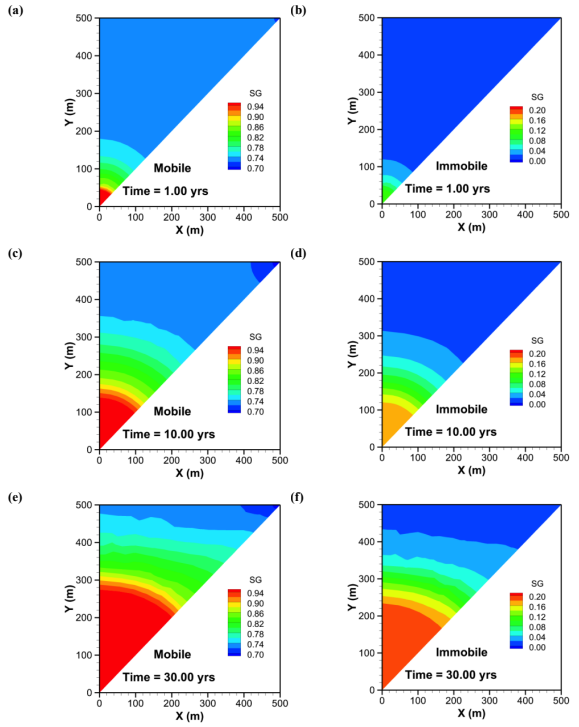

Figure 12. Simulated gas saturation in the reservoir after 1 year ((a) and (b)), 10 years ((c) and (d)), and 30 years ((e) and (f)) in the two continua. Different color scales are used for each continuum.

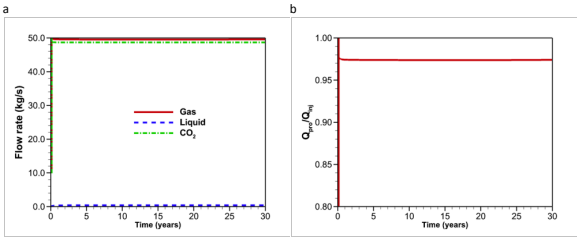

Figure 13. (a) Simulated gas and liquid phase flow rates as well as CO_2 component flow rate and (b) Ratio of CO_2 injection rate and production rate. Because the total injection (pure CO_2) rate and the total production (mixture) rate are equal, this ratio is also a measure of how much CO_2 enters the production stream.

CONCLUSIONS

ECO2N V2.0 is an extension and upgrade of ECO2N V1.0, a fluid property module for the multiphase, multicomponent simulator TOUGH2, Version 2.1. It provides capabilities for modeling advective and diffusive flow and transport in multidimensional heterogeneous systems containing H_2O - NaCl - CO_2 mixtures. Process capabilities include coupling between fluid and heat flow, partitioning of H_2O and CO_2 among different phases, and precipitation/dissolution of solid salt. The code represents thermophysical properties of brine-CO_2 mixtures generally within experimental accuracy for the range of conditions of interest in geologic disposal of CO_2 and CO_2 enhanced geothermal reservoirs. A fluid property table provided with ECO2N V2.0 covers temperatures from ambient to 307°C and pressures from ambient to 600 bars. Super- as well as sub-critical conditions may be modeled, but the code currently has no provisions to treat separate liquid and gas CO_2 phases, or transitions between them.

ACKNOWLEDGMENT

This work was partly supported by the TOUGH Royalty Fund, the Director, Office of Science, Office of Basic Energy Sciences of the U.S. Department of Energy, and by the Zero Emission Research and Technology project (ZERT) under Contract No. DE-AC03-76SF00098, and the Assistant Secretary for Energy Efficiency and Renewable Energy, Geothermal Technologies Program of the U.S. Department of Energy under Contract No. DE-AC02-05CH11231.

REFERENCES

Corey, AT. The interrelation between gas and oil relative permeabilities, *Producers Monthly*, 19(1), 38-41, 1954.

Pan, L. N. Spycher, C. Doughty, and K. Pruess. ECO2N V2.0: A TOUGH2 fluid property module for mixtures of Water, NaCl, and CO_2, *Rep. LBNL-6930E*, Lawrence Berkeley National Lab., Berkeley, CA, 2015.

Pruess, K., ECO2M: A TOUGH2 fluid property module for mixtures of water, NaCl, and CO_2, including super- and sub-critical conditions, and phase change between liquid and gaseous CO_2, *Rep. LBNL-4590E*, Lawrence Berkeley National Lab., Berkeley, CA 2011.

Spycher, N. and K. Pruess. CO_2-H_2O Mixtures in the Geological Sequestration of CO_2. II. Partitioning in Chloride Brines at 12–100 ˚C and up to 600 bar, *Geochim. Cosmochim. Acta,* 69, 13, 3309–3320, doi:10.1016/j.gca.2005.01.015, 2005.

Spycher, N. and K. Pruess. A phase partitioning model for CO_2-brine mixtures at elevated - temperatures and pressures: Application to CO_2-enhanced geothermal systems, *Transport in Porous Media*, 82, 173-196. doi: 10.1007/s11242-009-9425-y. 2010.

Spycher, N. and K. Pruess. A model for - thermophysical properties of CO_2-brine mixtures at elevated temperatures and pressures, PROCEEDINGS, Thirty-Sixth Workshop on Geothermal Reservoir Engineering, Stanford University, Stanford, California, January 31- February 2, 2011.

van Genuchten, M.Th. A closed-form equation for predicting the hydraulic conductivity of unsaturated soils, *Soil Science Society of America Journal,* 44(5), 892–8, 1980.

THE EFFECT OF NATURAL GROUNDWATER FLOW ON CO_2 MIGRATION AND TRAPPING: THE CASE OF THE JURASSIC SALINE AQUIFER OF THE NEGEV (ISRAEL)

Ravid Rosenzweig and Ran Calvo

Geological Survey of Israel
30 Malkhe Israel st.
Jerusalem, 95501, Israel
e-mail: rravid@gsi.gov.il

ABSTRACT

Mathematical modeling of migration and trapping of injected CO_2 in geologic media is an essential tool in the evaluation of the performance and safety of CO_2 storage projects. Simulations of injection scenarios require detailed knowledge of the geometry, petrophysical properties and flow characteristics of the host formation to provide a reliable prediction. In many of the previous studies, it was assumed that the water in the host aquifer is stagnant and the velocity of the groundwater wasn't taken into consideration. Although the velocity of the saline aquifers considered for CO_2 storage is typically small, in many aquifers it is not zero. In the current research the effect of the groundwater velocity on CO_2 migration and trapping is examined by considering the case study of the Jurassic aquifer of the Negev, Israel.

The Jurassic aquifer of the Negev is a saline, multi-layered aquifer. Previous studies found a pressure gradient of 0.44 bar/km across the aquifer. This pressure gradient amounts to a velocity of about 10 cm/year.

In the current research we perform three-dimensional simulations of CO_2 injection into the Jurassic aquifer using the TOUGH2 /ECO2N or TOUGH2/ECO2M simulators. We compare the migration and trapping of CO_2 with and without groundwater velocity for different structural settings typical of the aquifer and by considering either a homogeneous aquifer or the full layered geometry. We show that in some cases considering groundwater velocity is important for the accurate determination of the extent of CO_2 migration and the degree of trapping.

INTRODUCTION

Injection of carbon dioxide (CO_2) into deep geological formations bearing saline water is widely considered as a promising approach for the reduction of greenhouse gas emissions (IPCC, 2005; Orr, 2009).

As injection projects involve a substantial capital investment and a certain degree of environmental risks, mathematical modeling of the injection, migration and trapping of CO_2 is essential for the evaluation of the performance and safety of CO_2 storage projects. Reliable models require detailed information of the geometry, the petrophysical properties and of the flow characteristics of the host formation. In most studies, it was assumed that there is no natural groundwater flow (e.g., Tran Ngoc et al., 2013; Zhou et al., 2010) while in many cases groundwater has small, yet nonzero, velocity (e.g, Alberta basin, Canada, Bachu et al., 1994; the Frio formation, Texas, USA, Szulczewski et al., 2012).

While ignoring natural groundwater flow can simplify modeling by using a two-dimensional radially-symmetric geometry instead of the full three-dimensional, groundwater flow can affect migration and trapping dynamics in several ways. First, the extent of the CO_2 plume may be elongated in the flow direction, while it may be shortened or even arrested in the counter-flow direction. Second, natural flow dynamics may affect trapping. In particular, groundwater flow can remove CO_2-saturated brine from the plume/brine interface, replacing it with unsaturated brine, thus enhancing dissolution.

In this work we study the effect of natural groundwater flow on CO_2 migration and trapping for different structural settings of the

Jurassic aquifer of the Negev. The aquifer is modeled either as a homogeneous permeable medium or as a multilayered medium. For each setting we compare the results of the homogeneous and multilayered simulations with and in the absence of natural groundwater flow.

RESEARCH SITE

The Jurassic middle aquifer is located in the Negev, Israel and extends between the Mediterranean Sea and the Dead sea Valley. The aquifer is exposed at the three craters of the Negev and deepens towards the north-west where the depth of the top of the aquifer reaches more than 2500 m. In about 70% of the research area the top of the aquifer is deeper than 800 m. The aquifer thickness ranges from 100 m in the south to more than 2400 in the north-west (Calvo and Gvirtzman, 2013).

The hydrogeology of the aquifer was studied by Nativ et al. (1987). The stratigraphic sequence of the aquifer as identified by Nativ et al. (1987) and later modified by Calvo and Gvirtzman (2013) is presented in Figure 1. The units of the Jurassic aquifer are marked in red and the units of the overlying aquitard are marked in green. The aquifer strata consist of a gypsum-carbonate base (Ardon) overlaid by a thick porous sandstone layer (Inmar, up to 20% porosity and 100 md permeability) which is divided by a carbonate layer (the Queren member). On top of the Inmar, the lithostratigaphy is of alternating layers of carbonate, shale and sandstone (Daya and Sherif formations) while the top formation (Zohar) consists of fractured carbonate rock having low matrix porosity (Nativ et al., 1987). The aquifer is bounded on top by an aquitard made out of low-permeability shales (Kidod, Beer Sheva and Haluza formations having permeability of 0.1-0.01 md, Calvo and Gvirtzman, 2013).

Calvo et al. (2014) studied the petrophysical properties of the aquifer rocks. They used a database of over 2000 petrophysical analyses conducted throughout the years at the Geological Survey of Israel (GSI). The rock samples were taken from cores that were recovered from boreholes penetrating the aquifer. The distributions of the porosity and permeability of the aquifer and aquitard formations is presented in Figure 2. The median porosity of the individual geological units of the aquifer ranges from just below 4% to over 13%, while the permeability spans three orders of magnitude.

Nativ et al. (1987) found, by analyzing pressure well-test data, an average pressure gradient of -0.44 bar/km towards the south east, indicating a slow groundwater flow towards the Dead Sea Valley. The water salinity at the wells (in terms of TDS) ranges between 4200 mg/l to 190,000 mg/l, where higher salinity was found in the western part of the aquifer (Calvo and Gvirtzman, 2013).

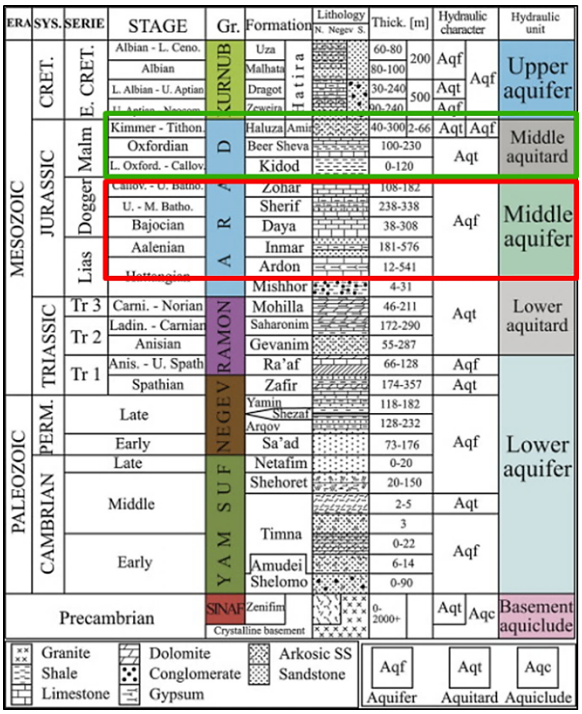

Figure 1. Stratigraphic and hydrostratigraphic sequence of the Negev (Calvo and Gvirtzman, 2013). The Juassic aquifer and sealing aquitard are marked in red and green, respectively.

MODEL SETUP

To study migration and trapping of CO_2 in the saline aquifer, two types of models were used: homogeneous models where representative parameters were assumed for the entire aquifer thickness and layered models in which the aquifer was assumed to consist of several homoge-

neous layers, each with its own set of parameters.

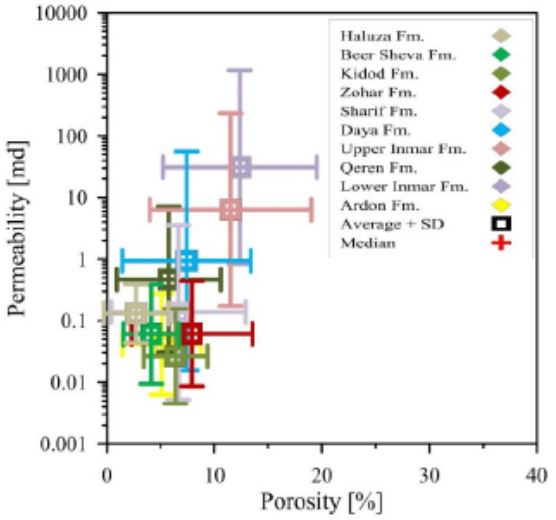

Figure 2. Porosity and permeability distribution of the units of the Jurassic aquifer and the overlaying aquitard (Calvo et al., 2014).

Conceptual and geometrical model

The 3D aquifer was modelled by using a domain of 40 km in the streamwise direction, 1000 m in the vertical direction, and 20 km in the spanwise direction, representing half of the width of the aquifer. The injection well was located at the midpoint of the aquifer length (x= 0) and at y = 0, exploiting the symmetry in the y direction. The thickness of the aquifer was taken as 1000 m and 1050 m in the homogeneous and layered simulations, respectively. These values are close to the mode of the distribution of the thickness of the Jurassic aquifer (Calvo et al., 2014). The length of the domain was chosen such that the pressure pulse generated by CO_2 injection would not affect the distant boundary.
The well injects CO_2 into the bottom 100 m of the aquifer at a rate of 50 kg/s (25 kg/s for half of the aquifer) for 30 years. All simulations modeled additional 200 years of the post-injection phase.

A hydrostatic pressure distribution and a geothermal gradient of 21 ^{o}C/km (Calvo and Gvirtzman, 2013) were specified in the vertical direction as initial conditions. It was assumed that the top of the aquifer is at a depth of 900 m below the surface and that the surface temperature is 15 ^{o}C. For simulations where natural groundwater flow was considered, a horizontal pressure gradient of -44 bar/km was specified in addition. Water salinity was assumed to be 2%. Constant pressure boundaries were assigned in the lateral boundaries to represent open boundaries while no-flow boundary condition was specified for the top and bottom boundaries. Before injection, simulations were left to run for 500-1000 years, to reach a steady state.

Three structural settings were investigated; a horizontal aquifer, an anticline and a sloping aquifer. An anticline was generated by varying the topography of geological units of the aquifer according to a 2D Gaussian function with the top of the Gaussian located at the origin,

$$z = A_z \cdot \exp\left(-\frac{x^2}{2\sigma_x^2} - \frac{y^2}{2\sigma_y^2} \right) \quad L_z \qquad (1)$$

where L_z, A_z σ_x, and σ_y are the z coordinate of the base of the curved surface, the maximum height of the Gaussian and the width parameters in the x and y directions, respectively. Values of $\sigma_x = 1165\,m$, $\sigma_x = 2330\,m$ and $A_z = 200\,m$ were assigned to represent an anticline of 200 m height and 5 km x 10 km dimensions in the x and y directions, respectively. These dimensions are characteristics of the Negev Syrian arc folds. Boundary conditions were slightly modified to generate the desired temperature distribution along the vertical direction given the curved geometry of the anticline. At the bottom boundary, a constant heat flux was specified to maintain the geothermal temperature gradient while at the top boundary the temperature was kept constant by enlarging the specific heat of the top 1 m to 10^{40} J/kg/C.

For the sloping aquifer, a tilt angle of 4.5^{o} was chosen. This angle represents the average slope of a 20 km section in the Jurassic aquifer calculated along a seismic line. It was assumed that the highest point of the modeled domain lies in a depth of 900 m such that in all the aquifer the CO_2 would be in a supercritical state. The geometry of the computational domain of the sloping aquifer was a little different than the one generated for the horizontal and anticline settings. Since the migration of the CO_2 in the upstream (and downdip) direction is expected to be small,

a domain length of 30 km was chosen where the well was located at 10 km from the upstream boundary. The other dimensions were similar to those of the other two settings.

Homogeneous model

The petrophysical properties assigned for the homogeneous aquifer are given in Table 1. The values of permeability and porosity were taken from the high end of the range of the measurements (Figure 2) to simulate the "worst case scenario" of maximum CO_2 migration. Also, the effective permeability of the fractured formations is much higher than the one measured from rock cores. Therefore the measured values presented in Figure 2 are expected to underestimate the effective permeability of some of the formations.

Table 1. Petrophysical properties used for the homogeneous simulations.

Property	Description	Value
k (md)	permeability	100
ϕ	porosity	0.1
m	van Genuchten's fitting parameter	0.457
S_{wr}	Residual water saturation	0.2
S_{gr}	Residual gas saturation	0.1
$1/\alpha$ (Pa)	van Genuchten fitting parameter	19,560
ρ_s (kg/m^3)	Grain density	2600
C (J/kg/ºC)	Specific heat	1000
C_r (1/ Pa)	Pore compressibility	4.5E-10

Multilayered model

A layered model that takes into account the properties of the individual geological units was assembled. The thickness and petrophysical properties of the units are listed in Table 2. Representative thicknesses were obtained from Calvo (2014). Porosity values were taken as the median values in Figure 1. The median permeability values of Table 1 were also used for the sandstone formations (Upper and lower Inmar) and for the Queren member. For the other formations (Daya, Sherif and Zohar), effective permeability values were taken from well tests reported in Nativ et al. (1987). These permeabilities are much higher than those obtained from cores. This discrepancy probably reflects the presence of fractures in the formations. Grain density values were taken either from the database of the GSI or from Helium piconometry measurements (Calvo et al., 2014).

The parameters of the capillary curve (S_{wr}, m, and α) were taken from mercury injection porosimetry measurements conducted for representative cores (Calvo et al., 2014). The measured capillary curves were fit to van Genuchten's (1980) relation. It was assumed that the empirical parameters obtained for the capillary curve can also be used to describe the relative permeability function of the water by using the Mualem (1976)-van Genuchten (1980) function. The other parameters were left identical to those used in the homogeneous simulation (Table 1).

Numerical solution

The ECO2N and ECO2M modules of the TOUGH2 package were used (Pruess et al., 1999). ECO2M was used for the case of the sloping aquifer since an extended temperature range (T <110 C^0 instead of T<100 C^0) was needed to account for the temperature at the deepest parts of the tilted aquifer.

A structured computational grid was constructed by the graphical user interface Petrasim. The grid was refined near the well and near the top boundary to resolve the flow in areas where large gradients are expected. The overall number of cells was between 59,520 and 72,800.

Table 2: Geometrical and petrophysical properties of the geological units used in the layered simulation.

Property / Layer	Thickness (m)	ϕ	k (md)	m	S_{wr}	$1/\alpha$ (Pa)	ρ_s (kg/m^3)
Lower Inmar	100	0.11	61.8	0.657	0.044	4371	2651
Queren	130	0.039	0.4	0.408	0.116	40	2720
Upper Inmar	160	0.106	10	0.546	0.056	3022	2648
Daya	180	0.054	8.5	0.521	0.123	3.9E5	2693
Sherif	320	0.047	16.3	0.152	0.000	1250	2707
Zohar	160	0.07	19.9	0.233	0.000	5425	2705

RESULTS AND DISCUSSION

Homogeneous model

Contours of CO_2 saturation along a vertical cross-section at y = 0 taken at the end of the simulation (200 years post-injection, 230 years after the beginning of the injection) are shown in Figure 3. The difference in plume spread between the three structural settings is evident. While the CO_2 plume injected below the anticline is fully contained within the anticline, in the horizontal and sloping aquifer cases a thin CO_2 plume is generated below the caprock. The CO_2 plume stretches in the streamwise and in the updip direction (for the sloping aquifer), showing the effect of groundwater flow on the shape and extent of the CO_2 plume.

Figure 4 shows the evolution of the plume extent (maximum distance of mobile CO_2 in the upstream and downstream directions) for the three structural settings and for the case of a horizontal aquifer with no groundwater flow. Again it is shown that the structural setting of the aquifer controls the extent of the plume. While the anticline dimensions control the extent of the plume, in the horizontal and in particular in the sloping aquifer case the plume extends to 8 and 20 km (the entire domain length), respectively. It is also shown that groundwater flow has a substantial effect on plume migration where the plume extent in the no-flow case reaches only 6 km, with respect to 8 in the flow case. It is interesting to note that the difference between the two cases is particularly shown in the post-injection phase.

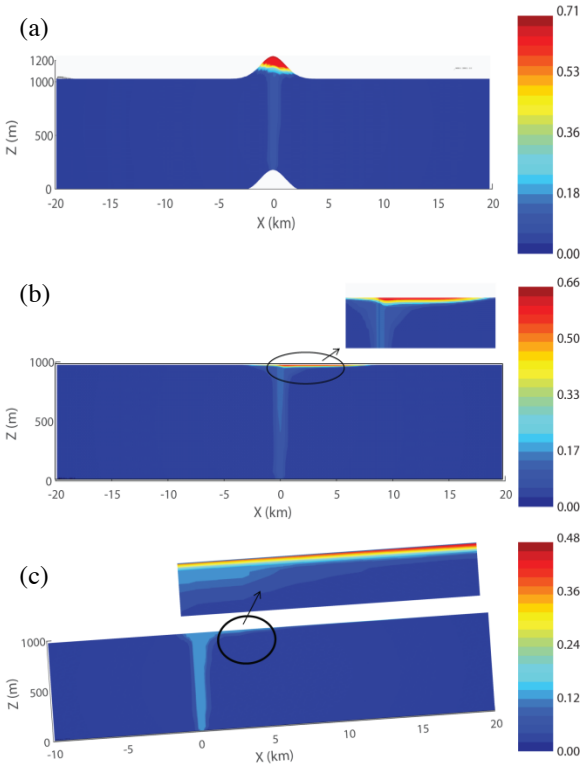

Figure 3. CO_2 saturation along a vertical cross section at y = 0 at the end of the simulation (200 years post-injection) obtained for the homogeneous aquifer. The injection well is located at x = 0. Groundwater flow is from left to right. (a) injection below an anticline (b) horizontal aquifer (c) sloping aquifer.

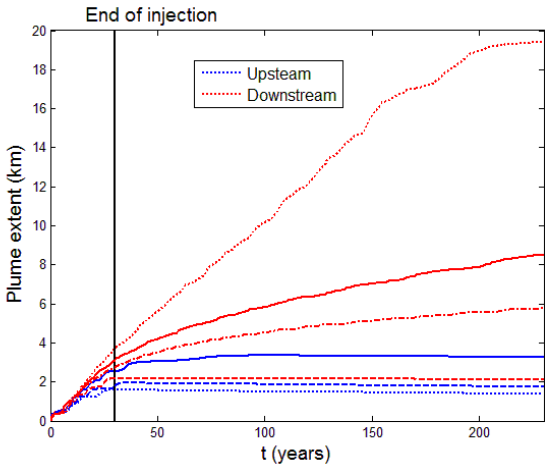

Figure 4. Evolution of the plume extent in the upstream (blue) and downstream (red) directions for the homogeneous simulations. Solid curve- horizontal aquifer, dashed-dot- horizontal aquifer with no-flow, dashed-injection below an anticline, dot- sloping aquifer.

Figure 5 depicts the evolution of mobile, capillary-trapped ($S_g < S_{gr}$) and dissolved CO_2 in time. It is shown that during the post-injection period the CO_2 slowly dissolves, decreasing the fraction of mobile CO_2. The fraction of trapped CO_2 remains nearly constant in time and is strongly dependent on the value of S_{gr} specified (data not shown). It is shown that the fraction of dissolved CO_2 is the smallest when the CO_2 is injected below an anticline and the largest for the case of a sloping aquifer. The mobile CO_2 fraction is the largest when the CO_2 is injected below an anticline and the smallest for the case of a sloping aquifer. This can be the result of a limited interfacial area between the CO_2 plume and the brine in the anticline versus a large interfacial area in the sloping aquifer. As the interfacial area increases, the macroscopic dissolution rate increases and more CO_2 dissolves. Thus, there is a tradeoff between plume extent and CO_2 dissolution. The curves for the horizontal no-flow case exhibit lower dissolution with respect to the horizontal-flow case, leading to more mobile CO_2. Again, this difference is evident in the post-injection phase.

Multilayered model

Figure 6 presents the CO_2 saturation in a vertical cross-section at y = 0 taken at the end of the simulation (200 years post-injection) for the three structural settings and for the layered aquifer. Figure 7 shows the evolution of the plume extents for the layered simulations. The shapes of the plumes are very different from the ones obtained in the homogeneous aquifer. A strong secondary-seal effect is shown where the low permeability Queren unit and, to a lesser extent, the Daya unit impedes the upward migration of CO_2. After 200 years post-injection, the plume reaches only the bottom three layers because of permeability and capillary effects. The lateral migration of the plume is also hindered as compared to the homogeneous simulation. As in the homogeneous simulations, groundwater flow enhances plume spreading in the streamwise direction; this is particularly noticeable in the horizontal simulation. No significant differences were found in the fraction of mobile, dissolved and capillary-trapped CO_2 between the flow and no-flow cases. This is probably because of the smaller difference in the extent of the plume and the higher saturations in the layered simulations which reduce contact between CO_2 plume and brine.

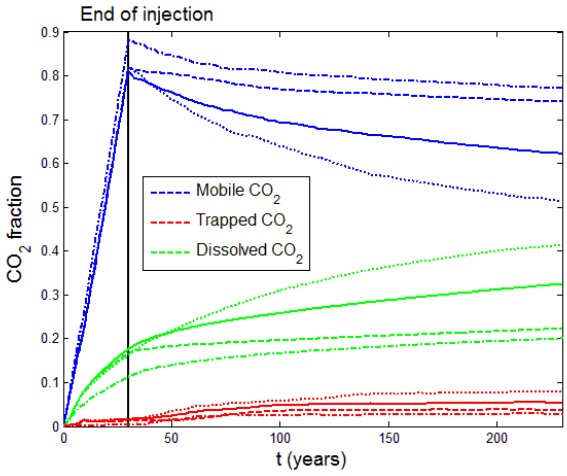

Figure 5. Fractions of mobile (blue), capillary-trapped (red) and dissolved (green) CO_2 obtained for the homogenous simulations. Solid curve- horizontal aquifer, dashed-dot- horizontal aquifer with no-flow, dashed-injection below an anticline, dot-sloping aquifer.

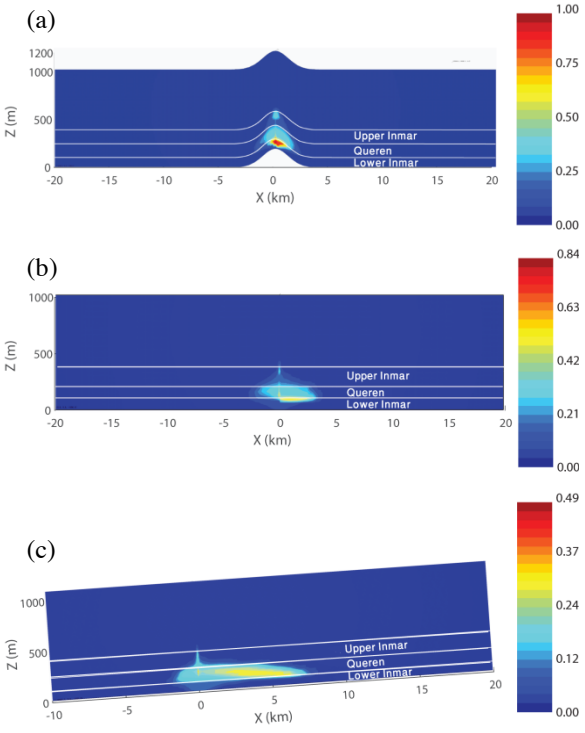

Figure 6. CO_2 saturation along a vertical cross section at y = 0 at the end of the simulation (200 years post-injection) obtained for the multilayered aquifer. The injection well is located at x = 0. Groundwater flow is from left to right. (a) injection below an anticline (b) horizontal aquifer (c) sloping aquifer. The three bottom layers are indicated.

SUMMARY AND CONCLUSIONS

In this study CO_2 migration and trapping in the Jurassic aquifer of the Negev was simulated. In particular, the effect of natural groundwater flow on the plume extent and the trapping efficiency was investigated. The aquifer was modeled either as a permeable homogeneous medium or as a multilayered aquifer consisting of six distinct geological units with each having its own set of petrophysical parameters. Three structural settings were investigated: horizontal aquifer, sloping aquifer and an anticline.

The results of the homogeneous simulations show that the structural setting of the aquifer plays a significant role in CO_2 migration and trapping. While anticlines of the size of the Negev arcs are able to stratigraphically trap the injected CO_2 and limit its migration, injection into sloping aquifers result in very large plumes that spread to a distance of tens of kilometers. It was shown that there is a tradeoff between the size of the plume and the fraction of mobile CO_2. When the plume is confined to a small area, more CO_2 remains mobile while large plumes are associated with high dissolution rates and less mobile CO_2. An effort should be made to maximize dissolution rates while minimizing the plume size.

A comparison between the flow and no-flow case of the horizontal aquifer indicates that groundwater flow enhances plume migration at the downstream direction and CO_2 dissolution at the post-injection phase.

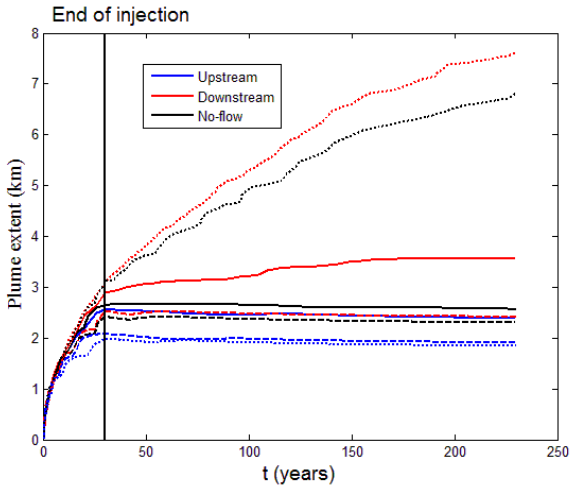

Figure 7. Evolution of the plume extent in the upstream (blue) and downstream (red) directions and for the no-flow case (black) obtained for the layered simulations. Solid curve- horizontal aquifer, dashed-injection below an anticline, dot- sloping aquifer. The plume extent for the no-flow sloping aquifer was taken in the updip direction.

The results of the layered simulations show the importance of accounting for the individual geological units that comprise the aquifer. A strong secondary seal effect is demonstrated where low permeability and capillary effects impedes the vertical and lateral migration of CO_2. This results in a much smaller plume area and generally in higher saturations with respect to the homogeneous case.

Although a significant effect of groundwater flow on the trapping efficiency wasn't found in the layered simulations, it was shown that groundwater flow still plays a significant role in plume migration. Groundwater flow enhances plume spread in the downstream direction and slightly limits the spread at the upstream direction.

We conclude that it is important to account for natural groundwater flow when modeling CO_2 storage even when water velocity is fairly small.

ACKNOWLEDGMENT

The generous financial support of the Israeli ministry of National Infrastructures Energy and Water under research and development grant No. 213-17-013 is gratefully acknowledged.

REFERENCES

Bachu, S., W.D. Gunter, and E.H. Perkins, Aquifer disposal of CO_2 - hydrodynamic and mineral trapping, *Energy Conversion and Management,* 35(4) 269-279, 1994.

Calvo, R., *A comparative study for potential CO_2 storage units in the subsurface Paleozoic-Mesozoic section in southern Israel: the Arad group*, GSI report GSI/25/14: Jerusalem, Israel, 2014.

Calvo, R., and Z. Gvirtzman, Assessment of CO_2 storage capacity in southern Israel, *International Journal of Greenhouse Gas Control,* 14(0) 25-38, 2013.

Calvo, R., R. Knafo, and R. Rosenzweig, *A comparative study for potential CO_2 storage units in the subsurface Paleozoic-Mesozoic section in southern Israel: Petrological and petrophysical dataset*, GSI report GSI/24/2014: Jerusalem, Israel, 2014.

IPCC, *Underground geological storage*, In: Metz, B., Davidson, O., de Coninck, H.C., Loose, M., Meyer, L.A. (Eds.), IPCC Special report on carbon dioxide capture and storage. Cambridge university press: Cambridge, UK, 2005.

Mualem, Y., New Model for Predicting Hydraulic Conductivity of Unsaturated Porous-Media, *Water Resources Research,* 12(3) 513-522, 1976.

Nativ, R., Y. Bachmat, and A. Issar, Potential use of the deep aquifers in the Negev desert, Israel- A conceptual model *Journal of Hydrology,* 94(3-4) 237-265, 1987.

Orr, F.M., Onshore Geologic Storage of CO2, *Science,* 325(5948) 1656-1658 2009.

Pruess, K., C. Oldenburg, and G. Moridis, *TOUGH2 user's guide, version 2*, Report LBNL-43134 Lawrence Berkeley National laboratory: Berkeley, California, 1999.

Szulczewski, M.L., C.W. MacMinn, H.J. Herzog, and R. Juanes, Lifetime of carbon capture and storage as a climate-change mitigation technology, *Proceedings of the National Academy of Sciences of the United States of America,* 109(14) 5185-5189 2012.

Tran Ngoc, T., C. Doughty, R. Lefebvre, and M. Malo, Injectivity of carbon dioxide in the St. Lawrence Platform, Quebec (Canada): A sensitivity study, *Greenhouse Gases: Science and Technology,* 3(6) 516-540, 2013.

van Genuchten, M.T., A closed-form equation for predicting the hydraulic conductivity of unsaturated soils, *Soil Science Society of America Journal,* 44 892-898, 1980.

Zhou, Q., J.T. Birkholzer, E. Mehnert, Y.F. Lin, and K. Zhang, Modeling basin-and plume-scale processes of CO2 storage for full-scale deployment, *Groundwater,* 48(4) 494-514, 2010.

RISK SCENARIO ANALYSIS FOR HETEROGENEOUS GEOLOGICAL MODEL IN A CARBON SEQUESTRATION APPLICATION IN CENTRAL TAIWAN

Chi-Wen Yu, Shih-Chang Lei

Sinotech Engineering Consultants Inc.
3F, No. 280, Xinhu 2nd Rd., Neihu Dist.
Taipei City 11494, Taiwan, R.O.C
e-mail: yu1014@sinotech.org.tw and leishihjhang@sinotech.org.tw

ABSTRACT

In this study, scenario analyses to reveal the geo-sequestration risk of the cap rock system associated with a heterogeneous rock formation within the Tai-Hsi Basin were carried out. Three deep-seated and typical target storage cap and reservoir systems (R-1, R-2, and R-3) of the candidate sequestration site were identified by a 3000 m deep borehole and considered to consist mainly of interlayered sandstone, siltstone, and shale. The intra-formational seal capability characterized by multi-layered shale baffles to act as the primary or ultimate cap system were taken into account by homogeneous and heterogeneous models. The relevant ranges of input parameters for porosity (20~35%) and permeability (0.0001~1000 mD) for the sandstone (storage layers) and shale (seals) have been selected, according to results of a large amount of laboratory core tests. Typical injected plume migration scenarios were stochastically simulated, including a 20-year continuous injection (one Mt-CO_2 per year) followed by a 1000-year post-injection monitoring period. The corresponding 2-D maximum horizontal migration distances (MHMD) of the CO_2 plume in the storage reservoir were calculated for heterogeneous reservoir models and their homogeneous counterparts. Moreover, the induced pressures at critical monitoring points above the injection zone were also evaluated. As a result, the shale baffles forming an intra-formational seal in a saline aquifer are shown to play a vital role, and to be capable of ensuring the safe carbon storage operation at a basin scale with a depth range of about 2100 to 2500 mRT (meters below rotary table).

INTRODUCTION

Carbon sequestration is a vital approach to combat the high CO_2 emissions causing the problem of global warming. It has been recommended by scientists that preferred sequestration sites be targeted in deep saline aquifers usually found in vast sedimentary basins. Additionally, it is more economical to select deep saline aquifers that are adjacent to high emission sources such as coal-fired power stations in coastal areas. However, to be considered safe, a competent cap rock system must exist, in order to minimize the geo-sequestration risk of forming a leakage pathway.

In many empirical cases, cap rock systems associated with interlayered sandstone and shale are encountered in shallow sedimentary basins around the world. Unlike a well-defined thick layer of cap rock possessing a great lateral extent, an intra-formational seal type of cap rock system characterized by frequently occurring intervening thin shale lenses, or baffles, within the main sandstone reservoirs is regarded as the realistic seal mechanism in most cases.

Sinotech Engineering Consultants, Inc. (Sinotech Inc.) has been commissioned by Taiwan Power Company (Tai-Power) since 2009 to investigate the Tai-Hsi Basin through on-site seismic surveys (Sinotech Inc., 2011; Yu et al., 2011) and deep drilling around a candidate site located in Chang-Hua coastal industrial park in Central Taiwan. A 3000 m deep pilot drilling (M-1 well) was launched in July 2012 and concluded in November 2013 (Yu et al., 2014).

The above-mentioned studies confirmed the local stratigraphic sequence and the top depth (by mRT) and thickness (m) of major formations, and obtained more than 1390 m long cores from depths of 1505 mRT to 3005 mRT. These cores

were sampled and extensively examined by laboratory analysis and testing. According to some preliminary as well as comprehensive results, it is confirmed that many target - sandstone-rich formations or deep saline reservoirs within Tai-Hsi Basin are very suitable (e.g., IEA, 2009; DNV-GL, 2012) for developing geological storage (Yu et al., 2011, 2014; Sinotech Inc., 2014).

Table 1 shows the on-site stratigraphic sequence and the thickness (m) of all the major formations revealed in the recently completed M-1 well (Sinotech Inc., 2014). The large amount of core recovered has shown that the lithological units are dominated by interlayered sandstone and shale, and indicates that these rocks were deposited in a shallow marine environment.

CONCEPTUAL GEOLOGICAL MODEL

Area of Interest

As shown in **Fig. 1**, some 30 km radial distance around the drilling site of M-1 well has been allocated (Sinotech Inc., 2011, 2014) as an area of interest for developing the geological model for the purpose of CO_2 sequestration. Some exploratory wells drilled by CPC (Taiwan Petroleum Company) are sparsely distributed around the highlighted area, and also a coal-fired power plant is located 15 km to the north of the M-1 drilling site. The area of interest is located inside a Geological Subzone of Taiwan, locally named Tai-Hsi Basin (Lin et al., 2003). This relatively young basin is basically a foreland basin produced by an orogenic activity starting in the Early Pliocene. The candidate site is part of a foreland bulge that lies within the southern flank of the foreland basin. The rock formations below the Chin-shui (CS) Formation (see Table 1) may have been deposited by sedimentation - originating from mainland China, during the time before the Taiwan islands were uplifted during the latest orogeny. In contrast, rock formations younger than the Chin-shui Formation are believed to be derived from the ancient Taiwan Central Range on the east side during the orogenic episode.

Regional Geological Model

The geological profile shown in **Fig. 2** illustrates the off-shore and on-shore regional geological model with seismic data. This profile runs in the W-E direction, roughly normal to the coastal line as shown in Fig. 2, and across the Well M-1 drilling site. Based on evidence of different scale seismic surveys, it had been noted that the thickness of each of the formations of interest is decreasing towards to the west (from inland to offshore), with a dip angle approximately 3~5^{o} dipping gently to the east. No active faults have been found in this area of interest, and only very limited seismic activity, exceeding magnitude 3 has been recorded so far.

To ensure the safety and security of carbon storage, some screening criteria had been preliminarily chosen to redefine the area of interest, as shown below:

(1) cap rock thickness at least 30 m,

(2) at least 5 km away from any suspicious active faults,

(3) storage depth greater than 800 m,

(4) injection operation depth less than 3000 m.

Table 1. Stratigraphic sequence and the thickness of major formations revealed in M-1 well.

Regional Geological Units (Formation/ Member)	Abbr. Formation Name	NN Zoning by Core Analysis	Drilling Interval	Conceptual Model after 3000 m Drilling	Reservoir Potential
0-17 Ma			mRT	Formation Thickness (m)	
Recent sediments	Overburden	-	G.L.-841	841	Ultimate Cap
Tou-ko-shan	TKS-	NN-19	841-1717	876	Primary Cap R-1
Cho-lan	CL	NN-19a	1717-2135	418	R-1
Chin-shui	CS	NN-18	2135-2295	160	Primary Cap R-2
Kei-chu-lin / Yutengping	KCL	NN-17	2295-2450	155	R-2
Kei-chu-lin / Shihliufeng	Absent	NN-17	Absent	Unconformity	-
Kei-chu-lin / Kuantaoshan	Absent	NN-17	Absent	Unconformity	-
Nan-chung / Shangfuchi	Absent	NN-16	Absent	Unconformity	-
Nan-chung / Tunkeng	Absent	NN-16	Absent	Unconformity	-
Kuanyinshan	KYS	NN-13~16	2450-2608	158	R-2
Ta-lu	TL	NN-5,6	2608-2800	192	Primary Cap R-3
Pei-liao	PL	NN-3,4	2800-3005	205	R-3

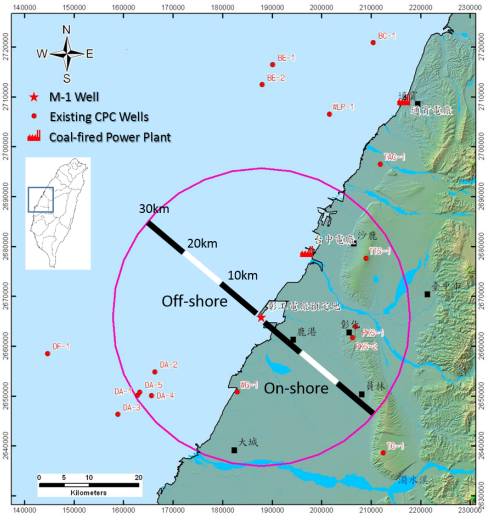

Figure 1. Area of interest (with M-1 well in the center).

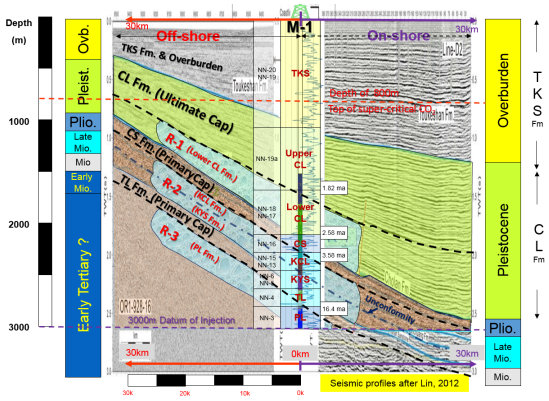

Figure 2. Geological profile across the western coast in W-E direction in middle Taiwan. (Note: M-1 well in the center)

Fig. 3 shows the 3-D geological model and the realistic area of interest which meets the sand-stone reservoir selection criteria. The 3000 m pilot drilling also helps to identify a multi-layered reservoir system underneath the area of interest. Consequently, three high potential storage systems were identified, namely R-1, R-2, and R-3, from top to bottom. Their effective storage capacities have been evaluated as 4.9, 6.3, and 2.5 Giga-ton, respectively. Well logging data (by Schlumberger) obtained from the M-1 well were taken as a crucial tool to examine the adequacy of the selected reservoirs. **Fig. 4** shows the well logging porosity data of the multi-layered reservoir system from 1500 m below ground, down to the 3000 m depth of the M-1 well.

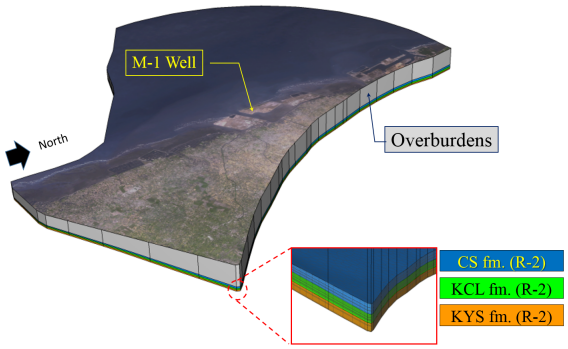

Figure 3. Realistic area of interest with reference to R-2 by site selection criteria.

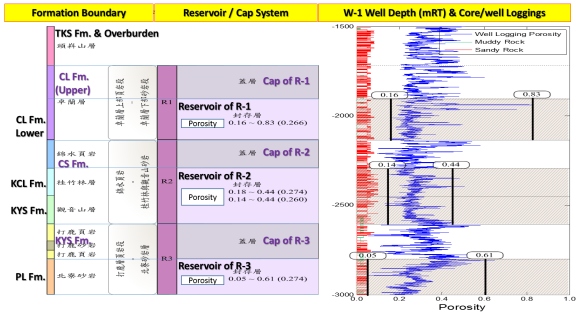

Figure 4. Vertical distributions of the multi-layered reservoir systems of R-1, R-2, and R-3.

Reservoir Rock Injectivity

Roughly seven major geological formations (see Table 1) can be identified by the 3000 m drilling as mapped along with the regional sedimentary geology. All of them are sedimentary rocks - originating in a shallow marine environment, and are interpreted as litho-facies belonging to shoreface, inter-tidal zone, upper to lower offshores, etc. This candidate sequestration site is thus believed to have been adjacent to a passive continental shelf in Early Pleistocene to Middle Miocene times. Alternation of sandstone, siltstone, and mudstone (or shale) encompass the basic lithological units all the way down to 3000 m deep.

Statistically speaking, no massive sandstone or mudstone layers with thickness exceeding 15 m can be logged, and most often the thickness of all mappable layers or lithological units are several meters only, and can be grouped as below:

- Sandstone interbedded with shale: laminated layers, millimeter to centimeter thick,

- Sandstone intercalated with shale: thin layers, centimeter to meters thick,
- Massive Sandstone: several meters to tens of meters thick.
- Massive Shale: several meters to tens of meters thick.

CO2CRC (2011) defined reservoir rock injectivity (or injection rate) as a function of (1) wellbore contact area, (2) injection pressure, and (3) rock permeability. Among them, the rock permeability is the prime factor that can be used to examine the injectivity before the in-situ test is conducted. From core-scale tests, the absolute permeability of most sandstones and some siltstones are in range from 1 to 1000 mD (miliDarcy), while most of the mudstones and some siltstones are in range from 0.00001 to 1 mD. Relative permeability tests also show the injectivity of most tested sandstones meet the general requirements of empirical values.

Fig. 5 shows the statistics of neutron porosity values from the in-situ well logging for four major reservoirs within R-1, R-2 and R-3. Some of the porosity values may not be realistic when they are greater than 0.5. Such a discrepancy may represent an overcut of the wellbore and/or drilling mud contamination. Nevertheless, the histograms shown in Fig.5 provide useful information on the rock porosity values, which are mostly in the range of 0.15-0.45. Rock permeability can be predicted by establishing an empirical relationship between porosity and permeability as long as enough test data are available.

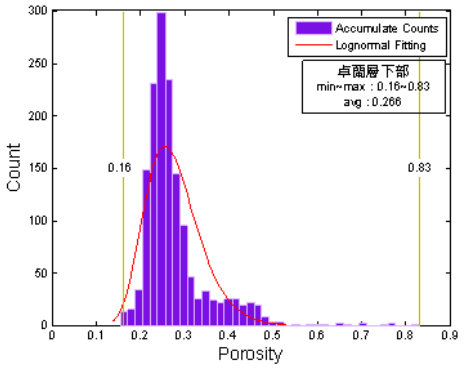

(a) [R-1] in CL Formation

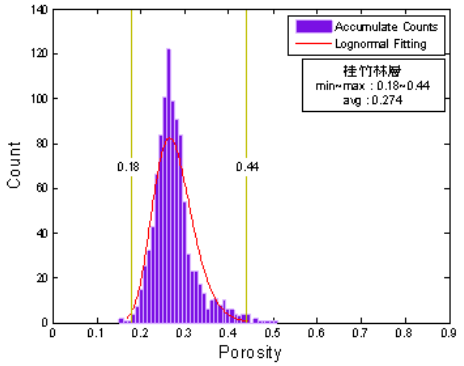

(b) [R-2] in KCL Formation

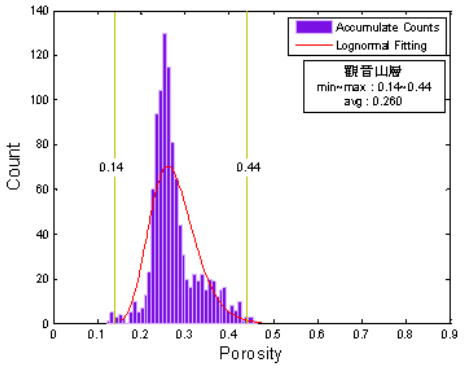

(c) [R-2] in KYS Formation

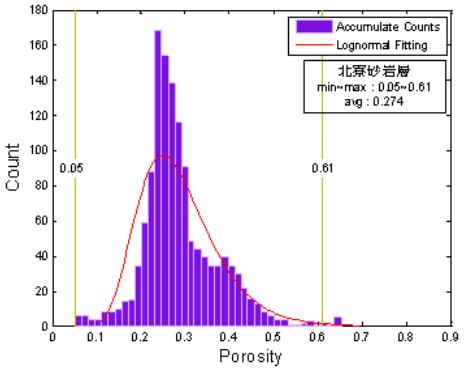

(d) [R-3] in PL Formation

Figure 5. Neutron porosity from the in-situ well logging for four major reservoirs.

Cap Rock Seal Potential

Above the Top most R-1 Reservoir (2295-2450 mRT) and all the way up to the ground surface, almost 2000 m thick of overlying rock can be expected to act as an ultimate or competent cap system. This can serve as the final barrier for securing unwanted leakage path of deep sequestered CO_2, despite the fact that no distinct, massive shale formation was found to be suitable for a good primary seal.

Table 2 summarizes the cap rock seal potential underneath the area of interest, derived from a large amount of typical core test results. The potential can be justified by three criteria recommended by IEA (2011). These criteria selected for site-specific reservoir systems are:

- Seal Capacity: max. CO_2 column that can be retained by cap rock
- Seal Geometry: thickness and lateral extent of the cap rock
- Seal Integrity: geo-mechanical properties of cap rock

Maximum CO_2 column heights calculated from MICP data (Mercury injection capillary pressure, Daniel, 2006) for most tested cores showed that quite high seal capacities can be expected for most mudstone (shale) and some siltstone. Distinct and continuous massive shale can only be found at depths between 2135-2146 mRT, with a thickness of 11 m, located on the top of the CS Formation. Nevertheless, numerous pairs of thin sandstone and shale layers from 3000 m deep up to the ground surface are generally laterally extensive and would form a relatively competent barrier to hinder vertical CO_2 flow.

As a consequence, the intra-formation seal (Gibson-Poole, 2009; IEA, 2011; Kameya et al., 2011) or multilayered cap rock system would then be expected to ensure the safety and security of CO_2 storage in such geological conditions. However, an uncertainty scenario analysis should be carried out to assess the effect of still insufficient geological data, as depicted in the following section.

NUMERICAL MODELLING TO CHECK THE INTRA-FORMATION SEAL

Define Homogeneous and Heterogeneous Models

Horizontal CO_2 migration distances for the candidate site during CO_2 injection are of prime importance for checking the safety of carbon storage. Here, homogeneous and heterogeneous site models were both used as shown in **Fig 6**. In both models, only the R-2 reservoir was considered, and the injection zones were predetermined as an injection interval length of 155 m, equivalent to the entire drilling thickness of the KCL Formation (2295-2450 mRT). The injection zones are assumed to be located in the existing M-1 well. **Table 3** shows the porosity and permeability values of the homogeneous and heterogeneous cases used in this study.

In the homogeneous model, the porosity of the injection zone is a uniform value of 35% compared with a cap rock (e.g. CL Formation) porosity of 20%. By correlation, the permeability of the injection zone is a uniform value of 59 mD, compared with a cap rock permeability of 0.0277 mD. These values represent the results of a large amount of core tests.

In the heterogeneous model, the rough lithological units of inter-bedding sandstone and shale, according to the findings of drilling, are used instead of Major Geological Formation, e.g. KCL Formation, to reflect the more realistic multilayered cap rock system. In general, a porosity value of 35% and a permeability of 59 mD are used for all the sandstone layers, while a porosity value of 20% and a permeability of 0.0277 mD are used for all the shale. Shale rocks are regarded as the layers which can provide a primary seal or act as the baffles in the intra-formational seal condition.

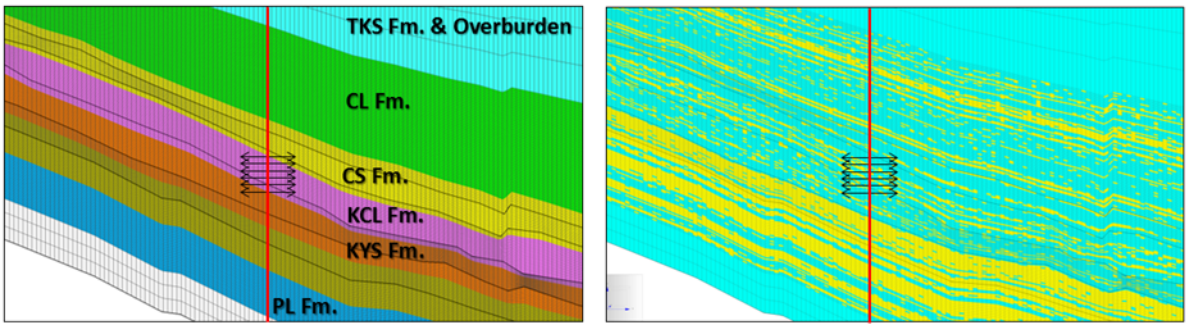

(a) Homogeneous Model
(Layering by Major Geological Formation)

(b) Heterogeneous Model
(Shale baffles are shown in yellow color)

Figure 6. Geological profiles for homogeneous and heterogeneous models for R-2 sequestration.

Table 2. Cap rock seal potential within area of interest.

Cap Rock Seal Potential	R-1 Cap	R-2 Cap	R-3 Cap
(1) Seal Capacity	66-152m*	583m*	967m*
	○	◉	◉
(2) Seal Geometry	Thickness 218m Lateral extension fair to good	Thickness 160m Lateral extension good	Thickness 192m Lateral extension good
	⊙	◉	◉
(3) Seal Integrity	Sandstone intercalated with shale	Sandstone intercalated with shale	Sandstone interbedded with shale
	○	⊙	⊙

* Max CO_2 column height calculated from MICP
○ May need to be further confirmed or verified ⊙ Moderate condition ◉ Good condition

Scenario Analysis for Homogeneous and Heterogeneous Models

TOUGH2 / ECO2N (Pruess, 2005) has been used to conduct uncertain scenario analysis. Two kinds of geological model have been considered to emphasis the difference in horizontal CO_2 migration distances between a homogeneous and a heterogeneous model. Numerical simulations was carried out in a 2-D model where the grid size of 200 m (in lateral of X direction)*5 m (in vertical or Y direction) is used for both models.

Fig. 7 shows the CO_2 migration results in the scenario analysis for both models after 20 years of injection plus 1000 years of monitoring. The CO_2 injection amount of the simulation is set at one million metric tons per year per well, and injection operation is continuously done with a duration of 20 years. The post-injection monitoring is designed up to 1000-year period. The **m**aximum **h**orizontal **m**igration **d**istance (MHMD) for both models are towards the west due to the eastward gentle dipping angle within the geological model. At the end of the monitoring, MHMD reaches 10 km for the homogeneous case, while the case in the heterogeneous model shows a much reduced MHMD of 3.1 km.

It can be noted that in the case of heterogeneous model, more components of injected CO_2 can move upward and penetrate into the lower part of cap rock (e.g. CL Formation) and are ultimately trapped by a single shale unit with good thickness of lateral extension. This should be the quite typical situation in an intra-formation seal mechanism where a multi-layered primary seal exists or an ultimate seal acts as a barrier, which can prevent further vertical CO_2 movement in the long run. The thickness of such ultimate seal does not have to be very thick because most of the mobile CO_2 has been residually trapped in the rock voids through their upward journey.

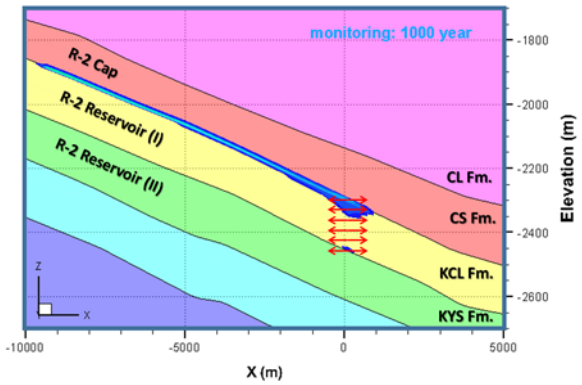

(a) Homogeneous model

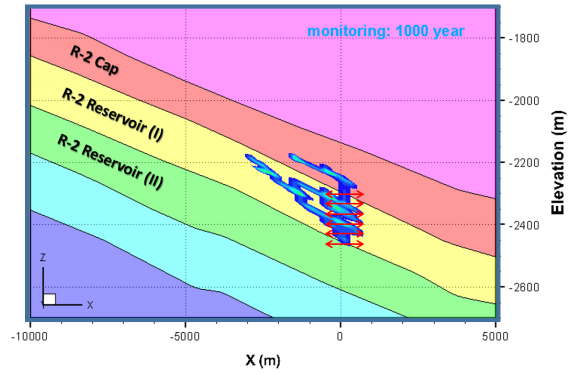

(b) Heterogeneous model

Figure 7. MHMD results in scenario analysis showing the fate of the injected CO_2 plume at 1020 years. Both of CO_2 plume are overlapped on geological profile.

Scenario Analysis with Uncertain Parameters in the Heterogeneous Model

The migratory analysis for the heterogeneous model shown in Fig.7 is regarded as a quite realistic scenario for storage in the candidate deep saline aquifer within Tai-his Basin. However, a probabilistic study is necessary to check the uncertainly when the assumed nominal parameters might be changed. **Fig.8** shows the relationship of porosity and permeability from the results of laboratory core tests. The upper and lower bound of permeability values can be defined at porosity values targeted at 20% and 35%, in addition to the nominal permeability values. Consequently, overall 9 scenario cases can be used to cover all of the input uncertainties, and reflect almost all possibility of porosity and permeability variations.

Table 3 shows the input data and the results of MHMD (m) in the scenario analysis considering all 9 cases with the heterogeneous model. With a maximum permeability of sandstone (1312 mD), coupled with minimum permeability of shale (0.0277-0.00001mD), the most credible MHMD values can reach 4.7 km (Case-2, and Case-3), about 1.6 km more compared with the nominal value of 3.1 km (Case-5). Accordingly, **Fig. 9** illustrates the MHMD (m) evolution for 1020 years for all the cases. All 9 cases of the heterogeneous model showed that the MHMD (m) will substantially stabilize around 100 years after CO_2 injection ends. In the case of the homogeneous model, in contrast, the continuing horizontal movement of the injected plume can last for hundreds of years without apparent stabilization.

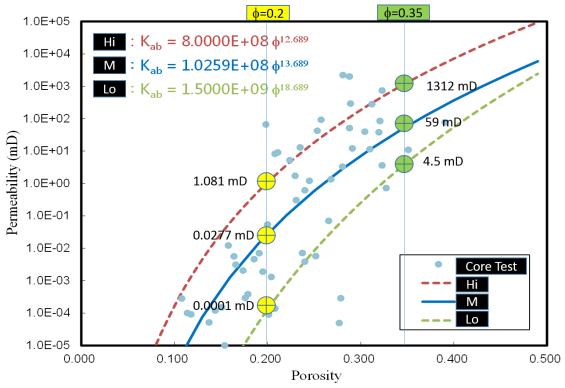

Figure 8. Empirical relationship between porosity and permeability based on laboratory core test.

In addition to the MHMD, the induced pressures inside the cap rock formation at a critical monitoring point above the injection zone (2162 mRT) are evaluated and acted as a pressure control tool. **Fig. 10** shows the induced pressures calculated for the 9 scenario cases using the heterogeneous models. As a rule of thumb, Case-1 to Case-3 are grouped as high permeability cases in which the MMHD is high and hence the induced pressure tends to be low (< 1000 kPa). In contrast, Case-7 to Case-9 can be grouped as low permeability cases with lower MMHD, but higher induced pressure reaching 10,000 kPa (e.g., Case-9). Case-4 to Case-6 are regarded as moderate cases which possess moderate induced pressure.

Table 3. Parameters values of the main parameters of the heterogeneous analysis.

Scenario Case No.	**Main Litho-Units**	**Input Porosity (%)**	**Input Permeability (mD)**	**MHMD (m)** after 20 year of injection	**MHMD (m)** After 1000 years of monitoring
1	Sandstone Shale	35 20	1312 1.081	≈1.9 km	≈3.3 km
2	Sandstone Shale	35 20	1312 0.0277	≈2.3 km	≈4.7 km
3	Sandstone Shale	35 20	1312 0.0001	≈2.3 km	≈4.7 km
4	Sandstone Shale	35 20	59 1.081	≈0.7 km	≈2.1 km
5*	**Sandstone Shale**	**35 20**	**59 0.0277**	**≈0.7 km**	**≈3.1 km**
6	Sandstone Shale	35 20	59 0.0001	≈0.7 km	≈3.3 km
7	Sandstone Shale	35 20	4.5 1.081	≈0.3 km	<1 km
8	Sandstone Shale	35 20	4.5 0.0277	≈0.5 km	<1 km
9	Sandstone Shale	35 20	4.5 0.0001	≈0.5 km	<1 km

*Base case for heterogeneous model and parameters of homogeneous model.

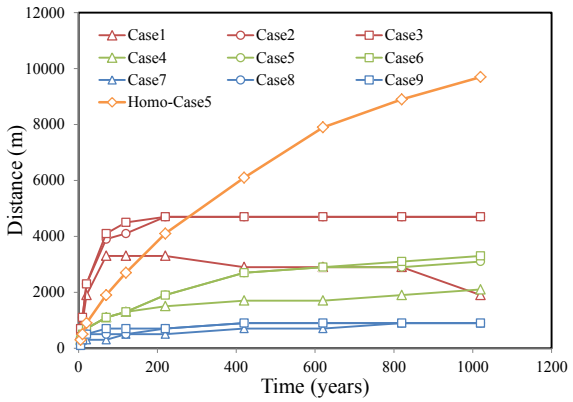

Figure 9. Comparisons of the maximum travel distances of plume migration up to 1020 year (red color represents high permeability; green color represents medium permeability; blue color represents low permeability).

CONCLUSION

The geological carbon sequestration model within the Tai-Hsi Basin on the western coast of Middle Taiwan is established, based on existing seismic survey data and the newly completed 3000 m pilot drilling with coring data. A deep saline aquifer beneath the area of interest, which is characterized by alternating sandstone, siltstone, and mudstone (or shale) is found to be suitable for development. An intra-formation seal mechanism can be utilized for developing the three deep-seated reservoirs within the basin, known as R-1, R-2, and R-3, with a total effective storage capacity of 13.7 Gt CO_2.

The intra-formation seal accompanied by the multilayered cap rock system is expected to be capable of ensuring the safety and security of CO_2 storage. Scenario analyses considering homogeneous and heterogeneous models were carried out to check the MHMD values corresponding to realistic injection scenarios.

In the heterogeneous model case studies, the range of input parameters of porosity (20~35%) and permeability (0.0001~1000 mD) covers the low values of the shale (seals) to the high values for the sandstone (storage layers), and have been selected according to results of laboratory core tests. Probabilistic study is necessary and has been conducted to check the uncertainly when the assumed nominal porosity and permeability parameters might be changed. With 9 cases of uncertain scenario analysis, the migration of the injected plume for the heterogeneous model were carried out and regarded as quite realistic scenarios for the storage in the candidate deep saline aquifer, compared to that of a homogeneous model.

Both the MHMD of the injected CO_2 plume in the R-2 storage reservoir, and the induced pressures at critical monitoring points above the injection zone have been calculated for 9 possible scenarios. As a result, the intra-formation shale baffles have been proven to be capable of playing a vital role for ensuring the safe carbon storage operation within R-2 of Tai-Hsi Basin within a depth range between 2100 and 2500 mRT.

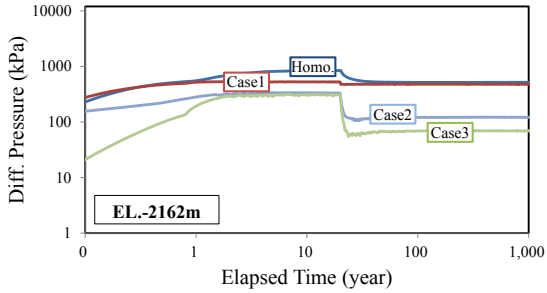

(a) Case-1~Case-3

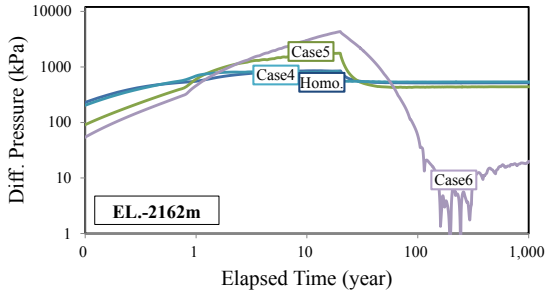

(b) Case-4~Case-6

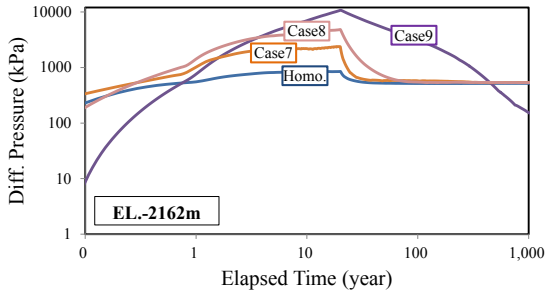

(c) Case-7~Case-9

Figure 10. Overview of induced pressures calculated from the 9 scenario cases for the heterogeneous models.

However, there is still not enough scientific evidence to validate the real safety of a cap rock system associated with the intra-formational seal mechanism, thus an on-site pilot scale injection test and more extensive geo-risk scenario evaluations are strongly recommended prior to making the decision to do large scale sequestration design and operation at the candidate site.

REFERENCES

Lin, T., A. B. Watts and S. P. Hesselbo, Cenozoic stratigraphy and subsidence history of the South China Sea margin in the Taiwan region, *Basin Research* 15, 453–478, 2003.

Pruess, K., *ECO_2N: A TOUGH2 Fluid Property Module for Mixtures of Water, NaCl, and CO_2*, Report LBNL-57952, Lawrence Berkeley National Laboratory, Berkeley, CA, 2005.

IEAGHG Programme, *CCS SITE CHARACTERISATION CRITERIA: Site selection criteria for ensuring the safety and security of CO_2 storage*, Technical Study Report No. 2009/10, 2009.

Gibson-Poole, C.M., L. Svendsen, J. Ennis-King, M.N. Watson, R.F. Daniel and A.J. Rigg, Understanding stratigraphic heterogeneity: A methodology to maximize the efficiency of geological storage of CO_2, In: M. Grobe, J.C. Pashin and R.I. Dodge (Editors), Carbon dioxide sequestration in geological media - State of the science, AAPG Studies in Geology; pp.347-364, 2009.

CO2CRC, Carbon capture and storage workshop, Taipei, Taiwan, Aug. 13, 2011.

Kameya, H., M. Ono, J. Takeshima, H. Azuma, S. Hiramatsu, N. Ohmukai, Evaluation for the capillary-sealing efficiency of the fine-grained sediments in Japan, *Energy Procedia* 4, 5146–5153, 2011.

Sinotech Inc., *Investigation, Pilot Planning and Research of Preferred Test Site for Carbon Geo-Sequestration*, Research Report submitted to Taiwan Power Company by Sinotech Engineering Consultants, Inc., 2011.

Yu, C.W., Chen, S, Shao, K.S., Chiao, C.H., Hwang, L.T., Chen J.L., Development of CCS Technology for Coal-fired Power Plant in Taiwan, *Energy Procedia* 4, 4806–4813, 2011.

Sinotech Inc., *Development a two-phase test facility*, Research Report submitted to Taiwan

Power Company by Sinotech Engineering Consultants, Inc., 2011.

IEAGHG Programme, *Cap rock systems for CO_2 geological storage*, Report of IEA Greenhouse Gas R&D Programme (IEAGHG), 2011.

DNV-GL. DNV-RP-J203, Geological Storage of Carbon Dioxide and DNV-DSS-402 Qualification Management for Geological Storage of CO_2, 2012.

Yu, C.W., Ko, W.C., Chiao, C.H., Hwang, L.T., Yang, M.W., Planning a Pilot Injection Test for a 3000m Deep Saline Aquifer in a Preferred Carbon Sequestration Site, *Energy Procedia*, 37, 4960-4967, 2013.

Sinotech Inc., *Investigation, On-site investigation and planning for a pilot test program in a preferred carbon sequestration reservoir (Phase-1)*, Research Report submitted to Taiwan Power Company by Sinotech Engineering Consultants, Inc., 2014.

Yu, C.W., C.H. Chiao, L.T. Hwang, M.H. Yang, M.W. Yang, A Pilot 3000m Drilling for Characterizing a Candidate Deep Saline Aquifer in Western Taiwan, *Energy Procedia*, 63, 5071-5082, 2014.

Daniel, R.F., *Carbon Dioxide Seal Capacity Study*, Wunger Ridge, Bowen-Surat Basin, southern Queensland., CO2CRC Report No. RPT05-0039, Appendix 10.6.5 of Report No. RPT05-0225, 2006.

EFFECT OF BOUNDARY OPENNESS, DOMAIN SIZE AND RELATIVE PERMEABILITY ON PRESSURE AND CO_2 SATURATION PREDICTIONS BY NUMERICAL SIMULATION UNDER GEOLOGIC CARBON STORAGE CONDITIONS

Liwei Zhang, Robert Dilmore and Grant Bromhal

U.S. Department of Energy, National Energy Technology Laboratory
626 Cochrans Mill Road,
Pittsburgh, Pennsylvania 15236, United States
e-mail: liwei.zhang@netl.doe.gov

ABSTRACT

A TOUGH2 simulation was conducted to investigate how the changes of important modeling parameters (i.e., boundary openness, domain size and relative permeability) affect simulation results of pressure increase and CO_2 saturation in the scenario of CO_2 injection into a deep CO_2 storage reservoir. Boundary openness does not have a significant impact on pressure increase and CO_2 saturation results, given a domain size of 100 × 100 km and a formation permeability of 10^{-13} m^2. However, if a smaller domain size (i.e., 10 × 10 km) is used in the simulation, the scenario with an open boundary predicts much slower pressure increase than the scenario with a semi-closed boundary. As to CO_2 saturation results, the scenario with an open boundary predicts slightly faster CO_2 plume migration given a simulation time of 130 years, compared with the scenario with a semi-closed boundary. Both the changes in formation permeability and choice of CO_2 relative permeability model significantly affect pressure increase results. Findings from this study imply that the boundary openness and formation permeability must be picked in accordance with the properties of the target CO_2 storage reservoir to ensure the accuracy of numerical simulation results.

INTRODUCTION

One motivation to use numerical simulation to study CO_2 sequestration is to obtain information about how the pressure and CO_2 saturation will evolve through, and long after of the period of active CO_2 injection (e.g., 100 years to 1000 years post injection), which obviously cannot be obtained by laboratory or field studies. In numerical simulations, some control variables (e.g., boundary conditions, domain size and effective permeability of CO_2) need to be appropriately prescribed. It is widely known that important control variables have a big impact on numerical simulation results (Zhou et al., 2008; Smith et al., 2011; Heath et al., 2014), but there is a lack of comprehensive studies to quantitatively determine how big the impact is. In this study, a TOUGH2-based integral finite difference model is developed to evaluate the effects of boundary openness, domain size and effective permeability of CO_2 on pressure and CO_2 saturation simulation results in the CO_2 storage reservoir. This study aims to understand the relationships between the control variables (boundary openness, domain size and effective permeability of CO_2) and model outputs (pressure and CO_2 saturation), and to provide quantitative information about how the changes of those control variables affect pressure and CO_2 saturation outputs from numerical simulation.

METHODOLOGY

Numerical simulation code

TOUGH2 (Transport of Unsaturated Groundwater and Heat, Version 2) coupled with the graphical user interface (GUI) code PetraSim was used as the numerical modeling tool to simulate pressure and CO_2 saturation response of the storage formation after injection of CO_2. TOUGH2 uses the integral finite difference method for space discretization, and first-order fully implicit time differencing. A choice of a sparse direct solver or various preconditioned conjugate gradient algorithms is available for linear equation solution. The code has been widely used in projects investigating geological CO_2 storage, oil and gas production operations, environmental remediation, and hydraulic fracturing processes. The reliability of TOUGH2 has been established through comparison of results with many different analytical and numerical solutions, supported by results from

laboratory experiments and field observations (e.g., Pruess et al., 1996; Pruess, 2002; Leonenko and Keith, 2008). To specify the components to be incorporated into the model, TOUGH2 utilizes multiple equation-of-state (EOS) modules, which define phases and related thermophysical properties (such as density, viscosity, and enthalpy) of the fluid or mixture being considered. In this study, the module ECO2N was used to simulate the migration of injected CO_2 and pressure build-up induced by CO_2 injection (Pruess et al., 2012).

Configuration and important parameters of the model

A 3-D TOUGH2 model was developed to simulate the injection of CO_2 into a deep saline reservoir. The model was constructed with five vertically stacked horizontal layers (Figure 1a) and the domain dimensions were 100,000 m × 100,000 m × 220 m. The plane of interest (all simulation results presented in this study are at the plane of interest) was located at Z=100 m (Figure 1a, corresponding to a depth of 1000 m below the surface). In the central region surrounding the CO_2 injection well, relatively small grid blocks were used and grid blocks with larger sizes were used in other regions outside the central region (Figure 1b). The model had 40,768 active grid blocks in total for the base case. For the convenience of result presentation, two monitoring cells on the plane of interest were chosen and most results presented in this paper were at the two monitoring cells. The location of the two monitoring cells can be found in Figure 1c. Important parameters used in the base case scenario can be found in Table 1.

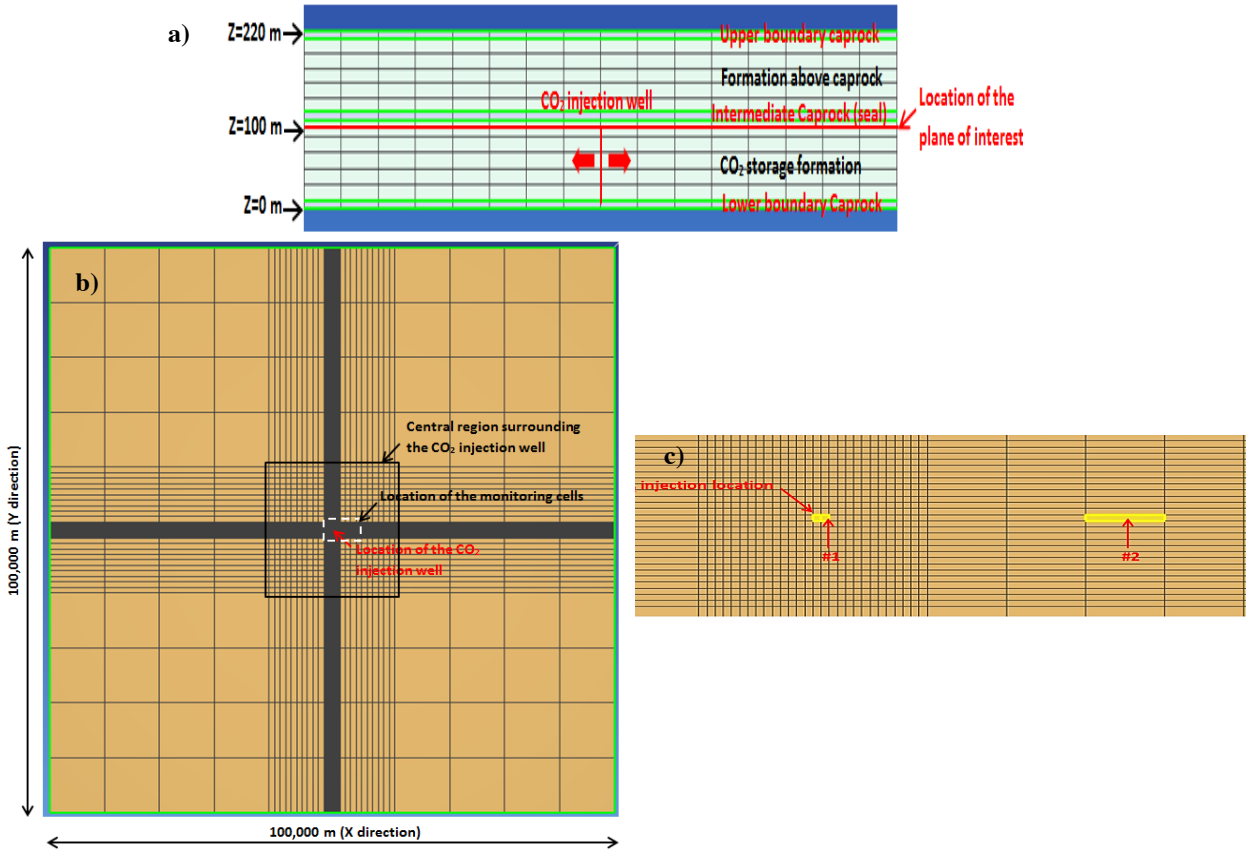

Figure 1. a) Model set-up and location of the plane of interest (Z = 100 m) in the CO_2 storage formation (side view); b) bird-eye view of the plane of interest (Z = 100 m) in the storage formation. The CO_2 injection well is in the middle of the plane; c) locations of the monitoring cells on the plane of interest (bird-eye view). The center of Cell #1 is 50 m away from the injection well; the center of Cell #2 is 3830 m away from the injection well.

Table 1: Modeling parameters used for the base case.

Parameter	Value
Density of rock in Layers 1-5	2600 kg/m^3
Initial pressure at Z=100 m	10.1 MPa
Pressure gradient	10^4 Pa/m
Temperature in Layer 3	47 °C
Horizontal permeability (storage formation and formation above seal caprock)	10^{-13} m^2 (0.1 D)
Vertical permeability (storage formation and formation above caprock)	10^{-14} m^2 (0.01 D)
Horizontal permeability (caprock)	10^{-19} m^2 (10^{-7} D)
Vertical permeability (caprock)	10^{-20} m^2 (10^{-8} D)
Simulation time step	Automatic adjustment (initial step = 1000 s)
CO_2 injection period	30 years
Post-CO_2 injection period	100 years
Boundary condition	Open and fixed pressure boundary
CO_2 injection rate (constant rate from t=0 to t=30 years)	31.7 kg/s (1M tons per year)
Brine residual saturation	0.15
CO_2 residual saturation	0.1
van Genuchten 1/α for capillary pressure calculation	2×10^4 Pa
van Genuchten m for capillary pressure calculation	0.46
Thickness of caprock layers	10 m
Thickness of the storage formation	100 m
Thickness of the formation above caprock	90 m
Salt (NaCl) mass fraction in brine	0.1
Porosity (storage formation and formation above seal caprock)	0.1
Porosity (caprock)	0.05
Maximum simulation time	130 years

RESULTS AND DISCUSSION

Effect of boundary openness and domain size on pressure results

Figure 2 shows the pressure evolution at monitoring cells #1 and #2 as a function of time after the initiation of CO_2 injection, given different domain sizes (100 × 100 km and 10 × 10 km) and different boundary conditions. "Semi-closed boundary" means that the boundary cells are assigned a volume factor of 10,000, which enables boundary cells to contain 10,000 times more fluid than their actual volume. For the 100 × 100 km scenario, the boundary openness did not have an impact on pressure simulation results at the monitoring cells. That is to say, if the domain size is big enough, the intervention of boundary conditions on pressure simulation can be minimized. For the 10 × 10 km scenario, however, the boundary openness had a significant impact on pressure simulation results at the two monitoring cells.

Cell #1

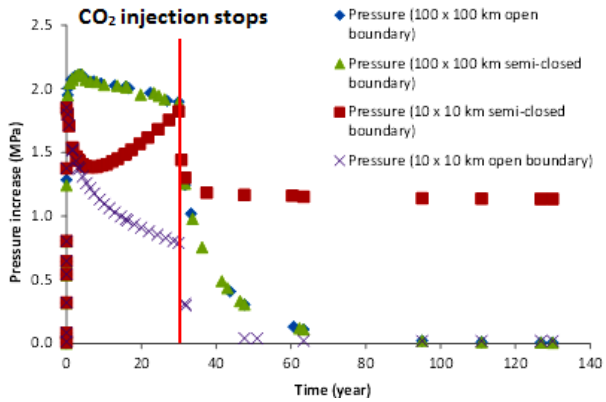

Cell #2

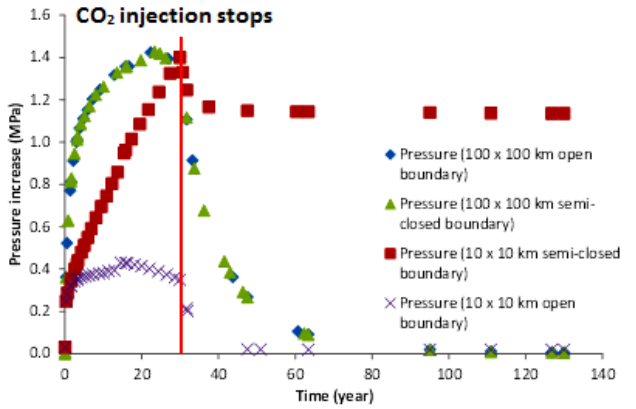

Figure 2. TOUGH2-predicted cell pressure increase at Cells #1 and #2.

Effect of boundary openness and domain size on CO_2 saturation results

Figure 3 shows the cross-sectional profiles of CO_2 plume migration after 130 years (30 years of CO_2 injection + 100 years of observation post CO_2 injection) in four scenarios. The scenario

with a large domain (100 × 100 km) and an open boundary predicted the fastest migration of CO_2 plume, whose front was 4,740 m away from the injection well after 130 years of simulation. The scenario with a small domain (10 × 10 km) and a semi-closed boundary predicted the slowest migration of CO_2 plume, whose front was 3,642 m away from the injection well. Overall, the speed of CO_2 plume migration in different scenarios did not differ from each other much.

Effect of CO_2 effective permeability on pressure results

Because the effective permeability of CO_2 equals the permeability of the storage formation × relative permeability of CO_2, the permeability of the storage formation is expected to have a significant impact on pressure results. Figure 4 shows pressure simulation results at Cell #1 and Cell #2 given different storage formation permeability (from 10^{-12} m^2 to 10^{-15} m^2). The lower the permeability of the formation rock, the higher the pressure built up in the region close to the injection well in the initial stage of CO_2 injection. When the permeability equaled 10^{-12} m^2, the pressure build-up in the region close to the injection well was almost invisible due to fast pressure dissipation. In the region relatively far away from the injection well (Cell #2), the scenario with a permeability of 10^{-14} m^2 had the highest pressure build-up. When the permeability was 10^{-15} m^2, there was no pressure increase at Cell #2, because the low formation permeability does not allow the pressure increase to reach Cell #2 within 10 years of simulation time.

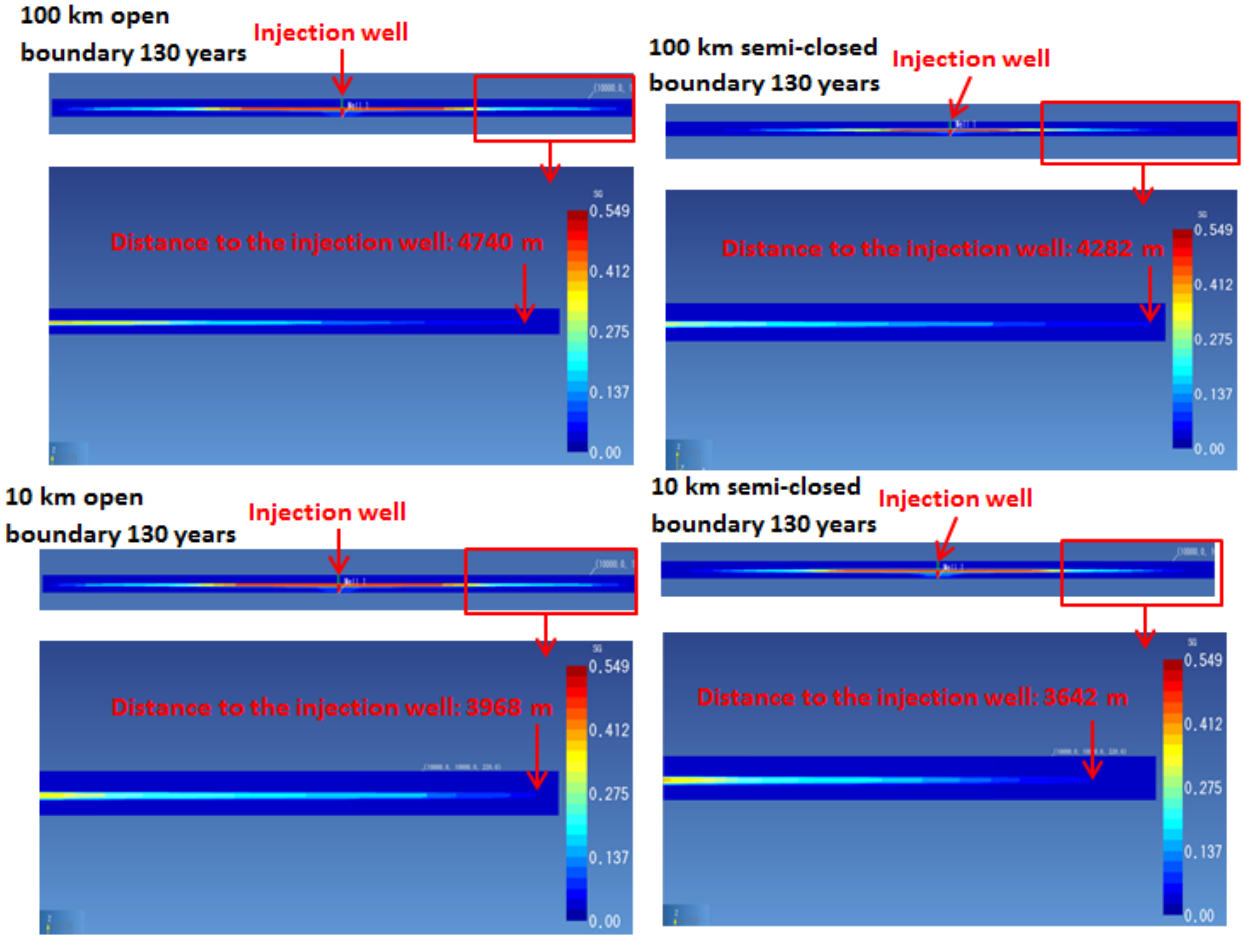

Figure 3. TOUGH2-predicted CO_2 plume migration results after 130 years (30 years of CO_2 injection plus 100 years of post CO_2 injection), given different domain sizes (100 × 100 km and 10 × 10 km) and different boundary conditions.

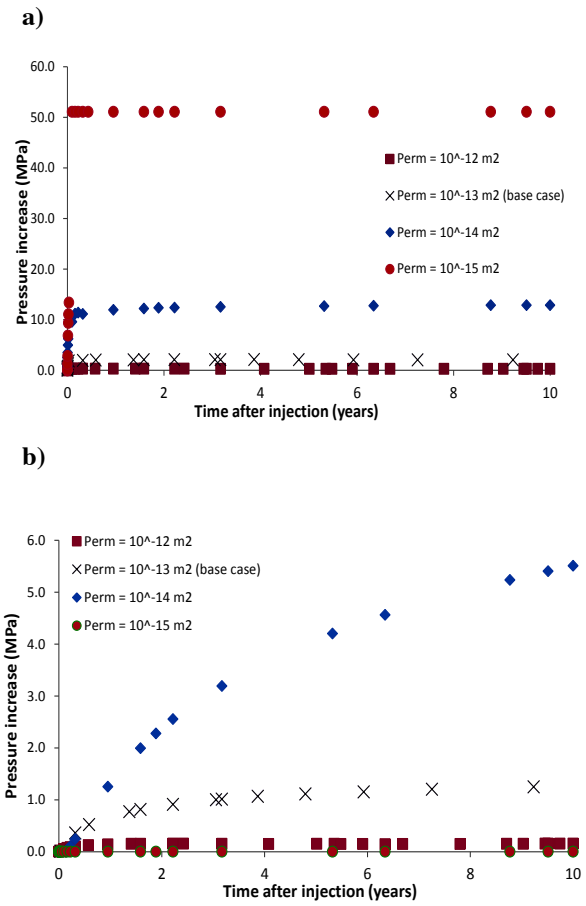

Figure 4. TOUGH2-predicted cell pressure results at Cell #1 (a) and Cell #2 (b), given different CO_2 storage formation permeability.

Figure 5 shows pressure increase results of scenarios with the use of a linear relative CO_2 permeability function and van Genuchten relative CO_2 permeability function (Van Genuchten, 1980) at Cells #1 and #2. The scenario with the use of the van Genuchten function predicted a much higher pressure increase than the other scenarios with the use of a linear function. Moreover, the change in CO_2 residual saturation in the linear function did not have a big impact on pressure build-up. However, at Cell #2 (3,830 m away from the injection well, where no phase transition occurs), all scenarios predicted identical pressure increase during the 130 years modeling period. Therefore, the choice of CO_2 relative permeability model only affects pressure results at cells close to the injection well, where a phase transition occurs.

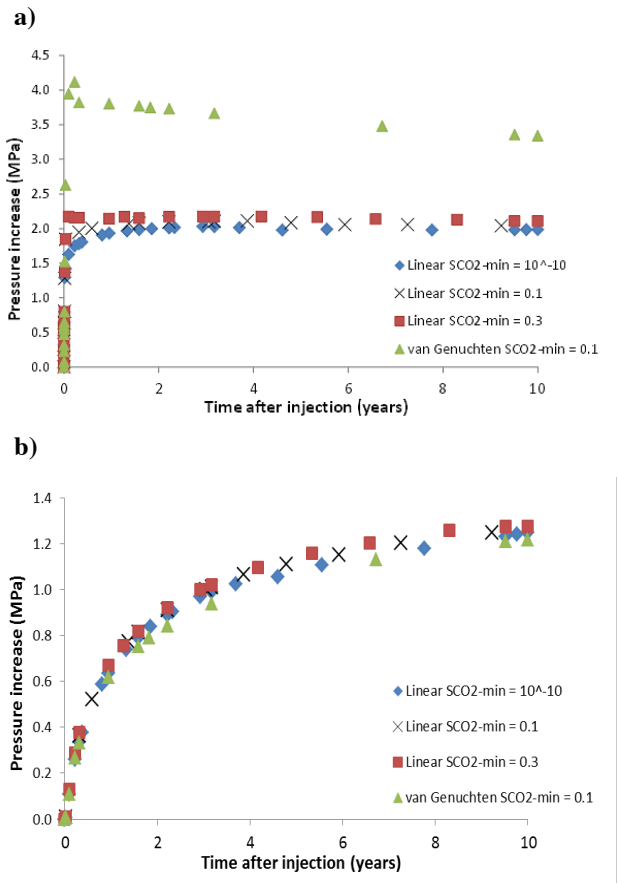

Figure 5. TOUGH2-predicted cell pressure results at Cell #1 (a) and Cell #2 (b), using linear CO_2 relative permeability function and van Genuchten CO_2 relative permeability function.

CONCLUSIONS

- Given a domain size of 100 × 100 km and a horizontal storage formation permeability of 10^{-13} m^2 (100 mD), the effect of boundary openness on pressure and CO_2 saturation simulation results is small.

- Given a domain size of 10 × 10 km and a horizontal storage formation permeability of 10^{-13} m^2 (100 mD), boundary openness significantly affects pressure simulation results. However, the impact of boundary openness on CO_2 plume migration is relatively small.

- A decrease in storage formation rock permeability results in higher pressure build up at all cells monitored given a permeability range of 10^{-12} m^2 to 10^{-14} m^2. However,

when the permeability is reduced to 10^{-15} m^2, significant pressure increase is only observed at the cell close to the CO_2 injector, and no pressure increase is observed at the cell far away from the CO_2 injector.

- The choice of CO_2 relative permeability model significantly affects pressure results at cells close to the CO_2 injector, while the choice of CO_2 relative permeability function has little to no effect on pressure results at cells far away from the CO_2 injector.

ACKNOWLEDGMENT

This work was completed as part of National Energy Technology Laboratory (NETL) research for the Department of Energy's Research and Development Program. The authors would like to thank NETL and National Risk Assessment Partnership (NRAP) for funding support.

REFERENCES

Heath, J. E., McKenna, S. A., Dewers, T. A., Roach, J. D., & Kobos, P. H. Multiwell CO_2 injectivity: Impact of boundary conditions and brine extraction on geologic CO_2 storage efficiency and pressure buildup. *Environ. Sci. Technol.*, 48(2), 1067-1074, 2014.

Leonenko, Y., & Keith, D. W., Reservoir engineering to accelerate the dissolution of CO_2 stored in aquifers. *Environ. Sci. Technol.*, 42(8), 2742-2747, 2008.

Pruess, K., Simmons, A., Wu, Y. S., Moridis, G., *TOUGH2 software qualification*, Rep. LBL-38383; Lawrence Berkeley National Laboratory, Berkeley, Calif., 1996.

Pruess, K., Numerical simulation of multiphase tracer transport in fractured geothermal reservoirs. *Geothermics*, 31 (4), 475–499, 2002.

Pruess, K., Oldenburg, C. and Moridis, G., *TOUGH2 User's Guide, Version 2*. Rep. LBNL-43134, Lawrence Berkeley National Laboratory, Berkeley, Calif., 2012.

Smith, D. J. Noy, D. J., Holloway, S. and Chadwick, R. A., The impact of boundary conditions on CO_2 storage capacity estimation in aquifers. *Energ. Procedia* 4, 4828–4834, 2011.

Van Genuchten, M. T., A closed-form equation for predicting the hydraulic conductivity of unsaturated soils. *Soil Sci. Soc. Am. J.*, 44(5), 892-898, 1980.

Zhou, Q., Birkholzer, J. T., Tsang, C. F., & Rutqvist, J., A method for quick assessment of CO2 storage capacity in closed and semi-closed saline formations, *Int. J. Greenh. Gas Con*, 2(4), 626-639, 2008.

THERMAL PERTURBATIONS INDUCED BY CO_2 PRODUCTION FROM THE KEVIN DOME CO_2 RESERVOIR

Quanlin Zhou [a], Curtis M. Oldenburg [a], Jonathan Ajo-Franklin [a], Stacey Fairweather [b], Lee H. Spangler [b]

[a] Earth Sciences Division, Lawrence Berkeley National Laboratory, Berkeley CA 94720, USA
[b] Big Sky Carbon Sequestration Partnership, Montana State University, Bozeman MT 59717, USA
e-mail: qzhou@lbl.gov

ABSTRACT

The Big Sky Carbon Sequestration Partnership recently drilled a well into Kevin Dome, a natural CO_2 reservoir, to source the CO_2 needed for its Phase III CO_2 injection project. At the perforations in the well at a depth of 1000 m, the measured pressure and temperature were 81.0 bar and 27.0 °C, conditions at which CO_2 is in its liquid phase rather than supercritical form. A series of production tests of different rate and duration were conducted in the well. During the last production test, constant-rate production lasted 2.5 days with 10 days for recovery. Before and after the test, the baseline profiles of pressure and temperature were measured, showing an interface between gaseous and liquid CO_2 in the well. The bottomhole gauge showed a significant temperature drop to close to 0 °C from initially 26 °C, along with a bottomhole pressure drop of 70 bar. To understand the significant thermal perturbation and its impact on the CO_2 productivity of the initially two-phase CO_2-water-filled reservoir, we simulated the production and recovery process using TOUGH2/ECO2M, which is needed to model potential three-phase (liquid CO_2, gaseous CO_2, and aqueous phases) flow in any of seven possible phase combinations. The simulation results indicated that the interface between gaseous and liquid CO_2 that forms in the well moves quickly into the reservoir with CO_2 production. The transition from liquid to gaseous CO_2 in the well and in the reservoir near the well, along with the Joule-Thomson cooling effect, was likely responsible for the observed thermal perturbation. It was inferred that the combined cooling effect may result in the formation of CO_2 hydrate and ice in the thermally-perturbed region near the well perforations. The ice/hydrate formation may result in lowered effective permeability in the reservoir near the perforations, including those caused by relative permeability effects.

INTRODUCTION

Significant thermal perturbations have been observed during CO_2 injection and storage in the field. Examples of these field projects include the Frio I test (Muller et al., 2007), the Cranfield large-scale demonstration project (Zhou et al., 2014), the In Salah industrial-scale project (Bissell et al., 2011), and the Shenhua Ordos project (Jiang et al., 2014). The thermal perturbations are caused by the significant difference between the temperature of injected CO_2 at the wellhead and the in situ temperature of the reservoir, along with a temperature increase (or decrease) by thermal gain (or loss) along the injection well. Modeling the thermal perturbations by using coupled wellbore-reservoir models is straightforward (Pan et al., 2011) when only supercritical CO_2 is involved without phase change.

In a few cases with low temperatures of both injected CO_2 and the reservoir, both gaseous and liquid CO_2 are present in the injection well. Examples of such CO_2 injection projects include the Sleipner industrial-scale project (Alnes et al., 2011; Lindeberg, 2011). At Sleipner, both CO_2 phases co-exist in the upper portion of the injection well, even though supercritical or liquid CO_2 may prevail at the injection point and in the reservoir itself. Modeling these thermal perturbations is more difficult because of phase changes and their induced strong change in CO_2 enthalpy. However, experience has been gained by modeling CO_2 leakage along a leaky fault involving three phases (gaseous, liquid, and aqueous), which was simulated by Pruess (2011a) using TOUGH2/ECO2M (Pruess, 2011b).

In this work, we analyze a CO_2 production and recovery test that involved CO_2 phase change in the wellbore and the reservoir near the perforations. We conduct numerical simulations with TOUGH2/ECO2M to understand the thermal perturbations by calibrating the pressure and temperature changes observed at the botthom-hole gauge and at the wellhead.

CO_2 PRODUCTION/RECOVERY TESTS

A well for CO_2 production for the Big Sky Carbon Sequestration Partnership (BSCSP) Phase III project was drilled into the Duperow formation in Kevin Dome in northern Montana to a total depth of 1158 m. Perforations were made for the interval between 977.80 and 1016.80 m, with a perforated zone of length 18.30 m. Seventeen short vent events releasing CO_2 from the well from Dec. 5 to 24, 2014 indicated that the Middle Duperow is a natural CO_2 reservoir that may source the CO_2 needed for the BSCSP Phase III CO_2 injection project (Zhou et al., 2013). To assess well CO_2 productivity, a production test was conducted between Dec. 26 and 28, 2014. The production test lasted 60 hours, with a fairly constant and controlled production rate of about 40 MSCFD (thousand standard cubic feet per day). A recovery test followed for 10 days, by which time pressure and temperature had completely recovered from the production test.

The in situ pressure and temperature of the CO_2-filled well were measured at different depths by lowering a P/T gauge before the production test and by pulling the gauge after the recovery test. As shown in Figure 1, the same pressure profile is obtained by the two types of measurements, with a change in pressure gradient at the depth of 685.50 m. The upper well section is filled with gaseous CO_2 with an average pressure gradient of 0.0174 bar/m, while the lower section is filled by liquid CO_2 with an average gradient of 0.0704 bar/m. In contrast to pressure measurements at each depth that are at equilibrium, temperature measurements are not at equilibrium, leading to deviation of the down-gauging profile from the up-gauging one. The down-gauging temperatures are smaller than the "actual" temperatures, while the up-gauging ones are higher than the "actual" values. The equilibrium temperature profile was estimated by constraining the two temperature profiles using the CO_2 phase diagram with the pressure profiles (see Figure 2). The minimum temperature of the gaseous CO_2 in the upper section of the well for a given pressure was used for determining the equilibrium temperature profile (white symbols and line in Figure 2).

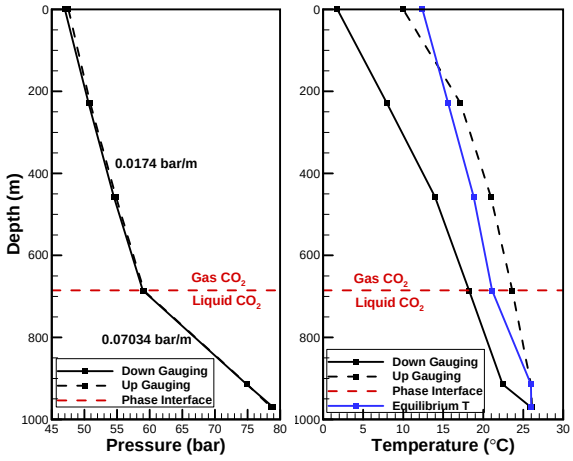

Figure 1. Vertical profiles of pressure and temperature during the well shut-in conditions measured before the production test (down-gauging) and after the recovery test (up-gauging), with the interface between gaseous and liquid CO_2 at a depth of 685.5 m.

The P/T gauge was located at a depth of 968.86 m, 8.9 m above the top of the perforated zone. The in situ pressure at the gauge is 78.97 bar and the in situ temperature is 25.89 °C. The in situ pressure/temperature indicates that the natural CO_2 in the reservoir occurs in liquid form at this depth. The series of pressure and temperature measurements at the gauge during the production and recovery tests are shown in Figure 3, while Table 1 shows the pressure, temperature, and CO_2 density and enthalpy at five key times. After one hour of CO_2 production, the pressure drops from 78.97 bar to 5.59 bar, while the temperature drops from 25.89 to 2.15 °C. The quick drop in pressure may be attributed to the slow supply of CO_2 from the reservoir to the wellbore. The quick temperature drop is caused by CO_2 phase transition from liquid to gaseous CO_2 in the wellbore, and to a lesser degree by the Joule-Thomson effect associated with the quick pressure drop. After the first hour, pressure remains relatively stable between 5.0

and 9.0 bar for the remainder of the production period. The temperature gradually increases to 23 °C within 10 hours, and then slowly increases to 24 °C by the end of the production period.

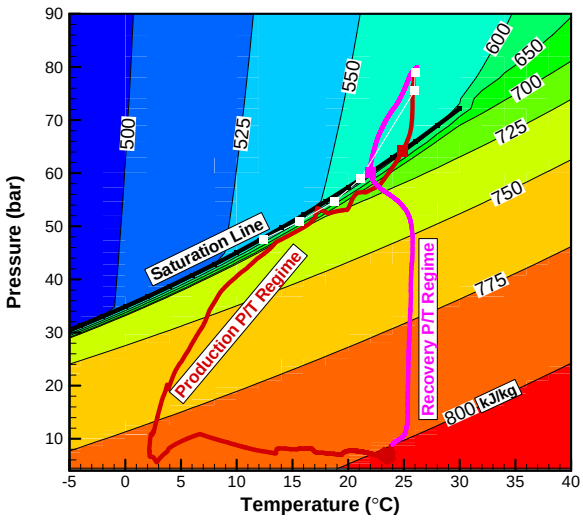

Figure 2. Color contour of CO_2 enthalpy with overlay of the in situ pressure and temperature along the well during the shut-in conditions (white line and symbols), and the pressure/temperature evolution during the production test (red line) and during the recovery test (pink line). The red and pink symbols show the crossing points at the saturation line during the production and recovery tests.

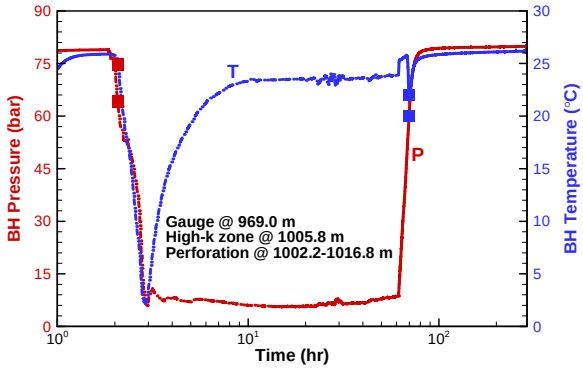

Figure 3. Series of pressure and temperature measurements at the bottom hole gauge at a depth of 969.0 m during the production test (dashed lines) and the later recovery test (solid lines). The symbols show the pressure and temperature on the saturation line during production and recovery.

The measured pressure and temperature during production and recovery are also shown in Figure 2 with a P/T phase diagram of CO_2 to show the CO_2 phase transition and associated enthalpy change. During the production test, liquid CO_2 transitions to gaseous phase at 13 minutes after the start of production (also see Table 1). It can be seen that CO_2 enthalpy increases by 127.6 kJ/kg for a 70% reduction in CO_2 density. During recovery, the gaseous CO_2 prevailing at the gauge during production transitions to liquid CO_2 8.3 hours after production ceases.

Table 1. Pressure (bar), temperature (°C), CO_2 density (kg/m^3), and CO_2 enthalpy (kJ/kg) at different times (hours) during the production and recovery tests, measured with a P/T gauge at a depth of 968.86 m.

Time	Pressure	Temp.	Density	Enthalpy
0	78.97	25.89	762.6	569.2
0.224*	64.22	24.89	244.0	696.8
1.022	7.62	2.15	15.45	781.6
59.67	8.84	23.97	16.51	799.9
67.97*	60.09	22.02	212.7	705.6

* Conditions on the saturation line.

PRELIMINARY MODELING

1D Wellbore Modeling for In Situ Conditions

A one-dimensional wellbore model was developed for all formations to a depth of 966.7 m from the ground surface. Two thermal gradients were used, with temperatures of 13.1, 21.1, and 27.69 °C at depths of 0, 682.14, and 1063.45 m, respectively. The 1D model was used to simulate phase transitions and pressure and temperature along the well. The top boundary was a no-flow condition. TOUGH2/ECO2M was used for the simulations.

2D Radial Wellbore-Reservoir Modeling

The 2D radial mesh was generated by combining a 2D wellbore-associated submesh and a 2D reservoir-associated submesh. In the former, 12 different radial columns of different materials at different depths were used to consider CO_2 in tubing, steel for tubing and casing, water for annulus, cement between casing, and rock of different types (shale, sandstone, and limestone).

The maximum radius considered was 0.25 m, and beyond that heat exchange was calculated using an analytical solution as implemented in TOUGH2 (Zhang et al., 2011). In the vertical direction, 100 layers with different thicknesses were used.

A reservoir submesh was generated using 121 radial columns and 79 layers to discretize the natural CO_2 reservoir, with local refinement near the wellbore (see Figure 4).

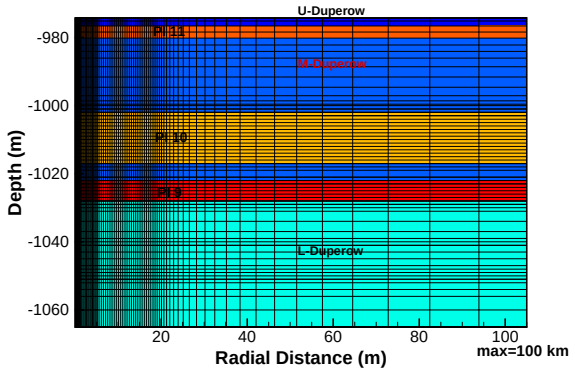

Figure 4. A portion of the reservoir submesh within a radius of 100 m, with two high-permeability zones (red and yellow) for the natural CO_2 reservoir.

Preliminary simulation results were obtained and are currently being analyzed in light of the field observations.

CONCLUSIONS

CO_2 production and recovery tests conducted in Kevin Dome, Montana were analyzed, indicating that gaseous and liquid CO_2 occur in the wellbore under a shut-in condition and liquid CO_2 prevails in the reservoir. During the production test, the bottomhole temperature dropped from 26 to 2 °C, while pressure dropped from 79 to 5 bar, showing significant thermal perturbations with CO_2 phase changes.

To understand the production and recovery test, a coupled wellbore-reservoir model was developed to simulate the thermal perturbations. TOUGH2/ECO2M was used for the numerical simulations. Preliminary results were obtained, the analyses of which are ongoing.

REFERENCES

Alnes, H., O. Eiken, S. Nooner, G. Sasagawa, T. Stenvold, and M. Zumberge, Results from Sleipner gravity monitoring: updated density and temperature distribution of the CO_2 plume, *Energy Procedia* 4, 5504-5511.

Bissell, R.C., D.W. Vasco, M. Atbi, M. Hamdani, M. Okwelegbe, M.H. Goldwater, A full field simulation of the In Salah gas production and CO_2 storage project using a coupled geo-mechanical and thermal fluid flow simulator, *Energy Procedia* 4, 3290–3297, 2011.

Jiang, P., X. Li, R. Xu, R. Wang, M. Chen, H. Wang, B. Ruan, Thermal modeling of CO_2 in the injection well and reservoir at the Ordos CCS demonstration project, China, *Int. J. Greenhouse Gas Control* 23,135–146, 2014.

Lindeberg, E., Modelling pressure and temperature profile in a CO_2 injection well, *Energy Procedia* 4, 3935–3941, 2011.

Muller, N., T.S. Ramakrishnan, A. Boyd, S. Sakruai, Time-lapse carbon dioxide monitoring with pulsed neutron logging, *International Journal of Greenhouse Gas Control* 1, 456-472, 2007.

Pan, L., C.M. Oldenburg, K. Pruess, Y.-S. Wu, Transient CO_2 leakage and injection in wellbore–reservoir systems for geologic carbon sequestration. *Greenhouse Gas Sci. Technol.* 1 (4), 335–350, 2011.

Pruess, K., Integrated modeling of CO_2 storage and leakage scenarios including transitions between super- and subcritical conditions, and phase change between liquid and gaseous CO_2, *Gas Sci. Technol.* 1(3), 237-247, 2011a.

Pruess, K., ECO2M: A TOUGH2 fluid property module for mixtures of water, NaCl, and CO_2, including super- and sub-critical conditions, and phase change between liquid and gaseous CO_2, Rep. LBNL-4590E, Lawrence Berkeley National Laboratory, Berkeley, Calif., 2011b.

Zhang, Y., L. Pan, K. Pruess, and S. Finsterle, A time-convolution approach for modeling heat

exchange between a wellbore and surrounding formation, *Geothermics* 40, 261–266, 2011.

Zhou, Q., J.T. Birkholzer, C.M. Oldenburg, Analysis of injectivity at four representative geological CO_2 injection sites, The thirteenth Annual Carbon Capture, Utilization, and Storage Conference, Pittsburgh, PA, April 28 - May 1, 2014.

Zhou, Q., C.M. Oldenburg, N. Spycher, L. Pan, and A. Cihan, LBNL Deliverable to the Big Sky Carbon Sequestration Partnership: Milestone Report on summary of site characterization, data collection and review, development of static geologic model, and preliminary multiphase flow and reactive transport modeling activities, Rep. LBNL-6519E, Lawrence Berkeley National Laboratory, Berkeley, Calif. 2013.

Geothermal

MANAGING LARGE GEOTHERMAL RESERVOIR MODELS UNDER THE iTOUGH2 PLATFORM

Grimur Bjornsson[1] and Andri Arnaldsson[2]

[1]Warm Arctic ehf, Skjolbraut 22, 200 Kopavogur Iceland
grimur.bjornsson@gmail.com
[2]Vatnaskil Consulting Engineers, Sidumuli 28, 108 Reykjavik, Iceland
andri@vatnaskil.is

ABSTRACT

Through 20 years of continuously developing and recalibrating 3-D numerical reservoir models for the geothermal industry, a fairly standardized work progress has been established. Fundamental components of the work are the TOUGH2 and the iTOUGH2 simulators, coupled with Linux operating systems and a handful of open source software. Data handling and interpretation is done exclusively using true geographical Cartesian coordinates, the depth coordinate is elevation, true dates are used when working with transient data, GIS related information is stored under appropriate visualization software and, finally, invite to the modeler team other geoscientists working on the reservoir under question. This team has to agree on a conceptual reservoir model that will be basis for the numerical model mesh. Identical, multi-layered meshes are practiced, on the order of 50x50 km in total area or more. Outer elements are few and large, while inner wellfields are of hexagon shape, typically 100-200 m wide elements, allowing for any fault orientation and better simulation of radial flow. Single porosity rock matrix is regarded as sufficient for simulating enthalpy changes in such fracture specific meshes.

A linear thermal gradient is assigned to the model outermost boundaries. Top and base model layers are defined as inactive. The former one has finite permeability to serve as a primary constant pressure boundary, while the latter is tight and assigned a temperature distribution that roughly complies with the field downhole temperature data. Generation histories are resampled using cumulative production. Time stepping, initial and final model times are supported by the DATE feature in iTOUGH2. Transient field data in the observation block of the inverse file is thereby better managed and visualized in space and time. Calibration is done through a series of forward and parallel inverse runs, using a cluster of Linux booted multi core desktops connected by a LAN. Natural state and production models are one and the same, with model initial time set as negative 100 thousand years and steady state reached typically when the time step exceeds 10 thousand years. Annotations specified in the inverse file serve as a mean to automate post processing of model and field data. Graphics are then mass produced with help of Linux scripts. Model parameters being estimated range between 20 and 60. Number of active elements is between 20 and 60 thousand while number of data sets and time steps easily exceed 100 each. With a best model at hand, a comprehensive report with many future production and injection scenarios is written, now with an audience outside the geothermal community like business developers, bankers and lenders. Finally, by using the iTOUGH2 platform, recalibration of existing models is greatly simplified, particularly if no new wells have come on line since last calibration and the conceptual reservoir model remains the same.

INTRODUCTION

With maturing geothermal industry worldwide most geothermal steam field operations have accumulated a large volume of field data. This situation is ideal for calibrating numerical 3-D well-by-well reservoir models. The number of wells drilled may exceed 20, and production, injection and drawdown histories span decades. Also the quality and volume of field data have gone from low and scarce in the early development to good and high with the digital age. A reservoir modeler team has to be capable of introducing all these data to their model work, a non-trivial task when considering the volume of field data and irregularity in space and time.

When iTOUGH2 became available, a new dimension opened for successfully developing such large scale models (Finsterle, 2007). The inverse calibration algorithms namely should do a better job with a growing number of data sets and observation times. Such an inverse model development can be divided into four phases.

1) Gather and organize all relevant field data at hand and come up with a conceptual reservoir model being mutually accepted by the owner resource team and the modelers.

2) The joint team then develops a model mesh that can capture basic features of the conceptual reservoir model, and have the flexibility to move structures around without necessarily changing the mesh geometry.

3) Then incorporate all relevant field data into the inverse file of iTOUGH2. Secure that these data are properly introduced in space and time. Followed by a combination of forward and inverse calibration runs to validate and calibrate the model.

4) Final step is to run future predictions, forecasting and sensitivity analysis. The model effort concludes with reporting; now of the quality and layout deemed necessary for the field developer to support its business models and for passing various due diligence tests.

This paper outlines how such a modeling campaign has developed into a more or less a standard process. The field data management is discussed, how the data interpretation results in a conceptual reservoir model, and how a model mesh is developed on the basis of the conceptual model using recent software STEINAR. The model layering and boundary conditions are addressed and how irregular production and injection histories are resampled into a gener block using a principle of cumulative mass flow. Moving scattered field data into the observation block of the iTOUGH2 inverse file is devoted to a special chapter, with emphasis on the convenient date format supported by the code. Then model calibration best practice and forecasting studies follow plus some housekeeping tips that may become handy when doing large models.

MANAGING THE FIELD DATA

Each numerical geothermal reservoir model is subject to the various field data made available. In particular these data have to provide the foundation for a sound conceptual reservoir model, here being the basis for the numerical model mesh and for specifying the model outer boundary conditions. Initial reservoir pressures and temperatures in wells need to be defined and also all histories of mass and heat flow to and from the reservoir, i.e. extraction from production wells and injection. Finally pressure histories in observation and production wells are extremely important, particularly with extended production, as those are the primary constraints for the reservoir model outer permeabilities.

Figure 1 shows as an example how initial pressure and temperature profiles (red dashed lines) are estimated by cross correlating all downhole profiles with other information like simplified lithology, well design, feedzone location, boiling point with depth profile (pink) and MT resistivity model clay cap (yellow band at 1600 mSL). In our view this analysis is the most critical step in detailing the conceptual reservoir model.

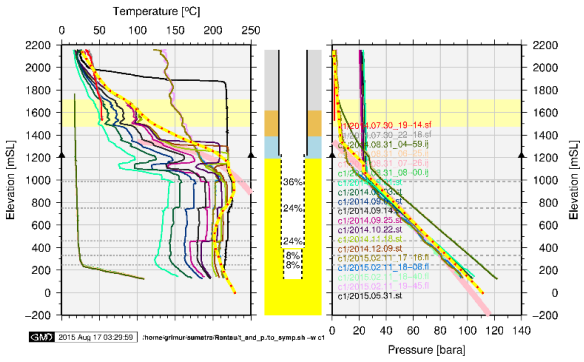

Figure 1. Initial temperature and pressure profiles in a geothermal well. See text for legend.

We also find it essential that a broad expert team is put on the task to ensure all available data have been considered and that the owner resource team is comfortable with the analysis. With three or more deep wells drilled, the initial temperature and pressure profiles then serve for making plots of the reservoir pressure and temperature distribution in plane and cross sections. Such graphics help to assess heat reserves, to make decisions on additional drilling and to set goals for future power plant staging and time-

lines. Finally, these will form basis for the numerical model mesh geometry and layering.

Figure 2 shows S to N temperature cross section in Steamboat, Nevada (Bjornsson et al., 2014). Such graph is a key component in defining a conceptual reservoir model, here consisting of hot 240 °C upflow zone to the S, diagonal ascent of the fluid to about 1000-1400 mSL and lateral flow onwards to the north. The geothermal fluid is either discharged to the surface as hot springs and fumaroles (yellow and red symbols on upper x axis) or consumed by alluvium to the north. Based on the figure the most relevant features of a numerical model can be defined. Like upflow zone location and inflow temperature, shallow layering for mass flow to the north, boundary conditions there that allow fluid to escape and, in the process, help the model to capture the observed temperature distribution.

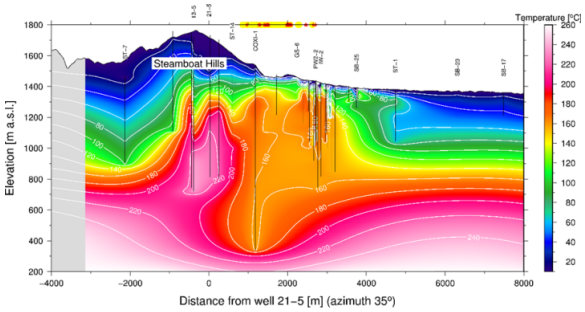

Figure 2. Temperature cross section serving as basis for the Steamboat numerical model (Bjornsson et al., 2014).

We prefer to couple the TOUGH2 mesh and GIS field information with QGIS, a free and open source software (QGIS development team, 2015), here supported with scripts and tools that convert the various model input and output files to formats used in modern GIS software. A handful of other publicly open projects assist with proper management and plotting of GIS data, with the Open Street Map (openstreetmap.org/), Google Earth, and the ASTER digital elevation map (aster-web.jpl.nasa.gov/gdem.asp) topping the list. In addition to these the modeler must also include other important GIS themes such as near vertical structures, hot springs and fumaroles locations, thermally altered grounds, volcanic craters and summits, other surface geological polygons of interest, wellpads, wellheads, welltracks, feedzone locations in directional wells, access roads, power plant locations etc.

Such large volume of field data can get complex to manage. Therefore hosting them all under a quality platform like QGIS is recommended. Furthermore, the model team should consider the GIS application as primary database and always ensure that new field data are uploaded there. Proper tools can then be used to export the GIS information to other software of preference.

Figure 3 shows such basic GIS features of the Olkaria III wellfield in Kenya (Owens et al., 2015). The deepest map layer is a high resolution aerial map, complemented with interpreted structures drawn as black, dashed lines. Next come in white, hexagon style ~160 m wide model elements of the inner wellfield with the TOUGH2 element names in yellow. Wells are drawn by blue lines. Characters refer to where these wells are intercepting the numerical model layers; the purple style is for existing wells and the cyan for a planned wells. Red and white circles refer to well feedzones. The Olkaria III power station is in center left half of the picture.

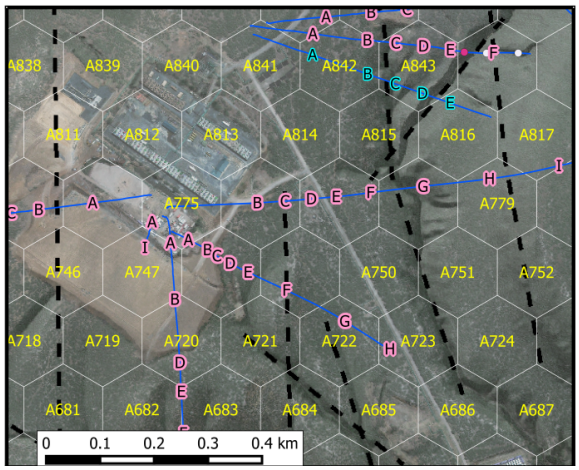

Figure 3. GIS information for Olkaria III.

THE MODEL MESH

The model mesh is the modeler's style of importing the conceptual reservoir model into the numerical one. Various methods are practiced in designing the mesh in the geothermal industry, with rectangular elements being fairly common. This method has the disadvantage of generating high number of elements at the model outer boundaries.

The authors instead prefer to use the AMESH code (Haukwa, 1989). Firstly as it allows for drastically reducing the number of elements assigned to outer boundaries of the numerical models, and secondly because it is an open source software. By selecting AMESH a third important step is taken, namely always generate the mesh in true geographic coordinates of the field being modeled. No need is to rotate the mesh boundaries into a local coordinate system aligned to a preferred fault strike. Instead, just align the element centers to the preferred structures that are to be captured in the mesh. The convenience of making this decision is immense, particularly as it allows for much better dialog with other earth sciences teams working on the same resource. Secondly the likelihood of making errors is drastically reduced.

By using the AMESH approach, another interesting convenience pops up when merging true coordinates of elements to other model properties such as distribution of temperature or pressure in a certain layer. Namely that the input file of AMESH contains the unique 5 character name of each model element, followed with its x, y and z coordinates and finally the layer thickness. Thus, simple Linux commands like `grep`, `sort` and `paste` can be used efficiently to generate text files of data point location and its model value like temperature, pressure or saturation in each model layer. The link is to use the element name as a key. Standard Linux tools then find its coordinates in the AMESH input file and model values in the TOUGH2 output file, before sorting and pasting into xyz files for plotting.

Another prerequisite adopted in the mesh management is to reserve the first character of each element name for the model layer name. The model top layer has the name A, next is B and so forth. Also spaces in element names have been eliminated to make field counting in Linux commands easier. The second column in the element name is also given a character, starting with A, and then B and so on. The remaining three characters follow a number sequence starting with `AA110` and ending with `AA999` prior to jumping to `AB110` and then repeating the sequence. This allows for ~23 thousand elements in a layer, and 26 layer maximum in the model mesh. This system fully complies with the standard TOUGH2 `(A3,I2)` element names.

By standardizing the mesh making, by removing spaces in element names, setting the first character as the layer name, make all layers in the model mesh identical in the horizontal plane, and by automatically generating the AMESH input file from a series of x, y coordinates, it became evident that a system was at hand for speeding up pre- and post-processing of TOUGH2 mesh files. This later led to development of the STEINAR Windows based software for mesh generation and mesh management. STEINAR is financed by Icelandic power companies and consulting firms, under the leadership of Mannvit and Vatnaskil. Please see www.vatnaskil.is/steinar for a free download.

Figure 4 shows an artificial 10x10 km single layer model consisting of coarser rectangular outer elements and finer inner part. The inner part is on purpose composed of hexagon shape elements. A primary advantage of this design is flexibility and better representation of radial flow fields near wells. It also provides much easier management of the model rock properties within the wellfield. For example the red colored fault in Figure 4 can be rotated or shifted to the left or right without rebuilding the mesh geometry. Numerous other features are handy in this software, particularly importing `SAVE` files to STEINAR as `INCON` file and then visualize temperature, pressure or saturation by selecting that property in the properties menu. Elements can also be added or removed, without changing names of the existing elements.

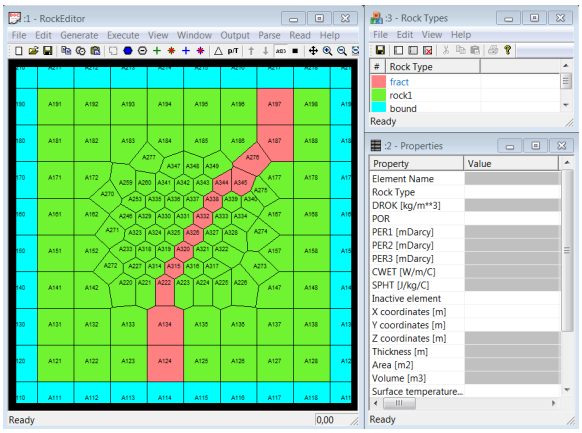

Figure 4. The STEINAR user's interface. Model is 10x10 km with course outer mesh and finer inner hexagons. Fracture in red.

The visual inner and outer mesh control made possible in STEINAR leads to an interesting concept in the model development. Namely that in the early work the modelers "freeze" the mesh geometry in the horizontal plane. Consequent work is then to focus on the rock properties, location and strength of sinks and sources and the model outer boundary conditions.

LAYERING AND BOUNDARIES

With the model mesh horizontal geometry in place, we prefer to simultaneously split the reservoir model into layers and decide on the outer boundary conditions. Again, a process that should have large audience since decisions made at this step can have major impact on the model behavior, particularly its long term response to production and injection.

The model horizontal extent is amongst the first decision to make. Here our rule of thumb is to make them extensive, say 50x50 km or more. There are two reasons for this. Firstly, to place the outermost elements sufficiently far away for them to hardly see the inner model pressure changes. Secondly, to define the outer rim elements as a constant temperature boundary, corresponding to a regional linear gradient. Such a gradient ranges from ~30 °C/km in continental crust to a maximum of 100 °C/km if using field data from the extensively drilled volcanic crust of Iceland. The light blue color property `bound` in Figure 4 is specifying such elements of constant temperature gradient. The STEINAR code can automatically assign thermal gradient to them and a corresponding pure water pressure gradient. Our preference is to only set the temperature as steady state, simply be defining high (10^{50}) heat capacity for the rock property `bound`. Additionally these elements should have horizontal permeability not exceeding 1 mD, while the vertical permeability should be less than or equal to 0.1 mD for fresh water reservoirs. Reduce both by factor 10 if the fluid is saline.

The vertical layering is then largely based on the conceptual reservoir model and strongly influenced by the modelers experience and preference. As a rule of thumb most models get away with thicker layers (200-400 m) in their shallow parts that roughly correspond to clay type thermal alteration and minor vertical flow. As soon as entering the active geothermal reservoir, particularly those with shallow natural steam caps or likely to develop such during production, the model layers need to get thinner, say down to 50 m or less. When below potential steam zones, model layers can grow gradually in thickness and the deepest ones may be as thick as 500 m.

Also for consideration is the model total thickness. In reservoirs that seem to get fairly tight with depth one may decide to conservatively place the deepest active model layer at a center depth corresponding to the deepest well drilled. In other cases, like in Steamboat, field data is pointing towards a significant deep vertical convection. That will justify defining active model layers below the deepest wells drilled (Bjornsson et al., 2014).

Model top and base layers need special consideration. The model top layer is preferred as a constant pressure and temperature boundary. Elements are set as inactive and of temperature and pressure corresponding to that of the local groundwater. A different approach may however be needed if the reservoir under question is characterized by regional lateral flow like seen in Olkaria in Kenya (Ofwona, 2002) or in the Hengill system in Iceland (Gunnarsson et al., 2011). Here the modeler can specify one row of upstream and downstream boundary elements as constant but different pressure, in addition to the top layer. The inverse calibration is then to find permeabilities to these boundaries that best reproduce the natural state temperature and pressure distribution.

Steady state temperature and pressure distribution is preferred for the model base layer, and of very low vertical permeability. Outer rim temperatures in this deepest model layer will comply with the linear style regional gradient assumption. Likewise a hot spot will show up in the center model by contouring downhole temperature from deep wells.

Finally note that elevation is selected as the model vertical depth coordinate. One reason is that various surfaces in GIS themes are in mSL, meaning easier cross correlation to the model mesh. Another is that working with downhole data collected in directional wells is easier when using elevation as depth reference.

THE TOUGH2 GENER BLOCK

Natural state mass and heat sources need to be introduced to the model prior to calibrating. This happens in the GENER block in the forward file. The definition is influenced by the modeler's experience and preference but also by details in the conceptual reservoir model. In general the hot upflow zone is the most important, its location, mass strength and enthalpy. Fumaroles and hot springs also are often defined as mass and heat sinks, ideally flowing against constant downstream pressure (DELV).

Well feedzone locations and relative strength is a special category and often require sizable attention in the calibration process. A good GIS database and the hexagon inner mesh geometry allow for assigning feedzones to closest elements and right layers. Furthermore, as wellfield hexagon elements are only 100 to 200 m across, sub-gridding of feedzone elements is not done. Relative contribution of feedzones to the total flow is however required, often assisted by analysis like those shown in Figure 1.

Lately the authors have done most of their models by specifying forced flow from production wells during the calibration phase. As this has the risk of pulling element pressures to zero, a minor change in the QUV2 subroutine of iTOUGH2 (t2f.f) has been made. Namely that feedzone flow is shut off if the element pressure falls below a value assigned to the HX property in the MASS generation line.

The two column format of a gener point in iTOUGH2 is much appreciated. And also the MOMOP feature that forces the time stepping to stop at all changes in generation. This ensures wells come on or off line exactly when specified so in the GENER block.

Generation histories of geothermal fields is then a special category and often tricky. Main reason is that two phase well discharge may only be measured once or twice a year, and interpolation therefore needed to make the production history more complete. Some developers account for this by maintaining a wellhead output curve relative to position of a control valve. Thus even daily record of well flow is possible. We have written simple Linux tools to read such irregularly spaced data series, assign element names to individual feedzones and specify the mass contribution from each one. These tools write out a resampled generation history for every well feedzone in a model, in a format that can be pasted directly into the GENER section of the forward file. The algorithm converts dates to seconds after an initial date, then computes the cumulative mass flow with time from that particular well, resamples the cumulative flow at preferred time interval before converting the volumetric flow back to rates.

THE iTOUGH2 OBSERVATION BLOCK

The last part in developing iTOUGH2 forward and inverse input files, prior to calibration, comprises of specifying field observations in the observation block of the inverse file. Now a text file heaven is entered by devoted Linux users, as the inverse file observation block is easy to manage with relatively simple scripts.

The iTOUGH2 STEADY STATE SAVE feature is revolutionary when calibrating a numerical model by inverse technology. Reason is that all field data support the parameter estimation in the same model run, contrary to earlier style of calibrating separately steady-state and production models. In previous section we have shown the considerable effort needed in building 3-D models and assigning feedzones and other features of interest to the right xyz coordinate and the right model element. The fourth dimension, the time, now becomes very important in the model management.

Conveniently the standard iTOUGH2 source code includes subroutines that can handle DATE strings in the inverse file. Table 1 below demonstrates how dates make the modeler's life easier. Firstly, set the steady state model time as zero. Secondly when time is first introduced as DATE, this date is in true date format, here January 1, 1981. All other dates in the observation block will be referenced to this date by iTOUGH2. Thirdly we instruct iTOUGH2 to stop at the five dates shown in the table for comparing measured and computed model values.

There are numerous other factors that need attention when working with times in iTOUGH2. For example it is convenient to have a general time block in the inverse file that is equally spaced throughout the production history, say on

the 15th of every month. The resampling of generation data, discussed above, should also coincide on those exact dates as it will reduce number of time steps in forward runs. Additionally there may be short intervals of dense data sampling in the field history, for example pressure interference test only lasting for a few days. Here another time block can be incorporated in the inverse file, now at much shorter time intervals to ensure these data contribute sufficiently to the iTOUGH2 objective function.

Table 1. Using dates in iTOUGH2

```
> OBSERVATION
   >> STEADY-STATE at TIME : 1
        0.0
   >> TIME: 1 DATE
      01-JAN-1981
      0.0
   >> TIME : 5 DATE
      1981-03-15
      15-MAY-1985
      1989-11-15
      01-01-2000
      23-SEP-2015
```

It is also important to observe that the initial time in the forward file, both in the PARAM block but also in the GENER block, should be given the same large negative value. We often set it as −100,000 years. The forward execution will then ideally reach the inverse file STEADY STATE SAVE time step of say 10 thousand years. Or, in case of slow convergence; the execution will consume the negative 100 thousand years and then advance into the production model. Either case, the execution will continue throughout the production history and ideally end at the maximum date value specified in the TIMES part of the inverse file OBSERVATION block.

It is convenient to give the maximum model time in the forward file PARAM and GENER blocks also a large number, say thousand years. Reason is that iTOUGH2 end of forward run is supplied by the TIME section of the inverse file. Thus, by simply adding a times block to the inverse file for dates that belong to a forecasting period, the forward run will continue with all wells flowing at their last rate specified in the GENER block. This allows for easy preview of the field future performance, by adding only 20-30 date lines to the inverse file.

The authors are keen to use strict annotation style for datasets and select ">>> PLOTFILE: ICELAND" as a mean to greatly simplify post-processing of computed and measured values. Bearing in mind that datasets in geothermal models are basically five, the following prefix is added to their annotations:

1) An element pressure observation, P%
2) An element temperature observation, T%
3) Enthalpy history observation, en%
4) Pressure drawdown history, dd%
5) Mass flow, mm%

The % sign serves as a field separator in the annotation text string, to automate the post-processing. For example the drawdown history of a well named NJ-41 that is connected to element GB265 can be annotated as dd%GB265%NJ-41. The post processing then extracts computed and measured values from the requested Iceland plot format ".ice", using the annotation first field for data type, second for element name and third for the graph heading.

Table 2 demonstrates two temperature observations that relate to a model with time zero on January 1, 1981. The first is for a well that was only completed in November 2007, while the latter is for a well that existed on time zero. iTOUGH2 will either automatically assign a time window to each observation that corresponds to the data dates, or use the inverse file window. In this example the default time stepping was 1 month. Thus by having two months in the date window, we ensure there will be taken at least one time step with data corresponding to that element and observation. Additionally note the different standard deviation for the two observations, intended to make the latter one more influential in the model misfit analysis.

Table 2: Defining dates for well initial temperatures

```
>> TEMPERATURE
   >>> ELEMENT : DB978
       >>>> ANNOTATION : T%DB978%21-05
       >>>> DEVIATION  :  15.0
       >>>> DATA DATES
            2007-10-02      70.77
            2007-12-01      70.77
       <<<<
   >>> ELEMENT : BC265
       >>>> ANNOTATION : T%BC265%25-13
       >>>> DEVIATION  :  5.0
       >>>> WINDOW     : -100.0 100.0
       >>>> DATA DATES
            1980-01-01     159.09
       <<<<
```

MODEL CALIBRATION

iTOUGH2 is second to none when it comes to calibrate complex geothermal reservoir models. This applies both to forward runs and automatic parameter calibration by inversion. Several reasons are for the convenience. Firstly, the field observations are all part of the input files, secondly the model misfit analysis is considering all field data during same execution and, thirdly, after every forward run iTOUGH2 provides an assessment on the misfit between data and model in the objective function. Other features of help come from the correlation of parameters, how individual data sets are contributing to the objective function and which model parameters being inverted for are the most sensitive.

We prefer to pack all the bits and pieces of the various model input blocks to only two files, the inverse file, always named "`ii`", and the forward file, always called "`fi`". Post processing of the forward and inverse runs is carried out by a suite of Linux tools, plotting field and model data either with depth or time. Auto scaling is essential, including the time axis. The generalization of annotation names allows for plotting graphs using Linux shell scripts.

The `kit` and `prista` tools of iTOUGH2 are of great help during the model calibration phase, particularly when doing inverse calibration with `PVM` (Finsterle,1988). Our experience is that `STEADY STATE SAVE` forward runs need close attention as models with extensive boiling occasionally suffer from lack of convergence, i.e. never reach the 10 thousand year criteria set. Simple command like `tail -f ~/it2_*/fi.out | grep " ST ="` works great for keeping an eye on this. When coupled with the Gnuplot package (http://www.gnuplot.info/), the model behavior can even be watched graphically in real time as shown in Figure 5 below. Zig zagging of the time step length in the first 7000 years is related to elements either flashing or condensing, thereby reducing length of time steps temporarily. After this the model stabilizes and advances fast to the desired 10 thousand year `STEADY STATE SAVE` time step.

The model calibration is then largely consisting of cycles of forward and inverse runs for about 2-4 weeks of calendar time. It requires a lot of finger work and typing errors are prone to happen. We therefore like to do this as a team; with one member "flying" iTOUGH2 by typing and editing while the other is the "co-pilot", watching his work on a large display. The "co-pilot" also has his own large display ideally with STEINAR and QGIS images used to better understand the numerical model behavior with respect to the conceptual reservoir model.

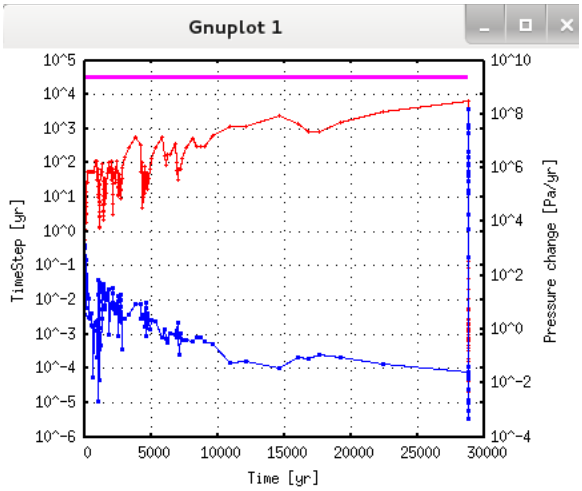

Figure 5. Length of time steps (red) and maximum pressure change (blue) during natural state forward run.

Specifying one `RESTART` time in the inverse file, say 300 seconds into production, makes iTOUGH2 write a `SAVE1` file to the disk. Prior to starting next model run, this file replaces the previous `INCON` block in the forward file.

At best, a typical work day during calibration may therefore consist of first viewing results of an overnight inverse calibration. Based on these, a handful of forward runs are to follow, checking out individual parameters and their impact on the model. Sometimes importing the new model calibration to STEINAR is needed, make changes in rock properties there and come back to a forward run. Ideally this work is successful in either reducing the model objective function or correcting annoying misfit in some of the observation data sets. The work day may therefore end by another overnight `PVM` inverse run.

The number of parameters used in the calibration is a combination of the model size, complexity and number of CPU processors available for the parallel `PVM` calibration. Typically these range from 20 to 60, paying close attention to any possible over- or underparameterization.

Care is needed in specifying allowable ranges for the various parameters to be estimated and their maximum change in iteration can also be restricted. The modeler experience and intuition is important here. Additionally, allowed parameter ranges should be cross correlated. For example do not allow outer and tighter rock domains to reach higher permeabilities than the fractured inner model mesh.

FORECASTING AND REPORTING

Any modeler at some point needs to decide that his or her model has achieved a "best model" status. At this point the work progresses to forecasting. Once again the procedure is dependent on the modeler background and preferences. Not mentioning the desire of the field developer to get as many MWh as possible out of its investment over a reasonable length of time.

Our style here has lately been to continue forced production from wells into the forecasting period, particularly in reservoirs where pressure drawdown with time is moderate. Intuition and flow penalty analysis are then performed, based on the predicted future pressure and enthalpy histories of individual feedzones, to assess need for make-up wells. Wells on deliverability are also studied.

Note that in the forecasting phase we prefer to start all forward runs at the same large negative time as during the calibration stage. The production history is then re-computed each time up to the prediction time period. This is to verify that the prediction scenarios are all using the same model calibration. The number of scenarios considered may however become large and then the computer cluster becomes handy with many forecasting runs executed simultaneously.

All this work is completed by writing a comprehensive report that may exceed two hundred pages in length and incorporate over one hundred images. Now the Linux plotting scripts are helpful as they can regenerate images at minimum effort with only a few command lines. It is important to keep in mind that such reports can have a wide range of audience outside numerical modelers and geothermal experts, like business developers, bankers and lenders. Furthermore, the model forecasting may become the basis for very large investment decisions, sometimes exceeding tens to hundreds of millions of USD. Reporting such model development is therefore a challenge and in itself a material for another paper.

HOUSEKEEPING

As our style of model calibration is to extensively use parallel computing with `PVM`, and for various other household issues, Linux operating systems are regarded essential for successful calibration of complex geothermal models. The numerical calculations are performed on a stack of new generation, LAN connected multi-core desktops. Graphics use open source tools like Gnuplot (http://www.gnuplot.info/) and the Generic Mapping Tool (Wessel et al., 2013). The latter is preferred for near automatic mass production of x-y graphs and for contouring xyz data with the help of Linux scripts.

A typical folder structure for a large model is shown in Figure 6. In green are folders that are mostly attended when getting field data into the format of the iTOUGH2 forward and inverse files. The `model` and `mesh` folders (blue) are more active during the calibration stage. Subfolder naming uses a simple trick that couples the date of making a folder to its name. The Linux command `cp -Rp old_folder new_folder` ensures that a successful older model folder is not touched by editing. Instead copy that one to a new name and continue there. Various other Linux tools like `rsync` are ideal for backups and maintaining mirror copies of model folders with time. Finally the secure shell access tool of Linux allows the modeler team to be distributed around the world.

Note the convenience of putting a time stamp on graphs made, together with the command used to plot and the graph folder location (lower left hand corner of Figure 1). This makes recalibration studies in particular faster as the modeler can always find the script that generated an image using the time stamp.

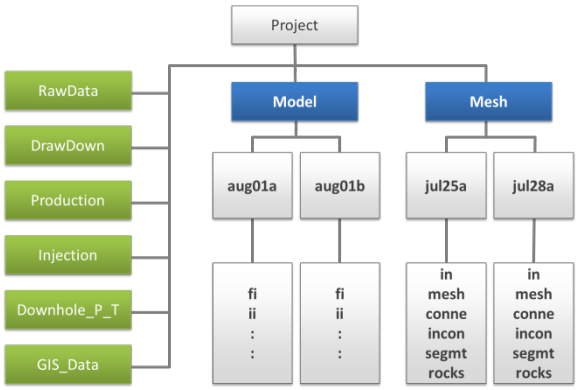

Figure 6. Folder tree for a model project.

DISCUSSION

Calibrating a large geothermal numerical reservoir model is complex and challenging endeavor. It will require a broad expertise in geothermal sciences, field data, numerical modeling, computer skills, programming and data management. The modelers' community should therefore consider a team approach and move to general solutions in file processing, formats and storing. These namely allow the team to better share information and ideas thereby contribute to a better model in a shorter amount of time.

The large audience suggested for a model development and calibration is here regarded as a tool to have numerical models both better supported and calibrated more quickly than earlier. Main reason is that with the team effort and parallel iTOUGH2 on a cluster, the number of calendar days required to deliver a model has been reduced while the cumulative man hours may remain the same. This is important from the field developer's point of view, as the power project may have put in large steam field investment at time of calibration. Consequently there is urgent need to make a fast and professional decision on power plant technology, size, staging, and steam field production and injection strategies. All these topics are addressed by the numerical model and should lead to a better power project implementation.

Typically such a model calibration effort takes no more than 3-4 months. Ideally, it should allow both modelers and the owner field experts to visit each other for speeding up data analysis and development of the iTOUGH2 inverse and forward files.

The numerical model reports being delivered can at times be confidential and proprietary, particularly if a project is passing delicate financial close stages or when negotiating power prices, land rights or other such business related issues. Open publications, unfortunately, are therefore scarce. Those who are interested in our previous work on large models under iTOUGH2 are directed to several TOUGH2 symposium papers on the Hellisheidi 300 MW and Nesjavellir 120 MW projects in Iceland (Bjornsson et al., 2003; Bjornsson et al., 2006; Gunnarsson et al., 2011), the >500 MW Olkaria development (Axelsson et al., 2013; Owens et al., 2015), the Steamboat and the Jersey Valley reservoirs in Nevada (Bjornsson et al., 2014; Drakos et al., 2011).

Open source software solutions like QGIS and the Generic Mapping Tool have greatly assisted in recent model calibration campaigns. There is however one particular issue that still needs to be solved, namely moving the field data storage into appropriate table structure, using the well-established SQL language of databases. Furthermore, one needs to ensure the table structure is complying with basic rules of data bases like normalization, and allow many to have access to the data stored. The authors have developed a beta version of such a data base using MySql and with a front end that allows users to access the data, insert, retrieve and plot via ordinary web browsers. Bearing in mind that data manipulation can consume up to 50% of the work hours put into a numerical model development, such a standardized data platform may therefore proof of help to modelers and ideally the resource developers also.

The architecture of the iTOUGH2 inverse file becomes very handy when a field developer likes to have a reservoir model recalibrated. Assuming no new wells have been drilled or changes made in the conceptual reservoir model, the recalibration effort may only consist of extending the `GENER` block in the forward file and adding a few lines of new drawdown and enthalpy observations to the inverse file. Then the name of the game is to rerun the model with the previous parameter set to assess its performance, and then recalibrate with the inverse parallel technique if new field data require so.

Another interesting opportunity coming with iTOUGH2 is to calibrate 3-D reservoir models much sooner in a resource development history than was considered realistic earlier (Sarmiento and Bjornsson, 2007). The reason is a combination of the iTOUGH2 capacities and much better field data being collected.

A well-kept numerical model can also prove valuable as a decision making tool in reservoirs that are to be stepwise expanded with extended history of production and drilling. The Olkaria III development history in Kenya is a good example, in which the developer has had the iTOUGH2 numerical model recalibrated every time prior to expanding the power plant's capacity (Porras et al., 2010; Owens et al., 2015).

ACKNOWLEDGMENT

We thank Ormat Technologies and Supreme Energy for publishing some of their field data. Fruitful and long standing feedback, visits and support by colleagues at the Earth Sciences Division of the Lawrence Berkeley National Laboratory is very much appreciated.

REFERENCES

Axelsson G., A. Arnaldsson, H. Ármannsson, K. Árnason, G. Einarsson, H. Franzson, T. Fridriksson, G. Gudmundsson, S. Gylfadóttir, S. Halldórsdóttir, G.P. Hersir, A.K. Mortensen, S. Thordarson, S. Jóhannesson, C. Bore, C. Karingithi, V. Koech, U. Mbithi, G. Muchemi, F. Mwarania, K. Opondo and P. Ouma, Updated Conceptual Model and Capacity Estimates for the Greater Olkaria Geothermal System, Kenya. *Proc., 38th Stanford Workshop on Geothermal Res. Eng. SGP-TR-198, 2013*

Björnsson, G., A. Hjartarson, G. Bödvarsson, B. Steingrimsson, Development of a 3-D geothermal reservoir model for the greater Hengill volcano in SW-Iceland, *Proceedings of TOUGH Symposium 2003, Lawrence Berkeley Natl. Lab., Berkeley, California, May 12-14, 2003*.

Björnsson, G., E. Gunnlaugsson, A. Hjartarson, Applying the Hengill Geothermal Reservoir Model in Power Plant Decision Making and Environmental Impact Studies, *Proceedings of TOUGH Symposium 2006, Lawrence Berkeley National Laboratory, Berkeley, California, May 15-17, 2006*.

Björnsson, G., A. Arnaldsson and J. Akerley, A 3D Numerical Reservoir Model for Steamboat, Nevada. *GRC Transactions, Vol. 38, 2014*

Drakos, P., P. Spielman and G. Björnsson, Jersey Valley Exploration and Development. *GRC Transactions, Vol. 35, 2011*.

Finsterle, S., *iTOUGH2 User's Guide*, Report LBNL-40040, Lawrence Berkeley National Laboratory, Berkeley, Calif., 2007.

Finsterle, S., *Parallelization of iTOUGH2 Using PVM*, Report LBNL-42261, Lawrence Berkeley Natl. Lab., Berkeley, Calif., October 1998.

Gunnarsson, G., A. Arnaldsson and·A. Lilja Oddsdóttir, Model Simulations of the Hengill Area, Southwestern Iceland. *Transport in Porous Media 90:3–22, 2011.*

Haukwa, C.B., AMESH — A Mesh Creating Program for the Integral Finite Difference Method, *Report LBNL-45284, Lawrence Berkeley National Laboratory, Berkeley, Calif., 1998*.

Ofwona C.O., *A Reservoir Study of Olkaria East Geothermal System, Kenya*. M.Sc. Thesis. UNU Geothermal Training Programme. Rep. 1, 2002

QGIS Development Team, QGIS Geographic Information System. *Open Source Geospatial Foundation Project. http://qgis.osgeo.org, 2015*

Owens L., E. Porras, P. Spielman and P. Walsh, Updated Geologic and Geochemical Assessment of the Olkaria III Field Following Recent Expansion to 110MW. *Stanford Geothermal. Workshop, 2015*

Porras, E., E. Mabwa, P. Spielman, G. Bjornsson, P. Hirtz, and M. Broaddus. Analysis and Interpretation of NDS Tracer Test Results at the Olkaria West Geothermal Field, Kenya. *GRC Transactions, Vol. 34, 2010*.

Sarmiento, Z.F. and G. Björnsson, Reliability of Early Modeling Studies for High-Temperature Reservoirs in Iceland and the Philippines. *Proc., 32nd Stanford Workshop on Geothermal Reservoir Eng. SGP-TR-183, 2007*.

Wessel, P., W. H. F. Smith, R. Scharroo, J. F. Luis, and F. Wobbe, Generic Mapping Tools: Improved version released, *EOS Trans. AGU, 94, 409-410, 2013*.

SIMULATIONS OF CO_2 PUSH-PULL IN FRACTURES TO ENHANCE GEOPHYSICAL CONTRAST FOR CHARACTERIZING EGS SITES

Andrea Borgia[1], Curtis M. Oldenburg[1], Rui Zhang[2], Lehua Pan[1], Stefan Finsterle[1], T.S. Ramakrishnan[3]

[1]Earth Sciences Division 74-316C, Lawrence Berkeley National Laboratory, Berkeley, CA 94720.
[2]School of Geosciences, College of Sciences, University of Louisiana at Lafayette, Lafayette, LA 70504.
[3]Schlumberger-Doll Research, One Hampton Street, Cambridge, MA 02139.
e-mail: aborgia@lbl.gov

ABSTRACT

We propose the use of CO_2 in push-pull well tests to improve geophysical identification and characterization of fractures in enhanced geothermal systems (EGS). Using TOUGH2-ECO2H, we carried out numerical experiments of push-pull injection-production cycling of CO_2 into single fractures to produce pressure-saturation-temperature conditions that are modeled for their geophysical and wellbore logging response. Our results show that there is a strong difference between injection and production. While the CO_2-plume grows regularly during injection, not all CO_2 is recovered during the following production phase: about 10-20% of the volume of the pores remains filled with CO_2. We find that across the CO_2 saturation range, C11 (the normal stiffness in the horizontal direction perpendicular to the fracture plane) varies by about 15%. It reaches a maximum at around 6%, decreasing exponentially to a minimum at higher saturations. These results are preliminary and are subject to refinement.

INTRODUCTION

Fracture permeability is needed to provide sufficient fluid production for sustainable geothermal energy. A small number of large fractures often dominate fluid production at enhanced geothermal system (EGS) sites and stimulation is used to create a more pervasive network of fractures to access the entire volume of hot rock more efficiently. In order to design and evaluate reservoir stimulation strategies, effective fracture network characterization is needed both of the natural and stimulated reservoirs. To achieve adequate characterization, we propose to use CO_2 in push-pull well testing combined with active-source geophysical monitoring and well logging to enhance the contrast between fractures and matrix and thereby improve fracture characterization. In this part of the project, we carried out push-pull injection-production cycling of CO_2 into single fractures to produce pressure-saturation-temperature conditions that can be modeled for their geophysical and wellbore logging response.

CONCEPTUAL MODEL

Fractures may be conceptualized using five independent topologies (Fig. 1), which serve to define basic model geometries. While these end-member topologies may not represent the complexity of geothermal fields nor relate to tectonic stresses of any given site, they are useful abstractions to understand fundamental behaviors that will be observed in natural systems. Unconnected horizontal fractures belong to Topology 1 where horizontal fractures are perpendicular to the z-axis, or Topology 2 where vertical fractures are perpendicular either to the x- or y-directions. As the fractures in one of these two topologies become more and more interconnected, other topologies emerge. If vertical or horizontal parallel fractures become fully connected in the horizontal or vertical directions, respectively, Topology 3 occurs. Topology 4 develops if there are two sets of vertical fractures. Topology 5 includes three sets of fractures, each perpendicular to one of the main axes.

Injecting CO_2 into fractures results in hydrologic and geophysical property changes, which contrast with previous fully liquid-saturated conditions. Specifically, CO_2 has contrasting wetting properties and very low viscosity relative to hot brine, which promote its flow in the fractures while excluding it from the matrix (Borgia et al., 2012). Therefore, imaging the growth or shrinkage of a CO_2 plume during injection or production tests may give better estimates of the fracture-dominated fluid- and

heat-flow parameters. On the geophysical side, CO_2 causes a significant reduction in seismic velocity, even at low CO_2 saturations, potentially providing a sensitive indicator of the presence of a CO_2-filled fracture. Also, the electrical resistivity of brine/CO_2 mixtures varies continuously across the full range of CO_2 saturation (e.g., Nakatsuka et al., 2010). The combination of seismic and electrical methods is therefore complementary to push-pull well testing and modeling in monitoring the presence of CO_2 and providing constraints on the fracture-dominated hydrologic system.

NUMERICAL MODEL

Fractures in EGS are mostly vertical, which creates challenges for CO_2 push-pull testing because the CO_2 tends to rise upward by buoyancy and resists production during the pull cycle. By using a simple vertical fracture in our numerical model, we maximize the buoyancy effect of the CO_2 In order to evaluate and address the buoyancy challenge.

We model how the CO_2 plume develops during injection and shrinks during production, and geophysical signature of CO_2 saturation, by constructing a 3D vertical fractured volume composed of a single fracture embedded in the rock matrix at 1500 m depth (Fig. 2). On both sides of the fracture, a damage zone and the adjacent un-fractured matrix are present (Table 1). This system represents a single independent productive fracture which is a minimum requirement for a productive geothermal well.

Our domain is 500 × 500 × about 10 m^3, with cells that are 10×10 m^2 parallel to the fracture, and in thickness range from ½ the fracture aperture, to the damage zone thickness, and to the thickness of a set of matrix bocks that increases from 10^{-} m to 10 m. The boundary conditions are varied from those representing an unconfined, to a poorly confined and finally to a fully confined fracture.

We are not considering at the moment the presence of different fractures sets.

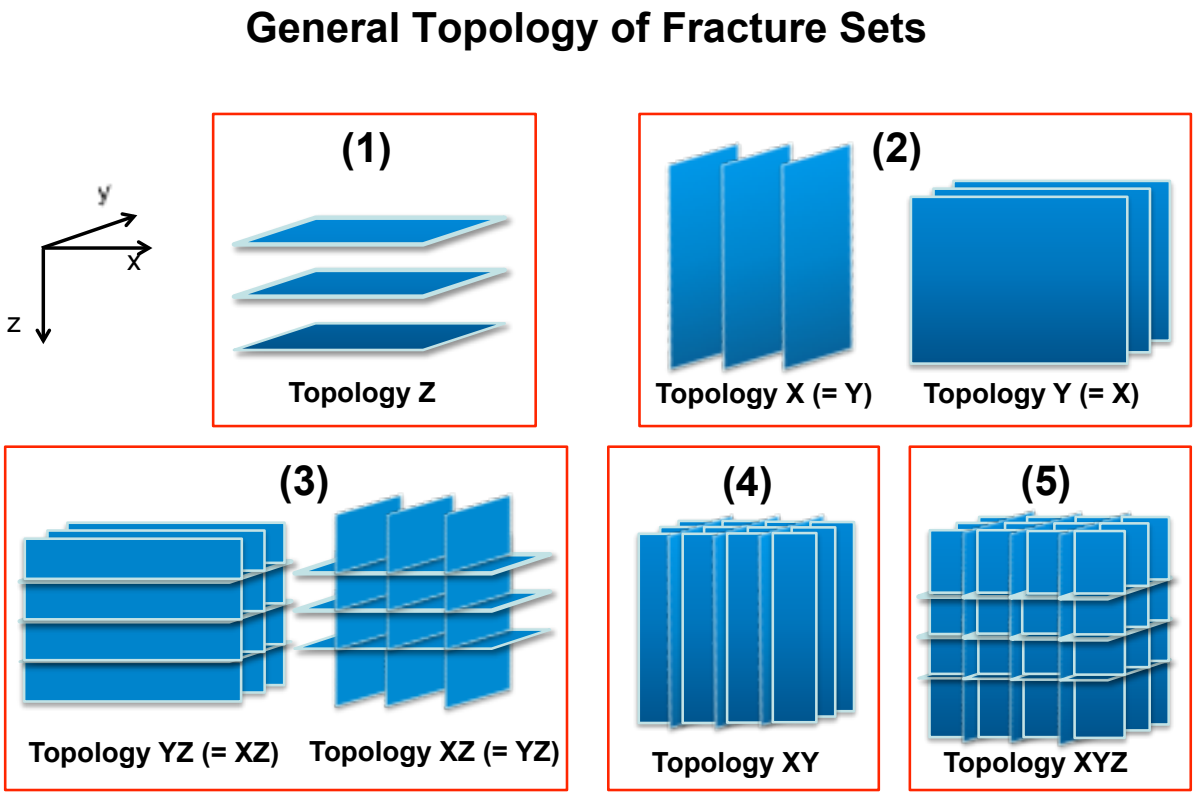

Fig. 1. The five independent fracture topologies.

Table 1. *Characteristic fracture geometry used in our model.*

A = fracture aperture	$= 10^{-4} - 10^{-5}$ (m)
d = damage zone thickness	$= 10^{-2} - 10^{-3}$ (m)
S = fracture spacing	$= 1 - 10^{3}$ (m)
D = fracture density = 1/S	$= 1 - 10^{-3}$ (fracture/m)
H = fracture zone thickness	$= 1 - 10^{3}$ (m)
L = fracture length	$= 1 - 10^{3}$ (m)
W = fracture width	$= 1 - 10^{3}$ (m)

In addition to modeling non-isothermal two-phase flow with TOUGH2 V2.0 (Pruess et al., 2012) using the equation-of-state module ECO2H, we include the effects created by capillary pressure, and salt precipitation and dissolution with, respectively, the associated permeability reduction and increase.

We inject CO_2 at 20-40 °C with a constant pressure of +2 MPa relative to hydrostatic (Fig. 2). During the production test we recover fluids against a constant depressurization of -4 MPa relative to hydrostatic. Production needs a larger pressure difference for minimizing the effect of CO_2 buoyancy, thus allowing a higher CO_2 recovery. Our experiments also include tests for injection and production at the constant flow rates of 100-500 kg/s.

RESULTS

For large injection pressure or flow rate, because CO_2 has a lower viscosity than saline water, a high pressure gradient forms around the well, which tends to extend outward, decreasing in magnitude as the CO_2 plume develops (Fig. 3). During production the high pressure gradient moves back toward the well. The CO_2 plume pervades the fractures, pushing the gas-brine interface away from the well (Fig. 4).

CO_2 injection and production into a vertical fracture

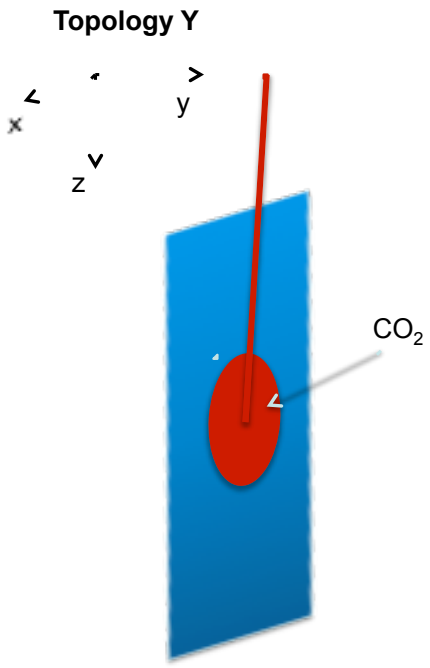

Geometry
The geometry is a simple vertical fracture (topology ***y***), which has dimensions of:
x = 500 (m), with 5 (m) cell side length;
y = 10^{-4} (m), just 1 cell;
z = 500 (m), with 5 (m) cell side length.
Gravity is parallel to z.

Boundary conditions
To simulate a well-connected fracture, all four boundaries are constant P, T, x (conditions don't change)

Rock properties
Density = 2650 kg/m^3
Porosity = 0.20;
Two cases:
1) Permeability = 1.0 *10^{-12} m^2 in all directions;
2) Permeability = 1.0 *10^{-13} m^2 in all directions;
Formation heat conductivity = 2.1 W/m ^{o}C;
Rock grain specific heat = 1.0 *10^3 J/kg ^{o}C.

Fig. 2. Numerical model.

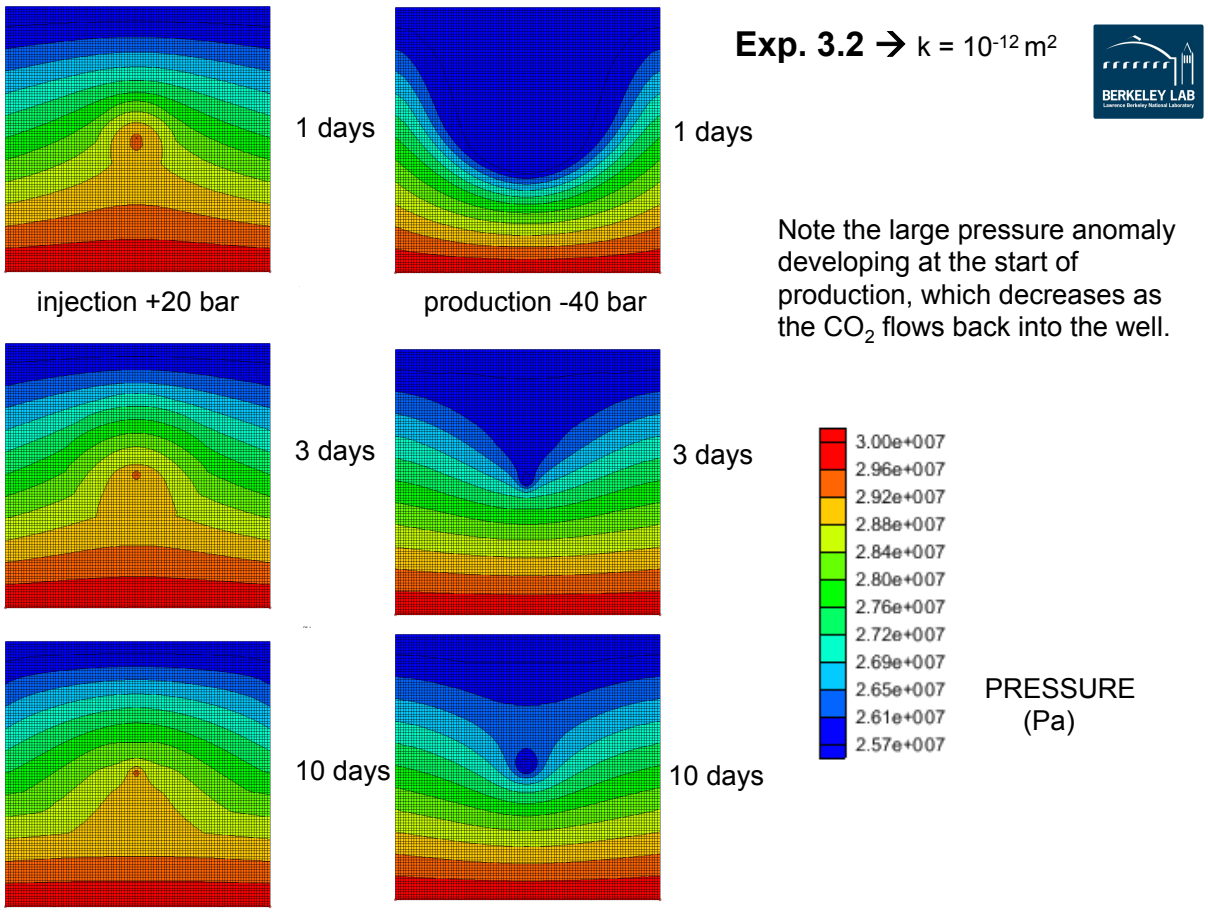

Initial conditions
Pressure = hydrostatic;
NaCl mass fraction in the aqueous solution = 0.10;
CO_2 mass fraction in the aqueous solution = 1.0 *10^{-6};
Temperature = 200 ^oC

Injection run (Push)
Pressure = 20 *10^5 Pa above hydrostatic only in the injection element (= bf150 o injec);
NaCl mass fraction in the aqueous solution = 0.10 throughout;
CO_2 mass fraction in the gas phase = 0.99 only in the injection element (= bf150 o injec);
Temperature = 20 ^oC only in the injection element (= bf150 o injec).

Production run (Pull)
Initial conditions are equal to those at the end of the injection period.
Pressure = 40 *10^5 Pa below hydrostatic only in the injection element (= bf150 o injec);
NaCl mass fraction in the aqueous solution = 0.10 all throughout;
CO_2 mass fraction in the gas phase = 0.99 only in the injection element (= bf150 o injec);
Temperature = 20 ^oC only in the injection element (= bf150 o injec).

Fig. 3. Numerical results: pressure variations

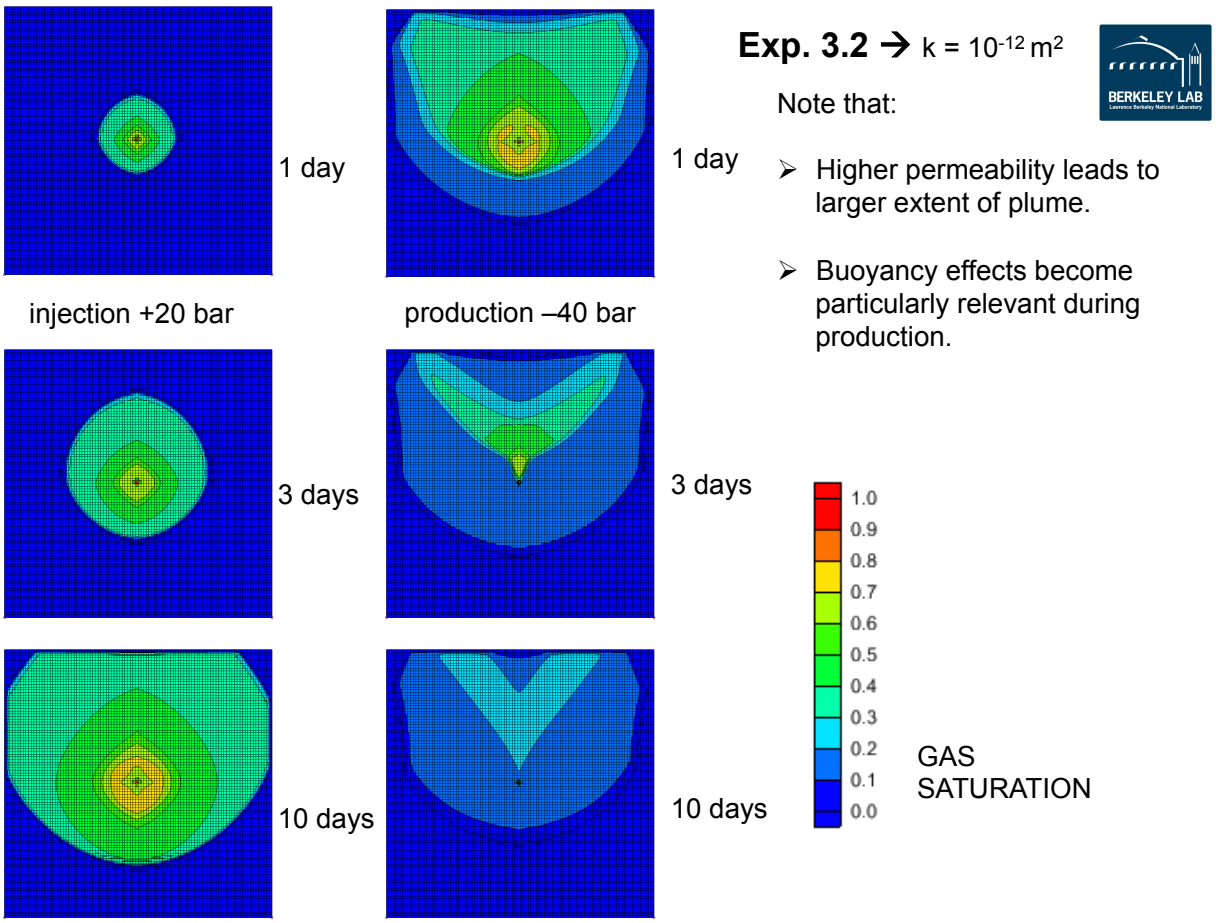

Fig. 4. Numerical results: CO_2 saturation

While close to the well the gas saturation becomes almost immediately unity, the front of the plume has an average gas saturation of 0.3-0.6%. Due to the high surface tension of the water/gas interface, the CO_2 plume remains confined to the fracture and the damage zones. Results are shown in Figs. 3 and 4. As shown, the CO_2 essentially does not enter the matrix even after 10 days of injection. This allows for a remarkably good filling of the fracture and optimal potential for fracture characterization based on the contrast in fluid properties both in space and time (e.g., time-lapse seismic for fracture characterization). Also, buoyancy effects of the plume are limited, but become more important during the following production test. Buoyancy is larger for higher permeability and longer simulation times. Salt precipitates as the CO_2 gas plume dries out the fracture, but tends to re-dissolve into the brine during the following production test as the brine reenters the fracture. The thermal component to the process of CO_2 plume development is insignificant.

There is a strong difference between injection and production. While the CO_2-plume grows approximately symmetrical during injection, not all CO_2 is recovered during the production Phase because of upward CO_2 flow due to buoyance: about 10-20% of the volume of the fracture remains filled with CO_2 (Fig. 4).

In the experiments with higher fracture permeability (10^{-12} m^2 relative to 10^{-13} m^2), a significantly larger CO_2 plume is developed, making the CO_2-push-pull experiment very effective in measuring fracture porosity and permeability.

PRELIMINARY MODELING OF GEOPHYSICAL RESPONSE

Seismic data are sensitive to subsurface fluid properties because different saturated fluids can lead to distinguishable elastic properties of rock (Batzle and Wang, 1992). By using a fracture rock physics model (Nakagawa and Schoenberg, 2007), we estimate the four elements of the stiffness tensor varying with CO_2 saturation as shown in Fig 5. C11 represents normal stiffness in the horizontal direction, which is perpendicular to the fracture plane. C22 represents normal stiffness in the vertical direction, which is parallel to the fracture plane; C33 represents normal stiffness along the fracture plane and C12 is transitional stiffness.

We find that across the CO_2 saturation range, C11 varies by about 15%. It reaches a maximum at around 6%, decreasing exponentially to a minimum at higher saturations. These results are preliminary and are subject to refinement.

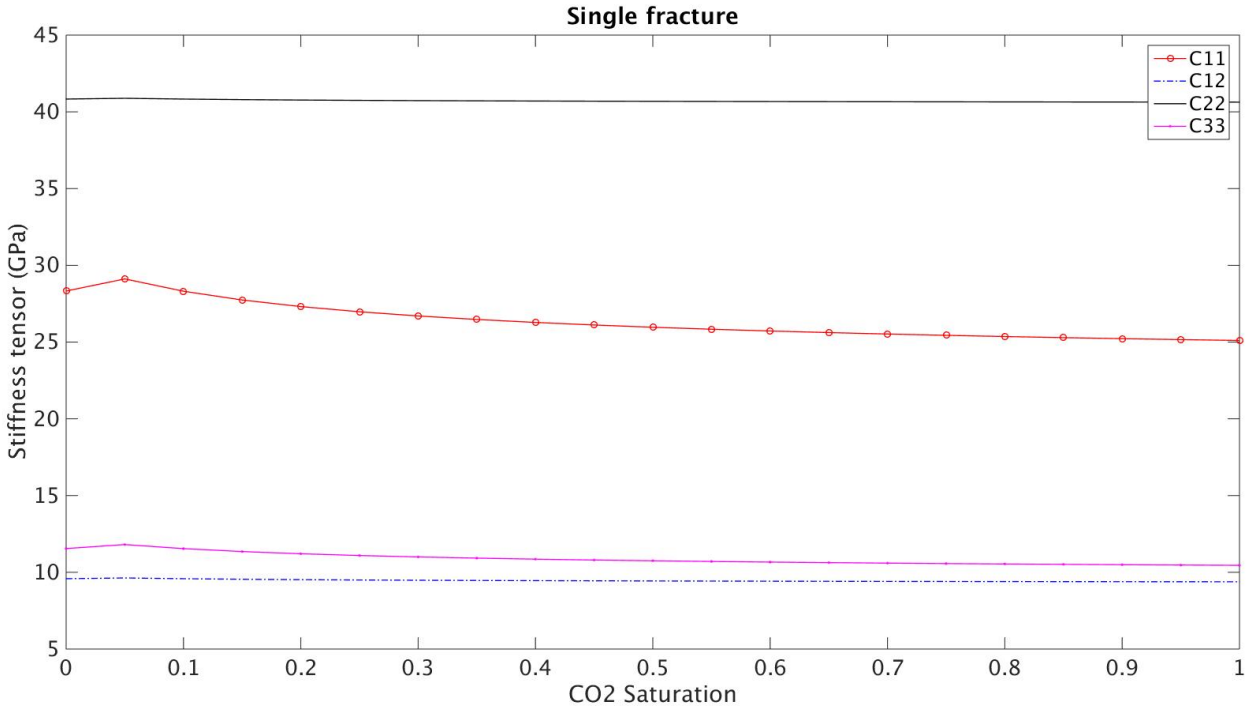

Fig. 5. Stiffness tensor elements as a function of CO_2 saturation.

CONCLUSIONS

For a 2 MPa over-pressure for injection, there is very little influence to the flow by CO_2 buoyancy in the short injection period. This influence is higher for larger permeability and for longer time.

There is a strong difference between injection and production. While the CO_2-plume grows regularly during injection, not all CO_2 is recovered during the production phase: about 10-20% of the volume of the pores remains filled with (trapped) CO_2.

Thermal influence is significant in the injection period (very small porosity), while there is little change in the temperature field during production. In the experiments with higher rock permeability (10^{-12} m^2 relative to 10^{-13} m^2), a significantly larger CO_2 plume is developed, making the CO_2-Push-Pull experiment very effective in measuring permeability.

Depending on the modeled seismic and geophysical logging contrasts arising from the CO_2 in the fracture, more effective fracture characterization may be possible at EGS sites.

The geophysical modeling suggests a change in elastic moduli (stiffness tensor) related to CO_2 displacing brine in a fracture. The moduli change depends on the component of the stiffness tensor being considered. This variability can be used to design the geometry of data acquisition for monitoring experiments.

ACKNOWLEDGMENTS

This work was supported by the Assistant Secretary, Office of Energy Efficiency and Renewable Energy, Geothermal Technologies Program, Enhanced Geothermal Systems, of the U.S. Department of Energy under Contract No. DE-AC02-05CH11231.

REFERENCES

Batzle M and Wang Z., Seismic properties of pore fluid, Geophysics, 57(11), 1992.

Borgia A., Pruess K., Kneafsey T.J., Oldenburg C.M., Pan L., Simulation of CO2-EGS in a fractured reservoir with salt precipitation. *Energy Procedia*, *37*, 6617-6624, doi:10.1016/j.egypro.2013.06.594, 2013.

Nakagawa S and Schoenberg M., Poroelastic modeling of seismic boundary conditions across a fracture, J. Acoust. Soc. Am, 122(2), 2007.

Nakatsuka, Y., Xue, Z., Garcia, H. and Matsuoka, T., Experimental study on CO2 monitoring and quantification of stored CO2 in saline formations using resistivity measurements, International Journal of Greenhouse Gas Control 4, 209–216, 2010.

Pruess, K., C. Oldenburg, and G. Moridis, *TOUGH2 User's Guide, Version 2.0*, Report LBNL-43134 (revised), Lawrence Berkeley National Laboratory, Berkeley, Calif., 2012.

3D DUAL POROSITY MODELING OF TRACER TRANSPORT IN PALINPINON I GEOTHERMAL FIELD, PHILIPPINES

Anthony E. Ciriaco[1] and Michael O'Sullivan[2]

[1]Energy Development Corporation, 38F One Corporate Center, Julia Vargas corner Meralco Avenue, Pasig City
[2]University of Auckland, Auckland, New Zealand

[1]ciriaco.ae@energy.com.ph

ABSTRACT

A small-scale three-dimensional dual-porosity model was developed to simulate the results of the 2009 multi-production/multi-injection NDS tracer test carried-out in Palinpinon I Geothermal Field, Philippines. A single porosity model was first generated using the windows-based pre- and post- processing software for TOUGH2 known as PETRASIM. Partitioning of the single porosity mesh into two computational volume elements to create a double-porosity grid was done using the program called GMINC. Calibration of the model focused on the tracer return data from the four most responsive production wells only. An acceptable match of the tracer recovery profiles for the four observation wells was obtained. Results of the simulation suggest that both the highly permeable faults and the lithologic boundaries provide pathways for transport of tracer chemicals from the injection well to the production area.

INTRODUCTION

Tracer testing has received a significant amount of attention in the geothermal industry. In the Philippines alone, several tracer tests had already been conducted in the past investigating the cause of significant cooling in the production area brought about by the injection of brine, a cooler separated fluid being injected back into the reservoir for environmental compliance and pressure support, a secondary benefit. Shook (2005) reported that more than 100 geothermal tracer tests had been carried out worldwide in the previous 40 years.

In 2009, three (3) different NDS tracers were injected in three (3) different injection wells in the Palinpinon 1 sector of Southern Negros Geothermal Production Field (SNGPF), more commonly known as Palinpinon I Geothermal Field. The amount of tracer recovered in the production wells was analyzed and interpreted using the programs TRINV and TRMASS in the software package ICEBOX (United Nations University Geothermal Training Programme, 1994).

The latest study attempts to simulate the 2009 Palinpinon 1 tracer test results using a small scale 3D reservoir model. The objective of this endeavor is to determine the dominant flow path of fluid transport, whether it is lithologically or structurally-controlled. And since the study is still at the initial stage of investigation, the following simplifications will be imposed in the model:

1) Use the dual-porosity approach in creating the model. This is the closest numerical representation of a highly fractured hydrothermal system like the Palinpinon field.

2) Only the results from one of the three tracer tests will be used as calibration parameters.

3) The tracer recovered only from the top four wells of the selected test will be treated as observation data. These production wells with the highest tracer recovery can be treated as strongly connected to the injection well where the tracer was introduced.

THE PALINPINON GEOTHERMAL FIELD

The Palinpinon Geothermal Field is located in Valencia, Negros Oriental, central Philippines. It was commissioned in 1983 with a total installed capacity of 192.5 MWe. The field is divided into two sectors: the Palinpinon-1 (112.5 MWe) and Palinpinon-2 (80.0 MWe). Early studies conducted in the field suggest that the main structures (Figure 1) that provide channels to the fluid flow are Lagunao Fault, Ticala Fault and its splays, and Puhagan Fault in Palinpinon 1.

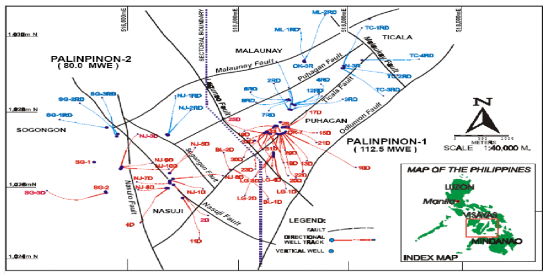

Figure 1. The structural map of Palinpinon I Geothermal Field.

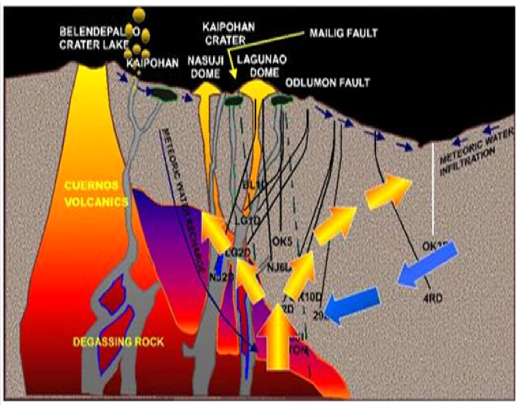

Figure 2. The conceptual model of Palinpinon I Geothermal Field.

The Palinpinon Geothermal Field is a high temperature, liquid-dominated geothermal system with localized two-phase zones in the shallow levels of the reservoir. The conceptual model of the field is shown in Figure 2. Pressure, temperature and geochemical pre-exploitation data suggest a major south-south-west of the Puhagan area. Also, the integrated data indicates presence of two outflow zones – one towards the northeastern sector and the other one towards the western sector of the field.

EARLY TRACER TESTS AND ANALYSES

Urbino (1986) attempted to determine the structural flow paths of injected fluid based on tracer tests conducted in 1981. The study suggests that the rapid and strong returns of the tracer injected indicated direct flowpaths between the injection and production wells provided by faults which have been observed at the surface and subsurface. Bullivant (1988) used computer simulation to analyze the results of the tracer test conducted in 1985. The computer simulator is based on a model of the fluid flow in the reservoir which can include the effects of injection wells, production wells, a single fracture and background flow. Malate (1990) conducted a modeling study to model the silica changes observed in one of the production wells which affected by injection breakthrough. Urbino (1991) used algorithms developed in Operations Research to determine the rate and extent of communication between the injection and production sectors. The last tracer test, before the 2009 test, was in 2005 where Napthalene Disulfonate (NDS) was injected to investigate fluid flow paths at Nasulo and Sogongon sectors. The result shows that around 24% of the chemical tracer injected in SG2RD was recovered at NJ3D (Maturgo et. al, 2006). The result also predicted that an injection rate of 105 kg/s, a thermal breakthrough will be realized in 6 months. In this paper, the thermal effect of injected fluid in SG2RD was simulated using lumped-parameter modelling method. The temperature decline was modelled by integrating the chloride mass balance model into a one-dimensional fracture flow model and by matching the calculated TQTZ in the well.

THE 2009 NDS TRACER TEST

In 2009, a multi injection well/multi production well tracer test was carried out in Palinpinon I on November 23-26 to quantitatively evaluate the effect of the RI loading from three major injection wells and identify the fluid flow paths. The tracers used were 2,7 NDS tracer, 2,6 NDS and 1,5 NDS tracer. Tracer recirculation and the amount of tracer recovered were both corrected and estimated, respectively using the softwares TRINV and TRMASS. There are still some wells, despite after pre-processing, with tracer return profile that suggests presence of re-circulated tracer. Figure 3 shows the plot of 2,7 NDS tracer recovered from the top four most responsive production wells.

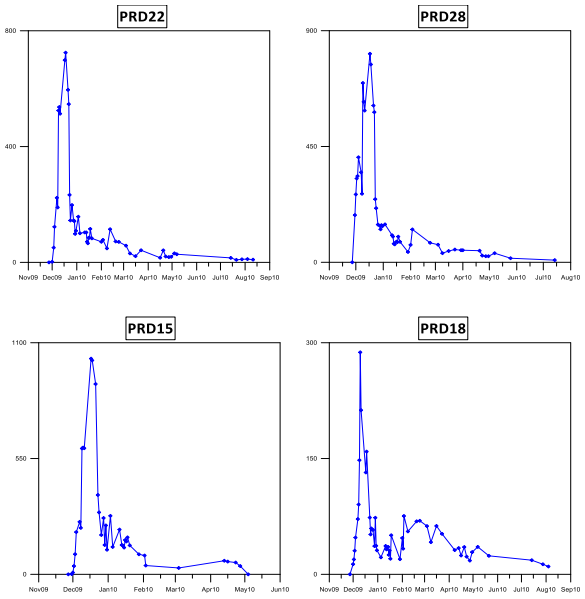

Figure 3. Plots of concentration of tracer recovered from the top four responsive production wells.

MODELLING

To gain an additional insight on the fluid movement from injection sink to production area, the results of 2009 tracer tests were incorporated in a small-scale 3D numerical model as a calibration parameter. There were 3 tracer tests conducted simultaneously, however, due to the complexity of matching all the results from all the tests, it was decided to just use only one of the three results. The selection was based on the nearest proximity of the test injection well to the production area.

Tracer Transport Model Development

Figure 4 shows a sketch of the grid drawn in the map of Palinpinon-1 and was oriented parallel to the major structure. The model grid was limited to cover the Palinpinon I only since the test was intended just for this sector. Three different programs were used in the modeling study: PETRASIM, GMINC (Pruess, 1983) and AUTOUGH2. A uniform porous model was created using a windows-based pre- and post-processor for TOUGH2 (Pruess, 1981) called PETRASIM. The ELEME and CONNE data lifted from the generated model were then used as an input data for the conversion to a dual porosity mesh, which was done using the software known as GMINC. The volume fraction was initially set at 0.001 while the fracture spacing value used was 10. The block was partitioned into two computational meshes, to be able to create a simple model that has matrix and fracture blocks.

The final model has a total of 4 layers that extends from -2200 m to -100 m. Each layer has 5000 blocks and each block has a size of 50 meters x 80 meters. The layering was set-up based on the feed zone distribution at depth per well.

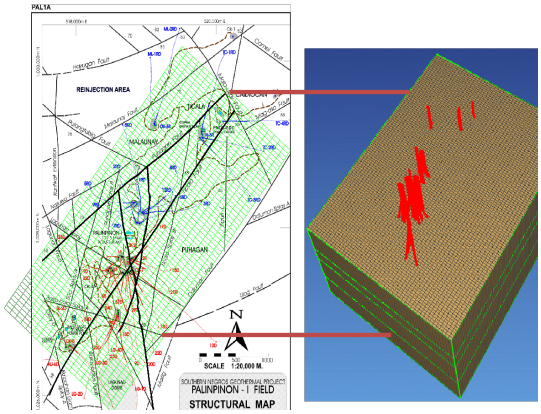

Figure 4. The Palinpinon I Geothermal Field tracer transport model grid.

Boundary Condition

A recharge boundary condition was chosen to allow flow from both sides of the model. The selected blocks on the side were treated as injection wells and were put under the deliverability option.

Pre-Tracer Test Model Calibration

The sequence of an ideal reservoir model calibration process starts with the matching of most if not all of the pre-exploitation data of the field followed by calibration of the model using production data. This is a vital procedure to perform specifically if the model will be used to predict future behavior of the field. But since the main interest of this study is to match the tracer test results and the model will not be used for forecasting, the pre-tracer test model calibration will follow a simplified calibration process: the first one involves getting an acceptable pressure and temperature distribution that agrees with the considered pre-exploitation data of the field and then calibrate this model against the production data of the field. The last production

data that will be used for matching is the day before the tracer test was carried out. The calibrated model will then be referred to as the initial condition for the tracer return profile matching.

Tracer Return Data Matching

Once an acceptable initial condition has been achieved, the model will now be matched against the tracer data. This time, the model will be calibrated against three critical data of a tracer return profile: these are the arrival time, peak concentration and shape of the curve.

The critical calibration parameter in getting the correct tracer arrival time is the volume fraction of the dual porosity block. Tweaking of permeability assignment was most useful in matching the peak concentration and shape of the tracer curve.

Inverse Modeling

An inverse modeling approach was implemented during the calibration of the tracer return data to speed up the calibration time. A freeware called PEST (Doherty, 2005), short for parameter estimation, was used in the process.

DISCUSSION OF RESULTS

Figure 5 shows the plot of the simulated tracer flow against the actual data. A good shape of the curve was obtained for wells PRD22 and PRD28. The model was able to get the correct arrival time. However, the simulation peak concentration is lower than the actual data. The locations of feedzones of wells PRD22 and PRD28 are in the same layer where the tracer was injected. The horizontal permeability distribution at this layer suggests that the flow of tracer towards the production area is controlled by both structures and the lithologic boundary. Different values were assigned for the horizontal permeability both in x and y direction of the blocks.

Of the four observation wells, the simulated tracer profile for well PRD18 is the one closest to the actual curve. The breakthrough time was also accurately matched. The fit for the peak concentration is very close. The slight difference between the match of the tail end is possibly due to the recycling of tracer in the actual data, which was not captured by the model and should have been corrected during the analysis of the data.

The match of the tracer return for well PRD15 needs further improvement. Although the arrival time and the late portion of the tail end of the curve were matched, the shape and the peak concentration are far from the actual data. The feedzone of well PRD15 is located 2 layers below from where the tracer was injected. The difference between the feed location and tracer injection depth may have affected the match obtained for PRD15. This may explain the reason why the tracer return match was not as good as the rest of the wells.

The match between the actual and simulated tracer data for well PRD15 may be improved by adjusting further the permeability assignment not just along the layer where it is located but also the vertical permeability of the blocks where the tracer was injected to allow more tracers to flow down to this layer.

The horizontal and vertical permeability values used in the model that gave a reasonable match of all the calibration dataset for the four wells range from 0.0562 md to 1000 md. Several trial and error runs were made to determine the volume fraction that will produce the first tracer arrival time. Increasing the permeability value helps in increasing the tracer flow towards the well but during the course of calibration, it was found out that the volume fraction has the greater effect. The final volume fraction that gave an acceptable match of the arrival time is 0.002.

FUTURE WORK

Additional work could be done in order to further constrain the model and to gauge the limitation of the 3D dual porosity model for modeling tracer transport. These are the following:

- Match all the other wells with tracer recovery. Aside from the four wells that were matched in this exercise, there are some more wells with minimal tracer recovery. Attempting to match the tracer data for these remaining wells will give extra information on the hydrology of the field.

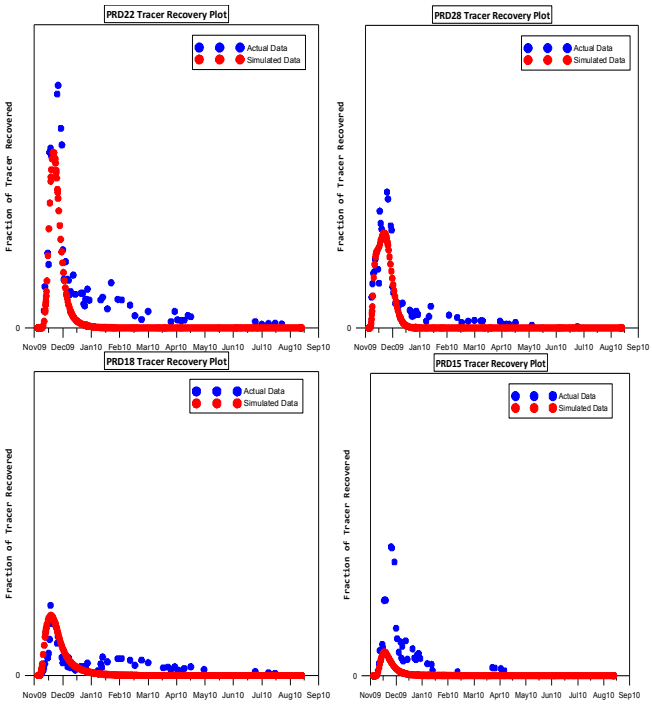

Figure 5. Plots of measured and simulated fraction of tracer recovered from top four responsive production wells.

- Include the results from the two remaining tracer tests to further constrain the model. Interestingly, some of the wells that were matched in the model also have tracer recovery of the other two tracer chemicals injected in different wells. Being able to reproduce these results using the same model will provide additional information about the flow dynamics of the field and will further strengthen the understanding of the connections between the injection sink and the production area.

- Do a process model of the 2011 3D numerical model of Palinpinon Geothermal Field. There is a recently completed 3D reservoir model for Palinpinon I that has successfully matched the steady-state and production data of the field. A process model may be carried out by considering only a small section of the field in the model and then use the tracer the data to further calibrate the selected portion of the model.

- Do a prediction scenario of the likely thermal changes and formulates and injection strategy. The ultimate goal of any tracer testing is to be able to come up with realistic injection optimization strategies. By performing a cooling prediction from a 3D model, the effects and timing of thermal breakthrough can be forecasted. This information will serve as valuable input for a successful resource management.

CONCLUSION

The tracer match for the observation wells was generally acceptable. The simulated tracer curve for three of the four wells is very close to the shape of the profile of the measured data. The arrival time was perfectly matched for most of the wells. Further refinement of permeability values is needed to improve the match for the peak concentration. Overall, this exercise proved that a 3D dual porosity model can be used to model the latest tracer results carried out in Palinpinon I Geothermal Field, Philippines.

ACKNOWLEDGMENT

This project was completed under the supervision of Prof. Michael O'Sullivan of The University of Auckland. The author wishes to thank the Energy Development Corporation management.

REFERENCES

Bullivant, D. P., Malate, R. C. M., O'Sullivan, M. J. and Sta. Ana. F. X. M. (1988). Computer Simulation of a Tracer Test at Palinpinon-I. *Proceedings,* New Zealand Geothermal Workshop.

Doherty, J. (2005). PEST Model-Independent Parameter Esimation User Manual. Watermark Numerical Computing.

Malate, R. C. M. and O'Sullivan, M. J. (1990). Modelling of Silica Breakthrough in Well PN-26, Palinpinon, Philippines. *Proceedings,* New Zealand Geothermal Workshop.

Maturgo, O. O., Sanchez, D. R., Barroca, G. B. and Bayrante, L. F. (2006). Injection Return Management: Initial Results of NDS Tracer Tests in Palinpinon-II and Its Implications to Future Resource Development. *Proceedings,* PNOC-EDC Geothermal Conference

Maturgo, O. O., Sanchez, D. R. and Barroca G. B. (2010). Tracer Test Using Naphthalene Disulfonates in Southern Negros Geothermal Production Field, Philippines. *Proceedings,* World Geothermal Conference.

Pruess, K. (1991). TOUGH2 – A General Purpose Numerical Simulator for Multiphase fluid and Heat Transfer. *Lawrence Berkeley Report No. LBL-29400*.

Prues, K. (1983). GMINC – A Mesh Generator for Flow Simulations in Fractured Reservoirs. *Lawrence Berkeley Laboratory, report LBL-15227*.

Shook, G. M. (2005). A Systematic Method for Tracer Test Analysis: An Example Using Beowawe Tracer Data. *Proceedings*, Stanford Geothermal Workshop (2005)

Urbino, M. E. G., Horne, R. N. (1991). *Optimizing* Reinjection Strategy at Palinpinon, Philippines, Based on Chloride Data. *Proceedings,* Stanford Geothermal Workshop.

Urbino, M. E. G., Zaide, M. C. M., Malate, R. C. M. And Bueza, E. L. (1986). Structural Flowpaths of Reinjected Fluids Based on Tracer Tests – Palinpinon I, Philippines. *Proceedings,* New Zealand Geothermal Workshop

EXPERIMENTAL STUDY ON FLOW FRICTION AND HEAT TRANSFER PERFORMANCE OF A SINGLE ROUGH FRACTURE IN GRANITIC ROCK UNDER CONFINING PRESSURE

Xiaoxue Huang, Jialing Zhu, Jun Li

Tianjin University
92 Weijin Road, Nankai District
Tianjin 300072, China
e-mail: xiaoxue@tju.edu.cn

ABSTRACT

For better understanding of flow and heat transfer in the fractured rock in Enhanced Geothermal System (EGS), experiments were conducted to investigate the single phase convective heat transfer and flow through a single fracture in a cylindrical granite with a length of 100 mm and a diameter of 50 mm. Rock temperature was changed to simulate various underground conditions in EGS. It is found that the Poiseuille numbers and the average Nusselt numbers significantly deviate from those of conventional theories. The large relative roughness raises the flow friction and reduces the heat transfer coefficient. Correlations were provided for predicting Po and Nu. The roughness-viscosity model (RVM) was used to explain the deviation and a satisfactory agreement between the RVM predicted results and the experimental data was reached.

INTRODUCTION

Enhanced Geothermal System (EGS) would provide access to a much larger fraction of deep geothermal resources. To utilize these hot dry rock (HDR) resources, hydraulic stimulation is required to create interconnected fractures for lower flow resistance.

Among the studies of EGS, prediction of the artificially fractured reservoir performance presents considerable challenges due to limited knowledge of the detailed nature of flow and heat transfer in the fractured rock.

Theories for laminar flow through ideal parallel plates demonstrate that when introducing the characteristic length equal to 4 times the hydraulic radius (R_h), the Poiseuille number (Po), product of the Reynolds number (Re) and the friction factor (f), is only determined by the cross-section dimensions of the channel. Accordingly, the widely employed cubic law which indicates the linear relationship between the ratio of flow rate to hydraulic gradient and the cube of fracture aperture was derived (Witherspoon et al., 1980). For the hydraulic behavior of water flowing through the rock fracture, the effect of roughness of the microscale fracture should be taken into account as the surface-to-volume ratio is large and the surface condition influences flow significantly. According to the studies of Shen et al. (2006), Po is not fixed and thus the cubic law needs modification to take account of the roughness influence.

Simultaneously, heat transfer of water through the fracture is also of great significance to EGS as thermal energy is extracted through the fluid-rock heat exchange, whereas it is often ignored as local thermal non-equilibrium is assumed.

A roughness-viscosity model (RVM) was proposed by Mala and Li (1999) and applied to quantify the effects of the surface roughness on laminar flow in microtubes and trapezoidal microchannels. Generally, the model regards the fluctuations near the wall as a so urce of augmented momentum transfer, and the increased momentum transfer is modelled by means of a local roughness viscosity. Thus, flow friction is increased due to the larger effective viscosity (μ_{eff}), sum of the fluid viscosity (μ_f) and the roughness viscosity (μ_r).

To study the fluid flow and heat transfer process in the fractured rock, high temperatures is attained to simulate the underground conditions of granite in EGS, low temperature water is pumped through the rough fracture. Relations

for dimensionless variables are formulated from fitting the measured data. The roughness-viscosity model is applied to predict hydraulic and heat transfer performances.

EXPERIMENTS

A cylindrical rock sample with a diameter of 50 mm and a length of 100 mm was cored from a granite block. It was then split into two halves under tensile stress by sharp wedges loaded by uniaxial compressive apparatus, which are standard procedures of the Brazilian test. Adhesive was applied to the lateral sides of the fracture to prevent fluid leakage.

Surface Topology Measurement

A Laser Scanning Microscope was used to perform non-contact 3D scan of the coarse tensile fracture surfaces. The average surface roughness R_a was derived as 20 μm.

Experimental Apparatus and Procedure

Fig. 1 shows the experimental apparatus. The fractured rock wrapped by thermal shrinkable sleeve was immersed in the anti-wear hydraulic oil that fills the high pressure triaxial cell. Deionized water was pumped to the test section through a Teledyne Isco syringe pump. An electric heater with temperature control was wrapped around the cell. Operating mode of constant flow was chosen, and the pressure was recorded automatically by the pump. Pt100 sensors were used to measure the inlet and outlet fluid temperature, together with the rock's outer surface temperature. Rock displacement was monitored by the attached transducer. A high-speed data acquisition system was used to collect the experimental data.

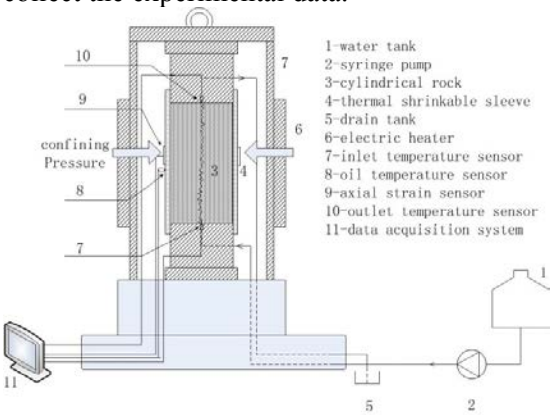

Figure 1. Schematic of experimental apparatus.

DATA REDUCTION

f is related to the fluid pressure drop over the fracture as

$$f = \frac{4\delta^3 b^2 \Delta P}{\rho L Q^2} \tag{1}$$

The geometry parameters, δ, b and L represent aperture, width and length of the fracture respectively.

Re is defined as

$$\mathrm{Re} = \frac{2\rho Q}{\mu_f b} \tag{2}$$

Po is the product of f and Re.

$$\mathrm{Po} = f\mathrm{Re} = \frac{8\delta^3 b \Delta P}{\mu_f L Q} \tag{3}$$

RESULTS AND DISCUSSION

Flow Friction

At different rock outer surface temperature (t_0), a larger pressure gradient is required at lower temperature as kinetic viscosity increases as shown in Fig. 2. The linear variation of pressure gradient with flow rate indicates that the conventional theories for flow between ideal parallel plates might also be applicable but need modifications for the fracture.

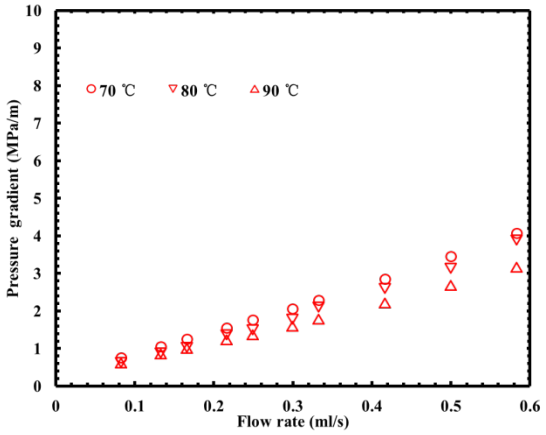

Figure 2. Measured flow rates and pressure gradients.

For fully developed laminar flow through rectangular channels, the conventional theories demonstrate that Po is only determined by the aspect ratio, and fixed at 96 with the width-to-height ratio approaching ∞. However, Po is not fixed as shown in the previous experiments on

microchannels, and it is due to the effects of surface roughness. Based on the experiments in this study, correlations for Po and Re is derived as Eq. (4), Fig. 3 shows Po based on the measured data, together with Po predicted by Eq. (4). It is demonstrated that Po decreases with Re, especially at low Re, and the slope is decreasing with Re, suggesting that Po may approach a fixed value if Re keeps increasing. Po is inversely proportional to the rock temperature as viscosity is lower at higher temperatures.

$$\mathrm{Po} = 96^{2.3053}\,\mathrm{Re}^{-0.2902} \qquad (4)$$

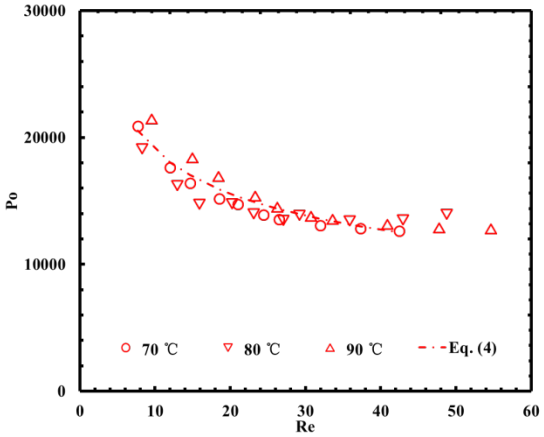

Figure 3. Poiseuille number vs. Reynolds number.

Heat Transfer

For fully developed laminar flow, the average Nusselt number based on hydraulic diameter of cross section with height-to-width ratio approaching 0 and assuming constant wall temperature is 7.54 according to Holman (2010), whereas in the fracture, Nu is about two orders of magnitude smaller.

The experimental result of average Nusselt number versus the non-dimensional length L_h^+ is plotted in Fig. 4.

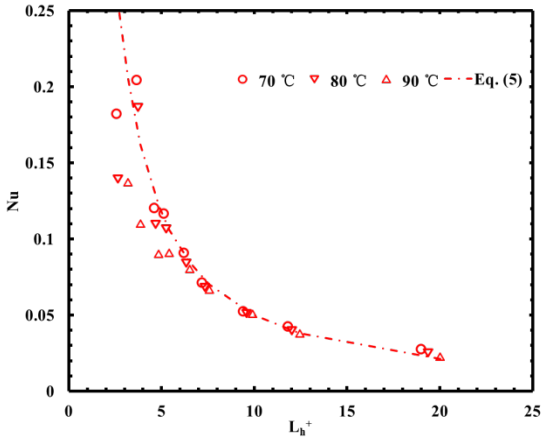

Figure 4. Nusselt number vs. Reynolds number.

According to Fig. 4, Nu decreases with L_h^+, which is obvious as heat transfer is enhanced at higher Re and Pr. However, the slope of Nu against L_h^+ is getting less steep along the positive x axis. A similar trend was presented by Shen et al. (2006), and this was explained that the thermally developed flow is approached. The relation for Nu is concluded as Eq. (5).

$$\mathrm{Nu} = 7.54^{-2.8569}\,\mathrm{Re}^{1.2205}\,\mathrm{Pr}^{1.3437} \qquad (5)$$

The curve predicted by Eq. (5) is also presented in Fig. 4 for comparison with the measured data. From the above equation, Nu is much lower than the constant 7.54, and increases with Re as heat transfer is enhanced by larger velocity. Another point to note is the exponent of Prandtl number is over 1 while those in the empirical relations of conventional theories are usually lower than 1, which can be explained by the roughness-viscosity model as the fluid viscosity used for the Prandtl number is lower than the effective viscosity.

Roughness-viscosity Model Prediction

Previous studies demonstrated that the relative roughness of such an order of magnitude as in this study may have profound effects on the velocity field and the temperature field, therefore the pressure drop and heat transfer coefficient are greatly affected by the surface roughness and conventional theories cannot be directly applied.

RVM by Mala and Li is employed to account for the deviation from conventional theories.

In a manner similar to the eddy viscosity in turbulent flow, the roughness viscosity was

introduced to the momentum equation. The effective viscosity can be obtained through RVM, therefore the flow rate can be computed. Fig. 5 compares the experimental data of flow rates with Re and the RVM predicted results. The agreement between the RVM predicted curves and the experimental results implies that the roughness-viscosity model proposed can be used to predict flow through the fracture.

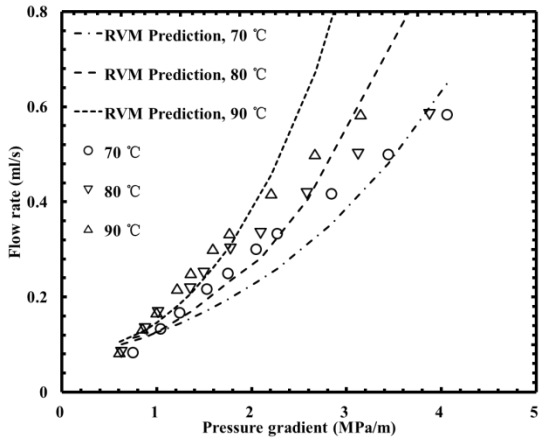

Figure 5. Comparison of experimental data with numerical results based on the roughness-viscosity model (flow friction).

With the velocity distribution obtained, temperature distribution can be easily acquired by a numerical solution. Nu predicted by RVM is shown in Fig. 6 for comparison with the experimental data. The numerical results exhibit the same trend as the experimental ones, generally, a satisfactory agreement is obtained.

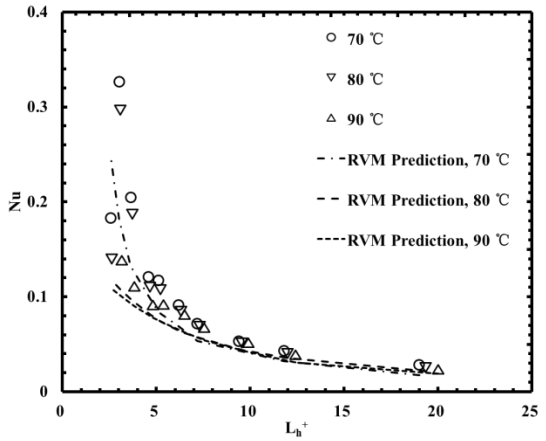

Figure 6. Comparison of experimental data with numerical results based on the roughness-viscosity model (heat transfer).

CONCLUSION

Flow and heat transfer characteristics of water through a fractured cylindrical rock sample were studied. The rock outer surface temperatures were kept at 70, 80 and 90°C.

For a certain volumetric flow rate, the pressure gradient required to force water passing through the fracture is much higher than that predicted by the conventional theories, meanwhile heat transfer coefficient is lowered by about two orders of magnitude. The roughness-viscosity model (RVM) proposed in previous studies was employed for numerical prediction, and the numerical solution agrees well with the experimental results. These results imply that for consideration of the roughness effect on fracture flow and fluid-rock heat transfer without local non-equilibrium assumption, the effective viscosity can be used to substitute the fluid viscosity and satisfactory numerical results can be readily obtained.

ACKNOWLEDGMENT

The authors gratefully acknowledge the support of this work by the National Natural Science Foundation of China (Grant No. 41272263).

REFERENCES

Witherspoon PA, Wang JSY, Iwai K, Gale JE. Validity of Cubic Law for Fluid Flow in a Deformable Rock Fracture. *Water Resources Research.* 1980;16(6):1016-24.

Shen S, Xu JL, Zhou JJ, Chen Y. Flow and Heat Transfer in Microchannels with Rough Wall Surface. *Energy Conversion and Management.* 2006;47(11-12):1311-25.

Mala GM, Li D. Flow Characteristics of Water in Microtubes. *International Journal of Heat and Fluid Flow.* 1999; 20:142-8.

Holman JP. *Heat Transfer.* 10 ed: McGraw Hill, 2010.

STRESS FIELD RESPONSE TO MASSIVE INJECTION OF COLD WATER INTO A GEOTHERMAL RESERVOIR: TOUGH-FLAC SIMULATION

Pierre Jeanne, Jonny Rutqvist

Earth Sciences Division
Lawrence Berkeley National Laboratory
Berkeley, CA 94720, USA
e-mail: pjeanne@lbl.gov

ABSTRACT

We study the evolution and distribution of the stress tensor within the northwest part of The Geysers geothermal field during 9 years of injection (from 2003 to 2012). Based on a refined 3D structural model, developed by Calpine Corporation, where the horizon surfaces are mapped, we use the GMS™ GUI to construct a realistic three-dimensional geologic model of the Northwest Geysers geothermal field. This model includes a low permeability graywacke layer that forms the caprock for the reservoir, an isothermal steam zone (the Normal Temperature Reservoir) within metagraywacke, a hornfels zone (the High Temperature Reservoir), and a felsite layer that is assumed to extend downward to the magmatic heat source. This model is mapped into a rectangular grid for use with the TOUGH-FLAC numerical simulator. Then, we reproduce the injection history of seven active wells between 2003 and 2012. Finally, our results are compared with previously published works where the stress tensor was studied from the inversion of focal plane mechanism in the same area and during the same period. As in these publications we find that: (1) changes in the orientation of principal horizontal stress are very small after one decade of injection, and (2) at injection depth significant rotations of the initially vertically oriented maximum compressive principal stress occur in response to changes in the fluid injection rates. As observed in the field, we found that σ_1 tilted towards the σ_2 direction by approximately 15° when injection rates were at their peak level. Such a rotation consequently results in a local change in the state stress from a normal stress regime ($S_v > S_{Hmax} > S_{hmin}$) to a strike slip regime ($S_{Hmax} > S_v > S_{hmin}$) above and below the injection zone. Our results show that thermal processes are the principal cause for the stress tensor rotation.

INTRODUCTION

The stimulation of geothermal reservoirs by massive injection of cold water is frequently accompanied by induced seismicity (Davis and Frohlich, 1993) and it is important to understand the geomechanical processes responsible for this phenomenon. Here, we focus our study on injection-induced stress changes occurring at reservoir depth. Several scientific studies performed at The Geysers geothermal field, California, and based on the inversion of focal plane mechanism were recently published on this topic (Martinez-Garzón et al., 2013 and 2014; Boyle and Zoback, 2014). These studies all indicate that The Geysers is subject to a normal/strike slip faulting regime ($S_V \approx S_{Hmax} > S_{hmin}$) with an average S_{Hmax} orientation ranging around N20. Boyle and Zoback (2014) also showed that, at the scale of the entire Northwest Geysers area, neither thermal stresses nor the pressure front associated with movement of fluids and steam, caused by the injection and production activities over the past 50 years, have perturbed the orientation of S_{Hmax}. Martinez-Garzón et al. (2013) highlighted, around one injection well, significant rotations of the orientation of the maximum compressive principal stress (σ_1) in response to changes in the fluid injection rates. They observed that σ_1 tilted from vertical towards the original σ_2 direction (S_{Hmax}) by approximately 20° when injection rates were at their peak level. Martinez-Garzón et al. (2013) also observed a normal faulting regime at the reservoir depth bounded by a strike –slip regime above and below.

Even if these studies found the same general results (stress regime and S_{Hmax} orientation), they focused on different scales and locations of The Geysers (entire Geysers, part of northwest Geysers, and around one injection well) where the stress regime inside the geothermal field

changes with depth. These studies show the complexity to fully describe the spatio-temporal evolution of the stress state caused by fluid production and massive injection of cold water in a geothermal field. Here, we present a three-dimensional Thermo-Hydro-Mechanical (THM) numerical simulation to study the evolution and distribution of the stress tensor within the northwest part of The Geysers geothermal reservoir and in particular a detailed study of the transient evolution around one well (Prati-9) until 2012.

MODELING APPROACH

We use the TOUGH-FLAC numerical simulator (Rutqvist et al., 2002; Rutqvist, 2011), which has the required capabilities for modeling of non-isothermal, multiphase flow processes coupled with stress changes in a steam-dominated geothermal reservoir such as The Geysers.

Calpine Corporation developed a refined 3D structural model where the boundaries of the main geological units are mapped. Based on these subsurface horizons, we use the Groundwater Modeling System (GMS; Aquaveo, LLC in Provo, Utah) to construct a realistic three-dimensional geologic model of the Northwest Geysers geothermal field (Fig. 1a). GMS is a graphical user environment which consists of a graphical user interface (the GMS program) providing tools for model conceptualization, mesh and grid generation. Our model includes, from the top down, a low permeability graywacke layer (caprock), an isothermal steam zone within metagraywacke (the normal temperature reservoir: NTR), a hornfels zone (the high temperature reservoir: HTR), and a felsite layer that is assumed to extend downward to the magmatic heat source. We then map this model onto a rectangular grid for use with the TOUGH-FLAC numerical simulator. The numerical model extends vertically from 650 to -6500 m (elevation relative to sea level) and 8250×10750 m horizontally. At the bottom of the domain in the felsite, we impose constant temperature, constant saturation and low-permeability boundary. Laterally we set no-flow boundaries (no mass or heat flow), while at the top we use a fully aqueous-phase-saturated constant atmospheric pressure boundary condition. The initial thermal and hydrological conditions (vertical distributions of temperature, pressure, and liquid saturation) are established through steady-state, multiphase flow simulations (Fig.1b, c and d). The initial reservoir temperature in the NTR is approximately 240°C down to the HTR, and then gradually increases up to 370°C toward the bottom boundary at a depth of -6.5 km (this lower value was used because it is the upper temperature limited of the TOUGH module used). At The Geysers, the steam pressure within the hydraulically confined NTR is only a few megapascals. Null displacement was imposed on the bottom and side boundaries, only the top boundary is free to move.

Common to all the simulations carried out during this study, an initial normal stress regime ($S_V \geq S_{Hmax} > S_{hmin}$) is imposed throughout the models at the beginning of the simulations. S_V is equal to the lithostatic stress. S_{Hmax} is oriented N020E (Boyle and Zoback, 2014), $S_{hmin} = 0.34 \times S_V$ (Jeanne et al., 2014) and $S_{Hmax} = 0.99 \times S_V$. The orientation of the stress tensor is extracted from the simulation results once every month. We extract the nine components that completely define the 3D state of stress given by matrix A (Eq.1) and we calculate its eigenvectors to find the vector coordinates of σ_1, σ_2 and σ_3. S_{Hmax} magnitude is calculated using Equation (2), where θ is S_{Hmax} orientation relative to North. In our model z is vertical and the x and y axes are oriented N050 and N130 respectively.

Table 1: properties used in the 3D model

	Caprock	NTR	HTR	Felsite
Young's modulus (GPa)	28	28	28	28
Poisson's ratio (-)	0.25	0.25	0.25	0.25
Thermal conductivity (W/m°C)	3.2	3.2	3.2	3.2
Thermal expansion coefficient (°C $^{-1}$)	10^{-5}	10^{-5}	10^{-5}	10^{-5}
Specific heat (J/kg°C)	880	880	880	880
Permeability (m^2)	10^{-25}	10^{-14}	5×10^{-15}	5×10^{-16}
Porosity (%)	5	5	2	1

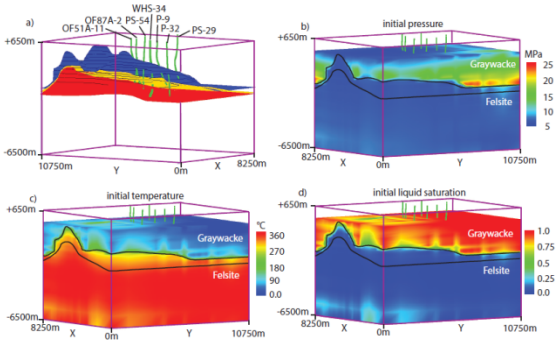

Figure 1: (a) Subsurface horizons of the bottom of the caprock and top of the NTR in blue, top on the HTR in yellow and top of the Felsite in red. The injection wells are green. Initial distributions of (b) pressure, (c) temperature and (d) liquid saturation.

$$A = \begin{pmatrix} \sigma xx & \sigma xy & \sigma xz \\ \sigma yx & \sigma yy & \sigma yz \\ \sigma zx & \sigma zy & \sigma zz \end{pmatrix} \quad (1)$$

$$S_{Hmax} = \sigma_{xx} \cos^2 \theta + 2\, \sigma_{xy} \sin\theta \cos\theta + \sigma_{yy} \sin^2 \theta \quad (2)$$

MODELING RESULTS

Evolution of the stress tensor over the Northwest Geysers area from 2003 to 2012

Figure 2 presents several map views of pressure and temperature distribution, and the vertical rotations of σ_1 (β) and σ_2 (α) at the end of 2012 after nine years of injection and the horizontal rotation of S_{Hmax} (θ). These map views are located inside: the NTR (z = -1900m), the HTR (z= -2316m), and the felsite (z = -3031m).In the simulation, only changes in temperature affect the orientation of S_{Hmax}, which slightly rotates in the vicinity of the injection wells where the temperature drops (Fig. 2g, h). S_{Hmax} rotates up to ≈13° close to the wells but the rotation quickly decreases below 10° at some distance from the wells. No change in S_{Hmax} orientation is observed inside the felsite where no significant change in temperature is calculated.

Evolution of S_{Hmax} and S_V around Prati-9 from 2007 to 2012

Figure 3 present the stress tensor distribution around Prati-9 at the end of 2012 along a cross section oriented N050. We select several control points where the 3D rotation of the stress tensor is calculated. Relative to the injection zone these control points are located: above (CP1), beside (CP2), and below (CP3 to CP12).

Above the injection well (CP1, z = -1420 m):

It is where the smallest changes in pressure and temperature are calculated with ΔP ≈ 0.6 MPa and ΔT ≈ 0°C (Fig.4a). However, it is also where the largest rotation of σ_1 is calculated with a rotation up to ≈ 70° after five years of injection (Fig.4b). As noticed previously σ_1 rotates towards σ_2 direction which in turn rotates by the same angle (α = 90-β). The rotation of S_{Hmax} is very small, only few degrees (Fig.4c). Figure 3 shows that these changes in the stress tensor are very localized and do not extend far away above the injection well. These rotations result from: (i) a reduction of the vertical stress caused by the stress reduction within the cooling area, and (ii) by the associated stress redistribution above the cooling area (Fig.4d) as shown in Rutqvist et al., (2007).

Beside the injection well (CP2, z = -1886 m):

Interestingly compared to CP1 and CP3, this is the location where the largest changes in temperature are calculated (ΔT ≈ -50°C) (Fig.4e) but also where the calculated rotation of σ_1 is the smallest (up to 14 degrees) and follows the seasonal variations of the injection rate (Fig.4f).

Every year, the largest rotation of σ_1 occurs during the winter when injection rate is at its peak level. It is also the location where the largest changes in S_{Hmax} direction occur with a horizontal rotation up to 16° (Fig.5g). These changes in stress tensor direction are mostly caused by the stress-reduction. Beside the injection well, the liquid zone and so the cooling area tends to expand laterally, which results in a vertical stress reduction almost equal to the horizontal stress reduction (Fig.5h). Over the years, these small differences between S_V and S_{Hmax} result in small and progressive variations of σ_1 direction. Moreover, the seasonal variations of the injection rate produce a higher cooling during winter (at high injection rate) than during summer (at low or null injection rate). Indeed, when the injection rate decreases or stops during the summer, the temperature stop dropping and slightly increases. The consequences is that during winter (at injection peak), S_V decreases a slightly more than S_{Hmax} leading to the rotation of σ_1, and during summer S_V increases a slightly more than S_{Hmax} and so the stress tensor rotates back towards its initial value.

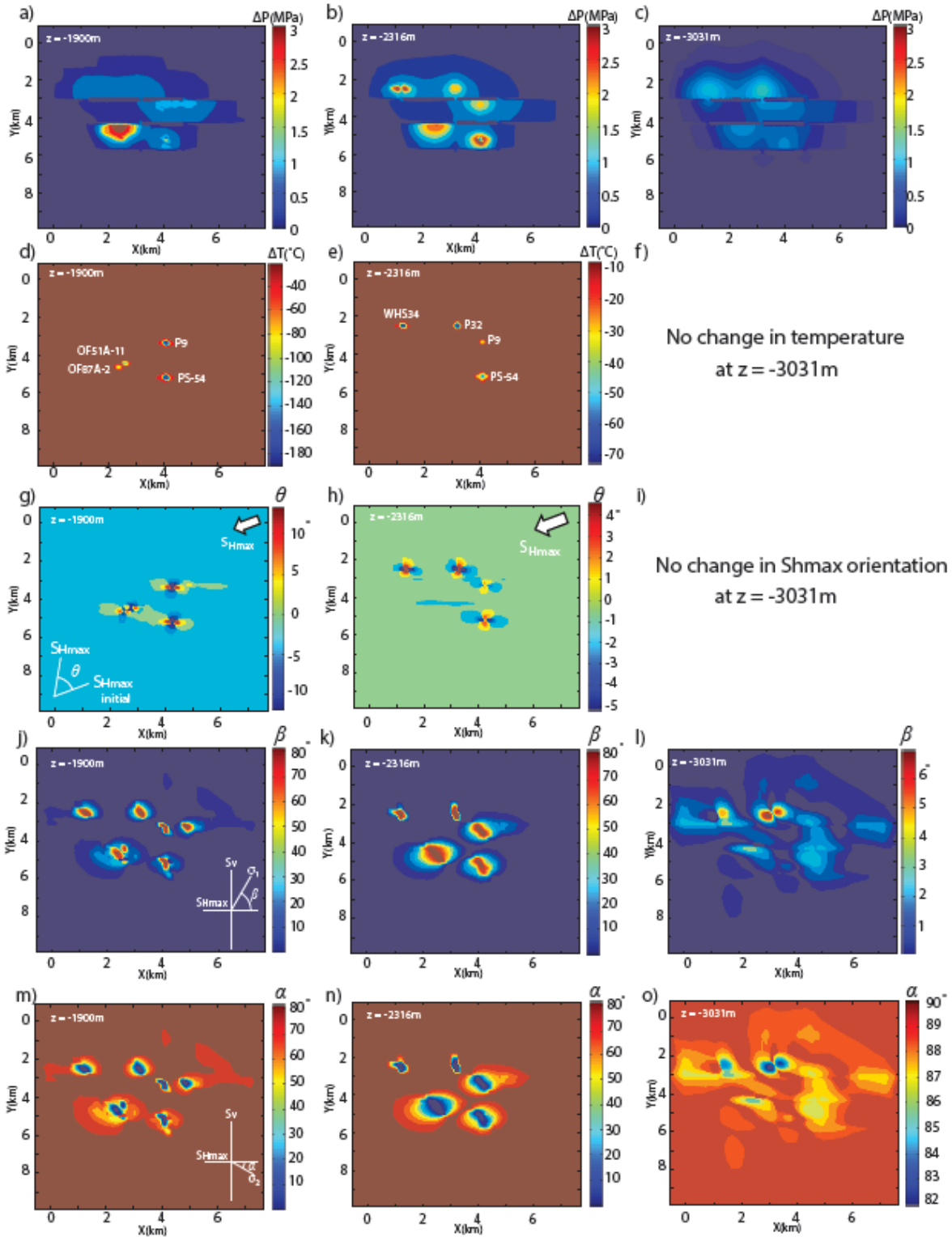

Figure 2: Calculated (a,b,c) pressure and (d,e,f) temperature change distribution, (g,h,i) orientation of S_{Hmax} , and vertical rotation of (j,k,l) σ_1 and (m,n,o) σ_2 inside: the Normal Temperature Reservoir, the High Temperature Reservoir and the felsite at the end of 2012.

Below the injection well (CP3, z = -2101 m):

At CP3, the temperature slightly decreases ($\Delta T \approx -20°C$) and changes in pressure are higher than those calculated at CP1 (up to $\Delta P \approx 1.8$ MPa) (Fig. 5k), however, the rotations of the stress tensor are very similar. In less than one year, σ_1 rotates as much as 60° towards the σ_2 direction and reaches a quasi-equilibrium state, which is slightly influenced by changes in temperature. At the same time, changes in the S_{Hmax} direction are less than 10 degrees. Figure 6a shows at nine control points located below the injection well Prati-9 (CP 4 to 12 in Fig. 4) how far and how quickly changes in σ_1 orientation propagate below the injection zone, which is located between -1550 and -2050 m below sea level in our simulation. We observe that (i) the perturbations of the stress tensor propagate much farther than the temperature variations, and (ii) from the bottom of the injection well to 800 m deeper, the orientation of σ_1 changes from vertical (90°) to almost horizontal (20°) creating a strike-slip stress regime just below the well and a normal stress regime 800 m deeper. We also notice that the part of the reservoir subject to a strike-slip stress regime (σ_1 oriented 20°) deepens at a rate of approximately 100m per year. Figures 6c to6e present the evolution of S_V and S_{Hmax} at three control points below the injection well: CP4 (z = -2173 m), CP 7 (z = -2387 m), and CP10 (z = -2602 m). It appears that the stress rotation is caused by a decrease in S_V (due to the vertical stress drop in the upper part, inside the cooling area), and by an increase in S_{Hmax} caused by stress redistribution around the cooled area.

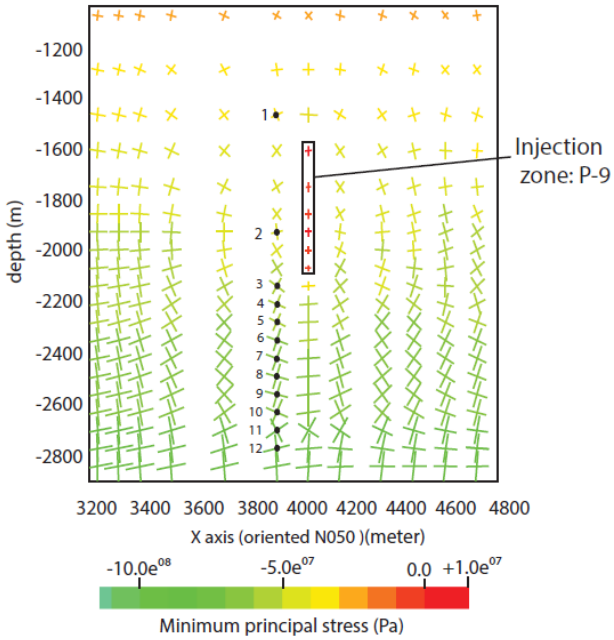

Figure 3: Stress tensor distribution around Prati-9 after 5 years of injection (end 2012) with the location on the different control points used during this study (From CP1 to CP12).

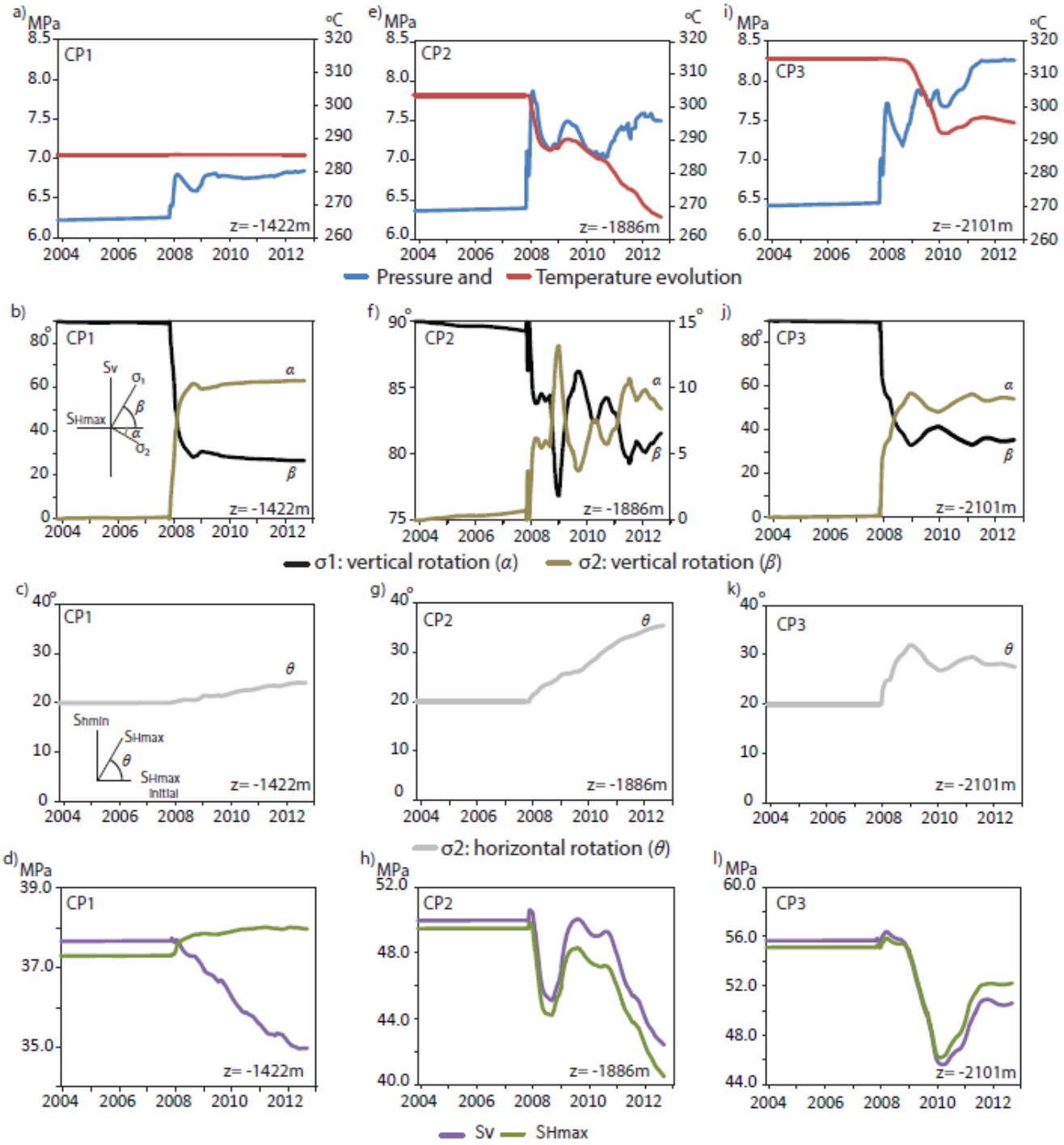

Figure 4: Calculated evolution changes in fluid pressure, temperature, rotation angles of: σ_1 and σ_2 relative to the horizontal plane and rotation of S_{Hmax} at monitoring points above (a, b, c, d) beside (e, f, g, h) and below (i, j, k, n) the injection zone.

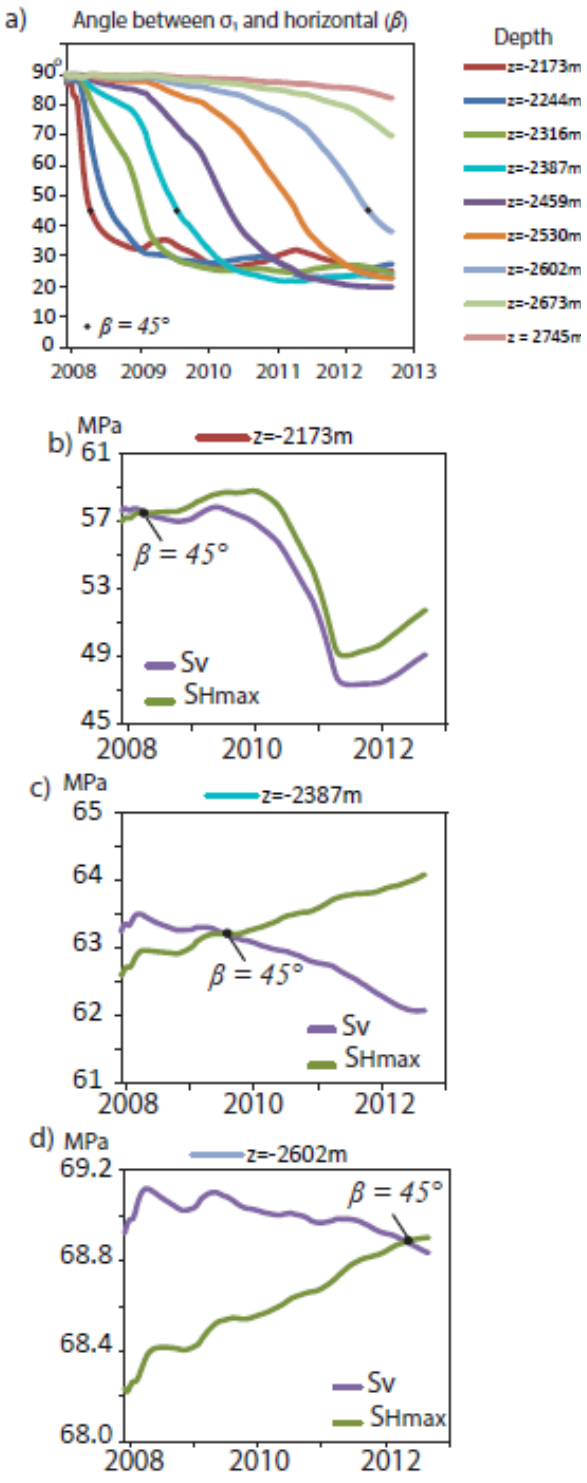

Figure 5: Calculated evolution of (a) σ_1 orientation and (b) temperature at nine control points located between 173 m and 745 m below the injection well. Calculated evolution of S_{Hmax} and S_V at (c) z =-2173m, (d) z = -2387 m and (e) z= -2602 m.

DISCUSSION

As observed by Boyle and Zoback (2014), we find that the direction of S_{Hmax} around the injection wells stay very similar to the regional orientation of S_{Hmax}. Excepted for a rotation in S_{Hmax} of 15° very close the injection well, we observe only a slight rotation in S_{Hmax} of less than 10° (Fig. 5). Such a small angle falls within the nodal plane uncertainty of the focal mechanisms and therefore may be not detected by the analyses of focal plane mechanism.

Also, consistent with observations from focal plane mechanisms by Martínez-Garzón et al. (2013), we calculated significant rotations of the orientation of the main principal stress (σ_1) in response to the seasonal changes in the fluid injection rates with σ_1 rotating from vertical towards the σ_2 direction. Martínez-Garzón et al. (2013) highlighted that σ_1 tilted by approximately 20°, and this value is similar to our results, where σ_1 tilted by up to 14° at the injection depth.

CONCLUSION

In this paper, we used the TOUGH-FLAC numerical simulator to investigate the spatio-temporal changes of the stress state within the northwest part of The Geysers geothermal field caused by injection of cold water. Good correlations were found between our results and previously published seismic focal plane mechanism studies on northwest Geysers stress changes. Our main finding is that changes in stress tensor orientation are caused by injection-induced progressive cooling of the reservoir affected by seasonal variations of the injection rate. Because of the gravity flow and cooling around a liquid zone formed by the injection, the vertical stress reduction is significant and propagates far below the injection well. At the same time, the horizontal stress increases because of the stress redistribution associated with stress reduction inside the cooling area. These two phenomena cause the rotation of the stress tensor and the appearance of a strike slip regime above, inside and below the cooling area.

ACKNOWLEDGMENT

This work was conducted with funding provided by the Assistant Secretary for Energy Efficiency and Renewable Energy, Geothermal Technologies Program, of the U.S. Department under the U.S. Department of Energy Contract No. DE-AC02-05CH11231

REFERENCES

Davis, S. D. and Frohlich, C., 1993, "Did (or will) fluid injection cause earthquakes? Criteria for a rational assessment," Seismological Research Letters, v. 64, p. 207-224.

Martínez-Garzón, P., M. Bohnhoff, G. Kwiatek, and G. Dresen (2013), Stress tensor changes related to fluid injection at The Geysers geothermal field, California, Geophys. Res. Lett., 40, 2596–2691, doi:10.1002/grl.50438.

Martínez-Garzón, P., G. Kwiatek, H. Sone, M. Bohnhoff, G. Dresen, and C. Hartline (2014), Spatiotemporal changes, faulting regimes, and source parameters of induced seismicity: A case study from The Geysers geothermal field, J. Geophys. Res. Solid Earth, 119, doi:10.1002/2014JB011385.

Boyle, K. and Zoback, M. (2014). The stress state of the northwest geysers, California geothermal field, and implications for fault-controlled fluid flow. Bulletin of the Seismological Society of America, 104(5).

Rutqvist, J., Wu, Y-S., Tsang, C-F., Bodvarsson, G., 2002. A modeling approach for analysis of coupled multiphase fluid flow, heat transfer, and deformation in fractured porous rock, *Int. J. Rock Mech. Min. Sci.,*39: 429-442.

Rutqvist, J., 2011. Status of the TOUGH-FLAC simulator and recent applications related to coupled fluid flow and crustal deformations. *Comput. & Geosci.* 37: 739-750.

Jeanne, P., Rutqvist, J., Dobson, P.F., Garcia, J., Walters, M., Hartline, C., 2014c. The Impacts of Mechanical Stress Transfers Caused by Hydro-mechanical and Thermal Processes on Fault Stability During Hydraulic Stimulation in a Deep Geothermal Reservoir. Int. J. Rock Mech. Min. Sci. 72, 149–163.

TOUGH2-EOS1 MODELING OF THE LONG TERM EXPLOITATION OF THE PARATUNSKY GEOTHERMAL FIELD, KAMCHATKA

Kiryukhin A.V.[1], Asaulova N.P.[2], Vorozheikina L.A.[2], Obora N.V.[2], Rozhenko A.I.[3], Zhuravlev N.B.[1], Kiryukhin P.A.[4], Polyakov A.Y.[1], Voronin P.O.[1], Kartasheva E.V.[1]

[1]-Institute of Volcanology & Seismology FEB RAS, Piip 9, Petropavlovsk Kamchatsky, Russia 683006
[2]-SUE KamchatskBurGeoTermia, Krasheninnikova 1, Termalny, Russia, 684035
[3]- United Institute of Computer Science SB RAS, Lavrentieva 6, Novosibirsk, Russia, 630090
[4]- Exigen Services Ltd, Pulkovskoe 40/4, Saint-Petersburg, Russia, 196158

email: AVKiryukhin2@mail.ru

ABSTRACT

The Paratunsky geothermal reservoir was geometrically characterized. Four hot water upflows were identified from hydrogeological data, and the distribution of feed zones and 3D temperatures were constrained by spline approximation. TOUGH2-EOS1 model setup was based on a polygonal three-layer (upper confining bed, reservoir, foundation) grid with a final total number of model elements of 9,792. Conductive and convective sources were assigned in a model base layer, while fixed pressure was specified in the upper caprock layer, where discharge of thermal waters took place. The reservoir (middle layer) was zoned based on temperature and feed-zone distributions. A natural-state iTOUGH2-EOS1 inversion with 13 adjustable parameters was used to estimate hot water upflow rates and enthalpies, production reservoir vertical and horizontal permeabilities, upper caprock permeability and pressure boundary condition based on pre-exploitation temperature and pressure measurements. Modeling of the thermohydrodynamic history of exploitation between 1965 and 2014 with updating of natural state conditions based on the data from six pressure monitoring wells and the temperature change observed in nine production wells helped to re-evaluate production reservoir compressibility and horizontal permeability. TOUGH2-EOS1+tracer modeling of chemical (Cl-) history of exploitation between 1965 and 2014 reveals the necessity of reservoir layer division into six sub-layers; it also provides an explanation of gradual Cl- growing in N and NP sites due to the inflow of sea waters through the NE boundary of geothermal reservoir.

CONCEPTUAL MODEL OF THE RESERVOIR

Input data for reservoir conceptual model development included (but was not limited to): topographical map (scale 1:200 000), well data on geological unit intersections and feed zone distributions, bottom hole temperature data, well head pressure data, geological cross sections (L.T. Naumov, 1968, pers. com.) and geological maps (scale 1:200,000).

Water isotope (δD, δ18O) data

45 samples from 44 production wells and 1 from the Karymshina river (a tributary of the Paratunsky river) were sampled (May, 2014) and analyzed in LGR IWA 45EP. A Craig diagram analysis pointed out that recharge of the Paratunsky geothermal field production wells consists of snow and ice melt from the Viluchinsky volcano, located 25 km south from the field. SR site is the heaviest part of the field (-107 δD ‰, -15 δ ^{18}O ‰), which may be caused by local groundwater inflow into the reservoir.

Temperature Distributions

Fig. 1 shows the Paratunsky geothermal field temperature distributions at -750 masl, and Fig.2 shows vertical cross-sectional temperature distributions calculated in a 3D area using library data that approximate LIDA-3, developed at the Computer Center SB RAS. Based on the above, four main upflows were identified by temperature anomalies, and the reservoir's lateral spread was controlled by 60°C geoisotherm at an altitude of -750 m.

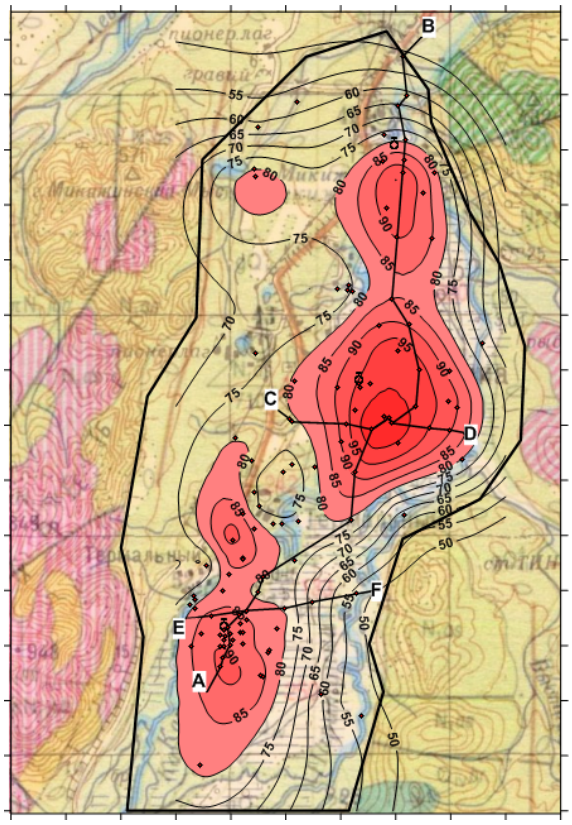

Figure 1. Paratunsky geothermal field temperature distributions at -750 masl were calculated using LIDA-3 3-dimensional approximation package. Geological features and topography are on the background.

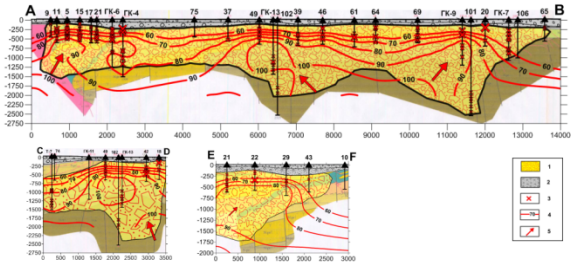

Figure 2. Paratunsky geothermal field hydrogeological cross sections. Cross section positions are shown in Fig.1. Notes: 1 – production reservoir, 2 – upper caprock, 3 - feedzones (shown proportionally to inflow rate), 4 – geoisotherms ^{o}C, calculated using LIDA-3 3-dimensional approximation package, 5 – hot water upflows.

Geological Setting, Reservoir Lateral and Vertical Extent

Laterally the reservoir is confined by the Paratunka river graben. Feed zones analysis also shows that the production reservoir is restricted by the 60^{o}C geoisotherm at -750 masl (Fig. 1), adjacent to the less permeable units with a total area of 69 km^2 (thick line on Fig. 1). Average vertical thickness of the production reservoir, which consists of neogene volcanic and sedimentary rocks (Nal tuffs, tuffs-sandstones; N_1pr_3 tuffs, tuffs-sandstones; N_1pr_2 basalts, tuffs of andesite-basalts are accounted to ~ 1200 m (AB cross section), 1090 m (CD cross-section) and 1330 m (EF cross section). Upper caprock consists of sand-gravel deposits (Q), conglomerates and sandstones (Q_1), having an average vertical thickness of ~ 180 m (Fig. 2). The reservoir basement has a heterogeneous structure and includes three more permeable channel zones with hot water upflows (SR, NP and N), which is reflected by the 80^{o}C geoisotherm at -750 masl (Fig. 1).

TOUGH2-EOS1 MODEL SETUP

Model Geometry and Grid

Model lateral extension is shown in Fig.1. Model vertical stratification included three layers: Layer 1, upper caprock, thickness 120 m, assigned in a depth interval +20 ÷ -160 masl; Layer 2, reservoir, thickness 1200 m, assigned in the interval -160 ÷ -1360 masl; Layer 3, basement, thickness 2640 m, assigned in a depth interval -1360 ÷ -3000 masl.

In generating a computational grid we have chosen a polygonal three-layer (upper caprock, reservoir, foundation) scheme of division into the elements with point centers at the horizontal coordinates of the wells; the total number of model elements is 3672.

On the final stage of modeling Layer 2 was divided into 6 sub-layers 200 m thick each, in this case the number of model elements increased to 9792.

Initial & Boundary Conditions

The EOS1 module with pressure and temperature as primary variables is used to simulate the liquid-dominated reservoir. In Layer-1 (caprock, -70 masl) a constant temperature of 10°C and a pressure of 9 bars were assigned. These conditions correspond to areal hot water discharge into the Paratunsky Valley alluvial deposits from the geothermal reservoir below. Pressure and temperature conditions in Layers 2 and 3 were defined based on a natural state modeling (see below).

Model Zonation & Material Properties

Layer 1 (caprock) was divided into CAPRK (Paratunsky river lowered basin, low permeable) and CAPR2 (Paratunsky uplifted terraces, impermeable) (Fig. 3).

Layer 2 (reservoir) was divided into RESE3 (low permeable reservoirs, temperature below 60°C), RESER, RESE2 (high permeable, temperature between 60°C and 80°C), RESSR (SR-site, temperature above 80°C), RESNP (NP-site, temperature above 80°C), RES_N (N-site, temperature above 80°C), RES_M (M-site, temperature above 80°C) (Fig. 3).

Layer 3 (basement) was divided into BASE (low permeable, outside upflow zones) and BASE* (high permeable upflow zones, where * is SR, NP, N, M, corresponding to the sites) (Fig. 3).

Table 1 shows material properties assigned in the model. It is a known difficulty to simultaneously estimate porosity and compressibility in an inversion. Hence, model porosity 0.1 was assigned as an analogous value for the Mutnovsky geothermal field, where the following estimates are available: Quaternary volcanic rocks 0.15-0.30 and more, Upper Pliocene 0.05-0.15, Miocene-Pliocene less than 0.10, and few percent in the oldest rock units (Kiryukhin et al., 2010). Heat conductivity is assigned according to the measurements conducted by Chernyak et al. (1987).

Table 1 Model material properties assigned and to be estimated (in bold). * - reserved for additional domains definition.

Material Parameters		Model Domain					
		CAPRK	CAPR*	RESER	RES**	BASE	BASE*
Grain Density, kg/m^3	ρ			2600	2600	2600	2600
Porosity	θ			0.1	0.1	0.1	0.1
H Permeability, мД	k	3.1	0.01	0.001	1410	1	741
V Permeability, мД	k	3.1	0.01	0.001	167	1	167
Heat Conductivity W/m°C	λ	1.0	1.0	1.4	1.4	2.0	2.0
Specific heat, J/kg°C	c			1000	1000	1000	1000
Compressibility, Pa^{-1}	C			4.1 10^{-8}	4.1 10^{-8}	10^{-8}	10^{-8}

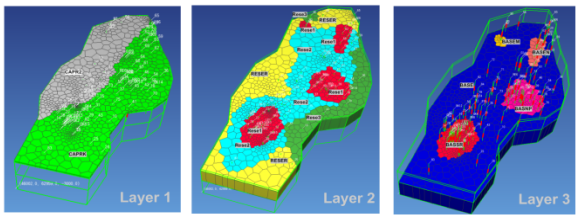

Figure 3. Paratunsky model zonation.

Base Sources

Base sources were defined in the 3-Layer (basement). They reflect conductive heat flow (0.06 W/m^2) and mass flows in upflow zones defined as a result of natural state modeling (see below).

Wells

Wells were assigned with a time dependent rate (monthly averaged) during history exploitation modeling. In case of several producing wells linked into a single production pump system, the rates of those wells were divided equally.

NATURAL STATE MODELING

Observational Data

3D temperature distribution calculations using the spline approximation package LIDA-3 (1°C standard deviation accepted) were used to generate temperature calibration points (77 points at -760 masl, and -2180 masl) in the corresponding grid elements. Wellhead pressure data, which had been measured before exploitation, were converted into reservoir pressures to be used as a pressure calibration points (20 points at -760 masl).

Model Parameterization and Inversion

The 13 estimated parameters include: mass fluxes (kg/s m^2) (which were converted into mass flows using known upflow areas: 4.27 km^2

(SR), 4.77 km^2 (NP), 2.18 km^2 (N) and 0.64 km^2 (MK)) and enthalpies (kJ/kg) in each of the four upflow zones (SR, NP, N, MK), vertical and horizontal permeabilities in productive model domains (RESER Rese1 Rese2 BASSR BASNP BASEN), permeability of non-productive domain (Rese3), permeability and pressure of the upper caprock domain CAPRK (where discharge conditions are assumed).

The following summarizes the iTOUGH2-EOS1 parameter estimates (model 3C4): 87 kg/s and 366 kJ/kg or 87°C (SR site), 70 kg/s and 415 kJ/kg or 99°C (NP site), 26 kg/s and 464 kJ/kg or 111°C (N site), 7 kg/s and 336 kJ/kg or 80°C (MK site); generalized horizontal and vertical reservoir permeabilities of the model's 2-layer and the feeding channels in the foundation third layer of 741 and 168 mD, respectively; permeability of the upper relative confining bed and peripheral sections of productive reservoir – 3 mD, pressure in the upper caprock discharge zone is 12.2 bar (at -90 masl).

iTOUGH2-EOS1 inversions yield reasonable model matches to the observed temperature data (MEAN=-0.6°C, STD=6.5°C), while a less reasonable match was obtained for the pressures (MEAN=0.0002 bar, STD=0.63 bar (where MEAN – is average deviation, STD – standard deviation). Most of the estimated parameter correlations are less than 0.6, while some parameters show correlation values of 0.8 (e.g., mass flux and enthalpy at N-site and production reservoir horizontal permeability).

The most significant input to the objective function, which is a measure of model and data mismatch, came from pressure (79%) data. Nevertheless, at a given reservoir permeability estimate of 741 mD, the pressure distribution should be rather homogenous throughout the entire geothermal field (0.1 bar variation). Hence, STD=0.63 bars must be assigned to mostly observational data errors, which may be caused either by disturbances from the pre-exploitation well head pressures, or hydrostatic pressure calculation errors caused by unknown temperature distributions.

In spite of reasonable temperature model and data match as a whole, it should be mentioned that model temperature is underestimated by 19.9 °C in deep well 103 (SR site) at -2180 masl). It is difficult to judge this case, since just three measurements were performed in the well 103 (82°C/1267 m, 96°C/1682 m and 99°C/2372 m) long ago.

Geochemical thermometry (Na-K-Ca, Fournier, Truesdell, 1973) based on 44 chemical analyses from the samples taken from production wells was also used to verify the inverse modeling estimates. All samples were taken by V. Gavryusev in May 2014, and they were analyzed in Central Chemical Lab of the Institute of Volcanology & Seismology by A.A. Kuzmina, V.V. Dunin-Barkovskaya, O.V. Shulga, and S.V. Sergeyeva. It should be noted that the variability of possible secondary mineral phases makes geothermometers rather uncertain at temperatures below 150°C. Nevertheless, the following average estimates were obtained: 75.7°C (N site), 79.3°C (NP-site), 79.6°C (SR site) and 77.4°C (MK site), that are somewhat lower than the corresponding inverse modeling estimates of 110°C, 99°C, 87.4°C and 80.2°C (see also Fig.2).

MODELING OF THERMOHYDRO-DYNAMIC HISTORY OF 1965-2014 EXPLOITATION

Observational Data

Exploitation flowrates were assigned in the model from January 1964 until June 2014 in the form of monthly averaged rates (Fig. 5).

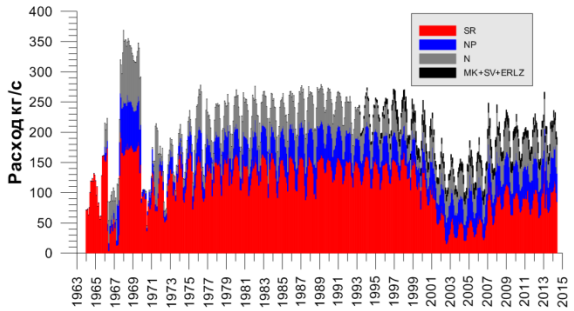

Figure 4. History of exploitation of the Paratunsky geothermal field (flowrates extracted in sites SR, NP, N and MK).

Reservoir pressures (at -760 masl) were calculated on the basis of the measured wellhead pressures in the monitoring wells by assuming hydrostatic conditions with a water density of

979.4 kg/m^3 (75^{o}C) as used for model calibration. Pressure shift parameter is used due to the uncertainty of absolute pressures estimations. The six most informative (model sensitive) monitoring wells (9, 52, ГК8, ГК12, 39 and 66) were used for the calibration.

Wellhead temperatures in the selected thirteen production wells (20, 42, 57, 5, 8, ГК2, ГК3, T2 and T8) at specified time intervals were used for model calibration. The selection criterion was that the temperature drop due to heat losses through casing is less than 1^{o}C (estimated using a local TOUGH2 model at a given well flowrate and casing construction). A temperature shift parameter is used to compensate for incomplete penetration of wells into the production formation.

Model Parameterization and Inversion

The estimated parameters are: production reservoir compressibility and horizontal permeability (domains RESSR, RESNP, RESEN, Rese2, RESEM, RESER, see Fig. 3). Observational data were either shifted to mean values (estimated at the preliminary inversion run), or shift estimations parameters were added within final inversions runs. Natural state re-estimation was implemented along the history of exploitation inversion runs.

Inversion output for modeling scenario (4E_P_1, when only pressure data is used for model calibration): compressibility 2.5×10^{-8} Pa^{-1} (2σ confidence interval 2.3×10^{-8} - 2.6×10^{-8}), permeability 285 mD (2σ confidence interval 270 – 307 mD). Pressure shifts estimates for wells 9, 52, ГК8, ГК12, 39 and 66: -2.3 bar, -3.1 bar, -2.5 bar, -1.6 bar, -2.0 bar, -2.7 bar, correspondingly. Correlation is less than 0.55, and allows for reliable estimates. Model vs. data standard deviations is 0.17 – 0.26 bars (Fig. 5); observational data shows high model sensitivity.

Relatively high model vs pressure data standard deviations are explained by large seasonal variations of wellhead (e.g. reservoir) pressures caused mainly by seasonal pressure changes in the discharge area (that is actually alluvial deposits of the Paratunsky river basin, or upper layer caprock assigned as CAPRK domain in the model). This seasonal cycling is not accounted for in the current model, but may potentially significantly improve the model vs pressure data matches.

Inversion output for modeling scenario 4E_PT_1, when pressure and temperature data are used for model calibration: compressibility 1.9×10^{-8} Pa^{-1} (2σ confidence interval 1.8×10^{-8} - 2.0×10^{-8}), permeability 460 mD (2σ confidence interval 442 – 478 mD). Fig. 6 shows model vs temperature data matches. Model vs data temperature deviations σ are 0.8 – 1.9 ºC, while no significant temperature changes are observed. Hence, we can conclude rather stable temperature conditions during exploitation period confirmed either by observational data or by modeling results.

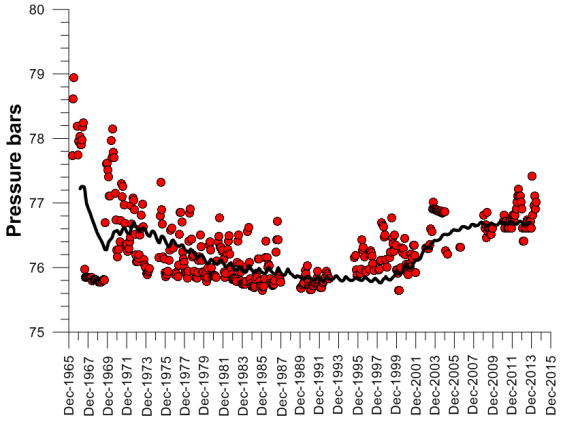

Figure 5. Modeling (4e_P_1) and observation based pressure match in well 9. Note: estimated shift parameter added to modeling results.

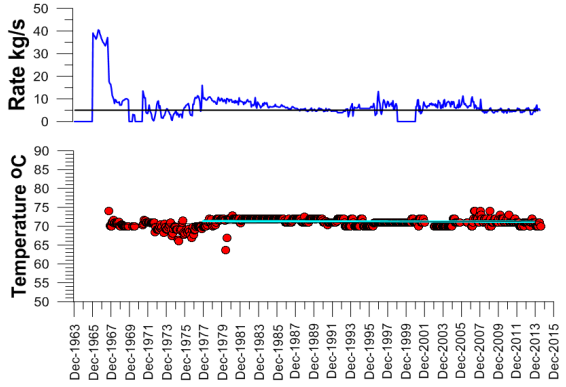

Figure 6. Lower graph: modeling (shifted, 4e_PT_1) and observational temperature match in well 20. Upper graph is well 20 flow rate, where horizontal line is lower threshold when temperature data are used for model calibration.

Inversion modeling for modeling scenario 4F_P_1, that is modified from 4E_P_1 by switching domain RESER (yellow domain on Fig. 3) to a lower permeability (0.01 mD) yields the following estimates: compressibility 4.08×10^{-8} Pa^{-1}, permeability 1.41 D.

MODELING OF HYDROCHEMICAL (CL^-) HISTORY OF EXPLOITATION 1965-2014

Conceptual Models of Chloride Ion Changes

The chemical history of Paratunsky geothermal field exploitation is characterized by gradual Cl- increase in N site and partial in NP site (NP2, NP3, NP4). The rate of growth is 1-3 ppm/year (or 20-40% during the whole period of exploitation).

The first conceptual model considers Cl^- rise in N site as a result of inflow of more concentrated fluids from NP site. TOUGH2-EOS1+tracer are used for this conceptual model verification. Although it was found possible to reproduce some Cl^- rise in N site, it casts unreliable hydrodynamic assumptions: localization of permeability between N and NP sites as a narrow channel, hydrodynamic isolation of N and NP sites from the rest of the Paratunsky field.

The second conceptual model explaining Cl^- rise was the attraction of more concentrated fluids from depth, especially taking into consideration shallow wells exploitation in N site. To verify this, more vertically detailed models were used, and a reservoir layer was divided into six sublayers (-160, -360; -360 - -560; -560 - -760; -760 – 960; -960 - -1160; -1160 - -1260 masl). Nevertheless, significant Cl^- rise was not reproduced in this model.

The third conceptual model considers lateral inflow of Cl^- concentrated waters through the NE boundary of the Paratunsky geothermal field, located just 8 km from Avachinsky Bay (that is directly linked to Pacific Ocean) and the adjacent NNW structure, which may be channeling sea water inflows. Having large Cl- concentrations in sea water (19383 ppm), just a small 1% fraction may cause Cl^- rise from 200 to 400 ppм.

TOUGH2-EOS1+tracer modeling

TOUGH2-EOS1+tracer modeling was used for sea water inflow conceptual model verification (third conceptual model). Models 4G2_2* (* - C, D, E that were derived as tracer models from model 4F_P_1) were used for this purpose. Natural state Cl^- modeling was used before to estimate Cl^- mass fluxes (e.g., Cl^- mass fractions) in the corresponding upflow areas: 60-115 ppm (SR site), 345-900 ppm (NP site), 375 ppm (N site), 50 ppm (MK site). Then modeling of the Cl^- history during exploitation was performed. In this case Cl^- high concentration (350 ppm) elements of a fixed state near the NE boundary were introduced in the model. In this way reasonable matches of the model vs Cl^- observational data were obtained (Fig. 7).

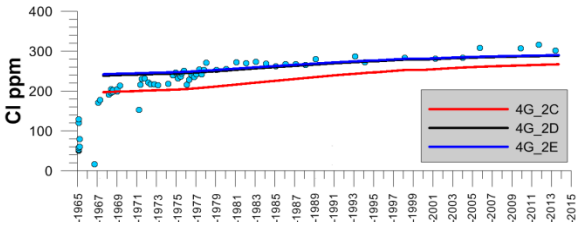

Figure 7. Modeling of Cl^- history of exploitation of the Paratunsky geothermal field (models 4G_2*): modeling vs Cl^- observational data in production well 20 (N site).

All modeling scenarios show reasonably good matches in N site wells 20, ГК9, 69, 63 and 67. Only well 62 shows Cl^- decline, which may be caused by meteoric inflows, indirectly confirmed by a heavier water isotope composition.

Despite the fact that the Cl^- history at the NP site is described by models 4G2_2* in average terms, they don't clearly show the Cl^- growth observed in NP2, NP3 and NP4. On the other hand, modeling shows Cl^- growing in SR4, although rather stable conditions are observed there. That may indicate a hydrodynamic isolation of the SR and NP sites, paralleled by a broader extension of the NE chloride inflow boundary that was not accounted for in the current model. SR site observational Cl^- data show a range of values from 44 ppm (SR1) to 80 ppm (SR2), which pointed either to non-uniform Cl^- distribution in SR upflow zone, or to a

different degree of production wells penetration. MK site wells Cl^- observational data are stable and reasonably matched by the modeling results.

CONCLUSIONS

1. The Paratunsky geothermal reservoir was geometrically characterized. Four hot water upflows inside were identified using hydrogeological data, with feed zone distributions and 3D temperatures constrained by spline approximation. A TOUGH2 model was set up based on the above.

2. Natural state iTOUGH2-EOS1 13-parametric inversion modeling was used to estimate hot water upflows rates and enthalpies, production reservoir vertical and horizontal permeabilities, upper caprock permeability and pressure boundary condition based on pre-exploitation temperature and pressure measurements.

3. iTOUGH2-EOS1 modeling of the thermohydrodynamic history of 1965-2014 exploitation with updating of natural state conditions based on the data of the six pressure monitoring wells and temperature change of nine production wells helps to re-evaluate production reservoir compressibility of 4.1×10^{-8} Pa^{-1} and horizontal permeability of 1410 mD.

4. TOUGH2-EOS1+tracer modeling of chemical (Cl^-) history of 1965-2014 exploitation reveals the necessity of reservoir layer division into six sub-layers and provides explanation of gradual Cl growing in N site and NP sites due to the inflow of sea origin waters through the NE boundary of geothermal reservoir.

ACKNOWLEDGMENT

Authors appreciate S. Finsterle's useful advice, and Dmitry Fage's efforts to extend the range of LIDA-3 package application to geothermal problems. Thanks to V.V. Kiryukhina for helping in manuscript translation.

REFERENCES

Chernyak V.P., Ryzhenko I.A. et al. Laboratory Estimation of Filtrational and Heat Properties of Rocks at Temperatures up to 120°C and Pressures 50 MPa Aiming at Exploration of the YuzhnoBerezhny and NizhneOzernovsky Sites of Kamchatka. Report ITTF AN USSR. Kiev, 1987.

Finsterle S. iTOUGH2 User's Guide. Rep.LBNL 40040, Lawrence Berkeley Natl. Lab., Berkeley, California. 1999.

Fournier, R.O., 1981. Application of Water Chemistry to Geothermal Exploration and Reservoir Engineering. In: Rybach, L., Muffler, L.J.P. (Eds.), Geothermal Systems. Principle and Case Histories. J. Wiley and sons, pp. 109–143.

Kiryukhin A.V., Kiryukhin V.A., Manukhin Y.F. Hydrogeology of Volcanic Areas \\ S-Petersburg, Nauka Publ., 2010, 395 p. (in Russian).

Kiryukhin A.V. High Temperature Fluid Flows in the Mutnovsky Hydrothermal System, Kamchatka // Geothermics, v.23, No:1, 1993, p.49-64.

«LIDA-3» Program Library to Approximate Functions and Digital Filtration of Signals and Pictures. Siberian Department of USSR Academy of Sciences. Novosibirsk. 1987. 169 p. (in Russian).

Manukhin Y.F., Vorozheikina L.F. Hydrogeology of Paratunsky Hydrothermal System and Conditions of its Formation. In: «Hydrothermal Systems and Geothermal Fields of Kamchatka». DVNC AN USSR. Vladivostok, 1976. p. 143-178.

Pruess, K., C. Oldenburg, and G. Moridis, *TOUGH2 User's Guide, Version 2.0*, Report LBNL-43134, Lawrence Berkeley National Laboratory, Berkeley, Calif., 1999.

MODELING LABORATORY EXPERIMENTS OF FLUID FLOW AND HEAT TRANSFER IN SUPERCRITICAL-CO2-SATURATED CORES WITH ECO2N V2.0

Mario Magliocco[1], Christine Doughty[2], Tim Kneafsey[2], and Steve Glaser[1,2]

[1]Department of Civil and Environmental Engineering
[2]Lawrence Berkeley National Laboratory
University of California
Berkeley, CA, 94720, USA
e-mail: mag@berkeley.edu

ABSTRACT

We have investigated heat transfer in a set of laboratory experiments where we flowed dry CO_2 through a bed of heated sand. Our laboratory apparatus is capable of operating at temperatures up to 200°C, pressures up to 340 bar, and flow rates up to 400 ml/min. In our system, we measure temperature throughout the sample. We designed the experimental system such that measurements and controls at the boundaries could be readily modeled with TOUGH2 and the ECO2N fluid property module. Significant cooling occurs over the course of an experiment resulting in large CO_2 property changes. Past modeling attempts failed to achieve a good match between simulation results and experimental data, likely due to the lack of effective thermal conductivity updating of CO_2 saturated grid blocks during the course of the simulation.

We found that temperature changes caused the effective thermal conductivity in our sample to vary from 1 to 0.2 W/m·K during a single experimental run. In order to take this behavior into account, optional code was included in the improved ECO2N V2.0 distribution package that estimates the thermal conductivity of the saturated rock as a function of rock properties, NaCl concentration, CO_2 saturation, and the varying thermal conductivity of CO_2. We performed five CO_2 flood experiments at various flow rates and system pressures to collect temperature, pressure, and mass flow rate measurements for use in model validation. A detailed model of our system was implemented in TOUGH2 and ECO2N using the optional thermal conductivity code. We found that the new code capabilities provided a significantly better fit to the experimental data than when a single effective thermal conductivity value was used.

INTRODUCTION

Numerical modeling tools are necessary for studying, planning, and operating geologic-based CO_2 sequestration and CO_2-based geothermal energy projects. Project viability and safety is dependent on the results of computer simulations of heat and mass flow in porous media, therefore model validation is an important concern. Models can be tested against closed form solutions, compared with other models (Pruess, 2004), or ideally they can be compared with measurements of actual physical systems. The data sources for validation either come from field data, that is usually sparse in space and time and very expensive, or laboratory experiments, which are often denser in space and time but usually lack the proper scaling.

Previous experiments collected data from a specially constructed apparatus that injected cold CO_2 into a heated porous sample and compared the results to a numerical model of the system implemented in the TOUGH2 family of codes using the ECO2N equation of state module (Magliocco et al., 2015). TOUGH2 is a general-purpose non-isothermal, multiphase, multicomponent fluid flow simulator for porous and fractured media developed at Lawrence Berkeley National Laboratory (LBNL) (Pruess, 2004). In previous work it was impossible to achieve a reasonable match between experimental and model results by trial and error. Our analysis found that the constant effective thermal conductivity of the saturated medium assumption used in TOUGH2/ECO2N was a likely source of error in the model results.

Since the initial experiments were performed, the ECO2N module has been updated and optional code (TCSUB) created that allows for

more accurate effective thermal conductivity modeling (Pan et al., 2015). Using an updated version of our apparatus a new set of data was captured that includes the mass flow at the outlet of the vessel and was used to perform the first comparison of the results of the new thermal conductivity modeling code to measured data. This paper presents the results of the experimental and numerical studies and examines what effects the updated thermal conductivity model has on the simulation accuracy.

CORE FLOOD EXPERIMENTS

Experimental Apparatus

Temperature, pressure, and flow rate measurements were taken with the experimental apparatus shown in Figure 1, which was an updated version of the system used for previous work (Magliocco et al., 2015). The experiment was designed to generate data for numerical model validation purposes by careful implementation of boundary conditions, the layout and density of temperature measurements, and the selection of experimental parameters such as flow rate and porous medium grain size. The inlet to the test vessel was controlled as a constant temperature and constant mass flux boundary by means of the computer controlled pumps and a laboratory chiller. The outlet was controlled as a constant pressure boundary condition by means of a back pressure regulator. Constant pressure and constant mass flux boundary conditions were easily implemented in a TOUGH2 model. The vessel was insulated by a custom fabricated aerogel insulation blanket in order to impose a relatively low heat flux at the exterior surfaces of the vessel. The pressure vessel was a hollow type 304 stainless steel cylinder with an inside diameter of 9.1 cm, outside diameter of 12.7 cm, and a 50.8 cm height between the type 316 stainless steel end caps secured by 4430 alloy steel caps.

Instrumentation and flow access to the interior of the vessel was through three axial passages through the bottom end cap, and one passage through the top. The vessel was oriented vertically such that the flow path was in the same orientation as the gravity-induced pressure gradient in order to minimize instabilities and maintain radial symmetry in the system.

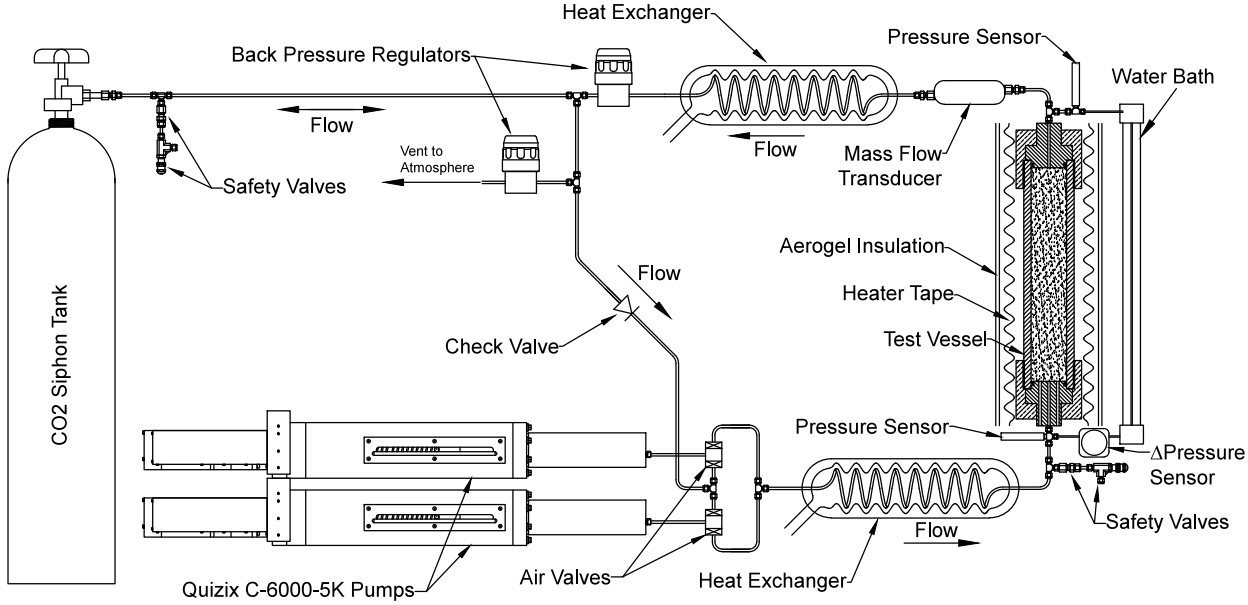

Figure 1. Diagram of experimental apparatus. Fluid was supplied by a siphon style CO_2 tank. Fluid was driven by a pair of pumps and fed through air-actuated valves. The fluid was chilled before it passed into the bottom inlet of the vertically oriented pressure vessel. A differential pressure sensor was connected hydraulically to the inlet and outlet of the vessel. Pressure and mass flow sensors were located at the outlet (top) of the vessel.

Temperature measurements within the sample were made with 23 small diameter (0.79mm) stainless-steel clad type-T thermocouples. The thermocouples were arranged at several elevations and radii in the sample (Table 1). At one elevation in the porous media, two thermocouples were mirrored so that they were both at the same radial distance from the central axis of the vessel to test our assumption of a radial symmetry in the heat transfer process.

Table 1. Thermocouple location and numbering. This table excludes the thermocouple that duplicates the radial position of TC15.

TC#	*Z* (cm)	*R* (cm)	TC#	*Z* (cm)	*R* (cm)
1	0	0	12	25.4	0
2	0	2.3	13	30.5	0
3	0	4.6	14	30.5	1.5
4	10.2	0	15	30.5	3.0
5	10.2	1.5	16	30.5	4.6
6	10.2	3.0	17	40.6	0
7	10.2	4.6	18	40.6	1.5
8	20.3	0	19	40.6	3.0
9	20.3	1.5	20	40.6	4.6
10	20.3	3.0	21	50.8	0
11	20.3	4.6	22	50.8	2.3

Porous Core Sample

The core sample consisted of dry-packed, well-sorted, spherical shaped quartz silica sand. The shape and sorting of the media were chosen to further simplify the system (Magliocco et al., 2015). Many conceptual models of porous media flow make use of a packed bed of spheres to represent the solid matrix. 4.9489 kg of prepared sand was packed into the mounted vessel in 15 separate lifts with manual tamping with a rounded aluminum rod between lifts. The porous sample properties are listed in Table 2.

Experimental Results

Five single-phase CO_2 experiments were performed under the conditions listed in Table 3. All experiments were operated above the critical pressure of CO_2 to ensure no gas phase was present in the system.

Table 2. Porous sample properties

Porous Core Properties	
Total Core Length	L =50.8 cm
Cross Sectional Area	$A = 6.54 \times 10^{-3} m^2$
Crystalline Quartz Density	$\varrho_R = 2650$ kg/m^3
Crystalline Quartz Specific Heat	$C_R = 830$ J/(kg K)
Crystalline Quartz Thermal Conductivity	8W/(m K)
CO_2 Saturated Sand Thermal Conductivity	λ_{eff} = 0.22-1.0W/(m K)
Permeability	$K = 9.3 \times 10^{-13} m^2$
Porosity	$\phi = 41\%$
Mean Grain Size	$d_{50} = 0.105$ mm

Table 3. Experimental conditions.

Experiment #	Injection Flow Rate	Outlet Pressure
1	200 ml/min	108 bar
2	50 ml/min	147 bar
3	200 ml/min	108 bar
4	100 ml/min	108 bar
5	50 ml/min	108 bar

The CO_2 was injected in the liquid phase at a temperature of 11°C. The temperature data from the twenty-two thermocouples (ignoring the redundant thermocouple) from a typical experimental flow run are shown in Figure 1. The sample was saturated with CO_2 at the desired experimental pressure and heated to the desired initial temperature and allowed to equilibrate. Before injection initiation a vertically oriented thermal gradient was present in the vessel with the highest temperature at the top of the vessel and the lowest temperatures at the bottom. Injection initiation can be seen as the temperature at the sample inlet (solid green line) drops shortly after flow initiation at time zero. The temperature at the vessel wall (dotted lines) decreases at a slower rate due to the heat energy stored in the stainless steel. After the initial temperature front has passed a strong thermal gradient develops in the inward radial direction as the heat is drawn out of the vessel wall by the passing CO_2.

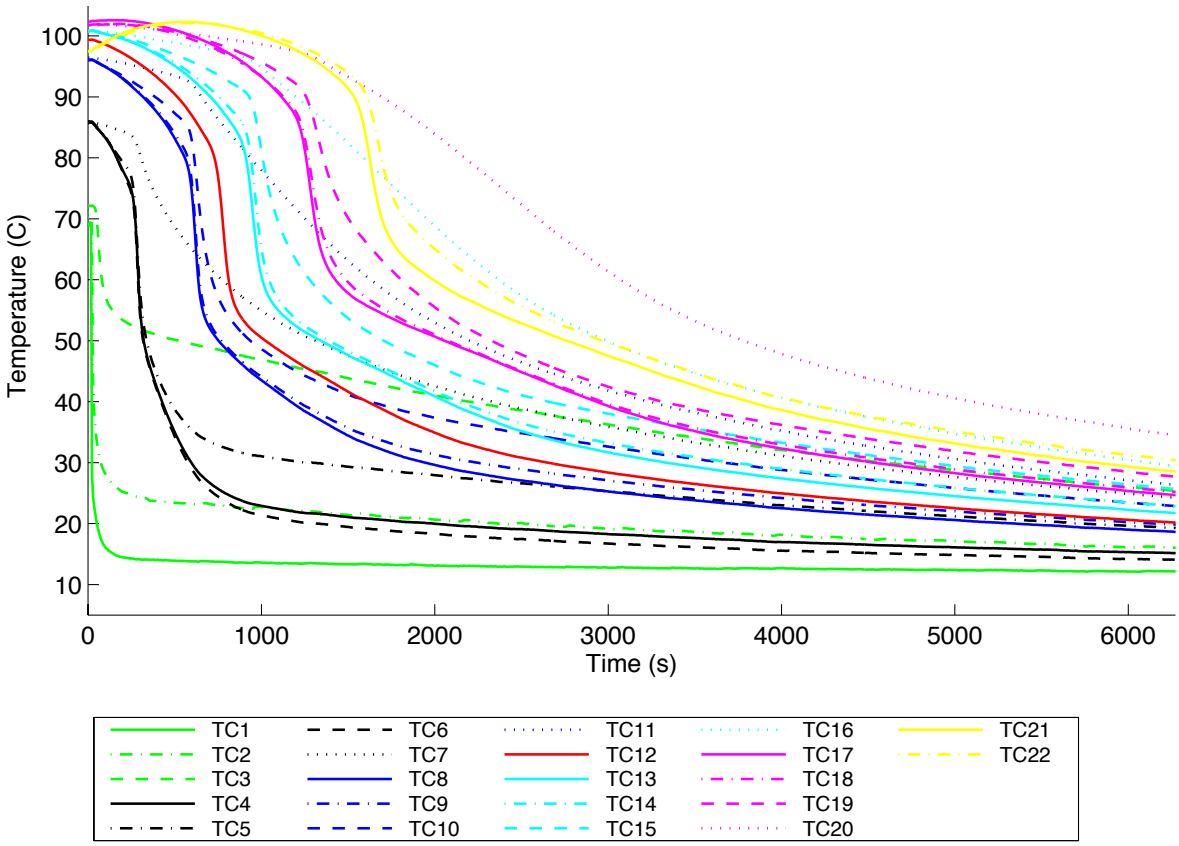

Figure 2. Temperature vs time data from twenty-two thermocouples from experimental flow run #3 operated at 200ml/min flow rate, 108 bar pressure, and an initial vessel temperature of 100 ◦C. Line color indicates elevation of the sensor, green being at the vessel bottom and yellow at the top. Line style indicates radial location with solid lines at the vessel axis and dotted lines at the exterior. Thermocouples are numbered in order of radial location and then by elevation starting at the bottom of the sample axis.

MODELING

A 2D axisymmetric model of the system was developed for evaluation in TOUGH2, a numerical simulator for non-isothermal flows of multi-component, multiphase fluids in one, two, and three- dimensional porous and fractured media, and the ECO2N property module which is capable of modeling mixtures of water, NaCl, and CO_2. Version 2.1 of TOUGH2 and version 2.0 of ECO2N were used with the included optional TCSUB code which implements effective thermal conductivity updating as a function of CO_2 thermal conductivity, rock thermal conductivity, and a pore shape parameter (Zimmerman, 1989; Pan et al., 2015).

During simulations, the standard TOUGH2/ECO2N code will vary the thermal conductivity of grid blocks based only on the degree of saturation by calculating a value based on the thermal conductivity of the dry and fully saturated block. Without TCSUB enabled, ECO2N does not update the effective thermal conductivity of CO_2 saturated grid blocks despite the fact that the thermal conductivity of CO_2 can vary greatly as a function of pressure and temperature (Magliocco et al., 2015). The functionality of TCSUB was enabled and disabled by changing the value of the IE(10) parameter in the SELEC block of the input file. An IE(10) value equal to zero will use the default TOUGH2 thermal conductivity handling, and an IE(10) value equal to 1 makes use of the new updating scheme based on effective medium theory (Zimmerman, 1989).

TOUGH2 with the ECO2N module was compiled on 64-bit intel Core i3 and Core 2 Duo processors running Ubuntu 14.04 and Mac OS X 10.10 respectively using the GNU Fortran compiler GFortran (4.8.2 on Ubuntu and 4.9.2

on the Macintosh). The Mac system was used primarily for model development with coarse meshes while the more computationally robust Linux system was used for finer resolution simulations.

A suite of custom Matlab scripts was created that would sequentially generate the model mesh, initialize the model input files based upon the experimental data, initiate the TOUGH2 simulation, import the results into Matlab and analyze and plot the results compared to experimental data. The Matlab mesh generation function was capable of producing a mesh of the appropriate dimensions with user selectable resolution. Besides the pressure and mass flow rate, the TOUGH2 simulation was initialized with an initial temperature distribution that was derived from the experimental temperature data.

Mesh Design

The model mesh geometry was based upon measurements of the experimental vessel with the exterior surface of the vessel taken as the system boundary (Figure 3). The mesh is 2D axisymmetric described on the R-Z plane and revolved around the Z axis creating a series of stacked and nested annuli with the appropriate 3D volumes and surface areas. The mesh blocks were assigned to one of seven different domains: the inlet block, outlet block, passage through the end caps, stainless steel vessel body and end caps, carbon steel vessel nuts, packed sand sample, and sand in contact with the vessel walls.

Interpolation was employed in order to approximate the modeled temperature values at thermocouple locations when a larger than thermocouple diameter grid-block size is used, the results of which vary depending on the temperature gradient and the mesh resolution especially near boundaries. To explore the sensitivity of the results to grid-block size, simulations were run with various mesh resolutions. Ultimately a mesh resolution was chosen of approximately 4 mm in the *z* direction and 8 mm in the *r* direction.

Domain Properties

The majority of the domain properties such as density, specific heat, and thermal conductivity were based on standard reference values (Avallone, Baumeister, and Sadegh 2006). Other values such as the sample porosity and permeability were based on laboratory measurements. To impose a constant temperature on the injection fluid, the injection cell domain was given a very large density and specific heat, and was initialized with the desired injection temperature.

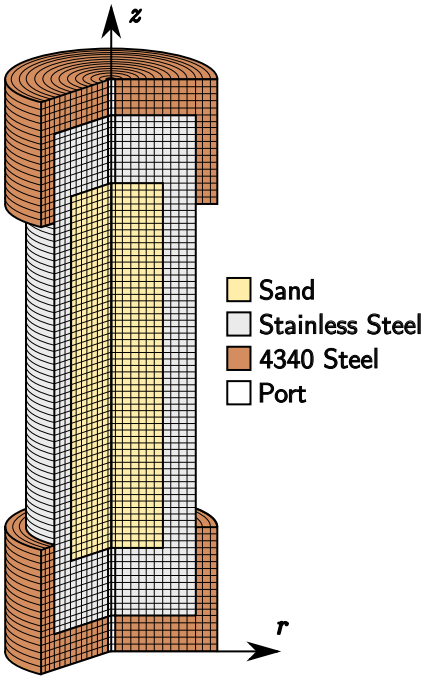

Figure 3. *Partially revolved model mesh, with colors indicating material type. Not to scale and not representative of final mesh resolution.*

Boundary Conditions

Three boundary conditions were included in the model, a constant pressure condition at the outlet, a mass flux at the inlet, and heat loss to the lab environment at the vessel exterior. The inlet cell was set as a generation cell with the type set to single phase CO_2 at either a constant mass flow, or a flow rate that varied over time, based on the measured experimental conditions. The outlet cell behavior takes advantage of a TOUGH2 computational shortcut in which the cell is marked as "inactive" and is not included in any of the mass or energy balance equations to ensure that the state does not change from the initial values. It was found that including heat loss at the boundary did not significantly improve the fit of the model to measured data.

Model Calibration

The choice of the thermal conductivity input parameters for the model was dependent on the thermal conductivity handling method chosen in the model input file using the IE(10) parameter which enables the TCSUB option. The standard TOUGH2/ECO2N code only changes the thermal conductivity of the grid block based on fluid saturation. The experiments we conducted were under fully saturated conditions at all times so the chosen saturated thermal conductivity value was used throughout the simulation. The modeler must choose a single pressure and temperature at which to make their estimate for thermal conductivity out of the range of pressures and temperatures that occur over time and space during a single experiment. This choice was problematic due to the fact that any estimate will only be valid for limited locations and times within the sample. Furthermore, the value would have to be estimated and calibrated separately for each experimental run based on the unique operating parameters, making the model less deterministic.

Due to the characteristics of the prepared core sample, estimates of effective thermal conductivity made use of a well-tested (Woodside and Messmer, 1961) model based on an unconsolidated packed bed of uniformly sized spheres (Kunii and Smith, 1960). Estimated effective thermal conductivity is a function of the sample porosity and reference values for the thermal conductivities of CO_2 and quartz. The calculated values ranged from approximately 0.2 to 1 W/(m K) with the lower value associated with cold injection CO_2 and the higher value with the hot CO_2 present at the initial conditions.

When the new TCSUB option was enabled, the model inputs are the thermal conductivity of the dry rock and a parameter, α, that relates to the shape of the pore space. By basing the thermal conductivity on physical parameters, the model becomes more deterministic and should produce accurate results for all operating conditions. Three limiting shapes have been identified that describe the pore spaces as flat discs (α = 0), spherical (α = 1), and needle- like pores (α > 1) (Zimmerman 1989). For the initial choice we used an α value equal to one, and a thermal conductivity reference value for quartz grains situated in random orientations (Woodside and Messmer, 1961). These values generated simulation results with a good initial fit to experimental data and allowed us to study the sensitivity of our model to other parameters such as heat loss, the effect of higher porosity at the vessel wall, and mesh resolution.

During calibration it was found that the modeled temperature consistently mismatched the experimental data near the end caps of the vessel. This was most likely due to the radial flow that occurs near the end caps, which results in very high pore velocities near the injection and outlet ports. The high pore velocities around the inlet and outlet are well outside of the Darcy flow regime and the theoretical capabilities of TOUGH2.

The model also consistently under-predicted the temperature front arrival time at the lower elevations in the sample. This was more apparent in the higher flow rate experiments, indicating this may be due to the upstream prediction errors at the injection end cap propagating up the sample column. When comparing the misfit between simulations, the temperature data at the bottom two thermocouple elevations (numbers 1 through 7) and the highest thermocouples located near the outlet end cap (numbers 21 and 22) were disregarded.

In order to differentiate results, a quantitative approach was applied using the weighted mean square error summed over all experiments as a measure of model misfit

$$\Phi = \frac{1}{5}\sum_{j=1}^{5}\frac{1}{k_j}\sum_{t=1}^{k_j}\frac{1}{13}\sum_{i=8}^{20}\frac{\left(d_{ij}(t)-s_{ij}(t)\right)^2}{\sigma^2}, \quad (2)$$

where $s_{ij}(t)$ is the simulation result at thermocouple number i at time t from experiment number j, k is the number of simulation time steps, $d_{ij}(t)$ is the recorded experimental data, and σ is the standard deviation of the measurements (estimated from mirrored thermocouple data). The misfit values for some different thermal conductivity choices are shown in Table 4.

Table 4. Misfit values for various thermal conductivity parameter choices.

Model Parameter	Misfit
TCSUB Enabled	
$\alpha = 0.03$	8.26
$\alpha = 0.04$	7.08
$\alpha = 0.07$	6.56
$\alpha = 0.08$	6.34
$\alpha = 0.11$	6.73
$\alpha = 0.12$	7.04
$\alpha = 0.5$	9.31
TCSUB Disabled	
$\lambda_{eff} = .5$	37.31
$\lambda_{eff} = 1$	16.42
$\lambda_{eff} = 2$	7.78
$\lambda_{eff} = 3$	7.11
$\lambda_{eff} = 3.5$	7.87

The lowest misfit value was achieved with an α value of 0.08, while the lowest misfit for a single, constant effective thermal conductivity was 3 W/(m K) which was out of the range of expected values. Without the TCSUB code enabled, it would have been difficult to calibrate the model using realistic effective thermal conductivity values using this calibration method.

MODELING REULTS

Using the TCSUB option (α = .08), the calibrated model simulation results for the central thermocouples (radial location = 0) are shown in Figure 4 with diamond markers, along with the experimental results shown without markers. The general temperature trends and front arrival time predictions produced by the simulation are relatively good at locations which are not in contact with the end caps.

The use of the TCSUB option allowed for relatively good fits with a wide range of α

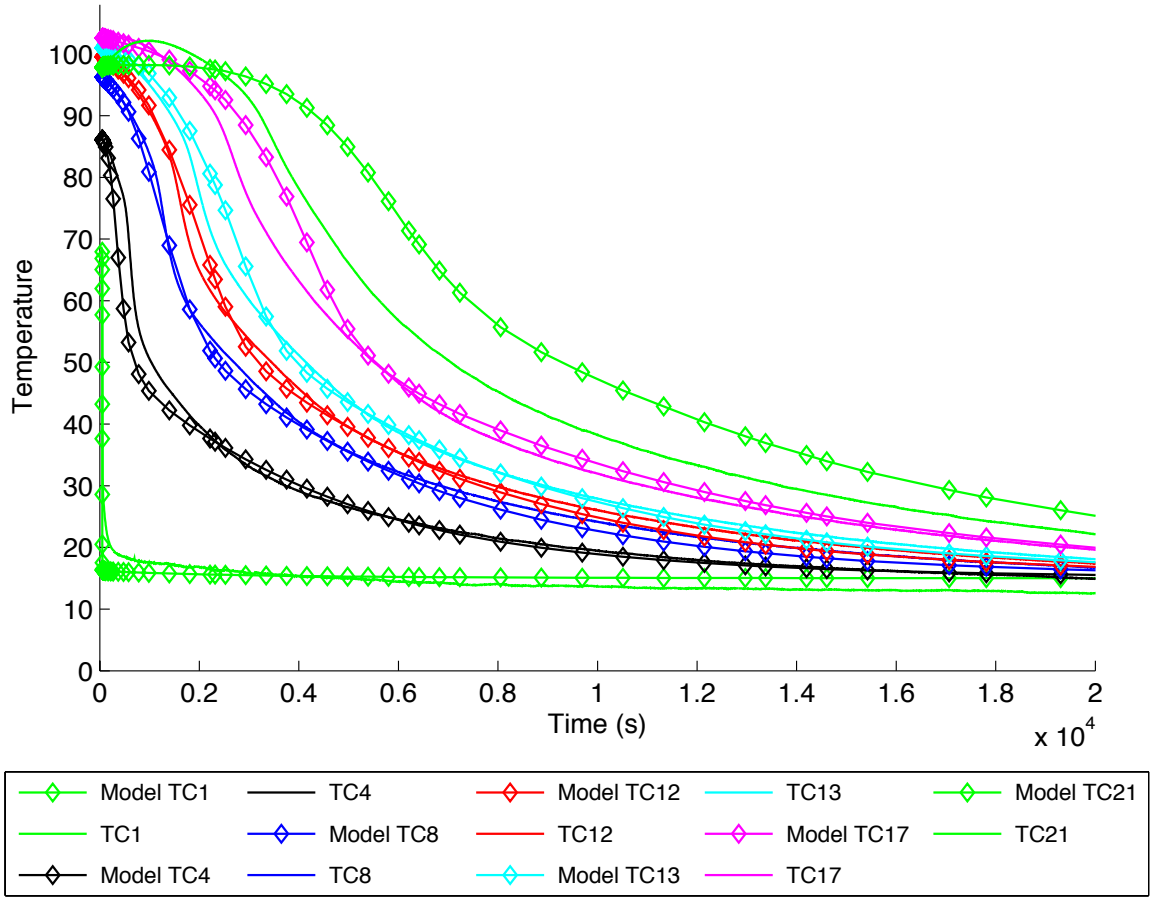

Figure 4. *Simulations results (α = 0.08) compared to data from experiment #5 operated at 50 ml/min flow rate, 108 bar pressure, and an initial vessel temperature of 100 ◦C*

choices (Table 4), and allowed for much easier model calibration. This indicates that the theoretical basis of the TCSUB code was more accurate than the assumption of constant thermal conductivity of the CO_2 saturated rock. In the original attempts at modeling experiments without TCSUB (Magliocco et al., 2015), it was difficult to choose a reasonable λ_{eff} that could be used to identify and correct other deficiencies in the model. A good overall fit could be achieved for individual experiments using a carefully chosen and often unrealistic effective thermal conductivity value that was outside of the range supported by theory and research findings. Using reasonable values for λ_{eff} resulted in an overall poor match for all experiments.

CONCLUSION

We measured experimental data using an experimental apparatus capable of producing temperature, pressure, and mass flow measurements of cold CO_2 flow through a heated porous sample. Five experiments were conducted under well-controlled conditions, and the resulting data was subsequently used for model validation. The results of the experiments and the modeling show that TOUGH2 with the TCSUB option enabled in the ECO2N module is capable of simulating heat transfer in CO_2 saturated porous media with reasonable accuracy with minimal calibration using reference values for material properties and direct measurements of our system. This was an improvement over the previous version of ECO2N that required the modeler to choose a possibly unreasonable value for the effective thermal conductivity of the CO_2 saturated media for each separate experiment in order to get a reasonable model fit. The new method enabled by the use of TCSUB was more deterministic in nature and more conceptually sound. While the TCSUB code does require the modeler to choose a pore shape parameter, the sensitivity of the system to the choice was not as great as the sensitivity to the choice of effective thermal conductivity when TCSUB was disabled, allowing more rapid and reasonable model calibration.

REFERENCES

Avallone, E. A, T. Baumeister, and A. Sadegh (2006). "Marks' Standard Handbook For Mechanical Engineers (Standard Handbook for Mechanical Engineers)".

Magliocco, M., T. Kneafsey, K. Preuss, & S. Glaser, (2015) Laboratory and Numerical Studies of Heat Extraction from Hot Porous Media by Means of Supercritical CO_2. *Transport in Porous Media*, 2015, 10.1007/s11242-015-0474-0

McCune, L.K., and R.H. Wilhelm (1949). "Mass and Momentum Transfer in a Solid-Liquid System". In: Industrial & Engineering Chemistry 41.6, pp. 1124–1134.

Pan, L., N. Spycher, C. Doughty, and K. Pruess (2015). ECO2N V2.0: A TOUGH2 Fluid Property Module for Mixtures of Water, NaCl, and CO_2. Report LBNL-6930E. Lawrence Berkeley Lab., CA (United States).

Pruess, K. (2004). "The TOUGH codes: a family of simulation tools for multiphase flow
and transport processes in permeable media". In: Vadose Zone Journal 3.3, pp. 738–746.

Woodside, W.T., and J.H. Messmer (1961). "Thermal conductivity of porous media. I. Unconsolidated sands". In: Journal of applied physics 32.9, pp. 1688–1699.

Zeng, Z. and R. Grigg (2006). "A criterion for non-Darcy flow in porous media". In: Transport in Porous Media 63.1, pp. 57–69.

Zimmerman, R. W. (1989). "Thermal conductivity of fluid-saturated rocks". In: Journal of Petroleum Science and Engineering 3.3, pp. 219–227.

SIMULATING SUPERCRITICAL WATER IN MAGMATIC GEOTHERMAL RESERVOIRS

Lilja Magnusdottir and Stefan Finsterle

Lawrence Berkeley National Laboratory
Earth Sciences Division, MS 74-316C
Berkeley, California, 94720, USA
e-mail: SAFinsterle@lbl.gov

ABSTRACT

In geothermal reservoir modeling, the heat source is usually assumed to be below the model's depth range, and the model is driven by boundary conditions in the bottom layer of the model. Including the heat source in the model poses a variety of modeling challenges due to the large changes in fluid properties near the critical point, and due to various unknowns such as the depth range of the water circulation and the time varying spatial distribution of the heat sources. To address these issues, a new equation-of-state module termed EOS1sc was developed for iTOUGH2 to provide forward and inverse modeling capabilities at supercritical conditions, which are encountered near the heat source of magmatic geothermal reservoirs. The IAPWS-IF97 and IAPWS-95 thermodynamic formulations were implemented. iTOUGH2-EOS1sc thus has a significantly higher operational range for pressure and temperature (from sub- to supercritical conditions), better accuracy (specifically near and above the critical point at 374°C and 22.064 MPa), and higher computational speed (through an extension of the IAPWS-IF97 formulation). Moreover, temperature dependence of permeability and thermal conductivity was implemented, where the related parameters can be analyzed using the toolsets of the iTOUGH2 framework.

INTRODUCTION

High enthalpy fluids extracted from magmatic geothermal reservoirs are becoming more desirable for energy production with advancing technology. Moreover, wells drilled into magma indicated that the heat sources could be located at a shallower depth than assumed. Finally, to accurately predict the thermal behavior in geothermal systems, the magmatic heat source of the geothermal systems should be incorporated into the numerical modeling.

Modeling supercritical conditions poses a variety of challenges due to the large gradients in fluid properties near the critical point. This work focused on using the iTOUGH2 simulator to model the extreme temperature and pressure conditions in magmatic geothermal systems.

Supercritical equation-of-state modules have been previously implemented into TOUGH2-based codes (Brikowski, 2001; Kissling, 2004; Croucher and O'Sullivan, 2008), using different thermodynamic formulations. The IAPWS-95 and IAPWS-IF97 thermodynamic formulations were implemented into iTOUGH2 to provide forward and inverse modeling capabilities of high-temperature magmatic geothermal reservoirs. Thus, the operational range of temperature and pressure was extended to 1,000°C and 1,000 MPa when using the IAPWS-95 formulation (IAPWS, 2009), and to 800°C and 100 MPa as well as 2,000°C for pressure within 50 MPa, when using the IAPWS-IF97 formulation (IAPWS, 2007). In addition, the possibility of extrapolating the formulation was investigated because IAPWS-IF97 is significantly faster than IAPWS-95. The operational ranges tested and accepted by IAPWS for water's thermodynamic formulations are summarized in Table 1.

Finally, the temperature dependence of permeability and thermal conductivity was also implemented. This new equation-of-state module will be used for forward modeling as well as inversions for the characterization and prediction of deep or very hot geothermal systems.

Table 1. Temperature and pressure range for international thermodynamic formulations.

Standard	Simulator	Temp. range (°C)	Pres. range (MPa)
IFC-67	TOUGH2, iTOUGH2	0–800	0–100
IAPWS-95	iTOUGH2-EOS1sc	0–1000	0–1000
IAPWS-IF97	AUTOUGH2, iTOUGH2-EOS1sc	0–800	0–100
Revised Region 5 of IAPWS-IF97	iTOUGH2-EOS1sc	800–2000	0–50

METHOD

The IAPWS-95 formulation serves as the international standard for water's thermodynamic properties. The IAPWS-IF97 formulation is a separate, faster formulation based on IAPWS-95. It is maintained for industrial use and replaces the IFC-67 formulation currently used in standard TOUGH2.

The IAPWS-IF97 formulation is given in terms of five regions nominally defined as liquid, vapor, supercritical, two-phase, and high temperature vapor as shown in Figure 1. Regions 1, 2 and 5 in Figure 1 are individually covered by a fundamental equation for the specific Gibbs free energy as a function of pressure and temperature. Region 3 is covered by a equation for the specific Helmholtz free energy and is given in terms of density and temperature. Region 4, which is the saturation curve, is given by a saturation-pressure equation.

In the new EOS1sc module, the supercritical equation-of-state (EOS) used in AUTOUGH2 was incorporated into iTOUGH2. In AUTOUGH2, Regions 1–4 of the IAPWS-IF97 formulation were implemented, as described by Croucher and O'Sullivan (2008). In EOS1sc, Region 5 was included as well to extend the applicability of the EOS to 2,000°C for pressures at or below 50 MPa.

In the IAPWS-95 formulation, which is also implemented in iTOUGH2, the primary variables are density and temperature for the entire state space. Thus, iterative function inversions are required when using IAPWS-95 outside of the supercritical region.

In EOS1sc, there are three options to select the thermodynamic formulation: (1) IFC-67, which is only valid for subcritical conditions, (2) IAPWS-IF97, or (3) IAPWS-IF97 for temperature below 800°C and IAPWS-95 for temperature equal or greater than 800°C. For the last option, IAPWS-95 is not used for the whole temperature range because IAPWS-IF97 is significantly faster and accurately approximates IAPWS-95 within its operational range of 800°C.

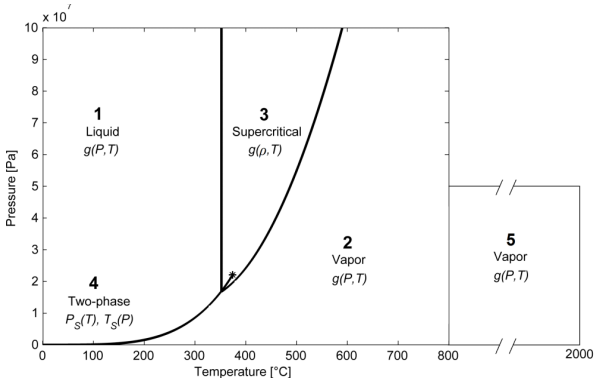

Figure 1. Regions of the IAPWS-IF97 thermodynamic formulation.

EXAMPLE: COOLING PLUTON

Model set-up

The forward and inverse capabilities of EOS1sc in iTOUGH2 were demonstrated for a cooling pluton with an initial temperature of 1,100°C. The IAPWS-IF97 formulation with Region 5 extrapolated in EOS1sc was used to investigate the groundwater flow and heat transfer in the hydrothermal system as the pluton cools down. An inverse analysis was used to estimate the initial temperature of the pluton, and the permeability of the geothermal reservoir using observations of injection pressure, production temperature, and production rate after the reservoir had reached steady state.

The model is two-dimensional with dimensions 4×10 km^2, and a nominal thickness of 1 m. The pluton is emplaced at a depth of 2.5 km; the

dimension of the pluton is 0.5 × 1.5 km^2. The basaltic rock consists of four regions.

The surface temperature and pressure were set constant at 20°C and 1 atm. A temperature gradient of 100°C/km and hydrostatic pressure were modeled. The initial temperature of the pluton was set as 1,100°C, thus assuming that there is a heat source beneath from which the pluton intruded. The initial pressure was defined approximately 10% less than lithostatic pressure. Therefore, the initial pressure of the pluton is significantly higher than the hydrostatic pressure of the surrounding geothermal system.

Natural state after pluton intrusion

First, the forward problem is studied of the pluton cooling down until the reservoir reaches steady state. The temperature distribution 5,000 years after the magma intrusion is shown in Figure 2. The geothermal system is highly permeable (k = 10^{-14} m^2) which results in heat transfer dominated by advection. The density-driven fluid migration is rapid, and an upwelling plume with temperatures higher than 250°C forms directly above the cooling pluton.

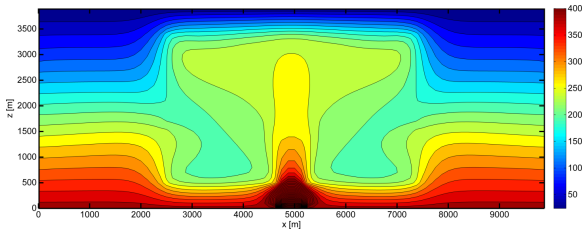

Figure 2. Temperature distribution (°C) at 5,000 years after the intrusion. The maximum temperature at elements below the intrusion is 1,100°C.

Demonstration of inverse analyses

iTOUGH2 provides a variety of analysis options for the TOUGH2 simulator, including (1) parameter estimation by automatic history matching, (2) local and global sensitivity analyses, (3) uncertainty propagation analysis, and (4) data-worth analysis. Here, we simply perform an inversion of synthetically generated exploitation data from the system previously described to demonstrate an iTOUGH2 application in combination with the new EOS1sc module.

Fluid with an enthalpy of 500 kJ/kg is injected at a constant rate; the injection pressure is monitored. Temperature and extraction rates are observed in a production well located above the intrusion. The pressure, temperature, and production-rate data are corrupted by Gaussian noise with standard deviations of 2 bars, 3 °C, and 0.1 kg/s, respectively. Data are collected monthly during the first 5 years of production. The calibrated model is then used to predict reservoir performance for an additional 15 years.

For this demonstration, the logarithm of reservoir permeability and initial pluton temperature are considered the unknown parameters to be estimated by history matching. Since the initial pluton temperature is updated during the inversion, a natural-state calculation starting from the time of the intrusion is needed, followed by a simulation of the transient behavior during reservoir exploitation.

The parameters are estimated by solving a non-linear weighted least-squares problem using five iterations of the Levenberg-Marquardt minimization algorithm. Estimation and prediction uncertainties are approximately calculated assuming the model is linear within the confidence region, and the errors are normally distributed.

Figure 3 shows the true system behavior, the noisy synthetic observations used as calibration points during the first five years of production, the long-term system behavior, and the corresponding model predictions with the initial (i.e., uncalibrated) and calibrated models. It is obvious that even relatively minor errors in the two parameters examined here lead to grossly different predictions of reservoir behavior; a calibration step is thus essential. iTOUGH2 is capable of identifying the true parameter set within a few iterations, thus matching the calibration data and yielding a reasonable prediction of future reservoir behavior, specifically the considerable long-term temperature decline in the production well despite the nearby presence of a hot pluton.

This generic data inversion and associated analyses demonstrate that the newly developed equation-of-state module for sub- and supercritical water was successfully integrated into the iTOUGH2 simulation-inversion framework. It

also indicates that simulating the deep heat source is essential, as it influences reservoir performance and the estimation of parameters that are correlated to the properties and conditions of, for example, an intrusion.

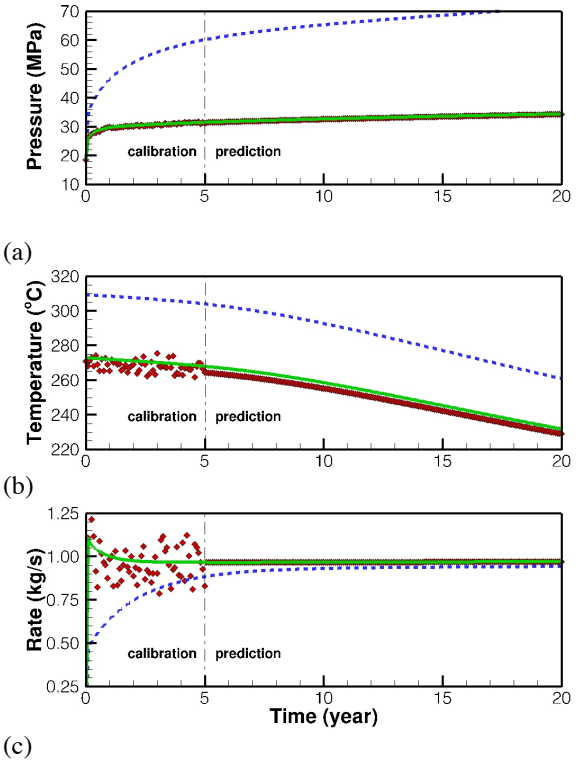

Figure 3. (a) Injection pressure, (b) production temperature, and (c) production rates simulated with the uncalibrated model (dashed lines), and calibrated model (solid lines); the synthetic data used for model calibration during the first five years of production are shown as symbols.

CONCLUDING REMARKS

A new equation-of-state module, termed EOS1sc, was developed to extend the operation range of iTOUGH2 to temperatures and pressures up to 2000°C and 50 MPa. Such extreme conditions are likely to occur in magmatic geothermal reservoirs where the heat sources can reach relatively shallow depths. It allows inclusion of the heat source—which is a key boundary condition—into a geothermal reservoir model. Moreover, the temperature and location of this heat source can be estimated (along with other reservoir properties) using iTOUGH2's inverse modeling capabilities. More details can be found in Magnusdottir and Finsterle (2015).

ACKNOWLEDGMENT

Gratitude goes to the Geothermal Research Group (GEORG) for funding this study. The second author was supported, in part, by the U.S. Dept. of Energy under Contract No. DE-AC02-05CH11231.

REFERENCES

Brikowski, T.H., Modeling supercritical systems with TOUGH2: Preliminary results using the EOS1SC equation of state module, *Proceedings*, 26th Workshop on Geothermal Reservoir Engineering, Stanford University, Stanford, Calif., 2001.

Croucher, A.E., and M.J. O'Sullivan, Application of the Computer Code TOUGH2 to the Simulation of Supercritical Conditions in Geothermal Systems, *Geothermics*, 37, 662-634, 2008.

International Association for the Properties of Water and Steam, *Revised Release on the IAPWS Industrial Formulation 1997 for the Thermodynamic Properties of Water and Steam*, IAPWS Release, Switzerland, 2007.

International Association for the Properties of Water and Steam, *Revised Release on the IAPWS Formulation 1995 for the Thermodynamic Properties of Ordinary Water Substance for General and Scientific Use*, IAPWS Release, The Netherlands, 2009.

International Formulation Committee of the 6th International Conference on the Properties of Steam, *The 1967 IFC Formulation for Industrial Use*, Verein Deutscher Ingenieure, Düsseldorf, Germany, 1967.

Kissling, W.M., Deep Hydrology of the Geothermal Systems in the Taupo Volcanic Zone, New Zealand, PhD Thesis, University of Auckland, New Zealand, 2004.

Magnusdottir, L., and S. Finsterle, An iTOUGH2 equation-of-state module for modeling supercritical conditions in geothermal reservoirs, *Geothermics*, *57*, 8–17, 2015.

GEOCHEMICAL MODELING OF TOURMALINE FORMATION AT ELBA ISLAND

* Giordano Montegrossi[1], Giovanni Ruggieri[1],Barbara Cantucci[2]

[1]CNR-IGG. Via La Pira 4, I-50121, Florence, Italy.
[2] INGV, Fluid Geochemistry Lab. Rome 1 Section, Via di Vigna Murata 605, Rome, 00143, Italy
montegrossi@igg.cnr.it

ABSTRACT

Geochemical numerical models require a comprehensive and coherent thermodynamic database. Although today's geochemical databases are quite complete, including the most common reaction and reaction constants, some reactions typical of specific environments are not included yet.

As part of the EU FP7-funded Integrated Methods for Advanced Geothermal Exploration (IMAGE) project, a building up of a thermodynamic database focused on thermal aureole minerals and B-metasomatic process, with Pitzer formalism was carried out.

Therefore, the thermodynamic properties of several minerals have been added to the TOUGHREACT Pitzer default database (data0.ypf). Input data, in a modified format were also added to the provided TOUGHREACT (Thermok.dat) and PHREEQC (llnl.dat) databases, to be used both in Debye-Hückel [1] and in the Pitzer [2] aqueous model.

The data were taken from available literature on thermodynamic properties of minerals, and in particular from the thermodynamic data collections of Holland and Powell [3] and Holland et al. [4] among many others.

The new data collection allows carrying out simple models of interest in fossil high-temperature geothermal systems in Eastern Elba Island (Italy), by means of TOUGHREACT-Pitzer.

The model involves the formation of tourmaline from the biotite present in micaschist of Eastern Elba Island by interaction with boron-rich fluids. As a secondary step for the uprising hot fluid, which is enriched in Fe^{+2} after the biotite dissolution and tourmaline precipitation, we have the deposition of magnetite as soon as the fluid reaches a horizon with higher redox potential. This process opens new interesting perspectives on the Fe source of iron deposits associated with the emplacement of leucogranite intrusions and B-metasomatism.

To be within the validity range of TOUGHREACT equation of state (EOS2 is used in this model), we choose the correct condition in terms of chemical composition of the hot fluid, so that the biotite-tourmaline alteration process could take place at temperature lower than 350°C, although higher temperature likely characterized the B-metasomatism in Eastern Elba Island.

THERMODYNAMIC BACKGROUND

Geochemical numerical models require a comprehensive thermodynamic database. Although today's geochemical database are quite complete, including the most common reactions and reaction constants, some reactions typical of specific environments are not included. In this work (carried out in the framework of EU FP7-funded Integrated Methods for Advanced Geothermal Exploration (IMAGE) project) we attempt to develop a model that can be applied to B-rich fluids released by crystallizing magmatic intrusions.

In fact, boron metasomatism and deposition of tourmaline in veins are common processes around granite intrusions, which release late magmatic fluids to the wall-rocks in both fossil (e.g. Elba Island, Italy; Scotland, U.K.; Utah and South Dakota, U.S.A.) and active (e.g. Larderello, Italy) hydrothermal systems (Wilson and Long, 1983; Shearer et al., 1984; Woodford et al., 2001; Dini et al., 2008).

A well exposed example of this process is in eastern Elba Island (Tuscany, Italy), where the emplacement of numerous Late Miocene shallow crustal tabular, tourmaline bearing, leucogranite intrusions induced widespread and selective biotite replacement by tourmaline

metasomatism and veining into the Calamita Schist hosts (Dini et al, 2008).

Therefore, the thermodynamic properties of some minerals relevant to our model that involve tourmaline formation from biotite dissolution have been added to the THOUGHREACT Pitzer default database (data0.ypf). Input data, in a modified format were also added to the provided TOUGHREACT (Thermok.dat) and PHREEQC (llnl.dat) databases, to be used both in Debye-Hückel (Debye and Hückel, 1923) and in the Pitzer (Pitzer, 1973) aqueous model.

The data0.ypf database follows the EQ3/6 V7.2b code formalism (Wolery, 1992), where solid phases are written as a dissolution reaction of mineral in its ionic and aqueous components. In particular the following dissolution reactions were added: Almandine (Holland and Powell, 2011), Andalusite (Helgeson et al. 1978), Annite (Helgeson et al. 1978), Fe-actinolite (Holland and Powell, 2011), Mg-cordierite anhydrous (Johnson et al., 1992), Mg-cordierite (Helgeson et al. 1978), Fe-cordierite anhydrous (Holland and Powell, 2011), Dravite (Ogordova et al., 2012), Elbaite (Ogordova et al., 2012), FeO (Helgeson et al. 1978), Grossular (Helgeson et al. 1978), Magnetite (Helgeson et al. 1978), Muscovite (Helgeson et al. 1978), Paragonite (Helgeson et al. 1978), Phlogopite (Helgeson et al. 1978), Pyrope (Holland and Powell, 2011), Schorl (Ogordova et al., 2012), Sillimanite (Helgeson et al. 1978), Spessartine (Holland and Powell, 2011), Fe-sudoite (Holland and Powell, 2011) and Sudoite (Holland and Powell, 2011).

Here are reported the mentioned dissolution reactions:

$$Fe_3Al_2Si_3O_{12}(almandine) + 12\,H^+ \leftrightarrow 3\,Fe^{+2} + 2\,SiO_{2(aq)} + 2\,Al^{+3} + 6\,H_2O$$

$$Al_2SiO_5(andalusite) + 6H^+ \leftrightarrow 2\,Al^{+3} + 1\,SiO_{2(aq)} + 3\,H_2O$$

$$KFe_3AlSi_3O_{10}(OH)_2(annite) + 10\,H^+ \leftrightarrow 3\,Fe^{+2} + 3\,SiO_{2(aq)} + 1\,Al^{+3} + 1\,K^+ + 6\,H_2O$$

$$KFe_3AlSi_3O_{10}(OH)_2(annite1) + 3\,Mg^{+2} \leftrightarrow 3\,KAlMg_3Si_4O_{10}(OH)_2(phlogopite) + 3\,Fe^{+2}$$

$$Ca_2Fe_5Si_8O_{22}(OH)_2(Fe-actinolite) + 14\,H^+ \leftrightarrow 2\,Ca^{+2} + 5\,Fe^{+2} + 8\,SiO_{2(aq)} + 8\,H_2O$$

$$Mg_2Al_4Si_5O_{18}(Mg-cordierite\ anhydrous) + 16\,H^+ \leftrightarrow 2\,Mg^{+2} + 4\,Al^{+3} + 5\,SiO_{2(aq)} + 8\,H_2O$$

$$Mg_2Al_4Si_5O_{18}H_2O(Mg-cordierite) + 16\,H^+ \leftrightarrow 2Mg^{+2} + 4\,Al^{+3} + 5\,SiO_{2(aq)} + 9\,H_2O$$

$$Fe_2Al_4Si_5O_{18}(Fe-cordierite\ anhydrous) + 16\,H^+ \leftrightarrow 2Fe^{+2} + 4\,Al^{+3} + 5\,SiO_{2(aq)} + 8\,H_2O$$

$$NaMg_3Al_6(BO_3)_3Si_6O_{18}(OH)_4(dravite) + 25\,H^+ \leftrightarrow 6Al^{+3} + 3\,Mg^{+2} + 1\,Na^+ + B(OH)_3 + 6\,SiO_{2(aq)} + 10\,H_2O$$

$$NaMg_3Al_6(BO_3)_3Si_6O_{18}(OH)_4(dravite1) + 3Fe^{+2} \leftrightarrow 1\,Schorl(aq) + 3\,Mg^{+2}$$

$$NaLiAl_{1.5}B_3Si_6O_{27}(OH)_4(elbaite) + 25\,H^+ \leftrightarrow 7.6\,Al^{+3} + 1\,Li^+ + 1\,Na^+ + 3\,B(OH)_3 + 6SiO_{2(aq)} + 10\,H_2O$$

$$FeO + 2\,H^+ \leftrightarrow 1Fe^{+2} + 1\,H^+$$

$$Ca_3Al_2(SiO_4)_3(grossular) + 12\,H^+ \leftrightarrow 2\,Al^{+3} + 3Ca^{+2} + 3SiO_{2(aq)} + 6H_2O$$

$$Fe_3O_4(magnetite) + 6H^+ \leftrightarrow 3Fe^{+2} + 0.5\,O_{2(aq)} + 3\,H_2O$$

$$Fe_3O_4(magnetite1) + 8H^+ \leftrightarrow 1\,Fe^{+2} + 2Fe^{+3} + 4\,H_2O$$

$$KAl_3Si_3O_{10}(OH)_2(muscovite) + 10\,H^+ \leftrightarrow 1K^+ + 3Al^{+3} + 3SiO_{2(aq)} + 6H_2O$$

$$NaAl_3Si_3O_{10}(OH)_2(paragonite) + 10\,H^+ \leftrightarrow 1Na^+ + 3\,Al^{+3} + 3SiO_{2(aq)} + 6\,H_2O$$

$$KAlMg_3Si_4O_{10}(OH)_2(phlogopite) + 10\,H^+ \leftrightarrow 1Al^{+3} + 1\,K^+ + 3Mg^{+2} + 3SiO_{2(aq)} + 6\,H_2O$$

$$Mg_3Al_2Si_3O_{12}(pyrope) + 12\,H^+ \leftrightarrow 2\,Al^{+3} + 3\,Mg^{+2} + 3\,SiO_{2(aq)} + 6\,H_2O$$

$$NaFe_3Al_6(BO_3)_3Si_6O_{18}(OH)_4(schorl) + 25\,H^+ \leftrightarrow 6Al^{+3} + 3Fe^{+2} + 1Na^+ + 3B(OH)_{3(aq)} + 6\,SiO_2 + 10\,H_2O$$

$$Al_2SiO_5(sillimanite) + 6H^+ \leftrightarrow 1SiO_{2(aq)} + 2\,Al^{+3} + 3H_2O$$

$$Mn_3Al_2Si_3O_{12}(spessartine) + 12\,H^+ \leftrightarrow 2\,Al^{+3} + 6\,H_2O + 3Mn^{+2} + 3SiO_{2(aq)}$$

$$Mg_2Al_4Si_5O_{18}(OH)_4(sudoite) + 16\,H^+ \leftrightarrow 4Al^{+3} + 2Mg^{+2} + 3SiO_{2(aq)} + 12\,H_2O$$

$$Fe_2Al_4Si_5O_{18}(OH)_4(Fe-sudoite) + 16\,H^+ \leftrightarrow 4Al^{+3} + 2Fe^{+2} + 3SiO_{2(aq)} + 12\,H_2O$$

The chemical equilibrium of the above reported reactions is ruled by the logarithm of equilibrium constant (log K) at standard temperature and pressure condition (i.e. 25°C and 1.0132 bar). To calculate the equilibrium constant at a different temperature, TOUGHREACT uses an analytical regression curve computed with eight equilibrium constants defined at eight specific temperatures and pressures, from 0°C up to 300°C along the liquid-vapor saturation curve of pure water. The log K grid is organized for temperatures of 0, 25, 60, 100 °C at 1.0132 bar and 150, 200, 250, 300 °C at steam/liquid water pressure. The analytical equation has the following form:

$$\text{Log K} = a[\![\log]\!]_n(T) + b + cT + d/T + e/T^2 \quad (1)$$

where T is temperature in Kelvin.

For the dissolution reactions of Mg-cordierite, Mg-cordierite anhydrous, Annite, FeO, Grossular, Muscovite, Paragonite, Phlogopite, Magnetite, Andalusite and Sillimanite, no complete thermodynamic data are found in the recent literature. Thus, the log K values were taken from the EQ3/6 database (data0.dat) by thermodynamic source data of Helgeson et al. (1978). The EQ3/6 database is one of the most complete sources of data and constitutes the original source from which most thermodynamic databases have been developed. Moreover, EQ3/6 data are consistent with recent literature and small changes only reflect a newer "best fit" to more recent thermodynamic data.

Calculation of log K for Dravite, Schorl, Fe-actinolite, Elbaite, Fe-cordierite anhydrous, Fe-

sudoite, Sudoite, Almandine, Pyrope and Spessartine were carried out by means of the code SUPCRT92 (Johnson et al. 1992). This code allows calculation of the standard molal thermodynamic properties of a wide variety of minerals, gas and aqueous species and their equilibrium reactions from 1 to 5000 bars and 0 to 1000°C.

The SUPCRT92 package is composed of three programs: i) the MPRONS92 is used to add or modify formation thermodynamic data of each species; ii) the CPRONS92 converts database generated by MPRONS92 in SUPCRT format, and iii) the SUPCRT92 reads and calculates the standard molal Gibbs free energy, enthalpy, entropy, heat capacity, volume and log K for each equilibrium reaction. The SUPCRT original default database (SPRONS92.DAT) contains thermodynamic data for approximately 500 minerals, gases, and aqueous species.

Because Almandine, Fe-actinolite, Fe-cordierite, Dravite, Elbaite, Pyrope, Schorl, Spessartine, Fe-sudoite, and Sudoite were not included in the SPRONS92.DAT database, they were added by means of MPRONS92 interactive program.

For each solid phases MPRONS92 requires: i) the standard Gibb free energy of formation ($\Delta G°f,298$) at 298.15K [cal mol-1]; ii) the standard enthalpy of formation ($\Delta H°f,298$) at 298.15K [cal mol-1], iii) standard entropy ($S°$) at 298.15K [cal mol-1K-1]; iv) the volume of minerals [cm3 mol-1], v) the standard heat capacity ($C°p$) at constant pressure and 298.15K [cal/mol K], iv) temperature-dependent $C°p$ coefficients (a, b, c) for use in extrapolating the data to elevated temperatures, using the Maier-Kelly equation (Maier and Kelley 1932):

$$[\![C°]\!]_p = a + bT + c/T^2 \qquad (2)$$

where T is absolute temperature in Kelvin. The heat capacity coefficients a,b,c are expressed as a, $b \times 10^3$, and $c \times 10^{-5}$.

Thermodynamic data representing experimental mineral solubility based on infinite dilution were extracted from the literature after a careful bibliographic research and reported in Table 1. Tourmaline (i.e., Elbaite, Dravite and Scholr) source data are from Ogorodova et al. (2012), whereas garnet (i.e., Almandine, Pyrope, and Spessartine), as well as amphibole (i.e., Fe-actinolite), Fe-cordierite, and chlorite (i.e., Sudoite and Fe-sudoite) data are from Holland and Powel (2004, 2011).

After conversion of modified MPRONS92 in the SUPCRT format, by means of CPRONS92 utility programs, the equilibrium constants at the T-P grid were calculated.

Reactions involved ions, aqueous species (i.e., H_2O and $SiO_2(aq)$), originally reported in the SPRONS92.DAT database were used, after checking the consistency with more recent data.

All collected Log K values were adapted to be used as input for TOUGHREACT (Thermok.dat) and PHREEQC databases (llnl.dat), both in Debye-Hückel (Debye and Hückel, 1923) and in the Pitzer (Pitzer, 1973) aqueous model.

Thermok.dat and llnl.dat databases require for each dissolution reaction the log K at EQ3/6 temperature grid and the coefficients for the analytic regression curve, to calculate equilibrium constant at different temperatures. On the basis of the log K obtained so far, the coefficients for analytic regression curve were calculated by means of Equation (1) for TOUGHREACT and by Equation (3) for PHREEQC:

$$[\![\log]\!]_{10}K = A_1 + A_2T + A_3/T + A_4[\![\log]\!]_{10}T + A_5/T^2 + A_6\,T^2 \qquad (3)$$

where T is temperature in Kelvin.

Regression coefficients for Equation (1) were computed by the utility program Kreg1 provided by TOUGHREACT, whereas for Equation (3), a modified version of Kreg1, accounting for the differences between Equations (1) and (3), was used.

To guaranty the inter-comparison among the thermok.dat, llnl.dat and data0.ypf databases, all thermodynamic data were uniformed.

Table 1. Summary of thermodynamic properties for new solid phases.

Mineral	ΔG°f,298 cal mol-1	ΔH°f,298 cal mol-1	S° cal mol-1K-1	V cm3mol-1	a cal $mol^{-1}K^{-1}$	$bx10^3$ cal $mol^{-1}K^{-2}$	$cx10^{-5}$ cal K mol^{-1}	
Almandine	-1179853.78*	-1256487.67	81.69	115.25	161.77	-	-9.02	Holland and Powel, 2011
Fe-actinolite	-2349611.52*	-2508800.30	169.581	284.20	308.1119	7.16826	-20.19	Holland and Powel, 2011
Fe-cordierite	-1898695.66*	-2016824.35	110.11	237.10	220.69	-	-16.82	Holland and Powel, 2011
Dravite	-3456824.92	-3680624.06	151.67	319.19	278.57	19.24	-87.05	Ogorodova et al., 2012
Elbaite	-3427446.80	-3658889.03	150.23	305.82	222.82	88.79	-58.53	Ogorodova et al., 2012
Pyrope	-1417224.17*	-1500464.56	64.37	113.13	151.31	-	-12.42	Holland and Powel, 2011
Schorl	-3244729.26	-3463273.77	171.49	319.45	242.79	82.89	-69.19	Ogorodova et al., 2012
Spessartine	-1272170.33*	-1359908.19	80.09	117.92	154.51	-	-10.82	Holland and Powel, 2011
Fe-Sudoite	-1737765.69*	-1886913.36	108.91	204.00	350.22	-11.32	-2.83	Holland and Powel, 2011
Sudoite	-1905223.33*	-2060506.98	94.34	203.00	343.01	-11.65	-6.57	Holland and Powel, 2011

* ΔG°f data are from Holland and Powell, 2004.

MODEL OF TOURMALINE FORMATION

To model the tourmaline formation from Elba Island Calamita Schist (i.e. biotite-bearing micaschists) due to an 'hydrothermal event', we assumed as initial steady state a column 1x1 km with 5 km height, with hydrostatic (from 1 bar to nearly 433 bar) pressure gradient, and with a normal thermal gradient (from 20 to nearly 200 °C). The mineralogy of the column is reported in table 2, and is uniform in the model.

Table 2. Volume fraction of minerals

Mineral	Volume Fraction of Solid
Albite	0.4
k-feldspar	0.001
Annite	0.3
Quartz	0.09
Phlogopite	0.2
Dravite	0.0000
Schorl	0.0000
Magnetite	0.0000

The fracture is modeled using 5 elements with high permeability ($1e^{-13}$ m^2, mesh size 4 cm) in the central ones and 2 elements at each side with lower permeability ($1e^{-15}$ m^2, mesh size 3 cm), while micaschists have $1e^{-17}$ m^2 in the whole column.

The hydrothermal event were modeled using an inflow of hot water (330 °C) with high boron concentration (2 mol/kg), with 1 kg/s constant inflow in the fracture center for 50 years.

The most extended effect, after 50 years, is the pH variations; the hydrolysis pH for the given rock composition is 11.15, but it is easily re-buffered at a pH nearly 7.2, while the hot boron-rich fluid reach a buffer at a pH of 4.53 at the fracture bottom, causing biotite dissolution.

In Figure 1 we could observe e.g. Annite dissolution, which produces an iron-rich zone according to the dissolution reactions before mentioned. In a zone slightly below (Figure 2), the hot boron-rich fluid allows the schorl precipitation, while the iron excess present in the uprising fluid is readily precipitated as magnetite in an upper zone (Figure 3), i.e. as soon as the mixing with formation water provides enough dissolved oxygen to allow magnetite precipitation, and the fluid is cooled down as well.

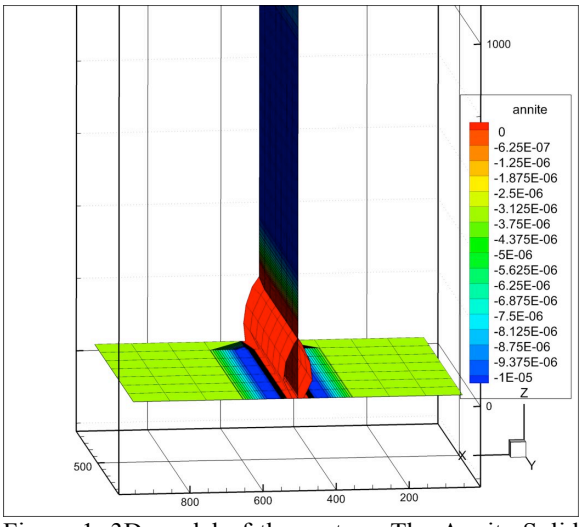

Figure 1. 3D model of the system. The Annite Solid Volume Fraction variation for a 0.3 years step after 40 years is shown.

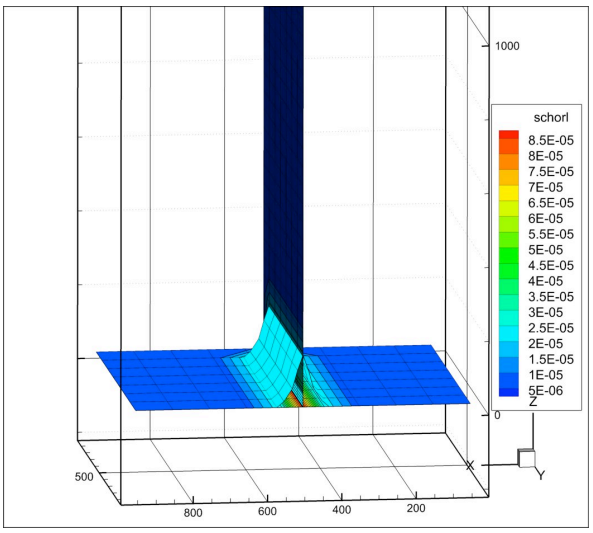

Figure 2. 3D model of the system. The Schorl Solid Volume Fraction variation for a 0.3 years step after 40 years is shown.

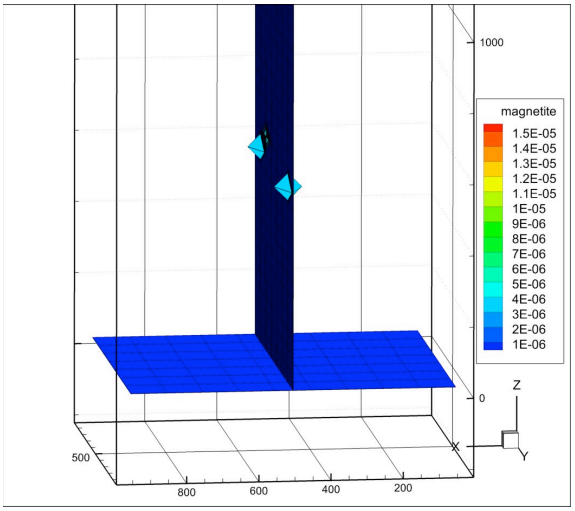

Figure 3. 3D model of the system. The Magnetite Solid Volume Fraction variation for a 0.3 years step after 40 years is shown.

CONCLUSION

This model show that the biotite dissolution due to a boron-rich fluid could lead to the precipitation of tourmaline at relatively low temperature, with a related iron oxide deposition in to the upper zone. Although dissolution should have occurred at higher temperature (e.g. 600 °C?) in the presence of a boron-rich saline fluids issued from the lecogranitic intrusions of Eastern Elba Island, the model were limited by the up-to date maximum temperature available with TOUGHREACT-EOS2, but still succeeded in modeling the mineral evolution processes.

An important consequence of our model is that partial dissolution of biotite, besides allowing tourmaline crystallization, could have also provided significant amount of iron which precipitated as magnetite and may form Fe-ores. This is exactly what we can observe in the Southeastern part of Elba Island where the Calamita Schist also host part of the famous Elba Island Fe-deposits mined in the past. .

REFERENCES

Debye P., Huckel E., Zur Theorie der Elektrolyte. *Phys. Z.,* 24, 185-206, 1923.

Dini A, Mazzarini F, Musumeci G., Rocchi S., Multiple hydro-fracturing by boron-rich fluids in the Late Miocene contact aureole of eastern Elba Island (Tuscany, Italy). *Terra Nova,* 20(4), 318-326, 2008.

Helgeson, H.C., Delany, J.M., Nesbitt, H.W., and Bird, D.K., Summary and critique of the thermodynamic properties of rock-forming minerals, *Amer. J. Sci*., 278a, 229 p., 1978.

Holland, T.J.B., Powell, R., An improved and extended internally consistent thermodynamic dataset for phases of petrological interest, involving a new equation of state for solids. *J. Metamorphic Geol.,* 29(3), 333–383, 2011.

Holland, T.J.B., Powell, R., An internally consistent thermodynamic data set for phases of petrological interest. *J. Metamorphic Geol.,* 16(3), 309–343, 1998.

Johnson, J.W., Oelkers, E.H., Helgeson, H.C., SUPCRT92: A software package for calculating the standard molal thermodynamic properties of minerals, gases, aqueous species, and reactions from 1 to 5000 bar and 0 to 1000°C. *Computers & Geosciences,* 18(7), 899-947, 1992.

Maier, C. G., Kelly, K. K., An equation for the representation of high temperature heat content data. *Am. Chemical Soc. Jour*., 54(8), 3243-3246, 1932.

Ogorodovaa, L.P., Melchakova, L.V., Kiseleva, I.A., Peretyazhko, I.S., Thermodynamics of natural tourmalines—Dravite and schorl. *Thermochimica Acta,* 539, 1– 6, 2012.

Pitzer K.S., Thermodynamics of electrolytes - I. Theoretical basis and general equations. *Journal of Physical Chemistry*, 77, 268-277, 1973.

Shearer, C.K., Papike, J.J., Simon, S.B., Laul, J.C. and Christian, R.P., Pegmatite ⁄ wallrock interactions, Black Hills, South Dakota: progressive boron metasomatism adjacent to the Tip Top pegmatite. *Geochim. Cosmochim. Acta,* 48, 2563–2579, 1984.

Wilson, G.C., Long, J.V.P., The distribution of lithium in some Cornish minerals, ion microprobe measurements, *Mineralogical Magazine,* 47, 191-199, 1983.

Wolery T. J., *EQ3NR, a computer program for geochemical aqueous speciation-solubility calculations: theoretical manual, User's Guide, and related documentation (version 7.0),* UCRL-MA-110662 PT III. Lawrence Livermore National Lab, Livermore, CA., 1992.

Woodford, D.T., Sisson, V.B. and Leeman, W.P., 2001. Boron metasomatism of the Alta stock contact aureole, Utah: evidence from borates, mineral chemistry and geochemistry. *Am. Mineral.,* 86, 513–533, 2001.

MODELING A CO_2 THERMOSIPHON IN A PARTIALLY SATURATED RESERVOIR USING T2WELL WITH EOS7CMA

Lehua Pan, Christine Doughty, Barry Freifeld, and Curtis M. Oldenburg

Earth Sciences Division, Lawrence Berkeley National Laboratory
University of California, One Cyclotron Road
Berkeley, CA 94720, USA
e-mail: lpan@lbl.gov

ABSTRACT

CO_2 as a working fluid for geothermal heat extraction is considered to have many advantages over conventional water. One of the advantages is the potential to establish a self-sustaining CO_2 thermosiphon by taking advantage of the strong temperature dependence of CO_2 density so that no additional energy would be needed to drive the circulation of working fluid in the geothermal system. In this paper, we have demonstrated an approach to simulate and analyze the thermosiphon phenomenon with an eye on development of a CO_2-based geothermal system. In particular, we have expanded T2Well, a fully coupled wellbore-reservoir numerical simulator, to be able to simulate the entire loop of fluid circulation in the fully coupled system consisting of the injection/production wells, the reservoir, and the surface devices (heat exchanger, flow-rate regulator, and fluid filter, etc.). Combined with the newly developed EOS7CMA, the modified T2Well was used to simulate the circulation of a CO_2-H_2O-CH_4 mixture in a geothermal system, which was designed based on a planned demonstration test at an operating CO_2 injection site. The main focus is to reveal the conditions for starting and sustaining the thermosiphon in a partially saturated reservoir.

INDRODUCTION

The goal of these modeling exercises is to predict the performance of a planned demonstration test at an operating CO_2 injection site, using the parameters estimated during the SECARB Cranfield Phase III injection test conducted at the DAS site (Hovorka et al., 2013). The results could be used to help design field tests of the thermosiphon including the surface infrastructure and the sequencing of procedures.

CONCEPTUAL MODEL AND GRID

Reservoir

The target reservoir is simplified as a flat reservoir of 23.16 m thickness at a depth of 3173.58 m below land surface. The reservoir consists of six layers with various thicknesses and properties, which were based on well logs from the injection well (Hosseini et al., 2013) (Table 1). Pore compressibility, heat conductivity, and specific heat are 3E-9 (Pa^{-1}), 2.51 (W/(m °C)), and 920 (J/(kg °C)), respectively, for all rock types.

Table 1 Formation layers and their properties

Name	Thickness (m)	Porosity	Lateral perm. ($\times 10^{-15}$ m^2)	Vertical perm. ($\times 10^{-15}$ m^2)
Layer1	6.86	0.169	8.60	1.058
Layer2	6.10	0.254	130.7	1.058
Layer3	2.90	0.288	230.0	47.94
Layer4	0.90	0.139	2.4	0.082
Layer5	3.00	0.315	349.2	84.87
Layer6	3.40	0.283	225.7	2.229
skins	0.1679 (lateral)	0.139	1.35	0.1058

A full 3D grid with varied lateral resolutions is developed to represent a 10 km by 10 km reservoir (Figure 1a), with the outer distance chosen to minimize boundary effects. Locally refined grid cells (down to 0.05 m in width) are used in the regions near the injection well and the production well (Figure 1b). The vertical resolution of the model is the thickness of each layer.

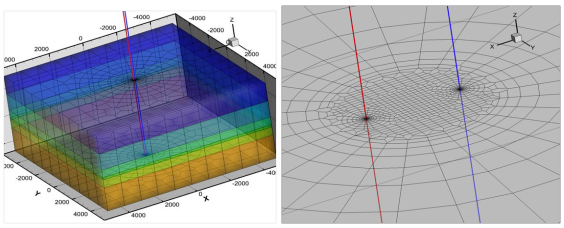

Figure 1. 3D grid of the reservoir with two wells. Blue line indicates the injection well and red line indicates the production well. Entire mesh (left) and local refinements (right).

The rocks near the injection wellbore (within a range of 0.168 m) are assumed to be affected by well completion (skin effects). A new rock type "skins" (Table 1) is assigned to these affected grid cells. No skin effect is included for the production well. Both wells are perforated in Layers 2-6.

The geothermal gradient is assumed to be 35.6 degree/km with $T = 127°C$ at a depth of 3000 m.

Wellbore

Two wells located in the center region of the simulated reservoir are 100 m apart and are assumed to have the same geometry (Table 2).

Table 2. Geometry and roughness of the wellbores

Length (above ground)	2.89 m
Length (below ground)	3196.74 m
I.D. (tubing)	2.4 in (0.06096 m)
I.D. (casing)	5.5 in (0.1397 m)
Wall roughness	1.5e-6 (smooth PVC)

The inner diameter of the casing (0.1397 m) is used for the wellbore grid cells within the reservoir (below -3173.58 m), whereas the inner diameter of the tubing is used for the wellbore above -3150.28 m. In-between -3150.28 m and -3167.58 m, the diameter of the simulated wellbore is assumed to change from 0.061 m (tubing I.D.) to 0.140 m (casing I.D.). A one-dimensional grid is created to represent the wellbore above the targeted reservoir. The vertical resolution of the wellbore grid is 10 m in most places, except that it is gradually reduced to about 3 m near the ground surface, to 4 m near top of the reservoir, and is the same as that used for the formation layers in the reservoir.

System and surface devices

The system consists of various surface devices besides the wells and the reservoir during different stages of the operation. The surface devices are represented as a series of grid cells in the numerical grid. The models include the entire system (the reservoir, the wellbores, and the surface devices) as depicted in Figure 2. During an initial filling stage, CO_2 comes from an external source. Therefore, the production well, the condenser, and the filter are not included in the model and the loop is not closed.

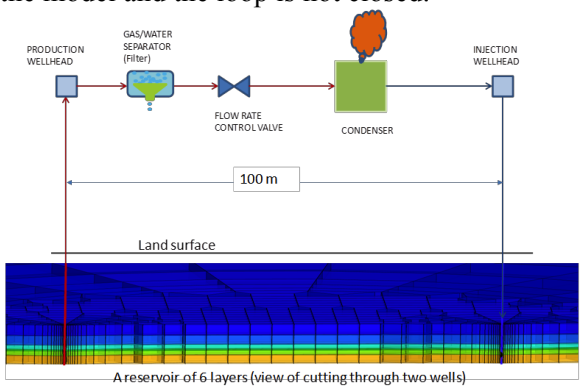

Figure 2. A sketch of the geothermal siphon model.

SIMULATOR

The simulations are carried out using a modified version of T2Well with EOS7CMA, a research version of the EOS7C code (Oldenburg et al., 2004) that includes air as a pseudo component. T2Well/EOS7CMA simulates non-isothermal, multi-phase, and multicomponent (H_2O, brine, and three non-condensable gas components) fluid and energy flow in the integrated wellbore-reservoir system. The code has been verified against some numerical solutions and field CO_2 production testing data, and has been applied to solve various problems involving coupled wellbore-reservoir flow processes (Pan and Oldenburg, 2013).

To facilitate the simulation of the geothermal siphon processes, we have modified the code by adding additional capabilities for simulating the Gas/Liquid separator, the flow-rate control valve, and the condenser (cooling device) simultaneously with other processes in wellbores and reservoir. Brief descriptions of the approaches and implementations are provided below:

1) The gas/liquid separator (the filter) is simulated by inserting an adaptive sink of water in the designated grid cell whose strength is defined as follows:

$$q^w_{\sin k} = q^w_{inlet}\,\lambda \quad (1a)$$

$$q^h_{\sin k} = \left(q^h_{gas} X^w_{gas} + q^h_{aqu} X^w_{aqu}\right)\lambda \quad (1b)$$

Where, q is flow rate, λ is the filtering efficiency, and the superscript w or h indicates water component or energy, respectively. "*aqu*" and "*gas*" indicate phase. X is the mass fraction. This adaptive sink will effectively remove λ fraction of the inflow water and energy (in both phases if any) from the grid cell.

2) The flow rate control valve is simulated as a special connection between wellbore cells through which the mixture velocity is fixed at a constant value (the value is internally calculated from the user-specified mass flow rate at that connection with the upstream densities.) The difference between the pressure drop across the valve and the pressure drop over the same length of a normal section of the same flowing pipe is a measure of the siphon force that can be calculated as below:

$$Siphon\ force = \Delta P_{valve} - \Delta P_{normal} \quad (2)$$

For any given mass flow rate, if Siphon force >=0, a thermosiphon is possible. Otherwise, a pump is required to maintain the flow rate.

3) The condenser is simulated as a special well cell which is connected to a virtual (constant temperature) grid cell through an interface that is impermeable to fluid but has a constant heat exchange coefficient. The conductive heat loss (q_{heat}) through the condenser is calculated as follow:

$$q_{heat} = \alpha\left(T_{fluid} - T_{envir}\right) \quad (3)$$

Where, α is the heat exchange coefficient (75.01 W/°C in this study), T_{fluid} is the fluid temperature, and T_{envir} is the reference temperature (or cooling fluid temperature, 10 °C in this study).

INITIAL AND BOUNDARY CONDITIONS

All boundaries of the domain are closed for fluid flow for the thermosiphon modeling. The heat exchange between the injection/production tube (the wellbore above the top of the reservoir) and the surrounding formations is calculated analytically (Ramey, 1962). The heat exchange between the reservoir and the caprock is also calculated analytically (Vinsome and Westerveld, 1980). The heat exchange in the condenser is simulated as described above.

The initial condition before thermosiphon testing is obtained by two stages of numerical simulation: the initial filling stage and the kick-off stage. During the initial filling stage, CO_2 from an external source is injected through the injection well into the reservoir initially filled with liquid water. The initial injection is assumed to take place for 1582 days (3.33 year, 12/1/2009-4/1/2014) with a total mass flow rate of 3.35 kg/s (the average injection rate over 3.33 year). In particular, the CO_2 injection rate is 3.25 kg/s and the CH_4 rate is 0.10 kg/s. The CO_2/CH_4 fluid in the external source (e.g., delivered through a pipe) is assumed to be at 3000 psi and 40°C when it arrives at the site (estimated from the data measured during the SECARB Cranfield Phase III injection tests). The reservoir pressure before initial injection is about 32.3 MPa (>hydrostatic pressure) and the temperature is about 127°C. The reservoir conditions and wellbore conditions after the initial filling stage are shown in Figure 3 and Figure 4, respectively. During the kick-off stage, the injection fluid still comes from the external source but a condenser is added to the injection line to cool the injection fluid while the production well is still closed at its wellhead. This operation lasts for 12 hours.

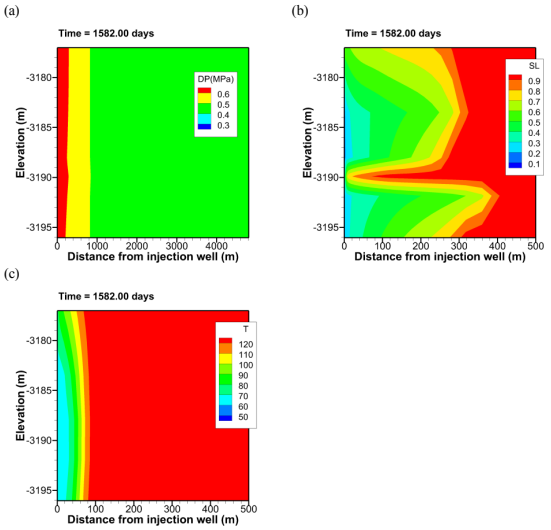

Figure 3. Reservoir conditions after the initial fill: a) pressure perturbation (*DP*); b) liquid saturation; and c) temperature.

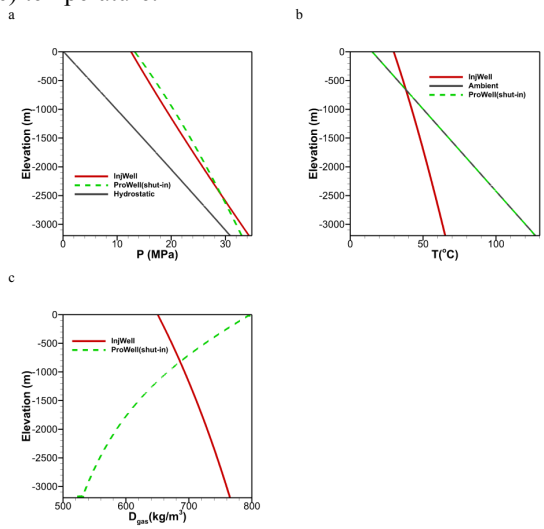

Figure 4. Wellbore conditions after the initial fill: a) pressure, b) temperature, and c) gas phase density.

RESULTS

Cooling injection with a condenser

The purpose of the kick-off is to increase the overpressure of the production wellhead over the injection wellhead. One possibility would be to release gas from the production well to the atmosphere. Instead, we assume that the ongoing injection of CO_2 from the outside source could be cooled by a condenser, which would increase the overpressure by reducing the injection wellhead pressure. Figure 5 shows the effects of such cooling.

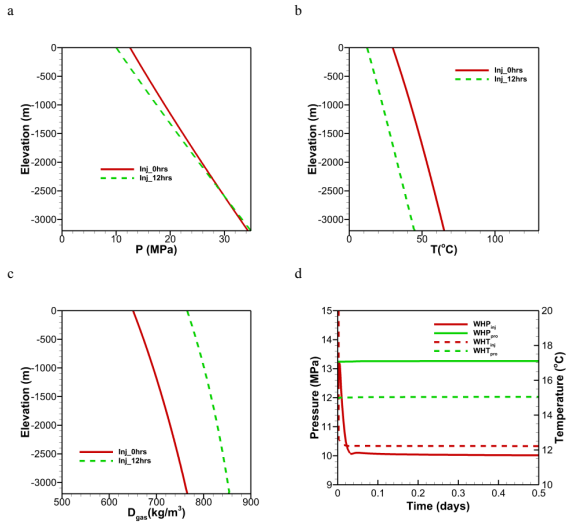

Figure 5. Effects of cooling injection fluid: a) pressure profiles in wells, b) temperature profiles in wells, c) gas density profiles in wells, and d) wellhead pressure and temperature responses to the cooling.

Siphon operation (Base case)

The thermosiphon test is designed to consist of three step-tests, each a week apart (Figure 6). Each test consists of four mass flow rates sequentially, namely, 2, 4, 6, and 8 kg/s. Each step lasts for 12 hours. Between the three step-tests, the mass flow rate is maintained at a constant value of 5 kg/s. A 2-hour shut-in period is inserted before the third step-test to see if the system can restart the thermosiphon without an external pump or high-pressure gas source after a short time shut-down (e.g., occasional equipment breakdown).

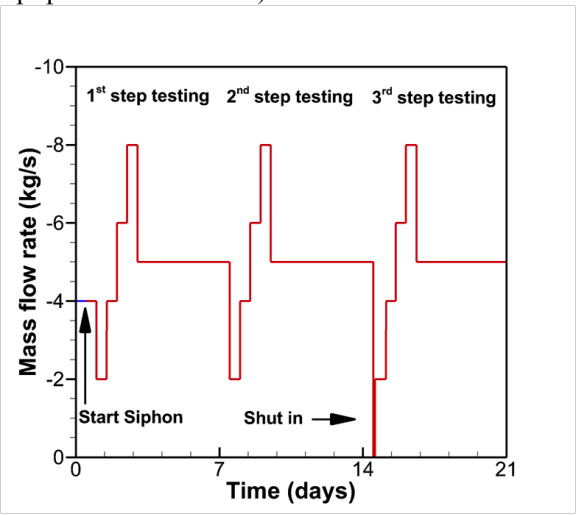

Figure 6. Prescribed mass flow rate during thermosiphon testing.

The siphon force increases with a decrease of the mass flow rate and vice versa (Figure 7a). While the trend of a decreasing siphon force during the first step-test is noticeable, the response of the siphon force to the mass flow rate is quite stable after 7 days. As mass flow rate increases to 8 kg/s, the siphon force becomes negative, indicating an additional pump is needed to maintain this flow rate, thus a thermosiphon is not sustainable at this rate for this system. The wellhead pressure responses to the mass flow rate are opposite between the production well and the injection well (Figure 7b). As mass flow rate increases, the production wellhead pressure decreases but the injection wellhead pressure increases. However, the magnitude of this response is larger in the injection well than in the production well. Meanwhile, the production well bottom pressure is much less sensitive to changes in mass flow rate than is the injection well bottom pressure. Similar patterns can be seen in the temperatures responses (Figure 7c). The liquid saturation at various locations changes little except immediately after a switch in mass flow rate.

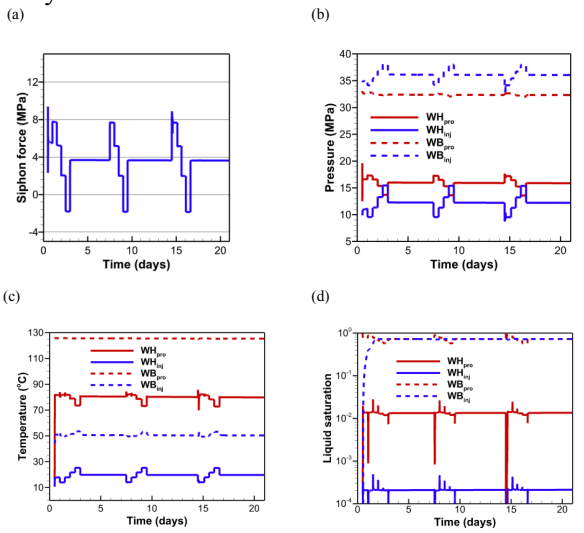

Figure 7. Base case: (a) siphon force, (b) pressure, (c) temperature, and (d) liquid saturation.

As the mass flow rate decreased from 5 kg/s to 0 kg/s when the shut-in period started, the siphon force jumped by more than 4 MPa (Figure 8a) because of a simultaneous increase in the production wellhead pressure and a decrease in the injection wellhead pressure (Figure 8b). However, the siphon force then decreases with time (Figure 8a) as the wellhead pressure decreases in the production well and increases in the injection well (Figure 8b). This is because the temperature in the production well decreases due loss of heat to the surrounding caprock and the temperature in the injection well increases due to heat gain from the surrounding caprock (Figure 8c). During the shut-in period, both wellheads dry out as liquid water quickly flows down the wells (Figure 8d). Although the well bottom pressures quickly approach the same value in the two wells, the pressure difference at the wellheads is still large at the end of the two-hour shut-in period (Figure 8b), even though this pressure difference is decreasing. Therefore, a short-term shut-in would still allow the system to restart thermosiphon operations without an external pump.

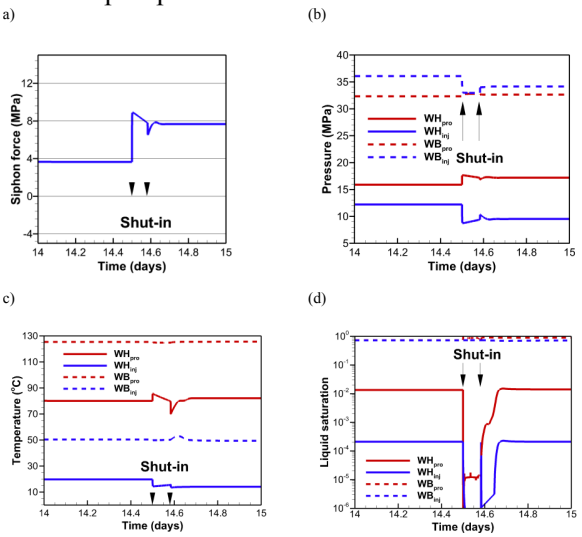

Figure 8. System performance during shut-in of two hours. (a) siphon force, (b) pressure, (c) temperature, and (d) liquid saturation.

Effects of aqueous phase mobility in the reservoir

We simulated an alternative case in which the residual liquid saturation is very high (=0.95 compared to 0.01 for the base case), which effectively makes the liquid phase water immobile in the reservoir formation. As a result, the siphon force is significantly larger in this "DryCase" than in the previous base case (Figure 9a). In this case, the siphon force becomes positive even when the mass flow rate is as high as 8 kg/s. This is because the wellhead pressure at the production well is higher and the wellhead pressure at the injection well is lower

in the "DryCase" than in BaseCase (Figure 9d) because the wells are drier (Figure 9d). The well bottom pressures are also less sensitive to the mass flow rate variations in the "DryCase" (Figure 9c) whereas the responses in terms of temperature are quite similar between the two cases in both wells (Figure 9e and f).

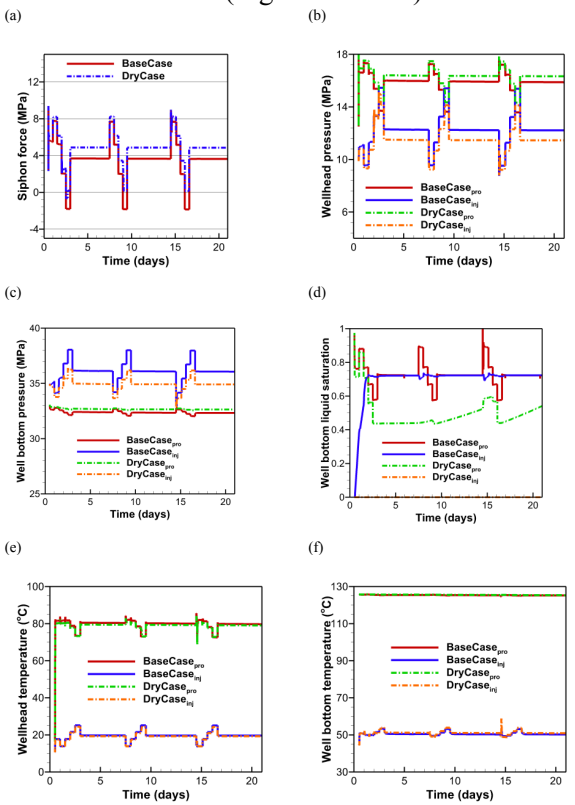

Figure 9. Effects of aqueous phase mobility in the reservoir on the system performance. (a) siphon force; (b) wellhead pressures; (c) well bottom pressures; (d) liquid phase saturation at well bottom; (e) wellhead temperature; and (f) well-bottom temperature. "DryCase" indicates the case in which the residual liquid saturation in the reservoir is so high that the water can only be transported in vapor form through the formation.

Effects of relative permeability in the reservoir

Although the immobilization of liquid water in the reservoir could have a significant impact on the siphon force as shown above, the "DryCase" is an idealized assumption that would not likely occur in the real world. Therefore, we have simulated the entire process (initial filling, cool injection and siphon testing) with an alternative set of hydraulic parameters, chosen to match lab experiments conducted on a sample from the Cranfield reservoir. The only difference is that the alternative case has higher gas permeability and lower liquid permeability than the base case. The effects of these differences in the relative permeability on the system performance can be seen by examining the siphon force (Figure 10). Overall, the siphon force decreases to negative value only at the mass flow rate of 8 kg/s which is similar to the base case but the siphon force in the "Alt" case could be higher than the base case (if mass flow rate is 2 kg/s) or lower (if mass flow rate is 8 kg/s). During the first step-test (Figure 10a), the siphon force in the "Alt" case is almost the same as that in the "Dry" case when the mass flow rate decreases to 2 kg/s. However, it is smaller than the base case when the mass flow rate increases to 8kg/s. For the flow rates of 4 and 6 kg/s, the siphon force of the "Alt" case is between the base case and the "Dry" case (Figure 10b). These "in-between" phenomena are diminished in the later tests (Figure 10c and d), but the behavior for high (8kg/s) or low (2 kg/s) flow rates remains the same.

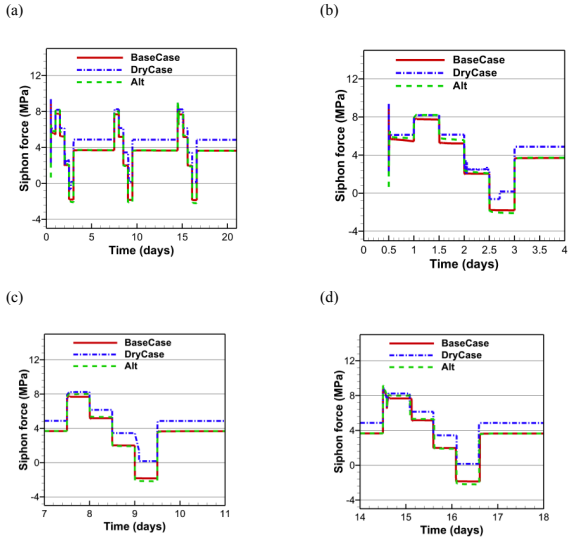

Figure 10. Comparison of siphon force for different cases. (a) entire test, (b) first step-test, (c) second step-test, and (d) the third step-test. "DryCase" indicates the case in which the liquid water in the formation is artificially immobilized during testing but the reservoir conditions are the same as the base case at the start of testing. "Alt" indicates the case in which the relative gas phase permeability is higher and the relative liquid phase permeability is lower than the base case (including initial fill and cooling injection periods).

To understand why the effects are mass-flow-rate-dependent, we plot the pressure drops over different sections of the system during testing (Figure 11). While the pressure drops in the injection well are similar between the two cases, the pressure drop in the production well is lower in the "Alt" case than in the base case for all mass flow rates. This is because the fluid entering the production well is expected to be drier (i.e., less liquid phase) in the "Alt" case than the base case due to lower liquid phase permeability and higher gas-phase permeability of the formation. In the injection well, the composition of the fluid is similar in both cases due to application of the liquid/gas separator resulting in similar pressure drops.

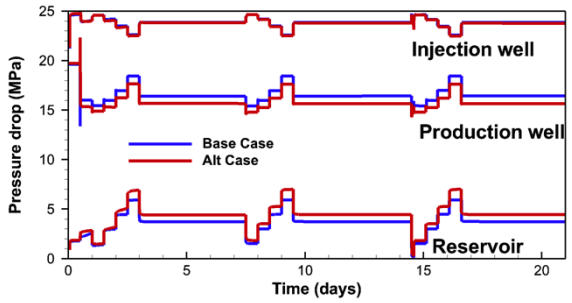

Figure 11. Pressure drops over different sections of the system, injection well (WBP_{inj}-WHP_{inj}), production well (WBP_{pro}-WHP_{pro}), and the reservoir (WBP_{inj}-WBP_{pro}), respectively. The two lines are effectively overlapping for the injection well.

The benefit of less pressure drop in the production well for the "Alt" case due to the relative mobility difference is somewhat offset by the larger pressure drop needed to drive the fluid through the reservoir (Figure 11). Except for the early time of the test, the difference in the pressure drop through the reservoir between the "Alt" case and the base case increases with the mass flow rate. As a result, the "Alt" case performs better at low mass-flow rate but worse in high mass-flow rate than the base case.

These different responses in pressure drop to the mass flow rate between the two cases are rooted in their different liquid saturations in the reservoir. As shown in Figure 12, at end of initial filling, the "Alt" case has a more extended plume of injected gas but inside the plume the liquid saturation is higher. For example, in the neighborhood around 100 m away from the injection well (where the production well will be installed), the dominant liquid saturation (in high permeability layers) is between 0.6-0.8 in the "Alt" case whereas it is below 0.6 in the base case. This is a typical phase interference scenario. The higher saturation of the less mobile phase (water) reduces the effective cross section area for the more mobile phase (gas) to go through. Therefore, the apparent resistance to the gas flow is higher in a wetter reservoir even though the relative permeability of gas phase is higher. Note that the hypothetical "Dry" case (in which the liquid phase is assumed to be immobile) discussed above has the same phase saturation in the reservoir as the base case and is designed to see how a drier production well would affect the performance of the system. This should not be confused with the "Alt" case that is used to investigate how the relative permeability of the reservoir would affect the system.

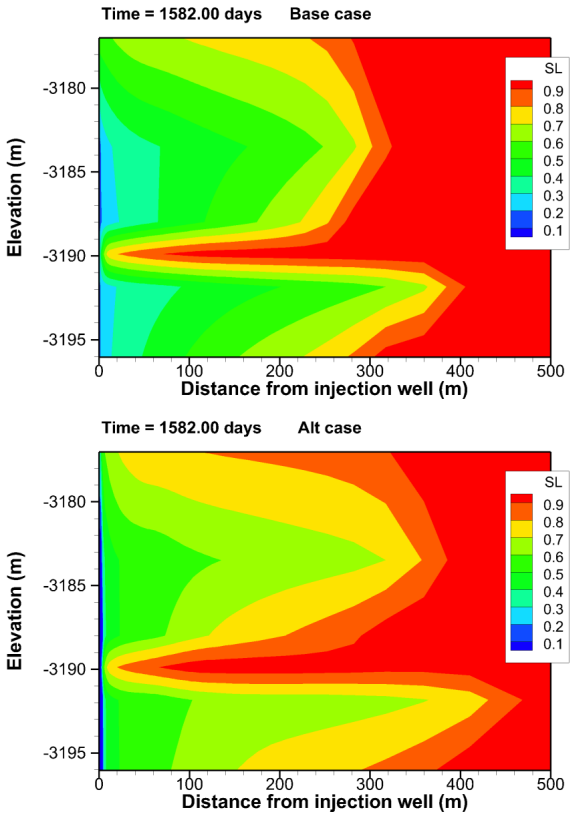

Figure 12. Liquid saturation in the reservoir after initial filling. The production well will be located 100 m away from the injection well.

CONCLUSIONS

Starting a thermosiphon without an additional pump is possible at the Cranfield site mainly because the injection well is an ongoing injection well so that its wellhead pressure is significantly lower than that at the static production well, because the injected gas is much colder than that in the production well. Installation of a condenser (a chiller) could further reduce the injection temperature which could result in even lower wellhead pressure at the injection well. Such cooling of the current injection before starting a thermosiphon operation is recommended to ensure a successful thermosiphon operation (e.g., no back flow) and zero release of CO_2.

The thermosiphon can be sustainable for a mass flow rate up to 6 kg/s for the given conditions. However, at a mass flow rate of 8 kg/s, the thermosiphon cannot be achieved.

The system responds quickly to the step changes in mass flow rate. a short-term shut-in would still allow the system to restart thermosiphon operations without an external pump or external gas source.

The liquid water in the produced fluid is low (less than a few percent). Therefore, the gas/liquid separator may be optional for the thermosiphon test.

Although the inlet temperature of the condenser (80°C) is much higher than that originally designed (34°C), the condenser is still able to meet the needs of thermosiphon testing.

Aqueous phase mobility in the formation could negatively impact the performance of the system. Our BaseCase simulations show liquid water is only a few percent of the produced fluid. If liquid water was assumed to be immobile, it could result in a significantly higher siphon force and expand the siphonable mass flow rate range up to 8 kg/s.

However, low mobility of the liquid phase has adverse effects on the system performance because it is harder to develop a drier reservoir with lower relative permeability of liquid phase for the same injection of gas phase. As a result, the benefits of a drier production well caused by low mobility of the liquid phase could well be canceled by the effects of a wetter reservoir on the effective permeability of gas through phase interference. Following this logic, a local alteration (intended or unintended) of hydraulic properties near the production well could significantly affect the system performance.

ACKNOWLEDGMENT

This work was funded by the Assistant Secretary for Energy Efficiency and Renewable Energy, Geothermal Technologies Program of the U.S. Department of Energy under Contract No. DE-AC02-05CH11231.

REFERENCES

Hosseini, S.A., H. Lashgari, J.W. Choi, J.-P. Nicot, J. Lu, and S.D. Hovorka, Static and dynamic reservoir modeling for geological CO2 seuestration at Cranfield, Mississippi, U.S.A., International Journal of Greenhouse Gas Control, 18, 449-462, 2013.

Hovorka, S.D., T.A. Meckel, and R.H. Trevino, Monitoring a large-volume injection at Cranfield, Mississippi - Project design and recommendations, International Journal of Greenhouse Gas Control, 18, 345-360, 2013.

Oldenburg, C.M., G.J. Moridis, N. Spycher, and K. Pruess, EOS7C Version 1.0: TOUGH2 Module for Carbon Dioxide or Nitrogen in Natural Gas (Methane) Reservoirs, Lawrence Berkeley National Laboratory Report *LBNL-56589*, March 2004.

Pan, Lehua, and Curtis M Oldenburg T2Well—An integrated wellbore-reservoir simulator. Computers & Geosciences 65 (2014) 46–55, 2013.

Ramey Jr, H.J., 1962. Wellbore heat transmission. *Journal of Petroleum Technology, 225*, 427–435.

Vinsome, P.K.W. and J. Westerveld, A simple Method for predicting Cap and Base Rock Heat Losses in Thermal Reservoir Simulators, J. Canadian Pet. Tech. Vol. 19, No. 3, pp. 87-90, July-September 1980.

A NUMERICAL CODE TO INCORPORATE GRAVITY DATA INTO GEOTHERMAL RESERVOIR MODELS

Sophie C.P. Pearson-Grant

GNS Science
Wairakei Research Center
Taupo, New Zealand
e-mail: s.pearson@gns.cri.nz

ABSTRACT

TOUGH2 models are a powerful way to look at the dynamics and sustainable potential of geothermal reservoirs. Because repeat gravity measurements are sensitive to changes in density, they can provide information about shallow fluid flow and phase changes that supplement often spatially sparse well temperature and pressure data. Repeat gravity measurements are collected in several countries (for example New Zealand and Japan) as a method of monitoring changes in reservoir characteristics, but they are not always incorporated into numerical reservoir models. Here we create a code to calibrate TOUGH2 models with gravity data. We use a synthetic model to test the code, and to look at what coupled TOUGH2-gravity modeling can tell us.

TOUGH2 model outputs include information about fluid density, changes in which can be used to calculate gravity signals at the Earth's surface. In the purest case, the gravity signal can be calculated directly from a point-source change in density. However, reality is rarely pure and never simple, and changes in density tend to have more complex, three-dimensional distributions. TOUGH2's grid structure makes it ideal for integrating densities over each cuboid grid cell to calculate gravity more rigorously. We use Python scripts to implement the method of Okabe et al. (1979) for single- and dual-porosity models. We then use PEST to couple the TOUGH2 model and the gravity code, facilitating sensitivity analysis and inverse modeling.

Tests of the gravity code show that it can match point-source approximations where point-source assumptions are valid. Creating a simple three dimensional synthetic model of a geothermal reservoir, with changes in boiling over time, then helps us to understand what the gravity data can tell us in a geothermal setting. By perturbing the model and then running PEST in parameter estimation mode, we find that this process can tell us the most about fracture volume, porosity, host rock fracture permeability and relative permeability, while some other parameters like host rock matrix permeability, source enthalpy and specific heat capacity need to be kept fixed to get reasonable model solutions. Coupled gravity-TOUGH2 modeling can be useful for both refining geothermal reservoir models, and optimizing use of gravity data collected at a geothermal field.

INTRODUCTION

In geothermal energy use, reservoir models are used extensively to guide field management (O'Sullivan et al., 2001). They allow us to test conceptual models, to bring together diverse datasets, and to estimate sustainable extraction and reinjection rates. They are based primarily on well temperatures and pressures, which can give detailed information but are often very sparse spatially.

Gravity measurements are sensitive to broad-scale changes in mass, and can therefore be used to deduce subsurface changes in fluid flow that cannot be detected by any other measurement tool. Shallow phase changes and/or fluid inflow and outflow result in changes in density that cause a potentially measurable change in gravity at the earth's surface. Gravity measurements however can be very difficult to interpret because a range of density changes can result in the same signal. By calibrating a pre-existing TOUGH2 model with gravity data, we can test and refine the model, and optimize the use of the gravity data. In this study, we created a forward

gravity modeling code using Python and coupled it with TOUGH2 using PEST.

GRAVITY MODELLING

Point-Source Approximation

In the simplest case, density change at a point results in a potentially measurable change in gravity at another point. Gravity change at a particular measurement location is given by the equation:

$$\triangle g(x,y,z) = -G\triangle\rho \int \frac{z-\gamma}{l^3} dV$$

where:
G = gravitational constant
ρ = density of body
$l = \sqrt{(x-\alpha)^2+(y-\beta)^2+(z-\gamma)^2}$, the radial distance between the measurement coordinates (x,y,z) and the body coordinates (α,β,γ; Figure).

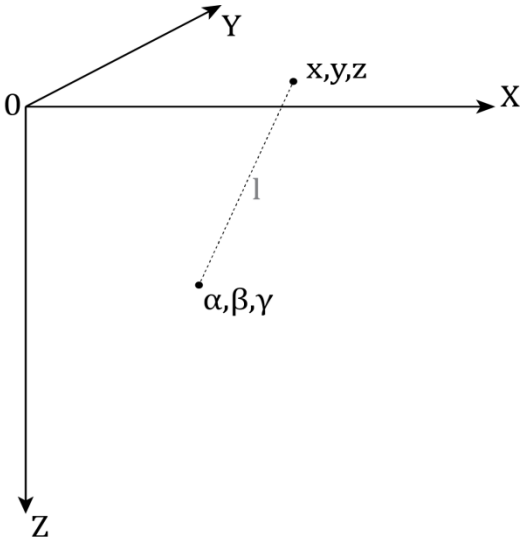

Figure 1. Schematic illustration of the terms used to calculate the gravity signal at a measurement point due to a point source.

This equation is valid where the density source is confined to a single point, or the distance from the source to the measurement point (i.e. l) is sufficiently large that the source can be approximated as a point. In a geothermal reservoir this is almost never the case; the most common source of density changes is phase changes, which typically occur over a region rather than at a point. These changes are also relatively small, meaning that detectable signals are often only in the shallow subsurface (<500 m) and so the distance to the measurement point is not large enough to assume that the source can be approximated as a point. Therefore a more sophisticated approach is necessary.

Three-Dimensional Distribution

To approximate a three-dimensional density distribution, it is necessary to integrate over three dimensions. In real-life applications, the body causing changes in gravity is unknown and so it is not a simple case of approximating a sphere or cube. Numerous approaches to modeling complex gravitation bodies can be found in the literature as summarised by Li and Chouteau (1998). In our study we use the method of Okabe (1979) because it is valid whether the measurement point is above, below or inside the source body.

A TOUGH2 grid is ideally suited to be used as the foundation for gravity calculations because the TOUGH2 model is already divided into a finite number of polygons. We implemented the relatively simple case of a rectangular grid with both single- and dual- porosity models. The gravity signal at a measurement point resulting from a cuboid cell is given by (Okabe, 1979; Figure 2):

$$\triangle g = -G\triangle\rho \sum_{i=1}^{2}\sum_{j=1}^{2}\sum_{k=1}^{2} \mu_{ijk}\left[x_i ln(y_j + l_{ijk}) + y_j ln(x_i + l_{ijk}) + 2z_k arctan\frac{x_i + y_j + l_{ijk}}{z_k}\right]$$

where:
$\mu_{ijk} = (-1)^i(-1)^j(-1)^k$
(x,y,z) = measurement coordinates
(α,β,γ) = body coordinates
$l_{ijk} = \sqrt{(x-\alpha_i)^2+(y-\beta_j)^2+(z-\gamma_k)^2}$

The gravity signal due to each cell can then be summed to give the total gravity signal at the measurement point (x,y,z). In this way every TOUGH2 grid cell is considered explicitly and assumptions are not made about the source distribution or the distance from the source.

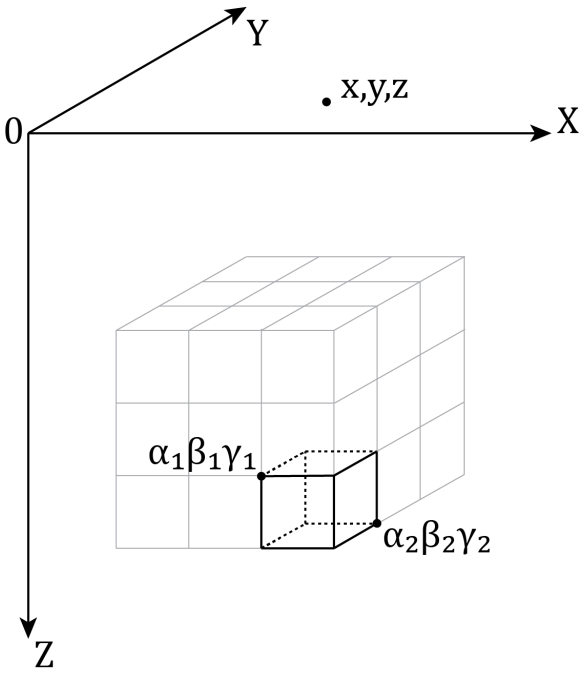

Figure 2. Schematic illustrating the method of gravity calculation for a three-dimensional volume.

GRAVITY CODE

The code to model gravity was written in Python because of its ubiquity, flexibility and lack of license limitations. PyTOUGH was also used where appropriate (Croucher, 2011). For readability and efficiency, the code was divided into several different scripts to carry out different functions as described below.

Cellcorners.py

This script is used to calculate the cell corners of each grid block as required for the calculation. This is necessary because TOUGH2 is grid-independent and does not include this information.

Gravityfactor.py

This script implements Okabe's gravity equation described above without the time-dependent density term. The resultant value is here called the gravity factor. The script uses the output from cellcorners.py as well as a file of station locations to calculate the gravity factor due to each cell for each measurement location. The gravity factor is based on the coordinates of each cell and so only has to be calculated once for each TOUGH2 model grid.

Density.py

Each TOUGH2 output contains several density terms. Rock density can be read from the TOUGH2 output directly. However, the fluid density is a function of both the steam and water densities, given by:

$$\rho = \varphi * (DG * SG + DW * SW)$$

where φ is porosity and D, S, G and W are density, saturation, vapour phase and fluid phase respectively as implemented in a TOUGH2 output file.

For a dual-porosity model, the fracture density due to both phases is calculated using the equation above, as is the matrix density, and then the two are summed.

As fluid density changes with time this script is run for each timestep or at specified times.

Gravity.py

The gravity script takes the density of each cell as calculated by density.py and multiplies it by the gravity factor as calculated in gravityfactor.py. This gives the gravity at one measurement point for one grid cell at a particular timestep.

For each measurement point, the gravity is summed over all the cells. This is repeated for every measurement point, and for each timestep. The output is a table of modeled gravity at each given measurement location at the times specified. This can then be plotted using Python or another plotting tool.

PEST COUPLING

To allow quantitative comparisons of modeled and measured gravity signals, PEST was used. This is parameter estimation software by Doherty et al. (1994). It creates an input file - in this case a TOUGH2 input file (Pruess et al. 1999) - based on a template file. Specified parameters are varied within pre-assigned ranges and TOUGH2 is called to run the model and create an output file.

Several steps were required to calibrate a reservoir model, which were run through PEST and a batch file (Figure). Firstly, the change in

gravity was calculated from the TOUGH2 density as described in the previous section. PEST was then used to compare the modeled and measured gravity signals. The input file was then modified automatically by PEST to attempt to reduce the misfit. As the final step in each iteration, the TOUGH2 model was rerun. This was repeated until the misfit between the calculated gravity signal and the measured one was below a specified threshold, or the fit was no longer improving. Statistics were also calculated by PEST. Using this methodology, gravity measurements could be used to refine a TOUGH2 model with relatively little user intervention.

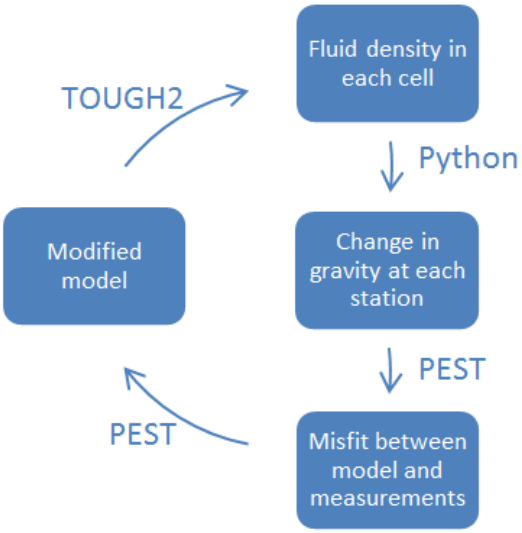

Figure 3. Methodology used to refine TOUGH2 model using gravity data.

CHECKING THE CODE

As the code contains several steps and is fairly complex, it is easy to misassign variables. Therefore it was tested thoroughly. Firstly, the forward gravity calculation was checked using a TOUGH2 model with 2 x 2 x 2 grid blocks and two, then six, measurement stations. The calculations were carried out by hand and in Excel, and gave results consistent with our code. Two measurement stations at large distances were also used to check if our code agreed with the point-source approximation described in the earlier section. It showed excellent agreement.

A slightly more complex model was then created, of 10 x 10 x 10 cells and six stations, to test the methodology as a whole. The gravity was calculated using the Python script, and then TOUGH2 parameters like permeability and porosity were changed to see if the methodology could recover the original model. PEST found the original parameters to within five decimal places (so within rounding error).

REFINING TOUGH2 MODELS USING GRAVITY DATA

To determine the reservoir parameters that gravity signals can most help to refine, a synthetic model was used. This was fairly simple, with 20 x 20 x 20 grid blocks and a single homogeneous rock type. The model was dual-porosity because fluid flow in geothermal reservoirs is often thought to be fracture dominated. A hot fluid source was placed at the base of the center of the model to induce boiling in the liquid-dominated reservoir (Figure). The TOUGH2 model was run using specified initial parameters, and the resulting gravity signal was calculated as a synthetic solution.

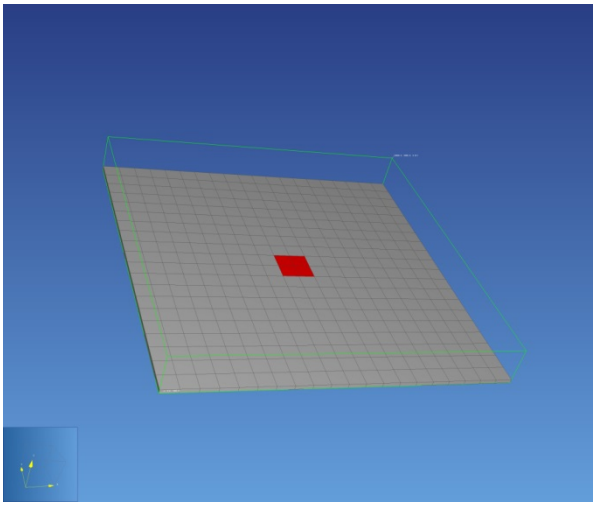

Figure 4. TOUGH2 model used to test gravity code with synthetic data.

Using the resulting synthetic model, parameters were varied one at a time through PEST to determine if the original values could be recovered. The sensitivity that was calculated within PEST was plotted to identify which TOUGH2 model parameters could be best refined using high-precision gravity data.

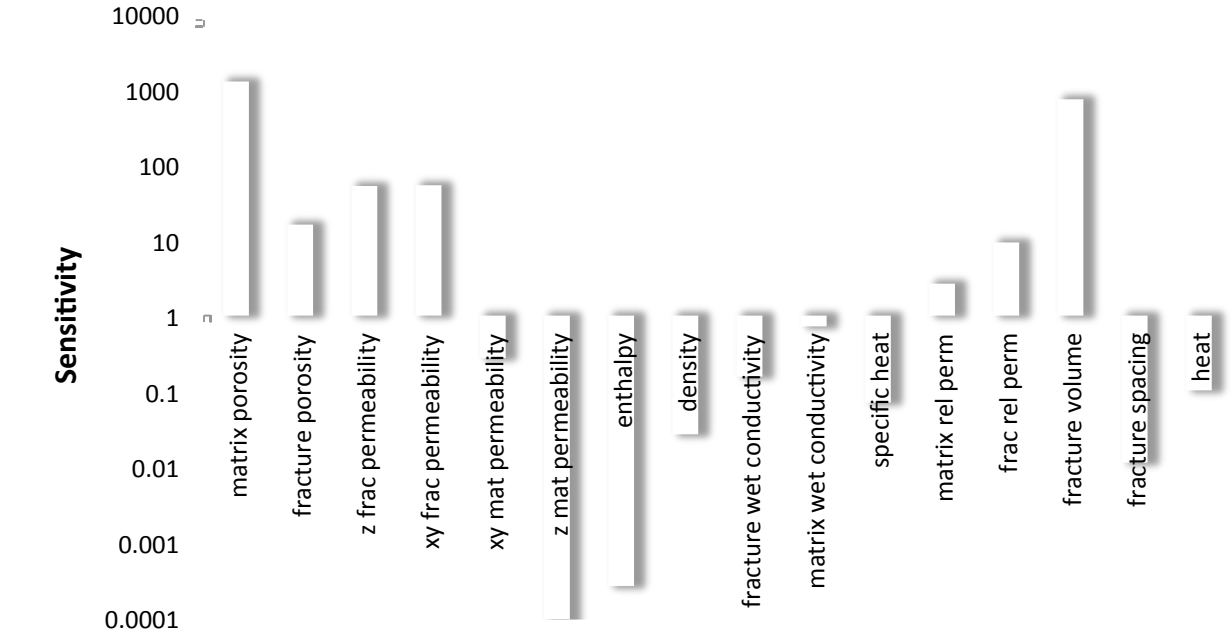

Figure 5. Results of synthetic modeling.

Figure 5 shows the results of the synthetic modeling process. There were seven variables that showed sensitivity of 1 or above and so are the best candidates to be refined through gravity measurements. These were matrix and fracture porosity, lateral and vertical fracture permeability, matrix and fracture relative permeability, and fracture volume.

As flow was predominantly fracture controlled, it makes sense that permeability of the fracture, its porosity and the proportion of the rock that was taken up by fractures (i.e. fracture volume) were important variables. Matrix porosity determines how much of the rock contains fluid. However, it is interesting that the amount of hot fluid coming into the system, and how hot it is, does not cause mass change differences strongly enough to be determinable from the surface gravity signals.

This model is a simplified version of a typical geothermal reservoir model. Therefore the sensitive parameters are an example, but different models will have different sensitivities. This does still provide a starting point for calibration with gravity, and it shows that some parameters that are generally not well constrained or considered in detail, for example relative permeability, can actually be important for shallow fluid flow. Gravity measurements can therefore be used to refine them.

In a real-life situation, there are many unknown variables. Figure 5 also helps to identify which parameters should not be included in calibration with gravity data because it is insensitive to them. By including them, the ability to determine other parameters will be reduced.

CONCLUSIONS

In this paper we developed a series of Python scripts that allow gravity signals to be calculated directly from TOUGH2 output. By coupling through PEST, we can refine a TOUGH2 geothermal reservoir model using gravity data and carry out some statistical analysis.

Applying this technique to a synthetic dual-porosity model shows that fracture properties are the parameters that gravity signals are most sensitive to, along with matrix porosity, relative permeability and fracture volume. This provides an indication of what gravity data can tell us in a geothermal reservoir model, and what parameters need to be considered most closely when modeling shallow fluid flow.

ACKNOWLEDGMENT

This project was funded in part by Geothermal Resources of New Zealand project 'Reservoir Modelling', and by MBIE project 'Geothermal Supermodels'. The codes are open source and can be accessed by contacting the author.

REFERENCES

Croucher, A.E., *PyTOUGH: a Python scripting library for automating TOUGH2 simulations.* Proceedings of the New Zealand Geothermal Workshop, 2011.

Doherty, J., L. Brebber, and P. Whyte, *PEST: Model-independent parameter estimation*. Watermark Computing, Corinda, Australia, 1994.

Li, X., and M. Chouteau, Three-dimensional gravity in all space, *Surveys in Geophysics*, 19, 339-368, 1998.

Okabe, M., Analytical expressions for gravity anomalies due to homogeneous polyhedral bodies and translations into magnetic anomalies, *Geophysics*, 112, 553-561.

O'Sullivan, M.J., K. Pruess, and M.J. Lippmann, State of the art of geothermal reservoir simulation, *Geothermics*, 30(4), 395-429, 2001.

Pruess, K., C. Oldenburg, and G. Moridis, *TOUGH2 User's Guide, Version 2.0*, Report LBNL-43134, Lawrence Berkeley National Laboratory, Berkeley, Calif., 1999.

GEOTHERMAL EXPLORATION THROUGH NUMERICAL MODELING OF COLD CO_2 SOIL FLUXES

Loïc Peiffer[1], Christoph Wanner[2], Lehua Pan[3]

lpeiffer@ier.unam.mx, christoph.wanner@geo.unibe.ch, lpan@lbl.gov

1. Instituto de Energías Renovables, Universidad Nacional Autónoma de México, Privada Xochicalco s/n, Centro, 62580 Temixco, Morelos, Mexico.
2. Institute of Geological Sciences, University of Bern, Baltzerstrasse 3, 3012 Bern, Switzerland.
3. Lawrence Berkeley National Laboratory, 1 Cyclotron Road, Berkeley, CA 94720, USA.

ABSTRACT

The most commonly accepted conceptual models to explain surface degassing of cold magmatic CO_2 in volcanic-geothermal systems involve the presence of a deep gas reservoir. Although these models are well detailed, they do not give any quantitative insights on the CO_2 degassing dynamic. In this study, numerical simulations using the TOUGH2-ECO2N V2.0 package were performed to get quantitative insights on how these fluxes and the surface temperature are related to the reservoir and fluid properties (geometry, permeability, depth, temperature gradient, and CO_2 dissolved content). Although the modeling is based on flux data measured at a specific geothermal site characterized by an extraordinarily high temperature gradient (140°C/km), the Acoculco caldera (Mexico), some general insights have been gained through a large set of simulations.

Both the CO_2 fluxes at the surface and the depth at which CO_2 exsolves are highly sensitive to the dissolved CO_2 content of the deep fluid, especially under high temperature gradient conditions. When CO_2 mainly exsolves above the hydrothermal reservoir within a fracture system, the surface CO_2 fluxes are not sensitive to the size of the reservoir but do depend on the CO_2 dissolved content and the rock permeability. For gas exsolution below the top of the reservoir, surface CO_2 fluxes depend on the gas saturation of the deep fluid as well as the reservoir size and the rock permeability. The absence of thermal anomalies at the surface is linked to the type of fluid primarily carrying the heat (i.e. low enthalpy of CO_2) and the magnitude of the fluid fluxes. Limited temperature anomalies (a few degrees above normal) may occur when permeability conditions allow some water flow towards the surface. Nevertheless, above a certain CO_2 flux limit at surface (~37,000 g m^{-2} day^{-1} of CO_2 at the surface), the heat carried by the CO_2 rich phase (gas or supercritical) uprising towards the surface exceeds the heat flux that can be balanced by heat conduction with wall-rock, and as a consequence the surface temperature increases.

Finally, specific results were obtained for the Acoculco geothermal site, such as the possible depth of the reservoir, the CO_2 dissolved content and the gas saturation state of the deep fluid. Our simulations show that CO_2 flux measurements are a powerful exploration tool if they can be combined with complimentary tools (e.g., geophysical surveys). For further details, please refer to:
Peiffer, L., Wanner, C., Pan, L. Numerical modeling of cold magmatic CO_2 flux measurements for the exploration of hidden geothermal systems. Journal of Geophysical Research, (in press).

GEOTHERMAL EXPLORATION THROUGH NUMERICAL MODELING OF COLD CO_2 SOIL FLUXES

Loïc Peiffer[1], Christoph Wanner[2], Lehua Pan[3]

lpeiffer@ier.unam.mx, christoph.wanner@geo.unibe.ch, lpan@lbl.gov

1. Instituto de Energías Renovables, Universidad Nacional Autónoma de México, Privada Xochicalco s/n, Centro, 62580 Temixco, Morelos, Mexico.
2. Institute of Geological Sciences, University of Bern, Baltzerstrasse 3, 3012 Bern, Switzerland.
3. Lawrence Berkeley National Laboratory, 1 Cyclotron Road, Berkeley, CA 94720, USA.

ABSTRACT

The most commonly accepted conceptual models to explain surface degassing of cold magmatic CO_2 in volcanic-geothermal systems involve the presence of a deep gas reservoir. Although these models are well detailed, they do not give any quantitative insights on the CO_2 degassing dynamic. In this study, numerical simulations using the TOUGH2-ECO2N V2.0 package were performed to get quantitative insights on how these fluxes and the surface temperature are related to the reservoir and fluid properties (geometry, permeability, depth, temperature gradient, and CO_2 dissolved content). Although the modeling is based on flux data measured at a specific geothermal site characterized by an extraordinarily high temperature gradient (140°C/km), the Acoculco caldera (Mexico), some general insights have been gained through a large set of simulations.

Both the CO_2 fluxes at the surface and the depth at which CO_2 exsolves are highly sensitive to the dissolved CO_2 content of the deep fluid, especially under high temperature gradient conditions. When CO_2 mainly exsolves above the hydrothermal reservoir within a fracture system, the surface CO_2 fluxes are not sensitive to the size of the reservoir but do depend on the CO_2 dissolved content and the rock permeability. For gas exsolution below the top of the reservoir, surface CO_2 fluxes depend on the gas saturation of the deep fluid as well as the reservoir size and the rock permeability. The absence of thermal anomalies at the surface is linked to the type of fluid primarily carrying the heat (i.e. low enthalpy of CO_2) and the magnitude of the fluid fluxes. Limited temperature anomalies (a few degrees above normal) may occur when permeability conditions allow some water flow towards the surface. Nevertheless, above a certain CO_2 flux limit at surface (~37,000 g m^{-2} day^{-1} of CO_2 at the surface), the heat carried by the CO_2 rich phase (gas or supercritical) uprising towards the surface exceeds the heat flux that can be balanced by heat conduction with wall-rock, and as a consequence the surface temperature increases.

Finally, specific results were obtained for the Acoculco geothermal site, such as the possible depth of the reservoir, the CO_2 dissolved content and the gas saturation state of the deep fluid. Our simulations show that CO_2 flux measurements are a powerful exploration tool if they can be combined with complimentary tools (e.g., geophysical surveys). For further details, please refer to:
Peiffer, L., Wanner, C., Pan, L. Numerical modeling of cold magmatic CO_2 flux measurements for the exploration of hidden geothermal systems. Journal of Geophysical Research, (in press).

DESCRIPTION OF EXPLICIT SURFACE FEATURES USING UPDATED FIELD DATA OF ROTORUA GEOTHERMAL FIELD

Thomas M.P. Ratouis, Michael J. O'Sullivan and John P. O'Sullivan

Department of Engineering Science, The University of Auckland,
Auckland, 1142, New Zealand
t.ratouis@auckland.ac.nz

ABSTRACT

The Rotorua geothermal field is a shallow geothermal reservoir lying directly beneath Rotorua City in New Zealand. It is renowned for its abundance of natural geothermal manifestations including the geysers and hot springs at Whakarewarewa. However intensive extraction of the geothermal fluid in the 1970s led to a general decline of aquifer pressures and surface activity of the natural features. In 1986 a Wellbore Closure Programme was enforced which resulted in the recovery of reservoir pressures and many of the surface features. Efforts to develop a robust numerical model which accurately captures the responses of the geothermal aquifer and its surface features are ongoing. UOA Model 5 already includes seasonal variations in production rates, reinjection rates and precipitation and now research focuses on matching the behaviour of important, individual surface features. A simple post-processing method is implemented and the resulting temperature match with field data are promising.

INTRODUCTION

The Rotorua Geothermal Field (RGF) is a geothermal reservoir that lies within the Rotorua Caldera and the Taupo Volcanic Zone of New Zealand. Surface activity is mainly confined to three areas within the Rotorua Township: Whakarewarewa/Arikikapakapa to the south, Kuirau Park/Ohinemutu to the northwest and Government Gardens//Ngapuna to the northeast (Figure 1, Figure 2). The Rotorua geothermal system is unique in that it contains one of New Zealand's last remaining areas of major geyser activity at Whakarewarewa (Figure 1).

Production of geothermal fluid from shallow bores from the 1950s onwards lead to a widespread decline of springs and geyser activity in the late 1970s. Increasing concern over the impact of declining aquifer pressures led to the introduction of the Rotorua Geothermal Monitoring Programme (RGMP) in 1982. By 1986, aquifer pressures declined to the lowest levels since the monitoring programme began (Bradford, 1992). A Wellbore Closure Programme became effective in 1986 and enforced closure of all bores within a 1.5 km radius of Pohutu Geyser (Whakarewarewa) and closure of all government owned wells in Rotorua township (Figure 1) (Gordon *et al.*, 2005). By 1988 the programme contributed to a 75% decrease in net withdrawal (Bradford, 1992) which resulted in an immediate increase in reservoir pressures and the recovery of some surface features was observed.

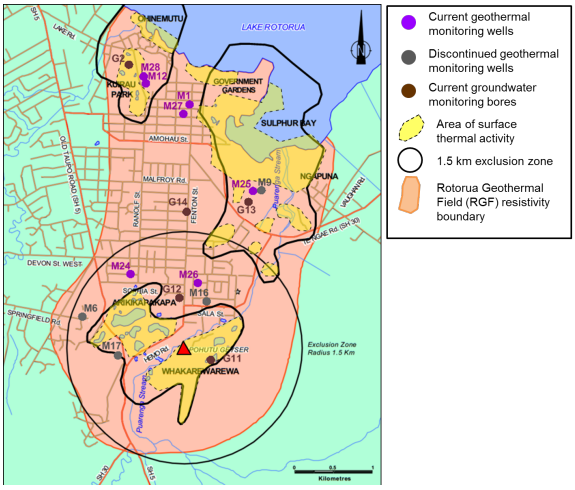

Figure 1. Map of the Rotorua Geothermal Field showing the extent of the field, and areas of surface thermal activity.

In 1991 Environment Bay of Plenty (EBOP) assumed responsibility for managing the field under the Resource Management Act. A management plan for the hot water resource was developed to monitor the recovery and behaviour of geothermal features and protect the surface manifestations while providing allocation of the resource for present and future

efficient use (EBOP, 1999). As such, a comprehensive database of the surface features was compiled with 1570 sites identified and referenced (Figure 2). 41 representative features (Figure 2) were selected for further observations and have been monitored on a monthly basis since May 2008.

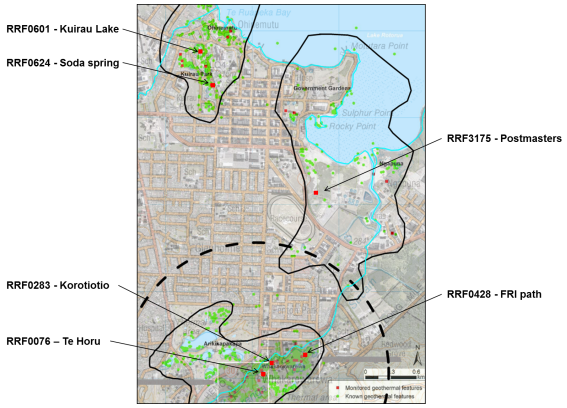

Figure 2. Map of Rotorua City showing the locations of know geothermal features (green) and monitored features (from GNS report 306, Graham et al., 2013)

In order to support the management plan a detailed numerical model of the RGF has been developed in collaboration with EBOP and GNS Science. In the next section the conceptual and numerical model are summarized. Then the behaviour of the model during the natural state and production stage is presented. The final section discusses of the challenges involved in accurately representing individual surface features and presents a new approach for modelling their behaviour.

COMPUTER MODELLING

Conceptual model

A conceptual model of the RGF was developed that is primarily based on Wood's description of the Rotorua geothermal system (Wood, (1992), isotopic and chemical observations from Stewart et al. (1992) and gravity anomalies interpreted by Hunt (1992). It is illustrated in Figure 3 which shows the main upflows and high temperatures encountered at shallow depths. For more information regarding the geological, structural and hydrothermal settings of the Rotorua model refer to Ratouis *et al*. (2015).

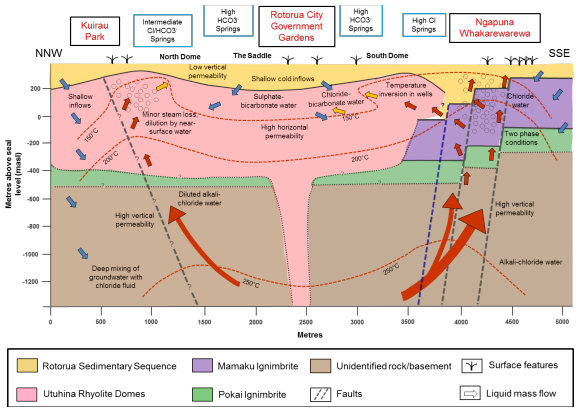

Figure 3. NNW – SSE Cross section of the RGF conceptual model

Model specifications

UOA Model 5 includes transport of chloride and CO_2 using the EWASG (Water – Salt – Gas) equation of state module (Battistelli *et al*., 1997) and is solved using the numerical simulator AUTOUGH2 (Yeh *et al*., 2012), the University of Auckland's version of TOUGH2 (Pruess, 1991). The main model parameters are summarized in Table 1.

Table 1. Comparison of grid and model parameters.

Category	*UOA Model 5*
Grid area	12.4 km x 18.3 km
Grid depth	2,000 m
Blocks	48,034
Layers	30
Minimum block size	125*125 m^2
Minimum block height	5 m
Surface	Topography & lake bathymetry
Equation of State (EOS)	EWASG (Water, NaCl, CO_2)

For further information on the details of the model refer to Ratouis *et al*. (2015).

Boundary Conditions

Top boundary

Atmospheric conditions are assigned at the top surface (1 bar, 15^0C). Below the lake surface, the pressure is set to the hydrostatic pressure

corresponding to the depth of the lake assuming a water temperature of 10^0C.

Historic rainfall recorded at Whakarewarewa from 1900 to 2014 provided by EBOP is represented by cold water injected into the top of the model. Over the urbanized zone an infiltration rate of 8% is used, instead of the 10% used elsewhere, to account for paved areas and the existing drainage system.

Side boundaries

The side boundaries are assumed to be closed.

Base boundary

Constant inflow of high enthalpy water is applied at the base of the inferred faults (Table 2) and a conductive flow of heat of 80 mW/m^2 is applied elsewhere.

Table 2 Deep inflows at the bottom layer of the model.

Area	*Mass t/day*	*Temp (˚C)*
Kuirau Park	8,300	255
Ngapuna Stream	23,100	270
Whakarewarewa	42,900	245
Total	74,300	

Production estimates

The number of production and reinjection bores prior and after the Wellbore Closure and annual mean rates since 1950 have been estimated by EBOP (Gordon *et al*., 2005) and are shown in Figure **4** and Figure **5**.

Following the 1986 Bore Closure Programme, the total production has gradually reduced to 9 tonnes/day and net production down to 1,000 tonnes/day in 2005 (Figure **5**). This is due to requirements in the Rotorua Geothermal Plan for each consent holder to comply with maximum daily take as well as a policy of full reinjection of the geothermal fluid.

Differences between winter and summer mass withdrawal values have been included in the model. Prior to 1991, a 20% difference between summer and winter values was used and after 1991 a 10% figure was used (Figure **5**) (Bradford, 1992).

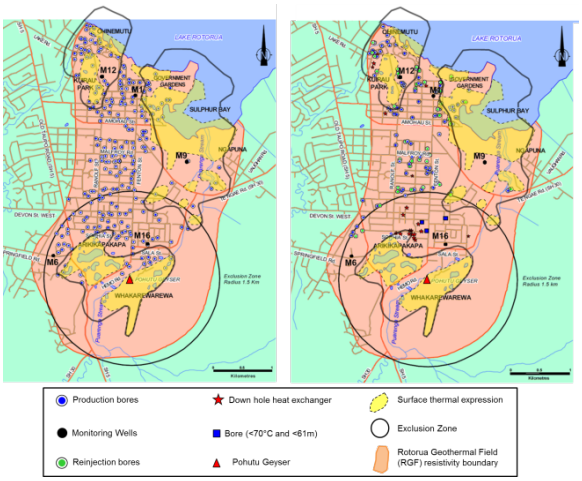

Figure 4. Location of production and reinjection wells distribution before and after the Wellbore Closure Programme

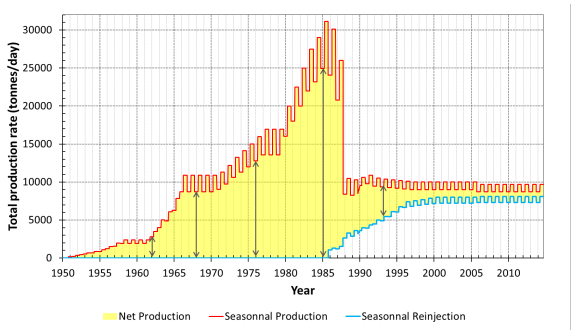

Figure 5. Seasonal mass production and reinjection estimates from 1950 to 2014

SIMULATION RESULTS: LARGE SCALE BEHAVIOUR

Natural State: Prior to 1950

Simulations were carried out to represent the natural state of the reservoir and the model has been calibrated against downhole temperature profiles for 191 wells from Ministry of Works reports (Candra and Zarrouk, 2013). The location and magnitude of surface heat and mass flow, and pre-exploitation pressures inferred by Grant *et al*. (1985) were also used for calibration.

A good overall match between the model and the available data had been obtained (Figure **6**, Figure **7**).

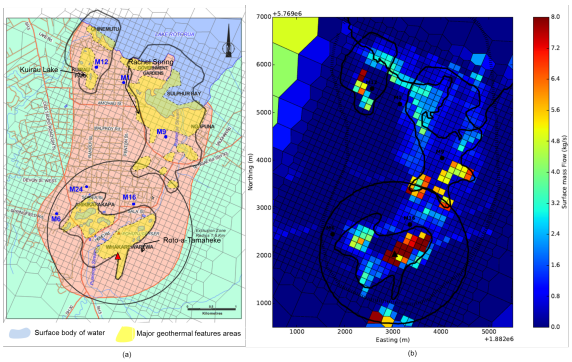

Figure 6. (a) Areas of geothermal surface activity and (b) natural state surface mass flow (kg/s) for UOA Model 5.

Areas of surface activity in the model, as shown by surface mass flows, are located within the model blocks that correspond with the known locations of surface discharging features. The most important areas of surface activity; Kuirau Park, Ohinemutu, Government Gardens, Ngapuna/Puarenga stream sector, Arikikapakapa and Whakarewarewa are well represented in the model (Figure **6**).

The modelled temperatures versus depth are also in good agreement with the field data (Figure **7**). For a more detailed comparison of results see Ratouis *et al*. (2015).

Production Modelling: from 1950 to 2014

The production simulation run which include production and reinjection estimates was carried out from 1950 to 2014. The model was calibrated against reservoir pressure information from the monitoring wells and from heat and mass flow estimations at Whakarewarewa, Ngapuna and Kuirau Park.

The model produces similar surface heat flow estimates as heat flow measurements at Whakarewarewa. In 1986, the heat flow measured at Whakarewarewa had dropped from 300 MW to an estimated 158 MW (Cody and Lumb, 1992); the simulation produces a decline of similar order of magnitude (Figure **8**, Table 5). Heat flow estimation in 2000 revealed a recovery of the surface activity at Whakarewarewa from 158MW to a value above 216MW (Gordon *et al*., 2005). The model captures this behaviour relatively well as it predicts that by 2000 the heat flow at Whakarewarewa had recovered to its pre-exploitation state. However, it can be seen that the model underestimates the heat flow reduction at Whakarewarewa from 1950 to 1986 and overestimates the recovery of the system as field observations show that some of the surface features are yet to regain full activity.

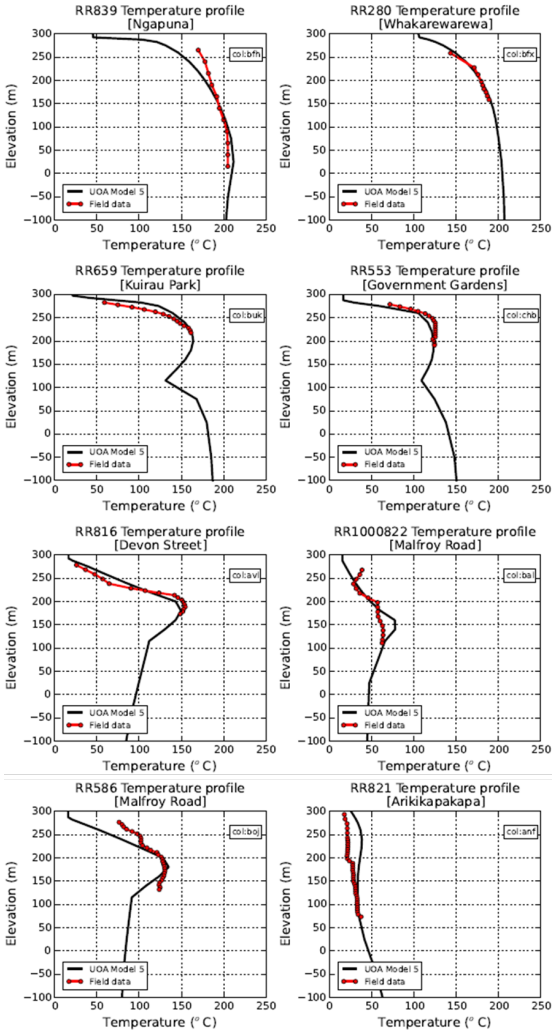

Figure 7. Temperature vs depth well profile (field data and UOA Model 5 results).

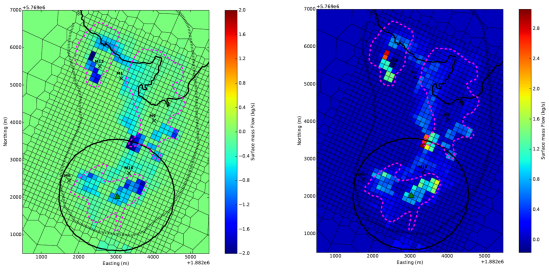

(a) (b)

Figure 8. (a) Modelled heat flow decline 1950 - 1986 (b) Modelled heat flow recovery 1950 - 2000.

Along the Puarenga Stream area the model predicts a heat flow of 96 MW in 1990 which is a close match to the estimated figure of 77±20 MW (Glover, 1992). Table **3** summarizes comparisons of the model predictions and field heat flow estimates:

Table 3. Estimated field heat flow vs modelled surface heat flow at Whakarewarewa and Ngapuna

Surface features	*Date*	*Measured*	*UOA Model 5*
Whakarewarewa Heat Flow (MW)	1950	300	278
	1985	158	245
	2000	>216	280
Ngapuna Heat Flow (MW)	1990	77	96

In Figure 9 the modelled temperatures, surface mass flows and pressures are plotted against time for the blocks corresponding to two important surface features located within the geothermal areas of Kuirau Park. The recorded rainfall data is also included.

The model results are consistent with observations that Kuirau Park Lake essentially ceased overflowing and sinter-lined basins went dry in the early 1980s. The model predicts a full recovery of surface features at Kuirau Park from 1990. This is consistent with field observations that these features started discharging in the 1990s with fluids which were chemically similar to those observed in the 1960s (Mroczek *et al*., 2002), indicating a recovery to near pre-closure status.

Additional results and comments on the natural state and production phase for UOA Model 5 are given Ratouis et al., (2015).

(a)

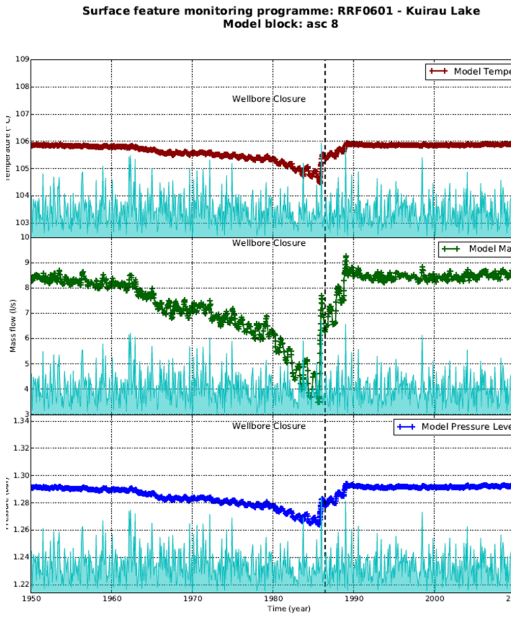

(b)

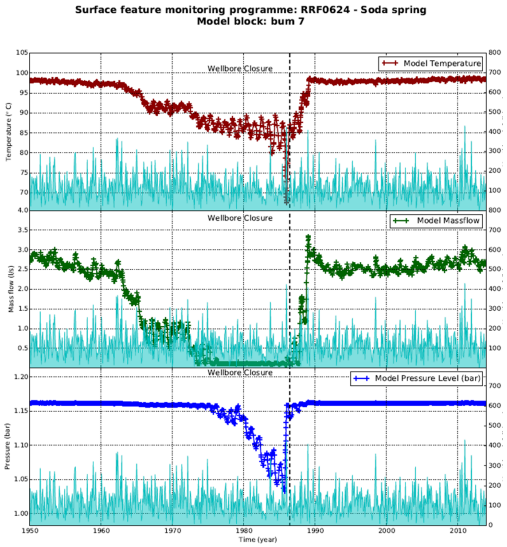

Figure 9. Modelled Temperature, mass flow and pressure for surface blocks at Kuirau Park (a) Kuirau Lake (b) Soda Spring.

SMALL SCALE BEHAVIOUR OF SURFACE FEATURES

Shallow temperature contours

To include the behaviour of individual surface features a re-evaluation of the down-hole temperature data available from direct-use bores was initiated. By combining and cross referencing DSIR and EBOP databases, 191

distinct wells have been identified and referenced (Candra and Zarrouk, 2013). Three-dimensional contours were generated which offer an accurate picture of the subsurface temperature distribution of the Rotorua system.

The model temperatures at the ground surface and at 220 masl are compared with the 3D temperature contours of field data at the same elevations in Figure **10**.

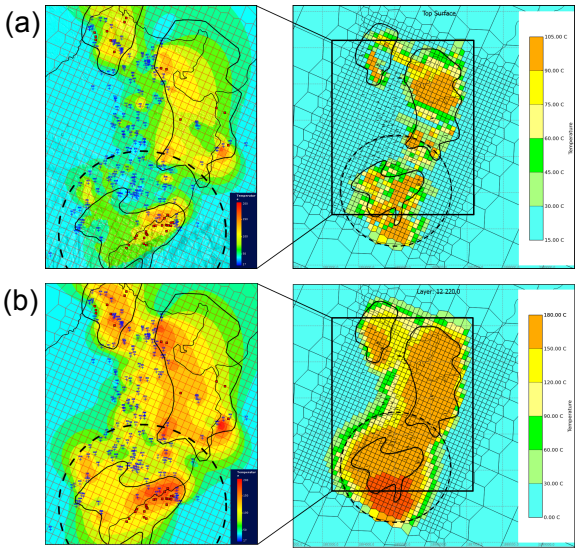

Figure 10. 3D temperature contour (a) Surface level (b) at 220 masl. Wells are indicated in blue and monitored surface features are designated by a red square.

It can be seen that the isotherms of the field data and modelled temperature at the surface and at 220 masl compare well. Surface temperatures range from 17°C to 180°C in the field and from 15°C to 120°C in the model. At 220 masl the field data temperatures range between 20°C and 190°C and modelled temperatures between 12°C and 185°C. However, a comparison between well temperatures versus depth and modelled temperatures indicate that further model calibration is required, particularly south of Whakarewarewa where the model is too hot.

In general, it is difficult to make accurate quantitative comparisons of surface temperatures for two reasons. First, a lack of field measurements for the shallow surface temperature means that the temperature contours are poorly constrained at the surface. Second, a minimum model block thickness of 5 m restricts the accuracy of the modelled surface temperatures.

Challenges associated with matching individual surface features

Of the 1570 geothermal sites identified, 41 surface features have had their temperature, mass flow and water level monitored by EBOP since May 2008. In the model the surface features are represented by the mass flow from surface blocks measuring 125 × 125m × 5m. Due to the size of the blocks, many surface features may be represented by a single block (Figure 11). The mass flow from the model block can be thought of as the sum of mass flows from the surface features and the model block temperature as the average of the temperatures of the surfaces features and surrounding terrain.

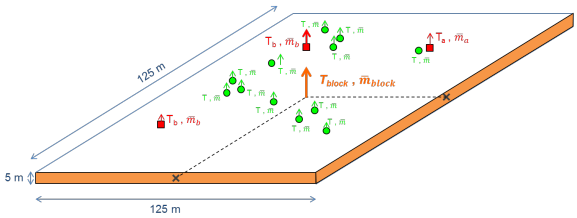

Figure 11. Schematic illustration the challenges of matching discrete surface features in a model. Know geothermal features are represented by a green circle and monitored features by a red square.

This averaging effect means that the magnitude of the temperature variations recorded in the surface features is significantly larger than those predicted for the corresponding model block. Unfortunately, there are no model blocks for which all the surface features enclosed are included in the subset of 41 that are monitored. This makes it impossible to accurately quantify and compare total mass flows or attempt to calculate average temperatures.

Another factor is that the model boundary conditions at the surface only take into account the rainfall that infiltrates into the subsurface. In reality, a certain amount of the rainfall that does not infiltrate into the subsurface runs off into the surface features reducing their average temperatures and affecting their temperature variation.

The cooling of fluid once it has left the subsurface is not taken into account in the model. Cooling occurs as a result of boiling, conduction, and radiation as well as mixing with other surface fluid already present in the feature.

Finally, the very shallow groundwater system is not represented accurately in the model. For examples, hot pools that are not overflowing must have a hot inflow but may also have an unknown outflow that combines with losses to the atmosphere to control the water level.

Surface feature model

The objective of the surface feature model is to represent the historic behaviour of the surface feature as accurately as possible and to provide a method for predicting its future behaviour in response to changes in the deeper geothermal system. The model proposed below is simple enough that it can be applied as a post-processing tool run after the reservoir simulations are complete. The model for each surface feature can be written in the following form:

$$h = \frac{\bar{m}_1 h_1 + x\,\bar{m}_2 h_2}{\bar{m}_1 + x\,\bar{m}_2} - c \qquad \textbf{(1)}$$

where h is the surface feature's enthalpy, h_1 and $\bar{m}_1$ are the enthalpy and mass flow of the hot fluid coming from the subsurface, h_2 and $\bar{m}_2$ are the enthalpy and mass flow of the rainfall runoff, x is a calibration parameter representing the dilution due to rainfall runoff entering the surface feature and c is a calibration parameter representing heat losses from boiling, conduction, and radiation.

Once the calibration parameters x and c have been determined, another parameter y is determined by comparing the recorded mass flow of the surface feature with mass flow obtained in Equation 1.

$$\bar{m} = y(\bar{m}_1 + x\,\bar{m}_2) \qquad (2)$$

The parameter y can be thought of as the proportion of the mass flow leaving the model block that contributes to the individual surface feature.

For all 41 thermal features a different set of parameters (x, c and y) were chosen to match the monitoring data as closely as possible.

Results

The post-processing model was applied to the model temperatures and surface mass flows for the blocks containing the monitored features (locations in Figure **2**). As described above, the calibration parameters (x, c and y) were then determined to obtain the best match with the monitored data. The following figures compare the enthalpy and mass flow for the numerical model block, the post-processing model and the recorded field data for selected surface features. The rainfall during the monitoring period is also included.

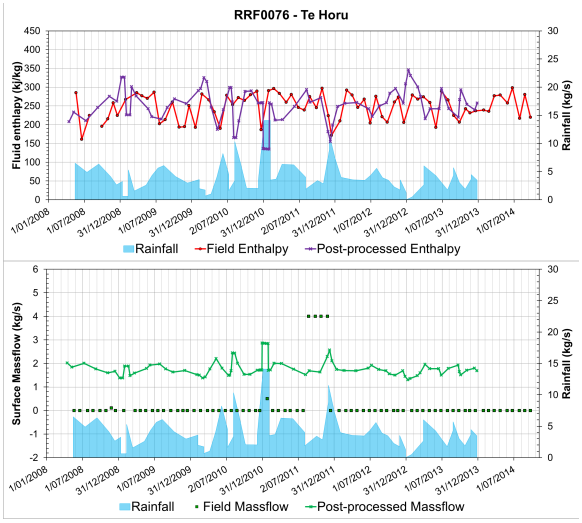

Figure 12. RRF0076 – Te Horu at Te Puia in Whakarewarewa geyser Valley.

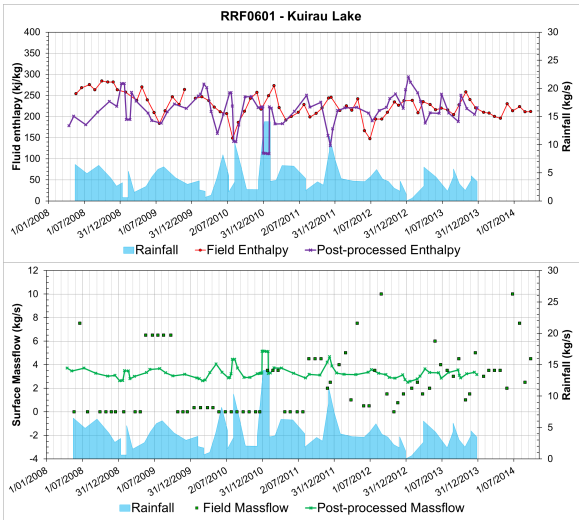

Figure 13. RRF0601 – Kuirau Lake at Kuirau park

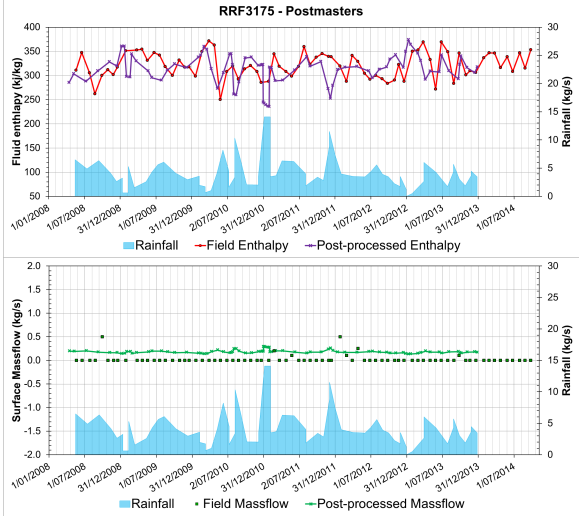

Figure 14. RRF3175 – Postmaster in Ngapuna

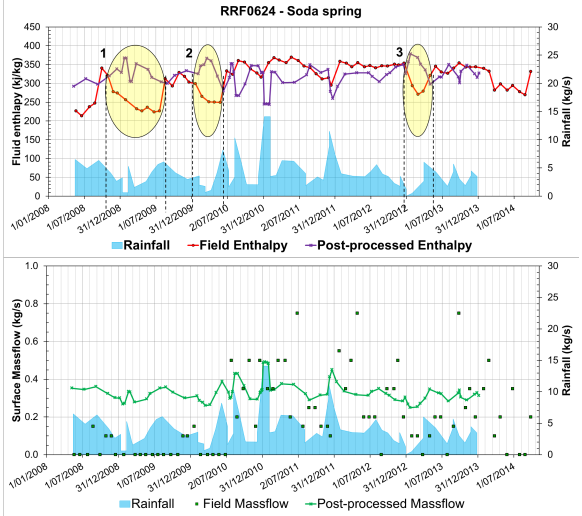

Figure 16. RRF0624 – Soda Spring at Kuirau Park

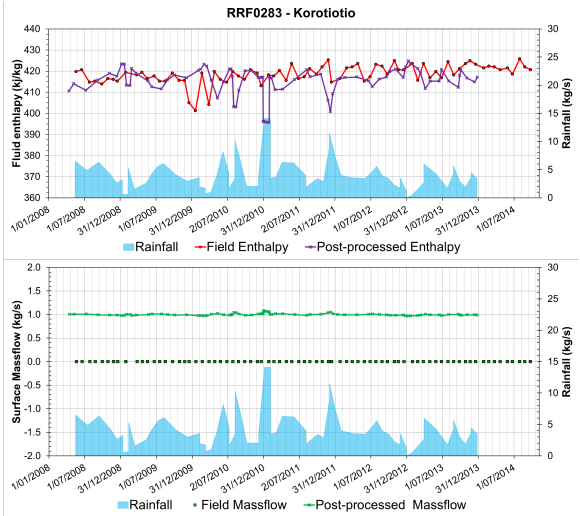

Figure 15. RRF0283 – Korotiotio in Whakarewarewa Village in Whakarewarewa geyser Valley.

In Figures 12-15 the post-processing model enthalpies and the field data curves are in close agreement and follow the same seasonal trends where high rainfall events are linked with temperature lows. It is worth noting that the model block temperatures for these features were already showing strong correlation with rainfall however the magnitude of the variation was too small to be compared to the field data as discussed above.

The matches between measured mass flow and the modelled mass flow are quite poor and largely qualitative. The reasons for this are discussed in the following section.

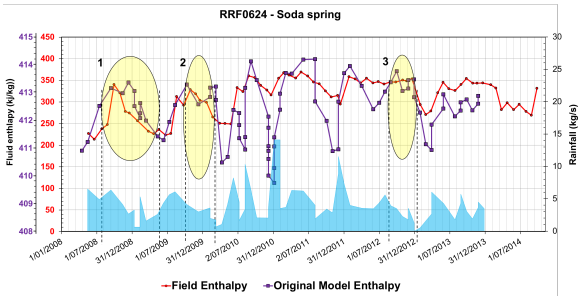

Figure 17. RRF0624 – Soda Spring at Kuirau Park. Field enthalpy (red) and original model block enthalpy (purple) from May 2008 to July 2014

In Figure 16 the post-processing model enthalpy and field data are not clearly correlated. In some periods the modelled enthalpy has an opposite trend than the field data (indicated by 1-3 in Figure **16**). The measured temperatures for Soda Spring (RRF0624) are in fact much more correlated with the original model block temperatures (caused by seasonal variations of production and reinjection) though the model block is hotter (Figure **17**). This indicates that rather than cooling the surface feature with additional rainwater dilution, the numerical model needs further calibration in this area to reduce the temperature of the flow from the subsurface.

Production near Kuirau Park seems to have a direct impact on the temperature of the neighboring Soda Springs (Soengkono *et al.*, 2001). This correlation is well captured in our model.

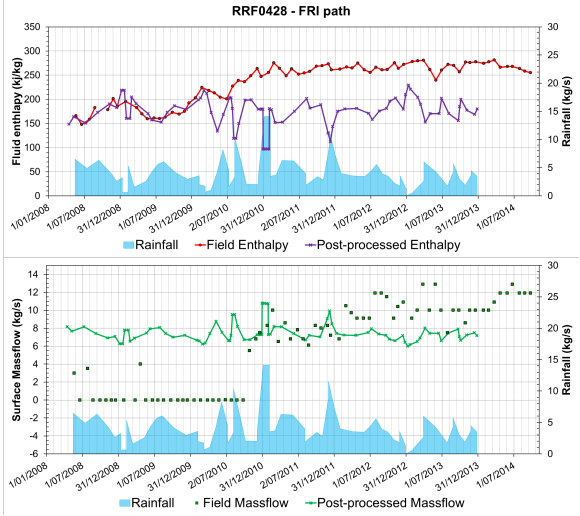

Figure 18. RRF0428 – FRI path in Whakarewarewa Village in Whakarewarewa geyser Valley.

For monitored surface feature RRF0428 – FRI path, the modelled temperatures match the field data very well up to 2010. However in 2010 the surface features experienced an increase in temperature (90 kJ/kg) that is not represented in our model. This temperature increase is not related to the rainfall or to a change in production nearby. More data is required to identify whether this change represents a new steady state for the surface feature or if it is the result of an unidentified transient event.

This is not an isolated case as several other monitored surface features have experienced increasing or decreasing temperature trends not represented in the model or related to rainfall or production variation. The temperature of Papakura geyser (RRF0028) increased by 50°C in September 2013, thermal features RRF0426 – 426 temperature increased from 35°C to 85°C in April 2010, and Tawewa Spring (RRF0653) from 60°C to 95°C in January 2009. While other springs such as Lake Roto-a-Tamaheke (RR0337) experienced a gradual increase in temperature since May 2008 from an average temperature of 35°C to approximately 50°C. Conversely, surface feature RRF0352 - Waipatuhuka experience gradual decrease in temperature from 70°C to 50°C in 2011 to stabilize at this lower value.

Discussion

There are several difficulties that geothermal modellers face when attempting to match measurements of discharging surface features.

For example the temperature of a boiling surface feature will be measured at close to 100°C where the reservoir model will often predict a temperature in excess of 100°C. In the field the temperatures are usually recorded at the surface of the surface features where in the model the temperature is taken in the centre of the surface block. Therefore the comparison does not include any cooling that take place between the surface and a few meters deep. High temperature gradients near the surface of geothermal systems mean that this effect could be quite large. This could be taken into account by creating a more complex post-processing model for which cooling from boiling, radiation, and conduction are calculated from known atmospheric conditions and size of the thermal feature.

Also, field measurements of the surface feature mass flows do not include losses by vaporization and shallow seepage. For example, Korotiotio is a large boiling alkali spring that has no measured mass flow (Figure **15**). However, while its water level is approximately 1m below the surrounding terrain and it does not obviously overflow, recording its mass flow as zero neglects the mass flow from vaporization and possible seepage to the neighboring Puarenga stream (Figure 19). More accurate estimates of the mass flow for the features are needed to compare with model predictions and develop more accurate models.

Figure 19. Picture of Korotiotio at Whakarewarewa on 30/07/2013 (GNS report 306, Graham et al., 2013)

CONCLUSION

A new model of the Rotorua geothermal field has been developed that represents the shallow unsaturated zone and includes the seasonal variations that impact the geothermal system. The model has a good match with the large scale behaviour of the system.

In order to provide a useful tool for assessing the impact of various production schemes on the important surface features a post-processing model has been developed to represent their behaviour. Good matches have been obtained for the temperature and mass flow variations of most of the monitored surface features. UOA Model 5 represents the first attempt to model such small scale activity as a result of large scale system behaviour.

ACKNOWLEDGMENTS

The authors thank Samantha Alcaraz from GNS Science for her assistance building representative three-dimensional temperature contours of the Rotorua system. We also thank the Environment Bay of Plenty (EBOP) for providing information on current and past consented geothermal bores as well as temperature versus depth data.

REFERENCES

Battistelli, A., Calore, C. and Pruess, K., The simulator TOUGH2/EWASG for modeling geothermal reservoirs with brines and non-Condensible gas, *Geothermics*, 26(4), 437 - 464, 1997.

Bradford, E. 1992. Pressure changes in Rotorua geothermal aquifers, 1982-90. *Geothermics 2111-2: 231-248.*

Candra, A., Zarrouk, S. 2013. Testing Direct Use Geothermal Wells in Rotorua, New Zealand. *Proc. 35th New Zealand Geothermal, Workshop, Rotorua, New Zealand, 18-20 November 2013.*

Environment Bay of Plenty Regional Council (EBOP). 1999. Rotorua Geothermal Regional Plan. *Resource Planning Publication 99/02. ISSN 1170 9022.*

Gordon, D. A., Scott, B., & Mroczek, E. K. 2005 Rotorua geothermal field management monitoring update: 2005. Environment Bay of Plenty Environmental publication 2005/12.

Graham, D.J., Pearson, S.C.P., Seward, A., O'Halloran, L. 2013. Rotorua Geothermal System: Measurements and Observations July to September 2013. GNS Science Consultancy Report 2013/306.

Grant, M.A., McGuiness, M.J., Dalziel, S.R., Razali, Yunus and O'Sullivan, M.J. 1985. A model of Rotorua geothermal field 586 and springs. In: The Rotorua geothermal field - Technical report of the monitoring programme 1982-1985. *Ministry* 587 *of Energy, Wellington.*

Hunt T.M. 1992. Gravity anomalies, caldera structure, and subsurface geology in the Rotorua area, New Zealand. *Geothermics, Vol. 21, No. 1/2, pp. 65-74.*

Pruess, K. 1991. TOUGH2: A general-purpose numerical simulator for multiphase nonisothermal flows. Rep. LBNL-29400, *Lawrence Berkeley Lab., California USA.*

Ratouis T.M.P., O'Sullivan M., and O'Sullivan J. 2014. Modelling of the Rotorua geothermal field including chemistry. *Proc. 36th New Zealand Geothermal Workshop, University of Auckland, Auckland, New Zealand, 18-21 November 2014.*

Ratouis T.M.P., O'Sullivan M. and O'Sullivan J. 2015. An Updated Numerical Model of Rotorua Geothermal Field. *Proceedings World Geothermal Congress 2015 Melbourne, Australia, 19-25 April 2015*

Soengkono S., Suhanto E., Teece C., Tuah A. H. A., Mejia Diaz C. E., Tansupo K. 2001. Temperature, resistivity and self potential investigations of Kuirau Park, Rotorua geothermal field, New Zealand. *Proceedings of the 23rd New Zealand Geothermal Workshop, 7-9 November 2001.*

Stewart, M.K, Lyon, GL, Robinson, BW and Glover, RB. 1992. Fluid Flow in the Rotorua Geothermal Field Derived from Isotopic and Chemical Data. *Geothermics 21 (1/2) Special Issue: Rotorua Geothermal Field, New Zealand, 141-163.*

Wood, C.P. 1992. Geology of the Rotorua geothermal system. *Geothermics, 21(1), 25-41.*

Yeh, A., Croucher, A. & O'Sullivan, M.J. 2012. Recent developments in the AUTOUGH2 simulator. *Proceedings TOUGH Symposium 2012, Berkeley, California. 17-19 September 2012.*

INTERPRETATION OF PRODUCTION TESTS IN GEOTHERMAL WELLS WITH T2WELL-EWASG

Ester Maria Vasini[(1)], Alfredo Battistelli[(2)], Paolo Berry[(1)], Stefano Bonduà[(1)], Villiam Bortolotti[(1)], Carlo Cormio[(1)], Lehua Pan[(3)]

[(1)]DICAM Dept., Bologna University,40131 Bologna, Italy
[(2)]AMBEN Dept., Saipem SpA, 61032 Fano (PU), Italy
[(3)]Earth Sciences Division, Lawrence Berkeley National Laboratory, Berkeley, CA 94720, United States

estermaria.vasini2@unibo.it; alfredo.battistelli@saipem.com; paolo.berry@unibo.it
stefano.bondua@unibo.it; villiam.bortolotti@unibo.it; carlo.cormio3@unibo.it; lpan@lbl.gov

ABSTRACT

A crucial aspect of geothermal reservoir engineering is the performance and interpretation of field tests, such as production tests, flowing temperature and pressure logs - both during injection and production, and down-hole pressure transient recording. Such tests are of great importance in order to evaluate the reservoir properties and to predict wells production capacity. However, production tests duration is often limited by environmental constraints related to the disposal of brines, and the running of downhole measurements is constrained by safety and cost considerations related to the use of expensive tools in high temperature high productive wells.

From this point of view, the capability to simulate the whole production tests can be extremely useful to improve the data interpretation and reduce the impact of lacking field data. In particular, the coupled simulation of transient fluid flow within the wellbore and the reservoir with the matching of output production curve, flowing logs, and downhole pressure transients, should result in a more reliable evaluation of reservoir properties. This can be done using T2Well, a coupled wellbore-reservoir numerical simulator, with proper equation of state (EOS) modules. EWASG is an EOS module for high enthalpy geothermal fluids consisting of mixtures of water, salts and a non-condensable gas (NCG). We have recently plugged it into T2Well and also improved the analytical computation of heat exchange between the well and the surrounding formations at early time, which may be important for reproducing the transient results of production tests. The resulted wellbore-reservoir simulator, T2Well-EWASG, is capable to simulate high enthalpy geothermal wells. We verified and validated T2Well-EWASG against flowing pressure and temperature logs taken from published literature and against field data collected during a short discharge test performed in a productive well drilled in a new prospect in Dominica.

INTRODUCTION

A crucial aspect in geothermal reservoir engineering is the performance and interpretation of field tests, both during injection and production. Such tests are of great importance in order to evaluate the reservoir properties and to predict wells production capacity. Typical field tests performed in geothermal wells are: production tests, dynamic temperature and pressure logs (either during injection and production), downhole pressure transients. Production tests are fundamental for the determination of the fluid enthalpy and to obtain the well deliverability curve (i.e. flow rate versus the well head pressure). The dynamic P&T (pressure and temperature) logs permit to evaluate the locations of feed-zones, the thermodynamic behavior of produced fluids and are useful for the calibration of coupled wellbore-reservoir models.

Finally, pressure transient analysis is executed to determine the main hydraulic parameters, such as the formation permeability-thickness product and the storage coefficient, the wellbore skin factor and wellbore storage capacity (Axelsson, 2013). However, production tests duration is often limited by environmental constraints related to the disposal of discharged separated brines, while the running of downhole measurements is constrained by safety and cost consid-

erations related to the use of expensive tools in high temperature high productive wells.

From this point of view, the capability to simulate the whole production tests can be extremely useful to improve their interpretation and reduce the impact of lacking field data. In particular, the coupled simulation of transient fluid flow within the wellbore and the reservoir with the matching of output production curve, flowing logs, and downhole pressure transients, should result in a more reliable evaluation of reservoir properties. This can be done using a coupled wellbore-reservoir numerical simulator for high enthalpy geothermal fluids consisting of mixtures of water, salts and a non-condensable gas. We have therefore plugged into the wellbore-reservoir numerical simulator T2Well (Pan and Oldenburg, 2013) the EWASG equation of state (EOS) for high enthalpy geothermal fluids (Battistelli et al., 1997; Battistelli, 2012). We also improved the analytical computation of heat exchange between the well and the surrounding formations at early time. The resulted integrated wellbore-reservoir numerical simulator, T2Well-EWASG, can be used to simulate high enthalpy geothermal systems.

T2Well

To address the need to simulate the coupled wellbore-reservoir flow, Pan and Oldenburg (2013) developed T2Well, a numerical simulator for non-isothermal, multiphase, and multi-component coupled wellbore-reservoir flow modeling.

T2Well extends the existing numerical reservoir simulator TOUGH2 (Pruess et al., 1999) to calculate the flow in both the wellbore and the reservoir by introducing a special wellbore sub-domain into the numerical grid. The wellbore flow is simulated using the Drift Flux Model (Zuber and Findlay, 1965). As TOUGH2, T2Well can be used with different EOS in order to describe different fluid mixtures. Up to now it has been used with ECO2N (Pruess, 2005) for applications related to CO_2 sequestration, with ECO2H (Pan et al., 2015) for enhanced geothermal system simulations, and with EOS7C (Oldenburg et al., 2013) for applications related to compressed air energy storage.

The heat exchanges between wellbore and the surrounding formation can be simulated numerically or optionally calculated with the semi-analytical Ramey's method (Ramey, 1962) or the Zhang's convolution method (Zhang et al., 2011).

EWASG EOS MODULE

EWASG is an EOS TOUGH2 module used primarily for modeling hydrothermal systems containing dissolved solids and one NCG such as CO_2, CH_4, H_2S, N_2 and H_2. EWASG can handle phase equilibria and fluid properties calculations up to 350°C and 1000 bar for H_2O-NaCl-NCG mixtures conventionally found in low and high enthalpy geothermal reservoirs (Battistelli et al., 2012), with the limitation of low to moderate NCG partial pressures.

In the course of time, EWASG has been partially or totally included within other simulator of the TOUGH family of code or used as the starting point for developing new EOS. Among others (Battistelli, 2012): iTOUGH2, TOUGH-MP, ECO2 and ECO2N, TMVOC V.2.0, TMGAS and EOSM.

New analytical function for heat exchange between wellbore and formation

The use an analytic computation of the heat exchange between wellbore and formation is a useful feature because it allows a substantial simplification of discretization grid, reducing both the efforts to manage the model and the computational time.

Unfortunately, both methods implemented in the original version of T2Well have some limitations. Ramey method works properly only for times longer than approximately a week, therefore it is not suitable to study short transient phenomena. On the other hand, the Zhang's method uses a simplified design, assuming there is no thermal resistance related to well completion. To overcome these limitations, we have implemented in T2Well (in both the original T2Well-ECO2N and the T2Well-EWASG) the Carslaw and Jeager function as reported by Kanev et al.(1997), with some additional empirical modifications.

Carslaw and Jeager function $f(t)$ uses a dimensionless time defined as:

$$t_D = \frac{\alpha t}{r^2}$$

where t is the time (s), r is the wellbore radius (m) and α is the thermal diffusivity and is equal to $k/(c\rho)$, where k is the thermal conductivity (W m^{-1} K^{-1}), ϱ is the density (kg m^{-3}) and c is the specific heat (J kg^{-1} K^{-1}) of the formation.
It is a discontinuous function depending on three specific jump discontinuity times, $t_0 < t_1 < t_2$.

If $t_D \geq t_2$, then at long times function is used:

$$f(t) = \frac{2}{\ln(4t_D) - 2\gamma} - \frac{\gamma}{\left(\ln(4t_D) - 2\gamma\right)^2}$$

If $t_0 < t_D \leq t_1$, then at short times function is used:

$$f(t) = \frac{1}{\sqrt{\pi t_D}} + \frac{1}{2} - \frac{1}{4}\sqrt{\frac{t_D}{\pi}} + \frac{1}{8}t_D$$

If $t_D \leq t_0$ then a constant time function is used:

$$f(t_0) = \frac{2}{\sqrt{\pi t_0}} + \frac{1}{2} - \frac{1}{6}\sqrt{\frac{t_0}{\pi}} + \frac{1}{16}t_0$$

Finally if $t_1 < t_D < t_2$ then:

$$f(t) = fac + \frac{\ln\frac{t_D}{t_1}}{\ln\frac{t_2}{t_1}}(temp - fac)$$

Where *fac* and *temp* are respectively equal to:

$$fac = \frac{1}{\sqrt{\pi t_1}} + \frac{1}{2} - \frac{1}{4}\sqrt{\frac{t_1}{\pi}} + \frac{1}{8}t_1$$

$$temp = \frac{2}{\ln(4t_2) - 2\gamma} - \frac{\gamma}{\left(\ln(4t_2) - 2\gamma\right)^2}$$

The values of the three reference dimensionless times we have individuated are:

$t_0 = 10^{-6}$
$t_1 = 1$
$t_2 = 10$

Code verification

To verify the T2Well-EWASG code coupling, a short well-test chosen from the literature (well W2, Barelli et al., 1982) was reproduced and the performance of Carslaw & Jeager function was tested on a simple case study.

Regarding the latter, a 1000 m depth wellbore characterized by a linear thermal gradient between 11 °C at well-head and 40°C at the bottom, producing 100 kg/s of water at 100°C at the bottom of wellbore was used. The simulations using the analytical Carslaw & Jeager function and a pure numerical one have produced a good match both using T2Well-ECO2N and T2Well-EWASG, as it is shown in Figure 1 and Figure 2.

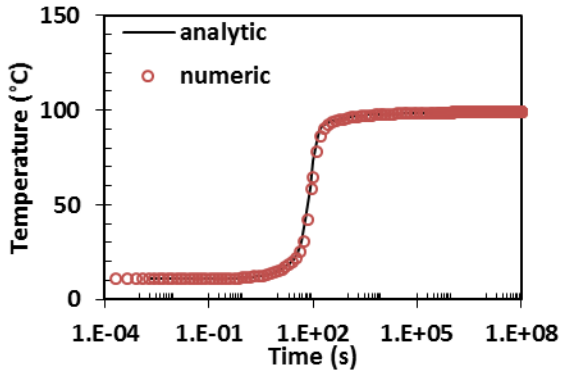

Figure 1. T2Well-ECO2N. Comparison of wellhead temperature vs time as obtained with the Carslaw & Jeager analytic relation and the ones obtained by a pure numerical computation.

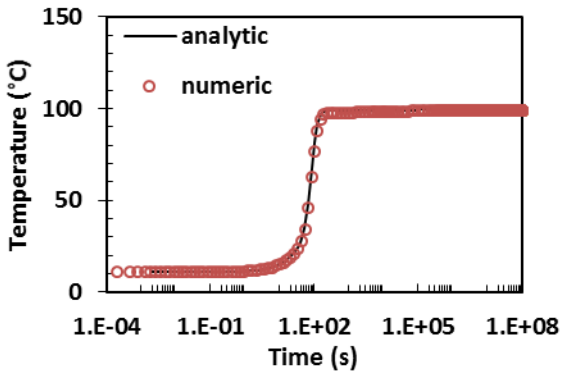

Figure 2. T2Well-EWASG. Comparison of wellhead temperature vs time as obtained with the Carslaw & Jeager analytic relation and the ones obtained by numerical computation.

The well W2 is 1355 m deep and produces low salinity brine (9600 ppm) with large amounts of CO_2 (2-10%). The flowing bottom temperature is 225°C and the pressure is equal to 98 bar. In Figure 3 the profiles of temperature and pressure used as initial conditions are displayed. The mesh used has 47 elements, with constant boundary conditions set at the bottom. The initial conditions for CO_2 a NaCl content are 30000 ppm 9600 ppm, respectively.

Figure 4 shows the simulated flowing T-P profiles after 11 hours of production at 34.1 kg/s. As shown in the Figure, the match between the simulated results and the field data is reasonably good.

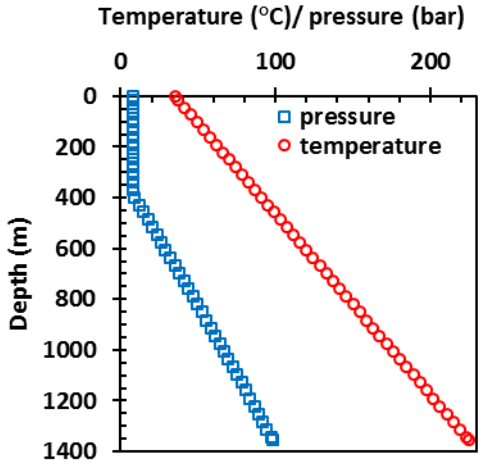

Figure 3. Profile of pressure and temperature used as initial conditions for the simulation of well W2.

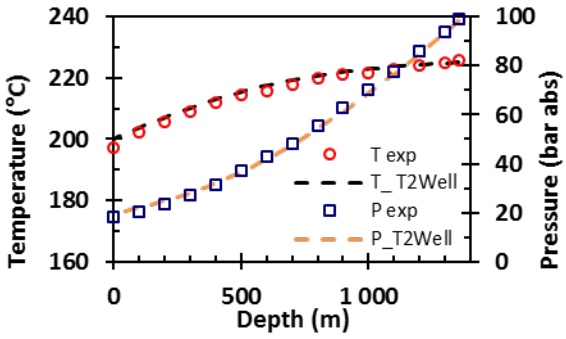

Figure 4. Comparison between experimental data and simulation results for the wellbore W2 after 11 hours of production.

Code validation

To evaluate the adequacy of T2Well-EWASG, a full coupled wellbore-reservoir simulation was performed. The field data are related to well WW-01, a productive slim hole drilled in the Wotten Waven Field, Roseaux Valley, Dominica (ELC, 2013; Osborne et al., 2014). WW-01 is a vertical slim hole 1200 m deep and producing from a liquid-dominated reservoir. The fluid inside the wellbore reaches a maximum temperature of 238°C and at the bottom the pressure is equal to 102 bar. The developed WW-01 well-reservoir model includes the cap-rock from 0 to -230 m (depth referred to the ground), and three main inferred feed zones: the first located between -297 m and -344 m (feed1), the second between -710 m and -734 m (feed2) and the third between -880 m and -940 m (feed3). The model is completed by reservoir layers called resv1 and resv2 between the feed zones, and by a less permeable rock domain (bottom) beneath the third feed zone. The well is completed with a 7" production casing (the CSG, internal diameter 159.42 mm) and a 4 ½" slotted liner (internal diameter 101.6 mm). The liner hanger is set at a depth of 263 m. The 2D radial grid used for the wellbore-reservoir system extends to an outer radius of 1500 m with the wellbore located on the axis of symmetry, for a total number of 1658 elements. In Figure 5 is displayed a vertical cross section of the model in which the main feed zones can be seen (in yellow, green and cyan lighter color). The cap-rock has not been included in the model: the heat exchange between wellbore and cap-rock has been simulated using the analytical solution.

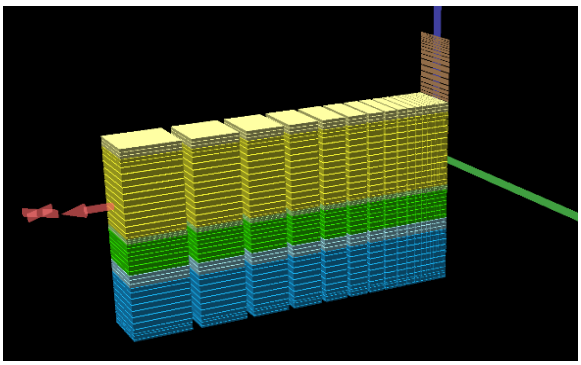

Figure 5. 2D vertical section of WW-01 wellbore-reservoir model. The main feed zones are the one with the lighter colors (yellow, green and cyan colors). The visualization of the model is performed by TOUGH2Viewer (Bonduà et al., 2012)

Figure 6 shows the shut-in temperature and pressure logs measured in WW-01 believed to be close to reservoir natural state and then used as

tentative initial conditions for the steady state simulation (initial T well and initial P). In addition, there is also the formation temperature assumed for the production simulation. The different temperature assigned to feed2 and feed3 was necessary in order to match the flowing experimental data with the simulated ones. This suggest that probably the shut-in T log was not yet stabilized after the disturbances due to drilling operations and completion tests. The production history (see Table 1) has been assigned to the model using a time dependent fluid extraction from the top element of the wellbore grid. The first step of matching process is the reproduction of downhole flowing pressure by calibrating the overall hydraulic transmissivity of feed zones. The downhole pressure was continuously recorded at the depth of 800 m and 1180 m during the performance of two pressure transient tests. For this first application of T2Well-EWASG to WW-01 tests data, the possible contribution of feed1 was neglected, by assuming that only feed2 and feed3 are producing.

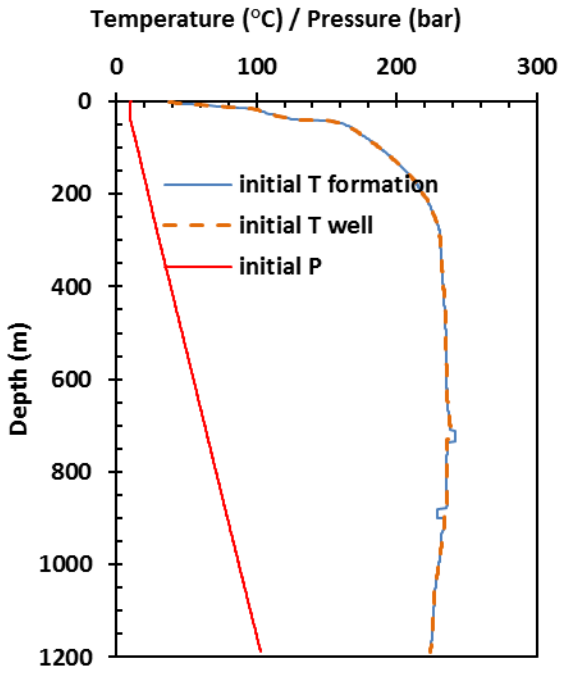

Figure 6. Initial pressure and temperature conditions assumed for the wellbore-reservoir model.

In Table 1 is reported the production history of wellbore WW-01 and in Figure 7 the comparison between the simulated rate and the measured one is shown.

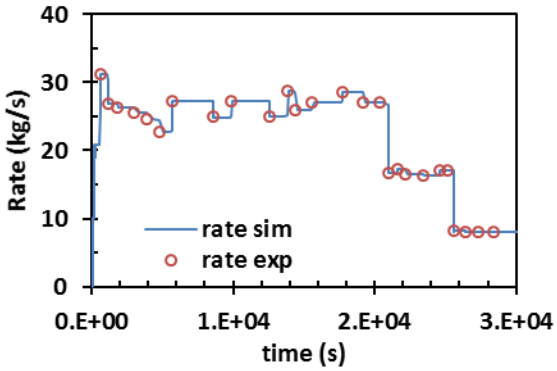

Figure 7. Comparison between simulated and measured rate.

The second step of the calibration process is the reproduction of flowing P&T logs, wellhead pressure (WHP) and production enthalpy. In Table 2 are reported the horizontal permeability values obtained by the calibration of the model. For this preliminary study, we have assumed that the skin coefficient of the wellbore is zero for both producing feed zones.

Table 1. Production history of wellbore WW-01

Time	Total flow (kg/s)	WHP (bar a)	Enthalpy (kJ/kg)
08:55		4.5	
09:05	31.25	18.0	1087.6
09:14	26.89	18.0	1124.8
09:25	26.26	17.8	1236.6
09:45	25.55	17.8	1280.4
10:00	24.53	17.9	1222.6
10:15	22.65	17.9	1170.4
10:30	27.27	17.5	1289.9
11:18	24.99	17.5	1331.9
11:40	27.28	17.5	1230.1
12:25	25.01	17.5	1292.2
12:45	28.72	17.5	1162.6
12:55	26.00	17.9	1222. 6
13:15	27.09	17.9	1178.1
13:50	28.60	17.8	1155.9
14:15	27.05	17.7	1155.2
14:45	16.77	19.4	1147.7
14:55	17.32	20.2	1094.9
15:05	16.44	20.2	1168.7
15:25	16.31	20.2	1156.7
15:45	17.15	20.3	1105.0
16:02	8.25	20.8	1155.9
16:15	8.03	20.8	1184.1
16:30	8.03	20.8	1184.1
18:00	0.00		

Table 2. Reservoir formation permeability (horizontal) as obtained by model calibration.

Rock domain	Permeability XY (m^2)
feed1	$18.0*10^{-15}$
resv1	$1.8*10^{-15}$
feed2	$180.0*10^{-15}$
resv2	$0.8*10^{-15}$
feed3	$30.0*10^{-15}$
bottm	$0.02*10^{-15}$

Figure 8 shows a reasonably good match of the measured flowing pressure profile with the simulated one. Figure 9 shows the comparison of recorded and simulated temperatures.

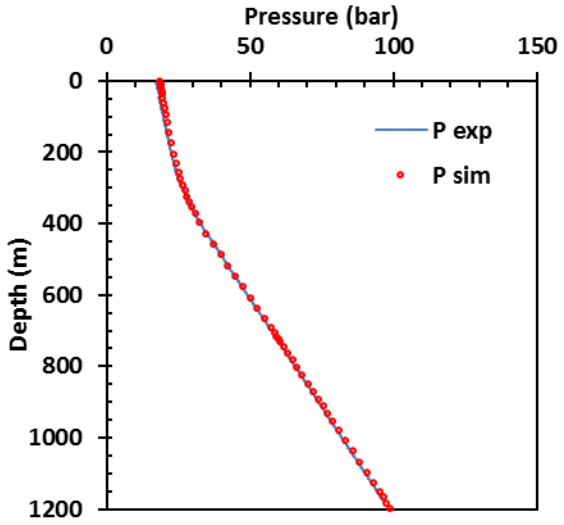

Figure 8. Comparison between the measured flowing pressure and the flowing simulated pressure at the time 10:40 am. The two set of data show a good agreement.

In Figure 10 the pressure recorded at 800 m, 1180 m and at wellhead is shown together with the simulated results. The agreement between downhole recorded and simulated pressure is rather good, while the WHP is underestimated between 21,000 and 27,000 s.

Figure 11 shows the comparison between the production enthalpy computed using field data and the numerical simulation results.

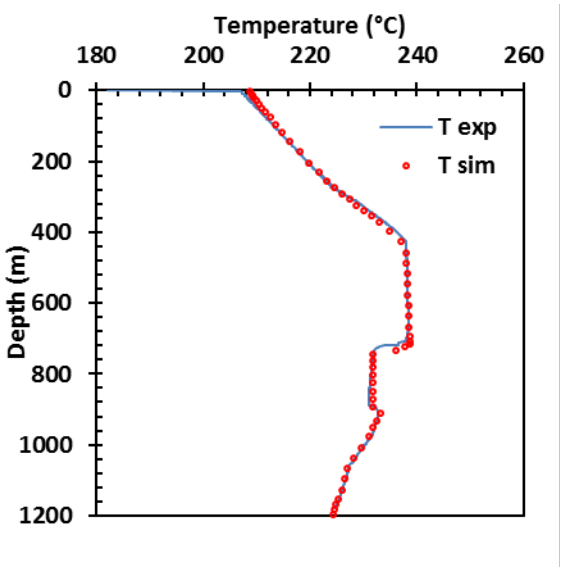

Figure 9. Comparison between the measured flowing temperature and the flowing simulated temperature at the time 10:40. The two set of data show a good agreement.

The simulated result give an almost constant production enthalpy of about 1000 kJ/kg which corresponds to a flash temperature of about 232°C. This result is in agreement with the production from a liquid dominated geothermal reservoir.

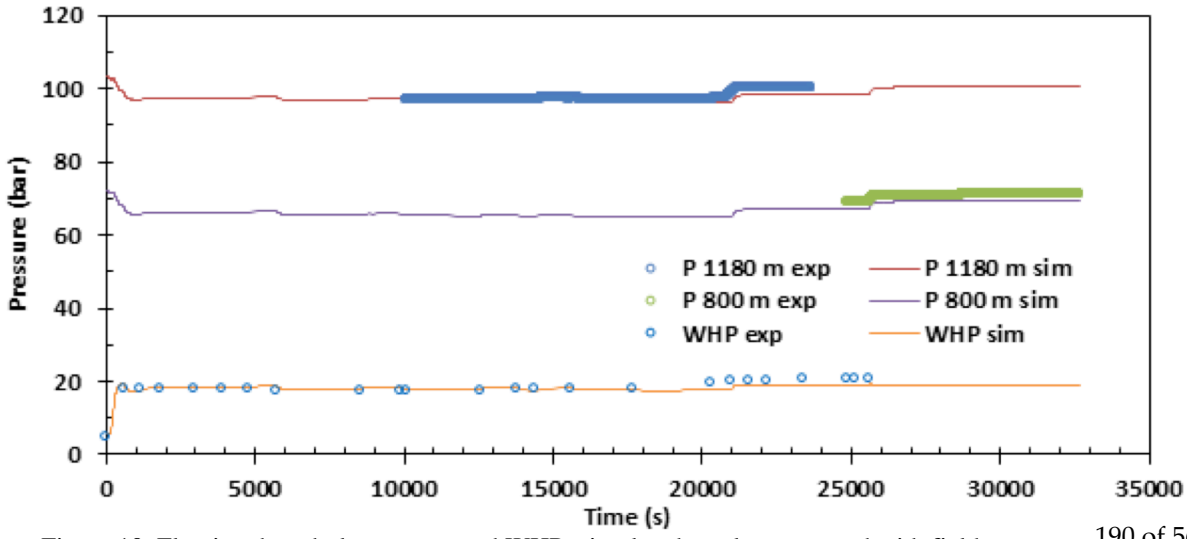

Figure 10. Flowing downhole pressure and WHP: simulated results compared with field measurements.

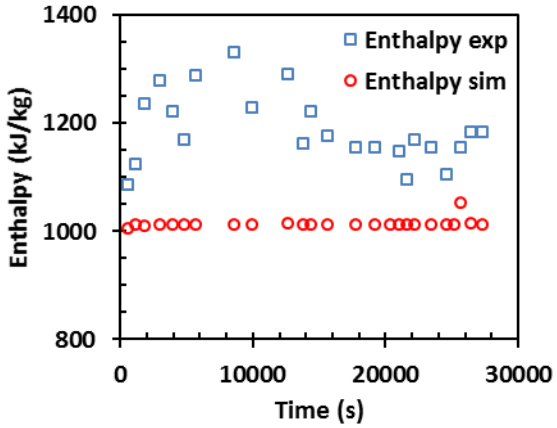

Figure 11. Measured and simulated production enthalpy.

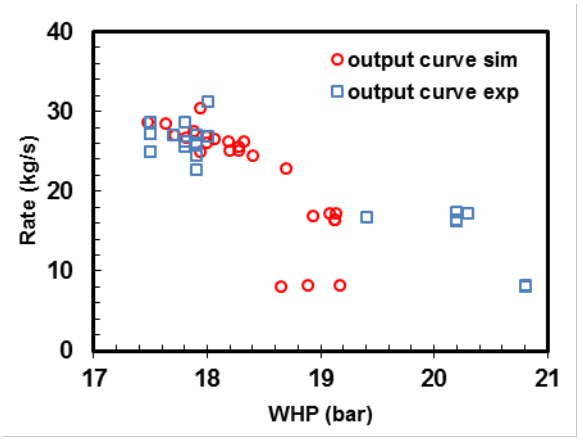

Figure 12. Output curve: comparison between simulated results and measured data.

The higher enthalpy estimated from field data were already pointed out in ELC (2013). The quite short production test was performed using the Russell James method with a lip pipe discharging into an atmospheric pressure separator and measuring the separated brine flow with a V-shaped weir. The higher estimated enthalpy could be due to either:

1. measurements errors during the production tests; and/or
2. the contribution of the first feed zone neglected in the present model.

In this preliminary study we have only adjusted the horizontal permeability of feed2 and feed3 in order to match the field data without attempting to simulate in a more detailed way the behavior of all the feed zones. For this reason, point 2 will be the object of further study because the first feed zone below the cap-rock is likely to be in two-phase conditions. Feed1 could then increase the production enthalpy by discharging a two-phase mixture with excess steam with respect to the static feed temperature.

Figure 12 shows the comparison between the experimental and simulated output curves. While measured WHP is well reproduced at rates exceeding 20 kg/s, at lower rates the simulated WHP underestimates the measured values. As the maximum discharge pressure is closely related to the production enthalpy, this may suggest that production enthalpy could actually be higher than that simulated due to the inflow of higher enthalpy fluid from the upper feed (feed1) neglected in this preliminary study.

CONCLUSIONS

We have plugged the EWASG EOS into T2Well. Furthermore, we have also enhanced the analytical computation of heat exchange between wellbore and formation and test it comparing the analytical results with the numerical ones. The resulted wellbore-reservoir simulator, T2Well-EWASG, is capable to simulate the flow in high enthalpy geothermal wells as shown by the verification made with a full set of wellbore data obtained from literature. The simulator has been validated against flowing pressure and temperature profiles. The application of the simulator to a coupled wellbore-reservoir system, as is represented by the case study of well WW-01 in the Wotten Waven Field (Commonwealth of Dominica), demonstrates that T2Well-EWASG can successfully be used as a tool to complement the integrated interpretation of surface and downhole measurements collected during the performance of production tests in geothermal wells. An important step forward would be the use of inverse simulation techniques to improve the reproduction of field measurements with the coupled wellbore-reservoir flow simulations.

ACKNOWLEDGEMENTS

The Geothermal Project Management Unit (PMU) of the Commonwealth of Dominica and ELC-Electroconsult SpA are acknowledged for the permission to use well WW-01 field data. During the 2011 - 2012 drilling campaign, Iceland Drilling Company (IDC) was the drilling contractor, Iceland GeoSurvey (ISOR) provided geologic, geochemical, and well testing services,

Geothermal Resource Group (GRG) provided supervision of drilling and well testing activities and ELC-Electroconsult supplied technical assistance to PMU. This work was partially supported by Saipem SpA under the R&D project "Simulation of production tests with TOUGH2-T2Well".

REFERENCES

Axelsson, G., Geothermal well testing, Presented at "Short Course V on Conceptual Modelling of Geothermal Systems", organized by UNU-GTP and LaGeo, in Santa Tecla, El Salvador, February 24-March 2, 2013.

Barelli, A., Corsi, R., Del Pizzo, G. and Scali, C., A two-phase flow model for geothermal wells in the presence of non-condensable gas, *Geothermics*, Vol.11, No.3, pp.175-191, 1982.

Battistelli, A., Calore, C., Pruess, K., The simulator TOUGH2/EWASG for modelling geothermal reservoirs with brines and a non-condensible gas. Geothermics, Vol. 26, No. 4, pp. 437-464, 1997.

Battistelli, A., Improving the treatment of saline brines in EWASG for the simulation of hydrothermal systems, In: Proceedings of TOUGH Symposium 2012. Lawrence Berkeley National Laboratory, Berkeley, California. Sept. 17-19, 2012.

Bonduá, S., Berry, P., Bortolotti, V., Cormio, C., TOUGH2Viewer: A post-processing tool for interactive 3D visualization of locally refined unstructured grids for TOUGH2. *Computers & Geosciences*, 46, p. 107-118, 2012.

ELC, *Wotten Waven Geothermal Field, Commonwealth of Dominica, West Indies: Feasibility Study*. Report for the Ministry of Public Utilities, Energy and Ports, Commonwealth of Dominica, 2013 (*unpublished*).

Kanev, K., Ikeuchi, J., Kimura, S. and Okajima, A., Heat loss to the surrounding rock formation from a geothermal wellbore, *Geothermics*, Vol. 26, No. 3, p. 329-349, 1997.

Oldenburg, C. M., Pan, L., Porous media compressed-air energy storage (PM-CAES): theory and simulation of the coupled wellbore reservoir system, *Transport in Porous Media*, DOI 10.1007/s11242-012-0118-6, 2013,

Osborn, W., Hernández, J., George, A., Successful Discovery Drilling in Roseau Valley, Commonwealth of Dominica. Proc., 39th Workshop on Geothermal Reservoir Engineering Stanford U., Stanford, CA, Feb. 24-26, 2014 SGP-TR-202, 2014.

Pan, L., Oldenburg, C.M., T2Well – An integrated wellbore-reservoir simulator, *Computer & Geoscience*, 2013. http://dx.doi.org/10.1016/j.cageo.2013.06.005.

Pruess, K., Oldenburg, C., Moridis, G., *TOUGH2 USER'S GUIDE, VERSION 2.0*, Earth Sciences Division, Lawrence Berkeley National Laboratory, University of California, Berkeley, California 94720, 1999.

Pan, L., Freifeld, B., Doughty, C., Zakem, S., Sheu, M., Cutright, B., Terrail, T., 2015, Fully coupled wellbore-reservoir modelling of geothermal heat extraction using CO_2 as the working fluid, *Geothermics*, 53, 100-113, 2015.

Pan, L., Spycher, N., Doughty, C., and Pruess, K., ECO2N V2.0: *A TOUGH2 Fluid Property Module for Mixtures of Water, NaCl and CO2*, Report LBNL-6930E, Lawrence Berkeley National Laboratory, Berkeley, Calif., February 2015.

Ramey, H.J. Jr., Welbore heat transmission, Mobil Oil Co., Santa Fe Springs, California, 1962.

Zhang, Y., Pan, L., Pruess, K., Finsterle, S., A time-convolution approach for modeling heat exchange between a wellbore and surrounding formation, *Geothermics*, 40, 4, 261-266, 2011.

Zuber, N., Findlay, J.A., Average volumetric concentration in two-phase flow systems, *Journal of Heat Transfer*, 87, 453, 1965.

Numerical Methods

IMPLEMENTATION OF A SIMPLE WELL-BORE MODEL IN iTOUGH2 FOR HIGH ENTHALPY WELLS

[1]Jean-Claude Berthet, [1]Andri Arnaldsson, [1]Snorri Kjaran
[1]Vatnaskil Consulting Engineers
Síðumúli 28
108 Reykjavík, Iceland
e-mail: berthet@vatnaskil.is

ABSTRACT

A simple well-bore model for intermediate to high enthalpy wells has been developed and implemented into iTOUGH2. The purpose of the model is to simplify the process of modelling constant well-head pressure production in geothermal wells. The well-bore model can be applied to wells containing one or two feed-zones.

The original version of the well-bore model, which was implemented into TOUGH2, required a user-specified table of flowing bottom-hole pressure values as a function of flow rate and enthalpy for a specified wellhead pressure. The model allowed for the definition of only one feed-zone for each prodution well.

The latest well-bore model presented here applies a new improved approach from the original version. The model has two operating modes: one to simulate production at a user-specified flow rate (the model then calculates the well-head pressure), the other to simulate production at a user-specified well-head pressure (the model then calculates the flow rate). The model has the ability to automatically switch between the two modes during the simulation time period. For each well, the user specifies a minimum well-head pressure and a maximum production rate. At the beginning of a model simulation, wells are allowed to produce at their maximum production rates as long as the well-head pressure remains above the defined minimum pressure. Once the well-head pressure declines and reaches the minimum pressure, the program reduces the production rate by the necessary amount to keep the well-head pressure constant at the minimum pressure value.

This new modelling approach more accurately simulates the way in which many geothermal wells are operated. The model relies on a set of empirical equations based on a pressure-discharge relationship for pure steam wells to estimate the well-head pressure. Four input parameters per feed-zone are required to describe each well. These four parameters are calibrated with a well-bore simulator before running iTOUGH2 using available wellhead pressure data, flow rates, well-design parameters and other appropriate data. The model allows for the definition of up to two feed-zones for each well. For dual feed-zone wells, the model calculates the relative contribution from each feed-zone based on reservoir pressure and user-specified well parameters.

The well-bore model was applied to the Þeistareykir geothermal wellfield in northeast Iceland. The well-bore simulator WellSim was used to calibrate the appropriate input parameters for the well-bore model and was also used to test the model. The productivity indices of the wells were calibrated using iTOUGH2 with the newly implemented well-bore model. A 30-year production scenario was run using the existing wells and proposed wells distributed within the wellfield.

INTRODUCTION

The TOUGH2 modelling suite is widely used in geothermal reservoir engineering to estimate reservoir volume, predict pressure trends and simulate injection. The calibration of reservoir models requires downhole pressure measurements which can be expensive and difficult to obtain. Such measurements are often performed during well maintenance by lowering a probe that records the pressure and temperature over a depth range. Thus, data from production wells are generally only available on a limited basis. Surface measurements, on the contrary, are easier to obtain and pressure and temperature are regularly recorded while wells are producing.

Pressure is lost in the reservoir when the extracted fluid ascends through the well. Estimating the pressure loss correctly is important in order to accurately predict the electric potential of a reservoir. Several programs have been developed to model well-bore processes. The main limitation with these programs is that they do not include a fully developed well-bore model coupled with a reservoir simulator. Thus, it is not possible to use surface data to calibrate the reservoir model. Also, for wells operated at constant head pressure, the flow rate in the reservoir model cannot be automatically adjusted to match the targeted head pressure. Over the last decades, several projects have attempted to incorporate well-bore simulators into TOUGH2. Results have been published; however, none of the simulators have become widely accepted and utilized. In 1990, an attempt was made to link the WFSA simulator to TOUGH2 (Hadgu, Zimmerman, & Bodvarsson, 1995). The WFSA simulator is one of the components of the WellSim simulation package. The project was abandoned in the following years. In 2000's, a project was undertaken to couple TOUGH2 to the well-bore simulator HOLA (Bhat, Swenson, & Gosavi, 2005). A more recent project, FloWell, is currently in progress but definitive results have yet to be presented (Gudmundsdottir, Jonsson, & Palsson, 2012; Gudmundsdottir, Jonsson, & Palsson, 2013; Guðmundsdóttir, 2012). Currently, the TOUGH2 program offers three options to model production from geothermal wells. The simplest method is called 'MASS' and requires the user to specify the production rate (Puess, Oldenburg, & Moridis, 1999). This method is suitable for matching historical data when the production rate is known. However, it is inconvenient when running future scenarios because when the well-head pressure drops below the minimum pressure required by the splitters, the program keeps producing at the specified flow rate until the area dries out and the program crashes. The second method for defining the production rate is the 'deliverability model'. With this method, the well produces at a specified constant bottom-hole pressure. The third method simulates production at constant well-head pressure. However, since there is no well-bore simulator in TOUGH2, the user is required to provide a table of flow rates and enthalpies versus bottom-hole pressures for each well. This method is rather cumbersome, and therefore the deliverability method is more commonly used despite the fact that it is less appropriate.

The work presented in this article has two objectives. The first is to simplify the process of simulating geothermal fields which contain wells producing at constant well-head pressure. The number of input parameters needed to describe the wells is reduced in the current well-bore model. The second objective is to create a model that can automatically choose between production at a constant flow rate and production at constant well-head pressure. The current model has been implemented for both single and dual feed-zone wells, and a description of both methods are presented below.

MODEL

Definitions and assumptions

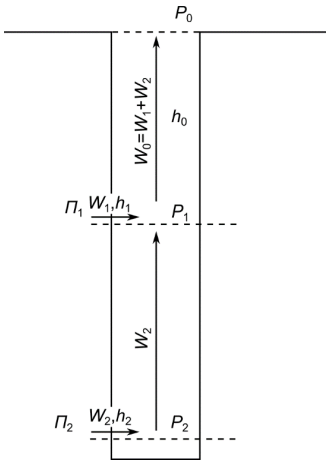

Figure 1. Conceptual drawing of wellbore.

P_0: well-head pressure
P_1: pressure in well at the elevation of the upper feed-zone
P_2: pressure in well at the elevation of the lower feed-zone
Π_1: pressure in the reservoir around the upper feed-zone
Π_2: pressure in the reservoir around the lower feed-zone
W_0: flow of fluid out of the well at the surface
W_1: flow of fluid from the reservoir into the well at the upper feed-zone

W_2: flow of fluid from the reservoir into the well at the lower feed-zone
h_0: specific enthalpy in the well after the fluids from the two feed-zones have mixed
h_1: specific enthalpy of the fluid flowing into the well at the upper feed-zone
h_2: specific enthalpy of the fluid flowing into the well at the lower feed-zone
υ_1: linear drawdown factor of the upper feed-zone
υ_2: linear drawdown factor of the lower feed-zone

The flow is assumed to be inelastic, therefore:

$$W_0 = W_1 + W_2 \quad (1)$$

The pressure difference between the reservoir and the well at the feed-zones is assumed to be a linear function of the flow from the reservoir into the well:

$$\Pi_1 = P_1 + \frac{W_1}{\upsilon_1} \quad (2)$$

$$\Pi_2 = P_2 + \frac{W_2}{\upsilon_2} \quad (3)$$

For steam-dominated wells, the relationship between the flow rate, the pressure at the upper feed-zone and the well-head pressure can be described by the following family of equations:

$$\left(\frac{W_0}{a_0}\right)^2 + \left(\frac{P_0}{b_0}\right)^2 = P_1^2 \quad (4)$$

The relationship between the pressures at the two feed-zones and the flow rate is described by the same family of equations but with a slight alteration:

$$\left(\frac{W_2}{a_1}\right)^2 + \left(\frac{P_1}{b_1}\right)^2 = P_2^2 \quad (5)$$

The enthalpy lost during the ascent of the fluid is assumed small and ignored. The enthalpy of the fluid in the well after the fluids from the two feed-zones have mixed is assumed to be:

$$h_0 = \frac{W_1 h_1 + W_2 h_2}{W_1 + W_2} \quad (6)$$

This is also assumed to be the enthalpy of the fluid coming out of the well at the surface.

Enthalpy

For a given pair of parameters a_0 and b_0, the relationships described by equations 5 and 6 are valid only for specific enthalpies. Therefore, because the enthalpy of the fluid can significantly change with time, parameters a_0 and b_0 are defined as functions of the enthalpy.

Several functional forms were tested, and a trial and error process led to the following simple forms which provide the best compromise between simplicity and accuracy:

$$a_0(h_0) = \alpha_0 h_0 + \beta_0 \quad (7)$$

$$b_0^2(h_0) = \gamma_0 h_0 + \delta_0 \quad (8)$$

$$a_1(h_2) = \alpha_1 h_2 + \beta_1 \quad (9)$$

$$b_1^2(h_2) = \gamma_1 h_2 + \delta_1 \quad (10)$$

Solutions for single feed-zone

Two solutions to the model described above are required. The first solution applies when the production rate is known. This solution is used mainly to run historical scenarios. The second solution applies when the well produces at constant well-head pressure. One of the goals for improving the model is to allow the program to determine which of the solutions is appropriate. Then the user can specify a flow rate which represents the needs of the geothermal power plant and a minimum well-head pressure. When the wellhead pressure drops below the minimum, the program adjusts the flow rate to keep the pressure constant.

Solution for a known flow rate

The flow rate W_0 is known and W_1 and W_0 are the same. The well-head pressure can be calculated using equations 2 and 4.

Solution for a known well-head pressure

When the well produces at constant well-head pressure, the flow rate is calculated from the solution of the quadratic equation:

$$\left(\frac{1}{a_0^2} - \frac{1}{\upsilon_1^2}\right) W_0^2 - \frac{2\Pi_1}{\upsilon_1} W_0 + \left(\frac{P_0}{b_2}\right)^2 - \Pi_1^2 = 0 \quad (11)$$

Solutions for dual feed-zones

Solution for a known flow rate

When the total flow rate W_0 is known, then W_1 and W_2 must be calculated first. It can be shown by combining equations 1, 2, 3 and 5 that W_1 is the root of a quadratic equation. The equation is

solved analytically. Then the head pressure is calculated using equation 4.

Solution for a known well-head pressure

It can be shown by combining equations 1–5 that for a known enthalpy h_0, the flow rate W_1 is the root of a quartic equation. Because h_0 is not known, the equation must be solved iteratively. The quartic equation is first solved analytically for a user-estimated initial enthalpy h_0. Then h_0 is re-estimated from the set of W_1 and W_2 obtained, and the process is repeated iteratively. The resulting algorithm converges very rapidly. Typically, a good solution is obtained within a few iterations.

iTOUGH2

Input

The model described above and its solutions were implemented in iTOUGH2. The input and output routines were modified to allow for the input of the parameters describing the model as well as the output of extra information. Three new generation type keywords were added: WHP0, WHP1 and WHP2. The first one is used to input single feed-zone wells. The next two are used for defining dual feed-zones wells. The keyword WHP1 is used to describe the upper feed-zones and WHP2 the lower feed-zones. In the input, the WHP2 entry must immediately follow WHP1. The keyword WHP0 and WHP1 are followed, in order, by a productivity index, the minimum well-head pressure and the target flow rate (Table 1). The two lines following the WHP entries contain the α_0, β_0, γ_0, δ_0 parameters describing the section of the well between the feed-zone and the surface. The keyword WHP2 is followed by the productivity index of the lower feed-zone. The two following lines contain the α_1, β_1, γ_1, δ_1 parameters that describe the section of the well between the two feed-zones.

The linear drawdown factors υ_1 and υ_2 defined earlier (Equations 2 and 3) are calculated in TOUGH2 from the productivity indices specified by the user:

$$\upsilon = P_i \left(\frac{S_l k_{rl} \rho_l}{\mu_l} + \frac{S_v k_{rv} \rho_v}{\mu_v} \right) \qquad (12)$$

where S_l, k_{rl}, ρ_l, μ_l, S_v, k_{rv}, ρ_v, μ_v are the saturation, the relative permeability, density and viscosity, respectively, of the liquid and vapor phases.

Output

An example of output produced by the modified iTOUGH2 is shown in Table 2. A new column P(WH) was added to the output to show the well-head pressure calculated by the program. In the example, the two feed-zones, BA581 and DA581, belong to the same well. Therefore, at each time step both display the same head pressure. At the beginning of the run, the pressure is above the minimum threshold (P_0 = 15×10^5 Pa). The flow rates from the feed-zones sum up to the total target flow rate specified by the user: W_0 = -11.1 kg/s. When the well-head pressure reaches the minimum pressure, the total production rate is adjusted to keep the well-head pressure constant. Thus the total flow rate decreases in steps from 11.1 kg/s to 9.3 kg/s, 7.9 kg/s, etc.

Table 1. iTOUGH2 input for the well-head module.

```
GENER----1----*----2----*----3----*----4----*----5----*----6----*----7----*----8
BA581sth91                    2     WHP1     Pi1         P0          W0
       α0          β0
       γ0          δ0
DA581sth91                    2     WHP2     Pi2
       α1          β1
       γ1          δ1
```

Table 2. Output example. The last column P(WH) shows the well-head pressure calculated by the program.

ELEMENT	SOURCE	INDEX	GENERATION RATE (KG/S) OR (W)	ENTHALPY (J/KG)		FF(GAS)	FF(AQ.)	P(WB) (PA)	P(WH) (PA)
BA581	sth91**		-0.27612E+01	0.17730E+07	...	0.44243E+00	0.55757E+00	0.18417E+07	0.15070E+07
DA581	sth91**		-0.83388E+01	0.13253E+07	...	0.00000E+00	0.10000E+01	0.53694E+07	0.15070E+07
BA581	sth91**		-0.17397E+01	0.20330E+07	...	0.58541E+00	0.41459E+00	0.18783E+07	0.15825E+07
DA581	sth91**		-0.93603E+01	0.14902E+07	...	0.11441E+00	0.88559E+00	0.41339E+07	0.15825E+07
BA581	sth91**		-0.16757E+01	0.18656E+07	...	0.73131E+00	0.26869E+00	0.16839E+07	0.15000E+07
DA581	sth91**		-0.76642E+01	0.18656E+07	...	0.38220E+00	0.61780E+00	0.26617E+07	0.15000E+07
BA581	sth91**		-0.99496E+00	0.18296E+07	...	0.91052E+00	0.89481E-01	0.16917E+07	0.15000E+07
DA581	sth91**		-0.69128E+01	0.18296E+07	...	0.36467E+00	0.63533E+00	0.27141E+07	0.15000E+07
BA581	sth91**		-0.88592E+00	0.18192E+07	...	0.93237E+00	0.67634E-01	0.16944E+07	0.15000E+07
DA581	sth91**		-0.67243E+01	0.18192E+07	...	0.35948E+00	0.64052E+00	0.27323E+07	0.15000E+07
BA581	sth91**		-0.74707E+00	0.17070E+07	...	0.94303E+00	0.56967E-01	0.17302E+07	0.15000E+07
DA581	sth91**		-0.67809E+01	0.17070E+07	...	0.28629E+00	0.71371E+00	0.30266E+07	0.15000E+07
BA581	sth91**		-0.70377E+00	0.16487E+07	...	0.94295E+00	0.57049E-01	0.17500E+07	0.15000E+07
DA581	sth91**		-0.68665E+01	0.16487E+07	...	0.24754E+00	0.75246E+00	0.32172E+07	0.15000E+07
BA581	sth91**		-0.70009E+00	0.16431E+07	...	0.94285E+00	0.57152E-01	0.17520E+07	0.15000E+07

CALIBRATION OF THE MODEL

The well-bore model presented is not a complete well-bore simulator. Therefore, like for the old constant well-head module in TOUGH2, an external well-bore simulator must be used to find the right parameters to describe the well. The protocol used to find these parameters is described below.

First, a series of well-head pressures versus flow rates are generated for several feed-zone pressures (Figure 2). Then, a linear regression analysis is performed to fit the curves to equation 4. A first pair of a_0 and b_0 parameters is created, which is valid for one specific enthalpy. The procedure is repeated for several specific enthalpies. Then, a new regression analysis is performed to fit the a_0 and b_0 parameters against equations 7 and 8 to find α_0, β_0, γ_0 and δ_0 (Figure 3). If the well has a second feed-zone, the whole procedure is repeated for the lower section of the well.

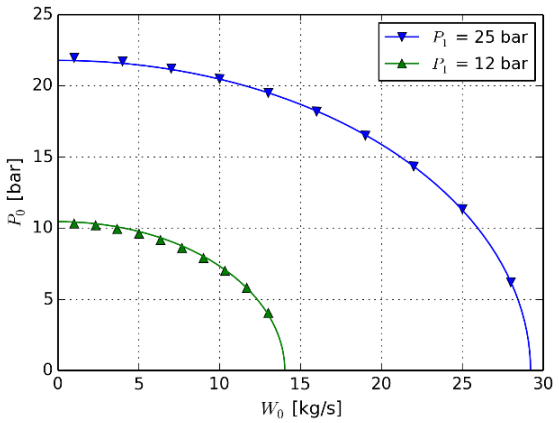

Figure 2. The well-head pressures calculated by WellSim are fitted against equation 4 to find a_0 and b_0 for a given specific enthalpy.

APPLICATION TO THE ÞEISTAREYKIR WELLFIELD

The model was applied to the Þeistareykir wellfield in northeast Iceland to run a future production scenario. At the time when this work was performed, nine wells had been drilled, eight tested and six were known to be suitable for production. The Þeistareykir wellfield is in its initial exploratory stage, but the goal is to construct a 90 MW electrical power plant. A TOUGH2 model of the reservoir was designed to assist with the management of the wellfield and estimate the number of required production wells and their life spans. Data from existing wells were used to construct the model, and their characteristics were entered into the well-bore simulator WellSim and the protocol described above was used to find the parameters α_0, β_0, γ_0, δ_0, α_1, β_1, γ_1 and δ_1 for each well. An example of this procedure for well ÞG-04 is given below.

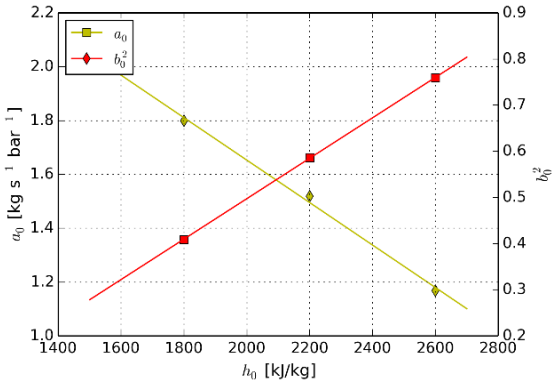

Figure 3. The a_0 and b_0 parameters are fitted against equations 7 and 8 to find the parameters α_0, β_0, γ_0 and δ_0.

Well-bore calibration

The calibration protocol was applied to the deviated well ÞG-04. The characteristics of the well (casing, liner lengths and diameters) were entered into WellSim. The well-head elevation of ÞG-04 is at 350 m a.s.l., and for the iTOUGH2 model two feed-zones were assumed at elevations 0 m a.s.l. and -1175 m a.s.l. The α_0, β_0, γ_0, δ_0, α_1, β_1, γ_1, and δ_1 parameters for the well were calculated and are provided in Table 3.

Table 3. Well-bore model parameters for well ÞG-04 (in SI units).

α_0	β_0	γ_0	δ_0
-3.11e-11	1.09e-04	2.80e-07	2.31e-01
α_1	β_1	γ_1	δ_1
-6.80e-12	2.60e-05	4.06e-07	-2.34e-01

Then, comparisons between WellSim and the well-bore model were performed to check that the two produce similar results. The tests were performed bottom-up such that pressures, flow rates and enthalpies were specified at the feed-zones, while the pressures, flow rates and enthalpies at the top calculated by the model were compared with values calculated by WellSim.

The comparisons are shown in Figures 4–6. Similar checks were performed with the other wells in the wellfield.

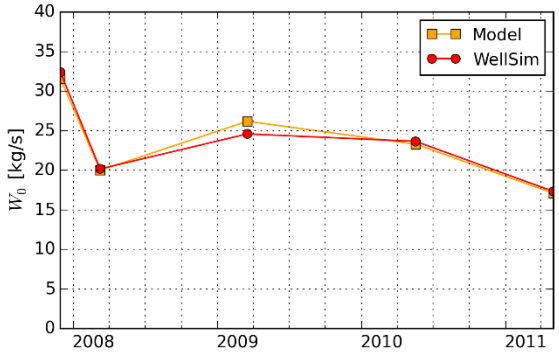

Figure 4. Well-head flow rate (W_0) calculated by the model and WellSim for well ÞG-04.

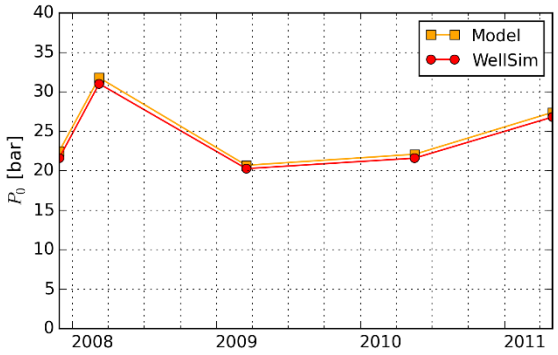

Figure 5. Well-head pressure (P_0) calculated by the model and WellSim for well ÞG-04.

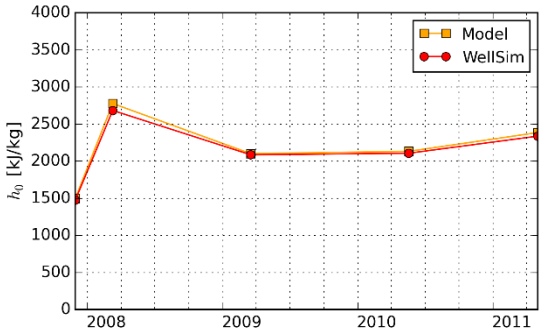

Figure 6. Well-head specific enthalpy (h_0) calculated by the model and WellSim for well ÞG-04.

Productivity indices calibration

After the well-bore calibration, data from discharge tests were used to calibrate the productivity indices of the feed-zones. Examples of flow rates, well-head pressures and specific enthalpies are shown for well ÞG-04 in Figures 7–9.

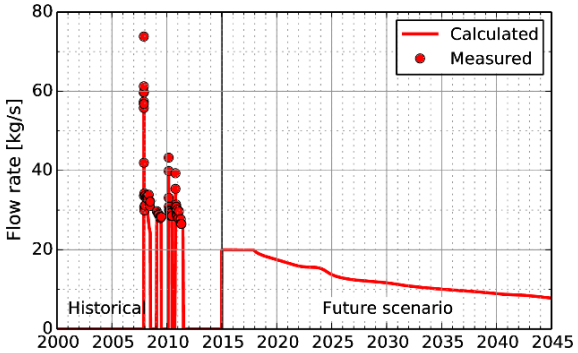

Figure 7. Flow rate for well ÞG-04, historical and future production scenario.

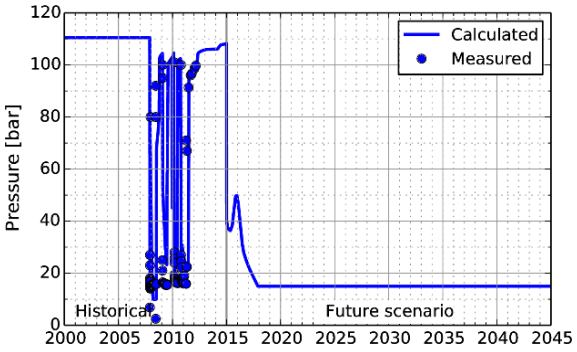

Figure 8. Well-head pressure for well ÞG-04, historical and future production scenario.

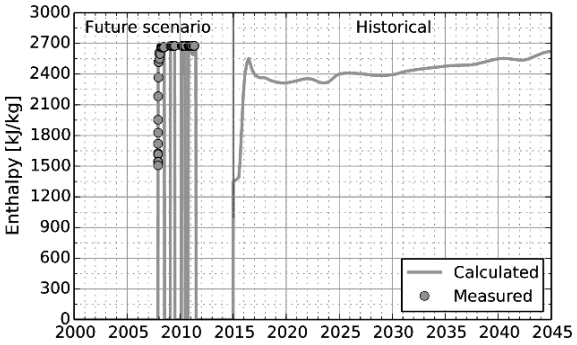

Figure 9. Well-head specific enthalpy for well ÞG-04, historical and future production scenario.

Ninety megawatts scenario

A 30-year production scenario was run with production beginning in 2015. Quickly, the model showed that the existing wells were not sufficient to provide 90 MW of electrical power. Therefore, proposed future wells were gradually added to the model (Figure 9). In addition to the six existing wells suitable for production, nine additional wells were necessary for the 90 MW production. As the productivity of the wells declined, extra make-up wells were needed to sustain the desired production, one well every two years for the first decade and one well every three years in the second decade of the scenario. In total, twenty-five wells were needed to maintain the electrical power above 90 MW over the thirty-year scenario.

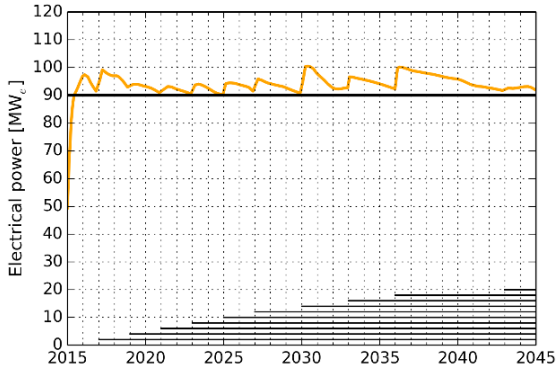

Figure 1. Electrical power output for the thirty-year scenario. The black lines at the bottom indicate when make-up wells open.

CONCLUSION

A well-bore model aimed at simplifying the simulation of constant well-head pressure wells in iTOUGH2 has been developed and tested. To describe the pressure loss in the well-bore, equations were developed that provide a satisfying level of accuracy and minimize the number of user-defined input parameters required. A solution based on empirical equations used to describe steam wells was used. Five input parameters are required per feed-zone to describe a well. For a single feed-zone well, four parameters are used to describe the well-bore and one parameter is needed for the productivity index of the feed-zone. The model is mostly suitable for intermediate to high enthalpy wells (roughly 1400–2800 kJ/kg). The model was used to run a thirty-year production scenario for the Þeistareykir wellfield in northeast Iceland. The parameters describing the well-bore were calibrated using the well-bore simulator WellSim. The productivity indices for the feed-zones were estimated by matching the iTOUGH2 output to real discharge data.

This model will be used in the future to model another geothermal field in Krafla in northeast Iceland. Several existing wells in Krafla have low enthalpies in the range of 1000–1200 kJ/kg. An evaluation of the suitability of the model for these wells will be performed. Changes will be made to extend the applicability of the model to include lower enthalpies.

ACKNOWLEDGMENT

This work was supported by HS Orka and Landsvirkjun. Special thanks are due to Landsvirkjun for allowing the materials for the Þeistareykir wellfield to be republished in this article.

REFERENCES

Bhat, A., Swenson, D., & Gosavi, S. (2005). Coupling the Hola wellbore simulator with TOUGH2. *Thirthieth Workshop on Geothermal Reservoir Engineering.* Standford: Standford University.

Guðmundsdóttir, H. (2012). *A Coupled Wellbore-Reservoir Simulator utilizing Measured Wellhead Conditions.* Reykjavik: University of Iceland.

Gudmundsdottir, H., Jonsson, M. T., & Palsson, H. (2012). Coupling wellbore simulator with reservoir simulator. *Thirty-Seventh Workshop on Geothermal Reservoir Engineering* (p. 9). Standford: Standford University.

Gudmundsdottir, H., Jonsson, M. T., & Palsson, H. (2013). The wellbore simulator Flowell. *Thirty-Eighth Workshop on Geothermal Reservoir Engineering* (p. 9). Standford: Standford University.

Hadgu, T., Zimmerman, R. W., & Bodvarsson, G. S. (1995). Coupled reservoir–wellbore simulation of geothermal reservoir behavior. *Geothermics, 24*(2), 145–166.

Puess, K., Oldenburg, C., & Moridis, G. (1999). *TOUGH2 User's Guide, Version 2.0.* Berkeley, California, USA: Lawrence Berkeley National Laboratory.

3D VORONOI PRE- AND POST- PROCESSING TOOLS FOR THE MODELING OF DEEP SEDIMENTARY FORMATIONS WITH THE TOUGH2 FAMILY OF CODES

Stefano Bonduà[(1)], Alfredo Battistelli[(2)], Paolo Berry[(1)], Villiam Bortolotti[(1)], Alberto Consonni[(3)], Carlo Cormio[(1)], Claudio Geloni[(3)], Ester Maria Vasini[(1)]

[(1)]DICAM Dept., Bologna University,40131 Bologna, Italy
[(2)]AMBEN Dept., Saipem SpA, 61032 Fano (PU), Italy
[(3)]GEOLAB Dept., eni SpA, 20097 San Donato Milanese (MI), Italy

stefano.bondua@unibo.it, alfredo.battistelli@saipem.com, paolo.berry@unibo.it, villiam.bortolotti@unibo.it
alberto.consonni@eni.com, carlo.cormio3@unibo.it, claudio.geloni@eni.com, estermaria.vasini2@unibo.it

ABSTRACT

Full three-dimensional (3D) unstructured grids offer a great degree of flexibility to perform accurate reservoir numerical simulations. However, when the space discretization is done using the Integral Finite Difference Method (IFDM), the requested orthogonality between the segment connecting the nodes and the blocks interface area complicates the construction of grids with irregular shape blocks. Nevertheless, the full 3D Voronoi approach guarantees the IFDM constraints and allows reproducing geological formations geometry, to follow the shapes of objects such as faults and directional wells, and allows increasing grid resolution in volumes of interest (local grid refinement). Here we present applications of the 3D Voronoi pre- and post-processing software tools dedicated to the TOUGH family of codes, (developed by the Geothermal research group of the DICAM Department, University of Bologna), to study the migration of non-condensable gases (NCG) in deep sedimentary formations at basin scale.

Several algorithms, mainly developed by the scientific community, are already available to calculate the Voronoi tessellation from a given set of seed points. In particular, the voro++ library is a well-known and powerful open source code to carry out 3D computations of the Voronoi tessellation. Based on voro++, VORO2MESH is a new software coded in C++ able to rapidly compute the 3D Voronoi tessellation for a given domain and to create a ready-to-use TOUGH2 MESH file, up to million blocks. The program can also directly generate the set of Voronoi seed points, using a set of geological surfaces as input. The resulting grid is a mixed grid with regular blocks (orthogonal prisms) and irregular blocks (polyhedron Voronoi blocks) at the contact between different geological formations. The use of regular blocks in regions sufficiently far from the contact surface allows limiting the number of connections. In order to easily inspect the 3D Voronoi discretization and to better visualize the subsequent numerical simulation results, the functionality of the TOUGH2Viewer post-processor has been extended. The software handles the visualization of 3D grids (structured and unstructured), the 3D vector representation of heat and mass fluxes, the iso-surfaces of the simulated variables and 2D contour maps. Different 3D grids of a deep sedimentary formation have been created with VORO2MESH, and the simulation results analysed with TOUGH2Viewer. In particular, the migration of NCG in a large sedimentary formation occupying an area of about 25,000 km^2 and with an average thickness of 800 m, extending from -2000 to -7000 m asl, has been simulated using TOUGH2-TMGAS. The use of unstructured grids as compared to the use of structured regular grids has substantially improved both the reproduction of the geological model and the simulation results of the NCG migration.

INTRODUCTION

The TOUGH (Pruess et al., 1999) family of codes uses the Integral Finite Difference Method (IFDM) for space discretization. This implies that the grid must comply with the orthogonality constraint, that is, each interface must be orthogonal with the connection line between two adjacent nodes. Cartesian grids implicitly satisfy this requirement, but they are not suitable to reproduce complex shapes such as the geometry of geological formations in sedimentary envi-

ronments. On the other hand, unstructured 3D Voronoi grids both satisfy IFDM constraints and reproduce the geometry of geological formations permitting to refine grids in volume of interest. Up to now, several software tools have been implemented to build Cartesian, 2.5D Voronoi grids (layered replication of a 2D Voronoi grid along one direction) and to analyse simulation results. As far as we know, software tools developed by scientific groups are MulGeom (O'Sullivan and Bullivant, 1995); GeoCad (Burnell et al., 2003); G*Base (Sato et al., 2003); Simple Geothermal Modelling Environment (Tanaka and Itoi, 2010); TOUGHER (Li et al., 2011); PyTOUGH (Croucher, 2011; Wellmann et al., 2012), and TOUGH2GIS (Berry et al., 2014). Commercial software are Petrasim (Alcott et al., 2006), WinGridder (Pan, 2003), mView (Avis et al., 2012) and Leapfrog (Newson et al., 2012). Regarding the full 3D Voronoi tessellation computation, a few algorithms have been developed by the scientific community. Among others, it is worth to mention Qhull (Barber et al. 1996), TetGen (Hang Si, 2015) and voro++ (Rycroft, 2009). To take full advantage of a full 3D Voronoi grid, we developed a tool, VORO2MESH, to generate ready-to-use TOUGH2 grids. On the other hand, with the growing of grid geometric complexity and consequently with the use of unstructured 2.5D or 3D grids, it is even more necessary to use enhanced tools that interactively allow to inspect simulation results. The large use of Finite Element Models has led the scientific community to primarily develop visualization software able to display tetrahedrons, which are not suitable for 3D unstructured IFDM grids constituted by polyhedron blocks. Therefore, we improved TOUGH2Viewer (Bondua et al., 2012) in order to visualize 3D unstructured grids for the TOUGH family of codes as generated by VORO2MESH. TOUGH2Viewer and its user manual are freely available at http://software.dicam.unibo.it, while the first version of VORO2MESH will be soon released and freely available at the same web address.

VORO2MESH

VORO2MESH is a software program developed by the Geothermal Research Group of DICAM Department, University of Bologna. The software is coded in C++ and allows realizing a space discretization of a convex domain from a set of seed points (the nodes of the grid) using the 3D Voronoi tessellation. The vertices coordinates, surface area and volume of each polyhedron block of the grid are computed using the voro++ library. The software can also assign a rock type at the blocks and, optionally, mark with a user-defined rock type the boundary blocks. By using a set of geological surfaces, VORO2MESH can also automatically generate the seed points. The loadable surfaces are now limited to a set of points on a regular 2D grid in an ASCII file format compatible with GRASS ASCII Grid format (see Appendix A). The result is a mixed grid with orthogonal prisms (regular blocks) in regions far from the surfaces and Voronoi blocks at the contact between different geological formations. The use of regular blocks in regions sufficiently far from the contact surface allows limiting the average number of connections. Figure 1a shows a cubic domain discretized by VORO2MESH using a set of seed points generated by TetGen (Hang Si, 2015). Figure 1b shows an example of discretization of a square domain enclosed between two surfaces.

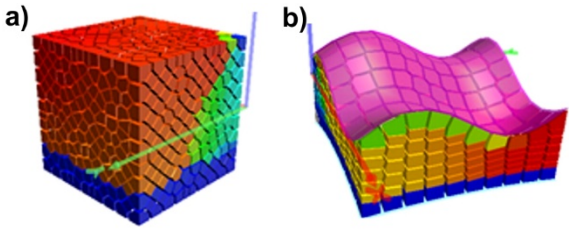

Figure 1: (a) Voronoi tessellation with seed points generated by TetGen; (b) Voronoi tessellation of a geological layer defined by two boundary surfaces, as plotted by TOUGH2Viewer.

In a 3D space, a surface can be represented as a regular grid of elevation points. This implies that it may be decomposed with a set of squares (hereinafter called 3D squares) whose corners are represented by four elevation coordinates. Therefore, a Voronoi tessellation including the surface can be obtained by forcing a pair of points (called drive nodes) on both sides of each 3D square, which represent the nodes of the 3D Voronoi blocks neighbouring the surface.

The remaining internal nodes between the two boundary surfaces can be inserted in several ways: (i) using the conjunction line between top and bottom drive nodes and vertically splitting

the space with the same number of points (Figure 2a, 2b); (ii) using a vertical line passing from the 3D squares centre and vertically splitting the space with the same number of points (Figure 2c, 2d); (iii) using the vertical line passing from the 3D square centre and vertically splitting the space imposing to the points to have the same elevation value (Figure 2e, 2f). This last method allows obtaining regular grids in region far from the surface, therefore limiting the number of connections.

VORO2MESH input files

The VORO2MESH input is at least composed of two files: the parameters and the data files. The former file contains geometric parameters about the 3D domain size, as requested by the voro++ library, domain cutting planes, and directives about the seed points to be used. The latter file can be of two types. The first contains just the list of nodes: id (a unique key); (x, y, z, coordinates); rocktype (optional, for material assignment). Note that if rocktype is set to a value less than zero, the node will be used during the tessellation computation, but the corresponding block will not be included in the MESH file and not visualized by the viewer. The second type uses a set of surfaces to discretize the domain defined in the parameters file, and a supplementary file containing the ordered list (from top to bottom) of the necessary geological boundary surfaces. Surface files must be present, in the format specified in Appendix A, in the folder from which the input files are loaded. Optionally the domain can be cut with planes expressed in the implicit form Ax+By+Cz+D=0, and the list of planes parameters A, B, C, D must be present in the WallList.dat file. Points external to the domain limited by the cutting planes, are not used for the Voronoi tessellation.

VORO2MESH output files

The output of a VORO2MESH run consists of several files:

- Tough2viewer.dat, which contains all the geometrical information to visualize the model with TOUGH2Viewer;

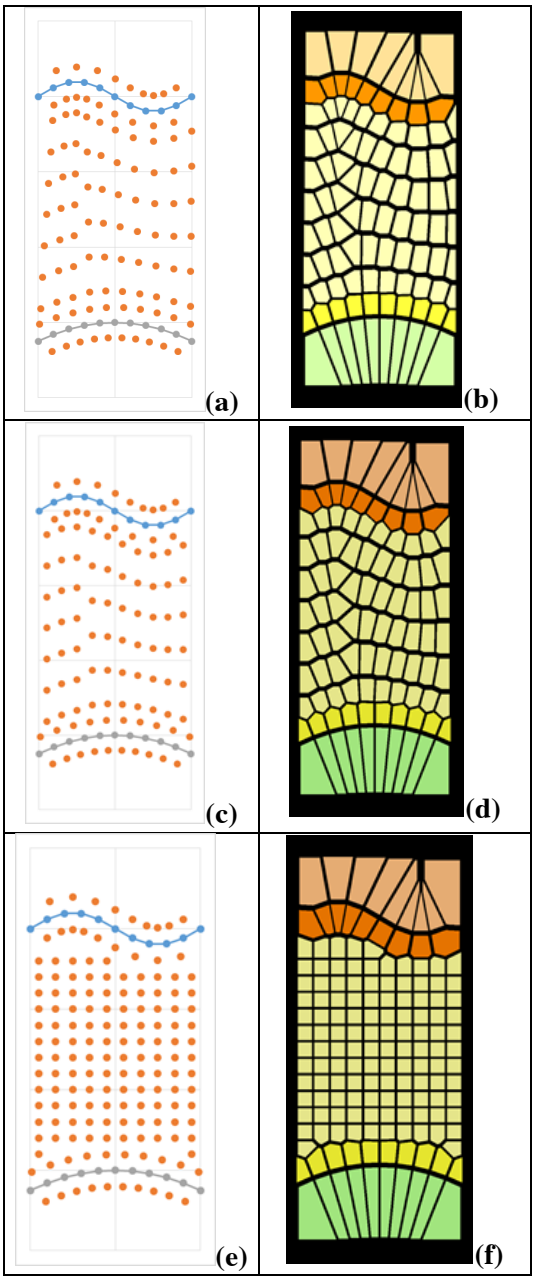

Figure 2: Vertical discretization of a volume included between two surfaces. (a), (c) and (e) show the distribution of seed points. (b), (d) and (f) show sections of the corresponding discretized domain.

- MESH, a ready-to-use TOUGH2 MESH file. If the input data file contains the rocktype, then the MESH contains also this information. If the data file is of surface type, a progressive rocktype index is assigned to each layer;
- statistic.dat, which contains statistical grid information (e.g., minimum and maximum

volume for each rocktype, elements number, connection area);

- Optional grid file in vtu format (ParaView VTK Unstructured Data) for visualization with ParaView;
- Optionally, a ready-to-use TOUGH2 INCON file can be generated. The value of each primary variable X_i used by the simulator can be also computed with a linear combination between the coordinates of the node and parameters defined by the user.

TOUGH2Viewer

As already stated, TOUGH2Viewer, which is developed in Java using the Java3D library, was improved with new functionalities to allow managing fully unstructured grids created with VORO2MESH or with the voro++ library. In a 3D virtual scene, each block is represented accordingly with the vertices coordinate and face information contained in the geometrical file. Other rendering are added to the Shape3D (Bouvier, 2000) object to obtain the final representation. Each vertex coordinate is shrunk, to separate each block from another, to get a better perception of the blocks shape. The entire model is visualized jointly with Cartesian axis and optionally with the geological boundary surfaces. Several tools are available in TOUGH2Viewer for inspecting the grid: predefined view, block shifting, definition of volume of interest, block search, threshold filtering, vertical 2D profile of the variables, neighboring blocks visualization, logarithmic color scale etc. Due to the great popularity and functionality of the free open source code Paraview, a filter to both export the simulation results and the geometry of the grid was implemented in TOUGH2Viewer. A file in vtu format can be exported for each simulated time step.

TOUGH2Viewer Input files

To allow TOUGH2Viewer to visualize a 3D virtual scene, it is necessary to provide:

- The geometrical file Tough2viewer.dat. See Appendix B for details;
- The TOUGH2 MESH file, its content can be visualized along with simulation results;
- The simulation file results. Each block is represented in a color scale, proportionally to the value of the variable shown (pressure, temperature, etc.). Other information, such as blocks convergence problems, number of phase changes, etc. can also be visualized. In order to preliminarily inspect the grid before running a simulation, this file can also be omitted;
- Optional input files. As aforementioned, the geological formations can be gridded by VORO2MESH with boundary surfaces features (generally top and bottom). The surface file used by VORO2MESH, can be directly imported in TOUGH2Viewer, allowing an easy inspection and comparison of the quality of the generated grid with respect to the geological layer surfaces.

SOFTWARE VALIDATION

To test the new tools, different grids of a deep sedimentary formation were created with VORO2MESH, and both grids and simulations results analysed with TOUGH2Viewer. In particular, the migration of non-condensable gases (NCG) in a large sedimentary formation encompassed between two geological boundary surfaces, occupying an area of about 25,000 km^2 and with an average thickness of 800 m, has been simulated using an enhanced version of TOUGH2-TMGAS (Battistelli and Marcolini, 2009). NCG injections blocks were set in a portion of the domain at the bottom left quarter of the grid, and an escape blocks was set at the top left corner (see Figures 4 and 5).

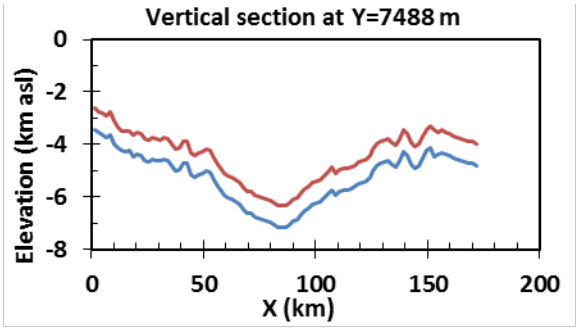

Figure 4: Generic vertical section of the domain showing the two boundary surfaces defining the geological layer, used to test VORO2MESH and TOUGH2Viewer.

The geological boundary surfaces were provided as grids (x, y, z, points file) with a resolution of 1700 × 1700 m^2, covering 180,000 m along X and 146,000 m along Y, and an elevation from -2000 down to -7000 m asl. The discretization of the volume between the two boundary surfaces was obtained inserting, for each 3D square centre, one drive node at the distance of 70 m on the normal to the plane that best interpolates the four vertices of the 3D square. The remaining region inside the two boundary surfaces was discretized with a regular grid with blocks of 1700 × 1700 × 140 m^3. In the unrefined grid, surface data refer to a rectangular domain, but the finished off grid has an irregular 2D shape as showed in Figure 5.

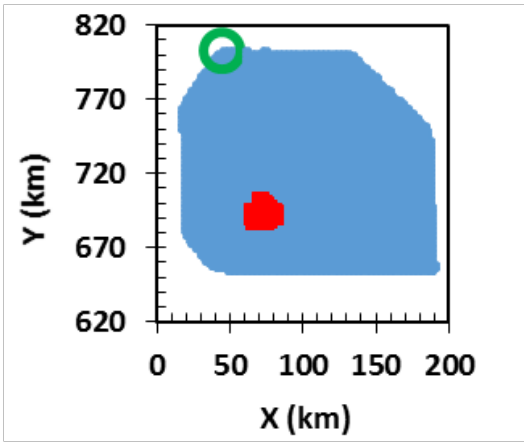

Figure 5: 2D view of the gridded surface. Highlighted in red color the position of the injection blocks (injection is performed at the bottom, see text). In green, the boundary block used to represent an open point of the system.

To define the sedimentary formation volume to be discretized, a convex hull encompassing the whole domain was used. In addition, a set of vertical planes was used to cut the domain to discard regions of no interest.

In Figure 6 is showed the resulting 3D grid as visualized by TOUGH2Viewer.

Figure 7 shows a portion of the 3D Voronoi grid with the two geological boundary surfaces (purple wireframe).

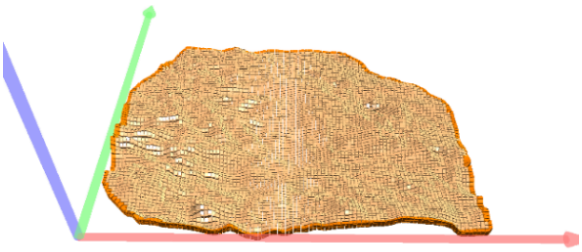

Figure 6: The finished off 3D grid (vertical exaggeration 5×).

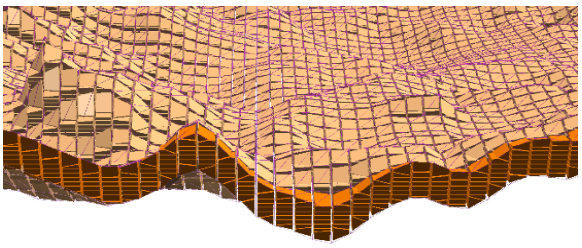

Figure 7: Grid and surfaces (purple wireframe) representing geological upper and bottom limits (vertical exaggeration 5×).

Figure 8 shows the same local maximum (a structural high) discretized with two different grids: the structured grid in Figure 8a; and the 3D Voronoi grid in Figure 8b. Clearly, the 3D Voronoi grid fits much better the geological surface shape (white wireframe). This has undoubtedly vantages when it is necessary to discretize geological domain rich of heterogeneities. Figure 8 is obtained with Paraview using a data set exported by TOUGH2Viewer. Therefore, the 3D Voronoi grid is compared with a classic structured regular discretization with blocks of 1700×1700×140 m^3. The structured grid was generated between the two geological boundary surfaces, skipping all points outside of the convex hull and the two surfaces. The cutting walls were applied as in the full 3D Voronoi grid. A statistical comparison between the two grids is reported in Table 1.

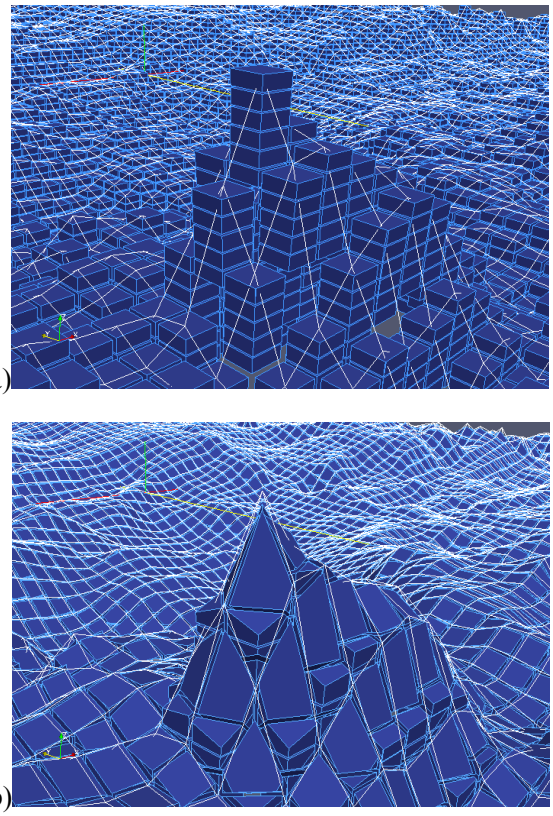

Figure 8: The same region gridded with: (a) regular discretization; (b) 3D Voronoi tessellation. The white wireframe represents the geological boundary surface (vertical exaggeration 5×).

Table 1 – Statistical parameters for the two grids. Volumes are in m^3 and areas in m^2.

	Regular model	3D Voronoi model
Number of blocks	48482	36258
Min Volume cell	1.5172e+08	3.128e+08
Max Volume cell	6.069e+08	1.9197e+09
Total Volume	1.9465e+13	1.9528e+13
Mean Volume	4.0148e+08	5.386e+08
Number of connections	122610	192186
Min num. connections	1	6
Max num. connection	6	25
Min connection area	1141.4	1.0
Max connection area	4.335e+06	7.225e+06

In Figure 9 is shown the distribution of the total volume of gas in place after 10^6 years of simulated injection for the regular grid, 9a, and 3D Voronoi grid, 9b. The two plots were obtained with Paraview. Also a simple visual check of Figure 9, shows that, as expected, a 3D Voronoi grid reproduces a NCG accumulation more localized in structural highs. On the other hand, in structured regular grids the NCG plume is more dispersed.

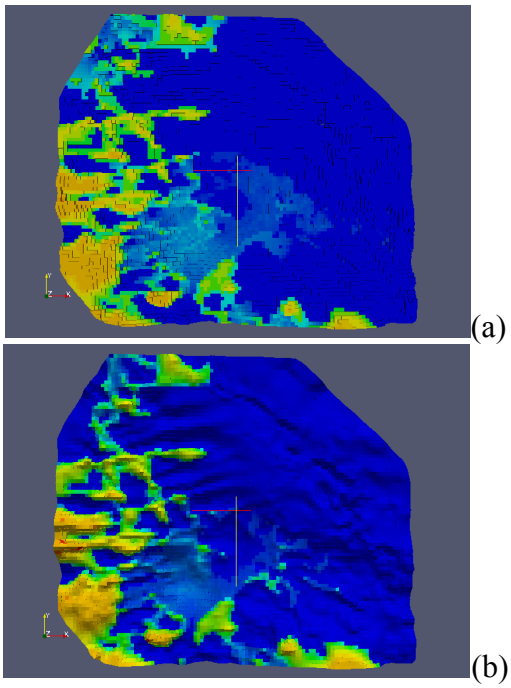

Figure 9 – Top view of non-aqueous phase saturation S_{NA} after 10^6 years of CO_2 injection: (a) regular grid; (b) 3D Voronoi grid, as plotted by Paraview.

In Figure 10a is shown the total volume of injected NCG as function of time. The different trend of the two curves after about 2 10^{13} s, is due to the fact that with the 3D Voronoi grid the NCG reaches the boundary block held at constant conditions earlier than in a regular structured grid. Figure 10b shows the time stepping behavior. Note that to reach 10^6 years, the regular grid required 62,605 time steps against the 88,454 time steps requested by the 3D Voronoi grid. The computation time, using a PC equipped with a processor Intel® Core™ i7-3770K CPU @ 3.50 GHz, with 8 GB RAM, for the 3D Voronoi grid was 182% of that required by the regular grid. The use of 3D Voronoi grids, tends to increase the number of connections and consequently increase the time required to assemble and solve the Jacobian at each Newton-Raphson iteration. The higher number of connections increased also the problems associated to the appearance/disappearance of the non-aqueous (NA) phase present in these simulations.

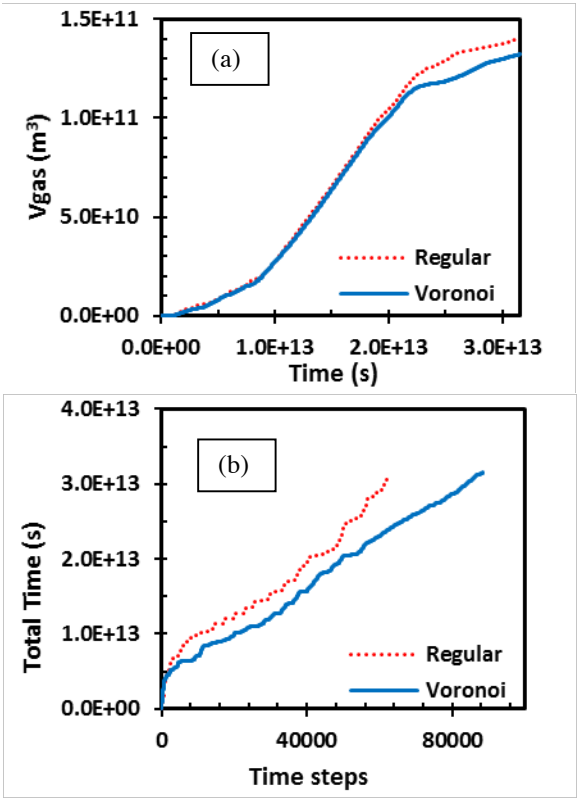

Figure 10: Comparison of simulation results: (a) total volume of gas vs time; (b) time steps vs. total time.

On the other hand using a 3D Voronoi grid, the simulation better reproduces the NCG migration and accumulation patterns within the geological formation studied. In particular, from Figure 8 it appears that the structured regular discretization doesn't allow a good approximation of the shape of geological formations compared with the 3D Voronoi discretization. Therefore, especially in case of two-phase flow, the better reproduction of geological structural highs and closure becomes of great importance as it allows modelling in more realistic way the NCG migration and its accumulation in structural highs.

CONCLUSIONS

The 3D Voronoi approach guarantees to produce grids complying with the IFDM, better reproducing the shapes of geological formations in sedimentary basins. On the other hand, 3D Voronoi grids must be carefully generated because even if considering a simulation volume discretized with a comparable number of blocks as in a regular mesh, the number of connections can dramatically grow, making computationally highly demanding the simulation of the multi-phase flow.

Nevertheless, this work has clearly highlighted that the use of full 3D unstructured grids, respect to the use of structured regular grids, substantially improved both the reproduction of the geological model and a more realistic simulation of fluids migration and accumulation.
However, due to the complexity of the full 3D unstructured grids, they can be effectively adopted only if adequate pre- and post-processing tools are available. VORO2MESH and TOUGH2Viewer have shown to be adequate to manage full 3D unstructured grids, from their creation to results analysis.

ACKNOWLEDGMENTS

This work was performed within the R&D project "Gas Systems" financed and coordinated by eni SpA. The management of eni SpA is acknowledged for the permission to publish the present work.

REFERENCES

Alcott, A., Swenson, D., Hardeman, B., *Using PetraSim to create, execute, and Post-Process TOUGH2 models*, Proceedings of TOUGH Symposium 2006, Lawrence Berkeley National Laboratory, Berkeley, California. May 15-17.

Avis, J., Calder, N.,Walsh, R., 2012. *MVIEW e a powerful pre- and post-processor for TOUGH2*, Proceedings, TOUGH Symposium 2012, Lawrence Berkeley National Laboratory, Berkeley, California. Sept. 17-19 1996.

Barber, C.B., Dobkin, D.P., and Huhdanpaa, H.T., 1996. *The Quickhull algorithm for convex hulls*, ACM Trans. on Mathematical Software, 22(4),469-483, http://www.qhull.org.

Battistelli, A., Marcolini, M. (2009). *TMGAS: a new TOUGH2 EOS module for the numerical simulation of gas mixtures injection in geological structures*, Intl. J. Greenhouse Gas Control, 3, 481-493.

Berry, P., Bonduá, S., Bortolotti, V., Cormio, C., Vasini, E.M., 2014. *A GIS-based open source pre-processor for georesources numerical modeling*, Environmental Modelling & Software, 62, 52-64, ISSN 1364-8152.

Bonduá S., Berry P., Bortolotti V., Cormio C. (2012). *TOUGH2Viewer: A post-processing tool for interactive 3D visualization of locally refined unstructured grids for TOUGH2*, Computers & Geosciences, 46, 107-118, 2012.

Bouvier, J., *Java 3D API Tutorial*, Sun Microsystems Java 3D Engineering Team, 2000.

Croucher, A., *PyTOUGH: a Python scripting library for automating TOUGH2 simulations*, Proceedings of the New Zealand Geothermal Workshop 2011, Auckland, New Zealand, 21-23 November 2011.

Hang Si., *TetGen, a Delaunay-Based Quality Tetrahedral Mesh Generator*, ACM Trans. on Mathematical Software, 41 (2), Article 11 (February 2015), 36 pages, 2015. DOI=10.1145/2629697 http://doi.acm.org/10.1145/2629697.

Li, Y., Niewiadomski, M., Trujillo, E., Sunkavalli, S.P., *Tougher: a user-friendly grafical interface for TOUGHREAC,* Comput. Geosci. 37 (6), 775-782, 2011.

O'Sullivan, M.J., Bullivant, D.P., *A graphical interface to the TOUGH family of flow Simulators*, Proceedings of the TOUGH Workshop 1995, Lawrence Berkeley National Laboratory, Berkeley, California, March 20-22, 1995.

Pan, L., *WinGridder: an interactive grid generator for TOUGH2*, Proceedings, TOUGH Symposium 2003, Lawrence Berkeley National Laboratory, Berkeley, California, May 12-14, 2003.

Pruess, K., C. Oldenburg, and G. Moridis, *TOUGH2 User's Guide, Version 2.0*, Report LBNL-43134, Lawrence Berkeley National Laboratory, Berkeley, Calif., 1999.

Rycroft, C.H, *Voro++: A three-dimensional Voronoi cell library in C++*, Chaos, 19, 041111, 2009.

Sato, T., Ohsato, K., Shiga, T., *G-STAR-BASE (G*BASE). A data base system for underground information and post-processing for TOUGH2*, Proceedings, TOUGH Symposium 2003, Lawrence Berkeley National Laboratory, Berkeley, California. May 12-14, 2003.

Tanaka, T., Itoi, R., *Development of numerical modeling environment for TOUGH2 simulator on the basis of Graphical User Interface (GUI)*, Proc. of the World Geothermal Congress, Bali, Indonesia, April 25-29, 2010.

Wellmann, J.F., Croucher, A., Regenauer-Lieb, K., *Python scripting libraries for subsurface fluid and heat flow simulations with TOUGH2 and SHEMAT*, Comput. Geosci. 43, 197-206, 2012.

Appendix A – Gridded surface file format

The geological surface file (GRASS ASCII) has a header section that describes the location and size of the data, followed by the elevation of the surface points.

The header has 6 lines:

```
north:   xxxxxx.xx
south:   xxxxxx.xx
east:    xxxxxx.xx
west:    xxxxxx.xx
rows:    r
cols:    c
```

The north, south, east, and west field values entered are the coordinates of the edges of the geographic region. The rows and cols field values entered describe the dimensions of the matrix of data to follow. The following are *r* rows of *c*, integer, float or double data.

Example:

```
north: 2000.0
south: 0.0
east:  1000.0
west:  0.0
rows:  21
cols:  11
-700.0 -673.0 -652.0 -637.0 -
 628.0 -625.0 -628.0 -637.0 -
 652.0 -673.0 -700.0
..
```

Appendix B – tough2viewer.dat file format

The geometrical TOUGH2Viewer file has no header. For each block, the data structure is as follows (blank space separated values):

```
id x y z n_vertex
[n_vertex(x,y,z)] n_faces
[n_faces(i_vertex, i_vertex+1,
…)] [n_faces(vx,vy,vz)]
```

where:

Id: integer, block label. Not used.

x y z: block node coordinate

n_vertex: integer: number of block vertexes.

[n_vertex(x,y,z)]: sequence of x, y, z coordinates for each vertex enclosed between bracket. Coordinates are relative to the blocks center node.

n_faces: number of faces of the cell

[n_faces(i_vertex, i_vertex+1, …)]: bracket sequences (one for each face) of integers representing the vertex of each face.

[n_faces (vx, vy, vz)]: for each face, a bracket sequence of double representing normalized vector of the normal to the face.

To generate this file format from voro++, it is necessary to use the following command line options: "%i %q %w %p %s %t %l".
Example, one line for one block (in the following only one line is reported):

```
0 27.4053 27.4053 -202.79 10 (-
27.4053,-4.62727,-83.8273)
(80.8347,-27.4053,-33.616) (-
27.4053,-27.4053,198.378)
(61.7832,61.7832,10.0153) (-
27.4053,80.8347,-33.616)
(13.0548,72.5947,-14.6858)
(72.5947,13.0548,-14.6858)
(61.2534,61.2534,6.96889) (-
5.43639,-27.4053,-84.3027) (-
27.4053,-27.4053,-92.4444) 8
(1,6,7,5,4,0,8) (1,2,3,6)
(1,8,9,2) (2,4,5,3) (2,9,0,4)
(3,7,6) (3,5,7) (8,0,9)
(0.451894,0.451894,-0.769145)
(0.906139,-0.0132613,0.422771)
(3.18904e-016,-1,1.22161e-017)
(-0.0132613,0.906139,0.422771)
(-1,9.51153e-016,-1.68966e-015)
(0.924535,0.314346,-0.215455)
(0.314346,0.924535,-0.215455)
(0.327509,0.334319,-0.883724).
```

GENERATING ONE-COLUMN GRIDS WITH FRACTAL FLOW DIMENSION

Christine Doughty

Earth Sciences Division
Lawrence Berkeley National Laboratory
#1 Cyclotron Rd
Berkeley, California, USA 94720
email: CADoughty@lbl.gov

ABSTRACT

The grid generation algorithm of MESHMAKER for creating one-column grids with linear or radial geometry is generalized to create one-column grids with fractal (non-integer) flow dimension. Such grids are useful for representing flow through fracture networks or highly heterogeneous geologic media with fractal geometry. The fractal grid generation method is verified by comparing numerical simulation results to an analytical solution for a generalized Theis solution for integer and non-integer dimensions between 1 and 3. It is then applied to examine gas production decline curves from a hydraulically fractured shale that is modeled as a fractal-dimensioned fracture network.

INTRODUCTION

TOUGH2 uses the integral-finite-difference method (Narasimhan and Witherspoon, 1976) for spatial discretization. In this method, the volumes of grid blocks and the areas of interfaces between grid blocks are specified, without reference to a global coordinate system. This feature enables creation of one-column grids that can represent

- linear flow geometry (all grid blocks have equal volumes and interface areas),
- radial flow geometry (grid-block volume increases in proportion to r^2 while interface area increases in proportion to r),
- spherical flow (volume increases in proportion to r^3 while area increases in proportion to r^2),

where r is the distance from the origin of the grid to a given grid block.

Linear and radial grids are familiar to most TOUGH users and can be created automatically using the MESHMAKER module. The MESHMAKER grid generation algorithm can be generalized to non-integer flow dimensions (i.e., fractal dimensions). For a flow dimension d ($0 < d \leq 3$), one can create a one-column grid to represent d-dimensional flow simply by making grid-block volume proportional to r^d and interface area proportional to r^{d-1}.

This paper is organized as follows. First, we review and illustrate the concept of fractal flow dimension in the context of flow through fracture networks or heterogeneous porous media. We then describe the fractal grid generation method and show examples of its use for two problems. The first problem compares numerical simulation results to an analytical solution for a generalized Theis solution (Barker, 1988) and serves to verify that the created grid does possess the desired fractal flow dimension. The second problem considers gas production from a hydraulically fractured shale, and illustrates how the early-time slope of the pressure decline curve can be related to the fractal flow dimension.

THE CONCEPT OF FRACTAL FLOW DIMENSION FOR GEOLOGIC MEDIA

A fractal dimension is simply a non-integer dimension. The usual concept of a spatial domain being 1-, 2-, or 3-dimensional can be generalized to allow d-dimensional spaces, where d need not be an integer. In the present paper we distinguish between the intrinsic fractal dimension of a geologic medium, d_i, and the fractal flow dimension, d, that describes flow through the medium to a particular source or sink, with the latter being the relevant dimension for grid generation.

To understand the intrinsic fractal dimension, it is helpful to first consider the usual integer dimensions. Two examples of media with $d_i = 3$ are a thick body of uniform sand, and a highly connected fracture network. In contrast, an extensive thin sand body over- and underlain by low permeability clay, and an isolated fracture plane are examples of media with $d_i = 2$. An intrinsic fractal dimension between 2 and 3 can be useful to describe the intermediate cases between these two extremes: thin sand bodies only partially isolated by clay lenses, and anisotropic fracture networks with great connectivity in two directions and sparse connectivity in the other direction. Similarly, a tube-like channel of high permeability is an example of a medium with $d_i = 1$. A sparsely connected network of tubes could be described by a fractal dimension d_i between 1 and 2. Altogether, we can imagine a variety of geologic media with intrinsic fractal dimensions ranging from 1 to 3.

However, when considering the dimension that the fluid flow field will have in these media, we need to consider not only the intrinsic fractal dimension of the medium but also the source or sink of fluid. The simplest case is a point source or sink, in which case $d = d_i$. Fractal flow dimension can range from 1 to 3, with $d = 3$ corresponding to a uniform medium surrounding the point, $d = 2$ corresponding to a planar feature surrounding the point, $d = 1$ representing a tube-like channel ending at the point, and all values of d between 1 and 3 possible to represent intermediately connected structures.

Next is the case of a line source or sink, the familiar representation of a well fully penetrating a formation. For a uniform medium with $d_i = 3$, the flow dimension will be 2: radial flow toward the well. For a uniform planar feature with $d_i = 2$ that is aligned with the well, the flow dimension will be 1: linear flow toward the well. Generally, for a line source with uniform flow along the whole line, $d = d_i - 1$. In particular, if the flow feature has intrinsic fractal dimension less than 2, then the fractal flow dimension will be less than 1, which represents flow that must diverge from the flow feature to the well. In contrast, if flow is not uniform along the line source (e.g., a short perforated interval along a long well), then flow from the medium will converge to the perforated interval, yielding a fractal flow dimension $d > 2$.

Finally, consider a plane source or sink. For a uniform medium with $d_i = 3$, the flow dimension will be 1: linear flow toward the plane. For a flow feature with intrinsic fractal dimension $d_i < 3$, the fractal flow dimension will be less than 1, again representing diverging flow to the plane. In contrast, if only localized regions of the plane are permeable, then flow from the medium will converge to those parts of the plane, yielding a fractal flow dimension $d > 1$.

FRACTAL GRID GENERATION METHODOLOGY

The essential concept to create a one-column grid with fractal dimension d is to set grid-block volume proportional to r^d and interface area proportional to r^{d-1}, where r is the distance from the origin of the grid to a given grid block. One additional feature to consider is how to define the volume and area of the first block of the grid, which represents the fluid source or sink.

For consistency in comparing grids with different values of d, we usually require that the area of the first grid block, which is the source/rock interface, be the same for all dimensions (an alternative definition will be discussed for the second example problem, described in Section 5). This area is denoted A_w.

For $d = 2$, a line source representing a well,

$$A_w = 2\pi r_w b, \qquad (1)$$

where r_w is the well radius and b is the thickness of the layer penetrated by the well.

For $d = 3$, a point source of radius r_w,

$$A_w = 4\pi r_w^2. \qquad (2)$$

The values of A_w will be the same for $d = 2$ and $d = 3$ if we set $b = 2r_w$. Note that for a one-column grid, there is no loss of generality in defining b this way. For $d = 3$, there is no b in the problem, and for $d < 3$, we can think of b as a unit thickness and scale injection rate to account for thicker or thinner models. We apply the definition $A_w = 4\pi r_w^2$ to all values of d.

Combining the concept that $A \sim r^{d-1}$ and the requirement that $A_w = 4\pi r_w^2$, yields a prescription for A as a function of r for all values of d:

$$A(r) = 4\pi r_w^{3-d} r^{d-1}. \quad (3)$$

Or in the discrete notation of a grid, for the ith grid block, with outer radius r_i

$$A_i = 4\pi r_1^{3-d} r_i^{d-1}, \quad (4)$$

where $r_1 = r_w$. To determine gird-block volume, V_i, we integrate the expression for A_i from r_{i-1} to r_i, yielding

$$V_i = \frac{4\pi r_1^{3-d}}{d}\left(r_i^d - r_{i-1}^d\right). \quad (5)$$

VERIFICATION AGAINST BARKER'S GENERALIZED THEIS SOLUTION

Barker (1988) developed analytical solutions for the pressure-transient response to hydraulic tests in fractured rock with flow dimension ranging from 1 to 3, including non-integer dimensions. Figure 1 shows a schematic view of his conceptual model for integer dimensions.

For a constant volumetric injection rate Q into an infinite medium, Barker found that the pressure change may be expressed as

$$\Delta P = \frac{Q\mu r^{2\nu}}{4\pi^{1-\nu} k (2r_w)^{3-d}} \Gamma(-\nu, u) \quad (6)$$

where $\Gamma(-\nu,u)$ is the complementary incomplete gamma function, $\nu = 1 - d/2$, and

$$u = \frac{\phi C \mu r^2}{4kt}. \quad (7)$$

The dimensionless parameter u is related to dimensionless time t_D as $u = 1/(4t_D)$. Medium properties are porosity ϕ, permeability k, and compressibility C, and μ is fluid viscosity.

Figure 2 shows Γ as a function of t_D. For $d < 2$, for long times the solution becomes linear with slope ν, where $\nu = 1 - d/2$. For $d = 2$, $\Gamma(0,u)$ is identical to the exponential integral $E_1(u)$ of the Theis solution.

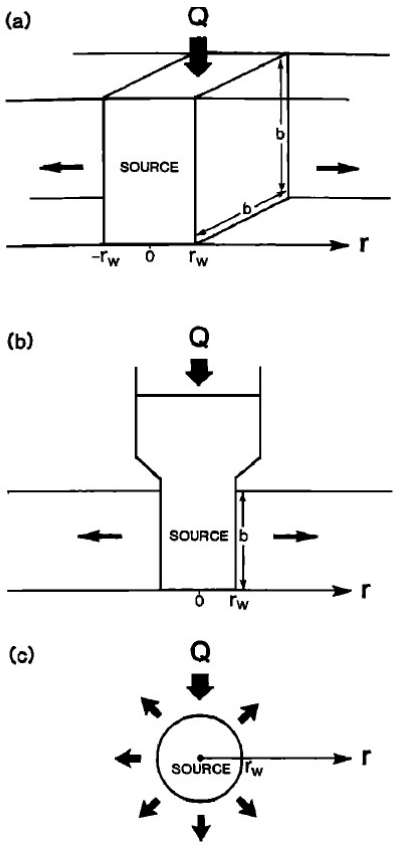

Figure 1. Schematic well tests for (a) $d = 1$ with a plane source, (b) $d = 2$ with a line source, and (c) $d = 3$ with a point source. Modified from Barker (1988).

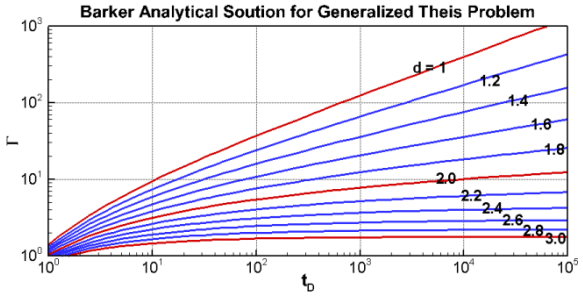

Figure 2. Barker (1988) analytical solution, where d is fractal flow dimension. For $d < 2$, the late-time slope is $\nu = 1 - d/2$.

Figure 3 shows the results of isothermal TOUGH simulations using EOS1 for single-phase water at 20°C initially at 1 bar, with constant-rate injection of water, for one-column grids created with values of d ranging from 0.4 to 3. The grids all begin with a source with r_w = 0.1 m, and contain 100 elements with steadily increasing radial increments (increase factor 1.1), to allow good near-well resolution, but a grid that extends far enough from the well for

the medium to be infinite-acting. Injection rate is kept small enough so that density does not change significantly, to conform to the assumptions for the analytical solution. The late-time slopes for $d < 2$ show the expected slope $\nu = 1 - d/2$, indicating that the mesh correctly represents fractal flow geometry.

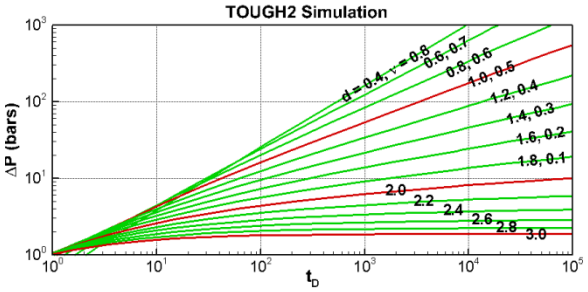

Figure 3. TOUGH2 simulation results for Barker (1988) generalized Theis problem. The first number on each curve is the fractal flow dimension d and the second number (when $d < 2$) is the late-time slope ν.

To compare the solutions in detail, we must correct for the different assumptions made for A_w when $d = 1$ by Barker ($A_w = 2b^2$) and by the fractal grid generator ($A_w = 4\pi r_w^2 = \pi b^2$). Recall from Darcy's law that for a given volumetric flow rate, pressure change is inversely proportional to the cross-sectional area through with flow occurs. Since for $d = 1$ the fractal grid generator A_w is $\pi/2$ times bigger than the Barker A_w, we need to multiply the simulated pressure change for $d = 1$ by $\pi/2$ to compare to Barker's analytical solution. Both methods assume the same value of A_w for $d = 2$ and $d = 3$, so we need a correction that is fully invoked for $d = 1$, makes no change for $d \geq 2$, and also does the right thing for $1 < d < 2$. This can be accomplished by multiplying the simulated pressure change by $(\pi/2)^{(2-d)}$ for all values of $d < 2$. This correction shifts the curves but does not alter their slope. The shifted numerically simulated results match the analytical solution (Figure 4), except at very early times, where the analytical solution's assumption of a vanishingly small wellbore is not met by the numerical solution.

Note that Barker presents his analytical solution only for the range $1 \leq d \leq 3$ (Barker, 1988, Figure 2), but that mathematically, it also holds for $0 < d < 1$. Figure 4 confirms that it also agrees with the TOUGH simulation results for this extended range of d, if the correction factor $(\pi/2)^{(2-d)}$ is applied.

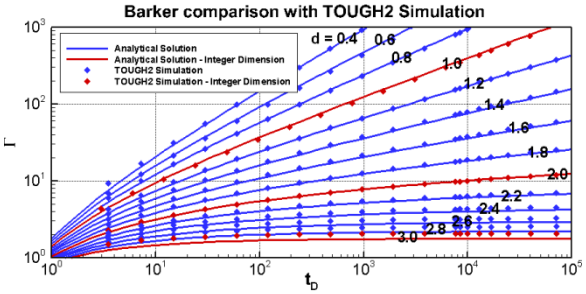

Figure 4. Comparison of Barker (1988) analytical solution and TOUGH2 simulation results for fractal flow dimension ranging from 0.4 to 3. TOUGH2 results for $d < 2$ have been shifted, to account for different assumptions about A_w when $d = 1$.

APPLICATION TO GAS PRODUCTION FROM HYDRAULICALLY FRACTURED SHALE

A typical conceptual model for gas production from a hydraulically fractured shale is illustrated in Figure 5, which shows several fracture stages along a horizontal well (Figure 5a). Each fracture stage (Figure 5b) consists of a stimulated reservoir volume (SRV) of thickness $2D$, consisting of a planar primary fracture of areal extent A perpendicular to the wellbore and a network of smaller secondary fractures orthogonal to the primary fracture. It is assumed that for a tight gas reservoir, production only occurs from the SRV. Additionally, it is assumed that the permeability of the primary fracture is so great that the pressure in the primary fracture is uniform and equals the pressure in the well. Although the fracture network making up the SRV will likely be irregular (as illustrated schematically in Figure 5b), it is assumed that flow through it toward the primary fracture can be modeled with a single value of fractal flow dimension.

The fluid is assumed to be single-phase, constant-compressibility gas, which flows according to Darcy's law. The system is assumed to remain at constant temperature. Initially, the gas in the reservoir and the well is at a constant pressure, p_R; at time zero the pressure at the well is dropped to p_W, where it is held constant during the production process.

With the assumption that fractal flow dimension of the SRV is d =1, the early-time production decline (before the effect of the no-flow boundary a distance D away from the primary fracture is felt) is linear on a log-log plot, with a slope -1/2 (Silin and Kneafsey, 2012). The assumption that d = 1 implies that gas flows uniformly through the SRV toward a planar primary fracture with uniform high permeability, as illustrated schematically in Figure 6b. Gas flow to the primary fracture has linear flow geometry, and this flow is uniform over the entire area of the fracture.

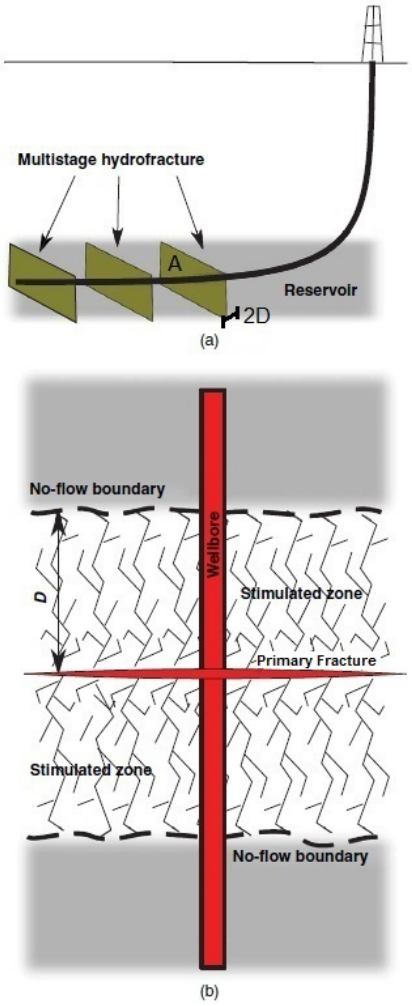

Figure 5. Schematic of the idealized hydraulic fracture problem (modified from Silin and Kneafsey, 2012).

However, if one considers a non-uniform primary fracture, with localized regions of high permeability, it is possible to imagine flow from the SRV converging to these portions of the fracture, yielding d > 1 (Figures 6c and 6d). In the extreme case of just one point on the primary fracture providing high permeability, with spherically symmetric flow from the SRV entering the facture at that one point, one would have d = 3. If quasi-linear regions of the primary fracture provided high permeability, with radial flow from the SRV entering the fracture along those lines, then one would have d = 2 (Figure 6d). Different patterns of localized high permeability in the primary fracture could produce non-integer values of $1 < d < 2$ (Figure 6c). On the other hand, if the primary fracture had uniform, high permeability, but flow paths through the SRV were limited due to a sparse or poorly connected fracture network, then d < 1 would also be possible (Figure 6a).

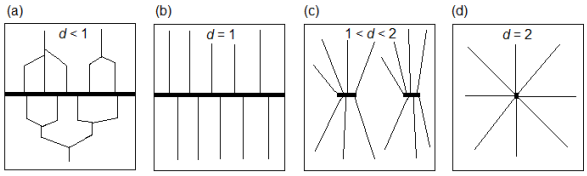

Figure 6. Schematic diagrams of flow from the fracture network (thin lines) to high-permeability regions of the primary fracture (thick lines), showing (a) diverging geometry for d < 1, (b) linear geometry for d = 1, (c) slightly converging geometry for $1 < d < 2$, and (d) strongly converging geometry for d = 2. The plots show a cross section perpendicular to the plane of the primary fracture.

Thus, we want to be able to analyze stimulated reservoir volumes (SRVs) in which the fracture network has a fractal flow dimension ranging from less than one to more than two. The essential difference between d < 1 and d > 1 is that for d < 1, there is a diverging geometry for the flow from the fracture network to the primary fracture, and for d > 1, there is a converging geometry.

A series of numerical simulations was done with TOUGH2 using the equation of state module EOS7C (Oldenburg et al., 2004) to investigate gas production from a hydraulically fractured medium, for a range of flow dimensions for the network of fractures making up the SRV and the primary hydraulic fracture. Grids with d = 0.25, 0.5, 0.75, 1, 1.25, 1.5, 2, 2.5, and 3 were created to model gas production from the SRV. One end of the one-column grid (r = 0) is the planar primary fracture and the opposite end (r = D) is

a no-flow boundary, to represent the outer limit of the SRV, beyond which permeability is assumed to be negligible. The length of the column (D = 150 m) and the number of grid blocks (300) are the same for each grid.

In keeping with the conceptual model illustrated in Figure 6, for $d \leq 1$, the area of the primary fracture (A_w) is equal to the area of the SRV, A, and area decreases as r increases, to represent a sparse fracture network, according to Equation (4). In contrast, for $d > 1$, the area at $r = D$ is set at A, and area decreases proportional to r^{d-1} as r decreases, to represent flow converging to the heterogeneous primary fracture, yielding

$$A_w = A r_w^{d-1} / D^{d-1}. \quad (8)$$

Simulation results (Figure 7) indicate that the early-time production rate is linear with a slope of -½ on a log-log plot for d = 1, which is consistent with many studies of shale-gas production (e.g., Silin and Kneafsey, 2012; Patzek et al., 2013; Lunati and Lee, 2014). For d < 1, we find production rate is linear with a slope $-\nu$, where $\nu = 1 - d/2$, similar to the Barker problem. For $d > 1$, the relationship between ν and d is not so simple, but it can be fit with a quadratic expression

$$\nu = 0.1195(3\text{-}d)^2 + 0.026. \quad (9)$$

Production decline data measured in the field (Figure 8) often show linear trends with a range of slopes, not just -½, at early times, and numerical simulations using fractal-dimension grids can be used to infer fractal flow dimension of the SRV from production data. Because the relationship between slope $-\nu$ and dimension d is quite simple, doing such an inversion will yield a unique value of d for an observed value of ν. However that does not mean that a unique description of the SRV has been obtained. Other authors (e.g., Olorode et al., 2012; Cinco-Ley and Samaniego, 1981) have hypothesized entirely different, non-fractal geometries for the primary fracture/secondary fracture network components of the SRV and also obtained early-time slopes different from -½.

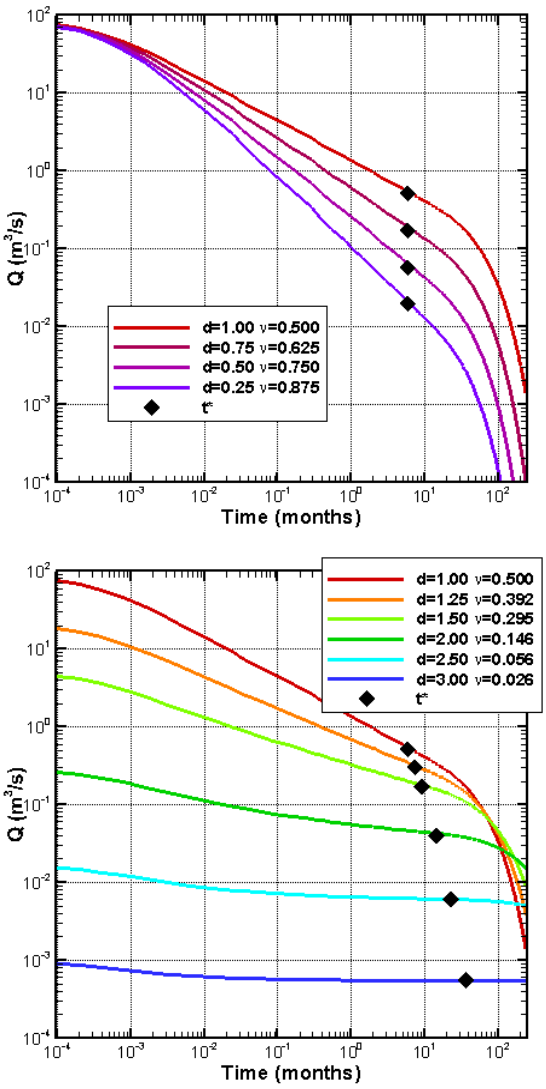

Figure 7. TOUGH2 simulation results showing production rate versus time for the hydraulic fracture problem. The black diamond shows the time at which the outer boundary of the SRV is felt.

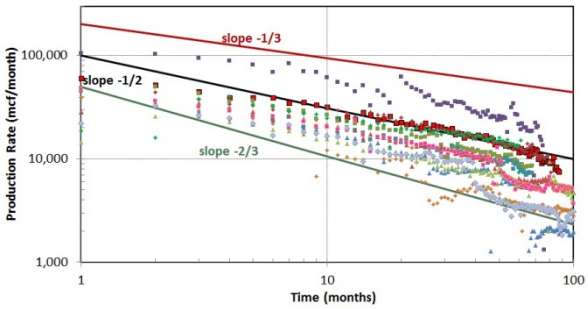

Figure 8. Production decline data (symbols) from shale-gas wells (Texas Railroad Commission data). Log-log slopes of -1/3, -1/2, and -2/3 are also shown (lines).

CONCLUSIONS

The integral finite difference formulation of TOUGH2 makes it straightforward to create one-column grids with fractal (non-integer) flow dimension. Such grids can be used to study fluid flow through geologic media with fractal dimension, and may be particularly useful in inverse methods, where pressure transient or production rate data are available, in order to infer the fractal dimension of the geologic medium.

ACKNOWLEDGMENT

This work was performed at Lawrence Berkeley National Laboratory of the US department of Energy (DOE) under Contract No. DE-AC02-05CH11231. It was funded by the Research Partnership to Secure Energy for America (RPSEA) through the Ultra-Deepwater and Unconventional Natural Gas and Other Petroleum Resources program authorized by the US Energy Policy Act of 2005. RPSEA is a non-profit corporation whose mission is to provide a stewardship role in ensuring the focused research, development, and deployment of safe and environmentally responsible technology that can effectively deliver hydrocarbons from domestic resources to the citizens of the US. RPSEA, operating as a consortium of premier US energy research universities, industry, and independent research organizations, manages the program under a contract with DOE's National Energy Technology Laboratory.

REFERENCES

Barker, J.A., A generalized radial flow model for hydraulic tests in fractured rock, *Water Resources Research*, 24(10), 1796-1804, 1988.

Cinco-Ley, H. and F. Samaniego, Transient pressure analysis for fractured wells, SPE 7490, *Journal of Petroleum Technology*, 33, 1749-1766, September 1981.

Lunati, I. and S.H. Lee, A dual-tube model for gas dynamics in fractured nanoporous shale formations, *Journal of Fluid Mechanics*, 757, 943-971, 2014.

Narasimhan, T.N. and P.A. Witherspoon, An integrated finite difference method for analyzing fluid flow in porous media, *Water Resources Research*, 12(1), 57 – 64, 1976.

Oldenburg, C.O., G.J. Moridis, N. Spycher, and K. Pruess, EOS7C Version 1.0: TOUGH2 module for carbon dioxide or nitrogen in natural gas (methane) reservoirs, Rep. LBNL-56589, Lawrence Berkeley National Laboratory, Berkeley, CA, 2004.

Olorode, O.M., C.M. Freeman, G.J. Moridis, and T.A. Blasingame, High-resolution numerical modeling of complex and irregular fracture patterns in shale gas and tight gas reservoirs, SPE 152482, presented at SPE Latin American and Caribbean Petroleum Engineering Conference, Mexico City, Mexico, 16-18, April 2012.

Patzek, T.W., F. Male, and M. Marder, Gas production in the Barnett Shale obeys a simple scaling theory, *Proceedings, National Academy of Science*, 110(49), 19731-19736, 2013.

Silin, D. and T. Kneafsey, Shale gas: nanometer-scale observations and well modelling, SPE 775 149489, *J. Canadian Petroleum Technology*, 464-475, November 2012.

UNSTRUCTURED 3D MESH GENERATION FOR GEOLOGICAL APPLICATIONS USING LaGriT

Carl W Gable[1]
Manuel Lorenzo Sentís[2]

[1]Computational Earth Science, Earth & Environmental Sciences
Los Alamos Natl. Lab.
gable@lanl.gov

[2] Section Disposal and Analysis
Swiss Federal Nuclear Safety Inspectorate, ENSI
Manuel.Sentis@ensi.ch

ABSTRACT

There are many applications in science and engineering modeling where accurate representation of complex geometry is important. In applications of flow and transport in subsurface porous media this is manifest in models that must capture complex geologic stratigraphy, structure (faults, folds, erosion, deposition) and infrastructure (tunnels, boreholes, excavations). Model setup, defined as the activities of geometry definition, mesh generation (creation, optimization, modification, refining, de-refining, smoothing) and assigning material properties, initial conditions and boundary conditions requires specialized software tools to automate and streamline the process. Also, some model setup tools will provide more utility if they are optimized to interface with and meet the needs of a particular flow and transport software suite. For example, the TOUGH2 (Pruess et al., 1997) code, as well as other well known codes (MODFLOW-USG, PFLOTRAN, FEHM) use a control volume discretization that is most accurate when the underlying control volumes are 2D or 3D Voronoi tessellations.

INTRODUCTION

The continuous increase of computer performance has made it possible to simulate numerically more complicated representations of the reality. In the groundwater field these models include extended representations of complicated stratigraphy (sloping layers, etc.) or complex geologic structures like faults, folds, erosion and deposition. It is also possible to represent complex man-made underground structures such as wells and tunnels for deep geological repositories, CO_2 sequestration, reservoir and geothermal systems. Huge three-dimensional numerical models for potential underground repository sites are used more and more frequently for the evaluation of water flow and potential contaminant transport in the subsurface (Senger, 2008;, Enssle, 2012; Zhang 2011; Poller, 2011).

Hand in hand with improvements in computer performance, many developments have been made in the numerical methods, the discretization methods and software tools used to describe and solve these challenging models. In this report we will concentrate on the discretization of complex models with the software tools in LaGriT, Los Alamos Gridding Toolbox. The LaGriT mesh generation and model setup software package, which is freely available (http://lagrit.lanl.gov), has been developed with geologic applications and Voronoi control volume solvers as the target application.

We provide an overview of some of the key capabilities of the mesh generation and model setup modules and present applications taken from a range of geologic applications such as the modelling with TOUGH2 within the FORGE (Fate Of Repository Gases) Project of gas migration in a geological repository for radioactive waste. The benchmark within the FORGE project includes a complex geometry of 100 waste tunnels and multiple drifts as well as waste package, backfill and a damage zone associated with each waste tunnel. We will present the approach used to build this geometri-

cally complex model and present results from a two-phase TOUGH2 (Pruess et al., 1999) flow model.

Examples from other applications, such as discrete fracture networks (thousands of intersecting 2D polygons in 3D space), CO_2 capture and storage, environmental monitoring at the former Nevada Test Site (complex sedimentary and volcanic stratigraphy with hundreds of nuclear detonation cavities) will also be discussed. We will also discuss some of the trade-offs in ease of mesh generation with model solution accuracy when one relaxes the desirable orthogonally properties of Voronoi tessellations as the basis of computational control volumes.

LaGrit

LaGriT (http://lagrit.lanl.gov) is a library of user callable tools that provide mesh generation, mesh optimization and dynamic mesh maintenance in one, two and three dimensions for a variety of applications. The program LaGriT is developed by Los Alamos National Laboratory. A variety of techniques for distributing points within these geometric regions are provided. Mesh generation is generally based on (2D and 3D) Delaunay triangulation algorithms that can optionally conform to complex geometry and internal material interfaces. The data structures created to implement the algorithms are compact, powerful and expandable to include hybrid meshes (tet, hex, prism, pyramid, quadrilateral, triangle, line); however, the main algorithms are for triangle and tetrahedral meshes. A prescribed material is assigned to each region of the model and the mesh elements inherit the material properties of the region they belong to.

The Swiss Federal Nuclear Safety Inspectorate has utilized the meshing and model setup capabilities of LaGriT in modelling work within the FORGE (Fate of Repository Gases, 2009-2013) project. The second benchmark of FORGE dealt with a complex model of a generic deep geological repository including many tunnels, drifts and materials. The analysis of different preprocessing programs for TOUGH2 listed in the TOUGH2 website (http://esd1.lbl.gov/research/projects/tough/software/processors.html) for such complex geometries showed the versatility of LaGriT.

EXAMPLES OF APPLICATIONS OF LAGRIT

In this section different examples will be shown of the application of LaGriT to create grids for complex geologic geometries.

Mesh Generation for Yucca Mountain

In Figure 1 a geological model of a cross section at Yucca Mountain is shown. In this example the representation of the layers in the small grey rectangle will be discussed.

The advantages of using an unstructured mesh were analyzed during the Yucca Mountain project for a deep geological repository.

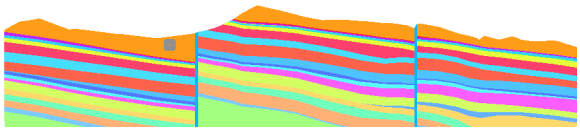

Figure 1: Geological model of a cross section at Yucca Mountain.

In Figure 2 a mesh with adaptive refinement to features is accomplished using a quadtree refinement algorithms. The mesh is shown with 31,428 elements. The mesh resolution is adapted here to the geometry of interest. In cases where a physics solver is not able to utilize the quadtree type mesh the quadrilateral mesh can be converted to a triangular mesh or a Voronoi mesh.

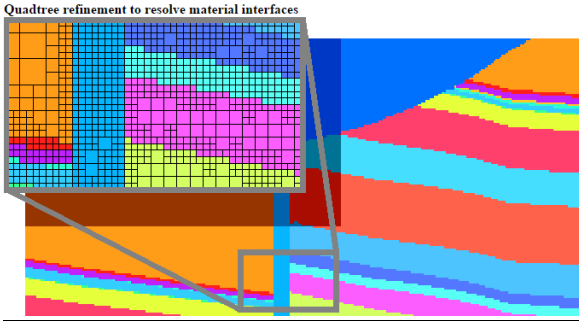

Figure 2: Structured quad-tree mesh.

In Figure 3 the mesh is unstructured with 7,880 triangular elements, whose position cannot be defined in a systematic way and whose connectivity is more arbitrary, for example the nodes have a varying number of triangles attached to them. This unstructured approach, however, allows us to create meshes that actually conform to the mountain's varied material interfaces.

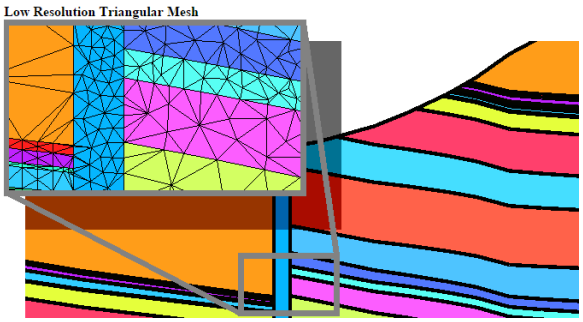

Figure 3: Low-resolution unstructured triangular mesh.

Comparing Figure 2 and Figure 3 it can be seen that with four times fewer elements the geological interfaces are still better represented with the unstructured mesh. The refinement can be increased everywhere or only in particular regions of interest, resulting in a mesh with more elements as shown in Figure 4 with a mesh of 31,520 elements.

The simple ideas illustrated with quadtree meshing and triangle meshing can be extended to 3D using octree meshing and tetrahedral meshing.

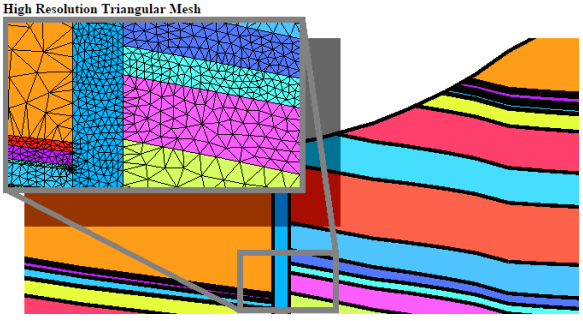

Figure 4: High-resolution unstructured triangular mesh.

Calculations with TOUGH2 for the FORGE Project

The FORGE project modeling exercise and the flow and transport software TOUGH2-MP was chosen as an example of the application of LaGriT to create an unstructured grid. In FORGE the generation and transport of gas in different materials was analyzed (https://www.bgs.ac.uk/forge/). Within FORGE benchmark exercises were defined to compare the results of gas transport between different programs (Wendling, 2010).

Geometric model

In one of the benchmarks of FORGE a generic repository with 50 waste emplacement cells on each side of the access drift and a main drift to connect to the rest of the modules is prescribed. The cross section of the waste and bentonite plugs in the cells is circular and surrounding these elements there is a 0.5 m thick circular ring representing the excavation disturbed zone (EDZ). The cross section of the access drift and main drift is square and is surrounded by a 1 m thick EDZ.

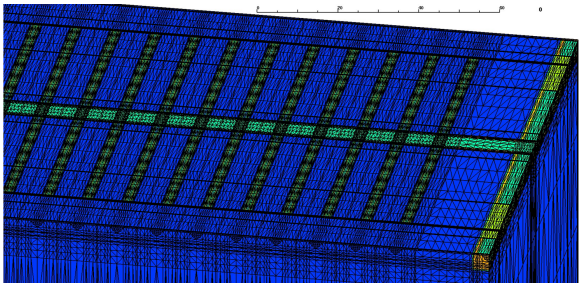

Figure 5: Illustration of the discretization of the model along the emplacement tunnels.

A detail of the cross sections of the model is shown in Figure 6. The mesh representing the geometry and distinct materials has been created with precise circular and square meshes of the correct dimension embedded in the same model.

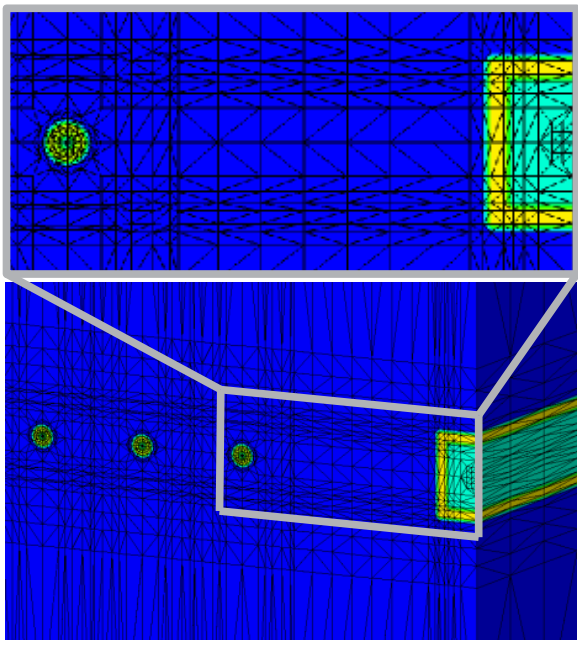

Figure 6: Illustration of the discretization of the model in a cross sectional area.

Generation of the mesh

The procedure for defining the mesh for TOUGH2 consists of several steps. In a first step the program LaGrit is used to create a tetrahedral mesh. The vertices are distributed following geometrical patterns (Cartesian or cylindrical distribution, etc.). Afterwards these distributions of vertices can be combined using different operations (addition, subtraction, union, intersection). The vertices can be translated in a modular way allowing one to build a precise representation of just one tunnel and then use translation, rotation and reflection to create the 100 tunnels. Once the vertices are defined LaGriT calculates the corresponding Delaunay tetrahedral mesh. In a second TOUGH2 specific step, all this information is processed in order to obtain the geometric parameters that are needed for TOUGH2 control volume solution that uses two-point fluxes computed on the dual Voronoi tessellation of the Delaunay mesh. Some of the parameters are already available as output of LaGriT, while other parameters (like the distances or the cosines) have to be calculated. A subroutine Lagrit2Tough2 processes and calculates these parameters and creates a TOUGH2 compatible input. The resulting TOUGH2 input contains the geometry coefficients (control volume, area of each control volume face, length of each connection of the mesh edge graph, angle between edge connection and vertical gravity vector) and must be augmented with other TOUGH2 input specifications (material properties, times, boundary conditions).

Some results

In the FORGE benchmark (Wendling, 2010) several calculations were defined and parameters like mass flow, pressure, concentrations, saturations were prescribed in different locations of the model. The mesh generated with LaGriT was used for the calculations with TOUGH2. In this section some results of these calculations are compared with the calculations performed also with TOUGH2 but with another mesh generator. For the results of this benchmark using the combination LaGriT TOUGH2 the reader is referred to Sentis (2015). For a detailed evaluation of the benchmark the reader is referred to Wendling (2013).

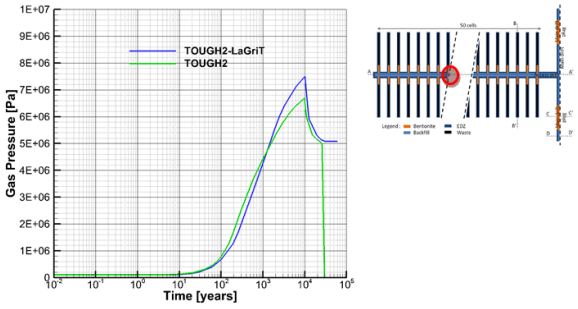

Figure 7 Results for the gas pressure within the red circle in the middle of the model.

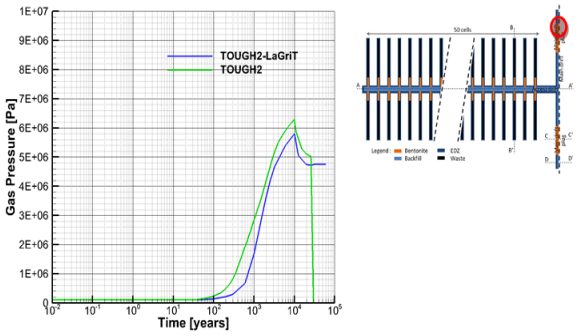

Figure 8: Results for the gas pressure within the red circle in the lateral end of the model.

Stratigraphy, Faults and Tunnels in a 3D Geological Mesh

The next example illustrates meshing strategies to capture a range of geometric features such as stratigraphy, faults and tunnels for flow and transport modeling work in the former Nevada Test Site. In this example stratigraphy and structure (faults) are resolved by progressively and locally refining volumes of the mesh by factors of two until the geometric complexity of model is resolved. The center image shows the full model volume, the upper image shows the Delaunay tetrahedral mesh and the lower image shows the Voronoi control volumes used for calculations. In addition the interior of the model can be refined to resolve tunnels that exist within the interior of the volume. Once the mesh is refined sufficiently to resolve the features of interest, material properties can be assigned to the mesh cells to represent material properties associated with the various features.

a)

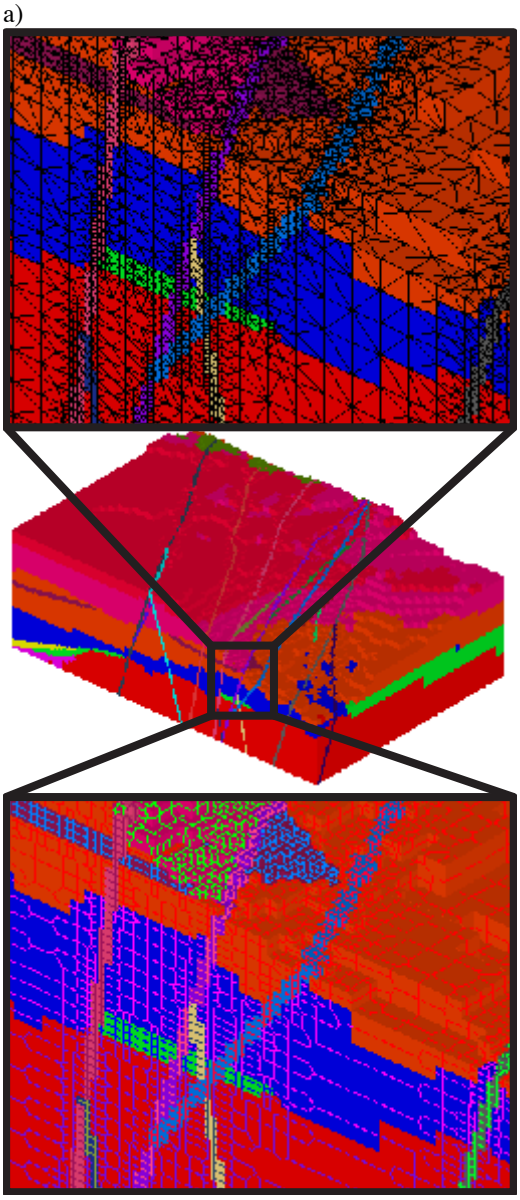

b)

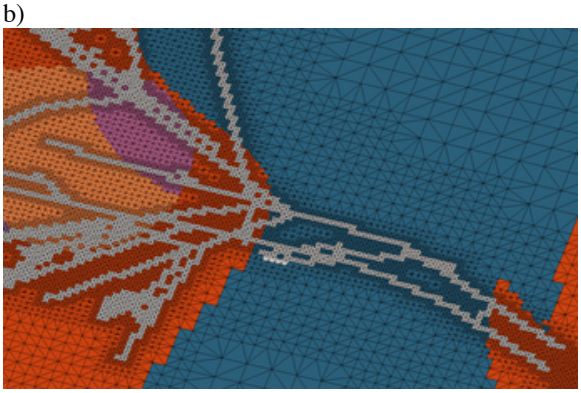

Figure 9: a) Delaunay and Voronoi meshes for a complex stratigraphy structure (faults and stratigraphy) and b) infrastructure (tunnels).

ACKNOWLEDGMENT

The research related to the project FORGE in this report has received funding from the European Atomic Energy Community's Seventh Framework Programme (FP7/2007-2011) under Grant Agreement no230357, the FORGE project.

REFERENCES

Enssle, C. P., J. Croisé, A. Poller, G. Mayer, J. Wendling, *Full scale 3D-modelling of the coupled gas migration and heat dissipation in a planned repository for radioactive waste in the Callovo-Oxfordian clay*. Physics and Chemistry of the Earth, doi: 10.1016/j.pce.2011.07.033 (2011).

Finite Element Heat and Mass Transfer Code (FEHM), Los Alamos National Laboratory, <http://fehm.lanl.gov>, 2015.

Los Alamos Grid Toolbox, LaGriT, Los Alamos National Laboratory, <http://lagrit.lanl.gov>, 2015.

McDonald, M.G., and Harbaugh, A.W. (1988). A modular three-dimensional finite-difference ground-water flow model (PDF). Techniques of Water-Resources Investigations, Book 6. U.S. Geological Survey.

MODFLOW-USG, http://water.usgs.gov/ogw/mfusg, 2015.

PFLOTRAN, <http://pflotran.org>, 2015.

Poller, A., C.P. Enssle, G. Mayer, J. Croisé, J. Wendling, *Repository-scale modeling of the long-term hydraulic perturbation induced by gas and heat generation in a geological repository for high- and intermediate-level radioactive waste: methodology and example of application,* Transport in porous media, doi: 10.1007/s11242-001-9725-x (2011).

Pruess, K., C. Oldenburg, and G. Moridis, *TOUGH2 User's Guide, Version 2.0*, Report LBNL-43134, Lawrence Berkeley National Laboratory, Berkeley, Calif., 1999.

Pruess, K., S. Finsterle, G. Moridis, C. Oldenburg and Y.-S. Wu, *General-purpose reservoir simulators: the TOUGH2 family*, GRC Bulletin, 53–57. February 1997.

Senger, R., K. Zhang, J. Avis, P. Marshall, *Three-dimensional modeling of gas migration in a deep low/intermediate level waste repository* (Switzerland). Proc. XVII Int. Conf. Computational Methods in Water Resources, San Francisco, California, July 6-10, 2008.

Sentis, M. L., C. Gable, *Two-phase flow modelling of a 3D deep geological repository within the second benchmark of the FORGE project,* submitted for publication in *Nuclear Technology* this year.

Sentis, M. L., *Two-phase flow modeling with Tough2-Mp of a deep geological repository within the first benchmark of the FORGE project*, Nuclear Technology, 187(2), 117-130, 2014.

Wendling, J., et al., *FORGE WP1.2: Benchmark specifications at a sub set of a repository containing several tens of HLW cells (module scale)*. 2010, Euratom 7th Framework project: FORGE 2010.

Wendling, J., L. Yu, E. Treille, M. Dymitrowska, D. Pellegrini, E. Ahusborde, M. Jurak, B. Amaziane, F. Caro, A. Genty, P. Poskas, D. Justinavicius, M. Sentis, S. Norris, A. Bond, H, Leung, N.J. Calder, *Final report on benchmark studies on repository-scale numerical simulations of gas migration, Part 1 : cell scale benchmark, Part 2: module scale benchmark,* European Commission FORGE Deliverable D1.6-R, 2013.

Zhang, K., Y. Wu, K. Pruess, *User's guide for TOUGH2-MP, A massively parallel version of the TOUGH2 Code*, Lawrence Berkeley National Laboratory, Berkeley, Calif., 2008.

Zhang, K., J. Croisé, G. Mayer, *Computation of the Couplex-Gaz exercise with TOUGH2-MP: hydrogen flow and transport in the pore water of a low-permeability clay rock hosting a nuclear waste repository,* Nuclear Technology, 174, 364-374 (2011).

TOUGH3: A NEW BASE VERSION OF THE TOUGH SUITE OF CODES

Yoojin Jung, George Pau, and Stefan Finsterle

Earth Sciences Division, Lawrence Berkeley National Laboratory
One Cyclotron, MS 74R316C
Berkeley, CA 94720, USA
e-mail: yoojinjung@lbl.gov

ABSTRACT

The TOUGH suite of nonisothermal multiphase flow and transport simulators has been updated to address a vast range of challenging subsurface problems by various developers over many years. Unfortunately, new or improved processes and features are frequently introduced independently, resulting in multiple versions of TOUGH2 that (1) introduce inconsistencies in feature implementation and usage, (2) make code maintenance and development inefficient, and (3) cause confusion to users and developers. TOUGH3 is developed to resolve these issues. TOUGH3 consolidates both the serial (TOUGH2) and parallel (TOUGH2-MP) implementations, enabling simulations to be performed on desktop computers and supercomputers using a single code. TOUGH3 also incorporates many new features that have been developed since the Version 2.1 release of TOUGH2, addresses bugs, and improves the flexibility of data handling. New PETSc-based parallel linear solvers are added to the existing solvers in TOUGH2 and TOUGH2-MP. To improve software management and prevent duplicate efforts in development, testing, and bug fixing, TOUGH3 is placed under a version control system (Mercurial/Bitbucket). The newly available features are fully tested and documented to enhance user support. Due to the improved capabilities and usability, TOUGH3 is more robust and efficient for solving tough and computationally demanding problems in diverse scientific and practical applications related to subsurface flow.

INTRODUCTION

The TOUGH suite of codes is developed to simulate nonisothermal multiphase flow and transport in porous and fractured media (Pruess et al., 2012), and has been updated and evolved to address a vast range of challenging subsurface problems (Pruess et al., 1997; Pruess, 2004; Finsterle et al., 2008, 2012, 2014). As a result, the current TOUGH codes include several branches, each with multiple modules. This diversity of branches and modules makes the codes powerful and efficient, but at the same time, makes code maintenance and development inefficient. Some of the features that have been developed after the Version 2 release of TOUGH2 are available only for certain modules or branches despite their usefulness and benefits. The existence of separate codes for serial (TOUGH2) and parallel (TOUGH2-MP, Zhang et al., 2008) simulations resulted in each version taking different development paths. iTOUGH2 (Finsterle, 2004), which is a computer program that provides inverse modeling capabilities for the TOUGH2 code, also contains slightly modified versions of some of the TOUGH2 modules. Finally, TOUGH+ (Moridis et al., 2008) is a version that focuses on advanced applications involving, for example, gas hydrates.

Such discrepancies between modules or branches will cause confusion to users and developers and result in duplicating efforts in development, testing and bug fixing. To improve the codes' robustness, usability, and dependability, it is therefore necessary to update the codes, partially consolidate the features, and place the codes under version control within a software configuration management system.

TOUGH3 is developed as a new base version of TOUGH to fulfill the needs addressed above and ultimately to promote the wider application of TOUGH. TOUGH3 currently includes all EOS (equation-of-state) modules of the Version 2 of TOUGH2, as well as ECO2N (Pruess, 2005), ECO2M (Pruess, 2011), and TMVOC (Pruess

and Battistelli, 2002). Details of the improvement and new features will be described in the following sections.

ENHANCEMENTS AND BUG FIXES

Recent developments and bug fixes implemented only for certain modules or branches are integrated into the TOUGH3 code to enhance flexibility, accuracy, and applicability. The list of the enhancements and bug fixes incorporated into TOUGH3 is shown in Table 1.

Table 1. Partial list of enhancements and bug fixes in TOUGH3.

Modification/Enhancement/Bug Fix	**Description**
Array allocation	Dimension arrays using dynamic memory allocation
Minimum number of Newton-Raphson (NR) iterations	Provide option to force at least two NR iterations (Finsterle, 2015)
Adjustment of NR increment weighting	Identify if NR iterations oscillate, then automatically decrease/increase NR increment weighting (Finsterle, 2015)
Porosity update	Add porosity update in MULTI to obtain correct storage term
Length of element names	Allow 5-to-9-character element names (Finsterle, 2015)
Brine Properties	Provide internally consistent H_2O-NaCl EOS (Battistelli, 2012)
Water properties	Provide option to use water properties from International Association for Properties of Water and Steam (1997)
Enthalpy of liquid water	Provide option to include potential energy in enthalpy of all phases (Finsterle, 2015)
Leverett scaling of capillary pressure	Rescale capillary pressure if element-specific permeabilities are specified (Finsterle, 2015)
Addition of modified Brooks-Corey (BC) model and modified van Genuchten (VG) model	Modify BC and VG characteristic curves to prevent the capillary pressure from decreasing toward negative infinity as the effective saturation approaches zero (Finsterle, 2015)
Hysteresis model	Add hysteretic capillary pressure and relative permeability functions (Doughty, 2013)
Consistent relative permeability and capillary pressure functions	Combine two-phase and three-phase functions and provide a single, consistent argument list to call relative permeability and capillary pressure functions
Air-entry pressure in BC capillary pressure curve	Provide options to interpolate air-entry pressure in BC capillary pressure curve (Finsterle, 2015)
Active fracture concept	Account for active and inactive fractures to describe gravity-dominated, non-equilibrium, preferential liquid flow in fractures (Liu at al., 1998)
Tabular input of time-dependent GENER rates	Allow tabular input of time-dependent rates, and time can be given in date format (Finsterle, 2015)
Time-dependent Dirichlet boundary conditions	Read time-dependent Dirichlet boundary conditions from the input file or from a separate data file (Finsterle, 2015)
Thermodynamic properties of non-existing phase	Calculate the density, viscosity, and enthalpy of non-existing phase to ensure these values are continuous at the interface where two-phase conditions are either evolving or disappearing (O'Sullivan et al., 2014)
Conversion of hydrocarbon vapor pressure	Correct the conversion factor in Subroutine SATO for TMVOC
Biodegradation reactions	Add the modeling capability of biodegradation reactions within TMVOC (Battistelli, 2004)

CONSOLIDATION OF SERIAL AND PARALLEL VERSIONS

In TOUGH3, serial (TOUGH2) and parallel (TOUGH2-MP) implementations are consolidated into a single code. TOUGH3 can be compiled either in serial or parallel mode depending on the computational requirements. TOUGH3 has access to not just the existing serial solvers and the Aztec parallel linear-equation solver, but also all the solvers in Portable, Extensible Toolkit for Scientific Computation (PETSc). This new solver option will be further discussed in the following section. The diagnostic, warning, and error messages in the two implementations are also consolidated, making all debugging information in TOUGH3 available regardless of the compilation mode.

WHAT IS NEW IN TOUGH3?

Controlled Software Development Environment

To improve version control of the codes and to avoid the redundancy of development efforts, the codes are placed under Bitbucket, a web-based hosting service for code management, and Mercurial is used as a tool for source control. Under this controlled software development environment, it is easy to track the revisions and convenient for multiple developers to collaborate since it is platform-independent and each local clone contains the whole development history, making most actions local and fast.

New PETSc-based Solvers

TOUGH3 has access to all PETSc-based sparse and dense linear solvers. By default we use a bi-conjugate gradient method and incomplete LU factorization as preconditioner. Different Krylov subspace algorithms and preconditioners can be selected through the specification of a PETSc option file (.petscrc), an example of which is shown in Figure 1. Users should refer to PETSc's documentation (http://www.mcs.anl.gov/petsc/documentation/index.html) for a list of updated Krylov subspace algorithms and preconditioners. However, it should be noted that selecting an appropriate algorithm and preconditioner typically relies on a good understanding of the linear system constructed by TOUGH3 for the specified problems. Users must also be aware of the tradeoff between efficiency and robustness.

```
# monitor solves
-ksp_monitor
# biconjugate gradient
-ksp_type bicg
# additive Schwarz preconditioner
-pc_type asm
# relative tolerance
-ksp_rtol 1e-7
```

Figure 1: An example of .petscrc

Automatic Build System

The automatic build system utilizes CMake (http://www.cmake.org/) and a shell script (configure.sh) to handle compiling of the code on multiple platforms[1]. The use of an advanced numerical library such as PETSc makes compiling the code a multi-step process; the automatic build system simplifies this process. For many systems, executing the provided script in the repository will successfully build the code. Additional options may need to be specified for other systems; a list of available options can be displayed by executing ./configure.sh --help.

Flexible Output (CSV File Format)

Users can choose the number and kind of variables and parameters for printout. A lumped set of primary variables or secondary parameters can be selected, and the coordinates of grid blocks can be included as well for plotting purposes. The header and unit of variables/parameters selected for printout will be generated accordingly. Separate output files will be generated for element-, connection-, and sinks/sources-related outputs at each specified printout time. Users can also specify the amount of time-dependent data for specific elements, connections, or sinks/sources. All output data will be saved in the CSV file format for ease of post-processing.

CONCLUDING REMARKS

TOUGH3 is developed to improve the capabilities, usability, and maintenance of the code. The

[1] On Windows machine, only Cygwin is supported by the automatic build system. Use of Visual Studio requires user's ingenuity.

broad user community can use TOUGH3 as a robust tool for diverse scientific and practical applications related to subsurface flow problems. The enhanced user support (i.e., detailed documentation and error messages) will help the users fully utilize the features and capabilities. Under the controlled software development system, it will be clear and easy to control/manage the version of the codes and track the changes, preventing duplicate efforts in development, testing, and bug fixing.

ACKNOWLEDGMENT

This work was funded by the TOUGH Development Grant through the U.S. Dept. of Energy under Contract No. DE-AC02-05CH11231.

REFERENCES

Battistelli, A., Modeling biodegradation of organic contaminants under multiphase conditions with TMVOCBio. *Vadose Zone Journal*, 3, 875–883, 2004.

Battistelli A., Improving the treatment of saline brines in EWASG for the simulation of hydrothermal systems. In: Finsterle et al. (Eds.), Proceedings of the TOUGH Symposium 2012. Report LBNL-5808E. Lawrence Berkeley National Laboratory, Berkeley, Calif., 2012.

Doughty, C., *User's Guide for Hysteresis Capillary Pressure and Relative Permeability Functions in TOUGH2*, Report LBNL-6533E, Lawrence Berkeley National Laboratory, Berkeley, Calif., 2013.

Finsterle, S., C. Doughty, M.B. Kowalsky, G. Moridis, L. Pan, T. Xu, Y. Zhang, and K. Pruess, Advanced vadose zone simulations using TOUGH. *Vadose Zone Journal*, 7, 601–609, 2008.

Finsterle, S., M.B. Kowalsky, and K. Pruess, TOUGH: model use, calibration and validation. *Transactions of the ASABE*, 55(4), 1275–1295, 2012.

Finsterle, S., *Enhancements to the TOUGH2 Simulator Integrated in iTOUGH2*, Report LBNL-TBD, Lawrence Berkeley National Laboratory, Berkeley, Calif., 2015.

International Association for the Properties of Water and Steam, *Release on the IAPWS Industrial Formulation 1997 for the Thermodynamic Properties of Water and Steam*. Erlangen, Germany, 1997.

Liu, H.H., C. Doughty, and G.S. Bodwarsson, An active fracture model for unsaturated flow and transport in fractured rocks. *Water Resources Research*, 34, 2633-2646, 1998.

Moridis, G.J., M.B. Kowalsky, and K. Pruess, *TOUGH+HYDRATE v1.0 User's Manual: A Code for the Simulation of System Behavior in Hydrate-Bearing Geologic Media*, Report LBNL-149E, Lawrence Berkeley National Laboratory, Berkeley, Calif., 2008.

O'Sullivan, J., A. Croucher, A. Yeh, and M. O'Sullivan, Further improvements in the convergence of TOUGH2 simulations. In: Oñate et al. (Eds.), 11th World Congress on Computational Mechanics (WCCM XI), 5th European Congress on Computational Mechanics (ECCM V), 6th European Congress on Computational Fluid Dynamics (ECFD VI), 5: 5929-5940, 2014.

Pruess, K., S. Finsterle, G. Moridis, C. Oldenburg, and Y.-S. Wu, General-purpose reservoir simulators: the TOUGH2 family. *GRC Bulletin*, 53–57, 1997.

Pruess, K., C. Oldenburg, and G. Moridis, *TOUGH2 User's Guide, Version 2.1*, Report LBNL-43134, Lawrence Berkeley National Laboratory, Berkeley, Calif., 2012.

Pruess, K., The TOUGH codes—a family of simulation tools for multiphase flow and transport processes in permeable media, *Vadose Zone Journal*, 3, 738–746, 2004.

Pruess, K., *ECO2N: A TOUGH2 Fluid Property Module for Mixtures of Water, NaCl, and CO_2*, Report LBNL-57952, Lawrence Berkeley National Laboratory, Berkeley, Calif., 2005.

Pruess, K., *ECO2M: A TOUGH2 Fluid Property Module for Mixtures of Water, NaCl, and CO_2, Including Super- and Sub-critical Conditions, and Phase Change between Liquid and Gaseous CO_2*. Report LBNL-4590-E, Lawrence Berkeley National Laboratory, Berkeley, Calif., 2011.

Pruess, K. and A. Battistelli. *TMVOC, A Numerical Simulator for Three-Phase Non-isothermal Flows of Multicomponent Hydrocarbon Mixtures in Saturated–Unsaturated Heterogeneous Media*. Report LBNL-49375, Lawrence Berkeley National Laboratory, Berkeley, Calif., 2002.

pTOUGH+: Status of Re-engineering Parallel TOUGH+

Noel Keen, Jeff Johnson, George Moridis, Matt Reagan
Lawrence Berkeley National Laboratory

Email: ndkeen@lbl.gov

TOUGH+ is a code in the TOUGH family that simulates multiphase, non-isothermal subsurface coupled flow and transport. Used with appropriate EOS modules, it can be used to model different systems, i.e. hydrate-bearing geologic media (TOUGH+HYDRATE), or reservoirs with mixed gases, water, and salt (TOUGH+RealGasBrine). We have developed a new high performance version of this code using MPI, named pTOUGH+. pTOUGH+ will maintain the ability to run in serial or in parallel and across various machines (workstations, clusters). The domain (mesh) is partitioned using Metis and each partition is distributed amongst the machine processors at runtime. pTOUGH+ uses the PETSc toolkit (developed at Argonne National Laboratory [ANL]) to perform the linear solve in parallel. We will show the performance improvements of this version over the serial version. We will also show performance comparisons between pTOUGH+ and a previous parallel version of TOUGH+ which was based on work in TOUGH2-MP and used the Aztec solver to perform parallel linear solves. We will show parallel performance of pTOUGH+ on two different problems exhibiting different simulation dynamics. The target machine for this work is a Cray XC30 at NERSC named Edison. We also discuss general software improvements made during development such as a more modular design to accommodate different equations of state, bug fixes, and the build process.

MESHMAKER V2.0S AND V2.0P: NEW GRID GENERATORS FOR COMPLEX HETEROGENEOUS DOMAINS IN TOUGH2/TOUGH+ SIMULATIONS

George J. Moridis and Noel Keen

Earth Sciences Division, Lawrence Berkeley National Laboratory
1 Cyclotron Rd
Berkeley, CA 94720
E-mail: GJMoridis@lbl.gov

ABSTRACT

MeshMaker V2.0S and V2.0P are the new versions (serial and parallel, respectively, and referred to as MM2S and MM2P and collectively as MM2S/P) of the older MeshMaker facility that had been developed for the discretization of domains involved in simulations of the TOUGH family of codes. The MM2S/P codes are not revisions but completely new codes. They are written in FORTRAN 95/2003, and use a namelist-based data input structures with easily recognizable keywords to generate the MESH file needed by the TOUGH family of codes. They can create grids comprising in excess of $5x10^9$ elements with 5- or 8-character long names, with any number of heterogeneous subdomains of complex geometries, and with any number of boundaries, time-invariable or transient. The MM2S/P codes allow the description of domains of irregular geometries through the options of "exclusion" and "inclusion" zones that reshape an original regular grid by removing from (or adding to) it subdomains of arbitrary geometry. An important new capability of the MM2S code is the partial mesh data generation option, which enables the simultaneous piece-wise creation of very large meshes involving millions of elements and connections by assigning them to individual processors or computers, thus drastically reducing the time frame for the MESH file creation. The MM2S/P codes generate grids that are directly usable by members of the TOUGH+ and of the conventional TOUGH2 families of codes, and can also create file that can be used for visualization of complex domains using the standard VTK file format.

INTRODUCTION

The TOUGH family of codes (Pruess et al., 1999; 2012) and its most recent TOUGH+ (Moridis et al., 2008; Moridis and Pruess, 2015) generation are based on the Integral Finite Difference space discretization method (Narasimhan and Witherspoon, 1972), a finite-volume method. The corresponding meshes that are needed for such simulations are quite different from the ones created by standard gridding software because they do not use global coordinates, but only local coordinates that describe the relative positions of the centers of the gridblock elements and do not provide any information on the corners of the elements of the grids. These grids pose a problem in the plotting of the corresponding results because they do not provide the geometric data needed by the standard VTK format used by common visualization software.

Pruess et al. (1999; 2012) provided a simple mesh-making facility named "MeshMaker" (hereafter referred to as MM1) for use with the TOUGH family of codes. The MM1 facility is not a stand-alone code, but it is completely integrated within the TOUGH2 code (Pruess et al., 1999). While useful in creating automatically TOUGH meshes, MM1 has some serious shortcomings. It is applicable to homogeneous domains, and is limited to the creation of Cartesian or cylindrical meshes of regular geometry. MM1 is limited to 5-character element names and its numbering system is inflexible (proceeding invariably along the X, Y and Z directions, always in that order), thus often preventing the computational and memory savings that could be attained during the matrix solving process by a reduction in the matrix bandwidth (a direct result of a more efficient element numbering). Additionally, the MM1 grids cannot provide the necessary information needed for the description of the more complex boundary specifications that are available options in the TOUGH+ family of codes (Moridis et al., 2008). For the solution of

problems involving heterogeneous systems of complex geometry, other gridding software–e.g., WinGridder (Pan, 2008)–have to be used, or the MM1-created grids have to be modified either manually or by using mission-specific software.

The MeshMaker V2.0S and V2.0P codes (serial and parallel, respectively, hereafter referred to as MM2S and MM2P, and collectively as MM2S/P) are not simple revisions of the older MM1 facility, but new stand-alone software that operate independently of the TOUGH codes. They were developed for the discretization of domains involved in simulations of all members of the TOUGH family of codes, and address all the shortcomings of MM1. The MM2 codes can describe large (in terms of number of elements) systems with heterogeneous subdomains of arbitrary geometry and complex boundary conditions, and create VTK files for the visualization of the simulation results using standard packages. In the following sections we describe the approach and capabilities of the MM2 codes.

CODE DESCRIPTION

Code Approach and Structure

The MM2S/P codes are written in FORTRAN 95/2003, making use of the significant advantages of the language: object-oriented programming, modular structure, matrix operations and manipulation, operator extension and overloading, advanced I/O options, and the creation and use of objects, pointers, derived-type variables, dynamic data structures, generic procedures and modules. The input files comprise between 2 (minimum necessary) and 6 (maximum) data blocks, the beginning of which is denoted by the '>>>' identifier followed by appropriate keywords, and the end is denoted by the '<<<' identifier. Inputs are read using the `namelist` facility, a powerful FORTRAN I/O option that allows maximum flexibility and clarity.

The two minimum data blocks are identified by the keywords `GENERAL_INFO` and `DISCRETIZATION`. In addition to them, there are four additional optional data blocks (`REGIONS`, `BOUNDARIES`, `EXCLUSIONS`, and `INCLUSIONS`). The function and general description of each one of these data blocks is discussed in the following sections.

The `GENERAL_INFO` Data Block

Figure 1 is an example of a `GENERAL_INFO` data block as it appears in a MM2 input file. It includes all the possible namelist options, and shows the power and flexibility of this I/O facility. Figure 2 shows the definition of the namelist `Grid_Specifications` used in this data block. As Figure 1 shows, namelists in the input files begin with the '&' character, followed by their name, then the names of the variables to which values are assigned, and closing with the '/' character). The components of a namelist can be entered in any order and format (e.g., all in a single line, or just one on every input line, or in any desired way). Comments (identified by a preceding '!') can be entered at any point or can be used to eliminate ('comment-out') a specific data entry. Note that not all namelist data entries are necessary: the optional ones are identified by the italics font in Figure 1, and can be omitted (in which case built-in defaults apply).

As its name suggests, this data block provides a general description of the specifications of the domain to be discretized. The use of conversational English names as variable inputs in the namelist renders unnecessary the explanation of most of the data entries. Practically all current TOUGH2 and TOUGH+ applications require the option `output_file_format='old'`. The element names may be 5- or 8- characters long. Of particular importance are the following variables:

(1) `level_of_grid_generation`: it allows the generation of a partial element and connection list when set equal to '`P`'; otherwise, it is set internally to '`P`", yielding the full element and connection list. The partial element and connection lists are stored in the external files `name_of_element_file` and `name_of_connection_file`, respectively (the default names are '`ELEMENTS`' and '`CONNECTIONS`'. Similarly, the complete mesh is stored in the file specified by the `name_of_mesh_file` variable (see Figure 1); the default value is '`MESH`'. Grid generation in complex multi-million element domains can take several days when run on a single processor for reasons that will be discussed later. This capability allows the simultaneous use of MM2S on several processors of one or more multi-

processor computers, thus significantly reducing (linearly) the grid generation time. In the parallel MM2P version, the process of allocation to several processors is done automatically, but in the serial MM2S version it is controlled by the variables `begining_of_partial_LLoop` and `end_of_partial_LLoop`, which refer to the largest of the 2 (in radial systems) or 3 (in Cartesian systems) numbers of subdivisions along the principal axes of the system, i.e., to the subdivisions of `max{MaxNum_D_Subdivisions}`, where **`D`**`=R,Z` for cylindrical systems and **`D`**`=X,Y,Z` for Cartesian domains. In the example of Figure 1, the partial grid will include all the X and Y subdivisions that are included between the 1060th and 1090th subdivision along Z (where the maximum number of subdivisions `MaxNum_Z_Subdivisions` = 2320 occurs).

(2) `VTK_output`: if set equal to **`.TRUE.`**, it allows the creation of the user-specified external file `name_of_corners_file` (see Figure 1) that conforms to the VTK format specifications required by several 3D visualization software.

(3) `old_style_inactive_elements`: if equal to **`.TRUE.`**, then the inactive elements conform to the standard TOUGH2 (Pruess et al., 1999) description of inactive elements, i.e., by placing them at the end of the element list following an element with zero volume. Otherwise, the more general TOUGH+ approach (Moridis et al., 2008) is followed, which allows identification of various types of inactive elements (i.e., boundaries) by an element activity character variable without altering the element order.

(4) `renumbered_inactive_elements`: the default is **`.TRUE.`** for both TOUGH2 and TOUGH+ inactive elements, but needs to be set to **`.FALSE.`** for parallel TOUGH+ simulations which describe inactive elements by assigning very large volumes to them without altering their order in the list. Heterogeneous Regions

The `DISCRETIZATION` Data Block

Figure 2 describes 2nd mandatory data block in MM2S/P and represents the discretization data block for a 3D Cartesian grid. Discretization along each direction involves sub-data-blocks that are marked by the appropriate keywords (**`D`**`-Discretization`, with **`D`**`=X,Y,Z`) and identifiers (**`:::>>>`** and **`:::<<`** at the beginning and end of the data blocks, respectively). As it is evident from Figure 2, discretization can involve either uniform-sized subdivisions or on-uniformed ones that are read according to a user-specified format. A discretization data block for a cylindrical system is entirely analogous, with `X` replaced by `R` and without Y-subdivisions.

The Optional Data Blocks

The four additional optional data blocks (`REGIONS`, `BOUNDARIES`, `EXCLUSIONS`, and `INCLUSIONS`) in MM2S/P are used to describe heterogeneity in the distribution of properties in the domain and/or irregular geometry. In all cases, each one of the four data blocks involves a general description (which is data block-specific) and a geometric description that is based on the use of the same type of generic namelists (which only differ in their name).

Figure 3 shows the first namelists in each of the four optional data blocks. The names of the variables in each ones of the namelists are self-explanatory and require no further clarification.

The first namelists are followed by additional namelists that describe the geometry and shape of each subdomain. A complete list of the additional namelists is shown in Figure 4. Depending on the data block, the variable ***`Subdomain`*** in Figure 4 can have one of the following 4 values: '`HetRegion`', '`boundary`', '`ExclZone`' or '`InclZone`'. Inspection of the list indicates the ability of MM2S/P to describe the following types of geometric shapes of the various subdomains: rectangular, cylindrical of any orientation, elliptical cones of any orientation, spherical, and irregular.

There are 3 ways to describe irregular subdomains: either by 3D bounding equations describing the bounding surfaces of the subdomain, or by interpolating in tables describing the bounding surfaces (designated by the ***`n`*** character in Figure 4, which can only assume the values of 1 or 2). If the subdomain has a constant thickness in any direction (e.g., a geologic formation extending over a large area), then it is possible to describe the bounding surfaces with respect to a reference surface defined by an equation or a table.

The function and applications of the optional data blocks are discussed in detail in the ensuing sections. Note that, (a) one or more of these data blocks may be missing from the input files for MM2S/P applications, but (b) the order of their appearance (denoted by the order in which they are described below) must be followed.

The `REGIONS` Data Block

This data block describes the spatial heterogeneity of the flow properties of a domain. This is accomplished by describing the geometry of each subdomain with distinctly different properties. There is no limit in the number of heterogeneous domains that can be described.

Figure 5 shows an example of the use of the `REGIONS` data block. The system described here has the material '`M1Sand`' as the dominant medium, but also includes an additional medium called '`Envlp`'. This medium is defined by a constant-thickness zone, the elevation of the bottom of which (i.e., the z-coordinate) is determined as a function of the x- and y-coordinates from interpolation in the table '`SaltFlnk`'. The interpolation process seeks to identify the triangle (defined by three entries in the table) to which the (x,y) coordinates are internal. The search algorithm limits the search radius for the identification of the 3 points to 150 m from the (x,y) location and to 500 interrogation points within this radius. The (x,y) range over which the two heterogeneous regions are defined is easily identified from the data in Figure 5. The names of the various variables involved in this (and all other) data blocks are self-explanatory.

The `BOUNDARIES` Data Block

No-flow boundaries in all TOUGH2/TOUGH+ simulations are automatically created at the end of the domain. This data block describes domain boundaries of any geometry and shape where constant conditions (e.g., constant pressure or temperatures) exist, i.e., identifying the *inactive* elements in the TOUGH+/TOUGH2 terminology. In the TOUGH+ family of codes, elements belong to such boundaries are designated by the '`I`' or '`III`' descriptor when time-invariant, and by the '`V`*`nn`*' descriptor when time-dependent (with *`nn`* being a two-digit number identifying the number of the boundary, thus allowing up to 99 such boundaries). If the `old_style_inactive_elements=.T.` option is used in the `GENERAL_INFO` data block, then MM2S/P will create a standard TOUGH2 (Pruess et al., 1999; 2012) element list with the inactive elements placed after the end of the active ones and observing the irregular geometry of their occurrence.

Figure 6 shows an example of the use of the `BOUNDARIES` data block. Two boundaries of constant thickness are described here. The first boundary is of type '`I`' and has the material name '`Upper`'. One of its bounding surfaces is defined by interpolation in table '`M1Sand`', and the second is at fixed stratigraphic distance of 1.5 m above the first. The second boundary is of type '`III`' and has the material name '`Lower`'. Their elevations are determined after interpolation in table '`M1Sand`'. The surfaces of this boundary are defined at fixed distances of 15 m (*stratigraphic*) below the '`M1Sand`' and of another 1.5 m below the first surface (i.e., this boundary has a constant *vertical* thickness of 1.5 m). The various variables involved in the description of this data block are entirely analogous to those described earlier. There is no limit in the number of boundary subdomains that can be defined in MM2S/P.

The `EXCLUSIONS` Data Block

The function of this data block is subtractive, i.e., it eliminates from the domain regions that are of no interest and/or consequence to the TOUGH2/TOUGH+ problem. The subdomain geometry is defined in the same general way discussed earlier, and all elements belonging to the `EXCLUSIONS` subdomains are removed. The number of possible exclusions is arbitrary.

Figure 7 shows an example of the use of the `EXCLUSIONS` data block. Two exclusion zones are described here. The bounding surfaces of the first one are defined by polynomial equations. The bounding surfaces of the second exclusion zone are defined by an equation and from interpolation in table '`M1Sand`'. All elements belonging to these two subdomains are eliminated from the MESH file.

All variables here have been previously identified, and are self-explanatory. The only exception is the variable `exclusion_zone_type`

='ABS', which appears in the namelist ExclZone_GeneralInfo. This variable indicates that the corresponding exclusion zone cannot be modified, i.e., it cannot be overridden by a subsequent INCLUSION zone (see below).

The INCLUSIONS Data Block

The function of this data block is additive, i.e., it into the domain regions new subdomains, often following an exclusion process. An example of such an application is the addition of a domal structure on top of an inclined formation. The process to do that often includes first the elimination of the domain above the inclined subdomain using the definition of appropriate zones in the EXCLUSION data set, and then the addition the domal structure using the INCLUSIONS data set. Note that such addition can only occur of the eliminated subdomain does not carry the exclusion_zone_type ='ABS' value. There is no limit in the number of inclusions.

Figure 8 shows an example of the use of the INCLUSIONS data block. It involves the addition to a previously excized domain of two chimneys (geological structures with elliptical cone shape). The geometric characteristics of the two chimneys 'ChimA' and 'Chim' can be easily identified in the inputs.

An example of a complex mesh developed using MM2S/P is shown in Figure 9. It involves two heterogeneous regions, 2 boundaries, 16 exclusion zones, and 2 inclusion zones. The original (untrimmed) domain involves 480x830x2311 = 920,702,400 elements in (x,y,z), and the final mesh has 6,2 million elements.

Sequence of Computations

As indicated earlier, the optional data blocks *must* appear in the input file in the sequence of their description above. One or more may be omitted. The computations in MM2S/P proceed in the following sequence: An element is first interrogated to determine if it belongs in an exclusion zone, and, if removed, it is added back if it belongs to an inclusion zone. Then MM2S/P determines if the element in question occurs on a boundary, and whether this should override an inclusion existing at the same point.

If multiple subdomains occur within a given optional subdomains, the order in which they should appear in the input files is as follows: first regular geometry (rectangular, cylindrical, spherical elliptical) descriptions, then polynomial subdomain definitions, and lastly table interpolations.

SUMMARY AND FUTURE WORK

We developed MeshMaker V2.0S and V2.0P for the discretization of domains involved in simulations of the TOUGH family of codes. These codes are written in FORTRAN 95/2003, and use a namelist-based data input structures with easily recognizable keywords. They can create grids comprising billions of elements with 5- or 8-character long names, with any number of heterogeneous subdomains and of boundaries. They can describe domains of irregular geometries using "exclusion" and "inclusion" zones that reshape an original regular grid by removing from (or adding to) it subdomains of arbitrary geometry, and allow the option of partial mesh generation option, which enables the simultaneous piece-wise creation of very large meshes. They can also create files in the standard VTK format for visualization purposes.

ACKNOWLEDGMENT

This study was supported by the Bureau of Ocean Energy Management, Department of the Interior, through Interagency Agreement #M14PG00044 with the Lawrence Berkeley National Laboratory.

REFERENCES

Edwards, A.L., TRUMP: A Computer Program for Transient and Steady State Temperature Distributions in Multidimensional Systems, National Technical Information Service, National Bureau of Standards, Springfield, VA, 1972.

Moridis, G.J. and K. Pruess, User's Manual Of The TOUGH+ Core Code V1.5: A General-Purpose Simulator Of Non-Isothermal Flow And Transport Through Porous And Fractured Media Report LBNL-6871E, Lawrence Berkeley National Laboratory, Berkeley, CA, 2014.

Moridis, G.J., M.B. Kowalsky and K. Pruess, TOUGH+HYDRATE v1.0 User's Manual: A Code for the Simulation of System Behavior in

Hydrate-Bearing Geologic Media, Report LBNL-0149E, Lawrence Berkeley National Laboratory, Berkeley, CA, 2008.

Narasimhan, T.N. and P.A. Witherspoon, An Integrated Finite Difference Method for Analyzing Fluid Flow in Porous Media, Water Resour. Res., 12(1), 57 – 64, 1976.

Pan, L., User's Information for WinGridder V3.0. Report LBNL-273E, Lawrence Berkeley National Laboratory, Berkeley, Calif., 2008.

Pruess, K., C. Oldenburg, and G. Moridis, TOUGH2 User's Guide, Version 2.0, Report LBNL-43134, Lawrence Berkeley National Laboratory, Berkeley, Calif., 1999.

Pruess, K., C. Oldenburg, and G. Moridis, TOUGH2 User's Guide, Version 2.1, Report LBNL-43134, Lawrence Berkeley National Laboratory, Berkeley, Calif., 2012.

```
>>>GENERAL_INFO
&Grid_Specifications coordinate_system  = 'Cartesian',
                     output_file_format = 'old',
                     length_units = 'm',
                     grid_numbering_system  = 'standard',
                     ElemName_NumCharacters = 8,
                     MaxNum_X_Subdivisions  = 485,
                     MaxNum_Y_Subdivisions  = 835,
                     MaxNum_Z_Subdivisions  = 2320,
                     AxesOrigin_X = 5.5d3,
                     AxesOrigin_Y = 5.0d2,
                     AxesOrigin_Z = -1.135d3,
                     inclination_angle = 0.0d0,
                     areas_for_HeatExch_Solution = .TRUE.,
                     level_of_grid_generation    = 'E',
                     beginning_of_partial_LLoop  = 1050,
                     end_of_partial_LLoop        = 1100,
                     VTK_output = .TRUE.,
                     renumbered_inactive_elements = .FALSE.,
                     old_style_inactive_elements  = .FALSE.,
                     name_of_mesh_file    = 'ELEMENTS_07',
                     name_of_corners_file = 'CORNERS_07'
                     /
<<<
```

Figure 1. An example of a `GENERAL_INFO` data block in a MM2S/P input file.

```
NAMELIST/Grid_Specifications/     coordinate_system, output_file_format, &
                                  length_units, grid_numbering_system, &
                                  ElemName_NumCharacters, &
                                  MaxNum_X_Subdivisions, MaxNum_R_Subdivisions, &
                                  MaxNum_Y_Subdivisions, MaxNum_Z_Subdivisions, &
                                  AxesOrigin_X, AxesOrigin_Y, AxesOrigin_Z, &
                                  inclination_angle, areas_for_HeatExch_Solution, &
                                  media_by_number, level_of_grid_generation, &
                                  beginning_of_partial_LLoop, end_of_partial_LLoop, &
                                  VTK_output, renumbered_inactive_elements, &
                                  old_style_inactive_elements, name_of_mesh_file, &
                                  name_of_elem_file, name_of_conx_file, &
                                  name_of_corners_file
```

Figure 2. Definition of the `Grid_Specifications` namelist that shows the complete list of its components. The variables in italics are optional.

```
NAMELIST/Heterogeneous_Regions/   number_of_regions, number_of_periodic_regions, &
                                  total_number_periodic_subdomains, dominant_medium

NAMELIST/Boundary_Regions/        number_of_boundaries

NAMELIST/Exclusion_Zones/         number_of_exclusion_zones, &
                                  number_of_periodic_ExclZones, &
                                  total_number_periodic_ExclZones

NAMELIST/Inclusion_Zones/         number_of_inclusion_zones, &
                                  number_of_periodic_InclZones, &
                                  total_number_periodic_InclZones
```

Figure 3. Definition of the first namelist in the REGIONS, BOUNDARIES, EXCLUSIONS, and INCLUSIONS data blocks, respectively. The variables in italics are optional.

```
NAMELIST/Subdomain_GeneralInfo/   Subdomain_name, Subdomain_shape, length_units
NAMELIST/Rectangular_Subdomain/   X_min, Y_min, Z_min, X_max, Y_max, Z_max
NAMELIST/Periodic_Subdomain/      X_min,R_min,Y_min,Z_min,X_max,R_max,Y_max,Z_max, &
                                  number_of_periodic_occurrences, &
                                  axis_of_periodicity, &
                                  location_of_1st_periodic_occurrence,
                                  &width_of_periodic_region,period_of_occurrence
NAMELIST/Cylindrical_Subdomain/   CylBase1_center_coordinates, &
                                  CylBase2_center_coordinates,                cylinder_Rmin,
                                  &cylinder_Rmax, cylinder_radius1, cylinder_radius2
NAMELIST/Spherical_Subdomain/     sphere_center_coordinates, sphere_Rmax, sphere_Rmin
NAMELIST/Elliptical_Subdomain/    Base1_center_coordinates, Base2_center_coordinates,&
                                  ellipse_long_axis_angle, plane_of_ellipse_bases, &
                                  Base1_Long_Axis, Base2_Long_Axis, Base1_Short_Axis,&
                                  Base2_Short_Axis, Long_Axis, Short_Axis
NAMELIST/Irregular_Subdomain/     dependent_variable_of_surfaces, type_of_equation1,&
                                  type_of_equation2, X_min, R_min, Y_min, Z_min, &
                                  X_max, R_max, Y_max, Z_max, &
                                  interpolation_data_file_name1, &
                                  interpolation_data_file_name2, &
                                  vertical_or_stratigraphic1, &
                                  vertical_or_stratigraphic2, reference_surface1, &
                                  reference_surface2, thickness0, thickness1, &
                                  thickness2, ref_interpolation_data_file
NAMELIST/Irregular_Subdomain_Surfn/equation_order_of_bounding_surfacen,Xn_shift, &
                                  Yn_shift, Zn_shift, Rn_shift, exponentn, signn, &
                                  BoundSurfacen_EquCoeff_A, BoundSurfacen_EquCoeff_B,&
                                  BoundSurfacen_EquCoeff_C, BoundSurfacen_EquCoeff_D
NAMELIST/Irregular_Subdomain_IntTablen/ number_of_rows, number_of_columns, &
                                  RowCol_DepVariable, RowCol_IndVariable_1, &
                                  RowCol_IndVariable_2,read_data_by_row, &
                                  read_data_format, interpolation_search_radius, &
                                  num_interrogated_points
NAMELIST/ Irregular_Subdomain_RefTable/number_of_rows, number_of_columns, &
                                  RowCol_DepVariable, RowCol_IndVariable_1,&
                                  RowCol_IndVariable_2, read_data_by_row, &
                                  read_data_format, interpolation_search_radius, &
                                  num_interrogated_points
```

Figure 4. A complete list of the possible options to describe the geometry and shape of the various subdomains in the REGIONS, BOUNDARIES, EXCLUSIONS, and INCLUSIONS data blocks, respectively. The appropriate names are obtained by using the appropriate name for ***Subdomain*** and value for ***n*** (1 and 2 are the only options).

```
>>>REGIONS
&Heterogeneous_Regions  number_of_regions = 2, dominant_medium = 'M1Snd' /
       &HetRegion_GeneralInfo  region_name  = 'Envlp',
                               region_shape = 'Irregular', length_units = 'm'  /
           &Irregular_HetRegion  type_of_equation1 = 'Inte',
                                 type_of_equation2 = 'Fixe',
                                 X_min=  1.0970d3, X_max= 2.055d3,
                                 y_min= -2.0000d0, y_max= 1.135d3,
                                 dependent_variable_of_surfaces = 'z',
                                 interpolation_data_file_name1  = 'SaltFlnk'
                                 vertical_or_stratigraphic2 = 'S',
                                 thickness2 = 2.0d1 /
           &Irregular_HetRegion_IntTable1 number_of_rows    = 76929,   ! 4910,
                                          number_of_columns = 3,
                                          RowCol_DepVariable   = 3,    !
                                          RowCol_IndVariable_1 = 1,
                                          RowCol_IndVariable_2 = 2,
                                          read_data_by_row  = .TRUE.,
                                          read_data_format  = '*',
                                          interpolation_search_radius = 1.0d2,
                                          num_interrogated_points = 500   /
<<<
```

Figure 5. An example of the `REGIONS` data block in a MM2S/P input file.

```
>>>BOUNDARIES
&Boundary_Regions  number_of_boundaries = 2  /
      &Boundary_GeneralInfo  boundary_name  = 'Upper'
                             boundary_shape = 'Irregular',
                             boundary_type  = 'I  ', length_units   = 'm' /
           &Irregular_Boundary   type_of_equation1 = 'Inte',
                                 type_of_equation2 = 'Fixe',
                                 X_min=  0.0e0, X_max= 5.731d3,
                                 Y_min=  0.0d0, Y_max= 3.170d3,
                                 dependent_variable_of_surfaces = 'z',
                                 interpolation_data_file_name1  = 'M1Sand'
                                 vertical_or_stratigraphic2 = 'V',
                                 thickness2 = 1.5d0  /
           &Irregular_Boundary_IntTable1 number_of_rows = 13788, number_of_columns = 3,
                                         RowCol_DepVariable   = 3,
                                         RowCol_IndVariable_1 = 1,
                                         RowCol_IndVariable_2 = 2,
                                         read_data_by_row  = .TRUE.,
                                         read_data_format  = '*',
                                         interpolation_search_radius = 1.0d2,
                                         num_interrogated_points = 500  /
      &Boundary_GeneralInfo  boundary_name  = 'Lower', boundary_shape = 'Irregular',
                             boundary_type  = 'III', length_units   = 'm'  /
           &Irregular_Boundary   type_of_equation1 = 'Fixe',
                                 type_of_equation2 = 'Fixe',
                                 X_min=  0.0e0, X_max= 5.731d3,
                                 Y_min=  0.0d0, Y_max= 3.170d3,
                                 dependent_variable_of_surfaces = 'z',
                                 ref_interpolation_data_file = 'M1Sand'
                                 vertical_or_stratigraphic1  = 'S',
                                 vertical_or_stratigraphic2  = 'V',
                                 reference_surface1 = '0',
                                 reference_surface2 = '1',
                                 thickness1 = -15.0d0,
                                 thickness2 = -1.50d0
                                 /
<<<
```

Figure 6. An example of the `BOUNDARIES` data block in a MM2S/P input file.

```
>>>EXCLUSIONS
&Exclusion_Zones  number_of_exclusion_zones = 2 /
&ExclZone_GeneralInfo      exclusion_zone_shape = 'Irregular',
                           exclusion_zone_type = 'ABS' /
         &Irregular_ExclZone   type_of_equation1 = 'Poly',
                               type_of_equation2 = 'Poly',
                               dependent_variable_of_surfaces = 'y',
                               X_min=  5.5e3, X_max= 6.00d3,
                               Z_min= -5.0d3, Z_max= 0.0d0 /
         &Irregular_ExclZone_Surf1  equation_order_of_bounding_surface1 =  1,
                                    BoundSurface1_EquCoeff_A = 1.8d4, -2.0d0 /
         &Irregular_ExclZone_Surf2  equation_order_of_bounding_surface2 = 1,
                                    BoundSurface2_EquCoeff_A = -6.0d3, 2.0d0 /
&ExclZone_GeneralInfo  exclusion_zone_shape = 'Irregular',
                              length_units = 'm' /
           &Irregular_ExclZone   type_of_equation1 = 'Inte',
                                 type_of_equation2 = 'Poly',
                                 X_min = 0.0e0, X_max= 1.000d4,
                                 Y_min =-2.0d1, Y_max= 1.000d4,
                                 dependent_variable_of_surfaces = 'z',
                                 interpolation_data_file_name1  = 'M1Sand' /
           &Irregular_ExclZone_Surf2  equation_order_of_bounding_surface2 = 0,
                                      BoundSurface2_EquCoeff_A = 0.0d0 /
<<<
```

Figure 7. An example of the EXCLUSIONS data block in a MM2S/P input file.

```
>>>INCLUSIONS
&Inclusion_Zones  number_of_inclusion_zones = 2
/
      &InclZone_GeneralInfo  inclusion_zone_name  = 'ChimA',
                             inclusion_zone_shape = 'Elliptic',
                             inclusion_zone_type  = '   ',
                             length_units = 'm' /
      &Elliptical_InclZone  Base1_center_coordinates= 6690.0d0, 9510.0d0,-3000.0d0,
                            Base2_center_coordinates= 6690.0d0, 9510.0d0,-1135.0d0,
                            plane_of_ellipse_bases  = 'XY',
                            ellipse_long_axis_angle = 142.0d1,
                            Base1_Long_Axis  =  2.50d3,
                            Base2_Long_Axis  =  30.0d0,
                            Base1_Short_Axis =  4.00d2,
                            Base2_Short_Axis =  30.0d0  /
      &InclZone_GeneralInfo  inclusion_zone_name  = 'ChimB',
                             inclusion_zone_shape = 'Elliptic',
                             inclusion_zone_type  = '   ',
                             length_units = 'm' /
      &Elliptical_InclZone  Base1_center_coordinates=6750.0d0, 700.0d0, -3000.00d0,
                            Base2_center_coordinates=6750.0d0, 700.0d0, -1180.50d0,
                            plane_of_ellipse_bases  = 'XY',
                            ellipse_long_axis_angle = 0.0d0,
                            Base1_Long_Axis  =  9.0d2,
                            Base2_Long_Axis  =  30.0d0,
                            Base1_Short_Axis =  8.5d2
                            Base2_Short_Axis =  30.0d0 /
<<<
```

Figure 8. An example of the INCLUSIONS data block in a MM2S/P input file.

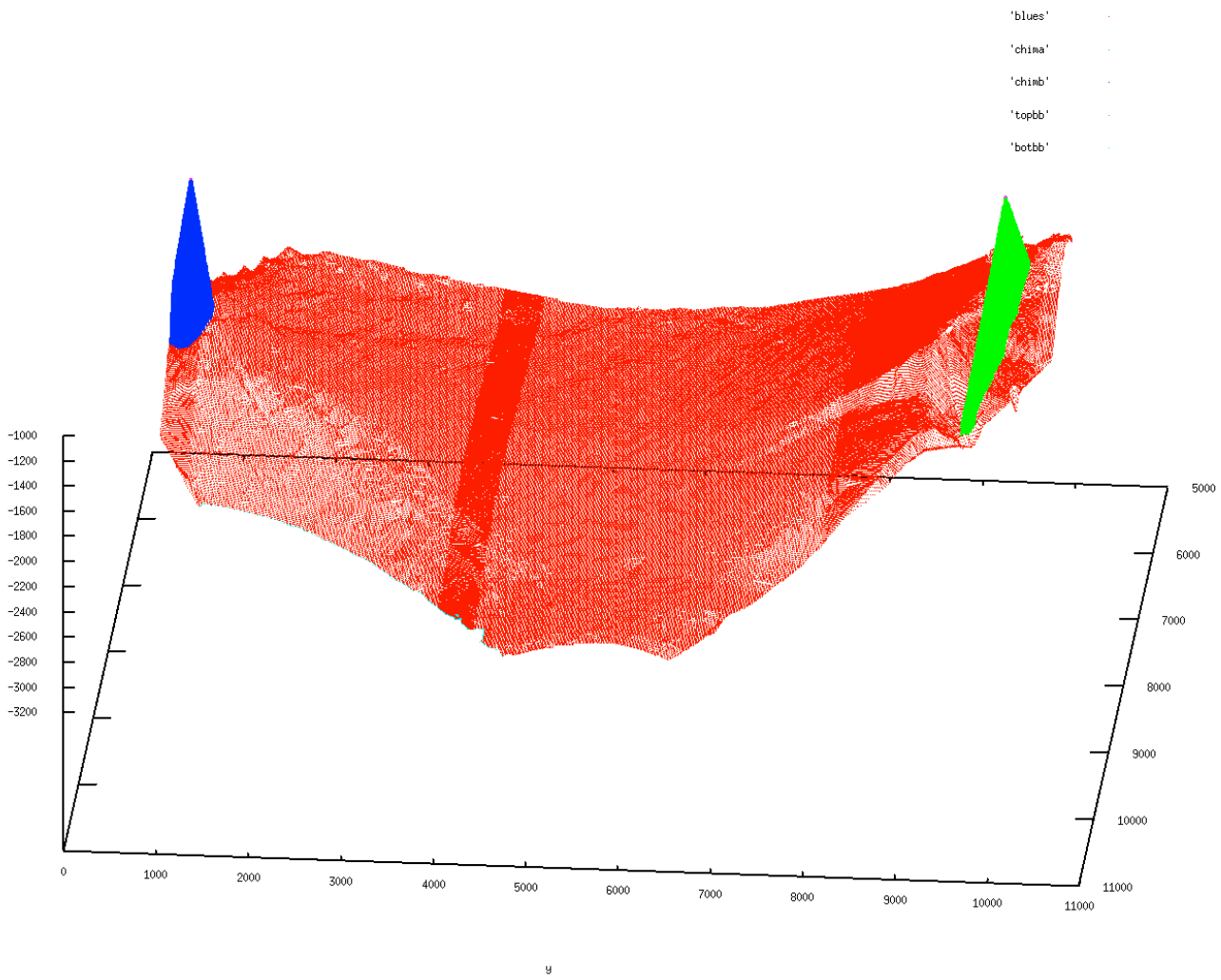

Figure 9. A complex grid comprising over 6 million elements generated by MM2S/P. The two chimneys with elliptical cone shapes that are clearly discernible were added through the `INCLUSIONS` data block, and the irregular shape of the domain was obtained through the definitions of multiple exclusion zones.

QUALITY ASSURANCE FOR THE TOUGH2 FAMILY OF CODES USING THE CODE SITA

Martin Navarro, Holger Seher, Stephan Hotzel, Jens Eckel

Gesellschaft für Anlagen- und Reaktorsicherheit (GRS) gGmbH
Schwertnergasse 1, 50667 Cologne, Germany
e-mail: martin.navarro@grs.de, holger.seher@grs.de, stephan.hotzel@grs.de, jens.eckel@grs.de

ABSTRACT

GRS uses the code TOUGH2 to analyze the safety of deep geological disposal systems for radioactive waste and continuously extends the code. The code extensions are gathered under the name TOUGH2-GRS.

In the context of radioactive waste disposal it is of great concern whether the code is correct and the simulation results are reliable. GRS has therefore set up a quality assurance program for TOUGH-derived codes. This includes the development of SITA, which is a tool for automated code testing.

In the present paper, we introduce the GRS quality assurance program for TOUGH2 and give a brief overview on TOUGH2-GRS and SITA. We present a common verification test for TOUGH2/EOS7R and TOUGH2-GRS. This test is part of a larger TOUGH verification procedure, which is still under development.

INTRODUCTION

GRS is a German technical safety organization in the field of nuclear safety conducting safety analyses for deep geological disposal systems for radioactive waste. GRS uses the code TOUGH2 (Pruess et al., 1999) in connection with the **E**quation **O**f **S**tate modules EOS7 and EOS7R to simulate multi-phase flow and radionuclide transport in repository systems. The code TOUGH2 has proved particularly useful to this task due to the availability and legibility of the source code. This gives sufficient flexibility to implement new processes and to understand and eliminate numerical problems that may arise. GRS is constantly extending the code. The code extensions are gathered under the name TOUGH2-GRS (Navarro, 2013).

In the context of radioactive waste disposal it is of major importance that the simulation code has undergone quality assurance processes and that the simulation results are thus reliable. The main measures to confirm reliability are code verification and validation.

Validation aims at showing that the physical model on which the code is based is appropriate to the problem that has to be solved. Regarding verification, part 4 of the IAEA General Safety Requirements (IAEA, 2008) distinguishes between *model verification*, as the "process of determining that a computational model correctly implements the intended conceptual model or mathematical model" and *system code verification*, which is "the review of source coding in relation to its description in the system code documentation". However, we will use the term code verification in a broader sense that includes both verification aspects mentioned in IAEA (2008).

The time frames considered in safety assessments for radioactive waste repositories usually range between 10,000 years and 1,000,000 years, depending on national regulation. In light of the extraordinary length of this time frame the possibility of code validation against experiments is limited. Facing these limits, code verification gains additional importance. Analytical solutions for simplified and idealized systems are available for all time-scales so that code verification is always possible, in principle.

If code development is a long-term project there is a need for frequent code verification. If a large set of verification tests has to be executed on a regular basis it is reasonable to automatize the testing procedure. Therefore, GRS has developed the code SITA for automatic code testing.

SITA is a "**SI**mulation and code **T**esting **A**ssistant" suitable for TOUGH codes.

Code testing with SITA may include intercomparison of different code versions. Different codes may have individual input and output format, which complicates the automation of cross-code comparisons. SITA solves this problem by introducing data interfaces for each code undergoing the testing procedure. These data interfaces allow SITA to generate code specific simulation input and to read code specific output data. By means of this concept SITA is able to handle a variety of TOUGH based codes.

In the present paper we describe the quality assurance concept of GRS for the codes TOUGH2 and TOUGH2-GRS. In the methodological chapter we will address the main elements of quality assurance, the aspects of verification standards and criteria, and methods of deriving test cases. The following chapters present the SITA code and give a short overview of TOUGH2-GRS. A common verification test for EOS7R and the radionuclide module of TOUGH2-GRS will be presented afterwards. The paper closes with a discussion of general quality assurance aspects and the conclusions.

METHODOLOGY

Quality Assurance

GRS's quality assurance concept for TOUGH2 and TOUGH2-GRS complies with the quality assurance guideline of GRS for software development projects (GRS, 2013). However, the general requirements defined by the guideline had to be interpreted and prioritized for the specific context of radioactive waste disposal, which has its focus on code reliability. Most crucial for demonstrating code reliability is code validation as well as the demonstration of the correctness (tested by code verification), robustness, testability, and maintainability of the code. In the present paper, we will concentrate on the aspects of verification, robustness, testability, and maintainability.

Code verification can be accomplished by test simulations. Specific problems connected to the development of verification tests will be considered in the following two chapters. Another effective means of code verification is the review of the source code. Code reviews are facilitated if the source code is well structured, well commented, and understandable.

Code reviews may or should be conducted as separate tasks by external reviewers. However, most programming activities inevitably involve partial code reviews by code developers. This is beneficial, because programmers will likely scrutinize other aspects of the source code than external reviewers. Code reviews by code developers do not comply with the standard review approach, which leaves this task to external reviewers. However, the additional involvement of developers in the review process appears to be reasonable in order to increase the quality of the code. In practice, effective code reviews by non-developers might be much more difficult to establish because the people who understand the source code well enough to judge its quality often are developers of the code.

The aspect of *code robustness* aims at safety against failures. In a broader sense this does not only apply to runtime failures but also to the likelihood of failures produced by false or non-optimal input data. For this reason, the code TOUGH2-GRS includes plausibility tests for input data and an extended warning and monitoring system.

Also, the code has to be easily *testable*. This is particularly important if tests are carried out frequently. Provided that frequent conduct of verification tests is a requirement, the code SITA makes the code TOUGH2-GRS testable.

Code *maintainability* is not only a matter of convenience but also a matter of reliability. If a code is badly maintained it might sooner or later become impossible to recall which changes have been made to which version of the source code and for which reason. This might lead to a deterioration of the code. GRS uses the software versioning and revision control system *Apache Subversion* (SVN) (Pilato et al., 2004) to coordinate different lines of code development and to record changes in a traceable way. SITA provides easy access to all lines of code development that are stored in the SVN repository.

Amongst others, this allows comparisons between different lines of code development.

Verification Standards and Criteria

Verification tests need a standard of comparison. From a physical point of view, the most desirable standard is provided by analytical solutions, which, however, might not always be available. For more complex problems, where analytical solutions cannot be found, comparisons of codes that implement the same physics can provide a means of verification. Parallel to the further development of a code, inter comparison with previous versions can be used to test whether the new code has deteriorated. This is not verification in a strict sense but it will help to detect coding errors.

In practice, accurate quantitative criteria that are able to decide whether a code is correct or incorrect are difficult to determine. Evaluation of code correctness therefore involves a significant amount of expert judgment. For this reason the basis of such evaluations, i.e. the results of the verification tests, should be documented in a traceable way.

Derivation of Verification Tests

If verification tests for a certain process show good agreement with analytical solutions, the physical process is not necessarily fully verified. There might be other test cases that perform badly due to coding errors that are only encountered under special circumstances. Yet, it is not practical to consider every conceivable verification test. Only a few tests can be taken into account so that code verification will depend on how test cases are selected. In order to increase the likelihood of error detection, GRS uses the following, diverse methods of selecting or deriving test cases:

- Published test cases are reproduced.
- Test cases are derived for all new processes added to TOUGH2-GRS as well as for basic processes of TOUGH2. Test case development is guided by the availability of analytical solutions for each process.
- For each process module, complete code coverage is envisaged (SITA is able to display code coverage information). Incomplete code coverage initiates the setup of new test cases.
- Test cases are developed for simulation problems observed in the past.
- Test cases are developed for code parts that developers or independent code reviewers have identified as potentially critical.
- Test cases are designed to cover both, natural and "synthetic" situations (see below).

Our term *synthetic test case* refers to simple test cases with few elements and idealized conditions that do not resemble natural conditions. It has been observed at GRS that synthetic test cases are very suitable to disclose coding errors. This may owe to extreme or idealized conditions (e.g. rounded numerical values) that may occur in synthetic test cases. Extreme or idealized conditions can activate conditional parts of the source code that are seldom encountered and thus not well tested. Also, small deviations from the expected behavior are easier to detect if idealized conditions are expected (e. g. zero fluxes). Eventually, if test cases are very simple, there often is a good understanding of how the system should evolve.

Whether code developers should be involved in constructing test cases can be judged differently. There might be a danger that developers try to hide flaws of their code if they have reason to fear a disclosure. However, the developers are the ones who are most apt to give valuable hints to critical parts and possible flaws of the code.

SITA

General Features

SITA is a tool for automatic code testing, which has been developed by GRS in the programming language Perl. Furthermore, SITA can run TOUGH simulations with regular TOUGH input files and serve as a pre- and post-processing tool. SITA interacts with the simulators by means of data interfaces. This enables SITA to handle other simulators like, for instance, the transport code MARNIE (Martens et al., 2002), which has been developed by GRS. SITA interacts with auxiliary programmes like Fortran compilers and *GNU make*. It uses *gnuplot* and

ghostscript to create plots, which are embedded in SITA's HTML output. SITA can be executed on a stand-alone computer or on a computer cluster. On a cluster, SITA will wait for the completion of all simulations before analyzing the simulation results.

Verification tests are defined by separate files using the JSON format. Test files include simulation input as well as information on how to analyze the simulation results. Test case files may contain EOS-specific parts to allow for a comparison of EOS modules. Time series or profiles can be plotted against other simulations results, xy-data or analytical functions.

Automatic compliance checks have not yet been implemented. This is not regarded as a major drawback by GRS because automatic compliance checks might restrain the user from scrutinizing the simulation results.

Source Code Management

Traceable verification tests have to state explicitly what exactly has been tested. This makes it necessary to distinguish between the categories *code*, *code version*, *code development line* and *executable* for the TOUGH code.

GRS uses the term *code* for independent sets of source codes. For example, "TOUGH2", "TOUGH2-GRS" and "TOUGH2-MP" are perceived as separate codes. *Code versions* refer to major changes in code functionality. Codes of the same version must, by our definition, have the same intended functionality as well as the same input and output format. Since SITA has to compare codes of different version it must be able to cope with different input and output formats.

Developers who work on the source code in order to correct the code, to implement new features, or provide snapshots of the code at a certain stage of development usually do this in separate directories. Each of these directories holds a complete version of the source code. SITA is able to address these source code directories, each of which corresponds to a *code development line,* according to our definition.

Eventually, *executables* are the entities that are subjected to the testing procedure. Every source code may produce different executables depending on the chosen EOS module, compiler and compiler options. SITA documents the applied compiler and compiler options in order to make the verification tests traceable.

TOUGH2-GRS

TOUGH2-GRS has been derived from version 2.0 of the TOUGH2 code, which has been developed by the DOE's Lawrence Berkeley National Laboratory. This version has been supplemented by the solver package t2cg22 of version 2.1 of the TOUGH2 code.

TOUGH2-GRS involves modules for additional processes as well as auxiliary modules that control and improve code performance. The code also includes plausibility checks for input data. This is regarded as an essential element for assuring the robustness of code application.

The following physical processes have been introduced to TOUGH2-GRS:

- Decay, sorption and transport of multiple radionuclides
- Compaction of backfill composed of crushed salt driven by the convergence of salinar host rock
- Generation of gas due to the corrosion of waste canisters, controlled and limited by water supply
- Permeability change of seals due to corrosive fluids
- Time-dependent change of seal permeability
- Pressure- or time-dependent dilation of microscopic gas pathways
- Alternative physical properties of the gas component
- Infiltration of gas into the salt host rock

New code parts have been implemented entirely in Fortran90/95. Implicit declaration of variables and use of COMMON blocks have been avoided because these are common sources of coding errors. As far as possible, the source code of new process models has been implemented as Fortran modules in separate files. This makes it easier to

evaluate how much of the source code has been covered by a set of test simulations.

EXAMPLE VERIFICATION TEST

In order to verify EOS7R and TOUGH2-GRS with regard to radionuclide decay and transport we have reproduced the verification test SAMR1 published by Oldenburg et al. (1995). The test covers radioactive decay as well as advective and diffusive flow of radionuclides. In the following, we will first introduce the radionuclide module of TOUGH2-GRS in detail before describing the verification test.

Radionuclide Module

The development of the radionuclide module (termed RNmod in the following) was initiated by the conception that transported radionuclides in conceivable contaminant transport conditions do not influence fluid flow significantly because of their low concentrations. In this context, the approach of EOS7R to solve the mass balance equations of main TOUGH2 components and radionuclides together is probably not optimal because both sets of balance equations can be solved successively. Also, the standard TOUGH2 tolerance limits for residuals are too large for radionuclide traces so that additional tolerance limits for radionuclides have to be introduced. The very low tolerance for radionuclide residuals can have a negative effect on code performance if the mass estimation for main components continues to converge during the Newton iteration loop thereby disturbing the estimation of radionuclide mass fractions.

RNmod therefore introduces radionuclides independently from the EOS module. Radionuclides are transported by diffusion and advection using the phase flows and phase distributions previously calculated by TOUGH2. RNmod can be used in connection with any EOS module.

Transport and linear adsorption of radionuclides are calculated by time integration using the Bulirsch-Stoer method (Stoer, 1980). With this approach TOUGH2-GRS follows the approach implemented in the code MARNIE (Martens et al., 2002), which is a flow and transport simulator designed for repositories in salt rock formations.

RNmod uses the same equations for advection and diffusion as TOUGH2/EOS7R. However, in contrast to TOUGH2/EOS7R, RNmod has a more accurate implementation of radioactive decay because it assumes exponential decay during a time step instead of linear decay.

Problem Description

In test case SAMR1, the model domain is a fully saturated horizontal column of 7 m length with inactive elements on both sides. The column is divided in horizontal direction into 200 grid elements of same volume and size.

The column material has a porosity of 30 % and a permeability of $1.24 \cdot 10^{-9}$ m². An initial steady state flow field with a pore velocity of 0.1 m/day is imposed on the column by applying a pressure of 100001.75 Pa to the left inactive element and a pressure of 100000 Pa to the right one (center-interface distances of inactive elements are set to $5 \cdot 10^{-6}$ m). Brine properties are set equal to those of pure water.

The parent radionuclide RN1 with assumed half-lifes of λ=20 d and $\lambda \rightarrow \infty$ is placed in the left inactive element with a mass fraction of 0.01. Radionuclide diffusion is characterized by a molecular diffusivity of $1.162 \cdot 10^{-7}$ m²/s and a tortuosity of 1. We assume that radionuclides are not adsorbed which corresponds to a retardation factor of R=1. The analytical solution of the problem is given in van Genuchten (1985) and details of the underlying equations and the boundary conditions can be found there. We have implemented the program CHAIN introduced by van Genuchten (1985) and have recalculated the analytical solution.

Results

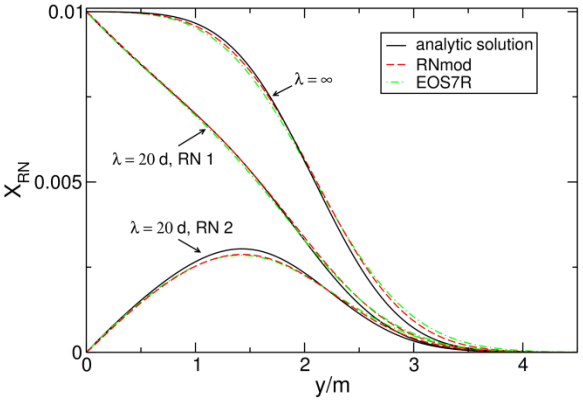

Figure 1. Horizontal profile of radionuclide mass fractions X_{RN} for parent radionuclide RN1 and daughter radionuclide RN2 at 20 days. The half-life of RN1 is λ=20 d and λ →∞ respectively. The upper time step width is 20000 s.

Figure 1 compares the analytical solution of van Genuchten (1985) with the results of two simulations performed with TOUGH2-GRS/EOS7R and TOUGH2-GRS/EOS7/RNmod. The comparison shows a satisfying agreement indicating that the relevant physics is correctly implemented within TOUGH2-GRS. Note that the concentration of the daughter radionuclide RN2 is not shown in Oldenburg et al. (1995). Results including adsorption with a retardation factor R=2 show similar agreement with the analytical solution but are not shown here.

In both, EOS7R and RNmod, the differential equations for radioactive decay are decoupled from the transport and energy equations. Radionuclide transport during a time step therefore takes place without radioactive decay. This suggests that the simulation results should deviate from the analytical solution if the time step width increases. Also, the error connected to the linear approximation of the decay process during a time step should increase with increasing time step. Possibly for this reason, Oldenburg et al. (1995) have suggested that the upper time step width limit should be well below the shortest half-life of the modelled radionuclides.

As a default, TOUGH sets no upper limit for the time step width thereby leaving the control of time step widths to the automatic time stepping mechanism. Consequently, time step width is mainly controlled by the differential equation solver but not by radionuclide half-lives. If the user refrains from defining an upper limit for the time step width – maybe because the simulations are time-consuming and require adaptive time stepping – the automatic time stepping mechanism could generate time step widths well above the shortest half-life resulting in significant errors. We have investigated this by recalculating the SAMR1 test without upper time step limit (see Figure 2).

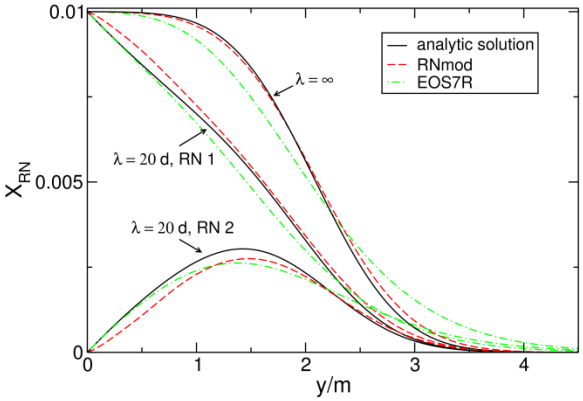

Figure 2. Horizontal profile of radionuclide mass fractions X_{RN} for parent radionuclide RN1 and daughter radionuclide RN2 at 20 days. The parameters are the same as in Figure 1, but there is no upper time step limit.

The observed deviations between the analytical solution and the results of EOS7R and RNmod (in connection with TOUGH2-GRS) are striking and underpin the importance of a fine-grained time discretization. However, it has to be noted that the observed deviations depend on the implemented time stepping mechanism.

The deviation of the TOUGH2-GRS/EOS7R results from the analytical solution for the case of no radioactive decay (λ→∞) was unexpected because no error should be caused by undue time discretization of the decay process. Possibly, the observed deviations are due to time-dependent numerical dispersion. This might explain the higher accuracy of the RNmod results because RNmod further subdivides every time step for the Bulirsch-Stoer method.

DISCUSSION

IAEA Safety Guide SSG-23 (IAEA 2012) states that "it should be ensured, as far as possible, that […] adequate quality assurance and quality control measures are applied to the software used". The expression "*as far as possible*" possibly reflects the principal problems of validation and verification briefly mentioned above.

Code verification tests can only cover a limited range of physical conditions and numerical states. Restrictions to code validation are introduced by assessment time frames well beyond human life expectation. Further on, there are modelling strategies that do not allow any validation at all because they do not aim at a realistic system description. This applies to conservative assumptions, over- or underestimations as well as to what-if considerations.

Requirement 18 of part 4 of the IAEA General Safety Requirements (IAEA 2008) states that "any calculational methods and computer codes used in the safety analysis have to undergo verification and validation to a sufficient degree". The meaning of "*sufficient degree*" is difficult to define and there obviously would be a problem if a "sufficient degree" would be impossible to achieve due to the validation and verification restrictions mentioned above.

There are no hard criteria to decide whether a simulation code used for repository system performance assessment is sufficiently verified or validated. This lack of criteria stresses the importance of documenting the basis of such decisions or of making statements on the degree of validation and verification.

Besides correctness, code robustness is important for the reliability of simulations too. Measures to improve code robustness may involve plausibility checks for input data. Also, the code may provide tools to aid the interpretation of simulation results thereby giving clues to erroneous input data. Eventually, it is possible to introduce procedures that care for the consistency of input data, especially if data acquisition and model setup take a long time and involve multiple revisions of data and assumptions. In a strict sense, data consistency is not a matter of code quality but it touches the question whether simulation results are reliable or not.

CONCLUSION

We have shown that automatic verification tests for TOUGH2 are possible using the code SITA, which has been developed by GRS. SITA is able to perform cross-code comparisons and comparisons with analytical solutions for code verification. The development of SITA and the definition of verification tests is part of a larger quality assurance programme of GRS for the TOUGH2 code that focusses on the reliability of the simulation results and thus on the quality of the code and the input data.

As an example, we have applied the SAMR1 verification test of Oldenburg et al. (1995) to TOUGH2/EOS7R and TOUGH2-GRS/EOS7/RNmod. Both codes show good agreement with the analytical solution for the combined process of radionuclide advection, diffusion and decay. However, appropriate time discretization is necessary to achieve accurate results.

ACKNOWLEDGMENT

This study has been funded by the German Federal Ministry for the Environment, Nature Conservation, Building and Nuclear Safety (BMUB) under the support code UM13A 03400.

REFERENCES

GRS (Gesellschaft für Anlagen- und Reaktorsicherheit): *Qualitätsmanagementhandbuch, Teil 1: Qualitätsmanagementprogramm.* Unpublished, 51p, Cologne, 2013.

GRS (Gesellschaft für Anlagen- und Reaktorsicherheit), Software Management Group: *Maßbahmen zur Qualitätssicherung bei der Erstellung von Computerprogrammen in der GRS.* – Attachment IV of part 3 of the GRS QM handbook, unpublished, Cologne, 2013.

IAEA (International Atomic Energy Agency), *The safety case and safety assessment for the disposal of radioactive waste: specific safety guide.* – IAEA safety standards series, no. SSG-23, ISBN 978–92–0–128310–8, 140p, Vienna, 2012.

IAEA (International Atomic Energy Agency), *Safety assessment for facilities and activities: general safety requirements*. – IAEA safety standards series, no. GSR part 4, ISBN 978–92–0–112808–9, 56p, Vienna, 2008.

Martens, K.-H., Fischer, H., Romstedt, P.: *Beschreibung des Rechenprogrammes MARNIE*. GRS-A-3027, 135 Seiten, Gesellschaft für Anlagen- und Reaktorsicherheit (GRS) mbH, Cologne, 2002.

Navarro, M.: *Handbuch zum Code TOUGH2-GRS.00a, Erweiterungen des Codes TOUGH2 zur Simulation von Strömungs- und Transportprozessen in Endlagern.* GRS-310, ISBN 978-3-939355-89-2, Gesellschaft für Anlagen- und Reaktorsicherheit (GRS) mbH, Cologne, 2013

Oldenburg, C.M. and Pruess, K.: *EOS7R: Radionuclide Transport for TOUGH2*. – Report LBL-34868, Lawrence Berkeley National Laboratory, Berkeley, Calif., 1995.

Pilato, C. M., Collins-Sussman, B., Fitzpatrick, B. W.: *Version Control with Subversion*. – O'Reilly, ISBN 0-596-00448-6, 1st edition, 2004.

Pruess, K., C. Oldenburg, and G. Moridis, *TOUGH2 User's Guide, Version 2.0*, Report LBNL-43134, Lawrence Berkeley National Laboratory, Berkeley, Calif., 1999.

Stoer J. and Bulirsch R.: *Introduction to Numerical Analyses*, Springer Verlag, New York, 1980.

FAST METHOD TO PREDICT OIL PRODUCTION FROM FRACTURED RESERVOIR

George Shu Heng Pau[1*], Stefan Finsterle[1], Kyung Jae Lee[1],
Rishi Parashar[2], and Yingqi Zhang[1]
[1]Lawrence Berkeley National Laboratory, Earth Sciences Division, Berkeley, California
[2]Desert Research Institute, Division of Hydrologic Sciences, Reno, Nevada
e-mail: gpau@lbl.gov

ABSTRACT

The success of a thermal water flood for enhanced oil recovery (EOR) depends on the geometrical and hydraulic details of the fracture network, which induces discrete, channelized flow behavior. The network also determines the effectiveness with which heat and brine penetrates the rock matrix, mobilizing and displacing the oil. Simulating an EOR operation using a discrete fracture network embedded in a low-permeability matrix is computationally very demanding, mainly because the detailed representation of the fracture network requires high mesh resolution. We propose to use the Proper Orthogonal Decomposition Mapping Method (PODMM) to reconstruct fine-resolution solutions based on efficient coarse-resolution solutions. In this reduced-order modeling (ROM) approach, the temporal evolution of the system is simulated for a relatively short time period using both a fine and coarse representation of the fractured reservoir. These results are then used as training snapshots to develop the ROM. During the prediction phase, only the coarse model is needed to calculate an approximation of the future system behavior, and the subgrid-scale dynamics of the discrete fracture network is then reconstructed very efficiently using the PODMM approach. We will demonstrate this novel application of PODMM by simulating a cyclic EOR operation in which hot brine is injected and oil produced from a single well.

INTRODUCTION

Thermal water flood is a common enhanced oil recovery (EOR) technique. However, economic viability of this EOR technique depends on whether we can predict the oil production rate accurately and thus justify the cost of employing the technique. Prediction of the oil production rate is typically obtained by constructing a numerical model that accurately captures the geometrical and hydraulic details of the fracture network, which induces discrete, channelized flow behavior. The network also determines the effectiveness with which heat and brine penetrates the rock matrix, mobilizing and displacing the oil. Simulating an EOR operation using a discrete fracture network embedded in a low-permeability matrix is computationally very demanding, mainly because the detailed representation of the fracture network requires high mesh resolutions.

In this paper, we apply a reduced order modeling (ROM) technique known as the Proper Orthogonal Decomposition Mapping Method (PODMM), first proposed by Robinson et al. (2012), that allows us to reconstruct the high-resolution solutions (which include the fracture network) based on coarse-resolution solutions obtained using models that only have upscaled, effective properties of the fracture network and thus can be efficiently simulated. This technique was recently enhanced and applied to land surface models to accurately reconstruct hydrological states, heat fluxes and carbon fluxes (Pau et al., 2014; Pau et al., 2015).

METHODS

Fracture Network Models

We demonstrate the proposed PODMM model-reduction approach for an EOR operation conducted in a fractured hydrocarbon reservoir. An individual cycle of the operation consists of four phases: (1) injection of hot water at 10 kg/s for 3 days, (2) an inactive soaking period of 4 days, (3) production of oil and water for 6 days at a total rate of 5 kg/s, and (4) a inactive period of 1 day. This two-week cycle is repeated 105 times for a total simulation time of 1470 days. The distribution of oil in the reservoir and the oil production rates are the key prediction variables of interest.

Simulating a long sequence of injection-production cycles is computationally expensive, especially if it is essential to capture the exchange of fluids between the reservoir rock (which contains the oil) and a network of discrete fractures embedded in that matrix (which provides the pathway for oil extraction). Moreover, system behavior and computational costs depend on the resolution with which the fracture network is represented in the model. The PODMM approach described below predicts the high-resolution behavior using a computationally efficient low-resolution model. Two models of different resolutions are thus developed: The high-resolution model (HRM) provides data for a relatively short training phase, and is used to demonstrate the accuracy of the ROM. The low-resolution model (LRM) provides approximate, efficient solutions for the entire simulation period; these solutions are then combined with PODMM to provide high-resolution predictions of the cyclic EOR operation. We examine three alternative LRMs (with a grid spacing of 5 m): an upscaled heterogeneous fracture-matrix model (LRM-fracture), a simple homogeneous model (LRM-homo), and a dual-porosity model (LRM-minc).

We consider a fracture network within a model domain of dimensions 100×50×30 m. Fractures are generated by randomly sampling values of size, orientation, and aperture from appropriate, truncated probability distributions. Two fracture sets with an average fracture spacing of 4 m are generated using the code ThreeDFracMap (Parashar and Reeves, 2011). Upscaled, anisotropic permeability modifiers are calculated and mapped onto structured TOUGH2 (Finsterle et al., 2014; Pruess et al., 1999) meshes with resolutions of 5 m and 2 m for the LRMs and HRM, respectively (see Figure 1). The LRM-fracture thus has about 15 times fewer elements than the HRM, making it significantly more efficient at the expense of loss of accuracy in representing discrete flow behavior in the fractures and fluid exchange with the matrix.

Figure 2 shows the oil saturation after the initial water flood. The LRM is a smooth representation of the considerably more intricate distribution obtained with the HRM. The PODMM procedure attempts to approximate and predict the HRM results based on the LRM results.

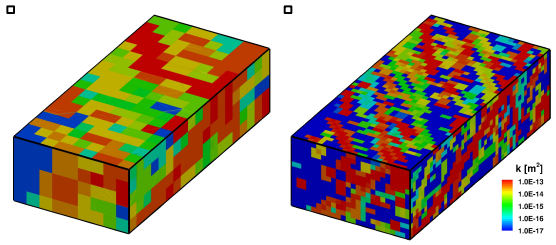

(a) (b)

Figure 1. Discrete fracture network mapped onto TOUGH2 continuum grid using (a) a low resolution of 5 m (LRM-fracture), and (b) a high resolution of 2 m (HRM).

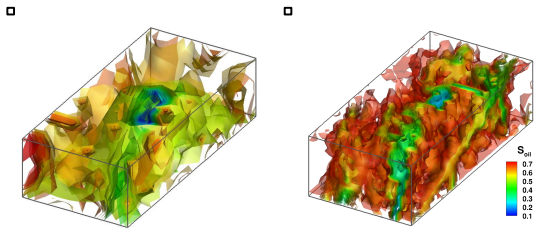

(a) (b)

Figure 2. Oil saturation after 3 days of hot water injection, calculated with (a) LRM-fracture and (b) HRM.

Proper Orthogonal Decomposition Mapping Method

We summarize the Proper Orthogonal Decomposition Mapping method (PODMM) here; more details can be found in Pau et al. (2014). The method consists of a training stage and a prediction stage. During the training stage, we determine N coarse- and fine-resolution solutions (**g** and **f**). We denote these solutions as the training set, and for the current problem it consists of solutions obtained at 1-day intervals from multiple consecutive injection-production cycles. We then perform a singular value decomposition (SVD) of the following matrix **W:**

$$\mathbf{W} = \begin{bmatrix} \mathbf{f}_1 - \overline{\mathbf{f}} & \cdots & \mathbf{f}_N - \overline{\mathbf{f}} \\ \mathbf{g}_1 - \overline{\mathbf{g}} & & \mathbf{g}_N - \overline{\mathbf{g}} \end{bmatrix} \qquad (1)$$

where

$$\overline{\mathbf{f}} = \frac{1}{N}\sum_{i=1}^{N}\mathbf{f}_i, \quad \overline{\mathbf{g}} = \frac{1}{N}\sum_{i=1}^{N}\mathbf{g}_i \ , \qquad (2)$$

to determine the POD bases, $\zeta_i \ , i = 1,\ldots M$, which can be decomposed into

$$\zeta_i = \begin{bmatrix} \zeta_i^{\mathbf{f}} \\ \zeta_i^{\mathbf{g}} \end{bmatrix} \quad (3)$$

where $\zeta_i^{\mathbf{f}}$ and $\zeta_i^{\mathbf{g}}$ are components associated with the HRM and LRMs, respectively; and M is the chosen number of POD bases to use in an approximation.

During the prediction stage, we first determine a coarse-resolution solution $\mathbf{g}$, and solve

$$\boldsymbol{\alpha}(\mathbf{g}) = \arg\min_{\gamma} \| \mathbf{g} - \overline{\mathbf{g}} - \sum_{i=1}^{M} \gamma_i \zeta_i^{\mathbf{g}} \|_2 \quad (4)$$

where $\| \cdot \|_2$ is the root mean square of a vector and γ_i is the mixing coefficient of POD basis $\zeta_i^{\mathbf{g}}$. The downscaled fine-resolution solution $\mathbf{f}^{\mathrm{PODMM}}$ is then given by

$$\mathbf{f}^{\mathrm{PODMM}} = \overline{\mathbf{f}} + \sum_{i=1}^{M} \alpha_i(\mathbf{g}) \zeta_i^{\mathbf{f}} . \quad (5)$$

The parameter M is the main model parameter for the ROM since it controls the accuracy and stability of the approximation. By using a larger M, we include more POD bases and the resulting approximation is expected to be more accurate. However, depending on the dimension of $\mathbf{g}$, larger M can also leads to overfitting when solving minimization problem given by equation (4). We describe how we determine an appropriate M in the next section.

Training and Validation Datasets

As a reference, the HRM we use is a fine-resolution discrete fracture network model with uniform grid spacing of 2 m. Using this computationally demanding model, we simulate a relatively short period (i.e., the initial few injection-production cycles) to train the ROM. To distinguish between the various ROMs, we use ROM-fracture, ROM-homo, and ROM-minc to denote ROMs constructed using the low-resolution heterogeneous fracture model (LRM-fracture), the homogeneous model (LRM-homo) and the dual-porosity model (LRM-minc), respectively. We focus on the prediction of oil saturation (S_{oil}) and oil production rate (Q_{oil}). ROMs for S_{oil} jointly considered S_{oil}, pressure (P) and temperature (T). ROMs for Q_{oil} are trained based on the fluxes of oil (F_{oil}), water (F_{water}) and heat (F_{heat}).

We examined two training periods: 5 and 15 EOR cycles (i.e., 70 and 210 days). Daily solutions from the coarse and fine models within these periods are used to train the ROMs. Since the injection-production cycle consists of three distinct stages (injection, soaking and production), separate ROMs are constructed for the three stages because the solutions in each stage can have unique characteristics. For example, F_{oil} is close to zero during the soaking stage, and of different characteristics during the injection and production stages. To determine an appropriate M to use in the ROMs (M_R), one additional cycle is simulated for each training period using HRM and LRMs. M_R is then given by M that minimizes the absolute error between the solutions obtained with the ROM and HRM within that cycle. We note that M_R will be different for the three stages.

In the results section, we study the accuracy of the ROMs using validation sample sets consisting of the daily HRM solutions determined up to the 105$^{\mathrm{th}}$ cycle (Day 1470). Depending on the training periods, the validation sample set starts from the 6$^{\mathrm{th}}$ cycle (Day 71) for ROM trained using 5 cycles, and the 16$^{\mathrm{th}}$ cycle (Day 211) for ROM trained using 15 cycles.

RESULTS

Production Rate

The ROMs are able to reproduce the oil production rates (Q_{oil}) very accurately. Figure 3(e)-(f) show that the relative error between Q_{oil} of HRM and ROM-fracture, constructed using 15 training cycles, is less than 6% averaged over the production stage during the 55$^{\mathrm{th}}$ cycle. The error stays approximately the same even when predicting 105 cycles. Compared to the Q_{oil} obtained using LRMs (Figure 3(a)-(b)), ROM-fracture reduces the LRM-fracture's biases by 83% and 85% respectively for the 55$^{\mathrm{th}}$ and 105$^{\mathrm{th}}$ cycles. In addition, it is clear that 5 training cycles are sufficient to accurately predict Q_{oil}. Instead of simulating 105 cycles using the HRM, we will only need to calculate 6 cycles using the HRM, thus reducing the computational cost by a factor of 17; running the LRM and setting up and evaluating the ROM is computationally very efficient.

Comparing the three different ROMs, Figure 3 shows that ROM-fracture is consistently more accurate than ROM-homo and ROM-minc. This is expected as (1) LRM-fracture is more accurate than LRM-homo and LRM-minc (Figure 3(a)-(b)), and (2) the approximation error decreases more uniformly with M, resulting in a more accurate determination of M_R. Both reasons can be attributed to the fact that LRM-fracture is a better approximation of the HRM since it retains some of the heterogeneous structure of the HRM.

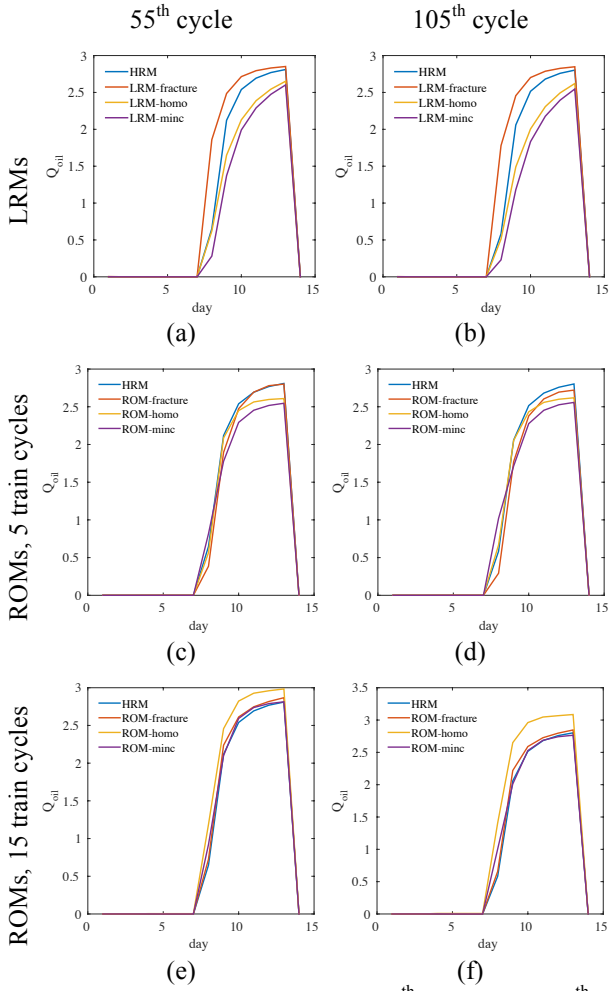

Figure 3. Oil production rates at 55th cycle and 105th cycle using LRMs and ROMs, compared to HRM, using 5 and 15 training cycles. ROMs reduce the biases in the LRM. ROM-fracture is consistently better than ROM-homo and ROM-minc.

When the ROMs are trained using 15 training cycles, ROM-minc can be as accurate as ROM-fracture (Figure 3(e)-(f)). ROM-homo, however, consistently overpredicts Q_{oil}. This overprediction is likely due to overfitting. Since the approximation error increases with time, M_R should decrease over time to avoid overfitting. We will study how M_R should be reduced over time in the future. We note that if we have determined M_R by minimizing the absolute error of Q_{oil} between the ROMs and the HRM over the entire validation period, we are able to get good approximations for all ROMs. However, this approach is not practical since we want to avoid simulating the HRM over an extended period of time.

Reproduction of Fine-scale Solution

We first determine how the accuracy of the ROMs changes over time. Initial tests suggest that ROM-homo and ROM-minc cannot reproduce the heterogeneity in the solution obtained using the HRM; therefore, we will only discuss results obtained using ROM-fracture in this section. To measure the accuracy of the approximation, we define the daily root mean square error (RMSE) of the ROM approximation over the validation sample set as $\varepsilon_{\text{RMSE}}$.

Figure 4 shows that the error increases with the number of days after the initial training period. The use of 15 instead of 5 training cycles reduces mean $\varepsilon_{\text{RMSE}}$ by 35%. In addition, $\varepsilon_{\text{RMSE}}$ of ROM-fracture trained with 5 cycles grows much faster than ROM-fracture trained with 15 cycles. The initial transient dynamics in the first 5 cycles are most likely poor representations of the long-time behavior of S_{oil}, resulting in the poor approximation. Subsequent slower growth of $\varepsilon_{\text{RMSE}}$ indicates that S_{oil} changes more slowly at later times. Compared to the approximation of Q_{oil}, the use of the larger number of training cycles has a more significant impact on the approximation of S_{oil}.

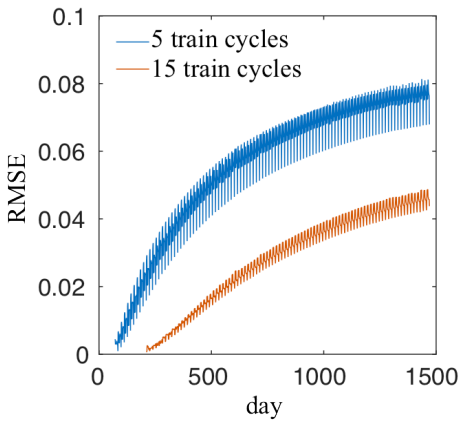

Figure 4. The RMSE of soil increases with number of days after the training period.

We now determine how well PODMM reproduces the S_{oil} distribution. Figure 5(c)-(d) shows the heterogeneous structure in S_{oil} at the end of the 55th cycle (Day 770) and 105th cycle (Day 1470). Figure 5(g)-(h) shows that ROM-fracture trained with 15 cycles is able to reproduce most of the intricate structure of S_{oil} on the 2 m scale. However, ROM-fracture is not able to reproduce the very high S_{oil} values, i.e., the approximated solutions are smoother. This discrepancy can be attributed to the neglected POD bases; 0.04% of the variance in the training snapshots is not captured by the ROM (M_R=9). Consistent with the results in Figure 4, ROM-fracture trained with 5 cycles has poorer predictive capability (Figure 5(e)-(f)). Nonetheless, in both cases, ROM-fracture added significant amount of small-scale structure to the LRM results (Figure 5(a)-(b)). In this respect, the PODMM can be viewed as a downscaling procedure. With 15 training cycles (plus one additional cycle for determining M_R), the computational cost of simulating 105 cycles is reduced by a factor of 6.5.

CONCLUSIONS AND FUTURE WORK

We have demonstrated that PODMM is capable of predicting long-time behavior of the oil production rate (Q_{oil}) and oil saturation (S_{oil}). The main conclusions are:

(1) The number of training cycles depends on the properties of the variables we are approximating. We showed that Q_{oil} is accurately approximated using only 5 training cycles while 15 training cycles are needed to reproduce the intricate structure of S_{oil} using the PODMM method.

(2) The approximation errors grow with time, indicating that the resulting ROMs have a limit to how far they can predict into the future without significant loss of accuracy. How that limit can be determined without simulating the HRM for an extended period of time will be studied in the future.

(3) Different LRMs can be used with PODMM. For some variables (e.g., Q_{oil}), simpler LRMs (e.g., a dual-porosity model) can produce a ROM that is sufficiently accurate for predictive purposes. However, ROMs constructed using more complex LRMs that are better representations of the HRM will typically have more consistent predictive capabilities.

For future work, we plan to study how PODMM can be used in cases where parameters such as injection rate, injection duration, production rate and production duration, are varied. In addition, applicability of PODMM to higher-resolution models and more complex models (e.g., subsurface flow coupled to geomechanics) will be studied. We will continue to study how we can improve the robustness of PODMM.

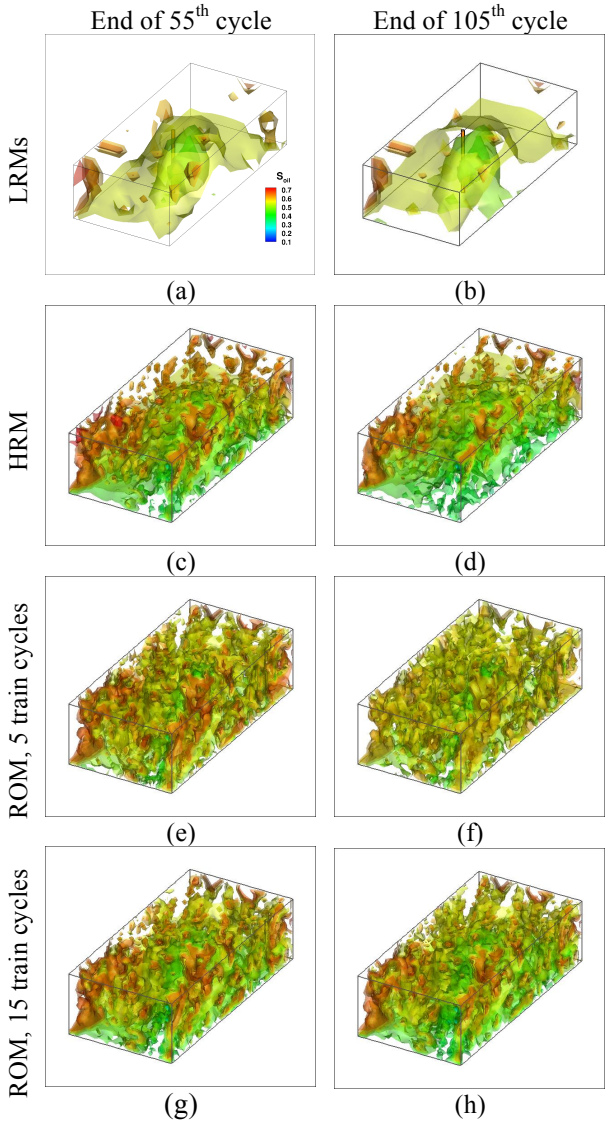

Figure 5. Oil saturation S_{oil} of LRM-fracture, HRM, ROM-fracture (5 training cycles) and ROM-fracture (15 training cycles) for the last day of the 55th and 105th cycles.

ACKNOWLEDGMENT

This research was supported, in part, the U.S. Department of Energy under Contract #DE-AC02-05CH11231.

REFERENCES

Finsterle, S., E. L. Sonnenthal, and N. Spycher, Advances in subsurface modeling using the TOUGH suite of simulators, *Computers & Geosciences*, 65, 2-12, 2014.

Parashar, R. and D. M. Reeves, Computation of flow and transport in fracture networks on a continuum grid, Golden, CO2011, 2011.

Pau, G. S. H., G. Bisht, and W. J. Riley, A reduced-order modeling approach to represent subgrid-scale hydrological dynamics for land-surface simulations: application in a polygonal tundra landscape, *Geosci. Model Dev.*, 7, 2091-2105, 2014.

Pau, G. S. H., C. Shen, and W. J. Riley, Accurate and efficient prediction of fine-resolution hydrologic and carbon dynamics from coarse-resolution models, 2015. Submitted.

Pruess, K., G. Moridis, and C. Oldenburg, TOUGH2 User's Guide, Version 2.1, Report LBNL-43134, Lawrence Berkeley National Laboratory, Berkeley, California, 1999.

Robinson, T., M. Eldred, K. Willcox, and R. Haimes, Strategies for multifidelity optimization with variable dimensional hierarchical models, 47th AIAA/ASME/ASCE/AHS/ASC Structures, Structural Dynamics, and Materials Conference, Reston, Virigina, 2012.

iMatTOUGH: AN OPEN-SOURCE MATLAB-BASED GRAPHICAL USER INTERFACE FOR PRE- AND POST-PROCESSING OF TOUGH2 AND iTOUGH2 MODELS

Anh Phuong Tran, Baptiste Dafflon, Susan Hubbard

Lawrence Berkeley National Laboratory
Earth Sciences Division
Berkeley, CA, 94720, USA
e-mail: APTran@lbl.gov

ABSTRACT

TOUGH2 is a nonisothermal multi-phase, multi-component model that simulates the heat and fluid flows in porous and fracture media (Pruess *et al.*, 1999). iTOUGH2 is a program that is used for parameter estimation, sensitivity analysis and uncertainty propagation analysis for TOUGH2 (Finsterle, 1999). Although the input and output in TOUGH2 and iTOUGH2 are well organized and structured, the natural complexity of these models and the text file editor have caused many difficulties for users to manage them. As a result, it is beneficial to develop a graphical user interface (GUI) to facilitate model setup.

However, so far there is no program that processes input and output of both TOUGH2 and iTOUGH2. In this study, we present a Matlab-based code (iMatTOUGH) that allows users to generate all necessary inputs for TOUGH2 and iTOUGH2, execute these models, visualize and analyze their outputs. The idea of development of this program is to hide the complicate input and output data from users to help them to concentrate on analyzing the model performance.

OVERVIEW

Prior to the development of iMatTOUGH, several GUIs supporting TOUGH2 have been developed. For example, Li *et al.* (2011) developed TOUGHER to control the input and output of TOUGHREACT. Adrian Croucher (University of Auckland, New Zealand) developed a library of Python scripts (named PyTOUGH) for automating setup and execution of TOUGH simulations. Using PyTOUGH, Wellmann *et al.* (2012) developed a workflow that processes grid generation, model setup, execution, and result analysis. Berry *et al.* (2014) developed TOUGH2GIS, a GIS-based pre-processor that allows the user to create locally refined unstructured (Voronoi) grids and to assign rock types to grid blocks.

In addition to these open-source programs, there are commercial products that support the development of TOUGH2 models, e.g. PetraSim (http://www.thunderheadeng.com/petrasim/), mView (http://geofirma.com/software/mview/), and Leapfrog (http://www.leapfrog3d.com/).

PROGRAM STRUCTURE AND GRAPHICAL INTERFACE

Main Control

Figure 1 presents the workflow supported by iMatTOUGH. The program can generate TOUGH2 and iTOUGH2 input files (pre-processing), execute them and visualize their results (post-processing). All of these processes can be called from the Main control interface as shown in Figure 2. It is worth noting that because iMatTOUGH obtains the soil material information from the ROCK block in the TOUGH2 input file and shows it in the iTOUGH2 user interface, the TOUGH2 input file must be created first. One typical characteristic of the program is its context-based approach, i.e., when possible, it automatically fills information for users to reduce their workload and mistakes. For example, if users select to perform sensitivity analyses, the program will show requirements related to sensitivity analysis and hide optimization requirements. If the observation variable is temperature, the program will understand that it is observed at an element and shows information related to elements. By contrast, if the observation is flow rate, the program will present the requirements for connections. This context-based approach is applied for both pre- and post-processing.

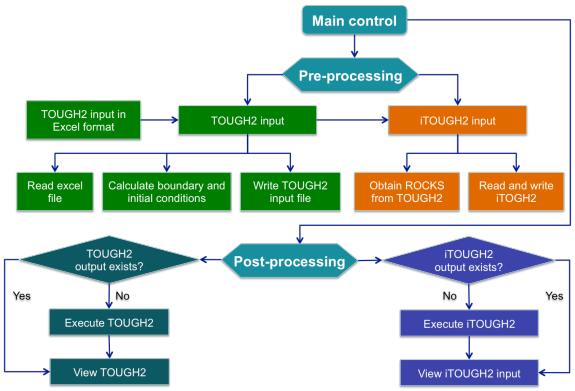

Figure 1. Workflow of the iMatTOUGH for pre- and post-processing TOUGH2 and iTOUGH2 models.

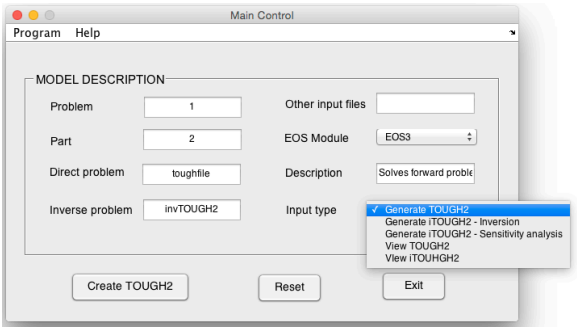

Figure 2. Main control interface.

Pre-Processing

Figure 3 shows the GUI of the TOUGH2 input generation. Users need to provide required information for TOUGH2 in a formatted EXCEL file as shown in Figure 4. The EXCEL file includes 15 sheets corresponding to different blocks in TOUGH2 and additional information for the mesh making (MESHMAKER), and specifying boundary information (BOUND) and initial conditions (INITIAL). The program will read the EXCEL file, process initial and boundary conditions (if necessary) and write the TOUGH2 input file.

Figure 5 presents the GUI of the iTOUGH2 input generation. This interface is divided into three sections, namely, PARAMETER, OBSEVATION and COMPUTATION. The PARAMETER section asks for information about the estimated parameters, the OSERVATION requires information related to observation data, and the COMPUTATION requires optimization/sensitivity analysis information (e.g., optimization algorithm, sensitivity analysis method, type of objective function, convergence criteria, output options).

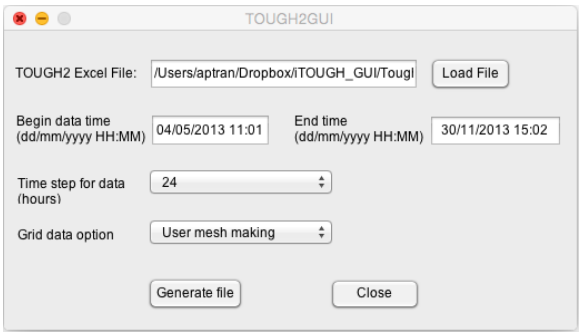

Figure 3. User interface for TOUGH2 input file generation.

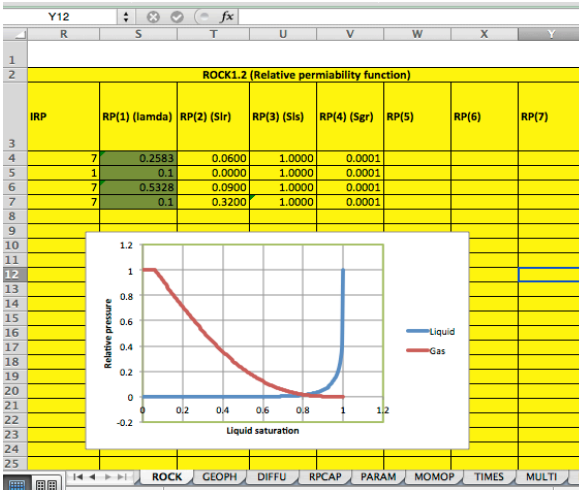

Figure 4. Excerpt from the TOUGH2 EXCEL spreadsheet, showing the input of relative permeability function parameters.

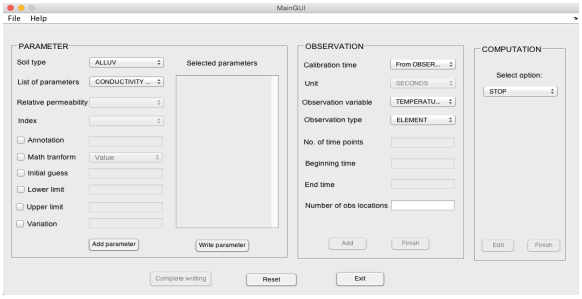

Figure 5. User interface for iTOUGH2 input generation.

Mesh generation

One of the hardest tasks of TOUGH2 pre-processing is to generate the computational mesh. iMatTOUGH can internally create the rectangular mesh. To do that, users need to provide the number of grid cell increments and grid sizes in X, Y, and Z directions. The program automatically sets the name of elements and makes the connections between them. It also

can assign the materials for the elements when users provide the spatial ranges of materials.

Initial and boundary conditions

TOUGH2 is a package that was developed for modeling flow in porous and fractured media, in as a general way as possible. Consequently, processing initial and boundary conditions that are usually different for different case studies are important. For the special case of nonisothermal flow simulation, the following features are implemented in iMatTOUGH:

- Adjust the atmospheric pressure from the standard one with consideration of the elevation of the study site
- Calculate the air mass fraction of the atmosphere from air temperature, relative humidity and atmospheric pressure
- Convert rainfall units (inch/hour) to source units (kg/s)
- Estimate the soil surface temperature (top temperature boundary condition) from the air temperature
- Approximate the bottom temperature boundary condition from the soil surface temperature using the analytical solution of the heat transport equation
- Estimate the bottom pressure boundary condition from the groundwater table depth using the hydrostatic equation
- Estimate the initial profile of temperature by interpolating the measured temperature data at the beginning of the simulation period
- Approximate the initial profile of the gas saturation in the unsaturated zone from the measured matric potential data at the beginning of the simulation using the water retention function

Post-processing

The program first checks if the output file of TOUGH2/iTOUGH2 is available. If it is not available, the program will execute TOUGH2/iTOUGH2. Figure 6 presents the user interface for viewing TOUGH2 and iTOUGH2 results. The program allows users to view all variables (e.g., temperature, gas saturation, heat rate, gas and fluid rate) from the TOUGH2 output file at different locations (elements and connections) and times in 1, 2 or 3 dimensions. In iTOUGH2 viewer, users can see the sensitivity of the model outputs with respect to different parameters at different locations and times so that they can identify the most sensitive parameters/locations/times. The program allows comparing measured and modeled data with different plotting types. The statistical criteria that evaluate the agreement between observation and modeling in iTOUGH2 are also shown.

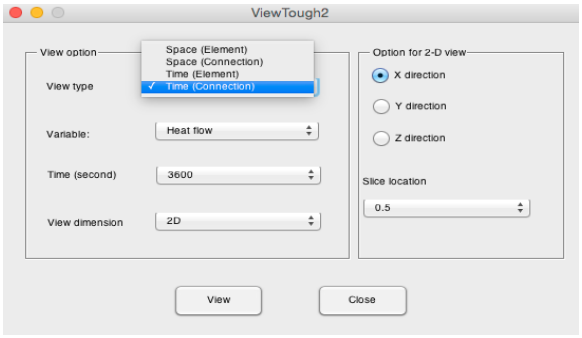

(a)

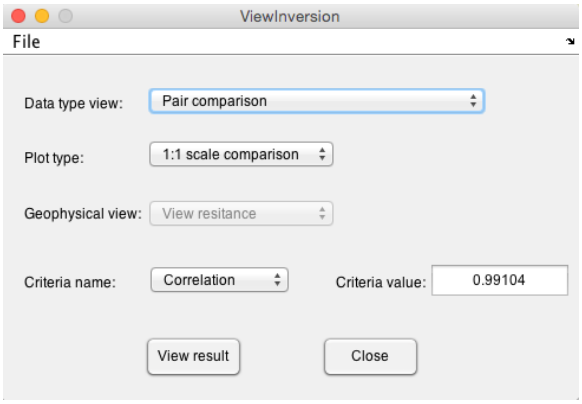

(b)

Figure 6. User interface for viewing (a) TOUGH2 and (b) iTOUGH2 outputs.

EXAMPLE

In order to show the capability of iMatTOUGH, we applied it for a case study that used iTOUGH2 to estimate the hydrological, thermal and petrophysical parameters from matric potential, temperature and Electrical Resistivity Tomography (ERT) data. Figure 7 shows the computational mesh generated by iMatTOUGH. The computational domain was divided into 30 equally spaced columns, each with a size of 1 m in the horizontal direction. In the vertical direction, the cell size is 0.05 m for the uppermost 2

m, 0.3 m for the next 1.5 m and 0.6 m for the last 3 m. Figure 8 shows an example of the temperature at time *t*=100 (hour) in 3-D plotted by iMatTOUGH from the TOUGH2 output. Figure 9 shows the comparison between modeled and measured temperature at a depth of 1.5 m from iTOUGH2 output.

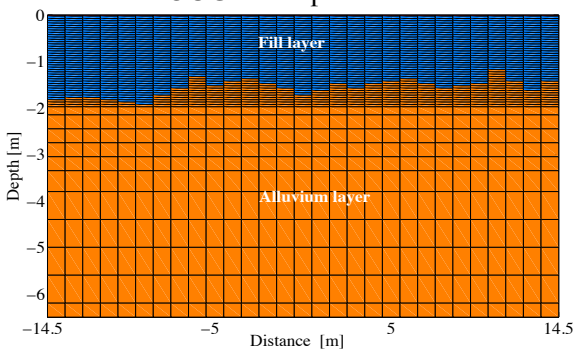

Figure 7. Computational mesh of the Rifle case study generated by iMatTOUGH.

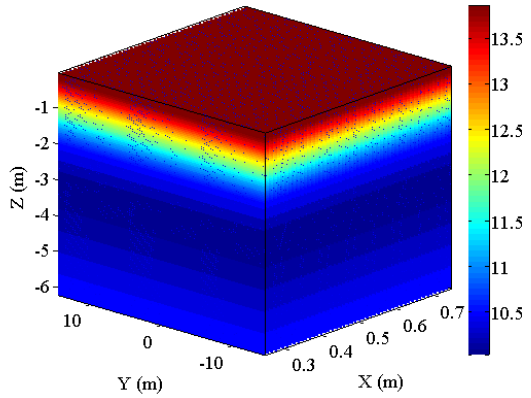

Figure 8. 3-D plot of the subsurface temperature at time t=100 hour obtained from the TOUGH2 output.

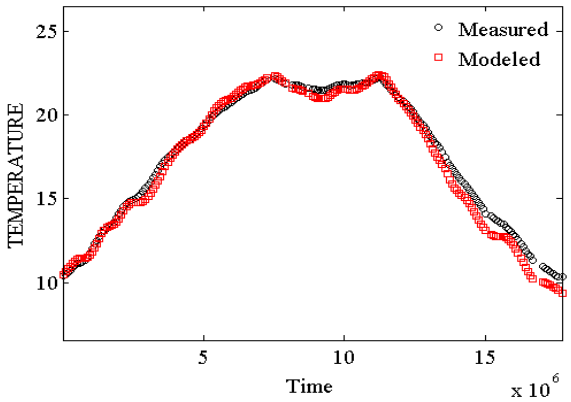

Figure 9. Comparison of measured and modeled temperature at depth z=1.5 m obtained from the iTOUGH2 output.

CONCLUDING REMARKS

iMatTOUGH is a new, Matlab-based software tool that allows convenient generation of TOUGH2 and iTOUGH2 input files. Moreover, it provides basic model setup and visualization capabilities. The program requires Matlab and Excel to perform all of its tasks.

ACKNOWLEDGMENT

This material is based upon work supported as part of the Subsurface Science Scientific Focus Area funded by the U.S. Department of Energy, Office of Science, Office of Biological and Environmental Research under Award Number DE-AC02-05CH11231. The authors would like to thank Stefan Finsterle for reading and editing the manuscript.

REFERENCES

Berry, P., S. Bonduá, V. Bortolotti, C. Cormio, E.M. Vasini, 2014. A GIS-based open source pre-processor for georesources numerical modeling, *Environmental Modelling & Software* 62, 52-64.

Finsterle, S. (1999), iTOUGH2 User's Guide, Lawrence Berkeley National Laboratory, Berkeley, CA.

Li, Y., Niewiadomski, M., Trujillo, E., Sunka-valli, S.P., 2011. Tougher: a user-friendly graphical interface for TOUGHREACT. *Computers & Geosciences* 37 (6), 775-782.

Pruess, K., C. Oldenburg, and G. Moridis (1999), TOUGH2 user's guide, version 2.0, Lawrence Berkeley National Laboratory, Berkeley, CA.

Wellmann, J. F., A. Croucher, and K. Rege-nauer-Lieb, 2012. Python scripting libraries for subsurface fluid and heat flow simulations with TOUGH2 and SHEMAT." *Computers & Geo-sciences* 43, 197-206.

DEVELOPMENT OF NUMERICAL APPROACHES FOR SIMULATION OF SLURRY FLOW IN FRACTURE/POROUS MEDIA

Xiaoyu Wang[1], Keni Zhang[1,2], Lehua Pan[2], Chaobin Guo[3]

[1] College of Water Sciences, Beijing Normal University, Beijing 100875, China
[2] Earth Sciences Division, Lawrence Berkeley National Laboratory, Berkeley, CA 94720, USA
[3] School of Mechanical Engineering, Tongji University, Shanghai 200092, China
e-mail: keniz@bnu.edu.cn

ABSTRACT

Drill cutting disposal by reinjection into the subsurface is an economic and environmentally friendly solution for oil and gas operations under zero-discharge requirements. For permanently and safely isolating the cuttings, the slurry of refining cuttings is injected into deep formations. Injection of slurry involves a complex flow process, because of its rheology and interaction with the formations. A new module for the TOUGH2 family of codes for modeling Bingham-like slurry flow is developed in this paper. The new development treats the slurry as a Bingham fluid by using an effective potential gradient to characterize its flow pattern. In this study, the mixed fluid properties of slurry and groundwater, precipitation-dissolution of slurry, and the impact of precipitation on formation porosity and permeability are investigated. The new code can be used for analyzing slurry transport, pressure distribution, and sealing capability of the cap rock. It predicts the injectivity and the storage capacity of the formation, the time when the formation breaks down, and further helps determining the optimal injection scheme. Simulations show that a short period intermittent slurry injection with lower density into shallower formations is preferable for fracturing. However, it may lead to a quick formation breakdown with the associated leakage risk. The simulated pressure oscillation matches well with the counterpart of monitoring data in a Texas cuttings re-injection project.

INTRODUCTION

Cuttings re-injection (CRI) is a cost-effective and environmentally friendly solution for drill waste disposal. It avoids transportation risks, achieves zero-discharge, and offers long-term safe disposal. CRI technology has been widely used. However, the supporting numerical simulators are still in the developing phase, because of the difficulty in dealing with 1) the complicated slurry rheology; 2) the interaction between the slurry and underground fluid flow; and 3) the reaction of subsurface formation to slurry injection. Most studies focus on the fracture propagation during slurry reinjection, because it is a crucial issue for both environmental safety and storage capacity (Shioya et al., 2002; Yamamoto et al., 2004; Shadizadeh et al., 2011). Potential blockage in both well and formation by cutting settling is one of the major risks in CRI projects (Guo et al., 2004). Therefore, the process of slurry flow plays an important role in slurry storage site characterization. Solid transport models depict slurry flow as two-phase flow of (1) a high-viscosity, non-linear fracturing fluid, and (2) a solid, i.e., the cuttings particles (Shioya et al., 2002). A development is added in the model by improving the slip velocity formula and considering the effect of solid particles on fluid viscosity (Yamamoto et al., 2004). These solid transport models could not show the miscibility of the slurry with groundwater. A power law relationship is used to characterize the rheology of slurry without considering particle settlement (Shadizadeh et al., 2011).

In this paper, a numerical method is developed to simulate Bingham-like slurry flow in subsurface systems. The rheology of slurry, the mixed fluid properties of slurry and groundwater, sediment-dissolution of slurry, and the impact of sediment on formation properties are investigated. The new development treats the slurry as a Bingham fluid by using an effective potential gradient to characterize its flow pattern (Wu et al., 1998), values the minimum potential

gradient of Bingham fluids with yield stress and permeability (Pascal, 1986), and computes yield stress by a linear relationship with the concentration of the gelatinizer (xanthan gum) in the slurry. The simulator developed in this paper is an extension of TOUGH2/EOS7. It is able to deal with three-dimensional slurry transport in anisotropic porous and fractured media. The simulator discretizes the continuum equations using the integral finite difference method (IFDM) (Edwards, 1972; Narasimhan et al., 1976). Numerical examples are simulated to investigate the impacts of engineering parameters on slurry flow, such as slurry density, injection depth, and intermittent injection schemes. In addition, a case study is discussed for a site-scale model of a Texas oil field.

METHODOLOGY

The miscible slurry flow in subsurface systems is modeled as consisting of an aqueous phase (groundwater and Bingham-like slurry) and solid phase (particle sediment). The slurry first dissolves in the groundwater flow system. The mixed fluid complies with multiphase Darcy's law, and acts as a Bingham fluid if the mass fraction of the slurry in the mixed flow is high enough. The aqueous phase with Bingham characteristics stops flowing and begins precipitating after several hours if the fluid pressure gradient is below a threshold; the sediment will be stirred up again and form a slurry when the pressure gradient is high enough. The porosity and permeability of the formation will change due to precipitation and dissolution, which later affects the underground fluid flow.

The new code can be used for analyzing slurry transport, pressure buildup, and sealing capability of the cap rock. It predicts injectivity for different formations, the storage capacity of the formation, the time when the formation breaks down, and further helps determining the optimal injection scheme.

Governing Equation

In this study, the subsurface system contains two components, water and slurry. Water stays in teh aqueous phase, while the slurry may precipitate into a solid phase or dissolve into the aqueous phase. These two components follow the mass balance equation, and each phase can be described by multiphase Darcy's law:

$$\frac{\mathrm{d}}{\mathrm{d}t}\int_{V_n} M^\kappa \mathrm{d}V_n = \int_{\Gamma_n} \boldsymbol{F}^\kappa \cdot \boldsymbol{n}\mathrm{d}\Gamma_n + \int_{V_n} q^\kappa \mathrm{d}V_n \quad (1)$$

$$M^\kappa = \phi \sum\nolimits_\beta s_\beta \rho_\beta X_\beta^\kappa \quad (2)$$

$$\boldsymbol{F}^\kappa = \sum\nolimits_\beta \boldsymbol{F}_\beta X_\beta^\kappa \quad (3)$$

$$\boldsymbol{F}_\beta = -k\frac{k_{r\beta}\rho_\beta}{\mu_\beta}\left(\nabla P_\beta - \rho_\beta \boldsymbol{g}\right) \quad (4)$$

In the equations, V_n is an arbitrary subdomain in the flow system, with boundary Γ_n. The quantity M represents mass per volume for each component κ (water, slurry). $\boldsymbol{F}$ is mass flux, and q denotes sinks and sources. $\boldsymbol{n}$ is a inward normal vector on the surface element $\mathrm{d}\Gamma_n$. In Eq. (2), Φ is porosity, S_β is the saturation of phase β (aqueous, solid), ρ_β is the density of phase β, and X_β^κ is the mass fraction of component κ present in phase β. Similarly, $\boldsymbol{F}^\kappa$ is also obtained by summing over the fluid phases β. k is absolute permeability, $k_{r\beta}$ is relative permeability to phase β, μ_β is viscosity, P_β is the fluid pressure in phase β, and $\boldsymbol{g}$ is the vector of acceleration of gravity.

Bingham Fluid Rheology

A Bingham fluid is a viscoplastic material, performing rigidly at low stresses and viscoplastic at high stresses. It is suitable to describe mud or slurry flows in drilling engineering, with the mathematical model given by Eq. (5). If the stress is beyond a certain value (called yield stress), the shear rate of the Bingham fluid increases linearly with increasing shear stress:

$$\tau = \eta\frac{\mathrm{d}v}{\mathrm{d}y} + \tau_0 \quad (5)$$

Here, τ is shear stress, η is apparent viscosity, and $\mathrm{d}v/\mathrm{d}y$ is shear rate, which stays zero if shear stress τ is less than the yield stress τ_0.

It is more efficient to use an effective potential gradient method than to characterize an apparent viscosity for Bingham fluids (Wu et al., 1998). Darcy's law of Bingham fluid flow is presented as Eq. (6) and Eq. (7) (Wu et al., 1998) with an effective potential gradient:

$$v = -\frac{kk_r}{\mu_b}\nabla\Phi e \quad (6)$$

$$\Phi e = \begin{cases} \mathrm{sgn}(\Phi)(|\Phi| - G) & |\Phi| \geq G \\ 0 & |\Phi| < G \end{cases} \quad (7)$$

where k is the permeability; k_r is the relative permeability; v denotes the Darcy velocity; μ_b is the Bingham plastic viscosity coefficient, which is influenced by the mass fraction of the slurry in the aqueous phase, $\nabla \Phi e$ is the effective potential gradient defined by Eq. (7). In Eq. (7), G presents the minimum potential gradient of the Bingham fluid. G is controlled by the yield stress of the Bingham fluid, shown as Eq. (8) (Pascal, 1986), in which α is an experimental coefficient or a fitting parameter:

$$G = \alpha \tau_0 / \sqrt{k k_r} \quad (8)$$

The yield stress is mainly affected by additives and the medium density (The Lubrizol Corporation, 2002). Xanthan gum is one of the most popular additives for thickening drilling mud, which increases the viscosity and the carrying capacity of the slurry. According to laboratory data, the yield stress increases with the concentration of xanthan gum (Figure 1). The yield stress passes the significance test of a linear model: $\tau_0 = b \cdot c_{xg} + a$, in which c_{xg} is the concentration of xanthan gum per barrel.

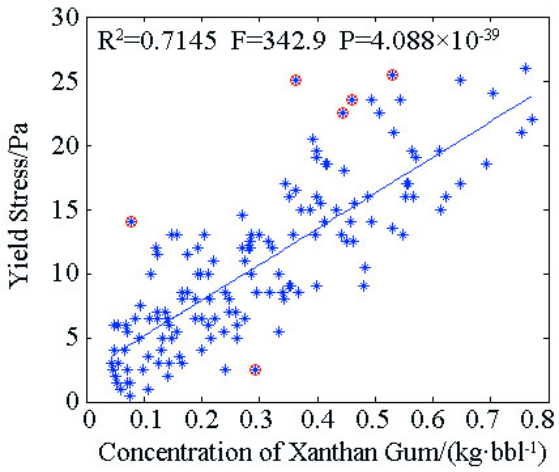

Figure 1: Yield stress versus the concentration of xanthan gum /(kg·bbl^{-1})

Mixture Fluid Properties

In the model, the aqueous phase consists of water and slurry. Assuming the volumes of water and slurry have additive properties, and the expansivity and compressibility of them are equal at all temperatures and pressures, the density of the water-slurry mixture ρ_{mix} is given by:

$$\frac{1}{\rho_{mix}} = \frac{X_{sly}}{\rho_{sly}} + \frac{1 - X_{sly}}{\rho_w} \quad (9)$$

$$\frac{\rho_{sly}(P,T)}{\rho_{sly}(P_0,T_0)} = \frac{\rho_w(P,T)}{\rho_w(P_0,T_0)} \quad (10)$$

where ρ_w is water density, ρ_{sly} is slurry density, and X_{sly} is the mass fraction of slurry in the aqueous phase. The density of the reference slurry at P_0 and T_0 is specified by the user.

The viscosity of the mixture is evaluated as a function of slurry concentration with a polynomial correction to the viscosity of water (Herbert et al, 1988):

$$\mu_{mix}(P,T,X_{sly}) = \mu_w(P,T) f(X_{sly}) \quad (11)$$

$$f(X_{sly}) = 1 + v_1 X_{sly} + v_2 X_{sly}^2 + v_3 X_{sly}^3 \quad (12)$$

where μ_{mix} is mixture viscosity, μ_w is water viscosity, and v_1, v_2, v_3 are fitting coefficients, which are determined by experimental data.

Precipitation Model

The mixture stops flowing when the fluid pressure gradient is less than the minimum potential gradient G. After several hours particle settlement occurs. When the fluid pressure gradient is large enough, the sediment will be stirred up and flow again as a slurry. The sediment-dissolution process is treated as a phase conversion of the slurry component. The slurry releases water to precipitate, and the sediment absorbs water to form the slurry. The volume of the suspension and the liquid phase are assumed to be additive.

In the process of precipitation, if slurry settlement of ΔX_{sly} occurs within a time step Δt, the solid saturation s_s at $t^{k+1} = t^k + \Delta t$ is given by:

$$s_s^{k+1} = s_s^k + \frac{\Delta X_{sly}}{X_{sly}^k} \frac{X_s^k \rho_{sly}^k}{\rho_s^k} \frac{X_{sly}^k \rho_w^k}{(1 - X_{sly}^k)\rho_{sly}^k + X_{sly}^k \rho_w^k} \quad (13)$$

and the mass fraction of slurry in the aqueous phase is

$$X_{sly}^{k+1} = \frac{X_{sly}^k - \Delta X_{sly}}{1 - \Delta X_{sly} X_s^k} \quad (14)$$

In the process of dissolution, if Δs_s sediment rejoins the slurry, the solid saturation s_s at $t^{k+1}=t^k+\Delta t$ is given by:

$$s_s^{k+1} = s_s^k - \Delta s_s \tag{15}$$

and the mass fraction of slurry in aqueous phase is:

$$X_{sly}^{k+1} = \left[\left(1-s_s^k\right)s_{sly(liq.)}^k + s_s\Delta s_{s(sly.)}^k\right]\rho_{sly}^k / \left\{\left[\left(1-s_s^k\right)\left(1-s_{sly(liq.)}^k\right) - \Delta s_s\left(1/s_{s(sly.)}^k - 1\right)\right]\rho_w^k + \left[\left(1-s_s^k\right)s_{sly(liq.)}^k + s_s\Delta s_{s(sly.)}^k\right]\rho_{sly}^k\right\} \tag{16}$$

where, ρ_s is the density of particles in the slurry, $s_{sly(liq.)}$ and X_{sly} are slurry saturation and mass fraction in the aqueous phase, and $s_{s(sly.)}$ and X_s are particle saturation and mass fraction in the slurry.

The Impact on Formation Properties

The impact of solid settlement on the formation porosity is quite simple, while it is quite complex on the formation permeability. The permeability changes not only due to the reduction of porosity, but also to its detailed shape. For instance, clogging pore throats may lead to a large reduction in permeability (Verma et al., 1988). The permeability change is modeled the same way as in TOUGH2/EWASG and TOUGH2/ECO2N with a tubes-in-series model (Verma et al., 1988). The relative change in permeability k/k_0 is given by:

$$\frac{k}{k_0} = \theta^2\frac{1-\Gamma+\Gamma/\omega^2}{1-\Gamma+\Gamma\left[\theta/\left(\theta+\omega-1\right)\right]^2} \tag{17}$$

$$\theta = \frac{1-s_s-\phi_r}{1-\phi_r} \tag{18}$$

$$\omega = 1+\frac{1/\Gamma}{1/\phi_r-1} \tag{19}$$

where Γ is the fractional length of the pore bodies (Figure 2), and Φ_r denotes the fraction of the original porosity at which permeability is reduced to zero.

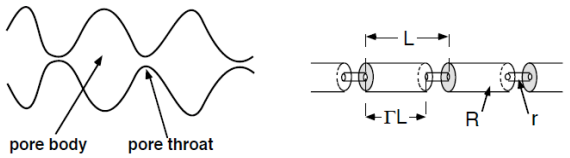

(a) conceptual model (b) tubes-in-series

Figure 2: Model for converging-diverging pore channels (Pruess et al., 1999)

For parallel-plate model (Verma et al., 1988), the relationship between relative change in permeability k/k_0 and porosity ($1-s_s$) is similar:

$$\frac{k}{k_0} = \theta^3\frac{1-\Gamma+\Gamma/\omega^3}{1-\Gamma+\Gamma[\theta/(\theta+\omega-1)]^3} \tag{20}$$

For a simple straight capillary tubes model (Verma et al., 1988), $\Gamma=0$ $\Phi_r=0$, Eq. (17) simplifies to:

$$\frac{k}{k_0} = \left(1-s_s\right)^2 \tag{21}$$

APPLICATION EXAMPLES

Cuttings re-injection in a sandy formation was simulated to observe the slurry flow and pressure oscillation by using the Bingham-like slurry flow model. A simple idealized model and a Texas CRI project case study are investigated.

Idealized Model Study

The idealized model consists of three sandy storage aquifers and two mudstone aquicludes. Numerical experiments indicate that a radial model domain of R = 10 km is sufficient for treating the boundary as a first-type boundary. The numerical model covers the depth from 1900 ~ 1960 m. The radial model domain was discretized with a minimum grid width of 2 m and a maximum width of 50 m, and vertically into 22 model layers (Figure 3). Only the middle sandstone formation is perforated for injection. Hydrostatic pressure is used as initial condition. Model parameters are listed in Table 1.

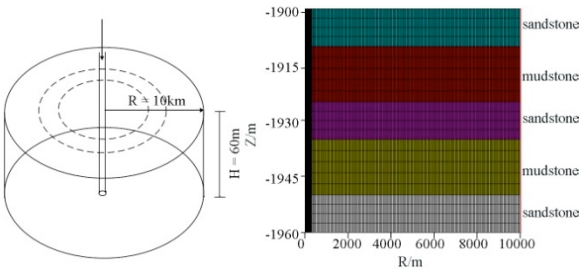

Figure 3: Radial-symmetric model

Table 1: Hydrogeologic parameters

parameter	value	
porosity	0.24	
sandstone permeability	$2.0\times10^{-13}m^2$	$k_x=k_y=10k_z$
mudstone permeability	1.0×10^{-17} m^2	$k_x=k_y=10k_z$
breakdown pressure	$1.5\times P_0$	P_0 is hydrostatic pressure

The Impact of Slurry Density

Slurry reinjection with different density is simulated to investigate the slurry flow pattern and pressure distribution. The slurry is continuously injected until the formation breaks down or 10 years, with an injection rate of 2 kg/s. The slurry density is set in the range between 1050 and 1350 kg/m^3, the plastic viscosity is 21 mPa·s, and the concentration of gelantinizer (xanthan gum) is 0.186 kg/bbl.

Figure 4 shows the simulated maximum pressure increment under different slurry density cases. It is supposed that the formation breaks down at 9.405 MPa pressure buildup (a half of the hydrostatic pressure). Slurry reinjection with lower density tends to make the formation breaks down earlier. In other words, it is preferable for a fracturing injection scheme.

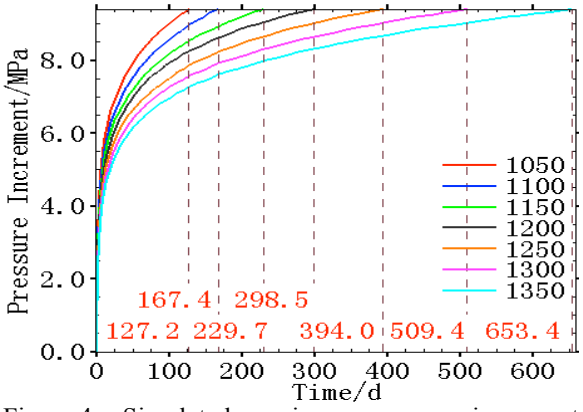

Figure 4: Simulated maximum pressure increment under different slurry density cases

The Impact of Injection Depth

Injection depth is another important factor for CRI project, because its competing influence on safety and economy. Slurry reinjection with the injection depth from 925 m to 2425 m is simulated. The slurry is continuously injected until the formation breaks down or 10 years. The slurry density is 1250 kg/m^3. Other model parameters are the same as in the first model.

Lower injection depth dramatically accelerates formation breakdown time (Figure 5). It takes 2.41 days to reach the formation breakdown pressure buildup (4.548 MPa) for a 925 m deep CRI project. For a fracturing CRI project, lower injection depth is preferable under the premise of safety. For a formation with poor property, fracture propagation may lead to leakage, and the injection depth should be carefully designed.

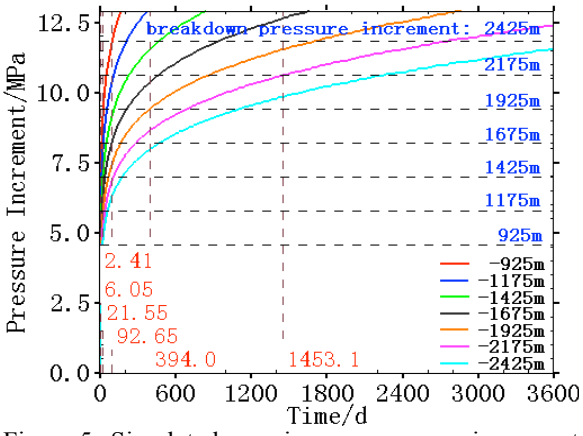

Figure 5: Simulated maximum pressure increment under different injection depth cases

The Impact of Intermittent Injection

Intermittent injection is a common scheme in CRI projects. It has significant influence on the pressure distribution of the formation. Several intermittent injection cases are simulated and compared with two continuous injection cases. The injection scheme is listed in Table 2. Other model parameters are the same as in the first model.

Table 2; Injection schemes

	Injection rate/(kg·s^{-1})	period/d
continuous injection	1	--
	2	--
intermittent injection	2	10
		20
		40
		60
		120

As shown in Figures 6 to 8, the formation pressure quickly increases during injection and rapidly decreases at the beginning of shut-ins. Particles rarely settle during the injection time, but do so frequently during shut-ins. The pressure distribution, mass of sediment and slurry all periodically change.

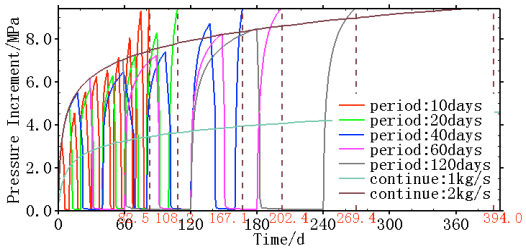

Figure 6: Simulated maximum pressure increment under different intermittent injection cases

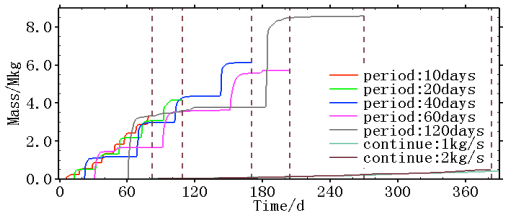

Figure 7: Simulated mass of sediment under different intermittent injection cases

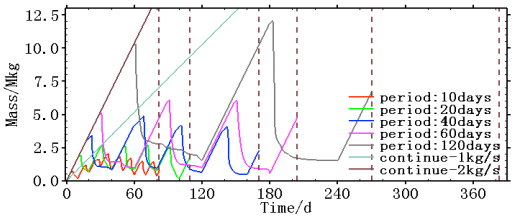

Figure 8: Simulated mass of slurry under different intermittent injection cases

Intermittent injection leads to several fracturing events. A scheme with short periods significant shortens the formation breakdown time. The pressure slowly increases under the continuous injection scheme, compared to the intermittent injection scheme.

Case Study

The CRI project intends to inject slurry in sandy aquifers distributed between a depth of 2112.9 and 2268 m, which are interlayered by mudstone formations. The injection well was drilled through 7 sandy storage aquifers, with a thickness of several meters and a porosity between 15% and 24%. Storage layers are numbered as Lyr01 ~ Lyr07. Only Lyr04 ~ Lyr07 were perforated for injection. The permeability of each formation is unknown, so empirical values were assigned based on porosity, and further treated as fitting parameters in the case study.

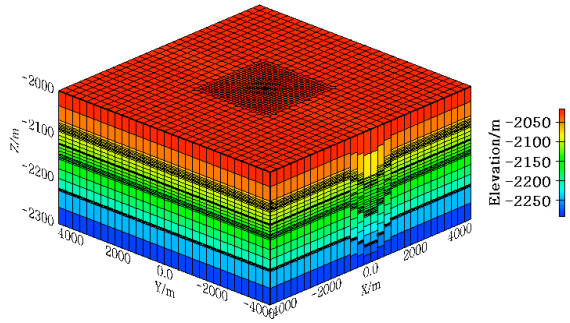

Figure 9: Model for Texas CRI project

A field model is established based on a Texas oil field with a domain size of 9 km × 9 km and vertically the depth from 2000 to 2300 m (Figure 9). The injection well is located at the center of the model domain. The model domain was discretized into 1523 grid-blocks for each model layer, and 34 model layers, with four levels of refinement around the injection well (Figure 10). Model parameters are listed in Table 3 according to empirical values given by Ehrenberg (2005). The sandstone permeability is proportionally adjusted and marked by the value of Lyr04~06 with the range between 0.7D and 1.1D. Hydrostatic pressure is used as initial condition, and a first-type boundary is set as boundary condition. The slurry injection of first 50 days is simulated with intermittent injection scheme.

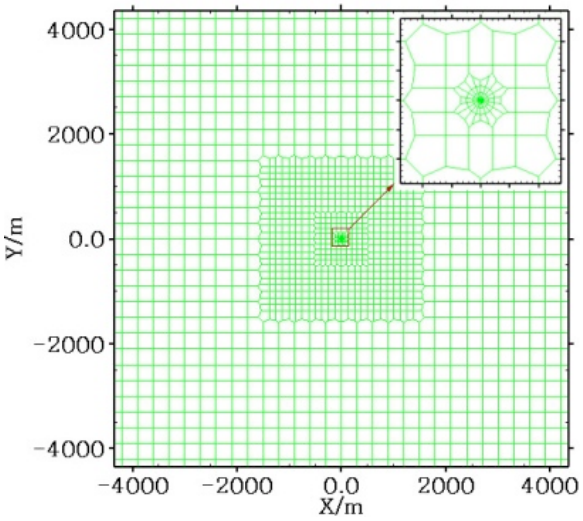

Figure 10: Plan view of the mesh grid

Table 3 Hydrogeologic parameters

model layer	lithology	permeability /mD	porosity
Lyr01~03	sandstone	243	0.24
Lyr04~06	sandstone	95	0.20
Lyr07	sandstone	40	0.15
aquiclude	mudstone	0.01	0.15

Figure 11 shows the comparison of maximum formation pressure between monitoring data and simulated results. The trend of pressure oscillation matches well with the monitoring data, especially at the beginning of injection. The pressure fluctuations stabilize somewhat at the late injection period, which may be caused by formation fracturing. The simulator developed in this study, however, is not ready for coupling the mechanical fracturing processes, so it has difficulty to match fracturing injection data. Among all cases, the curve with 0.9D permeability has the best fit to monitoring data.

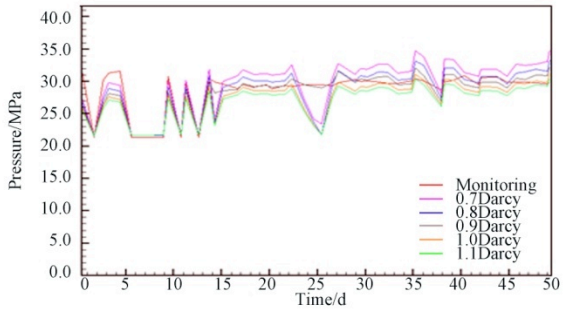

Figure 11: Pressure oscillation of each fitting case

For the best fit case, Figure 12 shows the plan view and vertical view of slurry distribution on the 50th day. Most of the slurry is captured in the injection layer Lyr4 within the first 50 days, due to the small injection volume. The influence radius is about 30 m after 50 days.

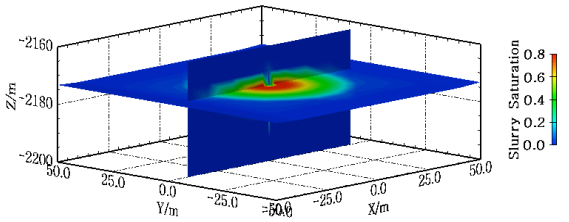

Figure 12: Plan view and vertical view of slurry distribution on the 50th day for 0.9D cases

CONCLUSION

A new module for the TOUGH2 family of codes for modeling Bingham-like slurry flow is developed in this paper. The rheology of slurry, the mixing fluid properties of slurry and groundwater, sediment-dissolution of slurry, and the effect of precipitation on formation porosity and permeability are investigated. The Bingham rheology is characterized by an effective potential gradient approach, and the minimum potential gradient is carefully valued by yield stress and permeability. The simulator is able to simulate three-dimensional slurry transport in anisotropic porous and fractured media.

The model has been applied to the site-scale slurry injection simulations for a Texas CRI project, which matches well with the pressure oscillation of the monitoring data. This model can simulate the slurry injection process, and obtain slurry flux distributions and pressure oscillations. The new code can predict the sediment process, the storage capacity of the formation, the time when the formation breaks down, and further helps in determining the optimal injection scheme. Simulations show that a short period intermittent slurry injection with lower density into shallower formation is preferable for fracturing. However, it may lead to a quick formation breakdown with associated leakage risks.

ACKNOWLEDGMENT

This work was sponsored by Jereh Energy Services Corporation. The authors would like to thank Hu Xianxian of Tongji University for his contribution to program testing.

REFERENCES

Edwards, A.L., TRUMP: A Computer Program for Transient and Steady State Temperature Distributions in Multidimensional Systems, National Technical Information Service, National Bureau of Standards, Springfield, VA, 1972.

Ehrenberg, S.N., and P. H. Nadeau, Sandstone vs. carbonate petroleum reservoirs: A global perspective on porosity-depth and porosity-permeability relationships, AAPG Bulletin, 89(4):435-445, 2005.

Guo, Q., and T. Geenhan, An overview of drill cuttings re-injection – Lessons learned and recommendations, 11th International Petroleum Environmental Conference Albuquerque, New Mexico, 2004.

Herbert, A.W., C.P. Jackson, and D.A. Leve, Coupled Groundwater Flow and Solute Transport with Fluid Density Strongly Dependent on Concentration, Water Resour. Res., 24(10):1781-1795, 1988.

Narasimhan, T. N., and P. A. Witherspoon, An integrated finite difference method for analyzing fluid flow in porous media, Water Resour. Res., 12(1):57 – 64, 1976.

Pascal, H., A theoretical analysis on stability of a moving interface in a porous medium for bingham displacing fluids and its application in oil displacement mechanism, Can. J. Chem. Eng., 64:375–379, 1986.

Pruess, K., C. Oldenburg, and G. Mcridis, TOUGH2 User's Guide, Version 2.0, Report LBNL-43134, Lawrence Berkeley National Laboratory, Berkeley, CA, 1999.

Shadizadeh, S. R., S. Majidaie, and M. Zoveidavianpoor, Investigation of drill cuttings reinjection: Environmental management in Iranian Ahwaz oilfield, Petroleum Science and Technology, 29(11):1093-1103, 2011.

Shioya, Y., K. Yamamoto, T. Fujieda, et al, Cuttings reinjection to shallow undersea formation: The geomechanical acceptance analysis using hydraulic fracturing simulator, Abu Dhabi International Petroleum Exhibition and Conference, Abu Dhabi, United Arab Emirates, 2002.

Verma, A. K., K. Pruess, C. F. Tsang, et al, A study of two-phase concurrent flow of steam and water in an unconsolidated porous medium, Proc. 23rd National Heat Transfer Conference, Am. Society of Mechanical Engineers, Denver, CO, 1985.

Verma, A. and K. Pruess. Thermohydrologic Conditions and Silica Redistribution Near High-Level Nuclear Wastes Emplaced in Saturated Geological Formations, J. of Geophys. Res., 93(B2): 1159-1173, 1988.

The Lubrizol Corporation, Measurement understanding yield value home formulations, 2002-01 [2014-11-13], http://www.lubrizol.com/Home-Care/Documents/Technical-Data-Sheets/TDS-244-Measurement-Understanding-Yield-Value-Personal-Care-Formulations.pdf

Wu, Y. S., and K. Pruess, A numerical method for simulating non-Newtonian fluid flow and displacement in porous media, Advances in Water Resources, 21:351-362, 1998.

Yamamoto, K., and T. Koyama, Geometry of the fracture for cuttings reinjection operation and solid concentration: A numerical study, the 6th North America Rock Mechanics Symposium, Houston, Texas, 2004.

Coupled Fluid Flow and Geomechanics

EXTENSION OF THE TOUGH-FLAC SIMULATOR TO ACCOUNT FOR FINITE STRAINS

Laura Blanco-Martín, Jonny Rutqvist and Jens T. Birkholzer

Lawrence Berkeley National Laboratory, Earth Sciences Division
One Cyclotron Road, MS 74R-316C
Berkeley, California, 94720, United States
e-mail: lblancomartin@lbl.gov

ABSTRACT

The well-established TOUGH-FLAC simulator for coupled flow and geomechanics analyses has recently been extended to the finite strain framework. In this paper, we present the main modifications to the simulator and we explain how to run a simulation under finite strains.

INTRODUCTION

The understanding and correct assessment of a wide variety of geosciences problems require the analysis of interactions between thermal, hydraulic and mechanical processes (Stephansson et al., 2004). For instance, the underground injection of fluids modifies the stress state in the target formation and may also affect the under and/or overburden. In addition, when underground structures such as tunnels or boreholes are excavated, the stress state around the openings changes and the flow properties of the material (permeability, porosity, etc.) may be influenced. Furthermore, the mechanical response of several rock types, like rock salt, is affected by temperature.

In most cases, the interactions between thermal, hydraulic and mechanical processes are complex, and this complexity often increases when the particularities of a case study (geology, anisotropy, etc.) are accounted for. Therefore, numerical modeling is commonly used for their study (Olivella et al., 1994; Rutqvist et al., 2002).

In the TOUGH Symposium 2003, the TOUGH-FLAC simulator was presented as a new tool to investigate coupled flow and geomechanics processes (Rutqvist and Tsang, 2003). Since then, this simulator has been successfully applied in different application fields, including geological carbon sequestration, geothermal reservoir engineering, oil recovery and nuclear waste disposal (Rutqvist et al., 2002; Rutqvist, 2011).

TOUGH-FLAC is based on an explicit sequential method to couple flow and geomechanics. The multiphase fluid and heat flows are computed by TOUGH2 (Pruess et al., 2012), and the geomechanical response of the system is calculated using FLAC^{3D} (Itasca, 2012). Since TOUGH-FLAC is a sequential simulator, the governing equations of the flow and geomechanics sub-problems are solved one-by-one within a time step, using the intermediate solution information technique (Settari and Mourits, 1998). In addition to its flexibility to be used in a broad variety of applications, one main advantage of TOUGH-FLAC is that both TOUGH2 and FLAC^{3D} are actively used internationally and are under constant development.

Recently, the TOUGH-FLAC simulator has been extended to account for finite (or large) strains and creep processes (Blanco-Martín et al., 2015a). Indeed, several engineering problems that involve thermal-hydraulic-mechanical (and chemical) coupled processes entail deformations that invalidate the assumptions on which the infinitesimal strain theory is based. For instance, in reservoir engineering, large deformations are common in unconventional reservoirs (Moridis et al., 2013). In addition, rocks that show a time-dependent rheology, such as rock salt, distort under the effect of temperature and deviatoric stresses, and if damage and sealing occur, significant volume changes may take place (Hunsche and Hampel, 1999). Compaction and dilation of geo-materials also involve large deformations. The updated version of TOUGH-FLAC for large strains allows the study of these engineering problems. This way, the fields of application of the simulator are extended.

In this paper, we first describe the main modifications, features and structure of the updated TOUGH-FLAC simulator, and we also explain how to use TOUGH-FLAC under the finite strain framework.

TOUGH-FLAC FOR FINITE STRAINS

Overview

In the analysis of coupled thermal-hydraulic-mechanical (and chemical) THM(C) processes, finite strains originate from the mechanical response of the domain: compaction of aggregates, consolidation, time-dependent rheology, etc. Consistently, FLAC^{3D} has a capability to compute finite strains. On the other hand, two main modifications have been necessary into TOUGH2 for its adaptation to the finite strain framework:

1. Update of the geometrical data required by the code (these data are contained in blocks ELEME and CONNE in the input), and
2. Extension of the balance equations to account for volume changes.

These two modifications are explained in the next sections. We note here that in addition to the more straightforward approach of directly updating the geometrical data, other approaches are available in the literature to compute coupled fluid flow and geomechanics under the finite strain framework (Bathe et al., 1975; Coussy, 1995).

Main modifications

Geometry

After every call to FLAC^{3D}, the geometrical data updated in TOUGH2 are: volume of the elements, distances of the centroids of two connected elements to their common interface, common interface area, and cosine of the angle between the gravitational acceleration vector and the line between the centroids of two connected elements. In a regular TOUGH2 input file (or MESH file), these data are contained in blocks ELEME and CONNE.

Since the resolution method used in TOUGH2 is based on the Voronoi partition (Pruess et al., 2012), deformed discretizations updated during a coupled run should still comply with the resolution method of the code. Bearing this in mind, we use the software library Voro++ (Rycroft, 2009) to ensure that the mesh used in TOUGH2 conforms to the principles of the Voronoi tessellation.

As the mesh deforms in the geomechanics sub-problem, Voro++ is executed to compute the corresponding Voronoi structure (Blanco-Martín et al. 2015b). In the current approach, the centroids of the deformed geomechanics mesh are transferred to Voro++, which computes the corresponding Voronoi discretization. Geometrical data of the new Voronoi mesh (volumes, common interface area between two adjacent grid blocks, etc.) are then transferred to TOUGH2 through a text file.

Figure 1a shows a detail of the initial and deformed flow grids corresponding to a 2D model to investigate long-term THM processes in a nuclear waste repository in rock salt, and Figure 1b shows a 2D slice of a 3D model for a similar application.

As it can be seen, the flow sub-problem uses Voronoi cells, both in the initial and the deformed configurations. In addition, it can be seen in the figures that the grid blocks at the boundary between two different domains (waste package, backfill and host rock) are slim and have the same thickness. This way, Voro++ will conserve the volume of each domain even when the mesh deforms (the generators of the Voronoi mesh are the centroids of the mesh used in FLAC^{3D}).

The geometrical update is made during the first iteration of the TOUGH2 Newton-Raphson process (Pruess et al., 2012). In this iteration, the primary variables and porosity remain equal to those at the end of the previous time step (only geometrical data are different), and the code checks whether the system continues to be in thermodynamic equilibrium for a new time increment and new geometry. If the maximum residual exceeds a preset convergence tolerance, an iterative process is carried out. In this process, the geometry is kept unchanged (i.e., the geometry is updated in TOUGH2 after every FLAC^{3D} call, but is constant within each time step) and consistency in the balance equations is ensured through the porosity correction formulation, explained in the next section.

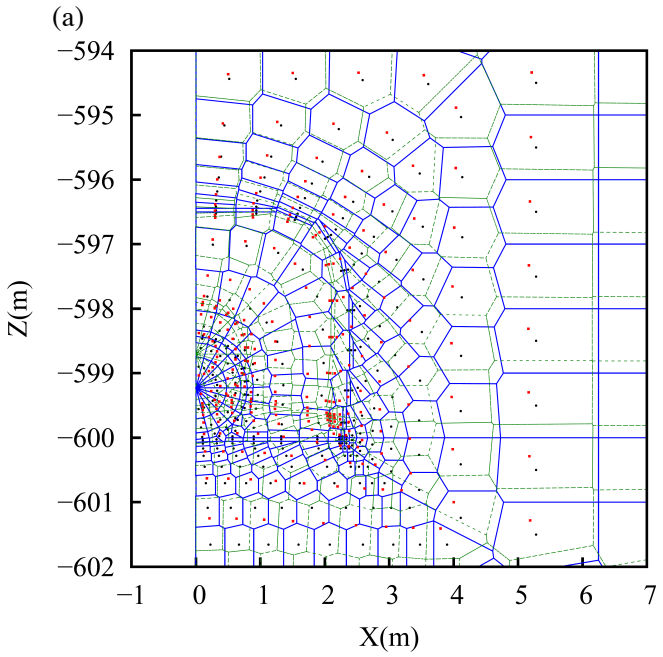

Figure 1. Voronoi structures used in the flow sub-problem under finite strains (THM coupling). (a): 2D model, with blue lines corresponding to the original domain; (b): 2D slice of a 3D drift (black lines correspond to the original domain).

Balance equations

The balance equations solved in TOUGH2 have been reformulated to ensure mass and energy conservation as geometry changes. The mass balance equations for a grid block *n* read

$$\frac{d\left(M_n^\kappa V_n\right)}{dt} = \sum_m A_{nm} F_{nm}^\kappa + q_n^\kappa \rightarrow$$
$$\rightarrow \frac{dM_n^\kappa}{dt} + M_n^\kappa \frac{dV_n}{Vdt} = \frac{1}{V_n}\left(\sum_m A_{nm} F_{nm}^\kappa + q_n^\kappa\right) \quad (1)$$

for κ=1, *NK* (*NK* is the total number of fluid components [air, water, etc.]). Note that a similar approach is carried out for the heat equation. In Eq. (1), M_n^κ is the accumulation term, V_n is the volume of the grid block (new volume after each FLAC^{3D} call), q_n^κ denotes sink/sources rates, and F_{nm}^κ is the flow of component κ across surface A_{nm} (new value after each FLAC^{3D} call). We note that for second and further iterations, the term $M_n^\kappa \frac{dV_n}{Vdt}$ is not computed. The accumulation terms read

$$M_n^\kappa = \phi \sum_\beta S_\beta \rho_\beta \chi_\beta^\kappa \quad (2)$$

where ϕ is porosity, S_β is the saturation of phase β, ρ_β is the density of phase β, and χ_β^κ is the mass fraction of component $\varkappa$ in phase β. Porosity changes during a time step (for second and further iterations) are calculated using a porosity variation, $d\phi$, which includes a correction term, $\Delta\phi$, from geomechanics. The porosity variation has the form

$$d\phi = A(\alpha, \phi, K)dP + B(\alpha_{th})dT + \Delta\phi \quad (3)$$

In Eq. (3), α [-] is the Biot coefficient, α_{th} [K^{-1}] is the linear thermal expansion coefficient, K [MPa] is the drained bulk modulus, and $\Delta\phi$ is the porosity correction from geomechanics (it has been adapted from Kim et al., 2012). The porosity correction is constant for a given time step.

Structure of the updated TOUGH-FLAC

Similarly to TOUGH-FLAC, the updated version is based on the fixed-stress split sequential method to couple flow and geomechanics. Accordingly, the flow sub-problem is solved first in the sequential scheme, using an explicit evaluation of the volumetric component of the total stress tensor. TOUGH2 is the master code of the simulator and it moves the simulation

forward in time, once convergence has been reached in each time step.

Currently, the modeling sequence is as follows. TOUGH2 moves the simulation forward and FLAC^{3D} is executed once within a TOUGH2 time step, just before the Newton-Raphson iteration process to solve the residual nonlinear equations. A schematic view of the coupled THM modeling sequence is displayed in Figure 2. The highlighted area corresponds to a time step from t^n to t^{n+1}. The pressure, P^n, temperature, T^n, liquid saturation, $S_l{}^n$, and porosity, ϕ^n, of each grid block computed at the end of the previous time step (from t^{n-1} to t^n) are transferred to FLAC^{3D}. The pressure transferred depends on the definition of pore pressure in geomechanics (Coussy, 2004). A new subroutine has been written to enable the use of the equivalent pore pressure using the van Genuchten function for capillary pressure (van Genuchten, 1980).

From flow to geomechanics, the pore-pressure change, $\Delta P=P^n-P^{n-1}$, and the temperature change, $\Delta T=T^n-T^{n-1}$, corresponding to two successive TOUGH2 time steps are accounted for as a correction to the total stress tensor, σ_{ij} (direct coupling). These changes are computed internally in FLAC^{3D} once the new values P^n and T^n are transferred. The corrected total stress tensor, σ_{ij}^c, has the form

$$\sigma_{ij}^c = \sigma_{ij} - \alpha\Delta P\delta_{ij} - 3\alpha_{th}K\Delta T\delta_{ij} \qquad (4)$$

where δ_{ij} [-] is the Kronecker delta. Compressive stresses are defined negative here. From Eq. (4), it can be inferred that the coupling from flow to geomechanics (TOUGH2 to FLAC^{3D}) affects only the volumetric component of the stress tensor. Moreover, during the geomechanics sub-problem P and T remain constant. Porosity and liquid saturation are used to update the body forces in the quasi-static governing equations of the geomechanical analysis. These equations account for the thermal strains that result from the temperature change ΔT.

Once all the updates are made, FLAC^{3D} runs until a new equilibrium mechanical state is obtained (stresses σ^n and strains ε^n in Figure 2). In FLAC^{3D}, the new static equilibrium is established internally through a dynamic-solution approach, solving the equation of motion in which the inertial terms are used as numerical means to reach the equilibrium state of the system under consideration.

From geomechanics to flow, geometrical changes are first accounted for, as described in the previous section. Additionally, the new mechanical state obtained at t^n is used through several coupling functions to compute mechanically induced changes in permeability and capillary pressure (Δk and ΔP_c in Figure 2). The coupling functions depend on each material (and the phenomena it goes through) and should be based on specific laboratory and theoretical results (Blanco-Martín et al., 2015a; Rutqvist et al., 2002). The mechanically modified flow properties (k'^n, ϕ'^n and $P_c{}'^n$ in Figure 2) are used to solve the residual equations of the flow sub-problem. Within a time step, the Newton-Raphson iteration process is continued until the residuals are reduced below a preset convergence tolerance. At the end of the current time step (time t^{n+1} in Figure 2), a new set of primary thermodynamic variables (P^{n+1}, T^{n+1} and $S_l{}^{n+1}$ in Figure 2) and new flow properties (k^{n+1}, ϕ^{n+1} and $P_c{}^{n+1}$ in the figure) are obtained.

CONCLUSIONS

We have presented an updated version of the TOUGH-FLAC simulator, suitable to conduct analysis under the large strain and creep frameworks. This enhancement has been motivated to study coupled THM processes related to the underground disposal of heat-generating nuclear waste in saliferous formations (natural salt host rock and crushed salt backfill), but the approach is general and can be applied to other application fields.

In the updated version of TOUGH-FLAC, the general structure and overall steps to run a coupled THM(C) simulation are the same as in standard TOUGH-FLAC. Although the data transferred between the two codes is slightly different (geometry information is now transferred), the user needs to prepare the same input files. In order to ensure that a Voronoi partition is used in TOUGH2 even when the geometry changes during a coupled simulation (large strains are computed by FLAC^{3D}), the software library Voro++ (open source) has been

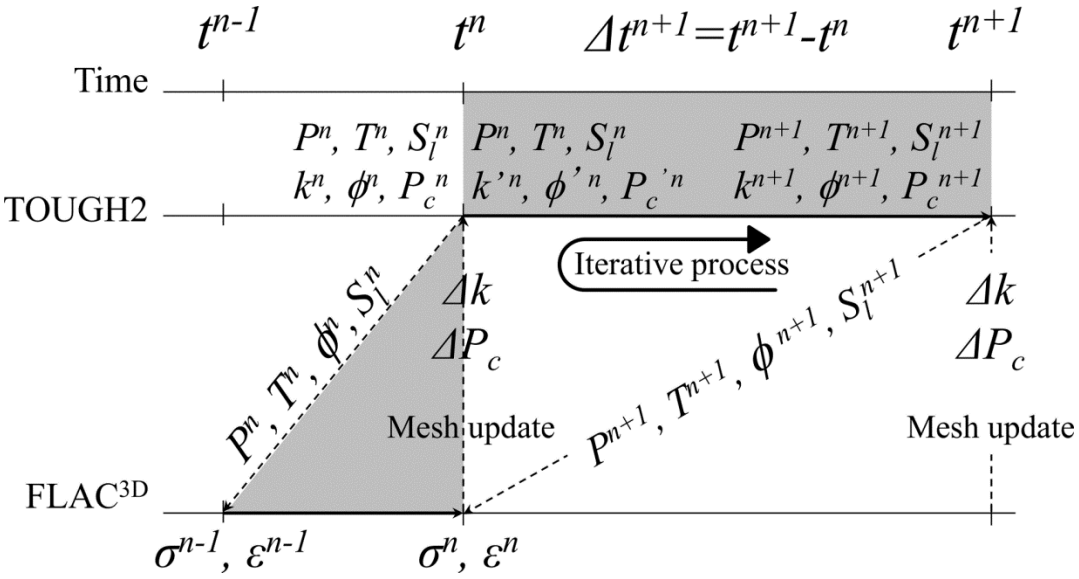

Figure 2. TOUGH-FLAC explicit sequential scheme (adapted from Rutqvist et al., 2002). The highlighted zones correspond to the time step between time t^n and t^{n+1}.

linked to the coupling scheme, and is used to compute the Voronoi partition corresponding to the current geometry, calculated by FLAC^{3D}.

The coupling between flow and geomechanics has also been implemented into iTOUGH2 (iTOUGH2-FLAC simulator) (Blanco-Martín et al., 2015c). In its current state, iTOUGH2-FLAC can be used in forward mode, and also in inverse mode for the estimation of flow parameters (for mechanical parameters, or flow *and* mechanical parameters, the PEST protocol and TOUGH-FLAC [or iTOUGH2-FLAC] have to be used, see Finsterle et al. [2010] for details on the use of iTOUGH2-PEST). As a general rule, the capabilities of iTOUGH2 (parameter estimation, sensitivity analysis, uncertainty propagation and data-worth analyses) can be used on flow parameters, but the system response will also account for geomechanics processes if iTOUGH2-FLAC is used, because the forward runs are actually coupled simulations. Also, the enhancements included in iTOUGH2 for direct flow problems (such as restart times, flexible assignment of initial and boundary conditions, MOMOP options, etc.) are available in iTOUGH2-FLAC.

The implementation of the finite strain framework into TOUGH-FLAC (and also iTOUGH2-FLAC) is an important new capability that will enable the use of the simulator in the analysis of a variety of engineering problems, thus extending its current areas of application.

ACKNOWLEDGMENT

Funding for this work has been provided by the Used Fuel Disposition Campaign, Office of Nuclear Energy of the U.S. Department of Energy, under Contract Number DE-AC02-05CH11231 with Lawrence Berkeley National Laboratory.

REFERENCES

Coussy, O., *Mechanics of porous continua*, Chichester: Wiley, 1995.

Coussy, O., *Poromechanics*, 1st ed. Chichester: Wiley, 2004.

Bathe, K.-J., E. Ramm, and E.L. Wilson, Finite element formulations for large deformation dynamic analysis, *Int. J. Numer. Methods Eng.*, 9(2), 353-386, 1975.

Blanco-Martín, L., J. Rutqvist, and J.T. Birkholzer, Long-term modeling of the thermal-hydraulic-mechanical response of a generic salt repository for heat-generating nuclear waste, *Engineering Geology*, 193, 198-211, 2015a.

Blanco-Martín, L., R. Wolters, J. Rutqvist, K.-H. Lux, and J.T. Birkholzer, Comparison of two simulators to investigate thermal-hydraulic-mechanical processes related to nuclear waste isolation in saliferous formations, *Computers and Geotechnics,* 66, 219-229, 2015b.

Blanco-Martín, L., J. Rutqvist, C. Doughty, Y. Zhang, S. Finsterle, and C.M. Oldenburg, iTOUGH2-FLAC modeling of thermal-hydraulic-mechanical processes related to steam-assisted heavy oil recovery from diatomite, TOUGH Symposium, Sept. 28-30, 2015c.

Finsterle, S., *iTOUGH2 Universal Optimization Using the PEST protocol – User's Guide*, Report LBNL-3698E, Lawrence Berkeley National Laboratory, Berkeley, Calif., 2010.

Hunsche, U., and A. Hampel, Rock salt – the mechanical properties of the host rock material for a radioactive waste repository, *Engineering Geology*, 52, 271-291, 1999.

Itasca Consulting Group, *FLAC^{3D} (Fast Lagrangian Analysis of Continua in 3D) Version 5.0 – User's Guide*, Minneapolis, MN, 2012.

Kim, J., E.L. Sonnenthal, and J. Rutqvist, Formulation and sequential numerical algorithms of coupled fluid/heat flow and geomechanics for multiple porosity materials, *Int. J. Numer. Methods Eng.*, 92(5), 425-456, 2012 .

Moridis, G.J., J. Kim, M.T. Reagan, and S.-J. Kim, Feasibility of gas production from a gas hydrate accumulation at the UBGH2-6 site of the Ulleung basin in the Korean East Sea, *Journal of Petroleum Science and Engineering*, 108, 180-210, 2013.

Olivella, S., J. Carrera, A. Gens, and E. Alonso, Nonisothermal multiphase flow of brine and gas through saline media, *Transport in porous media*, 15, 271-293, 1994.

Pruess, K., C. Oldenburg, and G. Moridis, *TOUGH2 User's Guide, Version 2.1*, Report LBNL-43134 Rev., Lawrence Berkeley National Laboratory, Berkeley, Calif., 2012.

Rutqvist, J., Y.S. Wu, C.F. Tsang, and G. Bodvarsson, A Modeling Approach for Analysis of Coupled Multiphase Fluid Flow, Heat Transfer, and Deformation in Fractured Porous Rock, *Int. J. Rock Mech. Min. Sci*., 39, 429-442, 2002.

Rutqvist, J., and C.-F. Tsang, TOUGH-FLAC: a numerical simulator for analysis of coupled thermal-hydrologic-mechanical processes in fractured and porous geological media under multi-phase flow conditions, TOUGH Symposium, May 12–14, 2003.

Rutqvist, J., Status of the TOUGH-FLAC simulator and recent applications related to coupled fluid flow and crustal deformations, *Computers and Geosciences*, 37, 739-750, 2011.

Rycroft, C.H, *Voro++: a three-dimensional Voronoi cell library in C++*, 2009. http://math.lbl.gov/voro++/

Settari, A, and F.M. Mourits, A coupled reservoir and geomechanical simulation system, *SPE J*, 3(3), 219–226, 1998 (SPE 50939).

Stephansson, O., J. Hudson, and L. Jing, Coupled Thermo-Hydro- Mechanical-Chemical Processes in Geo-Systems: Fundamentals, Modelling, Experiments, and Applications, G*eo-Engineering Book Series*, vol. 2. London: Elsevier, 2004

van Genuchten, M.T., A closed-form equation for predicting the hydraulic conductivity of unsaturated soils, *Soil Sci. Soc. Am. J.* 44(5), 892-898, 1980.

SIMULATIONS OF FLUID-DRIVEN FRACTURING WITHIN DISCRETE FRACTURE NETWORKS USING TOUGH-RBSN

Kunhwi Kim, Jonny Rutqvist, Seiji Nakagawa, James Houseworth, and Jens Birkholzer

Lawrence Berkeley National Laboratory
1 Cyclotron Rd.
Berkeley, CA 94720, USA
e-mail: KunhwiKim@lbl.gov

ABSTRACT

This paper presents numerical modeling of fluid-driven fracturing processes using the TOUGH-RBSN code for coupled THM analyses. The simulation tool combines TOUGH2 with the rigid-body-spring network (RBSN) model which enables a discrete representation of individual fractures and fracture networks in rock. The discrete fractures are directly mapped onto unstructured Voronoi grids via an automated geometric scheme. First, for verifying our modeling approach, a fracturing simulation on a simple 2D model is conducted, and the result is compared to available analytical solutions. Subsequently, hydraulic fracturing simulations are conducted to make predictions of planned laboratory experiments using analogue rock samples containing designed, pre-existing fractures. The results show selective fracturing and fluid infiltration along the pre-existing fractures, with some additional fracturing of the intact matrix. Qualitative interpretations of the fracture propagation speed are also provided, which is strongly affected by the specific storage of the fluid injection system.

INTRODUCTION

Fracture initiation, propagation and reactivation due to pressurization by fluids are relevant to many geoengineering applications. For example, hydraulic fracturing and stimulation of fracture networks are utilized by the energy industry (e.g., shale gas extraction, enhanced geothermal systems, etc.) to increase permeability of geological formations. From the opposite perspective, related to nuclear waste disposal and underground CO_2 sequestration, fracturing of the repository rock could be detrimental and increase the risk of contaminant leakage. Fluid-driven fracturing generally requires tightly coupled hydro-mechanical processes to be considered in its modeling. Especially in the presence of multiple fractures (e.g., propagating fractures and pre-existing natural fractures), modeling the fracturing processes can be very challenging because of the complex interactions between propagating fractures and natural fractures (e.g., Fu et al., 2013).

The purpose of this study is to extend the current TOUGH-RBSN modeling capabilities for coupled hydro-mechanical processes. The simulation tool combines TOUGH2 with the rigid-body-spring network (RBSN), a lattice modeling approach for geomechanical and fracture-damage behavior. Fractures are considered as discrete features so that discontinuities in the system can be explicitly represented. Discrete fracture networks (DFNs) are configured by mapping their geometry onto an unstructured Voronoi mesh, which is shared by both TOUGH2 and the RBSN.

A 2D fracturing model is used to verify the TOUGH-RBSN code for simulations of fluid-driven fracturing, in which the resulting fracture geometry is compared with an analytical solution. Next, predictive simulations are conducted for hydraulic fracturing within laboratory test specimens containing a network of pre-existing fractures. The discretization method employed by the modeling allows a close representation of the actual fracture geometry used in the experiment. The simulation results exhibit hydraulic fracture propagation consistent with our predictions. Additionally, a sensitivity analysis is conducted for qualitative interpretations.

MODEL CONSTRUCTION

Voronoi Discretization

Voronoi discretization is not only an effective method for partitioning a spatial domain, but is also an essential part of the RBSN model formulation. The Voronoi diagram serves to scale the element coefficients for the system equations.

The discretization process is carried out basically in three steps: nodal point insertion, Delaunay tessellation, and Voronoi tessellation. Within the domain, nodal points are positioned in regular or irregular formation. For random point generation, a minimum allowable distance l_{min} is used to define the desired nodal density of the unstructured grid. The Delaunay tessellation is conducted based on the nodal positions, where each Delaunay edge defines the nodal connection of the corresponding lattice element. Through the dual Voronoi tessellation, the spatial domain is collectively filled with discrete polyhedral cells that render the elemental volumes. More detailed procedure of the domain partitioning is presented elsewhere (Yip et al., 2005; Asahina and Bolander, 2011).

Discrete Fracture Representation

Fractures within geological systems may facilitate storage and flow of fluids as well as contribute to discontinuous mechanical responses. In this study, such fractures and discontinuities are explicitly modeled as discrete features within the Voronoi grid.

The Voronoi grid represents the matrix component of geomaterial structures, and pre-existing or newly generated fractures are placed on the Voronoi cell boundaries. Descriptors of fractures (e.g., orientation, length, curvature) can be obtained by field mapping, computer-generated statistical representations, or the simulation outcomes of mechanical models. An example of the discretization procedure in 2D modeling involving a straight fracture path is as follows:

i. Generate a Voronoi unstructured grid for the spatial domain.

ii. Overlay the reference fracture path onto the grid.

iii. Test all connections of natural neighboring nodes to check if they cross the fracture path. For example, compare connections *ij* and *jk* in Fig. 1.

iv. The collection of the Voronoi cell boundaries corresponding to the nodal connections that cross the reference fracture (such as *ij*) forms discretized fractures.

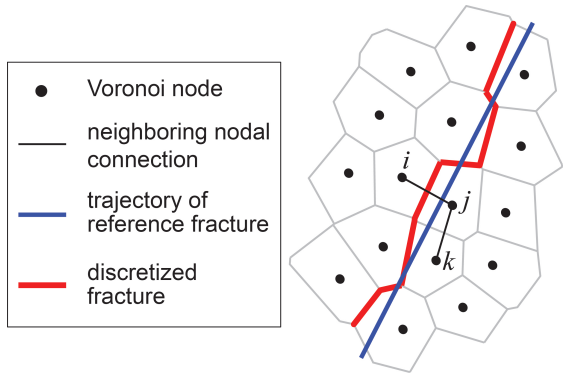

Figure 1. Fracture mapping and discretization within an unstructured Voronoi grid.

By repeating the above process for multiple fractures, a network of discrete fractures can be generated. This fracture discretization process is completely automated and can be easily extended to more complicated geometries in 3D modeling. The grid size should be carefully chosen to obtain a sufficiently accurate representation of the reference fracture. With a finer grid, the discretized fractures correspond more closely to the reference path, but the computational expense may be increased.

METHODOLOGY

TOUGH2 Simulator

TOUGH2 is a general-purpose simulator for flow and mass transfer in porous and fractured media (Pruess et al., 2011), which has an applicability to diverse modeling problems by adopting various equation-of-state (EOS) modules. Simulations presented in this paper use the EOS1 module for single-phase flow problems of water in isothermal conditions.

The modeling approach is based on the integral finite difference method (IFDM), thus possesses the advantage of being compatible with regular or irregular gridding in any spatial dimensions.

It also allows for flexibility of fracture representation, in which fractures and fracture networks form in response to the hydro-mechanical forces and conditions (Zhang et al., 2004; Rutqvist et al., 2013).

In the TOUGH2 simulations using a basic Voronoi grid, flow and mass transfer are enacted only through the connections of the neighboring matrix nodes (called matrix-matrix connections in Fig. 2a). However, if fracturing occurs within the matrix, substantial flow may arise through the fracture apertures. For the DFN approach, dynamic formation of such flow channels is implemented by introducing fracture nodes and the associated connections within the Voronoi grid. As shown in Fig. 2b, a fracture node is inserted on the Voronoi cell boundary where the matrix-matrix connection crosses. The original matrix-matrix connection is divided into two matrix-fracture (and vice versa) connections by the newly inserted fracture node. In addition, the connections between the fracture nodes are established to activate flow channels in discrete fractures. Hydrological properties of the discrete fractures are related to the grid geometry and the local fracture aperture. Fracture geometries can be either assigned as a pre-existing fracture property or computed by the mechanical-damage analysis of the RBSN model.

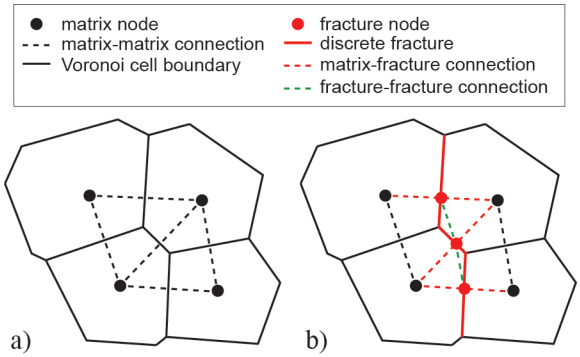

Figure 2. Adjustment of nodal connections for flow modeling with discrete fractures: a) original matrix nodes and connections; and b) insertion of fracture nodes and connections

Rigid-Body-Spring Network Approach

Elasticity and fracture damage of geomaterials are modeled using the rigid-body-spring network (RBSN), as a kind of discrete modeling approach, which represents the system behavior by a collection of simple lattice (two-node) elements. The RBSN formulation is based on the concept of the rigid-body-spring model (RBSM), first introduced by Kawai (1978).

The RBSN approach adopts the Voronoi diagram to partition the computational domain and the dual Delaunay tessellation to define the lattice structure. A lattice element consists of: 1) a zero-size spring set located at the centroid of the common Voronoi cell boundary; and 2) two rigid arm constraints that relate the spring set to the nodes. For 3D modeling, a spring set is formed from three axial springs and three rotational springs with a stiffness matrix $\mathbf{D} = \mathrm{diag}[k_n, k_s, k_t, k_{\phi n}, k_{\phi s}, k_{\phi t}]$ in local *n*-*s*-*t* coordinates. The *n*-axis is normal, and the *s*-*t* plane is parallel to the Voronoi cell boundary. The spring coefficients are defined according to the geometrical features of Voronoi diagram:

$$k_s = k_t = \alpha_1 k_n = \alpha_1 \alpha_2 E \frac{A_{ij}}{h_{ij}}, \qquad (1)$$

$$k_{\phi n} = E \frac{J_p}{h_{ij}}, \; k_{\phi s} = E \frac{I_{22}}{h_{ij}}, \; k_{\phi t} = E \frac{I_{11}}{h_{ij}}$$

where E is the elastic modulus, J_p, I_{22}, and I_{11} are the polar and two principal moment of area of the Voronoi cell boundary with respect to the centroid, respectively. The spring coefficients are scaled by the element length h_{ij} and the area of the Voronoi cell boundary A_{ij}. Effective Poisson ratio can be represented by adjusting α_1 and α_2. In this paper, by setting $\alpha_1 = \alpha_2 = 1$, the models behave with elastic homogeneity under uniform straining, albeit with zero effective Poisson ratio (Bolander and Saito, 1998; Asahina et al., 2011).

The fracturing process is represented by the damage/breakage of the springs. For the damaged spring set, the local spring coefficients are reduced to

$$\mathbf{D}' = (1 - \omega)\mathbf{D} \qquad (2)$$

where ω is a scalar damage index with a range from 0 (undamaged) to 1 (completely damaged).

A lattice element undergoes a fracture event when the stress state in the spring set violates the Mohr-Coulomb failure criterion (Fig. 3). The fracture surface is defined by three parameters: the internal friction angle ψ; cohesive strength c;

and the tensile strength f_n (tension cut-off). To determine the criticality of the stress state, a stress ratio is calculated for each element:

$$R_f = \overline{OP}/\overline{OP_o} \quad (3)$$

where $P(\sigma_n, \sigma_s, \sigma_t)$ is the stress measures applied in the three axial springs, and P_o is the vectorial description of the point at which $\overline{OP}$ intersects the fracture surface. For the element with $R_f \geq 1$, a fracture event entails a reduction of spring coefficients (Eq. 2) and a release of the associated elemental forces.

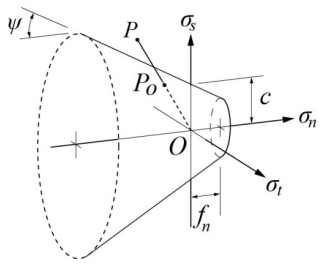

Figure 3. Mohr-Coulomb fracture surface with tension cut-off.

Coupling of Hydrological and Mechanical Modeling Codes

This section describes the linkage between the TOUGH2 simulator and the RBSN approach. Several advantages of the TOUGH-RBSN simulator stem from the availability of sharing the same grid geometry based on the Voronoi discretization, which simplifies coupling of nodal quantities and data exchange between the two numerical models.

The general coupling procedure of TOUGH-RBSN is basically similar to that of the TOUGH-FLAC simulator (Rutqvist et al., 2002), but the coupling modules are substantially modified for the DFN approach. Fig. 4 shows a schematic flow diagram of the coupling procedure between TOUGH2 and RBSN, which are linked through external modules that handle two-way coupling of the relevant quantities at each time step.

First, the TOUGH2 to RBSN link, shown on the left side of Fig. 4, supplies pressure and degree of saturation to update the mechanical quantities. From the pore pressure P, the effective (grain-to-grain) stress $\sigma_n{}'$, applied to the lattice element, is calculated using Biot's theory (Biot and Willis, 1957):

$$\sigma_n{}' = \sigma_n + \alpha_p P \quad (4)$$

where σ_n is the total normal stress obtained from overall loading, including external loads; α_p is Biot's effective stress parameter. Note that tensile stress is taken to be positive. By averaging the nodal pressure, Eq. 4 can be modified to calculate the effective stress applied to a lattice element *ij* in incremental form:

$$\Delta\sigma' = \Delta\sigma + \alpha_p(\Delta P_i + \Delta P_j)/2 \quad (5)$$

where ΔP_i and ΔP_j are the pressures increments measured at nodes *i* and *j*. It is assumed that the saturation change induces the strain increment in the element *ij* as follows:

$$\Delta\varepsilon_s = \alpha_s(\Delta S_i + \Delta S_j)/2 \quad (6)$$

where ε_s is shrinkage/ swelling strain; and α_s is the hydraulic shrinkage coefficient. If an expansible matrix material is subjected to constant stress conditions in an elastic region, the effective stress can be affected by the swelling/ shrinking strain as

$$\Delta\sigma' = \Delta\varepsilon_s E \quad (7)$$

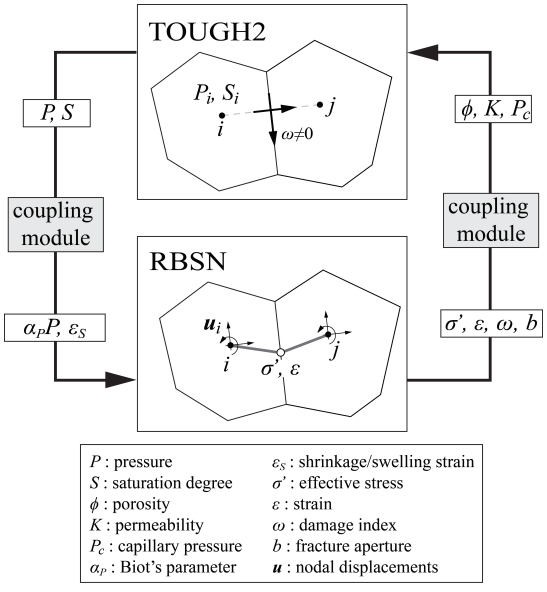

Figure 4. Flow diagram of the coupling procedure between TOUGH2 and RBSN (adapted from Asahina et al., 2014).

Thereafter, the RBSN to TOUGH2 link, shown on the right side of Fig. 4, supplies the effective stress and the strain calculated at the lattice element to update the hydrological properties of the corresponding Voronoi cells *i* and *j* in the TOUGH2 model. Porosity, permeability, and capillary pressure are generally related with the effective stress and strain values (Rutqvist and Tsang, 2002).

If fracturing occurs at the element *ij* (i.e., $\omega \neq 0$), the associated fracture node and additional connections are activated in the TOUGH2 model. The permeability of an individual fracture can be defined by the fracture aperture *b* (Bear, 1972; Bear et al., 1993), however, herein the fracture is simply assumed to have a constant permeability very high relative to that of the rock matrix.

Model Verification for Fluid-Driven Fracture Simulations

Fracture initiation and propagation incurred by the pressurized fluid are simulated to validate the TOUGH-RBSN simulator. A 2D rectangular domain with dimensions of 100×120 m is prepared, in which an unstructured Voronoi grid is generated with graded nodal density for computational efficiency (Fig. 5a). To provoke a single straight fracturing path, a reference line is prescribed in the middle of the domain. Symmetric boundary conditions are applied through a slipping (roller) configuration on the left side boundary. The point of fluid injection is located on this boundary at the end of the reference line.

The fracture geometry from the simulation result is compared to the analytical approximations for given fracture opening and length. Classic 2D fracture models, such as the Khristianovic-Geertsma-de Klerk (KGD) model (Khristianovic and Zheltov, 1955; and Geertsma and de Klerk, 1969) and the Perkins-Kern-Nordgren (PKN) model (Perkins and Kern, 1961; and Nordgren, 1972), have considered that the cross section of the fracture would be an elliptical shape based on the linear elastic fracture mechanics theory and the assumption of uniform fluid pressure along the fracture length.

In the result, the aperture width is measured by the generalized displacement of the fractured lattice element, and the fracture profiles are plotted at times 10, 15, and 20 sec. in duration of fluid injection (Fig. 5b). As the hydraulically driven fracture gets wider and longer with time, the fracture profiles retain elliptic shapes, which are analytically drawn for the fracture length and the wellbore aperture as the radii.

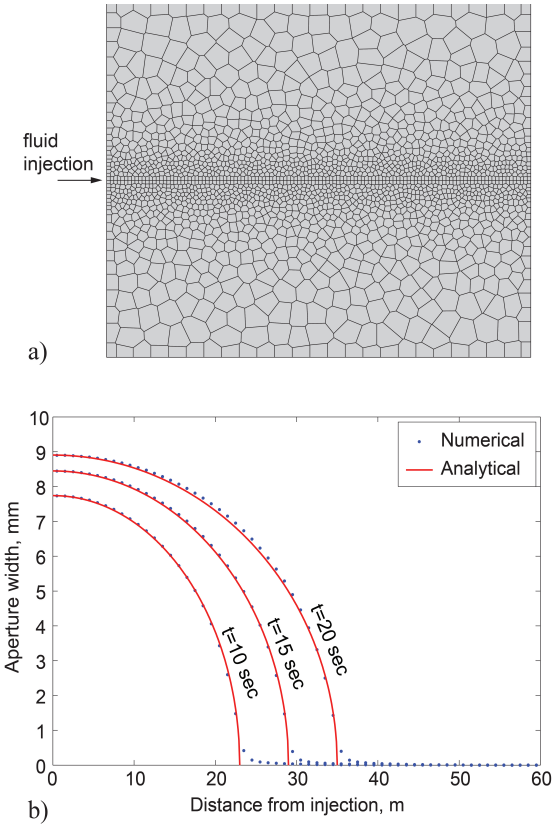

Figure 5. Hydraulic fracturing simulation of a single fracture: a) 2D model set up; and b) comparison between the numerical model and the analytical approximation in terms of fracture aperture profiles.

HYDRAULIC FRACTURING WITHIN DISCRETE FRACTURE NETWORKS

Model Configurations

Laboratory hydraulic fracturing experiments are being conducted using soda-lime glass blocks in which designed pre-existing fractures are generated by the 3D laser-engraving technique (Fig. 6a). The numerical model replicates the discrete fractures by mapping the fracture patterns onto the unstructured grid (Fig. 6b).

For simplicity, the matrix (soda-lime glass) is assumed to be impermeable and non-porous. An

88.9 mm square domain is discretized for modeling. Mechanical properties of the matrix are as follows: Young's modulus E =73.8 GPa, tensile strength f_t =30 MPa. Parameters for the Mohr-Coulomb fracture criterion are cohesive strength c =22.5 MPa and internal friction angle ϕ =45°.

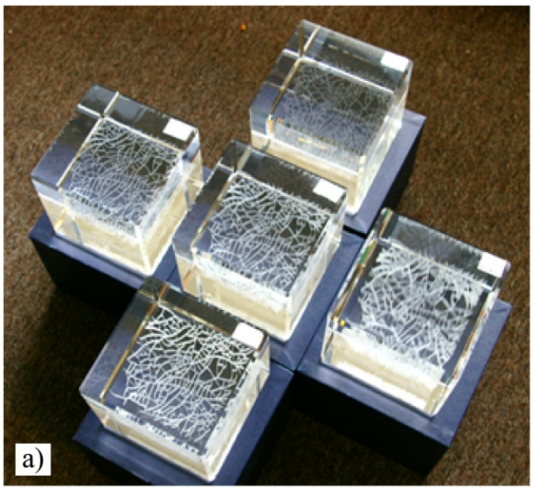

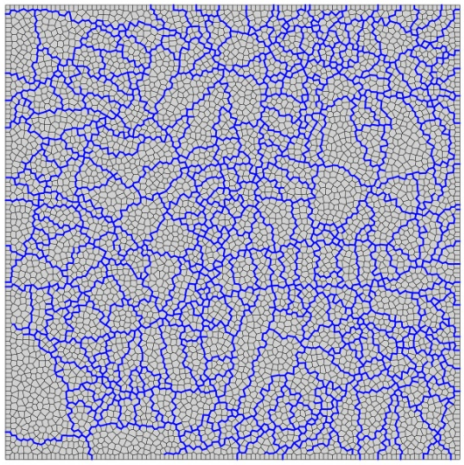

b)

Figure 6. Physical and numerical representations of complex fracture networks: a) 3D laser-engraved fractures in glass specimens; and b) mapping of the fracture pattern onto the Voronoi grid.

Because the glass is prone to brittle fracturing, the injection needs to be performed very carefully to capture the fracture propagation. In this simulation, water is injected into a borehole, placed at the center of the domain, with the rate of 2×10^{-7} kg/s per unit millimeter. Anisotropic confining stresses of 7.24 MPa and 4.83 MPa (in the vertical and horizontal directions, respectively) are applied at the boundary edges.

In the experiment, the pre-existing fractures are fabricated as clouds of thermally induced, isolated micro-cracks. The overall strength of the pre-existing fractures can be varied by modifying the microcrack density (reflected by the opaqueness of the fractures in Fig. 6a). Because we have not determined the strength of these fractures at this point, for the numerical modeling, we assume that pre-fractured elements have Young's modulus and tensile strength reduced from those of the intact glass by 50%. Hydrological properties of the pre-existing fractures are set as those of the intact glass unless the fractures are activated by subsequent hydro-mechanical responses. Once a new fracture occurs or a pre-existing fracture is activated, the mechanical resistance is removed and the permeability and the porosity are increased (e.g., a permeability of 1 darcy and a porosity of 0.8) for the fractured element while compressibility remains at zero. The borehole is assigned a permeability of 1 darcy, porosity of 1, and zero compressibility.

Results and Discussion

Fig. 7 presents the pressure distribution and hydraulic fracturing paths (in red) overlaid on the pre-existing fracture network (in blue). Two dominant fractures are shown stretching from the borehole in the direction sub-parallel to the maximum confining stress. As the hydraulic fractures advance, the fluid migrates into newly created volume along the fractures, thus the fracture paths reflect higher pressure than the surrounding matrix (Fig. 7a). As indicated by red segments in Fig. 7b, the details of the fracturing paths show a preference for forming along pre-existing fractures.

A sensitivity analysis for fracture formation was conducted by varying the storage coefficient as an independent variable. For accurate modeling of the system response, it is crucial to represent the specific storage of the injection device correctly (including the storage resulting from the compliance of the borehole) as well as the storage created by the opening of hydraulic fractures. The storage coefficient is related to the compressibility of the model domain. Two cases

of the compressibility parameters for the borehole blocks are considered: zero and 4.6×10^{-9} Pa^{-1}. Note that all the other conditions and parameters, including the injection rate, are identical in the simulations.

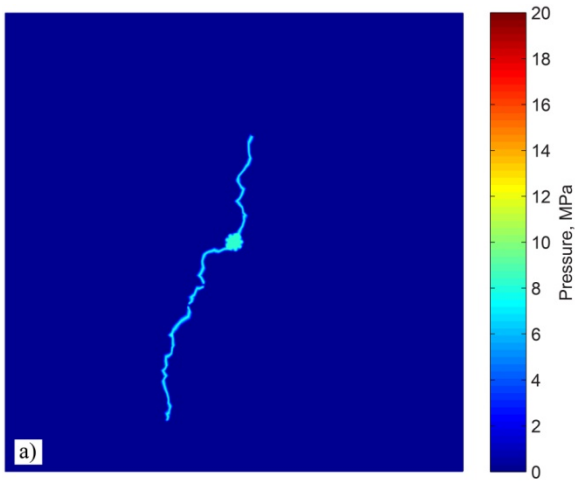

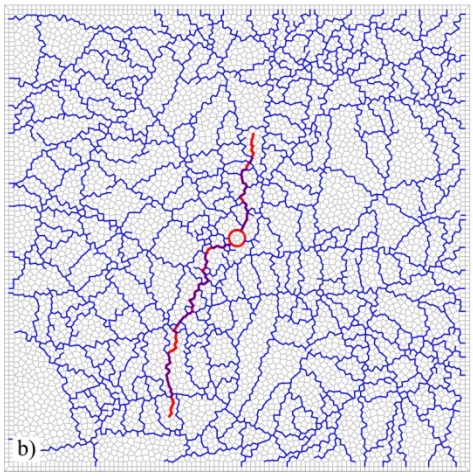

Figure 7. Simulation results at a final stage of hydraulic fracturing (t=1.25 sec): a) contour plot of internal pressure distribution; and b) fracture propagation paths overlaid on the pre-existing fracture network.

Fig. 8 compares the pressure evolutions at the borehole for the two cases. As depicted by the blue curve, zero compressibility allows gradual fracture propagation from the borehole with intermittent pressure release at the borehole. In contrast, the red curve for the higher compressibility case leads to a longer period for pressure development up to the triggering pressure and rapid fracture propagation to the model boundary with a subsequent instantaneous pressure drop. This analysis suggests that a stiff injection system with a low storage coefficient is desirable for producing stable propagation of hydraulic fractures.

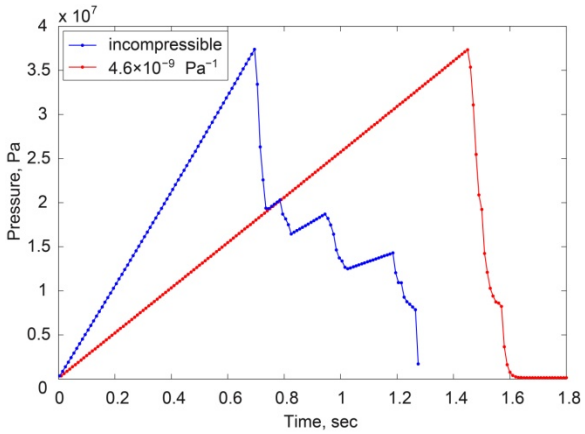

Figure 8. Evolutions of injected fluid pressure for different compressibility coefficients of the borehole region.

CONCLUDING REMARKS

In this study, an effective coupling between the TOUGH2 and the RBSN approach has been implemented and applied to hydraulic fracturing simulations. The simulator provides a discrete representation of hydrological (fluid flow through fracture networks) and mechanical (fracture initiation and propagation) responses within geomaterials.

The numerical program is verified through a simulation of a single fluid-driven fracture, in which the fracture geometry is in close agreement with the analytical approximation based upon the linear elastic fracture mechanics theory. Subsequently, predictive simulations including a sensitivity study of the effect of injection system compliance are conducted for hydraulic fracturing within complex pre-existing fracture networks. The simulation results demonstrate relevant modeling capabilities of TOUGH-RBSN, and the sensitivity analysis provides insights for controlling hydraulic fracture propagation.

Finally, the simulations presented in this paper employ constant hydrological properties for the fractured elements, regardless of varying fracture aperture. In our future study, to provide more realistic simulations and quantitative

investigations on fluid-driven fracturing, permeability, porosity and fluid storage parameters will be directly related with the fracture aperture.

ACKNOWLEDGMENT

This research is supported by the Assistant Secretary for Fossil Energy, Office of Natural Gas and Petroleum Technology, through the National Energy Technology Laboratory, and by the Used Fuel Disposition Campaign, Office of Nuclear Energy, of the U.S. Department of Energy under Contract No. DE-AC02-05CH11231 with Lawrence Berkeley National Laboratory.

REFERENCES

Asahina, D. and J.E. Bolander, Voronoi-based discretizations for fracture analysis of particulate materials, *Powder Technology*, 213, 92–99, 2011.

Asahina, D., J.E. Houseworth, J.T. Birkholzer, J. Rutqvist and J.E. Bolander, Hydro-mechanical model for wetting/drying and fracture development in geomaterials, *Computers & Geosciences*, 65, 13–23, 2014.

Bear, J., *Dynamics of Fluids in Porous Media*, Elsevier, New York, New York, 1972.

Bear, J., C.-F. Tsang and G. de Marsily, *Flow and Contaminant Transport in Fractured Rock*, Academic Press, San Diego, Calif., 1993.

Biot, M.A. and D.G. Willis, The elastic coefficients of the theory of consolidation, *Journal of Applied Mechanics*, 24, 594–601, 1957.

Bolander, J.E. and S. Saito, Fracture analyses using spring networks with random geometry, *Eng. Fract. Mech.*, 61, 569–591, 1998.

Fu, P., S.M. Johnson and C.R. Carrigan, An explicitly coupled hydro-geomechanical model for simulating hydraulic fracturing in arbitrary discrete fracture networks*, Int. J. Numer. Anal. Meth. Geomech.*, 37, 2278–2300, 2013.

Geertsma J., F. de Klerk, A rapid method of predicting width and extent of hydraulically induced fractures, *Journal of Petroleum Technology*, 21, 1571–1581, 1969.

Kawai, T., New Discrete Models and their Application to Seismic Response Analysis of Structures, *Nuclear Engineering and Design*, 48, 207–229, 1978.

Khristianovic, S.A., Y.P. Zheltov, Formation of vertical fractures by means of highly viscous liquid, *Proceedings of the Fourth World Petroleum Congress, Rome*, 579–586, 1955.

Nordgren, R.P., Propagation of a vertical hydraulic fracture, *Society of Petroleum Engineers Journal*, 12, 306–314, 1972.

Perkins, T.K. and L.R. Kern, Widths of hydraulic fractures, *Journal of Petroleum Technology*, 13, 937–949, 1961.

Pruess, K., C. Oldenburg and G. Moridis, *TOUGH2 User's Guide, Version 2*, Report LBNL-43134 (Revised), Lawrence Berkeley National Laboratory, Berkeley, Calif., 2011.

Rutqvist, J., C. Leung, A. Hoch, Y. Wang and Z. Wang, Linked multicontinuum and crack tensor approach for modeling of coupled geomechanics, fluid flow and transport in fractured rock, *J. RockMech. Geotech. Eng.*, 5, 18–31, 2013.

Rutqvist J. and C.-F. Tsang, A study of caprock hydromechanical changes associated with CO_2-injection into a brine formation, *Environmental Geology*, 42, 296–305, 2002.

Rutqvist, J., Y.-S. Wu, C.-F. Tsang and G. Bodvarsson, A modeling approach for analysis of coupled multiphase fluid flow, heat transfer and deformation in fractured porous rock, *International Journal of Rock Mechanics & Mining Sciences*, 39, 429–442, 2002.

Yip, M., J. Mohle and J.E. Bolander, Automated modeling of three-dimensional structural components using irregular lattices, *Computer-Aided Civil and Infrastructure Engineering*, 20(6), 393–407, 2005.

Zhang, K., Y.S. Wu, G.S. Bodvarsson and H.H. Liu, Flow focusing in unsaturated fracture networks: a numerical investigation, *Vadose Zone Journal*, 3, 624–633, 2004.

Development of a Hydro-geomechanical Model to Simulate Coupled Fluid Flow and Reservoir Geomechanics

Mamun Miah[1], Laura Blanco Martín[2] William Foxall[2],
Jonny Rutqvist[2], Antonio P. Rinaldi[3], Christopher Mullen[1], [2]

[1]University of Mississippi, Department of Civil Engineering, University, MS, 38677
[2]Lawrence Berkeley National Laboratory, Earth Sciences Division, Berkeley, CA, 94720
[3]ETH Zürich, SED, NO H 57 Sonneggstrasse, 58092 Zuerich
mmiah@go.olemiss.edu, lblancomartin@lbl.gov, bfoxall@lbl.gov, jrutqvist@lbl.gov, antonio-pio.rinaldi@sed.ethz.ch, cvchris@olemiss.edu

Keywords: Induced seismicity, hydro-geomechanical coupling, dynamic earthquake, rate- and state-friction, geothermal

ABSTRACT

We present development of a sequentially coupled hydro-geomechanical methodology to simulate subsurface flow and geomechanics using two available open-source codes, TOUGH2 and PyLith [CIG, 2014]. TOUGH2 is used to model fluid mass and energy balance equations through porous and fractured rock. PyLith is a USGS-developed finite-element code primarily used for large-scale geomechanical crustal deformation and earthquake simulation (static, quasi-static and dynamic modes). Our coupled framework divides the entire simulation period into a number of time steps for sequential computation of fluid flow and mechanical deformation. At each time step through the period of injection, the pressure field is passed to the geomechanical code PyLith to compute the stress change and associated deformation in the subsurface porous and fractured rock volume. Our eventual goal is to model nucleation of slips on faults and fractures due to reduction in effective normal stress under constant-rate tectonic shear loading, and subsequent dynamic earthquake rupture and elastic wave propagation. In the current contribution, the code will be benchmarked against available other codes i.e. TOUGH-FLAC [Rutqvist et al, 2002] and iGPRS [Jha and Juanes, 2014].

LITERATURE REVIEW

The complex interaction of coupled flow and geomechanics has received a great deal of attention in engineering and the geosciences. Among other applications, knowledge of hydro-geomechanical coupling behavior is critical in improving understanding of enhanced geothermal systems, enhanced oil recovery, assessing the environmental impact of groundwater use-, and induced seismicity, and monitoring and evaluating subsurface liquid waste disposal, geological carbon sequestration, and reservoir stimulation processes (e.g., Kohl et al, 1995; Morris, 2009; Rutqvist and Tsang, 2012; Zoback and Gorelick, 2012). For example, in scientific and engineering studies of CO_2 injection for geological sequestration, understanding the interaction behavior of supercritical CO_2 with a reservoir and caprock requires coupled modeling. Similarly, modeling coupled fluid flow and geomechanical deformation in fractured and porous media enables us to calculate the subsurface pressure and stress changes that can lead to coseismic slip on faults and fractures, which enhances permeability in geothermal systems. In faulted and fractured reservoirs, stress- and shear slip-dependent permeability changes are of special interest both at a local and field scales (Gutierrez et al., 2001). Fluid-induced stress and strain changes in the reservoir and overburden also impact wellbore stability, and therefore are of importance to the oil and gas industry (Zuluaga et al., 2007; Zoback, 2007).

Since coupled mechanisms play a significant role in understanding complex interactions across multidisciplinary areas, developing an accurate modeling scheme is of great interest. Therefore, coupled fluid and heat flow and deformation modeling have been studied quite extensively (Settari and Mourits, 1994; Minkoff et al., 1999; Thomas et al., 2000; Mainguy and Longuemare, 2002 Tran et al., 2004; Jha and Juanes, 2007; Kim, 2009). Unlike these studies,

in the work described here, we develop a computational methodology to model coupled thermal-hydraulic-mechanical mechanisms specifically to simulate both permeability changes and the nucleation, dynamic rupture, and subsequent ground motions during earthquakes induced by subsurface fluid injection. At present we are not accounting for complete thermo-poroelasticity effects (e.g., Kohl et al., 1995, 1998; Ghassemi et al., 2003), but fluid pressure effects on effective stress and shear strength as well as stress-dependent permeability changes as the coupling parameter from mechanics to flow.

COUPLED COMPUTATIONAL ALGORITHMS

Fully Coupled vs. Sequentially Coupled

For a typical multiphysics problem there are usually three approaches: fully coupled, loosely coupled, and one-way coupled (Minkoff et al., 2003). In a fully coupled simulator, a single set of nonlinear, coupled partial differential equations are derived and solved by incorporating all the relevant physics of flow and mechanics. In a loosely coupled approach, the governing equations for flow and mechanics are solved separately but sequentially. In that sense, a fully coupled approach might be more rigorous in simulating the complex multiphysics involved, but it is difficult and expensive. Unlike a fully coupled approach, where the full set of regular flow/mechanics time steps are used, in loose coupling, large jumps in time occur in the flow simulation due to the infrequent time steps dictated by the mechanics simulator. Also, in a fully coupled approach, a single computational grid is used for both of the codes whereas in a loosely coupled approach, the spatial grids can be different. The advantage of using a loosely coupled algorithm is that it can capture much of the complexity of the underlying physics of a coupled problem at considerably less time and cost (Minkoff et al., 2003). In a loosely coupled sequential algorithm, a high-level interface couples the two codes by calling each code sequentially and repeatedly. A time step, Δt_1 ($\Delta t_1 = t_1 - t_0$), for example, is specified to run the flow code first. The flow code usually breaks up that time step into number of smaller intervals in order to converge to its solution by the end of the given time step. The pressure output from the flow code is then passed to the mechanics code, which runs a simulation for the same time interval, Δt_1. To converge to its solution, the mechanics code may take one time step or a number of sub-steps that are generally different from those used in the flow calculation. The pore pressures are used as loads in the geomechanical governing equations in order to calculate effective stresses which are, in turn, used to calculate new porosity and permeability of the reservoir. The updated values of these flow parameters are then used in the flow code for the next time step. Thus a loosely coupled algorithm is staggered in time and involves a two-way sequential passage of information. On the other hand, in a one-way coupling output from one code is passed to the other code but only in one direction. It could be, for example, passing pore water pressure from flow code to mechanics code but no passage of information from mechanics code to the flow code. An example of one-way coupling is well failure prediction in Belridge Field, California (Fredrich et al., 1996).

Computational Scheme

Our sequential computational scheme is based on a loose coupling algorithm (Settari and Mourits, 1994; Minkoff et al., 2003) and divided in two parts. The first part is focused on the modeling of fluid and heat transport through porous and fractured strata under high injection pressure and calculation of changes in the fluid pressure field due to the injection. The second part deals with earthquake nucleation, i.e. triggering of shear slip on pre-existing highly stressed faults, due to the changes in the reservoir stress conditions resulting from fluid injection.

In order to accomplish the first part, the LBNL-developed code TOUGH2 (Pruess et al., 1999) is used. TOUGH2 is a finite difference-based suite of codes that contain multi-dimensional numerical models for simulating the coupled transport of water, vapor, non-condensible gas, and heat in porous and fractured media. For the second part the geomechanics code PyLith (PyLith 2.0.3, 2014) is used. PyLith is an open-source finite-element code for dynamic and quasi-static simulation of earthquakes developed by the

Computational Infrastructure for Geodynamics (CIG, 2014).

In the first step of the calculation, we model the fluid transport through a porous rock volume by means of the flow simulator TOUGH2. At the end of the flow simulation step, TOUGH2 provides us with the pore fluid pressure state in the reservoir system. The pore pressure is output at the centers of all of gridblocks in the computational domain. In second step, we map the pore pressure of each gridblock from the flow grid to the geomechanics grid. In the third step, we run PyLith for the same time interval as for the TOUGH2 run. The newly calculated pore pressures are used in the calculation of effective stresses and associated material deformation by the modified Drucker-Prager plastic constitutive model. In the fourth step, we estimate new permeability of the fractured and faulted zones by using an effective stress-dependent permeability model. We obtain the permeability output at the center of the geomechanics grid and map it from the geomechanics grid to the TOUGH2 grid. The updated permeability is then used as input in the next cycle of TOUGH2 run.

SUMMARY AND FUTURE WORK

We have successfully been able to link the two codes TOUGH2 and PyLith by modifying each of them. Specifically, we implemented a modified Drucker-Prager constitutive model in order to account for pore pressure in the material elastic deformation and associated plastic deformation or failure. We are currently in the process of verifying our coupled simulator with TOUGH-FLAC3D (Rutqvist et al., 2002). In our current coupled framework, we only consider a single phase flow and do not include fully thermo-poroelastic effects that may arise from changes in temperature, saturations, and the pore volume of the porous and fractured rock in a geothermal reservoir. These aspects will be addressed in the near future. Our goal is to apply this coupling approach to realistic and complex reservoir systems with arbitrary fault orientations. Our main objective is to eventually apply the framework in induced seismicity risk assessment to calibrate it fast-running approximate seismicity catalog simulations.

REFERENCES

Armero, F. and Simo, J.C. (1992). A new unconditionally stable fractional step method for non-linear coupled thermo mechanical problems. Int J Numer Methods Eng 35: 737–766.

Cappa, F., and J. Rutqvist. (2011). Modeling of coupled deformation and permeability evolution during fault reactivation induced by deep underground injection of CO2, Int. J. Greenhouse Gas Control, 5, 336–346, doi:10.1016/j.ijggc.2010.08.005.

Computational Infrastructure for Geodynamics (CIG, 2014). http://geodynamics.org

Cappa, F., and J. Rutqvist. (2012). Seismic rupture and ground accelerations induced by CO_2 injection in the shallow crust, Geophys. J.Intl., 190, 1784-1789.

CUBIT 14.1, Sandia National Laboratories, 2014. https://cubit.sandia.gov/

Fredrich, J., Arguello, J., Thorne, B., Wawersik, W., Deitrick, G., de Rouffignac, E., Myer, L., Bruno, M.,(1996). Three-dimensional geomechanical simulation of reservoir compaction and implications for well failures in the Belridge Diatomite. Proceedings of the SPE Annual Technical Conference and Exhibition, No. 36698. SPE, Richardson, TX, pp. 195– 210.

Ghassemi, A., Tarasovs, S., Cheng, A.H.-D., (2007). A three-dimensional study of the effects of thermo-mechanical loads on fracture slip in enhanced geothermal reservoir. International Journal for Rock Mechanics & Mining Science 44, 1132–1148.

Ghassemi, A., Zhou, X., (2010). A three-dimensional thermo-poroelastic model for fracture response to injection/extraction in enhanced geothermal systems. Geothermics 40(2011)39-49

Gutierrez M., Lewis R.W., and Masters I. (2001). Petroleum reservoir simulation coupling fluid flow and geomechanics. SPE Res. Eval. Eng. 164–172.faulting: Geol. Soc. America Bull., v. 70, p. 115-166

Jha B. and Juanes R. 2007. A locally conservative finite element framework for the simulation of coupled flow and reservoir geomechanics.*Acta Geotechnica* **2**: 139–153.

Kim J. (2009). Sequential formulation of coupled geomechanics and multiphase flow. Ph.D. Dissertation, Stanford University.

Kohl, T., Evans, K.F., Hopkirk, R.J., Ryback, L., (1995). Coupled hydraulic, thermal, and mechanical considerations for the simulation of hot dry rock reservoirs. Geothermics 24, 345–359.

Kohl, T., Hopkirk, R.J., (1995). "FRACimage"—a simulation code for forced fluid flow and transport in fractured, porous rock. Geothermics 24 (3), 333–343.

Mainguy M. and Longuemare P. 2002. Coupling fluid flow and rock mechanics: formulations of the partial coupling between reservoir and geomechanics simulators. *Oil Gas Sci Tech* **57**: 355–367.

Miga M.I., Paulsen K.D., and Kennedy F.E. (1998). Von Neumann stability analysis of Biot's general two dimensional theory of consolidation. Int J Numer Methods Eng 43: 955–974.

Minkoff S.E., Stone C.M., Bryant S., Peszynska M., and Wheeler M.F.(2003). Coupled fluid flow and geomechanical deformation modeling.*J Petrol Sci Eng* **38**: 37–56.

Morris J. (2009). Injection and Reservoir Hazard Management: The Role of Injection-Induced Mechanical Deformation and Geochemical Alteration at In Salah CO2 Storage Project. Lawrence Livermore National Laboratory.

Pruess, K., Oldenburg, C., Moridis, G., (1999), TOUGH2 user's guide, version 2.0, Lawrence Berkeley National Laboratory Report, LBNL-43134, Berkeley, p.198.

PyLith 2.0.3. Computational Infrastructure for Geodynamics, 2014. http://geodynamics.org/cig/software/pylith/

Rutqvist, J., Y.-S. Wu, C.-F. Tsang, and G. Bodvarsson. (2002). A modeling approach for analysis of coupled multiphase fluid flow, heat transfer, and deformation in fractured porous rock, Int. J. Rock Mech. Min. Sci., 39, 429–442, doi:10.1016/S1365-1609(02)00022-9.

Rutqvist, J., Tsang, C.-F. (2012). Multiphysics processes in partially saturated fractured rock: experiments and models from yucca mountain. Rev. Geophys. 50(3), http://dx.doi.org/10.1029/2012RG000391.

Settari, A. and Mourits, F.M.(1994): "Coupling of geomechanics and reservoir simulation models," Computational Methods and Advances in Geomechanics, Siriwardane and Zeman (eds.), Balkema, Rotterdam, The Netherlands (1994) 2151.

Thomas L.K., Chin L.Y., Pierson R.G., and Sylte J.E. 2003. Coupled geomechanics and reservoir simulation. SPE J 8(4): 350–358.

Tran D., Settari A., and Nghiem L. 2004. New iterative coupling between a reservoir simulator and a geomechanics module. SPE J 9(3):362–369.

Zoback M.D. (2007). Reservoir Geomechanics. Cambridge, UK: Cambridge University Press.

Zoback, M.D., Gorelick, S.M. (2012). Earthquake triggering and large-scale geologic storage of carbon dioxide. Proc. Natl. Acad.Sci.,http://dx.doi.org/10.1073/pnas.1202473109.

Zuluaga E., Schmidt J.H., and Dean R.H. (2007). The use of a fully coupled geomechanics-reservoir simulator to evaluate the feasibility of a cavity completion. SPE Ann Tech Conf Exhib (SPE109588), Anaheim CA, 11-14 Nov.

TOUGH2-SEED: A COUPLED FLUID FLOW MECHANICAL-STATISTICAL MODEL FOR THE STUDY OF INJECTION-INDUCED SEISMICITY

Massimo Nespoli[a,b], Antonio P. Rinaldi[c], Stefan Wiemer[c]

[a]INGV – Sezione di Bologna
via D. Creti 12, 40128 Bologna, Italy
e-mail: massimo.nespoli@ingv.it

[b]Università di Bologna – Dipartimento di Fisica e Astronomia
via Berti-Pichat 6/2, 40127 Bologna, Italy

[c]Swiss Seismological Service, ETH Zürich
Sonneggstrasse 5, 8041 Zürich, Switzerland

e-mail: antoniopio.rinaldi@sed.ethz.ch, stefan.wiemer@sed.ethz.ch

ABSTRACT

Understanding the injection-induced triggering mechanism is a fundamental step towards controlling the seismicity generated by deep underground exploitation. Here we propose a modeling approach based on coupling the TOUGH2/EOS3 simulator with a geomechanical-statistical model. The THM-statistical model provides a good representation of several mechanisms influencing each other during and after the injection phase. Each mechanism affects the induced seismicity in a different way and at different times during the reservoir stimulation, confirming that a complex interaction is on effect, and confirming that more sophisticated and physics-based coupled with statistical model are required to explain such a complex interaction.

INTRODUCTION

Deep underground exploitation sometimes leads to an increase of the local seismicity, posing potential hazard for the local community (Ellsworth, 2013). Thus, understanding how to avoid large earthquakes plays a crucial role in the success of deep geoenergy exploitation.

The correlation between underground fluid injection and seismicity is an issue that has been extensively studied (e.g., Shapiro and Dinske, 2009; Ellsworth, 2013). During fluid injection, although seismicity is generally controlled by fluid overpressure (e.g., Rinaldi et al., 2014), it is not possible to rule out some other mechanisms, such as static stress transfers between neighboring asperities, or temperature effects (Catalli et al., 2013; Dublanchet et al., 2013). In these conditions, the relationship between fluid pressure and induced seismicity is much more complex. Moreover, while current modeling approaches focus mostly on the active injection phase, the static stress transfer may become important at later stages during the post-injection phase (Catalli et al., 2013).

Many efforts in the last years aimed at a full understanding of coupled fluid flow and geomechanics processes, as well as induced seismicity. Studies have been performed accounting for lab experiments (e.g., Samuelson and Spiers, 2012; Guglielmi et al., 2015) as well as numerical modeling. The latter include: (a) fully coupled thermo-hydro-mechanical 3D numerical models (e.g., Rutqvist et al., 2002; Rutqvist, 2011; Rutqvist et al., 2015), (b) purely statistical models (Bachmann et al., 2011; Shapiro et al., 2010), and (c) hybrid models combining statistical and physical considerations (e.g., Bachmann et al., 2012; Goertz-Allmann and Wiemer, 2013; Gischig and Wiemer, 2013; Gischig et al., 2014).

Following the so-called "seed model" proposed by Gischig and Wiemer (2013), we present an improved version of the modeling approach, in which the transient pressure and temperature from TOUGH2 are used to calculate the stress changes on distributed "seed points", representing potential earthquake hypocenters. Assuming a Mohr–Coulomb failure criterion, we evaluate at each time step if a seed point has the critical condition for reactivation given the pressure and

temperature change at the seed location. The previous models (Gischig and Wiemer, 2013; Gischig et al., 2014) were improved by using TOUGH2 (Pruess et al., 2012) as the fluid flow simulator, which allows a full 3D formulation. We also account for transient, implicit permeability changes, which depend on pressure variation. If a seed is reactivated, we calculate a further permeability enhancement (either slip- or plastic strain-dependent) that is then fed back to TOUGH2.

The geomechanical-statistical model was also improved by accounting a 3D stress field including the orientation (dip and strike) for each possible earthquake location (seed). Furthermore, the TOUGH2-SEED model can also account for static stress transfer, allowing the reactivation of cascade events at the same time step.

NUMERICAL MODELING APPROACH

The model proposed here closely follows the one proposed by Gischig and Wiemer (2013). However, in the updated version presented here, we use (i) TOUGH2 as fluid flow model, and (ii) we updated and improved the stochastic part of the code to account for a more realistic 3D model. The working scheme of our model is represented in Figure 1. We follow an explicit coupling scheme: at each time step the TOUGH2 simulator computes fluid flow through the porous medium, and both temperature (T) and pore pressure (p) are interpolated to a random uniform distribution of seeds (i.e., potential earthquake hypocenters). Such a scheme has been proven to be successful for coupled simulations (e.g., TOUGH-FLAC; Rutqvist, 2011). The diagonal terms of the effective stress tensor of each seed are updated according to $\sigma'_{kk}=\sigma_{kk}-p+\beta K \Delta T$, where K is the bulk modulus and β is the volumetric thermal expansion coefficient.

While in Gischig and Wiemer (2013) the stress regime is defined by the two principal stress

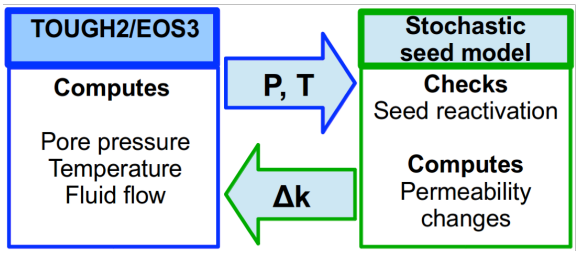

Figure 1. Coupling scheme between TOUGH2 and the stochastic seed model.

components, in our improved version we can define a more general 3D stress field, accounting for both strike-slip and dip-slip stress regime. In our model the initial three principal stress components of each seed are proportional to the lithostatic, depth-dependent pressure (p_{lit}), plus a random variation to mimic heterogeneities in the stress field. Assuming a fault orientation for each possible hypocenter (seeds), the shear τ and normal stress σ_n component variations are computed at each seed location. The stress tensor is projected to an arbitrarily oriented fault plane, defined by a strike (φ) and dip angle (θ), and shear and normal effective stresses are computed following Zoback (2010). Finally, reactivation of a seed occurs following a Mohr-Coulomb criterion. Friction angle (μ) and cohesion (C) are assigned a priori with random deviation around an average value. After activation, which occur for $\tau \geq \tau_c$, with $\tau_c=C+\mu\sigma_n$, the seed model calculates a stress drop. The stress drop, according to Gischig et al. (2014), is proportional to the shear stress: $\Delta\tau=\Delta\tau_{coeff}(\tau-c)/\mu$, where $\Delta\tau_{coeff}$ is an arbitrary coefficient and the shear stress is updated accordingly to $\tau_{new}=\tau-\Delta\tau$.

The activation of a seed point is then associated to a seismic event, whose magnitude is randomly assigned from a power-law distribution with a b-value corresponding to the seed differential stress (Gischig et al., 2014). We also account for permeability changes due to (i) pressure and/or (ii) slip on a given seed.

The first permeability dependence is a reversible pressure-dependent permeability changes (Eq. 1) (updated after Rinaldi et al., 2014).

$$\kappa_{hm} = \kappa_0 e^{C_1\left(\frac{\Phi_{hm}}{\Phi_0}-1\right)}, \Phi_{hm} = \left(\Phi_0 - \Phi_r\right)e^{\alpha\Delta p} + \Phi_r \qquad (1)$$

where C_1 and α are two empirical coefficients to obtain a two-fold increase in permeability over a 10 MPa pressure increase. Φ_0 and Φ_r are initial stress-free porosity and the residual porosity, respectively. κ_0 is the initial permeability.

The second mechanism accounts for permeability variations due to the earthquakes, and it is based on a slip-dependent equation (Eq. 2) (Gischig et al., 2014)

$$\kappa_{hm} = \kappa_0 \left[1 + C_2 \left(1 - e^{-\frac{\Delta d}{d^*}} \right) \right]^n, \Delta d = \frac{M_0}{G\pi} \left(\frac{16\Delta\tau}{7M_0} \right)^3 \qquad (2)$$

C_2 is a constant coefficient, d^* represents the slip scale, M_0 is the seismic moment and G is the shear modulus. This mechanism represents a very localized permeability variation, close to the triggered seeds (e.g., fracture opening, or slip on a fault zone), but in our model the permeability change is assigned to the gridblock containing the reactivated seed. It is worth of note that this permeability depends on the seismic moment, hence on the magnitude, which is randomly assigned.

MODELING RESULTS

The model domain is 4 × 4 km wide and 4 km deep (from -2 to -6 km depth), with a total of 20,412 elements. The mesh is finer in the central area of the domain, where we simulated a step-injection of cold water up to 30 days, followed by 60 days of constant injection (up to 90 days). The flow rate increases up to 30 kg/s at a depth of 4000 m at the center of the numerical domain. All the boundaries are open with fixed hydrostatic and geothermic conditions. The initial permeability is uniform over the entire domain corresponding to 10^{-16} m^2, while the porosity is 0.01.

Both hydraulic and geomechanic initial conditions were chosen to achieve a steady-state condition. 50,000 seeds are uniformly distributed all over the domain. This assumption does not necessarily represent a real case, in which we could assume different densities of seeds in different zones of the domain, according to the measured seismicity of the area. Table 1 reports the values of the parameters that we used in the simulations.

Table 1. List of constant parameters used in the simulation.

Thermal expansion (β)	$3 \cdot 10^{-5}$ °C^{-1}
Shear modulus (G)	5 GPa
Bulk modulus (K)	8.3 GPa
Stress drop coeff. ($\Delta\tau_{coeff}$)	0.09
Initial porosity (Φ_0)	0.01
Residual porosity (Φ_r)	0.005
Initial permeability (k_0)	10^{-16} m^2
C_1	15
C_2	2
α	10^{-8} Pa^{-1}
Critical slip (d^*)	$2 \cdot 10^{-3}$ m
Min-Max magnitude	0.85-9
Min-max differential stress for b-value	0-136 MPa

Base case results

The base case simulations are aimed to present the TOUGH2-SEED model, and as a comparison with the previous seed model (Gischig and Wiemer, 2013; Gischig et al., 2014).

For these base case simulations, we assume a local stress field (strike-slip regime) with $\sigma_{max} \approx 1.55 p_{lit}$, $\sigma_{min} \approx 0.7 p_{lit}$, $\sigma_{med} \approx p_{lit}$, respectively oriented along x-, y-, and z-axis. Each seed represents a strike slip fault with a strike angle $\varphi = 60°$ and a dip angle $\theta = 90°$.

Simulation 1 only accounts for reversible pressure-dependent permeability changes (Eq. 1) while Simulation 2 accounts also for slip-dependent permeability (Eq. 2). In both simulations, we do not account for the stress transfer at this stage.

Figure 2 shows the horizontal and vertical distribution of pore pressure changes for the two base case simulations at shut-in (90 days). The pressure variation in Simulation 1 reaches a maximum around injection zone of about 30 MPa (Figure 2a), while in Simulation 2 the pore pressure variations are lower given a larger permeability changes: at 90 days do not exceed 10 MPa (Figure 2b).

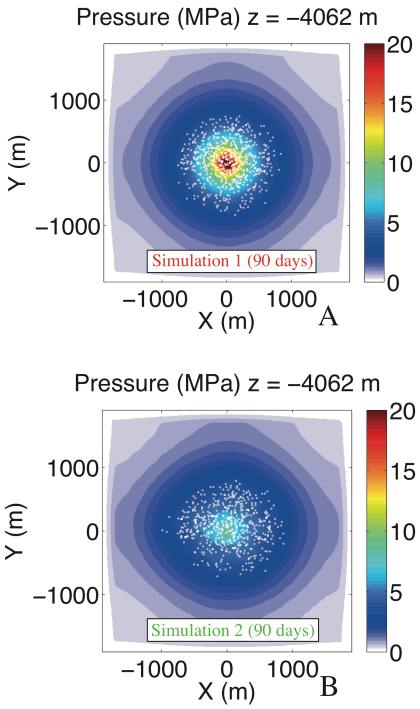

Figure 2. (a) Simulations 1 and (b) Simulation 2 horizontal sections of pressure at 90 days. The dots represent the triggered seeds after 90 days of injection.

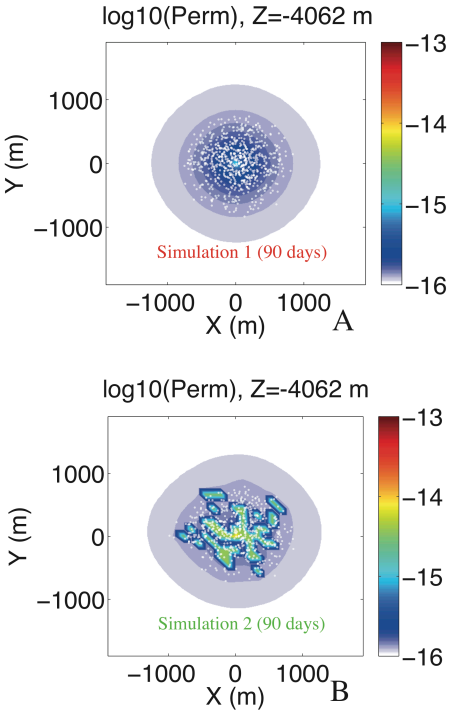

Figure 3. (a) Simulations 1 and (b) Simulation 2 horizontal sections of permeability at 90 days. Color= Permeability (m^2), dots=triggered seeds.

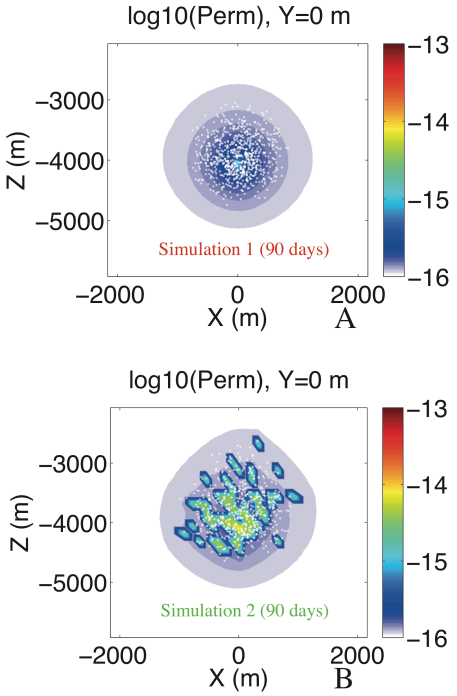

Figure 4. (a) Simulations 1 and (b) Simulation 2 vertical sections of permeability at 90 days. Color= Permeability (m^2), dots=triggered seeds.

Figures 3 and 4 shows the horizontal and vertical sections of permeability in the two simulations at the end of the injection period, respectively. Simulation 1 shows permeability changes up to a maximum increase of about one order of magnitude (up to 10^{-15} m^2) nearby the injection zone (Figure 3a). Given Eq. 1, the permeability evolution strictly follows the pore pressure distribution.

In Simulation 2 the effects of the two mechanisms of permeability enhancement are overlapped (Figure 3b). Indeed, given Eq. 2, a triggered seed produces a localized permeability increase, whose magnitude depends on the stress drop and seismic moment that is randomly assigned for each event. In Simulation 2, this relation between permeability and slip leads to scattered permeability changes up to 10^{-14} m^2 (i.e., a two orders-of-magnitude increase).

Worth of note is that the chosen permeability dependency may lead to a different shape of overpressure in the domain: while in Simulation 1 the injection-induced overpressure evolves along an almost spherical front, in Simulation 2 the evolution is slightly anisotropic.

Our 3D model allows us also to capture the simulation behavior along the *z*-axis that we expect to be quite different from the horizontal one. Figure 4 shows the vertical sections of permeability at 90 days for the two base cases simulations.

The vertical distribution of the cloud of events in both simulations has not a spherical shape but rather a drop shape: the model favors the seismicity at lower depth. This behavior is due to the combination of depth-dependent stress field and the 3D fluid flow computed by TOUGH2.

Well pressure and number of events

In the Simulation 1 we obtained a total of 757 events over the entire simulated period, and 572 in the Simulation 2. Figure 5 shows the well overpressure and the number of events at each time step (maximum 0.5 days) for the two base cases simulations. The well pressure in Simulation 1 increases of about 27 MPa during the step-injection (up to 30 days). During the constant injection period (30 to 90 days) the pressure shows a slower increase, reaching about 28 MPa at shut-in. In Simulation 2 after an initial pressure increase, a fast drop of about 3 MPa occurs, following then an irregular pattern during the entire step-injection phase (30 days) due to reactivation of seeds nearby the injection zone. The maximum pressure reached during the stimulation never exceeds 11 MPa.

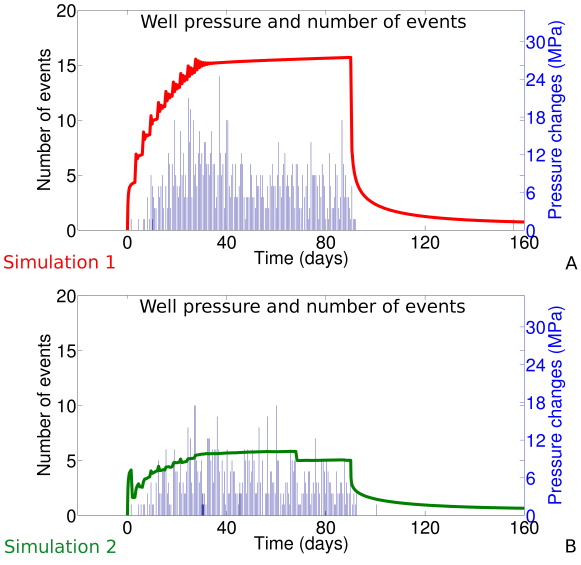

Figure 5. Well overpressure (lines) and number of events (histograms) for Simulation 1 (a) and Simulation 2 (b).

Generally, accounting for slip-dependent permeability means that when a large number of events occur, the permeability will feature a larger and faster permeability variation, resulting in spiked-like pressure changes (Figure 5b).

In both simulations, the number of events increase during the first 30 days and remains about constant during the late stage of injection. In both simulations few events occur during the post-injection phase (i.e. t>90 days).

Stress transfer

In the base case simulations we neglected the effect of static stress transfer. To account for such an effect on seed reactivation, and hence permeability and pressure distribution, we used a model first proposed by Baisch et al. (2010), which has been generalized for a full 3D formulation. In brief, when a given seed is reactivated, the shear stresses of the eight neighboring seeds on the fault plane are increased, considering a greater stress transfer along slip direction (Figure 6a). Therefore the stress transfer makes seeds closer to the failure condition and may also involve a triggering or a re-triggering of several seeds within the same time step.

Figure 6b shows an example of application of the stress transfer in TOUGH2-SEED. Assuming that the central blue dots is a triggered seed, the stress transfer function identifies the eight nearest seeds lying in nearby the oriented fault plane (red dots) and it increases their tangent stress component τ according to the scheme shown in Figure 6a.

In next subparagraphs we will show the result of two simulations: (i) Simulation 3 that is based on Simulation 2 but also accounting for the stress transfer (strike slip seeds); (ii) Simulation 4, aimed to study a case of dip slip regime.

Strike slip regime

The horizontal sections of permeability changes for Simulation 3 are shown in Figure 7a-c, at 30, 90, and 160 days, respectively, at a depth of

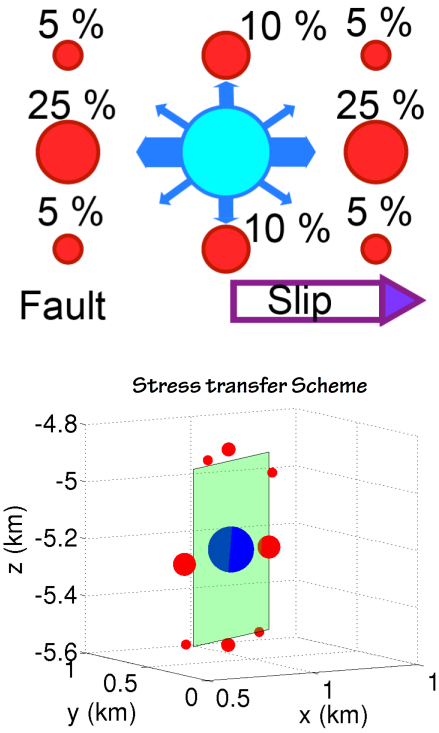

Figure 6. (a) Scheme of stress transfer, modified from Baish et al. (2010). (b) Example of stress transfer for the strike slip fault (green) used in the simulations. Blue dot is the triggered seed. Red dots are the 8 closest seeds lying in the fault plane. The dimensions are proportional to the magnitude of stress transfer.

4000 m. The red line in figures represents the seeds' strike orientation (60°). Generally the stress transfer involves a greater number of events during the first stage of simulation, and its effects on the seed distribution are even more empathized in the medium-later stage of injection. At 30 days the stress transfer produces a visible alignment of events (Figure 7a). After 90 days is difficult to distinguish the effect of the stress transfer in the injection zone, due to the large number of triggered seeds. The effects of the stress transfer are mainly visible at the edges of the seismic cloud, where several fringes oriented along the direction of strike develop (Figure 7b). At 160 days new fringes are produced and the cascades of events induced by stress transfer increase the dimension of pre-existing fringes (Figure 7c).

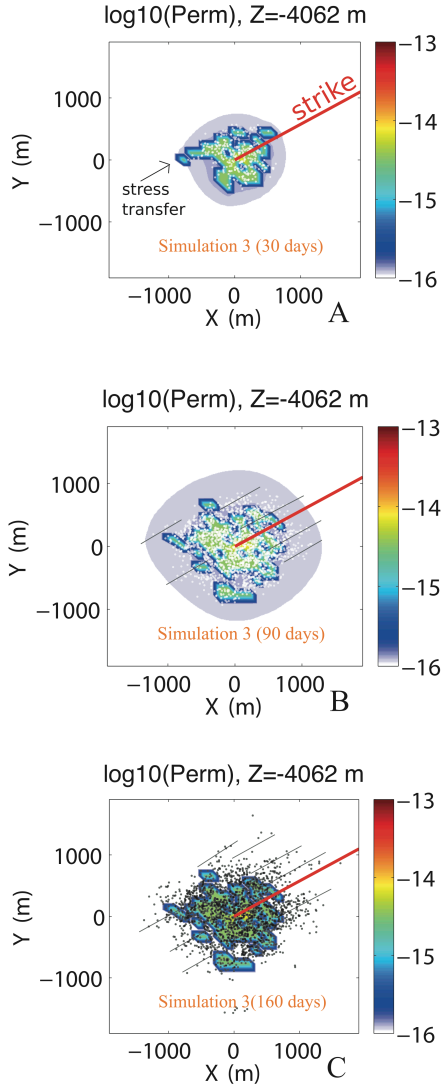

Figure 7. Horizontal sections of Simulation 3 at (a) 30, (b) 90 and (c) 160 days. Color is permeability. The red line is the strike direction and the black lines highlight the stress transfer interaction.

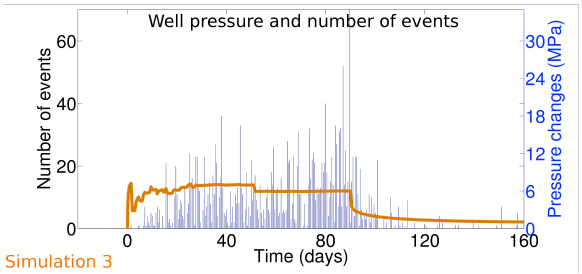

Figure 8. Well overpressure (line) and number of events (histograms) of simulation 3.

Unlike the previous base cases, in Simulation 3 we obtained a large number of seismic events also after shut-in. The well overpressure presents a temporal evolution similar to the one observed for the base case (Figure 8, orange line), although reaching a lower maximum value (about 7 MPa), probably because of the larger number of events.

In Simulation 3, the temporal evolution of the seismic events also distributes differently when compared to the base cases. The number of events progressively increases during the first 40 days of injection, remaining almost constant at the middle of the injection phase (40 to 60 days).

The occurrence of events increases at later stage of injection because of the stress transfer (60 to 90 days), and finally after shut-in the occurrence of events largely decreases, but 273 events are still triggered during the post-injection phase. The total number of events increased from 572 in the base case to more than 2000 if the stress transfer is taken into account.

Dip slip regime

The TOUGH2-SEED model is also capable of represent an arbitrary 3D domain, with fault (seeds) oriented in any direction. The fault type, as well as the stress field regime, can be assigned as initial input by the user. In order to investigate this capability, we performed a further simulation (Simulation 4), assigning a different regional stress field (with the minimum principal stress component oriented along the z axis: $\sigma_{max} \approx 1.3 p_{lit}$ (x-axis), $\sigma_{min} \approx 0.6 p_{lit}$ (z-axis), $\sigma_{med} \approx p_{lit}$ (y-axis) to mimic a dip-slip regime. All seeds represent faults with the same strike angle φ=0° and dip angle θ=20°.

Figure 9 shows the vertical sections of permeability of Simulation 4 at 30 and 90 days. At 30 days the seismicity is mostly localized in a central area of 0.5x0.5 km and there the permeability increased of about one order of magnitude around the injection-zone (Figure 9a). After 90 days the seismicity extends to a greater area and seems, with a preferential path oriented along to the dip direction and propagating toward shallower depths. The stress transfer, in fact, makes it easier to trigger events along the dip direction, consequently leading to dip-oriented permeability changes.

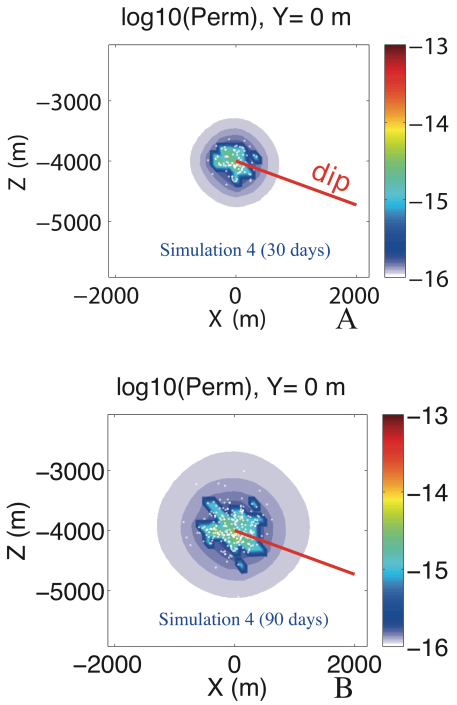

Figure 9. Vertical sections of Simulation 4 at (a) 30, (b) 90 days. Color is permeability. The red line is the dip direction.

DISCUSSION AND CONCLUSION

In this paper we presented some features of the code TOUGH2-SEED. Such a simulator couples the capabilities of TOUGH2 as fluid flow simulator to a geomechanical-statistical code for the study of injection-induced seismicity during deep underground exploitation.

We presented four different simulations. Simulation 1 and Simulation 2 showed the effects of two different permeability enhancement processes. Assuming a reversible pressure-dependent permeability we obtained a regular and well-defined seismicity zone around the injection well. Considering irreversible slip dependent permeability changes we obtained a more scattered permeability evolution that can consequently influence the pore pressure evolutions and then the whole seismicity. In both simulations the vertical section shows that the seismicity cloud is anisotropic but rather assumes a drop shape.

Simulation 3 showed the stress transfer effects. The most trivial consequence of the stress transfer is that it brings the seed closer to failure, and it may lead to cascade events. The stress trans-

fer, however, not only influences the number of events, but also their spatial and temporal distribution. In the strike-slip case the stress transfer produces several strike-oriented fringes in the seismicity clouds, triggering events to a greater distance than the base case simulation. In the dip-slip case (Simulation 4) the stress transfer leads to larger permeability changes along the dip direction.

Finally the stress transfer can also massively influence the temporal distribution of the events: indeed a large number of events are observed at a later stage of injection and even after shut-in. This behavior is somewhat in agreement with real observation. For example at EGS project in Basel, the major events only occurred after shut-in, and the temporal distribution of the seismicity showed that the number of events increased at the later stage of injection (Catalli et al., 2013).

With the TOUGH2-SEED model we can simulate up to a certain, limited extent the complex joint interaction between fluid flow and geomechanics. Compared to the previous model, we account for a more sophisticated fluid flow simulator, such as TOUGH2. Moreover, our improvements to the geomechanical-statistical seed model allow capturing effects that are impossible to represent on a simpler 2D model.

Although several effects are not considered (e.g., poroelasticity, fracture creation/propagation), the TOUGH2-SEED model represents an initial step to the representation of physics-based processes in a statistical model. The mechanical coupling can influence the seismicity at very different spatial and temporal scales, leaving open the way for the creation of more complex and realistic models.

REFERENCES

Bachmann, C.E., Wiemer, S., Woessner, J., and Hainzl, S., Statistical analysis of the induced Basel 2006 earthquake sequence: introducing a probability-based approach for Ehnhanced Geothermal System, *Geophysic. J. Int.*, 186, 793-807, 2011.

Bachmann, C.E., Wiemer, S., Goertz-Allmann, B.P., and Woessner, J., Influence of pore-pressure on the event-size distribution of induced earthquake, *Geophys. Res. Lett.*, 40(1), 72-77, 2012.

Baisch, S., Vörös, R., Rother, E., Stang, H., Jung, R., and Schellschmidt, R., A numerical model for fluid injection induced seismicity at Soultz-sous-Forêts, *Int. J. Rock Mech. Min. Sc.*, 47(3), 405-413, 2010.

Catalli, F., Meier, M.-A., and Wiemer, S., The role of Coulomb stress changes for injection□ induced seismicity: The Basel enhanced geothermal system, *Geophys. Res. Lett.*, 40(1), 72-77, 2013.

Dublanchet, P., Bernard, P., and Favreau, P., Interactions and triggering in a 3-D rate-and-state asperity model, *J. Geophys. Res. – Solid Earth*, 118(5), 2225-2245, 2013.

Ellsworth, W., Injection-induced earthquakes, Science, 341, 2013.

Gischig, V., and Wiemer, S., A stochastic model for induced seismicity based on non-linear pressure diffusion and irreversible permeability enhancement, *Geophys. J. Int.*, 194(2), 1229-1249, 2013.

Gischig, V., Wiemers, S., and Alcolea, A., Balancing reservoir creation and seismic hazard in enhanced geothermal system, *Geophys. J. Int.*, 198, 1585-1598, 2014.

Goertz-Allmann, B. and Wiemer, S., 2013. Geomechanical modeling of induced seismicity source parameters and implications for seismic hazard assessment. *Geophysics*, 78(1), KS25– KS39.

Guglielmi, Y., Cappa, F., Avouac, J.-P., Henry, P., and Elsworth, D., Seismicity triggered by fluid injection-induced aseismic slip, *Science*, 348(6240), 1224-1226, 2015.

Pruess, K., C. Oldenburg, and G. Moridis, *TOUGH2 User's Guide, Version 2.1*, Report LBNL-43134, Lawrence Berkeley National Laboratory, Berkeley, Calif., 2012.

Rinaldi, A.P., Rutqvist, J., and Cappa, F., Geomehcanical effects on CO_2 leakage through fault zones during large-scale underground injection, *Int. J. Greenh. Gas Contr.*, 20, 171-131, 2014.

Rutqvist, J., Status of TOUGH-FLAC simulator and recent applications related to coupled fluid flow and crustal deformations, *Comput. Geosci.*, 37, 739-750, 2011.

Rutqvist, J., Wu, Y.-S., Tsang, C.-F., Bodvarsson, G., A modeling approach for analysis of coupled multiphase fluid flow, heat transfer, and deformation in fractured porous rock, *Int. J. Rock Mech. Min. Sc.*, 39, 429-442, 2002.

Rutqvist, J., Rinaldi, A.P., Cappa, F., and Moridis, G.J., Modeling of fault activation and seismicity by injection directly into a fault zone associated with hydraulic fracturing of shale-gas reservoirs, *J. Petrol. Sc. Eng.*, 127, 377-386, 2015

Samuelson, J., and Spiers, C.J., Fault friction and slip stability not affected by CO_2 storage: Evidence from short-term laboratory experiments on North Sea reservoir sandstones and caprocks, *Int. J. Greenh. Gas Contr.*, 11, S78-S90, 2012.

Shapiro, S. A., and Dinske, C., Scaling of seismicity induced by non-linear fluid-rock interaction, *J. Geophys. Res.*, 114, B09307, 2009.

Shapiro, S.A., Dinske, C., Langebruch, C., and Wenzel, F., Seismogenic index and magnitude probability of earthquakes induced during reservoir fluid stimulations, *The Leading Edge – Special Section: Microseismic*, 304-309, 2010.

Zoback, M., *Reservoir Geomechanics*, Cambridge University Press, pp. 449, 2010.

INVERSE MODELING OF COUPLED FLUID FLOW AND GEOMECHANICS WITH iTOUGH2-PEST AND TOUGH-FLAC: APPLICATION TO IN SALAH CO_2 STORAGE SITE

Antonio P. Rinaldi[a,b], Jonny Rutqvist[a], Stefan Finsterle[a], Hui-Hai Liu[c]

[a]Lawrence Berkeley National Laboratory, Earth Sciences Division
1 Cyclotron Rd., Berkeley, CA, 94720, USA
e-mail: aprinaldi@lbl.gov, jrutqvist@lbl.gov, safinsterle@lbl.gov

[b]Swiss Seismological Service, ETH Zürich
Sonneggstrasse 5, 8041 Zürich, Switzerland
e-mail: antoniopio.rinaldi@sed.ethz.ch

[c]Aramco Research Center
16300 Park Row, Houston, TX, 77084, USA
e-mail: hhliu@lbl.gov

ABSTRACT

In this study we perform an inverse modeling analysis of coupled fluid flow and geomechanics of CO_2 injection at the In Salah CO_2 storage site by using iTOUGH2-PEST linked to TOUGH-FLAC. First we improved the previous modeling with TOUGH-FLAC at the injection well KB-502 by considering elasto-plastic behavior with Mohr-Coulomb failure criterion in both the storage reservoir and a vertical fracture zone.

Mechanical and hydraulic properties of the injection reservoir and those of fracture zones were determined through inverse modeling with iTOUGH2-PEST by matching the simulated spatial and temporal evolution of uplift to the corresponding InSAR ground displacement observations as well as by matching simulated and measured pressures. This included determination of properties related to stress-dependent permeability and elastic (bulk) modulus.

We found an excellent match between simulated and observed variables, with residuals consistent with observation errors. The estimated values for the parameterized mechanical and hydraulic properties are in agreement with previous numerical results.

INTRODUCTION

The In Salah project in Algeria was in operation between 2004 and 2011. It was the first on-shore, industrial-scale demonstration site for CO_2 sequestration. About 4 million tons of carbon dioxide were stored in a 20 m thick, water-filled reservoir at a depth of about 2000 m. Injection occurred through three injection wells (1 to 1.5 km long). A large caprock overburden, with a thickness of about 900 m, prevented the CO_2 from escaping to shallow depths (Ringrose et al., 2012).

The In Salah demonstration site is also well known for the unique monitoring network, consisting of wellhead sampling, down-hole logging, core analysis, surface gas and groundwater aquifer monitoring, 4D seismic, microseismic monitoring, induced seismicity, and satellite InSAR data (Mathieson et al., 2011)

The InSAR data provide essential information for the analysis of coupled fluid flow and geomechanics, and to develop a proper forward model needed for an inverse analysis.

In this paper, we analyze the evolution of deformation and pressure at the KB-502 injection well, where a double-lobe uplift feature has been observed by analysis of satellite data. Such a feature has been explained as caused by a deep fracture opening, and both semi-analytical and numerical modeling confirmed such a hypothesis (Vasco et al., 2010; Rutqvist et al., 2010; Rinaldi and Rutqvist, 2013). Analysis of 3D seismic images also confirmed the presence of such a linear feature at reservoir depth (Gibson-Poole and Raikes, 2010; Wright, 2011).

Starting from the results achieved by Rinaldi and Rutqvist (2013), here we improved the forward

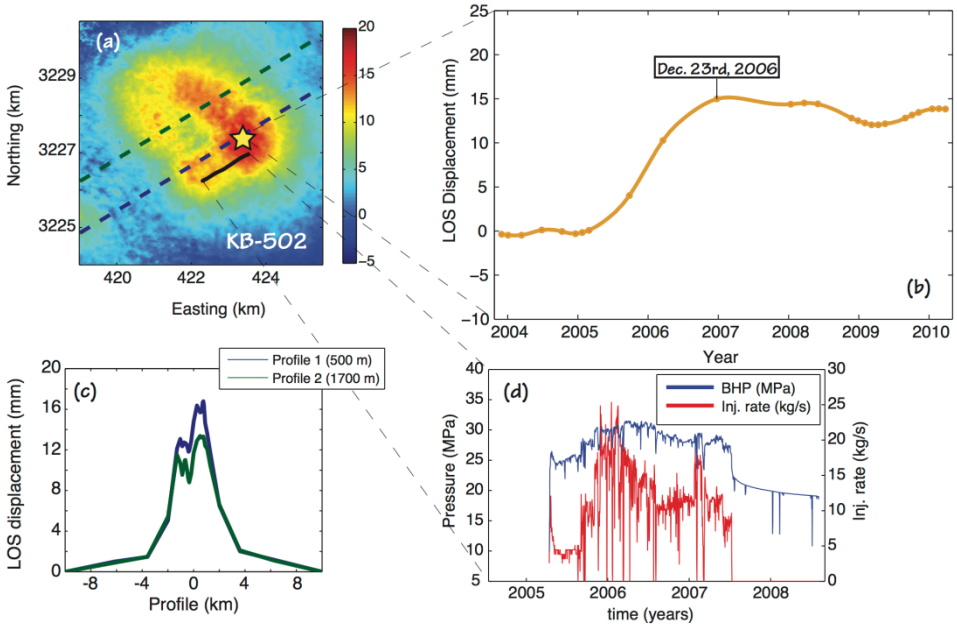

Figure 1. Observations at KB-502 injection well: (a) pattern of deformation, (b) transient evolution of ground uplift (dots indicate the days when satellite data were acquired), (c) profiles of ground uplift at 500 m (blue) and 1700 m (green) from injection well, (d) bottomhole pressure (blue) and injection rate (red).

model with TOUGH-FLAC (Rutqvist, 2011), by accounting for a reactivation criterion for the fracture zone and the injection reservoir. We also accounted for permeability changes associated with the stress evolution. Parameter estimation, sensitivity and uncertainty analyses were carried out using the inverse modeling program iTOUGH2-PEST (Finsterle and Zhang, 2011).

FIELD DATA AND MODELING AT KB-502 INJECTION WELL

Figure 1 shows some of the data collected at the KB-502 injection well. Here we focus on the first injection period, which lasted for about two years (mid-2005 to mid-2007).

The pattern of deformation, featuring a double-lobe uplift, is shown in Figure 1a. The snapshot was taken at about 600 days after injection started and shows a maximum uplift of about 15 mm. Figure 1b shows the transient evolution of the displacement on the satellite's Line of Sight (LOS) at a point located near the maximum observed uplift. The uplift undergoes a strong increase after the first few months of injection (up to about 15 mm in 1 year), followed by a slower subsidence rate after shut in. The double-lobe uplift is also clear in Figure 1c, which shows the uplift along two profiles. The ground surface reached about 16 mm and 12 mm displacement at 500 m and 1700 m NW of the injection well, respectively.

The In Salah project was not only characterized by InSAR monitoring. Indeed, wellhead pressure and injection rate were carefully monitored. Figure 1d shows the injection rate (red) and the bottomhole pressure (blue) calculated from the monitored wellhead pressure.

Seismic survey and well log analysis, as well as *in situ* measurements, provided an estimate for the principal stress orientation and helped to determine the seismic velocity field (Iding and Ringrose, 2010; Shi et al., 2012).

Model setup

The model presented here closely follows the one proposed by Rinaldi and Rutqvist (2013).

The forward runs were performed using the TOUGH-FLAC simulator (Rutqvist, 2011), which couples the TOUGH2 simulator for fluid flow in porous media (Pruess et al., 2011) with the FLAC3D simulator for geomechanics and deformation (Itasca, 2009). Figure 2 shows the computational domain with *x*-direction corresponding to the NW-SE direction.

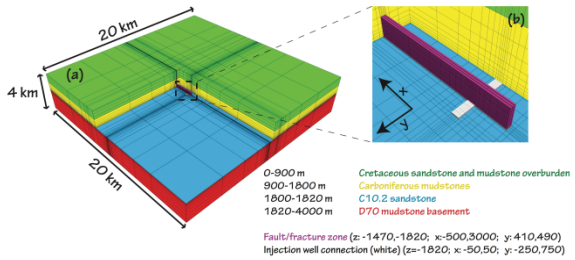

Figure 2. Computational domain (Rinaldi and Rutqvist, 2013).

Table 1. Hydrogeological properties used in the forward model (Rinaldi and Ruqtvist, 2013). Stress-dependent parameters in bold.

	Depth (m)	Φ_0 (-)	κ_0 (m^2)
Shallow	0-900	0.1	10^{-12}
Caprock	900-1800	0.01	10^{-21}
Reservoir	1800-1820	0.17	$\mathbf{0.8\times10^{-14}}$
Basement	>1820	0.01	10^{-19}

Table 2. Geomechanical properties based on log analysis (Gemmer et al., 2012). Depths were slightly modified to fit our geological model (Table 1). Stress-dependent parameters in bold.

Depth (m)	Young's modulus E (GPa)	Poisson's ratio ν(-)
0-900	3	0.25
900-1650	5	0.3
1650-1780	2	0.3
1780-1800	20	0.25
1800-1820	**10**	0.2
1820-4000	15	0.3

The model consists of four layers, whose properties are listed in Table 1. The mechanical properties, listed in Table 2, closely follow estimates from well log analyses (Gemmer et al., 2012).

Initial temperature and pressure gradients are taken from field investigations. The injection reservoir is at an initial temperature of 90 ˚C with about 18 MPa pore pressure. Lateral boundaries are at constant condition, while the bottom boundary is set as a no-flow and no-vertical displacement boundary.

The CO_2 injection takes place in a 20 m thick reservoir at a depth of 1820 m. Injection rates closely follow the values shown in Figure 1d.

The medium is poroelastic, with the exception of the storage reservoir and deep fracture zone, both subjected to a failure criterion. The initial stresses also follow field observations, with: σ_{xx}=15.8 MPa/km, σ_{yy}=22.2 MPa/km, and σ_{zz}=25.1 MPa/km.

Following the modeling approach by Rinaldi and Rutqvist (2013), we model the opening of a deep fracture zone at reservoir depth, extending for 350 m upward into the lower caprock. The novelty of the approach presented here consists in the use of a Mohr-Coulomb criterion to determine when such a pre-existing fracture zone reactivates. After reactivation, the tensile opening is simulated by using an orthotropic model.

All the hydraulic and mechanical parameters are constant, with the exception of reservoir permeability and bulk modulus, which change as a function of mean effective stress.

Stress-dependent reservoir permeability and bulk modulus

We assume that the injection reservoir is highly fractured, and if the principal stresses σ_1 and σ_3 within the injection reservoir satisfy the Mohr-Coulomb failure criterion for a given friction angle φ_{res}, defined by:

$$f = \sigma_1 - \frac{1+\sin\varphi_{res}}{1-\sin\varphi_{res}}\sigma_3 \qquad (1)$$

the permeability and the bulk modulus start to change as a function of the mean effective stress. A relationship between fracture aperture and normal effective stress was derived by Liu and Rutqvist (2013). Accounting for a cubic law (Witherspoon et al., 1980), and referring the relation to the initial state of stress and the mean effective stress, a stress-dependent permeability can be derived (Rinaldi et al., 2014):

$$\frac{\kappa_{hm}}{\kappa_i} = \left(\frac{b}{b_i}\right)^3 = \left(\frac{\gamma_e + \gamma_t e^{\frac{\sigma'_m}{K_{t,f}}}}{\gamma_e + \gamma_t e^{\frac{\sigma'_{m,i}}{K_{t,f}}}}\right)^3 \qquad (2)$$

where b and b_i are the current and initial apertures, and κ_{hm} and κ_i are the permeabilities at the current and initial state of stress, respectively. $K_{t,f}$ refers to the bulk modulus of the reservoir fractures, and σ'_m is the effective mean stress. γ_e and γ_t represent the unstressed volume fraction

for the hard and soft parts of a body rock, respectively.

Following Liu and Rutqvist (2013) and assuming a constant bulk modulus for the porous matrix, we have an effective bulk modulus given by:

$$\frac{1}{K_{eff}} = \frac{1}{K^{i}_{eff}} + \Theta_f \frac{\gamma_t}{K_{t,f}} \left(e^{\frac{\sigma'_m}{K_{t,f}}} - e^{\frac{\sigma'_m}{K_{t,f}}} \right) \qquad (3)$$

where K_{eff} and K^{i}_{eff} are the current and the initial bulk modulus, respectively, and Θ_f is the volume fraction occupied by fractures, assumed to be 1%.

RESULTS

Inverse modeling is conducted to estimate the values for some of the mechanical and hydraulic properties that minimize the misfit between simulation and observed data.

Parameters to be estimated are: (i) friction angle of the injection reservoir, (ii) friction angle of the deep fracture zone, (iii) bulk modulus for stress-dependent permeability (Eq. 2), and (iv-vi) the three Young's moduli in the three directions for the deep fracture zone (E_x, E_y, and E_z). Initial guesses for the parameters can be found in Table 3.

Simulation results are compared with four field observations: (i) bottom-hole pressure, (ii) transient evolution of the LOS displacement on a single point located above the injection well, and (iii) and (iv) two different profiles located at 500 m and 1700 m, respectively, northwest and parallel to the injection well.

We use the Levenberg-Marquardt algorithm to minimize the misfit between model results and field data. A reasonably good match was achieved with three iterations (Rinaldi et al., 2014); here we used six iterations to account for the increased number of parameters.

The best estimate for the parameters after inversion can be found in Table 3. All the parameters are estimated with a relative error smaller than 1%. The objective function value was reduced from the initial 1189.6 to 99.23, and the maximum weighted residual was reduced from about 45 to 15.

Figure 3 shows the comparison between model results and field observations. We find an excellent match for the bottomhole pressure (Figure 3a), with the simulated pressure (orange line) consistent with the expected error of the field observations (gray area). Major differences are found after shut-in, probably related to phase or temperature changes within the borehole that the model is unable to reproduce. Figure 3b and 3c show the comparison between simulated and observed LOS ground surface uplift, along the two profiles. Also in this case we achieve a good match, although we overestimate the uplift in the region far from the double-lobe region. Finally, Figure 3d shows the resulting transient evolution of the LOS displacement at a single point. The simulated evolution is in excellent agreement with the observed variation.

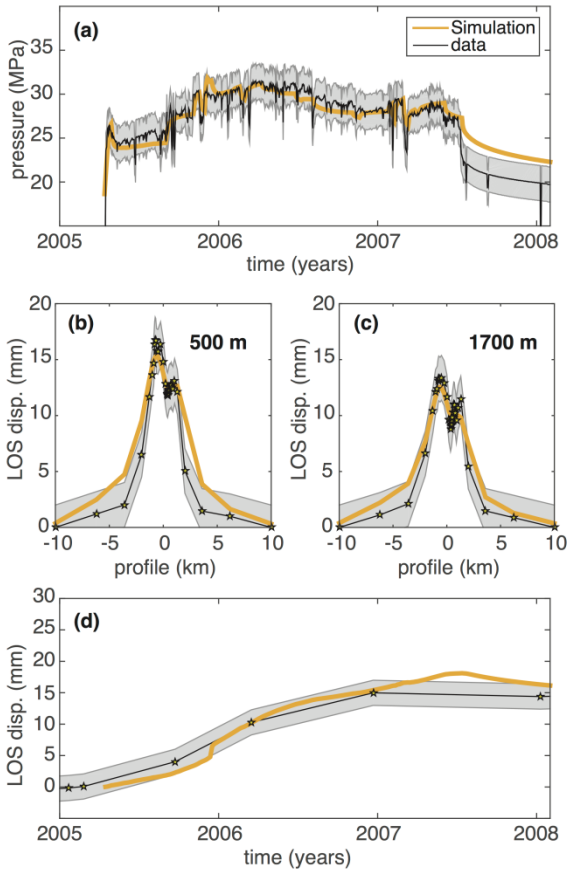

Figure 3. Comparison between simulation and observed data at KB-502: (a) temporal evolution of bottomhole pressure, (b) profile of ground uplift at 500 m after 618 days, (c) profile of ground uplift at 1700 m after 618 days, (d) temporal evolution of ground uplift.

Table 3. Estimated parameters for KB-502 injection well (initial guess E_x, E_y, and E_z fom Rinaldi and Rutqvist, 2013).

	Initial Guess	Best estimate
K_t (Pa)	$10^{7.0253}$	$10^{6.90\pm0.01}$ (7.94 MPa)
ϕ_{res} (˚)	31	27.9±0.3
ϕ_{frac} (˚)	31	30.6±0.2
E_x (Pa)	0.17×10^9	$10^{8.71\pm0.05}$ (0.51 GPa)
E_y (Pa)	0.14×10^9	$10^{8.13\pm0.03}$ (0.13 GPa)
E_z (Pa)	10^9	$10^{9.06\pm0.02}$ (1.15 GPa)
Objective func.	1189.6	99.23
Max. Residual	44.89	14.52

For completeness, we also show the comparison between the simulated and observed pattern of deformation (Figure 4), although we do not use the entire map as observation for the inverse analysis. Figure 4 shows how the simulation is able to reproduce the observed double-lobe uplift.

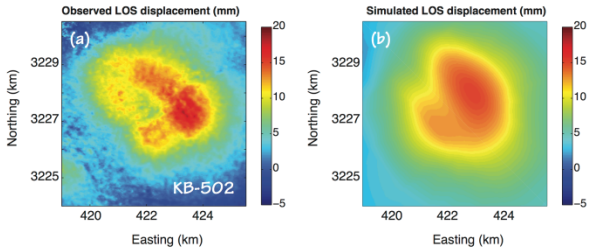

Figure 4. Resulting deformation after inversion. (a) Observed LOS displacement, (b) simulated LOS displacement.

Sensitivity Analysis

Thanks to the capabilities of iTOUGH2-PEST, we can perform a full sensitivity analysis, and results are shown in Figure 5.

Figure 5a shows that the bottomhole pressure is very sensitive to a change in K_t (parameter largely affecting the permeability). The sensitivity analysis shows that the pressure is also affected by mechanical parameters, such as the bulk modulus of the deep fracture zone in vertical direction (E_z). The friction angle of the fracture zone (ϕ_{res}) has a minor effect, visible only at the time of reactivation (around 2006).

Figures 5b and 5c show the sensitivities for the LOS displacement along the two profiles. As expected, the surface uplift highly depends on the Young's moduli of the deep fracture zone in the three different directions. The profiles are inversely correlated to E_z and directly correlated to E_y, suggesting more opening compared to the uplift of the fracture zone (the vertical Young's modulus increases, while the horizontal Young's modulus decreases). It is worth noting that the parameter K_t has also some effect on deformation, suggesting that a coupled fluid and geomechanics model is essential to capture all the feature of a complex, interacting system. Interestingly, the LOS displacement along the profiles is not sensitive to parameter changes in the far field (i.e., 5 km from the injection region along the profile). Finally, Figure 5d shows the sensitivity analysis for the transient evolution of the LOS displacement. This observation has a sensitivity similar to the one seen for the profiles, but it is also interesting to note that the transient evolution of the LOS displacement is not sensitive (or minimally sensitive) to the chosen parameters before fracture reactivation.

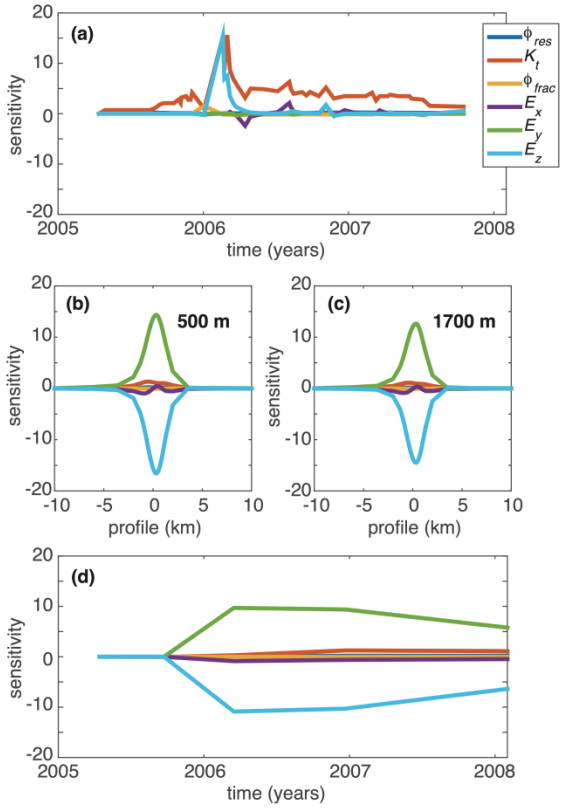

Figure 5. Sensitivity analysis: (a) temporal evolution of bottomhole pressure, (b) profile of ground uplift at 500 m after 618 days, (c) profile of ground uplift at 1700 m after 618 days, (d) temporal evolution of ground uplift.

Residual Analysis

The results of the analysis of the misfit between simulation and field observation are shown in Figure 6. All the simulated results are in very good agreement with the field observations, with residuals within the assumed errors for each observation.

Figure 6a shows the misfit for the bottomhole pressure. The misfit between simulation and data is limited to the range -2 to 2 MPa, with only few exceptions after shut-in. We accounted for such large error in pressure because the bottomhole pressure is calculated from wellhead pressure and the injection rate by using the code T2Well (Pan et al., 2011). Such calculation increased the error associated with the real measure of wellhead pressure. For the LOS displacement along the profiles, the misfit is limited in the range -2 to 2 mm for most of the observations. Residuals are small in the double lobe region (less than 2 mm), and increase in the far field, probably because of the coarse numerical grid (Figures 6b and 6c). The analysis of the residual for the temporal evolution of LOS displacement shows that the misfit between simulation and field data is always smaller than the 2 mm error associated with InSAR measurements (Figure 6d).

CONCLUSION

We conducted a joint inversion of coupled fluid flow and geomechanics associated with the CO_2 storage operation at the KB-502 injection well at the In Salah demonstration site.

Starting from numerical simulations performed in the past, we first improved the forward model with TOUGH-FLAC. We then performed an inverse analysis using iTOUGH2-PEST to estimate uncertain parameters. Thanks to the capabilities of iTOUGH2 (Finsterle, 2007) we were also able to evaluate the error associated with the parameters, as well as to study the sensitivity of the model to the parameters of interest.

Results show that the inverse modeling approach is able to fit the observations after only a few iterations. A sensitivity analysis on the chosen parameters shows that hydraulic parameters (e.g., stress-dependent permeability parameters) may influence geomechanical observations. Results also show that the hydraulic observations (e.g. bottomhole pressure) may depend on mechanical parameters, such as the bulk modulus of the fracture zone at depth.

The current inverse modeling approach, coupling iTOUGH2-PEST with TOUGH-FLAC, is a powerful tool to estimate unknown properties for complex coupled fluid flow and geomechanics problems, providing the errors and sensitivities associated with such properties. Future works will include the study and parameterization of the deep fracture zone geometry, as well as the study of the effect of mesh discretization.

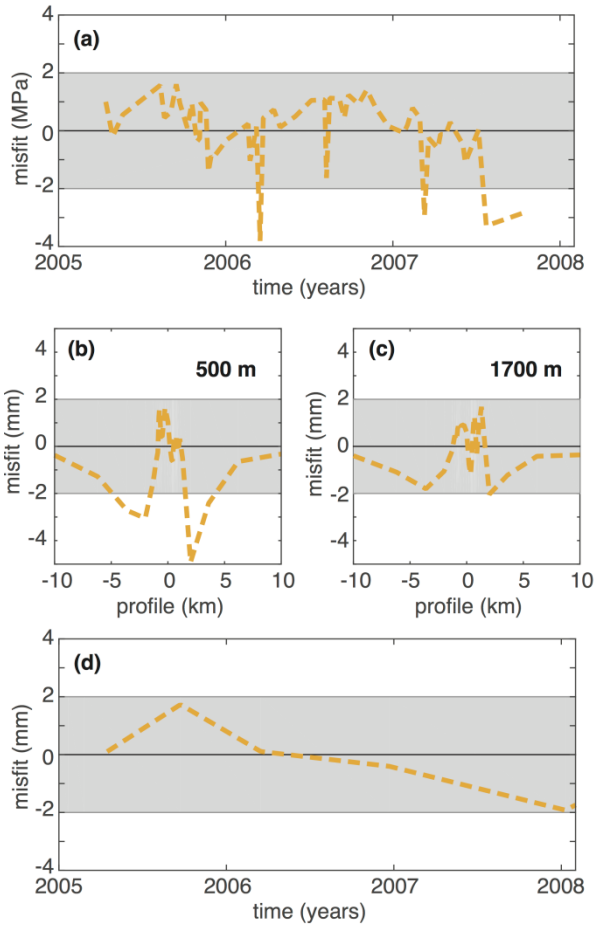

Figure 6. Residual analysis: (a) temporal evolution of bottomhole pressure, (b) profile of ground uplift at 500 m after 618 days, (c) profile of ground uplift at 1700 m after 618 days, (d) temporal evolution of ground uplift.

ACKNOWLEDGEMENTS

This work was jointly supported by the Assistant Secretary for Fossil Energy, Office of Natural Gas and Petroleum Technology, through the National Energy Technology Laboratory, and the In Salah JIP and their partners BP, Statoil, and Sonatrach under the U.S. Department of Energy Contract No. DE-AC02-05CH11231.

REFERENCES

Finsterle, S., *iTOUGH2 User's Guide*, Report LBNL-40040, Lawrence Berkeley Natl. Lab., Berkeley, CA, USA, 2007.

Finsterle, S., and Zhang, Y., Solving iTOUGH2 simulation and optimization using PEST protocol, *Environ. Modell. Softw.*, 26(7), 959-968, 2011.

Gemmer, L., Hansen, O., Iding, M., Leary, S., and Ringrose, P., Geomechanical response to CO_2 injection at Krechba, In Salah, Algeria, *First Break*, 30, 79-84, 2012.

Gibson-Poole, C.M., and Raikes, S., Enhanced understanding of CO_2 storage at Krechba from 3D seismic, *9th Annual Conference on Carbon Capture and Sequestration*, Pittsburgh, PA, USA, Ma 10-13, 2010.

Iding, M., and Ringrose, P., Evaluating the impact of fractures on the performance of the In Salah, CO_2 storage site, *Int. J. Greenh. Gas Contr.*, 4, 242-248, 2010.

ITASCA, *FLAC3d v5.0, Fast Lagrangian Analysis of Continua in 3 Dimensions, User's Guide*, Itasca Consulting Group, Minneapolis, MN, USA, 2009.

Liu, H.H., and Rutqvist, J., Coupled hydrome-chanical processes associated with multiphase flow in a dual-continuum system: formulations and an application, *Rock Mech. Rock Eng.*, 46(5), 1103-1112, 2013.

Mathieson, A., Midgley, J., Wright, I., Saoula, N., and Ringrose, P., In Salah CO_2 storage JIP: CO_2 sequestration monitoring and verification technologies applied at Krechba, Algeria, *Energy Procedia*, 4, 3596-3603, 2011.

Pan, L., Oldenburg, C. M., Pruess, K., and Wu, Y.-S., Transient CO_2 leakage and injection in wellbore-reservoir system for geological carbon sequestration, *Greenh. Gas. Sci. Tech.*, 1(4), 335-350, 2011.

Pruess, K., Oldenburg, C.M., and Moridis, G., *TOUGH2 User's Guide, Version 2*.1, Paper LBNL-43134 (revised). Lawrence Berkeley Natl. Lab., Berkeley, CA, USA, 2011.

Rinaldi, A.P., and Rutqvist, J., Modeling of deep fracture zone opening and transient ground surface uplift at KB-502 CO_2 injection well, In Salah, Algeria, *Int. J. Greenh. Gas Contr.*, 12, 155-167, 2013.

Rinaldi, A.P., Rutqvist, J., Finsterle, S., and Liu, H.H., Forward and inverse modeling of ground surface uplift at In Salah, Algeria, *48th US Rock Mechanics/Geomechanics Symposium*, Minneapolis, MN, USA, 1-4 June, 2014.

Ringrose, P.S., Mathieson, A.S., Wright, I.W., Selama, F., Hansen, O., Bissell, R., Saoula, N., and Midgley, J., The In Salah CO_2 storage project: lessons learned and knowledge transfer, *Energy Procedia*, 37, 6226-6236, 2012

Rutqvist, J., Status of TOUGH-FLAC simulator and recent applications related to coupled fluid flow and crustal deformations, *Comput. Geosci.*, 37, 739-750, 2011.

Rutqvist, J., Vasco, D.W., and Myer, L., Coupled reservoir-geomechanical analysis of CO_2 injection and ground deformations at In Salah, *Int. J. Greenh. Gas Contr.*, 4, 225-230, 2010.

Shi, J. Q., Sinayuc, C., Durucan, S, and Korre, A., Assessment of carbon dioxide plume behaviour within the storage reservoir and the lower caprock around the KB-502 injection well at In Salah, *Int J. Greenh. Gas Contr.*, 7, 115-126, 2012.

Vasco, D.W., Rucci, A., Ferretti, A., Novali, F., Bissell, R.C., Ringrose, P.S., Mathieson, A.S., and Wright, I.W., Satellite-based measure-ments of surface deformation reveal fluid flow associated with the geological storage of carbon dioxide, *Geophys. Res. Lett.*, 37, L03303, 2010.

Witherspoon, P.A., Wang, J.S.W., Iwai, K., and Gale, J.E., Validity of cubic law for fluid flow in deformable rock fracture, *Water Res. Res.*, 16(6), 1016-1024, 1980.

Wright, I., In Salah CO_2 storage JIP lessons learned, *10th Annual Conference on Carbon Capture and Sequestration*, Pittsburgh, PA, USA, 2011.

AN OVERVIEW OF TOUGH-BASED GEOMECHANICS MODELS

Jonny Rutqvist

Lawrence Berkeley National Laboratory
1 Cyclotron Rd.
Berkeley, CA 94720, USA
e-mail: Jrutqvist@lbl.gov

ABSTRACT

After the initial development of the first TOUGH-based geomechanics model 15 years ago based on linking TOUGH2 to the FLAC3D geomechanics simulator, at least 15 additional TOUGH-based geomechanics models have appeared in the literature. This paper provides a brief overview of these models and approaches, focusing on some of the most recent ones that are complementary and have been more frequently applied to a diverse set of problems associated with geomechanics and its couplings to hydraulic, thermal and chemical processes.

INTRODUCTION

A growing demand and interest for modeling coupled multiphase flow and geomechanical processes has resulted in the development of an increasing number of TOUGH-based geomechanics models. This development started with the need for analyzing the effect of geomechanics on multiphase fluid flow behavior and transport properties around nuclear waste emplacement tunnels at the previously proposed U.S. high-level nuclear repository site at Yucca Mountain, Nevada. The TOUGH-FLAC simulator was developed as a pragmatic approach, linking the two existing codes, TOUGH2 and FLAC3D (Rutqvist et al., 2002). The TOUGH-FLAC simulator has since been adapted and applied for a wide range of geoscientific research and geoengineering applications, such as geologic CO_2 sequestration, enhanced geothermal systems, and gas production from gas hydrate bearing sediments (Rutqvist (2011) and references therein).

Following the development of the TOUGH-FLAC simulator, a number TOUGH-based geomechanical models have been and are being developed. In fact, at least 15 additional TOUGH-based geomechanics models of various sophistications have appeared in the literature. This include simulators such as TOUGH+ROCMECH (Kim and Moridis, 2013), TOUGH-RDCA (Pan et al., 2014a), TOUGH-CSM (Winterfeld and Wu, 2015), TOUGH-RBSN (Kim et al., 2015a), and many more linking TOUGH to geomechanics codes, as well as various approaches linking geomechanics models to TOUGHREACT for modeling coupled thermal, hydraulic, mechanical and chemical THMC processes (e.g., Taron et al., 2009; Zhen et al., 2014; Kim et al., 2015b). In recent years additional interest and demand have been fueled by the need to stimulate reservoirs through fracturing (e.g., for enhanced geothermal systems or tight gas and shale gas formations), to understand the risk of leakage (e.g., at carbon storage sites), and to address the issue of induced seismicity, issues that have received substantial public and media attention over the last few years.

This paper provides a brief overview of the current TOUGH-based geomechanics models, including capabilities, applications and potential future developments. In general the codes and approaches differ in the assumptions about the mechanical behavior of porous and fractured geologic media, the numerical method used to perform the stress–strain calculation, the discretization scheme and how state variables and parameters calculated for potentially different meshes are mapped to each other, and the way to couple fluid flow and geomechanics. Although the TOUGH-based geomechanics approaches are developed for modeling coupled thermal-hydraulic-mechanical (THM) or, in some cases, even THMC processes, the couplings of fluid flow and geomechanics, i.e., HM couplings, are central to most applications and is a delicate numerical modeling issue. Therefore, HM coupling schemes are discussed in the next section. This is followed by descrip-

tions of TOUGH-FLAC, TOUGH-ROCMECH, TOUGH-RDCA, TOUGH-CSM, and TOUGH-RBSN, which are complementary approaches and have been more frequently applied to a diverse range of problems associated with geomechanics and its coupling to hydraulic, thermal and chemical processes.

HM COUPLING SCHEMES

Figure 1 shows a schematic of the couplings between hydraulic and mechanical processes in a deformable porous media such as soil and rock (Rutqvist and Stephansson, 2003). The arrows indicate the couplings, which can be divided into two categories: direct (solid line arrows) and indirect (dashed line arrows). Direct couplings are associated with pore-volume changes and their instantaneous and direct effect on fluid mass balance and effective stress, whereas indirect couplings are occurring indirectly through changes in mechanical and hydraulic properties.

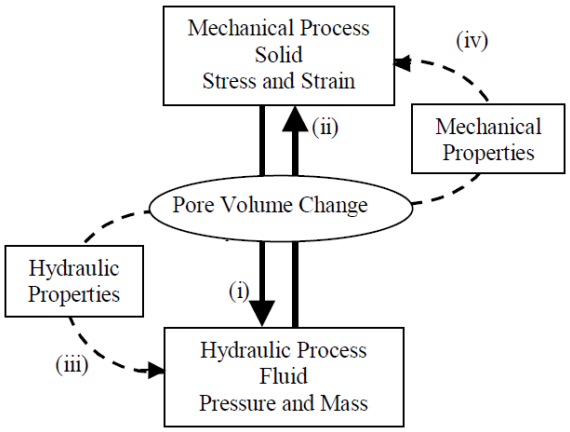

Figure 1. Hydromechanical couplings in geological media; (i) and (ii) are direct couplings through pore volume interactions, while (iii) and (iv) are indirect couplings through changes in material properties (Rutqvist and Stephansson, 2003).

Depending on the type of problem being solved and the porous medium properties, the importance of different HM couplings varies. In relatively permeable fractured hard rock, the indirect coupling in the form of permeability changes with stress might be most important. In relatively impermeable, soft and porous clay, on the other hand, direct pore-volume coupling may be most important. For example, when a porous deformable media is suddenly loaded mechanically, the pores will deform and squeeze the pore fluid to a higher pore pressure that will impact the fluid mass balance in the hydraulic part. This increase in pore-fluid pressure would in turn have an instantaneous effect on effective stress and volumetric strain in the mechanical part. These are instantaneous two-way couplings between hydraulic and mechanical processes that can be challenging to resolve numerically.

A number of numerical schemes have been employed for the analysis of coupled fluid flow and geomechanics (Mincoff et al., 2003; Kim, 2010). These include so-called fully coupled (monolithic) methods and sequentially coupled methods. In monolithic solutions, all the equations for fluid flow and mechanics including coupling terms are assembled into a large matrix system and solved simultaneously. Most of the coupled fluid flow and geomechanics finite element codes developed in rock and soil mechanics since the 1980s have employed fully coupled numerical schemes (e.g., Noorishad et al., 1982). The fully coupled method usually provides unconditional and convergent numerical solutions for mathematically well-posed problems (Kim, 2010).

When linking two different codes for fluid flow and geomechanics, it is generally not possible to use the monolithic solution scheme. Consequently, in most TOUGH-based geomechanics models to date, including TOUGH-FLAC, the equations for fluid flow and geomechanics are solved sequentially. Sequential coupling methods might be prone to numerical instability and inaccuracy when solving problems involving strong direct pore-volume coupling. However, as shown by Kim (2010), by choosing an appropriate coupling scheme with so-called stress fixed iterations in the sequential scheme, the sequential solution becomes unconditionally stable. In a stress fixed sequential solution, flow is solved first, fixing the total stress field, and then geomechanics is solved from the variables obtained at the previous flow step. The stress fixed sequential scheme is achieved in the computation by calculating an appropriate porosity correction term while keeping the pore-

compressibility non-zero and active in the reservoir simulator.

The sequential coupling method is used in all TOUGH-based geomechanics approaches except in one-way coupled approaches and in TOUGH-CSM in which a monolithic solution is employed (Winterfeld and Wu, 2015). In their approach a simplified mean stress geomechanics approach is used and the fluid flow and geomechanics is solved simultaneously, adding just one primary variable to the system.

For strong pore-volume coupling, the various TOUGH-based codes, including TOUGH-FLAC, TOUGH+ROCMECH and TOUGH-CSM, have been verified against analytical solutions involving poro-elasticity such as one-dimensional consolidation (Terzaghi) and the 2D Mandel-Cryer effects showing good agreement for both the fully coupled scheme in TOUGH-CSM (Winterfield and Wu, 2015) and sequentially coupled schemes in TOUGH+FLAC (e.g., Kim et al., 2012) and TOUGH+ROCMECH (e.g., Kim and Moridis, 2013). This shows that both monolithic and sequential coupling schemes can be used to solve problems involving strong pore-volume coupling, though there may be some limitations in the length of time steps that can be taken.

In the development of coupled HM numerical models, a lot of effort is usually dedicated to verification of algorithms related to pore-volume coupling, partly because there are poro-elastic analytical solutions for such problems. However, in much of the multiphase flow applications encountered, direct two-way pore-volume couplings may not be important, or can be ignored by choosing an appropriate pore-compressibility in the flow simulator. More common is that indirect couplings by property changes dominate. Moreover, in many cases one-way coupling is sufficient, for example hydraulic-to-mechanical coupling considering how fluid pressure gives rise to mechanical deformation and failure.

TOUGH-FLAC

The TOUGH-FLAC simulator was originally developed in the late 1990s as part of the Yucca Mountain nuclear waste disposal project (Rutqvist et al., 2002; Rutqvist and Tsang, 2003a). At that time TOUGH2 was the main code used for the analysis of unsaturated zone flow and transport of the Yucca Mountain site, but there was a need to analyze how flow and transport was affected by geomechanical processes (Rutqvist and Tsang, 2003b). The idea was then to link TOUGH2 to a geomechanics code; the FLAC3D code was selected, because it had the required geomechanics capabilities, was a continuum code compatible with the TOUGH2 continuum approach, and was already qualified and applied in the Yucca Mountain Project (Rutqvist and Tsang, 2012).

While FLAC3D (Itasca, 2012) is a commercial code and the source code is not distributed, it contains a script programming capability called FISH, which makes it possible to reach and modify internal variables and thereby enabled the linking with the TOUGH2 code. FLAC3D also has the capability of implementing user defined constitutive models through C++ programing added in a dynamic link library file. Thus, despite not having access to the source code, FLAC3D provides sufficient flexibility for research applications and specialized developments to a wide range of applications. In addition, FLAC3D contains a large number of constitutive models, including elasto-plastic and visco-elastic (creep) models for solids as well as the possibility of including some discontinuities as interfaces between solid elements.

As described in the previous section, TOUGH-FLAC uses sequential coupling between TOUGH2 and FLAC3D, whereby fluid flow variables, such as pore pressure, temperature, and saturation calculated by TOUGH2, are transferred to a compatible numerical grid for FLAC3D, which then calculates effective stresses and associated deformations, returning updated values for porosity, permeability, and capillary strength parameter to the flow simulator (Rutqvist et al., 2002). Over the past 15 years the TOUGH-FLAC simulator has been extensively applied

to analyze a wide range of problems, including CO_2 sequestration (e.g., Rutqvist and Tsang, 2002), nuclear waste disposal (e.g., Rutqvist and Tsang, 2003b), geothermal systems (e.g., Rutqvist et al., 2015), underground compressed air energy storage (e.g., Rutqvist et al., 2012a), and gas production from hydrate bearing formations (e.g., Rutqvist and Moridis, 2012b). Over these 15 years, about 60 peer reviewed journal paper on TOUGH-FLAC and its application have been published, with those appearing until 2011 listed in a 2011 TOUGH-FLAC status paper (Rutqvist, 2011).

Since the 2012 TOUGH Symposium, significant advancements have been made, extending the simulations to more complex geomechanical processes, especially related to modeling injection-induced fault activation and induced seismicity (e.g., Rutqvist et al., 2014a; Rinaldi et al., 2015), advanced constitutive models for expansive clay in nuclear waste isolation (Rutqvist et al., 2014b; Vilarassa et al., 2015), and modeling of salt geomechanical processes coupled with temperature and multiphase flow (Blanco Martin et al., 2015). Fault activation and induced seismicity have been modeled in 3D using strain-softening (slip-weakening) fault friction models that enable modeling of sudden seismic slip (Rinaldi et al., 2015). This includes recent 3D modeling of injection-induced fault activations associated with both underground CO_2 injection and during stimulation of shale-gas reservoirs (Rutqvist et al., 2015b; Rinaldi et al., 2015). In some cases this has involved fully dynamic calculations of the fault activation and resulting ground surface motion (Rutqvist et al., 2014a). Implementation of more advanced fault frictional laws is underway; Urpi et al. (2015) present a first step in the implementation of a rate-and-state fault friction law into the TOUGH-FLAC framework.

The recent extension of the TOUGH-FLAC simulator for modeling THM processes associated with nuclear waste disposal in salt has been accomplished through collaboration between LBNL and Clausthal Technical University, Germany (Blanco Martin et al., 2015b). This includes the development, implementation and application of an advanced constitutive model from Clausthal Technical University (the Lux/Wolters constitutive model) for THM induced damage, healing and sealing of salt host rocks and compaction of crushed salt. Moreover, this involves modeling of large strain along with the compaction of the crushed salt backfill from a porosity of about 30% to less than 1% (Blanco Martin et al., 2015a, b). Clausthal Technical University uses a different coupling scheme in which FLAC3D is the main code driving the simulation forward, and denotes this simulator FLAC-TOUGH rather than TOUGH-FLAC (Blanco Martin et al., 2015b).

Related to THM in clay, the implementation of the Barcelona Basic Model for mechanical behavior of unsaturated soils (Rutqvist et al., 2014b), and the Barcelona Expansive Model (Vilarassa et al., 2015) for mechanical behavior of expansive soils are important additions for rigorous modeling of bentonite based backfill material. Moreover, the consideration of two structural levels, i.e., macro- and micro-structures in the expansive model, provides a link between mechanics and chemistry for more mechanistic modeling of THMC behavior. Two recent papers by Zheng et al. (2014; 2015) describe different types of chemical-mechanical coupling behavior in bentonite, i.e., effects of chemistry on the mechanical evolution of the bentonite material. In this case TOUGHREACT is linked to FLAC3D to model CM couplings, such as salinity effects on swelling pressure. Such chemical-mechanical coupling effects might be especially important when considering higher temperature disposal systems (Zheng et al., 2015).

FLAC3D is a well-established code with a large user base. It makes available many geomechanical constitutive models and has the flexibility to extend and implement new constitutive models, which is one of the most appealing features for selecting FLAC3D as the geomechanics code to be linked to TOUGH. One drawback with the current TOUGH-FLAC simulator is that it runs exclusively on Windows (because FLAC3D only runs on Windows), which prevents us from applying the approach

on existing large-scale Unix clusters. However, there are plans to port FLAC3D to Linux and to develop an mpi version in the near future (personal communication with Itasca, June 2015).

TOUGH-ROCMECH

TOUGH-ROCMECH is developed as an alternative to TOUGH-FLAC, in which the source code of the geomechanics part is available and therefore enabling a more efficient linking between multiphase flow and geomechanics, and the possibility of porting the simulator for computer clusters and massive parallel processing (Kim and Moridis, 2013). ROCMECH is an LBNL in-house developed finite element code that was tailored first for linking with TOUGH+ (Kim and Moridis, 2013) and later with TOUGHREACT (Kim et al., 2015) and iTOUGH2 (Finsterle, 2015). The codes are sequentially coupled, including the fixed stress split algorithms implemented and verified by Kim and Moridis (2013).

The current basic ROCMECH version has the capability of modeling mechanical failure within solid elements through elasto-plastic Drucker-Prager or Mohr-Coulomb models. This has recently been extended to consider failure on multiple shear planes representing fracture sets of different orientation and applied for the analysis of shear stimulation related to an enhanced geothermal project at the Newberry Volcano, Oregon (Smith et al., 2015). A new multiporosity approach was also developed and implemented by Kim et al. (2012). This version of TOUGHREACT-ROCMECH has also been applied for modeling THMC processes for flow along fractures, considering mechanical and chemical (precipitation) effects on porosity and permeability (Kim et al., 2015). These are processes important for the long-term sustainability of enhanced geothermal systems, but are also important related to sealing of fractures associated with CO_2 sequestration and nuclear waste disposal.

In a version of TOUGH+ROCMECH, capabilities for modeling 3D fracture propagation along a vertical pre-defined plane have been implemented. The model was applied for the analysis of hydraulic fracture propagation associated with stimulation of shale-gas reservoirs (Kim and Moridis, 2013; 2015). The approach is similar to that of Ji et al. (2009), in which the fracture propagates along the boundary of the model domain through a nodal-splitting algorithm.

In the case of modeling hydraulic fracturing in tight shale, the TOUGH+RealGasH2O with ROCMECH has been applied (Kim and Moridis, 2013; 2015). The vertical fracturing is modeled by adding traction boundary conditions at locations where nodes have been split. Moreover, once a fracture has been created adjacent to the solid element, the initial single continuum element in TOUGH is changed to multiple continuum for considering the local leak-off from the fracture to the surrounding porous rock.

Fracturing conditions for node-splitting are based on tensile strength rather than toughness. A fracturing criterion considering the effects of both effective stress normal to the fracture and shear stress enables a mix-mode fracturing criterion. Using this model, Kim and Moridis (2015) were able to model multiphase flow driven hydraulic fracturing and found significant effects of complex two-phase flow processes, including vertical gravity segregation that are processes important for estimating the fracture volume and leak-off to the surrounding rock.

TOUGH-RDCA

Pan et al. (2014a) coupled TOUGH2 to RDCA (rock discontinuous cellular automaton), a code capable of simulating nonlinear and discontinuous deformation behavior, such as plastic yielding and the initiation, propagation and coalescence of cracks induced by changes of fluid pressure and temperature.

RDCA uses a special displacement function to represent internal discontinuities (Pan et al., 2014b). A level-set method tracks the

fracturing path, and a partition of unity method is used to improve the integral precision of fracture surface and fracture tip calculations. The mechanical state is evaluated by a cellular automaton updating rule. In this approach, the discontinuity of a crack is incorporated independently of the mesh, such that the crack can be arbitrarily located within an element, i.e., the method does not require any re-meshing for crack growth, which greatly simplifies the modeling procedure and its sequential integration with TOUGH2 through external coupling modules.

In TOUGH-RDCA, the fracturing condition can be evaluated either by linear elastic fracture mechanics using fracture toughness or by a modified Mohr-Coulomb criterion. The toughness-based criterion includes mixed Mode I (extension) and Mode II (shear) fracture propagation, whereas the Mohr–Coulomb criterion is modified with a tension cut-off, enabling modeling of both shear and tensile failure.

TOUGH-RDCA has been verified against analytical solutions and against TOUGH-FLAC for poro-elastic behavior and injection-induced ground surface uplift (Pan et al., 2013). A number of simulation applications have been presented related to fluid driven fracture propagation and CO_2 leakage through fractures. This includes multiple fracture propagation with intersections to pre-existing fractures (Pan et al., 2014c). The code is currently limited to modeling fracture propagation in 2D, whereas a 3D RDCA code is under development.

TOUGH-CSM

TOUGH-CSM is being developed at the Colorado School of Mines (CSM), with the ultimate goal of an efficient code tailored for massive parallel processing simulations (Winterfeld and Wu, 2012; 2015). The geomechanics part is accomplished by adding a mean stress equation for thermo-poroelastic multi-porosity media to the standard set of governing multiphase flow equations of TOUGH2-MP. In this formulation, the mean total stress is included as an additional primary variable, and the coupled thermal–hydrological–mechanical system is solved fully implicitly, obtaining volumetric strain and associated changes in porosity and permeability. Geochemical reactions based on the TOUGHREACT code have also been included in this formulation (Zhang et al., 2012; Winterfeld and Wu, 2012).

A few applications of TOUGH-CSM related CO_2 sequestration in deep sedimentary formations and geothermal systems have been published (Hu et al., 2013; Wu and Winterfeld, 2014). In the case of CO_2 sequestration, the effect of fracturing through the caprock overlying a reservoir was studied in Huang et al. (2015). Since only the mean stress was solved in the fully coupled simulation, some other relationships and assumptions were used to estimate the horizontal stress needed for evaluating the possibility of vertical fracturing through the caprock. The application example related to geothermal included simulation of ground subsidence at the Geyser geothermal field with comparison to the previous results obtained with TOUGH-FLAC (Hu et al., 2015).

As concluded in Hu et al. (2015), calculations limited to mean total stress as opposed to the total stress tensor is a simplification that may be a shortcoming since it cannot analyze phenomena dependent on shear stress, such as rock failure. However, currently a new algorithm is being developed and tested in which the stress tensor, including all normal and shear stress components, are solved in a sequential manner (Winterfeld and Wu, 2015). This approach of calculating the stress components was verified against analytical solutions showing the potential of this approach and for efficient coupled geomechanical simulations with TOUGH.

TOUGH-RBSN

TOUGH-RBSN is being developed at LBNL with the main goal of modeling mass transport through permeable media under dynamically changing hydrologic and mechanical conditions in 3D heterogeneous geological media (Asahina et al., 2014; Kim et al., 2015). A strong motivator is the potential of modeling discrete fracture propagation through heterogeneous geological

media in 3D (Kim et al., 2015). The simulation tool combines TOUGH2 with the rigid-body-spring network (RBSN) model, which enables a discrete (lattice) representation of elasticity, individual fractures and fracture networks in rock.

One advantage of linking TOUGH2 and RBSN resides in their common utilization of a set of nodal points and properties of the corresponding Voronoi tessellation (e.g., natural neighbor and volume rendering definitions). Shared use of the Voronoi tessellation facilitates every stage of the analyses, including model construction and results interpretation. In such a system, the discrete fractures are directly mapped onto unstructured Voronoi grids via an automated geometric scheme (Asahina et al., 2011). A fracture is represented by the controlled breakage of the springs (1D lattice elements) linking adjacent Voronoi cells along the fracture trajectory. Fractures can propagate along Voronoi cell boundaries as THM-induced stresses evolve and exceed prescribed material strength values. The fracturing process is represented by the damage/breakage of the springs. A Mohr-Coulomb criterion with tension cut-off is used to judge when a lattice element undergoes a fracturing event.

The RBSN code has been extensively used and validated for fracturing in concrete materials, including heterogeneities such as large grain inclusions, whereas the linked TOUGH-RBSN code has been verified against analytical solutions and other numerical tools for various features, including poro-elasticity, swelling, and fracture deformation (Asahina et al., 2014; Kim et al., 2015). Applications include validation against experimental results on desiccation cracking in a fine-grained sediment (mining waste), and most recently modeling of fracture propagation through a heterogeneous laboratory sample that includes pre-existing weaknesses (Kim et al., 2015).

Currently a new dynamic simulation framework for RBNS is being developed. In the new methodology, nodal kinematic information (displacements, velocities, and accelerations) is calculated through the explicit time integration scheme, by which the code implementation with parallelization can be easily realized. The parallelization will be a requirement for being able to solve large-scale problems in 3D with this approach.

OTHER TOUGH-GEOMECHANICS CODES AND APPROACHES

In addition to the above developments, a number of TOUGH-based geomechanics models and approaches have been developed, though some of them have not been as extensively applied.

Some of the earlier work includes Gosavi and Swenson (2005) who linked TOUGH2 to the finite element code GeoCrack3D for a more tightly coupled code, and later applied it to geothermal energy applications. Javeri (2007) linked TOUGH2 and FLAC3D in a similar manner to Rutqvist et al. (2002) and applied it to study geomechanical effects of gas generation and pressure buildup in a nuclear waste repository. Hurwitz et al. (2007) linked TOUGH2 to the USGS coupled hydro-mechanical finite element code Biot2, named the simulator TOUGH2-Biot and applied it to study hydrothermal fluid flow and deformation in large calderas. Recently another simulator named TOUGH2Biot was presented (Lei et al., 2015), which is linking TOUGH2 to an in-house finite element code and verified against previous TOUGH-FLAC simulations of the Geysers geothermal system as well as applied to simulate CO_2 injection of a site in China. Note that TOUGH2biot is not the same a TOUGH2-biot mentioned above, although both involve linking TOUGH2 to a poro-elastic finite element code.

Taron et al. (2009) at Penn State University linked TOUGHREACT to FLAC3D and have since applied this approach for modeling THMC processes mostly associated with geothermal systems (Taron et al., 2009; Izada and Elsworth, 2015). Taron et al. (2009) used THMC modeling to study the evolution of permeability associated with mechanical, thermal, and chemical (precipitation and dissolution) effects. In Izada and Elsworth (2014; 2015), the FLAC domain was populated with an implicit fracture network for the analysis of injection-induced micro-seismicity during hydraulic stimulation.

Other efforts includes Rohmer and Seyedi (2010) who linked TOUGH2 to the French open source finite element code Code_Aster and simulated deep underground CO_2 injection. Loschetter et al. (2012) used the TOUGH2-Code_Aster combination to model enhanced coalbed methane production. Aoyagi et al. (2013) linked TOUGH2 to FrontISRM, an open source finite element code in Japan, based on TOUGH-FLAC links, and demonstrated it by modeling a generic CO_2 injection simulation.

Some of the most recent efforts include Lee at al. (2015) who linked TOUGH2 to UDEC, which is a distinct element code, enabling modeling the geomechanical behavior of fracture networks in 2D. Miah et al. (2015) present on-going work on linking TOUGH2 with PyLith, which is a USGS-developed finite-element code primarily used for large-scale geomechanical crustal deformation and earthquake simulation (static, quasi-static and dynamic modes). PyLith has advanced fault frictional models that will be applied and benchmarked against TOUGH-FLAC implementations of rate-and-state frictional models.

Finally, simpler TOUGH-based geomechanics approaches have been developed for specialized applications, including Walsh et al. (2012) who added the effects of an external, vertical stress change to the porosity update that is performed at the end of each time step. This approach was recently applied to model effects of glaciation in the safety assessment of a hypothetical nuclear waste repository (Calder et al., 2015). Another example is TOUGH2-SEED, a coupled fluid flow and mechanical statistical model for the study of injection-induced seismicity (Nespolia et al., 2015). With TOUGH2-SEED, the authors were able to model several mechanisms influencing each other during and after the injection phase.

CONCLUDING REMARKS

After the first development of the TOUGH-FLAC simulator 15 years ago, at least 15 additional TOUGH-based geomechanics codes and approaches have appeared in the literature. Seven of those involved linking TOUGH2 to an in-house developed or open source finite element code, using sequential coupling techniques as in TOUGH-FLAC, but with access to the source code for the geomechanics part. One of the main motivations related to those developments is the access to the source code and the potential of more efficient coupling as well as the possibility of running the codes together on computer clusters. Among the codes linking TOUGH to an in-house or open source finite element code, TOUGH-ROCMECH is the one that has been applied most extensively to date. Most of these finite element codes are limited to simple poro-elasticity, although ROCMECH includes some elasto-plasticity with Drucker-Prager and Mohr-Coulomb constitutive models. To extend such geomechanics codes to more sophisticated constitutive models that are currently available in FLAC3D would require a substantial effort, but is feasible. TOUGH-CSM includes an unorthodox mechanical approach that with the current addition for calculation of the full stress tensor can be an efficient and useful approach for modeling large systems.

TOUGH-FLAC still remains the most applied TOUGH-based geomechanics model. It is the combination of the TOUGH2 library of fluid equations-of-states (EOS) and the FLAC3D library of geomechanical constitutive models that make it possible to extend TOUGH-FLAC to new areas of research and geo-engineering applications within a relatively short time. The fact that FLAC3D only runs on Windows has been viewed as a bottleneck leading to long simulation times. However, the computation time is only one part of the effort. Extension into a new research area or other types of geological media usually involves development and implementation of new constitutive models, to build the mesh and populate the model with material properties, boundary conditions, to run the models, to interpret the results and to publish it in scientific journals. FLAC3D has the user interface and flexible meshing and post-processing capabilities that can be used to construct models for both FLAC3D and TOUGH in an efficient way. A LINUX and mpi version of FLAC3D is planned to be developed in the next few years (personal communication with Itasca, June, 2015).

Currently there is a need for effective model simulations of fracturing and fracture propagation in heterogeneous geological media. The ability to model discrete fracture propagation in 2D has been demonstrated for TOUGH-RDCA; the fractures can propagate through the mesh without the need for remeshing. A 3D version of RDCA is under development, but this will require substantial effort and 3D fracture propagation through a 3D heterogeneous rock mass will be challenging. Discrete fracture propagation has also been demonstrated for TOUGH-ROCMECH, in 3D, but limited to a pre-defined path, such as vertical fracture along the boundary of the model domain. Other approaches, such as TOUGH-UDEC and TOUGH-PyLith, could be useful additions for modeling complex hydraulic stimulations and induced seismicity. TOUGH-RBSN has the potential for modeling complex fracturing processes in 3D in heterogeneous geological media, though more developments are required before it can be applied for large-scale systems.

ACKNOWLEDGMENTS

This paper was completed with funding from the Assistant Secretary for Fossil Energy, Office of Natural Gas and Petroleum Technology, through the National Energy Technology Laboratory, and the Used Fuel Disposition Campaign, Office of Nuclear Energy, and the Assistant Secretary for Energy Efficiency and Renewable Energy, Geothermal Technologies Program, of the U.S. Department of Energy under Contract No. DE-AC02-05CH11231 with Lawrence Berkeley National Laboratory. The author thanks Stefan Finsterle, Chris Doughty and Carol Valladao at the Lawrence Berkeley National Laboratory for their review of the initial manuscript.

REFERENCES

Aoyagi A., R. Imai, J. Rutqvist, H. Kobayashi, O. Kitamura and G. Nobuhisa, Development of TOUGH-FrontISTR, a numerical simulator for environmental impact assessment of CO2 geological storage, *Energy Proceedia*, 37, 3655–3662, 2013.

Asahina, D. and J.E. Bolander, Voronoi-based discretizations for fracture analysis of particulate materials, *Powder Technology*, 213, 92–99, 2011.

Asahina, D., J.E. Houseworth, J.T. Birkholzer, J. Rutqvist and J.E. Bolander, Hydro-mechanical model for wetting/drying and fracture development in geomaterials, *Computers & Geosciences*, 65, 13–23, 2014.

Blanco Martín L., J. Rutqvist and J.T. Birkholzer, Long-term modelling of the thermal-hydraulic-mechanical response of a generic salt repository for heat-generating nuclear waste, *Engineering Geology*, 193, 198–211, 2015.

Blanco Martín L., R. Wolters, J. Rutqvist, K.-H. Lux and J.T. Birkholzer, Comparison of two simulators to investigate thermal-hydraulic-mechanical processes related to nuclear waste isolation in saliniferous formations. *Computers & Geotechnics*, 66, 219–229, 2015.

Calder N., J. Avis, E. Kremer and R. Walsh, Application of 1D hydromechanical coupling in TOUGH2 to a deep geological repository glaciation scenario. *Proceedings of the TOUGH Symposium 2015*, Lawrence Berkeley National Laboratory, Berkeley, California, 2015.

Finsterle, S., What's new in iTOUGH2?. *Proceedings of the TOUGH Symposium 2015*, Lawrence Berkeley National Laboratory, Berkeley, California, 2015.

Gosavi S. and D. Swenson, 2005, Architecture for a coupled code for multiphase fluid flow, heat transfer and deformation in porous rock, *Proceedings of the Thirtieth Workshop on Geothermal Reservoir Engineering* Stanford University, Stanford, California, January 31-February 2, 2005.

Hu L., P.H. Winterfeld, P. Fakcharoenphol and Y.-S. Wu, A novel fully-coupled flow and geomechanics model in enhanced geothermal reservoirs, *Journal of Petroleum Science and Engineering*, 107, 1–11, 2013.

Huang Z.-Q., P.H. Winterfeld, Y. Xiong, Y.-S. Wu and J. Yao, Parallel simulation of fully-coupled thermal-hydro-mechanical processes in CO2 leakage through fl uid-driven fracture zones. *International Journal of Greenhouse Gas Control*, 34, 39–51, 2015.

Hurwitz S., L.B. Christiansen and P.A. Hsieh, Hydrothermal fluid flow and deformation in large calderas: inferences from numerical simulations, *Journal of Geophysical Research* 112, BO2206, 2007.

Itasca, *FLAC3D V5.0, Fast Lagrangian Analysis of Continua in 3 Dimensions, User's Guide.* Itasca Consulting Group, Minneapolis, Minnesota, 2012.

Izadia G. and D. Elsworth, Reservoir stimulation and induced seismicity: Roles of fluid pressure and thermal transients on reactivated fractured networks, *Geothermics*, 51, 368–379, 2014.

Izadia G. and D. Elsworth, The influence of thermal-hydraulic-mechanical- and chemical effects on the evolution of permeability, seismicity and heat production in geothermal reservoirs, *Geothermics*, 53, 385–395, 2015.

Javeri V., Three dimensional analysis of combined gas, heat and nuclide transport in a repository in clay rock including coupled thermo-hydro-geomechanical processes, *Physics and Chemistry of the Earth*, 33, S252–S259, 2007.

Ji L, A. Settari and R.B. Sullivan, A novel hydraulic fracturing model fully coupled with geomechanics and reservoir simulation, *SPE Journal*, 14, 423–430, 2009.

Kim J., *Sequential methods for coupled geomechanics and multiphase flow*. Ph.D. Thesis, Department of Energy Resources Engineering, Stanford University, California, 264 pp, 2010.

Kim J. and G.J. Moridis, Development of the T+M coupled flow–geomechanical simulator to describe fracture propagation and coupled flow–thermal–geomechanical processes in tight/shale gas systems, *Computers &* Geosciences, 60, 184–198, 2013.

Kim J. and G.J. Moridis, Numerical analysis of fracture propagation during hydraulic fracturing operations in shale gas systems, - *International Journal of Rock Mechanics & Mining Sciences*, 76, 127–137, 2015.

Kim J., G.J. Moridis, D. Yang and J. Rutqvist, Numerical studies on two-way coupled fluid flow and geomechanics in hydrate deposits, Society of Petroleum Engineers, SPE-141304-PA, *SPE Journal*, 17, 485–501, 2012.

Kim J., E. Sonnenthal and J. Rutqvist, A modeling and sequential numerical algorithms of coupled fluid/heat flow and geomechanics for multiple porosity materials, *International Journal of Numerical Methods in Engineering*, 92, 425–456, 2012.

Kim K., J. Rutqvist, S. Nakagawa, J. Houseworth and J. Birkholzer, Simulation of fluid-driven fracturing within discrete fracturing within discrete fracture networks using TOUGH-RBSN. *Proceedings of the TOUGH Symposium 2015*, Lawrence Berkeley National Laboratory, Berkeley, California, 2015a.

Kim J., E. Sonnenthal and J. Rutqvist, A sequential implicit algorithm if chemo-thermo-poro-mechanics for fractured geothermal reservoir. *Computers & Geosciences*, 76, 59–71 2015b.

Lee J., K.-B. Min and J. Rutqvist, TOUGH-UDEC simulator for the coupled multiphase fluid flow, heat transfer, deformation in fracture porous media. *Proceedings of 13th Congress of the ISRM*, Montreal, Quebec, Canada, May 10 - 13, 2015.

Lei H., T.F. Xu, and G. Jin. TOUGH2Biot – A simulator for coupled thermal–hydrodynamic–mechanical processes in subsurface flow systems: Application to CO2 geological storage and geothermal development, *Computers & Geosciences*, 77, 8–19, 2015.

Loschetter A., F. Smai, S. Sy, A. Burnol, A. Leynet, S. Lafortune and A. Thoraval, simulation of CO2 storage in coal seams: coupling of TOUGH2 with the solver for mechanics Code_Aster, *Proceedings of the TOUGH Symposium 2012*, Lawrence Berkeley National Laboratory, Berkeley, California, 2012.

Miah M., L. Blanco Martín, W. Foxall, J. Rutqvist, A.P. Rinaldi and C. Mullen, Development of a hydro-geomechanical model to simulate coupled fluid flow and reservoir geomechanics, *Proceedings of the TOUGH Symposium 2015*, Lawrence

Berkeley National Laboratory, Berkeley, California, 2015.

Minkoff S.E., C.M. Stone, S. Bryant, M. Peszynska and M.F. Wheeler, Coupled fluid flow and geomechanical deformation modeling, *Journal of Petroleum Sciences and Engineering*, 38, 37–56, 2003.

Nespolia M., A.P. Rinaldi, and S. Wiemer, TOUGH2-SEED: A coupled fluid flow and mechanical statistical model for the study of injection-induced seismicity. *Proceedings of the TOUGH Symposium 2015*, Lawrence Berkeley National Laboratory, Berkeley, California, 2015.

Noorishad J, M.S. Ayatollahi, and P.A. Witherspoon, A finite element method for coupled stress and fluid flow analysis of fractured rocks. *International Journal of Rock Mechanics and Mining Sciences*, 19, 185–193, 1982.

Pan P.-Z., J. Rutqvist, X.-T. Feng and F. Yan, Modeling of caprock discontinuous fracturing during CO2 injection into a deep brine aquifer, *International Journal of Greenhouse Gas Control*, 19, 559–575, 2013.

Pan P.-Z., J. Rutqvist, X.-T. Feng and F. Yan, An approach for modeling rock discontinuous mechanical behavior under multiphase fluid flow conditions. *Rock Mechanics and Rock Engineering*, 47, 589–603, 2014a.

Pan P.-Z., J. Rutqvist, X.-T. Feng, F. Yan and Q. Jiang. A discontinuous cellular automaton method for modeling rock fracture propagation and coalescence under fluid pressurization without remeshing, *Rock Mechanics and Rock Engineering*, 47, 2183–2198, 2014b.

Pan, P.-Z., J. Rutqvist, X.-T. Feng and F. Yan TOUGH–RDCA modeling of multiple fracture interactions in caprock during CO2 injection into a deep brine aquifer. *Computers & Geosciences*, 65, 24–36, 2014c.

Rinaldi A.P., V. Vilarrasa, J. Rutqvist and F. Cappa, Fault reactivation during CO2 sequestration: Effects of well orientation on seismicity and leakage. *Greenhouse Gas Sciences and Technology*, 5, 1–12, 2015.

Rohmer J., and D.M. Seyedi, Coupled large scale hydromechanical modelling for caprock failure risk assessment of CO2 storage in deep saline aquifers. *Oil & Gas Sci and Technol – Rev IFP*, 65, 503–517, 2010.

Rutqvist J. Status of the TOUGH-FLAC simulator and recent applications related to coupled fluid flow and crustal deformations. *Computers & Geosciences*, 37, 739–750, 2011.

Rutqvist J. and O. Stephansson, The role of hydromechanical coupling in fractured rock engineering. *Hydrogeology Journal*, 11, 7–40, 2003.

Rutqvist J. and C.-F. Tsang, TOUGH-FLAC: A numerical simulator for analysis of coupled thermal-hydrologic-mechanical processes in fractured and porous geological media under multi-phase flow conditions. *Proceedings of the TOUGH symposium 2003*, Lawrence Berkeley National Laboratory, Berkeley, May 12–14, 2003a.

Rutqvist J. and C.-F. Tsang, Multiphysics processes in partially saturated fractured rock: Experiments and models from Yucca Mountain, *Reviews of Geophysics*, 50, RG3006, 2012.

Rutqvist, J., and C.-F.Tsang, Analysis of thermal-hydrologic-mechanical behavior near an emplacement drift at Yucca Mountain. *Journal of Contaminant Hydrology*, 62–63, 637–652, 2003b.

Rutqvist J. and C.-F. Tsang. A study of caprock hydromechanical changes associated with CO2 injection into a brine aquifer. *Environmental Geology*, 42, 296–305, 2002.

Rutqvist J., Y.-S. Wu, C.-F. Tsang and G. Bodvarsson, A Modeling Approach for Analysis of Coupled Multiphase Fluid Flow, Heat Transfer, and Deformation in Fractured Porous Rock *International Journal Rock Mechanics & Mining Sciences*, 39, 429–442, 2002.

Rutqvist J., H.-M. Kim, D.-W. Ryu, J.-H., Synn, and W.-K. Song, Modeling of coupled thermodynamic and geomechanical performance of underground compressed air energy storage in lined rock caverns, *International Journal of Rock Mechanics & Mining Sciences*, 52, 71–81, 2012a.

Rutqvist J., G.J. Moridis, T. Grover, S. Silpngarmlert, T.S. Collett and S.A. Holdich, Coupled multiphase fluid flow and wellbore stability analysis associated with gas production from oceanic hydrate-bearing sediments. *Journal of Petroleum Science and Engineering*, 92–93, 65–81, 2012b.

Rutqvist J., F. Cappa, A.P. Rinaldi and M. Godano, Modeling of induced seismicity and ground vibrations associated with geologic CO2 storage, and assessing their effects on surface structures and human perception, *International Journal of Greenhouse Gas Control*, 24, 64–77, 2014a.

Rutqvist J., L. Zheng, F, Chen, H.-H Liu and J. Birkholzer, Modeling of Coupled Thermo-Hydro-Mechanical Processes with Links to Geochemistry Associated with Bentonite-Backfilled Repository Tunnels in Clay Formations. *Rock Mechanics and Rock Engineering*, 47, 167–186, 2014b.

Rutqvist J., P.F. Dobson, J. Garcia, C. Hartline, P. Jeanne, C.M. Oldenburg, D.W. Vasco and M. Walters. The northwest Geysers EGS demonstration project, California: Pre-stimulation modeling and interpretation of the stimulation. *Mathematical Geosciences*, 47, 3-26, 2015a.

Rutqvist J., A.P. Rinaldi, F. Cappa and G.J. Moridis, Modeling of fault activation and seismicity by injection directly into a fault zone associated with hydraulic fracturing of shale-gas reservoirs, *Journal of Petroleum Science and Engineering*, 127, 377–386, 2015b.

Smith T., E. Sonnenthal and T. Cladouhos, Thermal-hydrological-mechanical modelling of shear stimulation at Newberry Volcano, Oregon. *Proceedings of the 49th US Rock Mechanics/Geomechanics Symposium*, San Francisco, CA, USA, 28 June- 1 July 2015. American Rock Mechanics Association ARMA, Paper No. 15-680, 2015.

Taron, J., D. Elsworth and K.B. Min, Numerical simulation of thermal–hydrologic–mechanical–chemical processes in deformable, fractured porous media, *International Journal of Rock Mechanics Mining Sciences*, 46, 842–854, 2009.

Urpi L., A.P. Rinaldi and B. Wassing. Modelling fault reactivation and velocity dependent friction with TOUGH-FLAC. *Proceedings of the TOUGH Symposium 2015*, Lawrence Berkeley National Laboratory, Berkeley, California. 2015.

Vilarrasa V., J. Rutqvist, L. Blanco Martin and J.T. Birkholzer. Use of a dual structure constitutive model for predicting the long-term behavior of an expansive clay buffer in a nuclear waste repository, *ASCE's International Journal of Geomechanics* (Accepted, August 2015).

Winterfeld, P.H. and Y.-S. Wu, Development of an advanced thermal-hydrological-mechanical model for CO2 storage in porous and fractured saline aquifers. *Proceedings of the TOUGH Symposium 2012*, Lawrence Berkeley National Laboratory, Berkeley, California, 2012.

Winterfeld P. H. and Y.-S. Wu, Simulation of CO2 sequestration in brine aquifers with geomechanical coupling. *In Computational Models for CO2 Sequestration and Compressed Air Energy Storage*, edited by J. Bundschuh and R. Al-Khoury, Chapter 8, CRC Press, New York, NY, 2014.

Winterfeld, P.H. and Y.-S. Wu, A coupled flow and geomechanics simulator for CO2 storage in fracture reservoirs. *Proceedings of the TOUGH Symposium 2015*, Lawrence Berkeley National Laboratory, Berkeley, California, 2015.

Zhang, R., X. Yin, P.H. Winterfeld and Y.-S. Wu, A fully coupled model of nonisothermal

multiphase flow, geomechanics, and chemistry during CO2 sequestration in brine aquifers. *Proceedings of the TOUGH Symposium 2012*. Lawrence Berkeley National Laboratory, 2012.

Zheng L., J. Rutqvist, H.-H. Liu, J.T. Birkholzer and E. Sonnenthal, Model evaluation of geochemically induced swelling/shrinkage in argillaceous formations for nuclear waste disposal, *Applied Clay Science*, 97–98, 24–32, 2014.

Zheng L., J. Rutqvist, J.T. Birkholzer, and H.H. Liu. On the impact of temperatures up to 200ºC in clay repositories with bentonite

engineer barrier systems: a study with coupled thermal, hydrological, chemical, and mechanical modeling. *Engineering Geology* (Accepted August, 2015).

MODELLING FAULT REACTIVATION AND VELOCITY DEPENDENT FRICTION WITH TOUGH-FLAC

Luca Urpi[1], Antonio P. Rinaldi[2,3], Brecht Wassing[4]

[1]Utrecht University
Budapestlaan 4, 3584CD, Utrecht, The Netherlands
e-mail: l.urpi@uu.nl

[2]Swiss Seismological Service, ETH Zurich
Sonneggstrasse 5, 8092, Zurich, Switzerland
e-mail: antoniopio.rinaldi@sed.ethz.ch

[3]Lawrence Berkeley National Laboratory, Earth Sciences Division
1 Cyclotron Rd, 94720, Berkeley, CA, USA

[4]TNO Geo Energy
Princetonlaan 6, 3584CB, Utrecht, The Netherlands

ABSTRACT

Mechanical stability and sealing integrity of faults play a crucial role for a wide range of industrial activities involving fluid injection at depth, such as carbon capture and storage, geothermal reservoir exploitation, unconventional hydrocarbon resources, and waste water disposal. Stress and pressure perturbations acting on faults may change their mechanical and hydraulical behavior or even bring them to failure.

In this paper, the capabilities of TOUGH has been extended with the sequential coupling to the geomechanical finite difference FLAC solver, to evaluate stress perturbation on a sealing fault plane due to CO_2 injection in its vicinity. The novelties of the approach presented here are: (i) the representation of the fault through interface elements, (ii) the fully dynamic simulation of the rupture, and (iii) a more detailed evolution of the fault frictional properties.

The basis of the sequential coupling TOUGH-FLAC are already well established and can be summed up in such a way: pressure values calculated in TOUGH are given as input in FLAC as volumetric strain, which evaluates the new stress state for every grid element and shear and normal stress component for every interface element. Interface element obeys to a simple Mohr-Coulomb law, and the quasi-static solution is evaluated for failure: if the failure criterion is satisfied, the fault is set free to slide and the dynamic solution is calculated. The failure criteria can vary with time, to represent interaction between the fault material and the fluid injection. Spatial distribution in properties and changes in permeability due to volumetric strain, porosity change and shear strain can be included in the model.

INTRODUCTION

Fluid injection operation effects can extend well beyond the volume hosting the mass of fluid injected. Stress and pore pressure can be perturbed at distance from the injection point. Fault rupture and slip can be induced on fault.

Human-felt events associated with fluid injection have been associated with waste water disposal activities, including disposal of brine from hydraulic fracturing conventional and enhanced geothermal system, underground gas storage reservoir development: a comprehensive review of recent cases and of possible physical mechanisms (Ellsworth, 2013) points out the uncertainties in pinpointing the exact triggering process.

Carbon dioxide capture and geological storage (CCS) has not been associated up to now to induced seismicity events at CO_2 onshore and offshore storage sites (e.g. Martens et al. 2012). However, similar amount of fluid injected (10-

100 thousands of m^3) at bottom-hole pressures above in-situ condition (1-10 MPa) in proximity of a fault led to a range of different response, from human-felt event to large-scale aseismic motion. It has been argued that adopting large-scale CCS is a risky strategy, with seal integrity and social acceptance of CCS threatened by fault reactivation generating small-to moderate-sized earthquakes (Zoback and Gorelick, 2012). However, studies have shown that sedimentary basin, in which generally CO_2 injection occur, are rarely critically stressed (Vilarrasa and Carrera, 2015). Furthermore, numerical simulations have shown that compromising the sealing capacity of a storage site is generally not related to the seismicity (Rinaldi et al., 2014a). Moreover, heterogeneities along fault may also reduce both leakage and maximum event magnitude (Rinaldi et al., 2014b).

Numerical investigations have been performed at the reservoir scale, with the goal of assessing safety and integrity of CO_2 in aquifer (Rutqvist et al., 2012; Mazzoldi et al., 2012) or depleted hydrocarbon reservoir (Orlic, 2009; Orlic et al., 2011). Generally, these studies are rather conservative, assuming that if a fault is reactivated, all the excessive strain is released seismically and that the slip weakening mechanism is the dominant one in determining the frictional behavior of the sliding fault, overlooking slip-rate influence on frictional behavior.

In this study, an idealized CO_2-injection scenario is modelled with the TOUGH-FLAC hydro-mechanical coupled solver, to include injection pressure diffusion, effective stress change, and dynamic fault rupture, to overcome the limitation related to the quasi-static approach and to explore the possibilities of implementing complex frictional behavior into fault rupture simulation. Friction rate parameters can be obtained from rock sample representative of the materials that a fault may encounter. Reservoir and caprock may have different behavior with respect to friction evolution with slip rate. We will investigate the potential impact of different properties for the different formations.

Our goal is to design a worst-case scenario and to quantify the maximum slip that can be expected considering representative velocity-weakening and velocity-strengthening behavior; therefore we analyzed the influence of velocity-weakening transition with depth on the storage. Fault rupture nucleating below the reservoir can propagate through the reservoir and reach the overlying cap-rock, favoring CO_2 leakage if the shearing deformation enhances the permeability of the sealing material.

NUMERICAL APPROACH

The simulations here presented were performed coupling FLAC (Itasca, 2007), a commercially available finite difference software tool, capable of solving the mechanical poro-elastic problem with TOUGH2 (Pruess et al., 2012).

The different characteristic times for the hydrological and mechanical phenomena allows to solve the two process iteratively, computing the transient solution for pore pressure and fluid flow, while the stress tensor and the strain components are resolved with the quasi-static elastic solution. If the Mohr-Coulomb failure criterion for the interface is met, the computation to resolve stresses and strains will be full dynamic, to take into account the required level of detail of the rupture dynamics. This allows to efficiently cover the potentially long times between ruptures, because the time step must vary from tenth of milliseconds for the dynamic calculations to days/weeks or even longer for the quasi-static solution, which does not require to take into account the inertial effects.

To evaluate mechanical rupture on a fault, we use 1-D contact elements, so-called interfaces. Discontinuity in stresses and displacements across regular elements can then be taken into account. The use of these logical elements allows taking into account for discontinuity in stresses and displacements across regular elements. In Figure 1 shows a scheme to understand how an interface is defined. An interface is defined as a particular surface located on the boundary between elements (minimum 2) and it is defined by the boundary gridpoints of the elements. Since our simulation is 2-dimensional, the interface will be defined with segments. If the gridpoints located on opposite boundaries are in contact (tensile forces below imposed interface tensile strength and distance smaller than an imposed threshold), the contact length is computed for each gridpoint. When one gridpoint is in contact with another gridpoint on the opposite side of the interface, the sum of the half of the distances between the gridpoint and its two adjacent gridpoints is the contact length

contribution to the interface of that gridpoint. Contact length does not limit the shearing distance: which gridpoints are in contact and their contact length are updated at every calculation step, if the slip distance is large enough to offset elements on each side of the interface.

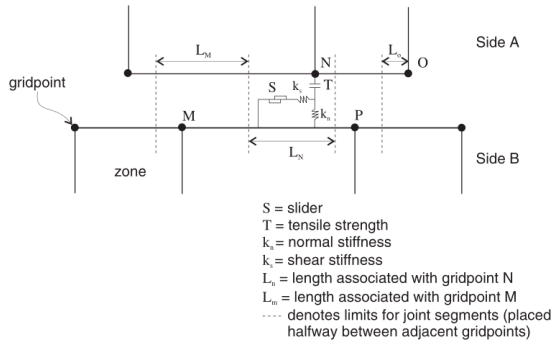

Figure 1. Scheme of the zero-thickness element representing the shearing plane (from Itasca 2007)

The coupling between the two codes is sequentially explicit: a fluid source term is applied to initial static hydro-mechanical equilibrium in TOUGH2, calculating the resulting pressure field. Results from this calculation are imported into FLAC, which takes into account the variation in the pressure field as change to the effective stress, performing then a quasi-static mechanical analysis. Volumetric and shear strain are then passed back to TOUGH2, optionally updating permeability and porosity, then the new pressure field will be derived. Fig. 2 depicts the iteration scheme

Normal and shear forces are evaluated on the single gridpoints composing the interfaces at each solution step, their magnitude are derived from the stress tensor acting on each elements, taking into account the contact length allocated to the gridpoint. The Mohr-Coulomb criterion gives a maximum admissible value for the shear force:

$$F_{smax} = c_0 L + \mu(F_n - pL) \qquad (1)$$

Where c_0 is the cohesion along the interface, L is the effective contact length, μ is the friction coefficient (varying with strain and shearing velocity), F_n is the normal force, p the pore pressure.

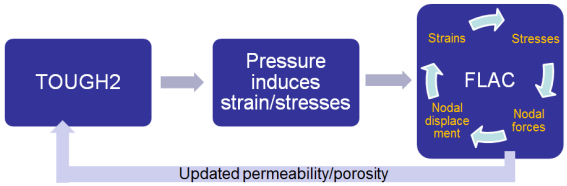

Figure 2. Representation of the explicit sequential coupling linking FLAC and TOUGH2.

Before rupture, there is continuity in both shear and normal displacement, while during shearing only normal displacement will be continuous (non-penetrating interface).

When the shear force is exceeded, the associated shear flow rule is applied, to evaluate the acceleration and velocities generated by the release of excessive shear stress. In our simulation the friction is evolving by a drop in its value at the very beginning of the rupture, friction evolves from its static value μ_s to a reference dynamic value μ_d linearly with increasing slip d, until the critical distance D_c is reached and the friction coefficient reaches the dynamic value (slip-weakening):

$$\mu = \mu_d + \frac{d}{D_c}(\mu_s - \mu_d) \qquad \text{if } d<D_C \quad (2)$$

Successivly, the friction evolution depends on the slip rate V, accordingly to the rate-and-state "slowness law" (Scholz, 1998):

$$\mu = \mu_d + (a-b)\log\left(\frac{V}{V_0}\right) \qquad \text{if } d>D_C \quad (3)$$

Where the sign of the term $(a-b)$ defines if the interface shows velocity strengthening behaviour (negative) or velocity weakening behaviour (positive), with respect to a reference low velocity V_0.

The coupled TOUGH2-FLAC approach has been already used in a number of similar studies to assess safety of CO_2 storage, to determine maximum fault slip and seismic wave transmission (Cappa and Rutqvist, 2012), maximum injection pressure (Rutqvist et al., 2007), influence of pre-existing tectonic stress on slip magnitude (Mazzoldi et al., 2012). The novelty of the approach presented here is the fully dynamic solution of the rupture process with dynamic friction coefficient evolving with the shear velocity (eq. 3). The 2-D approach here presented is representative of the central section of CO_2 injection from a long horizontal well. An evaluation about how to interpret the results of a

plane strain 2-D model to a 3-D scenario for a similar problem can be found in Rinaldi et al. (2015).

The main advantage of using zero-thickness interface elements versus the use of finite size (or volume) elements to reproduce the fault is the decoupling of plastic strain (shear) from the elements size. With interfaces the shearing displacement can be as large as the size of the bounding elements, without incurring in excessive deformation of the element itself, which would require time-consuming technique to recompute the grid. Since spatial and time resolution depends on the element size, the decoupling allows the use of a refined grid to reach higher resolution and at the same time to capture large displacement.

GEOMECHANICAL COUPLED MODEL

The coupled TOUGH2-FLAC solver has been used to investigate slip magnitude in a CO2-injection idealized scenario. We model different homogeneous and heterogeneous velocity dependent behavior for the fault, to investigate how the slip magnitude during failure is affected by different *(a-b)* values, depicting a worst-case scenario. The parameters choice for friction evolution, static and dynamic friction is not univocally possible: the different sets chosen in this analysis are designed to define a reasonable and comparable study with the current literature. Fig. 3 shows a scheme of the model.

A known fault with 80°dip located at 500 meters distance from the injection point. The fault cuts through the formation accommodating the injected CO_2 (the reservoir, from now on) and through the low permeability units lying above and below the reservoir (the cap-rock).

The fault is embedded in a 2x2 km elastic domain in plane-strain condition. In the reservoir zone the minimum size of the elements is 2.5 x 0.5 meters. The fault is represented by contiguous interfaces, one per each element in contact; the corresponding minimum interface length (at initial condition) is 0.5 meters.

Normal tectonic setting is imposed by assigning appropriate initial stress conditions (horizontal stress 0.7 times vertical lithostatic stress). Initially the pressure profile is hydrostatic, with injection taking place in a confined aquifer.

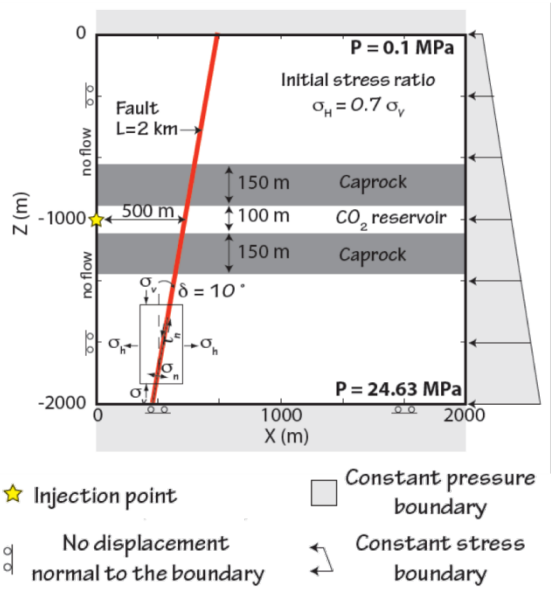

Figure 3. Domain scheme, showing different units and boundary conditions

Table 1. Mechanical properties

Density (kg/m^3)	Young's modulus (GPa)	Poisson's ratio	V_P (m/s)	V_S (m/s)
2300	10	0.25	2284	1319

Table 2. Hydraulical properties

	Porosity	Permeability (m²)
Overburden	0.1	10^{-14}
Caprock	0.01	10^{-19}
Reservoir	0.1	10^{-13}
Basement	0.001	10^{-18}
Fault core	0.01	10^{-15}

Tectonic stresses have been applied as a boundary condition to the lateral right boundary and free surface conditions at the top boundary. Roller boundary conditions (no displacement allowed in the directional perpendicular to the boundary) are applied to the left and to the bottom boundary.

Fixed pressure is imposed at the bottom and at the top of the model. A no-flow boundary is applied on the left boundary.

In the simulations, CO_2 is injected at a depth of 1000 meter, with constant rate of 0.05 kg/m/s. Considering a well with an injection section 1 km long, this will amount to 50 kg/s, if CO_2 is

injected at supercritical condition this equates about 80 l/s. This injection rate is expected to generate quite large overpressure in a confined aquifer in a short time, with reactivation of a favorably oriented fault expected to happen within few days or weeks from the start of the injection.

Mechanical properties are homogeneous and presented in Table 1. Hydraulical properties are summarized in Table 2.

When the failure criteria is satisfied, the simulation is run dynamically, solving the full equation of motions with a time-step of the order of the μ_s, to accurately solve the onset of the rupture, allowing the rupture to develop completely. The parameter D_C (Eq. 2) value has been chosen on the basis of results available in literature, from laboratory measurement.

In the framework of the slowness law, the critical distance can be interpreted as the sliding distance required in renewing the contact population, once the sliding is larger than this distance the friction coefficient reaches a steady-state value.

Finite-difference methods suffer from spurious amplification of high-frequency oscillations. In the dynamic simulation these amplifications may generate unrealistic seismic waves. On the other hand, the accuracy of the seismic wave generated by the rupture depends on its frequency and on the largest zone dimension: for accurate representation of wave transmission, the spatial element size must be smaller than about one-tenth of the wavelength associated with the highest frequency component. We applied a Rayleigh damping filter centered on 30Hz frequency, to damp the potential generation of high frequency content and at the same time to preserve the relatively high frequency content of the seismic wave propagation. Velocities and displacement are monitored at various localities along the fault, as well on the free surface, at the fault trace. Synthetic seismogram can be collected and analyzed to evaluate impact of ground motion on structure and persons (Rutqvist et al., 2014).

RESULTS

Spontaneous rupture takes place after 9 days of injection, with an overpressure in the vicinity of the injection point of ~7.5 MPa. A more detailed description of the hydraulic evolution of the system can be found elsewhere (Cappa and Rutqvist, 2012; Rinaldi et al., 2014a,b; Rutqvist et al., 2014). The rupture nucleates on 6 interfaces, for a total length of the nucleation zone of less than 10 meters, right below the reservoir, in the underlying cap-rock unit. The nucleation zone is the length where shear stress is larger than the maximum shear stress allowed by the Mohr-Coulomb criteria. The rupture length can be one order of magnitude larger, depending on the pre-existing stresses and on the stress released during rupture.

The nucleation zone is not directly affected by CO_2, therefore the mechanisms leading to the reactivation of the fault are reduction in effective stress due to pressurization of the reservoir and the poroelastic induced stress change due to the pressurization of the reservoir itself. It has been demonstrated analytically (Soltanzadeh and Hawkes, 2009) that failure is promoted on the bottom part of a normal fault bounding a reservoir undergoing fluid injection.

Repeated slip on the same fault can take place with continued injection: the slip magnitude is progressively decreasing, even with fault friction coefficient recovering to the initial value immediately after the rupture stops, because the injection rate used here is too high to allow the fault to be effectively reloaded by tectonic forces.

Results from the velocity-neutral model are visible in fig. 4, showing the stress evolution of a fault point located at the bottom of the reservoir. In fig. 5 the fault slip profile for the 4 consecutive ruptures.

Caprock integrity is preserved above the reservoir, while rupture tends to propagate downwards. The segment of the fault undergoing seismic slip is 600 meters length and the maximum slip peak occurs during the first event with a value of 5.3 cm.

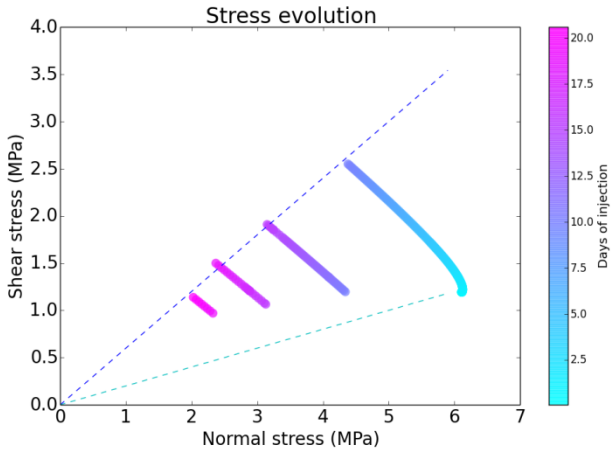

Figure 4. Stress evolution for a point located on the fault, at the bottom of the reservoir.

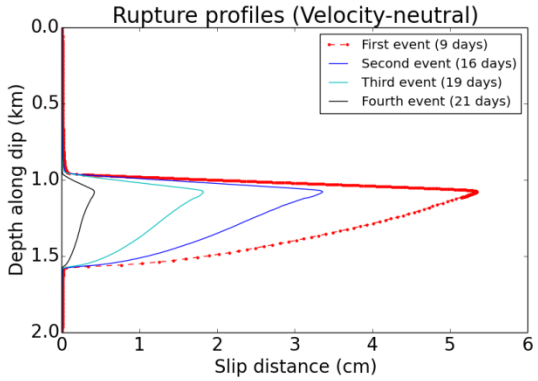

Figure 5. Final rupture profile, successive ruptures (continuous constant injection).

To evaluate the magnitude associated with this ruptured area and slip length, assuming the simplest circular source model, the seismic moment equals to (Kanamori and Anderson, 1975):

$$M_0 = G\bar{u}S \qquad (4)$$

With G representing the shear modulus, $\bar{u}$ the average slip and S the ruptured area. This moment can then be translated into magnitude according to the relation (Kanamori and Anderson, 1975):

$$\log_{10} M_0 = 1.5\, M_w + 16.1 \qquad (5)$$

A circular rupture of radius 600m and average slip 3.2 cm yields then a magnitude 2.9, which can be most certainly felt by the population being in the proximity of the fault, due to the shallow nucleation depth.

We will keep the slip and length of the fault ruptured as our reference value to assess the relative importance of the constitutive parameter *(a-b)* of the rate-and-state law. Values of this parameter can be determined from laboratory experiment, with all the due limitations due to size sample and measure uncertainty. For this study on co-seismic slip and slip-rate, the parameter (a-b) has been investigated in the range from -0.03 to +0.03.

The final slip profiles for the different parameter values are plotted in Fig. 6. Co-seismic displacement velocities and the maximum slip are reduced by velocity-strengthening behavior (positive *a-b*).

The magnitude corresponding to the maximum slip generated by a large, negative *(a-b)* is 4.1, assuming validity the equations (4) and (5) and their underlying assumptions. The maximum magnitude of the event induced by injection with strong velocity strengthening caprock instead is 2.0.

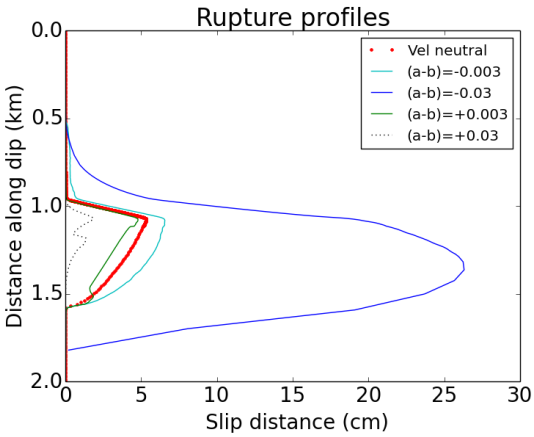

Figure 6. Final rupture profile, different fault rheology.

Since the strong velocity-weakening fault rupture can generate a synthetic seismic event one order of magnitude larger than the velocity-neutral fault, we evaluate the extreme cases of a strong velocity-weakening reservoir combined with a strong velocity-strengthening caprock and vice versa, to assess the relative impact. Results are shown in Fig. 7.

Rupture is minimally affected by the slip-rate dependency of the reservoir material. The results are almost the same as the ones previously obtained by assuming that the whole fault has

the same friction-dependency on velocity that the cap-rock has.

Synthetic waveform can be recorded at station on the surface. The waveforms from the heterogeneous fault rupture are shown in Fig. 8.

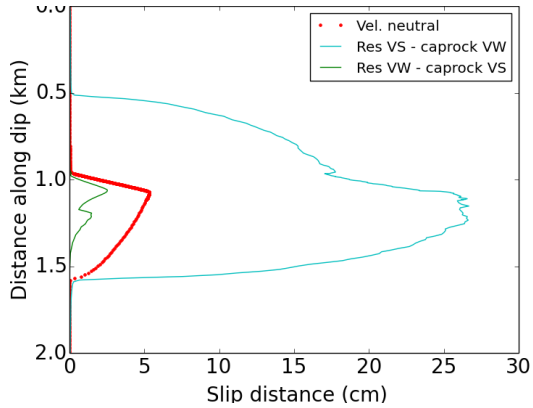

Figure 7. Final rupture profile, heterogeneous fault rheology (VS stand for velocity strengthening, VW for velocity weakening).

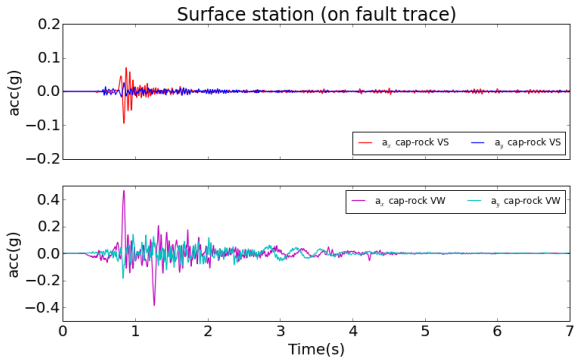

Figure 8. Synthetic waveform generated by the different caprock behaviors. Horizontal and vertical components. Ground roll is absent due to the station being on the fault trace.

We focused on the short-term co-seismic behavior of the fault and on successive rupture induced by high injection rate. However, the approach proposed here can include healing and long term reloading of the fault, to evaluate interaction between anthropogenic operations and tectonic natural load on pre-existing fault. Although nucleation of the rupture takes place on a very small length where stresses are perturbed by the injection activities, the final rupture is the result of the interaction between constitutive fault parameters and the in-situ stress state.

CONCLUSION

In this paper, we performed a forward simulation of rupture taking place on a fault affected by variation in the normal and shear stress acting on it due to fluid injection activity.

This deterministic approach has been used to investigate an idealized fluid injection scenario, loosely based on a real tectonic setting, where CO_2 is injected into a confined aquifer bounded by a low-permeable fault. The goal was to design a worst-case scenario, to investigate how rupture size can be affected by a complex friction coefficient dependent not only on slip distance (slip-weakening) but also on shearing velocity (velocity-weakening or velocity-strengthening).

The effect can be noticeable and some operational questions arise from the result of the numerical model, especially regarding the frictional properties of the material composing the fault below the unit accommodating the injected fluid. Rupture nucleated and propagated in these deeper units may propagate across the reservoir and break through the above sealing unit. Fault reactivation and the possible associated degradation of caprock sealing properties are depending not only on the caprock material itself, but also on the surrounding. The model presented here can model heterogeneity on the fault plane and provide constrain on the expected seismic slip, to achieve a safe injection and storage of CO_2 into a confined aquifer.

ACKNOWLEDGMENT

This research has been carried out in the context of the CATO-2-program (www.co2 cato.org), the Dutch national research program on CO_2 Capture and Storage technology (CCS). The program is financially supported by the Dutch government (Ministry of Economic Affairs) and the CATO-2 consortium parties.

REFERENCES

Cappa, F. and Rutqvist, J., Seismic rupture and ground accelerations induced by CO2 injection in the shallow crust, *Geophys J Int*, 190, 1784–1789, 2012.

Ellsworth, W. L., Injection-Induced Earthquakes, *Science*, 341, 1225942, 2013.

Itasca, FLAC: Fast Lagrangian Analysis of Continua, Version 7.00, *User Manual*, Itasca Consulting Group, Inc., Minneapolis, 2011.

Kanamori, H. and Anderson, D., Theoretical basis of some empirical relations in seismology, *Bulletin of the seismological society of America*, 65(5), 1073-1095, 1975.

Martens, S., et al., CO2 Storage at the Ketzin Pilot Site, Germany: Fourth Year of Injection, Monitoring, Modelling and Verification, *Energy Procedia*, 37, 6434-6443, 2013.

Mazzoldi, A., Rinaldi, A.P., Borgia, A. and Rutqvist, J., Induced seismicity within geological carbon sequestration projects: Maximum earthquake magnitude and leakage potential from undetected faults, *Int J Greenh Gas Contr.,*10, 434-442, 2012.

Orlic, B., Some geomechanical aspects of geological CO_2 sequestration, *Korean Journal of Civil Engineering*, 13 (4), 225–232, 2009.

Orlic, B., ter Heege, J., Wassing, B., Assessing the integrity of fault- and top seals at CO2 storage sites, *Energy Procedia*, 4, 4798-4805, 2011.

Pruess, K., C. Oldenburg, and G. Moridis, *TOUGH2 User's Guide, Version 2.1*, Report LBNL-43134, Lawrence Berkeley National Laboratory, Berkeley, Calif., 2012.

Rinaldi, A.P., Rutqvist, J. and Cappa, F., Geomechanical effects on CO 2 leakage through fault zones during large-scale underground injection, *Int J Greenh Gas Contr,* 20, 171–131, 2014a.

Rinaldi, A.P., Jeanne, P., Rutqvist, J., Cappa, F. and Guglielmi, Y., Effects of fault-zone architecture on earthquake magnitude and gas leakage related to CO 2 injection in a multilayered sedimentary system, *Greenh Gas Sci Techn*, 4, 99–120, 2014b.

Rinaldi, A. P., Vilarrasa, V., Rutqvist, J. and Cappa, F., Fault reactivation during CO_2 sequestration: Effects of well orientation on seismicity and leakage, *Greenhouse Gas Sci Technol.*, doi: 10.1002/ghg.1511, 2015.

Rutqvist, J., Birkholzer, J., Cappa, F, and Tsang, C.-F., Estimating maximum sustainable injection pressure during geological sequestration of CO_2 using coupled fluid flow and geomechanical fault-slip analysis, *Energy Conversion and Management*, 48, 1798-1807, 2007.

Rutqvist J., Cappa, F., Rinaldi, A.P. and Godano, M., Modeling of induced seismicity and ground vibrations associated with geological CO_2 storage, and assessing their effects on surface structures and human perception, *Int J Greenh Gas Contr.,*24, 64-77, 2014.

Soltanzadeh, H., and Hawkes, C. D., Assessing fault reactivation tendency within and surrounding porous reservoirs during fluid production or injection, *International Journal of Rock Mechanics and Mining Sciences*, 46(1), 1-7, 2009.

Vilarrasa, V. and Carrera, J., Geologic carbon storage is unlikely to trigger large earthquakes and reactivate faults through which CO_2 could leak, *PNAS*, Early Edition, 2015.

Zoback, M.D., and Gorelick, S.M., Earthquake triggering and large-scale geologic storage of carbon dioxide, *PNAS*, 109(26), 10164-10168, 2012.

A COUPLED FLOW AND GEOMECHANICS SIMULATOR FOR CO_2 STORAGE IN FRACTURED RESERVOIRS

P. H. Winterfeld and Yu-Shu Wu

Colorado School of Mines
Department of Petroleum Engineering
1600 Arapahoe St., Golden, CO, 80401, USA
pwinterf@mines.edu

ABSTRACT

Injecting large amounts of CO_2 into deep saline aquifers for long-term storage is a promising near-term approach for reducing CO_2 atmospheric emissions. This injected CO_2 forms large plumes in the formation, elevates pressure, and changes stress significantly. If vertical pathways are available or created through these changes, such as by reactivating fractures or faults, CO_2 may flow upward and escape.

We are developing a coupled flow-geomechanics reservoir simulator of CO_2 injection induced rock mechanical processes including fracture mechanical responses (opening and shear) and creation of new fractures. The fluid and heat flow portion of our thermal-hydrological-mechanical simulator is for multiphase, multicomponent, multi-porosity systems. The geomechanical portion consists of an equation for mean stress, derived from linear elastic theory for a thermo-multi-poroelastic system, and equations for stress tensor components that depend on mean stress and other variables. The application of this formulation to model fracture mechanical responses and creation of new fractures is then discussed. The integral finite-difference method is used to solve the governing equations for the simulator. The mean stress and reservoir flow variables are solved for implicitly and the remaining stress tensor components are solved for explicitly. Finally, our geomechanical formulation is verified using analytical solutions from the literature.

FLUID & HEAT FLOW FORMULATION

Our simulator's fluid and heat flow formulation is based on the TOUGH2 one (Pruess *et al*., 1999) for general multiphase, multicomponent, multi-porosity systems. Fluid advection is described with a multiphase version of Darcy's law. Heat flow occurs by conduction and convection, the latter including sensible as well as latent heat effects. The description of thermodynamic conditions is based on the assumption of local equilibrium of all phases and rock media. The conservation equations for mass and energy can be written in differential form as:

$$\frac{\partial M^k}{\partial t} = \nabla \cdot \mathbf{F}^k \quad q^k \tag{1}$$

where superscript k refers to a component, M is mass per unit volume, q is source or sink per unit volume, and $\mathbf{F}$ is mass or energy flux. Mass per unit volume is a sum over phases:

$$M^k = \phi \sum_l S_l \rho_l X_l^k \tag{2}$$

where ϕ is porosity, subscript l refers to a phase, S is phase saturation, ρ is phase mass density, and X is phase mass fraction. Energy per unit volume accounts for internal energy in rock and fluid and is the following:

$$M^{N+1} = (1-\phi) C_r \rho_r T \quad \phi \sum_l S_l \rho_l U_l \tag{3}$$

where ρ_r is rock density, C_r is rock specific heat, U is phase specific internal energy, and N is the number of mass components.

Advective mass flux is a sum over phases and phase flux is given by the multiphase version of Darcy's law:

$$\mathbf{F}_l = -k \frac{k_{rl} \rho_l}{\mu_l} \left(\nabla P + \nabla P_{c,l} - \rho_l \mathbf{g} \right) \tag{4}$$

where $\mathbf{F}_l$ is phase flux, k is absolute permeability, k_r is phase relative permeability, μ is phase

viscosity, P_c is phase capillary pressure, and **g** is the gravity vector. Capillary pressure is relative to the gaseous phase. Energy flux includes conductive and convective components:

$$\mathbf{F}^{N+1} = -k_t \nabla T + \sum_l h_l \mathbf{F}_l \quad (5)$$

where k_t is thermal conductivity and h is specific enthalpy.

MEAN STRESS FORMULATION

Our simulator's mean stress geomechanical formulation is based on the classical theory of elasticity extended to multi-porosity non-isothermal media. The stress-strain behavior of such media is described by an extended version of Hooke's law (Winterfeld and Wu, 2014):

$$\boldsymbol{\tau} - \left[\sum_j \left(\alpha_j P_j + 3\beta K \omega_j \left(T_j - T_{ref}\right)\right)\right]\mathbf{I} = 2G\boldsymbol{\varepsilon} + \lambda\left[tr\left(\boldsymbol{\varepsilon}\right)\right]\mathbf{I} \quad (6)$$

where K is bulk modulus, G is shear modulus, λ is the Lamé parameter, β is linear thermal expansion coefficient, subscript j refers to porous continuum, α_j is Biot coefficient, ω_j is volume fraction, and T_{ref} is reference temperature for a thermally unstrained state. Two other fundamental relations in the theory of linear elasticity are the relation between the strain tensor and the displacement vector:

$$\boldsymbol{\varepsilon} = \frac{1}{2}\left(\nabla \mathbf{u} + \mathbf{u}\nabla\right) \quad (7)$$

and the static equilibrium equation:

$$\nabla \cdot \boldsymbol{\tau} + \mathbf{F}_b = 0 \quad (8)$$

where $\mathbf{F}_b$ is the body force.

We combine Equations 6-8 to obtain the thermo-multi-poroelastic Navier equation:

$$\nabla\left[\sum_j \left(\alpha_j P_j + 3\beta K \omega_j T_j\right)\right] + \left(\lambda + G\right)\nabla\left(\nabla \cdot \mathbf{u}\right) + G\nabla^2 \mathbf{u} + \mathbf{F}_b = 0 \quad (9)$$

The trace of the stress tensor, an invariant, is obtained from Equation 6 as:

$$K\varepsilon_v = \tau_m - \sum_j \left(\alpha_j P_j + 3\beta K \omega_j \left(T_j - T_{ref}\right)\right) \quad (10)$$

where τ_m is the mean stress, the average of the normal stress tensor components, and ε_v is the volumetric strain, the sum of the normal strain components. Taking the divergence of Equation 9, combining with Equation 10, and noting that the divergence of the displacement vector is the volumetric strain, yields an equation relating mean stress, pore pressures, and temperatures (Winterfeld and Wu, 2014):

$$\nabla \cdot \left[\frac{3\left(1-\upsilon\right)}{1+\upsilon}\nabla \tau_m + \mathbf{F}_b - \frac{2\left(1-2\upsilon\right)}{1+\upsilon}\nabla\left(\sum_j \left(\alpha_j P_j + 3\beta K \omega_j T_j\right)\right)\right] = 0 \quad (11)$$

where υ is Poisson's ratio.

We couple fluid and heat flow to geomechanics by solving Equation 11 along with the mass and energy conservation equations (Equation 1) from the fluid and heat flow formulation. Mean stress is the primary thermodynamic variable associated with our geomechanical formulation and volumetric strain is an additional property arising from our geomechanical formulation that is calculated from Equation 10.

Rock properties, namely porosity and permeability, are correlated to effective stress, a general definition of which was given by Biot and Willis (1957):

$$\tau' = \tau_m - \alpha P \quad (12)$$

Correlations that are used for these properties appear in Winterfeld and Wu (2014).

STRESS TENSOR COMPONENT FORMULATION

Equation 9 sets a vector to zero; hence, all of the vector's components are zero as well. Consider the x-component of Equation 9:

$$\frac{\partial}{\partial x}\left[h\left(\mathbf{P},\mathbf{T}\right)\right] + \left(\lambda + G\right)\frac{\partial}{\partial x}\left(\nabla \cdot \mathbf{u}\right) + G\nabla^2 u_x + F_{b,x} = 0 \quad (13)$$

where

$$h\left(\mathbf{P},\mathbf{T}\right) = \sum_j \left(\alpha_j P_j + 3\beta K \omega_j \left(T_j - T_{ref}\right)\right) \quad (14)$$

Differentiating Equation 13 by x and eliminating strains and displacements in favor of stresses using Equations 6, 7, and 10 yields an equation relating the xx-normal stress component, mean stress, pore pressures, and temperatures:

$$\frac{\partial^2}{\partial x^2}\left[h(\mathbf{P},\mathbf{T})\right] + \frac{3}{2(1+\upsilon)}\frac{\partial^2}{\partial x^2}\left(\tau_m - h(\mathbf{P},\mathbf{T})\right)$$
$$\frac{1}{2}\nabla^2\left(\tau_{xx} - h(\mathbf{P},\mathbf{T}) - \frac{3\upsilon}{1+\upsilon}\left(\tau_m - h(\mathbf{P},\mathbf{T})\right)\right)$$
$$\frac{\partial}{\partial x}F_{b,\mathrm{x}} = 0 \tag{15}$$

Repeating this procedure for the y- and z-components of Equation 9 yield similar equations for the yy- and zz-normal stress components:

$$\frac{\partial^2}{\partial y^2}\left[h(\mathbf{P},\mathbf{T})\right] + \frac{3}{2(1+\upsilon)}\frac{\partial^2}{\partial y^2}\left(\tau_m - h(\mathbf{P},\mathbf{T})\right)$$
$$\frac{1}{2}\nabla^2\left(\tau_{yy} - h(\mathbf{P},\mathbf{T}) - \frac{3\upsilon}{1+\upsilon}\left(\tau_m - h(\mathbf{P},\mathbf{T})\right)\right)$$
$$\frac{\partial}{\partial y}F_{b,\mathrm{y}} = 0 \tag{16}$$

$$\frac{\partial^2}{\partial z^2}\left[h(\mathbf{P},\mathbf{T})\right] + \frac{3}{2(1+\upsilon)}\frac{\partial^2}{\partial z^2}\left(\tau_m - h(\mathbf{P},\mathbf{T})\right)$$
$$\frac{1}{2}\nabla^2\left(\tau_{zz} - h(\mathbf{P},\mathbf{T}) - \frac{3\upsilon}{1+\upsilon}\left(\tau_m - h(\mathbf{P},\mathbf{T})\right)\right)$$
$$\frac{\partial}{\partial z}F_{b,\mathrm{z}} = 0 \tag{17}$$

Consider the y-component of Equation 9:

$$\frac{\partial}{\partial y}\left[h(\mathbf{P},\mathbf{T})\right] + (\lambda + G)\frac{\partial}{\partial y}(\nabla\cdot\mathbf{u}) + G\nabla^2 u_y +$$
$$F_{b,\mathrm{y}} = 0 \tag{18}$$

Differentiating Equation 18 by x, differentiating Equation 13 by y, averaging the two, and eliminating strains and displacements as before yields an equation relating the xy-shear stress component, mean stress, pore pressures, and temperatures:

$$\frac{\partial^2}{\partial x\partial y}\left[h(\mathbf{P},\mathbf{T})\right] + \frac{3}{2(1+\upsilon)}\frac{\partial^2}{\partial x\ y}\left(\tau_m - h(\mathbf{P},\mathbf{T})\right)$$
$$\frac{1}{2}\nabla^2\tau_{xy} + \frac{1}{2}\left(\frac{\partial}{\partial x}F_{b,\mathrm{y}} + \frac{\partial}{\partial y}F_{b,\mathrm{x}}\right) = 0 \tag{19}$$

Repeating this procedure for the y- and z-components of Equation 9 yields an equation for the yz-shear stress component; repeating this procedure for the x- and z-components of Equation 9 yields an equation for the xz-shear stress component:

$$\frac{\partial^2}{\partial y\partial z}\left[h(\mathbf{P},\mathbf{T})\right] + \frac{3}{2(1+\upsilon)}\frac{\partial^2}{\partial y\ z}\left(\tau_m - h(\mathbf{P},\mathbf{T})\right)$$
$$\frac{1}{2}\nabla^2\tau_{yz} + \frac{1}{2}\left(\frac{\partial}{\partial y}F_{b,z} + \frac{\partial}{\partial z}F_{b,\mathrm{y}}\right) = 0 \tag{20}$$

$$\frac{\partial^2}{\partial x\partial z}\left[h(\mathbf{P},\mathbf{T})\right] + \frac{3}{2(1+\upsilon)}\frac{\partial^2}{\partial x\ z}\left(\tau_m - h(\mathbf{P},\mathbf{T})\right)$$
$$\frac{1}{2}\nabla^2\tau_{xz} + \frac{1}{2}\left(\frac{\partial}{\partial x}F_{b,z} + \frac{\partial}{\partial z}F_{b,\mathrm{x}}\right) = 0 \tag{21}$$

Equations 15-17 and 19-21 relate each normal or shear stress component to mean stress, pore pressures, and temperatures, the primary variables of the mean stress geomechanical formulation.

DISCRETIZATION AND SOLUTION OF SIMULATOR EQUATIONS

The fluid and heat flow and geomechanical equations are discretized in space using the integral finite difference method (Narasimhan and Witherspoon, 1976). In this method, the simulation domain is subdivided into grid blocks and those equations, for example Equation 1, are integrated over a grid block volume, V:

$$\frac{d}{dt}\int_V M^k dV = \int_\Gamma \mathbf{F}^k\cdot\mathbf{n}\,d\Gamma + \int_V q^k dV \tag{22}$$

where Γ is the grid block surface. Because geomechanical effects result in grid block geometry changes, the integrands of Equation 22 depend on strain. This dependence is formulated as:

$$\psi\left(\varepsilon_\psi\right)=\psi_0\left(1-\varepsilon_\psi\right),\psi= \quad A,D,orV \tag{23}$$

where subscript 0 refers to zero strain, A refers to area, D refers to distance, and V refers to volume. Replacing volume integrals with grid block volume averages and surface integrals with discrete sums over grid block surface segment averages yields the following discrete form of the simulator equations:

$$\left[M^k\left(1-\varepsilon_v\right)\right]^{i+1}-\left[M^k\left(1-\varepsilon_v\right)\right]^{i}- \frac{\Delta t}{V_0}\left[\sum_j A_0\left(1-\varepsilon_{\mathrm{A,j}}\right)F_j^k+V_0\left(1-\varepsilon_v\right)q^k\right]^{i^*}=0 \tag{24}$$

where the summation is over grid block surface segments, superscript i is time step, and superscript i^* bracketing the flux and generation terms denotes that those terms are evaluated at the previous time step (i) or the current one (i+1).

The simulator equations and primary variables comprising the single-porosity version our formulation are summarized in Table 1.

Table 1. Equations and associated primary variables for single-porosity formulation.

Equation	Primary Variables
Mass conservation	Pressure, N-1 mass fractions
Energy conservation	Temperature
Mean stress	Mean stress
Normal stresses	xx, yy, zz normal stresses
Shear stresses	xy, yz, xz shear stresses

This system of equations is solved in a sequential manner using the Newton-Raphson method. The Jacobian matrices consist of square sub matrices that are associated with a grid block or a connection between two grid blocks. Conservation of mass, energy, and the mean stress equation are solved simultaneously first. Normal and shear stresses appearing in those equations are evaluated at the previous time step and the rest of the primary variables are evaluated at the current time step. Solution of those equations yields pressure, mass fractions, temperature, and mean stress at the current time step. The size of that Jacobian's sub matrices is two plus the number of mass components. The normal and shear stress equations, Equations 23-25 and 27-29, are solved next. In those solutions, pressure, mass fractions, temperature, and mean stress are evaluated at the current time step. Normal and shear stresses appearing in the Laplacian terms are also evaluated at the current time step, and other instances of those stresses are evaluated at the previous time step. The Jacobian matrix for each stress tensor component is linear, independent of the other stress tensor components, and has a sub matrix size of one. Figure 1 is a flow chart illustrating this equation solution.

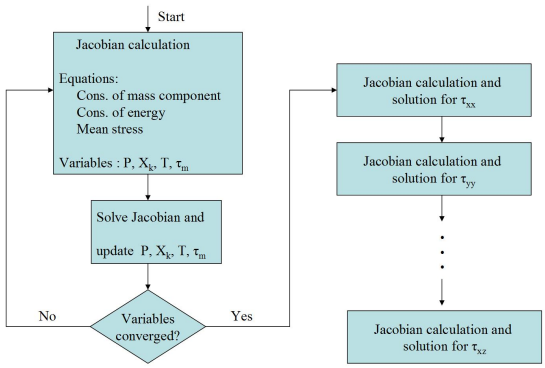

Figure 1. Flow chart for solution of mass, energy, and geomechanical equations.

Our simulator is massively parallel, with domain partitioning using the METIS and ParMETIS packages (Karypsis and Kumar, 1998; Karypsis and Kumar, 1999). Each processor computes Jacobian matrix elements for its own grid blocks and exchange of information between processors uses MPI (Message Passing Interface) and allows calculation of Jacobian matrix elements associated with inter-block connections across domain partition boundaries. The Jacobian matrix is solved in parallel using an iterative linear solver from the Aztec package (Tuminaro *et al.* 1999).

CO_2 INJECTION INDUCED ROCK MECHANICAL PROCESSES

During geologic sequestration of CO_2 into a permeable reservoir, the integrity of caprock that seals the reservoir must be preserved because super critical CO_2 is less dense than the in-situ brine and thus can migrate, through induced or opened fractures and activated faults, out of the injection zone.

We will include the capability to simulate fault and fracture activation, and induced fracturing,

into our model. Induced fracturing or tensile failure is thought to be able to occur when the pore pressure exceeds the least compressive principal stress (Zoback, 2007):

$$P > \sigma_3 \tag{25}$$

Induced or activated fractures form channels through which fluid can flow. The ability of the fracture to conduct fluid is a function of the fracture aperture, for example (Cappa and Rutqvist, 2011):

$$T = \frac{b_h^3}{12\mu} \tag{26}$$

where T is the fracture transmissibility and b_h is the fracture aperture. Fracture aperture changes have been correlated to normal stress (Rutqvist *et al*., 2002) for directional fractures or mean stress (Rutqvist and Tsang, 2002) for isotropic fractures.

A fault may be activated if the shear stress acting on its plane is great enough. This has been quantified as the Coulomb failure criterion (Jaeger *et al*., 2007) and can be written as:

$$\tau = c + \mu_s \sigma_n' \tag{27}$$

where τ is the shear stress for fault reactivation, σ_n' is normal effective stress on the fault plane, c is cohesion, and μ_s is the static friction coefficient. These normal and shear stresses would be obtained from the stress tensor components whose calculation is described above. Once activated, a fault would have a permeability and porosity that depends on effective stress.

VERIFICATION OF STRESS TENSOR COMPONMENT FORMULATION

We provide two example problems for verification of our stress tensor component calculation technique. The first is a comparison of simulation to the analytical solution for displacement caused by a uniform load on a semi-infinite elastic medium. There is no fluid or heat flow in this problem. The second is a comparison of simulation to the analytical solution for the two-dimensional Mandel-Cryer effect.

Displacement from Uniform Load on Semi-infinite Elastic Medium

Timoshenko and Goodier (1951) present analytical solutions for a uniform load over a circular area of radius a acting on the surface of a semi-infinite elastic medium. We used this analytical solution to verify calculation of normal stress tensor components. We approximated the semi-infinite medium as a large rectangular parallelepiped 194 m in the x- and y-directions and 1320 m in the z-direction. We subdivided this medium into a 200x200x800 Cartesian grid. Grid block x- and y-direction length in the vicinity of the center was 0.1 m and increased further away from it. Grid block z-direction length was 0.2 m in the vicinity of the surface and increased further away from it. The loaded circle was located at the center of the top xy-face and had a 1.0 m radius. Because our grid was Cartesian, we approximated this circle as 314 loaded squares of radius 0.1 m, as shown in Figure 2. The rest of the medium's surface had no load exerted on it.

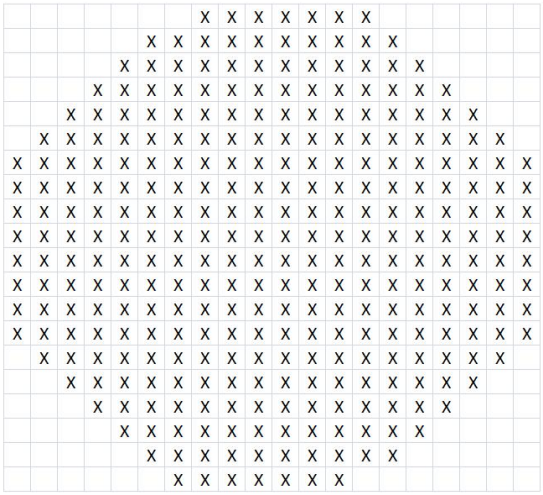

Figure 2. Approximation of loaded 1.0 m radius circle by 314 square grid blocks of length 0.1 m.

Our geomechanical formulation requires boundary conditions for mean stress and those stress tensor components that are calculated. We specified a mean stress of 0.48 MPa and a normal z-direction stress (the load) of 0.6 MPa over the loaded circle. The equal x- and y-direction normal stresses were then 0.42 MPa. There is no fluid or heat flow in this problem, so only mean stress and stress tensor components are solved for. We solve for mean stress first,

and calculate stress tensor components next using the mean stress solution. Because grid block geometry depends on stress tensor components that are evaluated at the previous time step, we must repeat these calculations over a number of steps until the stress tensor components are unchanged from one step to the next. These stress tensor components are those obtained by a fully coupled or fully implicit solution to our geomechanical formulation.

The displacement caused by the load is the change of the medium's overall length in the direction of the applied load, given by:

$$w = \sum D_{0,z}\varepsilon_{zz} \tag{28}$$

where $D_{0,z}$ is z-direction grid block unstrained length and the sum is over a *z*-direction column of grid blocks. The z-direction normal strain is calculated from Hooke's law:

$$\varepsilon_{zz} = \frac{1}{E}\left(\tau_{zz} - \upsilon\left(\tau_{xx} + \tau_{yy}\right)\right) \tag{29}$$

The analytical and simulated displacements are shown in Figure 3 and those for the z-direction normal stresses are shown in Figure 4. In both cases, they are hardly distinguishable.

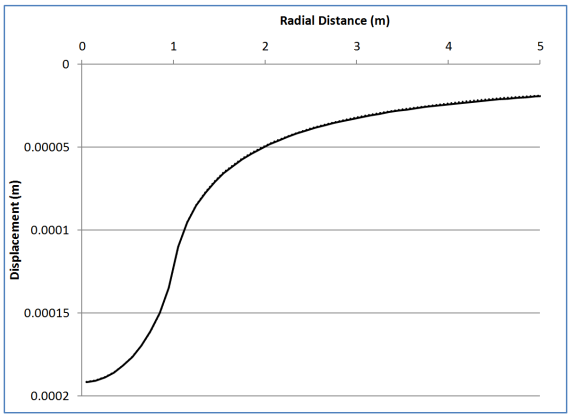

Figure 3. Analytical (solid line) and simulated (dotted line) displacements for semi-infinite medium subjected to circular load.

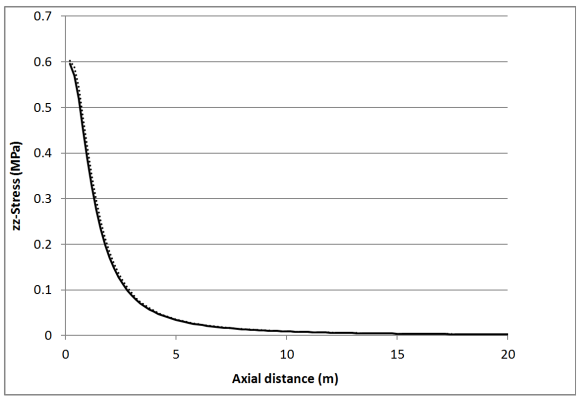

Figure 4. Analytical (solid line) and simulated (dotted line) z-direction normal stresses for semi-infinite medium subjected to circular load.

Two-Dimensional Mandel-Cryer Effect

Consider a fluid-filled poroelastic material with a constant compressive force applied to the top and bottom. There is an instantaneous compression and uniform pore pressure increase due to the force. Afterwards, the material is allowed to drain laterally. Drainage is accompanied by a decrease in pore pressure near the edges and the material there becomes less stiff, resulting in a load transfer to the center and a pore pressure there that reaches a maximum and then declines. This pore pressure behavior is the Mandel-Cryer effect (Mandel, 1953) and Abousleiman *et al.* (1996) derived an analytical solution to it. We use this analytical solution to verify our coupled fluid flow and geomechanics calculations.

Our simulation domain is 1000 m square and is subdivided into a uniform Cartesian 200x200 grid. Rock properties are the following: porosity is 0.094, permeability is 10^{-13} m^2, Young's modulus is 5.0 GPa, Poisson's ratio is 0.25, and the Biot coefficient is 1.0.

We first simulate the compression and next the drainage. The initial unstrained state is pore pressure and normal stress components at 2.0 MPa. The compressive portion of the simulation, with an imposed mean stress of 5.0 MPa at the top and bottom, is run until equilibrium is reached. After compression, the pore pressure has increased to 3.28 MPa and the mean stress becomes 5.0 MPa throughout the simulation domain. Because the lateral boundaries are free, the x- and y-direction effective stresses are zero, so the normal stresses

in those directions are 3.28 MPa, and the normal z-direction stress is therefore 8.44 MPa.

In the drainage portion of the simulation, the initial pore pressure (2.0 MPa) is imposed at the lateral boundaries. Because the effective stresses at those boundaries are zero, the x- and y-direction normal stresses there also equal the initial pore pressure. The normal z-direction stresses at the top and bottom remain at 8.44 MPa. The drainage simulation is run for 100,000 seconds with 100 second time steps. Figure 5 shows the match of centerline pore pressure with the analytical solution. The displacements in the

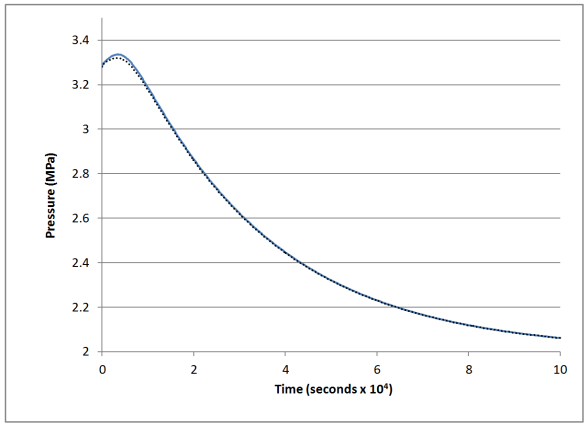

Figure 5. Match of simulated centerline pore pressure (dotted line) with analytical solution (solid line) for Mandel-Cryer effect.

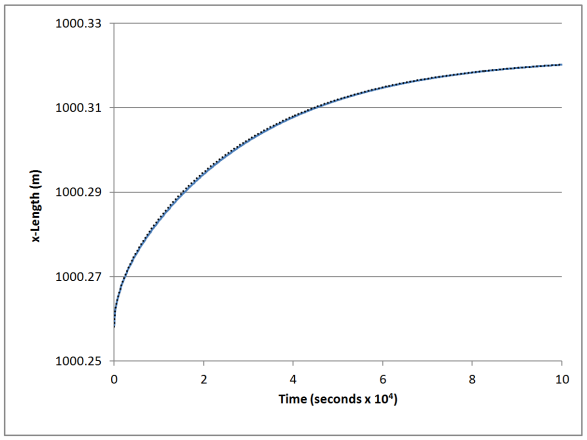

Figure 6. Match of simulated x-direction displacement (dotted line) with analytical solution (solid line) for Mandel-Cryer effect.

x- and z- directions are calculated from the normal strains in a similar manner as the displacement calculation from the previous example problem. The applied stress causes the system to contract in the z-direction and expand in the x-direction. The expansion, shown in Figure 6, is matched almost perfectly and the match of the contraction, shown in Figure 7, shows only a small deviation from the analytical solution at early times.

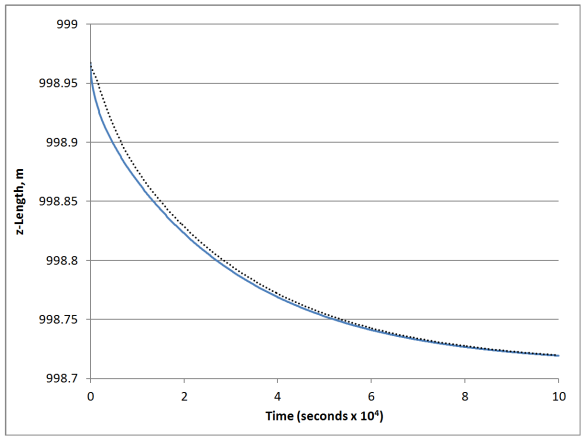

Figure 7. Match of simulated z-direction displacement (dotted line) with analytical solution (solid line) for Mandel-Cryer effect.

CONCLUSIONS

We developed a reservoir simulator for modeling THM processes in fractured and porous media. The simulator's geomechanical formulation consists of a momentum conservation equation for mean stress, pore pressures, and temperatures, along with additional equations relating each stress tensor component to mean stress, pore pressures, and temperatures. The fluid and heat flow formulation is for general multiphase, multicomponent, multi-porosity systems. The simulator is an extension of a THM one whose geomechanical formulation was the momentum conservation equation for mean stress alone.

We verified our stress tensor component calculation technique using analytical solutions for two problems, the displacement from a uniform load on semi-infinite elastic medium and the two-dimensional Mandel-Cryer effect. Analytical stress tensor component equations were matched by simulation extremely well,

verifying our technique for calculating them. In future work, we will apply this formulation to studying injection induced mechanical processes, such as fault and fracture activation and induced fracturing, during CO_2 sequestration.

ACKNOWLEDGMENT

This work was supported by the Foundation CMG, the EMG of the Colorado School of Mines, and by the National Energy Technology Laboratory of the U. S. Department of Energy.

REFERENCES

Abousleiman Y., Cheng, A. H.-D., Cui L., Detournay, E., and Roegiers, J.-C., Mandel's problem revisited, *Géotechnique,* 46 (2), 187-195, 1996.

Cappa. F. and Rutqvist, J., Modeling of coupled deformation and permeability evolution during fault reactivation induced by deep underground injection of CO_2, *Intl. J. of Greenhouse Gas Control*, 5, 336-346, 2011.

Biot, M.A. and Willis, D.G., The elastic coeffi-cients of the theory of consolidation, *J. Appl. Mech*, 24, 594–601, 1957.

Karypis, G. and Kumar, V., A parallel algorithm for multilevel graph partitioning and sparse matrix ordering, *Journal of Parallel and Distributed Computing,* 48, 71-85, 1998.

Karypis, G. and Kumar, V., A fast and high quality multilevel scheme for partitioning irregular graphs. *Siam J. Sci. Comput.,* 20 (1), 359-392, 1999.

Jaeger, J. C., Cook, N. G. W., and Zimmerman, R. W., *Fundamentals of Rock Mechanics*. Malden, MA: Blackwell Publishing, 2007.

Mandel, J.: Consolidation des sols (etude mathematique), *Geotechnique*, 3287–3299, 1953.

Narasimhan, T. N. and Witherspoon, P. A., An integrated finite difference method for analysis of fluid flow in porous media, *Water Resources Res.,* 12, 57–64, 1976.

Pruess, K., C. Oldenburg, and G. Moridis, *TOUGH2 User's Guide, Version 2.0*, Report LBNL-43134, Lawrence Berkeley National Laboratory, Berkeley, Calif., 1999.

Rutqvist, J. and Tsang, C.F., A study of caprock hydromechanical changes associated with CO_2-injection into a brine formation. *Environ. Geol.,* 42, 296–305, 2002.

Rutqvist, J., Wu Y.-S., Tsang, C.F. and Bodvarsson, G.A., Modeling approach for analysis of coupled multiphase fluid flow heat transfer and deformation in fractured porous rock, *Int. J. Rock Mech.and Min. Sci.,* 39, 429–442, 2002.

Timoshenko, S. and Goodier, J. N., *Theory of Elasticity*, McGraw-Hill Book Company, Inc, New York, NY, 1951.

Tuminaro, R.S., Heroux, M., Hutchinson, S.A. and Shadid, J.N., *Official Aztec User's Guide Version 2.1*, Massively parallel computing research laboratory, Sandia National Laboratories, Albuquerque, New Mexico, 1999.

Winterfeld P. H. and Wu Y.-S., Simulation of CO_2 sequestration in brine aquifers with geomechanical coupling. In *Computational Models for CO_2 Sequestration and Compressed Air Energy Storage,* edited by J. Bundschuh and R. Al-Khoury, Chapter 8, CRC Press, New York, NY, 2014.

Zoback, M.D., *Reservoir Geomechanics*, Cambridge Univ. Press, Cambridge, UK, 2007.

Nuclear Energy and Waste

APPLICATION OF 1D HYDROMECHANICAL COUPLING IN TOUGH2 TO A DEEP GEOLOGICAL REPOSITORY GLACIATION SCENARIO

Nicola Calder[1], John Avis[1], Erik Kremer[2] and Robert Walsh[1]

[1]Geofirma Engineering Ltd.
1 Raymond St. Suite 200
Ottawa, Canada K1R 1A2
e-mail: ncalder@geofirma.com,
javis@geofirma.com

[2]Nuclear Waste Management Organization
22 St. Clair Avenue East, Sixth Floor
Toronto, Canada M4T 2S3
e-mail: ekremer@nwmo.ca

ABSTRACT

Modelling glaciation events requires hydromechanical coupling in two-phase flow systems. Modelling systems such as TOUGH-FLAC have been developed, but can be very demanding to use, both computationally and in terms of human effort. Previously, we have described and tested a simplified one-dimensional hydromechanical coupling model implemented directly in TOUGH2 (Walsh et al., 2012). The approach was inspired by the methods described for pure vertical strain in Wang (2000) and Neuzil (2003), and is appropriate for modelling the effects of relatively uniform changes in mechanical loading over a large area, such as occurs during continental glaciations or laterally extensive erosion/deposition events.

The model has recently been applied to a glaciation scenario for a post-closure safety assessment of a hypothetical deep geological repository for used nuclear fuel in sedimentary rock formations. Previous glaciation analyses considered the sedimentary rock formations to be fully liquid saturated; however, there is evidence of residual gases in some of the rock formations where the repository is likely to be situated (INTERA, 2011). The 1D hydromechanical model implemented in TOUGH2 was applied to a 2D slice from an existing 3D sub-regional model, which was implemented in a conventional groundwater code. Comparisons of 2D single-phase flow results to the 3D sub-regional flow model results showed that the reduced dimensionality of the model did not impair its ability to reproduce the important features of the subglacial velocity field. As expected, the greater compressibility of gas significantly moderated the increase in head during glacial loading. Gas saturations during glacial loading also decreased due to the greater compression of gas relative to water during loading, resulting in a smaller volumetric ratio of gas. Moderation of heads during glacial cycles did not translate to a moderation of vertical velocities. Upward vertical velocities in the two-phase model increased in the formations containing the repository compared to liquid phase simulations, due to an increase in the vertical head gradient. The results of this modelling show that even low gas saturations can significantly impact hydromechanical coupling. Variations in gas saturations or rock properties between different formations can lead to interesting behavior which can only be assessed with a two-phase flow numerical model.

INTRODUCTION

The Nuclear Waste Management Organization (NWMO) has undertaken post-closure safety assessments of geological repositories for used fuel hosted in sedimentary rock formations in Canada (NWMO, 2013). As part of the post-closure safety assessment, a quantitative assessment of the impacts of glaciation events on a hypothetical deep geological repository is considered. Primary analyses have used a hydromechanical model coupled with a single-phase flow model.

In the Ordovician sedimentary rock formations under consideration, there is evidence of residual gases (INTERA, 2011). To determine the influence of residual gases on the glacial climate induced changes to geosphere flow behavior, a two-phase TOUGH2 model coupled with a 1D hydromechanical model was applied to a 2D vertical slice from the 3D sub-regional ground-

water flow model. This paper will focus on the impacts of two-phase flow on glaciation induced geosphere flow, providing an overview of the 1D hydromechanical model coupled with TOUGH2, previously described in detail within Walsh et al. (2012); a comparison of the two-phase flow glaciation model with the single-phase glaciation model; and a description of the sensitivity of the two-phase flow model to initial gas saturations.

1D HYDROMECHANICAL MODEL

External stresses arising from transient ice-sheet mechanical loading and elevated sub-glacial hydraulic head can potentially influence groundwater system dynamics and solute migration. The presence of gas in formations is expected to greatly reduce the magnitude of hydro-mechanical coupling. Fully coupled 3D hydro-mechanical models, such as TOUGH-FLAC (Rutqvist and Tsang, 2003) are demanding to use at the repository scale, in terms of computational and human effort, and may require some approximation in accounting for markedly increased fluid compressibility in a gas-water system. An approximate 1D solution to the coupled hydro-mechanical processes, relying on the simplifying assumptions of horizontally bedded formations and vertical uniaxial strain, is reasonable for a relatively homogeneous and extensive vertical load, such as occurs during continental glaciation or laterally extensive erosion/deposition events. The 1D assumption is not valid where vertical loads vary significantly across the model domain, as would occur during the early stages of a glacial advance when the ice margin is within the model domain. The interval during which the ice margin crosses the domain is typically short, and the one-dimensional hydromechanical model is reasonably accurate for the majority of the simulation time.

The 1D approach is described in detail for single-phase flow in Wang (2000) and Neuzil (2003), and two-phase flow in Walsh et al. (2012), and is implemented in TOUGH2.

In TOUGH2, the change in porosity as a function of pressure is analogous to the storage term in single-phase flow mass balance equations, and is included within the mass accumulation term of the governing mass balance equation (Pruess et al., 1999). Porosity (ϕ) is not a constant material property, but is transient and updated at the end of each time-step. Hydro-mechanical coupling is implemented as a change in porosity due to a change in the vertical load. The total change in porosity at the end of each time step, including storage and hydro-mechanical components, is described as follows:

$$\phi_t = \phi_{t-1} + \phi_{t-1} C_{pore} dp + S_{S-1D} \zeta d\sigma_{zz} \quad (1)$$

where

ϕ_{t-1} = porosity at time step $t-1$ (-);

C_{pore} = pore compressibility (Pa^{-1}), COM in the ROCKS record;

dp = change in pressure during time step $t-1$ (Pa);

S_{S-1D} = specific storage (Pa^{-1});

ζ = one-dimensional loading efficiency (-); and

$d\sigma_{zz}$ = change in vertical load during time step $t-1$ (Pa).

The fourth term in equation (1), ($S_{S-1D} \zeta d\sigma_{zz}$) is the new hydromechanical term. While the loading efficiency (ζ) and the storage coefficient (S_{S-1D}) are both functions of fluid compressibility, and therefore gas saturation in two-phase systems, the term $S_{S-1D}\,\zeta$ reduces to a function dependent only on material parameters:

$$S_{S-1D}\,\zeta = \frac{\left(\frac{1}{K}\right)(1+\nu)}{3(1-\nu)} \quad (2)$$

where

K = Drained bulk modulus (Pa), ($1/K = \phi C_{pore}$); and

ν = Poisson's Ratio (-).

As a result, the loading efficiency and storage parameters can be input as material-dependent parameters within TOUGH2.

As the hydromechanical term is not dependent on gas saturation, the change in porosity due to hydromechanical loading is the same regardless

of whether the system is single-phase groundwater or two-phase gas and groundwater. The influence of a gas phase on glaciation induced hydromechanical loading is indirect: the same change in porosity will result in a smaller pressure change in a gas-saturated pore than in a liquid-saturated pore, and this difference in pressure will affect porosity changes due to storage. The storage term in TOUGH2 is implemented as the change in porosity due to changes in pressure ($\phi_{t-1} C_{pore} dp$ in Eq. (1)).

GLACIATION SCENARIO

The hypothetical deep geological repository is located in a sedimentary rock formation, within the model domain shown in Figure 1. Glacial climate data for this scenario consists of ice sheet thickness at locations surrounding the repository as a function of time for a single glacial cycle occurring over a period of 120 ka, obtained from the Glacial Systems Model described in NWMO (2013). This cycle is repeated eight times to provide an approximately 1 Ma scenario.

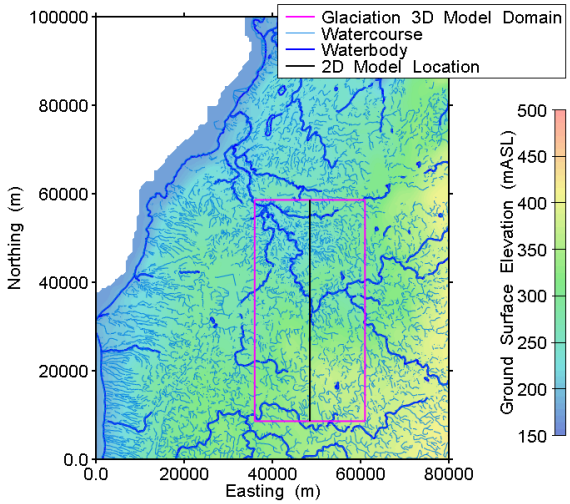

Figure 1. Location of model domain. Repository site location within this model domain selected for modelling purposes only.

An analytic glacial profile model (Oerlemans, 2005) is used to determine ice sheet shape and ice thickness near the toe. Figure 2 shows the ice thickness for the first cycle. Permafrost was ignored, a simplification justified by the negligible effect of permafrost in the 3D single phase models.

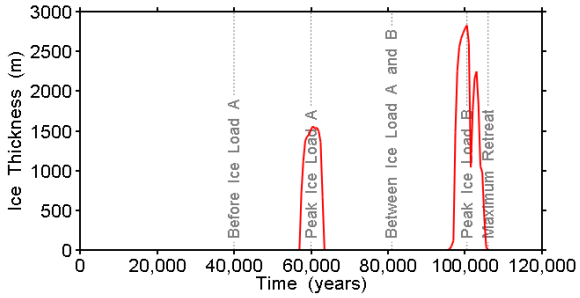

Figure 2. Ice thickness above repository for first cycle of the glaciation scenario.

MODELLING APPROACH

The 2D model is a vertical north-south slice, the assumed direction of glacial advance and retreat. The location of the 2D slice is shown in Figure 1. While the slice cuts through the repository location, repository details are not included in the model. The model focus is on effects of glaciation on the groundwater flow regime. With a single-phase model, the 2D model was found to compare well to a 3D model, indicating the 2D slice captures the essential flow attributes of the glacial groundwater flow regime. Figure 3 compares the hydraulic head between a 2D and 3D single phase model, both models using FRAC3DVS (Therrien et al., 2010), a 3D finite-element / finite-difference code for groundwater flow and solute transport that utilizes the same 1D hydromechanical model as implemented in TOUGH2.

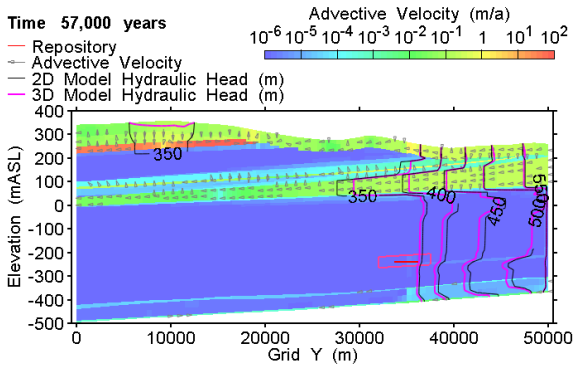

Figure 3. Hydraulic head comparison between single-phase 2D and 3D models.

Vertical discretization is based on digital elevation models of geologic formation tops, extending from the Pre-Cambrian to the top of bedrock, and including recent Pleistocene overburden

deposits at surface, as shown in Figure 4. The density of the grid on the right hand side is a result of formation sub-cropping merging into the weathered bedrock/overburden zone. The grid has 12 000 nodes.

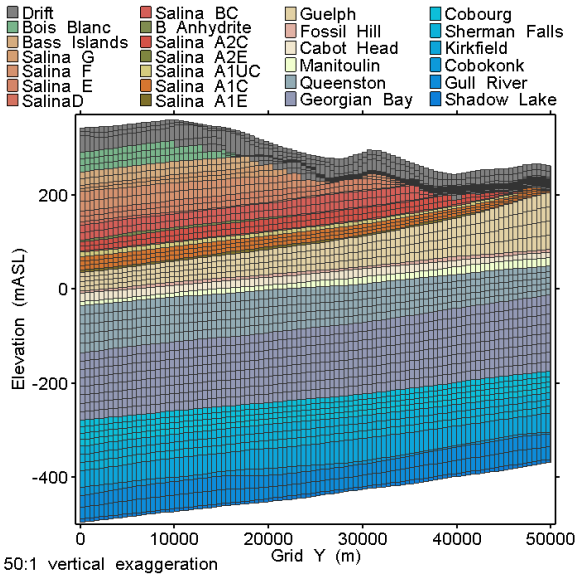

Figure 4. 2D vertical model slice grid and properties.

The repository is located within the Cobourg formation, which has a vertical permeability of 2×10^{-15} m^2, a porosity of 0.015, a van Genuchten $1/\alpha$ parameter of 61.7 MPa, a pore compressibility of 1.58×10^{-9} Pa^{-1}, and a loading efficiency of 0.8. Material properties for all formations are provided in NWMO (2013).

A warm-based glacier is assumed, with the result that the ice thickness can be converted to a hydraulic head surface boundary condition. The glacial ice thickness is converted to a pressure, assuming an ice density of 900 kg/m^3, and applied to the top of the model as a time-variable boundary condition. At the north and south sides of the model, time-variable boundary conditions are defined by propagating the surface pressure downwards. For glacial advance and retreat only, the vertical loading rate is calculated as the derivative of the surface hydraulic head with respect to time.

The gas in the Ordovician is assumed to be methane, with a Henry's coefficient of 7.2×10^{-11} Pa^{-1} (Quintessa and Geofirma, 2011).

Initial gas saturation within the formations is not known with precision, and reference case initial gas saturation is assumed to be 10% in all Ordovician units. In the 2D model shown in Figure 4, the Ordovician units are all units below and including the Queenston formation. All units above the Ordovician are assumed fully liquid water saturated. Sensitivity cases exploring different initial gas saturations are presented in a subsequent section.

COMPARISON OF SINGLE-PHASE AND TWO-PHASE RESULTS

The glacial groundwater flow regime for single-phase groundwater is compared to the flow regime for the two-phase flow reference case, with initial gas saturations of 10% in the Ordovician units.

Groundwater head and velocity changes correspond to glacial events. Figure 5 shows the groundwater head and velocity impacts during glacial advance, the glacier advancing from the right. The impacts of the glacial advance are more apparent in the fully saturated units. The presence of gas is apparent in the reduced heads in the Ordovician units, below approximately 0 mASL.

Figure 6 shows the gas saturation profile at various times during the fifth glacial cycle. The various profile times are illustrated in Figure 2. Gas saturation decreases during glacial loading, due to the greater compressibility of gas relative to water during loading, resulting in a smaller volumetric ratio of gas. Gas saturations begin to vary between formations, due to different capillary pressures in each zone, with gas preferring formations with low capillary pressure.

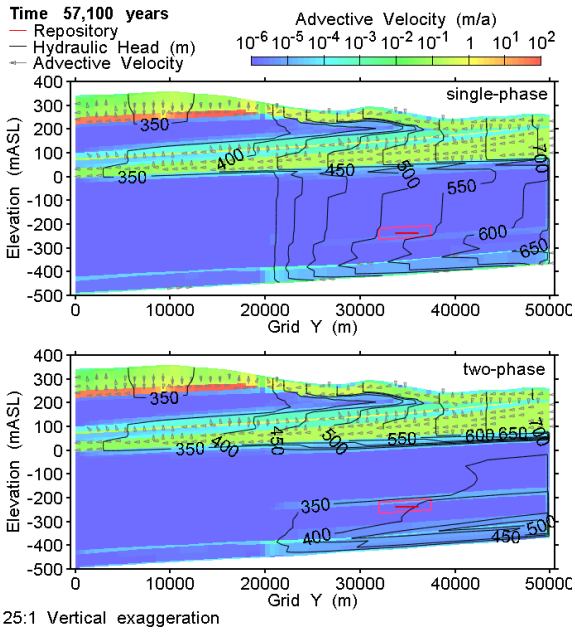

Figure 5. Groundwater head and velocity during glacial advance for the single phase case (above) and two-phase reference case with 10% initial gas saturation (below).

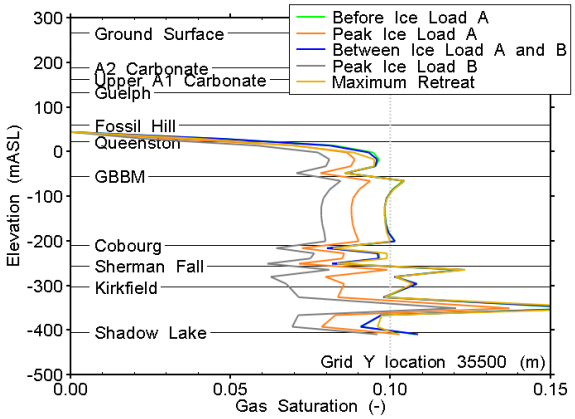

Figure 6. Gas saturation profiles at various times during the fifth glacial cycle.

As expected, the greater compressibility of gas significantly moderates the increase in head during glacial loading, as shown in Figure 7 for the fifth glacial cycle.

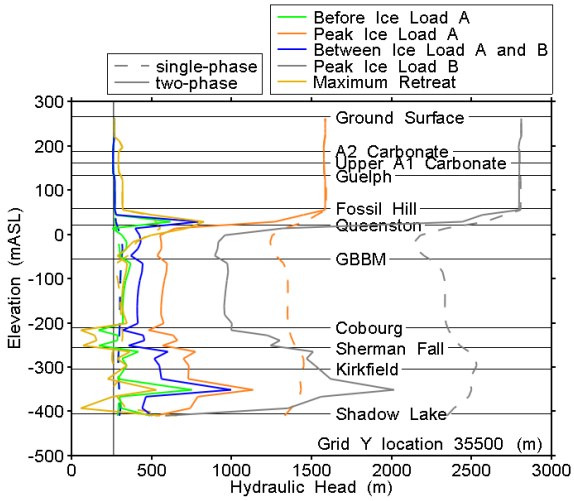

Figure 7. Hydraulic head profiles comparing single and two-phase groundwater flow.

Moderation of heads during glacial cycles does not translate to a moderation of vertical velocities. Maximum upward vertical velocities, of interest from a transport perspective, are shown in Figure 8 for three Ordovician formations during the fifth glacial cycle. Upward vertical velocities in the repository formation are increased due to differences in the vertical head profile, such as an increase in the head gradient during glacial loadings. The exception is the Queenston formation during glacial loading, when upward velocities are decreased.

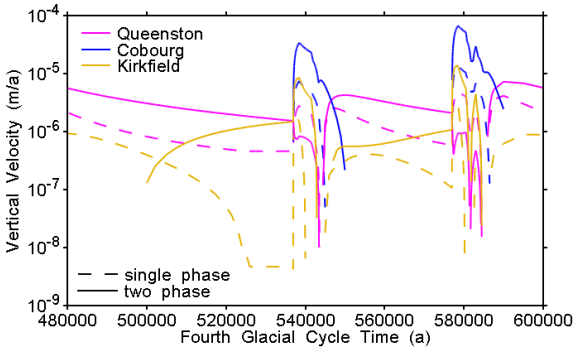

Figure 8. Maximum upward vertical velocities during fifth cycle in selected formations.

Figure 9 shows the head and vertical velocity at a single point at the repository horizon (in the Cobourg formation), over the course of all 8 glacial cycles. There is very little incremental change between each cycle, with a very small increase in head with each cycle and no apparent change in vertical velocity.

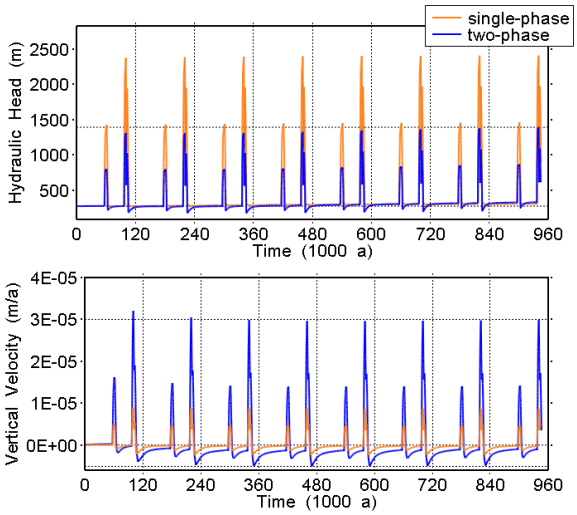

Figure 9. Head and vertical velocity at the repository location for all glacial cycles.

SENSITIVITY CASES – 2%, 5% AND 15% INITIAL GAS SATURATION

Three sensitivity cases investigated the impact of initial gas saturation. As might be expected, higher gas saturations result in greater moderation of heads, and conversely, lower gas saturations have less impact, as shown in Figure 10. The moderation in head is not linear, and the incremental decrease in head during glacial loading decreases with increasing saturation. Gas saturations, as shown in Figure 11 for the fifth glacial cycle, remain relatively constant in profile except when ice loads are applied. The change in saturation increases with increasing initial gas saturation, both between periods in the glacial cycle, and between formations; for example, the high gas saturations in the Coboconk formation located below the Kirkfield formation.

Maximum vertical velocities, while increased compared to the single-phase case, are similar between the different initial gas saturation sensitivity cases, as shown in Figure 12. This is due to the similarity of the head gradient (not head magnitude) within the Ordovician units of each case.

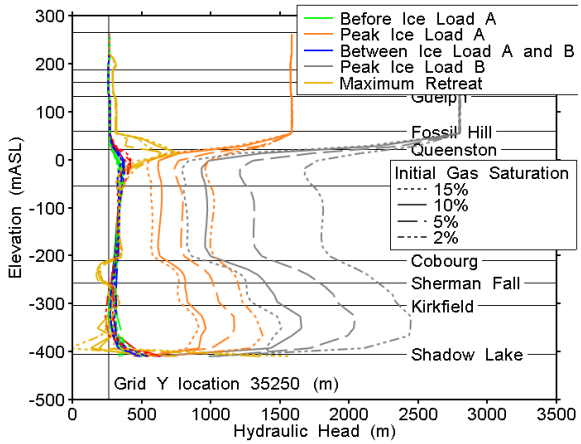

Figure 10. Hydraulic head profiles in the fifth glacial cycle, comparing various initial gas saturations.

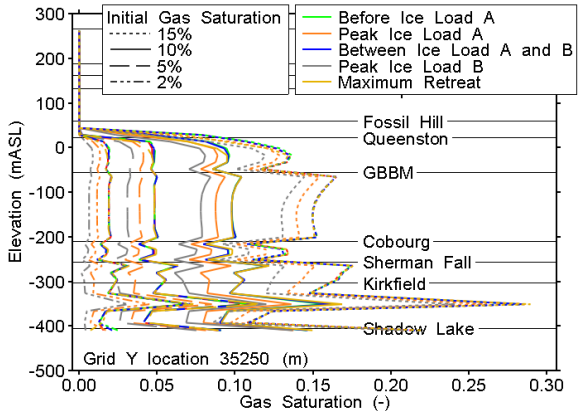

Figure 11. Gas saturation profiles in the fifth glacial cycle, comparing various initial gas saturations.

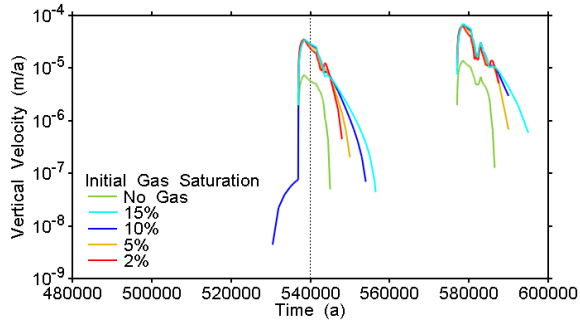

Figure 12. Maximum upward vertical velocities during fifth cycle in the Cobourg formation for various initial gas saturations.

CONCLUSIONS

TOUGH2, coupled with a 1D hydromechanical model, assessed the impact of glacial events on heads and velocities at a hypothetical deep geological repository in a sedimentary sequence. The results of this modelling show that the presence of gas, even at low saturations, can significantly moderate the head increase expected during glaciation events. This moderation in head does not necessarily translate to a reduction in velocities, which increased at the repository horizon for the case presented here. Increases or decreases in velocity, of interest from a transport perspective, will be affected by the change in the head profile caused by gas saturation and its distribution between different formations. While velocities at the repository horizon increased due to the presence of gas, the increase is small relative to the overall increase in velocity due to the glaciation event.

ACKNOWLEDGMENT

The authors thank the NWMO for continued support.

REFERENCES

INTERA, *Descriptive Geosphere Site Model*, Nuclear Waste Management Organization Report NWMO DGR-TR-2011-24 R000, Toronto, Canada, 2011.

Neuzil, C, *Hydromechanical coupling in geological processes*, Hydrogeology Journal, 11, 41-83, 2003.

NWMO, *Adaptive Phased Management Postclosure Safety Assessment of a Used Fuel Repository in Sedimentary Rock Pre-Project Report,* Nuclear Waste Management Organization Report NWMO TR-2013-07, Toronto, Canada, 2013.

Oerlemans, J, *Glaciers and Climate Change*, Swets and Zeitlinger BV, Lisse, 2001.

Pruess, K., C. Oldenburg, and G. Moridis, *TOUGH2 User's Guide*, Version 2.0, Report LBNL-43134, Lawrence Berkeley National Laboratory, Berkeley, Calif., 1999.

Quintessa and Geofirma, OPG's Deep Geologic Repository For Low and Intermediate Level Waste Postclosure Safety Assessment: Data, Nuclear Waste Management Organization Report NWMO DGR-TR-2011-32, Toronto, Canada, 2011.

Rutqvist, J., and C.F. Tsang, *TOUGH-FLAC: A numerical simulator for Analysis of Coupled Thermal-Hydrologic-Mechanical Processes in Fractured and Porous Geological Media under Multi-phase flow Conditions*, Proceedings, TOUGH2 Symposium 2003, Berkeley, California, 2003.

Therrien, R., R.G. McLaren, E.A. Sudicky, S.M. Panday and V. Guvanasen, *FRAC3DVS_OPG: a three-dimensional numerical model describing subsurface flow and solute transport. User's Guide*, Groundwater Simulations Group, University of Waterloo, Ontario, Canada, 2010.

Walsh, R., N. Calder and J. Avis, *A Simple Implementation of 1D Hydromechanical Coupling In TOUGH2*, PROCEEDINGS, TOUGH Symposium 2012, Berkeley, California, September 17-19, 2012.

Wang, H., *Theory of Linear Poroelasticity with Application to Geomechanics and Hydrology*, Princeton University Press, Princeton, USA, 2000.

MODELING OF GAS MIGRATION THROUGH LOW-PERMEABILITY CLAY USING INFORMATION ON PRESSURE AND DEFORMATION FROM FAST AIR INJECTION TESTS

Rainer Senger[1], Enrique Romero[2], Paul Marschall[3]

[1] Intera Incorporated, Richland, WA 99354
[2] Department of Geotechnical Engineering and Geosciences, UPC, Barcelona, Spain
[3] Nagra, Wettingen, Switzerland
e-mails: rsenger@intera.com; enrique.romero-morales@upc.edu; paul.marschall@nagra.ch

ABSTRACT

The characterization of gas migration through low-permeability clay formations has been a focus of R&D programs for radioactive waste disposal, which is also of great importance for shale-gas exploration, and cap-rock behavior of hydrocarbon reservoirs and CO_2 sequestration.

Laboratory tests on Opalinus clay cores from a shallow borehole in the Mont Terri Underground Research Laboratory (URL) and from a deep borehole in northern Switzerland included specific water and air injections tests, as well as oedometer and isotropic compression tests. For tests under different confining stress conditions, the rock compressibility was determined and the measured deformation was used to estimate changes in void ratio and to derive a relationship between void ratio and stress, and the corresponding changes in permeability as a function of changes in porosity.

For the shallow cores from Mont Terri, largely linear-elastic deformation associated with the gas injection test could be inferred and the change in void ratio was accounted for by the pore compressibility. The corresponding change in permeability was obtained from the results of the water tests, indicating a log-linear relation between permeability and porosity. The derived porosity change and corresponding change in permeability was implemented in the standard TOUGH2 code, which reproduced the measured gas test results using fitted water-retention data derived from laboratory measurements.

Similar injection tests performed on Opalinus clay cores from the borehole at greater depth showed overall similar behaviour, but at lower permeabilities, lower pore compressibilities and lower changes in porosity. These cases indicated non-linear behaviour which was implemented using an effective stress-dependent porosity change and associated change in permeability. In addition, the anisotropy associated with the bedding of the clay formation was considered by assuming different properties for "soft" and "hard' layers to account for storage capacity for the injected gas prior to gas breakthrough. The computed change in the overall porosity could be compared to the measured axial deformation during the gas injection test and was used for calibration of the parameters describing the relationship between the effective stress and porosity and the corresponding change in permeability and capillary pressure.

INTRODUCTON

The National Cooperative for the Disposal of Radioactive Waste (NAGRA), Switzerland has developed a comprehensive program to characterize gas flow in the Opalinus Clay (OPA), one of the host rocks for a deep geological repository, through laboratory tests to determine the relevant hydraulic, geomechanical and two-phase properties, and to develop appropriate constitutive models through numerical analyses of the laboratory tests.

Understanding gas transport processes is an important issue in the assessment of radioactive waste repository performance and is the focus of paper. The actual gas migration mechanisms may entail standard two-phase flow or more complex mechanisms involving coupled two-phase geomechanical (Marschall et al., 2005) and possibly geochemical phenomena.

Laboratory tests on OPA cores from a shallow borehole (~300 m depth) in the Mont Terri Underground Research Laboratory (URL) and from a deep borehole (~800 m depth) in

northern Switzerland were described in detail by Romero et al. (2012), Romero and Gomez (2013) and Romero and Gonzalez-Blanco (2015).

AIR INJECTION TESTS ON SHALLOW CORES

The air-injection tests were performed using a high-pressure triaxial cell, which was specifically designed to apply isotropic/ anisotropic stress states and to inject water at specified gradients or inject air at a controlled volume rate while measuring the outflow at a downstream chamber as well as the axial deformation. A detailed description of the experimental setup for the different tests and analyses is given in Romero et al., 2012a, b). A schematic of the test configuration is shown in Figure 1.

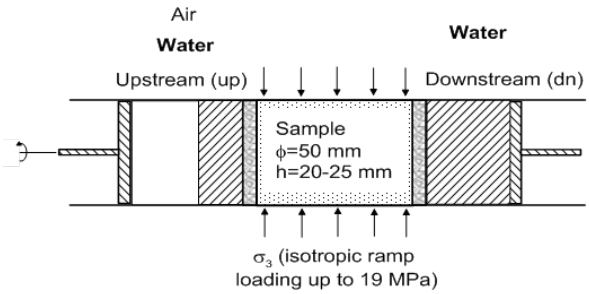

Figure 1. Schematic of the test configuration for the water and air injection tests under isotropic and anisotropic stress states (Romero et al., 2012b).

For the water test preceding the air-injection tests, prescribed gradient conditions were used to determine the hydraulic conductivities. For water tests under different confining isotropic stress conditions, the measured axial deformation on low-height specimen was used to estimate the change in void ratio and to derive a relationship between void ratio and stress, and the corresponding change in permeability as a function of changes in porosity.

The time evolutions of air-injection pressure during the fast controlled volume-rate air injection test at 100 mL/min on two shallow OPA core samples with two bedding plane orientations are shown in Figure 2 together with the pressure / volume outflow response and axial deformation. The injection pressure increased up to about 12 and 13 MPa (depending on the orientation), followed by a shut-in and recovery period. For the flow parallel to bedding, outflow response was observed immediately after shut-in, corresponding to a sudden drop in the injection pressure, followed by a subsequent gradual decline. The pressure in the fixed-volume outflow chamber rapidly increased until reaching 2 MPa, when a constant pressure was maintained through a release valve.

For the flow perpendicular to bedding, the injection pressure increased to 12 MPa and remained relatively flat after shut-in (Figure 2). The outflow response is significantly delayed compared to the case with flow parallel to bedding. Only after the apparent gas breakthrough did the injection pressure show a steep decline. This test indicated gas migration into the sample for certain time prior to gas outflow (i.e., gas breakthrough) at an injection pressure of 12 MPa which is significantly below the fitted van Genuchten (1980) capillary air-entry parameter of 18 MPa from the water retention data (Romero et al., 2012a).

The axial deformation revealed two different deformation regimes. For the test parallel to bedding (Figure 2), the initial pressure increase shows axial deformation at negative values indicating expansion. During the early period after shut-in, the pressure slightly decreased but the axial strain continued to increase. Afterwards, as the pressure continued to decrease, the axial deformation reversed indicating compression as the effective stress increased.

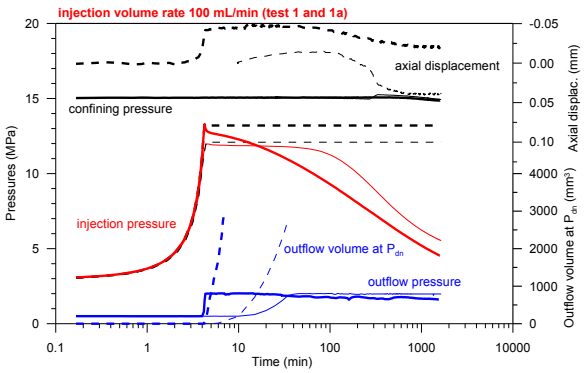

Figure 2. Measured pressures at the injection and outflow sides together with outflow data and axial displacements for the air injection test parallel (thick lines) and normal (thin lines) to bedding for shallow OPA core sample (from Romero et al., 2012a, b).

For the gas test with flow normal to bedding (Figure 2), the axial deformation indicates a similar pattern, although no measurements were available during the early injection period. During the early period after shut-in, very little change in pressure occurred, whereas the axial deformation went negative indicating expansion. At late time, the axial deformation reversed as the pressure decline steepened indicating compression. The axial deformation, reflecting the changes in void ratio, indicates that during the injection period expansion and a corresponding increase in void ratio occurred associated with gas migration into the pore space of the core sample and effective stress decrease due to pore pressure increase. This expansion continued beyond the shut-in as the gas pressure front propagated into the sample causing the fluid pressure to increase and the effective stress to decrease. At late time after the pressure in the outflow chamber started to increase, the injection pressure declined and the effective stress increased, indicating compression.

Modeling Approach

For the analysis of the air-injection tests, the test configuration was implemented in a numerical model using the two-phase flow code TOUGH2 (Pruess et al., 1999). In a first step, the measured results in terms of permeability, porosity, and pore compressibility, as well as the two-phase parameters derived from the water retention data were used as initial estimates for the inverse modeling using iTOUGH2 (Finsterle, 2007). The resulting simulations could not reproduce well the observed injection-pressure responses over the entire test and outflow responses for both air-pulse tests (parallel and normal to bedding). Moreover, the estimated parameters were significantly different from those derived from the measured retention curves and from the water tests (Senger et al., 2014).

A revised approach was then used taking into account the relations between void ratio and stresses (Romero et al., 2012a). Changes in porosity are accounted for in the standard TOUGH2 code through the pore compressibility, whereas the potential change in permeability is not. Assuming largely linear-elastic deformation associated with the gas injection test, the inferred change in void ratio can be accounted for by the pore compressibility. With the confining stress kept constant at 15 MPa during the air pulse injection tests, the variation in effective stress can be related to the variation in pressures. In TOUGH2 the effect of compressibility is accounted for by the change in porosity ($d\phi$) in response to a change in fluid pressure (dP) as:

$$d\phi = \phi C_p dP \qquad (1)$$

The corresponding change in permeability was obtained from the results of the water tests, indicating a log-linear relation between permeability and porosity (Romero et al., 2012a, b). For two-phase flow, the change in porosity/permeability also affects the capillary pressure, which is accounted for by the Leverett function (Leverett, 1941).

For the revised analysis only forward simulations were performed using the two-phase parameters based on the measured retention curve data and the estimated permeability from the water test (Table 1). The results of the simulations for the air-injection tests parallel and perpendicular to bedding planes are shown in Figure 3. The simulation, incorporating the coupling between the changes in porosity, due to pore compressibility associated with the increased pore-pressure, and the corresponding permeability changes reproduced both the injection pressure response and the outflow pressure response. The peaks of the outflow response are

due to the fact that the effect of the release valve at 2 MPa was arbitrarily set at a certain time after the gas breakthrough response.

Table 1. Model input parameter (shallow OPA)

	Test 1a (parallel)	Test 1 (normal)
Permeability: k (m^2)[a]	1.4E-19	4.3E-20
Porosity [-][a]	0.20	0.18
Pore compress. C_p [1/Pa][a]	2.0E-08	1.5E-08
van Genuchten: P_0 [Pa][b]	18.0E+6	18.0E+6
van Genuchten; n[b]	1.67	1.67
Res. water saturation: S_{lr}[c]	0.01	0.01
Res. gas saturation: S_{gr}[c]	0	0
Initial saturation (S_w)[c]	1	1

[a]measured, [b]fitted to WRC, [c]assumed

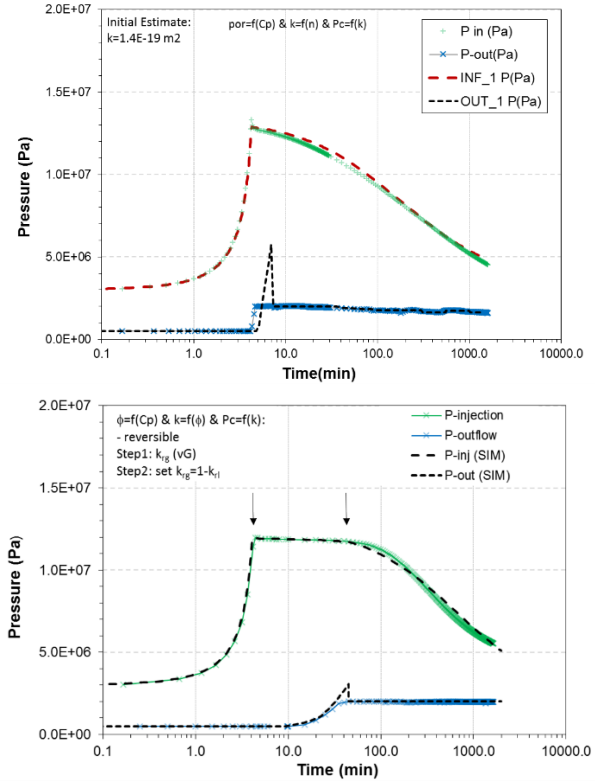

Figure 3. Simulated (dashed lines) and measured (solid lines) pressures for air-injection tests for flow parallel to bedding) (top), and for flow perpendicular to bedding (bottom) (modified from Senger et al., 2014); the arrows note the times for the profiles in Figure 4.

Figure 3 shows that the outflow response for the test perpendicular to bedding is significantly later than for the test parallel to bedding. That is, gas continues to migrate into the expanding pores prior to the breakthrough response. One can assume that preferential gas pathways are established resulting in higher gas mobility and less phase interference. This is represented by a Grant model for the gas relative permeability (e.g., $k_{rg} = 1\text{-}k_{rl}$), which produced the more rapid injection pressure decline following the gas breakthrough.

The computed changes in permeability due to the changes in porosity within the core during the air-injection test are shown together with the pressure and saturation profiles in Figure 4. After gas injection stopped (after 4.17 min), the gas pressure profiles indicate the gas front migrating into the sample. The computed permeability increases from the initial 4.3E-20 m^2 to 2.5E-19 m^2 corresponding to an increase in porosity from 0.18 to about 0.21 which, in turn, correlates to the axial displacements, shown in Figure 2. After 45 minutes - at about gas breakthrough - the increased permeability extends across the entire core corresponding to the maximum expansion of the core sample (Figure 2).

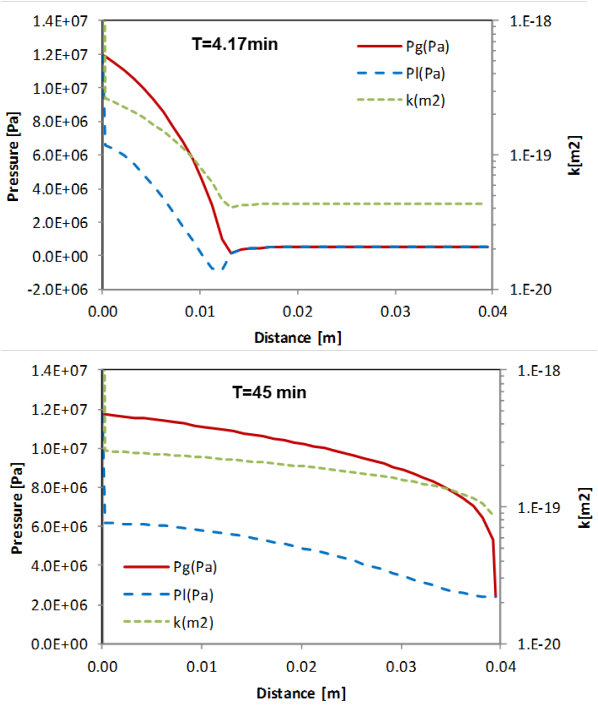

Figure 4. Computed vertical profiles of gas pressure (Pg), liquid pressure (Pl) and permeability (k) throughout the core height (perpendicular to bedding) after 4.17 min (top) and 45 min (bottom).

AIR INJECTION TESTS ON DEEP CORES

The air-injection tests on OPA core samples from a depth of about 800 m in the Schlattingen borehole in northern Switzerland showed overall similar responses (Figure 5) as those from the shallow borehole at Mont Terri (Figure 2). Only cores perpendicular to bedding were available from the deep borehole. Similar to the shallow analyses, a series of complementary tests were performed preceding the air injection tests, which included compression tests, water permeability tests, and water retention measurements which are described in detail in Romero and Gomez (2013).

The air injection test in Figure 5 was performed under isotropic stress conditions of 15 MPa. Compared to the shallow tests procedure, the deep tests measured the actual outflow volume increase instead of the pressure increase which was limited to a maximum of 2 MPa. Even though the overall response was similar, the deep cores indicated a significantly later outflow response (only after more than 100 min) compared to the shallow air injection test (Figure 2). Also, the injection pressure following shut-in after 4.2 minutes shows a more distinct decline, indicating gas flow into the sample. That is, the injected gas has to accumulate in the core until outflow response occurs.

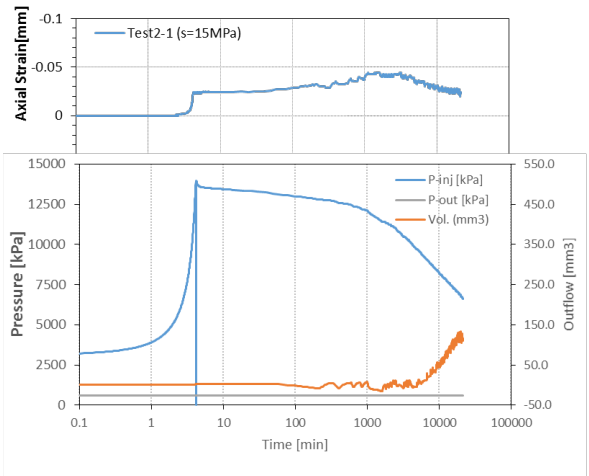

Figure 5. Measured pressures at the injection side and outflow volumes at the downstream side together with axial displacements for the air injection test perpendicular to bedding for a deep OPA core sample (after Romero and Gomez, 2013).

On the other hand, the maximum axial expansion of the deep core during the air injection test is similar to that of the shallow core (Figure 2). Moreover, the estimated compressibility from the compression tests and initial porosity is much lower than for the deep core sample. Potential non-reversible changes in the pore volume were indicated by the measured pore size distributions before and after the air-injection tests, changing to a bi-modal pore size distribution with new "pores" having two orders of magnitude higher entrance pore size (Romero and Gonzalez-Blanco, 2015).

Table 2 summarizes the properties of the deep OPA core sample, indicating also higher suction with a fitted van Genuchten parameter P_0 of 34 MPa (Romero and Gomez, 2013). This information together with the additional parameters is used as input for the numerical modeling described below.

Table 2. Model input parameter (deep OPA)

	Test 2-1 (normal)
Permeability: k (m^2)[a]	1.3E-21
Porosity: ϕ_r [-][a] (ϕ_o)	0.1 (0.15)
Pore compress. C_p [1/Pa][a]	1.0E-09
van Genuchten: P_0 [Pa][b]	34.0E+06
van Genuchten; n[b]	1.58
Res. water saturation: S_{lr}[c]	0.01
Res. gas saturation: S_{gr}[c]	0
Initial saturation (S_w)[c]	1
Coefficient: α [1/Pa] (soft)	1.0, (0.6)
Factor for k-ϕ: c	10
Enhancement factor for k_{rg}	10
[a]measured, [b]fitted to wrc, [c]assumed	

Modeling Approach

The observed responses from the deep core sample suggest more complex phenomena of gas migration through the clay implying non-linear behavior associated with pathway dilation.

For this analysis, the layering of the OPA is explicitly implemented by alternating layers of different material properties. This allows preferential gas migration into "softer" interlayers having somewhat higher permeability before migrating to the next interlayer. The gas migra-

tion front in the axial direction is thus retarded and provides greater storage capacity for the observed gas flow into the sample prior to gas breakthrough.

In addition, the potential changes in hydraulic properties are described as a function of effective stress, using the empirical function given by Rutqvist et al. (2002):

$$\phi = \phi_r + (\phi_0 - \phi_r)e^{-\alpha\sigma'} \qquad (2)$$

where ϕ_0 is zero effective stress porosity, ϕ_r is the residual porosity at high effective stress, and the exponent α is a rock parameter. The addition of the residual porosity ϕ_r results in a relatively steep increase in porosity in the low effective-stress range. An associated exponential function for permeability as a function of porosity is given by (Rutqvist et al., 2002):

$$k = k_0 e^{c(\frac{\phi}{\phi_0}-1)} \qquad (3)$$

where k_0 is the initial reference permeability and c is a rock specific parameter (Table 2). Figure 6 (top) shows the computed effective stress, based on the total stress of 15 MPa, and the injection pressure response through time. The computed porosity as a function of effective stress assumed a parameter α = 0.6 Pa^{-1} for the 'soft' interlayer (Table 2). The computed porosity shows a steep increase when the peak injection pressure and lowest effective stress is reached (Figure 6 top), which compares with the steep volume expansion indicated by the axial displacement (Figure 5).

The corresponding porosity and permeability as a function of effective stress (Figure 6, bottom) show an exponential increase with decreasing effective stress. The permeability depends largely on the coefficient 'c' in Equation (3), which was set to 10 (Table 2) in Figure 6 (bottom).

Compared to the previous air injection tests on the shallow OPA cores (Figure 1), the boundary condition on the outflow was changed. In order to directly simulate the volume increase, a relatively high pore compressibility was assigned to the element representing the outflow chamber.

Any mass flow into the outflow chamber and corresponding pressure increase is represented by an increase in porosity, which can be converted to a volume increase for comparison with the measured volume increase of the outflow chamber.

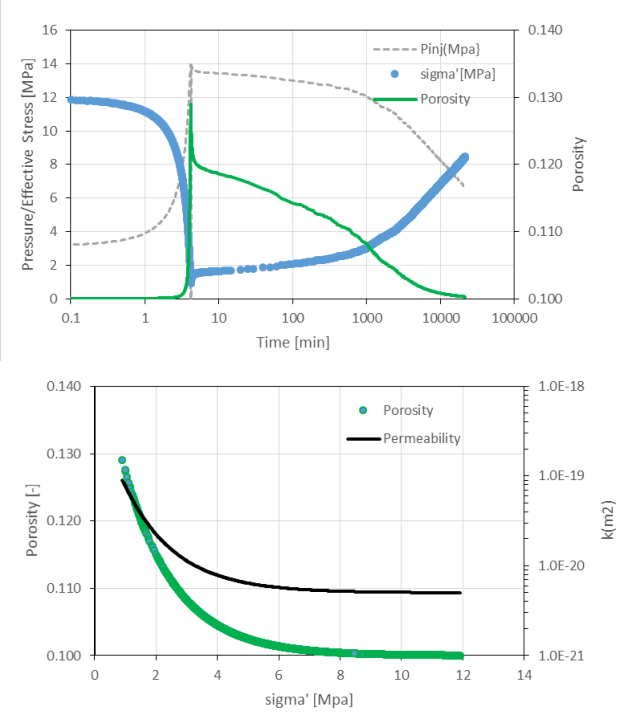

Figure 6. Injection pressure, effective stress and computed porosity based on Equation 2 (top) and corresponding permeability based on Equation 3 (bottom), representing the maximum changes at the upstream boundary of the core (see Figure 4).

In order to more realistically represent the bedding of the OPA core, a 2D random heterogeneous porosity/permeability field was generated to reproduce the typical anisotropy of the OPA formation. For the soft interlayers, the porosity increase was estimated using an α parameter of 0.6 Pa^{-1}, compared to the hard layers for which the parameter was set to 1 Pa^{-1}. An enhancement factor for the gas relative permeability has been also considered to account for the higher mobility when a gas path has developed (instead of arbitrarily setting $k_{rg}=1-k_{rl}$).

The results for this simulation are shown in Figure 7 in terms of time evolutions of the

simulated injection pressure (top) and the computed outflow volume (bottom). The simulated injection pressure shows relatively little decline following the shut-in and a later pressure recovery compared to the measured injection pressure. At late time, the pressure recoveries are similar. On the other hand, the computed outflow volume shows an earlier increase compared to the measured response, indicating an earlier gas breakthrough but at a similar rate. The comparison suggests a somewhat higher gas flow into the sample prior to the gas breakthrough, requiring an increase in gas permeability and associated accumulation of the injected air in the dilated pathways without a connection to the outflow boundary.

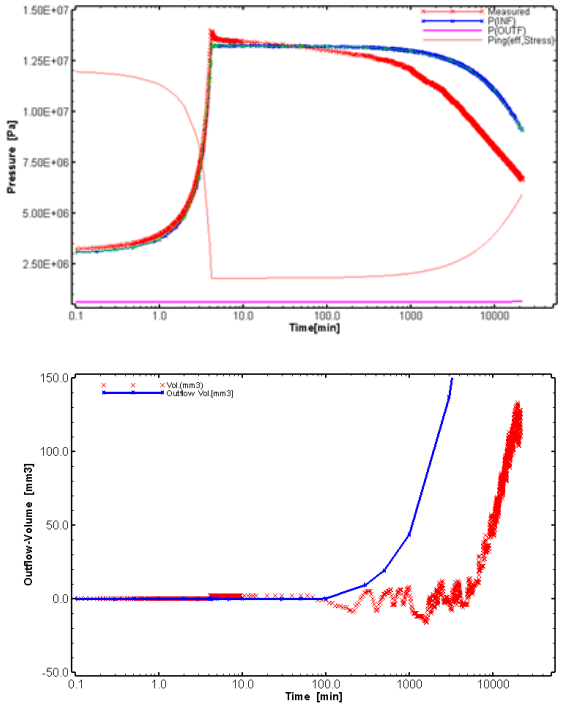

Figure 7. Simulated and measured injection pressures (top), and computed outflow volume increase for comparison with measured outflow volume.

The system response is depicted in Figure 8 in terms of the spatial distribution of gas saturation, porosity, and gas permeability after 100 minutes, when the gas front reaches the outflow boundary at the top. The gas saturation indicates relatively large variability due to the permeability variations within layers and between layers.

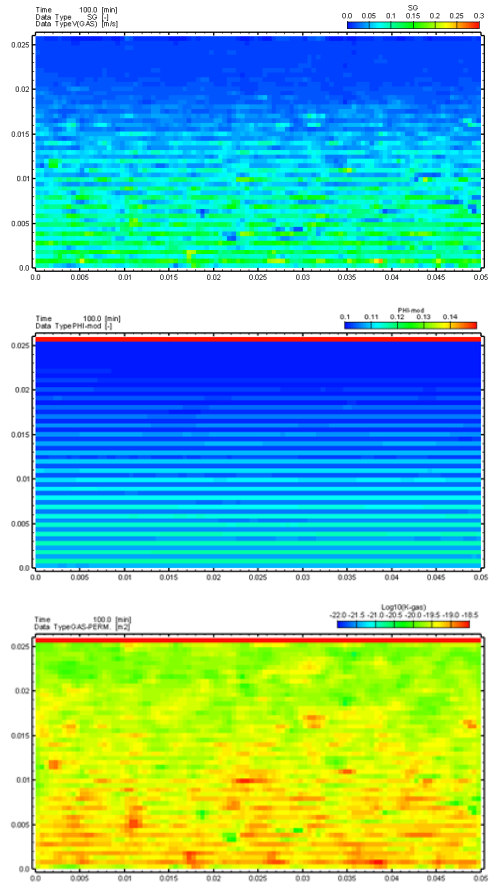

Figure 8. Simulated distribution of Sg (top), porosity (middle), and gas permeability (bottom) after 100 min.

SUMMARY AND OUTLOOK

The detailed analyses of laboratory experiments on Opalinus Clay cores were used to develop a conceptual and numerical model for simulating two-phase flow of gas through a low-permeability clay formation. The specific test configuration of the fast air-injection tests complemented by isotropic compression test, water permeability test, and water retention measurement provided consistent data sets which are enhanced by the measured displacement during the air-injection tests. The air-injection test responses for the shallow OPA cores could be reasonably well reproduced assuming standard two-phase flow accounting for the change in porosity associated with the measured pore compressibility and for the change in permeability and capillary pressure. The results of the air-injection tests of the deep OPA cores indicated overall similar behavior in terms of

pressure responses and measured axial displacement as the shallow cores. However, the implied changes in porosity and permeability required more complex processes associated with creation of additional pore space through pathway dilation. Existing models of stress-dependent porosity/permeability changes could not reproduce both the injection pressure response and outflow response, even when accounting for the layered structure of the OPA, assuming soft and hard layers. These models are limited in that the change in porosity is uniform for all pores. In reality, only certain pores or pore-size fraction may undergo micro fissuring producing oriented higher-permeable pathways. Such phenomena will be evaluated in further studies.

ACKNOWLEDGMENT

This study has been performed under contract from the National Cooperative for the Disposal of Radioactive Waste (NAGRA), Switzerland.

REFERENCES

Finsterle, S., *ITOUGH2 User's Guide*, Report LBNL-40040, Lawrence Berkeley National Laboratory, Berkeley, Calif., 2007.

Leverett, M.C., Capillary behaviour in porous solids, *Transactions of the AIME* 142, 159–172, 1941.

Marschall, P., Horseman, P., and T. Gimmi, Characterization of gas transport properties of the Opalinus Clay, a potential host rock formation for radioactive waste disposal, *Oil and Gas Science and Technology*, 60, 121-139, 2005.

Pruess, K., C. Oldenburg, and G. Moridis, *TOUGH2 User's Guide, Version 2.0*, Report LBNL-43134, Lawrence Berkeley National Laboratory, Berkeley, Calif., 1999.

Romero, E., Senger, R., and Marschall, P., Air injection laboratory experiments on Opalinus Clay, Experimental Techniques, Results and Analyses: 3rd EAGE Shale Workshop, Barcelona, 23-25 January, 2012a.

Romero, E., Senger, R., Marschall, P., and Gómez, R., Air tests on low-permeability claystone formations. Experimental results and simulations, *in* Multiphysical Testing of Soils and Shales. L. Laloui & A. Ferrari (eds.). Springer-Verlag, Berlin: 68-83, 2012b.

Romero, E., and Gomez, R., Water and air permeability tests on deep core samples from Schlattingen SLA-1 borehole; Material characterization and experimental set-up. Compressibility on loading, water permeability and air injection results, NAGRA Report NAB 13-51, 2013.

Romero, E. and Gonzalez-Blanco, L., Complementary water and air permeability tests on core samples from Schlattingen SLA-1 borehole, NAGRA Report NAB 15-06, 2015.

Senger, R.K., E. Romero, A. Ferrari, and P. Marschall, Characterization of gas flow through low-permeability claystone: Laboratory - experiments and two-phase flow analyses, in Norris et al., Clays in natural and engineered barriers for radioactive waste confinement, Geological Society, London, Special Publication, 400, 2014.

Rutqvist J, Wu Y-, Tsang C-, Bodvarsson G., A modeling approach for analysis of coupled multiphase fluid flow, heat transfer, and deformation in fractured porous rock, *Int J Rock. Mech Min Sci* 39, 429–442, 2002.

van Genuchten, M.Th. A closed-form equation for predicting the hydraulic conductivity of - unsaturated soils, *Soil Sci. Soc.Am. J.,* 44, 892 – 898, 1980.

PRELIMINARY ANALYSES AND NUMERICAL MODELING OF THE GAS PERMEABLE SEAL TEST (GAST) AT THE GRIMSEL TEST SITE, SWITZERLAND

T. Spillmann[1], R. Senger[2], George W. Lanyon[3], Niels Giroud[1], Paul Marschall[1]

[1] Nagra, Wettingen, Switzerland
[2] Intera Incorporated, Richland, Washington, USA
[3] Fracture Systems, Cornwall, United Kingdom
thomas.spillmann@nagra.ch, rsenger@intera.com, bill@fracture-systems.co.uk, niels.giroud@nagra.ch, paul.marschall@nagra.ch

ABSTRACT

Gases (hydrogen, methane, carbon dioxide) may accumulate in the emplacement caverns of a geological repository for low/intermediate-level waste (L/ILW) due to the corrosion and degradation of the wastes thereby producing hydraulic overpressures in case of a low permeability clay host rock. While it is assumed that the excavation damaged zone (EDZ) is the main pathway for gas pressure release, gas permeable backfill and tunnel seals have been proposed as an additional option to release a part of the gas into the operations and access tunnels while still maintaining low hydraulic conductivity thereby limiting radionuclide transport.

Laboratory tests indicated that mixtures of 80% sand, 20% bentonite combine the required low water permeability with enhanced gas permeability.

Two larger scale experiments have been implemented to demonstrate the effective functioning of the sand/bentonite mixture for gas permeable tunnel seals. The medium scale Mock-up experiment features a cylindrical sand/bentonite body of 0.6 m length and 0.54 m diameter. High-permeable filter elements at both ends facilitate water and gas tests with pressures up to the vessel's design pressure of 2 MPa. The design-analogue large scale Gas Permeable Seal Test (GAST; 8 m length, 3.0 m diameter) was implemented at the end of a gallery in the granitic rocks of the Grimsel Test Site and instrumented for detailed monitoring (e.g., total pressures, pore pressures, relative humidity, etc.). For GAST water and gas injection pressures up to 5 MPa were considered as design values and approximation of the expected hydrostatic pressures in a repository seal at ~500 m depth.

Simulations of the experiments were implemented in 3-D integrated finite-difference (IFD) grids using the TOUGH2 code. In a first phase, a number of scoping simulations were performed to explore the effect of the potential range in permeability of the sand/bentonite, the variation in the van Genuchten parameters and water-injection procedures on the saturation of the sand/bentonite and subsequent gas flow through the bentonite. In the second phase, interpretive models were developed to analyze the actual measurements.

Mock-up scoping simulations with water permeabilities of 10^{-16}, 10^{-17} and 10^{-18} m^2 resulted in saturation times of 7, 30 and 120 days and steady state flow of 2.4, 0.24 and 0.024 ml/min.

Scoping simulations for GAST predicted three to ten years for partial and full saturation. The available observations since construction in mid 2012 allowed first interpretive assessments of the material parameters and saturation behavior. The observations during the very early saturation phase showed the development of preferential flow paths and anisotropic permeabilities associated with the layer-wise construction of the sand/bentonite in the GAST. Modelling this behavior turned out to be a significant challenge.

INTRODUCTION

Opalinus Clay has become the preferred host rock for a repository for low and intermediate-level waste (L/ILW) in Switzerland (Nagra, 2014a). Opalinus Clay is characterized by a low permeability and is, therefore, an excellent barrier against radionuclide transport. Gas migration in a L/ILW repository is a critical component within the safety assessment of proposed deep repositories in low-permeability formations. In L/ILW repositories, anaerobic corrosion of metals and degradation of organic materials produce mainly hydrogen and methane. The generation, accumulation, and release of these gases from the disposal system may affect a number of processes that influence the long-term radiological safety of the repository (Nagra, 2008; Senger, 2011). It is anticipated that the main gas transport pathway is along the excavation damaged zone of the tunnel wall which has a higher permeability compared to the undisturbed clay host rock.

With the concept of the "engineered gas transport system" (EGTS), a backfill and sealing system was developed that allows the controlled transport of gases along the access structures. In order to enhance the understanding and estimate parameters at the larger scale required for reliable prediction, performance demonstration experiments have been built.

This paper presents simulations of two experiments aimed at improving the upscaling of the performance of an 80/20 sand/bentonite seal.

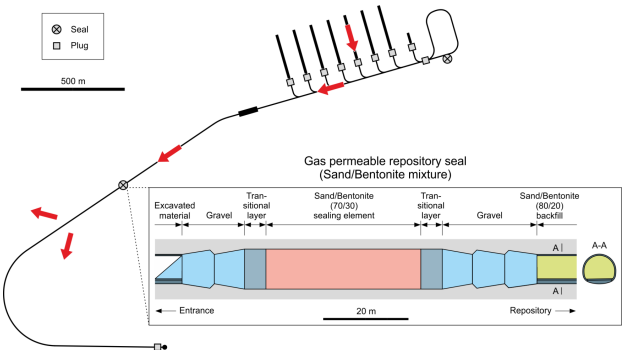

Figure 1. Nagra's generic concept for an L/ILW repository and EGTS gas migration paths (red arrows). Inlay shows access tunnel seal (after Nagra 2008).

EGTS CONCEPT

According to the generic repository concept (see Figure 1), the repository consists of seven to eight parallel caverns sealed off from a single access tunnel / ramp (Nagra, 2014b). The backfilling and seals constitute the EGTS. It has been developed to increase the gas transport capacity of the backfilled underground structures without compromising the radionuclide retention capacity of the engineered barrier system (Nagra, 2008).

High-porosity cementitious mortar will be used to fill the void spaces within the emplacement caverns (Figure 1). After backfilling of a cavern, it is closed with a concrete plug. Each emplacement cavern is linked to the operation tunnel by a branch tunnel. The repository seal (Figure 1) separates the access tunnel in the host rock from the backfilled ramp and contact with the overlying confining rock units.

Sand/bentonite mixture

The material foreseen for access tunnel backfill is a mixture of sand and bentonite. Sand/bentonite mixtures have significantly lower gas entry pressure than pure compacted bentonite of equivalent water permeability, and the sand content allows the gas permeability to be adjusted to a desired value. The use of bentonite in the mixture further ensures good sorption for many radionuclides, self-sealing and a low hydraulic conductivity and thus ensures the barrier functionality (Dixon et al., 2002; JAEA, 1999; Mata Mena, 2002).

Laboratory testing of 80/20 sand/bentonite (Kunigel V) as reported in Senger et al. (2006) for the RWMC Gas Migration Test (GMT) showed relatively low suction as a function of saturation. The wetting curve data was fitted with a van Genuchten parameter model using a capillary strength parameter P_0 ~40 kPa and a shape parameter n = 2.5.

For the large-scale tests considered here a mixture of 20% Wyoming MX-80 bentonite and 80% sand was used. Recent laboratory tests at EPFL (Nagra, 2013) for samples compacted at 1.5 and 1.8 Mg/m^3 were fitted with a van Genuchten model with entry pressures varying between 10 and 360 kPa dependent on dry density wetting/drying curve and the suction

range over which the model was fitted (see Figure 2).

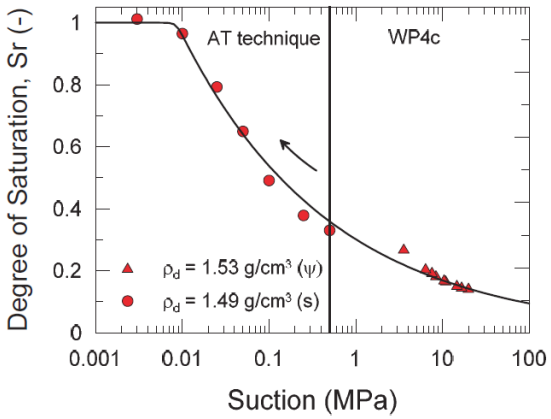

Figure 2. Water *retention curve (saturation versus suction) for 80/20 sand/bentonite mixture at 1.5 g/cm^3 dry density (from Nagra, 2013). AT: axis translation, WP4c: dewpoint psychrometer.*

Laboratory tests on the sand/bentonite have typically been at scales of cms. In order to investigate large scale saturation and gas transport behavior two large tests: the FORGE Mock-up and the GAST field test have been developed.

FORGE MOCK-UP EXPERIMENT SCOPING CALCULATIONS

The FORGE Mock-up is a fully instrumented medium scale experiment to investigate sand/bentonite water and gas permeabilities and investigate potential chemical interaction between cementitious mortar and sand/bentonite.

Figure 3 shows the confining steel cylinder which is 0.92 m long, having an outer diameter of 0.62 m, a 10 mm thick wall, and flange type covers at both ends (ID = 600 mm). To prevent bypass of the sand/bentonite buffer a 4.3 cm-thick annulus of granular bentonite surrounds the sand/bentonite body. Two highly permeable mortar filter elements (used for water and gas injection) confine the test cylinder. Figure 3b shows the simplified numerical grid model for mock-up scoping simulations. The numerically challenging permeability contrast between filter element and sand/bentonite body was alleviated by implementing a thin transition zone.

A key parameter in the model was the as-emplaced water permeability, which is a function of the dry density achieved by compaction.

a)

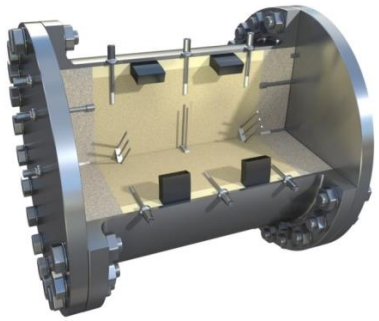

b)

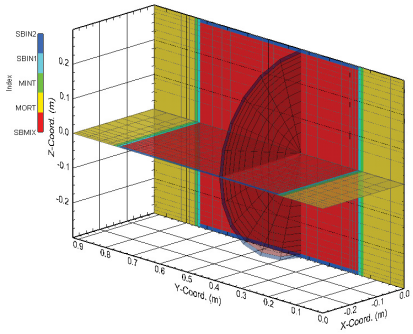

Figure 3. a) Cut-away view of FORGE Mock-up, showing the stainless steel cylinder, mortar filters, granular bentonite and sand/bentonite body and sensors; b) simplified mesh for TOUGH2 scoping calculations.

Simulations for selected modelling cases with water permeabilities of 10^{-16}, 10^{-17} and 10^{-18} m^2 predicted saturation times of 7, 30 and 120 days and prescribed injection pressure of 2 MPa, resulting in simulated steady state flow of 2.4, 0.24 and 0.024 ml/min. The low permeability case showed the best agreement with the Mock-up measurements and this value of water permeability was selected as the reference case for the full-scale GAST experiment simulations.

Subsequent gas injection tests (post-water saturation) and post-mortem dismantling indicated the development of a low permeability alteration layer within the Mock-up at the interface between the sand/bentonite with the mortar. It is therefore possible that the development of this layer may have affected late time response to saturation, resulting in an underestimate of the unaffected water permeability of the as-compacted sand/bentonite. Laboratory studies are under way to characterize potential chemical

alterations in sand/bentonite near the mortar interface.

GAST EXPERIMENT

EXPERIMENT AND MODEL DESIGN

To demonstrate the effective functioning of gas permeable tunnel seals, a large-scale experiment has been implemented in the crystalline rock in the Swiss Alps. The construction at the end of a 3.5 m diameter tunnel boring machine (TBM) tunnel in the Grimsel Test Site provides a stiff boundary with negligible Excavation Damage Zone (EDZ). The hydraulic conductivity of the EDZ in the vicinity of the GAST tunnel is believed to be in the same range or lower than that of the seal.

The seal element (Figure 4a) consists of 23 layers of compacted sand/bentonite with a length of 8m and target intrinsic permeability of 10^{-18} m^2. Vertical sand filters were emplaced at both ends for later water and gas injections. Two walls, made of compacted bentonite blocks and granular bentonite, constituted the watertight seal at the tunnel end and at the confining bulkhead.

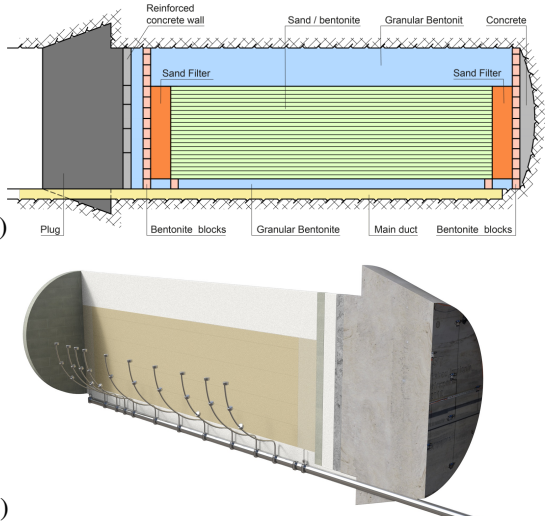

Figure 4. a) GAST experimental layout and b) cut-away visualization showing sand/bentonite and granular bentonite bodies and instrument risers and main duct below the tunnel.

Sensors are placed at the rock wall and at the tops of selected sand/bentonite layers. Cables and lines from the sensors are routed to the risers and then to the main duct that runs below the seal as shown in Figure 4b.

The radial rock/buffer interfaces and head space were filled with granular bentonite material to obtain a tight seal against the surrounding host rock and to minimize preferential water and/or gas flow paths along interfaces. Selected numerical meshes are shown in Figure 5a -c.

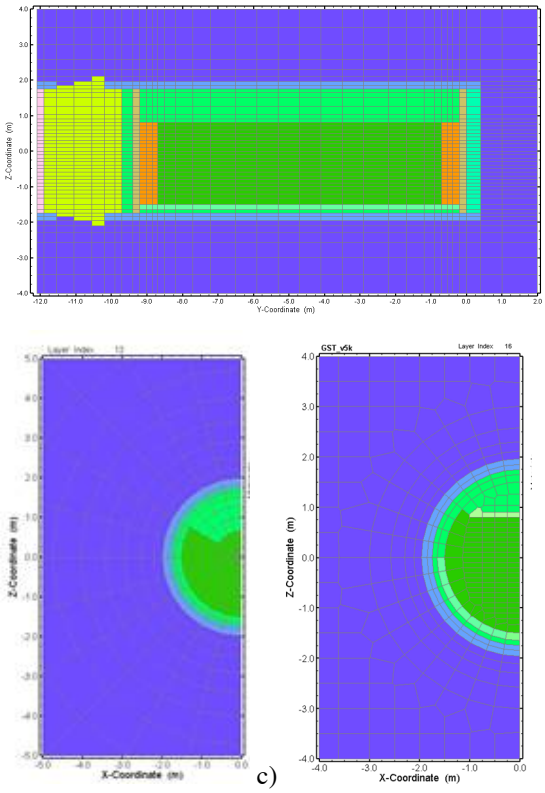

Figure 5. a) Numerical grid, longitudinal cross-section, b) head space scoping grid, c) realistic grid with head space at the top and interface zones at the bottom and top of the sand/bentonite..

A rigorous quality assurance programme including on-site and laboratory measurements provided a robust description of the as-emplaced system. The first phase of the experiment is saturation of the buffer after which hydraulic and gas tests will be performed to evaluate the efficiency and functioning of the seal.

MODELLING RESULTS

Scoping calculations

Scoping calculations for the GAST experiment were performed during the planning phase to

help design the saturation process and identify requirements for the injection equipment. Sensitivity studies varying the buffer material parameters and host-rock permeability were performed.

Model grids developed over time from (i) simple cylindrical representation of the sand/bentonite to (ii) detailed models accounting for the head space filled with granular bentonite(Figure 5b), and to (iii) more realistic representations of the as-emplaced system, approximating the layered sand/bentonite section surrounded by granular bentonite (Figure 5c).

The simulated saturation prediction from selected case (ii) is shown in Figure 6. In the models, water is injected at constant pressure (40 bar) from one of the filters (S14, at left in Figure 5a) while the downstream filter (S02) was kept at atmospheric pressure.

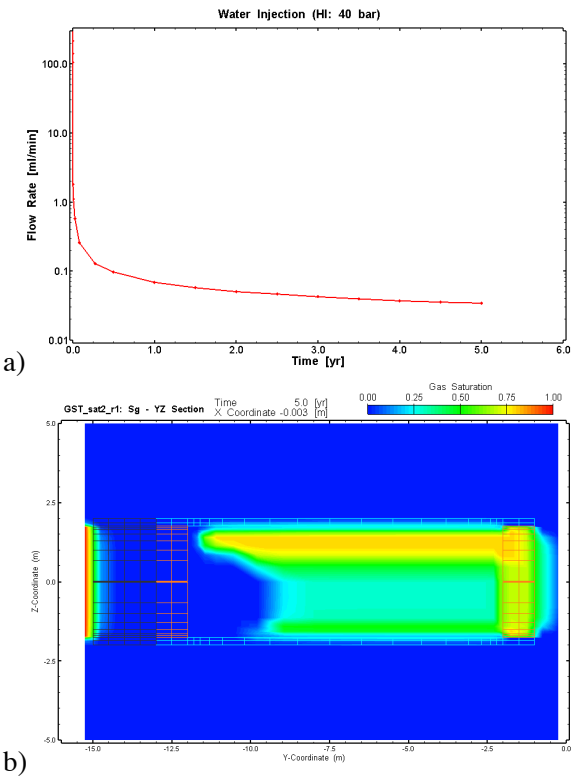

Figure 6. TOUGH2 scoping calculations showing a) injection flow versus time and b) gas saturation at 5 years.

The results of the scoping simulations using a constant pressure injection showed that between 30 to 50% of the buffer volume would be saturated within one to five years (Figure 6), respectively. Depending on the permeability, long-term flow rates of about 1 to 0.1 ml/min were established after one year and reduce gradually with ongoing saturation.

The effect of the granular bentonite headspace on buffer saturation time is small. Despite its higher initial suction, the lower permeability of granular bentonite limits water uptake and headspace saturation is retarded.

Interpretation modelling

A revised TOUGH2 model has been developed to support interpretation of the GAST experiment. The injection sequence was implemented as time-varying boundary conditions and best-estimate material properties based on the QA data from construction were used.

Figure 7 shows the injection rate and selected pore pressure data from the first 550 days from the start of injection. A low constant injection rate was set initially to minimize erosion or piping of the bentonite. The injection rate was increased after pore pressure response in the sand/bentonite buffer was observed. Key features of the measured response are the relatively low injection pressures and the pressurization of the downstream filter (S02) after approximately 350 days (Figure 7). The pressure response in the downstream filter (S02) suggests that a hydraulic flow path developed between the two sand filters possibly at the bottom of the bentonite along the connection of the risers (Figure 4b).

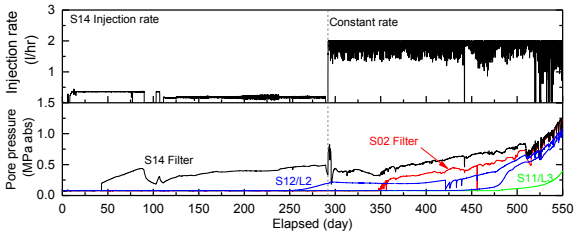

Figure 7. Injection rate and measured pore pressure over first 550 days from start of injection.

Figure 8 shows the simulated distribution of pressures (gas phase) and saturation at 350 days after the start of the injection. The potential permeability enhancement was accounted for by a significant increased permeability after 292 days along the bottom of the bentonite (by a factor of 10,000 in horizontal direction). The

simulation results show that the left (S14/water injection) sand filter is fully saturated and pressurized to approximately 5MPa. The sand/bentonite in the lower layers is also water saturated with some pressure developing. The base of the downstream filter (S02) has been saturated by water drawn from the upper part of the filter. The bulk of the buffer and granular bentonite is partially saturated and at atmospheric pressure. Some water from the surrounding granite rock has been drawn into the granular bentonite at the top of the head space.

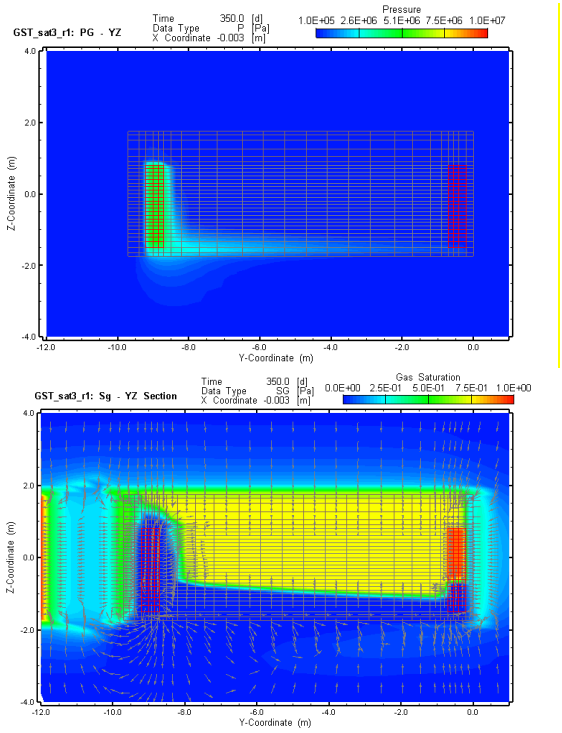

Figure 8. Interpretation model vertical cross-section along tunnel axis showing pressures (top) and gas saturations (bottom) at 350 days.

Figure 9 shows the predicted pressure and saturation at 500 days. The increased pressure in the water injection filter (~10MPa) at the base of the sand/bentonite is clearly seen. Simulated pressures have also developed in the granular bentonite above the S14 filter and in the rock below the filter. The right filter has also saturated through the lower layers of the sand/bentonite. The upper layers of the sand/bentonite and the granular bentonite above it remain partially saturated. The granular bentonite at the rear of the tunnel (right) also remains unsaturated.

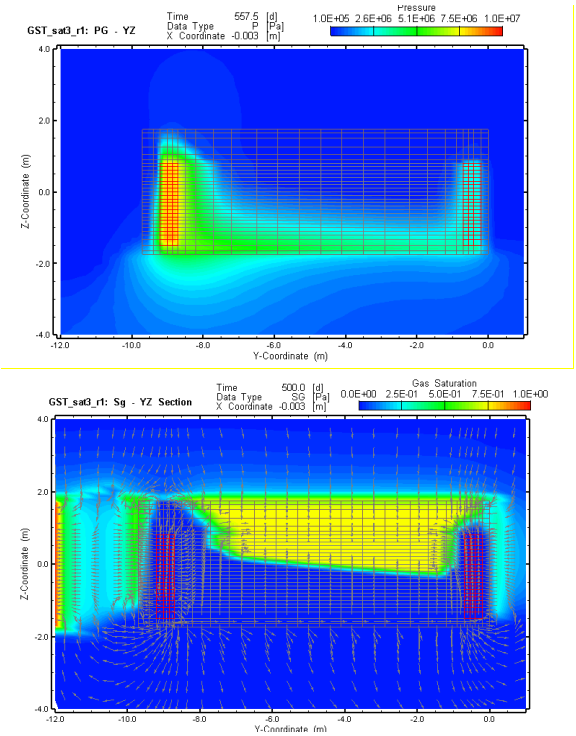

Figure 9. Interpretation model vertical cross-section along tunnel axis showing pressure (top) and saturation (bottom) at 500 days.

The high pressures in the initial interpretation simulations were inconsistent with the observations and a series of models were developed where:

1) Bentonite/sand permeability was increased by factor 100 at start of constant rate injection; or

2) The initial water saturation of the sand/bentonite was reduced; or

3) The horizontal bentonite/sand permeability was increased by a factor of 10 and a more permeable interface was included at the sides and top of the sand/bentonite (see Figure 5c).

The corresponding distributions of simulated pressures and gas saturations are shown in Figure 10 and 11. In this revised modeling case, the injection pressures were greatly reduced (~2MPa at 550 days) and the downstream (S02) filter becomes pressurized via flow along a high-permeable interface along the bottom of the tunnel.

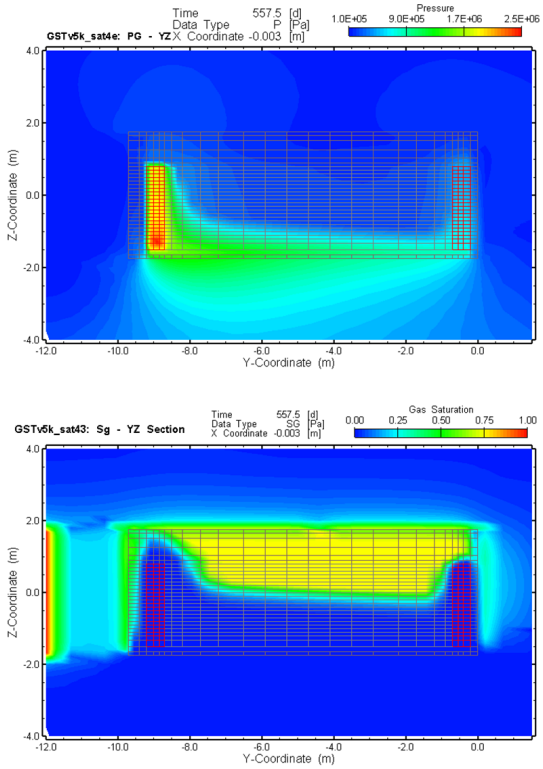

Figure 10. Revised Interpretation model vertical cross-section along tunnel axis showing pressures (top) and gas saturation (bottom) at 550 days.

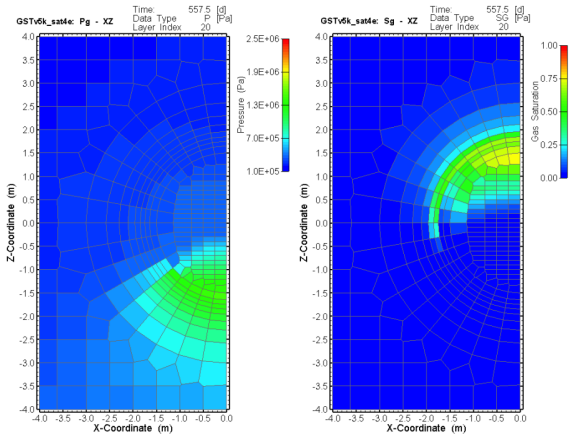

Figure 11. Revised Interpretation model vertical cross-section perpendicular to tunnel axis showing pressures (left) and gas saturation (right) at 550 days (shown in color area mode).

Figure 12 shows a comparison of the model and measured pressures for selected sensors during the early phase of saturation and for the first 258 days of the constant rate injection (2 l/hr) that was initiated after 292 days.

The modelled and measured pressures show reasonable agreement until the start of the constant rate injection (292 days) when the measured water injection (S14) filter pressure initially increases to approximately 0.85 MPa but then quickly drops despite the continued injection. The simulated pressure in the injection filter increases sharply to values considerably higher than the expected stresses.

In part the modelled over-estimate of filter pressure could be due to underestimate of the bulk sand/bentonite permeability but the observed pressure response also indicates potential hydromechanically coupled processes associated with possible low effective stress conditions within and around the buffer.

Flow along the simulated interface around the sand/bentonite results in a slightly slower pressurization of the downstream (S02) filter than was observed. Piezometer responses in the base of the sand/bentonite at Level 2 and Level 3 close to the S14 filter show reasonable matches.

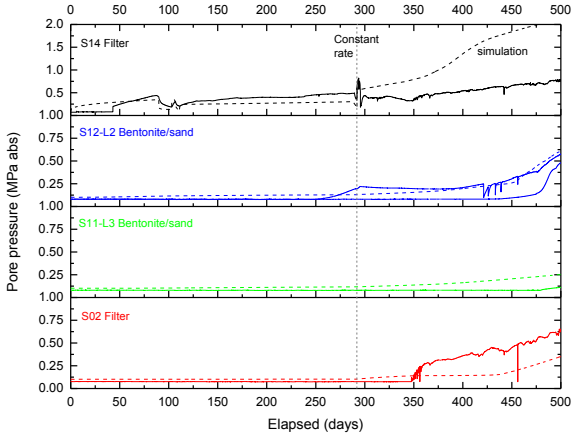

Figure 12. Comparison of simulated and measured pressure at the S14 (water injection) and S02 (gas injection) filters and three sensors in the lower part of the sand/bentonite in sections S12 and S11

OUTLOOK

TOUGH2 two-phase flow models have been used to design and interpret large-scale laboratory and field tests for a gas-permeable seal using a sand/bentonite buffer. These models have been based on small-scale laboratory characterization of the buffer material together with QA measurements from construction.

In order to obtain a better match to the observed saturation response in the GAST experiment it was necessary to include more permeable elements at the interface between the sand/bentonite and the granular bentonite providing a permeable path that links the two sand filters.

While the initial behavior of both the Mock-up and GAST field test were relatively well-described by the two-phase flow TOUGH2 models described here, additional processes relating to chemical interaction and coupled hydro-mechanical processes are believed to be potentially significant for understanding the long term saturation and gas injection (FORGE Mock-up) and higher pressure injection (GAST) phases of the experiments.

ACKNOWLEDGMENT

The authors would like to thank the GAST field team members from Aitemin, Solexperts and VSH. Dave McKey and Bruno Kunz (Nagra) are thanked for preparation of the visualizations in some the figures. The FORGE Mock-up experiment was performed within the framework of the EU FP7 Collaborative project (Forge 230357).

REFERENCES

Dixon, D., Chandler, N., Graham, J., & Gray, M. N. N. Two large-scale sealing tests conducted at Atomic Energy of Canada's underground research laboratory: the buffer-container experiment and the isothermal test. *Canadian Geotechnical Journal,* 39(3), 503–518. doi:10.1139/T02-012 2002.

JAEA, *H12: Project to establish the scientific and technical basis for HLW disposal in Japan* ("H12 report" in short). Japan Atomic Energy Agency, 1999.

Mata Mena, C. *Hydraulic behaviour of bentonite based mixtures in engineered barriers: The Backfill and Plug Test at the Äspö HRL (Sweden)*. Doctoral Thesis Universitat Politecnica Catalunya, Barcelona, 2003.

Nagra, *Effects of post-disposal gas generation in a repository for low- and intermediate-level waste sited in the Opalinus Clay of Northern Switzerland*. Nagra Technical Report NTB 08-07. Nagra, Wettingen, 2008.

Nagra, *FORGE (Fate of Repository Gases) Final Laboratory Report Deliverables D3.34 and D3.36*. Nagra Arbeitsbericht NAB 12-62. Nagra, Wettingen, 2013.

Nagra, *SGT Etappe 2: Vorschlag weiter zu untersuchender geologischer Standortgebiete mit zugehörigen Standortarealen für die Oberflächenanlage Sicherheitstechnischer Bericht zu SGT Etappe 2 Sicherheitstechnischer Vergleich und Vorschlag der in Etappe 3 weiter zu untersuchenden geologischen Standortgebiete*. Nagra Technical Report NTB 14-01. Nagra, Wettingen, 2014a.

Nagra, *Sensitivity analyses of gas release from a L/ILW repository in the Opalinus Clay in the candidate siting regions of Northern Switzerland*. Nagra Arbeitsbericht NAB 13-92. Nagra, Wettingen, 2014b.

Senger, R., G.W. Lanyon, P. Marschall, S. Vomvoris, and A. Fujiwara, *TOUGH2/iTOUGH2 analysis of the gas migration test (GMT) at the Grimsel Test Site (Switzerland)*. Proceedings, TOUGH Symposium 2006, Lawrence Berkeley National Laboratory, Berkeley, California, May 15–17, 2006.

Senger, R., J. Ewing, K. Zhang, J. Avis, P. Marschall, and I. Gaus, *Modeling Approaches for Investigating Gas Migration from a Deep Low/Intermediate Level Waste Repository (Switzerland)*, Transport in Porous Media, 90, 113-133, 2011.

COUPLED THMC MODELS FOR BENTONITE IN CLAY REPOSITORY FOR NUCLEAR WASTE USING TOUGHREACT-FLAC3D

Liange Zheng, Jonny Rutqvist and Jens T. Birkholzer

Lawrence Berkeley National Laboratory (LBNL)
Berkeley, California 94720, USA
e-mail: lzheng@lbl.gov

ABSTRACT

Illitization, the transformation of smectite to illite, could compromise some beneficiary features of an engineered barrier system (EBS) that is composed primarily of bentonite and clay host rock. It is a major determining factor to establish the maximum design temperature of the repositories because it is believed that illitization could be greatly enhanced at temperatures higher than 100°C and thus significantly lower the sorption and swelling capacity of bentonite and clay rock. However, existing experimental and modeling studies on the occurrence of illitization and related performance impacts are not conclusive, in part because the relevant couplings between the thermal, hydrological, chemical, and mechanical (THMC) processes have not been fully represented in the models. Here we present fully coupled THMC simulations of a generic nuclear waste repository in a clay formation with bentonite-backfilled EBS. Two scenarios were simulated for comparison: a case in which the temperature in the bentonite near the waste canister can reach about 200°C and a case in which the temperature in the bentonite near the waste canister peaks at about 100°C.

The model simulations demonstrate that illitization is in general more significant at higher temperatures. We also compared the chemical changes and the resulting swelling stress change for two types of bentonite: Kunigel-VI and FEBEX bentonite. Higher temperatures also lead to much higher stress in the near field, caused by thermal pressurization and vapor pressure buildup in the EBS bentonite and clay host rock. Chemical changes lead to a reduction in swelling stress, which is more pronounced for Kunigel-VI bentonite than for FEBEX bentonite.

INTRODUCTION

The temperature to which the EBS and natural rock can be exposed is one of the most important design variables for a geological repository. This is especially important for a clay repository, because argillaceous rocks have relatively small heat conductivity. All disposal concepts throughout the world, despite their differences in design concepts, unanimously impose a temperature limit of about 100°C (Hicks et al., 2009). Chemical alteration and the subsequent changes in mechanical properties are among the determining factors. A high temperature could result in chemical alteration of buffer and backfill materials (bentonite) within the EBS through illitization and cementation, which compromise the function of these EBS components by reducing their plasticity and capability to swell when wetting (Pusch and Karnland, 1996; Pusch et al., 2010; Wersin et al., 2007).

Regarding the concern of chemical alteration and the associated mechanical changes, Wersin et al. (2007), after reviewing a number of data sets, concluded that the criterion of 100°C for the maximum temperature within the bentonite buffer is overly conservative. The impact of a high temperature on bentonite and clay host rock behavior, and the consequences on repository performance, are largely open questions for a clay repository system. While various studies shed light on certain aspects of this question, there is no study that integrates the relevant THMC processes and considers the interaction between EBS and host rock.

In this paper we present coupled THMC modeling to evaluate the chemical alteration and mechanical changes in EBS bentonite and the NS (natural system) clay formation under various scenarios, attempting to provide necessary information for decisions on temperature limits.

THE THMC SIMULATOR TOUGHREACT-FLAC3D

The numerical simulations are conducted with TOUGHREACT-FLAC3D, which sequentially couples the multiphase fluid flow and reactive transport simulator, TOUGHREACT (Xu et al., 2011), with the finite-difference geomechanical code FLAC3D (Itasca, 2009). The coupling of TOUGHREACT and FLAC3D was initially developed in Zheng et al. (2012) to provide the necessary numerical framework for modeling fully coupled THMC processes. It included a linear elastic swelling model (Zheng et al., 2012; Rutqvist et al., 2014) to account for swelling as a result of changes in saturation and pore-water composition and the abundance of swelling clay (Liu et al., 2013; Zheng et al., 2014).

MODEL DEVELOPMENT

Modeling Scenario

The model is applied to a hypothetical bentonite-backfilled nuclear waste repository in clay rock, a repository example that involves a horizontal nuclear waste emplacement tunnel at 500 m depth (Figure 1) (Rutqvist et al., 2014). The Z-axis is set as vertical, while the horizontal Y- and X-axes are aligned parallel and perpendicular to the emplacement tunnel, respectively (Figure 1) in this 2-D model.

An initial stress field is imposed by the self-weight of the rock mass. Zero normal displacements are prescribed on the lateral boundaries of the model. Zero stress is applied to the top and vertical displacements are prevented at the bottom. An open boundary is applied to the liquid pressure at top and bottom and initially the model domain is in a hydrostatic state. The initial temperature at the top is about 11°C, with a thermal gradient of 27 °C/km, the initial temperature at the bottom is 38°C. The model simulation was conducted in a nonisothermal mode with a time-dependent heat power input (Rutqvist et al., 2014). The power curve in Figure 1 was adopted from representative heating data from the U.S. DOE's Used Fuel Disposition campaign for pressurized water reactor (PWR) used fuel. This heat load is then scaled in the 2D model to represent an equivalent line load, which depends on the assumed spacing between individual waste packages

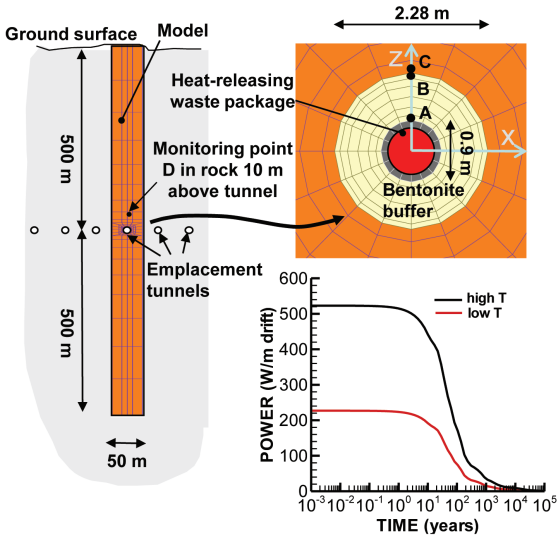

Figure 1. Domain for the test example of a bentonite back-filled horizontal emplacement drift at 500 m (Rutqvist et al., 2014). Modeling monitoring points: *A: inside the bentonite near the canister, B: inside the bentonite and near the EBS-NS interface, C: inside the clay rock formation and near the EBS-NS interface, D: inside the clay rock formation at a distance of 10 m from the canister. "High T": 200 ºC; "Low T": 100ºC.*

along an emplacement tunnel. The heat load for the "low-T" case corresponds to an initial thermal power of 3144 W for a 4-PWR-element waste package after aging for 60 years, a 50-m spacing between emplacement tunnels, and 3-m spacing between the 5-m long packages. The heat load for the "high T" case represents similar waste package and spacing, except with only 20 years of aging. The thermal and hydrological properties of bentonite and clay formation are listed in Table 1. Initially the EBS bentonite has a water saturation of 65% and the clay formation is fully saturated. From time zero, the EBS bentonite undergoes simultaneously re-saturation, heating, chemical alteration, and stress changes.

The two bentonites selected in this study, FEBEX and Kunigel bentonite, differ in their mineralogy and initial pore-water composition. They also have distinct hydrological and thermal parameters; however, the most relevant of these, thermal conductivity and permeability, are actually fairly similar for both bentonites. Therefore, in this paper, we use identical thermal and

hydrological parameters for both bentonites, but different chemical parameters. By having the same thermal and hydrological parameters, we can isolate the effect of variation in chemical parameters on stress changes.

Table 1. Thermal and hydrological parameters.

Parameter	Clay Formation	EBS Bentonite
Grain density [kg/m^3]	2700	2700
Porosity ϕ	0.162	0.33
Saturated permeability [m^2]	2.0×10^{-20}	2.0×10^{-21}
Relative permeability, k_{rl}	$m = 0.6$, $S_{rl} = 0.01$	$K_{rl} = S^3$
Van Genuchten α [1/Pa]	6.8×10^{-7}	3.3×10^{-8}
Van Genuchten m	0.6	0.3
Compressibility, β [1/Pa]	3.2×10^{-9}	5.0×10^{-8}
Thermal expansion coeff., [1/ºC]	1.0×10^{-5}	1.5×10^{-4}
Dry specific heat, [J/kg ºC]	860	800
Thermal conductivity [W/m ºC] dry/wet, Λ_d/Λ_w	1.47*/1.7$	1.1/1.5
Tortuosity for vapor phase	$\phi^{1/3} S_g^{10/3}$	$\phi^{1/3} S_g^{10/3}$
Bulk modulus, (GPa)	4.17	0.02
Shear modulus, (GPa)	1.92	0.0067

*calculated by $\Lambda_d=(1-\phi)\Lambda_w$

$from http://www.mont-terri.ch/internet/mont-terri/en/home/geology/key_characteristics.html

Mechanical Model

Details of the mechanical model implemented in TOUGHREACT-FLAC3D are given in Rutqvist et al., (2014). Here we briefly describe the mechanical models for the EBS bentonite and clay formation. For nonisothermal behavior of unsaturated soils, we may partition the total incremental strain into elastic (ε^e), plastic (ε^p), suction (ε^s), thermal strains (ε^T) and chemical strains(ε^c):

$$d\varepsilon = d\varepsilon^e + d\varepsilon^p + d\varepsilon^s + d\varepsilon^T + d\varepsilon^c \qquad (1)$$

where the suction strain represents the strain associated with changes in suction and chemical strain represents the strains associated with change in chemical conditions, including changes in ion concentration and abundance of swelling clays. Each of these types of strain, except chemical strain, is described in Rutqvist et al. (2014).

Similar to thermally induced strains, chemical strains are purely volumetric:

$$d\varepsilon^c = -A_n^* dC + A_{sc}^* dMs \qquad (2)$$

Where A_n^* is a constant that linearly relates ion concentration (C) variation and the corresponding strain change. A_{sc}^* is a constant that relates the change in mass fraction of swelling clay, *Ms*, to change in strain.

A linear elastic swelling model essentially defines the suction stress as a function of water saturation:

$$d\varepsilon^s = \beta_{sw} dSl \qquad (3)$$

where *Sl* is the water saturation and β_{sw} is a moisture swelling coefficient.

Under mechanically constrained conditions and considering the linear relationship between swelling stress and suction strain, $d\sigma_s = 3Kd\varepsilon^s$, we have a swelling stress that is linearly proportional to the saturation:

$$d\sigma_s = 3K\beta_{sw} dSl \qquad (4)$$

where *K* is the bulk modulus. Equation (4) is what was used for EBS bentonite in Rutqvist et al. (2011). In this work, β_{sw} is 0.048, calibrated based using the swelling pressure of 1 MPa for Kunigel bentonite (Börgesson et al., 2001) under the condition that bentonite is saturated with dilute solution (e.g. deionized water), and *K* is 20 MPa (Rutqvist et al., 2011).

To consider the swelling due to both moisture and chemical changes, we include the stress due to a change of ion concentration in the pore water and abundance of swelling clay:

$$\begin{aligned} d\sigma_s &= 3K(d\varepsilon^S + d\varepsilon^C) \\ &= 3K(\beta_{sw} dSl + A_n^* dC + A_{sc}^* dMs) \\ &= 3K\beta_{sw} dSl + A_n dC + A_{sc} dMs \end{aligned} \qquad (5)$$

where $A_n = 3KA_n^*$ is a constant that linearly relates ion concentration (C) variation and the

corresponding swelling stress change. $A_{sc} = 3KA^*_{sc}$ is a constant that relates the change in mass fraction of swelling clay, *Ms*, to change in swelling stress.

A_n is typically calculated from swelling pressures measured using a different solution (e.g. deionized water versus 1 M NaCl solution) to saturate the bentonite. Laredj et al. (2010) proposed the following expression for A_n:

$$A_n = \frac{(5.312\ln C - 23.596)}{\sqrt{C}} - \frac{7.252\times10^{-4}}{C^2} \quad (6)$$

An empirical value for A_{sc} is derived through a linear regression of swelling pressure versus smectite mass fractions (Zheng et al., 2014). A_{sc} is 2.5×10^6 Pa for Kunigel bentonite and 6.5×10^6 Pa for FEBEX bentonite.

Chemical Model

In these generic cases, it is assumed that the host-rock properties are representative of Opalinus Clay (Lauber et al., 2000), that the EBS backfill is composed of either Kunigel bentonite (Ochs et al., 2004) or FEBEX bentonite (ENRESA, 2000). The mineral compositions of the bentonites and the clay formation are listed in Table 2.

Table 2. Mineral volume fraction (dimensionless, ratio of mineral volume to total volume of medium) of the Kunigel (Ochs et al., 2004),FEBEX bentonite (ENRESA, 2000) and Opalinus Clay(Bossart 2011; Lauber et al., 2000).

Mineral	EBS Bentonite: Kunigel-V1	EBS Bentonite: FEBEX	Clay formation: Opalinus Clay
Calcite	0.016	0.0065	0.093
Dolomite	0.018	0.0	0.050
Illite	0.000	0.0	0.273
Kaolinite	0.000	0.0	0.186
Smectite	0.314	0.6	0.035
Chlorite	0.000	0.0	0.076
Quartz	0.228	0.026	0.111
K-Feldspar	0.029	0.0065	0.015
Siderite	0.000	0.0	0.020
Ankerite	0.000	0.0	0.045

The pore-water composition of the Kunigel bentonite (Sonnenthal et al., 2008), FEBEX bentonite (Fernández et al., 2001) and the clay formation (Fernández et al., 2007) are given in Table 3. Illitization is modeled as the dissolution of smectite and precipitation of illite. The overall reaction can be written as:

$$\text{Smectite} + 0.52H^+ + 0.63AlO_2^- + 0.6K = \text{illite} + 0.26H_2O + 0.08Mg^{+2} + 0.33Na^+ + 0.5SiO_2(aq) \quad (7)$$

Table 3. Pore-water composition of Kunigel bentonite (Sonnenthal et al., 2008), FEBEX bentonite Fernández et al., 2001) and Opalinus Clay (Fernández et al., 2007).

	EBS Bentonite: Kunigel-V1	EBS Bentonite: FEBEX	Clay formation: Opalinus Clay
pH	8.40	7.72	7.40
Cl	1.50E-05	1.60E-01	3.32E-01
SO_4^{-2}	1.10E-04	3.20E-02	1.86E-02
HCO_3^-	3.49E-03	4.1E-04	5.18E-03
Ca^{+2}	1.37E-04	2.2E-02	2.26E-02
Mg^{+2}	1.77E-05	2.3E-02	2.09E-02
Na^+	3.60E-03	1.3E-01	2.76E-01
K^+	6.14E-05	1.7E-03	2.16E-03
Fe^{+2}	2.06E-08	2.06E-08	3.46E-06
$SiO_2(aq)$	3.38E-04	1.1E-04	1.10E-04
AlO_2^-	1.91E-09	1.91E-09	3.89E-08

MODEL RESULTS

THC Evolution

The evolution of heat release from decaying waste is shown in Figure 1. The heat release rates have been adjusted to make two cases for comparison: a "high T" case, in which the temperature near the canister can reach 200 °C; and a "low T" case, in which the temperature near the canister peaks at about 100 °C. In this report, the temporal evolution at the four monitoring points (shown in Figure 1) is used to present thermal, hydrological, chemical and mechanical results: point A is inside the bentonite near the canister, point B is inside the bentonite near the EBS-NS interface, point C is inside the clay formation near the EBS-NS interface, and point D is inside the clay formation at a distance of 10 m from the canister. The temperature evolution at points A and D are

shown in Figures 2 and 3 respectively. After 100,000 years, as expected from the heat release function shown in Figure 1, the temperature drops to about 27 °C. The bentonite becomes fully saturated in about 20 years for the "low T" case and in about 35 years for the "high T" case. The clay formation near the EBS-NS interface goes through desaturation for a short time period. Pore pressure increases as a result of re-saturation and heating, as exemplified by the pore pressure evolution at point A in Figure 4.

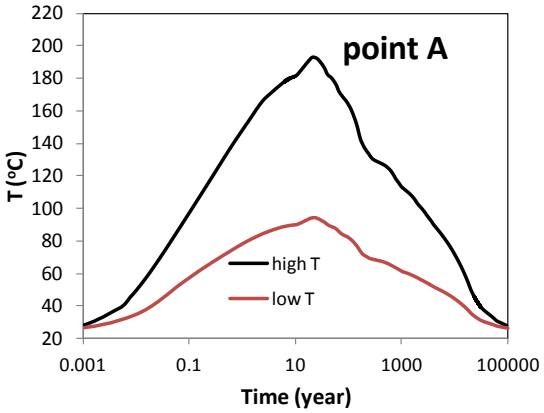

Figure 2. Temperature evolution at point A.

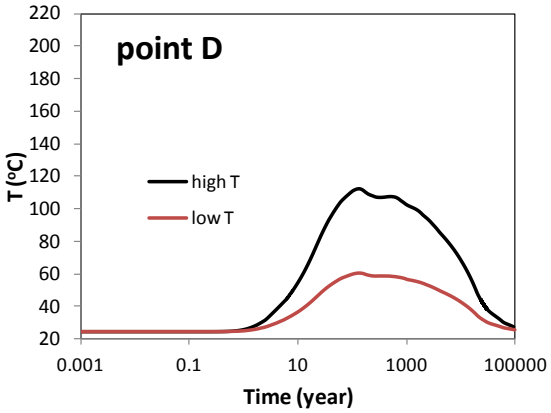

Figure 3. Temperature evolution at point D.

As shown in Equation (7), illitization is modeled as the dissolution of smectite and precipitation of illite. Smectite volume fraction changes at points A through D in Kunigel and FEBEX bentonite are shown in Figures 5–8. Wherever and whenever smectite dissolve, illite precipitates at similar magnitude (results are not shown). We will discuss the dissolution of smectite in Kunigel bentonite first.

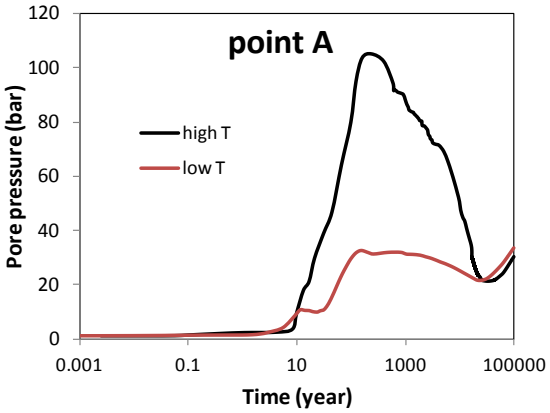

Figure 4. Pore pressure evolution at point A.

Figures 5 and 6 show that illitization (as shown by smectite dissolution) does occur in the Kunigel bentonite. In addition to temperature effects, illitization is affected by the initial disequilibrium between the pore-water solution and mineral phases. Initially, the pore water in the bentonite buffer is oversaturated with respect to illite and under-saturated with respect to smectite. In addition, the pore water in the clay formation contains a much higher concentration of K and Al, and thus provides a source of Al and K for the EBS bentonite alteration through diffusion and advection. Note that the increase in Al and K concentrations in bentonite is caused not only by diffusion and advection, but also by the dissolution of other minerals, such as K-feldspar. In fact, as shown in Liu et al. (2013), the dissolution of K-feldspar is the major source of K for illitization, especially in the area that is away from the EBS-NS interface, such as point A. The pore water in the clay formation also has a higher concentration of Mg and Na, which inhibits illitization. But it seems that the factors in favor of illitization outpace those against illitization. Smectite volume fraction changes are similar at points A and B in the first 2,000 years. However, illitization exhibits distinct behavior at points A and B for the "high T" case after 2000 years. At point A, illitization is stagnant. This is mainly caused by the drop of temperature, which significantly slowed down the dissolution of K-feldspar and subsequently the supply of K. The reduced temperature also significantly decreases the reaction rate of smectite and illite. Conversely, at point B, the illitization continues at fairly fast rate due to the interaction with clay formation. Although the

dissolution rate of K-feldspar at point B is significantly reduced (which limits the supply of K), bentonite near the EBS-NS interface receives K from the clay formation. This source of K is depleted before 2,000 years by illitization in the clay formation. However, illitization ceases in the clay formation after 2,000 years (see Figure 7) such that K is free to move into the bentonite. After 100,000 years, for the "high T" case, at point A, smectite volume fraction decreases by about 0.05, equivalent to 17% of the initial amount of smectite, while at point B, smectite volume fraction decreases by about 0.19, close to 60% of the initial amount of smectite. The difference between the illitization at points A and B shows that without interaction with the host rock, the thermal-induced chemical alteration in the EBS bentonite stabilizes after 2,000 years (e.g. results at point A), but the interaction with host rock may lead to dramatic changes in EBS bentonite as illustrated by the model results at point B. For the "low T", smectite volume fraction decreases about 0.03 (10% of initial amount) at points A and B after 100,000 years, which is substantially lower than that for "high T" case, especially at point B.

Figures 5 and 6 also show the dissolution of smectite in FEBEX bentonite. An examination of the model results for Kunigel and FEBEX bentonite reveals that some changes are common to both bentonites and some are distinct. Some common observations for both bentonites are as follows:

- Illitization (dissolution of smectite and precipitation of illite) occurs in bentonite and is enhanced at higher temperature.
- Bentonite near the NS-EBS interface undergoes more illitization than that near the waste package.
- Starting from about 1,600 years for the "high T" case, coincident with the time that smectite is depleted and illitization ceases in the clay formation near the NS-EBS interface, the dissolution of smectite is accelerated.

However, in comparison with the model results for Kunigel bentonite, several distinct features have been observed for FEBEX bentonite.

- There is less smectite dissolution for FEBEX bentonite for both "high T" and "low T" scenarios after 100,000 years. For the "high T" case, smectite volume fraction decreases about 0.03 at point A and 0.14 at point B, about 5% and 23% of the initial smectite volume fraction, respectively. These changes are significantly lower than a decrease of 0.05 (17% of initial amount) at point A and 0.19 (60% of the initial amount) for Kunigel bentonite.
- The enhancement of illitization by temperature is less pronounced for FEBEX, i.e. the difference between the amount of smectite dissolving for the "low T" and "high T" scenarios is less significant for FEBEX bentonite than for Kunigel bentonite.

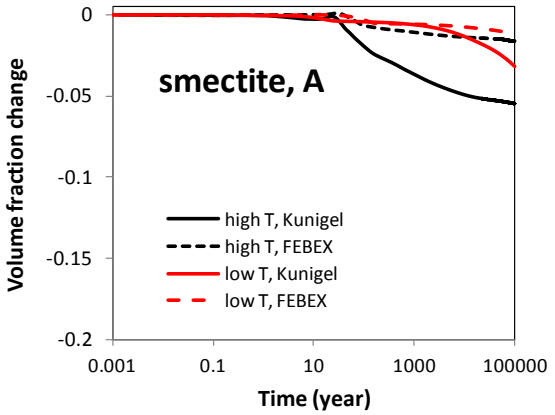

Figure 5. Temporal evolution of smectite volume fraction at points A for Kunigel and FEBEX bentonite. Negative value means dissolution.

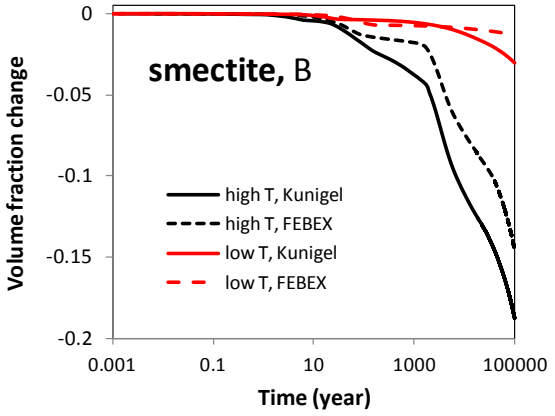

Figure 6. Temporal evolution of smectite volume fraction at points B for Kunigel and FEBEX bentonite. Negative value means dissolution.

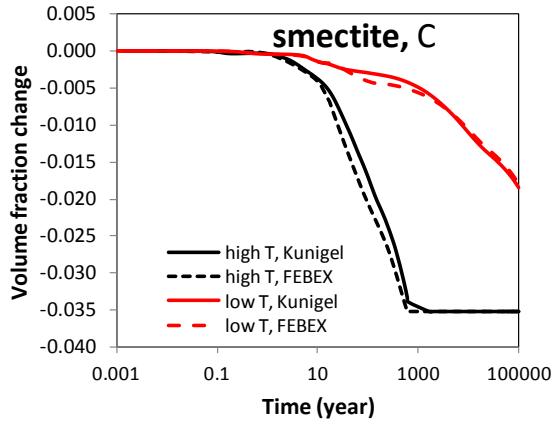

Figure 7. Temporal evolution of smectite volume fraction at points C in clay formation with Kunigel and FEBEX bentonite as EBS. Negative value means dissolution.

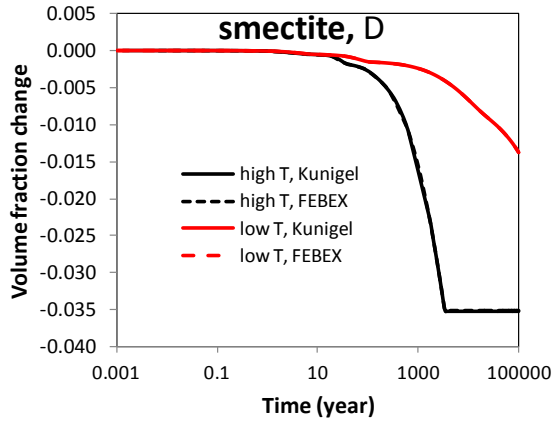

Figure 8. Temporal evolution of smectite volume fraction at points D in clay formation with Kunigel and FEBEX bentonite as EBS. Negative value means dissolution.

Figures 7 and 8 show that the clay rock undergoes a small degree of illitization similar to observations in geological systems (e.g. Wersin et al., 2007; Pusch and Madsen, 1995). Results at point D represent the chemical alteration in the clay formation induced only by the long term heating. The volume fraction of smectite in the clay formation, which initially is 0.035, is depleted after 3,500 years for the "high T" case and decreases by 0.0135 (about 40% of initial amount) for the "low T" case. A simulation that has no heat release from water package shows that clay formation undergoes a decrease in smectite volume fraction of 0.005 (14% of the initial amount) for undisturbed temperature conditions (Zheng et al., 2015). At point C near the EBS-NS interface, because the clay formation undergoes interaction with bentonite and experiences higher temperature, illitization is faster in comparison with that at point D. For the "high T" case, in only 650 years, the volume fraction of smectite decreases by 0.034 (about 97% of initial amount) and then in about 1,500 years, all smectite is transformed to illite; for the "low T" case, the volume fraction of smectite decreases about 0.017 (50% of the initial amount) in 100,000 years. As mentioned above, the quick depletion of smectite or the cessation of illitization in the clay formation near the EBS-NS interface has significant impact on the illitization in bentonite. Although the different types of EBS bentonite have almost no impact on the chemical changes in the clay formation away from the EBS-NS interface (illustrated by results at point D Figure 8), the type of bentonite does have a moderate impact on the clay formation near the EBS. As shown by the results at point C in Figure 7, with FEBEX bentonite, smectite dissolution occurs earlier in the clay formation. The reason is that FEBEX bentonite has a higher K concentration (see Table 3) so that the diffusion of K from the clay formation into the bentonite is at lower rate, and subsequently more K is available in the clay formation for illitization.

Stress Evolution

The increase in pore pressure due to hydration and thermal pressurization (a process caused by the difference in thermal expansion of the fluid and solid host rock), bentonite swelling, and thermal expansion lead to an increase in total stress in bentonite, as shown in Figure 9 at point A for Kunigel and FEBEX bentonite. The stress in bentonite peaks at about 100 years. After 100 years, the stress gradually goes down and stabilizes somewhat after 30,000 years. By the end of 100,000 years, the difference between the "high T" and "low T" cases is minimal. Because FEBEX bentonite has higher swelling pressure, the total stress for FEBEX bentonite are 3-4 MPa higher than that for Kunigel bentonite at the peak (100 years) and this difference persists until the end of the simulation at 100,000 years (Figure 9).

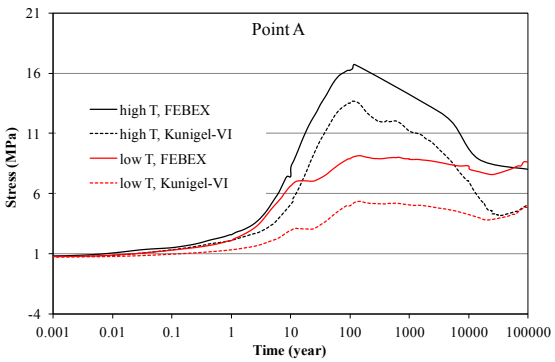

Figure 9. Temporal evolution of stress at points A for Kunigel and FEBEX bentonite.

The constitutive relationship described by Equation (5) provides an opportunity to evaluate the effect of chemical changes on swelling stress. In order to isolate the contributions of ion concentration changes versus smectite changes on swelling stress changes, we present three sets of calculated swelling stress. In the first set, denoted in Figure 10 as "σ=f(Sl,C,Ms)", the swelling stress is calculated according to Equation (5) as a function of liquid saturation changes (Sl), ion concentration (C) changes, and smectite (Ms) changes. In the second set, denoted as "σ=f(Sl,C)", the contribution from smectite changes in Equation (5) is disregarded, and the swelling stress is only a function of liquid saturation and ion concentration. In the third set, denoted as "σ=f(Sl)", all chemical effects are neglected, and the swelling stress is only a function of liquid saturation changes.

Figure 10 shows the swelling stress change in these three scenarios at point B for FEBEX bentonite. At early time (< 20 years), the fact that results for "σ=f(Sl,C,Ms)" and "σ=f(Sl,C)" cases are indistinguishable indicates that smectite changes have not yet contributed to the stress change because the volume fraction of smectite changes significantly only after about 20 years. Ion concentration changes start to affect stress at early times (< 20 years) and maintain such effects afterwards. The chemically induced swelling stress decreases at the end of 100,000 years are summarized in Table 4. In Table 4, stress reduction by ion concentration is the difference between the swelling stress obtained with "σ=f(Sl)" and "σ=f(Sl,C)", and the stress reduction by smectite dissolution is the difference between the swelling stress obtained with "σ=f(Sl,C)" and "σ=f(Sl,C,Sc)" where the relative amount (%) use the results from "σ=f(Sl)" as the basis. By the end of 100,000 years, Kunigel bentonite has lost more than half of its swelling capacity whereas FEBEX bentonite has lost about 13% of its swelling capacity. Generally speaking, in absolute numbers, Kunigel and FEBEX bentonites undergo similar magnitudes of reduction in swelling stress, but relative to their swelling capacity (the maximum swelling stress which is typically measured by hydrating bentonite with deionized water), chemical changes cause a stronger reduction in swelling capacity for Kunigel than for FEBEX bentonite. Therefore, using bentonite with a high swelling capacity such as FEBEX bentonite is always beneficial with respect to stress reduction caused by illitization.

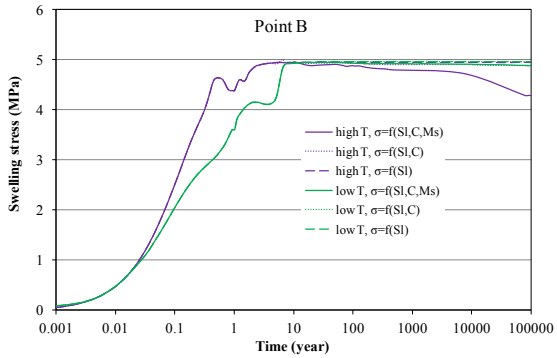

Figure 10. Simulation results of swelling stress at point B for FEBEX bentonite for the "low T" and "high T" scenarios, respectively.

Table 4. Geochemically induced swelling stress for Kunigel and FEBEX bentonite at points A and B for "high T" scenario.

	Kunigel-VI bentonite				FEBEX bentonite			
	Stress reduction by ion concentration		Stress reduction by smectite dissolution		Stress reduction by ion concentration,		Stress reduction by smectite dissolution	
	MPa	%	MPa	%	MPa	%	MPa	%
Point A	0.07	7	0.09	9	0.006	0.1	0.17	3.4
Point B	0.08	8	0.45	45	0.06	1.1	0.6	12

We developed two sensitivity runs in which the contribution of ion concentration and smectite volume fraction change to stress are alternatively neglected to check on the contribution of chemical changes on the stress in clay formation, as shown in Figure 11. Model results for these three cases show that the effects on stress are very small. By the end of 100,000 years at point C, the dissolution of smectite leads to a decrease in stress of about 0.14 MPa and ion concentration change cause another decrease in stress of about 0.14 MPa. Therefore, in total, the chemical changes in the clay formation result in about a 0.28 MPa decrease in stress, or 2.6%.

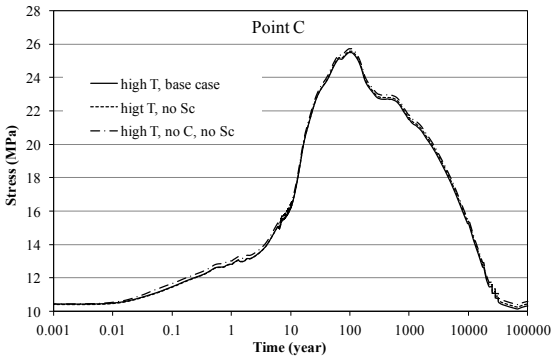

Figure 11. Simulation results of mean total stress at point C for the "high T" scenarios in three cases: the "high T, base case" in which the effect ion concentration and smectite change on stress are considered; the "high T, no Sc" case in which the contribution of smectite change to stress is neglected and the "high T, no C, no Sc" case in which both the contribution of smectite change and ion concentration to stress are neglected.

CONCLUSION

In this paper, coupled THMC modeling has been used to evaluate the chemical alteration and associated mechanical changes in a generic repository to consider the interaction between EBS bentonite and the NS clay formation. Two main scenarios were developed for comparison: a "high T" case in which the temperature near the waste package can reach about 200 ^{o}C and a "low T" scenario in which the temperature peaks at about 100 ^{o}C.

Our model results for 100,000 years show that illitization occurs in the EBS bentonite and NS clay formation and it is enhanced under higher temperature. Model results reveals that for the "high T" scenario, illitization is stabilized after about 2,000 years in bentonite near the waste package, but continues in bentonite near the EBS-NS interface. For the "low T" scenario, illitization is nearly stabilized after 2,000 years for the entire volume of EBS bentonite. The geochemical interaction between EBS bentonite and the clay formation has a strong effect on long term illitization in bentonite.

In terms of the effect of chemical changes on swelling stress for bentonite, the current modeling results show a significant reduction in swelling stress as a result of smectite dissolution after 100,000 years. For the "high T" case, Kunigel bentonite near the EBS-NS loses as much as 53% swelling capacity and FEBEX bentonite near the EBS-NS has about 13% reduction in swelling stress, whereas bentonite near the waste package undergoes a small reduction in swelling stress — 16% reduction for Kunigel and 3.4% for FEBEX bentonite, respectively. For the "low T" case, the stress reduction by chemical change is relatively homogeneous, 16% reduction for Kunigel bentonite and around 3% reduction for FEBEX bentonite after 100,000 years. Chemical change leads to about a 2.6% decrease in stress near the EBS-NS interface and about 0.7% in the far field in clay formation. In general, chemical change does not have significant impact on the stress in the clay formation.

ACKNOWLEDGMENT

This work was funded by the U.S. Department of Energy, Used Fuel Disposition Program.

REFERENCES

Börgesson, L., Chijimatsu, M., Nguyen, T.S., Rutqvist, J., Jing L. Thermo-hydro-mechanical characterization of a bentonite-based buffer material by laboratory tests and numerical back analyses. *Int. J. Rock Mech. & Min. Sci.* 38, 105-127, 2001.

ENRESA. *Full-scale engineered barriers experiment for a deep geological repository in crystalline host rock FEBEX Project*, European Commission: 403, 2000.

Fernández, A., Cuevas, J., Rivas, P., Pore water chemistry of the FEBEX bentonite. *Mat. Res. Soc. Symp. Proc.* 663, 573–588, 2001.

Fernández, A. M., Turrero, M. J., Sánchez, D. M., Yllera, A., Melón, A. M., Sánchez, M., Peña, J., Garralón, A., Rivas, P., Bossart, P. and Hernán, P. On site measurements of the redox and carbonate system parameters in the low-permeability Opalinus Clay formation at the Mont Terri Rock Laboratory. *Physics and Chemistry of the Earth*, Parts A/B/C 32(1-7): 181-195, 2007.

Hicks, T.W., White, M.J. and Hooker, P.J. *Role of Bentonite in Determination of Thermal Limits on Geological Disposal Facility Design, Report 0883-1, Version 2,* Falson Sciences Ltd., Rutland, UK, Sept. 2009.

Itasca, FLAC3D, *Fast Lagrangian Analysis of Continua in 3 Dimensions, Version 4.0, Minneapolis, Minnesota*, Itasca Consulting Group, 2009.

Laredj, N., Missoum, H. and Bendani, K., Modeling the effect of osmotic potential changes on deformation behavior of swelling clays. *Journal of Porous Media* 13(8): 743-748, 2010.

Lauber, M., B. Baeyens and Bradbury, M. H. *Physico-Chemical Characterisation and Sorption Measurements of Cs, Sr, Ni, Eu, Th, Sn and Se on Opalinus Clay from Mont Terri*. PSI Bericht Nr. 00-10 December 2000 ISSN 1019-0643, 2000.

Liu, H.H., J. Houseworth, J. Rutqvist, L. Zheng, D. Asahina, L. Li, V. Vilarrasa, F. Chen, S. Nakagawa, S. Finsterle, C. Doughty, T. Kneafsey and J. Birkholzer. *Report on THMC modeling of the near field evolution of a generic clay repository: Model validation and demonstration, Lawrence Berkeley National Laboratory*, August, 2013, FCRD-UFD-2013-0000244, 2013.

Ochs, M., Lothenbach, B., Shibata, M. and Yui, M. Thermodynamic modeling and sensitivity analysis of porewater chemistry in compacted bentonite. *Physics and Chemistry of the Earth*, Parts A/B/C 29(1): 129-136, 2004.

Pusch R. and Karnland, O. Physico/chemical stability of smectite clays, *Engineering Geology* 41: 73-85, 1996.

Pusch, R., Kasbohm, J. and Thao, H. T. M. Chemical stability of montmorillonite buffer clay under repository-like conditions—A synthesis of relevant experimental data. *Applied Clay Science* 47(1–2): 113-119, 2010.

Pusch, R. and Madsen, F. T. Aspects on the illitization of the kinnekulle bentonites. *Clays and Clay Minerals* 43(3): 261-270, 1995.

Rutqvist, J., Y. Ijiri and H. Yamamoto, Implementation of the Barcelona Basic Model into TOUGH–FLAC for simulations of the geomechanical behavior of unsaturated soils. *Computers & Geosciences* 37(6): 751-762, 2011.

Rutqvist, J., Zheng, L., Chen, F., Liu, H.-H. and Birkholzer, J., Modeling of Coupled Thermo-Hydro-Mechanical Processes with Links to Geochemistry Associated with Bentonite-Backfilled Repository Tunnels in Clay Formations. *Rock Mechanics and Rock Engineering*: 47(1): 167-186, 2014.

Sonnenthal, E. Chapter 5 in: Birkholzer, J. Rutqvist, E. Sonnenthal, and D. Barr, *Long-Term Permeability/Porosity Changes in the EDZ and Near Field due to THM and THC Processes in Volcanic and Crystalline-Bentonite Systems, DECOVALEX-THMC Project Task D Final Report*, 2008.

Wersin P., Johnson, L.H. and McKinley, I.G., Performance of the bentonite barrier at temperature beyond 100^{o}C: A critical review, *Physics and Chemistry of the Earth* 32: 780-788, 2007.

Xu, T., Spycher, N., Sonnenthal, E., Zhang, G., Zheng, L. and Pruess, K., TOUGHREACT Version 2.0: A simulator for subsurface reactive transport under non-isothermal multiphase flow conditions. *Computers & Geosciences* 37(6): 763-774, 2011.

Zheng, L., Li, L., Rutqvist, J., Liu, H. and Birkholzer, J.T., *Modeling Radionuclide Transport in Clays.* Lawrence Berkeley National Laboratory. FCRD-URD-2012-000128, 2012.

Zheng, L. J. Rutqvist, C. Steefel, K. Kim, F. Chen, V. Vilarrasa, S. Nakagawa, J. Zheng, J. Houseworth, J. Birkholzer. *Investigation of Coupled Processes and Impact of High Temperature Limits in Argillite Rock.* FCRD-UFD-2014-000493, LBNL-6719E, 2014.

Zheng, L. J. Rutqvist, K. Kim, J. Houseworth. *Investigation of Coupled Processes and Impact of High Temperature Limits in Argillite Rock.* FCRD-UFD-2015-000362, LBNL-187644, 2015.

Hydrocarbon Recovery and Reservoir Processes

iTOUGH2-FLAC MODELING OF THERMAL-HYDRAULIC-MECHANICAL PROCESSES RELATED TO STEAM-ASSISTED HEAVY OIL RECOVERY FROM DIATOMITE

Laura Blanco-Martín, Jonny Rutqvist, Christine Doughty, Yingqi Zhang,
Stefan Finsterle and Curtis M. Oldenburg

Lawrence Berkeley National Laboratory, Earth Sciences Division
One Cyclotron Road, MS 74R-316C
Berkeley, California, 94720, United States
e-mail: lblancomartin@lbl.gov

ABSTRACT

We present the current status of a coupled thermal-hydraulic-mechanical (THM) modeling effort undertaken to investigate key factors that may lead to systematic well failure in compactible reservoirs, and to evaluate the sensitivity of potential well failure to THM processes. The context for this study is the production of heavy oil using cyclic steaming. The reservoir rock is diatomite, a particular rock that has high porosity, low permeability and experiences non-recoverable volume decrease under increasing temperature. At this stage, we focus on local effects around wells, with the main target of evaluating whether thermally-induced compaction of diatomite is important to explain reservoir compaction and surface subsidence. The simulations are performed using iTOUGH2-FLAC, recently developed using the well-established TOUGH-FLAC simulator as a basis (forward simulation model). An enhanced version of EOS8 is being used in the flow subproblem. The modified Cam-Clay model has been provided with a capability to model non-recoverable volumetric strain. Although the results shown are preliminary, they suggest that temperature is a key factor to explain reservoir compaction and subsidence. Based on these findings, it seems that thermal effects within the reservoir have the potential to affect differential movements in the overburden, which may induce well failure. This will be investigated in the next stage of the research, in which a simulation will be set up to investigate large-scale THM-related differential movements.

INTRODUCTION

In order to produce heavy oil efficiently, a mechanism to decrease oil viscosity is required. One of the available mechanisms is cyclic steaming, in which steam is injected for a few days into the heavy oil reservoir to locally heat the oil, then the well is shut in for a few days, and then the warmed oil of reduced viscosity is produced. This operation is repeated as long as oil production is profitable. Since the same well is used to inject and to produce (huff-and-puff recovery method), and because the oil in place is originally very viscous and cannot be displaced over long distances, several of these wells (hundreds or even thousands depending on the size of the reservoir) operate in a field, sometimes at very close spacing (Fredrich et al., 2000).

It is well known that underground injection and production of fluids modify the stress state in the subsurface (target formation and likely the over- and/or under-burden), and, depending on the properties of the formations, may lead to non-recoverable effects, such as compaction, i.e., non-reversible reduction of the pore space (Crawford et al., 2006; Zoback, 2010). As a result, the following ground surface movements are expected, particularly if the reservoir is shallow (Bruno, 2001): subsidence if the reservoir undergoes compaction; uplift if, for instance, the pore pressure increases at a large scale (e.g., due to low permeability and/or reduced possibility for lateral flow), or if thermal expansion due to the injection of hot fluids is important.

Reservoir compaction and/or expansion, linked to differential movements in the overburden, have been observed to cause substantial well failure, triggering considerable economic impacts (Bruno, 1990; Hamilton et al., 1992; Hilbert et al., 1996; Fredrich et al., 2000; Yudovich and Morgan, 1989). A well-

documented example is the Belridge field in the San Joaquin Valley (California), where more than 1,000 wells have been reported to experience severe damage in a time period of about 20 years (Fredrich et al., 2000).

In this work, we perform coupled thermal-hydraulic-mechanical (THM) modeling to achieve two objectives: (1) to understand key factors that may lead to systematic well failure, and (2) to evaluate the sensitivity of potential well failure to THM processes. These objectives fit within a broader framework of subsurface integrity risk assessment, related to the production of heavy oil using cyclic steaming. The reservoir rock that we study is diatomite, a highly porous rock (initial porosity 50-70%), but showing low permeability (undisturbed permeability of about 10^{-15} - 10^{-14} m^2) as a result of fine grain size and relatively small pore-throat diameters. Laboratory studies on diatomite samples suggest that porosity, permeability and mechanical properties can change under the effect of temperature, due to dissolution/precipitation processes, and to silica diagenetic transformations (Crawford et al., 2006; Dietrich and Scott, 2007; Hascakir and Kovscek, 2010). In particular, while most materials experience expansion if the temperature increases, diatomite has been observed to experience non-recoverable volume decrease.

In this paper, we present a preliminary study conducted to investigate local effects around wells, and in particular, to determine whether the effect of temperature on the mechanical response of the reservoir rock plays an important role in explaining compaction and ground surface subsidence. Indeed, since the wells are flowed rather than pumped, pore pressure changes within the reservoir are small, and some other mechanism should be responsible for the reservoir and overburden movements. After a short description of the numerical tools used, we present our conceptual model and the current status of the modeling activities. Finally, we give the main conclusions and perspectives of this work.

NUMERICAL TOOLS

iTOUGH2-FLAC simulator

In the context of this research project, FLAC^{3D} (Itasca, 2012) has been integrated into iTOUGH2 (Finsterle, 2007) to conduct coupled flow and geomechanics analyses. In order to implement the coupling between the two codes, the general structure and sequential scheme of the well-established TOUGH-FLAC simulator (Rutqvist et al., 2002; Rutqvist and Tsang, 2003) have been used as a basis.

In its current version, iTOUGH2-FLAC can be used:

1. To perform forward coupled THM simulations, in a similar way as TOUGH-FLAC, but with additional enhancements (see below);
2. To perform parameter estimation, sensitivity analysis, uncertainty propagation, and data-worth analyses on flow parameters (like standard iTOUGH2 would perform), but on a model response that accounts for geomechanical effects, because the forward runs are actually coupled simulations (flow-geomechanics);
3. To perform parameter estimation, sensitivity analysis, uncertainty propagation, and data-worth analyses on mechanical parameters (or flow *and* mechanical parameters) using the PEST protocol. In this case, iTOUGH2 should be used as the main program, and TOUGH-FLAC (or iTOUGH2-FLAC) should be used as the user-provided model (for details on the use of iTOUGH2-PEST, see Finsterle, 2010).

In forward mode, iTOUGH2-FLAC inherits all the enhancements of iTOUGH2 as compared to standard TOUGH2: printout control and formatting, code robustness, secondary mesh, permeability assignments, MOMOP block, the flexible assignment of initial and boundary conditions, the possibility to use restart times (which was necessary to easily model a significant number of cycles in our particular case), etc. All these enhancements are detailed in Finsterle (2015).

The use of iTOUGH2-FLAC is similar to that of other iTOUGH2 special modules, such as GSLIB, parallel execution using PVM, or PEST:

a file named *it2flac.f* contains the full subroutines for the coupling, and if the coupling is desired, subroutine *isthisflac(flaconly)* in file *it2stubs.f* should be renamed.

Finally, we note that, similarly to TOUGH-FLAC, iTOUGH2-FLAC can be used in creep mode, and also for finite strain analyses (Blanco-Martín et al., 2015).

Enhancement of EOS8

In this work, the Equation-of-State module 8 (EOS8) of TOUGH2/iTOUGH2 has been used (Pruess et al., 2012). Three components are included in EOS8: water, air and oil, as well as three phases: gas, aqueous and non-aqueous phase liquid (NAPL). This module provides a simple capability to include an oleic phase, and the thermodynamics of the oil component are simplified, e.g., oil cannot volatilize into the gas phase, nor can it dissolve into the aqueous phase. Similarly, neither the air nor the water can dissolve into the NAPL phase. In other words, the oil is present only in the NAPL phase (Pruess et al., 2012), sometimes referred to as "dead oil". Also, as compared to the more sophisticated TMVOC module (Pruess and Battistelli, 2002), only one oil component can be accounted for (i.e., the number of components cannot be greater than 3). The main advantage of EOS8 as compared to TMVOC is that, due to the simplified thermodynamics, the module runs more smoothly, and several runs can be performed in a short time (sensitivity analysis, etc.). For the purposes of this research (investigate processes that could explain well failure and evaluate the sensitivity of well failure to THM processes [which requires several runs]), a detailed representation of the oil is not necessary, and a "dead oil" approximation, as often adopted in the literature, should be sufficient (Fredrich et al., 2000; Minkoff et al., 2000).

Notwithstanding, and following recommendations about the module (Pruess et al., 2012), some enhancements have been incorporated into EOS8 to get a more realistic description of three-phase mixtures:

1. The linear relative permeability function provided for the oil phase (see Eq. (15) in Pruess et al., 2012) has been made a power-law function. If in the block SELEC, parameter FE(19) ≠ 0, then the exponent of Eq. (15) will be 1 + FE(19);
2. Three-phase relative permeability functions available in TMVOC have been implemented (including Stone's (1970) and Parker's (1987) models);
3. Viscosity of the oil phase can be calculated as in TMVOC using an empirical correlation developed by Van Velzen et al. (1972);
4. The three-phase capillary pressure function from TMVOC (Parker's model [Parker et al., 1987]) is available.

The ternary plot in Figure 1 displays NAPL isoperms (i.e., lines of equal relative permeability) for Parker's model and the EOS8 oil relative permeability function (with FE(19) = 1). As the figure shows, for a given oil saturation Parker's model predicts higher relative permeability than the EOS8 function, and therefore higher mobility of the NAPL phase. The use of Parker's model over EOS8 had an important impact in our simulations, both to increase the oil production and also to reduce the pore pressure increase during steam injection.

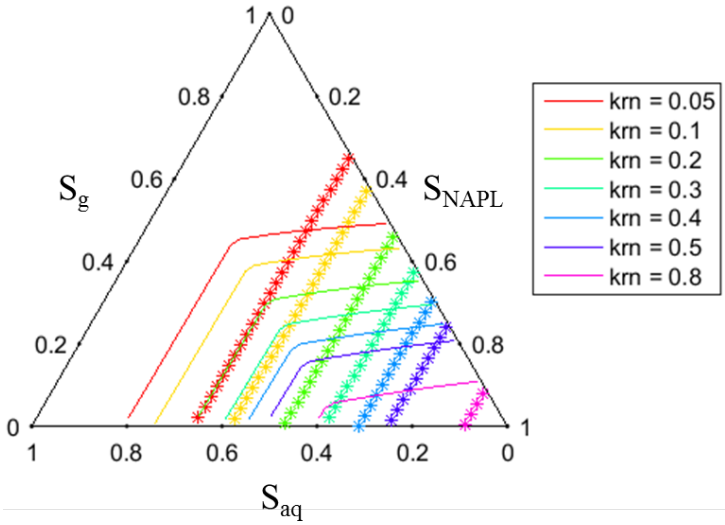

Figure 1. Ternary plot (3-phase system) with NAPL isoperms corresponding to Parker's model (solid lines) and EOS8 modified power-law function (stars). Each color corresponds to a relative permeability value (k_{rn} in the legend).

Previous modeling investigations had highlighted the importance of three-phase relative permeability models for predicting the perfor-

mance of heavy oil reservoirs (Kumar, 1990). We have adopted Parker's model because it yields isoperms similar to those of the linear interpolation model (Baker 1988), previously proposed as an accurate model for heavy oil reservoirs (Kumar, 1990).

MODELING RESULTS

We present results at a local scale around wells to investigate processes that could affect the mechanical response of the reservoir rock (diatomite), and to study related reservoir and overburden movements. To illustrate the effect of temperature, we first present results that neglect thermally-induced compaction, and then results that account for such an effect.

THM processes around a well neglecting thermally-induced compaction

Our conceptual model can be seen in Figure 2. We have accounted for typical well-to-well distances in heavy oil fields (Fong et al., 2001); as a result, the model domain extends considerably more in the *Z*-direction than in the *X*-*Y* plane.

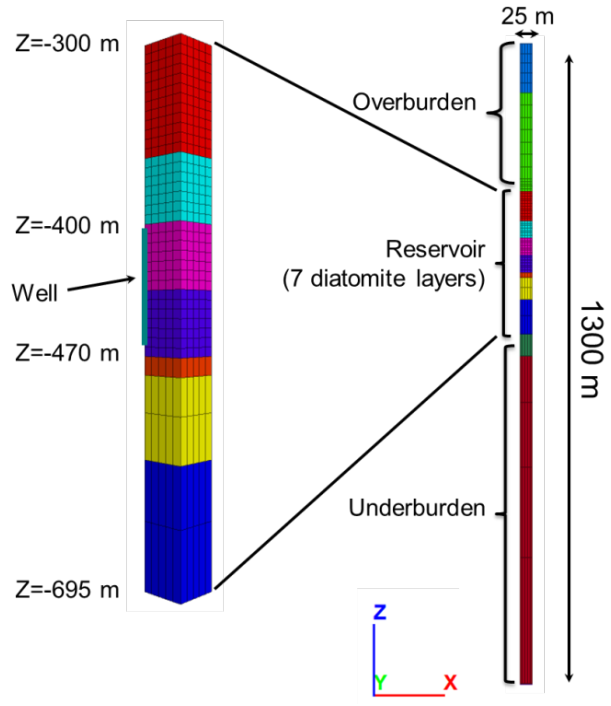

Figure 2. Conceptual model to study local THM effects around a well.

The model starts at the ground surface and extends to Z = -1300 m. The reservoir consists of seven diatomite layers (having different mechanical properties) and extends from Z = -300 m to Z = -695 m. The well is open over a thickness of 70 m, starting at a depth of about 400 m. It is placed in one of the corners and, for symmetry reasons, the lateral planes of the model are no-flow boundaries. Dirichlet boundary conditions are set at $Z = 0$ and $Z =$ -1300 m. The displacement normal to the lateral planes is blocked, as well as the vertical displacement at Z = -1300 m.

We model cycles as follows:

1. Six days of steam injection (500 STB/day/well, cold water equivalent);
2. Four days of soak;
3. Twenty-two days of production under self-flowing conditions.

Since compaction is important for diatomite, for the geomechanics sub-problem we need a cap model (i.e., both shear and hydrostatic failure are possible). From the FLAC^{3D} library, we select the modified Cam-Clay model (Itasca, 2012). This model has been used previously to model diatomite compaction at laboratory-scale (hydrostatic compression tests), see Crawford et al. (2006). Mechanical and flow properties for our THM simulations have been adopted from available literature for heavy oil reservoirs (Ambastha et al., 2001; Crawford et al., 2006; DOGGR, 1998; Fong et al., 2001; Fossum and Fredrich, 1998; Kumar and Beatty, 1995; Kumar, 1990).

Figure 3 displays the pore pressure and temperature evolution at the injection horizon, during 33 cycles (somewhat less than 3 years). Although the pore pressure changes within a cycle (due to injection/production), the average pore pressure does not change significantly over the time frame considered. A slight increase can be observed during the first year, due mainly to the low permeability of the reservoir and the injection of steam, and to the reservoir compaction (reduction of the pore space) as the yield surface (i.e., the *cap*) is reached. The slow decrease thereafter occurs as the overall viscosity of the fluids in the reservoir decreases: more low viscosity steam is present and water and oil viscosity decrease as the zone warmed by steam grows.

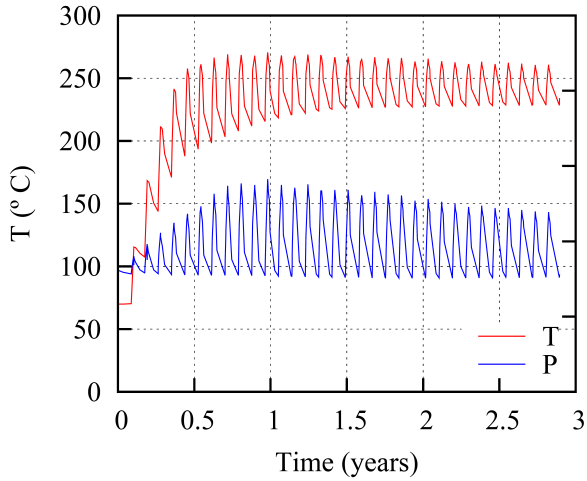

Figure 3. Pressure and temperature evolution at the injection horizon (Z = -400 m) during 33 cycles.

Figure 4a shows the temperature distribution within the reservoir after 33 cycles. Because the vertical permeability is half of the horizontal permeability, the temperature spread is preferentially horizontal. Also, because steam tends to move upwards, it can be seen in Figure 4a that the rock directly above the well has elevated temperature.

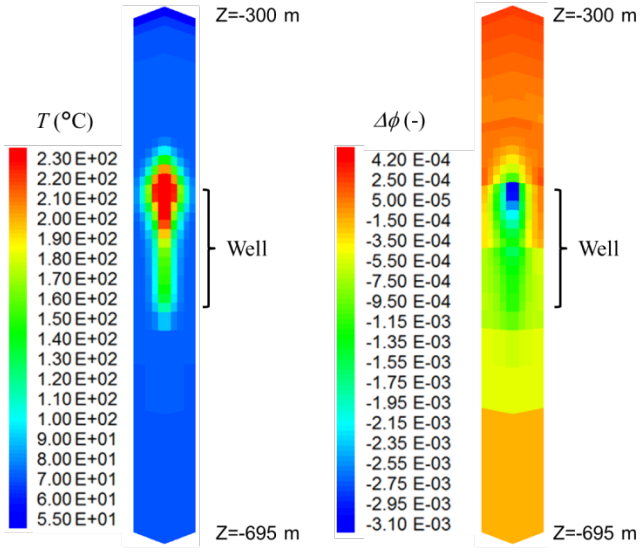

Figure 4. (a): temperature distribution in the reservoir after 33 cycles; (b): porosity change in the reservoir after 33 cycles.

Figure 5 displays the displacement predicted at the ground surface during 33 cycles (values shown correspond to the end of the soak phase). Despite the fact that the reservoir is compacting slightly around the well (see Figure 4b), the small lateral extent of this compaction and the pressure increase shown in Figure 3 are thought to be the main reasons for the predicted ground surface uplift. The negative value in the first cycle is due to the fact that the well is produced for 32 days before injection starts.

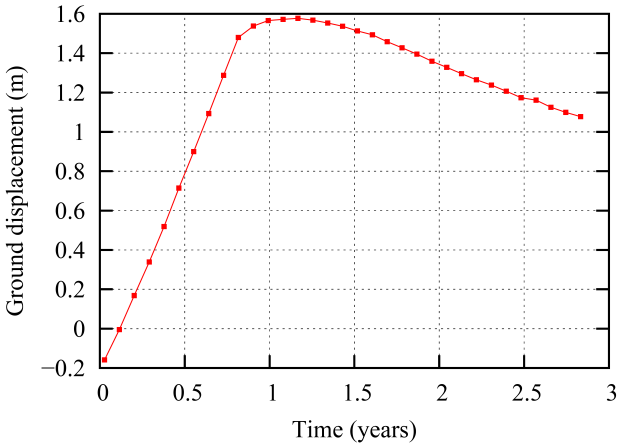

Figure 5. Predicted ground surface displacement over 33 cycles (without thermally-induced compaction).

After about one year, the ground displacement starts to reverse, although after 33 cycles the net balance still points to uplift. In the next section, we explore whether thermally-induced compaction could significantly affect these predictions, and accelerate ground surface subsidence.

THM processes around a well including thermally-induced compaction

Dietrich and Scott (2007) performed stress and temperature tests on several diatomite samples and observed that, under constant effective stress, diatomite compacts as temperature is raised. Upon cooling, little recovery of the strain was measured. Therefore, it seems that reservoir compaction is not only caused by a change in effective stresses, but also by a temperature increase.

In order to incorporate these phenomenological observations into our simulations, we have modified the Cam-Clay model available in FLAC^{3D} to include non-recoverable volumetric change due to a temperature increase.

Figure 6 compares ground surface displacement predicted when thermally-induced compaction is accounted for or disregarded. It can be seen that

when thermal effects are included, the reverse from uplift to subsidence starts earlier, and the slope of the subsidence part is higher than in the case without thermally-induced compaction. In addition, after 30 cycles the predictions point to net subsidence.

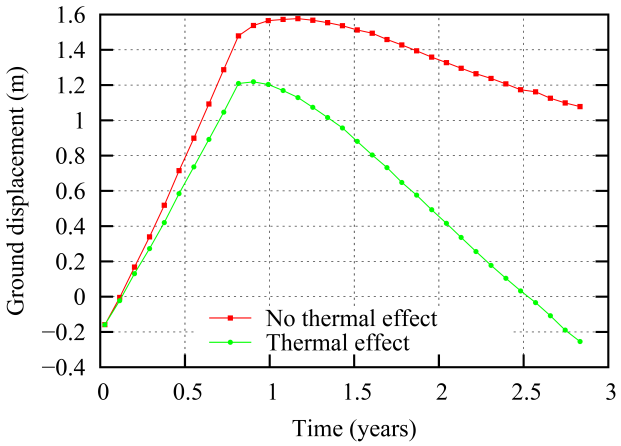

Figure 6. Predicted ground surface displacement over 33 cycles, accounting for and disregarding thermally-induced compaction.

Although these results are preliminary, they suggest that temperature is a key factor to explain reservoir compaction and subsidence.

CONCLUSIONS AND PERSPECTIVES

We are conducting THM modeling to investigate key factors that may lead to systematic well failure in compactible heavy oil reservoirs, and to evaluate the sensitivity of potential well failure to THM processes.

In this paper, we have presented preliminary, local investigations around a single well to determine whether thermally-induced compaction of diatomite could explain substantial reservoir compaction and ground surface subsidence, often observed in diatomite heavy oil reservoirs.

The simulations are performed using the newly developed simulator iTOUGH2-FLAC and an enhanced version of the EOS8 module. We have also modified the Cam-Clay model available in FLAC^{3D} to include non-recoverable thermal volumetric strain.

Although the results shown are preliminary, they suggest that temperature is a key factor to explain reservoir compaction and ground surface subsidence. Therefore, thermal effects within the reservoir will likely affect differential movements in the overburden, which have the potential to cause well failure, in particular in the presence of weak layers.

In the future, we intend to further validate our modified Cam-Clay model, and to perform a large-scale simulation including thermally-induced compaction, with the aim of capturing macro-scale movements that could relate to potential well failure.

ACKNOWLEDGMENT

Support for this work was provided in part by Lawrence Berkeley National Laboratory under Department of Energy Contract No. DE-AC02-05CH11231.

REFERENCES

Ambastha, A.K., M. Kumar, L.A. Skow, and G.M. Evola, Evaluation of cyclic steam operations at Cymric 1A Diatomite, SPE Annual Conference, Sept. 30-Oct.3, 2001 (SPE 71500).

Baker, L.E., Three-phase relative permeability correlations, SPE/DOE Symposium, April 17-20, 1988 (SPE/DOE 17369).

Blanco-Martín, L., R. Wolters, J. Rutqvist, K.-H. Lux, and J.T. Birkholzer, Comparison of two simulators to investigate thermal-hydraulic-mechanical processes related to nuclear waste isolation in saliferous formations, *Computers and Geotechnics*, 66, 219-229, 2015.

Bruno, M.S., Subsidence-induced well failure, SPE Calif. Regional Meeting, April 4-6, 1990 (SPE 20058).

Bruno, M.S., Geomechanical analysis and decision analysis for mitigating compaction related casing damage, SPE Annual Conference, Sept. 30-Oct.3, 2001 (SPE 71695).

Crawford, B.R., K.H. Searles, S.-Y. Hsu, W.L. Reese, A.H. Urdaneta, B.D. Carnahan, and J.W. Martin, Plastic compaction in diatomite: *in situ* stress versus temperature effects, 41st ARMA Symposium, June 17-21, 2006 (ARMA 06-1122).

Dietrich, J.K., and J.D. Scott, Modeling thermally-induced compaction in diatomite, SPE J. (SPE 97849), 2007.

DOGGR, California Department of Conservation (Division of Oil, Gas and Geothermal Resources), *California Oil and Gas Fields, Volume I, Central California*, Publication No. TR11, Sacramento, Calif., 1998.

Dusseault, M.B., M.S. Bruno and J. Barrera, Casing shear: causes, cases, cures, SPE Drilling & Completion, 2001 (SPE 72060).

Finsterle, S., *iTOUGH2 User's Guide*, Report LBNL-40040, Lawrence Berkeley National Laboratory, Berkeley, Calif., 2007.

Finsterle, S., *iTOUGH2 Universal Optimization Using the PEST protocol – User's Guide*, Report LBNL-3698E, Lawrence Berkeley National Laboratory, Berkeley, Calif., 2010.

Finsterle, S., *Enhancements to the TOUGH2 Simulator Implemented in iTOUGH2*, Report LBNL-TBD, Lawrence Berkeley National Laboratory, Berkeley, Calif., 2015.

Fong, W.S., L. Lederhos, L.A. Skow, G.M. Evola, and J. Choi, Analysis of a successful cyclic steam process at Cymric Field, California, SPE International Thermal Operations and Heavy Oil Symposium, March 12-14, 2001 (SPE 69702).

Fossum. A.F., and J.T. Fredrich, Estimation of Constitutive Parameters for the Belridge Diatomite, South Belridge Diatomite Field, Report SAND-98-1407, Sandia National Laboratories, Albuquerque, New Mexico, 1998.

Fredrich, J.T., J.G. Argüello, G.L. Deitrick, and E.P. de Rouffignac, Geomechanical modeling of reservoir compaction, surface subsidence and casing damage at the Belridge Diatomite filed, SPE Reservoir Eval. & Eng. 3(4), Aug. 2000 (SPE 65354).

Hamilton, J.M., A.V. Maller, and M.D. Prints, Subsidence-induced shear failures above oil and gas reservoirs, 33rd US Symposium on Rock Mechanics, 1992 (paper 263).

Hascakir, B., and A.R. Kovscek, Reservoir simulation of cyclic steam injection including the effects of temperature induced wettability alteration, SPE Western Regional Meeting, May 27-29, 2010 (SPE 132608).

Hilbert, L.B. Jr., J.T. Fredrich, M.S. Bruno, G.L. Deitrick, and E.P. de Rouffignac, Two-dimensional nonlinear finite element analysis of well damage due to reservoir compaction, well-to-well interactions, and localization on weak layers, 2nd North American Rock Mechanics Symposium, June 19-21, 1996 (ARMA-96-1863).

Itasca Consulting Group, *FLAC3D (Fast Lagrangian Analysis of Continua in 3D) Version 5.0 – User's Guide*, Minneapolis, MN, 2012.

Kumar, M., and F.D. Beatty, Cyclic steaming in heavy oil diatomite, SPE Western Regional Meeting, March 8-10, 1995 (SPE 29623).

Kumar, M. and T.N. Do, Effects of endpoint saturations and relative permeability models on predicted steamflood performance, SPE/DOE 7th Symposium, April 22-25, 1990 (SPE/DOE 20202).

Minkoff, S.E., C.M. Stone, S. Bryant, and M. Peszynska, Coupled geomechanics and flow simulation for time-lapse seismic modeling, *Geophysics*, 69(1), 200-211, 2004.

Parker, J.C., R.J. Lenhard, and T. Kuppusamy, A parametric model for constitutive properties governing multiphase flow in Porous Media, *Water Resour. Res.*, 23(4), 618 -624, 1987.

Pruess, K., and A. Battistelli, TMVOC, A Numerical Simulator for Three-Phase Non-isothermal Flows of Multicomponent Hydrocarbon Mixtures in Saturated-Unsaturated Heterogeneous Media, Report LBNL-49375, Lawrence Berkeley National Laboratory, Berkeley, Calif., 2002.

Pruess, K., C. Oldenburg, and G. Moridis, *TOUGH2 User's Guide, Version 2.1*, Report LBNL-43134 Rev., Lawrence Berkeley National Laboratory, Berkeley, Calif., 2012.

Rutqvist, J., Y.S. Wu, C.F. Tsang, and G. Bodvarsson, A Modeling Approach for Analysis of Coupled Multiphase Fluid Flow, Heat Transfer, and Deformation in Fractured Porous Rock, *Int. J. Rock Mech. Min. Sci*., 39, 429-442, 2002.

Rutqvist, J., and C.-F. Tsang, TOUGH-FLAC: a numerical simulator for analysis of coupled thermal-hydrologic-mechanical processes in fractured and porous geological media under multi-phase flow conditions, TOUGH Symposium, May 12–14, 2003.

Rutqvist, J., Status of the TOUGH-FLAC simulator and recent applications related to coupled fluid flow and crustal deformations, *Computers and Geosciences*, 37, 739-750, 2011.

Stone, H.L., Probability Model for Estimating Three-Phase Relative Permeability, *Trans. SPE of AIME*, 249, 214-218, 1970.

Van Velzen, D., R.L. Cardozo, and H. Langenkamp, A liquid viscosity-temperature-chemical constitutive relation for organic compounds, *Ind. Eng. Chem. Fund.,* 11(1), 20-25, 1972.

Yudovich, A., and D.R. Morgan, Casing deformation in Ekofisk, JPT, 1989 (paper 729).

Zoback, M.D., Reservoir Geomechanics, Cambridge University Press, 2010 (ISBN 9780521146197).

JOINT INVERSION OF HYDROLOGICAL AND GEOPHYSICAL DATA FOR ENHANCED RESERVOIR CHARACTERIZATION DURING ENHANCED OIL RECOVERY

Michael Commer[1], Stefan Finsterle[1], Yingqi Zhang[1], Michael Hoversten[2]

[1]Lawrence Berkeley National Laboratory, Berkeley, CA
[2]Chevron Energy Technology Company, San Ramon, CA
E-mail: MCommer@lbl.gov

ABSTRACT

We present two hydrogeophysical joint inversion studies that target the enhanced prediction of fluid saturations in CO_2-induced enhanced oil recovery (EOR) operations. Considered are two geophysical data types. The first study involves the combination of production data with time-domain electromagnetic (TEM) data. The second combines production with seismic amplitude-versus-angle (AVA) data. The pilot point method combined with geostatistical simulation is used to generate a spatially correlated, heterogeneous permeability field that is flexibly adjustable during the joint inversion process. Both geophysical data types promise an improved prediction of the CO_2 saturation, indicating potential benefits in both EOR as well as CO_2-sequestration monitoring operations.

INTRODUCTION

Understanding hydrocarbon reservoirs and predicting oil production requires detailed characterization of formation properties as well as the temporal evolution of the system state. In particular, the migration pattern of CO_2 injected for enhanced oil recovery (EOR) critically affects the effectiveness with which oil is mobilized and displaced towards a production well. While data collected at the injection or productions wells (such as pressures, oil, gas and water rates) can be used to estimate average reservoir properties, these data lack the spatial resolution needed to infer the distribution of CO_2. Conversely, while geophysical data may be used to image saturation changes in the reservoir, they do contain direct information about flow relevant properties.

We therefore propose to combine production with geophysical data (specifically from time-domain electro-magnetic and seismic amplitude-versus-angle surveys) in a joint inversion framework to concurrently estimate flow parameters and the evolution of the CO_2 plume. We apply the approach for a synthetic CO_2-EOR operation in a heterogeneous reservoir to demonstrate the benefits of analyzing complementary data for enhanced reservoir characterization.

RESERVOIR MODELING

Three-Phase Model for EOR Simulation

The reservoir simulation involves three-phase flow of an aqueous fluid (water), a non-aqueous phase liquid (NAPL or oil phase), and a non-condensible gas (CO_2). The thermophysical properties of mixtures of multicomponent oil, CO_2, and brine under reservoir conditions that may vary considerably during alternating injection of CO_2 and water is complex, specifically when accounting for changing miscibility and mixed wettability of the reservoir rocks. For simplifying this proof-of-concept demonstration, only three components were considered, namely a single oil component (with fluid properties similar to those of C11, undecane), one non-condensible gas (CO_2), and water. Each of these three components partitions into the three phases (aqueous, NAPL, and gas) according to the P-T conditions in each computational grid block. Phases may evolve or disappear. Three-phase flow is simulated using the multiphase extension of Darcy's law, with phase interference represented by three-phase capillary pressure and relative permeability functions. The simulator used for this analysis is referred to as TMVOC (Pruess and Battistelli, 2002), a module of the TOUGH2 suite of non-isothermal multiphase flow simulators (Pruess et al., 1999), as implemented in the iTOUGH2 simulation-optimization framework (Finsterle, 2004).

2D Model Design

The model contains heterogeneous stratigraphic units, with a low-permeability confining cap rock and an oil-bearing reservoir, which overlies a water-saturated zone. The heterogeneous permeability and porosity fields are shown in Figures 1a and 1b, respectively. For this conceptual study, a two-dimensional model was developed based on a 3D numerical model provided by industry. The size of the 3D model is approximately 960 m × 1350 m × 400 m. The top of the hydrological model domain (at Z=0 in Figure 1) is located at 1500 m below the land surface. An X-Z cross section at a fixed Y coordinate containing an injection and a production well was extracted from the 3D model, yielding the 2D model used for this analysis. The injection well is located at X_1=247.5 m, and the production well at X_2=652.5 m. The wells are perforated over the range from Z=0 to a model depth of -250 m. Initial water saturation was also taken from the 3D cross section. Initially, no CO_2 is present, hence the water saturation shown in Figure 1c also reflects the initial distribution of oil.

The 2D model has no-flow boundaries on all sides based on the assumption that the top and bottom layers are in contact with impermeable layers. The cross section is discretized into grid blocks of size 15 m (in X direction) and 20 m (in Z direction).

Geostatistical Inverse Modeling

We invert for the spatial distribution of the permeability field using the geostatistical simulation software GSLIB (Deutsch and Journel, 1992). The process includes (1) generation of random, spatially correlated property fields, and (2) the estimation of heterogeneous subsurface structures using the pilot point method (de Marsily et al., 1984; RamaRao et al., 1995; Finsterle and Kowalsky, 2007; 2008). Note that the "true" permeability and porosity (Figure 1) do not follow a known geostatistical model. Building a geostatistical model for the inversion using pilot points is part of the model development process. Thus, the final reservoir model is inherently unable to reproduce the true permeability and porosity structures, making the inversion more realistic and more challenging.

The initial oil saturation field (Figure 1c) is heterogeneous and is considered known.

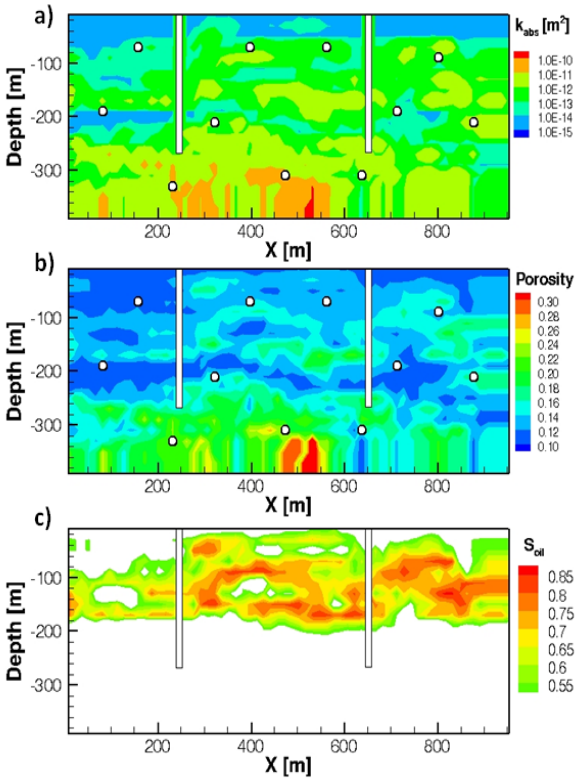

Figure 1: True (a) permeability field, (b) porosity field, and (c) initial distribution of oil saturation.

SYNTHETIC PRODUCTION DATA

We simulate an EOR operation in which CO_2 is injected at a constant rate of 30 kg/s for 10 days, followed by 30 days of water injection at 45 kg/s, and another 20 days of CO_2 injection at 30 kg/s. Production of oil, water, and CO_2 is assumed to occur against a fixed downhole pressure of 10 MPa.

Figure 2 shows the simulated gas saturation distribution at the end of each injection period (i.e., after 10, 40, and 60 days) resulting from the actual reservoir properties (Figure 1). Gas preferentially enters the reservoir at well depths where structures of relatively high permeability are spatially continuous, resulting in an intricate gas saturation distribution after 10 days (Figure 2a). Much of the injected free-phase CO_2 is displaced, compressed and dissolved during the 30-day water injection period (Figure 2b). Similar gas flow paths are established during the second injection period from 40 to 60 days,

leading to gas breakthrough at the production well (Figure 2c).

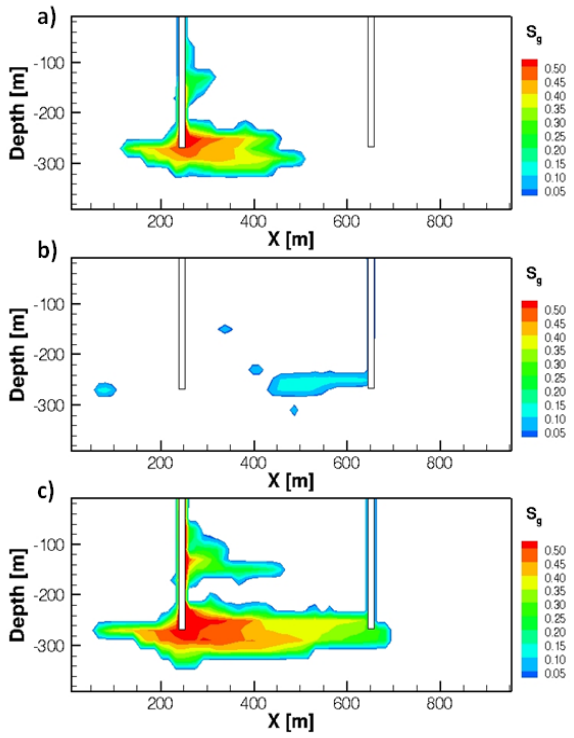

Figure 2: Gas saturation distribution (a) 10 days, (b) 40 days, and (c) 60 days into the CO_2-EOR operation, simulated from the actual reservoir properties (Figure 1).

Synthetic observation data are generated based on the model of Figure 1. Downhole pressure data at the injection well are recorded once a day, so are the oil and water production rates at the production well. These three time series constitute the hydrological data set for our inversion studies. All three data sets have considerable complexity which is a result of (1) nonlinearity in the displacement process, (2) heterogeneity in flow-relevant parameters, and (3) a non-uniform, spotty initial oil distribution (Figure 1c).

GEOPHYSICAL SIMULATIONS

The time-domain electromagnetic (TEM), or transient EM, technique provides the first type of geophysical data for the joint inversion scheme. We employ a modified version of the inverse flow- and transport simulator iTOUGH2 (Finsterle, 2004; Commer et al., 2014) with parallel hydrological domain decomposition, coupled with a parallel finite-difference TEM simulator (Commer and Newman, 2004). For this demonstration study, the hydrological-geophysical attribute linkage is provided through a simple petrophysical transformation function, given by (Archie, 1942):

$$\sigma = \sigma_f \Phi^m S^n \qquad (1)$$

The bulk electrical conductivity, σ, is calculated as a function of the fluid electrical conductivity σ_f, the porosity Φ, the cementation factor m=1.8, the water saturation S, and exponent n=2.0. Note that electrical conductivity, in units of S/m, is the inverse of resistivity, which is in units of Ωm.

The second geophysical data type considered here are seismic AVA data. They are simulated by a one-dimensional convolutional model (Hoversten et al., 2005), which has also been coupled with the iTOUGH2 inverse modeling framework. The mapping of the hydrological state to seismic attributes is based on a regression analysis obtained from well logs:

(1) Seismic P-wave velocity in m/s:

$$V_p = 6500 - 4000\Phi + 120S \qquad (2a)$$

(2) Seismic S-wave velocity in m/s:

$$V_s = 3600 - 2600\Phi - 40S \qquad (2b)$$

(3) Density in g/cm^3:

$$\rho = 2.8 - 1.2\Phi + 0.14S \qquad (2c)$$

Figure 3 shows the baseline model for the electrical conductivity before the CO_2-EOR operation. The conductivity ranges from approximately 10^{-3} S/m to 0.5 S/m. The central mesh discretization for the geophysical simulations have the same spatial sampling as is used for the hydrological modeling domain (indicated by the dotted box), with a grid interval of 15 m that gradually increases towards the domain boundaries. For this spatial grid sampling, the high conductivity of two steel-cased wells (injection well and production well) is approximated by one mesh column of size 15 m × 15 m that has an effective conductivity of σ=19.7 S/m, calculated from a conductivity averaging scheme (Commer and Newman, 2006).

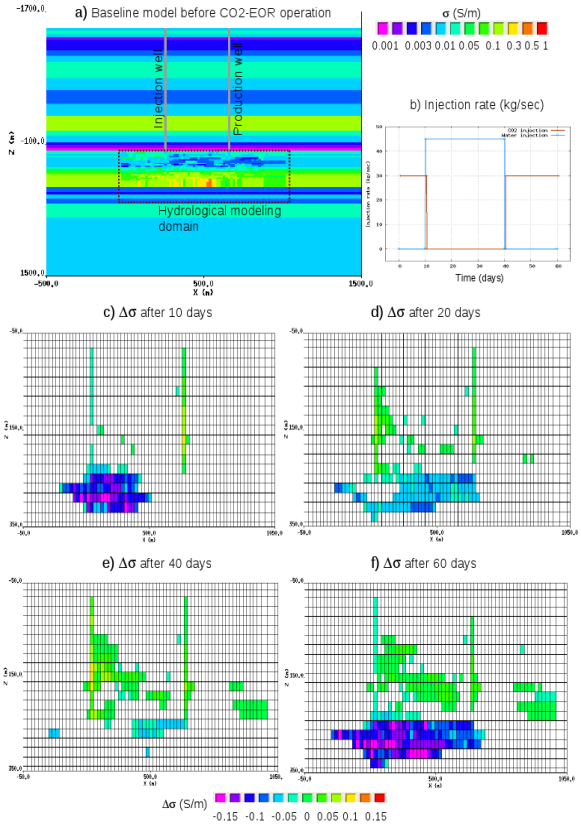

Figure 3: (a) Geophysical baseline model for the geophysical attribute (electrical conductivity) distribution before beginning of the EOR operation. (b) CO_2 and water injection rates over the 60-day injection period. Electrical conductivity changes with respect to the baseline are plotted for the times (c) 10 days, (d) 20 days, (e) 40 days, and (f) 60 days after beginning of the fluid injection.

COMPARATIVE INVERSE MODELING

Inversion of Production Data Only

In the following, we compare the outcomes of three inversion realizations, focusing on the complementary nature of the geophysical data for improved gas saturation prediction. The gas saturation, S_g, obtained from inverting the production data is plotted in Figure 4. Comparing to the true case (Figure 2), the gas saturation distribution resulting from the underlying geostatistical realization of the permeability field has little resemblance to the true distribution. This is expected, as production data inherently integrate information on the gas, water, and oil flow between the injection and production wells, i.e., they do not contain information about the spatial details of the permeability field.

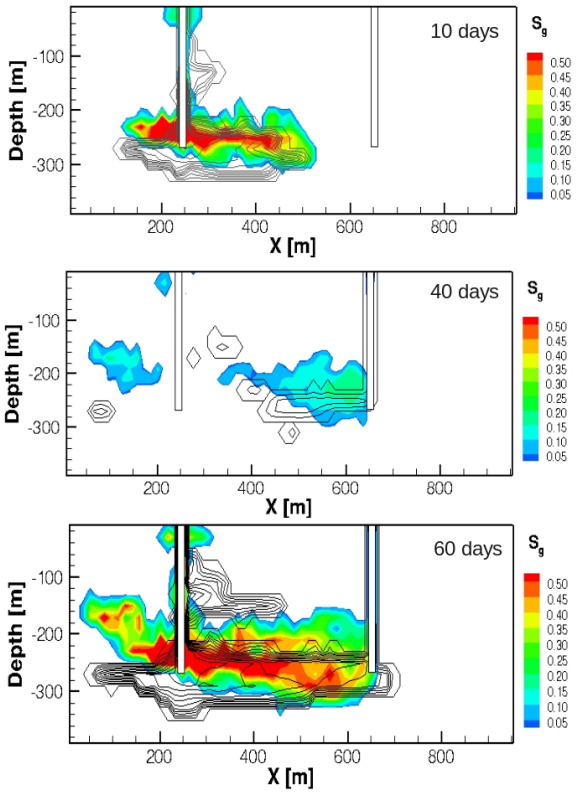

Figure 4: Gas saturation distributions (top) 10 days, (middle) 40 days, and (bottom) 60 days into the CO_2-EOR operation, simulated using the reservoir model calibrated against hydrological data alone and without conditioning to well permeability data. Black contour lines indicate the true gas saturation distribution (Figure 2).

Joint Inversion of Production and TEM Data

The second inversion approach combines the hydrological data set with two TEM data sets. The TEM data is calculated from a surface configuration with 21 detectors and a horizontal electric dipole transmitter, where horizontal electric fields (E_x) samples are taken at the time points 40 days and 60 days after beginning of the injection. Each TEM receiver records the transient electrical field over the time range from 1 ms to 100 ms, with 76 logarithmically spaced transient sampling times.

The result of the combined inversion is visualized in Figure 5, again comparing the predicted (color contours) and the actual (line contours) S_g distributions. For the early injection period, we observe a slightly improved image of S_g. This beneficial effect of combining data of complementary nature can be described as follows. The main role of the production data is

to make sure that the effective permeability between the injection and production wells are properly captured. The main role of the geophysical data is to place the high- and low-permeability features in the right location, i.e., to provide spatial resolution. Well data are used to condition the permeability fields; they thus support both respective roles of the production and geophysical data.

Figure 6 shows the concurrent match to the hydrologic data in the injection well (pressure) and production well (water and oil flow rates). Note that the joint inversion seeks a compromise between all available data types, which are weighted against each other using the expected magnitude of the residuals.

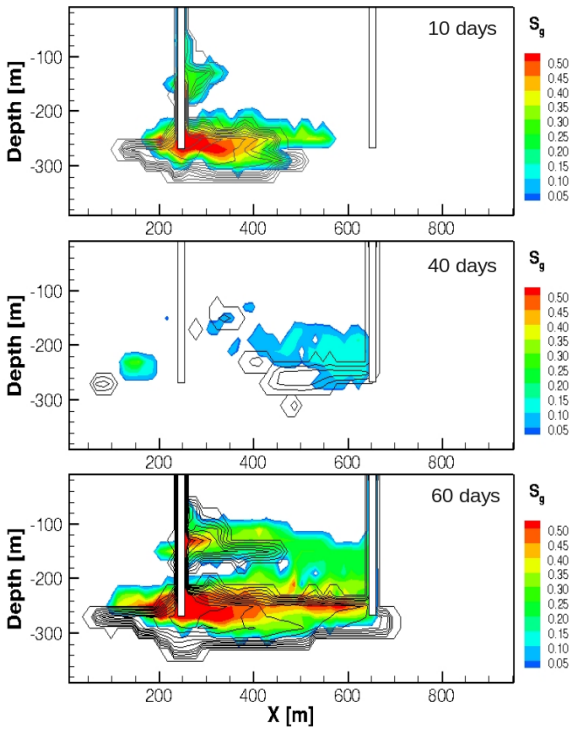

Figure 5: Gas saturation distributions (top) 10 days, (middle) 40 days, and (bottom) 60 days into the CO_2-EOR operation, simulated using the reservoir model jointly calibrated against production data and TEM data.

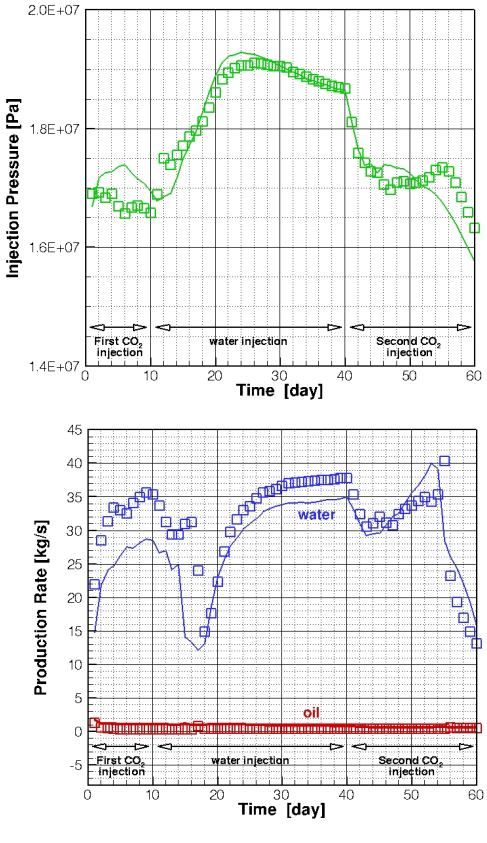

Figure 6: Comparison between measured (synthetic) and calibrated (a) injection and (b) production data during CO_2-EOR operation, simulated using the reservoir model jointly calibrated against production data and seismic AVA data.

Joint inversion using seismic AVA data

Finally, we invert production data together with seismic AVA data sets at the times 20 days, 40 days and 60 days after injection. One AVA set consists of a profile of 30 common depth points (CDP) on the surface. Further, each CDP contains seismic traces from 9 angles, with a sampling of 40 amplitudes per trace. Hence, the total number of AVA data points per set is 10,800. As shown by Figure 7, both the location and the size of the CO_2 plumes are reasonably well identified. Figure 8 further shows the matches to the production data.

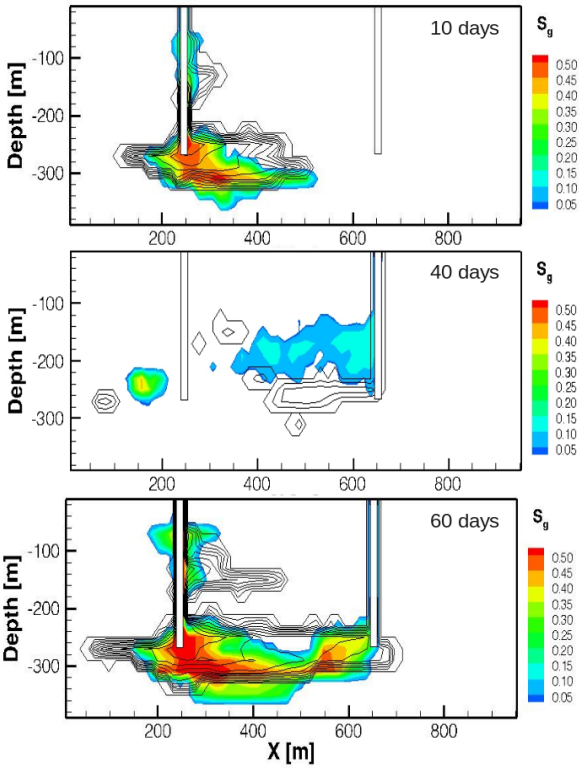

Figure 7: Gas saturation distributions (top) 10 days, (middle) 40 days, and (bottom) 60 days into the CO_2-EOR operation, simulated using the reservoir model jointly calibrated against production data and seismic AVA data.

CONCLUDING REMARKS

The parallel simulation-optimization code MPiTOUGH2-TMVOC is suitable for the joint analysis of production data along with either time-domain EM or seismic AVA data during a CO_2-EOR operation. Using geophysical and hydrological data in a joint inversion has the potential to yield improved estimates of property and system state distributions. Detailed analysis on the achievable property and state resolution, the need for prior information, conditioning, and other regularization, and on optimal survey configurations will be performed to examine the potential and limitations of this multi-physics joint-inversion approach for improved reservoir characterization.

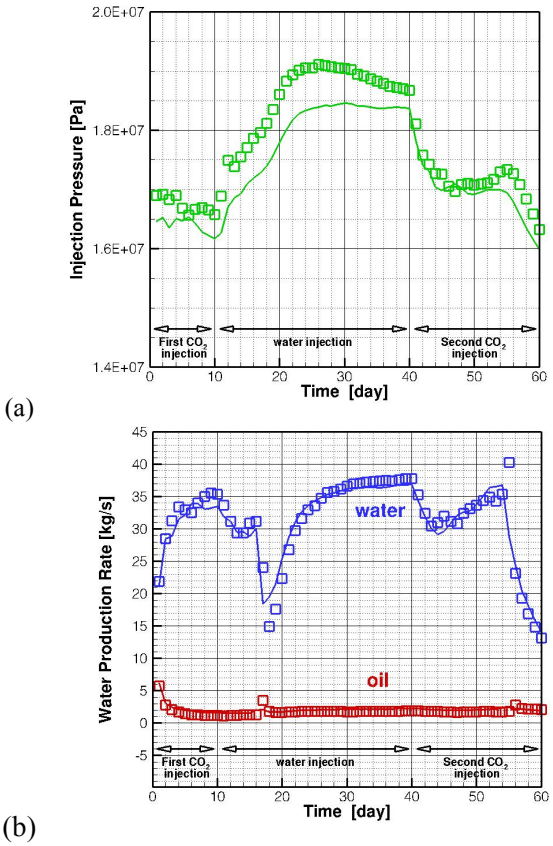

Figure 8: Comparison between measured (synthetic) and calibrated (a) injection and (b) production data during CO_2-EOR operation, simulated using the reservoir model jointly calibrated against production data and seismic AVA data.

ACKNOWLEDGMENT

This work was supported, in part, by the U.S. Dept. of Energy under Contract No. DE-AC02-05CH11231.

REFERENCES

Commer M., and G.A. Newman, A parallel finite-difference approach for three-dimensional transient electromagnetic modeling with galvanic sources, *Geophysics*, 69, 1192-1202, 2004.

Commer M. and G.A. Newman, An accelerated time domain finite difference simulation scheme for three-dimensional transient electromagnetic modeling using geometric multigrid concepts, *Radio Science*, 41, RS3007, doi:10.1029/2005RS003413, 2006.

Commer, M., M.B. Kowalsky, J. Doetsch, G. Newman, and S. Finsterle, MPiTOUGH2: A parallel parameter estimation framework for hydrological and hydrogeophysical applications, *Computers & Geosciences*, 65, 127–135, 2014.

de Marsily, G., C. Lavedan, M. Boucher, and G. Fasanino, Interpretation of interference tests in a well field using geostatistical techniques to fit the permeability distribution in a reservoir model, *in* Verly, G., David, M., Journel, A.G., and Marechal, A., Geostatistics for natural resources characterization: NATO Advanced Study Institute, ser. C 182, p. 831–849, 1984.

Deutsch, C.V., and A.G. Journel, *GSLIB, Geostatistical Software Library and User's Guide*, Oxford University Press, New York, New York, 1992.

Finsterle, S., Multiphase inverse modeling: Review and iTOUGH2 applications, Vadose Zone J., 3: 747–762, 2004.

Finsterle, S., and M.B. Kowalsky, *iTOUGH2-GSLIB User's Guide*, Report LBNL/PUB-3191, Lawrence Berkeley National Laboratory, Berkeley, Calif., June 2007.

Finsterle, S., and M. B. Kowalsky, Joint hydrological-geophysical inversion for soil structure identification, *Vadose Zone J.*, 7:287–293, doi:10.2136/vzj2006.0078, 2008.

Hoversten, G.M., J. Chen, E. Gasperikova, G.A. Newman, Integration of marine CSEM and seismic AVA data for reservoir parameter estimation, 75th Annual International Meeting, SEG, Expanded abstracts, 579-583, 2005.

Pruess, K., and A. Battistelli, *TMVOC, A Numerical Simulator for Three-Phase Non-Isothermal Flows of Multicomponent Hydrocarbon Mixtures in Saturated-Unsaturated Heterogeneous Media*, Report LBNL-49375, Lawrence Berkeley National Laboratory, Berkeley, Calif., April 2002.

Pruess, K., C. Oldenburg, and G. Moridis, *TOUGH2 User's Guide, Version 2.0*, Report LBNL-43134, Lawrence Berkeley National Laboratory, Berkeley, Calif., November 1999.

RamaRao, B. S., A. M. LaVenue, G. de Marsily, and M. G. Marietta, Pilot point methodology for automated calibration of an ensemble of conditionally simulated transmissivity fields, 1. Theory and computational experiments, *Water Resour. Res., 31*, 475–493, 1995.

WATER INJECTION CLOSE TO FAULT RISK ANALYSIS, FIELD APPLICATION

Julia DIESSL, Vahid SERAJIAN, Mike S. BRUNO

GeoMechanics Technologies
103 E. Lemon Street
Monrovia, California, 91016, U.S.A
e-mail: juliad@geomechancistech.com

ABSTRACT

A former producing well is considered for conversion into a water injector well to maintain reservoir pressure. There is a fault at about 85m distant from the well. The objective of this study is to evaluate the risk of fault reactivation due to water injection at this particular well. In this paper we focus on the 3D fluid and heat flow model developed with TOUGH2/EOS1 to estimate pressure and temperature changes induced by injection operations. The model is first calibrated and history matched to the observed pressure changes based on injection in a nearby well and subsequently applied to predict pressure and temperature effects at the fault due to a proposed injection scenario at the planned injector. The influences of different injection temperatures on pressure changes around the injector are discussed.

INTRODUCTION

Large-scale water injection is a common operation in oil and gas industry to enhance oil recovery and to manage produced water from a field. Injection of large volumes of water into the reservoir may change the pressure and temperature regime of the reservoir and cause unwanted phenomena such as caprock integrity damage and fault reactivation. Therefore, prior to the major water injection projects, the injection zone should be studied for possible geo-hazards and risks.

One of the potential operational risks during large volume fluid injection is fault reactivation. The injected mass could be water, CO_2, industrial wastes etc. The fault reactivation risk due to underground mass injection has long been investigated in mining, geotechnical and petroleum industries. Examples can be found in (Soltanzadeh and Hawkes, 2009), (Ozan et al., 2011), (Rutqvist et al., 2013).

Water injection can sometimes induce fault re-activation through two mechanisms. The first mechanism is related to poroelastic stresses induced by injection-related changes in pressure and temperature. That is, changing pressure and temperature in the injection zone causes the formation material to expand or contract, due to compressibility and thermal expansion effects. The surrounding material will act to restrict this deformation, thereby inducing stresses not only within the injection zone but also in the surrounding material. These stress changes may be sufficient to induce slip on nearby faults, depending on the stresses and their orientation, and type of fault.

The second fault reactivation mechanism involves direct migration of injected fluid into the fault zone. If the fault zone is sufficiently pressurized, the effective normal stress acting to keep the fault from slipping is reduced enough to allow the shear stresses acting on the fault to cause slip.

To analyze these two geomechanical effects on an injection well located near to a major fault, a feasibility study was carried out for a water injector well planned to inject up to 10,000m^3/day. The main objective is to assess the fault stability during water injection in that particular well.

This paper has focused on model assembly, history matching and sensitivity simulations of the fluid flow using TOUGH2 to simulate expected pressure and temperature changes around the injector and the adjacent fault. The outcomes of this study are used to support final decisions regarding fault stability.

TOUGH2 MODEL

Geological setting

The reservoir is located in a horst structure extending North-South between two assumed sealing faults. For the last couple of years the area of interest has been pressure supported by Water Injector 1 (WI-1) (shown in Figure 1) to improve the oil production of the wells located south of the current area of interest. These wells are NOT shown in the figures.

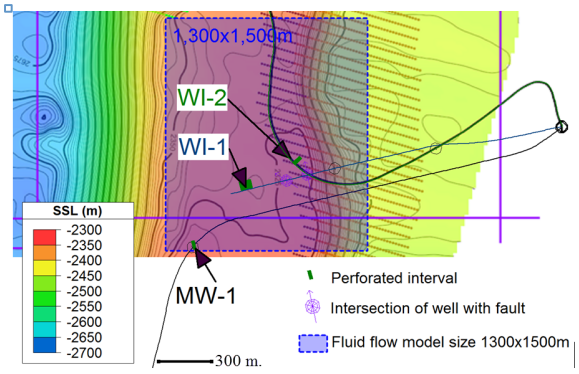

Figure 1. Structure map of the top of reservoir and the inclined wells trajectories at the area of interest.

An additional Water Injector 2 (WI-2) – a former producer – is placed at a distance of 80m from a fault. Water Injector 2 is approximately 340m from well WI-1. A couple of other wells penetrate the reservoir; one shut-in producer currently used as Monitoring Well (MW-1) is located ~840m from WI-2 – see Figure 1.

MW-1 and WI-2 are both fitted with down-hole pressure gauges. Pressure monitoring data during WI-1 injection for the past few years is available in those two wells and used for history matching in this study.

Fluid component

As a result of over 10 years of water injection operations at WI-1, most of the recoverable oil has been swept from the area of interest. Therefore, only residual oil saturations, or close to residual saturations, are now present in the pore spaces.

Consequently, water constitutes the majority of the flow. Water was therefore simulated as the single component of the fluid flow model. Using EOS1, an equation of state module available within the TOUGH2 code, the model was set for single porosity simulation. The software is also capable of modeling dual porosity behavior, which might be a future model variation to consider.

Grid generation

The fluid flow model's grid has been created in a way to match the main stratigraphic layers of the geological model provided by the operator. Please see Figure 2 for details of a cross section through the WI-1. The fluid flow model covers an area of 1300 by 1500m.

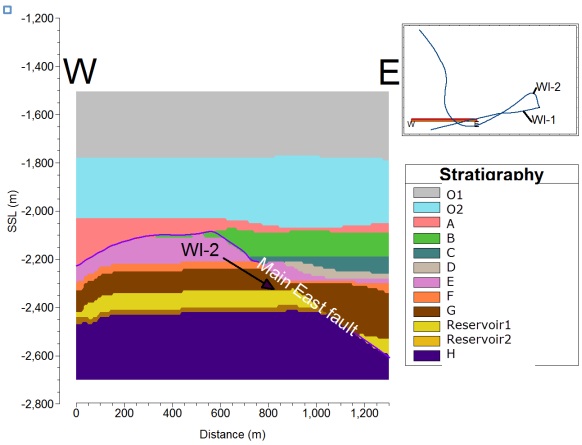

Figure 2. West-east cross section passing through the injector WI-2 and indicating the location of Water Injection well #2 in respect to the main fault.

A finer mesh zone was set up around the injection area to provide higher resolution of results at the perforation zones of both the monitoring and injecting wells. In total, the fluid flow model consists of 133,590 individual cells. The applied fluid flow boundary conditions are indicated in Figure 3. We assumed a no-flow boundary criterion at the top and bottom of the model, since the reservoir is sealed by thick over and underlying impermeable layers. We set the western fault as another no-flow boundary since this fault is assumed to be a sealing one.

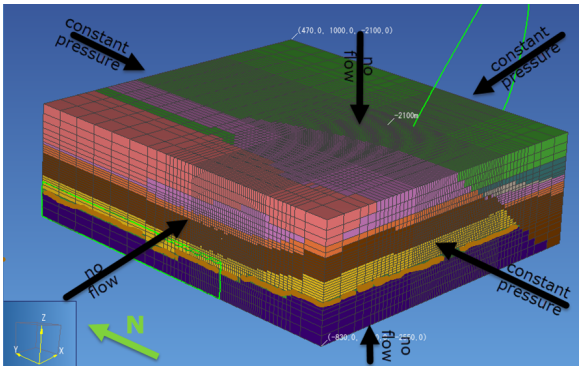

Figure 3. The 3D fluid flow model developed for the area of interest and the fluid flow assumptions on the model boundaries

All other boundaries are assumed as constant pressure boundaries. The structural offset caused by the main East fault forms a natural seal for the fluid flow (see Figure 2 for fault and injector locations).

Water has been injected historically into WI-1 (see Figure 1) to support ongoing oil production from the wells located beyond the South of the fluid flow model (not shown in Figure 1). On the other hand, the Monitoring Well 1 (MW-1) showed constant pressure during injection into Water Injector 1 (WI-1) – refer to Figure 6 later in text. In other words, MW-1 is located in an area between the WI-1 and the producers outside the model where the pressure remained constant during injection/production operations. Consequently we assume a constant pressure boundary condition at the South.

Regarding the boundary condition at the North, we assumed constant pressure due to the distance of the injector from the northern boundary and the flow being driven to the South due to production.

Initial conditions

We initialized the TOUGH2 model with information about pressure and temperature representing the reservoir state before starting water injection into the WI-2 close to the fault.

Based on pore pressure estimations from log data and measurements from both GeoTap® tools and active down-hole gauges, the current pore pressures are estimated with two gradients: one overburden gradient reflecting a virgin pressure gradient – 11.8kPa/m and another, a depleted reservoir pressure gradient, due to ongoing production – 9.4kPa/m. Field data used for pore pressure estimation is shown in Figure 4.

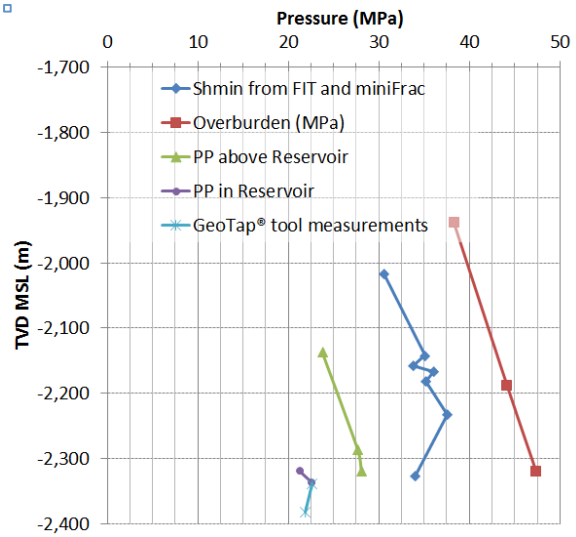

Figure 4. In situ pore pressure

The estimated geothermal gradient based on the temperature measurement at the reservoir is ~ 4.4°C/100m. The current temperature at reservoir depth is about 100°C.

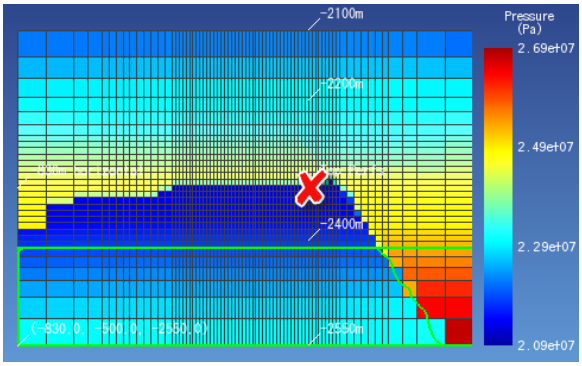

Figure 5: West-East cross section through WI-2 showing initial pressure gradient – X indicates WI-2 perforations

The model was run at isothermal conditions for 20 days to bring the model to an initial equilibrium condition.

Material properties

Table 1 and Table 2 present the average physical and thermal properties of the formations used in TOUGH2 simulations. These properties are

averaged based on log data analysis and adjusted based on history matching (discussed later).

The reservoir is divided into a high permeability upper zone (Reservoir1) and a low permeability deeper zone (Reservoir2). In this study, the effects of thermal expansion coeffient were ignored, as our simulations showed that it does not influence the results significantly for simulation of the short term (up to 1 year) water injection projects. Due to the lack of lab measurements, the values for heat conductivity and specific heat have been taken from literature (Incropera, et al, 1996) taking into account dominant lithology types in the different layers.

Table 1. The physical properties of the formations used in the model

Formation	Density (kg/m^3)	Effective Porosity (-)	X-perm (mD)	Y-perm (mD)	Z-perm (mD)
A	2715	0.14	101.3	101.3	60.8
B	2655	0.17	3.8	3.8	2.3
C	2908	0.26	1	1	0.6
D	2675	0.24	1	1	0.6
E	2557	0.09	1	1	0.6
F	2803	0.25	0.05	0.05	0.03
G	2617	0.08	0.001	0.001	0.0005
Reservoir1	2562	0.21	169	169	101
Reservoir2	2568	0.09	23	23	14
H	2578	0.07	0.8	0.8	0.5

Table 2. The thermal properties of the formations used in the model

Formation	Heat conductivity (W/m°C)	Specific Heat (J/kg°C)	Pore Compressibility (1/Pa)
A	2	1000	2.12E-09
B	2	1000	1.12E-09
C	2	1000	8.75E-10
D	2	1000	9.52E-10
E	2	1000	2.10E-09
F	2	1000	7.24E-10
G	1.3	880	2.10E-09
Reservoir1	2.9	745	9.66E-10
Reservoir2	2.9	745	2.25E-09
H	2	1000	2.15E-09

SIMULATION RESULTS

History match

We carried out reservoir scale simulations to history match recent pressure variations due to water injection into WI-1 – see Figure 6.

Validation of the fluid flow model is done by simulating historical injection at the WI-1 well. Two interference pressure measurements are available for this injection, at WI-2 and MW-1.

The modeled pressure change at the location of WI-2 is compared with the pressure changes observed in the field. Injecting with an average rate of $620m^3/h$ at WI-1 only increases the pressure at WI-2 between 5 and 9bar - see Figure 6, as mentioned in ***Geological setting*** above distance between those two wells is 340m.

Since pressure does not change significantly for MW-1, we assumed a no flow boundary at the South edge of the reservoir, as mentioned above.

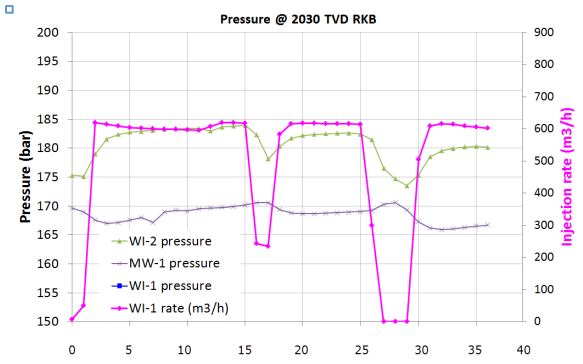

Figure 6. Injection rate of WI-1, pressures for WI-1, WI-2, MW-1 calculated to 2030m TVD based on measured data at gauge depths

An initial estimate of the average reservoir permeability was provided to us through the operator. Using TOUGH2, we ran a history matching scenario and tried to find a reasonable match between the permeability provided to us and the pressure decline between the two wells. The results of the history matching indicated that there is almost an order of magnitude difference between the permeability values provided and the estimates from the simulations.

A comparison between the pressure changes measured in the field and matched by simulations is shown in Figure 7. The comparison shows a good match between the measured and the simulated pressure values.

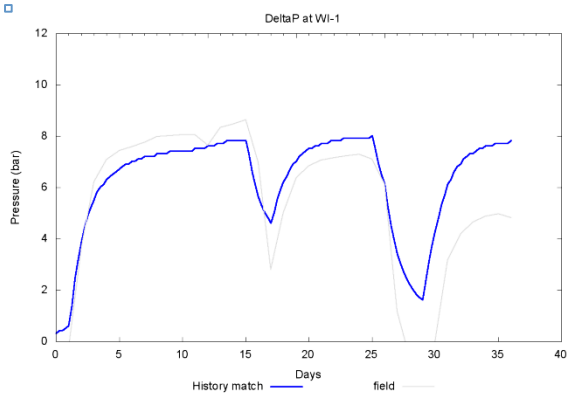

Figure 7. Delta pressure during injection at WI-2 measured and simulated

Modeling water injection close to the fault

After calibrating the model with historical injection data at WI-1 and updating the appropriate permeability values, the next simulations modeled the future injection plan using the WI-2 well. The simulations listed in Table 3, summarize the different configurations for the fluid flow simulations performed with TOUGH2.

All simulations are run with the maximum injection rate planned for WI-2, approximately 10,000m^3 per day. The first, baseline simulation (Run #1), was run with isothermal settings, which is equivalent to injecting water at reservoir temperature.

Table 3. Simulation matrix

Run ID	Isothermal	Inj. Temp (°C)	Duration (days)
#1	Yes	N/A	60
#2	No	70	60
#3	No	30	60
#4	No	100	60

All other runs were set to non-isothermal conditions, taking into account the temperature changes induced by the difference between formation and injected fluid temperatures.

Based on provided information from the operator, for the WI-2 well, the temperature of the injected water will be approximately 60°C to 70°C at the time of injection. Occasionally, it might be necessary to inject water at 30°C as well, which has also been accounted for in the simulations.

DISCUSSION

In this section, simulation results are described by referring to the evolution of simulated pressure and temperature over time, given at various monitoring points. Overall, we defined two monitoring points in different distances from the fault to evaluate how pressure and temperature change with respect to the distance from the fault.

The locations of these monitoring points are shown and explained in Figure 8 below.

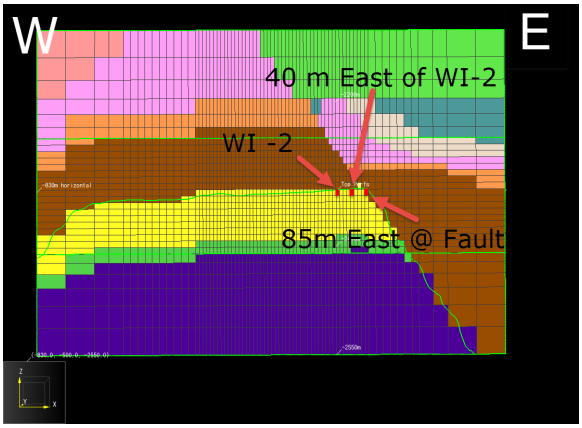

Figure 8. Location of monitoring points during simulation runs (red dots), West-East cross section through top of WI-1 perforations

Figure 9 shows a plan view of the pressure changes caused by 60 days of water injection into the target formation. The left and the right figures demonstrate the pressure changes close to the bottom and the top of the target zone, respectively. This is the isothermal case where the focus has been only on the pressure changes and therefore the thermal effects have been ignored. Pressure falls off faster toward the South as expected due to the production beyond the South boundary. The maximum pressure increase at the fault location is about 15 to 16bar for the isothermal case. Similarly, Figure 10 shows a contour plot of a West-East cross section through the formation at the WI-2 injection point for the same scenario.

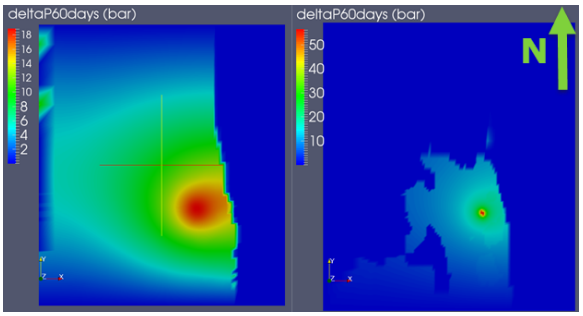

Figure 9. Pore pressure variations near the bottom (on left image) and the top of the target zone (on right image) isothermal conditions scenario (Run #1)

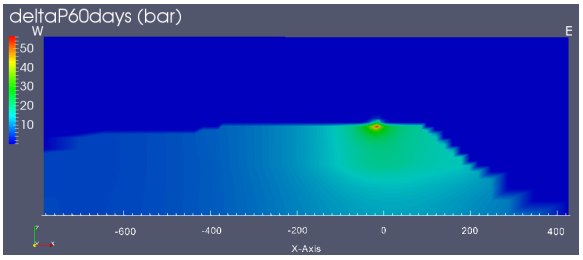

Figure 10. A West-East cross section passing through Water Injector 2 showing the pore pressure changes caused by water injection scenario (Run #1)

Non-isothermal conditions were considered next. Including temperature effects will influence geomechanical response in mainly two ways: First, the injected colder fluid will cool the formation causing thermal contraction. Second, injection of colder fluid increases the pressure response, due to viscosity effects because water at 30°C has about 4 times higher viscosity compared to 100°C water (Kemmer, 1979).

We ran different scenarios modeling injection temperatures of 30°C, 70°C, and 100°C and monitored the pressure and temperature changes at the monitoring cells shown in Figure 8.

30°C and 70°C are considered as the lower and upper bounds of the injected water temperature and 100°C is the water temperature chosen to be equal to the reservoir temperature for model verification purposes.

Figure 11 demonstrates the temperature changes at monitoring cell 40 meters from the fault caused by water injection with different temperatures. The initial reservoir temperature is 100°C and as expected, injecting 100°C water to the reservoir didn't change the monitoring cell's temperature.

In the reservoir with initial temperature of 100°C, injection of 70°C water cools down the monitoring cell to 70°C after about 40 days while using 30°C water cools down the monitoring cell temperature in about 15 days, see Figure 11.

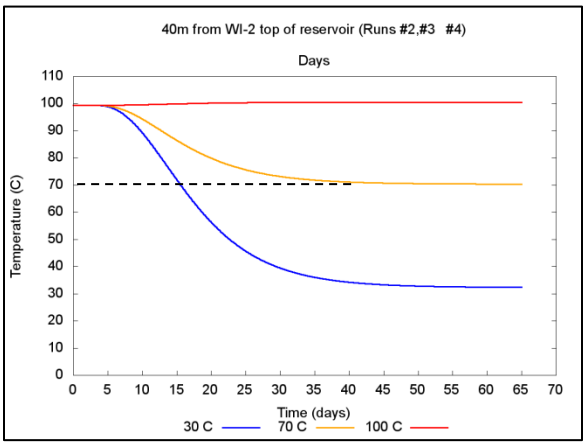

Figure 11. Effect of injected water temperature on changing the reservoir's temperature located 40m from the fault.

Farther away from the well and at the fault face, the change is even less pronounced, and the cooling effect is only apparent after about 50 days of injection and onward as shown in Figure 12.

The temperature development curves indicate that short injection of relatively cold water into the reservoir cannot change the initial reservoir temperature too far away from the injection well. Occasional injection of water at a temperature of 30°C for a short duration is therefore not significantly different from injection of 100°C water at the fault location. So, the main concern here is the operational injection pressure limits and not the thermal effects.

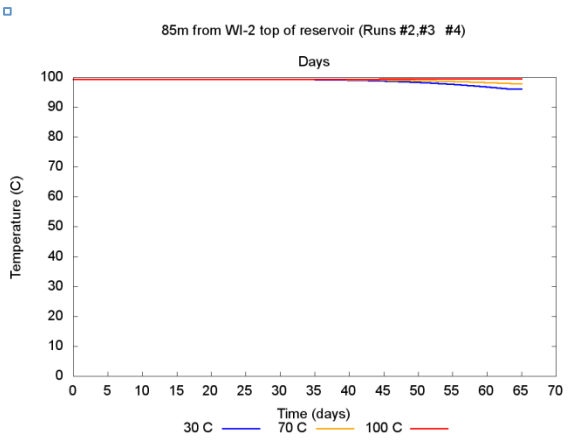

Figure 12. Thermal changes on the fault caused by injection water with different temperatures. The thermal changes on the fault are very small

Pressure increase at a distance 40m to the East of injection – heading direction fault – stays below 30bar for the different temperature scenarios modeled. There is a slightly higher increase for the 30°C water injection – see Figure 13.

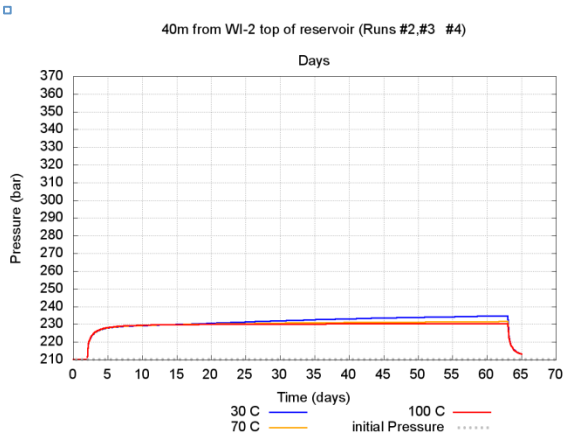

Figure 13. The effects of water temperature on changing the pressure values 40m from injection point, at 10,000m^3/day

The current reservoir pressure is about 210bar. At the fault location – 85m away from the injection point – injecting water will change the pressure from 210 to 230 bars. It is noted that change in the injected water temperature, doesn't make a significant change on changing the pressure induced on the fault (see Figure 14) as the pressure changes are similar to each other.

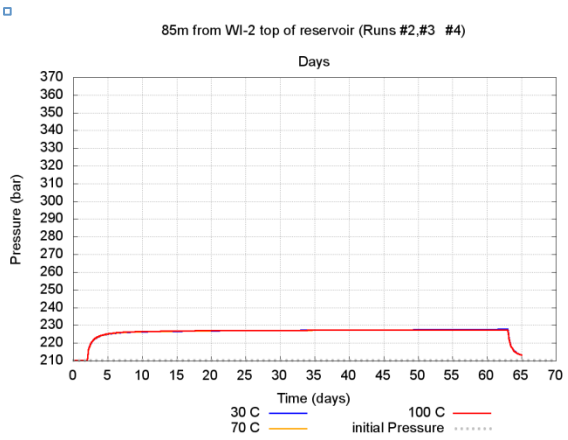

Figure 14. The effects of water temperature on changing the pressure values 85m from injection point, at 10,000m^3/day. It shows that injection water temperature effects vanish as the distance increases.

Next we looked at delta pressure and temperature values along the West-East profile at the injection depth (see Figure 15).

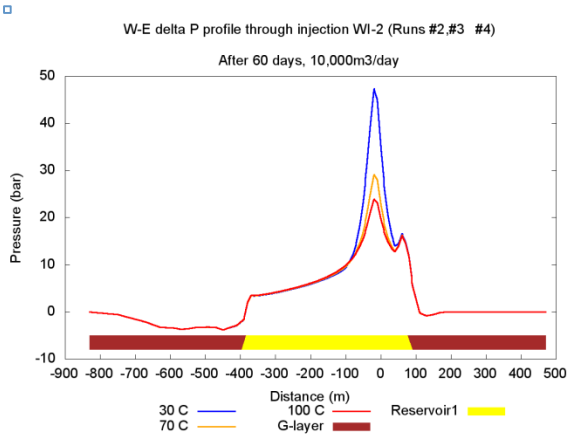

Figure 15. The pore pressure changes in a West-east cross sectional profile at -2325m SSL, overlaid with Formation G (brown) and Reservoir1 (yellow) formations

The pressure profiles indicate that there is no influence of cold water after a distance of 100 m away from injector. This is clearly seen in both directions, going west, where distance to West fault is about 400m and going east where the distance to fault is less than 100m. Temperature profiles shown in Figure 16 indicate similar area of influence.

Regarding the pressure increase after 60 days of water injection – as expected – the pressure increases more (up to 18bar) in the area of the

nearby East fault, while pressure increase toward the West decreases steadily and stays below 5bar 400m away from the injection point.

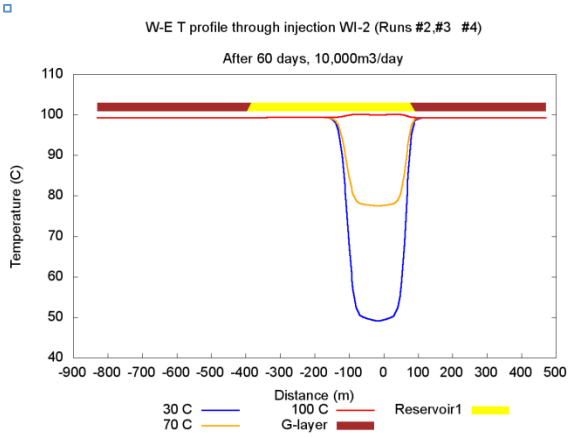

Figure 16. West-east cross sectional temperature profile at top of reservoir, overlaid with G-layer (brown) and Reservoir1 (yellow) formations

CONCLUSION

The results of our simulations show that injecting water at a rate of 10,000m^3/day and temperatures up to 60°C cooler than the reservoir will cause only minor temperature changes on the fault's face and the more pronounced thermal changes take place only near the injection well.

As expected, pressure build-up near the fault is higher than elsewhere – at the same distance from injection – in the reservoir. Due to continuous production to the South of the zone of interest, we believe the pressure increase at the fault is going to be less than 20bar or about 10% of the initial pressure.

FUTURE WORK

Using the simulation and history matching techniques presented in this paper, we will develop two extreme scenarios involving the continuous injection of the maximum amount of water for 1 year and assuming 100°C and 60°C injected water temperatures. The pressure and temperature changes caused by 1 year water injection from TOUGH2 will be exported and analyzed in a one-way coupled 3D Geomechanical model to assess the induced stresses on the fault. The ultimate goal will be to evaluate fault activation risks caused by the induced stresses.

ACKNOWLEDGMENT

Thanks to "Subsurface As" for technical support during the project completion. Also thanks to Mr. Bill Childers for valuable feedbacks and corrections.

REFERENCES

Incropera, F.P., DeWitt, D.P., "*Fundamentals of Heat and Mass Transfer*", John Wiley & Sons, 4th Edition, 1996.

Kemmer, F.N., *The NALCO Water Handbook*, McGraw-Hill, Inc., USA, 1979

Ozan, C., Brudy, M., & Van der Zee, W. *"Fault Reactivation Due to Fluid Production And Injection In Compacting Reservoirs"*. American Rock Mechanics Association. (2011).

Pruess, K., C. Oldenburg, and G. Moridis, *TOUGH2 User's Guide, Version 2.0*, Report LBNL-43134, Lawrence Berkeley National Laboratory, Berkeley, Calif., 1999.

Rutqvist, J.; Rinaldi, Antonio P.; Cappa, F; Moridis George J. *"Modeling of Fault Reactivation and Induced Seismicity During Hydraulic Fracturing of Shale-Gas Reservoirs"* Journal of Petroleum Science and Engineering, (2013)

Soltanzadeh, H.; Hawkes, Christopher D.;*" Assessing fault reactivation tendency within and surrounding porous reservoirs during fluid production or injection"* International Journal of Rock Mechanics & Mining Sciences 46 (2009)

MODELING STEAM, WATER, AND OIL FLOW OVERLYING A HEAVY OIL RESERVOIR UNDERGOING CYCLIC STEAMING

Christine Doughty, Laura Blanco-Martin, Yingqi Zhang, and Curtis M. Oldenburg

Lawrence Berkeley National Laboratory, Earth Sciences Division
One Cyclotron Road, MS 74R-316C
Berkeley, California, 94720, United States
e-mail: cadoughty@lbl.gov

ABSTRACT

We model the non-isothermal migration of steam, liquid water, and oil that leaks from a damaged well casing through the overburden of a hypothetical petroleum reservoir being produced with cyclic steaming. Of particular interest is to predict when, if ever, any leaking fluids reach the ground surface. Key modeling choices include the Equation of State (TMVOC or EOS8), model dimensionality (RZ, XZ, 1D vertical), the extent and resolution of the model, and how to resolve the cyclic steam operations in time. Preliminary findings indicate that it is difficult for leaking fluids to reach the surface, requiring the existence of preferential vertical flow paths that provide limited opportunity for lateral spreading.

INTRODUCTION

As part of an ongoing study to develop a risk assessment framework for oil and gas production, we are conducting flow modeling, geomechanical modeling, and data-worth analysis for a test case involving cyclic steaming of heavy oil in a high-porosity, low-permeability diatomite reservoir. This paper provides a progress report on the flow modeling. Companion papers describe geomechanical modeling (Blanco-Martin et al., 2015) and data-worth analysis (Zhang et al., 2015).

In cyclic steaming, steam is injected into a well for a few days, then the well is shut in for a few days, and then the well is produced. The energy from the steam heats the oil, reducing its viscosity and enabling it to flow into the well. Cyclic steaming is the preferred alternative to steam flooding when reservoir permeability is too low to allow significant communication between wells. In highly compressible diatomite formations, cyclic steaming may cause significant expansion and compaction of the overburden and reservoir, which can lead to stresses on wells and associated well failures. If undetected and unmitigated, well failures may result in leakage of steam and formation fluids into the overburden. The purpose of the present work is to model the non-isothermal migration of steam, liquid water, and oil that escapes through a hypothetical casing break above the producing formation and migrates upward through the overburden, which consists of a shallow oil reservoir, a groundwater-saturated clay layer, and an overlying vadose zone. Of particular interest is to predict when, if ever, any leaking fluids reach the ground surface, along with the composition and rate of leakage.

Model development is guided by two conflicting constraints. On the one hand, the model should be a realistic representation of the system, considered relevant by all stakeholders, and allow monitoring and mitigation strategies to be tested. On the other hand, a simpler model may help to identify key processes that are responsible for certain observations. In addition, the reduced computational cost can accelerate the corresponding sensitivity and data-worth analysis. In conjunction with the geological setting, balancing these two constraints informs the choices made for model development, as outlined in the sections below. Thereafter, example simulation results are presented, along with a discussion of the strengths and weaknesses of the underlying models, followed by a summary of the conclusions reached thus far and recommendations for future work.

GEOLOGIC SETTING

The test case is a hypothetical reservoir, denoted La Prueba, typical of the diatomite reservoirs in the southern San Joaquin Valley of California. Figure 1 shows a cross section perpendicular to

the long axis of an anticline structure that traps heavy oil. Cyclic steaming occurs in the Diatomite A formation, which overlies the lower-permeability, unproductive Diatomite CT formation. It is hypothesized that differential subsidence and uplift cause casing damage along plains of weakness in the overlying Tulare Formation, which is divided into layers labeled A through E. The Tulare Formation is highly heterogeneous, with lenses of heavy oil interspersed among water-saturated rock, and sub-vertical faults common near the crest of the anticline. The permeability of the Tulare Formation is high, but the oil is so viscous that it does not flow under ambient temperature conditions. The Corcoran Clay (green line) is a regional low-permeability clay layer within the Tulare Formation, approximately coincident with the top of the oil deposits and the water table. The overlying alluvium is expected to be similarly heterogeneous as the Tulare, and is initially partially saturated with air and water.

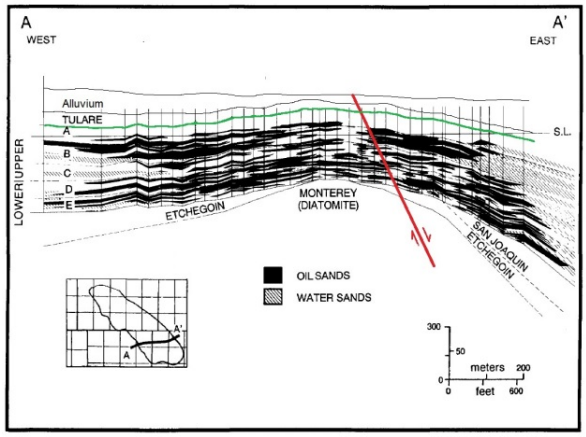

Figure 1. Conceptual model of La Prueba.

If the Tulare oil is heated by escaped steam, a variety of flow paths appear possible: lateral spreading under the shale lenses that presently trap oil within the Tulare Formation, lateral spreading under the Corcoran Clay, vertical flow through gaps in the Tulare Formation, and possible focused vertical flow through sub-vertical faults or abandoned and/or damaged wells.

The key hydrogeologic layers used to represent La Prueba are shown in Table 1. The depths and thicknesses shown are for the top of the anticline.

Table 1. Parameters for hydrologic layers of La Prueba.

Formation and Permeability	Depth of Top (m)	Thick-ness (m)	Feature
Alluvium k_h = 100 mD k_h/k_v = 100	0	74	Vadose zone (air and water)
Corcoran Clay k_h = 1 mD k_h/k_v = 10	74	26	Water Table
Tulare k_h = 1 D k_h/k_v = 10	100	200	Oil and water (casing break at 167 m depth)
Diatomite A k_h ~ 1.5 mD (decreasing with depth)	300	300	Oil and water (oil saturation, permeability, and porosity decrease with depth)
Diatomite CT k_h ~ 0.5 mD (decreasing with depth)	600	900	Oil and water (oil saturation, permeability, and porosity decrease with depth)

MODEL CHOICES

Equation of State: TMVOC or EOS8

The physical processes that must be considered are the multi-phase, multi-component fluid flow of steam, liquid water, and oil, along with heat flow and phase change. In terms of their proclivity for upward migration, steam is buoyant and low viscosity, but it is ephemeral – until sufficient heating of native rock and fluids occurs, it condenses into liquid water. Water may be buoyant, and has moderate viscosity, but it is already present everywhere in the system when steam injection begins. Oil is lighter than water but heavier than air, meaning it will only be buoyant below the water table. Additionally, oil viscosity is too high for it to flow at all unless it has been heated significantly. Thus, it is unclear a priori whether or how a distinct signal of casing failure will be manifested at the ground surface.

Two modeling approaches have been taken. The first, more rigorous, approach uses TMVOC

(Pruess and Battistelli, 2002) with five components: water, air, methane, and two oils (one composition for the Diatomite Formations and another heavier, more viscous composition for the Tulare Formation), and three phases: gas, aqueous, and non-aqueous phase liquid (NAPL, i.e., oil), with all components partitioning into all phases. Thus, even if oil does not flow upward as a separate phase, upward migration of oil may occur if the oil dissolves into the aqueous phase or volatilizes into the gas phase.

For flow and transport through the strongly heterogeneous medium considered, TMVOC runs very slowly, and often stops with convergence failures, motivating a simpler approach involving EOS8 (Pruess et al., 2012). EOS8 considers only three components: water, air, and oil, and three phases: gas, aqueous, and NAPL. The oil is considered "dead": it does not volatilize into the gas phase or dissolve into the aqueous phase, nor does water or air dissolve into the NAPL phase. EOS8 was customized to incorporate the viscosity temperature dependence used in TMVOC, which is necessary to capture the orders-of-magnitude decrease in oil viscosity that accompanies steam heating, and to generalize the linear oil relative permeability function built into EOS8 to a power-law function. (The three-phase relative permeability and capillary pressure functions from TMVOC have also been added to EOS8 (Blanco-Martin et al., 2015), but they are not used for the present studies.) TOUGH2/EOS8 runs faster and is more stable than TMVOC.

Comparison between simulations using TMVOC and EOS8 suggest that for the present problem, the simpler EOS8 representation adequately represents the main physical processes occurring, because the heavy oil of the Tulare Formation (API = 13), does not partition significantly into the aqueous or gas phases. Figure 2 illustrates spatial distributions of state variables after two years of steam injection, simulated with TMVOC using an RZ model. Frames labeled "NO" indicate states that do not exist in EOS8. None of these states should play a major role in enabling leakage of steam, liquid water, or oil to the ground surface.

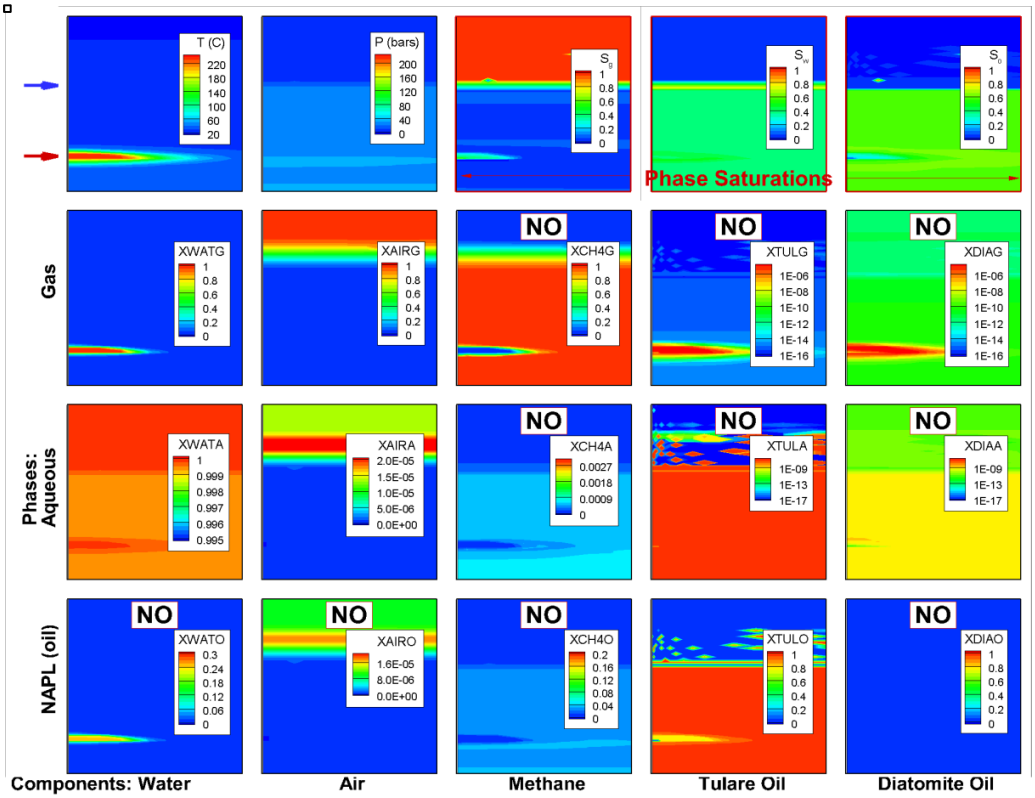

Figure 2. TMVOC Results: state variables after two years of steam injection in an RZ model. Frames labeled "NO" indicate that EOS8 does not consider the state. Blue arrow: water table. Red arrow: casing break. Horizontal:Vertical exaggeration 20:1.

Dimensionality: 3D, 2D, or 1D

The geometry of a well leaking steam into a heterogeneous formation is intrinsically three dimensional (3D) as buoyant fluid moves radially outward from the well and then upward through preferential flow paths. However, 3D models of sufficient resolution to properly simulate near-wellbore effects would be too computationally intensive to be practical in the context of a risk assessment framework. Two-dimensional (2D) models are much more computationally tractable, but we must be aware of the errors they inevitably introduce.

For problems involving a single well, an axisymmetric (RZ) model is a natural choice. The radial spreading of fluid and heat away from the well can be efficiently modeled with a grid whose radial resolution is fine near the well, then gradually coarsens with distance. If the well being studied is one of many similar wells penetrating a reservoir, a closed outer boundary acts as a line of symmetry, so the influence of neighboring wells is accounted for. Layered heterogeneity can be represented accurately, but any lateral variability must be interpreted carefully. Clay lenses of low permeability, such as could trap oil as shown in Figure 1, are actually ring structures. A vertical preferential flow path is actually an annulus, unless it is at the origin.

If a reservoir has an anticline structure as shown in Figure 1, a 2D vertical cross-section across the anticline (an XZ model) may be a good choice to represent the large-scale geology. Layering and lateral heterogeneities can be represented accurately if the assumption of negligible flow out of the XZ plane is met. However, representing a single leaking well is problematic. The actual well leakage rate and heat flow rate will be too low at early times and too high at late times to accurately represent the radial fluid and heat flow away from the well. Only if the well being modeled is actually one of a long line of similar wells, so that flow from each well will tends to be planar rather than radial, will the XZ model accurately represent leakage and heat flow from the well.

For the present work involving cyclic steaming, it is important to capture the radial geometry of fluid and heat flow outward from and inward to the well, so an RZ model is deemed preferable to an XZ model. The treatment of vertical preferential flow paths must therefore be regarded as more schematic: a flow path can be located accurately in terms of its distance from the well, but the focusing of flow through a tube-like channel that might occur in nature cannot be fully represented because the conduit is actually an annulus rather than a tube.

As an extreme simplification, we also developed a one-dimensional (1D) vertical column model to represent only vertical fluid flow through a hypothesized vertical preferential flow path. The purpose of such a simplified model was to study the sensitivity of the potential surface manifestation to the properties of a vertical leakage flow path. Conductive heat flow from the path to the surrounding overburden was represented via an analytical solution (Zhang et al., 2011). This model runs very quickly, enabling sensitivity studies to be conducted easily, but it is too simple to use in a meaningful data-worth analysis because it provides no opportunity to examine monitoring or mitigation strategies.

Model Extent and Grid Resolution

The vertical extent of the model must include the depths from the casing break at 167 m to the ground surface. Greater depths could also be included, with the bottom boundary being either the bottom of the Tulare Formation (300 m), the bottom of the productive diatomite (600 m), or the bottom of the entire diatomite (1500 m). For the 1D model, because we only model flow through the vertical conduit, the casing break is a reasonable lower boundary, but for the RZ model, where fluid flow through the Tulare Formation also occurs, the bottom of that formation should be used. If we want to include the reservoir response to production, we need to include the Diatomite A. Little fluid flow occurs in the underlying Diatomite CT, so it can be omitted from the model or represented very coarsely. The vertical resolution is finest (5 m) from the ground surface down through the upper two-thirds of the Tulare Formation, with a gradual coarsening with depth below that.

To represent one well in isolation, the lateral extent of the model is made very large to

approximate an infinite-acting model. Radial grid resolution is fine near the well, to resolve sharp pressure and temperature gradients, but coarsens with distance. Figure 3 shows the central portion of the RZ grid used for the La Prueba problem.

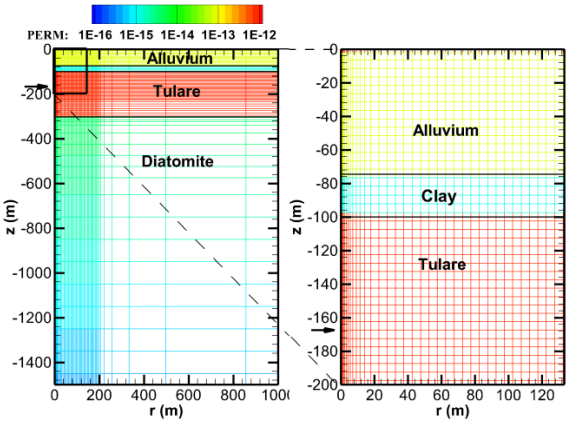

Figure 3. Central portion of the infinite-acting RZ grid used for La Prueba. The casing break at 167 m depth is shown by an arrow.

A useful method for helping decide grid extent and resolution for non-isothermal problems is to calculate the thermal penetration distance for conduction, L, which is defined as $L = (4\ D_{th}\ t)^{1/2}$, where D_{th} is thermal diffusivity (thermal conductivity divided by heat capacity) and t is time. Table 2 shows L for a range of times, for $D_{th} = 10^{-6}$ m^2/s. Thus, for a simulation time of 20 years, upward heat flow from the top of the Diatomite A at 300 m will not impact fluid flow around the casing break at 167 m, so the Diatomite Formation only needs to be included if the response in that formation itself is of interested. On the other hand, in 20 years radial heat flow will extend 50 m from the well, so if well spacing is less than 100 m, the interference between wells should be considered. Short-time penetration distances are also relevant, to make sure near-well grid resolution is appropriate for representing the injection-rest-production periods of the cyclic steaming operation.

Table 2. Thermal penetration distance for conduction as a function of time.

Time	1 day	10 days	1 mo	6 mos	1 yr	2 yrs	5 yrs	20 yrs
L (m)	0.6	1.9	3	8	11	16	25	50

Cycle Resolution

Cycle duration for cyclic steaming is taken to be 6 days of injection, 4 days of rest, and 22 days of production. Steam leakage is modeled as a water source (COM1) at the casing break, with a repeated step injection rate (on for 6 days, off for 26 days) of 500 CWE bbl/day (0.92 kg/s) and an enthalpy that represents 75% quality steam. The enthalpy is determined iteratively since the (P,T) conditions at the casing break, which controls enthalpy, are not known a priori. For the production period, the (P,T) conditions at the wellhead are held constant.

Because the simulation period in on the order of 10-20 years or more, taking short enough time steps to resolve all these cycles can be problematic. If we are not interested in the oil production from the Diatomite, but only the migration of fluids caused by steam leakage, an alternative is to assume constant steam injection at a rate of 6/32 times the actual rate, so that the correct amount of steam is added to the system.

NUMERICAL SIMULATIONS

The preliminary simulation results presented here use EOS8, the infinite-acting RZ model shown in Figure 3, and a constant steam injection rate of 0.17 kg/s with enthalpy 2376 kJ/kg at the casing break. Simulations run for 50 years.

Initial and boundary conditions

The ground surface is a constant-property boundary with atmospheric temperature and pressure. The bottom boundary of the model is closed. The outer radial boundary is closed, but it is so far away (19 km) that it has negligible impact. Initial conditions are a geothermal gradient for temperature and a hydrostatic pressure distribution. Fluid composition is an air/ water mixture in the Alluvium, water in the Corcoran Clay, and a water/oil mixture in the Tulare and Diatomite Formations. As permeability decreases with depth in the Diatomite Formations, so does oil saturation.

Characteristic curves

The relative permeability and capillary pressure functions used for steam and liquid water are generic van Genuchten (1980) functions with m

= 0.7, S_{lr} = 0.2, and S_{gr} = 0.02. Capillary pressure strength follows Leverett scaling (inversely proportional to the square root of permeability), with a value of 0.25 bars for the Tulare Formation. Oil relative permeability is a power law with exponent 2 and residual oil saturation S_{or} = 0.2. There is no capillary pressure between oil and water.

Base case

For the base case, there is no surface manifestation of steam injection. Figure 4 shows the spatial distributions of temperature, pressure, steam saturation, and oil saturation at the end of 50 years steam injection. The Corcoran Clay acts as an effective top seal to trap the injected steam. Note that the steam has displaced oil away from the well and created a bank of higher oil concentration at distance. This is an artifact of using a constant steam injection rate.

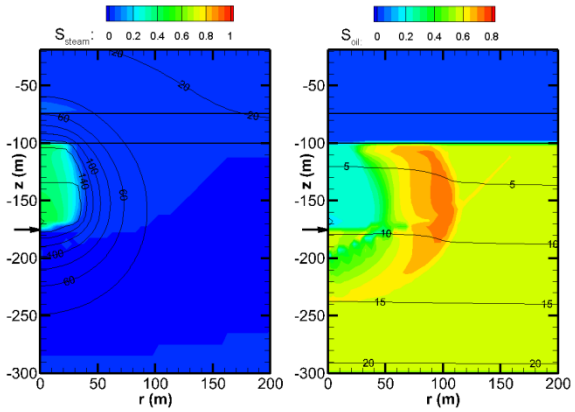

Figure 4. Base case simulation results after 50 years. The left frame shows steam saturation as color and temperature (°C) as contour lines. The right frame shows oil saturation as color and pressure (bars) as contour lines. The Corcoran Clay is delineated by the horizontal black lines.

Homogeneous sensitivity studies

A series of sensitivity studies were done, varying the permeability of various materials, to see if a surface manifestation of steam leakage could be achieved. First, the permeability of the Corcoran Clay layer was increased to equal that of the Alluvium (in other words, the clay was absent), but there was still no surface manifestation. Next, as an extreme measure, the vertical permeabilities of the Alluvium, Corcoran Clay, and Tulare were all increased to 1 Darcy, but that did not produce any surface manifestation. Doubling these vertical permeabilities to 2 D did produce a surface manifestation, with steam reaching the ground surface 18 years after steam injection began. Doubling vertical permeabilities again to 4 D shortened the breakthrough time to 6 years. Figure 5 shows spatial distributions at 50 years for the 4 D case. Note that oil has moved upward, but much less than steam. This is at least partly an artifact of the outward displacement of the oil caused by the constant steam injection rate.

The vertical permeability increase required to achieve a surface manifestation produces a rather unrealistic homogeneous, anisotropic medium in which vertical permeability is much greater than horizontal permeability. This motivated construction of two heterogeneous models, described below.

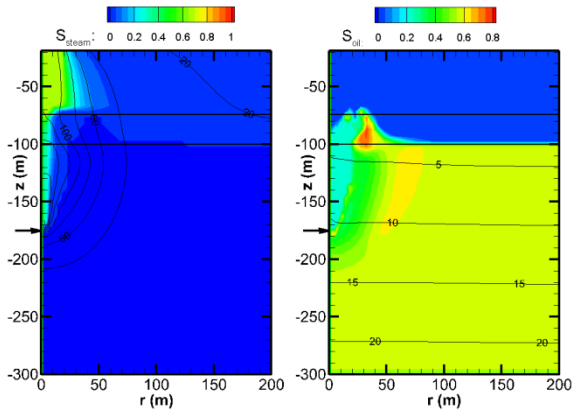

Figure 5. 4 D vertical permeability simulation results after 50 years.

Stochastic heterogeneity sensitivity studies

The Tulare Formation, the Corcoran Clay, and the Alluvium were all replaced by a stochastically generated heterogeneous formation in which low-permeability clay lenses are interspersed in a high-permeability sand. The clay permeability is 0.1 mD and the sand permeability is 4 D. Both materials are isotropic. Different heterogeneous formations were generated by specifying different maximum lengths for the clay lenses. It was anticipated that for long lenses, a surface manifestation would be less likely due to the circuitous path from the casing break to the ground surface. However, even for the shortest

maximum lens length, there was no surface manifestation. Then, as an extreme measure, clay lenses were removed by hand from a region near the well, leaving a continuous isotropic 4 D sand between the casing break and the ground surface. Even this did not produce any surface manifestation. Two examples of the heterogeneous simulation results after 50 years are shown in Figure 6. It is clear that although upward movement of steam does occur through gaps between the clay lenses, there is also much lateral spreading, which precludes a surface manifestation.

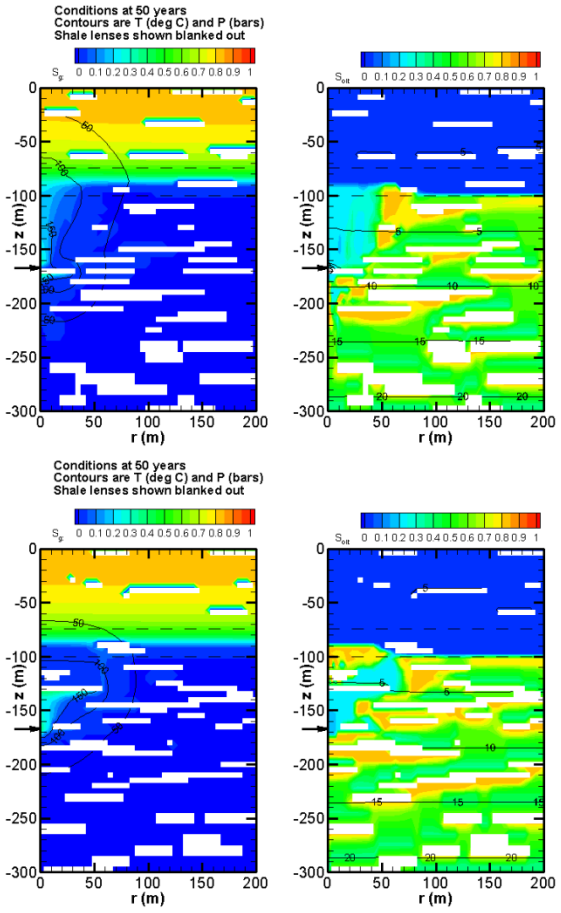

Figure 6. Heterogeneous simulation results for two different stochastic realizations. Left frames: gas saturation; right frames: oil saturation.

Deterministic heterogeneity sensitivity studies

Recall that for the homogeneous cases with a surface manifestation, although vertical permeability is 4 D, lateral permeability is 1 D in the Tulare Formation and 100 mD elsewhere. Thus, we hypothesize that the requisite conditions for surface breakthrough are a high-permeability vertical path with limited opportunity for lateral spreading. Models with deterministically-placed high-permeability conduits extending from the casing break to the ground surface embedded in a medium with base-case properties do show surface manifestations, confirming this hypothesis.

Interestingly, under some conditions, the surface manifestation is transient. For large conduits, the surface manifestation is steady once breakthrough occurs, but for small conduits, where lateral fluid flow is larger compared to vertical fluid flow, an initial surface manifestation may occur, which later decays as the subsurface heats up, enabling more lateral fluid flow and hence less vertical fluid flow to the surface. This subtle interplay of vertical and lateral fluid flow underscores the need to include the possibility of fluid flow in all directions, precluding use of our extremely simple 1D vertical conduit model.

CONCLUSIONS AND FUTURE WORK

A key result of the simulations is that it is difficult for leaking fluids to reach the ground surface. Although steam is buoyant relative to all other fluids, under typical subsurface conditions, geological heterogeneities promote lateral spreading in addition to upward buoyant flow, resulting in cooling and condensation. Oil is buoyant relative to groundwater, but not relative to vadose-zone air, again promoting lateral spreading rather than upward flow. Numerous two-dimensional (RZ) simulations using different representations of the geologic heterogeneity suggest that for leaking fluids to reach the surface, a high-permeability, continuous conduit, with limited opportunity for lateral migration, is necessary. Such a conduit could be provided by an abandoned well, a vertical fracture or fault, or a geochemically altered region caused by the steam itself (a so-called "wormhole"). This is consistent with field operations in the southern San Joaquin Valley diatomite fields, where many wells have casing failures that could cause leaks, but only a few surface manifestations of leaking fluids are observed.

Once a suite of sensitivity studies has been completed, it is valuable to revisit the modeling choices made. The simulations described above have many opportunities for improvement, which are the subject of ongoing and future work. These are listed below.

1. The individual cycles of injection-rest-production should be incorporated if the movement of oil is to be modeled correctly. This is straightforward to do, but will increase simulation times greatly by forcing smaller time steps. As a result, an efficient mesh is important.
2. A closed lateral boundary at 25 m (half the nominal well separation of 50 m) should be used, to represent one well among many, rather than one isolated well. Even if surface manifestation is a rare occurrence, casing failure is not, and even with an intact casing, conductive heat flow will propagate 25 m away from the well within 5 years.
3. The three-phase relative permeabilities from TMVOC have been incorporated in EOS8 (Blanco-Martin et al., 2015) and using them will increase oil relative permeability compared to the treatment of relative permeability used thus far.
4. Since the onset of this work, more realistic property values have been found for permeability and initial temperature of the producing Diatomite Formation, both of which will impact the (P,T) conditions in the wellbore and in particular at the casing break. The possibility of specifying steam injection at the wellhead and letting the code calculate the conditions at the casing beak will be investigated, rather than specifying the steam injection explicitly at the casing break, as is done now.

ACKNOWLEDGMENT

Support for this work was provided in part by Lawrence Berkeley National Laboratory under Department of Energy Contract No. DE-AC02-05CH11231.

REFERENCES

Blanco-Martin, L., J. Rutqvist, C. Doughty, Y. Zhang,S. Finsterle and C.M. Oldenburg, iTOUGH2-FLAC modeling of thermal-hydraulic-mechanical proceses related to steam-assisted heavy oil recovery from diatomite, Proceedings, TOUGH Symposium, 2015.

Pruess, K., and A. Battistelli, *TMVOC, A Numerical Simulator for Three-Phase Non-isothermal Flows of Multicomponent Hydrocarbon Mixtures in Saturated-Unsaturated Heterogeneous Media*, Report LBNL-49375, Lawrence Berkeley National Laboratory, Berkeley, Calif., 2002.

Pruess, K., C. Oldenburg, and G. Moridis, *TOUGH2 User's Guide, Version 2*, Report LBNL-43134 Rev., Lawrence Berkeley National Laboratory, Berkeley, Calif., 2012.

van Genuchten, M. Th., A closed-form equation for predicting the hydraulic conductivity of unsaturated soils, *Soil. Sci. Soc. Am. J.,* 44, 892-898, 1980.

Zhang, Y., L. Blanco-Martin, C. Doughty, S. Finsterle, Q. Zhou, and C.M. Oldenburg, Determining optimal monitoring strategies for managing risks of cyclic steam injection using data-worth analysis, Proceedings, TOUGH Symposium, 2015.

Zhang, Y., L. Pan, K. Pruess, S. Finsterle, A time-convolution approach for modeling heat exchange between a wellbore and surrounding formation, *Geothermics*, 40, 261-266, 2011.

A NEW SIMULATION MODEL OF KEROGEN PYROLYSIS FOR THE IN-SITU UPGRADING OF OIL SHALES

Kyung Jae Lee and George J. Moridis

Earth Sciences Division, Lawrence Berkeley National Laboratory
1 Cyclotron Rd
Berkeley, CA 94720
E-mail: kyungjaelee@lbl.gov

ABSTRACT

Oil shale is a vast, yet untapped energy source. Our study focuses on in-situ upgrading, which is applicable to all formation depths. Kerogen pyrolysis during in-situ upgrading process is represented by six kinetic reactions, resulting in 10 pseudo-components that are distributed among four phases. We expanded FTSim, a variant of the TOUGH+ simulator, and developed a simulator capable of modeling the kerogen pyrolysis and the accompanying system changes during the in-situ upgrading process. The simulator describes the coupled process of mass transport and heat flow through porous and fractured media and accurately accounts for the thermodynamics of phase equilibria and transitions, thus providing a powerful tool to evaluate the energy efficiency and the productivity of the in-situ upgrading processes. We applied our simulator to evaluate the three proposed methods for the in-situ upgrading, i.e., the Shell In-situ Conversion Process, the ExxonMobil Electrofrac method, and the Texas A&M Steamfrac method. We analyzed and compared the productivity and energy efficiency of each process.

INTRODUCTION

The global resources in oil shales with commercial potential are believed to exceed 2.5 trillion barrels, of which 2.0 trillion barrels are in the US. Commercial production of hydrocarbons from oil shales has not yet been realized because of the technical and economic challenges posed by the thermal processes that are needed for their development. At a temperature approaching 610 °F, kerogen in the oil shale is decomposed into fluid and solid products including hydrocarbons. At a higher temperature, heavy hydrocarbons crack into lighter hydrocarbons in subsequent reactions. In order to successfully produce hydrocarbons from oil shale reservoirs, these pyrolysis processes and accompanying system changes should be understood and evaluated properly.

In this paper, we use a non-isothermal, fully implicit, and multiphase-multicomponent simulator developed to describe kerogen pyrolysis in the in-situ upgrading of oil shales (Lee 2014; Lee et al. 2015). We apply the simulator to the diverse in-situ upgrading processes such as Shell In-situ Conversion Process (ICP), ExxonMobil Electrofrac, and Texas A&M (TAMU) Steamfrac. Through these simulation works, we will evaluate the producible total hydrocarbons, cumulative productions of fluid phases, remaining kerogen in the reservoir, and energy efficiency of each process.

METHODS

Simulator Development

Our own simulator for the kerogen pyrolysis was developed by expanding the FTSim, a variant of the TOUGH+ simulator, and was validated by matching with the field production data from Shell ICP implementation in Green River Formation (Lee et al. 2015). This simulator involves mass and heat flow in porous/fractured media, accurate computation of phase properties, phase equilibrium and transitions, and evolution of porosity and permeability.

Kerogen pyrolysis reactions are simply grouped into six kinetic reactions as shown in Table 1 (Wellington et al. 2005). The first reaction is the solid kerogen decomposition into fluid and solid products, which is activated from 290 °C. The second and third reactions are the cracking of heavy oil component into lighter hydrocarbons

and solid products in gaseous phase and liquid organic phase, respectively. The fourth and fifth reactions are the cracking of light oil component into hydrocarbon gas and solid products in gaseous phase and liquid organic phase, respectively. The second to the fifth reactions are activated from 320 °C. The sixth reaction is the coking of hydrocarbon gas into hydrogen and solid products, which is activated from 330 °C.

Table 1. Kinetic Reactions of Kerogen Pyrolysis.

Kinetic reactions
(1) Kerogen → 0.02691 H_2O + 0.009588 heavy oil + 0.01780 light oil + 0.04475 HC gas + 0.01049 H_2 + 0.00541 CO_2 + 0.5827 Prechar
(2) Heavy oil (G) → 1.8530 light oil + 0.045 HC gas + 2.4515 Prechar
(3) Heavy oil (O) → 0.2063 light oil + 2.365 HC gas + 17.497 Prechar
(4) Light oil (G) → 5.730 HC gas
(5) Light oil (O) → 0.5730 HC gas + 10.904 Prechar
(6) Hydrocarbon gas (G) →2.8 H_2 + 1.6706 Char

The reservoir system includes 10 components distributed in four phases as provided in Table 2. The four phases are aqueous phase, liquid organic phase, gaseous phase, and solid phase. The 10 components are the fluid products of:

(1) heavy oil ($C_{22}H_{46}$)
(2) light oil ($C_{11}H_{24}$)
(3) hydrocarbon gas (C_2H_6)
(4) water (H_2O)
(5) hydrogen (H_2)
(6) Carbon dioxide (CO_2)
(7) Nitrogen (N_2),

and the solid products of:

(8) kerogen
(9) prechar
(10) char

In the aqueous phase, the oil and gas components are dissolved in the liquid water. In the liquid organic phase, the water and gas components are dissolved in the mixture of heavy oil and light oil. In the gaseous phase, the water and oil components present as vapor, and the gas components present as free gas. In the solid phase, kerogen presents as solid hydrocarbon, and pre-char and char present as solid carbon.

Table 2. Phases and Components in the System.

Phases	Components
(1) Aqueous	(1) Heavy oil ($C_{22}H_{46}$)
(2) Liquid organic	(2) Light oil ($C_{11}H_{24}$)
(3) Gaseous	(3) Hydrocarbon gas (C_2H_6)
(4) Solid	(4) Water (H_2O)
	(5) Hydrogen (H_2)
	(6) Carbon dioxide (CO_2)
	(7) Nitrogen (N_2)
	(8) Kerogen
	(9) Prechar
	(10) Char

The simulator solves 11 mass and energy balance equations; 10 of them are the mass equations of components; one of them is the heat equation. These equations are described in a form of Eq. (1) (Pruess et al. 1999).

$$\frac{d}{dt}\int_{V_n} M^{\kappa(\theta)} dV_n = \int_{\Gamma_n} \mathbf{F}^{\kappa(\theta)} \cdot \vec{\mathbf{n}} d\widetilde{A} + \int_{V_n} q^{\kappa(\theta)} dV_n \qquad (1)$$

Here, V_n is the volume of element n; Γ_n is the contact area between elements; $M^{\kappa(\theta)}$, $\mathbf{F}^{\kappa(\theta)}$, and $q^{\kappa(\theta)}$ are the terms of accumulation, flux, and source/sink of component κ (θ, heat), respectively.

The mass changes due to the chemical reactions are accounted into the accumulation terms. The simulator computes the solutions of these mass and energy balance equations in a fully implicit manner, by using a Jacobian matrix of residual equations obtained from the Eq. (1). We used the Original Porous Medium (OPM) model to account for the amount of solid phase affecting effective porosity and permeability of reservoir rocks, but not affecting porosity and absolute permeability (Moridis 2014).

The initial condition of the simulation cases is listed in Table 3. Initial pressure and temperature of the reservoir are 207 bar and 35 °C, respectively. The pores are initially filled with aqueous phase of 30 % and solid phase of 70 %. The solid phase is initially composed of whole kerogen. We consider the oil shale formation containing natural fracture system as presented by Fowler and Vinegar (2009).

Table 3. Initial Condition.

Parameters	Values
Initial pressure (bar)	207
Initial temperature (°C)	35
Rock density (kg/m^3)	2,000
Initial S_A	0.30
Kerogen volume fraction	0.70

From the previous work of Lee et al. (2015), one of the possible reservoir model was found to have the properties provided in Table 4. It has oil shale grade of 25 gal/ton and corresponding organic matter content of 30.10 %. The initial effective permeability of fluid is 0.001 md, and the permeability of the natural fracture system is 150 md. Formation conductivity is 2.0 W/m-K.

Table 4. Reservoir Properties.

Parameters	Values
Oil shale grade (gal/ton)	25
Organic matter content (vol%)	30.10
Initial effective permeability (md)	0.001
Permeability of natural fracture network (md)	150
Formation thermal conductivity (W/m-K)	2.0

Case 1: Shell ICP

Shell ICP process implements the in-situ upgrading of oil shale by using multiple vertical heaters distributed as a hexagon. Oil shale formation is heated by heat conduction from the heaters, and converted fluids are produced from the two vertical producers located at the center of the hexagon. This process is utilized by using multiple hexagonal patterns as shown in Fig. 1.

We simulate a quarter of one hexagon by using a 2D model of 15*17 = 255 grid blocks. The model has 14*17 = 238-ft^2 area with 113 ft-height. The outer grey part is consisted of inactive cells, which are not accounted in the computation. There are six electric heaters and one producer in the simulation model. We use constant heater temperature of 320 °C through the process. The converted fluids from kerogen pyrolysis are produced by using variable flowing bottomhole pressure.

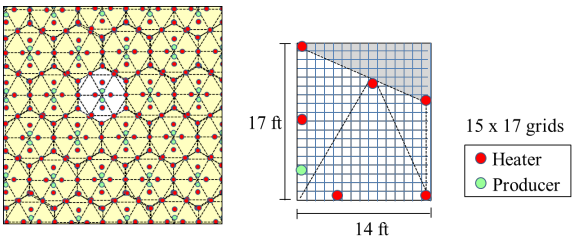

Figure 1. Simulation Model Geometry of Shell ICP.

Case 2: ExxonMobil Electrofrac Method

ExxonMobil Electrofrac method implements the in-situ upgrading of oil shale by using a horizontal well which has a longitudinal vertical fracture propped with electrical conductive material. The converted fluids are produced from the two vertical producers located in front of the fracture. This method is also can be utilized in the system with multiple fractures. The reservoir configuration and the simulation model are provided in Fig. 2. There are a number of horizontal wells having their longitudinal fractures and vertical wells located between the fractures.

We simulate an eighth of one fracture system by using a 3D model of 7*5*13 = 455 grid blocks as shown in Fig. 2 (b). It contains overburden and underburden formations of 40 ft-thickness. Heat is transferred from the horizontal well to the hydraulic fracture, and the heated hydraulic fracture linearly conveys heat to the formation. The horizontal well is maintained as a high temperature of 345 °C through the whole process. We produce the converted fluids at the top of the producer to avoid excessive water production by using variable flowing bottomhole pressure.

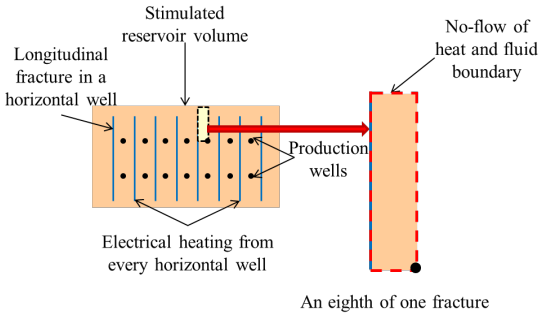

(a)

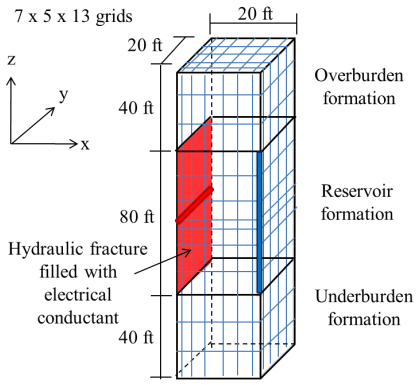

(b)

Figure 2. ExxonMobil Electrofrac–(a) Reservoir Configuration, (b) Simulation Geometry.

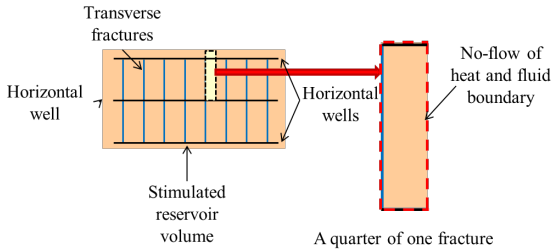

(a)

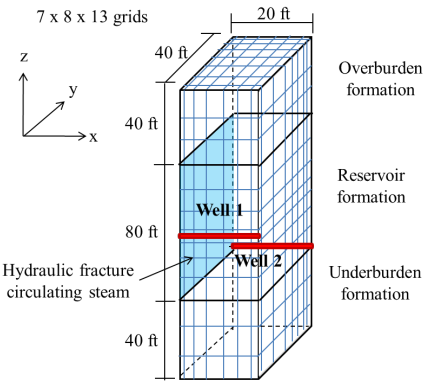

(b)

Figure 3. TAMU Steamfrac–(a) Reservoir Configuration, (b) Simulation Geometry.

Case 3: TAMU Steamfrac Method

TAMU Steamfrac method implements the in-situ upgrading by injecting steam into a horizontal well with multiple vertical hydraulic fractures. This method is proposed with the expectation of the effective heating by heat convection as well as heat conduction. The reservoir configuration is provided in Fig. 3 (a). Steam is injected into the horizontal well located at the center of the reservoir, and the fluids are produced simultaneously from the two horizontal wells located at the bottom edges of the reservoir. After 50 days, we switch the wells, inject steam into the two wells at the bottom edges, and produce fluids from the center well.

We simulate a quarter of one fracture system by using a 3D model having 7*8*13 = 728 element grids as shown in the Fig. 3(b). It contains overburden and underburden formations of 40 ft-thickness as the ExxonMobil case. There exists two wells in the simulation model by the principle of symmetry.

RESULTS

The simulation results of the Shell ICP for 340 days are provided in Fig. 4 and Table 5. They present the results of one hexagon. Fig. 4 shows the production rates of the fluid phases. We produce the fluids from 65 days. We can find that the aqueous phase, liquid organic phase, and gaseous phase are produced after 65 days, 100 days, and 130 days, respectively. The peaks of production rates of aqueous phase, liquid organic phase, and gaseous phase are reached after 120 days, 190 days, and 160 days, respectively. The aqueous phase production rate reaches to zero after 240 days, while the hydrocarbons are continuously produced until the end of the process.

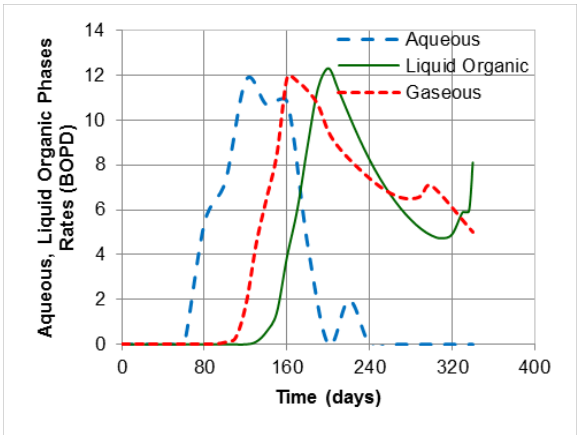

Figure 4. Phases Production Rates–Shell ICP Case.

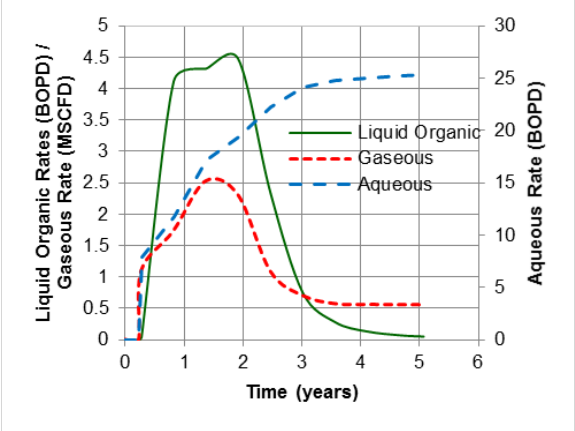

Figure 5. Phases Production Rates– ExxonMobil Electrofrac Case.

From the Table 5, we can find that the remaining kerogen after the process is 2.66 wt % of the initial mass in place. The total hydrocarbon production reaches to 1,762.6 BOE in one hexagon, where the liquid organic phase production reaches to 1,415 STB. We compute the energy input in BOE by converting the thermal energy into chemical energy and get 144 % of energy efficiency.

Table 5. Simulation Results of the Shell ICP Case.

Parameters	Values
Duration (days)	340
Heater temperature (°C)	320
Remaining kerogen (wt%)	2.66
Liquid organic phase production (STB)	1,415
Gaseous phase production (MSCF)	1,975
Aqueous phase production (STB)	1,050
GOR (MSCF/STB)	1.40
Total produced hydrocarbon (BOE)	1,762.6
Energy efficiency (%)	144

The simulation results of the ExxonMobil Electrofrac method for 5 years are provided in Fig. 5 and Table 6. They present the results of one fracture unit. Fig. 5 shows the production rates of the fluid phases. We produce the fluids from 100 days. We can find that the aqueous phase, liquid organic phase, and gaseous phase are produced simultaneously after 100 days. The peaks of production rates of liquid organic phase and gaseous phase are reached after 1.8 years and 1.5 years, respectively. The aqueous phase production rate continuously increases until the end of the process, while the production rates of liquid organic phase and gaseous phase continuously decrease after their peaks.

From the Table 6, we can find that the remaining kerogen after the process is 44.1 wt % of the initial mass in place. The amount of remaining kerogen is quite much, because the kerogen located at the lower part of the reservoir did not decompose. This is because we produced fluids from the top of the well, and heat rises. The total hydrocarbon production reaches to 3,676 BOE in one fracture unit, where the liquid organic phase production reaches to 3,305 STB. We get 177 % of energy efficiency, which is higher than the case of Shell ICP.

Table 6. Simulation Results of the ExxonMobil Electrofrac Case.

Parameters	Values
Duration (years)	5
Heating temperature (°C)	345
Remaining kerogen (wt%)	44.1
Liquid organic phase production (STB)	3,305
Gaseous phase production (MSCF)	2,110
Aqueous phase production (STB)	3.78E4
GOR (MSCF/STB)	0.64
Total produced hydrocarbon (BOE)	3,676
Energy efficiency (%)	177

The simulation results of the TAMU Steamfrac method for 2 years are provided in Fig. 6 and Table 7. They present the results of one fracture unit. Fig. 6 shows the production rates of the fluid phases. We produce the fluids from 20 days. We can find that the production rates of the phases fluctuate, because we switched the injection and production wells repeatedly in a few months intervals.

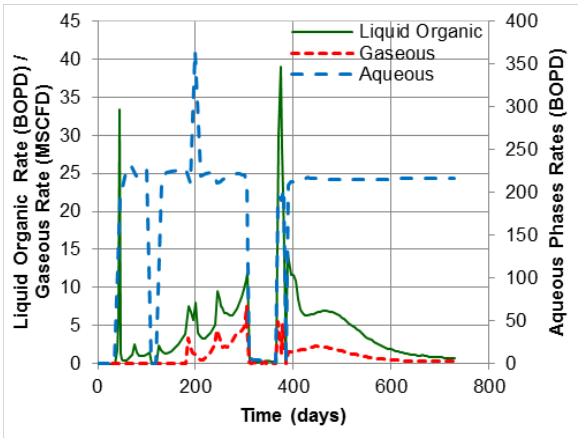

Figure 6. Phases Production Rates– TAMU Steamfrac Case.

From the Table 7, we can find that the remaining kerogen after the process is 42.9 wt % of the kerogen initial mass in place. The total hydrocarbon production reaches to 3,140 BOE in one fracture unit, where the liquid organic phase production reaches to 3,007 STB. We get 54.1 % of energy efficiency, which is the lowest among the three in-situ upgrading processes.

Table 7. Simulation Results of the TAMU Steamfrac Case.

Parameters	Values
Duration (years)	2
Remaining kerogen (wt%)	42.9
Liquid organic phase production (STB)	3,007
Gaseous phase production (MSCF)	754
Aqueous phase production (STB)	1.34E5
GOR (MSCF/STB)	0.25
Total produced hydrocarbon (BOE)	3,140
Energy efficiency (%)	54.1

CONCLUSIONS AND FUTURE WORK

In this study, we applied our developed simulator for kerogen pyrolysis to the diverse in-situ upgrading processes. We compared the total hydrocarbon production, liquid organic phase production, gaseous phase production, amount of remaining kerogen in the reservoir, and energy efficiency of each methods.

We find that the ExxonMobil Electrofrac method necessitates the longest period of process, but has higher energy efficiency than the Shell ICP and the TAMU Steamfrac method. The Shell ICP has the smallest amount of remaining kerogen after the process. The TAMU Steamfrac has the lowest GOR, but also shows the excessive water production.

For future work, we plan to parallelize the simulation codes to perform reservoir problems in large scale. Also, this codes will be included to the TOUGH+ as a new family code.

ACKNOWLEDGMENT

This research was supported by the Crisman Research Institute for Petroleum Research of Texas A&M University.

REFERENCES

Fowler, T. and Vinegar, H. 2009. Oil Shale Icp-Colorado Field Pilots. In SPE western regional meeting. Society of Petroleum Engineers.

Lee, K. 2014. Rigorous Simulation Model of Kerogen Pyrolysis for the In-situ Upgrading of Oil Shales, PhD dissertation, Texas A&M University, College Station, Texas (December 2014).

Lee, K. Moridis, G.J. and Ehlig-Economides, C.A. 2015. A Comprehensive Simulation Model of Kerogen Pyrolysis for the In-situ Upgrading of Oil Shales. Paper presented at Reservoir Simulation Symposium, Houston, Texas U.S.A. Society of Petroleum Engineers SPE-173299-MS.

Moridis, G. 2014. Tough+ Hydrate V1. 2 User's Manual: A Code for the Simulation of System Behavior in Hydrate-Bearing Geologic Media.

Pruess, K. 1985. A Practical Method for Modeling Fluid and Heat Flow in Fractured Porous Media. Society of Petroleum Engineers Journal 25 (01): 14-26.

Wellington, S.L., Berchenko, I.E., De Rouffignac, E.P. et al. 2005. In Situ Thermal Processing of an Oil Shale Formation to Produce a Desired Product. In: Google Patents (US6880633 B2).

NUMERICAL SIMULATION OF TRANSPORT BETWEEN FRACTURED TIGHT/SHALE GAS RESERVOIRS AND NEAR-SURFACE GROUNDWATER

Matthew T. Reagan, George J. Moridis, Noel D. Keen

Lawrence Berkeley National Laboratory
1 Cyclotron Rd
Berkeley, CA 94720, USA
e-mail: mtreagan@lbl.gov

ABSTRACT

Hydrocarbon production from unconventional resources and the use of reservoir stimulation techniques, such as hydraulic fracturing, has grown explosively over the last decade. However, concerns have arisen that reservoir stimulation may create permeable pathways connecting the stimulated reservoir with shallower fresh-water aquifers, thus resulting in the contamination of potable groundwater by escaping hydrocarbons or other reservoir fluids. This work investigates, by TOUGH+ simulation, gas and water transport between a tight-gas reservoir and a shallower overlying fresh-water aquifer following hydraulic fracturing operations, if such a connecting pathway has been created. We focus on two general failure scenarios: 1) communication between the reservoir and aquifer via a connecting fracture or fault, and 2) communication via a deteriorated, preexisting nearby well. We find that hydrostatic tight-gas reservoirs are unlikely to act as a continuing source of migrating gas, and such incidents of gas escape are likely to be limited in duration and scope. To further explore the envelope of failure, we also study the possible transport of reservoir brines, examine the effects of reservoir overpressure, perform parametric studies of key reservoir and aquifer properties, and examine a range of depths and pathway configurations. This extended abstract summarizes the methodology behind, and the conclusions of the transport studies.

INTRODUCTION

Hydrocarbon production from unconventional resources with ultra-low permeability (TG reservoirs) reservoirs has experienced tremendous growth over the last decade. Stimulation technology has made economical gas and oil production from these resources possible, by developing a new system of artificial fractures that increases the permeability of the system and increase the surface area over which reservoir fluids flow from the matrix to the permeable fractures. There are concerns that reservoir stimulation creates significant environmental threats via the creation of permeability pathways (via the fracturing of overlying formations or failure of the cement in imperfectly completed wells) connecting the stimulated TG reservoir to overlying fresh-water aquifers. This could result in contamination of potable groundwater resources by escaping hydrocarbons and other reservoir fluids.

The objective of this study is to evaluate *by means of numerical simulation* the short-term transport of contaminants from a TG reservoir toward a shallower aquifer, and to analyze the implications, identifying the dominant/important parameters and the main transport mechanisms. We do not address the likelihood of pathway formation—we considered pathways between the TG reservoir and a shallow aquifer a given and aimed to determine the extent of short-term contaminant transport covering the widest possible spectrum of system properties and conditions, and under realistic regimes of pressure in the TG reservoir and the aquifer.

It is important to clarify what the present study *is* and *is not*. It *is* a parametric study using generalized representations of single-well, single-pathway tight- and shale-gas systems to identify the processes and parameters that could lead to rapid gas transport from TG formations to groundwater resources. It *is not* a formal risk assessment. It *is not* a detailed representation of a specific formation, reservoir and aquifer, or of a particular hydraulic fracturing scenario or technique. The multiplicity of geologies and

geometries that may exist in such TG/aquifer systems make it impossible to predict all possible outcomes. However, by identifying the processes that enhance or mitigate flow and transport out of TG reservoirs, and by examining a range of geological parameters and production techniques, the envelope of potential system behavior (and of possible hazards) can be better defined.

This study was conducted by LBNL (Reagan et al., 2015) as part of a wider investigation headed by the EPA's Office of Research and Development. In this paper we focus exclusively on the contaminant transport component of the studies. The EPA study drafts may be found at: *http://www2.epa.gov/hfstudy*.

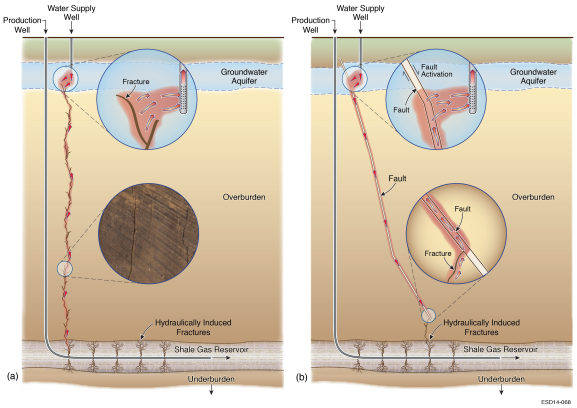

Figure 1. Fracture- or fault-driven pathways.

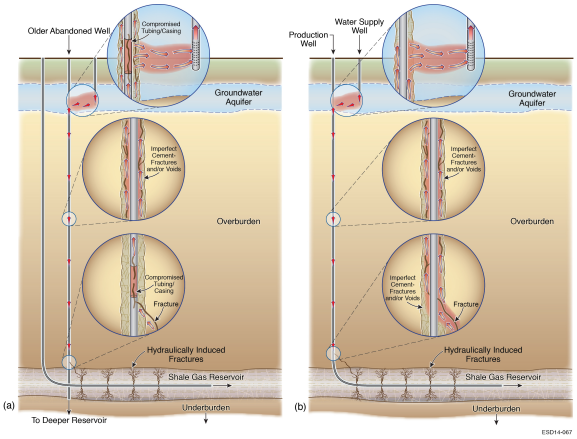

Figure 2. Well-failure pathways.

METHODOLOGY

System and Parameters

In the current study we investigate the contaminant transport potential of systems with the two general geometric configurations shown in Figures 1 and 2. These involve a vertical well in the shallow aquifer, a horizontal production well in the TG reservoir, and a connecting permeable feature that penetrates an impermeable overburden.

We vary (a) distance between the reservoir and aquifer, (b) type of permeable pathway connecting the TG reservoir to the aquifer, (c) formation conditions and properties, and (d) gas- and water-well production regimes. These base cases include:

1. Two types of permeable connecting features: *fractures* or *permeable faults* that can be either entirely hydraulically induced or a connection to a preexisting natural pathway, or *failed wells* that involve hydraulically-induced fractures that emanate from the TG reservoir and intercept older offset wells with deteriorated casings.
2. Three separation distances L between the TG reservoir and the aquifer: 200 m, 800 m, and 2000 m. While the value of L = 200 m may be an unlikely geometry, it is important to capture an end-case where contaminant transport is highly likely to contrast the result with more likely scenarios (i.e., larger separations).
3. Two aquifer permeability k_a values: $k_{a1} = 10^{-12}$ m^2 and $k_{a2} = 10^{-13}$ m^2 (1 D and 0.1 D, respectively).
4. Three TG reservoir matrix permeability k_s values: $k_{s1} = 10^{-18}$ m^2, $k_{s2} = 10^{-19}$ m^2 and $k_{s3} = 10^{-21}$ m^2 (1 mD, 100 nD and 1 nD, respectively).
5. Four water and gas production regimes: (a) both the gas well and the water well are producing, (b) only the water well is producing (inactive gas well), (c) only the gas well is producing (inactive water well), and (d) no water or gas production (both the water and the gas well are inactive).

6. A hydrostatic initial pressure distribution in the aquifer, TG reservoir, and any pathway, or a 50% overpressured reservoir.

From this set of geometries and parameters, 336 base simulations were performed to establish the envelope of potential releases. Additionally, we conducted well over 1,000 additional long- and short-term simulations to clarify problems, confirm specific observations, or test the validity of the underlying assumptions.

In all the base cases the aquifer and the TG reservoir are assumed to be infinite acting. For production, the horizontal well is operated at a constant bottomhole pressure $P_w = 0.5\ P_0$. When water is produced, it is withdrawn from the aquifer via the vertical well at a constant mass flow rate of $Q_w = 0.1$ kg/s (8.64 m^3/d).

The maximum time frame of the simulations in the first stage of this study is a relatively short two years, and was determined through initial scoping calculations that suggested a possible short-term nature of the gas release. Many simulations in fact reach a quasi-steady state well before two years, and thus stop for lack of significant changes in system properties. Certain scenarios with a potential of longer periods of non-steady-state behavior were simulated for up to 100 years.

Simulation Methods

We conducted the numerical studies using the TOUGH+RealGasBrine simulator (Moridis and Freeman, 2014), a member of the TOUGH family of codes. This simulator (T+RGB) describes the non-isothermal two-phase flow of water, a real gas mixture, and dissolved solutes, with a particular focus in TG reservoirs. The gas mixture is treated as either a single-pseudo-component having a fixed composition, or as a multicomponent system composed of up to 9 individual real gases. In addition to the capabilities of all TOUGH+ codes, T+RGB also includes: coupled flow and thermal effects in porous and/or fractured media, real gas behavior, inertial (Klinkenberg) effects, full micro-flow treatment (Knudsen diffusion and the Dusty-Gas Model (Webb and Pruess, 2003; Freeman et al., 2011) for multicomponent studies), Darcy and non-Darcy (Barree and Conway (2007)) flow through high-permeability features, single- and multi-component gas sorption onto the grains of the porous media following several sorption isotherms, discrete and equivalent fracture representation, complex matrix-fracture relationships, porosity-permeability dependence on pressure changes, and an option for full coupling with geomechanical models.. The simulations performed for this study involve 3 or 4 simultaneous equations per element, corresponding to the two mass balance equations for H_2O and CH_4, plus the heat balance equation of the entire system (i.e. non-isothermal), plus the optional salt component. We also use Langmuir sorption for CH_4 in the shale reservoir and micro-flow physics within the tight shale medium.

The TOUGH+ simulations for this study were run on three-dimensional Voronoi grids with geometric features informed by the geology of interest. We used the MeshVoro toolkit for generating these grids [Freeman et al., 2014]. There are two families of geometries that correspond to the two general types of the permeable/connecting pathways in the base cases of our study. In the F-cases, we describe a subdomain containing the planar fracture that represents a hydraulic fracture (or a hydraulic fracture intercepting a native fracture or permeable fault) connecting the deeper TG reservoir to the shallow aquifer. In the W-cases, we use a more complex geometry that includes (a) a cylindrical subdomain (which describes an abandoned well that descends below the aquifer into the TG reservoir overburden) intercepting (b) a planar subdomain that represents the hydraulic fracture emanating from the horizontal well in the TG reservoir. A schematic of the two cases is shown in Figure 3.

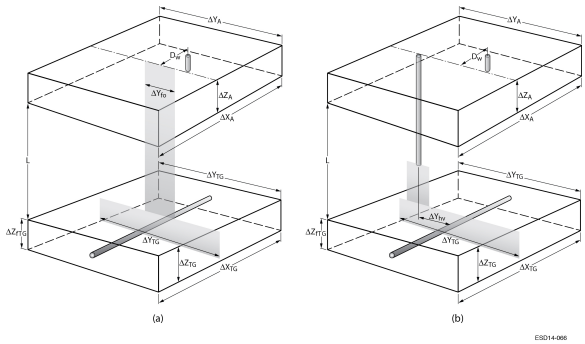

Figure 3. General schematic and dimensions of the F-cases (a) and W-cases (b).

The TG reservoir subdomain and the aquifer subdomain have the same dimensions in both the F- and W-family geometries. Thus, the thickness of the aquifer and of the TG reservoir are DZ_A = 100 m and DZ_{TG} = 100 m, respectively. The aquifer extends in the *x*- and *y*-directions to $DX_A = DY_A$ = 1000 m, with the fracture plane being at its center (Figure 3a and 3b). Because of the much lower permeability of the TG reservoir, infinite-acting behavior over the two years of the study could be ensured by DX_{TG} =100 m and DY_{TG} = 300 m. Elements near the boundaries of the TG reservoir (away from the fracture and well) are monitored to ensure no pressure or temperature changes propagate to these boundaries during the simulation timeframe.

The hydraulically induced fracture within the TG reservoir has dimensions of DZ_{fTG} = 100 m (the reservoir thickness) and DY_{fTG} = 300 m, with the horizontal well being at the center of the rectangle (Figure 3a and 3b). The fractures through the overlying formations (either hydraulic or natural) in the F-cases are assumed to have an average width of DY_{fO} = 20 m and the same aperture as the fractures within the TG reservoir (Figure 3a). The radius of the degraded region around the offset well (or the vertical part of the gas well) in the W-cases is meshed to approximately 0.5 m with a small porosity reflecting voids or deterioration in the region surrounding the well.

The meshes generated using these geometries contain 100,000 to 400,000 elements. Subsequent removal of unnecessary elements (i.e. those in likely static, impermeable regions) reduced the working meshes to 95,000 to 150,000 elements.

All the simulations were conducted non-isothermally, and the initial temperature followed the standard geothermal distribution with a mid-range geothermal gradient of dT/dz = 0.03 ^{o}C/m, with T_{tA} = 12 ^{o}C at the top of the aquifer. For the 200 m, 800 m, and 2000 m overburden thicknesses, this results in T_{tTG} = 21 ^{o}C, 40 ^{o}C, or 75 ^{o}C at the top of the TG reservoir. The significant temperature difference between the gas reservoir and the aquifer, and the strong dependence of gas density on both *P* and *T*, did not permit treating the problem as isothermal.

The aquifer and the overburden of the TG formation (including any connecting pathway) were fully water-saturated. The aqueous and gas saturations in the matrix of the TG reservoir were set at S_A = 0.3 and S_G = 0.7 respectively (highly undersaturated), which is consistent with earlier studies [Engelder, 2014] showing that many gas shales do not produce significant aqueous phase after flowback. Initial salt concentrations, when included, were *Y* = 15 wt% in the TG reservoir and 1 ppm in the aquifer.

Other important assumptions include: 1) The permeable connecting pathways (penetrating fractures and well casings) have uniform porosities and permeabilities throughout their entire length, and 2) the penetrating feature (well or fracture/fault) is the only permeable connection between the TG reservoir and the aquifer. The overburden is considered entirely impermeable.

CONCLUSIONS

We drew the following conclusions from this simulation study:

1. In the F-cases, the main factors affecting the transport of gas to the base of the aquifer and its appearance at a producing water well in the aquifer are (a) the production regime, i.e., an active gas well in the TG reservoir mitigates release, (b) the permeability k_f of the connecting fracture, and less so, (c) the separation between the TG reservoir and the aquifer.
2. Similarly, for the W-cases the main factors (by far) affecting the transport of gas to the base of the aquifer and its appearance at a producing water well in the aquifer are the permeability k_w of the connecting offset well, and the production regime (i.e., whether a gas well in the TG reservoir is active). Permeabilities $k_w <= 10^{-15}$ m^2 lead without exception to no gas arrivals at the aquifer for *L* as small as 200 m, and only the highest permeability leads to a large probability of release for all other parameters, and for larger separations, a producing TG well can mitigate release even for such high permeabilities. Generally speaking, gas transport through such a connecting feature conveys larger CH_4 amounts to the aquifer

than the connecting fractures/faults of the F-cases.

3. The TG reservoir appears unable to recharge the hydraulic fracture over short timescales for a hydrostatic pressure regime and an unfavorable evolution of relative permeability. Thus, the amount of gas available for immediate migration toward the shallower aquifer is limited to that initially stored in the hydraulically-induced fractures. Thus, the period of significant gas release is limited. This appears to be true even in cases where a TG well is not producing.
4. The dependence on production strategy is of particular interest because in the field, stimulation may not necessarily be followed immediately by production, and production may not be continuous (i.e. well shut-in). However, the opening of a highly permeable pathway is also likely to deliver significant quantities of water to the producing well, which would hamper gas production and provide a clear notice of the presence of such a pathway.
5. Aqueous flow in nearly all of our parametric cases is downward, with the exception of systems with very low permeability of the connecting features or exhibiting incomplete gas migration at the end of simulation time. This is true whether or not a TG well is producing and thus creating a downward driving force.
6. As a result of the downward flow, salt infiltration into the aquifer is not seen for any of the cases. This is consistent with field studies that suggest gas migration, but no migration of reservoir fluids. Overpressure does not change this result.

A presentation of the methods, parametric space, and full results of this simulation study can be found in Reagan et al. (2015) and Moridis et al. (2015).

ACKNOWLEDGMENTS

This research was funded by the U.S. Environmental Protection Agency's Hydraulic Fracturing Drinking Water Assessment through Interagency Agreement between EPA (DW-89-92235901-C, Stephen Kraemer, EPA Project Officer) and the Department of Energy Lawrence Berkeley National Laboratory (DE-AC02-05CH11231). The views expressed in this article are those of the authors and do not necessarily reflect the views or policies of the EPA. This research used resources of the National Energy Research Scientific Computing Center, which is supported by the Office of Science of the U.S. Department of Energy under Contract No. DE-AC02-05CH11231.

REFERENCES

Barree R.D., and M.W. Conway, Multiphase non-Darcy flow in proppant packs, Paper SPE 109561, 2007 Annual Technical Conference and Exhibition, Anaheim, CA, 11–14 Nov 2007.

Freeman, C.M., Moridis, G.M., Blasingame, T.A. (2011), A Numerical Study of Microscale Flow Behavior in Tight Gas and Shale Gas Reservoir Systems, Transport in Porous Media, 90(1), 253-268.

Freeman, C.M., K.L. Boyle, M.T. Reagan, J.N. Johnson, C. Rycroft, and G.J. Moridis (2014), MeshVoro: A Three-Dimensional Voronoi Mesh Building Tool for the TOUGH Family of Codes, Computers and Geosciences, 70, 26-34.

Moridis, G. J., and C. M. Freeman (2014), The RealGas and RealGasH2O options of the TOUGH+ code for the simu lation of coupled fluid and heat flow in tight/shale gas systems, *Comput. Geosci*. 65, 56-71.

Moridis, G.J., Reagan, M.T., Keen, N.D., (2015) Numerical Simulation of the Environmental Impact of Hydraulic Fracturing of Tight/Shale Gas Reservoirs on Near-Surface Groundwater, submitted to *Water Res. Res.*

Reagan, M.T., Moridis, G.J., Keen, N.D., Johnson, J.N., (2015) Numerical Simulation of the Environmental Impact of Hydraulic Fracturing of Tight/Shale Gas Reservoirs on Near-Surface Groundwater: Background, Base Cases, Shallow Reservoirs, Short-Term Gas and Water Transport, *Water Res. Res.,* 51(4).

Webb, S.W. and K. Pruess. The Use of Fick's Law for Modeling Trace Gas Diffusion in Porous Media. Transport in Porous Media, 51, 327-341, 2003.

METHANE DIFFUSION AND ADSORPTION IN SHALE ROCKS— A NUMERICAL STUDY USING THE DUSTY GAS MODEL IN TOUGH2/EOS7C-ECBM

Weijun Shen[1,3], Liange Zheng[2], Curtis M. Oldenburg[2],
Abdullah Cihan[2], Jiamin Wan[2] and Tetsu K. Tokunaga[2]

[1] Institute of Porous Flow and Fluid Mechanics, Chinese Academy of Sciences,
Langfang, Hebei 065007, China
[2] Earth Sciences Division, Lawrence Berkeley Laboratory,
1 Cyclotron Road, Berkeley, CA 94720, USA
[3] University of Chinese Academy of Sciences, Beijing 100190, China
e-mail: wjshen763@gmail.com

ABSTRACT

Gas production from gas shales plays a significant role in satisfying increasing energy demands. Compared with conventional reservoir rocks (sandstones and carbonates), shale rocks have low porosity, ultra-low permeability, and high organic carbon content. Slip flow, diffusion, and adsorption/desorption are the primary gas transport processes in shale matrix while Darcy flow is restricted to fractures. Understanding methane diffusion and adsorption, and gas flow and equilibrium in the low-permeability matrix of shale are crucial for gas shale formation evaluation and for predicting gas production. Modeling of diffusion in low-permeability shale rocks requires use of the Dusty Gas Model (DGM) rather than Fick's Law. The DGM is incorporated in the TOUGH2 module EOS7C-ECBM, a modified version of EOS7C that simulates multicomponent gas mixture transport in porous media. Also included in EOS7C-ECBM is the extended Langmuir model (ELM) for adsorption and desorption of gases. In this preliminary study, a one-dimensional shale model was constructed to simulate methane diffusion and adsorption through shale rocks. The process of binary CH_4-N_2 diffusion and adsorption was analyzed. A sensitivity study was performed to investigate the effects of pressure, temperature, and permeability on diffusion and adsorption in shale rocks. The result shows that with the temperature and permeability increasing, methane diffusion accelerates while its effect is very little in the low-permeability ($<1.0 \times 10^{-15}$ m^2) porous media. As the pressures increases, methane gas diffusion reduces and there is no effect on the adsorbed result when the pressure exceeds the Langmuir pressure.

INTRODUCTION

Because of the large reserves and the advantages of lower CO_2 emissions compared to other fossil fuels, shale gas is becoming one of the most important energy sources and has attracted increasing attention (Sutton et al., 2010; Kuuskraa et al., 2011; Michiel et al., 2011). Gas production from gas shales has drastically increased in the U.S.A. in recent years due to advances in horizontal drilling and hydraulic fracturing (Kuuskraa et al., 2011). According to a report from the U.S. Energy Information Administration (EIA), 34% of gas production in 2011 in the U.S.A is from shale and the percent is predicted to reach 45% by 2035. Unlike conventional sandstone and carbonate reservoirs, shale is relatively low in porosity (≤10%), can have ultra-low permeability (≤0.001mD) and high organic content (≥2%) (Chuck et al., 2006). Natural gas (primarily methane) in shale gas reservoirs exists in one of three forms: (1) free gas in fractures and pores; (2) adsorbed gas on organic matter and inorganic minerals surfaces; and (3) dissolved gas in oil and water (Strapoc et al., 2010). Compared with conventional gas reservoirs, transport in shale gas reservoirs is strongly influenced by diffusion, adsorption, and desorption (Moridis et al., 2010). Diffusion, adsorption and desorption are the primary mechanisms controlling transport in shale matrix while Darcy flow is dominant in fractures. Thus understanding methane diffusion and adsorption, and gas flow and equilibrium in the low permeability matrix of shale is crucial for gas shale formation evaluation and for forecasting gas production.

Gas diffusion is commonly described using Fick's law. However, the application of Fick's

law to gas diffusion in porous media has been questioned by some investigators (e.g., Thorsten and Pollock (1989), Abriola (1992), Webb (1998) and Oldenburg et al. (2004)) because it violated empirical relations and did not compare well with the measured data in some circumstances. The Dusty Gas Model (DGM), which is a more fundamental approach to analyzing gas diffusion, is preferable to Fick's law for low-permeability porous media (Thorstenson and Pollock, 1989; Webb, 2011). The DGM was incorporated in TOUGH2/EOS7C-ECBM, a modified version of EOS7C that simulates multicomponent gas mixture transport in porous media. It is known to be more accurate in low permeability systems using the DGM, where the pore sizes have the same scale with the mean free path of gas molecules. Besides, the extended Langmuir model (ELM) is also included in EOS7C-ECBM for adsorption and desorption of gases. In this work, a one-dimensional shale model was constructed to simulate methane diffusion and adsorption through shale rocks using the module EOS7C-ECBM. The process of binary CH_4-N_2 diffusion and adsorption was analyzed and the effects on diffusion and adsorption through shale rocks were evaluated.

NUMERICAL MODEL AND MODEL DESCRIPTION

Numerical model

EOS7C is a TOUGH2 module for nitrogen (N_2) or carbon dioxide (CO_2) in methane (CH_4) reservoirs (Oldenburg et al., 2004). EOS7C-ECBM (Webb 2011), a modified version of EOS7C, includes the extended Langmuir model (ELM) for gas adsorption and desorption and the Dusty Gas Model (DGM) for gas diffusion, which can be used to simulate multicomponent gas mixture transport in porous media.

The extended Langmuir model for gas adsorption and desorption (Law et al., 2002) may be expressed as

$$G_{si} = G_{sLi}\left[1-\left(w_a + w_{we}\right)\right]\frac{\frac{P\,y_i}{P_{Li}}}{1+P\sum_{j=1}^{nc}\frac{y_j}{P_{Lj}}} \qquad (1)$$

where G_{si} is gas storage capacity of component i, sm^3/kg; G_{sLi} is dry, ash-free Langmuir storage capacity of component i, sm^3/kg; w_a is ash weight fraction; w_{we} is equilibrium moisture weight fraction; P is pressure, Pa; P_L is Langmuir pressure, Pa ; and nc is number of components.

The general form of the Dusty Gas Model for the gas diffusion of component i (Thorstenson and Pollock, 1989; and Reid, 1987) may be written as

$$\sum_{j=1,j\neq i}^{n}\frac{y_i N_j^D - y_j N_i^D}{D_{ij}^*} - \frac{N_i^D}{D_i^{K*}} = \frac{\left(\nabla P_i - \rho_g g\right)}{RT} \qquad (2)$$

$$D_{ij,PT} = D_{ij}\left(P_0,T_0\right)\frac{P_0}{P}\left(\frac{T+273.15}{273.15}\right)^{\theta} \qquad (3)$$

where N^D is the molar diffusive flux; y is the gas phase mole fraction; D_{ij}^* is the effective binary diffusion coefficient; D^{K*} is the effective Knudsen diffusion coefficient; P is the pressure; R is the gas constant; T is the temperature; P_0 and T_0 are 10^5 Pa and 0℃, respectively.

Model description

In order to study the process of methane diffusion and adsorption in shale rocks, we build a one-dimensional shale model. The geometry of the model is shown in Figure 1 and the properties of the base model are summarized in Table 1. The model assumptions are as follows: (1) the column contains only gas; (2) the outer boundaries are closed except for the top boundary which is open; (3) the initial condition of the base-case model has a uniform constant temperature of 30 °C and constant pressure of 1MPa; (4) there is only nitrogen in the model system, and the top boundary is held at a constant concentration of 99% methane and 1% nitrogen; and (5) the porosity and permeability of the model are constant. The simulation was run for a base case, and in cases in which parameters were individually varied.

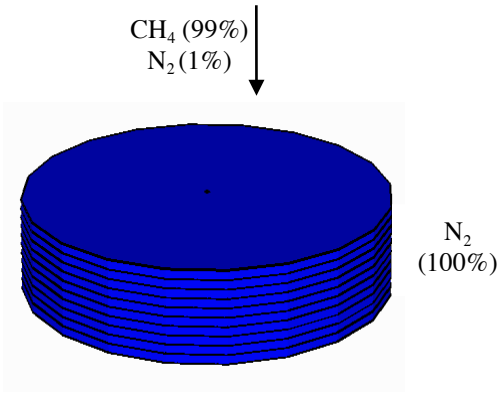

Figure 1. Schematic of the one-dimensional shale model for methane diffusion and adsorption.

Table 1. Properties of the one-dimensional model for CH_4 adsorption and diffusion.

property	Value
Model radius (m)	4.0e-2
Model height (m)	5.0e-3
Porosity (%)	5
Permeability (m^2)	1.0e-15
N_2 diffusivity(m^2s^{-1})	1.8e-5
CH_4 diffusivity(m^2s^{-1})	2.4e-5
Binary diffusivity (m^2s^{-1})	2.4e-6
Ash weight fraction (%)	92.91
Equilibrium moisture weight fraction (%)	0.8
Langmuir storage capacity (sm^3kg^{-1})	0.0037
Langmuir Pressure (Pa)	15694
Initial Temperature (℃)	30
Initial Pressure (Pa)	1.0e+6

RESULTS AND ANALYSES

Overview

In the beginning, the model system is stable and there is no driving force for advection. As the simulation goes on, CH_4 will diffuse downwards and N_2 in the system will diffuse upwards. The CH_4 gas diffusing downwards will be adsorbed on the shale until equilibrium is established. Figure 2 shows the total mass of CH_4 and N_2 in the system along with gas density versus time in the model system. As seen in Figure 2, CH_4 mass increases continuously until equilibrium, while N_2 mass decreases. In the process of CH_4 diffusion downwards and N_2 diffusion upwards, the gas density in the model system will decrease continuously until the time when the CH_4 partial pressure is equal to CH_4 partial pressure at the top boundary because of the large density of N_2 relative to CH_4.

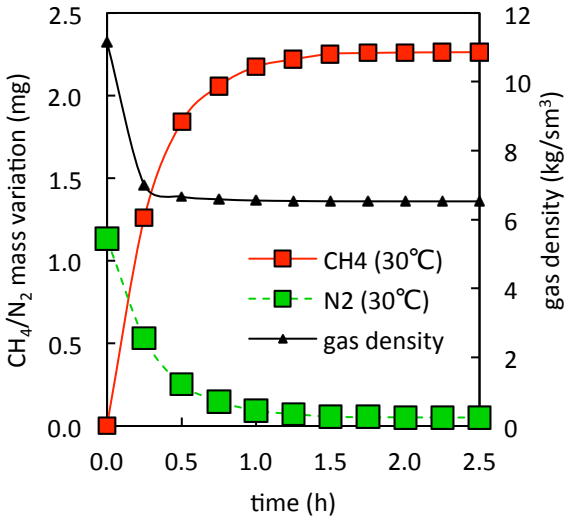

Figure 2. CH_4/N_2 mass variation and gas density versus time.

Pressure

Figure 3 shows different pressures effects where four cases were run by varying pressure from 1 to 15 MPa to study CH_4 diffusion and adsorption. From the result of Figure 3, with the pressure increasing in the model system, CH_4 mass variation decreases in the early stage but has only minor influence on the equilibrium adsorbed mass. Pressure is seen to affect gas diffusion rate. With the pressure increasing, the mean free path between gas molecule collisions decreases thereby reducing the gas diffusion rate. From Equation (2), it is known that the gas diffusion coefficient is inversely proportional to the pressures and gas diffusion rate will reduce with the pressure increasing. It will be seen that there is relatively small CH_4 mass variation until equilibrium when the pressure is 1MPa. The reason is that Langmuir pressure (1.57 MPa) is larger than the pressure (1 MPa), and the shale does not reach its maximum CH_4 adsorption capacity. When the CH_4 pressure significantly exceeds its Langmuir pressure, gas diffusion rates are influenced while the final adsorbed CH_4 mass simply equals the maximum capacity of the shale.

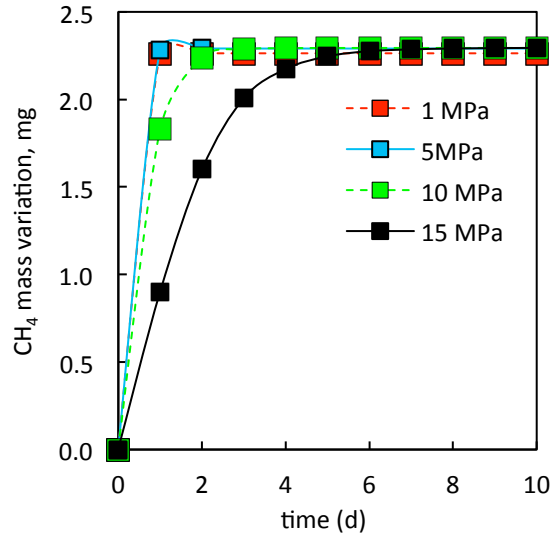

Figure 3. CH_4 mass variation versus time for different pressures.

Temperature

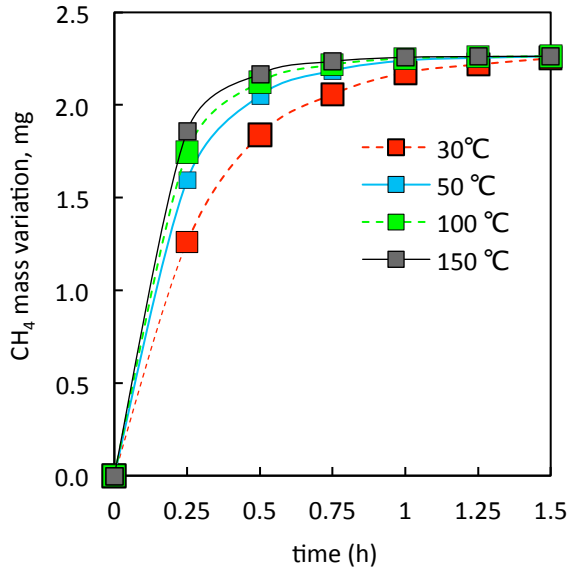

Figure 4. CH_4 mass variation versus time for different temperatures.

The time dependence of CH_4 uptake for different temperatures from 30 °C to 150 °C is shown in Figure 4 where it is seen that as temperatures increase, CH_4 mass variation increases. It means that the elevated temperature favors methane diffusion and adsorption in shale rocks. This is because the average kinetic energy of gas molecules will increase when temperatures increases. Thus methane gas diffusion will accelerate at the higher temperatures.

Permeability

Three cases of different permeability values from 1.0×10^{-12} m^2 to 1.0×10^{-18} m^2 are selected to study the effects of methane diffusion and adsorption in shale rocks, as shown in Figure 5. The result shows that gas diffusion slows down with the permeability value decreasing but there is a slight change after the permeability value reaches 1.0×10^{-15} m^2. This suggests that the permeability has a minor effect on the gas diffusion rate if the permeability is less than 1.0×10^{-15} m^2. From the result in Figure 5, it is seen that there is very little change in results between 1.0×10^{-15} m^2 and 1.0×10^{-18} m^2. This suggests that there is a limit of gas diffusion when permeability is very low at which the permeability is not the dominant factor influencing gas diffusion, especially in shale rocks.

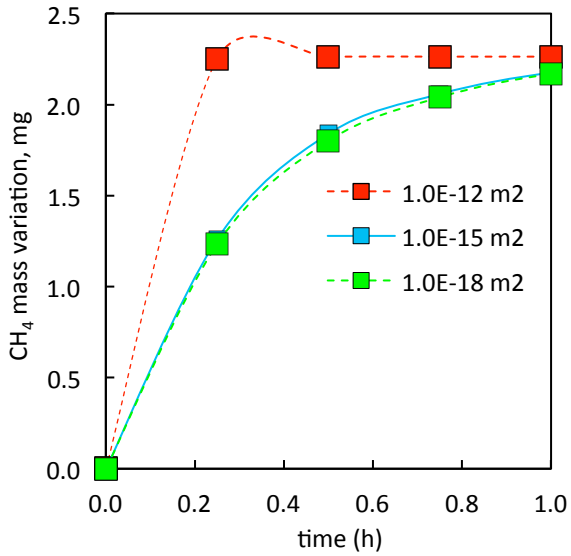

Figure 5. CH_4 mass variation versus time for different permeability values

SUMMARY AND FUTURE WORK

A one-dimensional shale model was considered to simulate methane diffusion and adsorption through shale rocks using the DGM and ELM in the module EOS7C-ECBM. The effects of different pressures, temperatures and permeability values on diffusion and adsorption through shale rocks were evaluated. With increase in temperature and permeability, methane diffusion speeds up. The permeability has minor effect on methane diffusion for permeability less than 1.0×10^{-15} m^2. As the

pressures increases, methane gas diffusion reduces and there is no effect on the adsorbed result when the pressure exceeds the Langmuir pressure. In future work we will conduct the experiment of methane diffusion and adsorption in shale rocks, and compare experimental and numerical results.

ACKNOWLEDGMENT

This work was supported by the National Energy Technology Laboratory under U.S. Department of Energy Contract No. ESD14085, "Understanding Water Controls on Shale Gas Mobilization into Fractures". This work was also supported by the Foundation of China Scholarship Council.

REFERENCES

Abriola, L.M., Fen C.-S., and Reeves H.W., Numerical Simulation of Unsteady Organic Vapor Transport in Porous Media Using the Dusty Gas Model, Subsurface Contamination by Immiscible Fluids, Rotterdam, pp. 195-202, 1992.

Chuck Boyer, John Kieschnick, Roberto Suarez-Rivera, et al, Production Gas from its Source. Oilfield Review, 18(3), 36-49, 2006.

Kuuskraa, Vello A., Scott H. Stevens,Keith Moodhe, EIA /ARI World Shale Gas and Shale Oil Resource Assessment, Virgin, Advanced Resources International, Inc., 2011, 5-6.

Law D. H.-S., Van Der Meer L.G.H., and Gunter W.D., Numerical Simulator Comparison Study for Enhanced Coalbed Methane Recovert Processes, Part 1: Pure Carbon Dioxide Injection, SPE-75669, 2002.

Michiel Soeting, et al., Shale Gas—A Global Perspective, KPMG Global Energy Institute, 2011, 1-18.

Moridis G.J., Blasingame T.A. and Freeman C.M., Analysis of Mechanisms of Flow in Fractured Tight-Gas and Shale-Gas Reservoirs, SPE-139250, 2010.

Oldenburg, C.M., Webb S.W., Pruess K., and Moridis G.J., Mixing of Stably Stratified Gases in Subsurface Reservoirs: A Comparison of Diffusion Models, Transport in Porous Media, 54:323-334, 2004.

Reid R.C., Prausnitz J.M., and Poling B.E., The Properties of Gases and Liquids, Fourth Edition, McGraw-Hill Book Company, New York, 1987.

Webb, S.W., EOS7C-ECBM Version 1.0, Report CRC2011-0002, Lawrence Berkeley National Laboratory, Berkeley, Calif., 2011.

Strapoc D., Mastalerz M., Schimmelmann A., et al, Geochemical Constrains on the Origin and Volume of Gas in the New Albany Shale (Devonian-Mississippian), Eastern Illinois Basin, AAPG Bull. 94, 1713-1740, 2010.

Sutton R. P., Cox S. A.，Barree R. D. Shale Gas Plays: A Performance Perspective, SPE 138447, 2010, 1-12.

Thorstenson D.D., and Pollock D.W., Gas Transport in Unsaturated Zones: Multi-Component Systems and the Adequacy of Fick's Laws, Water Resour. Res., 25:477-507, 1989.

Webb, S.W., Gas-Phase Diffusion in Porous Media – Evaluation of an Advective-Dispersive Formulation and the Dusty-Gas Model for Binary Mixtures, J. Porous Media, 1:187-199, 1998.

Webb, S.W., EOS7C-ECBM Version 1.0, Report CRC2011-0002, Lawrence Berkeley National Laboratory, Berkeley, Calif., 2011.

COMBINING TOUGH2 AND FLAC3D TO SOLVE PROBLEMS IN UNDERGROUND NATURAL GAS STORAGE

Robert Walsh, Othman Nasir, Nicola Calder, Sean Sterling, John Avis

Geofirma Engineering Limited
1 Raymond Street, Suite 200
Ottawa, Ontario, K1G 1R8, Canada
e-mail: rwalsh@geofirma.com

ABSTRACT

Geofirma was contracted to prepare engineering and modelling studies assessing the feasibility of increasing the maximum storage pressure in several underground natural gas storage reservoirs. This required an assessment of the potential for pressure and gas propagation in the caprock, and the geomechanical response to pressure change in the storage reservoir. To solve this problem in an efficient manner, TOUGH2 and FLAC3D models were combined in series. Two-phase flow models were developed in TOUGH2 and calibrated with data collected on-site. The mechanical response of the caprock to delta pressuring was modelled using FLAC3D, allowing assessment of the induced stresses in formations surrounding the reservoirs. Here we focus on two sites: In the first, field data was obtained from a deep borehole above the gas reservoir, which provided indirect observations of the geomechanical response of the caprock to pressure changes in the reservoir. In the second, open boreholes intersecting two thin caprock units immediately above the reservoir allowed gas flow to a shallower unit, significantly impacting the modelled fracture gradient.

INTRODUCTION

Imposed changes in pore pressure may have a considerable impact on effective and total stress in a host rock, with important implications in many subsurface engineering applications. Rutqvist and Tsang (2003) suggested that TOUGH2 could be combined with FLAC3D, leveraging the strengths of each code; simulating two-phase flow in TOUGH2, while mechanical processes are handled by FLAC3D. They showed one possible application, coupling these models to simulate CO_2 sequestration. Walsh et al. (2015) combined these codes in a different way to characterize damage development and flow in a tunnel excavation damaged zone. Depending on the problem, there are many different ways to combine these models. Here we present a straightforward application where TOUGH2 and FLAC3D were combined in series to solve problems in underground natural gas storage in depleted natural gas reservoirs.

Gas Storage in Pinnacle Reefs

Underground natural gas storage is common, representing a long-established, safe technique. The issues in this industry are analogous to those encountered in CO_2 sequestration, and in radioactive waste isolation where anaerobic degradation of organic material and ferrous metals may produce sufficient gas to pressurize a waste repository (Geofirma and Quintessa, 2011). Gas storage systems provide an opportunity to verify and refine modelling tools to assess gas flow and rock mechanical response in deep underground systems.

In Canada, most jurisdictions apply the most recent version of CSA Z341 to regulate the technical aspects of natural gas storage (CSA, 2014). This standard allows delta pressuring, or pressurization of the storage pool beyond the gas pressure that existed when the pool was initially discovered. The maximum delta pressuring must remain at or below 80% of the fracture gradient, defined as "the pressure gradient that, when applied to subsurface formations, causes the formations to fracture physically." Put another way, this condition requires that gas pressure be less than or equal to 80% of the minimum principal stress. To meet this standard, the operator must estimate how changes in the pressure of stored gas and movement of gas

drive changes in total and effective mechanical stress in the caprock above the storage pool.

In our work, we have modeled a large number of gas storage pools. Here we highlight modelling results and field measurements from two pools, which exemplify the geomechanical response to pool pressurization operations and movement of gas in the subsurface. Both gas storage pools are in Silurian age pinnacle reefs in close proximity to one another, and both have been safely operated as storage pools for decades. The ground surface elevation is 200 mASL (metres above sea level), and the minimum depth of both pools is roughly 500 m. The caprock overlying the reef consists of relatively thin anhydrite and shale units, overlain by a somewhat more permeable carbonate unit, a thin anhydrite, and an extensive and thick salt unit.

In both cases, the historical data set includes local data on key properties (permeability and porosity) of the reservoir and cap material, additional property data (retention curves, mechanical properties) from surrounding reefs, and micro-fracture test results at two nearby pinnacle reefs. Modelling was primarily two-dimensional, based on geological cross sections through the buried pinnacle reefs. For one of the pools a three-dimensional model was developed to verify the accuracy of the 2D model.

MODELLING PLAN

Two models were used to understand the hydromechanical behavior of each storage pool: a TOUGH2 model and a FLAC3D model. The TOUGH2 model was used to test and develop a two-phase flow model of the system, generating pore pressures for input into the FLAC3D model. The FLAC3D model was used to assess the impact of the changing pore pressure field on the distribution of stress in and above the storage pool. The FLAC3D model used the same grid and property distribution as the TOUGH2 model to facilitate interpolation of scalar values from one grid to the other.

The sequence of events for modelling the geomechanical consequences of pool pressurization were as follows:

1. Horizontal and vertical stresses were initialized using the lithostatic pressure curve and estimated stress boundary conditions. Initial pore pressures were set to hydrostatic in most of the model domain, and to discovery pressure in the reservoir.
2. As the initial stress distribution was only approximately correct, the FLAC3D model was stepped forward until it reached a stable equilibrium, representing the initial stress state more accurately given the variation in lithology across the cross-section.
3. Pore pressures were reset using output from TOUGH2. The saturation averaged pressure was passed to FLACD.
4. The geomechanical model was run to reach a new equilibrium, representing the mechanical impact of the applied pore pressure.

For the subsequent calculation of the percent fracture gradient the maximum fluid pressure was used, rather than the saturation averaged pore pressure passed to FLAC3D in step 3.

The EOS3 equation of state module was used to simulate the transport gas. Modifications to EOS3 were performed to use alternative gases, specifically methane (CH4). The modifications entailed changes to Henry's law constants, molecular weights, and viscosity calculations. EOS3 was also modified to correct methane density as function of pressure under conditions where methane compressibility diverges from ideal gas behavior (such as high gas pressures in the storage pool). This correction uses the Peng-Robinson equation; further details on the Peng-Robinson cubic equation of state can be found in Reid et al. (1987). Finally, EOS3 was altered to model a higher density liquid component (i.e. brine). This was done to achieve realistic saturated formation pressures without inducing unrealistic vertical flow gradients.

IN-SITU STRESS

The in-situ stress is the primary factor determining the fracturing pressure and therefore the safe operating pressure of a gas storage reservoir. The best available synopsis of the regional stress regime is presented in Lam and Usher (2011). Based on their report, the value of the minimum horizontal principle stress (σ_h) in this region and at these depths is between 1 and 1.2 times the vertical stress (σ_v), while the maximum horizontal principle stress (σ_H) is

likely between 1.5 and 2.1 times higher than the minimum horizontal principle stress. The orientation of the maximum principle stress is approximately ENE. A series of micro-fracture tests at two nearby gas storage pools confirmed that the minimum principle stress in the area is likely vertical, as it was very close to lithostatic.

Information on the other principle stresses could not be gleaned from the test data. To manage this uncertainty, the horizontal principle stress was assumed to be equal to the lithostatic stress gradient. This is likely a conservative assumption with respect to the potential for tensile hydraulic fracturing, but produces low shear stress as the horizontal and vertical principle stresses are nearly equal throughout the model domain. To assess the development of shear stress and the potential for shear failure, cases in which the horizontal stress was set to 2.5 times the vertical stress were also run. Shear failure was found to be an unlikely failure mode, and these results are not discussed further here.

STORAGE POOL A

Pool A was discovered in December 1970 at a pressure of 5981 kPag, and produced until August 1972, when it was shut-in at a pressure of 764 kPag, having produced 152 Mm^3 (at 15°C, 1 atm). Use of the pool for gas storage began in 1975. Pool A is of interest due to the installation of a pore pressure monitoring system in the water saturated formations directly above the buried pinnacle reef. At the time this model was prepared, the pool operated at a delta pressure gradient of 0.73 psi/ft (16.5 kPa/m).

In 2013, site characterization work was completed by Geofirma. This work included drilling one borehole to approximately 490 m deep, providing further site/geological information by coring through the formations directly above the pool. Core was sampled and tested for geomechanical properties, retention properties, permeability, and geochemical analysis. Subsequent to coring, a field hydraulic testing program was undertaken, providing in-situ measurements of formation permeability for these very low permeability formations. Thereafter, a multi-level piezometer with 12 intervals was installed and used to measure the pressure profile after allowing three months for pressure stabilization. After that, datalogger pressure probes were installed in seven intervals, to record the evolution of pressure in the caprock above the reservoir during pressure cycling. This monitoring continues to the present, and this data has been used for model development and analysis.

Model Setup

The grid and property distribution in the cross-sectional model for Pool A are shown in Figure 1. The general structure of the reef and surrounding formations is evident. The overlying caprock formations are generally very tight, with permeabilities on the order of 10^{-20} m^2 or less. The carbonate formation directly above the reef is divided into an upper zone with a permeability of $1.4x10^{-21}$ m^2, and a lower zone with permeability of $5.5x10^{-18}$ m^2. The reef itself has an average permeability of $7.2x10^{-15}$ m^2.

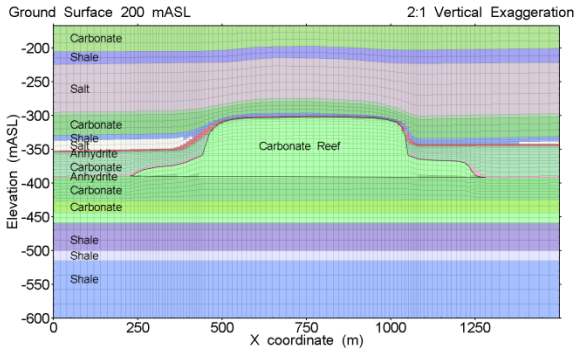

Figure 1. Grid and properties, Pool A model.

Stabilized inventories for Pool A between 1983 and 2013 were provided. These inventories were used to calculate average gas injection and withdrawal rates, which were applied as a methane source/sink term in the model. The methane injection/extraction rate is shown in the upper part of Figure 2. The source term was scaled for the smaller reef volume in the 2D model which had a nominal thickness of 1 m (as compared to the real 3D reef). Note that for the first 23 years the model used a simplified source term which allowed the model to run more quickly, matching maximum and minimum stabilized pressures and establishing a reasonable pressure history.

Model Results

Figure 2 also shows the comparison of measured and modelled storage pressures. In general, the

model does a good job of matching the actual pressure in the reef. While not a perfect fit, the match between modelled and measured pool pressures is good, particularly given that the model prediction is very sensitive to the production or injection rate of the source term.

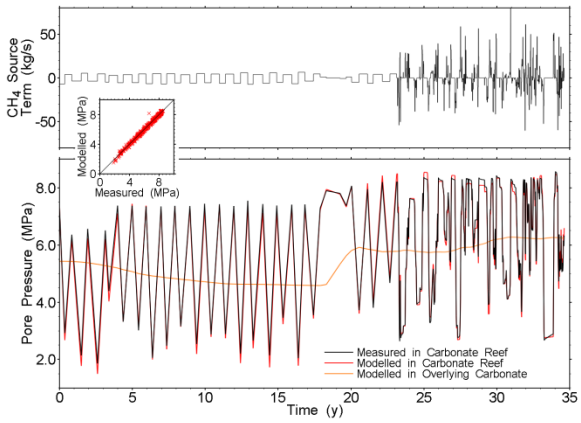

Figure 2. Methane source term and modelled and measured pool pressure, Pool A.

Figure 3 shows a measured pressure profile in the caprock directly above the gas storage pool. This profile was taken in September 2013 when the pool was at minimum pressure. The multilevel packer system had been installed for three months and pressures in most intervals were approaching equilibrium with the formation. The measurements show underpressures in shallower units (recall the surface elevation is 200 mASL), which have likely developed over geologic time and are perhaps linked to glaciation during the past 120 ka (Neuzil, 2014). Below these underpressured units measured pressures are near hydrostatic.

The carbonate formation directly above the reef, isolated from the storage pool by relatively thin layers of anhydrite and shale, is over-pressured with respect to hydrostatic. The genesis of this overpressure is uncertain. It is close to the pool discovery pressure, and may have been naturally present before discovery and development of the pool. Alternatively, this overpressure may be a consequence of the storage operation. We have conservatively assumed the second possibility is the true explanation, and starting with initial estimates of the properties of the thin anhydrite and shale caprock units, the model has been calibrated to fit the observed overpressure. The September 2013 pressure profile from the calibrated model is shown in Figure 3. The modeled pressure distribution in the overlying caprock units is reasonably close to the measured values, with the exception of the underpressured shallower units.

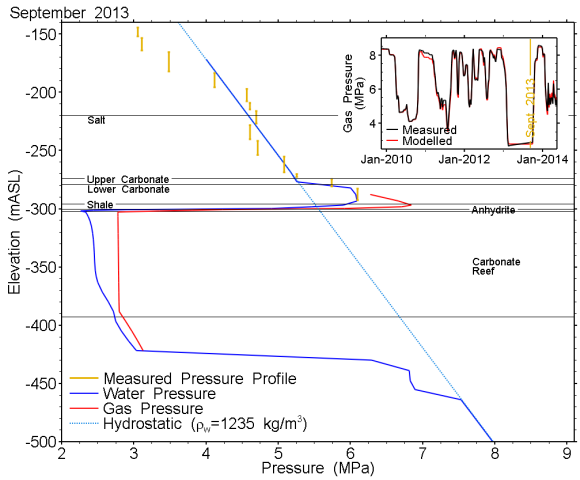

Figure 3. Pore pressure profile above reef, modelled and measured.

Figure 3 represents a single point in time. The orange line in Figure 2 shows the timeseries of average fluid pressure in the carbonate formation above the reef. The model predicts that over many years of operation pressures in the carbonate unit move toward equilibrium with the average storage pool pressure, tracking the average pressure during the preceding 4-5 years. This calibrated model allows small quantities of gas to seep into the lower part of the overlying carbonate during the decades-long operational period of the pool. The modelled overpressure in this formation does have implications for the effective stress and fracture gradient in this unit.

These pressures from TOUGH2 were interpolated onto a FLAC3D grid and imported into the previously initialized FLAC3D model. Figure 4 shows the model results, from both TOUGH2 and FLAC3D. The results are for a pool pressure maximum, under current operating conditions at the time the model was run. The first panel shows the gas saturation, the second shows the saturation averaged pore pressure which was exported to FLAC3D, the third shows the resultant total stress distribution (horizontal), and the final panel shows the calculated percent fracture gradient. The maximum percent fracture gradient was 65.4% at 0.73 psi/ft. Increasing the delta

pressure gradient to 0.8 psi/ft, by increasing injection and extraction rates, raised the maximum fracture gradient to 71.4%. In both cases, this maximum occurred at the top of the reef, and not in the overlying carbonate. The fracture gradient was calculated using the maximum fluid phase pressure, not the average gas and water pressure.

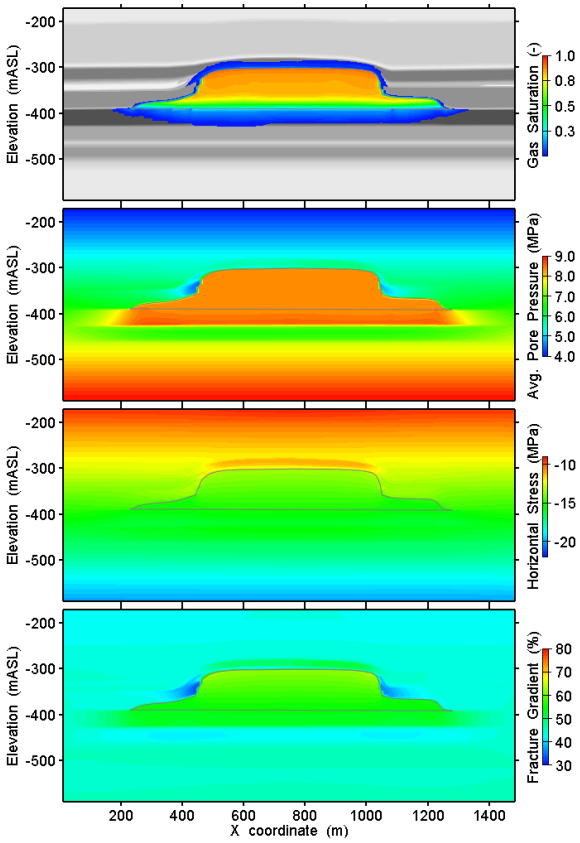

Figure 4. Pool A model results. In panel three, tensile stress is positive.

In Figure 4, panel 3, the reduction in horizontal compressive stress directly above the storage pool is evident. A vertical profile showing model results at the midpoint of the reef is shown in Figure 5. The reduced compressive stress above the pool is apparent, as is the increased stress at minimum storage pressure (second panel). The stress change is reduced in the salt unit, as it is more elastically compliant.

A 3D model for this pool was also developed. It confirmed that the 2D model adequately captures the important mechanical processes, predicting a maximum fracture gradient of 65.5%, as compared to the value of 65.4% returned by the 2D model (see Figure 6).

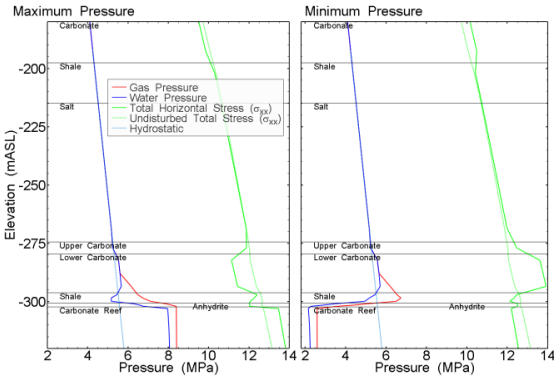

Figure 5. Stress profile at high and low pool pressures. Compressive stress is positive.

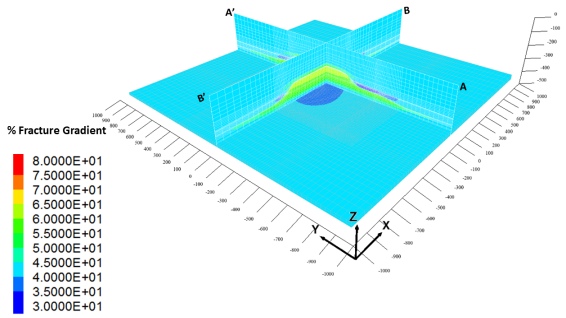

Figure 6. Percent fracture gradient in 3D model.

Indirect Measurement of Stress Change

As mentioned earlier, datalogger probes were installed in seven intervals above the storage reservoir, to record the evolution of fluid pressure in the cap during reservoir pressure cycling. The instruments were intended primarily to measure the in-situ pore pressure, and provide an early warning should the increased storage pressure cause detrimental pressure changes in the cap. Pressures from six dataloggers are shown in Figure 7. Data from the seventh, installed at -160 mASL, is difficult to interpret due to pronounced underpressure in the adjacent formation, which may be causing the packer to leak.

Figure 7 shows that, despite the variation in pool pressure between 3.5 and 8.2 MPa, the pore pressure measured in the caprock does not change significantly. The gradual pressure rise, especially apparent in ports 2, 3, and 4, is due to gradual equilibration between the initial water pressure in the isolated section of borehole, and the formation fluid pressure. Port 1, in the relatively permeable part of the overlying carbonate unit shows virtually no change during this time, as equilibration was more rapid.

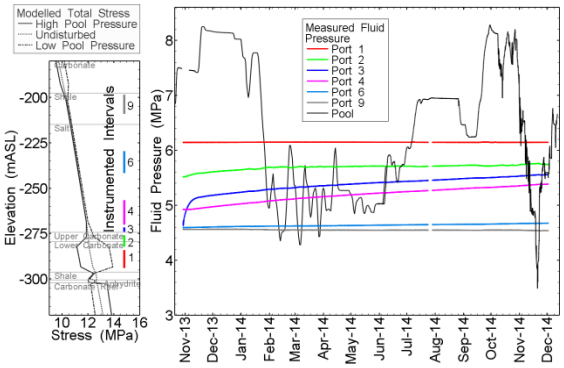

Figure 7. Measured pressure in caprock.

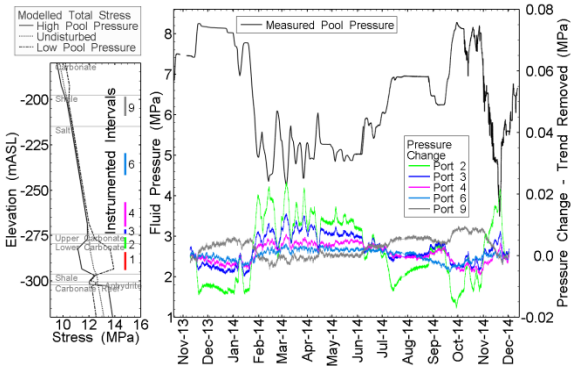

Figure 8. Pressure change in overlying caprock.

Even at the scale of Figure 7, small perturbations are evident in some of the pressure timeseries. To highlight these perturbations, a cubic spline fitting the overall trend of the pressure recovery curve was subtracted from the data. The resulting timeseries highlights the small pressure fluctuations, as shown in Figure 8. Plotted in this way, there is clearly a relationship between pressure changes in the storage pool and small pressure fluctuations in the cap. It is equally clear that this is not caused by movement of fluid, but rather by hydromechanical coupling. The observed pressure response is virtually instantaneous, and the pressure perturbations are inversely proportional to the pool pressurization.

Given the very low permeability of the caprock units, established through hydraulic testing and also evident in the long equilibration times, the pore pressure response measured by these sensors is likely not due to a change in formation pressure, but rather to borehole deformation.

There are no similar small pressure fluctuations in Port 1, in the lower carbonate, closest to the storage reservoir. Pressure at this port is remarkably stable. The permeability of this unit is approximately three orders of magnitude higher than other units, which may allow any hydromechanically induced pressure fluctuations in the borehole to dissipate much more rapidly. Alternatively, even very low gas saturations in the borehole would reduce the hydromechanical pressure response (e.g. Walsh et al., 2012).

It might be possible to model the observed borehole hydromechanical response to stress changes, and thereby use pore pressure changes in the borehole as a proxy measurement for changes in rock stress; however, this was beyond the scope of this project. In order to develop such a model, it would be necessary to have a very good understanding of the in-situ stress field, compliance of the packer and casing system (Westbay MP55 in this case), and rock mechanical properties for the entire isolated interval. If all of these conditions were met, this analysis could still be confounded by very low saturations of gas in the test interval. Low gas saturations could explain the lack of pressure response in Port 1, and may also affect the observed pressure change in other ports, albeit to a lesser degree. On the other hand, the observed pressure fluctuations do provide a qualitative confirmation of the modeled stress changes.

STORAGE POOL B

The pool was discovered in 1931 at a well head pressure of 6,029 kPaa. The pool has a depth to crest of 479.9 m, and this translates to a discovery gradient of 12.6 kPa/m (0.56 psi/ft). The pool was designated as a natural gas storage area in 1943 and currently operates between a cushion and maximum pressure of 3,447 kPaa and 7,320 kPaa (measured at well head).

In contrast to Pool A, the shale and anhydrite units separating the carbonate reef storage pool from the overlying carbonate formation are discontinuous. The casing of two production wells ends in the overlying carbonate, so the wells are open from the reef into the overlying carbonate. Three abandoned wells are also open to both the reef and the carbonate, with the seals

ending partway through the overlying carbonate. During drilling, gas shows were recorded in the overlying carbonate in four wells. The cross connections between the overlying carbonate and the reef and the initial presence of gas in the overlying carbonate mean that this unit likely acts as a secondary gas storage zone.

Model Setup

The grid and property distribution in the cross-sectional model of Pool B are shown Figure 9. Geologically, Pool B is very similar to Pool A. The primary difference between the pools is due to the five open boreholes perforating the anhydrite and shale cap. As a consequence, the caprock for Pool B is effectively the thick salt unit (plus another thin anhydrite layer). This is a dense and low permeability unit with an average thickness of 33.4 m over the reef. There is evidence, in the form of gas pressure observations, that a debris bed on the flanks of the reef forms a secondary storage zone.

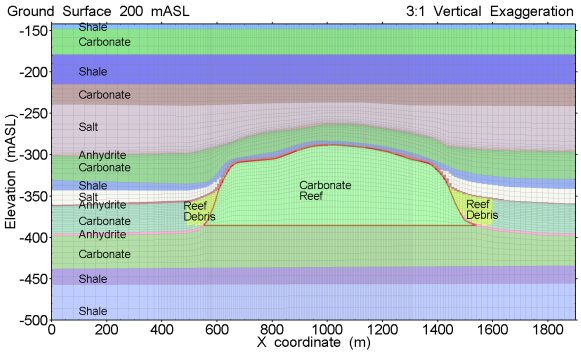

Figure 9. Grid and properties, Pool B model.

Stabilized inventories for Pool B between 1991 and 2015 were provided and used to calculate a methane source/sink term. A three month data gap exists starting in January 2003. The model commences after this gap.

Model Results

To assess suitability of the model, measured gas pressures in the storage pool, the flanking carbonate debris bed, and the overlying carbonate were compared to modelled pressures, as shown in Figure 10. The model does a good job matching the measured pool pressure, as well as those in the flanking debris bed and the overlying carbonate. The observation borehole in the overlying carbonate is above the reef flank (approximately Model X = 525 m). Modelled pressures directly above the pool are greater than the measured values above the flank.

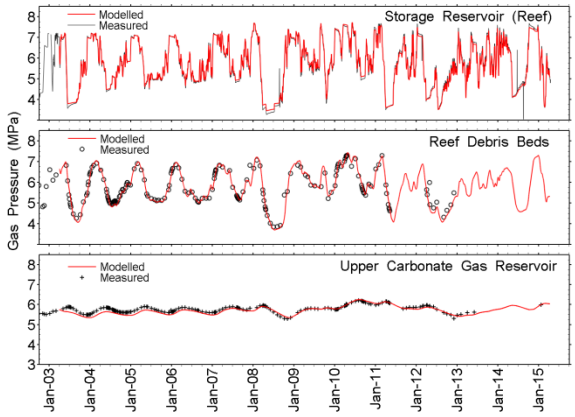

Figure 10. Modelled and measured pressure, Pool B.

To fit the overlying carbonate pressure, the model required a connection across the thin cap, as exists in five boreholes. This was approximated in the 2D model by a single line of nodes with high vertical permeability crossing the anhydrite and shale, and extending half-way into the carbonate. The observed pressure response in the overlying carbonate follows the pressure in the reef, with reduced amplitude and a time delay. Short duration pressure changes in the reef have minimal impact on pressures within the overlying carbonate. Permeability in the overlying carbonate unit was calibrated to fit the observed pressures. The calibrated permeability of 5×10^{-16} m^2 is close to the measured horizontal permeability of 4×10^{-16} m^2 for the same unit at an adjacent reef.

Figure 11 shows the model results, from both TOUGH2 and FLAC3D models. As in Figure 4, the results represent a pool pressure maximum. The panels show gas saturation, saturation averaged pore pressure, the total stress, and the calculated percent fracture gradient. The maximum percent fracture gradient was 70.4% at 0.70 psi/ft. Increasing the delta pressure gradient to 0.8 psi/ft, by increasing injection and extraction rates, raised the maximum fracture gradient to 80.4%. In both cases the maximum is located within the overlying carbonate unit. As in Pool A, the reduction in horizontal compressive stress directly above the storage pool is evident. When this is combined with the increased gas pressure in the same unit, the

increased maximum fracture gradient is the result. An adequate model of this system requires a model (or as in this case a series of models) which can represent the physics of gas flow processes affecting the pore pressure in the units above the storage pool, and the physics of stress redistribution above the pool resulting from expansion and contraction of the reef in response to pool pressure cycling. The use of TOUGH2 and FLAC3D in series allowed an efficient and defendable solution.

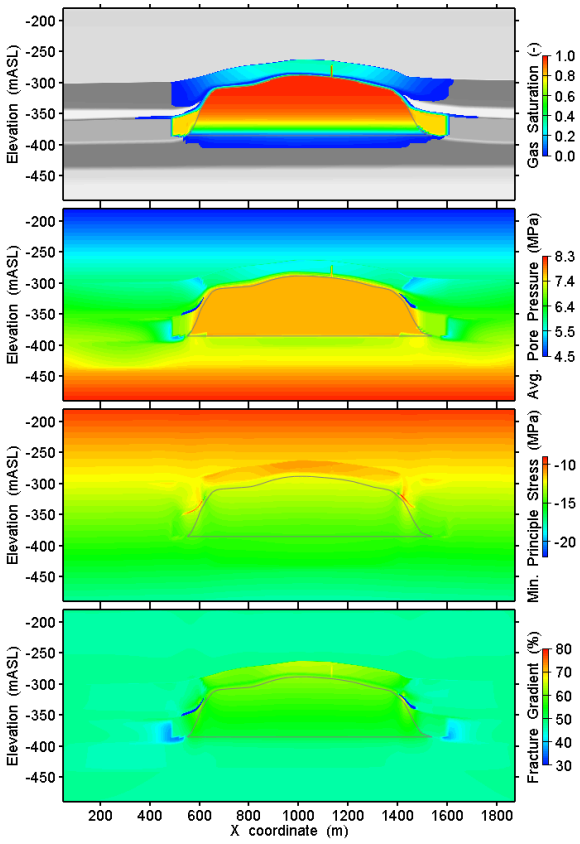

Figure 11. Pool B model results. In panel three, tensile stress is positive.

CONCLUSION

In this paper, we have briefly described two similar models developed to investigate gas flow and geomechanical processes in underground natural gas storage operations. This work provides an application example combining TOUGH2 and FLAC3D models to quantify the subsurface processes which occur when gas is injected into deep formations at pressures exceeding those that were naturally present. Uncertainty, which is present in all subsurface engineering, was managed through conservative, but plausible, assumptions, based on the available evidence. The use of all available field data to calibrate and confirm model predictions fostered confidence in the model. At Pool A, pore pressure measurements in a borehole above the pool provided qualitative confirmation of model predicted stress changes, and offered a potential method to estimate stress changes by the proxy measurements of pore pressure. The combined use of TOUGH2 and FLAC3D allowed us to establish the safety of proposed operating pressures for these pools, allowing the client to fully develop the value of their assets.

REFERENCES

CSA, *Storage of Hydrocarbons in Underground Formations*. Z341 Series-14, Canadian Standards Association, Mississauga, Ontario, Canada, 2014.

Geofirma and Quintessa, Postclosure Safety Assessment: Gas Modelling, DGR-TR-2011-31, Nuclear Waste Manag. Org., Toronto, ON, 2011

Lam, T and S. Usher, *Regional Geomechanics Southern Ontario*, DGR-TR-2011-13, Nuclear Waste Manag. Org., Toronto, ON, 2011.

Neuzil, C.E. and A.M. Provost, Ice sheet load cycling and fluid underpressures in the Eastern Michigan Basin, Ontario, Canada, *J. Geophys. Res. B: Solid Earth*, 119(12), 8748-8769, 2014.

Reid, R., Prausnitz, J., and B. Polling, *The Properties of Gases and Liquids, 4th Edition*, McGraw-Hill Inc, New York, 1987.

Rutqvist, J., and Tsang, C.F. TOUGH-FLAC: A numerical simulator for Analysis of Coupled Thermal-Hydrologic-Mechancial Processes in Fractured and Porous Geological Media under Multi-phase flow Conditions. *Proccedings, TOUGH2 Symposium 2003*, Berkeley, California, 2003.

Walsh, R., N. Calder, and J. Avis, A Simple Implementation of Hydromechanical Coupling in TOUGH2. *Proccedings, TOUGH2 Symposium 2012*, Berkeley, California, 2012.

Walsh, R., O. Nasir, H. Leung, and J. Avis, Numerical Characterization of the Excavation Damaged Zone in the HG-A Experiment. *Proccedings: International High-Level Radioactive Waste Management,* Charleston, SC, 2015.

Environmental Engineering and Vadose Zone

MULTIPHASE FLOW AND TRANSPORT OF METHANE IN SOIL UNDER VARYING SUBSURFACE AND ATMOSPHERIC CONDITIONS: BENCH-SCALE EXPERIMENTAL AND NUMERICAL STUDY

Chamindu Deepagoda[1], Kathleen Smits[1], Tissa llangasekare[1], Curtis M. Oldenburg[2], Abdullah Cihan[2]
[1] Colorado School of Mines
1500 Illinois Street
Golden, CO 80401, USA
[2] Lawrence Berkeley National Laboratory
1 Cyclotron Road
Berkeley, CA 94720
E-mail: kdeepago@mines.edu

ABSTRACT

Fugitive atmospheric emissions of methane, a potent greenhouse gas, from natural gas infrastructure have recently gained widespread attention. When methane leaks from an underground pipeline, its subsurface migration and ultimate release into the atmosphere are controlled by subsurface soil conditions (e.g., soil heterogeneity, moisture, and temperature) and are further affected by atmospheric boundary conditions (e.g., wind, barometric pressure, temperature). Nonetheless, the transport and attenuation of methane is not well understood, making it difficult to define the leakage rate based on estimates of methane concentrations at and above the soil surface. Based on bench-scale experiments using a porous media test facility coupled with a wind tunnel, this study investigated multiphase processes controlling migration of methane from a simulated point source (i.e., buried pipeline) under differently-saturated and texturally-heterogeneous subsurface conditions. In addition, potential effects of atmospheric boundary controls, wind (0.5 and 2.0 m s^{-1}) and temperature (24 and 38 ^{o}C), were also examined. A subsurface multiphase transport simulator, TOUGH2-EOS7CA, (Oldenburg, 2015) was used to numerically characterize the non-isothermal density-dependent methane-air-water flow and transport through the subsurface.

INTRODUCTION

Methane (CH_4) is a potent greenhouse gas with a global warming potential 25 times higher (over a 100-year time horizon) than CO_2 (EPA 2013). In addition to its significant impact on global climate change, elevated concentrations of CH_4 may increase ground-level ozone and thereby adversely affect terrestrial ecosystem functions. The presently higher atmospheric CH_4 concentrations (~ 1800 ppb) compared to preindustrial levels (~ 680-715 ppb) can be attributed to increased anthropogenic interference over the past few decades in which fugitive emissions from the natural gas industry have played a significant role (Miller et al., 2013). Natural gas distributed for commercial use is composed almost entirely of methane; emissions may occur from almost all processes from production at the gas reservoir, to distribution by pipeline, to end-use. As much of the natural gas infrastructure exists underground (e.g., wellbores, pipelines, gathering lines, and storage), the inspection, maintenance, and monitoring of leakage are extremely challenging. These challenges, combined with limited regulations, have resulted in huge gaps in emission inventories and the use of emission factors with limited empirical validation (e.g., US EPA's national inventory). Methane leakage from underground infrastructure is particularly prevalent across the United States from aging underground pipelines (EPA 2014). Moreover, leakage rates of methane from underground pipelines are typically calculated based on estimates from above-ground concentration measurements (e.g., Jackson et al., 2013) with limited consideration of the controlling mechanisms of the fate and transport of methane in the subsurface.

The fate and transport of methane in soil are primarily controlled by subsurface conditions such as heterogeneity, soil moisture, temperature, and pressure gradients. For example, gas migration in a texturally

heterogeneous soil system (e.g., in the presence of a low-permeability clay lens embedded in a sandy formation) will be markedly different from that of a homogenous soil system due to the different texture- (or porosity-) induced tortuosity effects. Similarly, soil moisture controls methane migration in variably-saturated soils due to the effects of methane solubility and water vapor transport in the soil gas phase. Furthermore, temperature affects molecular diffusion and thereby the diffusive flow of gases while the presence of pressure gradients leads to advective gas flow. Moreover, the wind- or temperature-induced near-surface fluctuations may also affect the subsurface migration and atmospheric emission of methane. However, experimental and numerical studies investigating subsurface methane migration under different subsurface conditions and atmospheric controls are limited.

This study investigated the multiphase processes contributing to the migration of methane in variably saturated soil under different surface and subsurface conditions with the goal of developing more accurate estimates of surface leakage of methane to the atmosphere. We studied changes in subsurface and atmospheric methane concentrations under two subsurface conditions (i.e., homogenous and layered with differently-textured sand) and two saturation conditions (i.e., at residual saturation and at -35 cm H_2O capillary pressure). Potential effects of two atmospheric boundary controls, wind (0.5 and 2.0 m s^{-1}) and temperature (24 and 38 ºC), were also examined. The dynamics of subsurface methane migration in the experimental domain were numerically modeled using the subsurface multiphase transport simulator TOUGH2 (Pruess et al., 2012) together with EOS7CA (Oldenburg, 2015), a research module developed for non-isothermal density-dependent flow of non-condensable gas (e.g., CH_4) and water flow in partially saturated soil.

MATERIALS AND METHODS

A series of bench-scale controlled laboratory experiments was conducted using a two-dimensional soil tank (35 cm x 55 cm) coupled with an open-loop boundary-layer wind tunnel (Figure 1).

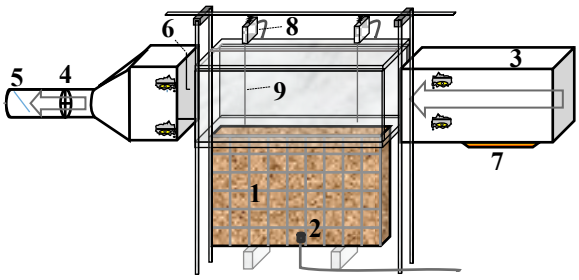

1. Sand-packed tank 2. Methane source 3. Galvanized steel duct
4. In-line fan 5. Damper 6. Pitot static tube 7. Heater assembly
8. Gas sampling head (2 Nos.) 9. Capillary tube (2 Nos.)

Figure 1. Schematic of the experimental set-up (not to scale). The arrows show the wind direction.

A point methane source (50,000 ppm, 0.5 lpm) was placed 2 cm above the bottom of the tank (at the centerline) to mimic a leaky shallow underground pipe. The tank was packed uniformly with a silica sand # 30/40 (identified by the effective sieve number) (Accusand, Unimin Corporation, Ottawa, MN) to represent a homogenous system. To represent a layered system, a 5-cm thick coarse-textured (#12/20) sand layer was sandwiched 15 cm below the surface. Experiments were conducted for near-dry (i.e., at residual saturation) and partially saturated (i.e., wet-packed and drained to -35 cm H_2O with respect to the center) conditions.

An integrated sensor network within the soil tank was used to measure soil temperature (Decagon Devices Inc. RT-1), moisture (Decagon Devices, Inc. ECH2O EC-5), and water pressure (only for partially saturated experiments) (Figure 2). Wind velocity was measured using a pitot static tube (Dwyer Instruments, Inc). Gas samples were extracted at steady state from selected ports within the soil tank and methane concentrations were determined using gas chromatography (Agilent 6850). Above-ground methane concentrations were continuously monitored using fast Flame Ionization Detection (FID) (HFR 400, Cambustion Ltd, UK).

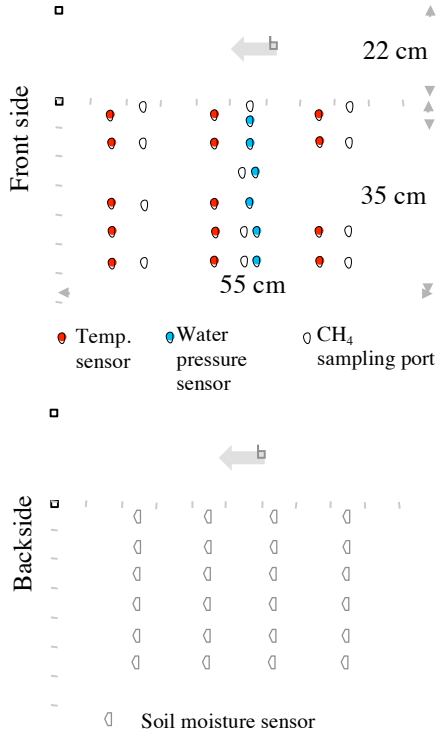

Figure 2. The schematic showing sensor locations and gas sampling ports in the front side (top) and the back side (bottom) of the tank. The arrow shows the direction of the wind in duct space.

RESULTS AND DISCUSSION

Effect of subsurface heterogeneity

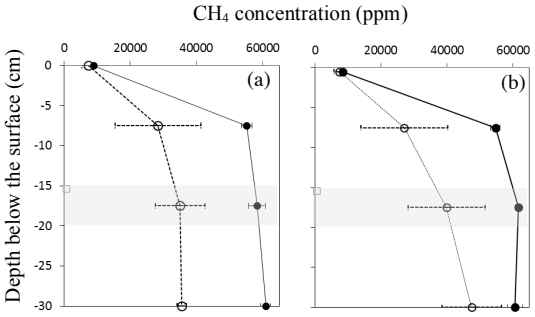

Figure 3. Depth-wise variation of methane concentration in homogenous (solid lines) and heterogeneous (layered) (dotted lines) soil systems at near-dry conditions under two different atmospheric wind velocities; (a) 0.5 ms^{-1} and (b) 2.0 ms^{-1}. The shaded area illustrates the embedded course-textured sand layer (#12/20).

Figure 3 shows the observed steady-state subsurface methane concentration profiles (i.e., depth vs. CH_4 concentration) for homogenous and layered soil systems under two above-ground velocity conditions: (a) 0.5 ms^{-1} and (b) 2.0 ms^{-1}.

A clear effect of textural heterogeneity in subsurface methane concentrations can be seen at both velocity conditions. The relatively lower concentrations in layered soil systems in comparison to the homogenous soil system (packed with #30/40 sand) can be attributed to the presence of the embedded high-porous and high-permeability sand layer (#12/20).

Effect of wind velocity and temperature

Despite the minimal effect on subsurface CH_4 concentrations, wind velocity showed a pronounced effect on above-ground (near-surface) CH_4 concentration (Figure 4).

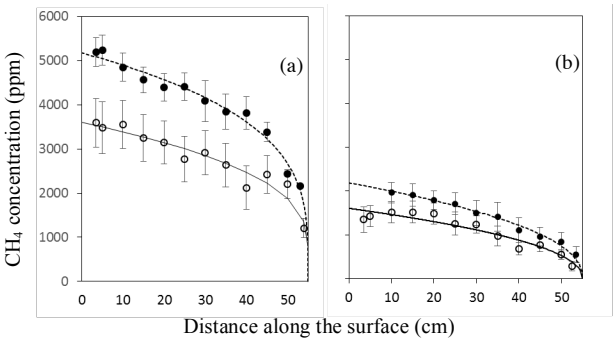

Figure 4. Methane concentration along the surface (measured from downstream to upstream) in homogenous (solid lines, open symbols) and heterogeneous (layered) (dotted lines, closed symbols) soil systems at near-dry conditions under two different atmospheric wind velocities; (a) 0.5 ms^{-1} and (b) 2.0 ms^{-1}. Measurements are shown by symbols, lines represent fitting functions given by Equation (1).

Note the nearly two-fold increase in above-ground CH_4 concentrations when the wind velocity decreases from 2.0 m s^{-1} to 0.5 ms^{-1}. To further characterize the wind-induced effects, we described the measured surface concentration, $C_s(x)$, based on a two-parameter nonlinear fitting function as presented below.

$$C_s(x) = C_{s,o}\left(\frac{L-x}{L}\right)^n \quad \mathbf{0 \le x \le L} \quad \mathbf{(n \ge 0)} \qquad (1)$$

where L (cm) is the length of the tank, $C_{s,o}$ (ppm) is the maximum surface concentration (i.e., at the downstream edge), and n (-) is a shape factor representing the shape of the surface CH_4 concentration buildup under wind- and temperature-induced atmospheric conditions. The fitted models are illustrated in Figure 4 as

lines. Generally, for wind velocities of 0.5 and 2.0 m s^{-1}, the *n* value varied in the ranges of 0.2-0.3 and 0.5-0.65, respectively.
The effect of atmospheric temperature on subsurface CH_4 concentration profiles (not shown) is not particularly evident though a noticeable increase in atmospheric CH_4 concentrations was observed with an increase in temperature.

Effect of soil moisture
Figure 5 illustrates the effect of soil moisture on steady state CH_4 concentration profiles in identical homogenously-packed (#30/40) soil systems under two different moisture conditions; (i) dry-packed at residual saturation (solid line), and (ii) wet-packed and subsequently drained to -35 cm H_2O (with respect to the centerline) (dotted line).

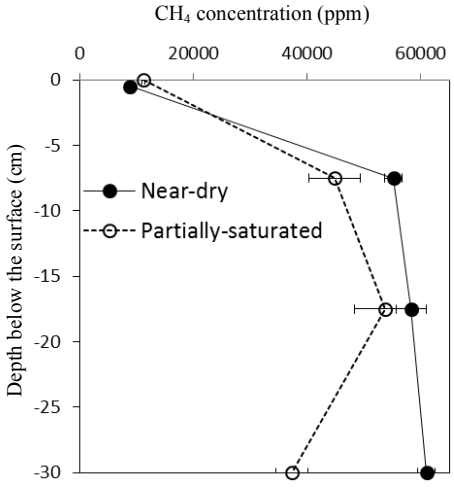

Figure 5. Depth-wise variation of methane concentration at steady state in homogenous soil systems (#30/40) under two different moisture conditions; near-dry (packed at residual saturation) (solid line), and wet-packed and drained to -35 cm H_2O (dotted line).

In the partially saturated soil system, a capillary fringe occurred nearly up to a depth of -35 cm causing unsaturated partially saturated zone near the methane source. The marked decrease in CH_4 concentration in the partially saturated system in comparison to the near-dry system at a depth of -30 cm is due to the effect of soil moisture. The near-surface soil layers in both soil systems are at residual saturation and therefore showed almost the same CH_4 concentrations. Experiments investigating the effect of soil moisture in layered soil systems are on-going.
Observed variations in CH_4 concentrations under different subsurface and atmospheric conditions will be numerically modeled using the TOUGH2/EOS7CA simulator to further characterize subsurface CH_4 dynamics.

SUMMARY

Based on a controlled laboratory experiment using a bench-scale porous media facility coupled with an open-loop wind tunnel, this study investigated the effects of soil conditions (heterogeneity and soil moisture) and atmospheric controls (wind and temperature) on methane dynamics in the subsurface. A distinct effect of soil heterogeneity and soil moisture on subsurface methane concentration profiles under steady state was observed. Wind velocity showed a more pronounced effect on atmospheric methane boundary layer compared to the temperature. TOUGH2/EOS7CA-based numerical modeling will be carried out to further characterize subsurface CH_4 dynamics.

ACKNOWLEDGMENT

This research was funded in part by the Department of Energy's *National Energy Technology Laboratory* (*NETL*), the Research Partnership to Secure Energy for America project (# RFP2012UN001) and the National Science Foundation Project Award Number 1447533.

REFERENCES

Miller, S. M., S.C.Wofsy, A.M. Michalak, A.E. Kort, A.E.Andrews, S.C. Biraud, E.J. Dlugokencky, J. Eluszkiewicz, M.L.Fischer, G. Janssens-Maenhout, B.R. Miller, J.B. Miller, S.A. Montzka, T. Nehrkorn, C.Sweeney, Anthropogenic emissions of methane in the United States. *Proc. Natl. Acad. Sci.* U. S. A. 110 (50), 20018–20022, 2013.

Oldenburg, C.M., EOS7CA Version 1.0: TOUGH2 module for gas migration in shallow subsurface porous media systems, Lawrence Berkeley National Laboratory Report, LBNL-175204, March 2015.

Pruess, K., C.M. Oldenburg, and G.J. Moridis. TOUGH2 User's Guide Version 2. E. O. Lawrence Berkeley National Laboratory Report LBNL-43134, 1999; and LBNL-43134 (revised), 2012.

US Environmental Protection Agency, Inventory of U.S. Greenhouse Gas Emissions and Sinks: 1990–2011, *Technical Report EPA 430-R-13-001* (Environmental Protection Agency, Washington), 2013.

US Environmental Protection Agency, Office of Inspector General, Improvements needed in EPA efforts to address methane emissions from natural gas distribution pipelines, *Report No. 14-P-0324*, 2014.

Jackson, R. B.A. Down, N.G. Phillips, R.C. Ackley, C.W. Cook, D.L. Plata, K. Zhao. Natural gas pipeline leaks across Washington, DC. *Environ. Sci. Technol*. 48 (3), 2051−2058, 2013.

A SEMI-ANALYTIC APPROACH FOR MODELING MATRIX DIFFUSION EFFECTS IN TOUGH2 AND OTHER GROUNDWATER TRANSPORT MODELS

Ronald W. Falta,
Department of Environmental Engineering and Earth Sciences
Clemson University

faltar@clemson.edu

ABSTRACT

Matrix diffusion occurs when groundwater contaminants present in high permeability zones diffuse into adjacent low-permeability zones. This process occurs in a variety of geologic settings including simple aquifer-aquitard systems, layered systems, strongly heterogeneous systems, and fractured porous media. In all cases, the contaminants that have diffused into the low permeability zones can represent a long term source of contamination following remediation of the high permeability zones due to back diffusion. Current numerical modeling approaches are not able to accurately resolve the local-scale matrix diffusion effects without resorting to extremely fine grids, with gridblocks numbering in the millions.

The TOUGH2 codes contain an option for modeling conductive heat transfer with low permeability confining beds using the semi-analytical method of Vinsome and Westerveld (1980). We have adapted this method for simulating the diffusive mass flux of contaminants between an aquifer and an aquitard. With this method, only the high permeability zone is discretized in the numerical model, and the interaction with the low permeability zone is accounted for in a time-dependent source/sink term that is computed analytically in each gridblock. The new method is extremely efficient, and it compares well with exact analytical solutions for diffusion into and out of clay aquitards.

Following the modifications outlined by Pruess and Wu (1993), the method is also applicable to modeling matrix diffusion in general layered or heterogenous media, as well as in fractured porous media.

REFERENCES

Pruess, K. and Y.-S. Wu, A new semi-analytical method for numerical simulation of fluid and heat flow in fractured reservoirs, SPE Advanced Technology Series, 1(2), 63-72, 1993.

Vinsome, P.K.W. and J. Westerveld, A simple method for predicting cap and base rock heat losses in thermal reservoir simulators, *J. Canadian Pet. Tech.*, 19(3), 87-90, July-September 1980.

DETERMINING IN SITU HEATING TEMPERATURE FOR OPTIMIZING RETURN ON INVESTMENT IN DNAPL SOURCE ZONE REMEDIATION

Amy Y. Fu*[1,3], Stefan Finsterle[2], Yingqi Zhang[2], Michael D. Annable[3]

[1]Ellis & Associates, Inc., 7064 Davis Creek Road, Jacksonville, FL 32256.
[2]Earth Sciences Division, Lawrence Berkeley National Laboratory, 1 Cyclotron Rd, MS 74R316C, Berkeley, CA 94720
[3]University of Florida, 365 Weil Hall, P.O. Box 116580, Gainesville, FL 32611
*Email: a.fu@ellisassoc.com

ABSTRACT

The technical challenge of dense nonaqueous-phase liquid (DNAPL) source removal has spurred interest in incorporating in situ thermal (IST) technologies in DNAPL treatment. However, the high electricity consumption associated with typical IST applications that raise subsurface temperature to approximately 100˚C has limited its general use. It is important to explore the effectiveness of low-temperature IST (i.e., 50˚C to 90˚C) in DNAPL source zone remediation, which may lead to a more sustainable application of the IST technology in environmental remediation. Using the TMVOC (Pruess et al., 2002) multiphase flow simulator, the effect of low temperature IST combined with a Soil Vapor Extraction (SVE) and a Multi-Phase Extraction (MPE) system has been evaluated for various DNAPL (e.g., perchloroethylene (PCE)) impacted site conditions. The results of the numerical simulation help better understand the physical processes of mass removal influence by low temperature IST, and investigate the feasibility of employing such technologies for DNAPL source zone treatment. Using the inverse modeling capability of iTOUGH2 (Finsterle, 1999), the optimum Return on Investment (ROI) in terms of total mass removal and remediation cost as a function of temperature settings of the IST heaters could also be examined. Simulation results indicate that significantly more PCE mass can be removed, and contaminant flux can be reduced even with the IST temperature set as low as 50˚C. In addition, the IST temperature associated with an optimum ROI of a DNAPL source zone remediation could be determined.

INTRODUCTION

Remediation of dense nonaqueous-phase liquid (DNAPL) source zones caused by perchloroethylene (PCE) releases is often considered “technically impracticable” (USEPA 1996), which spurred the use of in situ thermal (IST) technologies (e.g., Electrical Resistance Heating (ERH), Steam Injection (SI), and Thermal Conductive Heating (TCH)) in the late 1990s. The major limitation of the IST technologies, however, lies in the high electricity demand to raise subsurface temperature to approximately the boiling point of water (i.e., 100˚C). Moreover, a proportional amount of energy is also required to cool the extracted off-gas and groundwater to allow for contaminant recovery. To explore a more sustainable delivery of the IST technology, the effect of low temperature IST (i.e., 50˚C to 90˚C) combined with a Soil Vapor Extraction (SVE) and a Multi-Phase Extraction (MPE) system has been evaluated in this research for DNAPL source zone treatment.

This research is intended to achieve three major objectives. Firstly, we simulate three-phase, multicomponent, isothermal flow of a DNAPL release into unsaturated zone followed by redistribution of DNAPL in both unsaturated and saturated zones to establish baseline site conditions for remediation. Secondly, we evaluate the effectiveness and feasibility of low temperature IST (i.e., heater temperature set at 50˚C to 90˚C) in DNAPL source zone remediation through numerical simulation of three-phase, multicomponent, non-isothermal flow. Thirdly, we examine the optimum Return on Investment (ROI) in terms of total mass removal and remediation cost as a function of temperature settings of IST.

METHODS

Part A: DNAPL Release and Distribution

The simulation domain is 100 m long (x axis), 1 m wide (y axis), and 15 m deep (z axis). The water table is 5 m below ground surface (bgs) on the left and 5.5 m bgs on the right, resulting in a groundwater flow velocity of 18.9 m/year from left to right. The computational mesh is generated using evenly spaced 200 columns and 30 layers for a total of 6,000 elements. A DNAPL release caused by a total of 1,000 kilogram of steady PCE spill (x = 39.5 m) into the unsaturated zone over one year and re-distribution in both unsaturated and saturated zones for one more year upon cease of the PCE spill is simulated.

Part B: DNAPL Source Zone Remediation

A combined IST, SVE, and MPE system, shown on Figure 1 is used to simulate a typical DNAPL remediation. The SVE well (x = 40.5 m) is operated under 0.8 bar pressure with a well screen from 0.5 m bgs to 5.0 m bgs. The MPE well (x = 41.0 m) is operated under 0.4 bar pressure with its well screen from 5 m bgs to 14.5 m bgs. The IST well (x = 40.5 m) is represented by a heating well with its hot section from 0.5 m bgs to 15 m bgs. Part of the domain surface is turned impervious to prevent short circuiting of air from going into the SVE well. Two monitoring wells, MW-1 (x = 39.0 m) and MW-2 (x = 43.0 m) screened across the saturated zone are used to evaluate heat transfer and contaminant mass flux during DNAPL remediation.

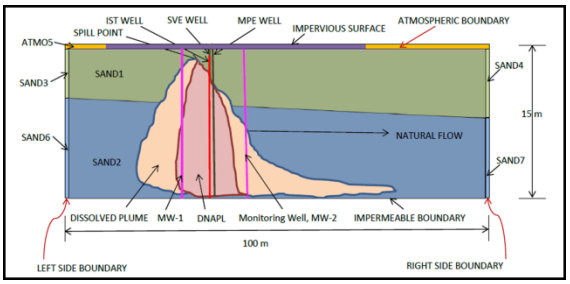

Figure 1. Conceptual model of 2-D DNAPL Source zone remediation.

RESULTS

Scenario A: Homogenous, No Adsorption, Sandy Soil

A typical sandy soil domain was simulated by setting absolute permeabilities along the three principal axes (i.e., x, y, and z) as 4.0×10^{-12} m^2, 4.0×10^{-12} m^2, and 1.0×10^{-12} m^2, respectively. Separate simulations were conducted with the temperature of the IST well set at 20˚C (isothermal), 50˚C, 60˚C, 70˚C, 80˚C, and 90˚C. No adsorption effect is considered.

The simulation results, as presented in Figures 2 and 3, indicate that significant improvements in terms of mass removal rate and cumulative mass removal could be achieved with the temperature of the IST well increased by as little as 30˚C (i.e., from 20˚C to 50˚C). In addition, with non-adsorptive sandy soil, a near complete mass removal of the DNAPL contamination could be accomplished by operating the combined IST, SVE, and MPE remedial system for less than one year. With the obvious trend that the higher the IST temperature is, the more effective the remediation becomes, the remediation is most effective while IST temperature is set at 90˚C.

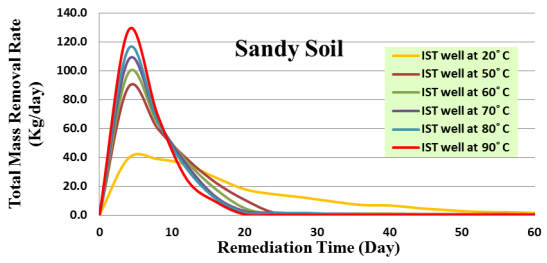

Figure 2. Mass removal rate during remediation in sandy soil domain.

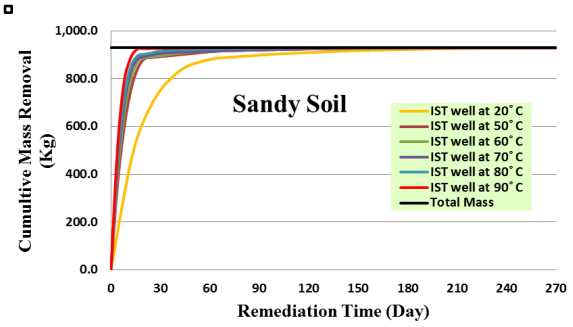

Figure 3. Cumulative mass removed during remediation in sandy soil domain.

Scenario B: Homogenous, No Adsorption, Silty Sand

A typical silty sand domain was simulated by setting absolute permeabilities along the three principal axes as 4.0×10^{-13} m^2, 4.0×10^{-13} m^2, and 1.0×10^{-13} m^2, respectively. By repeating the simulation steps of Scenario A, a near complete mass removal of the PCE contamination could only be accomplished by operating the combined SVE, MPE system and IST well at 90˚C during a one-year period. Significant tailing of mass removal is evident if the remedial system is operated under isothermal conditions (i.e., 20˚C). It is also obvious that asymptotic conditions have been reached during the first year of remediation, resulting in incomplete mass removal with the IST system operating below 90˚C. Prolonged remediation could only produce diminishing returns beyond this point.

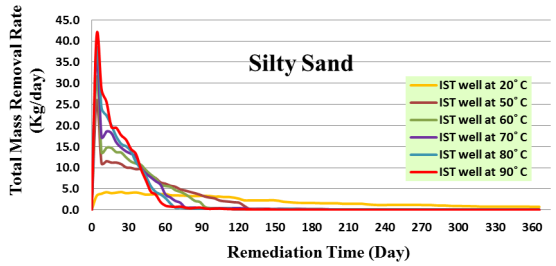

Figure 4. Mass removal rate during remediation in silty sand domain.

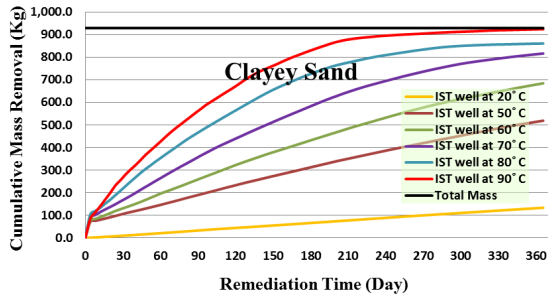

Figure 5. Cumulative mass removed during remediation in silty sand domain.

Scenario C: Homogenous, No Adsorption, Clayey Sand

A typical clayey sandy domain was simulated by setting absolute permeabilities along the three principal axes as 4.0×10^{-14} m^2, 4.0×10^{-14} m^2, and 1.0×10^{-14} m^2, respectively. By repeating the simulation steps of Scenario A, a near complete mass removal of the PCE contamination could only be accomplished by operating the combined SVE, MPE system and IST at 90˚C during a one-year period. Remedial effectiveness is considerably lower with the remedial system operating under isothermal conditions (i.e., 20˚C). In addition, significant mass removal would be unachievable using the selected remedial system without elevating the IST temperature, which is consistent with the general observation that contaminants in clayey sand are extremely difficult to recover.

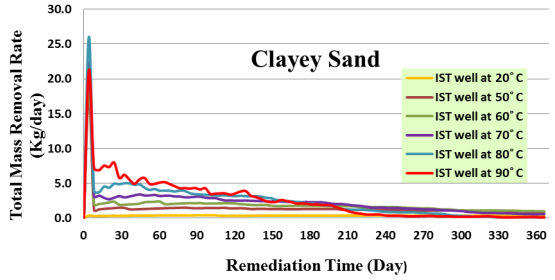

Figure 6. Mass removal rate during remediation in clayey sand domain.

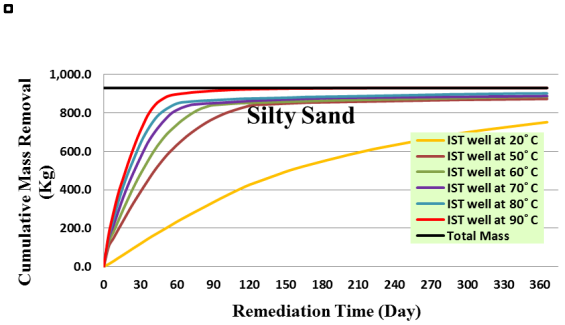

Figure 7. Cumulative mass removed during remediation in clayey sand domain.

CONCLUSIONS

Simulation results indicate that significantly more DNAPL mass can be removed at a substantially increased rate even with an IST system operating at 50˚C compared to ambient temperatures of 20˚C. In addition, remediation appears to be most effective and least affected by low- permeability soils with IST operating at 90˚C, likely due to the fact that localized boiling occurs around the IST well operating at 90˚C. This conclusion is consistent with the observation that the IST technologies are very tolerant of subsurface heterogeneities and actually perform comparably well in low-permeability silts and clay as in higher-permeability sands and gravels (Beyke and Fleming, 2005).

These preliminary forward simulations will be used as the basis for optimization runs with the aim to maximize ROI by employing in situ thermal remediation technologies that operate at reduced temperatures.

ACKNOWLEDGMENT

The author would like to acknowledge Lawrence Berkeley National Laboratory (LBNL) for providing the TOUGH2 and iTOUGH2 suite of simulators for this research. This work was supported, in part, by the U.S. Dept. of Energy under Contract No. DE-AC02-05CH11231.

REFERENCES

Beyke, G. and D. Fleming, In situ thermal remediation of DNAPL and LNAPL using electrical resistance heating, *Remediation*, Summer, 5-22, 2005.

Finsterle S. *iTOUGH2 user's guide*. Report LBNL-40040. Lawrence Berkeley National Laboratory, Berkeley, CA, 1999.

Pruess, K. and A. Battistelli, *TMVOC user's guide,* Report LBNL-49375, Lawrence Berkeley National Laboratory, Berkeley, Calif., 2002.

U.S. Environmental Protection Agency (1996). *Superfund reforms: Updating remedy decisions*, EPA 540/F-96/026, 9200.0-22, PB96-96532; U.S. Government Printing Office:
Washington, DC.

INFLUENCE OF PERMEABILITY ON THE INITIAL GAS BUBBLE EVOLUTION IN COMPRESSED AIR ENERGY STORAGE IN AQUIFERS

Chaobin Guo[1], Keni Zhang[1, 2], Cai Li[3]

School of Mechanical Engineering, Tongji University
No. 4800, Cao'an Road
Shanghai 201804, PR China
e-mail: guochaobin123@hotmail.com

College of Water Science, Beijing Normal University
No. 19, Xinjiekouwai Street
Beijing 100875, PR China
e-mail: keniz@bnu.edu.cn

School of Civil Engineering, University of Sydney
Sydney NSW 2006, Australia
e-mail: cali8165@uni.sydney.edu.au

ABSTRACT

Compressed air energy storage (CAES) is believed to be a potential choice for large-scale energy storage. Generally, using deep aquifers for energy storage would be more convenient than employing underground caverns because of the extensive presence of aquifers. During the first stage in a typical process of compressed air energy storage in aquifers (CAESA), a large amount of compressed air is injected into the target aquifer to develop an initial place (a gas bubble) for energy storage. Then a specific mass of compressed air is cyclically injected into or produced from the bubble, depending on the electricity production demand. The injection-production cycle is typically daily, and the injection mass is usually equal to the production mass in a cycle. In this study, numerical simulations were conducted to investigate the influence of aquifer's permeability on the initial gas bubble's formation and sustainability for the later cycling operation. The results show that, for a certain scale of CAESA system, there would be an optimum permeability range to select a candidate aquifer. Low permeability would make an aquifer not meet the target injectivity, while high permeability would make the bubble expand too quickly in the aquifer, reducing the effective volume of gas during the cycling process. An aquifer within this permeability range will not only satisfy the injectivity requirement but also sustain the cycle times above the desired number, which is a critical parameter to evaluate the efficiency of CAES.

INTRODUCTION

Compressed air energy storage is considered as one of the most attractive methods for large-scale store energy (especially for electricity). Energy storage can be very useful in the utilization of solar and wind energy because this kind of energy fluctuates greatly with time. The electricity energy that CAES stores and produces can be up to 400MW (Megawatt) (Nakhamkin et al., 2009). Generally, an underground cavern is ideal for a CAES system. However, such underground caverns suitable for a grid-scale CAES system are somewhat difficult to find. This is one of the main reasons why CAES has not yet been widely employed.

However, this geographical limitation can be removed if aquifers are used as the storage space for CAES, analogous to using aquifers for CO_2 geologic storage and natural gas storage.

The suitability of aquifers for CAES was positively proved through numerical simulations in previous studies (e.g., Oldenburg and Pan, 2013a; Hu et al., 2012; and Pan and Oldenburg, 2014).

Figure 1 schematically shows a CAESA system. Typically, there are two stages in running a

CAESA system. The first stage is to form a big gas bubble in the target aquifer, by injecting a large amount of air into the aquifer to displace the native water. This big bubble, called the initial gas bubble, should provide sufficient pressure support for the second stage, in which gas is cyclically injected into or produced from the bubble to adapt to the electricity generation demand. The effective volume of the gas bubble is believed to sustain the storage place and prevent the displaced water from returning to the well during the time when gas is pumped out to generate electricity. However, the effective volume of the bubble will contract gradually as the number of gas injection-production cycles increases. The bubble fringe will break somewhere due to the bubble volume changes during the injection/production operations. Once the bubble no longer maintains a continuous shape against the pressure from water in the aquifer, another large amount of gas must be injected to restore the storage place. Therefore, the initial bubble is supposed to support the gas injection-production process for as many cycle as possible before a restoring operation is needed.

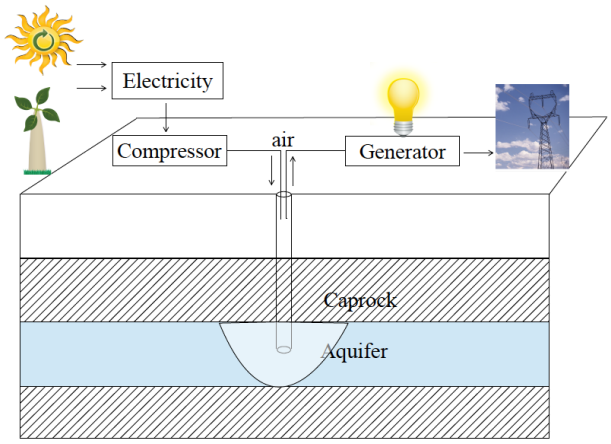

Figure 1. Schematic illustration of CAES in aquifers

The initial gas bubble was assumed stable in previous studies by Kushnir et al. (2010) and Oldenburg and Pan (2013a and 2013b). However, this kind of assumption is not appropriate for practical performance assessment of a CAESA system because performance changes are highly related to the initial gas bubble status. Many factors could affect the evolution and sustainability of the initial gas bubble, like geological structure, reservoir permeability, and depth of target aquifer. In analogous studies about the application of aquifers to natural gas storage and CO_2 storage, reservoir permeability was believed one of the most impacting factors (Entrekin et al., 2011; Juanes et al., 2006; Nakajima et al., 2014). In previous research, the impacts of reservoir permeability on CAESA performance have not been deeply addressed yet. Therefore, in this research with the assistance of numerical simulation, we investigated the influence of permeability on the initial gas bubble's formation and sustainability for later cycling operation. We contend that our results could help in designing a CAES system using aquifers as the storage place.

METHOD

CAESA Design

The energy supply/demand in our research was assumed to be 3 MW. In the first stage to form the initial gas bubble, air was injected into the target aquifer at 10 kg/s for 20 days. In the second stage of operational cycles, during each cycle, compressed air was firstly injected into the aquifer at 2 kg/s for 12 hours, after which electricity generation was suspended. After 4.5 hours of rest, the air was pumped out for electricity generation at 8 kg/s for 3 hours, and then another 4.5 hours of rest occurred before a new cycle began (Figure 2).

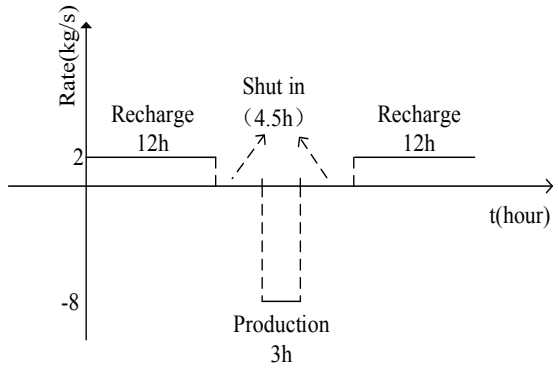

Figure 2. Schematic of daily cycle design

Modelling Approach

TOUGH2-MP/EOS3 (Zhang et al., 2008), the parallel version of the TOUGH2 simulator (Pruess et al., 1999) was used to do the numerical simulations in this study. The EOS3 module

was developed to describe the system consisting of H_2O-Air-Heat components in a porous medium.

An idealized model was built in a domain of 2 km radius horizontal and 250m thick. Figure 3 shows the domain and mesh discretization. The top of the reservoir is 800 m underground, as is shown in Figure 3(b). The major target reservoir properties are shown in Table 1 and Table 2. The overlying layer and underlying layer are both 100 m thick and assumed to have low permeability of 1.0×10^{-16} m^2 acting as the seal layers.

Table 1. Properties of the basic model.

Target aquifer properties	
Thickness	50 m
Porosity	0.20
Permeability	0.50×10^{-12} m^2
Density of grains	2.60×10^{3} kg/m^3
Compressibility	1.00×10^{-10} Pa^{-1}
Thermal conductivity of saturated reservoir formation	2.51 W/(m K)

Table 2. Parameters of the relative permeability and capillary pressure.

Relative permeability(k_r) model	van Genuchten-Mualem
Capillary pressure (p_{cap}) model	van Genuchten
Residual liquid saturation (S_{lr})	0.27
Residual gas saturation (S_{gr})	0.20
Maximal capillary pressure (p_{max})	1.0×10^{5}Pa
λ	0.20

Simulation Cases

Different cases were designed to investigate the influence of permeability on initial gas bubble formation and its sustainability for the later cycling operation. The range of permeability varies from 0.05 Darcy to 0.5 Darcy in low permeability cases and varies from 0.5 Darcy to 3.5 Darcy in high permeability cases (Table 3). The basic model to compare with has a permeability of 0.5 Darcy.

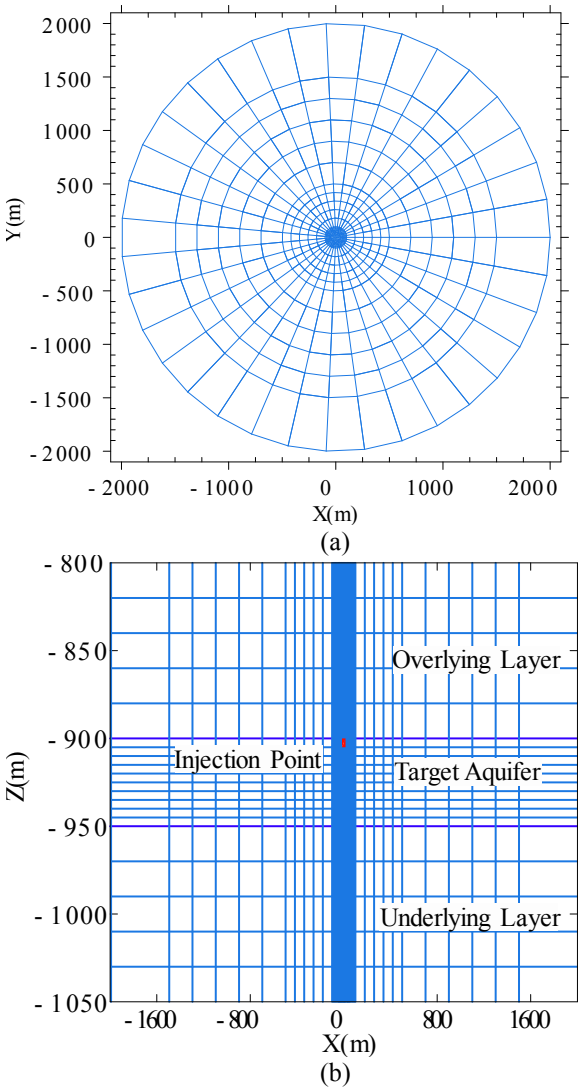

Figure 3. Model domain and mesh discretization

Table 3. Simulation cases design

Cases	Permeability(Darcy)				
Low Permeability	0.05	0.1	0.2	0.3	0.4
Basic model	0.5				
High Permeability	1.0	1.5	2.0	2.5	3.0

*(low and high with respect to the basic model)

RESULTS AND DISCUSSION

Basic Model Result Description

Results presented here focus on pressure variation and gas plume evolution. Figure 4 shows the pressure variations at the injection point through the whole simulation time. The pressure increased sharply at first because of the on-set of injection. The peak pressure in each operation

cycle noticeably decreased as the operation cycled in the first 500 hours, and then remained relatively stable around 9 MPa through the end of the simulation.

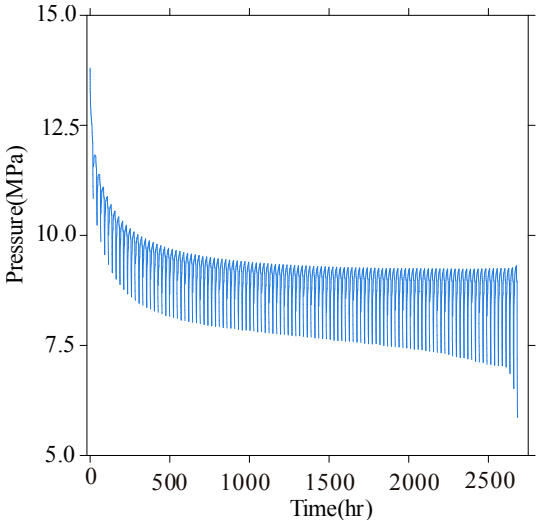

Figure 4. Pressure variation of the whole process.

Figure 5 shows the pressure variation at three places in the reservoir for two cycles in the middle of the simulation time. We choose one cycle to describe the processes, in which from Point 1 to 2 is the recharge period in Figure 2, from Point 2 to 3 is the first resting period, from Point 3 to 4 is the production period, and from Point 4 to 5 is the second resting period. Figure 5 indicates that the pressure variations between these operational points depend on the distance to the injection well. The closer to the injection well, the more obvious is the difference of pressure between the operational points. Very close to the injection well (r = 0.5m), the difference of pressure between Point 2 (the maximum pressure in one cycle) and Point 4 (the minimum pressure in one cycle) is nearly 2 MPa, while farther away (r = 23 m) such a difference is around 1.2 MPa, and at an even more distant location (r = 143.2 m) the difference is hardly seen.

Figure 6 shows the gas plume evolution during one cycle. The gas saturation of 0.2 is taken as the identifier of the fringe of the effective gas bubble because below this value in our model the gas would be immobile. At the beginning of the cycle, the bottom edge of the gas bubble is at a depth of about -923.2 m. Then pressure increases as the recharge goes on, pushing the bottom edge of gas down further to -928.0 m.

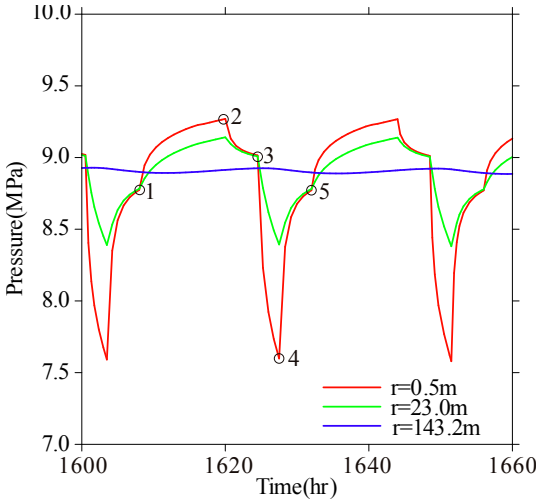

Figure 5. Pressure variation during the cycle (1600 hour-1660 hour)

During the rest period, the bottom edge moves upward. In the production period, the contour line gets close to -922.0 m. At the end of the cycle, after another period of rest, the contour line comes back to about -923.2 m, the same as the beginning status. The cycle can repeat if the bubble can provide sufficient pressure support.

Permeability Impact on Pressure Variation

Figure 7 shows that lower permeability leads to a larger pressure fluctuation. This is because the injected gas could not migrate away quickly during the injection period, causing high pressured air concentrated in vicinity of the injection well.

The large fluctuations of pressure would lead to formation instability, and have a negative influence on the CAESA system.

Permeability Impact on the Gas Bubble Evolution

The edge of the gas bubble migrates farther away from the well as permeability increases and that would cause a reduction of gas volume for cycles. Figure 8 shows the shape of gas bubble in different permeability cases right after the initial injection is finished. In the low permeability case (k=0.1D), the gas is mostly gathered near the well. As the permeability increases, the bottom edge of the gas moves up from -951.4m to -927.7m, while the lateral extent expands.

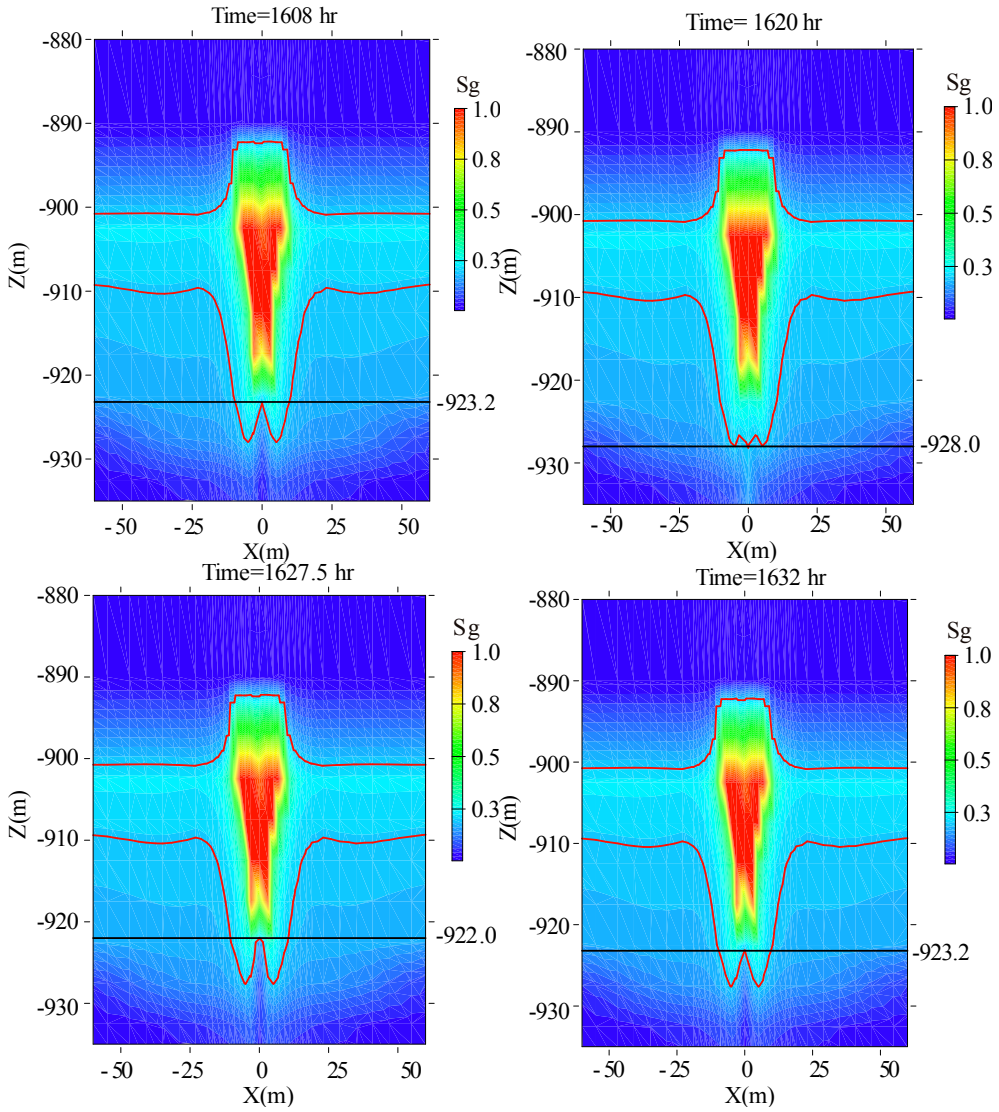

Figure 6. Gas plume during the cycle (67 day-68 day)

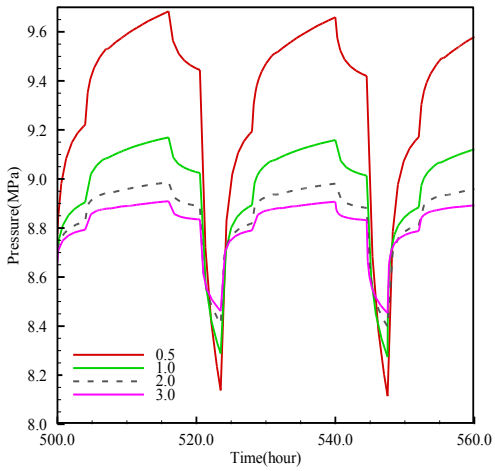

Figure 7. Detail pressure variation of two cycles for selected permeability cases (from the 500 hour to 560 hour).

It can be predicted that the lateral edge of the bubble extends farther when the aquifer permeability increase, but the pressure support that the bubble can provide decreases, which is actually not good for the later operational cycles, as will be shown in the next section.

In summary, low aquifer permeability may make it hard to meet the injectivity requirements, while high permeability may considerably reduce the number of operational cycle. Therefore, a suitable target aquifer should not only have a good injectivity but also sustainably support the operational cycles for a long time.

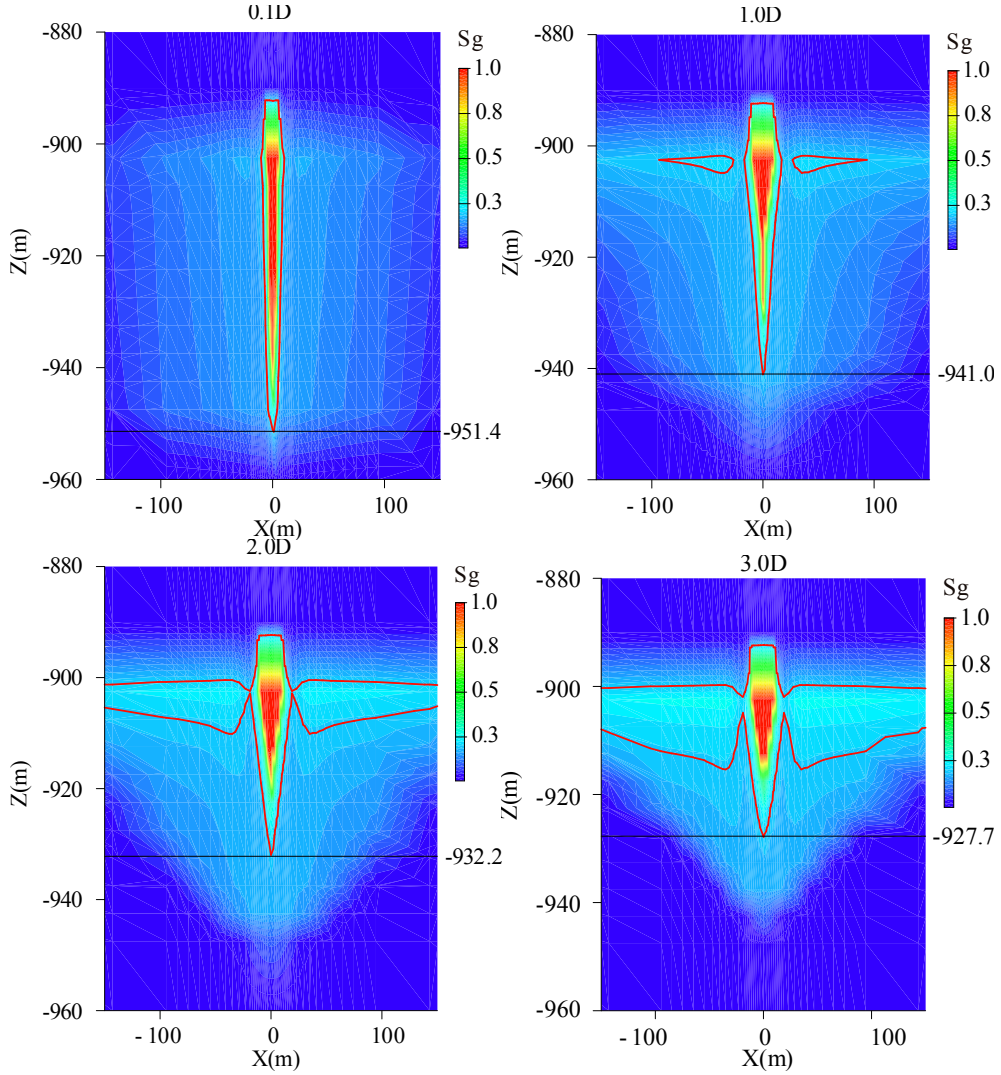

Figure 8. Gas plume of initial gas bubble in different permeability cases (0.1D, 1.0D, 2.0D, and 3.0D)

Permeability Impact on Operational Cycles

The effective volume of the gas bubble (which sustains the storage place) will reduce as the number of cycles increases, because the bubble edge gradually breaks into small bubbles, which dissipate in the aquifer. Operational cycles terminate when no air can be produced or water is produced from the well during the production period. The system cycle time (SCT) is the length of time that the system can continuously cycle before another injection operation to restore the initial gas bubble is required. A 20-day initial injection should support the assumed daily cycling schedule for around 7 months.

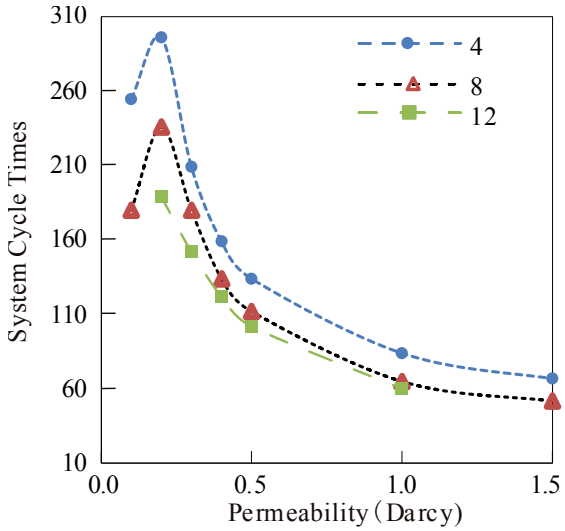

Figure 9. Variation of system cycle time with permeability for different production rates (kg/s)

Our results suggest that there is an optimal range of aquifer permeability to support a certain production rate. Figure 9 shows the relation between the system cycle time and the permeability of an aquifer under different production rates (kg/s). For the assumed operational cycles, an aquifer with a permeability of 0.2 Darcy achieves the best performance of cycle times. If we select 200 as the criteria of SCT for the production period at 8kg/s for 3 hours in a daily cycle, aquifers with permeability ranging from 0.15 ~ 0.22 Darcy could be the candidate target aquifer.

CONCLUSIONS

We took an idealized horizontal aquifer at a depth of 800 m and with a permeability of 0.5Darcy as the target aquifer for a CAES system and numerically investigated the impacts of aquifer permeability on formation of the initial gas bubble and the sustainability for later operational cycles. Our simulation results show that the aquifer permeability is crucial to a CAESA system. To achieve the best performance of operational cycles, the target aquifers should be within an optimal permeability range. Lower permeability would not meet the targeted injectivity, while higher permeability of the aquifer would make the bubble expand quickly, which may significantly reduce the number of operational cycles. If the projection operation runs at 8 kg/s for 3 hours in a daily operational cycle, an aquifer with 0.2 Darcy would achieve the best performance.

ACKNOWLEDGMENT

This research was funded partly by Fundamental Research Funds for the Central Universities. It was also supported by the China Scholarship Council.

REFERENCES

Entrekin, S., Evans-White, M., Johnson, B., and Hagenbuch, E. Rapid expansion of natural gas development poses a threat to surface waters. *Frontiers in Ecology and the Environment, 9*(9), 503-511, 2011.

Hu, L. T., Pan, L., and Zhang, K. N. Modeling brine leakage to shallow aquifer through an open wellbore using T2WELL/ECO2N. *International Journal of Greenhouse Gas Control, 9*, 393-401, 2012.

Juanes, R., Spiteri, E., Orr, F., and Blunt, M. Impact of relative permeability hysteresis on geological CO2 storage. *Water Resources Research, 42*(12), 2006.

Kushnir, R., Ullmann, A., and Dayan, A. Compressed air flow within aquifer reservoirs of CAES plants. *Transport in Porous Media, 81*(2), 219-240, 2010.

Nakajima, T., Xue, Z., Chiyonobu, S., and Azuma, H. Numerical Simulation of CO_2 Leakage Along Fault System for the Assessment of Environmental Impacts at CCS Site. *Energy Procedia, 63*, 3234-3241, 2014.

Nakhamkin, M., Chiruvolu, M., Patel, M., Byrd, S., Schainker, R., and Marean, J. Second generation of CAES technology-performance, operations, economics, renewable load management, green energy. *POWER-GEN International, Las Vegas,* 2009.

Oldenburg, C.M. and Pan, L. Porous Media Compressed-Air Energy Storage (PM-CAES): Theory and Simulation of the Coupled Wellbore-Reservoir System. *Transport in Porous Media, 97*(2), 201-221, 2013a. doi:10.1007/S11242-012-0118-6

Oldenburg, C.M. and Pan, L. Utilization of CO_2 as cushion gas for porous media compressed air energy storage. *Greenhouse Gases: Science and Technology, 3*(2), 124-135, 2013b.

Pan, L. and Oldenburg, C. M. T2Well-An integrated wellbore-reservoir simulator. *Computers & Geosciences, 65*, 46-55, 2014.

Pruess, K., Oldenburg, C., and Moridis, G. TOUGH2 User's Guide, Version 2.0. *Report LBNL-43134*, Lawrence Berkeley National Laboratory. Berkeley, Calif., 1999.

Zhang, K., Wu, Y.-S., and Pruess, K. User's guide for TOUGH2-MP-a massively parallel version of the TOUGH2 code. *Report LBNL-315E,* Lawrence Berkeley National Laboratory, Berkeley, Calif., 2008.

THOUGH2 APPLICATION FOR AN ASSESSMENT OF OPEN PIT SLOPE STABILITY USING SATURATED/UNSATURATED GROUNDWATER FLOW MODELING TO ESTIMATE HYDRAULIC FORCES, ARKHANGELSK KIMBERLITE PIPE, RUSSIA

I.L. Kharkhordin[(1)], V.V. Nazima[(2)], A.N. Gurin[(2)], I.E. Shkil[(3)]

1) Geostroyproekt Ltd, St. Petersburg, Russia, kharkhordin@rambler.ru
2) VNIMI Institute, St. Petersburg, Russia, v.v.nazima@gmail.com
3) Severalmaz Co., Arkhangelsk, Russia

For deep open pits, hydrogeological setting is a very important factor affecting the cost of mining. Generally, groundwater effects on mining are considered in the following areas: a) forecast of water discharge into mine, b) optimization of dewatering system, c) assessment of the environmental impact, d) estimation of groundwater impact on the pit slope stability. Frequently, the first three problems can be solved with regional models using traditional computer codes for saturated groundwater flow modeling. To solve the last problem a local saturated/unsaturated model is necessary, especially if groundwater discharge into the pit occurs at a few levels separated by unsaturated rocks. Such a situation was investigated at Lomonosov diamond field located in Arkhangelsk region, Russia.

Lomonosov diamond field is located in the north-west part of the Russian Plate. The seven main hydrogeological units were described as: quaternary deposits (Q), urzuga deposits (C2ur), kimberlite of crater phase (mD3-C2), kimberlite of conduit phase (iD3-C2), padun deposits (Vpd), mezen deposits (Vmz).

The geological massif nearby open pit was divided into eight sectors. We took into account the features of the geological cross-section, location of the elements of hydrogeomechanical monitoring systems (profiles of survey marks, boreholes with water pressure sensors) and location of the elements of the pit dewatering system. Presently the local saturated/unsaturated flow model was created for one sector only. The sector boundaries approximately correspond to flow lines and could be considered as impermeable. The water pressure at the boundary located outside the drainage well contour was recalculated from water heads obtained with the regional groundwater flow model. Rock properties were estimated using pumping tests, laboratory determinations and observations at the pit slope. The TOUGH2 code with EOS9 was used for calculations. The most difficulties with the TOUGH2 application were connected with approximation of the water seepage boundary at the pit slope. Two approaches were tested: a fictitious layer along the slope and delivery wells located along the pit slope at the seepage area.

Results of calculations were applied for pit slope stability analysis on the original computer code for limit equilibrium calculations. A grid of water saturation was used to calculate the weight of rock bodies and the pressure grid was used to take into account hydrostatic and hydrodynamic forces.

CONCLUSIONS

a) Using of a saturated/unsaturated groundwater flow model allows to obtain more reliable data on water saturation and pressure for estimation of groundwater impact on slope stability.

b) Calculation of the water pressure field as an application of the saturated groundwater flow model provides an additional estimate of slope stability.

COMPARISON BETWEEN EQUIVALENT CONTINUUM AND DISCRETE CRACK MODELS OF TRANSIENT RADON TRANSPORT AT THE SOIL-BUILDING FOUNDATION CRACK INTERFACE USING TOUGH2/EOS7RN

Zakaria Saâdi[1], and Jérôme Guillevic[1]

Institut de Radioprotection et de Sûreté Nucléaire (IRSN)
[1]PRP-DGE/SEDRAN/BERAM, 31 Avenue de la Division Leclerc
Fontenay-aux-Roses, 92262, France
e-mail: zakaria.saadi@irsn.fr, jerome.guillevic@irsn.fr

ABSTRACT

In the framework of radon risk management in France, it is necessary to enhance knowledge on radon transfer from its source to exposure areas (e.g., buildings) by developing simple, accurate, numerical models for transient radon transport in three-dimensional (3D) unsaturated porous materials. The equivalent continuum modelling (ECM) of flow and transport at the interface between the soil and cracks (fissures) in a building foundation (e.g., slab-on-grade, basement) is simple and more attractive, since equivalent (effective) continuum properties assigned to model cells can represent the combined effect of individual cracks and solid matrix of the cracked concrete of the foundation (slab and blocks walls). However, this approach has never been verified numerically. Thus the goal of the present work is to develop an ECM-model based on explicit and accurate numerical description of flow and transport in the crack (discrete crack model, DCM) through the use of a new version of the TOUGH2/EOS7Rn module, and to compare between these two approaches.

As a first step, the DCM-approach has been verified numerically through a comparison to a reference 3D-steady-state numerical solution for radon transport into a house with basement under constant negative pressure. Then, results of the DCM and ECM approaches were compared. Although the soil-gas pressure distributions calculated by ECM and DCM approaches were not similar, the radon concentration distributions were nearly identical. The final result is that the ECM approach is conservative and gave the same indoor radon concentration calculated by the DCM approach.

INTRODUCTION

Because of the complex geometry of the soil-house interface and the numerous processes that are involved (transient pressure-driven gas flow, radon production and decay, and diffusion and advection of radon), numerical models constitute a powerful tool for studying the proposed problem. Through the open literature one can distinguish two approaches for handling the problem of the mathematical modelling of soil gas inflow and gas components (radon, VOCs…) entry through openings (cracks, joints, and holes) at the soil-basement interface. The first modelling approach (DCM: discrete crack model for crack opening) focuses on explicit description of the geometry of the opening in the mesh. Calculations at the soil-opening interface can be done by two different numerical methods, which differ in their treatment of the opening itself: in the first, the crack is not discretized, whereas in the second it is. The first numerical method solves continuity equations for soil-gas pressure and velocity, as well as gas component concentration and flux density at the soil-opening interface. In order to solve these continuity equations, we can use either an iterative method (Loureiro, 1987; Loureiro et al., 1990; Revzan et al., 1991; Revzan and Fisk, 1992; Andersen et al., 2000) or explicitly write and discretize the continuity equations (treating the crack as a boundary condition) as a part of the non-linear global matrix system of flow and transport equations to be solved for soil gas pressure and concentration (Holford, 1994; Abreu and Johnson, 2005; Bozkurt et al., 2009). Both techniques give satisfactory results but with an advantage for the second one since it needs less CPU-time. As described in Loureiro (1987) the iterative procedure converges after

200 iterations in order that the maximum variation of dimensionless pressure and gas velocity at the soil crack/interface is lower than 5×10^{-5} and 1.5×10^{-3}. Except Holford (1994) and Bozkurt et al. (2009) who used finite element numerical models, all other authors used finite difference models. In these works, it was assumed that the crack with an aperture w (m) is dry and air flow in the crack is laminar Poiseuille flow between parallel plates with the intrinsic permeability k_c (m^2) is given by analogy to Darcy velocity, as follows:

$$k_c = \frac{(w)^2}{12} \quad (1)$$

As shown by Abreu and Johnson (2005) and Bozkurt et al. (2009), transient storage effects due to the simplified stationary model Eq. (1) are negligible and do not highly impact simulation results of gas inflow and gas components entry into a house basement. The second numerical method assumes implicitly continuity of gas pressure and concentration variables, and gas and gas component fluxes at the soil-opening interface. The small crack opening in the basement floor is considered as an extra-cell which is finely discretized and connected to the soil block mesh (Tsang and Narasimhan, 1992). The crack opening can also be idealized as in Eq. (1). This approach is much easier to implement when using mass conserving numerical schemes like the integral finite difference method (IFDM) (Tsang and Narasimhan, 1992; Pruess et al., 1999). This approach is much simpler to implement and conserves the physics of the problem without the need of iterative methods which can demand high CPU-time.

The second alternative approach for modelling gas inflow and gas components entry into the basement is the equivalent continuum modelling (ECM) approach. The physical characteristics of the porous materials constituting walls (concrete hollow blocks) and slab (concrete) with openings, such as porosity and permeability are modelled by effective properties (i.e., ϕ_E (-) and k_E (m^2), respectively) of a homogeneous porous material, which are estimated by (Yu et al., 2009):

$$\phi_E = F_c = \frac{V_c}{V} \quad (2)$$

$$k_E = F_m \times k_m + F_c \times k_c \quad (3)$$

where V is the volume of the slab or the wall (m^3); F_c is the volumetric fraction of the openings in the slab or the wall (-); and F_m is the volumetric fraction of the solid matrix in the slab or the wall (-), which is given by:

$$F_m = \frac{V_m}{V} = 1 - F_c \quad (4)$$

Looking at Eqs. (2)-(3), one can see that the second approach does not need information on solid matrix porosity (i.e., ϕ_m) of the walls and the slab of the basement foundation, nor the crack geometry and its dimension in the mesh in order to simulate flow and transport, but rather the volumetric fractions of fractures and solid matrix.

Yu et al. (2009) conducted a sensitivity analysis on the foundation slab fracture aperture, the indoor air pressure drop, the capillary fringe thickness, and the infiltration rate using the multi-phase compositional model CompFlow Bio and effective properties (Eqs. (1)-(4)) of the slab basement to study gas inflow and TCE (VOC) entry into a 2D basement above a heterogeneous aquifer. The model calculates acceptable physical results but has not been tested against experimental data. Saâdi (2015) also applied the ECM-approach and conducted a sensitivity analysis to simulate gas inflow and radon entry rate at the soil/foundation interface of a house with basement, where high radon levels were measured. He showed that the ECM-approach can simulate properly measured radon exhalation at the basement walls and slab as well as measured radon activity concentration within the basement. Although the ECM-approach can give satisfactory results, it has never been verified numerically in order to quantify uncertainties due to numerical errors.

The application of the first approach (DCM) to the case of a house basement is cumbersome, and difficult to carry out in practice, especially for making scenarios of 3D-problems. Complicated meshes are needed since they have to be much finer in the soil near the opening as well as in its vicinity, and mesh construction has to be performed for different values of the crack aperture. The numerical convergence of the

problem solution becomes more complicated when the transient two-phase (water-air) flow problem has to be solved for the instantaneous time-variations of the soil water saturation profile.

The present work aims to verify the applicability of Eqs. (2)-(3) and to develop an ECM-model based on an explicit and accurate numerical description of flow and transport in the crack (DCM-model) by using a new version of the TOUGH2/EOS7Rn module (Saâdi et al., 2012; 2014). As a first step, a DCM subroutine will be implemented in TOUGH2/EOS7Rn in order to ensure continuity of gas pressure, radon concentration in the soil-gas, and flux densities of gas and radon at the soil-crack interface within a new convergence iteration loop. To this end, a 3D-mesh, finer near the crack aperture and coarser in the soil far away from the building foundation, will be constructed, and soil/crack interfaces will be defined. Airflow in the cracks will be assumed to be laminar Poiseuille flow between parallel plates (Eq. (1)), and the foundation will be assumed to be impermeable to soil-gas except at these interfaces. As a second step, this subroutine will be verified through a comparison to a reference steady-state 3D-numerical solution (Loureiro, 1987; Loureiro et al., 1990) for radon transport into a house with basement under constant negative pressure. Finally, a comparison will be presented to show differences between ECM and DCM-models solutions, with an application to 2D radon transport from the soil to an under-pressurized house with basement.

THE MATHEMATICAL MODEL

Geometric Configuration – Hypotheses

Here we consider an idealized geometrical configuration of the model which will be used for the model verification and comparison between DCM- and ECM-modelling approaches. However, the model hypotheses remain the same for any geometrical configuration.

The geometrical configuration of the model is shown in Figure 1. The soil block under consideration is represented as a parallelepiped of dimensions $2L_x$, $2L_y$, and L_z. The house is also considered a smaller parallelepiped of dimensions $2l_x$, $2l_y$, and $(l_z + h)$ partially embedded in the center and upper part of the soil block. The basement, represented by the part of the house embedded in the soil block, has the dimensions $2l_x$, $2l_y$, and l_z.

In fact, due to the symmetry in the XY plane, the model will be developed in a reduced geometrical configuration represented by one quarter of the house, with the dimensions L_x, L_y, L_z and l_x, l_y, l_z for the soil block and the basement, respectively, as represented in Figure 2.

The entry route for soil gas into the basement is defined as the concrete shrinkage gap located at the wall-footer-floor joint along all the perimeter of the basement floor due to foundation settlement. A simplification of this configuration is assumed in the model (Figure 2). In this simplified geometry, the footer is not considered, and the crack is assumed to be located between the floor slab and the wall. Figure 3 represents a plan view of the basement floor, showing the extension of the crack all along the perimeter of the basement floor.

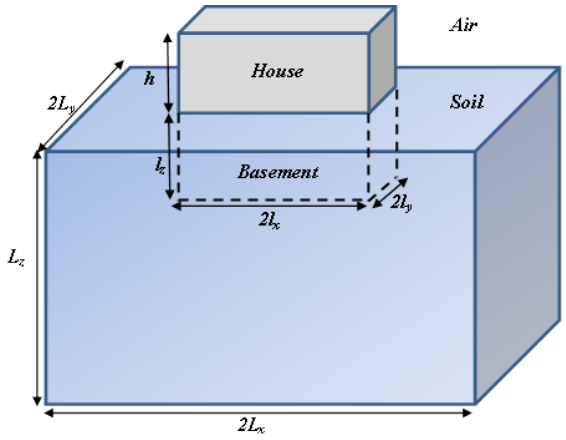

Figure 1. Geometric configuration of the soil block with the house and basement.

Boundary Conditions

At the top of the soil block (soil-air interface), first type boundary conditions are specified. There, the absolute pressure is equal to the atmospheric pressure P_{atm} (Pa). Since the concentration of radon in the atmospheric air is much smaller than that in the soil and since it is expected that air will flow from the atmosphere into the ground, driven by the negative disturbance pressure field, it is assumed that

soil-gas radon concentration is negligibly small (zero) at the soil-air interface. The boundary conditions at the interface between the gap (crack) and the soil underneath it required careful consideration. As discussed in the first section, we adopt here the second numerical method used in the DCM-approach to avoid iterative methods (first method). This method assumes implicitly the principle of continuity for flow and transport at the soil-crack interface where the crack opening in the basement floor is considered through adding an extra-cell connected to the soil block cells. This method can be applied very well by using the numerical model TOUGH2 (Pruess et al., 1999) which uses a spatially integrated approach for space discretization. Numerical trials showed small differences between soil gas pressure distributions calculated by both methods but with an advantage for the second method with less CPU-time. The basement-crack interface is set as a constant pressure boundary condition, with pressure lower than atmospheric pressure.

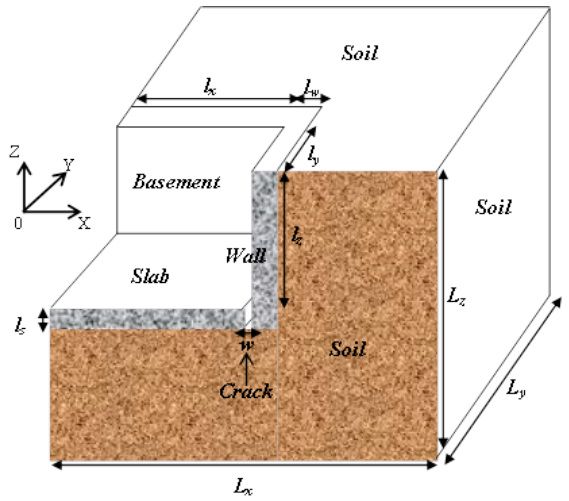

Figure 2. View of a quarter of the soil block used for the numerical solution

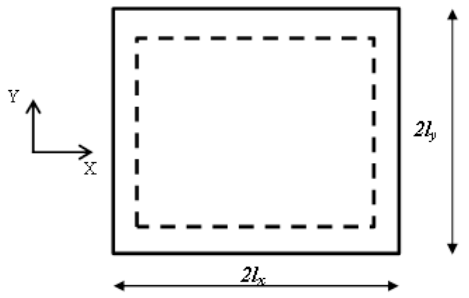

Figure 3. Plan view of the basement floor showing the crack as a dashed line.

The other regions illustrated in Figure 2 are treated as no-flow boundaries. The effective radon diffusion coefficient and the intrinsic permeability of concrete (walls and floor) are much smaller than their respective values in the soil and consequently both gas velocity and radon flux density are assumed to be zero. The bottom and lateral sides of the soil block are assumed to be located at a sufficiently large distance from the gap such that the disturbance pressure and radon concentration fields are essentially invariant with distance. Therefore, both gas velocity and radon flux density are also assumed to be zero. This assumption was supported by simulations to ensure that the size of the domain did not significantly affect the computed results. Finally, the internal surfaces of the soil block are treated as no-flow boundaries due to symmetry.

The numerical solution

Irregular meshing of the 2D or 3D-flow domain is carried out by an external program using either circular (Loureiro, 1987) or exponential techniques in order to locate crack cells, and to handle boundary conditions. The mesh was made finer near the crack and near the surface boundaries of the domain. Preprocessing of the mesh was done using PetraSIM (RockWare Inc.) to visualize the crack cells, to define connections between crack and soil cells, and to affect material properties to each cell (soil block, slab, walls, crack, atmosphere…). Extra-cells have been added in order to easily handle constant or time-variable boundary conditions at the soil surface and basement atmosphere.

For our calculations we used the two-phase flow and radon transport module EOS7Rn (Saâdi et al., 2012, 2014) of TOUGH2. 3D-simulations with larger numerical grids that need large computer memory were not possible *a priori* because of limitations of the TOUGH2 code version used in this work (Pruess et al., 1999). However, it was possible to use the module TOUGH2/EOS7R under PertaSIM to simulate only the 3D two-phase flow problem. The particularity of the former module is that the main physical properties for radon such as emanation, diffusion, adsorption at the solid/gas interface, and solubility are incorporated in the code with different choices for their modelling.

This module has been verified numerically by its comparison to steady-state analytical solutions for homogenous and layered soil materials under single-gas phase and unsaturated conditions (Saâdi et al., 2012; 2014), and comparison to the transient numerical solution of the code TRACI (Ferry et al., 2001) for a two-layered soil column (Saâdi and Guillevic, 2015). Experimental validation of the code has also been carried out through the experiment of Ferry et al. (2002) for radon transport in a two-layered pond under barometric pressure and rainfall fluctuations in time at the soil surface boundary (Saâdi and Guillevic, 2015).

Indoor radon activity concentration

Once the radon entry rate F_g^{Rn} (Bq.s^{-1}) into the basement through the crack/soil line and/or the solid matrix of slab and walls interfaces is simulated, the radon activity concentration C_H^{Rn} (Bq.m^{-3}) within the house or house basement volume V_H (m^3) is simulated by solving the following simplified mass-balance equation model:

$$(5)\ \frac{dC_H^{Rn}}{dt} = \frac{F_g^{Rn}}{V_H} - (\lambda + \lambda_H)C_H^{Rn} + \lambda_H C_{ATM}^{Rn}$$

where C_{ATM}^{Rn} is the outdoor radon activity concentration (atmosphere) (Bq.m^{-3}), supposed to be negligible compared to that in the basement; λ_H is the air exchange rate through window and door openings (s^{-1}), it corresponds to air volume entering per unit volume of the house or basement per unit of time; and λ is the radioactive decay of radon (2.1×10^{-6} s^{-1}).

Equation (5) assumes that radon activity within the basement is homogeneous; it is solved using the Euler implicit finite difference method.

NUMERICAL VERIFICATION: COMPARISON TO LOUREIRO (1987) SOLUTION

Loureiro (1987) and Loureiro et al. (1990) solved the steady-state single-gas-phase (dry soil environment) and radon transport problems for the basement and soil block configuration shown in Figures 1, 2 and 3, using a Patankar-Spalding finite difference technique with alternating direction iterative algorithm for the solution of the very large system of algebraic equations obtained from the application of the numerical discretization for 3D-problems. Both problems were solved independently in time to simulate the steady-state distribution of the soil gas pressure, Darcy gas velocity, radon activity concentration and radon flux density. The radon flux density through the gap and into the basement is also computed along with the resultant indoor concentration using the steady-state solution of Eq. (5). We do not have access to the code developed by Loureiro (1987) in order to make a direct comparison with our numerical solution for gas pressure and radon concentration distribution in the flow domain. So, comparison will be restricted to the values of average air inflow and radon entry rate through the gap crack as well as indoor radon concentration as tabulated by Loureiro (1987) (see Table 5.3, p. 109).

In order to compare our simulation results to those of the tabulated results of Loureiro (1987), we use the same input parameters (geometry of the basement and its foundation, and soil physical characteristics) given in Tables 1 and 2.

TOUGH2-simulations were run under single-gas phase flow conditions using the same mesh configuration of Loureiro (1987). The slab cells were deactivated, slab and walls materials were assumed impermeable to the gas-phase, and gravity effect has been neglected.

Table 1. Parameters defining soil block, and house foundation geometry and occupation.

House dimensions	
Basement slab, $2l_x \times 2l_y$ (m × m)	5 x 5
Basement height, l_z (m)	2
Height of the house, h (m)	3
Thickness of the walls, l_w (m)	0.15
Thickness of the slab, l_s (m)	0.15
Vacuum pressure, ΔP_H (Pa)	-5
Crack aperture, w *(m)*	0.001
Air exchange rate, λ_H (s^{-1})	1.39×10^{-4}
Volume of the house, V_H (m^3)	125
Soil block dimensions	
Distance from the house to domain boundaries (m)	10
Calculation domain	12.65 x 12.65 x 12.15

Table 2. Parameters defining soil radon source, and soil physical characteristics.

Radium-226 activity mass content (Bq.kg^{-1})	40
Emanation coefficient (-)	0.2
Dry bulk density (kg.m^{-3})	1325
Infinite soil-gas radon activity concentration (Bq.m^{-3})	21200
Bulk radon diffusion coefficient (m^2.s^{-1})	1×10^{-6}
Porosity (-)	0.5
Soil permeability (m^2)	1×10^{-12}

3D-Configuration

Figure 4 shows the mesh used for the TOUGH2/EOS7R numerical solution, as well as iso-surfaces of the steady state soil-gas pressure P_g (Pa), and velocity vectors along the gap line. Disturbance pressure and gas velocity are higher near the crack line (maximum velocity in basement corner). House under-pressurization can reach lateral boundaries as simulated by Loureiro (1987) as well.

For the same mesh configuration (21 x 21 x 21; Table 3), the average gas-phase velocity along the gap calculated by EOS7R underestimates the one calculated by Loureiro (1987) by 13.7%. Using a finite difference code with the second numerical method of the DCM-model (see first section), Abreu and Johnson (2005) predicted, in contrast to our results, soil gas entry rates greater than those of Loureiro (1987) by a range of ~ 1.2 to 2.5 for the cases tested with crack apertures of 0.001 and 0.0005 m and soil permeabilities ranging from 10^{-12} to 10^{-9} m^2. Whereas the source of the discrepancy between the three numerical models is unknown, the differences in pressure coupling and soil gas entry rate are likely attributable to differences in discretization of the soil-foundation gas flow boundary condition.

Table 3. Steady-state solutions of Loureiro (1987) and the current model using EOS7R and EOS7Rn modules of TOUGH2 (DCM and ECM models).

	Model-Dimension (Mesh)	Soil pore gas velocity (m.s^{-1})	Radon flux density (Bq.m^{-2}.s^{-1})	Indoor Radon concentration (Bq.m^{-3})
Loureiro (1987)[a]	DCM-3D[b] (21 × 21 × 21)	1.46E-04	1.59	7.20
	DCM-3D (29 × 29 × 29)	1.50E-04	1.63	7.38
TOUGH2/EOS7R	DCM-3D (21 × 21 × 17)	1.26E-04	-	-
	DCM-2D (29 × 25)	1.24E-04	2.91	6.60
TOUGH2/EOS7Rn	DCM1-2D (29 × 29)	1.25E-04	4.78	10.84
	ECM-2D[c] (29 × 29)	6.33E-05	6.49E-03	6.63

[a] Test cases #3 and #5 - Table 5.3, p. 109 of Loureiro (1987)

[b] Average values for gas velocity and radon flux density along the gap (crack/soil line interface)

[c] Average values for gas velocity and radon flux density along wall and slab surfaces

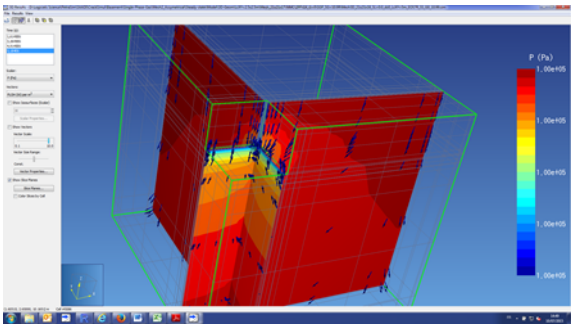

Figure 4. Iso-surfaces of soil-gas pressure, gas velocity, and the 3D-mesh used for the DCM-numerical solution.

2D-Configuration

Similar results are obtained for 2D-simulated gas phase velocity and gas pressure distributions (Figure 5), and normalized disturbance gas pressure (NDP, defined as the ratio $(P_g - P_{atm})/\Delta P_H$), Figure 6A. Figure 6B shows also isolines of the normalized radon activity concentration in the soil-gas (NRnC defined as the ratio $C_g^{Rn}/C_{g,\infty}^{Rn}$, with $C_{g,\infty}^{Rn}$ is the infinite soil-gas radon activity concentration given in Table 2). Note, however, from Table 3 the good agreement between indoor radon activity concentrations calculated by EOS7Rn and Loureiro (1987). Comparison between 2D and 3D-averaged gas- velocity DCM-simulations by EOS7R showed smaller differences (Table 3), which will justify our model analysis for the distribution of radon activity concentration in 2D flow domains.

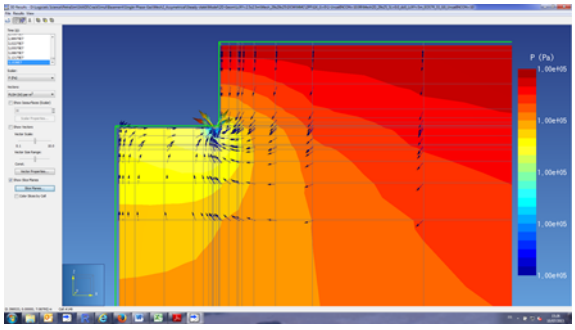

Figure 5. Iso-surfaces of soil-gas pressure and velocity, and the 2D-mesh (DCM-model).

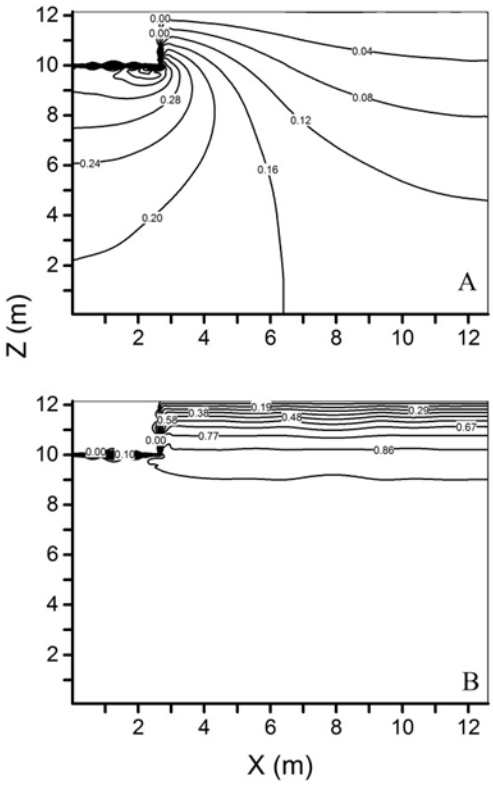

Figure 6. Isolines of (A) normalized disturbance gas pressure and (B) normalized radon concentration using the DCM model.

COMPARISON BETWEEN ECM AND DCM NUMERICAL SOLUTIONS

We consider the same 2D configuration above, and soil physical and basement foundation parameters given in Tables 1 and 2. However, for this comparison the slab and walls were considered as part of the modelled soil domain with smaller values of permeability (1×10^{-20} and 1×10^{-17} m^2, respectively) in order to introduce both ECM- and DCM-approaches on the same mesh configuration. We denote DCM1 as the DCM-model for this new configuration. Values of equivalent porosity ϕ_E and permeability k_E used in the ECM-model are equal to 8×10^{-4} and 6.67×10^{-11} m^2 for the cracked slab material according to Eqs. (2) and (3), respectively.

From Figure 7A we see that the disturbance pressure calculated by DCM is approximately twice that calculated by ECM. This is obvious because the latter model applied under-pressure to the whole basement surface area (walls and slab). However, comparison between isolines for NRnC (Figure 7B) did not show high discrepancies between ECM- and DCM models.

The astonishing result is that the radon entry rate in $Bq.s^{-1}$ is approximately the same for both DCM and ECM models, although radon entry rate distribution at wall and slab surface areas is different. We obtain approximately the same indoor radon activity concentration (Table 3, Figure 8).

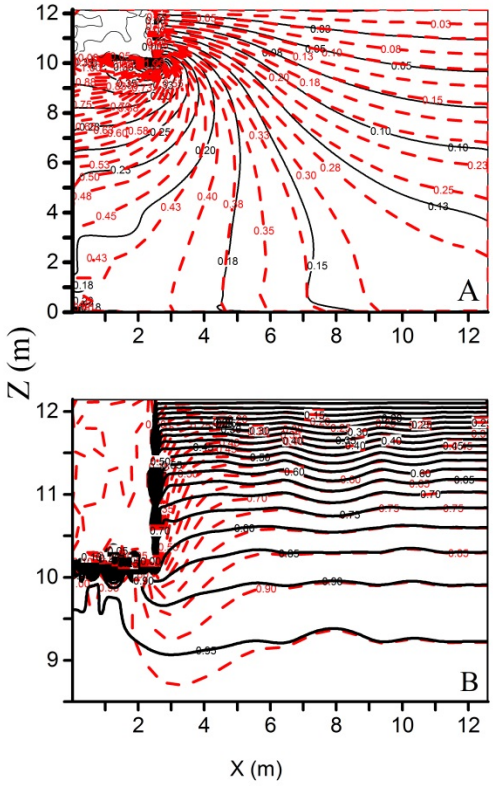

Figure 7. Isolines of (A) normalized disturbance gas pressure and (B) normalized radon concentration using DCM (black line) and ECM (red dashed line) models.

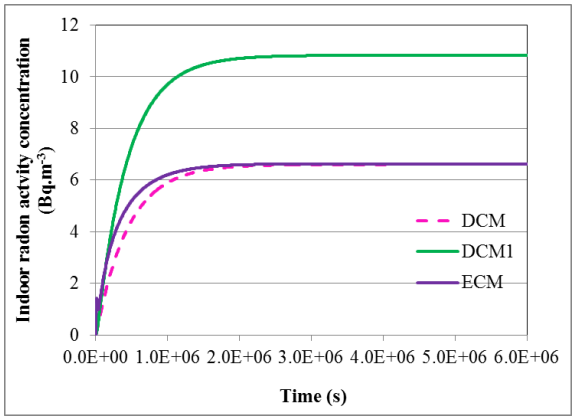

Figure 8. Transient simulations by EOS7Rn of the indoor radon activity concentration using DCM and ECM models.

REFERENCES

Abreu, L.V.D., and P.C. Johnson, Effect of vapor source-building separation and building construction on soil vapor intrusion as studied with a three-dimensional numerical model, *Environ. Sci. Technol.*, 39, 4550-4561, 2005.

Andersen, C.E., *Radon transport modelling: User's Guide to RnMod3d*. Risø National Laboratory, DK-4000 Roskilde, Denmark; Report Risø-R-1201(EN); 2000.

Bozkurt, O., K.G. Pennell, and E.M. Suuberg, Simulation of the vapor intrusion process for nonhomogeneous soils using a three-dimensional numerical model, *Ground Water Monitoring & Remediation*, 29(1), 92–104, 2009.

Ferry, C., P. Richon, A. Beneito, and M.C. Robé, Radon exhalation from uranium mill tailings: experimental validation of a 1-D model. *J. Environ. Radioactiv.*, 54(1), 99-108, 2001.

Ferry C., P. Richon, A. Beneito, and M.C. Robé, Evaluation of the effect of a cover layer on radon exhalation from uranium mill tailings: transient radon flux analysis. *J. Environ. Radioactiv.*, 63(1), 49-64, 2002.

Holford, D.J., *Rn3D: a finite element code for simulating gas flow radon transport in variably saturated, nonisothermal porous media. User's manual, version 1.0*, PNL-8943; Pacific Northwest Laboratory, DEO, 1994.

Loureiro, C.O., *Simulation of the steady state transport of Radon from soil into houses with basements under constant negative pressure*, Ph. D. Dissertation, University of Michigan, Rep. LBL-24378, Lawrence Berkeley Laboratory, Berkeley, CA, 1987.

Loureiro, C.O., L.M. Abriola, J.E. Martin, and R.G. Sextro, Three-dimensional simulation of Radon transport into houses with basements under constant negative pressure, *Environ. Sci. Technol.*, 24(9), 1338-1348, 1990.

Pruess K., C. Oldenburg, G.J. Moridis, *TOUGH2 User's Guide, Version 2.0*. Report LBNL-43134, Lawrence Berkeley National Laboratory, Berkeley, California, 1999.

Revzan, K.L., and W.J. Fisk, Modeling radon entry into houses with basements: the influence of structural factors, *Indoor air*, 2, 40-48, 1992.

Revzan, K.L., W.J. Fisk, and A.J. Gadgil, Modeling radon entry into houses with basements: model description and verification, *Indoor air*, 2, 173-189, 1991.

Saâdi Z., D. Gay, J. Guillevic, and R. Améon, EOS7RN—A New TOUGH2 module for simulating radon emanation and transport in the subsurface. In: Proceedings of the TOUGH Symposium 2012. Berkeley, California: Lawrence Berkeley National Laboratory; 481-489, 2012.

Saâdi, Z., D. Gay, J. Guillevic, and R. Améon, EOS7Rn—A New TOUGH2 module for simulating radon emanation and transport in the subsurface, *Comput. Geosci.*, 65, 72-83, 2014.

Saâdi, Z., and J. Guillevic, Comparison of two numerical modelling approaches to a field experiment of unsaturated radon transport in a covered uranium mill tailings soil (Lavaugrasse, France), *J. Environ. Radioactiv.*, Available online 9 April 2015, In Press, doi:10.1016/j.jenvrad.2015.03.019.

Saâdi, Z., Numerical modelling of radon transport from soil to a house basement under variable weather conditions, *In: Radon in the Environment 2015*, Oral communication, Krakow, Poland, 25th-29th May 2015.

Tsang, Y.W., and T.N. Narasimhan, Effects of periodic atmospheric pressure variation on radon entry into buildings, *J. Geophy. Res.*, 97(B6), 9161-9170, 1992.

Yu, S., A.J.A. Unger, and B. Parker, Simulating the fate and transport of TCE from groundwater to indoor air, *J. Contam. Hydrol.*, 107(3−4), 140−161, 2009.

SIMULATING WATER FLOW THROUGH A LAYERED SNOWPACK

Ryan W. Webb[1] and Stephen W. Webb[2]

[1] Department of Civil & Environmental Engineering
Colorado State University
Fort Collins, Colorado 80523-1372, USA
Email: rwebb@colostate.edu

[2] Canyon Ridge Consulting, LLC
Albuquerque, New Mexico 87047, USA
Email: Stephen.webb.crc@gmail.com

ABSTRACT

The distribution of snow across a landscape can be an important component in the hydrologic cycle of many mountainous watersheds. Snow dominated stream systems will vary in timing and volume of peak flow depending on when the snow melts and the lag time for the meltwater to reach the stream. As a snowpack accumulates during winter months, varying temperature and vapor gradients cause a metamorphosis of snow grains within a snowpack. Additionally, variable layers in a porous media such as snow have different hydraulic properties that can form capillary barriers at the interfaces between layers. Data from three snow pits located in the Spring Creek Intensive Study Area (Part of the NASA CLPX dataset) of Colorado were used for simulations. Data for north, south, and relatively flat aspect slopes were chosen to represent the variable metamorphosis that occurs under different conditions. The north and south aspect slopes each have a 20 degree slope whereas the flat location has a five degree slope. The data provided a maximum of 27 layers within a single snow pit for which hydraulic properties were estimated. Simulations were conducted at steady state infiltration rates of 0.1, 1.0, and 5.0 mm/hr that represent the range of expected snow melt rates using the EOS9 module of TOUGH2. Results demonstrate that conditions are present within a layered snowpack to produce multiple permeability barriers and capillary barriers, though capillary barriers were only present on the north aspect snowpack. These results suggest that during a snowmelt period water may be redistributed down slope prior to infiltrating the ground surface. A better understanding of a snowpack as a porous medium will improve future hydrologic modeling, in part due to snow layers generally having hydraulic conductivities that are orders of magnitude greater than most soils.

INTRODUCTION

The melting of a snowpack is known to be an important aspect of the hydrologic cycle and potentially sensitive to a changing climate (Caine, 1992; Bales *et al*., 2006; Adam *et al*., 2009; Harpold *et al*., 2012). Additionally, snowpacks have been understood to be layered porous media that produce variable infiltration of meltwater (Webb *et al*., 2015) and to have a strong influence on the timing and magnitude of snowmelt hydrographs (Kattelmann and Dozier, 1999; Waldner *et al*., 2004; Williams *et al*., 2010; Wever *et al*., 2014). However, the movement of water through snowpacks remains an area of snow science with much room to grow.

The understanding of water flow through a snowpack has been limited, in part, due to the destructive nature of observations, constraining results to discrete temporal resolution rather than continuous (Williams *et al.*, 2010; Kattelmann and Dozier, 1999). Furthermore, snow metamorphosis is accelerated during melt adding complexity with temporally varying hydraulic properties not normally associated with flow through porous media (Colbeck, 1987; Marsh, 1987).

The formation of a layered snowpack occurs throughout the entire winter season. Each snow storm event produces an additional layer that begins a metamorphosis that is dependent upon

the subsequent atmospheric and lower boundary conditions unique to each layer (Colbeck, 1991). As winter transitions to spring and the snowpack warms and melts, each layer will have varying grain sizes and densities that can be used to estimate hydraulic properties (Yamaguchi *et al.*, 2010).

Water flow through layered porous media such as soils and the physics of capillary barriers has long been studied and successfully modeled (Oldenburg and Pruess, 1993; Stormont, 1995; Webb, 1997; Ho and Webb, 1998). Recently, soil physics has been applied successfully to a layered snowpack in Switzerland using estimations of hydraulic properties and applying Richard's equation (Wever *et al.*, 2014). This study resulted in improved estimations of snowmelt runoff in a one-dimensional (vertical) setting. Other studies have qualitatively shown retention of percolating meltwater above layer interfaces as well as the transmission of meltwater downslope through the use of dye tracers as a means to visualize flow paths (Williams *et al.*, 2010; Walter *et al.*, 2013; Eirikkson *et al.*, 2013).

This study investigates the potential for layered snowpacks to produce capillary barriers with large diversion lengths through the following objectives: 1) simulate percolating water through layered snowpacks in complex terrain using TOUGH2 (EOS9), 2) identify grain size and density variations that predict the formations of capillary barriers, and 3) estimate potential diversion lengths of meltwater through a layered snowpack as a result of capillary barriers.

METHODS

Snowpack stratigraphy data for this study were collected from the National Aeronautics and Space Administration (NASA) Cold Land Process Experiment (CLPX) dataset (Elder *et al.*, 2003). Data for this study are from the Spring Creek intensive study area collected on March 30, 2003, part of the Rabbit Ears mesoscale study area in northern Colorado (Fig. 1) (for more information on NASA CLPX data collection see Elder *et al.*, 2009).

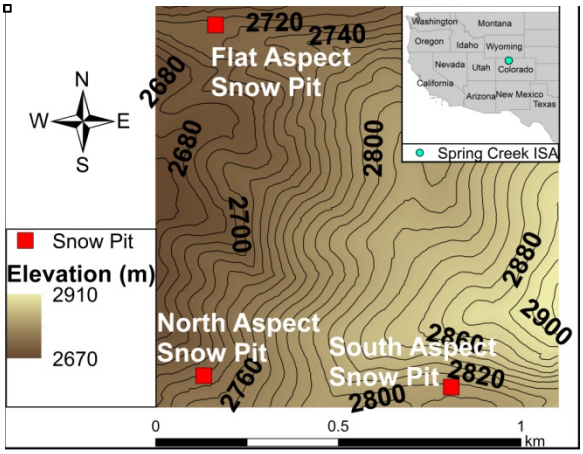

Figure 1. Map of Spring Creek Intensive Study Area showing snow pit locations for data used in this study and 10 meter contours.

Three snowpits were chosen for simulations from the NASA CLPX dataset based on slope and aspect (Fig. 1). Aspects chosen for simulations were flat, south, and north. The flat aspect has a slope of 5° whereas both the south and north snowpits have slopes of approximately 20°. Slopes and aspects were determined from airborne Light Detection and Ranging data collected for the intensive study area (Miller, 2004). Grain sizes of all three pits ranged in mean diameter from 0.2 mm to 1.5 mm and density ranging from 48.5 kg/m^3 for a layer of fresh snow to 461.0 kg/m^3 (Fig. 2).

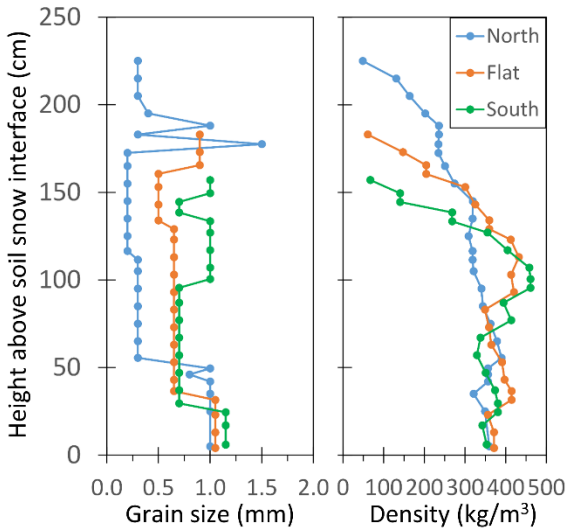

Figure 2. Stratigraphy data displaying grain size and layer density of the three snow pits (north aspect, flat aspect, and south aspect) chosen for TOUGH2 EOS9 simulations.

Hydraulic properties of snowpack layers were estimated from equations developed by Yamaguchi *et al*. (2010) based on mean grain size and snow density to estimate saturated hydraulic conductivity as well as van Genuchten (1980) unsaturated properties (Fig. 3). The purpose of this paper is to primarily investigate the role of capillary barriers in a snowpack, thus ice layers are only represented through density and grain size measurements.

The numerical code TOUGH2 is utilized for simulation of water in the unsaturated conditions of this study (Pruess *et al.*, 1999). TOUGH2 has been used in previous studies concerning effects of capillary barriers (Webb, 1997; Ho and Webb, 1998). The numerical code is capable of simulating multiphase transport of air, water, and heat in porous media. For the purposes of this study only the transport of liquid water was investigated using the TOUGH2 equation of state module EOS9. This module applies Richards' equation (Richards, 1931). The weighting of unsaturated hydraulic properties at element connections was chosen as upstream weighting as has been shown to accurately describe the behavior of capillary barriers (Webb, 1997).

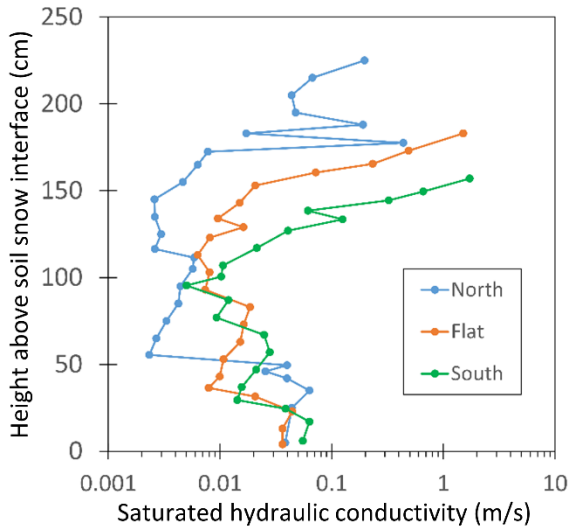

Figure 3. Estimated values of saturated hydraulic conductivity based on Yamaguchi *et al*. (2010).

A rectilinear grid was used to constrain the simulations to 25 m wide at 0.5 m horizontal resolution. Minimum vertical element separation at interfaces was 5 x 10^{-4} m with a growth rate factor of 1.4 away from all interfaces. Snowpack profiles had total depths of 1.9 m for the flat aspect, 1.6 m for the south, and 2.2 m for the north. The north aspect slope had the most layers at 27, resulting largely from the resolution of the data collection (Elder *et al*., 2009). Each modeled snowpit was used to simulate steady state melt rates of 0.1, 1.0, and 5.0 mm/hr generated in the uppermost row of the model. In cases where a 25 m width was not wide enough, capillary barriers were identified by using Ross' (1990) approximation for van Genuchten properties (Webb, 1997).

RESULTS

Results from the initial simulations display distinct barriers forming within the layered snowpacks. Multiple lateral diversions can be seen in each simulated flow field, displaying how a "stair step" flow path would develop as water flows through the medium, similar to that suggested by Colbeck (1975) concerning ice lenses (Fig. 4). The barriers observed in Fig 4 are primarily permeability barriers, though, rather than capillary barriers. Permeability barriers form in the case that the upper layer has a permeability greater than the lower layer such that if water is infiltrating at a higher rate than the infiltration capacity of the interface, lateral flow will occur, as is seen in these results. The primary difference between permeability barriers and capillary barriers is that permeability barriers allow steady state flux across the interface whereas capillary barriers will divert all of the flow for a predictable diversion length. The addition of permeability barriers to the theory adds more downslope flow paths that may develop. The flat and south aspect snowpits were successfully modeled as layered media, however the north aspect stratigraphy resulted in relatively large diversion at the uppermost interface. Ross approximations for the north aspect stratigraphy, however, suggest multiple capillary barriers with potential diversion lengths ranging from 0.5 to 350 m. Further simulations are being developed for the north aspect stratigraphy.

The flat aspect stratigraphy resulted in two distinct permeability barrier effects at heights of 35 cm and 130 cm above the soil-snow interface

(SSI) (153 and 58 cm below the snow surface, respectively) diverting water at all three infiltration rates (Fig. 4a). No significant capillary barriers were observed in simulation results for the flat aspect stratigraphy. The interface 35 cm above the SSI resulted from two layers of similar density, 414.5 kg/m^3, and a crystal grain size 0.4 mm larger in the layer below the interface. The interface at 130 cm above the SSI resulted from two layers with similar density, 359.5 kg/m^3, and the lower layer having a crystal diameter 0.2 mm larger. The maximum diversion length for each of these barriers occurred at a melt rate of 0.1 mm/hr and lengths of 6.5 m at 35 cm above the SSI and 3.0 m at 130 cm above the SSI. Diversion lengths for permeability barriers are considered to be the distance from the lateral boundary that infiltration rate above the interface is equal to the flux across the interface, though a larger flux continues laterally as simulation results show (Fig. 4).

The south aspect stratigraphy also resulted in two distinct permeability barrier effects at heights of 27 cm and 135 cm above the SSI (135 cm and 27 cm below the snow surface, respectively) (Fig. 4b). No capillary barrier effects were observed in the south aspect stratigraphy simulations. The two permeability barriers diverted water percolating at all three melt rates. The interface 27 cm above the SSI resulted from two layers of similar density, 380.5 kg/m^3, and a crystal grain size 0.5 mm larger in the layer below the interface. The interface at 135 cm above the SSI resulted from two layers with similar density, 268.5 kg/m^3, and the lower layer having a crystal diameter 0.3 mm larger. The maximum diversion length for each of these barriers occurred at a melt rate of 0.1 mm/hr and lengths of 9.0 m at 27 cm above the SSI and 5.5 m at 135 cm above the SSI.

The north aspect stratigraphy displayed a more stratified snowpack with five identified potential capillary barriers from the Ross (1990) and Webb (1997) approximation. The 25 m wide simulation resulted in a single permeability barrier diverting flow the entire 25 m (Fig. 4c). The Webb (1997) approximations suggest capillary barriers occur at 51, 113, 180, 190, and 200 cm above the SSI with initial estimated diversion lengths ranging from 0.5 m to 350 m (Table 1). These barriers occurred between layers with differences in density ranging from 0 kg/m^3 to 38 kg/m^3 and differences in crystal grain diameters from 0.1 to 1.2 mm (Table 1).

The largest diversion length estimate from all three snowpack stratigraphy data occurred 51 cm above the SSI on the north aspect. The diversion length of this barrier is estimated at 350 m at a melt rate of 0.1 mm/hr. All capillary barriers in this study resulted from layers of varying crystal grain sizes and lesser from differences in density though this may be a result of density measurements being measured at a 0.1 m resolution and unable to capture the variability between layers (Elder *et al*., 2009). The minimum difference in crystal grain diameter was 0.1 mm occurring twice within the north aspect stratigraphy and with the shortest estimated diversion lengths. The capillary barrier with the longest diversion length did not have the largest difference in crystal grain diameter with a difference of 0.7 mm and a difference in density of 33 kg/m^3.

Table 1. Summary of permeability (Per.) and Capillary (Cap.) barriers for the flat (F), south (S), and north (N) aspect locations showing the differences in grain sizes and densities between layers forming the barrier (note: all capillary barriers are only from Webb (1997) approximations).

Aspect	Barrier Type	Diff. in Grain Size (mm)	Diff. in Density (kg/m^3).	Max Diversion Length (m)
F	Per.	0.4	0	6.5
F	Per.	0.2	0	3.0
S	Per.	0.5	0	9.0
S	Per.	0.3	0	5.5
N	Per.	0	82.5	>25.0
N	Cap.	0.1	38	0.5
N	Cap.	0.6	34	90
N	Cap.	1.2	1.5	270
N	Cap.	0.1	0	3.1
N	Cap.	0.7	33	350

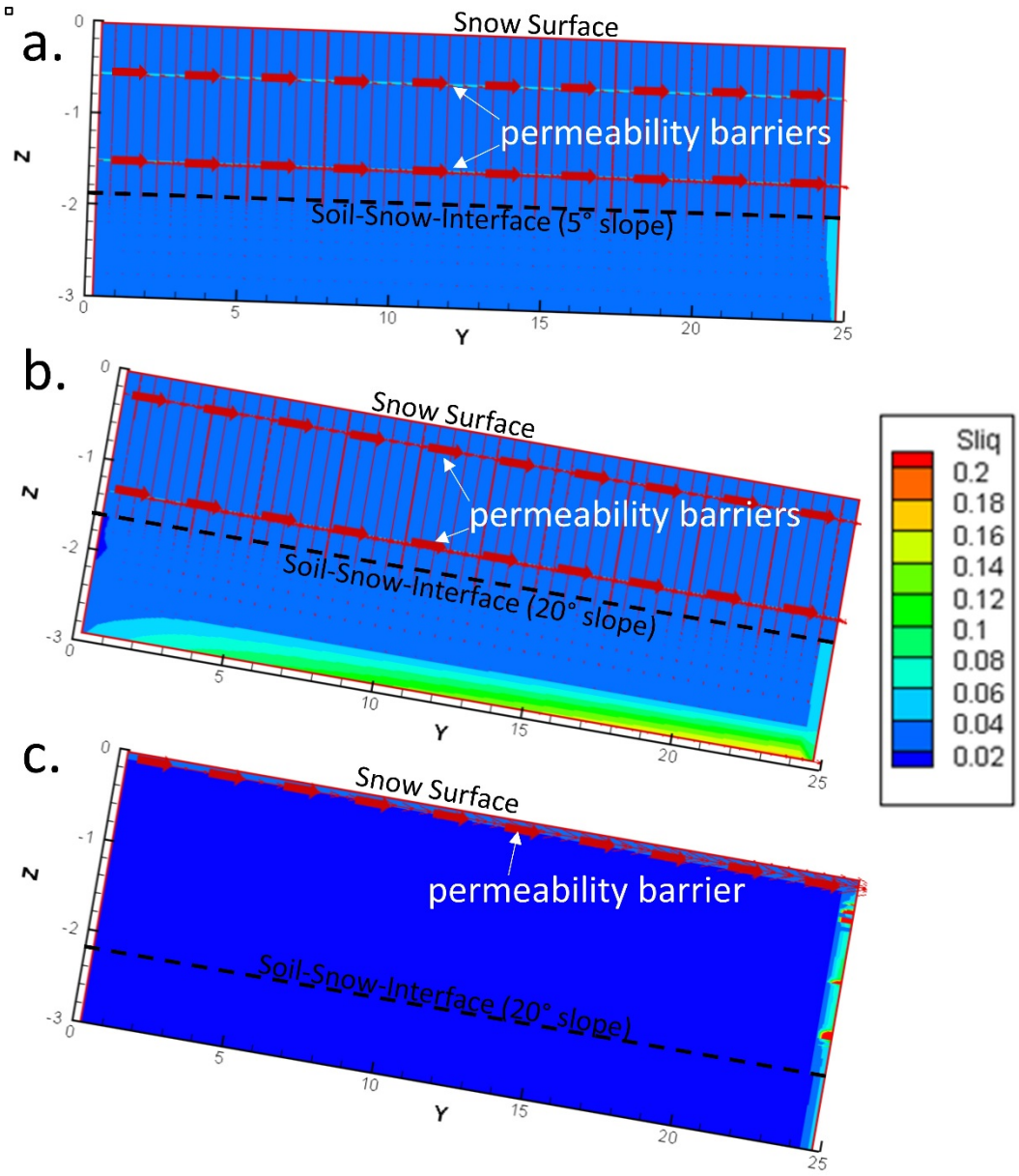

Figure 4. Simulation results from TOUGH2 EOS9 for a) flat aspect, b) south aspect, and c) north aspect stratigraphy. Results displayed are vector plots of the flow paths for melt rates of 1.0 mm/hr with the permeability barrier vector arrows enlarged for highlighting purposes. The color contour of each result is the steady state distribution of liquid saturation (Sliq).

DISCUSSION

In this study, we have shown that TOUGH2 is capable of simulating the percolation of water through a layered snowpack. Highly stratified snowpacks such as the north aspect location in this study add complexity to the modeling process, making it difficult to represent in a 25 m wide domain. The simulations resulted in the diversion of vertically infiltrating melt water from primarily permeability barriers with capillary barriers predicted and to be tested in future simulations being developed. These barriers had diversion lengths ranging from 0.5 to 350 m. The permeability barrier observed in the north aspect stratigraphy may be a result of calculating hydraulic properties from the equations developed by Yamaguchi *et al.* (2010). Yamaguchi *et al.* (2010) tested samples with densities near 500 kg/m^3 and the topmost

layer in the north aspect stratigraphy simulated in this study has a density of 48 kg/m^3. It is also likely that some of the layer interfaces cause diversions less than the resolution of these simulations or smaller scale heterogeneity that would cause fingering of the infiltrating water as shown in field studies (Williams *et al*., 2010; Eiriksson *et al*., 2013). However, it has been shown in previous studies that the homogenous layer approach is a reasonable approximation of the mean diversion length of heterogeneous realizations (Ho and Webb, 1998). Ultimately, these simulations display the potential for large diversion lengths of percolating water flowing through a porous snowpack.

Diversion lengths of the magnitude shown in this study may be unrealistic for the environment that the snowpit stratigraphy data were collected. In complex subalpine mountainous terrain such as the Spring Creek Intensive Study Area, it is unlikely that snowpack layers will remain continuous for the entirety of the larger diversion lengths. The scale of the spatial variability in snowpack layers will likely be controlled by the scale of the topographic and land cover variability causing a range of temperature and radiation gradients (Colbeck, 1991). In the case of subalpine mountainous terrain this variability can range from meters to tens of meters (Musselman *et al*., 2008; Sextone and Fassnacht, 2014). However, further investigation in regions of lesser topographic and land cover variability such as glacial watersheds could result in diversion lengths occurring at the hundreds of meters scale as this study has shown a layered snowpack has the potential to produce.

The primary differences between layers that formed capillary barriers were the crystal grain sizes. The differences ranged from 0.1 to 1.2 mm with a threshold being observed at 0.5 mm to produce a diversion length of 5 m or greater with lesser differences necessary for permeability barriers. Density did not vary as often as grain size between these layers though this may be a result of the sampling method (Elder *et al*., 2009). Density measurements were conducted using a 1 L wedge cutter that is only capable of 0.1 m resolution resulting in some layers being averaged together in density measurements. Further field data collection and testing would need to be conducted to quantify the impact this had on the simulation results.

It should also be noted that some of these simulated barriers occurred at locations that were observed to have melt-freeze crusts or ice layers present that were not accounted for in the model. These occurred at the south aspect stratigraphy 135 cm above the SSI, the north aspect at 51 cm, 180 cm, and 190 cm above the SSI. The flat aspect simulations did not produce any barriers at depths of observed crusts or ice layers. The north aspect melt-freeze crusts and ice layers occur at the largest potential capillary barrier diversion lengths displaying the effect that these crusts and layers can have on the predicted hydraulic properties through increased density and grain sizes. Further research is necessary to improve on the diversion potential of these melt-freeze crusts and ice layers as capillary barriers and/or permeability barriers.

Additionally, it has been shown in numerous studies that crystal growth is accelerated in the presence of liquid water (Colbeck, 1987; Marsh, 1987). Therefore, it is likely that the barriers shown in this study to exist in a layered snowpack may be short lived and only applicable over a short temporal scale. It is possible that as water is diverted, the crystal growth is rapid enough to alter the diversion length during the day that the melt is occurring. Further investigation of the rate at which *in-situ* crystals grow during melt would improve this hypothesis, though it has been shown at the day time scale (Kattelmann and Dozier, 1999) and hours time-scale in laboratory settings (Walter *et al*., 2013). The current capabilities of TOUGH2 do not allow for the temporal variability of material properties.

This study has implications to the distribution of water within a snowpack early in the melt season. During the transition from winter to spring as the snowpack ripens, meltwater may be diverted laterally as a result of capillary and/or permeability barriers. In complex subalpine mountainous environments such as the site for this study, meltwater may be diverted across multiple capillary and/or permeability barriers within the snowpack at lengths similar to those of the topographic and land cover varia-

bility. This would result in more water reaching the SSI at locations of topographic depressions or transition zones from open to under canopy conditions (for two examples). Variable infiltration such as this has been shown in previous studies of the shallow subsurface (Webb *et al*., 2015; Williams *et al*., 2009). Additionally, this may cause variable release rates of water from the snowpack at the SSI that may result in infiltration excess or run-off and run-on scenarios as has been observed at locations during snowmelt (Bales *et al.*, 2011).

Hydrologic processes such as groundwater recharge and streamflow generation from a melting snowpack would be improved through a better understanding of the snowpack as a porous media. As we have shown in this study, multiple barriers are likely to occur within a layered snowpack in subalpine mountainous terrain with diversion lengths ranging from less than a meter to 350 m. Vadose zone hydrologic studies may be improved through representing snowmelt as a variable process across the SSI for purposes of groundwater recharge, streamflow generation, and plant production quantifications.

CONCLUSION

We were able to represent water flowing through a layered snowpack using the EOS9 module of TOUGH2. A highly stratified snowpack as was observed from the north aspect snowpit data used for this study add complexities and difficulties for modeling purposes. Capillary barriers formed as a result in crystal grain sizes varying from 0.1 to 1.2 mm between snowpack layers but diversion lengths above 5 m were only estimated for grain size differences above 0.5 mm. Permeability barriers were also observed in simulations with differences in grain size as low as 0.0 mm and density differences from 0 up to 82.5 kg/m^3, though this may be a limitation in parameter estimation. Barriers were observed less often as a result of differences of density. The diversion lengths from estimated capillary barriers were as high as 350 m at a melt rate of 0.1 mm/hr displaying the large potential for percolating water to move laterally within a snowpack. Highly stratified snowpacks such as the north aspect snow pit in this study produce higher potential for lateral diversion of percolating melt water. These results have strong implications on the distribution of water within a layered snowpack during the transition period from winter to spring, though further studies are necessary to verify large capillary diversion in layered snowpacks in the field.

REFERENCES

Adam, J.C., A.F. Hamlet, and D.P. Lettenmaier, Implications of global climate change for snowmelt hydrology in the twenty-first century, *Hydrol. Porcess*., 23, 962-972, 2009.

Bales, R.C., N.P. Molotch, T.H. Painter, M.D. Dettinger, R. Rice, and J. Dozer, Mountain hydrology of the western United States, *Water Resour. Res.,* 42(8), W08432, doi: 10.1029/2005WR004387, 2006.

Bales, R.C., J. Hopmans, A.T. O'Geen, M. Meadows, P.C. Hartsough, P. Kirchner, C.T. Hunsaker, and D. Beaudette, Soil moisture response to snowmelt and rainfall in a Sierra Nevada Mixed-Conifer Forest, *Vadose Zone J*., 10, 786-799, 2011.

Caine, N., Modulation of the diurnal streamflow response by the seasonal snow cover of an alpine basin, *J. Hydrol*., 137, 245-260, 1992.

Colbeck, S.C., A theory for water flow through a layered snowpack, *Water Resour. Res*., 11(2), 261-266, 1975.

Colbeck, S.C., Theory of particle coarsening with a log-normal distribution, *Acta Metallica*, 35, 1583-1588, 1987.

Colbeck, S.C., The layered character of snow covers, *Reviews of Geophysics*, 29(1), 81-96, 1991.

Eiriksson, D., M. Whitson, C. Luce, H. Marshall, J. Bradford, S. Benner, T. Black, H. Hetrick, and J. McNamara, An evaluation of the hydrologic relevance of lateral flow in snow at hillslope and catchment scales, *Hydrol. Process*. 27, 640-654, 2013.

Elder, K. and D. Cline, edited by M. Parsons and M. Brodzik, CLPX-Ground: ISA snow pit measurements, version 2 [Spring Creek ISA], Boulder, Colorado USA: NASA National Snow and Ice Data Center Distributed Active Archive Center, http://dx.doi.org/10.5060/D4H41PBP, 2003.

Elder, K., D. Cline, G.E. Liston, and R. Armstrong, NASA cold land processes experiment

(CLPX 2002/03): field measurements of snowpack properties and soil moisture, *J. of Hydrometeorology*, 10, 320-329, 2009.

Harpold, A., P. Brooks, S. Rajagopal, I. Heidbuchel, A. Jardine, and C. Stielstra, Changes in snowpack accumulation and ablation in the intermountain west, *Water Resour. Res*., 48, W11501, doi: 10.1029/2012WR011949, 2012.

Ho, C.K. and S.W. Webb, Capillary barrier performance in heterogeneous porous media, *Water Resour. Res*., 34(4), 603-609, 1998.

Kattelmann, R. and J. Dozier, Observations of snowpack ripening in the Sierra Nevada, California, U.S.A., *J. of Glaciology*, 45(151), 410-416, 1999.

Marsh, P., Grain growth in a wet arctic snow cover, *Cold Reg. Sci. and Tech*., 14, 23-31, 1987.

Miller, S., CLPX-Airborne: infrared orthophotography and lidar topographic mapping, [Spring Creek ISA], Boulder, Colorado USA: NASA National Snow and Ice Data Center Distributed Active Archive Center. http://dx.doi.org/10.5067/KRWSPR2J1N2N, 2004.

Musselman, K.N., N.P. Molotch, and P.D. Brooks, Effects of vegetation on snow accumulation and ablation in a mid-latitude sub-alpine forest. *Hydrol. Process*., 22, 2767-2776, doi: 10.1002/hyp.7050, 2008.

Oldenburg, C.M., and K. Pruess, On numerical modeling of capillary barriers. *Water Resour. Res*., 29(4), 1045-1056, 1993.

Pruess, K., C. Oldenburg, and G. Moridis, *TOUGH2 User's Guide, Version 2.0*, Report LBNL-43134, Lawrence Berkeley National Laboratory, Berkeley, Calif., 1999.

Richards, L., Capillary conduction of liquids through porous mediums, *J. Appl. Phys*., 1, 318-333, doi: 10.1063/1.1745010, 1931.

Ross, B., The diversion capacity of capillary barriers, *Water Resour. Res*., 26(10), 2625-2629, 1990.

Sextone, G.A., and S.R. Fassnacht, What drives basin scale spatial variability of snowpack properties in northern Colorado?, *The Cryosphere*, 8, 329-344, doi: 10.5194/tc-8-329-2014, 2014.

Stormont, J.C., The effect of constant anisotropy on capillary barrier performance, *Water Resour. Res*., 31(3), 783-785, 1995.

van Genuchten, M.T., A closed-form equation for predicting the hydraulic conductivity of unsaturated soils, *Soil Science Society of America Journal*, 44, 892-898, doi: 10.2136/sssaj1980.03615995004400050002x, 1980.

Waldner, P.A., M. Schneebeli, U. Schultze-Zimmermann, and H. Flühler, Effect of snow structure on water flow and solute transport, *Hydrol. Process*., 18, 1271-1290, doi: 10.1002/hyp.1401, 2004.

Walter, B., S. Horender, C. Gromke, and M. Lehning, Measurements of the pore-scale water flow through snow using fluorescent particle tracking velocimetry, *Water Resour. Res*., 49, 7448-7456, doi: 10.1002/2013WR013960, 2013.

Webb, S.W., Generalization of Ross' tilted capillary barrier diversion formula for different two-phase characteristic curves, *Water Resour. Res*., 33, 1855-1859, 1997.

Webb, R.W., S.R. Fassnacht, and M.N. Gooseff, Wetting and drying variability of the shallow subsurface beneath a snowpack in California's Southern Sierra Nevada, Vadose Zone J., [in press], doi: 10.2136/vzj2014.12.0182, 2015.

Wever, N., C. Fierz, C. Mitterer, H. Hirashima, and M. Lehning, Solving Richards Equation for snow improves snowpack meltwater runoff estimations in detailed multi-layer snowpack model, *The Cryosphere*, 8, 257-274, doi: 10.5194/tc-8-257-2014, 2014.

Williams, M.W., T.A. Erickson, and J.L. Petrzelka, Visualizing meltwater flow through snow at the centimeter-to-metre scale using a snow guillotine, *Hydrol. Process*, 24, 2098-2110, doi: 10.1002/hyp.7630, 2010.

Williams, C.J., J.P. McNamara, and D.G. Chandler, Controls on the temporal and spatial variability of soil moisture in a mountainous landscape: the signature of snow and complex terrain, *Hydrol. Earth Syst. Sci*., 13, 1325-1336, 2009.

Yamaguchi, S., T. Katsushima, A. Sato, and T. Kumakura, Water retention curve of snow with different grain sizes, *Cold Reg. Sci. and Tech.*, 64, 87-93, doi: 10.1016/j.coldregions.2010.05.008, 2010.

Reactive Transport

MODELING PROCESSES AFFECTING CARBON DYNAMICS AT A BIOGEOCHEMICAL HOTSPOT IN A FLOODPLAIN AQUIFER

Bhavna Arora[1], Dipankar Dwivedi[1], Nicolas Spycher[1], and Carl Steefel[1]

Lawrence Berkeley National Laboratory
1 Cyclotron Road
Berkeley, CA 94720, USA
e-mail: barora@lbl.gov

ABSTRACT

Although carbon fluxes in soils and groundwater are critical components of the global carbon budget, significant uncertainty is associated with their predictions due to the presence of different hydrological and biogeochemical mechanisms that affect carbon turnover and distribution in the subsurface. In particular, redox reactions regulated by the presence of a large and diverse soil microbial population exert a dominant control on near surface soil CO_2 dynamics. This study investigates the transport and release of carbon within the saturated and unsaturated zone of an alluvial aquifer bordering the Colorado River at Rifle, Colorado. Localized biogeochemically reduced zones (referred to as naturally reduced zones or NRZs) have been identified as biogeochemical hotspots at this floodplain site, enriched with organic matter and reduced Fe and S phases. To quantify the spatial redox and microbial zonation on subsurface carbon fluxes at this site, a 2-D reactive transport model has been developed using TOUGHREACT. The model, making use of the EOS3 module, specifically accounts for spatially distinct pools of Fe and S minerals and functional microbial populations in the subsurface. Results suggest the need to include microbial contributions from chemolitho-autotrophic processes (e.g., sulfur and iron oxidation) as well as temperature gradients to match locally-observed high CO_2 concentrations in the unsaturated zone. Ignoring these processes leads to an underestimatation of carbon fluxes. Modeling such systems requires the capability to simulate reactive transport in both aqueous and gas phases under non-isothermal and variably saturated conditions.

INTRODUCTION

Export of organic and inorganic carbon fluxes from terrestrial sources to rivers are of critical importance to understanding trends in the global carbon budget. However, the magnitude and governing controls of spatio-temporal variability in subsurface carbon fluxes remain uncertain (Raymond et al., 2013; Tian et al., 2015).

Studies have shown that soil moisture and temperature represent two significant sources of temporal variability in carbon fluxes. For example, Michalzik et al. (2001) showed that an increase in dissolved organic carbon and nitrogen fluxes along a vertical profile in forests was positively correlated with increasing annual precipitation. Similarly, Arora et al. (2013) reported that temporal changes in several redox sensitive concentrations (including dissolved organic carbon) in groundwater were strongly correlated with rainfall events and/or water table fluctuations. Several studies have highlighted the role of antecedent temperature conditions on soil CO_2 fluxes and the effect of increasing temperature on heterotrophic decomposition processes (Bond-Lamberty and Thomson, 2010; Dawson et al., 2011; Moore and Dalva, 1993). In addition, the solubility of dissolved CO_2 and weathering of carbonate minerals are also dependent on temperature.

Spatial variability in carbon fluxes is inherently governed by flow and its interaction with geomorphology (Robertson et al., 1999). For example, spatial patterns in dissolved organic carbon fluxes have been correlated with hydrological connectivity (such as, distance from the source area) and landscape elements (such as, vegetation cover and type) (Canham et

al., 2004; Laudon et al., 2011; Manzoni and Porporato, 2011).

Here we assess the spatio-temporal variability in subsurface carbon fluxes at the Rifle field site in Rifle, Colorado. Specific objectives of the study are to: (a) examine the spatial variability in redox behavior and microbial populations at the site, and include the required level of detail within reactive transport models, (b) investigate the biotic and abiotic pathways responsible for carbon cycling at the site, and (c) evaluate the relative importance of water level, recharge, temperature, and atmospheric pressure variations on CO_2 efflux patterns from the site.

THE RIFLE SITE

The Rifle field site is a former Uranium Mill Tailings Remedial Action (UMTRA) site at Rifle, Colorado, located on the floodplain of the Colorado River (Figure 1). Groundwater beneath the Rifle site was contaminated by former vanadium and uranium ore-processing operations from 1924 through 1958 (U.S. Department of Energy, 1999). Mill tailings and other radioactive chemicals were removed in 1996 as part of UMTRA efforts. Site-wide field investigations continue at this site, including the present study on organic and inorganic carbon fluxes across the floodplain.

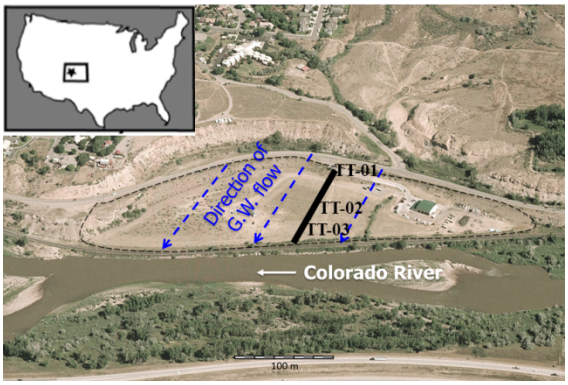

Figure 1. Location of the Rifle site and the modeled TT transect on the floodplain of the Colorado River.

Biogeochemical Hotspot at the Rifle Site

Cluster analysis was applied to classify multivariate geochemical data and dominant microbial populations across the Rifle floodplain. Spatial clustering was done using the PAM (Partitioning Around Mediods) method after the data were transformed and rescaled using medians. Figure 2 shows three significant clusters at the site – cluster 1 is associated with naturally reduced zones that are identified from geophysical delineation and are associated with large chemolithoautotrophic populations, cluster 2 is associated with high contaminant concentrations (uranium and vanadium) and is dominated by sulfate reducers, and cluster 3 is associated with low contaminant concentrations and dominated by iron reducers.

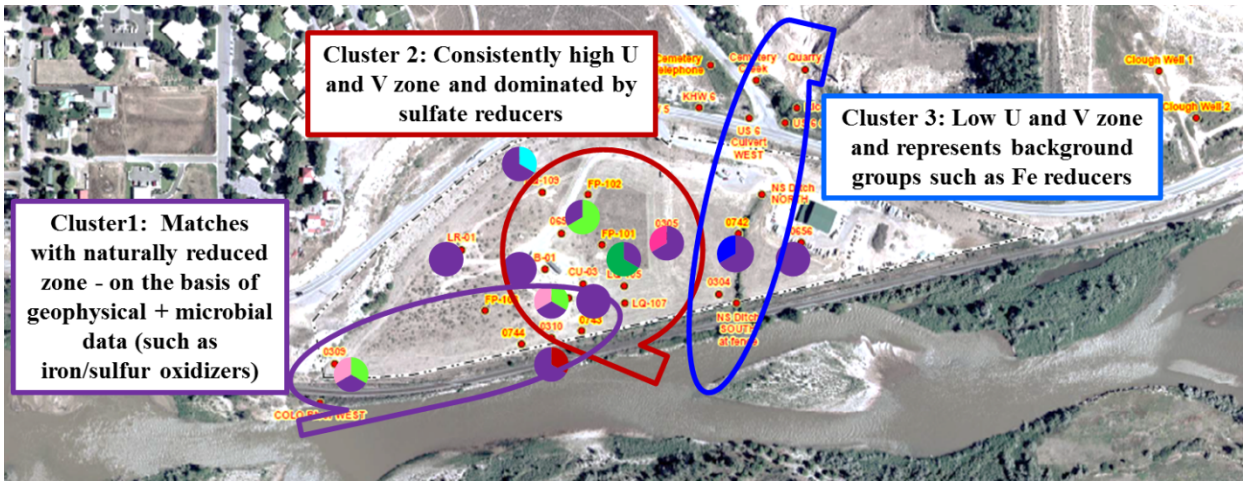

Figure 2. Results of PAM cluster analysis showing spatial variability in redox behavior and microbial populations at the Rifle site.

Naturally reduced zones (NRZs) as identified in cluster 1, have been found under many floodplains. These zones are considered to be biogeochemical hotspots, distinguished by elevated organic matter content, reduced Fe and S minerals, distinct microbial activities, and elevated contaminant concentrations (e.g. uranium).

APPROACH

In this study, we conduct biogeochemical reactive transport simulations using TOUGHREACT V2 and V3-OMP (Sonnenthal et al., 2014; Xu et al., 2011) with the EOS1 and EOS3 module (Pruess et al., 1999) to understand carbon dynamics at the site. The implemented reaction network and simulated cases are summarized below.

Geochemical Reaction Network

The model includes a multicomponent biotic reaction network with multiple terminal electron acceptors (TEAs), kinetic and equilibrium mineral precipitation and dissolution reactions, as well as spatially distinct pools of Fe and S minerals and functional microbial populations based on cluster analysis results as well as previous studies at the site.

Inorganic reaction system

The inorganic reaction processes included in this study are aqueous speciation and mineral precipitation and dissolution reactions. Reactive minerals considered in the model are goethite, pyrite, siderite and calcite. All mineral precipitation and dissolution reactions are described using kinetic rate laws (Table 1) as:

$$R_m = (k_{neutral} + k_{H^+}[a_{H^+}] + \Sigma k_j \prod_i [a_{ij}]) \quad (1)$$

where $k_{neutral}$, k_{H+} and k_j are rate constants for neutral, acid or additional (j^{th}) reaction mechanism, respectively; a_{ij} is the activity of the i^{th} aqueous species in the j^{th} reaction; and Ω_m is the saturation ratio of the m^{th} mineral phase.

Microbially mediated reaction system

The inorganic reaction system is coupled to the biotic reaction network in which redox is decoupled in the thermodynamic database. Acetate is produced by the decomposition of cellulose. The decomposition of acetate is represented by overall reactions for oxic respiration, denitrification, sulfate reduction, and iron reduction. Single Michaelis-Menten kinetics are used to represent the microbially mediated decomposition of acetate using:

$$R_S = \mu_{max} \frac{C_S}{K_{M,S}+C_S} \frac{C_{TEA}}{K_{M,S}+C_{TEA}} \frac{K_I}{K_I+C_I} \quad (2)$$

where μ_{max} is the maximum rate of reaction; C_S, C_{TEA} and C_I are the substrate, electron acceptor and inhibiting species concentrations, respectively; K_S and K_{TEA} are the corresponding half-saturation constants for the substrate and TEAs; and K_I is the inhibition constant. Further, the sequence of TEAs is realized using inhibition terms (such as, Reactions 5-10 in Table 1). In addition to the heterotrophic oxidation of acetate, chemolithoautotrophic oxidation of Fe^{+2} and HS^- were included in the simulation (Reactions 3, 4, 7 and 8, Table 1). The kinetic parameters were either obtained from literature or calibrated based on the analyses of pore waters at the site.

Simulated Cases

The reactive transport model is setup along a vertical 2D transect roughly parallel to the local groundwater flow gradient and instrumented at three locations (wells TT-01, TT-02, and TT-03) (Figure 3).

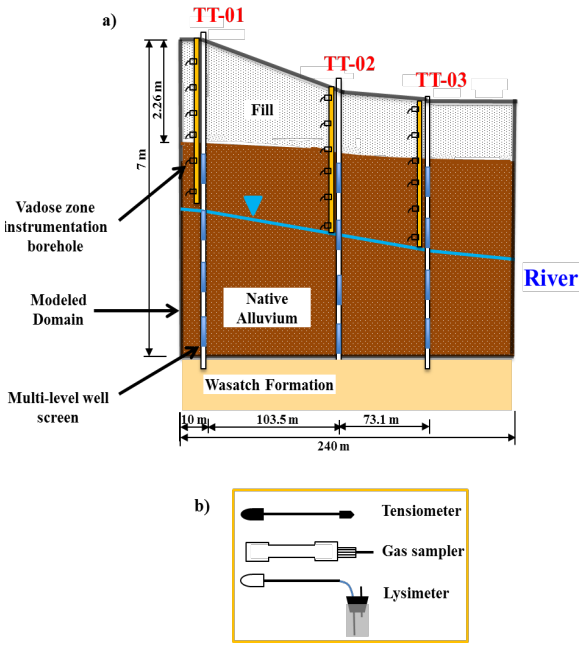

Figure 3. (a) 2-D cross-section of the model domain and (b) description of the borehole instrumentation after (Tokunaga et al., 2015).

Table 1. Important reactions considered in this study and their parameters

No.	Reaction stoichiometry	Kinetic parameters			
	Microbially mediated reactions	μ_{max} (/s)	$K_{M,s}$ (mol/L)	$K_{M,TEA}$ (mol/L)	K_I (mol/L)
1	$CH_3COO^- + 2O_2 \rightarrow 2HCO_3^- + H^+$	5.0×10^{-12} [a]		2.4×10^{-5} [b]	
2	$NH_3(aq) + 2O_2 \rightarrow NO_3^- + H_2O + H^+$	5.3×10^{-4} [a]	1.5×10^{-5} [c]	2.4×10^{-5} [b]	
3	$Fe^{+2} + 0.25O_2 + H^+ \rightarrow Fe^{+3} + 0.5H_2O$	5.3×10^{-11} [a]	1.0×10^{-5} [d]	2.4×10^{-5} [b]	
4	$0.5HS^- + O_2 \rightarrow 0.5H^+ + 0.5SO_4^{-2}$	2.4×10^{-8} [e]	1.0×10^{-5} [f]	2.4×10^{-5} [b]	
5	$CH_3COO^- + 4NO_3^- \rightarrow 2HCO_3^- + 4NO_2^- + H^+$	2.0×10^{-10} [g]		1.1×10^{-4} [b]	$K_{I,O2}=1.6 \times 10^{-8}$ [h]
6	$CH_3COO^- + 2.667NO_2^- + 1.667H^+ \rightarrow 2HCO_3^- + 1.33N_2 + 1.33H_2O$	3.0×10^{-8} [a]		1.1×10^{-4} [b]	$K_{I,O2}=1.6 \times 10^{-8}$ [h]
7	$Fe^{+2} + 0.2NO_3^- + 1.2H^+ \rightarrow Fe^{+3} + 0.1N_2 + 0.6H_2O$	7.0×10^{-8} [i]	1.0×10^{-5} [d]	1.1×10^{-4} [b]	$K_{I,O2}=1.6 \times 10^{-8}$ [h]
8	$HS^- + 1.6NO_3^- + 0.6H^+ \rightarrow SO_4^{-2} + 0.8N_2 + 0.8H_2O$	7.0×10^{-8} [i]	1.0×10^{-5} [f]	1.1×10^{-4} [b]	$K_{I,O2}=1.6 \times 10^{-8}$ [h]
9	$CH_3COO^- + 8Fe^{+3} + 4H_2O \rightarrow 8Fe^{+2} + 2HCO_3^- + 9H^+$	1.0×10^{-13} [a]			$K_{I,O2}=1.6 \times 10^{-8}$ [h] $K_{I,NO3}=1.0 \times 10^{-7}$
10	$CH_3COO^- + SO_4^{-2} \rightarrow 2HCO_3^- + HS^-$	3.0×10^{-12} [a]	1.0×10^{-3} [j]		$K_{I,O2}=1.6 \times 10^{-8}$ [h] $K_{I,NO3}=1.0 \times 10^{-7}$ $K_{I,Fe}=1.0 \times 10^{-12}$
	Mineral dissolution and precipitation	$\log k_{neutral}$	$\log k_{H+}$	$\log (k_j \Pi[a_{ij}])$	
11 [k]	$CaCO_3(s) + H^+ \rightleftarrows Ca^{+2} + HCO_3^-$	-5.8	-0.3	$-3.5 + \log [CO_3^{-2}]$	
12 [l]	$FeCO_3(s) + H^+ \rightleftarrows Fe^{+2} + HCO_3^-$	-8.6	-3.7		
13 [l]	$FeOOH(s) + 3H^+ \rightleftarrows Fe^{+3} + 2H_2O$	-6.9			
14 [m]	$FeS_{2(s)} + 3.5O_2 + H_2O \rightleftarrows Fe^{+2} + 2SO_4^{-2} + 2H^+$			$-7.6 + \log [Fe^{+3}]^{0.3}[Fe^{+2}]^{-0.47}[H^+]^{-0.32}$	
15 [m]	$FeS_{2(s)} + 14Fe^{+3} + 8H_2O \rightleftarrows 15Fe^{+2} + 2SO_4^{-2} + 16H^+$			$-7.1 + \log [O_2]^{0.5}[H^+]^{-0.11}$	

[a] Calibrated; [b] (Maggi et al., 2008); [c] (Wu et al., 2011); [d] (Mayer et al., 2002); [e] (Luther et al., 2011); [f] (Handley et al., 2013); [g] (Parkhurst and Appelo, 1999); [h] (Widdowson et al., 1988); [i] (Palmer et al., 2010); [j] (Li et al., 2010); [k] (Duckworth and Martin, 2004); [l] (Palandri and Kharaka, 2004); [l] (Steefel, 2000; Williamson and Rimstidt, 1994)

A detailed description of the numerical model setup and input data is provided elsewhere (Arora et al., 2014; Arora et al., in preparation). Only a brief description of the simulations considered in this study are provided here:

- C1 - Base case simulation or abiotic case: This case implements only mineral dissolution and precipitation reactions (Reactions 11-15, Table 1) and does not consider any microbially mediated reactions. This case was simulated for a period of 15 years, a little over twice the estimated groundwater residence time at the site (6 years), and a period after which steady hydrological and chemical conditions were reached. A fixed water table height and steady temperature (12ºC) conditions were applied.
- C2 - Biotic case: Restarting the base case simulation and simulating for 6 years, with

the addition of microbial contributions from heterotrophic and chemolithoautotrophic processes (Reactions 1-10, Table 1). The chemolithoautotrophic processes considered are microbially mediated Fe^{+2} and HS^- oxidation reactions (Reactions 3, 4, 7 and 8, Table 1).

- C3 - Water table variations: Restarting C1 and C2 for a seasonal time frame (April to June 2013), with the addition of water level fluctuations recorded during this period.
- C4 - Temperature gradients: Restarting C1 and C2 for a seasonal time frame (April to June 2013), with the addition of observed temperature gradients.

Simulations C1 to C3 were run using the EOS1 equation of state module. EOS3 was used for simulating non-isothermal multiphase reactive transport processes with C4.

RESULTS

Abiotic versus biotic pathways

Model simulations are used to quantify the release of carbon dioxide and consumption of oxygen via abiotic pathways and heterotrophic microbial oxidation of reduced species (Fe(II), S(-2)) and minerals (pyrite). Figure 4 compares observed and simulated profiles of dissolved oxygen with simulations C1, C2 and C3 at wells TT-01 and TT-03. Dissolved oxygen (DO) concentrations in groundwater show a more gradual decline in well TT-01 compared to TT-03. Simulated C1 profiles which capture only abiotic processes are consistent with DO profiles measured in TT-01. However, biotic with heterotrophic and chemolithoautotrophic processes (C2) are needed to represent the faster depletion of DO in well TT-03.

Water table fluctuations

Modeling efforts focused on the April through June 2013 time frame that corresponds to the time of spring snow melt, leading to an approximately 0.6 meter rise in the water table. Observed water table variations at a USGS gaging location near the Rifle site are shown in Figure 5.

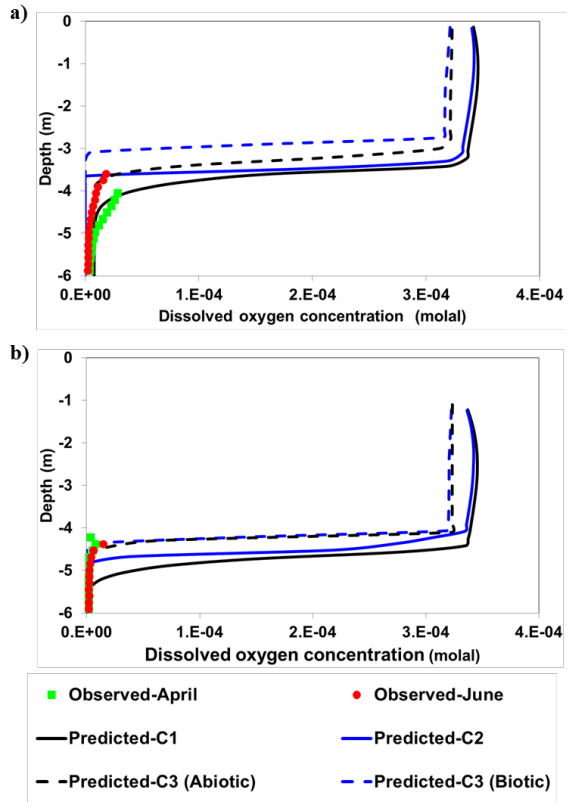

Figure 4. Observed and simulated dissolved oxygen concentrations at (a) TT-01 and (b) TT-03 wells for three modeled cases under steady (C1, abiotic; C2, abiotic+biotic with heterotrophic and chemolithoautotrophic pathways) and varying water table conditions (C3).

The changes in observed DO concentrations in the capillary fringe zone due to water table fluctuations between May and June 2013 are shown on Figure 4 at both TT-01 and TT-03 wells. Simulation C3 using abiotic pathways (dashed black line) best captures the observed DO profiles in June (red circles) in well TT-01.

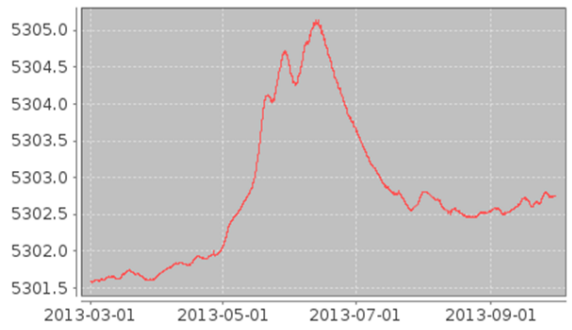

Figure 5. Observed USGS gage height for the Colorado River during 2013.

Simulation C3 using either abiotic or biotic pathways (dashed black and blue lines) capture the steeper DO profiles in well TT-03.

Temperature gradients

Figure 6 shows observed temperature gradients at well TT-03. Temperature variations of as much as 5ºC were observed at shallow depths (< 1.5 m), while at least some temperature variation (1ºC) occurred as deep as about 6 m during the April to June 2013 time frame.

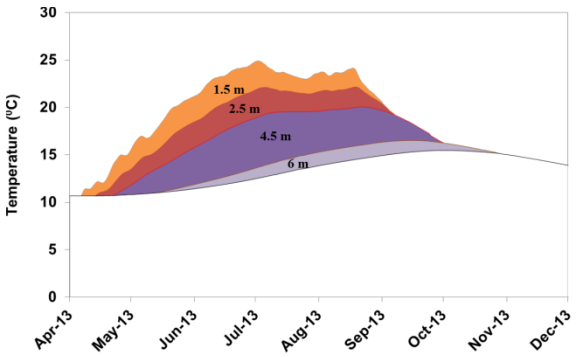

Figure 6. Observed temperature variations at 1.5, 2.5, 4.5 and 6 m depths at well TT-03 during 2013.

Figure 7 shows the computed effect of temperature gradients on model predictions. Results indicate that simulation C4 including the biotic pathways (solid blue line) is able to capture reasonably well the observed total carbonate concentration and soil CO_2 concentration profiles in June (red circles) in well TT-03. Note that simulation C4 using abiotic pathways (dotted black line) underpredicts soil CO_2 and carbonate concentrations especially in the vadose zone at well TT-03.

CONCLUSIONS

A 2D reactive transport model has been developed using TOUGHREACT to explore CO_2 dynamics in the saturated and unsaturated zones at the Rifle site. Results indicate that spatial and temporal variations in CO_2 concentrations resulting from variations in biogeochemical and microbial properties across the site can be qualitatively reproduced. Chemolithoautotrophic processes may play an important role in carbon dynamics and biogeochemical cycling at the site. Inclusion of

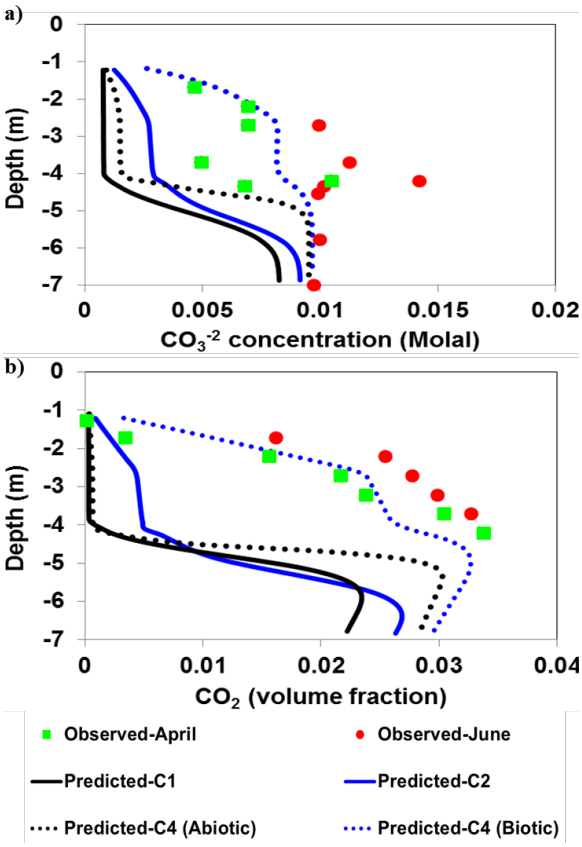

Figure 7. Observed and simulated (a) CO_3^{-2} concentrations and (b) CO_2 volume fractions at well TT-03 for three modeled cases under fixed (C1, abiotic; C2, abiotic+biotic with heterotrophic and chemolithoautotrophic pathways) and varying temperature gradients (C4).

temperature and hydrologic fluctuations in the model simulations was necessary to reproduce observed CO_2 concentration trends. An important conclusion from this study is that accurate prediction of subsurface carbon fluxes requires incorporation of site-specific microbial reactions and the use of a model that can handle reactive transport in both aqueous and gas phases under non-isothermal and variably saturated conditions.

ACKNOWLEDGMENT

Funding for this study was provided by the LBNL Sustainable Systems Scientific Focus Area under the U.S. Department of Energy contract DE-AC020SCH11231. We are grateful to M. Conrad, B. Faybishenko, T. Tokunaga, J. Wan, and K. Williams for providing data for this modeling study. The contribution of H.

Wainwright and E. Brodie with cluster analysis is also acknowledged.

REFERENCES

Arora, B., Mohanty, B. P., McGuire, J. T. and Cozzarelli, I. M.: Temporal dynamics of biogeochemical processes at the Norman Landfill site, Water Resour. Res., 49, 6909–6926, doi:10.1002/wrcr.20484, 2013.

Arora, B., Spycher, N. F., Molins, S., Steefel, C. I., Conrad, M. E. and Tokunaga, T.: Effect of spatial and temporal variability on subsurface carbon exports from a contaminated floodplain site, Biogeochemistry, n.d.

Arora, B., Spycher, N., Molins, S. and Steefel, C. I.: Modeling the biogeochemical response of a flood plain aquifer impacted by seasonal temperature and water table variations, in American Geophysical Union Fall Meeting Abstracts, p. 0019, 2014.

Bond-Lamberty, B. and Thomson, A.: Temperature-associated increases in the global soil respiration record., Nature, 464(7288), 579–82, doi:10.1038/nature08930, 2010.

Canham, C. D., Pace, M. L., Papaik, M. J., Primack, A. G. B., Roy, K. M., Maranger, R. J., Curran, R. P. and Spada, D. M.: A spatially explicit watershed-scale analysis of dissolved organic carbon in Adirondack lakes, Ecol. Appl., 14(3), 839–854, doi:10.1890/02-5271, 2004.

Dawson, J. J. C., Tetzlaff, D., Speed, M., Hrachowitz, M. and Soulsby, C.: Seasonal controls on DOC dynamics in nested upland catchments in NE Scotland, Hydrol. Process., 25(10), 1647–1658, doi:10.1002/hyp.7925, 2011.

Duckworth, O. W. and Martin, S. T.: Role of molecular oxygen in the dissolution of siderite and rhodochrosite, Geochim. Cosmochim. Acta, 68, 607–621, doi:10.1016/S0016-7037(00)00464-2, 2004.

Handley, K. M., VerBerkmoes, N. C., Steefel, C. I., Williams, K. H., Sharon, I., Miller, C. S., Frischkorn, K. R., Chourey, K., Thomas, B. C., Shah, M. B., Long, P. E., Hettich, R. L. and Banfield, J. F.: Biostimulation induces syntrophic interactions that impact C, S and N cycling in a sediment microbial community., ISME J., 7, 800–16, doi:10.1038/ismej.2012.148, 2013.

Laudon, H., Berggren, M., Ågren, A., Buffam, I., Bishop, K., Grabs, T., Jansson, M. and Köhler, S.: Patterns and dynamics of dissolved organic carbon (DOC) in boreal streams: The role of processes, connectivity, and scaling, Ecosystems, 14(6), 880–893, doi:10.1007/s10021-011-9452-8, 2011.

Li, L., Steefel, C. I., Kowalsky, M. B., Englert, A. and Hubbard, S. S.: Effects of physical and geochemical heterogeneities on mineral transformation and biomass accumulation during biostimulation experiments at Rifle, Colorado., J. Contam. Hydrol., 112(1-4), 45–63, doi:10.1016/j.jconhyd.2009.10.006, 2010.

Luther, G. W., Findlay, A. J., MacDonald, D. J., Owings, S. M., Hanson, T. E., Beinart, R. a. and Girguis, P. R.: Thermodynamics and kinetics of sulfide oxidation by oxygen: A look at inorganically controlled reactions and biologically mediated processes in the environment, Front. Microbiol., 2(April), 1–9, doi:10.3389/fmicb.2011.00062, 2011.

Maggi, F., Gu, C., Riley, W. J., Hornberger, G. M., Venterea, R. T., Xu, T., Spycher, N., Steefel, C., Miller, N. L. and Oldenburg, C. M.: A mechanistic treatment of the dominant soil nitrogen cycling processes: Model development, testing, and application, J. Geophys. Res. Biogeosciences, 113, 1–13, doi:10.1029/2007JG000578, 2008.

Manzoni, S. and Porporato, A.: Common hydrologic and biogeochemical controls along the soil-stream continuum, Hydrol. Process., 25(8), 1355–1360, doi:10.1002/hyp.7938, 2011.

Mayer, K. U., Frind, E. O. and Blowes, D. W.: Multicomponent reactive transport modeling in variably saturated porous media using a generalized formulation for kinetically controlled reactions, Water Resour. Res., 38(9), 13–1–13–21, doi:10.1029/2001WR000862, 2002.

Michalzik, B., Kalbitz, K., Park, J.-H., Solinger, S. and Matzner, E.: Fluxes and concentrations of dissolved organic carbon and nitrogen – a synthesis for temperate forests, Biogeochemistry, 52(2), 173–205, doi:10.1023/A:1006441620810, 2001.

Moore, T. R. and Dalva, M.: The influence of temperature and water table position on carbon dioxide and methane emissions from laboratory columns of peatland soils, J. soil Sci., 44(4), 651–664, 1993.

Palandri, J. L. and Kharaka, Y. K.: A compilation of rate parameters of water-mineral interaction kinetics for application to geochemical modeling., 2004.

Palmer, K., Drake, H. L. and Horn, M. A.: Association of novel and highly diverse acid-tolerant denitrifiers with N2O fluxes of an acidic fen., Appl. Environ. Microbiol., 76(4), 1125–34, doi:10.1128/AEM.02256-09, 2010.

Parkhurst, D. L. and Appelo, C. A. J.: User's guide to PHREEQC (version 2) – a computer program for speciation, batch-reaction, one-dimensional transport, and inverse geochemical calculations, Denver, CO., 1999.

Pruess, K., Oldenburg, C. M. and Moridis, G. J.: TOUGH2 User's Guide Version 2, Berkeley, CA., 1999.

Raymond, P. A., Hartmann, J., Lauerwald, R., Sobek, S., McDonald, C., Hoover, M., Butman, D., Striegl, R., Mayorga, E., Humborg, C., Kortelainen, P., Durr, H., Meybeck, M., Ciais, P. and Guth, P.: Global carbon dioxide emissions from inland waters, Nature, 503(7476), 355–359, doi:10.1038/nature12760, 2013.

Robertson, A. I., Bunn, S. E., Boon, P. I. and Walker, K. F.: Sources, sinks and transformations of organic carbon in Australian floodplain rivers, Mar. Freshw. Res., 50(8), 813, doi:10.1071/MF99112, 1999.

Sonnenthal, E., Spycher, N., Xu, T., Zheng, L., Miller, N. and Pruess, K.: TOUGHREACT V3.0-OMP reference manual: A parallel simulation program for non-isothermal multiphase geochemical reactive transport., 2014.

Steefel, C. I.: New directions in hydrogeochemical transport modeling: Incorporating multiple kinetic and equilibrium reaction pathways, Comput. Methods Water Resour. Vols 1 2 Comput. Methods Subsurf. Flow Transp. - Comput. Methods, Surf. Water Syst. Hydrol., 331–338, 2000.

Tian, H., Yang, Q., Najjar, R. G., Ren, W., Friedrichs, M. A. M., Hopkinson, C. S. and Pan, S.: Anthropogenic and climatic influences on carbon fluxes from eastern North America to the Atlantic Ocean: A process-based modeling study, J. Geophys. Res. Biogeosciences, 120(4), 757–772, doi:10.1002/2014JG002760, 2015.

Tokunaga, T., Kim, Y., Williams, K. H., Dong, W., Wan, J., Conrad, M. E., Bill, M., Robbins, M. J., Hobson, C., Faybishenko, B., Christensen, J. N., Dayvault, R. D., Long, P. E. and Hubbard, S. S.: Vadose Zone Borehole Instrumentation for Monitoring Water, Solute, and Gas Fluxes: Installations in a cobbly floodplain and initial results, Vadose Zo. J., 1–16, 2015.

U.S. Department of Energy: Final Site Observational Work Plan for the UMTRA Project Old Rifle Site, Grand Junction, CO., 1999.

Widdowson, M. A., Molz, F. J. and Benefield, L. D.: A numerical transport model for oxygen- and nitrate-based respiration linked to substrate and nutrient availability in porous media, Water Resour. Res., 24(9), 1553–1565, doi:10.1029/WR024i009p01553, 1988.

Williamson, M. A. and Rimstidt, J. D.: The kinetics and electrochemical rate-determining step of aqueous pyrite oxidation, Geochim. Cosmochim. Acta, 58, 5443–5454, doi:10.1016/0016-7037(94)90241-0, 1994.

Wu, Y.-S., Di, Y., Kang, Z. and Fakcharoenphol, P.: A multiple-continuum model for simulating single-phase and multiphase flow in naturally fractured vuggy reservoirs, J. Pet. Sci. Eng., 78(1), 13–22, doi:10.1016/j.petrol.2011.05.004, 2011.

Xu, T., Spycher, N., Sonnenthal, E., Zhang, G., Zheng, L. and Pruess, K.: TOUGHREACT Version 2.0: A simulator for subsurface reactive transport under non-isothermal multiphase flow conditions, Comput. Geosci., 37(6), 763–774, doi:10.1016/j.cageo.2010.10.007, 2011.

A REACTIVE TRANSPORT MODEL OF SULFUR CYCLING AND ISOTOPE FRACTIONATION DURING MICROBIAL RESERVOIR SOURING AND REMEDIATION

Yiwei Cheng[1], Li Li[2], Nicholas Bouskill[1], Christopher G. Hubbard[1], Sergi Molins[1], Liange Zhang[1], Eric Sonnenthal[1], Anna Engelbrektson[3], Mark E. Conrad[1], John D. Coates[3] and Jonathan Ajo-Franklin[1]

[1]Lawrence Berkeley National Laboratory, Berkeley, California, 94720, USA
[2]Pennsylvania State University, University Park, Pennsylvania, 16802, USA
[3]UC Berkeley, CA, USA
yiweicheng@lbl.gov

ABSTRACT

In this study, we describe the mechanistic incorporation of microbial metabolic reaction pathways and associated sulfur isotope fractionation into a reactive transport model (RTM) of souring/desouring (nitrate) dynamics, using the TOUGHREACT code. The RTM simulates the spatio-temporal evolution of the primary chemical species (e.g. sulfate, sulfide, nitrate, sulfate $\delta^{34}S$ and the microbial dynamics involved in the souring and desouring processes, as described in a recent laboratory experiment stimulating and treating sulfate reduction. The growth and inhibition dynamics of the various bacterial population (i.e. sulfate reducers and nitrate reducers) are explicitly represented within the RTM. In this work, we demonstrate the kinetic isotope fractionation capability of TOUGHREACT applied to the kinetics of the individual sulfate isotopologues, i.e. $^{32}SO_4^{2-}$ and $^{34}SO_4^{2-}$, with a modified dual Monod rate expression. The reaction network developed for nitrate amendment successfully reproduced measurements from the column experiments. The modification of the dual Monod rate expression in TOUGHREACT allows for another method of treating biologically-mediated isotopic fractionation to interpret chemical and isotopic data.

INTRODUCTION

Effective control of reservoir souring in the oil field is important from both economic and operational safety perspectives. Souring is a phenomenon associated with an increase in mass of hydrogen sulfide (H_2S) per unit mass of total produced oil in the field. Not only does H_2S pose health risks to workers on site (*Fuller and Suruda*, 2000), its corrosive nature compromises the integrity of metallic structure and pipeline equipment (*Vance and Thrasher*, 2005). Souring is most pronounced during the enhanced oil recovery (EOR) phase, when fluid is injected into the reservoir to maintain pressure and sweep the remaining oil out. In natural settings, water within the reservoir formation often contains low concentrations of sulfate, limiting the activities of the sulfate reducing bacteria (SRB) population. During EOR, re-injection of produced water mixed with seawater is common in offshore platforms. The injected mixture contains high concentrations of sulfate and DOC, stimulating the activity of the SRB.

Remediation methods of reservoir souring focus on inhibiting the growth and activities of SRB. In the past decade, a common alternative to biocide treatment has been the injection of nitrate (*Voordouw et al*, 2009; *Hubert et al*, 2010; *Gieg et al*, 2011). The microbiological mechanisms by which nitrate inhibits souring are: (1) competition between heterotrophic nitrate reducers (hNRB) and SRB for electron donors, (2) inhibition of sulfate reduction by nitrite (*Callbeck et al*, 2013), and (3) activity of nitrate reducing sulfide oxidizing bacteria (NR-SOB) (*Hubert and Voordouw*, 2007; *Haghshenas et al*, 2012).

In addition to geochemical data, isotopic data collected may also help to elucidate and quantify the microbial reactions associated with reservoir souring/desouring. In several field studies, measurements of stable sulfur isotope ratios have been used to determine whether the source of sulfide production in oil reservoirs was biogenic or thermochemical (*Martins et al*, 2006; *Nengkoda et al*, 2009). Sulfate reducing bacteria (SRB) favor the reduction of the lighter sulfate isotopologue ($S^{32}O_4^{2-}$) over the heavier isotopologue ($S^{34}O_4^{2-}$), leading to a progressive

and distinctive enrichment of the remaining sulfate in the heavier isotopologue as sulfate reduction proceeds. In an experimental study, $\delta^{34}S$ and $\delta^{18}O$ data were measured concurrently to tease apart the impacts of hNRB and that of the NR-SOB during nitrate treatment (*Hubert et al*, 2009). Finally, monitoring the $\delta^{34}S$ of sulfate has been proposed as an early indicator of sulfate reduction for oil reservoirs with significant sulfide scavenging potential (*Hubbard et al*, 2014).

Accurate modeling of reservoir souring and remediation is important for the design of field scale remediation efforts. In addition, models are focal points in which disparate processes observed in experiments are incorporated in synergy to provide more integrative perspectives. Descriptive and analytical models for reservoir souring have existed for two decades (*Ligthelm et al*. 1991, *Eden et al*., 1993). In line with the rapid growth in computational power, reservoir-souring models in recent years are more complex in their representation of key processes. An example of this is UTCHEM (*Farhadinia et al*., 2010), a multicomponent reservoir model which includes a biological souring module (*Haghshenas et al* 2011). The model was developed to simulate the control of reservoir-souring by nitrate amendments (*Haghshenas et al*. 2011), by explicitly simulating the growth of sulfate reducing bacteria (SRB), nitrate reducing bacteria (NRB) and nitrate-reducing-sulfide-oxidizing bacteria (NR-SOB). While the biological souring module of *Haghshenas et al* (2012) has incorporated the dynamics of NR-SOB, the interactive dynamics of NR-SOB with SRB and hNRB were not demonstrated in the validation simulations.

The objective of this paper is a rigorous mechanistic incorporation of microbiological reactions and associated kinetic sulfur isotope fractionation involved in reservoir souring and desouring treatments (nitrate), into TOUGHREACT. The overall aim is to provide a comprehensive understanding of the abiotic and biotic factors affecting SRB dynamics, the source of sulfidogensis in oil reservoirs. Specifically, this study simulates the interactions between SRB with other microbial populations such as NRB and NR-SOB during nitrate treatments respectively, to better understand how these interactions inhibit the production of hydrogen sulfide. Finally, the incorporation of isotope dynamics extends the capabilities of TOUGHREACT as a modeling tool to better interpret chemical and isotopic data, and predict biologically-mediated geochemical processes in the subsurface.

DESCRIPTION OF PREVIOUSLY CONDUCTED COLUMN EXPERIMENT

Datasets utilized in this modeling study were derived from the laboratory column studies described by *Engelbrektson et al* (2014). Briefly, the aim of the flow-through column study was to compare the effectiveness of nitrate amendments against (per)chlorate amendments, a novel biological control over the production of hydrogen sulfide. The columns were packed with a mixture of 50% San Francisco Bay sediment (microbial inoculum) and 50% glass beads (70-100 µm diameter), which resulted in a matrix with porosity 0.33. The columns were continuously flooded with San Francisco Bay water (19-33 mM sulfate) with 1 $g.L^{-1}$ yeast extract (labile complex carbon source) and 10 mM of either one of the following (depending on the treatment): sodium nitrate, sodium chlorate, sodium perchlorate, no treatment control. Between Day 35 and Day 37, the treatment concentration was briefly reduced to 5 mM. Each treatment consisted of triplicate columns. Two flow regimes were prescribed throughout the experiment. For the first 28 days, flow was alternated between periods of high flow (0.1 $mL.min^{-1}$) and zero flow. For the remainder of the experiment (Day 29 – 51), flow was continuous, at a flow rate of 0.025 $mL.min^{-1}$. Sulfur isotope ratios of dissolved sulfate samples from each treatment were also measured. The ratios were reported in standard delta notation relative to the Canyon Diablo Troilite standard (R_{std} = 0.0441216), $\delta\ ^{34}S = (R_{sample}/R_{std} - 1) \times 1000$, where $R = {}^{34}S/{}^{32}S$. $\delta^{34}S$ were reported in per mil (‰).

In this work, reactive transport modeling was conducted for the following cases: (1) No treatment (sulfate reduction only), and (2) Nitrate treatment. The RTM utilized and the

simulations conducted are described in the following sections.

CONCEPTUAL MODEL

A multicomponent, multi-phase reactive transport simulator, TOUGHREACT (*Xu et al*, 2011), was used to systematically elucidate the impacts of microbial processes and abiotic mechanisms (e.g. mineral precipitation) on sulfate, sulfide concentrations and sulfate isotopes. In this work, we also demonstrate for the first time, the kinetic isotope fractionation capability of TOUGHREACT applied to the kinetics of the individual sulfate isotopologues, i.e. $^{32}SO_4^{2-}$ and $^{34}SO_4^{2-}$, with a modified dual Monod rate expression.

Microbially Mediated Reactions and Kinetic Isotope Fractionation

In this work, reactive transport modeling is conducted for the following cases:
(i). No treatment, sulfate reduction only: We explicitly represent microbially mediated reduction of $^{32}SO_4^{2-}$ and $^{34}SO_4^{2-}$. Following the concepts as described by *Rittmann and McCarty* (2001), microbially mediated reactions are divided into two components: catabolic and anabolic. For each mole of electron donor/substrate utilized, a fraction, *fs*, is conserved by the microbial biomass for cell synthesis (anabolic) while the remaining fraction, *fe*, is used for energy production (catabolic). Values of fe and fs are 0.92 and 0.08 respectively, following values used in *Druhan et al*, 2014 (Table 1, Rxns 1-2).

As biologically mediated reactions, kinetics of isotope fractionation are best described by a Michaelis-Menten (MM) type function that occurs with reaction orders between zero and one. The isotopic fractionation factor: ratio of the rare to common isotope in the product species over the ratio of the rare to common isotope in the reactant species, is variant as the MM expression transition between zero and first order (*Druhan et al*, 2014). When substrates (sulfate and organic carbon) are not limiting, reaction order is zero order, fractionation factor is dependent on the concentrations of the isotopologues. On the other hand, as substrates become limiting, reaction order becomes first order, and fractionation factor is independent of the concentration of the isotopologues. Reactive transport models of isotope fractionation typically assume first order reactions (*Gibson et al*, 2011; *Wehrmann et al*, 2013). This can lead to erroneous predictions when the model transitions between reaction orders. A more general rate expression demonstrated by *Maggi and Riley* (2009) and more recently implemented in a reactive transport model, CRUNCHTOPE (*Druhan et al*, 2014) resolves this issue:

$$^{32}r = {}^{32}\mu[SRB]\frac{\left[{}^{32}SO_4^{2-}\right]}{\left[{}^{32}SO_4^{2-}\right] + {}^{32}K_s\left(1+\frac{\left[{}^{34}SO_4^{2-}\right]}{{}^{34}K_s}\right)} \quad (2)$$

$$^{34}r = {}^{34}\mu[SRB]\frac{\left[{}^{34}SO_4^{2-}\right]}{\left[{}^{34}SO_4^{2-}\right] + {}^{34}K_s\left(1+\frac{\left[{}^{32}SO_4^{2-}\right]}{{}^{32}K_s}\right)} \quad (3)$$

Where SRB is sulfate reducing bacteria. Next, by assuming a common half saturation constant for both ^{32}r and ^{34}r and accounting for the dependency on electron donor (dissolved organic carbon) concentration:

$$^{32}r = {}^{32}\mu[SRB]\frac{\left[{}^{32}SO_4^{2-}\right]}{\left[SO_4^{2-}\right] + K_S^{SO_4}}\frac{[DOC]}{[DOC] + K_S^{DOC}} \quad (4)$$

$$^{34}r = {}^{34}\mu[SRB]\frac{\left[{}^{34}SO_4^{2-}\right]}{\left[SO_4^{2-}\right] + K_S^{SO_4}}\frac{[DOC]}{[DOC] + K_S^{DOC}} \quad (5)$$

The fractionation factor (α) can be calculated as shown below. Note that the fractionation factors α and ε are related according to $\varepsilon \approx 1000.(\alpha - 1)$.

TABLE 1. Microbial and iron-sulfide reactions modeled.

Microbial Reactions	
1	**Sulfate Reduction** ($^{32}SO_4^{2-}$ -> $H_2{}^{32}S_{(aq)}$) (fs = 0.08, fe = 0.92)**
	$^{32}SO_4^{2-} + 1.082DOC + 3.05NH_4^+ \rightarrow 0.033C_5H_7O_2N_{SRB} + 2.1H_2O + 2CO_{2(aq)} + H_2{}^{32}S_{(aq)}$
2	**Sulfate Reduction** ($^{34}SO_4^{2-}$ -> $H_2{}^{34}S_{(aq)}$) (fs = 0.08, fe = 0.92)
	$^{34}SO_4^{2-} + 1.082\ DOC + 3.05NH_4^+ \rightarrow 0.033C_5H_7O_2N_{SRB} + 2.1H_2O + 2CO_{2(aq)} + H_2{}^{34}S_{(aq)}$
3	**Heterotrophic Nitrate Reduction** (NO_3^- -> NO_2^-) (fs = 0.5, fe = 0.5)
	$0.125DOC + 0.25NO_3^- + 0.025NH_{3(aq)} + 0.025H^+ \rightarrow 0.025C_5H_7O_2N_{NRB} + 0.1H_2O + 0.025CO_{2(aq)} + 0.1HCO_3^- + 0.25NO_2^-$
4	**Heterotrophic Nitrite Reduction** (NO_2^- -> N_2) (fs = 0.6, fe = 0.4)
	$0.125DOC + 0.133NO_2^- + 0.03NH_{3(aq)} + 0.163H^+ \rightarrow 0.03C_5H_7O_2N_{NRB} + 0.1617H_2O + 0.125CO_{2(aq)} + 0.095HCO_3^- + 0.0667N_{2(aq)}$
5	**Nitrate Reduction Sulfide Oxidation** (NO_3^- -> NO_2^-) (fs = 0.15, fe = 0.85)
	$0.425NO_3^- + 0.0075NH_{3(aq)} + 0.03CO_{2(aq)} + 0.0075HCO_3^- + 0.125H_2{}^{32}S_{(aq)} + 0.0075H_2O \rightarrow 0.0075\ C_5H_7O_2N_{NSOB} + 0.12^{32}SO_4^{2-} + 0.425NO_2^- + 0.2425H^+$
6	**Nitrite Reduction Sulfide Oxidation** (NO_2^- -> N_2) (fs = 0.25, fe = 0.75)
	$0.25NO_2^- + 0.0125NH_{3(aq)} + 0.05CO_{2(aq)} + 0.0125HCO_3^- + 0.125H_2{}^{32}S_{(aq)} + 0.0125H^+ \rightarrow 0.0125\ C_5H_7O_2N_{NSOB} + 0.125^{32}SO_4^{2-} + 0.125N_{2(aq)} + 0.1125H_2O$
7	**Nitrate Reduction Sulfide Oxidation** (NO_3^- -> NO_2^-) (fs = 0.15, fe = 0.85)
	$0.425NO_3^- + 0.0075NH_{3(aq)} + 0.03CO_{2(aq)} + 0.0075HCO_3^- + 0.125H_2{}^{34}S_{(aq)} + 0.0075H_2O \rightarrow 0.0075\ C_5H_7O_2N_{NSOB} + 0.12^{34}SO_4^{2-} + 0.425NO_2^- + 0.2425H^+$
8	**Nitrite Reduction Sulfide Oxidation** (NO_2^- -> N_2) (fs = 0.25, fe = 0.75)
	$0.25NO_2^- + 0.0125NH_{3(aq)} + 0.05CO_{2(aq)} + 0.0125HCO_3^- + 0.125H_2{}^{34}S_{(aq)} + 0.0125H^+ \rightarrow 0.0125\ C_5H_7O_2N_{NSOB} + 0.125^{34}SO_4^{2-} + 0.125N_{2(aq)} + 0.1125H_2O$
Iron-Sulfide Reactions	
9	$Fe^{2+} + H_2{}^{32}S_{(aq)} \leftrightarrow Fe^{32}S_{(am)} + H^+$
10	$Fe^{2+} + H_2{}^{34}S_{(aq)} \leftrightarrow Fe^{34}S_{(am)} + H^+$
11	$Fe(OH)_{3(s)} + 0.5H_2{}^{32}S_{(aq)} + 2.5H^+ \leftrightarrow Fe^{2+} + 0.5^{32}S_{(s)} + H_2O + 2.0OH^-$
12	$Fe(OH)_{3(s)} + 0.5H_2{}^{34}S_{(aq)} + 2.5H^+ \leftrightarrow Fe^{2+} + 0.5^{34}S_{(s)} + H_2O + 2.0OH^-$

** fs and fe values calculcated based on method and using free energy values as described in Rittman and MaCarty (2001).

$$\alpha = \frac{^{34}\mu}{^{32}\mu} \tag{6}$$

This modified dual Monod rate law adds to the existing capability of TOUGHREACT in terms of simulating isotope fractionation as recently developed by *Wanner and Sonnenthal* (2013). Cr isotope fractionation as simulated by *Wanner and Sonnenthal* (2013) occurs due to kinetic mineral precipitation of Cr(III)-hydroxide, an abiotic reaction between Cr(VI) and Fe(II). Rate expressions describing the kinetics of the isotopologues are assumed to be of first order.

(ii). Nitrate treatment: In this work, the focus is on simulating the dynamics of hNRB and NR-SOB. For each group the denitrification reaction is split into two parts: (1) $NO_3 \rightarrow NO_2^-$, then (2) $NO_3^- \rightarrow N_2$. Currently, reduction of nitrate to ammonia is not considered.

The hNRB competes with the SRB for the same electron donor but uses nitrate and nitrite as electron acceptors:

$$r^{hNRB}_{NO3->NO2} = \mu^{hNRB}_{NO3->NO2}[hNRB]\frac{[NO_3^-]}{[NO_3^-]+K_S^{NO_3}}\frac{[DOC]}{[DOC]+K_S^{DOC}} \tag{10}$$

$$r^{hNRB}_{NO2->N2} = \mu^{hNRB}_{NO2->N2}[hNRB]\frac{[NO_2^-]}{[NO_2^-]+K_S^{NO_2}}\frac{[DOC]}{[DOC]+K_S^{DOC}} \tag{11}$$

In order to represent the inhibitory impacts of nitrite the following term is multiplied to Eqns (4) and (5):

$$\frac{K_S^{NO2}}{[NO_2]+K_S^{NO_2}} \tag{12}$$

NR-SOB mediates souring by removing sulfide from the system. Nitrate/nitrite are used as electron acceptor while sulfide is utilized as the electron donor:

$$r_{NO3->NO2}^{NRSOB} = \mu_{NO3->NO2}^{NRSOB}[NRSOB]\frac{[NO_3^-]}{[NO_3^-]+K_S^{NO_3}}\frac{[^{32}S^{2-}]}{[^{32}S^{2-}]+K_S^S} \quad (13)$$

$$r_{NO2->N2}^{NRSOB} = \mu_{NO2->N2}^{NRSOB}[NRSOB]\frac{[NO_2^-]}{[NO_2^-]+K_S^{NO_2}}\frac{[^{32}S^{2-}]}{[^{32}S^{2-}]+K_S^S} \quad (14)$$

The above equations also apply to $^{34}S^{2-}$. Values associated with the kinetics parameters described above are listed in Table 2.

TABLE 2 | Associated kinetic and thermodynamic parameters of reactions listed in Table 2.

Microbial reactions (Rxn number from Table 2)	μ (1/s)	$K_{acceptor}$ (mol/kg H_2O)	K_{donor} (mol/kg H_2O)
1	7.0 x 10^{-4} (a)	5.0 x 10^{-3} (b)	1.0 x 10^{-4} (c)
2	6.867623 x 10^{-4} (a)	5.0 x 10^{-3} (b)	1.0 x 10^{-4} (c)
3	8.0 x 10^{-4} (d)	1.0 x 10^{-3} (e)	1.0 x 10^{-3} (e)
4	1.1 x 10^{-4} (d)	1.0 x 10^{-3} (e)	1.0 x 10^{-3} (e)
5	9.0 x 10^{-4}	5.0 x 10^{-4} (e)	5.0 x 10^{-4}
6	7.0 x 10^{-4}	5.0 x 10^{-4} (e)	5.0 x 10^{-4}
7	9.0 x 10^{-4}	5.0 x 10^{-4} (e)	5.0 x 10^{-4}
8	7.0 x 10^{-4}	5.0 x 10^{-4} (e)	5.0 x 10^{-4}
Mineral dissolution and precipitation (Rxn number from Table 2)	log$k$ (mol/m^2/s)	logK_{eq}	
9, 10	-7.0 (f)	3.5 (f)	
11,12	-10.0 (f)	-19.6 (f)	

(a) Range: 1.13x10^{-4} – 1.189 x 10^{-3} s^{-1} based on Druhan et al (2014), Jin and Roden (2011).

(b) Range: 0.01 – 7.5 mM based on Pallud and Van Cappellen (2006), Porter et al. (2007), Fang et al. (2009), Li et al. (2009), Jin and Roden (2011), Druhan et al (2014).

(c) Range: 0.0043 – 5.0 mM based on Pallud and Van Cappellen (2006), Porter et al. (2007), Fang et al. (2009), Li et al. (2009), Jin and Roden (2011), Druhan et al (2014).

(d) Adapted from Maggi et al (2008).

(e) Adapted from Maggi et al (2008).

(f) Values from Li et al. (2009), Druhan et al (2014).

Model Setup

The flow columns are modeled as porous medium with approximately 0.12 m (height of columns) long 1D flow path. As such the simulation domain is discretized into 120 units each 0.001 m. Porosity as calculated using known flow velocity and volume of the column is 0.33. A flux boundary condition is specified at the first cell of the model. Flow rates mirror the rates used in the column experiments (see **Description of Previously Conducted Column Experiment** and Figure 1). Composition of the injection fluid varies depending on treatment (no treatment and nitrate injection) and are listed in Table 3.

TABLE 3 | Aqueous species concentrations in Initial Water (IW) and Amendment Water (AW) for all three cases.

Species	Initial Water (IW) (mmol/kg H_2O)	Amendment Water (AW) (mmol/kg H_2O)
pH	7.2	7.2
Na(I)	483	483
Mg(II)	53	53
Ca(II)	10	10
Fe(II)	0.0	0.0
NH_4(I)	5.0	5.0
Cl(-I)	426	426
SO_4(-II)	19.0	Varying; see Fig. 1
HCO_3(I)	8.73	8.73
DOC*	20.0	20.0
S(-II)	0.0	0.0
For nitrate treatment		
NO_3(-I)	0.0	Varying; see Fig. 2

Results from the column experiment revealed a delay in sulfide breakthrough in comparison to the $\delta^{34}S$ breakthrough, suggesting the presence of iron mineral-sulfide reactions. These reactions are represented following the reaction network as utilized in *Li et al* (2009, 2010), *Druhan et al*. 2014).

RESULTS AND DISCUSSION

No treatment, sulfate reduction only

Despite the fluctuating influent sulfate concentrations (between 18 – 33 mM), the model was able to capture the timing of the effluent sulfate concentrations during both the batch and the continuous phases (Figure 1A).

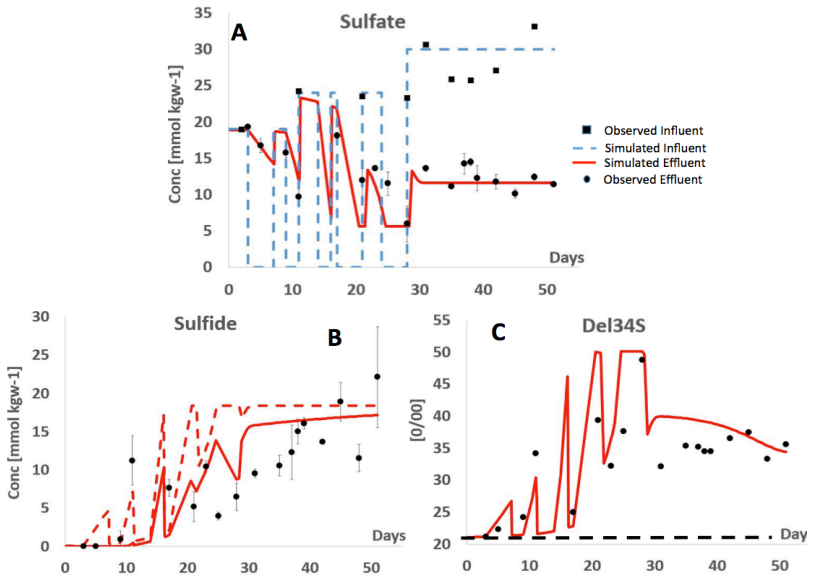

Figure 1. | No treatment control: (A) Observed and simulated influent and effluent sulfate concentration with time. (B) Observed and simulated influent and effluent sulfide concentration with time. Simulated sulfide for different iron content are also shown: No iron present (fine dashed line), and baseline (solid line). (C) Observed and simulated influent and effluent $\delta^{34}S$ with time. $\delta^{34}S$ for seawater is shown as the black dashed line.

Similarly, the model was able to capture the rising trend of sulfide concentration that is consistent with the observed effluent sulfide concentration (Figure 1B).

The model also captured the rise in $\delta^{34}S$ throughout the experiment. The kinetic fractionation factor, α, used in this study is 0.9804, similar to the experimental data. The α value is also within the reported range of 0.9579 – 0.987 used in previous modeling studies (*Waybrant et al*, 2002; *Guo and Blowes*, 2009; *Gibson et al*, 2011; *Druhan et al*, 2014). $\delta^{34}S$ values greater than the reference seawater signal of 21‰ (dashed black line) correspond to the decrease in effluent sulfate concentrations relative to influent values and represent the occurrence of microbial sulfate reduction.

The data revealed a delay in sulfide breakthrough in comparison to changes in both the effluent sulfate and $\delta^{34}S$ values, suggesting the possibility of iron mineral-sulfide reactions. Such delay in effluent sulfide had been observed in earlier field and column studies (*Druhan et al*, 2014) and points to $\delta^{34}S$ values as more reliable proxy for onset of sulfate reduction (*Hubbard et al*, 2014). Observed effluent sulfate and $\delta^{34}S$ pointed towards the occurrence of sulfate reduction as early as the first shutoff period (Day 3 – 7). Effluent sulfate decreased by as much as 4.0 mmol kgw^{-1} and effluent $\delta^{34}S$ increased by 4.0‰ by the end of first shutoff period. However, no rise in the effluent sulfide concentration was observed during the same period. Limited iron mineral data were available from the experiment. The iron-containing mineral was represented as $Fe(OH)_3$ with an assumed surface area of 40 m^2/g (*Poulton et al*., 2004) and logK of -10.0, consistent with geothite being a low reactive iron mineral (*Poulton et al*, 2004), and an optimal initial 0.1% of goethite. The reaction product between this iron mineral and sulifide was elemental sulfur (Table 2) (*Yang et al*., 2009; *Li et al*., 2009, 2010). In the absence of the iron mineral-sulfide reactions, sulfide breakthrough mirrored the changes in effluent sulfate and $\delta^{34}S$ (dashed red line in Figure 1B).

Nitrate Treatment

Observed effluent data showed that sulfate concentrations remained similar to the influent concentrations during much of the batch flow phase. However, beyond Day 20, sulfate reduction proceeded at detectable rate, as shown by the effluent $\delta^{34}S$ and sulfide data. Effluent sulfide concentrations increased as early as day 30 and reached a maximum of about 4 mmol kgw^{-1}. The model successfully captured the trends of the effluent $\delta^{34}S$, nitrate, sulfate and sulfide (Figure 2B). During batch phase,

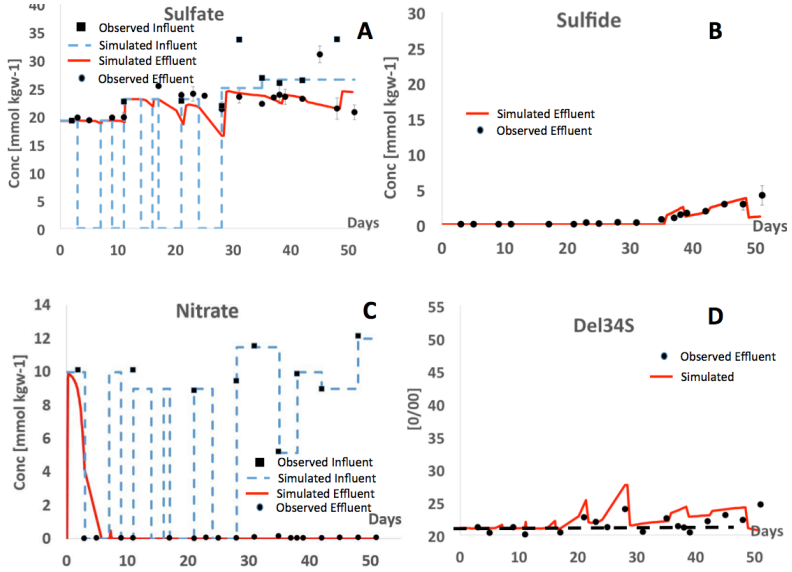

Figure 2 | (A) Observed and simulated influent and effluent sulfate concentration with time. (B) Observed and simulated influent and effluent sulfide concentration with time. (C) Observed and simulated influent and effluent nitrate concentration with time. (D) Observed and simulated influent and effluent $\delta^{34}S$ with time.

effluent nitrate concentrations remained zero suggesting rapid nitrate utilization. While no data were collected during periods of flow, it can be postulated that during periods of flow, effluent nitrate may be lower than the influent concentration given such high nitrate reduction rates. The model under predicted nitrate reduction rates in the first 5 days however reproduced the trend thereafter (Figure 2C).

Similar to *Haghshenas et al* (2012) our model represents the following processes: (1) direct inhibition by nitrite; (2) competition between hNRB and SRB for growth limiting carbon substrates; (3) re-oxidation of sulfide (coupled to nitrate and nitrite reduction) by NR-SOB. The model results shown here extend the nitrate treatment modeling study by *Haghshenas et al* (2012). While the biological module of the general purpose adaptive reservoir simulator (GPAS) developed by *Haghshenas et al* (2012) has incorporated the dynamics of NR-SOB, the interactive dynamics of NR-SOB with SRB and hNRB were not demonstrated in the validation simulations.

CONCLUSION

In this work, TOUGHREACT has shown promise as a numerical tool that is able to capture the first order dynamics of the microbial populations involved in souring/desouring. The inclusion of isotope dynamics within the model structure reveals dynamics previously not easily discernable from chemical data alone, which in turn can be used to better constrain reaction rates and associated model parameters.

ACKNOWLEDGMENT

This work was funded by the Energy Biosciences Institute.

REFERENCES

Callbeck, C. M., Agrawal, A., and Voordouw, G. Acetate production from oil under sulfate-reducing conditions in bioreactors injected with sulfate and nitrate. *Appl. Environ. Microbiol.* **2013**, 79, 5059-5068. Doi:10.1128/AEM.01251-13.

Druhan, J. L.; Steefel, C. I.; Conrad, M. E.; DePaolo, D. J. A large column analog experiment of stable isotope variations during reactive transport: I. A comprehensive model of sulfur cycling and $\delta^{34}S$ fractionation. *Geochim. Cosmochim. Acta,* **2014**, 124, 366-393.

Eden, B.; Laycock, P. J.; Fielder, M. *Oilfield Reservoir Souring*. HSE Books, 1993.

Engelbrektson, A.; Hubbard, C. G.; Piceno, Y.; Boussina, A.; Jin, Y. T.; Wong, H.; Carlson, H.; Conrad, M. E.; Anderson, G.; Coates, J. D. Inhibition of microbial sulfate reduction in a flow-through column system by (per)chlorate treatment. *Front. Microbiol.* **2014**, doi: 10.3389/fmicb.2014.00315.

Fang, Y. L.; Yabusaki, S. B.; Morrison, S. J.; Amonette, J. P.; Long, P. E. Multicomponent reactive transport modeling of uranium bioremediation field experiments. *Geochim. Cosmochim. Acta,* **2009**, 73, 6029–6051.

Farhadinia, M.A.;' Bryant, S.L.; Sepehrnoori, K.; Delshad, M. Development and implementation of a multidimensional reservoir souring module in a chemical flooding simulator. *Petroleum science and technology*, **2010**, 28(6): 535-546.

Fuller, D. C., and Suruda, A. J. Occupationally related hydrogen sulfide deaths in the United States from 1984 to 1994. *J. Occup. Environ. Med*. **2000**, 42, 939-942. Doi:10.1097/00043764-200009000-00019.

Gieg, L., Jack, T., and Foght, J. Biological souring and mitigation in oil reservoirs. *Appl. Microbiol. Biotechnol*. **2011**, 92, 263-282. Doi:10.1007/s00253-011-3542-6.

Haghshenas, M.; Sepehrnoori, K.; Bryant, S.; Farhadinia, M. Modeling and simulation of nitrate injection for reservoir souring remediation. *SPE International Symposium on Oilfield Chemistry*, 2011.

Hubbard, C. G., Cheng, Y., Engelbrekston, A., Druhan, J. L., Li, L., Ajo-Franklin, J. B., … Conrad, M. E. Isotopic insights into microbial sulfur cycling in oil reservoirs. *Frontiers in Microbiology*. **2014**, *5*, 480. doi:10.3389/fmicb.2014.00480

Hubert, C.; Voordouw, G. Oil field souring control by nitrate-reducing Sulfurospirillum spp. that outcompete sulfate reducing bacteria for organic electron donors. *Appl Environ Microbiol*. **2007**, 73(8): 2644 – 2652.

Hubert, C., Voordouw, G., and Mayer, B. Elucidating microbial processes in nitrate- and sulfate-reducing systems using sulfur and oxygen isotope ratios: the example of oil reservoir souring control. *Geochim, Cosmochim. Acta*, **2009**, 73, 3864-3879. Doi: 10.1016/j.gca.2009.03.025.

Hubert, C. "Microbial ecology of oil reservoir souring and its control by nitrate injection," in Handbook of Hydrocarbon and Lipid Microbiology, ed K. Timmis (Berlin; Heidelberg: Springer), **2010**, 2753-2766.

Li, L.; Steefel, C. I.; Williams, K. H.; Wilkins, M. J.; Hubbard, S. S. Mineral transformation and biomass accumulation associated with uranium bio-remediation at Rifle, Colorado. *Environ. Sci. Technol*. **2009**, 43, 5429–5435.

Li, L.; Steefel, C. I.; Kowalsky, M. B.; Englert, A.; Hubbard, S. S. Effects of physical and geochemical heterogeneities on mineral transformation and biomass accumulation during biostimulation experiments at Rifle, Colorado. *J. Contam. Hydrol*. **2010**, 112, 45–63.

Ligthelm, D. J.; de Boer, R.B.; Brint, J.F.; Schulte, W.M. Reservoir souring: an analytical model for H2S generation and transportation in an oil reservoir owing to bacterial activity. Paper SPE 23141 presented at the Offshore Europe, Aberdeen, 3 – 6 September, 1991.

Maggi, F.; Gu, C.; Riley, W. J.; Hornberger, G. M.; Venterea, R. T.; Xu, T.; Spycher, N.; Steefel, C.; Miller, N. L.; Oldenburg, C. M. A mechanistic treatment of the dominant soil nitrogen cycling processes: Model development, testing and application. *J. Geophys. Res*. **2008**, 113, G02016, doi:10.1029/2007JG000578.

Poulton, S. W.; Krom, M. D.; Raiswell, R. A revised scheme for the reactivity of iron (oxyhydr)oxide minerals towards dissolved sulfide. *Geochim. Cosmochim. Acta*, **2004**, 68(18), 3703-3715.

Rittman, B. E.; MaCarty, P. L. Environmental biotechnology: principles and applications. McGraw-Hill, New York, 2001.

Vance, I., and Thrasher, D. R. "Reservoir souring: mechanisms and prevention," in Petroleum Microbiology, eds B. Ollivier, and M. Magot (Washington, DC: ASM Press), 123-142.

Voordouw, G., Grigoryan, A. A., Lambo, A., Lin, S., Park, H. S., Jack, T. R. Sulfide remediation by pulsed injection of nitrate into low temperature Canadian heavy oil reservoir. Environ. Sci. Technol. **2009**, 43, 9512-9518. Doi:10.1021/es902211j.

Wanner C., and Sonnenthal, E. L. Assessing the control on the effective kinetic Cr isotope fractionation factor: A reactive transport modeling approach. *Chemical Geology*, **2013**, 337-338, 88-98.

Xu, T., Spycher, N.F., Sonnenthal, E., Zhang, G., Zheng, L., Pruess, K. TOUGHREACT version 2.0: a simulator for subsurface reactive transport under non isothermal multiphase flow conditions. *Computer & Geoscience*, **2011**, 37, 763–774.

TOUGHREACT WRAPPING USING PYTHON TOWARDS CODE INTERCOMPARISON

Dimier Alain [(1)], Zorn Roman[(1)], Gherardi Fabrizio [(2)]

[(1)] KIT Karlsruhe, EIFER Institute – Karlsruhe, Germany
[(2)] Consiglio Nazionale delle Ricerche, Istituto di Geoscienze e Georisorse – Pisa, Italy

e-mail: Alain.Dimier@eifer.uni-karlsruhe.de

ABSTRACT

A former study based on a code intercomparison using TOUGHREACT (Xu et al., 2004) and PHREEQC (Parkhurst and Appelo, 1999) fostered the idea that a unique geochemical formulation of all data linked to the physical problem to be modelled would favour the quality of the analysis developed in such studies. Therefore, the work initiated on the coupling environment for PHREEQC (Parkhurst and Appelo, 1999) and Elmer (Råback, 2008), wherein the two codes are used as Python shared objects, served as a basis for an extension to include the TOUGHREACT/EOS3 module in that environment. In this framework, TOUGHREACT/EOS3 is handled as a Python shared object, and its geochemical component is coupled to Elmer (Råback, 2008).

In this manuscript, we present the data model enabling a common formulation of a geochemical-transport model, and we illustrate the way TOUGHREACT/EOS3 can be wrapped in Python and used as a Python module.

INTRODUCTION

Geothermal activities at Eifer favored the development of a numerical tool where various multi-physical simulation softwares with disjunctive application fields, like PHREEQC (Parkhurst and Appelo, 1999) and Elmer (Råback et al., 2014), are gathered within one environment to broaden their respective application area. The targeted application is multidimensional (1D to 3D), multi-component, non-isothermal reactive solute transport studies, eventually coupled to geomechanics, limited to the linear elasticity field (2D/3D).

A previous study (Dimier and Gherardi, 2012) presented the idea of introducing the TOUGHREACT/EOS3 module in the aforementioned environment. This development was made in two steps. First, the initial platform data model was modified to enable a generic data introduction prior to the geochemical tool choice, PHREEQC or TOUGHREACT. The second development step was to wrap TOUGHREACT in Python to enable its use as a shared object; like PHREEQC, in the generic coupling tool algorithm.

GEOCHEMICAL MODEL

The first step was to set up a data model covering the physics to be handled. Herein every element of the physical model is associated to a class enabling a complete description and instantiation, of each physical element, going from the conceptual model to an instantiated one.

All necessary data to describe the geochemical model are gathered in one class called "GeochemicalSystem".

As an example, that class enables the description of all chemical elements needed to specify the initial and boundary conditions of the model. Specific to the use of TOUGHREACT, we have to give a list of primary and secondary species, aqueous complexes, minerals, gases, surface complexes, and exchangeable cations. This information can also be used to define a PHREEQC simulation in conjunction with the llnl.dat file and a specific PHREEQC water.dat database; the last one containing only water linked elements.

Linked to the database elements we have to define initial and boundary conditions. This is made for initial and boundary conditions in the same generic way; these two classes gather within their arguments a material and all elements necessary to the description of the relevant geochemistry:

```
ic= InitialCondition(name = "trial",
                     material = Rock1,
                     aqueousSolution = plugAS,
                     mineralSpecies=[calciteConc],\
                     gaseousSpecies = None,
                     cationExchange = None)
```

In the preceding initial condition example, Rock1 is an instantiation of a material class; that class entails all elements linked to the description of the solid matrix, effective diffusion, permeability, porosity, etc…

plugAqueousSolution is the instantiation of the AqueousSolution class which holds every aqueous species involved in the aqueous phase, its pH and its temperature.

```
plugAqueousSolution=AqueousSolution(
        elementConcentrations = [\
ElementConc('HCO3-',value=1.348e-3,unit="mol/l"),
ElementConc('Ca+2',value=79.13e-4,unit="mol/l"),
ElementConc('Na+',value=1.062e+0,unit= "mol/l"),\
ElementConc('Cl-',value=1.062e+00,unit= "mol/l"),\
ElementConc('SiO2(aq)',value=7.2e-4,unit="mol/l")],
pH = pH_ic, temperature = plugTemp,
balance = None, units = None)
```

Apart from the material, these elements are the major ones for the definition of the geochemical system. Others elements are linked to the definition of the problem: the tool to be used, the input parameters, the type and number of outputs, the type and size of the mesh it is applied on.

Once the whole problem is defined, the three TOUGHREACT standard input files are written using two command lines:

```
problem.flowTransportWriter()
problem.geochemicalTransportWriter()
```

Note that the way TOUGHREACT files are generated is independent of the way the tool will be used: only as a geochemical solver or as a coupled flow geochemical transport solver.

The use of such an object-oriented programming enables to define a case study through class instantiation and module parametrization. In that way, the user gains more insight in its studies due to the setup of comprehensive data / object bindings. Moreover, he doesn't need to do input file formatting through the automation of that part of the work.

WRAPPING

In the present context we want to transform, to some extent, the TOUGHREACT/EOS3 executable into a Python module, with methods exposed to the user. Those methods will enable the user to run a TOUGHREACT/EOS3 simulation in a similar way as the standalone code, or to use only its geochemical part for coupling with other flow or transport solvers in a specific Python frame. This development is related only to the TOUGHREACT/EOS3 executable. The wrapped tool will be called hereafter WEos3 that is a Python shared object with a Linux .so extension.

For efficiency and validation purposes, we initially compared standard TOUGHREACT outputs with the WEos3 ones, with the requirement that the tool development would be considered as validated once the respective output files are strictly identical apart from the CPU time reported.

To fulfill that requirement, while keeping the desired algorithm, we had first to create new subroutines overlapping initial subroutines of the 1.2 version of TOUGHREACT.

The first four methods which have been developed follow entirely the initial TOUGHREACT/EOS3 algorithm; they enable the verbose, the initialization, the launch and the execution of the simulation; the last one being the stop method. The only change made to the initial source code is a transfer of some initializations outside of the CYCIT call.

In Python, the TOUGHREACT/EOS3 simulation occurs in four steps:

```
WEos3.verbose("verboseFile")
WEos3.initialise()
WEos3.run()
WEos3.stop()
```

We did not observe any significant difference in simulation time when launching standard TOUGHREACT/EOS3 and WEos3 Python module, apart from a slightly faster (i.e. 2 to 3%) execution speed of the standalone code. Numerical outputs are indeed identical.

The second development step was to rewrite the cycit algorithm in Python.

Here we had to rewrite first, all the "goto" statements of the routine, replacing some of them with the fortran "do while" statement. The core of the routine can be then implemented in three main calls: i) the time step evaluation, ii) the loop between geochemical-transport and flow, and iii) an output call. In Python, these calls are wrapped in three methods:

```
WEos3.lastEndPrints(kcyc)
WEos3.geoFCTStep()
WEos3.timeStepUpdate()
```

The method geoFCTStep can be further divided using two methods called WEos3.flowStep and WEos3.chemTranStep.

The validation of the transfer of the TOUGHREACT algorithm to Python was made in the same way as before. Even in this case, we did not observe any difference in the output results between the treact12 subroutine of TOUGHREACT/Eos3 and its Python counterpart; execution times being as before similar.

The third and final step of the EOS3 module wrapping is a little bit different; we introduce new methods to handle the WEos3 module as a geochemical equilibrium solver.

To reach that step, we had to consider the coupling algorithm, between geochemistry and transport, implemented in the subroutine couple of the source code. That one is built on three sequential main loops, the aqueous species transport, the gas transport and the geochemical equilibrium. All those three elements were wrapped; but the only method we use to couple the Eos3 chemistry to Elmer is the WEos3.equilibrium.

Linked to that method we had to write further methods to deal with the evolution of species within the transport and the chemistry over time.
A transport step inducing a modification of the species distribution within each mesh cell, we need to retrieve the aqueous species field from the transport and to impose it to WEos3 via:

```
WEos3.setMobileConcentation
```

That call enables to update the Eos3 chemistry in order to simulate a new geochemical equilibrium which is evaluated through:

```
WEos3.equilibrium
```

on each cell. Once that one is reached, we have to retrieve the updated concentrations from WEos3 through:

```
WEos3.getMobileconcentration
```

Those three methods are the three main ones enabling the coupling between the Eos3 chemistry and the Elmer transport; but some other methods have been set up to handle specific outputs within the platform frame.

Here the validation couldn't be made in the same way as before, mainly for two reasons: i) in WEos3, the generic coupling algorithm and the flow-transport solver are different from TOUGHREACT/EOS3 ones; ii) this part of the code development is still in progress and further testing is needed.

Despite these limitations, preliminary tests indicate that even in this case WEos3 produces very similar results compared to the standalone version of the code when applied on simple analytical test cases. The only significant difference concerns the CPU time dedicated to transport, with Elmer being slower and less efficient compared to TOUGHREACT.

Nevertheless, the validation process of that phase is still an ongoing one, simply due to the fact that apart from simple test cases we could state differences which have to analyzed from a geochemical point of view; case definition, related assumptions.

CONCLUSIONS

We described the way TOUGHREACT/EOS3 has been used in conjunction with Python. First, a geochemical and transport platform frame has been defined. In that frame, every data necessary to the problem description is transformed into a Python instantiated object. This step enables to generate the necessary input files for the TOUGHREACT/EOS3 module.

We also described the different ways the tool has been wrapped. By means of these different

wrapping procedures, WEos3 can be used as a geochemical solver, and then possibly coupled to other flow/transport tools. For this application we used the flow/transport code Elmer. The wrapping was made while keeping the original algorithm structure of TOUGHREACT/EOS3. The WEos3 shared object so far created can be used to replicate the "original" TOUGHREACT/EOS3 coupling, as well as just used as a batch geochemical solver.

The validation of WEos3 as geochemical solver coupled to Elmer flow and transport engine has been performed through comparison with simple analytical tests. Based on this exercise, it emerged that WEos3 numerical outputs are almost identical to results obtained with TOUGHREACT/EOS3, with only minor differences due to the different discretization methods employed by the transport/flow engines TOUGH2 and Elmer.

The validation process is still in progress, and further major advancements are expected as soon as the implementation of the openfoam (www.openfoam.org) solver will be completed.

ACKNOWLEDGMENTS

That work has been financially supported by EDF and the KIT.

REFERENCES

Dimier A. and Gherardi F., Caprock integrity assessment by reactive transport modeling: A code intercomparison approach. Proceedings of the TOUGH Symposium 2012, pp. 600-604, Berkeley, Calif.., USA, September 17-19 2012.

Parkhurst, D.L. and Appelo, C.A.J., User's guide to PRHEEQC (version 2)--A computer program for speciation, batch-reaction, one-dimensional transport, and inverse geochemical calculations: U.S. Geological Survey Water-Resources Investigations Report 99-4259, 312 p., 1999.

Råback, P. Elmer - An open source finite element software for multiphysical problems, CSC – IT Center for Science, Espoo, Finland, May 2008.

Råback, P., Malinen, M., Ruokolainen, J., Pursula, A., Zwinger, T., Elmer Models Manual, CSC – IT Center for Science, Espoo, Finland, November 4, 2014.

Xu, T., Sonnenthal. E., Spycher, N., Pruess, K., TOUGHREACT User's Guide: A simulation program for non-isothermal multiphase reactive geochemical transport in variably saturated geologic media. Rep. LBNL-55460, 203 pp., Lawrence Berkeley National Lab., Berkeley, Calif., 2004.

CARBON SATUARTION AFFECTS SOIL C DYNAMICS?

Dipankar Dwivedi, William J. Riley, and Jinyun Tang

Earth Sciences Division, Lawrence Berkeley National Laboratory
1 Cyclotron Road
Berkeley, CA, 94720, USA
e-mail: DDwivedi@lbl.gov

ABSTRACT

Soil organic carbon stores a vast amount of carbon; this carbon is susceptible to release to the atmosphere as greenhouse gases. Various environmental factors control soil organic matter (SOM) decomposition. Here we focus on the role that C saturation (due to available mineral sites for sorption) has on SOM cycling. To investigate how C saturation at different depths impacts soil carbon dynamics, we modified and integrated a biotic and abiotic reaction network [Biotic and Abiotic Model of SOM (BAMS1); Riley et al., 2014] into a multi-phase reactive transport solver (TOUGHREACT). To evaluate the soil's ability to stabilize organic matter, we used a surface comeplexation model to represent soil minerals and organic carbon interactions, as the surface complexation model accounts for a finite number of sites that can hold organic carbon. Additionally, our reaction network includes above and belowground carbon inputs, multiple polymer and monomer carbon substrate groups, and bacterial and fungal activity. We applied the model to explore how SOM profiles and radiocarbon ($\Delta^{14}C$) values evolve over time. Results indicate that polymers rapidly approach their steady state values, but dissolved monomers and peptidoglycan vertical profiles take longer to stabilize and their monotonically depleting profiles with depth are controlled by interactions with soil minerals.

INTRODUCTION

Soils are the largest global pool of carbon that actively cycle organic C (Schmidt and Torn et al. 2011). This carbon is susceptible to release to the atmosphere primary as CO_2, which is a greenhouse gas, due to global warming. Therefore, understanding the relationship between environmental changes and soil organic matter (SOM) stabilization and modeling SOM dynamics are critical for projecting changes in soil carbon fluxes in a changing climate.

There are various models in the literature that can represent SOM biogeochemistry in the subsurface. These models range from simplified single-pool turnover-time models to those that follow the homogeneous soil layer structure and carbon pool dynamics of the CENTURY model, such as DAYCENT, FORCENT, or ROTHC (Jenkinson and Coleman 2008; Parton et al. 1998, 2010). Also, these CENTURY-like carbon pool models have also been integrated in vertically resolved climate-scale models (Braakhekke et al. 2011; Koven et al. 2013; Tang et al. 2013). Because these conceptual soil organic pools are not measurable, it is recommended to use measurable soil organic carbon pools (Skjemstad et al. 2004). Moreover, most of these models of SOM dynamics assume first order kinetics for the decomposition of various conceptual pools of organic matter, which means that equilibrium C stocks are linearly proportional to C inputs (Paustian et al. 1994; Six et al. 2002). Additionally, much emphasis has been placed on representing microbial activity explicitly in models of SOM dynamics; however, microbes are not represented explicitly in these types of SOM models. Furthermore, most of these models either do not include any mechanistic representation of mineral-organic interactions or apply empirical sorption models that do not account for the mineral surface area. Because representing microbes and sorption is important to understand and accurately model SOM dynamics in soil, the next generation of SOM decomposition models will likely include mechanistic treatment of microbial processes and sorption processes and their impacts on SOM dynamics.

Riley et al. (2014) proposed a Biotic and Abiotic Models of SOM (BAMS1) based on the emergent understanding of dynamics of SOM. BAMS1 represented the decomposition of SOM modeled as a biological process mediated by microbes. The model includes above- and below-ground inputs, multiple polymer and monomer carbon substrate groups; microbes consume polymers and monomers and respire CO_2 to the atmosphere. However, BAMS1 did not represent mineral-organic interactions mechanistically, which is important for understanding SOM stabilization in soils of different geologic ages formed under similar climatic and vegetation conditions. Efforts are underway by Dwivedi et al. (2015, in preparation) to describe the impact of mineral surface area on depth-resolved soil organic matter (SOM) and $\Delta^{14}C$ in grassland ecosystems. A key feature in SOM dynamics is the soil C saturation concept (i.e., that soils, at a particular time, have a limited capacity to stabilize SOM). A growing body of literature has shown the significance of C saturation in SOM cycling (Cotrufo et al. 2013; Six et al. 2002). The relationship between soil structure and its ability to stabilize SOM has not been explored in detail. We hypothesize that C saturation has a significant impact on the stabilization of SOM with depth in a soil column. The specific objective of this study is to explore how SOM profiles and radiocarbon ($\Delta^{14}C$) values of SOM evolve over time.

METHODOLOGY

We conducted this study using published data from marine terraces in Northern California (Masiello et al. 2004). These coastal sites range from 3.9ka to 240 ka in geologic age and experience a cool, temperate Mediterranean climate. We chose the intermediate site (29ka) for understanding time dependent stabilization of SOM in the context of C saturation. Mean annual air temperature and precipitation is recorded as 12^0C and ~1000 mm, respectively. More details are provided in (Masiello et al. 2004; Merritts, Chadwick, and Hendricks 1991).

Decomposition Reaction and Stoichiometry of Organic Monomers

Riley et al. (2014) developed the Biotic and Abiotic Models of SOM (BAMS1) that included a complex monomer structure and multiple polymers C substrates. BAMS1 represented microbial biomass explicitly (aerobic heterotrophic bacteria and fungi). BAMS1 was able to predict SOM with a reasonable accuracy in U.S. Great Plains grasslands (Riley et al. 2014). Because we do not have observations to validate the complex monomer pools used in that first set of simulations, we modified BAMS1 (termed BAMS1.1) so that it represents only one monomer pool (dissolved organic carbon). The BAMS1.1 reaction network includes above- and below-ground inputs as root exudates, leaf litter, and woody litter. Root exudates generate dissolved organic carbon (monomers); leaf litters generate monomers and polymers (cellulose and hemicellulose); woody litters generate monomers and polymers (cellulose, hemicellulose, and lignin). Heterotrophic aerobic bacteria and fungi are represented explicitly in BAMS1. Fungi are assumed to decompose polymers. Heterotrophic aerobic bacteria are assumed to consume monomers (as a source of energy and carbon) directly leading to biomass yield and CO2 production. Death of heterotrophic bacteria and fungi produce necromass (represented as peptidoglycan).

BAMS1 was integrated into TOUGHREACT using Michaelis-Menten kinetics as follows:

$$r_i = \sum_{s=1}^{M}\left[k_{i,s}\times\prod_{j=1}^{N_i}(\gamma_j^{v_{i,j}}C_j^{v_{i,j}})\times\prod_{k=1}^{N_{mi}}(\frac{C_{i,k}}{K_{M_i,k}+C_{i,k}})\right]$$

where i represents the number of stoichiometric reactions and r_i represents the reaction rate of each reaction. There are M pathways that are counted by the variable s. The first, second, and third terms on the right hand side of the above Equation are rate constants, product terms, and Monod terms, respectively. k is a rate constant (s^{-1}). The product term is the product of γ_j (activity coefficient of species j) and C_j (mol m^{-3} s^{-1}) (concentration of species j), and $v_{i,j}$ is a stoichiometric coefficient. In the Monod term, N_l is the number of reacting species in the forward rate term (also known as product terms), N_m is the number of Monod factors (Monod terms), and $C_{i,k}$ (mol m^{-3} s^{-1}) is the concentration of the k^{th} Monod species.

BAMS1 applied a kinetically rate limited sorption process, and assumed that soil minerals are not limited in their ability to stabilize C stocks. However, several studies have emphasized that bulk soil minerals have a finite number of sites that sorb dissolved organic carbon. Therefore, here we represented sorption of monomers and peptidoglycan with a surface complexation model. We used the bulk mineral surface area (a generic surface with no charge, as described in TOUGHREACT (Xu et al. 2011)), where a chemical reaction between the aqueous species and the specific surface sites (surface complexation) is described using an equilibrium sorption coefficient (Dzombak 1990).

Reactive Transport Solver

We integrated BAMS1 in the generic reactive transport solver TOUGHREACT. Darcy-Richards equation (Pruess et al., 1999) was used to model water flow. The mass balance equation was solved:

$$\frac{\partial C_i}{\partial t} = -\frac{\partial}{\partial z}\left[D\frac{\partial C_i}{\partial z} + vC_i\right] + \sum_k \frac{\partial C_i}{\partial t}\Big|_k$$

where t (s) is the time, D (m^2 s^{-1}) is the effective aqueous or gaseous diffusivity, and v (m s^{-1}) is bulk aqueous or gaseous velocity.

Climate Forcing, Boundary Conditions, and Initial Conditions

We performed all simulations with no soil carbon as an initial condition and constant climate forcing. We imposed carbon inputs from leaf, wood, and root litter based on simulations using CLM4.0 (Lawrence et al. 2011). We allowed simulations to come to the steady state for SOM; it took 5000 years for SOM to stabilize. We also performed simulations for 10,000 years and found SOM content comes to a steady state after ~4000-5000 years. Therefore, for computational tractability, we performed simulations for 5000 years in this paper.

Model Analysis

We performed a forward simulation to predict SOM in a soil column in the 29ka site. The range of the current mineral surface area and site density were chosen from the literature (Arora et al. 2014). Subsequently, we performed several simulations varying the mineral surface area and systematically imposed exponential decaying profiles of bulk soil mineral surface area with depth to match SOM. We used a site density of 4.258×10^{-6} mol_{sites} $m^{-2}{}_{mineral}$, and a bulk mineral surface area of 1.54×10^{6} $m^2{}_{mineral}$ $m^{-3}{}_{mineral}$. The range of values of LogK were adopted from the literature (Murphy, Lenhart, and Honeyman 1999).

To carry out simulations for $\Delta^{14}C$, we performed a parallel simulation for all modeled components. We imposed a first order radioactive decay (8267 y, the turnover time corresponding to the ^{14}C radioactive decay rate) to mimic the radioactive depletion of ^{14}C values. Because TOUGHREACT allows first order decay only in primary species, we modified the code to also account for first order decay in sorbed species (dissolved monomers and peptidoglycan), which are treated as secondary species in TOUGHREACT.

RESULTS AND DISCUSSION

SOM Predictions for the N. California Site

Observed SOM content at the 29ka site in Eureka, California ranges from 4% to 1% in the top 2 m of the soil column. BAMS1.1 was able to predict SOM values in the soil column that were broadly consistent with observations at depth (Fig. 1). Figure 1 also shows that SOM content builds from the top of the soil column towards the bottom over the 5000 years.

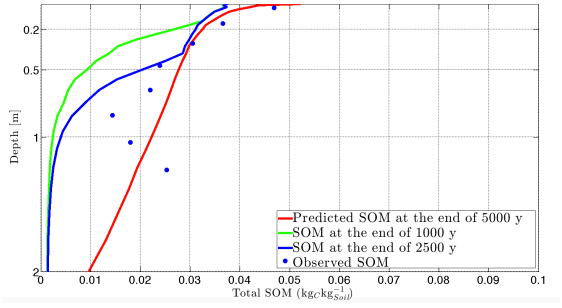

Figure 1. Predicted and observed SOM content for the 29ka grassland site after 1000 y, 2500 y, and 5000 years of simulation.

BAMS1.1 predicted SOM contents with a reasonable accuracy: R^2 and root mean square error (RMSE) values of predicted and observed SOM contents were 0.91 and 0.016,

respectively. Unlike CENTURY-like models, we did not need to impose any arbitrary depth dependent turnover times to predict depth-resolved SOM content.

$\Delta^{14}C$ Predictions for the N. California Site

We also performed simulations to predict transient $\Delta^{14}C$ values along the depth of the soil column. BAMS1.1 was able to relatively accurately reproduce observed SOM $\Delta^{14}C$ values in the soil column; R^2 and root mean square error (RMSE) values of predicted and observed $\Delta^{14}C$ values of SOM contents were 0.81 and 64 ‰, respectively. However, these metrics improved when considering values below 15 cm depth: $R^2 = 0.98$ and RMSE = 22 ‰.

Predicted $\Delta^{14}C$ values of SOM ranged from -80 ‰ near the surface to -400 ‰ at 2 m depth in the soil column. The gray area in Figure 2 shows the SOM $\Delta^{14}C$ depletion without adjusting for the nuclear weapons testing of the 1950s and early 1960s. As a result of those weapons tests, the atmospheric concentration of $^{14}CO_2$ approximately doubled. The higher $\Delta^{14}C$ values in the atmosphere then enriched $\Delta^{14}C$ in soil, as shown by the difference between the gray and green shading in Figure 2. $\Delta^{14}C$ values are a good indicator for the age of the carbon in soil; i.e., more negative values indicate older carbon. The monotonically decreasing $\Delta^{14}C$ values with depth indicate the carbon that is stabilized on mineral surfaces is progressively older with depth.

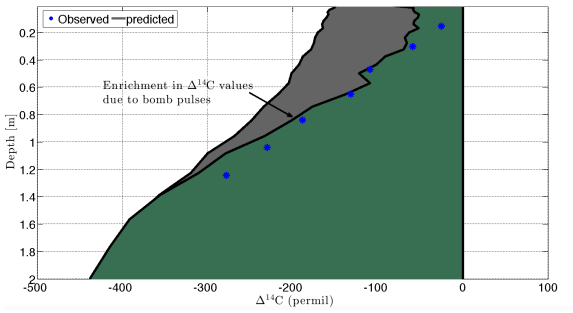

Figure 2. Predicted and observed $\Delta^{14}C$ values of total SOM at the end of a 5000-year simulation at the 29ka grassland site in Northern California.

BAMS1.1 predicted the decrease in $\Delta^{14}C$ with depth without imposing any model parameter changes at the 29ka site in Northern California. Rather, in BAMS1.1, compounds are unavailable to microbes when sorbed and readily decomposable when not sorbed, a model structure that produces the observed shape of $\Delta^{14}C$ profiles (Fig. 2).

Evolution of various components of SOM

Simulation results of individual components of SOM reveal several interesting patterns. Although experimental data are not available for individual SOM components to compare to our predictions, their vertical profiles showcase key processes predicted that control bulk SOM content. For example, the aerobic biomass comprised more than 90% of the total biomass (Fig 3A), which is consistent with other studies (Ekelund, Ronn, and Christensen 2001). Input polymers (cellulose, hemicellulose, and lignin) are in the top half-meter of the soil column (Fig 3 D, E, and G). Because, in BAMS1.1, input polymers do not transport, they come to a steady state relatively faster than other components of SOM (e.g., monomers and peptidoglycan). Fungal biomass and input polymers (cellulose, lignin, hemicellulose) have similar profiles (Fig 3B) over time because fungi consume cellulose, hemicellulose, and lignin.

Dissolved monomers and peptidoglycan interact with soil minerals and transport in the soil column. Additionally, aerobic bacteria consume dissolved monomers and peptidoglycan. Although monomers and peptidoglycan surface complexation is represented as an equilibrium process, it takes a long time for the soil to stabilize the vertical profile of organic matter. Because monomers and peptidoglycan are transported in the soil column and also consumed by aerobic bacteria, the protected (sorbed) monomers and peptidoglycan act as a buffer that can replenish dissolved monomers and peptidoglycan.

Soils have a C saturation capacity due to finite numbers of sorption sites. Available sorption sites are filled from the top of the column over time, as dissolved monomers are readily available near surface from inputs (root exudates, leaf and root litters). Moreover, microbial and fungal biomass is also higher near the surface (Fig. 3 A and B); therefore peptidoglycan (i.e., necromass) is higher near

the surface as well. Once available sorption sites are saturated near the top of the soil column, dissolved monomers and peptidoglycan are transported down the soil column where they can be sorbed and consumed by aerobic bacteria. As a result, dissolved and sorbed monomers and peptidoglycan have a profile in the soil column that changes with depth (Fig 3C, F, H, and I). Dissolved and sorbed monomers and peptidoglycan broadly evolve similarly in time because surface complexation is an equilibrium-based model. Aerobic biomass also displays a similar profile (Fig 3A) in time as dissolved monomers and peptidoglycan, because aerobic bacteria consume these substrates.

SUMMARY AND CONCLUSIONS

It is important to understand and model soil organic matter (SOM) dynamics accurately, since they are important contributors to land-atmospheric interactions and will undoubtedly affect future climate change. We developed and used a new model (Biotic and Abiotic Model of SOM; BAMS1.1) which is based on emerging understanding that SOM cycling is an emergent response to biological process, abiotic processes, edaphic properties, and environmental factors. Application of BAMS1.1 to a 29ka old site in Eureka, California suggested that (1) mineral sorption controlled centennial to millennial SOM vertical profile dynamics and (2) C saturation was strongly affected by mineral properties and organic matter interactions.

ACKNOWLEDGMENT

Funding for this study was provided by the Office of Biological and Environmental Research of the US Department of Energy, under contract number DE-AC02-05CH11231, as part of the Next-Generation Ecosystem Experiment (NGEE Arctic) project and under award number DE-AC02-05CH11231, as part of the Scientific Focus Area at Lawrence Berkeley National Laboratory.

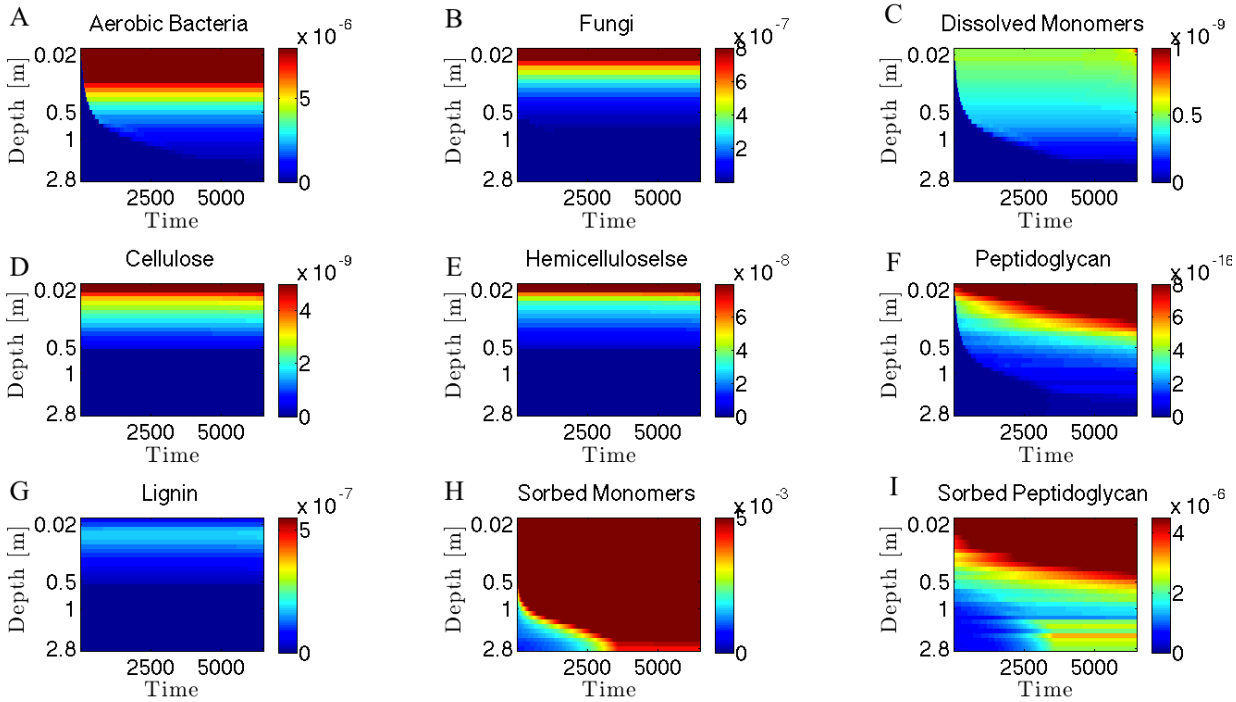

Figure 3. Evolution of modeled carbon components in 5000 years using the simulation at 29ka

REFERENCES

Falta, R.W., K. Pruess, I. Javandel, and P.A. Witherspoon, 1989. "Density-driven flow of gas in the unsaturated zone due to the evaporation of volatile organic compounds." *Water Resour. Res.*, *25*(10), 2159–2169.

Arora, B., S. Sevinç Şengör, N. F. Spycher, and C. I. Steefel. 2014. "A Reactive Transport Benchmark on Heavy Metal Cycling in Lake Sediments." *Computational Geosciences*. Retrieved May 9, 2015 (http://link.springer.com/10.1007/s10596-014-9445-8).

Braakhekke, M. C. et al. 2011. "Somprof: A Vertically Explicit Soil Organic Matter Model." *Ecological Modelling* 222:1712–30.

Cotrufo, M. F., M. D. Wallenstein, C. M. Boot, K. Denef, and E. Paul. 2013. "The Microbial Efficiency-Matrix Stabilization (MEMS) Framework Integrates Plant Litter Decomposition with Soil Organic Matter Stabilization: Do Labile Plant Inputs Form Stable Soil Organic Matter?" *Global Change Biology* 19(4):988–95. Retrieved February 20, 2015 (http://www.ncbi.nlm.nih.gov/pubmed/23504877).

Dzombak, D. A. 1990. *Surface Complexation Modeling: Hydrous Ferric Oxide*. John Wiley & Sons. Retrieved November 18, 2014 (http://books.google.com/books?hl=en&lr=&id=LGBtoHNUbWwC&pgis=1).

Ekelund, F., R. Ronn, and S. Christensen. 2001. "Distribution with Depth of Protozoa, Bacteria and Fungi in Soil Profiles from Three Danish Forest Sites." *Soil Biology and Biochemistry* 33(4-5):475–81. Retrieved July 17, 2015 (http://www.sciencedirect.com/science/article/pii/S0038071700001887).

Jenkinson, D. S. and K. Coleman. 2008. "The Turnover of Organic Carbon in Subsoils. Part 2. Modelling Carbon Turnover." *European Journal of Soil Science* 59:400–413.

Koven, C. D. et al. 2013. "The Effect of Vertically Resolved Soil Biogeochemistry and Alternate Soil C and N Models on C Dynamics of CLM4." *Biogeosciences* 10(11):7109–31. Retrieved October 1, 2014 (http://www.biogeosciences.net/10/7109/2013/).

Lawrence, D. M. et al. 2011. "Parameterization Improvements and Functional and Structural Advances in Version 4 of the Community Land Model." *Journal of Advances in Modeling Earth Systems* 3(1) M03001, 27 pp. Retrieved June 11, 2015 (http://doi.wiley.com/10.1029/2011MS00045).

Lutzow, M. v., I. Kögel-Knabner, K. Ekschmitt, E. Matzner, G. Guggenberger, B. Marschner ande H. Flessa. 2006. "Stabilization of Organic Matter in Temperate Soils: Mechanisms and Their Relevance under Different Soil Conditions - a Review." *European Journal of Soil Science* 57(4):426–45. Retrieved July 15, 2014 (http://doi.wiley.com/10.1111/j.1365-2389.2006.00809.x).

Masiello, C. A., O. A. Chadwick, J. Southon, M. S. Torn, and J. W. Harden. 2004. "Weathering Controls on Mechanisms of Carbon Storage in Grassland Soils." *Global Biogeochemical Cycles* 18:1–9.

Merritts, D. J., O. A. Chadwick, and D. M. Hendricks. 1991. "Rates and Processes of Soil Evolution on Uplifted Marine Terraces, Northern California." *Geoderma* 51:241–75.

Murphy, R. J., J. J. Lenhart, and B. D. Honeyman. 1999. "The Sorption of Thorium (IV) and Uranium (VI) to Hematite in the Presence of Natural Organic Matter." *Colloids and Surfaces A: Physicochemical and Engineering Aspects* 157(1-3):47–62. Retrieved July 17, 2015 (http://www.sciencedirect.com/science/article/pii/S0927775799001156).

Parton, W. J. et al. 2010. "ForCent Model Development and Testing Using the Enriched Background Isotope Study Experiment." *Journal of Geophysical Research: Biogeosciences* 115.

Parton, W. J., M. Hartman, D. Ojima, and D. Schimel. 1998. "DAYCENT and Its Land Surface Submodel: Description and Testing." *Global and Planetary Change* 19:35–48.

Paustian, K., C. E. Pankhurst, B. M. Doube, V. V. S. R. Gupta, and P. R. Grace. 1994. "Modelling Soil Biology and Biochemical Processes for Sustainable Agriculture Research." 182–93. Retrieved July 17, 2015 (http://www.cabdirect.org/abstracts/19951907614.html).

Pruess, K. C. Oldenburg, G. Moridis,1999. "TOUGH2 User's Guide Version 2." Rep. 43134, Lawrence Berkeley National Laboratory, Berkeley, Calif. Retrieved (http://escholarship.org/uc/item/4df6700h.pdf).

Riley, W. J. et al. 2014. "Long Residence Times of Rapidly Decomposable Soil Organic Matter: Application of a Multi-Phase, Multi-Component, and Vertically Resolved Model (BAMS1) to Soil Carbon Dynamics." *Geoscientific Model Development* 7(4):1335–55. Retrieved October 1, 2014 (http://www.geosci-model-dev.net/7/1335/2014/).

Schmidt, M. W. I. et al. 2011. "Persistence of Soil Organic Matter as an Ecosystem Property." *Nature* 478:49–56.

Six, J., R. T. Conant, E. A. Paul, and K. Paustian. 2002. "Stabilization Mechanisms of Soil Organic Matter: Implications for C-Saturation of Soils." *Plant and Soil* 241:155–76.

Skjemstad, J. O., L. R. Spouncer, B. Cowie, and R. S. Swift. 2004. "Calibration of the Rothamsted Organic Carbon Turnover Model (RothC Ver. 26.3), Using Measurable Soil Organic Carbon Pools." *Australian Journal of Soil Research* 42(1):79. Retrieved July 15, 2015 (http://www.publish.csiro.au/view/journals/dsp_journal_fulltext.cfm?nid=84&f=SR03013).

Tang, J. Y., W. J. Riley, C. D. Koven, and Z. M. Subin. 2013. "CLM4-BeTR, a Generic Biogeochemical Transport and Reaction Module for CLM4: Model Development, Evaluation, and Application." *Geoscientific Model Development* 6(1):127–40. Retrieved October 1, 2014 (http://www.geosci-model-dev.net/6/127/2013/gmd-6-127-2013.html).

Xu, T. et al. 2011. "Toughreact Version 2.0: A Simulator for Subsurface Reactive Transport under Non-Isothermal Multiphase Flow Conditions." *Computers and Geosciences* 37:763–74.

DEVELOPMENT OF SYN-DEPOSITIONAL MODELS OF CARBONATE DIAGENESIS: AN APPLICATION OF PyTOUGH TO COMPLEX GEOLOGICAL PROCESSES

Miles Frazer[1,2]; Fiona Whitaker[2]; Cathy Hollis[3]

[1] Chevron Energy Technology Company, Houston, TX
[2] School of Earth Sciences, University of Bristol, UK
[3] School of Earth, Atmospheric and Environmental Sciences, University of Manchester, UK

mf6064@bristol.ac.uk

ABSTRACT

Rock fabric modifications that occur by water-rock interaction during the development of a carbonate platform are critical to the determination of the final quality of geological reservoirs in carbonate successions. The distribution of facies, along with early modifications to the distribution and character of porosity defines the early template of permeability that is exploited by later stages of reactive fluid flow and during reservoir exploitation. As such, a clear understanding of these early porosity-arranging processes is the first step in predicting the distributions of reservoir quality in carbonate lithologies using process simulations.

Whilst the TOUGHREACT code is a forefront technology for the simulation of water-rock interaction processes, simulating syn-depositional processes using TOUGHREACT can be challenging because of the requirement for capturing evolving platform geometries and a growing sedimentary stratigraphy, as well as temporal changes in boundary conditions, within a reactive transport model. We have overcome this challenge by using a multi-stage modelling approach which is automated using the PyTOUGH library, along with a series of Python functions to deal with ongoing compactional reduction in porosity and permeability as sediments are buried. The workflow is applied to a case study of dolomite formation by geothermal convection of seawater during the deposition of a Carboniferous carbonate platform in North England.

Previous, single-stage reactive transport models (RTMs) of dolomitisation have suggested that, over many millions of years, it can produce a wedge-shaped dolomite body that thins with distance from the platform margin (Whitaker and Xiao, 2010). However, on this time scale, a carbonate platform can accumulate significant volumes of sediment and alter its overall geometry multiple times. This is not considered by these previous simulations.

We present a series of more advanced RTMs that consider concurrent platform growth, sediment compaction and dolomitisation by geothermal convection of seawater. The results of these models reveal that platform growth could significantly influence both the amount and distribution of dolomite formed by this mechanism. Specifically, they suggest that the distinct dolomite bodies described by Whitaker and Xiao (2010) are not applicable to cases where platform margins are non-static through time. Instead dolomite proportions increase with depth in the carbonate platform as it is the deepest, earliest sediments that exist longest at the elevated temperatures required to accelerate dolomitisation rates to significant levels.

REFERENCE

Whitaker, F.F., and Y. Xiao. Reactive transport modeling of early burial dolomitization of carbonate platforms by geothermal convection. *AAPG bulletin* 94.6 (2010): 889-917.

USE OF REACTIVE TRANSPORT MODELLING TO STUDY WELL INTEGRITY IN A NATURAL ANALOGUE FOR THE GEOLOGICAL CO_2 STORAGE

*Ana Hernández-Rodríguez[1,2], Giordano Montegrossi[3], Giorgio Virgili[1],Orlando Vaselli[2], Bruno Huet[4], Luigi Marini[1].

[1]West Systems s.r.l., Viale Donato Giannotti, 24, I-50126 Florence, Italy
[2]Dip. Scienze Terra, Università di Firenze, Via La Pira 4, I-50121, Florence, Italy.
[3]CNR-IGG. Via La Pira 4, I-50121, Florence, Italy.
[4]Lafarge Research Center. 95 Rue du Montmurier, 38070 Saint-Quentin-Fallavier, France.
a.hernandez@westsystems.com

ABSTRACT

This study presents the preliminary results obtained by investigating well integrity in a natural analogue for the geological storage of CO_2 in Tuscany. Reaction Path Modelling (RPM) and Reactive Transport Modelling (RTM) were used to investigate the integrity of an ideal well for CO_2 sequestration with different types of cementing material. Two models were implemented, both with a 2D radial cell arrangement and a logarithmic scale grid, increasing the number of cells and decreasing their size for the cement and the near-well zone. In one of the two models, a leaking zone was introduced 20 m above the casing shoe. It simulates either fracturing of casing and cement or cementing problems or both. The comparison between the model with the leaking zone and the model without it (which represents "ideal conditions" for casing without a damage zone), allows one to investigate the fate of fluids, cement and casing degradation, and rock alteration.

INTRODUCTION

The case study is located in southern Tuscany, where a thermal spa and a CO_2 production plant are present.

At considerable depth the upflow of deep CO_2 is mainly controlled by a regional NW-trending structure, parallel to the Apennine chain, whereas the local structures become important at shallow depth, as revealed by both boreholes drilled for CO_2 production and diffuse iso-CO_2 soil flux maps, the latter being obtained by means of the accumulation chamber method (Chiodini et al., 1998) in selected zones of the study area, to assess the natural CO_2 leakage. The measured CO_2 flux data were processed by means of log probability plots, partitioned in different populations following the approach of Sinclair and mapped by using geostatistical tools (semivariograms and Kriging). Merging the obtained data with those from previous studies (Frondini et al., 2008), it was possible to estimate a total diffuse output of deep CO_2 of ~48.7 ± 8.1 ton/day from an area of ~7400 m^2. Currently, no CO_2 flux measurements were carried out from the bubbling pools that are distributed in three areas located a few hundred meters from the CO_2 plants.

REACTION PATH MODELLING

In this study, RPM is used to investigate both hydration and carbonation processes in cement for a better understanding of wellbore integrity for the geological storage of CO_2.

Portland cement class G is normally used in a high pressure and high temperature context (e.g., oil and gas reservoirs). Hence, for this study Portland cement G-class has been adopted referring to the mineralogical composition given in Thomas and Jennings (2014), reported in Table 1.

Table 1. Mineralogical composition and concentration of Portland cement.

Clinker minerals	Formula	Moles
Alite (C3S)	Ca_3SiO_5	5.531
Belite (C2S)	Ca_2SiO_4	1.936
C3A	$Ca_3Al_2O_6$	0.678
Ferrite(C4AF)	$Ca_4Al_2Fe_2O_{10}$	0.360
Gypsum	$CaSO_4 \cdot 2H_2O$	0.472
Arcanite	K_2SO_4	0.006
Periclase	MgO	0.404
Thenardite	Na_2SO_4	0.029

Isothermal (25 °C) RPM was carried out to simulate first the progressive hydration of cement minerals and carbonation reactions afterwards. Simulations were performed by means of the geochemical code Phreeqc version 3.1.2 using a modified version of the thermodynamic database phreeqc_thermoddemv1.10_11dec2014.dat (http://thermoddem.brgm.fr/spip.php/rubrique14).

The first simulation constrains the solid phases precipitating during cement hydration. Thus, for a total amount of clinker and water of 9.42 moles and 55.6 moles, respectively, Phreeqc predicts the precipitation of Portlandite [$Ca(OH)_2$], Gibbsite [$Al(OH)_3$], Ca-monosulfoaluminate $Ca_4Al_2(SO_4) \cdot 12H_2O$, Hydrotalcite [$Mg_4Al_2O_7{\cdot}10H_2O$], CSH(1.6) [$Ca_{1.60}SiO_{3.6}{\cdot}2.58H_2O$] and Ferrihydrite [$Fe(OH)_3$], as shown in Figure 1.

Note that pH remains close to 12 during this process, owing to saturation with portlandite.

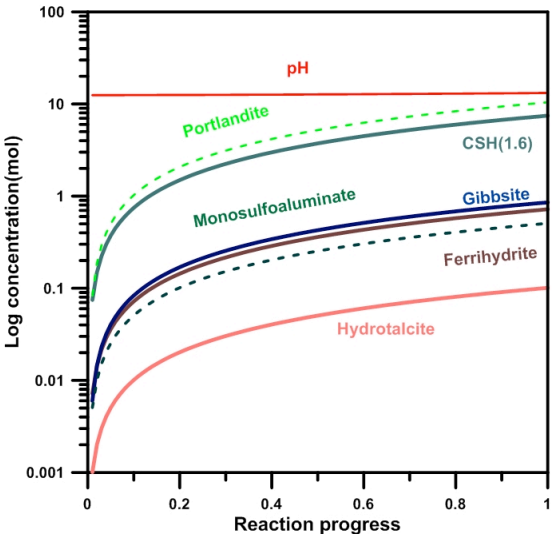

Figure 1. Cement hydration evolution. Solid phases evolution against the reaction progress.

The progressive carbonation of cement minerals was simulated by adding 25.5 moles of CO_2 at P=10 bar.

During the carbonation process different solid phases are predicted to be formed. When the carbonation is completed, as indicated by the excess of unreacted CO_2(g), the solid phases obtained are (Figure 2): Calcite, Amorphous Silica, Magnesite, Ferrihydrite, Gibbsite, and Gypsum.

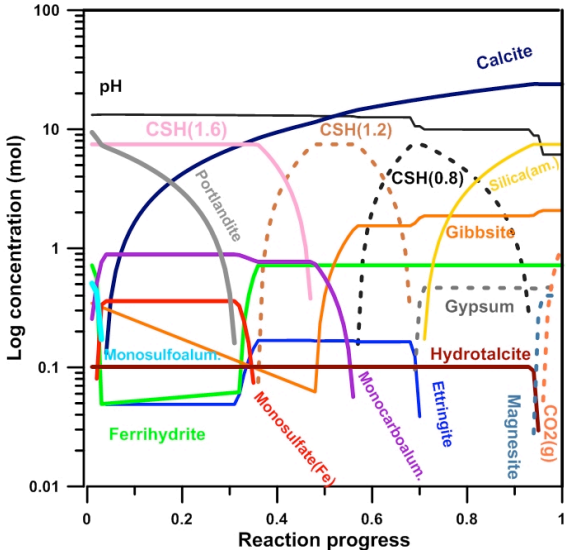

Figure 2. Cement carbonation simulation. Evolution of the solid phases against the reaction progress.

The pH decreases progressively during the carbonation process, passing though a series of constant or relatively constant values, which are dictated by different mineral assemblages acting as pH buffers. The final pH of the aqueous solution upon completion of the carbonation process is 6.13.

Thus, Portlandite is dissolved quickly to form other Ca-bearing solid phases. Ca-monosulfoaluminate is converted to Fe-monosulfate and Ettringite [$Ca_6Al_2(SO_4)_3(OH)_{12}{\cdot}26H_2O$], which have an ephemeral existence and produce Gypsum, representing the stable sulfate mineral at the end of the carbonation process.

CSH(1.6) is transformed into CSH(1.2) [$Ca_{1.2}SiO_{3.2}{\cdot}2.06H_2O$] first and CSH(0.8) [$Ca_{0.8}SiO_{2.8}{\cdot}1.54H_2O$] afterwards. All these minerals have an ephemeral existence and are destroyed, producing amorphous silica and stable Ca-bearing solid phases, namely Calcite and Gypsum.

Among the Al-bearing phases, Ca-monocarboaluminate is dissolved and substituted by authigenic Gibbsite. Hydrotalcite remains stable over most of carbonation but it is destroyed towards the end of the process to produce magnesite, which is part of the final mineral assemblage. The final mineral assemblages at the

end of both hydration and carbonation are summarized in Table 2.

Table 2. Stable mineral assemblages at the end of cement hydration and carbonation.

Hydration	Carbonation
Portlandite	Calcite
CSH(1.6)	CSH(0.8)
	CSH(1.2)
	SiO_2(am.)
Gibbsite	Gibbsite
Ca-monosulfoaluminate	Gypsum
Hydrotalcite	Magnesite
Ferrihydrite	Ferrihydrite

REACTIVE TRANSPORT MODELLING

Reactive Transport Modelling (RTM) was carried out by using the software package TOUGHREACT v2.1, with the ECO2N equation of state.

The items involved in RTM are: carbonate-rich host rocks, cement, stainless steel casing, and fluids flowing in the borehole. Fluids comprise a CO_2-rich gas phase and relatively saline Na-HCO_3 waters. The measured CO_2 flux data were used to constrain CO_2 saturation in the soil.

Physical parameters like permeability, porosity, pressure, viscosity, etc. are taken in account as well as chemical parameters for calculation with the RTM.

A CO_2-bearing layer has been defined based on local stratigraphic data and geostatistical data processing of the CO_2 fluxes from all the surveyed natural emissions and wellbores in the study area.

The wellbore considered in this study is an ideal well that attains a maximum depth of 100 m below ground level. The CO_2 (g) production interval is an 8-m-thick fractured zone at a depth of 80 m, whereas the overlying caprock consists of limestone with a high amount of silica.

The maximum radial distance considered in the model is 280 m, with logarithmic refinement up to the well casing (Figure 3).

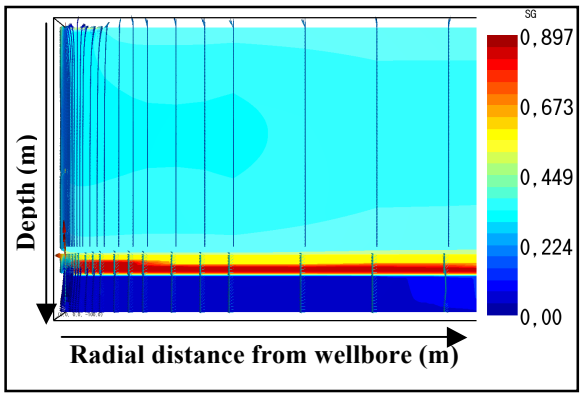

Figure 3. 2D radial model of the system showing the distribution of gas saturation (in Volume Fraction) at time zero. The well is 100 m in depth. It comprises an 8-m-thick fractured zone. The radial distance is 280 m.

In this model, the CO_2 flows at the top of the fractured zone, whereas the water flows at the bottom; the well is producing 2 ton/h of CO_2 and 2 ton/h of water. Casing is being corroded at the CO_2/water interface, and a leakage at nearly 53 m depth is added to better study the cement corrosion around the leakage zone. The production zone can be recognized in the radial model (Figure 3) because of the high gas saturation values distinguished in yellow and red color.

RESULTS AND CONCLUSION

A first calibration was carried out to assess the permeability of the soil cover, and a 2.5e-16 m2 (0.25 md) isotropic permeability was obtained on the basis of the measured CO_2 flux.

The wellbore pressure profile (from 24 bar at the production zone to 3 bar at wellhead) were computed by means of HOLA and used as boundary conditions for the fluid extraction.

The same thermodynamic database used for the batch reaction model was also used for the TOUGHREACT simulation. The minerals of the rock formation (made of Calcite, Quartz, Illite and Montmorillonite) were equilibrated with the natural CO_2 abundance in soil and the formation water. Thus, no chemical changes occur in the soil during the run of this model.

The observed changes consist of cement carbonation, which follows mainly the same steps reported in the batch reaction analysis with the exception of the CSH(0.8) and CSH(1.2) that

were not observed. It seems likely that in this system the carbonation goes directly to calcite (see Figures 4 and 5). This effect may be due to the small dimension of the transition zone and the cell size adopted in the RTM model (note that the cement thickness is less than 20 cm, with 1 cm of mesh size). In the natural system, kinetic reasons may also explain this cement carbonation path.

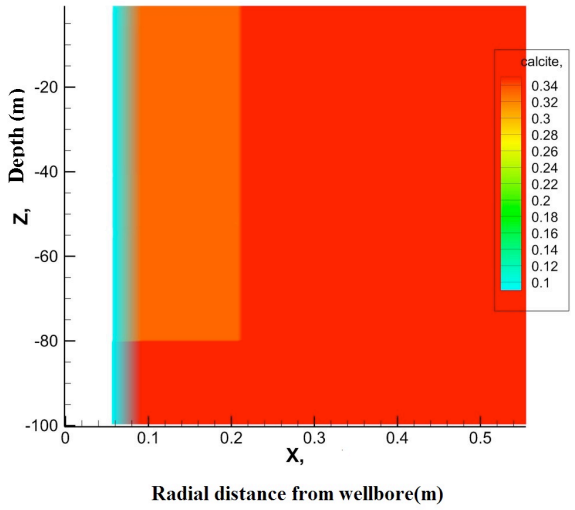

Figure 4. 2D radial model of the system showing the distribution of calcite after carbonation (in solid volume fraction).

The extent of the carbonation process is limited by water pH (7.126) in the soil, which corresponds to the reaction progress value of 0.7 in Figure 2, which is concurrent with the disappearance of Ettringite and before the appearance of a very small amount of magnesite. A lower pH is attained in the production zone (pH 6.26) and in the case of CO_2 leakage from the well. The cement is carbonated but it appears to be relatively stable in this system with some remnants of the hydrated product (i.e. ferrihydrite, gibbsite, CSH1.6), while cement carbonation would be complete in the case of gas leakage.

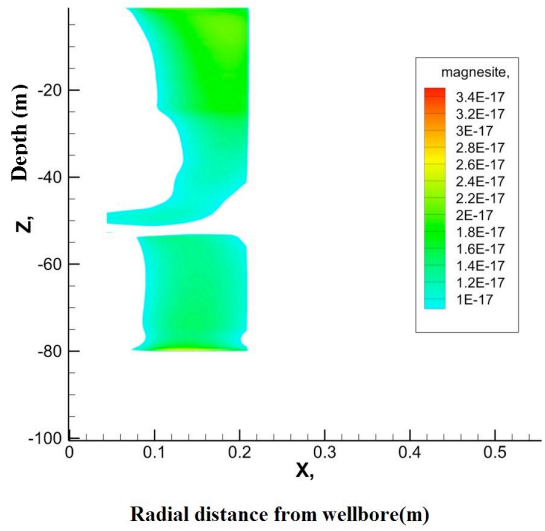

Figure 5. 2D radial model of the system showing the distribution of magnesite (in solid volume fraction), after carbonation.

ACKNOWLEDGMENT

This research was supported by the CO_2 react Marie Curie initial training network.

REFERENCES

Chiodini, G., R. Cioni, M. Guidi, L. Marini, B. Raco, Soil CO_2 flux measurements in volcanic and geothermal areas. *Appl. Geochem*. 13, 543–552, 1998.

Frondini, F., S. Caliro, C. Cardellini, G. Chiodini, N. Morgantini, F. Parello, Carbon dioxide degassing from Tuscany and Northern Latium (Italy). *Global and Planetary Change,* 61, 89–102, 2008.

C. Geloni, T. Giorgis, and A. Battistelli, Modeling of rocks and cement alteration due to co2 injection in an exploited gas reservoir, Transp Porous Med 90,183–200, 2011.

J. L. Palandri and Y. K. Kharaka, A compilation of rate parameters of water-mineral interaction kinetics for application to geochemical modeling, Open File Report 2004-1068, U. S. Geological Survey, California, 2004.

Thomas, J. and H. Jennings, Northwestern University, Evanston, (IL), Manufacture and composition of Portland cement, 2014. http://iti.northwestern.edu/cement/monograph/Monograph3_2.html

ANALYSIS OF FAULT 'SELF-SEALING' ASSOCIATED WITH CO_2-LEAKAGE IN GEOLOGIC CARBON SEQUESTRATION

Vivek V. Patil[1,3], Brian J. McPherson[1,3], Alexandra Priewisch[2], Joseph Moore[3], Nathan Moodie[1,3]

Department of Civil and Environmental Engineering, University of Utah[1]
110 Central Campus Drive, Salt Lake City, UT 84112, USA
E-mails: vivek.patil@utah.edu; b.j.mcpherson@utah.edu; nathan.moodie@m.cc.utah.edu

Department of Earth and Planetary Sciences, University of New Mexico[2]
Albuquerque, NM 87131, USA
Email: alexandra.priewisch@gmail.com

Energy and Geoscience Institute, University of Utah[3]
423 Wakara Way, Suite 300, Salt Lake City, UT 84108, USA
Email: jmoore@egi.utah.edu

INTRODUCTION

Rise in the atmospheric concentration of carbon dioxide (CO_2) due to human activities is believed to be contributing to global warming. Injecting CO_2 captured from anthropogenic sources into deep saline aquifers is a suggested method of mitigating the associated climate change. However, the possibility of its untimely migration into unintended areas owing to unforeseen heterogeneity in the subsurface is a concern. Pathways of such leakage could be permeable faults, abandoned wells, caprocks with weak integrity, and seepage through an unconfined aquifer. If CO_2-enriched water migrates along a fault or fracture, there will be CO_2-induced water-rock reactions that will affect the fluid-flow properties of the fault. Having a complete understanding of such effects is crucial for successful deployment of geologic CO_2 sequestration.

In this research, we investigated the reactive transport processes involved in the long-term leakage of CO_2-rich fluids along a vertical fault zone. Our hypothesis was that faults can self-seal but the choice of parameters for relative permeability, capillary pressure and reaction kinetics will have a huge impact on the quantitative prediction of fault sealing. To evaluate this hypothesis, we chose a natural example of fault self-sealing, the Little Grand Wash Fault zone (LGWF), near Green River in the Paradox basin in Central Utah. We developed idealized 1D reactive transport models based on the hydrogeologic conditions found at the LGWF as well as measured key geochemical parameters in the field.

MODEL DESCRIPTION

The Little Grand Wash Fault is a complex fault system located south of the town of Green River in the Paradox basin, Utah. Due to juxtaposing during faulting, the fault acts as a barrier to the NW-SE directed groundwater flow, but acts as a conduit to vertical flow of CO_2-brine mixture from deeper formations into the shallower formations. Flow of these CO_2-enriched fluids to the surface is evidenced by calcite cement in fractures and massive travertine deposition at the surface along the fault line. Travertines are freshwater limestone rocks that form at springs and seeps while carbonate veins form in horizontal and vertical faults and fractures (Figure 1). Both the travertines and the carbonate veins precipitate from CO_2-charged groundwater that is supersaturated with respect to $CaCO_3$ due to the loss of CO_2 pressure when the groundwater migrates along faults and fractures towards the surface. Kampman et al. (2014) along with previous studies cited therein provide a detailed description of the LGWF conceptual model, based on which we built our 1D models.

Our model had a 1D dual permeability domain extending from the surface to 300 m depth (z) and was non-uniformly discretized into 82 grid cells in each continuum. The top and bottom end cells acted as constant pressure boundaries. An overpressure of ~5 bars was specified at the

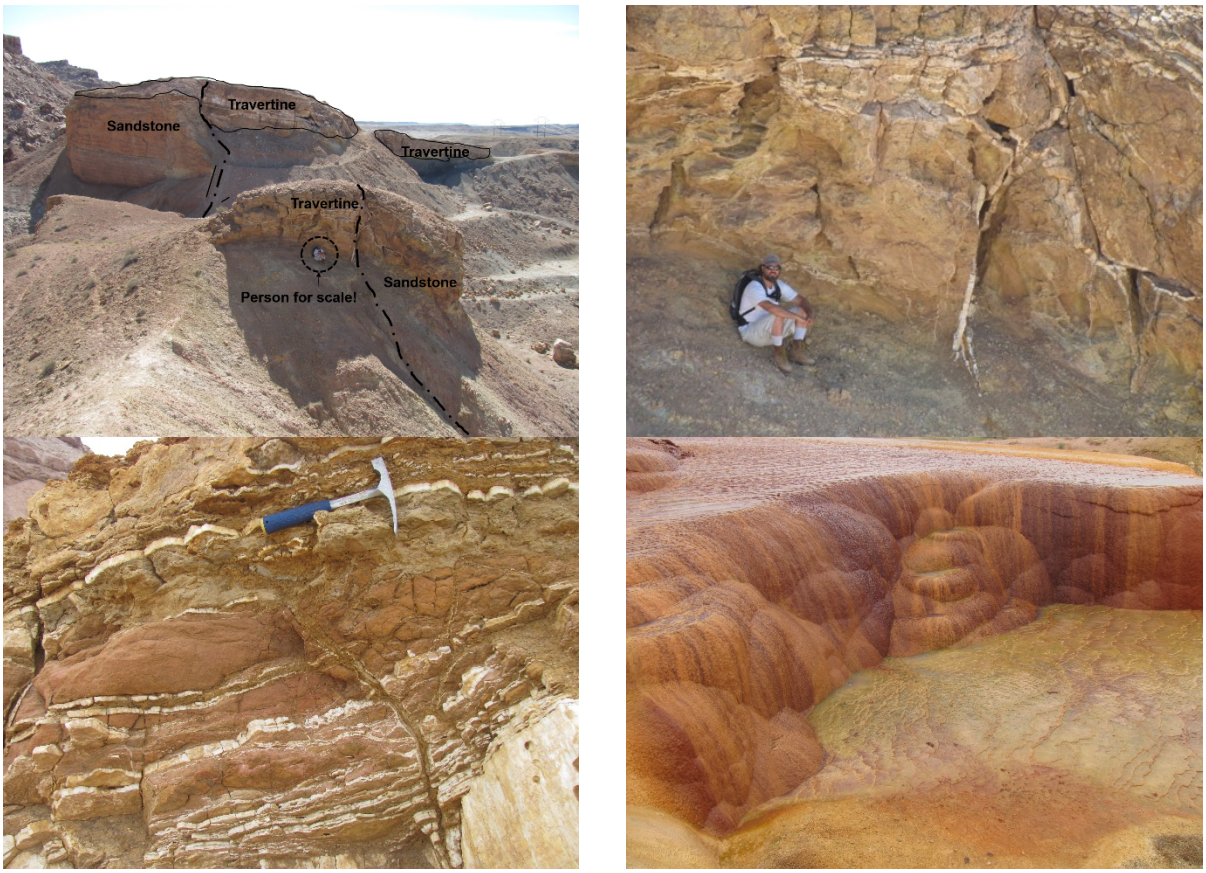

Figure 1: (Top left) Travertine precipitation along the fault trace. (Top right) Subsurface fractures in the fault zone filled with $CaCO_3$. (Bottom left) Aragonite ($CaCO_3$) layers inside a travertine mound. (Bottom right) Active travertine precipitation adjacent to the LGWF from the Crystal Geyser water. Golden red coloring is due to the presence of iron in the water.

bottom boundary to mimic the artesian conditions in the field and induce upward flow. The fault width (x) and thickness (y) were 5 m and 1 m respectively. Inherent to the 1D assumption, we assumed no cross-flow (x) from reservoirs into the fault. The two continua modeled by dual-permeability method using MINC processing represented the fault damaged zone (DZ) and the fault core (FC) and were assigned different flow properties (Table 1). For our base-case model, we followed the convention from several previous studies (e.g. (Pruess 2005)) and used the van Genuchten-Mualem model for relative permeability and van Genuchten function for capillary pressure with parameters taken from Moodie et al. (2015). Initial flow conditions were hydrostatic with no CO_2. A constant gas saturation of 10% was maintained at the bottom boundary which introduced CO_2 in gaseous and dissolved phases into the fault at the beginning of the simulation.

Table 1: Range of effective porosity-permeability values for the fault for different Fa values. The porosity-permeability values for damaged zone and fault core are 0.4, 10^{-12} m^2 and 0.02, 10^{-16} m^2 respectively. Effective porosity and permeability of the fault is calculated by taking a weighted average based on the DZ and FC widths. (Fa is the fault architecture coefficient (Caine et al. 1996) that is used to effectively model fault heterogeneity. It is calculated as Fa = damaged zone width (DZ) / total fault width (DZ+FC))

Fault property	**Fa values**				
	0.05	**0.25**	**0.5**	**0.75**	**0.95**
Effective porosity	0.04	0.12	0.21	0.31	0.38
Effective perm.	5.01 E-14	2.50 E-13	5.00 E-13	7.50 E-13	9.50 E-13

Geochemistry of the fault was partially determined from field data analysis. The initial fault mineralogy was assumed to be a weighted average of the individual mineralogy of the three

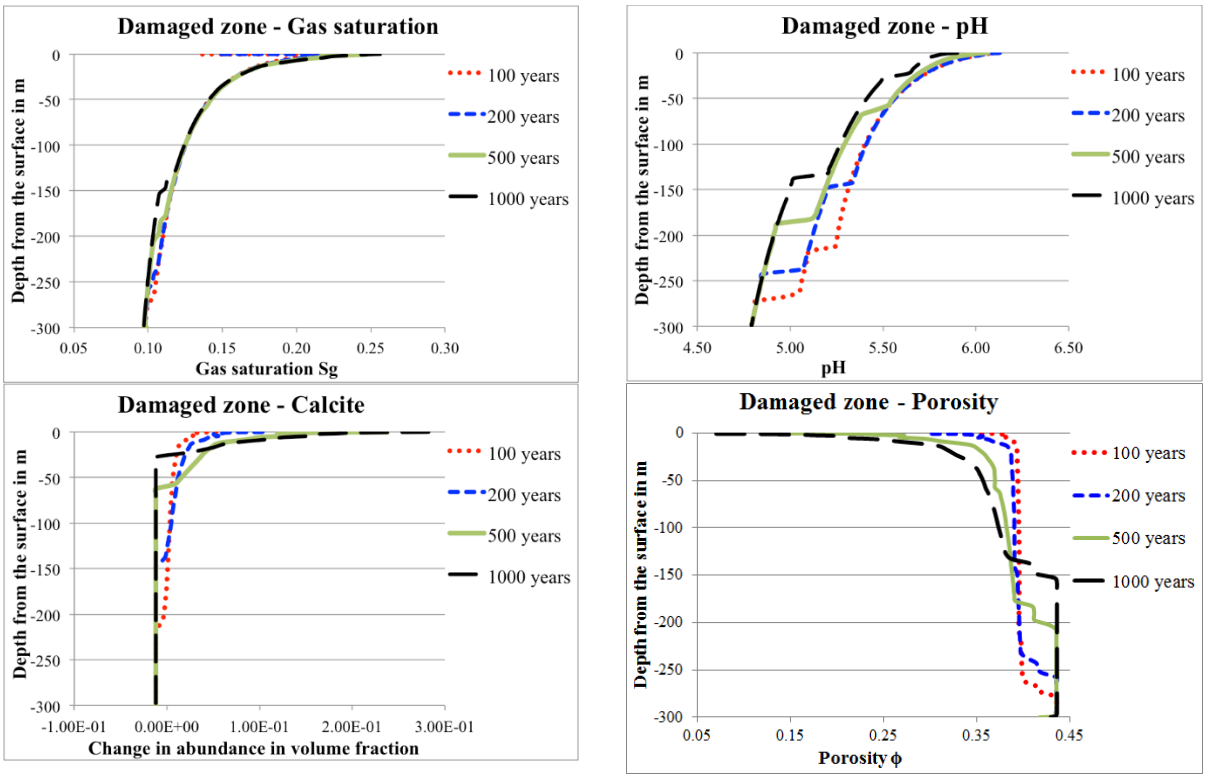

Figure 2: Selected damaged zone results- (top left) gas saturation, (top right) pH evolution, (bottom left) change in abundance of calcite and (bottom right) evolution of damaged zone porosity.

formations that it cuts through in the 300 m depth. Choice of secondary minerals were chosen based on saturation ratios of minerals in preliminary equilibrium modeling. We also collected rock samples from an outcrop of the fault. XRD results of the fault samples were used to constrain the choice of mineralogy. Kinetic parameters were taken from Palandri & Kharaka (2004). Table 2 gives the mineralogy used in our model.

Table 2: Primary and secondary mineral assemblage specified in the model. Initial weight fractions for all secondary minerals was zero.

Primary	Wt%	Secondary
Quartz	77	Na-smectite
K-feldspar	6	Ca-smectite
Oligoclase	2	Chlorite
Calcite	2	Gibbsite
Dolomite	2	Ankerite
Hematite	2	Dawsonite
Kaolinite	4	Siderite
Illite	3	Magnesite
Gypsum	2	Albite-low

The initial water chemistry was determined by reacting the primary minerals with NaCl water for 10,000 years. The resulting water composition was closely in equilibrium with the primary mineral assemblage. The water erupting from Crystal Geyser which lies along the fault is mostly sourced from the reservoir at 300 m depth. We measured this composition and applied it as a fixed bottom boundary composition (Table 3).

Table 3: Initial fault water composition in equilibrium with primary mineral assemblage is calculated using batch reaction modeling. Crystal Geyser water composition is an average of the measured values and is used at the bottom boundary. All values except that of pH in mol/kg H_2O.

Component	Initial water	Boundary water
pH	7.149	6.433
Ca^{++}	1.39E-02	2.81E-02
Mg^{++}	1.21E-03	1.07E-02
Na^{+}	1.30E-01	1.5E-01
K^{+}	1.41E-07	7.94E-03
Fe^{++}	6.50E-13	2.37E-04
Al^{+++}	4.61E-12	6.99E-06
$SiO_{2(aq)}$	3.08E-02	2.33E-04
HCO_3^{-}	4.49E-03	7.45E-02
SO_4^{--}	4.81E-02	2.19E-02
Cl^{-}	6.00E-02	1.09E-01
$O_{2(aq)}$	7.50E-10	1.94E-05

Multiphase flow through the described model was simulated for 1000 years using TOUGHREACT v2.0 (Xu et al. 2012).

RESULTS

Figure 2 shows the highlights of the results. Gas saturation (gaseous CO_2) in the domain ranged from a fixed 10% at the bottom to 26% at the top. pH became acidic due to CO_2 dissolution in the water and was buffered by dissolution of feldspars and kaolinite. Calcite precipitation in the top half of the fault depth was the most predominant mineral change associated with the CO_2 leakage. This is in tandem with the field observations (Figure 1). The precipitation mechanism is supersaturation of $CaCO_3$ due to loss of pCO_2. Other significant precipitating minerals were gypsum, dolomite, ankerite and illite. Two main reaction sequences were 1) carbonate precipitation due to pCO_2 loss, and 2) incongruent dissolution of feldspars accompanied by clay and quartz precipitation.

Porosity (and permeability) in the damaged zone (in turn the effective fault) changed dramatically over 1000 years. The porosity in the top half of the fault dropped from 40% to as low as 6% indicating that fault self-sealing is very much possible in such systems, especially at near-surface depths. However, temporal changes also suggest that initial precipitated calcite could dissolve back at a later time.

We also tested the sensitivity of the model results to key parameters. We found that our models were most sensitive to relative permeability parameters and the fault architecture. Different relative permeability functions, and more interestingly different parameter values in the same function, predicted significantly different sealing capacities. This demonstrated how relative permeability can impact reaction scenario in coupled reactive transport systems. For example, Corey curve models seemed to predict a more advanced reaction scenario at the same time compared to van Genuchten curve models.

SUMMARY

We developed 1D reactive transport models to simulate fault self-sealing due to CO_2-leakage. The base conditions that we investigated were found at the Little Grand Wash fault-zone in Utah. Our model successfully captured the reactive transport processes leading to the fault-sealing behavior in the LGWF area. We found that the results were most sensitive to the relative permeability parameters and the fault architecture. Major conclusions from this analysis are that a failed (leaking) engineered sequestration site may behave very similar to the LGWF and that under similar conditions some faults are likely to seal over time.

ACKNOWLEDGMENT

The authors would like to thank Dr. Weon Shik Han (and his students) from University of Wisconsin and Richard Esser and Richard Franz (formerly) from University of Utah for their support during field trips. This research was funded by the National Science Foundation.

REFERENCES

Caine, J., Evans, J. and Forster, C., 1996. Fault zone architecture and permeability structure. *Geology*, (11), pp.1025–1028. Available at: http://geology.gsapubs.org/content/24/11/1025.short [Accessed September 28, 2013].

N. Kampman, Bickle, M.J., Maskell, A., Chapman, H.J., Evans, J.P., Purser, G., Zhou, Z., Schaller, M.F., Gattacceca, J.C., Bertier, P., Chen, F., Turchyn, A.V., Assayag, N., Rochelle, C., Ballentine, C.J., Busch, A., 2014. Drilling and sampling a natural CO_2 reservoir: Implications for fluid flow and CO_2-fluid–rock reactions during CO_2 migration through the overburden. *Chemical Geology*, 369, pp.51–82. Available at: http://www.sciencedirect.com/science/article/pii/S0009254113005536 [Accessed February 27, 2014].

Moodie, N., McPherson, B., Lee, S.-Y., and Mandalaparty, P.,, 2015. Fundamental Analysis of the Impacts Relative Permeability has on CO_2 Saturation Distribution and Phase Behavior. *Transport in Porous Media*, 108(1), pp.233–255.

Available at: http://link.springer.com/10.1007/s11242-014-0377-5 [Accessed June 10, 2015].

Palandri, J.L. and Kharaka, Y.K., 2004. *A compilation of rate parameters of water-mineral interaction kinetics for application to geochemical modeling*, DTIC Document.

Pruess, K., 2005. Numerical studies of fluid leakage from a geologic disposal reservoir for CO_2 show self-limiting feedback between fluid flow and heat transfer. *Geophysical Research Letters*, 32(14), p.n/a–n/a. Available at: http://doi.wiley.com/10.1029/2005GL023250 [Accessed April 10, 2014].

Xu, T., Spycher, N., Sonnenthal, E., Zheng, L., and Pruess, K. , 2012. TOUGHREACT User's Guide: A Simulation Program for Non-isothermal Multiphase Reactive Transport in Variably Saturated Geologic Media, version 2.0. *Lawrence Berkeley National Laboratory: Berkeley, CA*.

NUMERICAL SIMULATIONS OF THE CHEMICAL IMPACT OF IMPURITIES ON GEOLOGICAL CO_2 STORAGE – COMPARISON BETWEEN TOUGHREACT V2.0 AND TOUGHREACT V3.0-OMP

Dorothee Rebscher [1], Jan Lennard Wolf [1], Jacob Bensabat [2], and Auli Niemi [3]

[1] Bundesanstalt für Geowissenschaften und Rohstoffe, BGR, Germany
Stilleweg 2, Hannover, 30655, Germany
e-mail: dorothee.rebscher@bgr.de, janlennard.wolf@bgr.de

[2] Environmental and Water Resources Engineering, EWRE Ltd.
Shaar Halevanon 3, Haifa 3445402, Israel e-mail: jbensabat@ewre.com

[3] Uppsala Universitet, Institutionen för geovetenskaper, Luft-, vatten- och landskapslära
Villav. 16, 752 36 Uppsala, Sweden
e-mail: auli.niemi@geo.uu.se

ABSTRACT

Numerical studies on the geochemical impact of impurities on the geological storage of CO_2 have been performed using the well established TOUGHREACT V2.0 and the more recent TOUGHREACT V3.0-OMP with OpenMP parallelization. The aim is to compare and differentiate results of identical injection scenarios which were obtained by the different modeling approaches. As to be expected, the main difference lies in the fact that a dry-out zone evolves in the V3.0-OMP simulations, but not in the V2.0 simulations due to the numerically needed coinjection of an additional aquatic phase in which the impurity has to be dissolved. The comparison indicates that in principle the influence of the acidic impurity on pH value and the continuous mineral reactions in the V2.0 simulations leads to an overestimation of the extent of the mineral changes in the system. Nonetheless, qualitative statements concluded from the V2.0 simulations are in good agreement with the newly achieved V3.0-OMP results.

INTRODUCTION

The scientific interest on the impact of impurities in CO_2 flue gas designated for geological storage grew in recent years. Experimental as well as computational methods are applied in order to assess the effects of the complex coupled flow and chemistry processes in reservoir rock formations of the deep subsurface.

Many studies on this topic rely on numerical simulations of the reactive transport of the injected CO_2, using for instance the THC codes TOUGHREACT (Xu et al., 2008) or STOMP (Bacon et al., 2009). Yet, previous versions of these codes were only capable of dealing with CO_2, water, and NaCl as constituents of fluid flow without any further gas phase components. Hence, the aqueous equilibrium concentration of an impurity was computed under the prevailing conditions (pressure, temperature, salinity) and artificial formation water containing the chosen amount of impurity was injected additionally to CO_2 in the simulations.

However, the recent release of advanced versions of these simulation codes (Bacon et al., 2014; Xu et al., 2014) allows the inclusion of additional trace gas species, therefore providing a more realistic description of reactive transport in the subsurface. In the context of the geochemical impact on CO_2 storage, it is now possible to inject a CO_2 stream with impurities e.g. SO_2, where SO_2 is directly dissolved in the gas phase. This is of special interest, as SO_2 is one of the most prominent impurities in CO_2 flue gas streams designated for geological storage while having the greatest impact on pH value and due to its relevance in redox reactions.

THE TEST SITE HELETZ

This numerical study presented is embedded in the European project CO2QUEST, short for Impact of the Quality of CO_2 on Storage and Transport (Brown et al., 2014; Jung et al., in prep.). Reservoir data, kindly provided by the MUSTANG Project (Niemi and Bensabat, in prep.; Niemi et al., in prep.), is based on the field scale experiment Heletz, which is located at the Southern Mediterranean Coastal Plain of Israel, within a saline aquifer at the edges of a depleted oil field, refer Figure 1. The target reservoir consists of three Lower Cretaceous sand layers at depth of about 1650 m below a shaly caprock (Shtivelman et al., 2011), parameters are listed in Tables 1 and 2. Injection tests of water and super-critical pure CO_2 have been conducted very recently, in summer 2015. Push-pull tests with SO_2 as an impurity in the CO_2 stream will start in fall 2015.

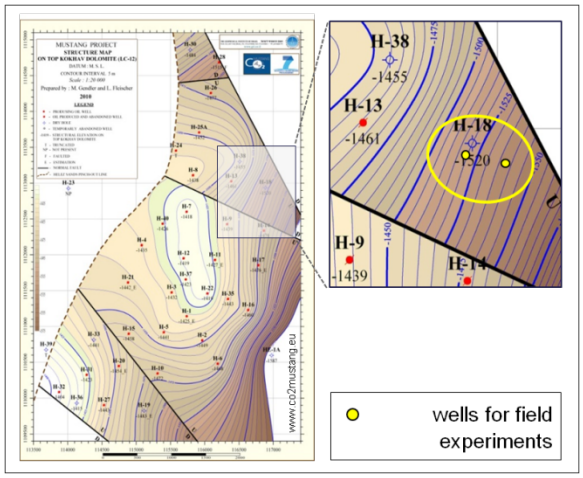

Figure 1. Location of the field scale experiment Heletz with the injection well H-18, modified after (Fagerlund et al., 2013).

Table 1. Parameters of the Heletz test site used in the simulations.

parameter	value
pressure	14.7 MPa
temperature	66 °C, isothermal
porosity	20 %
horizontal permeability	100 mD
vertical permeability	700 mD
thickness	18 m
rock density	2870 kg/m^3
salinity	0.055

Table 2. Initial mineral composition based on laboratory studies performed within the FP7-MUSTANG project.

primary minerals	fraction
carbonates	
ankerite $CaFe_{0.7}Mg_{0.3}(CO_3)_2$	3.7 %
feldspars	
K-feldspar $KAlSi_3O_8$	12 %
albite $NaAlSi_3O_8$	3.9%
clay minerals	
illite $K_{0.85}Al_{2.85}Si_{3.15}O_{10}(OH)_2$	3.9 %
kaolinite $Al_2Si_2O_5(OH)_4$	3.2 %
chlinochlore-7a $Mg_5Al_2Si_3O_{10}(OH)_8$	1.4 %
sulfur minerals	
pyrite FeS_2	2.1 %
anhydrite $CaSO_4$	0.4 %
oxide mineral	
quartz SiO_2	69.35 %
iron mineral	
goethite Fe_2OOH	0.05 %
secondary minerals	
carbonates	
calcite $CaCO_3$	
siderite $FeCO_3$	
iron mineral	
hematite Fe_3O_4	

MODEL SETUP

The 2D radial symmetric grid model represents three sandstone layers adjacent by two shale layers, covering a vertical extent of 18 m, refer Table 1, Figures 2a and 2b. In the vertical, each of these layers is represented by 3 to 20 cells. Dependent on the layer, the height of a cell ranges from 0.36 m to 1.4 m. The horizontal extent of the model covers 1000 m. In order to get a more detailed resolution close to the injection well, a horizontal incremental factor of 1.06 was chosen. Hence, cell lengths vary from 0.18 m at the injection point at the lower left

corner to 75 m at the edge of the model on the very right. The total number of cells is 37 x 100.

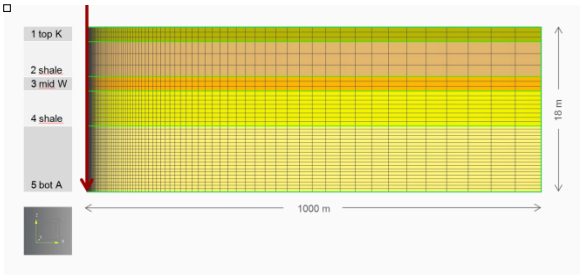

Figure 2a. The 2D radial symmetric reservoir grid consisting of the three Lower Cretaceous sandstone layers K, W, and A, separated by two shale layers (five gray blocks to the left corresponding to five grid layers in different shades of yellow-orange). The thickness of the shale layers amounts to 4 m each, the sandy layers from bottom to top 11 m, 1.5 m, and 1.5 m, respectively. The injection point is located at the lower left corner, marked by the red arrow.

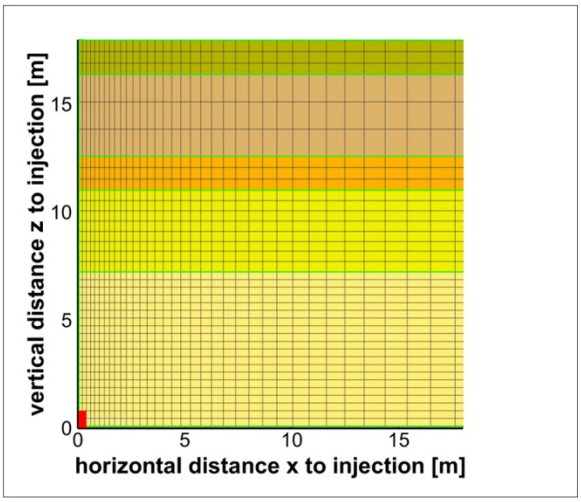

Figure 2b. Section of the 2D radial symmetric grid, covering the identical area of the Figures 3 to 9b, refer Figure 2a. The four injection cells at the lower left are marked in red.

The thermodynamic database is transferred from the Lawrence Livermore National Laboratory's geochemical software package EQ3/6, respecting some minor changes between primary and secondary species (Wolery, 1992). The kinetic data for mineral dissolution and precipitation is based on (Palandri and Kharaka, 2004) with minor additions (Xu et al., 2006; Zhang et al., 2011).

For the numerical simulations, the injection strategy conforms with the planned injection test. Over a time period of 100 h, CO_2 and SO_2 are coinjected with a rate of 0.28 kg/s and a ratio of 97 to 3. This injection phase is followed by a relaxation phase of 144 h.

INJECTION STRATEGIES

TOUGHREACT V2.0 (in the following referred to as V2) offers the feasibility to simulate reactive transport for pure gases but not gas mixtures. A common practice to introduce impurity compounds to a gaseous or supercritical CO_2 phase is to dissolve the compound in an aqueous phase (Xu et al., 2007). Accordingly, in the simulations presented here, the SO_2 is dissolved in an aquatic phase and coinjected with the CO_2. Besides this, the aquatic phase has the identical composition of the native brine, hence minimizing an unrealistic dissolution of the primary minerals. The distribution of the additional brine is shown in Figure 3, influencing an area of less than 10 m times 5 m.

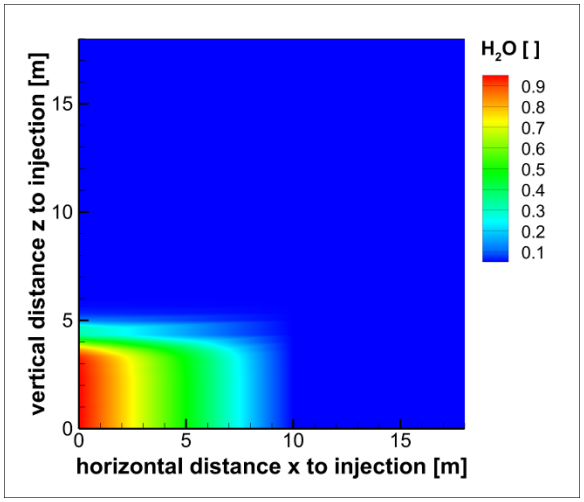

Figure 3. Distribution of the additional brine. calculated with Helium in the aquatic phase added as a tracer using 0.001 mol/kg H_2O in one V2 simulation.

However, as this composition is fixed during the simulation of injection, it cannot respond to particular activity changes in the injection zone induced by the dissolution of CO_2 or SO_2. This might lead to the precipitation of minerals solely originating from the injection mass flow but not from the dissolution of primary minerals. In the

case of TOUGHREACT V3.0-OMP (in the following referred to as V3), the SO_2 impurity is introduced into the system as a trace gas included in the injected CO_2. This methodological approach allows for consideration of the impact of gas phase transport on the spatial dissolution pattern as well as for avoiding the artificial influence of injection water as discussed above. Note, that the fluid flow of the CO_2 rich phase, i.e. the gas phase, is still computed assuming the flow of a pure CO_2 phase, whereas any impact of the impurity compound, for instance on density or viscosity of the phase, is neglected.

GEOCHEMICAL SIMULATION USING TOUGHREACT V2.0 AND V3.0-OMP

The fluid property model for geological sequestration in saline aquifers ECO2N (Pruess, 2005) was used, providing the properties of the tertiary mixture H_2O-NaCl-CO_2 and covering the required parameter ranges of the reservoir conditions in Heletz, refer Table 1. Using a Windows-based PC (i7-4770, 32 GB, Quad core, 8 threads), a V2 calculation needed 17 h, the V3 required 8 h, equivalent to a speed-up factor of about 2.

In order to emphasize the region where the important changes occur, only a section of the whole model is plotted in Figure 3 to 9, i.e. in the horizontal only the first 18 m are shown, while the vertical extent of 18 m covers the entire height of the model layers.

As the injected gas pushes the native brine away from the injection point, a distinct dry out zone emerges, within a region about 1 m around the injection cells. The preference of horizontal flow is due to the difference between horizontal and vertical permeability. High values in the gas saturation close to the injection are clearly visible in the V3 results, see Figure 4b. Whereas the dry out zone is omitted in the gas saturation values obtained with V2 due to the diluting effect of the additional brine, see Figure 4a.

The slight increase in gas saturation within the upper part of the lowest sand layer A, below the shale is very similar in both simulations, regarding concentration as well as geometry. Equivalent horizontal distances of about 10 m are found with both TOUGHREACT versions. The overlying shale layer is only affected in the first few meters and no differences between the two codes are detected. This is reasonable as no significant additional brine reaches regions above a few meters in the vertical. Hence, as expected, the main difference occurs in the bottom part of the model and close to the injection point, where the additional fluid dilutes the gas saturation.

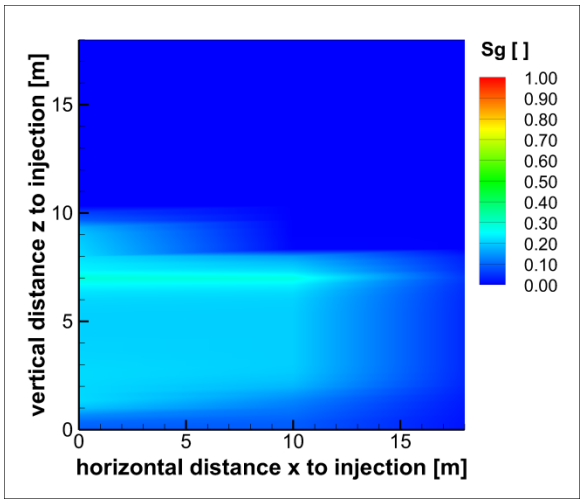

Figure 4a. Gas saturation after 10 days of coinjecting about 100 t CO_2+SO_2. There is no development of a dry out zone; simulation with TOUGHREACT V2.0.

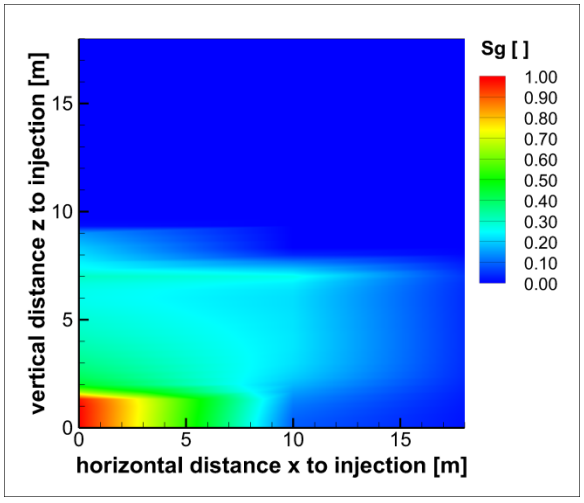

Figure 4b. Gas saturation after 10 days of coinjecting about 100 t CO_2+SO_2. Development of a dry out zone in the vicinity of the injection point; simulation with TOUGHREACT V3-OMP.

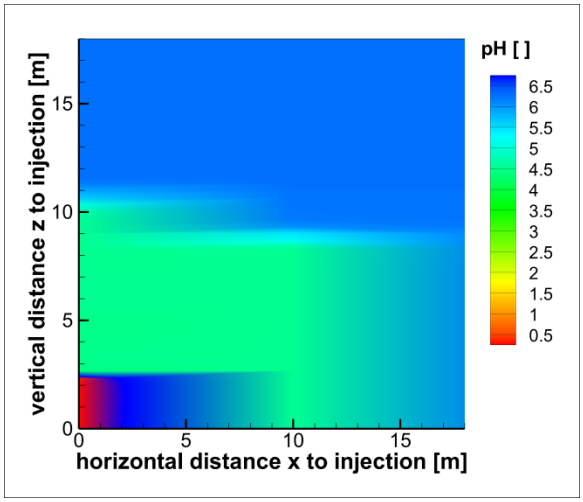

Figure 5a. Distribution of pH value after 10 days of coinjecting about 100 t CO_2+SO_2; simulation with V2.

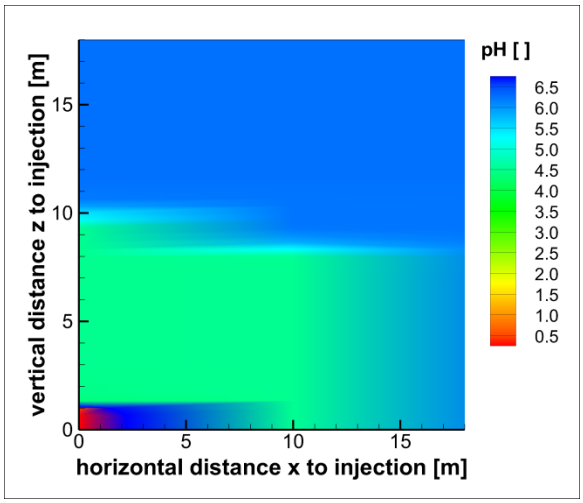

Figure 5b. Distribution of pH value after 10 days coinjecting about 100 t CO_2+SO_2; simulation with V3.

MINERAL ALTERATION

The comparison of numerical results from impure CO_2 injection scenarios into a saline aquifer using the two TOUGHREACT versions reveals several qualitative as well as quantitative differences in mineral alterations. In general, the geochemical behavior predicted is comparative. The numerical results of both code versions show the strongest impact of SO_2 to be related to the fast reacting, pH sensitive primary carbonate mineral ankerite, see Figures 5a to 6b.

However, the spatial extent and the degree of the ankerite the ankerite dissolution and the concomitant release of Ca^{2+} induces the immediate precipitation of anhydrite.

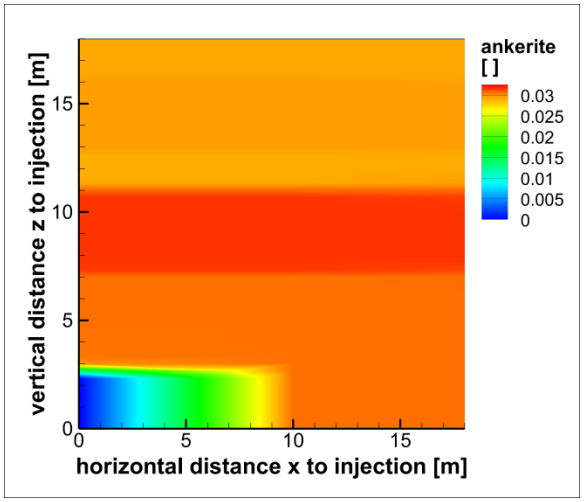

Figure 6a. Distribution of ankerite after 10 days of coinjecting about 100 t CO_2+SO_2; simulation with V2.

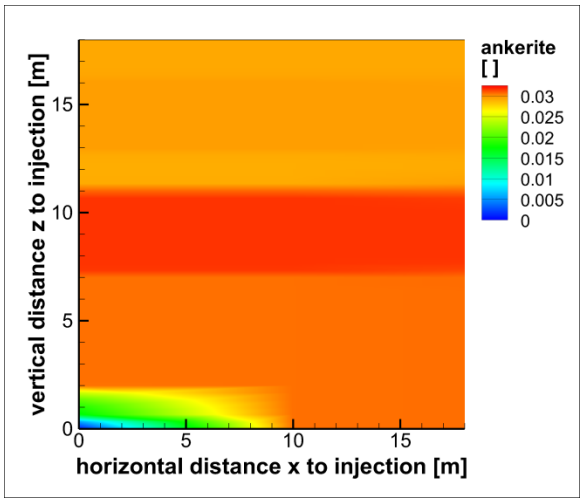

Figure 6b. Distribution of ankerite after 10 days of coinjecting about 100 t CO_2+SO_2; simulation with V3.

While the transformation of ankerite into anhydrite in the V3 simulation appears at the same grid cells, in the V2 simulation the released metal cations (e.g. Ca^{2+}) and sulfate ions from the SO_2 injection water become firstly displaced to slightly higher zones due to the "purging" effect of the injection water flow, refer Figures 8a and 8b.

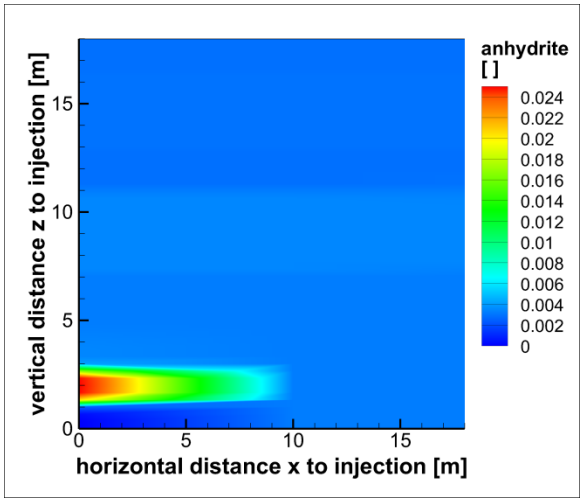

Figure 7a. Distribution of anhydrite after 10 days of coinjecting about 100 t CO_2+SO_2; simulation with V2.

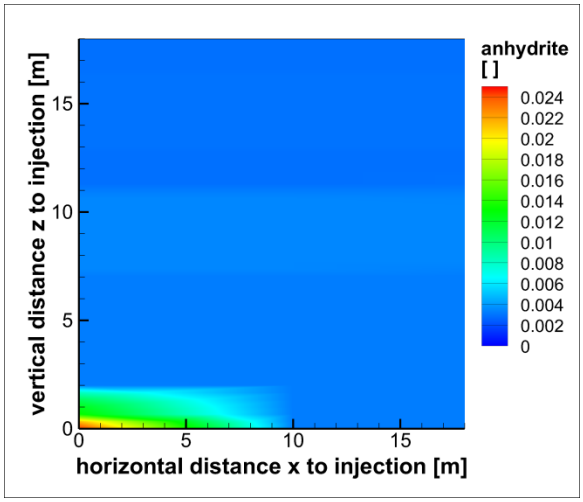

Figure 7b. Distribution of anhydrite after 10 days of coinjecting about 100 t CO_2+SO_2; simulation with V3.

This is also reflected in the spatial distribution of Ca^{2+} in the V2 simulation, where the impact of the injection water can be seen as a three-banded concentration profile within the sandy layer A. The lowest band (0 m to 1 m) is dominated by the lateral purging flow of the additional injection water with low Ca^{2+} concentration (0.02 mol/kg water) in order to prevent artificial anhydrite and calcite precipitation. Above (1.0 m to 2.5 m), acidic SO_2(aq) from the injection is available for dissolution of ankerite and subsequent precipitation of anhydrite, thereby leading to a slightly increased Ca^{2+} concentration compared to the injection water (approximately 0.04 mol/kg water. The third band (2.5 m to 5.0 m) lies still within the extent of the injection water plume as shown by including non-reactive He(aq) transport in the simulation, refer Figure 3. Thus, this band is still dominated by the injected water and its low Ca^{2+} concentration, but the acidifying SO_2(aq) is already totally consumed due to the formation of anhydrite in the intervening layer, i.e. between 1.0 m to 2.5 m.

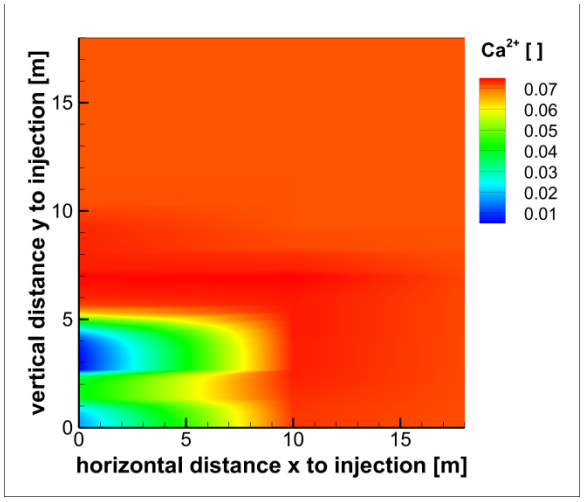

Figure 8a. Distribution of Ca^{2+} after 10 days of coinjecting about 100 t CO_2+SO_2; simulation with V2.

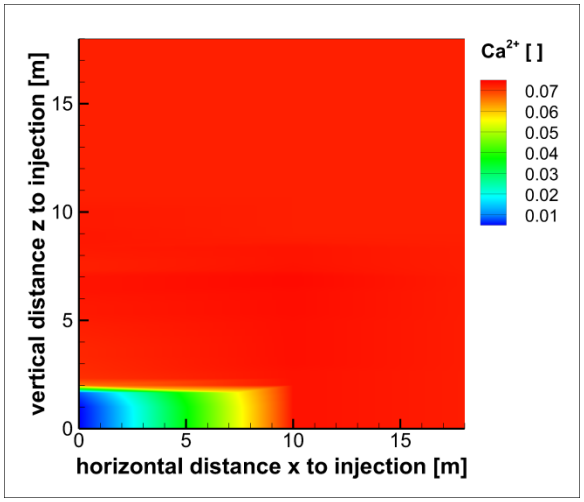

Figure 8b. Distribution of Ca^{2+} V3 after 10 days of coinjecting about 100 t CO_2+SO_2; simulation with V3.

The enhanced ankerite dissolution close to the injection zone in the V2 simulation compared to the V3 computation also leads to an increased release of Fe^{2+} ions, which is accompanied by an

enhanced precipitation pattern of pyrite (FeS_2). These three main mineral reactions – carbonate (ankerite) dissolution, sulfate (anhydrite), precipitation as well as pyrite precipitation – dominate the overall porosity change, which is more pronounced in case of the V2 simulation due to the higher amounts of reacting minerals, see Figures 9a and 9b.

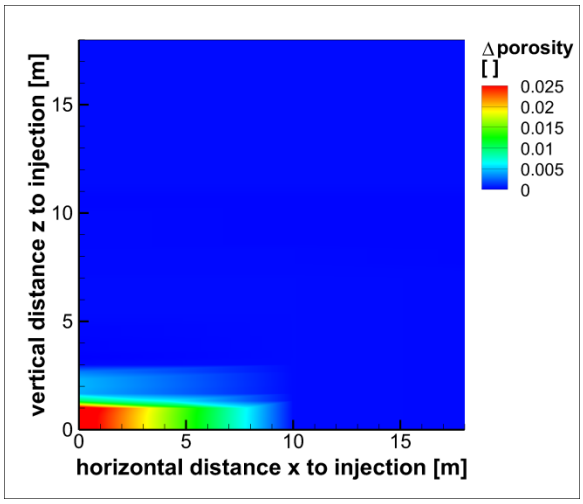

Figure 9a. Changes in porosity after 10 days of coinjecting about 100 t CO_2+SO_2; simulation with V2.

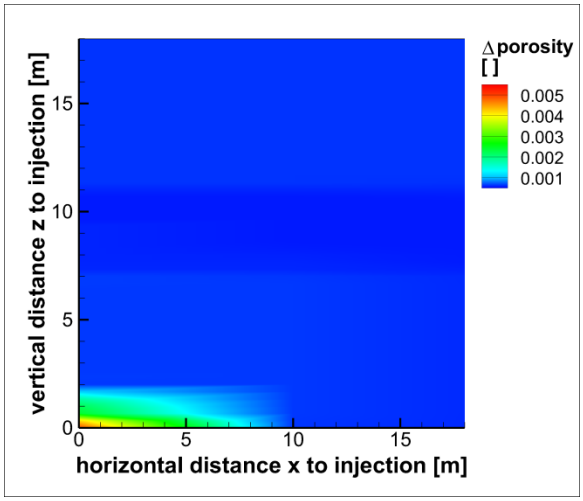

Figure 9b. Changes in porosity after 10 days of coinjecting about 100 t CO_2+SO_2; simulation with V3. Note the different scale in the legend compared to Figure 9a.

CONCLUSIONS

The TOUGHREACT V2.0 simulations are in good agreement with the newly achieved TOUGHREACT V3.0-OMP results, evidenced by comparing results of identical injection scenarios obtained by two different modeling approaches. As to be expected, the main difference lies in the fact that a dry-out zone evolves in the V3 simulations, but not in the V2 simulations due to the coinjected brine in the latter case. The comparison indicates that in principle the influence of the acidic impurity on pH value after 10 days and the continuous mineral reactions in the V2 simulations leads to an overestimation of the extent of the mineral changes in the system.

Both modeling approaches reveal the same dominant mineral alteration processes (ankerite dissolution, anhydrite and pyrite precipitation) as well as similar aqueous flow patterns of the main primary species (e.g. Ca^{2+}, Fe^{2+}, H^+ / pH). But the magnitudes of the mineral reactions in case of the V2 simulation seem to be significantly overestimated compared to the more realistic V3 computation due to the disregard in the V2 case of more pronounced spatial impurity distribution patterns. The additional injection of (aqueous) fluid and the subsequently increased displacement of formation water is presumably responsible for the enlarged spatial extent of mineral alteration in the V2 case. Nonetheless, qualitative statements concluded from the V2 simulations are in good agreement with the newly achieved V3 results. In scenarios were the close vicinity of the injection point is investigated, the use of V3 is recommended, whereas farther away, V2 is sufficient. The numerical simulations will be validated against experimental field data.

ACKNOWLEDGMENT

The authors would like to thank Nic Spycher (Lawrence Berkeley National Laboratory) and Franz May (BGR) for stimulating discussions and always insightful answers. Thanks are also extended to the partners within the CO2QUEST Project. The accessibility of data obtained within the MUSTANG Project is kindly acknowledged.

DISCLAIMER

The research leading to the results described in this presentation has received funding from the European Union 7th Framework Programme

FP7-ENERGY-2012-1-2STAGE under grant agreement number 309102. The presentation reflects only the authors' views and the European Union is not liable for any use that may be made of the information contained therein.

REFERENCES

Bacon, D. H., B. M. Sass, M. Bhargava, J. Sminchak, and N. Gupta, Reactive Transport Modeling of CO_2 and SO_2 Injection into Deep Saline Formations and Their Effect on the Hydraulic Properties of Host Rocks, *Energy Procedia*, *1*, 3283-3290, 2009.

Bacon, D. H., R. Ramanathan, H. T. Schaef, and B. P. McGrail, Simulating geologic co-sequestration of carbon dioxide and hydrogensulfide in a basalt formation, *Int. J. Greenh. Gas Con., 21*, 165-176, 2014.

Brown, S., S. Martynov, H. Mahgerefteh, M. Fairweather, R. M. Woolley, C. J. Wareing, S. A. E. G. Fallec, H. Rütters, A. Niemi, Y. C. Zhang, S. Chenf, J. Bensabat, N. Shah, N. Mac Dowell, C. Proust, R. Farret, I. G. Economou, D. M. Tsangaris, G. C. Boulougouris, J. van Wittenbergh CO2QUEST: Techno-economic Assessment of CO_2 Quality Effect on Its Storage and Transport, *Energy Procedia*, 63 2622-2629, 2014.

Fagerlund, F., A. Niemi, J., Bensabat, and V. Shtivelman, Design of a two-well field test to determine in situ residual and dissolution trapping of CO_2 applied to the Heletz CO_2 injection site. *Int. J. of Greenh. Gas Con.*, 19, 642-651, 2013.

Jung, B., J. L. Wolf, D. Rebscher, R. Segev, J. Bensabat, and A. Niemi, Hydromechanical and Geochemical Impacts of Impurity on Geological CO_2 Storage in Heletz Site, Israel, *Int. J. Greenhouse Gas Control*., in prep.

Niemi, A. and J. Bensabat, *Int. J. Greenhouse Gas Control,* Special edition, in prep.

Niemi , A., J. Bear, and J. Bensabat (eds.), Geological Storage of CO_2 in Deep Saline Formations, Springer-Verlag Berlin Heidelberg New York, in prep.

Palandri, J. L. and Y. K. Kharaka, A compilation of rate parameters of water-mineral interaction kinetics for application to geochemical modeling, Report 2004-1068, U.S. Geological Survey, Menlo Park, Calif., 2004.

Pruess, K., ECO2N: A TOUGH2 fluid property module for mixtures of water, NaCl and CO_2, *Report LBNL-57952*, Lawrence Berkeley National Laboratory, Berkeley, Calif., 2005.

Pruess, K., and N. Spycher, ECO2N – A fluid property module for the TOUGH2 code for studies of CO_2 storage in saline aquifers, *Energy Conversion and Management*, *48*(6), 2007.

Shtivelman, V., M. Gendler, and I. Goldberg, 3D geological model of potential CO2 reservoir for the Heletz test site. Geophysical Institute of Israel, POB 182, LOD 71100. *Geophysical Research Abstracts*, 13, EGU2011-1307-1, 2011.

Wolery, Th. J., *EQ3/6*: Software package for geochemical modeling of aqueous systems: Package overview and installation guide, version 7.0, *Report*, Lawrence Livermore National Laboratory, Livermore, Calif. 1992.

Xu, T., J. A. Apps, K. Pruess, and H. Yamamoto, Numerical modeling of injection and mineral trapping of CO_2 with H_2S and SO_2 in a sandstone formation, *Chem. Geol.*, *242*, 319-346, 2007.

Xu, T., E. Sonnenthal, N. Spycher, and K. Pruess, TOUGHREACT user's guide: a simulation program for non-isothermal multiphase reactive geochemical transport in variably saturated geologic media, V1.2.1. *Report LBNL-55460-2008*, Lawrence Berkeley National Laboratory, Berkeley, Calif., 2008.

Xu, T., E. Sonnenthal, N. Spycher, and L. Zheng, TOUGHREACT V3.0-OMP Reference Manual: A Parallel Simulation Program for Non-Isothermal Multiphase Geochemical Reactive Transport, *Report LBNL-DRAFT*, Lawrence Berkeley National Laboratory, University of Calif., Berkeley, 2014.

Zhang, W., Xu, T., Li, Y., Modeling of fate and transport of coinjection of H_2S with CO_2 in deep saline formations, *J. Geophys. Res.* (1978–2012), 116(B2) 13, 2011.

SIMULATING CO_2-BRINE-ROCK INTERACTIONS INCLUDING MERCURY AND H_2S IMPURITIES IN THE CONTEXT OF CO_2 GEOLOGIC STORAGE

Nicolas F. Spycher and Curt M. Oldenburg

Lawrence Berkeley National Laboratory
1 Cyclotron Road, MS 74R316C
Berkeley, California, 94705, USA
e-mail: nspycher@lbl.gov

ABSTRACT

Mercury (Hg) is a common contaminant in natural gas, remains at small concentrations in combustion products, and accompanies CO_2 in the amine separation capture process. The fate of Hg as a potential impurity accompanying CO_2 in geologic storage operations is unknown, and so is the question of whether Hg in the CO_2 injection stream could negatively impact injectivity by reducing permeability in the storage formation. Modeling investigations were undertaken to assess the potential for Hg to precipitate (or condense) from an injected stream of Hg-containing supercritical CO_2 into a sandstone formation at 106°C and 215 bar. Volumetric analyses show that any Hg deposition would have to occur on scales of centimeters to potentially affect permeability. Simulations using TOUGH2/EOS7C show that the evaporative concentration of aqueous Hg by (dry) supercritical CO_2 uptake of water is unlikely, because the volatility of Hg into the CO_2 stream is higher than that of water. Geochemical and reactive transport simulations using CHILLER and TOUGHREACT, respectively, predict that cinnabar (HgS) would readily precipitate from the CO_2 phase in the presence of aqueous sulfide naturally present in the formation. However, the precipitation of minerals other than cinnabar is predicted to dominate the evolution of porosity, including the precipitation of chalcedony from the dissolution of silicate minerals, and the replacement of Fe-chlorite by siderite, of calcite by dolomite, and of K-feldspar by muscovite. Liquid Hg is not expected to condense at the conditions of interest here (190 ppbV Hg gas), even in sulfide-free waters. Simulations with (200 ppm) and without H_2S as a co-contaminant yield similar results, except that pyrite alters to ankerite when H_2S is deficient. In all simulated cases, the predicted porosity change is negligible and not expected to affect permeability and CO_2 injectivity.

INTRODUCTION

Trace amounts of mercury (Hg) are found naturally in fossil fuels (coal, oil, and natural gas) (e.g., Bingham, 1990) resulting in combustion products that also contain Hg. Because concurrent capture of CO_2 and Hg from flue gas and from high-CO_2 natural gas is being considered (e.g., Cui et al., 2010), the question arises whether Hg in CO_2 streams injected into deep geologic formations could negatively impact geologic carbon sequestration (GCS), specifically through reducing injectivity.

Trace amounts of Hg in large volumes of injected CO_2 could reduce injectivity in at least two ways. First, the condensation of liquid Hg ($Hg_{(l)}$) from the compressed CO_2 gas phase could reduce the CO_2 relative permeability in the formation. In addition, the precipitation of Hg-containing minerals such as cinnabar ($HgS_{(s)}$) could reduce porosity of the formation, with associated effects on permeability. In this study, we present simple volumetric and equilibrium dew-point analyses, along with more complex reactive transport and geochemical modeling to investigate whether Hg condensation, precipitation as cinnabar, or reactions involving non-Hg minerals could substantially affect injectivity arising from injection. Details of our work can be found in Oldenburg and Spycher (2015), and Spycher and Oldenburg (2015).

APPROACH

In the first part of this study, we evaluated potential pore occupancy and evaporation-condensation processes of Hg injected as a trace

contaminant with a CO_2 carrier gas into an idealized, porous reservoir formation at a depth of approximately 2 km (~210 bar, 106 °C). The volumetric calculations, which assume that a cylindrical porous region around the wellbore is uniformly permeated with injected CO_2 and Hg, were made to evaluate the amount and volume of Hg injected with CO_2 and to assess the effects on porosity of different volumetric distributions of Hg and CO_2 within the target formation. Dynamic changes in aqueous Hg concentration were investigated by numerical simulation using TOUGH2/EOS7C (Pruess et al., 1999, 2012; Oldenburg et al., 2004) to simulate the evaporative concentration behavior of trace soluble gas species (such as Hg) of different volatilities.

In the second part of the study, we performed geochemical speciation and reaction path simulations using, respectively, GeoT (Spycher et al., 2014) and CHILLER (Reed, 1980, 1998) to investigate the products of incremental reaction between an Hg-bearing CO_2 phase, formation water, and reservoir minerals, with effects on porosity. The results of these simulations were then used to refine geochemical inputs for more complex reactive transport simulations using TOUGHREACT V2 (Xu et al., 2006, 2011) and TOUGHREACT V3-OMP (Sonnenthal et al., 2014) with the ECO2N equation of state module (Pruess and Spycher, 2007). This reactive multiphase flow simulator takes into account the non-ideal phase-partitioning of CO_2 and brine, aqueous and gas-phase transport (by advection and diffusion), aqueous complexation, and mineral precipitation/dissolution under equilibrium and/or kinetic constraints.

RESULTS

Volumetric and Evaporation-Condensation Analyses

Relevant properties and operational parameters of a hypothetical GCS reservoir and injectate composition are shown in Table 1. From these assumptions, the maximum porosity change from Hg deposition in a reservoir can be estimated by simple volumetric analyses, assuming that all of the available Hg either condenses or precipitates as cinnabar within a uniform cylindrical volume around the wellbore. The calculated Hg mass flow rate into the target formation is 400 kg/y (Table 1). However, the corresponding (maximum) volumes of Hg or cinnabar that could condense and precipitate (respectively) upon injection are very small (< 2 m^3) relative to the huge volume of injected supercritical CO_2. Given these small expected volumes, it is evident that a significant reduction in permeability from Hg deposition would only arise if deposition occurred within the pore space of a small and localized region of the reservoir.

If we assume that Hg deposition occurs uniformly along 300 m of a 0.25 m-diameter (10-inch) injection well, it is possible to roughly estimate by simple geometrical calculations the lateral extent of Hg deposition around the well versus porosity drop, or vice versa. In doing so, it is estimated that an absolute porosity drop of more than 1% would require precipitation of all of the injected Hg within less than ~0.2–0.4 m from the injection well (Figure 1). If, on the other hand, Hg deposition occurred over meters to tens of meters, as we might intuitively expect, the porosity drop would be correspondingly smaller, as would the impact on porosity and therefore on injectivity. Although this simple analysis does not consider the details of where deposition might occur, e.g., in pore throats versus within pore bodies, the small volume of Hg available to reduce porosity suggests minimal effects on injectivity. We note that TOUGHREACT-ECO2N numerical simulations (e.g., Pruess and Spycher, 2007) reveal that the distribution of CO_2 and Hg around the injection well cannot be assumed to be cylindrical in shape because the buoyancy of supercritical CO_2 results in an upward-widening conical plume around the wellbore.

Small quantities of water are known to evaporate into compressed CO_2 (e.g., Pruess and Müller, 2014), which results in the evaporative concentration of constituents in the formation water when large amounts of CO_2 flow through the formation in contact with that water (e.g., near the wellbore during CO_2 injection). Could such an evaporative concentration process affect the partitioning of Hg between the CO_2 phase and the formation water, and create the potential

for dissolved Hg to concentrate in the aqueous phase upon prolonged injection of CO_2? If such rise in aqueous Hg concentrations occurred, could Hg condense or precipitate as cinnabar during continued drying, causing significant reductions in porosity? This question was investigated using the three-grid-block numerical and conceptual model sketched in Figure 2a. As shown, CO_2 is injected into the first model grid block, which is initially filled with a small amount of aqueous phase that quickly dries up. This CO_2 flows directly into the second grid block that contains a two-phase mixture of supercritical CO_2 and water, where the aqueous phase contains Hg at concentration ~5.6×10^{-8} (mass fraction at equilibrium determined for the conditions of interest). In this second grid block, instantaneous equilibrium of the CO_2 and the Hg-bearing aqueous phase is calculated, resulting in equilibrium partitioning of Hg and CO_2 into the aqueous and gas phases. The CO_2-rich phase then flows into the third grid block which is an effective sink for whatever phases and components flow into it. The question we have posed can be answered by simply monitoring the aqueous phase concentration in the second grid block; in short, does the aqueous Hg concentration in the second grid block increase or decrease as dry CO_2 flows through?

Table 1. Model system parameters for simple volumetric analysis.

Input assumptions	**Value**	**Units**
Pressure	215	bar
Temperature	106	C
Porosity	0.15	
Residual CO_2 saturation	0.4	
Thickness of injection interval	300	m
CO_2 injection rate per injector	14.8	kg/s
Injection time period	40	Y
Hg concentration in CO_2	0.19	ppmV
H_2S concentration in CO_2	200	ppmV
Hg mass injection rate	399	kg/y
Volumetric injection rate as Hg(l)	0.0295	m^3/y
Volumetric injection rate as HgS(s)	0.0489	m^3/y
Results		
Reservoir volume with residual	6.35×10^8	m^3
Total Hg volume as Hg(l)	1.18	m^3
Total Hg volume as HgS(s)	1.95	m^3
Radius of CO_2 plume	821	m

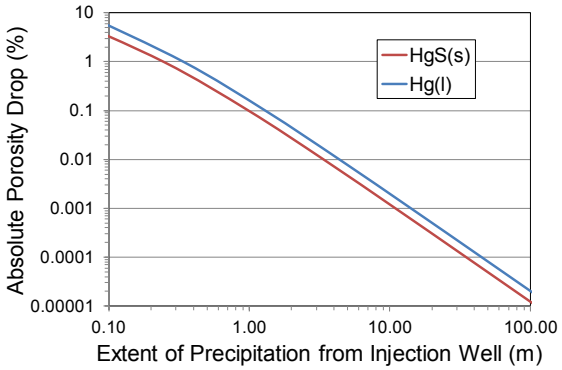

Figure 1. Absolute porosity change estimated for a given extent of homogeneous Hg deposition radially around an injection well (see Table 1 for assumptions and inputs).

Simulations were carried out using TOUGH2/EOS7C considering a tracer with various assigned values of Henry's Law constant (*Kh*). In one case, a *Kh* value representative of Hg was considered (with *Kh* ~8.2×10^8 Pa/mole fraction at the temperature and pressure of interest). In the other cases, hypothetical tracers more- and less-volatile than Hg were considered. Results are shown in Figure 2b by curves of CO_2-phase saturation (S_g, left-hand side vertical axis, representing the CO_2-rich phase volume fraction in the pore space) and Hg concentration (mass fraction in the aqueous phase) predicted in the second grid block, computed for various values of 1/*Kh*. S_g is predicted to increase steadily as the H_2O component evaporates from the aqueous phase. For Hg (at 1/*Kh* ~ 1.22×10^{-9} Pa^{-1}; solid blue curve), the Hg concentration is computed to rapidly decline with time, indicating that Hg will not concentrate in the aqueous phase as dry CO_2 flows through. Additional results for hypothetical solutes with various 1/*Kh* values are shown in Figure 2b. For 1/*Kh* values larger than 7.994×10^{-6} Pa^{-1}, the solute concentrates as evaporation occurs. This critical value of 1/*Kh*, separating concentrating from non-concentrating solutes, subject to contact with dry CO_2, represents the inverse of the saturation pressure of water at the considered *P-T* conditions. In other words, if a solute is more volatile than water in the CO_2 stream, its concentration decreases in the aqueous phase as drying occurs. If the solute is less volatile than water, its concentration increases. This result shows that the concentration of any aqueous Hg

in a two-phase groundwater-gas region is expected to decrease as dry CO_2 flows through, because the Hg component is more volatile (by several orders of magnitude) than the H_2O component into the CO_2 stream. This behavior implies that Hg will tend to be transported farther into the formation with the flowing CO_2 rather than accumulating around the near-well region where it could impact injectivity.

(a)

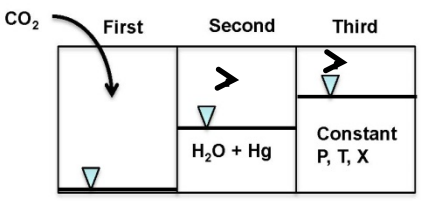

(b)

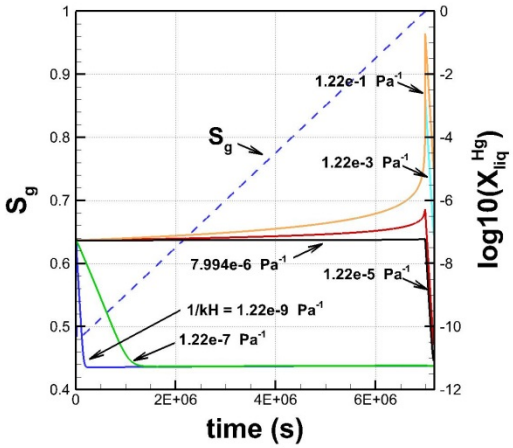

Figure 2. (a) Sketch of the three-grid-block model used to predict the evolution of aqueous Hg concentrations (in the second grid block) as water dissolves (evaporates) into the dry CO_2 flowing (arrows) above the solution. (b) TOUGH2/EOS7C results of CO_2-rich ("gas") phase saturation (S_g) and log mass fraction of Hg in the aqueous phase (in the second grid block) as a function of time, for different input $1/Kh$ values. The curve for Hg is shown by the blue solid line ($1/Kh = 1.22 \times 10^{-9}$ Pa^{-1}). Note that the sharp curve reversals near the right axis are caused by the aqueous phase drying up after 7×10^6 s (81 days).

Reactive geochemistry

The water composition in a deep formation at a temperature of 106°C and ~21.5 MPa was reconstructed by geochemical modeling (e.g., Palandri and Reed, 2001), using a water composition and mineralogical data obtained from the literature for a typical marine glauconitic sandstone/siltstone. The chemical reactions between the deep brine/sandstone assemblage and a CO_2+Hg mixture at 106°C and ~21.5 MPa were then simulated using CHILLER. This thermodynamic modeling exercise (which does not consider transport) yields a formation water pH (in-situ) initially dropping from about 7 to 4.7, then becoming buffered near 5.2 upon reaction with the formation minerals. Cinnabar is found to be thermodynamically stable as soon as the Hg-bearing CO_2 reacts with the formation water, however liquid Hg does not condense at any point during the simulation. The main reaction products are chalcedony forming mainly from feldspar dissolution, and siderite primarily from Fe-chlorite dissolution, with negligible porosity change.

The injection of Hg- and H_2S-bearing CO_2 into a similar deep sandstone formation was then simulated, with focus on the spatial distribution of Hg deposition and the porosity change around the injection well. The model was set up as a two-dimensional radial *X-Z* domain, considering 40 years of CO_2 injection at a rate of 14.8 kg/s through a 300 m interval perforated into a 400 m-thick formation, at a constant temperature of 106°C and average initial pressure ~21.5 MPa. The modeled domain was discretized into 9700 grid blocks, with 100 horizontal layers (Δz=4 m) and increasing grid spacing in the horizontal direction (Δx=0.08–2 m for the first 100 m). Three cases of injection were simulated, with CO_2 containing: (1) 200 ppmV H_2S and 190 ppbV Hg, (2) no H_2S and 190 ppbV Hg, and (3) 200 ppmV H_2S and 7 ppbV Hg. Similar results were obtained for these cases, with details presented in Spycher and Oldenburg (2015).

The porosity is predicted to change by a maximum of only about ±0.05% (absolute). An overall increase in porosity is predicted within the two-phase zone, resulting primarily from the combined effect of the replacement of Fe-chlorite by siderite, of calcite by dolomite, and of K-feldspar by muscovite, together with the precipitation of chalcedony. Similar to the CHILLER simulation results, the pH of the formation water is predicted to drop from 7 to ~4.5–5 near the well, and to ~5–6 farther away

in a zone initially invaded by CO_2 but where CO_2 eventually fully disappears by dissolution and buoyancy flow. A zone of cinnabar precipitation is predicted to develop in the vicinity of the injection well (Figure 3), with a shape mostly matching the single-phase CO_2 plume. The case with low Hg concentration (7 ppbV) in the CO_2 results in about two orders of magnitude less cinnabar precipitation than with the higher Hg concentration (190 ppbV). In the latter case, the total amount of Hg input into the system is large (~16 metric tons after 40 years). However, even though essentially this entire amount precipitates as cinnabar, the resulting porosity decrease is small (~0.005%, Figure 3) because of the high density of this mineral.

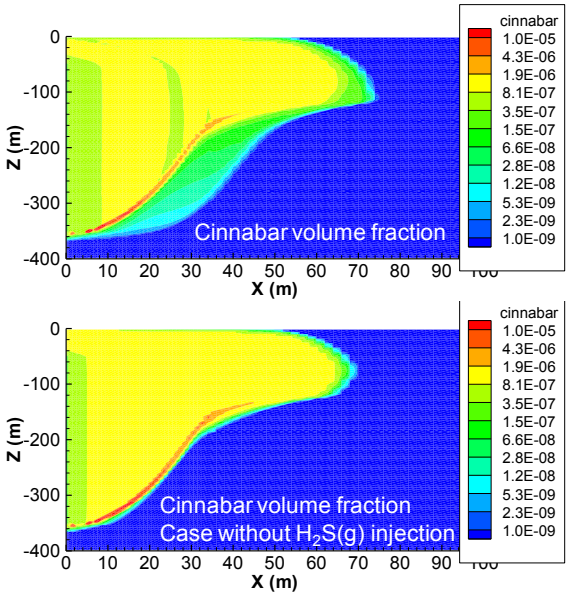

Figure 3. Simulated distribution of cinnabar precipitation after 40 years of CO_2 injection for cases with 190 ppbV Hg, without and with H_2S (200 ppmV), included as impurities in the CO_2. The contours show the precipitated (absolute) volume fraction (i.e., positive values correspond to negative porosity changes).

The results of these reactive transport simulations are consistent with the volumetric calculations presented earlier and in more detail in Oldenburg and Spycher (2015), in that the condensation of liquid mercury from the CO_2 phase is not expected in this system, even if sulfide-free. However, the presence of even a very small amount of dissolved sulfide in the formation water causes essentially all the Hg initially in the CO_2 to precipitate as cinnabar. This mineral has a very low solubility, and therefore the predicted dissolved Hg concentrations in the formation water are very small (ppb range). As discussed further by Oldenburg and Spycher (2015) and Spycher and Oldenburg (2015), the effect of cinnabar precipitation on porosity (and thus permeability) depends on the scale over which such precipitation takes place. More details on sulfide reactions forming cinnabar and pyrite are presented in the latter paper.

CONCLUSIONS

A series of analyses was carried out to assess the potential for Hg to impact injectivity through condensation of liquid Hg or precipitation of cinnabar from a stream of Hg-containing supercritical CO_2 injected into a geologic formation at ~21.5 MPa bar and 106°C. On the basis of simple volumetric analyses, the co-injection of small quantities of Hg (7 and 190 ppbV) with CO_2 into a deep geologic formation is not expected to significantly impact injectivity through Hg condensation or precipitation. More sophisticated geochemical and reactive transport simulations come to the same conclusions, although these clearly show that essentially all injected Hg should precipitate as cinnabar, which might be expected given the known strong affinity of Hg for sulfide (present in formation waters). Our analyses also show that evaporative concentration of aqueous Hg (from H_2O dissolution into CO_2) is unlikely because Hg is more volatile than H_2O and thus is expected to partition more strongly than H_2O into the CO_2 injectate. It should be noted, however, that at the *P-T* conditions modeled here, elevated Hg concentrations in the injected CO_2 (> ~2000 ppbV) could potentially lead to the condensation of liquid Hg in a sulfide-free system. It should also be noted that the phase partitioning of Hg between CO_2 and water predicted in this study relies on scarce thermodynamic data with significant uncertainty, as well as assumption of ideal gas behavior for Hg. For these reasons, future experimental work is encouraged to test the results of this modeling study.

ACKNOWLEDGMENT

We thank Nicholas J. Pester (LBNL) for constructive review of an earlier draft, and Eric Sonnenthal for making early versions of TOUGHREACT V3-OMP available. Support for this work was provided by Chevron with project management by Scott Imbus (Chevron). Additional support was provided by the Assistant Secretary for Fossil Energy (DOE), Office of Sequestration, Hydrogen, and Clean Coal Fuels, through the National Energy Technology Laboratory (NETL), and by Lawrence Berkeley National Laboratory under Department of Energy Contract No. DE-AC02-05CH11231.

REFERENCES

Bingham, M.K, Field detection and implications of mercury in natural gas. *SPE Production Engineering*, May 1990, 120–124, 1990.

Cui, Z., A. Aroonwilas, and A. Veawab, Simultaneous capture of mercury and CO_2 in amine-based CO_2 absorption process, *Industrial & Engineering Chemistry Research 49*(24), 12576–12586, 2010.

Oldenburg, C.M., G.J. Moridis, N. Spycher, and K. Pruess, *EOS7C Version 1.0: TOUGH2 Module for Carbon Dioxide or Nitrogen in Natural Gas (Methane) Reservoirs*, Lawrence Berkeley National Laboratory Report LBNL–56589, 2004.

Oldenburg, C.M., N. Spycher, Will mercury impurities impact CO_2 injectivity in deep sedimentary formations? I. Condensation and net porosity reduction. *Greenhouse Gases Sci. and Tech.*, *5*(1), 64–71, 2015.

Palandri, J., and M.H. Reed, Reconstruction of in situ composition of sedimentary formation waters. *Geochimimica et Cosmochimica Acta* 65, 1741–1767, 2001.

Pruess, K., C.M. Oldenburg and G.J. Moridis, *TOUGH2 User's Guide Version 2.0.* E. O. Lawrence Berkeley National Laboratory Report LBNL-43134, 1999.

Pruess, K., and N. Spycher, ECO2N – A Fluid property module for the TOUGH2 code for studies of CO_2 storage in saline aquifers. *Energy Conversion and Management*, 48 (6), 1761–1767, 2007.

Pruess, K., and N. Müller, Formation dry-out from CO_2 injection into saline aquifers: 1. Effects of solids precipitation and their mitigation. *Water Res. Research*, 45, W03402, doi:10.1029/2008WR007101, 2009.

Pruess, K., C.M. Oldenburg and G.J. Moridis, *TOUGH2 User's Guide Version 2.0.* E. O. Lawrence Berkeley National Laboratory Report LBNL-43134 (revised), 2012.

Reed, M.H., Calculation of multicomponent chemical equilibria and reaction processes in systems involving minerals, gases and an aqueous phase. *Geochimimica et Cosmochimica Acta*, 46, 513–528, 1982.

Reed, M.H., Calculation of simultaneous chemical equilibria in aqueous-mineral-gas systems and its application to modeling hydrothermal processes. In: Techniques in Hydrothermal Ore Deposits Geology, *Reviews in Economic Geology, Volume 10*. Richards J., Larson P. (eds), 109–124, 1998.

Sonnenthal, E.S., N. Spycher, T. Xu, L. Zheng, N. Miller, and K. Pruess, *TOUGHREACT V3.0-OMP reference manual: a parallel simulation program for non-isothermal multiphase geochemical reactive transport. Lawrence Berkeley National Laboratory*, Draft Report, 2014. http://esd.lbl.gov/files/research/projects/tough/documentation/TOUGHREACT_V3-OMP_RefManual.pdf

Spycher, N., and C.M. Oldenburg. Will mercury impurities impact CO_2 injectivity in deep sedimentary formations? II. Mineral dissolution and precipitation. *Greenhouse Gases Sci. and Tech.*, *5*(1), 72–90, 2015.

Spycher, N., L Peiffer, G. Saldi, E. Sonnenthal, M.H. Reed, B.M. Kennedy, Integrated multicomponent solute geothermometry. *Geothermics*, 51, 113–123, 2014. (http://esd.lbl.gov/research/projects/geot/)

Xu, T., E. Sonnenthal, N. Spycher, and K. Pruess, TOUGHREACT - A simulation program for non-isothermal multiphase reactive geochemical transport in variably saturated geologic Media: applications for geothermal injectivity and CO_2 geologic sequestration. *Computers & Geosciences*, 32, 145–165, 2006.

Xu, T., N. Spycher, E. Sonnenthal, G. Zhang, L. Zheng, and K Pruess, TOUGHREACT Version 2.0: A simulator for subsurface reactive transport under non-isothermal multiphase flow conditions. *Computers & Geosciences*, 37, 763–774, 2011.

POTENTIAL CHEMICAL IMPACTS OF CO_2 LEAKAGE ON UNDERGROUND SOURCE OF DRINKING WATER (USDWS) ASSESSED BY QUANTITATIVE RISK ANALYSIS

Ting Xiao, Brian McPherson, Feng Pan, Rich Esser

Department of Civil & Environmental Engineering; Energy & Geoscience Institute
The University of Utah
Salt Lake City, Utah, 84112, USA
e-mail: txiao@egi.utah.edu

ABSTRACT

To evaluate potential risks to Underground Sources of Drinking Water (USDWs) due to CO_2 leakage, a generic TOUGHREACT geochemical model is developed to interpret changes in water chemistry following CO_2 intrusion. A response surface methodology (RSM) based on these TOUGHREACT simulations was used to quantify associated risks. The case study example for this analysis is the Ogallala aquifer overlying the Farnsworth unit (FWU), an active commercial-scale CO_2-EOR field. Specific objectives of this study are to: (1) understand how CO_2 leakage is likely to influence geochemical processes in aquifer sediments; (2) quantify the potential risks to the Ogallala groundwater aquifer due to CO_2 leakage from the Farnsworth oil reservoir; (3) identify water chemistry factors for early detection criteria.

Results indicate that the leakage rate would be most likely range between 10^{-14} – 10^{-10} kg/(m^2·year). Within this range of CO_2 leakage rate, generally, groundwater quality won't be impacted. In worst-case scenarios, trace metal concentrations could be twice as much as the initial value. However, predicted magnitudes are still less than one-fifth of regulation-stipulated maximum contamination levels (MCL). Finally, results of this analysis suggest that TDS and nitrate could be effective geochemical markers of CO_2 leakage.

INTRODUCTION

Enhanced Oil Recovery (EOR) offers potential economic benefits of increased oil production, which could offset part of the costs for CO_2 capture and storage (IPCC, 2005). Therefore, it becomes a promising way for reducing CO_2 emissions from point sources. Most CO_2-EOR sites are overlain by groundwater aquifers located at shallow depth. Although the possibility of CO_2 leakage from a sequestration site is very low (Bachu and Watson, 2009; Gaus, 2010), there are still concerns of CO_2 leakage to potable aquifers through wellbores or faults, impacting water quality with acidification and trace metal mobilisation (IPCC, 2005; Gaus, 2010). Multiple environmental variables such as aquifer geology, mineralogy, and groundwater chemistry also play an important role on groundwater quality (Frye et al., 2012; Wilkin and Diguilio, 2010). Therefore, site-specific, quantitative risk assessments are essential for safe and effective application of carbon sequestration (Wilkin and Diguilio, 2010) and early detection criteria (Little and Jackson, 2010). To date, research on CO_2 leakage risk assessment mainly focused on lab-scale and small site-scale experiments in order to obtain early detection of aquifer quality changes in shallow groundwater aquifer and forecast the impact of groundwater quality as drinking water resources (Frye et al., 2012; Little and Jackson, 2010; Lu et al., 2010; Qafoku et al., 2013; Wells et al., 2007; Zheng et al., 2012). However, it is difficult to assess the long term impacts of groundwater quality with CO_2 leakage only with lab-scale experiments or field tests. Uncertainty analysis with numerical simulations becomes necessary for evaluations of long-term groundwater quality with CO_2 leakage, especially with site specific water chemistry, leakage flux, mineralogy and other parameters.

In order to quantify the uncertainty of potential risks to the groundwater quality due to CO_2 leakage, a response surface methodology (RSM) was applied in this study. RSM overcomes the disadvantage of "traditional" risk and uncertainty analysis methods (e.g. the basic Monte Carlo method) which require substantial time, cost, and effort (Box and Draper, 1987; Myers

and Montgomery, 1995). Recently, RSM has been successfully applied in risk assessment for carbon capture and storage (CCS) and EOR (Carroll et al., 2014; Dai et al., 2014; Rohmer and Bouc, 2010), which provides a new resolution for CO_2 leakage risk analysis. For example, Dai et al. (2014) developed a generic integrated framework for optimizing CO_2 sequestration with RSM. Results showed the distance between injection and production wells and the competing rates of water alternating gas (WAG) are the primary significant operational parameters for designing a CO_2-EOR pattern. Stages in the application of RSM include: (1) determine the major independent parameters; (2) carry out experiments according to the selected experimental matrix with verification of the RSM model equation; and (3) obtain the response surface plot and determination of optimum points.

The case study selected is the Farnsworth CO_2-EOR unit (FWU) and its overlying underground sources of drinking water (USDW) aquifer (the Ogallala aquifer) located in the northern Anadarko basin in Ochiltree County, Texas. For this site, potential risks to groundwater quality due to CO_2 leakage through wellbores are quantified. We selected this unit as our case study because: (1) there are considerable brine/water and mineralogy data available for both the FWU and the Ogallala aquifer; (2) the Ogallala aquifer is one of the largest USDWs in North America (George et al., 2011), and represents a typical drinking water resource in the USA. The main objectives of this study are to: (1) understand how CO_2 leakage is likely to influence geochemical processes in aquifer sediments; (2) quantify the potential risks to the Ogallala groundwater aquifer associated with changes in groundwater chemistry due to CO_2 leakage from the FWU; and (3) identify water chemistry factors as markers for early detection criteria.

This study is structured into three parts: (1) cement hydration simulations, to obtain the equilibrium composition of wellbores and wellbore fluids; (2) quantification of maximum possible CO_2 leakage from the FWU reservoir through wellbore fractures to the overlying USDW; (3) quantification of the potential risks to Ogallala groundwater quality due to CO_2 leakage. All the simulations of this study were performed with TOUGHREACT V2 (Xu et al., 2011) ECO2N module (Pruess, 2005).

METHODOLOGY

Simulation of Cement Hydration

Wells in the FWU are completed with Portland cement. When the cement mixes with water, it starts hydration with chemical reactions, and causes microstructure formations to form a harder structure (Li, 2011). Chemical reactions during hydration involve: (1) hydration of aluminates to form ettringite and monosulfate; (2) hydration of the silicates (i.e. alite and belite) to form calcium silicate hydrate (CSH); and (3) hydration of ferrite to form ettringite (Li, 2011; Mehta and Monteiro, 2014). CSH is the primary binding material of the cement and doesn't have a confirmed formula. Most of the reactions take place during a few hours and release a huge amount of heat. After a few days, the chemical reactions and hardening rate decelerate. However, hydration processes may take decades to reach an equilibrium state.

To obtain the equilibrium wellbore cement composition under the field environment, a batch simulation of cement hydration was conducted for an arbitrary but long value of 100 years. To avoid vigorous chemical reactions during the initial several hours, the initial Portland cement composition for this simulation was adopted from Table 3 of Scrivener et al. (2011), which is the cement hydration experimental result after 1 day. Water chemistry was adopted from average brine chemistry data of the FWU reservoir.

Simulation of CO_2 leakage flux through wellbores

In order to assess the CO_2 leakage rate through wellbore fractures, a vertical 1-D simulation was conducted for 100 years. The mineralogy result of the cement hydration batch model was used for this simulation. Based on the sizes of wells in the FWU, the diameter of the simulated well was set as 17 cm, and the thickness of the wellbore was assigned 2.5 cm. The bottom of the reservoir was 3,000 m, and the thickness was assigned 30 m. The overlying aquifer was set

with 100 m thickness, and the upper boundary was set with ambient pressure. Hydrostatic pressure was set as the initial pressure of the domain, and the initial temperature was set as 20 °C at the top of the domain with a 25 °C/km gradient. All parameters of the reservoir were set with monitoring data. Cement parameters were set according to reference. The USDW formation is a typical sand aquifer, and all the parameters were set as typical sand. The multiple interacting continua (MINC) in TOUGH2 code was used to imitate the micro fractures of the wells. Other hydrogeological parameters are shown in Table 1. The uncertainties of leakage flux were quantified by RSM with three independent uncertainty parameters (Table 2).

Table 1. Hydrogeological parameters.

Property	Value
Reservoir (Morrow)	
Thickness	30 m
Permeability	4.52×10^{-14} m^2
Porosity	0.1453
Rock density	2650 kg/m^3
Salinity	0.06
Cement	
Permeability	5.0×10^{-20} m^2 *
Porosity	0.08 **
Rock density	2400 kg/m^3
Fracture	
Permeability	1.0×10^{-14} m^2 *
Porosity	0.40 **
Rock density	2400 kg/m^3
USDW aquifer	
Thickness	100 m
Permeability	5.0×10^{-13} m^2
Porosity	0.30
Rock density	2600 kg/m^3
Salinity	0.00035

* Bachu and Bennion, 2009
** Rimmelé et al., 2008

Quantification of the risks with CO_2 leakage into the Ogallala formation

Model setup

A 2-D radial model was conducted to analyze the potential risks of groundwater quality due to CO_2 leakage. All simulations assumed that CO_2 dissolves in water instantly when it is injected; gaseous CO_2 was injected into the system with a constant rate, and water chemistry results in the Ogallala aquifer were examined for up to 200 years. Based on more than 100 fresh-water well drilling records on/near the FWU, the thickness of the aquifer was assigned 100 m, and the bottom depth was set as 150 m. Because the distance between monitoring wells of the FWU is around 1,000 m, the dimension of our model was set as 1,000 m × 100 m with a total of 230 grid cells. A regression model was created with RSM to assess the impacts to the USDW aquifer with four independent parameters (Table 3).

Geological formations

A constant temperature of 25 °C and hydrostatic pressure were used as initial conditions. The porosity was set as 0.3 (Beard and Weyl, 1973). The initial water chemistry was taken from the average of more than 100 water-analysis data sets of FWU groundwater monitoring tests. For the water indexes not available with the water samples, their values were adopted from Hopkins (1993). All element concentrations except Se did not exceed the Texas maximum contaminant level (MCL). On the other hand, Se did not exceed the EPA standard. Total dissolved solid (TDS) and nitrate concentration exceeded EPA MCL values, As and Mn were more than 1/10 of the standard value. In this study, TDS, nitrate, As, Se, Mn and pH were considered as potential contaminants for the water body. The initial dissolved oxygen was calculated using the oxidation reduction potential (ORP) value. A water-mineral equilibrium condition was obtained by performing the simulation without any injection for 100 years (Table 4). The initial mineralogy was set up based on geological data of the High Plains aquifer (Qafoku et al., 2013). Initial primary minerals are: quartz, calcite, kaolinite, K-feldspar and muscovite with volume fraction 0.6, 0.05, 0.085, 0.23, 0.025, respectively. The radius of mineral grains was set as 1 mm, according to the results of our size distribution tests for the Ogallala sand samples. Specific surface area (SSA) of each mineral was calculated by: $SSA=A \cdot v/(V \cdot MW)$, where A is sphere area, v is molar volume, V is sphere volume, and MW is molecular weight (Labus and Bujok, 2011). Molar volume and molecular weight were obtained from EQ3/6 database.

Table 2 Independent parameters for CO_2 leaking rate simulation.

Parameter name	Low (-1)	Mid (0)	High (+1)	Distribution
CO_2 saturation	0.1	0.5	0.9	Uniform
Reservoir pressure: bar	300	325	350	Uniform
Wellbore fracture proportion	0.01	0.055	0.10	Uniform

Table 3. Independent parameters for simulations of CO_2 leaking into USDW aquifer.

Parameter name	Low (-1)	Mid (0)	High (+1)	Distribution
Permeability: m^2	10^{-14}	10^{-13}	10^{-12}	Lognormal
Leaking rate: kg/(s·m^2)	10^{-21}	10^{-19}	10^{-17}	Lognormal
CEC: meq/100g	1	6.5	12	Uniform
Absorbent SSA	1	50.5	100	Uniform

Table 4. Selection of the initial water chemistry of the Ogallala aquifer.

Name	Concentration (mg/L)	Balanced Concentration (mol/kg)
H^+	pH 7.73	$10^{-7.52}$
Fe^{2+}	0.002 *	1.49×10^{-8}
NO_3^-	15.21	2.45×10^{-4}
$H_2AsO_4^-$	0.0024 (as As)	3.41×10^{-9}
Ba^{2+}	0.072	5.12×10^{-7}
Cd^{2+}	3.44×10^{-5}	2.18×10^{-10}
$Cr(OH)_2^+$	0.002 (as Cr)	3.28×10^{-8}
Cu^{2+}	0.014	9.19×10^{-8}
Pb^{2+}	8.7×10^{-4}	2.78×10^{-9}
F^-	1.73	9.12×10^{-5}
$HSeO_3^-$	0.003 (as Se)	1.10×10^{-8}
Mn^{2+}	0.0077	1.17×10^{-7}
Ag^+	3.61×10^{-5}	8.78×10^{-11}
Zn^{2+}	0.45	5.03×10^{-6}
TDS	570	548 mg/L

* TWDB, 1993

Chemical reactions

It is suggested that cation exchange capacity (CEC) and sorption processes with dissolution of carbonates might be the main factors driving the geochemical response to CO_2 injection (Zheng et al., 2012). In this study, aqueous complexation, cation exchange, adsorption/ desorption and mineral dissolution/precipitation were considered. The thermodynamic parameters for aqueous and mineral reactions were taken from EQ3/6 database (Wolery, 1992). The parameters for the kinetic rate law of minerals were taken from Palandri and Kharaka (2004). For the minerals not included, the kinetic parameters were assumed to be the same as the similar minerals in the same category.

For adsorption/desorption reactions, the Gouy-Chapman double diffuse layer model was used (Smith, 1999). Hydrous ferric oxide (HFO) was assumed to be the sorbent, because it is a widely existing mineral as a sorbent in natural systems, with the approximate formula $Fe(OH)_3$ used in this model. Constants and sorbent properties were taken from Dzombak and Morel (1990), with the strong site density 9.0×10^{-8} mol sites/m^2, and the weak site density 3.0×10^{-6} mol sites/m^2. Adsorption/desorption reactions are controlled by the total amount of sorption sites (product of amount of sorbent and sorbent SSA). The model sensitivity to the total amount of sorbent sites could be evaluated by varying one of these parameters (Zheng et al., 2012). In this study, sorbent fraction was set with 0.1% of the total mineral volume, and sorbent SSA was treated as an independent uncertainty parameter. Pure sorbent SSA is 600 m^2/g; however, the actual value is far less than this value. Based on tests of Fe concentrated clay surface areas (Fontes and Weed, 1996) and BET surface area tests for our Ogallala sand samples, 1 – 100 m^2/g sorbent SSA was used in our study.

The CEC of a sediment could often be considered constant (Appelo and Postma, 1994); however, as no measured data of the Ogallala formation overlying FWU is available, we treated CEC as an uncertainty independent parameter. Based on CEC values for various minerals, 1 – 12 meq/100 g was used in this study, which can cover typical values for sands (Ming and Dixon, 1987). The exchange reactions and their selectivity coefficients were adopted from Table 5.5 of Appelo and Postma (1994).

RESULTS AND DISCUSSIONS

Cement hydration

The solid phase changes during cement hydration are shown in Figure 1, which indicate that with the consumption of alite, belite, ferrite and aluminate, CSH, portlandite and ettringite precipitated as main products. These results match known cement hydration mechanisms (Li, 2011). The composition of cement became stable after less than 1 year, but there were still slight changes for decades. Although CSH doesn't have a confirmed formula, in this simulation, the average Ca/Si ratio was about 1.7, corresponding to former studies (Allen et al., 2007).

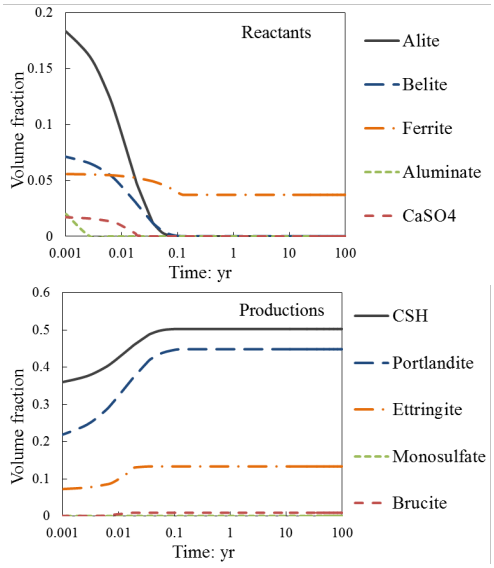

Figure 1. Composition changes during cement hydration.

CO_2 leakage flux through wellbore

The response of the CO_2 leakage rate into the overlying groundwater formation during the 100 year simulation was of particular interest. The correlation between original (fully modeled) simulation CO_2 leakage rates and RSM forecasted rates was above 0.9, which showed the RSM expression could represent the simulation results with high accuracy. The results show that CO_2 leakage rate increased during the first year, but then maintained a stable value for 100 years. The results show that no gaseous phase CO_2 was leaking, and only dissolved CO_2 entered the groundwater formation. Similar results were also found by Elison et al. (2012). The cumulative distribution function (CDF) of log CO_2 leakage rate after 100 year fits a normal distribution curve with P value < 0.005, which indicates that the leakage rate follows a log normal distribution. With more than 90% probability, leakage rate is between 10^{-21} – 10^{-17} kg/(m^2·s), which is about 10^{-14} –10^{-10} kg/(m^2·year). This leaking rate is far less than other estimations of former studies (Carroll et al., 2009; Elison et al., 2012). The best explanations for these resulting small flux values are: (1) the reactions between CO_2 and portlandite ($Ca(OH)_2$) of wellbore cement largely consumed CO_2; (2) porosity decreased due to the precipitation of $CaCO_3$, which further impacted the leakage pathway. Specifically, model simulations without chemical reactions were executed, and corresponding CO_2 leakage rate approached 10^{-6} kg/(m^2·s).

Risk assessments of CO_2 leakage into the Ogallala formation

Generally, the coefficient of determination (R^2) between simulation results and the responses of the regression (RSM) model for all the water indexes of interest exceeded 0.9, except a few points with more than 0.7, suggesting that the resulting trained ROMs are significantly effective for representing full-scale (non-ROM) simulation results. For up to 50 years of CO_2 leakage, there were no obvious changes of TDS, trace metals and pH over the domain. After 100 years of leakage, the changes became more obvious. After 200 years, there was more than a 10% possibility that TDS exceeded 780 mg/L (initially 540 mg/L), which was 50% different compared to the initial value (Figure 2); but pH was between 7.2 – 7.7 all over the domain (initially 7.5), less than 10% different (Figure 3). Concentrations of other elements (N, Mn, As, Se) showed similar trends with TDS (figures not shown). Both Figures 2 and 3 indicate CO_2 had a stronger impact on the upper layer of the domain, due to the buoyancy of CO_2. This probably facilitates early detection, because water quality monitoring test samples are typically taken from relatively shallow groundwater, and sometimes it is not possible to drill wells to the bottom of the aquifer formation. The aqueous plume affected by CO_2 reached more than 1000 m away from the leakage point following initial obvious changes, especially in the top layer of the aquifer.

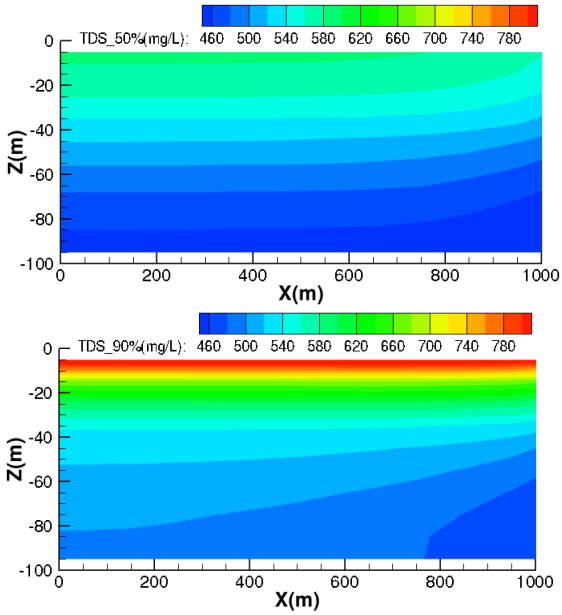

Figure 2. TDS distribution with 50th and 90th percentile after 200 years.

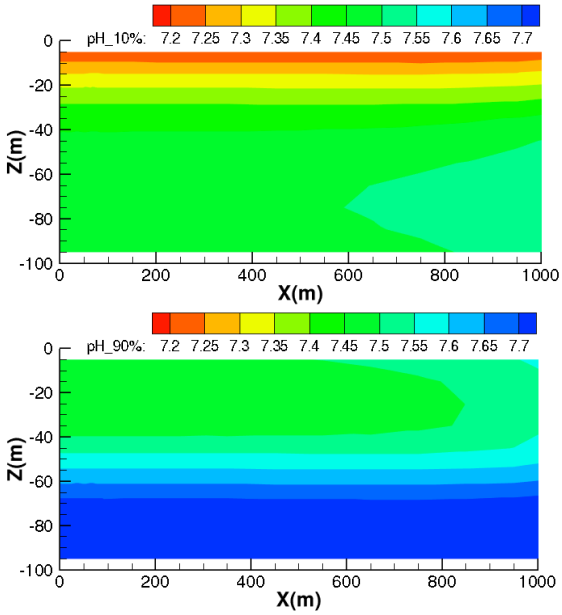

Figure 3. pH distribution with 10th and 90th percentile after 200 years.

The CDF of responses of TDS at 10, 50, 100 and 200 years (Figure 4) suggest that the uncertainty increased over time. It is obvious that in the first 50 years, no significant changes of TDS occurred. At 100 years, results suggested only ~10% possibility of being beyond 600 mg/L, which was not significant. After 200 years, ~40% possibility that TDS exceed 600 mg/L, and ~10% possibility of being over 50% variation from the initial value. Of note is that there was less than 4% possibility that the TDS would exceed the Texas MCL (1000 mg/L). Accordingly, the possibility is too low to be considered as a risk.

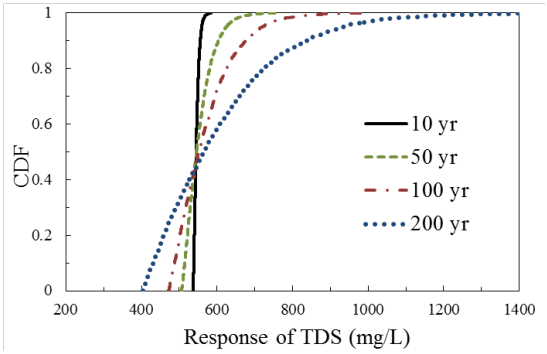

Figure 4. CDF of responses for TDS at 10, 50, 100, and 200 years.

It is usually believed that the closer the test wells are located, the earlier that detections may be made. However, based on this study, the CDF curves at 100, 500 and 1000 m away from the leaking point only show slight differences within 200 years. The existing monitoring wells are 1,000 m away (on average) from the operational wells in the FWU, which could detect groundwater quality changes due to CO_2 leakage in practical time, at least as suggested by the results of this study.

Figure 5 shows concentration changes of the water quality indexes that are of interest, with different percentiles at the current monitoring well position (1,000 m away from the leaking point). Within the 95th percentile, the concentrations wouldn't become twice the initial values, or exceed the MCL regulations. However, selenium (Se) already exceeds the Texas MCL (0.002 mg/L) value initially, and there is about a 50% possibility that the concentration will increase (worsen) during 200 years. On the other hand, EPA MCL standard requires no more than 0.05 mg/L Se in drinking water. Although simulated Se concentration exceeds Texas MCL standard, it is still ~10 times less than the EPA standard.

Usually groundwater chemistry varies over time due to multiple reasons such as groundwater flow, experimental errors and other reasons.

Some differences among tests are typically acceptable. Early detection of CO_2 leakage is more difficult by water chemistry tests if the change is very small, especially less than 10%. Consequently, suggested principles to choose markers for early detection include: (1) easy to be tested and (2) changes due to CO_2 leakage significant. Based on these principles, pH is not sensitive enough to become a marker. Although Mn, As and Se all have similar trends with TDS, these trace metals require inductively coupled plasma- mass spectrometry (ICP-MS) to detect, which is rarely available near the field. TDS is easy to be tested, and its amount is relatively abundant in groundwater, and thus it is recommended to be an early detection marker. Nitrate is also quite abundant and not complex to be tested and as such could also be treated as a marker for CO_2 leakage detection.

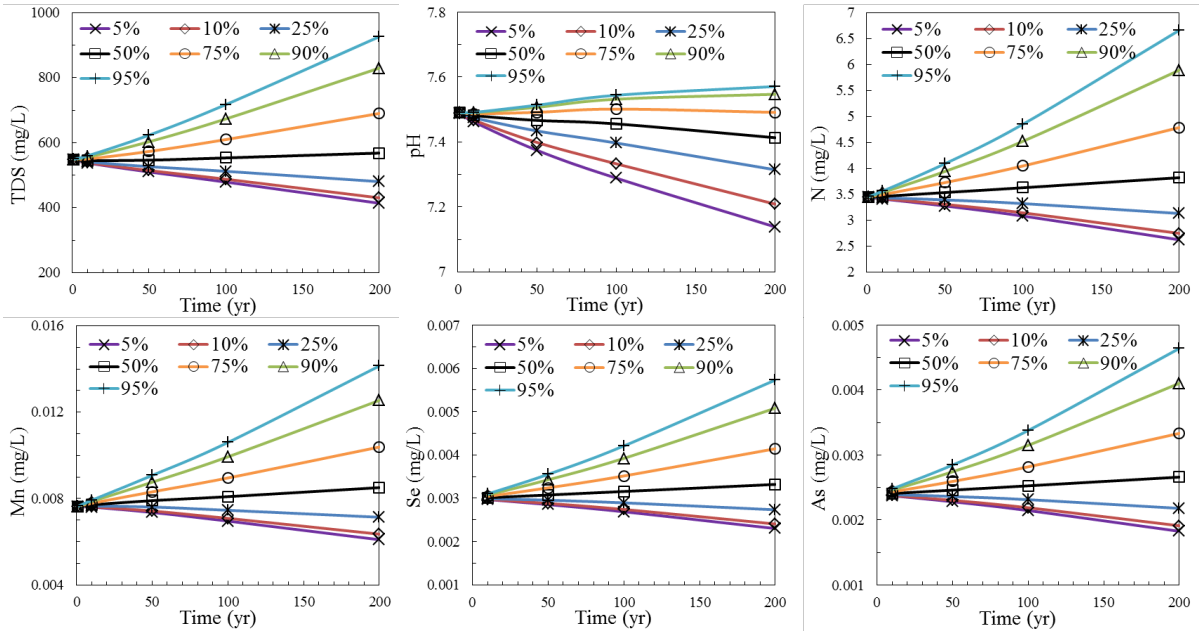

Figure 5. Selection of water factor changes via time at current monitoring wells with 5th-95th percentiles.

CONCLUSIONS

This study focuses on the assessment of potential risks of CO_2 leakage through wellbores on groundwater quality using a RSM approach and identification of water chemical factors for early detection criteria at a commercial-scale CO_2-EOR field. Before that, we evaluated the uncertainties of the CO_2 leakage rate with the consideration of CO_2 and cement chemical reactions. The coefficient of determination (R^2) between simulation results and the prediction responses of the regression (RSM) model for the water chemical factors exceeded 0.9, suggesting that the results of ROMs are significantly effective for representing the simulation results.

The results show that with more than 90% probability, leakage rate is between 10^{-14} – 10^{-10} kg/(m^2·year). The small CO_2 leaking rate is because the CO_2 reaction with portlandite ($Ca(OH)_2$) of wellbore cement largely consumed CO_2 and further decreased the fracture porosity, resisting the CO_2 pathways. Within the range of CO_2 leakage rate, trace metal concentrations could be twice as much as the initial value with the worst scenarios after 200 years. However, they are all less than 1/5 of the MCL limit, showing that the Ogallala groundwater quality won't be significantly impacted. Water quality at 100, 500 and 1000 m away from the leaking point show slight differences within 200 years, indicating that the current monitoring wells can detect the leakage in time. TDS and nitrate are suggested as markers for early detection, because they are abundant in water, show significant changes due to CO_2 leakage, and are easy to test compared to the trace metals.

ACKNOWLEDGEMENT

This study was supported by the U.S. Department of Energy and NETL, contract DE- FC26-05NT42591.

REFERENCES

Allen, A.J., J.J. Thomas, and H.M. Jennings, Composition and density of nanoscale calcium-silicate-hydrate in cement, *Nat. Mater.*, 6, 311-316, 2007.

Appelo, C.J.A., and D. Postma, *Geochemistry, groundwater and pollution*, A. A. Balkema, Rotterdam, Netherlands, 1993.

Bachu, S., and D.B. Bennion, Experimental assessment of brine and/or CO_2 leakage through well cements at reservoir Conditions, *Int. J. Greenh. Gas Control.*, 3, 494-501, 2009.

Bachu, S., and T.L. Watson, Review of failures for wells used for CO_2 and acid gas injection in Alberta, Canada, *Energy Procedia*, 1, 3531-3537, 2009.

Beard, D.C., and P.K. Weyl, Influence of texture on porosity and permeability of unconsolidated sand, *Am. Assoc. Petr. Geol. B.*, 57 (2), 349-369, 1973.

Box, G.E., and N.R. Draper, *Empirical model-building and response surfaces*, John Wiley and Sons, New York, NY, 1987.

Carroll, S., Y. Hao, and R. Aines, Geochemical detection of carbon dioxide in dilute aquifers, *Geochem. Trans.*, 10, doi:10.1186/1467-4866-10-4, 2009.

Carroll, S., K. Mansoor, and Y. Sun, *Second-generation reduced-order model for calculation of groundwater impacts as a function of pH, total dissolved solids, and trace metal concentration*, Report NRAP-TRS-III-002-2014, Lawrence Livermore National Laboratory, Livermore, CA, 2014.

Dai, Z., R. Middleton, H. Viswanathan, J. Fessenden-Rahn, J. Bauman, R. Pawar, S. Lee, and B. McPherson, An integrated framework for optimizing CO_2 sequestration and enhanced oil recovery. *Environ. Sci. Technol. Lett.*, 1, 49-54, 2014.

Dzombak, D.A., and F.M.M. Morel, *Surface complexation modeling-hydrous ferric oxide*, John Wiley & Sons, New York, 1990.

Ellison, K., R. Falta, L. Murdoch, and S. Brame, Behavior of brines containing dissolved CO_2 in abandoned wellbores, *Proceedings, TOUGH Symposium*, Lawrence Berkeley National Laboratory, Berkeley, CA, 2012.

Fontes, M.P.F., and S.B. Weed, Phosphate adsorption by clays from Brazilian oxisols: relationships with specific surface area and mineralogy, *Geoderma*, 72, 37-51, 1996.

Frye, E., C. Bao, L. Li, and S. Blumsack, Environmental controls of cadmium desorption during CO_2 leakage, *Environ. Sci. Technol.*, 46, 4388-4395, 2012.

Gaus, I., Review: Role and impact of CO_2-rock interactions during CO_2 storage in sedimentary rocks. *Int. J. Greenh. Gas Control.*, 4, 73-89, 2010.

George, P.G., R.E. Mace, and R. Petrossian, *Aquifers of Texas*, Report 380, Texas Water Development Board, Austin, TX, 2011.

Hopkins, J., *Water-quality evaluation of the Ogallala aquifer, Texas*, Report 342, Texas Water Development Board, Austin, TX, 1993.

International Panel on Climate Change (IPCC), *IPCC special report on carbon dioxide capture and storage*, Cambridge University Press, New York, NY, 2005.

Labus, K., and P. Bujok, CO_2 mineral sequestration mechanisms and capacity of saline aquifers of the upper silesian coal basin (central Europe) – modeling and experimental verification, *Energy*, 36, 4974-4982, 2011.

Li, Z., *Advanced concrete technology*, John Wiley & Sons, Hoboken, NJ, 2011.

Little, M.G., and R.B. Jackson, Potential impacts of leakage from deep CO_2 geosequestration on overlying freshwater aquifers, *Environ. Sci. Technol.*, 44, 9225-9232, 2010.

Lu, J., J.W. Partin, S.D. Hovorka, and C. Wong, Potential risks to freshwater resources as a result of leakage from CO_2 geological storage: a batch-reaction experiment, *Environ. Earth Sci.*, 60, 335-348, 2010.

Mehta, P.K., and P. Monteiro, *Concrete: microstructure, properties, and materials, 4th Edition*, McGraw-Hill Education, New York, NY, 2014.

Ming, D.W., and J.B. Dixon, Quantitative determination of clinoptilolite in soils by a cation-exchange capacity method, *Clays Clay Miner.*, 35, 463-468. 1987.

Myers, R.H., and D.C. Montgomery, *Response surface methodology: Process and product optimization using designed experiments*, John Wiley & Sons, New York, NY, 1995.

Palandri, J.L., and Y.K. Kharaka, *A compilation of rate parameters of water-mineral interaction kinetics for application to geochemical modeling*, Report 2004-1068, U.S. Geological Survey, Menlo Park, CA, 2004.

Pruess, K., *ECO2N: A TOUGH2 Fluid Property Module for mixtures of water, NaCl, and CO_2*, Report LBNL-57952, Lawrence Berkeley National Laboratory, Berkeley, CA, 2005.

Qafoku, N.P., A.R. Lawter, C.F. Brown, M. Bowden, G. Wang, O.R. Harvey, and C. Sullivan, *Geochemical impacts of leaking CO_2 from subsurface storage reservoirs to unconfined and confined aquifers*, PNNL-22420, Pacific Northwest National Laboratory, Richland, WA, 2013.

Rimmelé, G., V. Barlet-Gouédard, O. Porcherie, B. Goffé, and F. Brunet, Heterogeneous porosity distribution in Portland cement exposed to CO_2-rich fuids, *Cem. Concr. Res.*, 38, 1038-1048, 2008.

Rohmer, J., and O. Bouc, A response surface methodology to address uncertainties in cap rock failure assessment for CO_2 geological storage in deep aquifers. *Int. J. Greenh. Gas Control.*, 4, 198-208, 2010.

Scrivener, K.L., T. Füllmann, E. Gallucci, G. Walenta, and E. Bermejo, Quantitative study of Portland cement hydration by X-ray diffraction/rietveld analysis and independent methods, *Cem. Concr. Res.*, 34, 1541-1547, 2004.

Smith, K.S., Metal sorption on mineral surfaces: an overview with examples relating to mineral deposits, In: Plumlee, G.S., Logson, M.J. (Eds.), The Environmental Geochemistry of Mineral Deposits, *Rev. Econ. Geol.*, 6A-6B, 161-182, 1999.

Wells, A.W., J.R. Diehl, G. Bromhal, B.R. Strazisar, T.H. Wilson, and C.M. White, The use of tracers to assess leakage from the sequestration of CO_2 in a depleted oil reservoir, New Mexico, USA, *Appl. Geochem.*, 22, 996-1016, 2007.

Wilkin, R.T., and D.C. Digiulio, Geochemical impacts to groundwater from geologic carbon sequestration: controls on pH and inorganic carbon concentrations from reaction path and kinetic modeling, *Environ. Sci. Technol.*, 44, 4821-4827, 2010.

Wolery, T.J., *EQ3/6, a software package for geochemical modeling of aqueous systems: package overview and installation guide, version 7.0*, Report UCRL-MA-110662 PT I, Lawrence Livermore National Laboratory, Livemore, CA, 1992.

Xu, T., N. Spycher, E. Sonnenthal, L. Zheng, and K. Pruess, *TOUGHREACT user's guide: a simulation program for non-isothermal multiphase reactive transport in variably saturated geologic media, version 2.0,* Lawrence Berkeley National Laboratory, Berkeley, CA, 2012.

Zheng, L., J.A. Apps, N. Spycher, J.T. Birkholzer, Y.K. Kharaka, J. Thordsen, S.R. Beers, W.N. Herkelrath, E. Kakouros, and R.C. Trautz, Geochemical modeling of changes in shallow groundwater chemistry observed during the MSU-ZERT CO_2 injection experiment. *Int. J. Greenh. Gas Control.*, 7, 202-217, 2012.

Optimization, Parameter Estimation, Data-Worth Analysis

WHAT'S NEW IN iTOUGH2?

Stefan Finsterle

Lawrence Berkeley National Laboratory
Earth Sciences Division
One Cyclotron Road, MS 74-316C
Berkeley, CA 94720
e-mail: SAFinsterle@lbl.gov

ABSTRACT

iTOUGH2 supports the TOUGH suite of non-isothermal multiphase flow simulators by providing capabilities for sensitivity analyses, automatic parameter estimation, data-worth analysis, and uncertainty quantification. iTOUGH2 is continuously updated in response to scientific challenges and user needs, with new capabilities added to both the forward simulator and the optimization framework. This article summarizes some of these new iTOUGH2 features.

INTRODUCTION

iTOUGH2 (Finsterle, 2007abc) is a simulation-optimization framework for the TOUGH suite of nonisothermal multiphase flow models (Pruess et al., 2012; Finsterle et al., 2014). By running TOUGH simulations multiple times for different input parameter sets, iTOUGH2 can be used for parameter estimation through automatic model calibration, local and global sensitivity analyses, data-worth analyses, and for assessing the uncertainty of model predictions. iTOUGH2 updates are driven by scientific challenges and user needs, with new capabilities added to both the forward simulator and the optimization framework.

Recent advances within the inversion framework include: data-worth analysis, in which the benefit of adding potential data or the detriment of removing existing data is evaluated with respect to estimation or prediction uncertainty; evaluation of the relative effect of parameter uncertainty on prediction uncertainties; inclusion of time-domain electro-magnetic data for joint hydrogeophysical inversions; automatic resampling of paths that are unusable in a Morris global sensitivity analysis due to a convergence failure in the forward simulation; triangular probability density functions for Latin Hypercube sampling; generation of tornado plots; a skew exponential power objective function; and parallel execution of forward runs on multi-processor machines. Recent advances related to the forward simulator include: inclusion of coupled thermal-hydrological-rockmechanical processes; a new equation-of-state module for supercritical water up to 2000 °C; a chemical osmosis module; depth- or temperature-dependent permeability and heat capacity; reading and mapping of heterogeneous, anisotropic permeability fields; and various other user options. A selection of these new capabilities as well as other iTOUGH2 enhancements and additions will be summarized below.

CODE ENHANCEMENTS

The following subsections describe some of the features recently incorporated into iTOUGH2, starting with additions to the forward operator (i.e., TOUGH2), followed by enhancements of the inverse operator.

Enhancements of Forward Model

iTOUGH2 is wrapped around standard TOUGH2 (Pruess et al., 2012), calling it to obtain select outputs evaluated for a given parameter set. However, many modifications to the TOUGH2 simulator have been made. Some of these features are motivated by the fact that—if used within the iTOUGH2 optimization framework—the simulation problem has to be solved in a single run, i.e., it cannot be interrupted, for example, to edit the mesh, or to change boundary conditions. This requirement has led to a number of useful features, such as the ability to connect steady-state and transient simulations; to change geometric mesh information after internal mesh generation; to change

element volumes, primary variables, and certain material properties and flags at specified restart times; and to select alternative convergence criteria.

Other enhancements were driven by specific user needs, such as the incorporation of non-Darcy flow based on the Forchheimer equation and choked flow in gas wells; internal generation of spatially correlated, random property fields using geostatistics (Finsterle and Kowalsky, 2007); time-dependent Dirichlet and free-drainage boundary conditions; more flexible formulations of the van Genuchten and Brooks-Corey relative permeability and capillary pressure functions; Leverett scaling of capillary strength parameter; inclusion of the active fracture concept of Liu et al. (1998); material-related sinks and sources; vapor-pressure reduction to prevent disappearance of the liquid phase; and five- to nine-character element names.

A third group of enhancements includes features that simply increase user convenience, such as the signal handler, which allows a user to request printout or to gently terminate a TOUGH2 run at any point during the simulation; free-format and tabular reading of GENER and TIMES blocks; improved time-stepping and printout control; and intermediate saving of restart files.

Most of these options are now described in a dedicated report (Finsterle, 2015a). They are useful even if iTOUGH2 is only used to perform forward simulations. The following paragraphs describe capabilities and features that were recently added to the simulator in iTOUGH2.

Geomechanics

The coupling of TOUGH's multiphase flow and transport processes with rock mechanics is an active area of research and code development (for an overview, see Finsterle et al., 2014). These developments are partly motivated by the need to stimulate reservoirs through fracturing (e.g., for enhanced geothermal systems or tight shale gas formations), to understand the risk of compromising confining layers (e.g., at carbon storage sites or in heat-generating nuclear waste repositories), to address the issue of induced seismicity (either as a risk or monitoring option during reservoir stimulation), and many other applications (e.g., uplift and subsidence calculations caused by water and oil production).

Observable deformation data do not only contain information about geomechanical processes, but may help identify fluid and heat flow processes that caused stress changes in the reservoir. To be able (a) to determine geomechanical properties through inverse modeling, and (b) to make use of deformation data to constrain other properties and processes within a multi-physics joint inversion framework, non-isothermal fluid flow and geomechanics must be coupled. We integrated the ROCMECH simulator into iTOUGH2. ROCMECH calculates elastoplastic deformations caused by thermal and mechanical stresses using a sequential approach (Kim et al., 2012). Geomechanical properties (such as Young and shear moduli, Poisson ratio, Biot coefficient, yield stress, hardening parameter, friction and dilation angles, and thermal dilation coefficient) are added to the list of parameters that can be estimated, and deformation observations (magnitude and orientation) can be used as calibration data.

Figure 1 shows simulated deformations in response to steam injection into a reservoir for enhanced oil recovery (EOR). Pressure and temperature changes lead to effective and thermal stresses that result in considerable uplift and subsidence effects, which may be observed using InSAR or titltmeters. Such deformation data can then be used (in combination with injection, production and thermal data) to calibrate the reservoir model using iTOUGH2's multi-physics joint inversion capabilities.

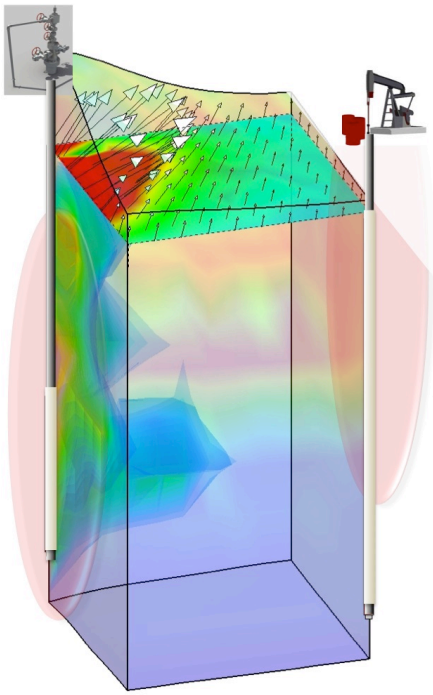

Figure 1. Simulation of coupled nonisothermal fluid flow and geomechanics. Isosurfaces of steam saturation indicate displacement of oil towards the production well. The EOR operation leads to uplift and deformations (vectors), which can be observed using InSAR and tiltmeters, potential data to be used within the multi-physics joint inversion framework of iTOUGH2.

Supercritical water

To simulate high-enthalpy fluids extracted from magmatic geothermal reservoirs, and to accurately predict the sustainability of the resource, the magmatic heat source of the geothermal systems should be incorporated into the numerical model. This requires an equation-of-state (EOS) module with temperature and pressure ranges that include supercritical conditions. The IAPWS-95 and IAPWS-IF97 thermodynamic formulations were implemented into iTOUGH2 to provide forward and inverse modeling capabilities of high-temperature magmatic geothermal reservoirs. Based on the work by Croucher and O'Sullivan (2008), the operational range of temperature and pressure was extended to 1,000°C and 1,000 MPa when using the IAPWS-95 formulation, and to 800°C and 100 MPa as well as 2,000°C for pressure within 50 MPa, when using the IAPWS-IF97 formulation. An extension of IAPWS-IF97 (which is significantly faster than the IAPWS-95 formulation) to 2,000°C is also provided. The five thermodynamic regions covered by the new EOS module are shown in Figure 2. A temperature dependence of permeability and thermal conductivity was also implemented. The new supercritical module EOS1sc is described in Magnúsdóttir and Finsterle (2015).

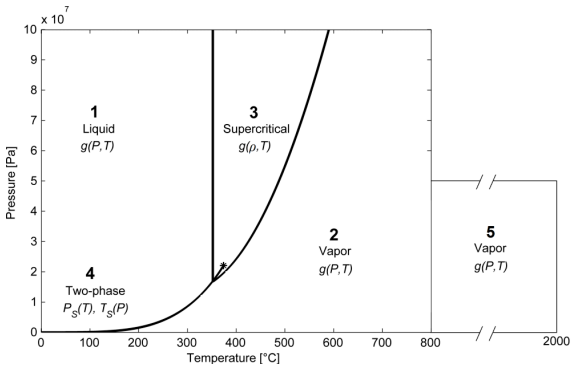

Figure 2. Thermodynamic regions implemented in iTOUGH2-EOS1sc.

Heterogeneous, anisotropic properties

Small-scale heterogeneity often is a key factor controlling the system behavior of interest. Element-by-element porosities and permeabilities can be specified or internally generated using geostatistical simulation (Finsterle and Kowalsky, 2007). However, a single modifier perturbs all three permeabilities in a given element. While this approach maintains the global anisotropy ratio of a material, it is often desirable to consider small-scale heterogeneity separately for each direction. Specifically, the upscaling and mapping of a discrete fracture network onto a continuum model requires anisotropic permeability modifiers. The code ThreeDFracMap (Parashar and Reeves, 2011) can be used to generate a fracture network by randomly sampling values for size, orientation, and aperture from appropriate, truncated probability distributions. Based on the resulting fractures and their intersections with each other as well as any given grid block, upscaled anisotropic permeabilities are calculated for each continuum element of the TOUGH2 model. Figure 3 shows the permeability structure as well as the oil saturation distribution resulting from a simulated water flood.

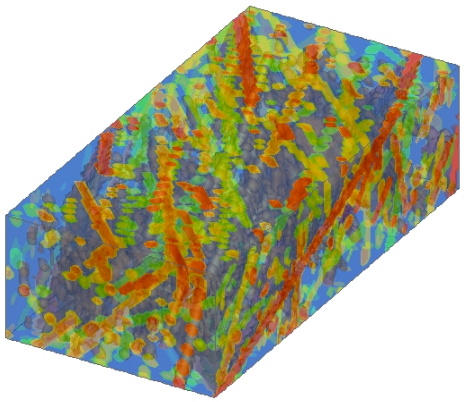

(a)

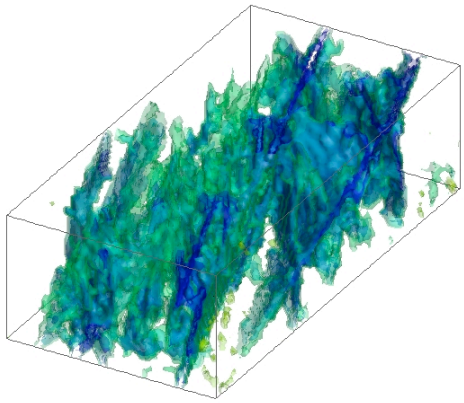

(b)

Figure 3. High-resolution continuum model with (a) anisotropic permeability modifiers to represent fracture network, and (b) result of water-flood simulation.

Enhancements of iTOUGH2 Framework

Multi-physics joint inversion framework

Figure 4 shows iTOUGH2's multi-physics joint inversion framework, where a diverse set of parameters can be estimated based on various types of observations.

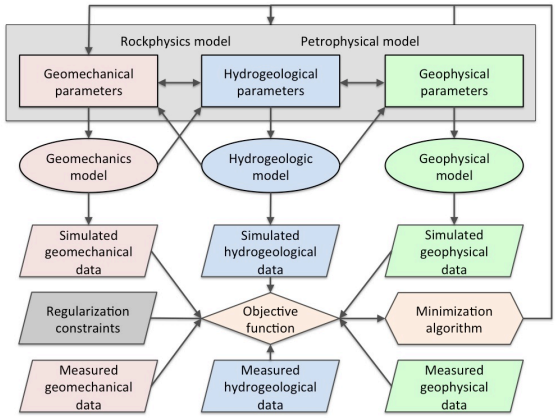

Figure 4. Multi-physics joint inversion framework.

The basic idea is that information contained in different data types is likely to be complementary to each other, helping to reduce the ill-posedness of an inverse problem if jointly analyzed. For example, geophysical data generally contain information about the subsurface structure and spatial phase distribution, whereas hydrogeological data contain information about flow and transport properties. Combining the two data sets allows for the determination of the spatial distribution of flow-relevant properties. Geomechanical data may serve a similar purpose, but may also be analyzed for their own sake.

Multi-physics joint inversion requires two-way coupling or one-way linking of hydrogeological, geomechanical, and geophysical forward models. Parameters to be estimated are either shared among these model components, or are connected through petrophysical relationships. Observations of all types enter a single, weighted objective function, which is minimized by concurrently updating all influential parameters.

The capabilities for jointly inverting hydrological and geophysical data for the estimation of hydrogeological, geophysical, and geostatistical parameters (Kowalsky et al., 2005) have been extended to include time-domain electromagnetic and seismic data. These capabilities are implemented in the parallel version referred to as MPiTOUGH2 (Commer et al., 2012). Time-lapse electrical DC resistivity data can also be simulated using the BERT finite-element code (Günther et al., 2006; Doetsch et al., 2013). A simple straight-ray seismic simulator is also available. New petrophysical relations relating hydrological properties and states to various geophysical attributes have been added.

Geomechanical modeling is fully integrated in iTOUGH2, allowing the user to estimate geomechanical parameters based on displacement observations (and other sensitive data).

The multi-physics joint inversion framework allows the estimation of parameters related to material properties, initial and boundary conditions, the geometry of the geological structure (Wellmann et al., 2014), geostatistical parameters (Finsterle and Kowalsky, 2008), and statistical properties of the residuals (Finsterle and

Zhang, 2011a). Moreover, the objective function, which includes a variety of observable variables, can be augmented by regularization terms (prior information and Tikhonov regularization). Finally, in addition to the fully incorporated hydrological, geomechanical, and geophysical models, any external code (e.g., a pre-processor, simulator, or post-processor) can be linked to iTOUGH2 through the PEST protocol (Finsterle and Zhang, 2011b).

Data-worth analysis

A data-worth analysis aims at identifying the relative contribution that each data point makes to the solution of an inverse problem and the subsequent predictive simulation. The basic idea is to examine how the addition of potential data (or removal of existing data) reduces (or increases) the uncertainty in select predictions made by a model that is calibrated against these data. Prediction uncertainty is proposed as the criterion for evaluating data-worth because it measures the usefulness of the data point for answering the specific modeling questions that support the ultimate project objectives.

Including calibration and prediction phases in a single data-worth analysis has considerable advantages, as it automatically identifies data that contain information about those parameters that are most influential on the predictions of interest. The approach consists of the following steps (see Figure 5):

(1) Selecting observable variables and categorization into actual observations, potential monitoring data, and target predictions, the uncertainty of which shall be reduced; (2) selecting potentially influential parameters; (3) developing calibration and prediction models that share these parameters; (4) evaluating estimation and prediction uncertainties with the reference data set; (5) removal of existing or addition of potential calibration data, and repetition of uncertainty analysis; and (6) calculating a composite uncertainty-reduction measure (ω), which reflects data worth.

Data worth depends not only on the reference parameter set, but also on the amount and quality of all the other data points presumed available for model calibration. The data-worth analysis is thus repeated for different reference parameter sets and different reference data sets with varying assumptions about the error structure of the residuals. The approach is further described in Wainwright and Finsterle (2015), and Finsterle (2015b).

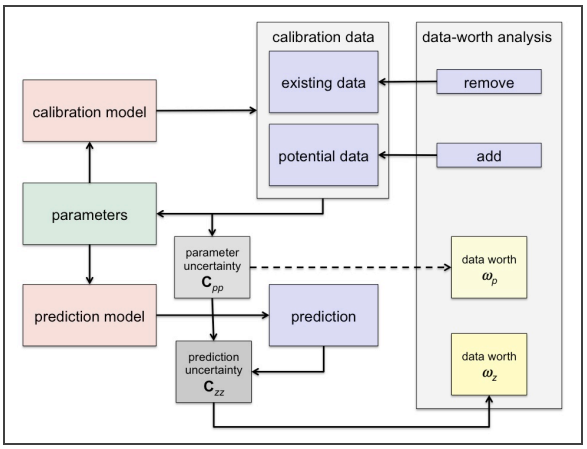

Figure 5. Elements of data-worth analysis. Influential parameters to be estimated from calibration data are shared with a prediction model to determine how the removal of existing or addition of potential data impacts prediction uncertainty. Data worth may also be calculated based on parameter uncertainty (dashed line).

Model reduction

iTOUGH2 analyses can be computationally very demanding as they require multiple solutions of the forward problem. Using fast surrogate models or response surface approximations is a promising approach to enable inversions, sensitivity, and uncertainty analyses of systems represented by large high-fidelity models. Advanced reduced-order modeling approaches are currently being developed and applied within the iTOUGH2 framework – they are discussed in separate communications (e.g., Pau et al., 2014). In addition, iTOUGH2 provides very simple response-surface interpolation schemes (based on inverse distance averaging), and supports the generation and storage of so-called snapshot results. This simple approach is useful to increase the sample size in certain uncertainty quantification approaches without undue computational burden.

Other features

The following additional user features have been added to iTOUGH2:

(1) A new objective function based on the skew exponential power function (Eq. 1) is available to better handle non-Gaussian, heteroscedastic, skewed residual distributions. The statistical parameters (β and ξ) can be specified or estimated.

$$p(r_i \mid \xi, \beta) = \frac{2\sigma_\xi}{\xi + \xi^{-1}} \omega_\beta \exp\left\{-c_\beta \left| r_{\xi,i} \right|^{2/(1+\beta)}\right\} \quad (1)$$

(2) Parallel execution of individual forward runs has been supported by iTOUGH2 since 1998 (Finsterle, 1998). This flexible and robust approach is based on the Parallel Virtual Machine (PVM) protocol, and allows access to multiple nodes and processors on a heterogeneous cluster of Unix-based workstations. A simpler parallelization scheme is now available, which does not require installation of PVM. However, it is limited to access multi-processor cores on a single machine (including PCs).

(3) Failed forward runs often lead to the premature termination of iTOUGH2. For certain analyses, iTOUGH2 attempts to recover from an incomplete run and to continue the analysis. Specifically, sampling-based approaches (e.g., Monte Carlo simulations or Morris global sensitivity analyses) may recover by simply resampling from the given distributions. iTOUGH2 may also recover from failed forward runs during certain stages in the Levenberg-Marquardt minimization algorithm.

(4) A new option has been added to automatically stop forward simulations as soon as it is identified that they do not lead to a reduction in the objective function. This may greatly reduce computational time when trial parameter sets are evaluated and in Monte Carlo simulations used for parameter estimation.

(5) The relative effect of parameter uncertainty on prediction uncertainties and a parameter identifiability measure is evaluated. the latter (appropriately scaled) is also used as the criterion for dynamically selecting a subset of parameters for updating during an inversion.

(6) iTOUGH2 now supports the generation of Tornado plots.

(7) In addition to (log-)normal and (log-) uniform distributions, (log-)triangular probability density functions can be specified for Monte Carlo and Latin Hypercube sampling.

(8) Total flow rates of phases or components across interfaces between two (or more) zones can be defined conveniently by specifying pairs of material names. The orientation of connections is automatically taken into account to yield consistent signs of individual flow rates before they are summed. This feature allows definition of total flow rates to or from well elements or across interfaces between geologic units or other performance boundaries.

(9) The weighting factor for increments dynamically reduced if residuals oscillate; they are increased again if oscillations are not the reason for convergence failures. Moreover, small residuals can be set to zero to avoid updating of primary variables, potentially making the solution more stable.

(10) As part of the enhancements described in this article, a number of bugs were fixed, and an unknown number of new bugs were introduced. There fate will be discussed at the TOUGH Symposium 2018.

WHAT'S NEXT?

We will continue to update iTOUGH2 and add new features and analysis methods to both its forward model and inversion framework in response to user requests and to address scientific challenges. While not all of the enhancements described in this article are released, a new version of iTOUGH2 will be made available for licensing.

ACKNOWLEDGMENT

I would like to thank all the developers and users who contributed to the formulation, implementation, and testing of new iTOUGH2 features. This work was supported, in part, by the U.S. Department of Energy under Contract No. DE-AC02-05CH11231.

REFERENCES

Commer, M., M.B. Kowalsky, J. Doetsch, G. Newman, and S. Finsterle, MPiTOUGH2: A parallel parameter estimation framework for hydrological and hydrogeophysical applications, *Computers & Geosciences*, *65*, 127–135, 2014.

Croucher, A.E., and M.J. O'Sullivan, Application of the Computer Code TOUGH2 to the Simulation of Supercritical Conditions in Geothermal Systems, *Geothermic*s, *37*, 662–634, 2008.

Doetsch, J., M.B. Kowalsky, C. Doughty, S. Finsterle, J.B. Ajo-Franklin, C.R. Carrigan, X. Yang, S.D. Hovorka, and T.M. Daley, Constraining CO_2 simulations by coupled modeling and inversion of electrical resistance and gas composition data, *International Journal of Greenhouse Gas Control*, *18*, 510–522, 2013.

Doherty, J., and R.J. Hunt, Two statistics for evaluating parameter identifiability and error reduction, *J. Hydrol.*, *366*, 119–127, 2009.

Finsterle, S., *Parallelization of iTOUGH2 Using PVM*, Report LBNL-42261, Lawrence Berkeley National Laboratory, Berkeley, Calif., October 1998.

Finsterle, S., *iTOUGH2 User's Guide,* Report LBNL-40040, Berkeley Lab, Berkeley, Calif., 2007a.

Finsterle, S., *iTOUGH2 Command Reference,* Report LBNL-40041, Berkeley Lab, Berkeley, Calif., 2007b.

Finsterle, S., *iTOUGH2 Sample Problems*, Report LBNL-40042, Berkeley Lab, Berkeley, Calif., 2007c.

Finsterle, S., and M.B. Kowalsky, *iTOUGH2-GSLIB User's Guide*, Report LBNL/PUB-3191, Berkeley Lab, Berkeley, Calif., 2007.

Finsterle, S., and M. B. Kowalsky, Joint hydrological-geophysical inversion for soil structure identification, *Vadose Zone J.*, *7*, 287–293, 2008.

Finsterle, S., and M.B. Kowalsky, A truncated Levenberg-Marquardt algorithm for the calibration of highly parameterized nonlinear models, *Computers and Geosciences*, *37*, 731–738, 2011.

Finsterle, S., and Y. Zhang, Error handling strategies in multiphase inverse modeling, *Computers and Geosciences*, *37*, 724–730, 2011a.

Finsterle, S., and Y. Zhang, Solving iTOUGH2 simulation and optimization problems using the PEST protocol, *Env. Modelling and Software*, *26*, 2011b.

Finsterle, S., E.L. Sonnenthal, and N. Spycher, Advances in subsurface modeling: The TOUGH suite of simulators, *Computers & Geosciences*, *65*, 2–12, 2014

Finsterle, S., *Enhancements to the TOUGH2 Simulator Integrated in iTOUGH2*, Report LBNL-TBD, Lawrence Berkeley National Laboratory, Berkeley, Calif., 2015a.

Finsterle, S., Notes on sensitivity and data-worth analysis, *Water Resour. Res.*, 2015b (in review).

Günther, T., C. Rücker, C., and K. Spitzer, Three-dimensional modelling and inversion of DC resistivity data incorporating topography - II. Inversion, *Geophys. J. Int.*, *166*, 506–517, 2006.

Kim, J., E. Sonnenthal, and J. Rutqvist, Formulation and sequential numerical algorithms of coupled fluid/heat flow and geomechanics for multiple porosity materials. *Int. J. Numer. Meth. Eng*. *92*, 425–456, 2012.

Kowalsky, M.B., S. Finsterle, J. Peterson, S. Hubbard, Y. Rubin, E. Majer, A. Ward, and G. Gee, Estimation of field-scale soil hydraulic parameters and dielectric parameters through joint inversion of GPR and hydrological data, *Water Resour. Res.*, *41*, W11425, 2005.

Magnúsdóttir, L., and S. Finsterle, An iTOUGH2 equation-of-state module for modeling supercritical conditions in geothermal reservoirs, *Geothermics*, 2015.

Morris, M.D., Factorial sampling plans for preliminary computational experiments. *Technometrics*, *33*(2), 161–174, 1991.

Parashar, R., and D.M. Reeves, Computation of flow and transport in fracture networks on a continuum grid, In: *Proceedings*, MODFLOW and More 2011: Integrated Hydrologic Modeling, 771–775, 2011.

Pau, G.S.H., Y. Zhang, S. Finsterle, H. Wainwright, and J. Birkholzer, Reduced order modeling in iTOUGH2, *Computers & Geosciences*, *65*, 118–126, 2014.

Pruess, K., C. Oldenburg, and G. Moridis, *TOUGH2 User's Guide, Version 2.1*, Report LBNL-43134, Berkeley Lab, Berkeley, Calif., 2012.

Saltelli, A., M. Ratto, T. Andres, F. Campolongo, J. Cariboni, D. Gatelli, M. Saisana, and S. Tarantola, *Global Sensitivity Analysis, the Primer,* 292 pp., John Wiley & Sons Ltd., West Sussex, England, 2008.

Schoups, G., and J.A. Vrugt, A formal likelihood function for parameter and predictive inference of hydrologic models with correlated, heteroscedastic, and non-Gaussian errors, *Water Resour. Res.*, *46*, W10531, 2010.

Wainwright, H., S. Finsterle, Y. Jung, Q. Zhou, and J.T. Birkholzer, Making sense of global sensitivity analyses, *Computers & Geosciences*, *65*, 84–94, 2014.

Wainwright, H.M., and S. Finsterle, *Global Sensitivity and Data-Worth Analysis in iTOUGH2, User's Guide*, Report LBNL-TBD, Lawrence Berkeley National Laboratory, Berkeley, Calif., 2015.

Wellmann, J.F., S. Finsterle, and A. Croucher, Integrating structural geological data into the inverse modelling framework of iTOUGH2, *Computers & Geosciences*, *65*, 95–109, 2014.

EFFECT OF ANISOTROPY ON MULTI-DIRECTIONAL PRESSURE-PULSE-DECAY EXPERIMENTS

Michael J. Hannon, Jr.[1]
Stefan Finsterle[2]

[1]The University of Alabama at Birmingham
1150 10th Ave. S., BEC 257
Birmingham, Alabama, 35294, USA
e-mail: mhannonj@uab.edu

[2]Lawrence Berkeley National Laboratory
One Cyclotron Road, MS 74-316C
Berkeley, California, 94720, USA
SAFinsterle@lbl.gov

ABSTRACT

To provide a greater understanding of critical parameters of ultra-tight geologic formations such as shales, multiple unsteady-state methodologies have been developed to estimate permeability of core samples. The original transient analysis technique, called the "Pressure Pulse Decay", showed significant time savings as compared to conventional steady-state analyses when measuring tight sandstone materials having permeabilities in the milli-Darcy to micro-Darcy range, but they have had limited success in measuring materials having nano-Darcy permeability. As industrial interest developed for these lithologies, most notably as source rocks for unconventional oil and gas recovery and as geologic confining zones for deep subsurface waste containment, the methodology was revised further by enhancing the surface area accessible to the pulse and allowing fluid ingress along arbitrary directions.

Despite the increasing complexity of the resultant flow field using such techniques, the most widely used models today assume isotropic cores. In this study we investigate the effect of assuming an isotropic fabric for materials that show strong anisotropic behavior, most notably layered media like shales. We begin by describing multiple forward models to simulate the anticipated pressure response for pressure-pulse-decay measurements performed on fractured cylindrical samples and crushed cuttings. Then, using the inverse modeling analyses available through iTOUGH2, we fit the various models to synthetic data and compare their results. We show that by assuming the fabric to be isotropic, such measurements yield a bulk permeability estimate with limited physical significance. However, anisotropy can be readily accounted for in the iTOUGH2 data-inversion framework, which allows for the assumption of an isotropic fabric to be relaxed.

INTRODUCTION

Site characterization of geologic formations begins with the collection of native core samples and analyzing them by benchtop laboratory experiments. Although these analyses occur on a minute sampling size with respect to the reservoirs under investigation, they are used as the "ground truth" against which field-scale data acquired by techniques such a wireline geophysical logs (Jorgensen, 1989) or seismic profiling (Parra, 2000) are calibrated. Perhaps nowhere is this protocol more important than in the measurement of permeability. Conventional steady-state measurements performed on samples from highly porous and permeable storage formations provide accurate estimates of intrinsic permeability in a reasonable amount of time. But for the ultra-tight caprock formations interlaced between them, measuring permeability is much more difficult. The ability to perform such measurements in a way that is both accurate and timely continues to elude interested parties, who require them for applications in Carbon Capture, Utilization and Storage (Bennion and Bachu, 2007) as well as in unconventional oil and gas exploration (Chhatre et al., 2014; Sondergeld et al., 2010).

UNSTEADY-STATE PERMEAMETRY

Increased interest in lower permeability materials led to experimental methodologies devised to analyze the transient responses to pressure gradients imposed on cylindrical core samples. The most common of these is the pressure-pulse-decay technique introduced by Brace et al. (1968), which is depicted in Figure 1.

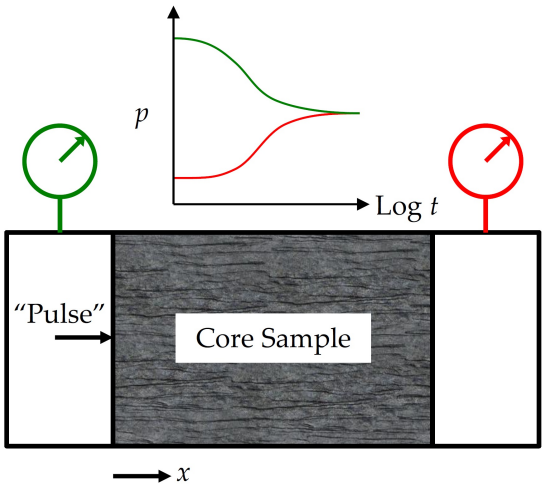

Figure 1. Conceptual schematic of the traditional pressure-pulse-decay experiment.

A closed fluid system, compartmentalized in two reservoirs on either end of a core sample and the pore volume therein, reaches equilibrium at a set pressure. The pressure in the upstream volume is instantaneously pulsed by a small percentage of the initial equilibrium pressure, and the pressure-decay curves in the upstream reservoir and/or the pressure increase in the downstream reservoir are recorded and fit to transient flow models.

An exact analytical solution to the governing equations of the pressure-pulse decay was derived for a liquid permeant by Hsieh et al. (1981) and adapted, by way of integral transformations, to a gaseous permeant by Haskett et al. (1988). Finsterle and Persoff (1997) later devised a numerical model to also account for experimental imperfections, such as the initial Joule-Thomson temperature fluctuations or system leakages, which do not lend themselves as easily to analytical solutions. Some notable experimental design adjustments were made to accommodate extremely low permeability (i.e., nano- to subnano-Darcy) materials. These methods, described in the following paragraphs, are able to do so by permitting fluid ingress into additional sections of sample surface area, thereby allowing transport along multiple directions.

Pressure-Pulse Decay of Fractured Cores

With brittle materials like shale, coring-induced fractures falling along the bedding plane of cylindrical samples are quite common. In order to quantify the influence of these fractures, Ning et al. (1993) designed the pulse-decay experiment depicted in Figure 2.

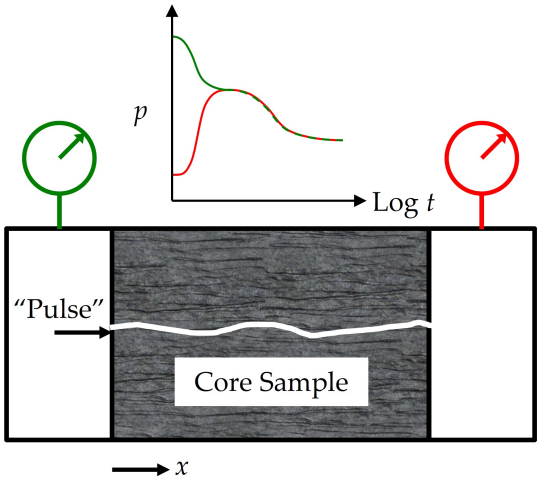

Figure 2. Conceptual schematic of the pressure-pulse-decay test of fractured cores.

A core sample of porous material oriented parallel to the native bedding plane with at least one fracture spanning its length is placed in a standard pressure-pulse-decay test cell. Once the pulse is performed, the pressures in both reservoirs quickly approach one another as the permeant travels through the highly permeable fracture. At this point, through the access given in the upstream and downstream faces and the additional access through the fracture, the pulse continues to infiltrate the matrix pore network. This results in both reservoir pressures continuing to decrease until a final equilibrium value is reached.

Ning et al. (1993) developed an analytical flow model to approximate the pressure response under this scenario. A history match of this model to the early-time behavior helps ascertain fracture permeability and the thickness of its zone of influence, while the remaining pressure

trace characterizes the matrix permeability and porosity. By enabling new pathways into matrix pores, permeability measurements in previously inestimable regimes now become accessible. Yet the flow model is limited by its assumption of isotropic flow. For the Bremen sandstones used for verification, this assumption is reasonable. But applying the same assumption to layered materials having principal permeabilities that can vary by orders of magnitude (Sondergeld et al., 2010), such as the Devonian shale specimens also analyzed in this paper, will result in an artificial bulk estimate with limited physical significance.

Pressure-Pulse Decay of Crushed Samples

To achieve maximization of accessible surface area for permeant ingress and the resultant minimization of equilibration time, Luffel and Curtis (1996) proposed crushing core samples into small cuttings and placing them into the test rig conceptualized in Figure 3. The pressure inside the pores of each particle and inside the test cell initially reaches equilibrium by filling the system with the gaseous permeant. After reaching equilibrium, the pressure in the test cell is instantaneously increased by a small percentage by adding a fluid "pulse" to the system. Assuming the pressure in the space between fragments responds immediately to the initial pressure disturbance in the cell, the system is immediately closed after the pulse is introduced. As the pulsed gas begins to infiltrate the pores of the fragments, it slowly decreases to a new equilibrium, as depicted in Figure 3.

This methodology, commonly referred to as the "GRI Method" after the Gas Research Institute who funded this research, is perhaps the most commonly used permeametry strategy employed by professional core laboratories for the characterization of the ultra-low permeability shales. Employing this technique allows a permeability estimate in the sub-nD regime to be attained within 15 – 20 minutes. However, as Figure 3 demonstrates, the shape, size and orientation of the cuttings cannot be described with a strong degree of accuracy. Based on sieve analyses and simplicity for model generation, flow models typically assume a cylindrical (Luffel and Curtis, 1996) or spherical (Profice et al., 2011) geometry for the cuttings. Although many of the models devised to analyze the data from these tests are not available in the public literature, those that are assume drill cuttings of an isotropic composition. As the material under investigation is no longer consolidated, it is also impossible to apply confining stress, which has a strong influence on permeability (Yang and Aplin, 2007). As a result of these limitations, permeability measurements from core laboratories employing this technique result in discrepancies of an order of magnitude or more (Chhatre et al., 2014; Sondergeld et al., 2010).

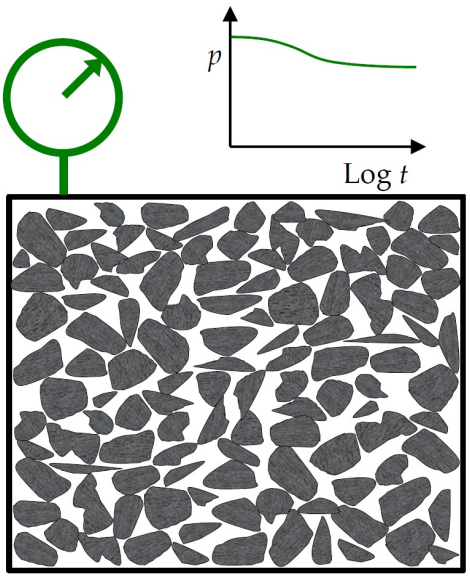

Figure 3. Conceptual schematic of the pressure-pulse-decay test of crushed samples.

NEW MODELS

Currently available experimental analyses are limited by their assumption of isotropic materials. In the paragraphs below, we introduce new models meant to take anisotropic effects into account and compare their results to publicly available models. For each experimental design (fractured sample as well as crushed samples), we introduce a unidirectional analytical model in addition to a multidirectional numerical model.

Fractured Samples

Flow of a gas with pressure p, density ρ and viscosity μ through a fractured sample of porosity n_m and directional permeabilities $k_{m,x}$ and $k_{m,z}$, with a single fracture network of

thickness h_f, porosity n_f and permeability k_f lying at the vertical centerline, should take into account both flow through the matrix and flow through the fracture. In the most general sense, flow in the matrix (subscript m) and fracture (subscript f) can be modeled using Equations 1 and 2, respectively.

$$k_{m,x}\frac{\partial}{\partial x}\left(\frac{\rho_m}{\mu}\frac{\partial p_m}{\partial x}\right) + k_{m,z}\frac{\partial}{\partial z}\left(\frac{\rho_m}{\mu}\frac{\partial p_m}{\partial z}\Big|_{z=\frac{h_f}{2}}\right) = \frac{\partial}{\partial t}(n_m\rho_m) \quad (1)$$

$$k_f\frac{\partial}{\partial x}\left(\frac{\rho_f}{\mu}\frac{\partial p_f}{\partial x}\right) - 2\,\frac{k_{m,z}}{h_f}\frac{\partial p_m}{\partial z}\Big|_{z=\frac{h_f}{2}} = \frac{\partial}{\partial t}(n_f\rho_f) \quad (2)$$

As indicated by the equations below, flow would enter and exit upstream (Eq. 3) and downstream (Eq. 4) reservoirs by way of flux across the upstream and downstream faces of the sample. Note that flux through the matrix pores must be integrated across the span wise direction y as the vertical extent of the sample ingress area h_m will change with it.

$$\frac{h_f D}{V_u}\frac{k_f}{\mu}\frac{\partial p_f}{\partial x}\Big|_{x=0} + \frac{2D}{V_u}k_m\int_0^D\int_{h_f}^{h_m(y)}\frac{\rho_m}{\mu}\frac{\partial p_m}{\partial x}\Big|_{x=0}dzdy = \frac{d\rho_u}{dt} \quad (3)$$

$$\frac{h_f D}{V_d}\frac{k_f}{\mu}\frac{\partial p_f}{\partial x}\Big|_{x=L} + \frac{2D}{V_d}k_m\int_{-R}^{R}\int_{h_f}^{h_m(y)}\frac{\rho_m}{\mu}\frac{\partial p_m}{\partial x}\Big|_{x=L}dzdy = -\frac{d\rho_d}{dt} \quad (4)$$

The subscripts u and d denote conditions in the upstream and downstream reservoirs, respectively, and $D = 2R$ is the thickness of the core in the y direction. In addition to the horizontal pressure gradient acting across the sample, a vertical pressure gradient is imposed by the gas in the fracture that allows ingress into the matrix. This is indicated by the $\partial/\partial z$ terms in Eqs. 1 and 2 as well as by imposing pressure equivalence at the interface between the fracture and matrix ($z = h_f/2$).

Unidirectional flow

The model described here neglects flow in the z direction, which allows us to obtain an analytical solution. Since we expect $k_{m,z}$ to be well under $k_{m,x}$ (Sondergeld et al., 2010), we assume flow to remain horizontal throughout the test and no pressure communication to occur between the fracture network and its neighboring matrix pores.

Multi-directional flow in anisotropic cores

Allowing flow to occur parallel and perpendicular to bedding introduces complexities in the governing equations and flow domain that require a numerical solution. Therefore, we employ simulations with TOUGH2 to approximate the flow response to the fully multi-directional case.

Crushed Samples

As one would expect, mimicking the exact flow domain in the case shown in Figure 3 is excessively difficult. Thus, some basic simplifying assumptions on the flow domain should be employed. As mentioned previously, the currently available methods assume the cuttings to be either isotropic spheres or isotropic cylinders, all of equal size. While there are many assumptions here we feel could be relaxed to improve the accuracy of the flow domain, we limit our analyses to a collection of equally sized cylindrical fragments having diameters equaling twice their heights (Luffel and Curtis, 1996). Such a test is conceptualized in Figure 4. We also assume all cylindrical fragments are composed of their own layering similar to the native formations (e.g. shales) from which the core materials are typically extracted. The central axis of each cylinder is oriented normal to bedding.

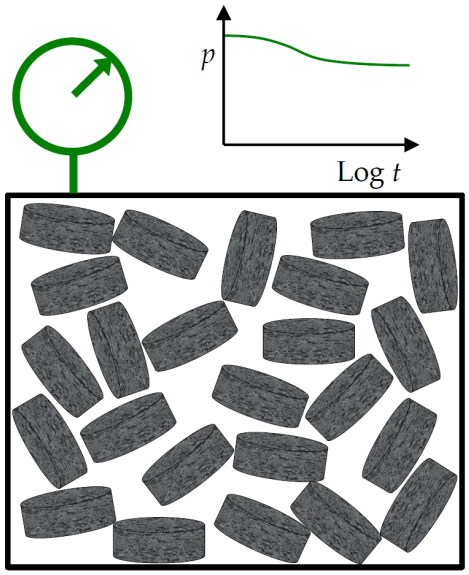

Figure 4. Conceptual schematic of the pressure-pulse-decay test of crushed cylindrical particles.

Unidirectional radial flow

As in the models used to analyze fractured samples, we begin by assuming flow to occur only along the direction parallel to bedding, which in this case is the radial direction of each cylindrical cutting. Doing so allows the governing equations to be solved analytically. This is a reasonable assumption for layered media, whose permeabilities perpendicular to bedding tend to be much lower (i.e. by an order of magnitude or more) than those parallel to it.

Multidirectional flow in anisotropic cylindrical cuttings

We again employ numerical simulations with TOUGH2 to approximate the flow response to the fully multi-directional case. In this case, we assume two constant permeabilities along the axial and radial directions of each cylinder.

RESULTS

Using the iTOUGH2 data-inversion framework, we plan to fit the flow models introduced in this study as well as published isotropic models to synthetic data generated by the numerical anisotropic models.

CONCLUSIONS AND FUTURE WORK

From our model analyses, we plan to demonstrate that bulk permeability estimates obtained from models assuming an isotropic core lie somewhere between the permeability parallel and perpendicular to the native bedding plane. Using the analytical models, which assume no flow perpendicular to the bedding plane, we arrive at a solution that has a comparable fit to the synthetic data at a value close to the permeability parallel to the bedding plane. The unidirectional model deviates from the synthetic data as vertical permeabilities approach horizontal permeabilities. However, anisotropy can be readily accounted for in the iTOUGH2 data-inversion framework, allowing for the estimation of directional permeabilities. Such a framework can be used to compare against experimental data, which we plan to perform in subsequent studies.

ACKNOWLEDGMENTS

This work was supported by the Alabama Power Company and Southern Company, under the project entitled, "Geologic Carbon Sequestration: Caprock Integrity Laboratory;" by Advanced Resources International, under Award Number DE-FE0010554 from the National Energy Technology Laboratory, entitled, "Commercial Scale CO_2 Injection and Optimization of Storage Capacity in the Southeastern United States;" by Montana State University, under Award Number DE-FE0004478 from the National Energy Technology Laboratory, entitled, "Advanced CO_2 Leakage Mitigation using Engineered Biomineralization Sealing Technologies;" by Oklahoma State University under Award Number DE-AC26-07NT42677 from the National Energy Technology Laboratory, entitled, "Petrophysics and Tight Rock Characterization for the Application of Improved Stimulation and Production Technology in Shale;" and by the U.S. Department of Energy under Contract No. DE-AC02-05CH11231 with the University of California, for the management and operation of Lawrence Berkeley National Laboratory.

REFERENCES

Bennion, D. and S. Bachu, Permeability and relative permeability measurements at reservoir conditions for CO_2-water systems in ultra low permeability confining caprocks, In *SPE Eur. Conf. Exhib.* London, UK: Society of Petroleum Engineers, 2007.

Brace, W.F., J.B. Walsh, and W.T. Frangos. Permeability of granite under high pressure, *J. Geophys. Res.*, 73(6), 1968.

Chhatre, S.S., E.M. Braun, S. Sinha, M.D. Determan, Q.R. Passey, T.E. Zirkle, A.C. Wood, J.A. Boros, D.W. Berry, S.A. Leonardi, and R.A. Kudva, Steady state permeability measurements of tight oil bearing rocks, In *Int. Symp. Soc. Core Anal.*, Avignon, France: The Society of Core Analysts, 2014.

Finsterle, S. and P. Persoff, Determining permeability of tight rock samples using inverse modeling, *Water Resour. Res.,* 33(8):1803 – 1811, 1997.

Haskett, S.E., G.M. Narahara, and S.A. Holditch, A method for simultaneous determination of permeability in low-permeability cores, *SPE Form. Eval.,* 3(3), 651 – 658, 1988.

Hsieh, P.A., J.V. Tracy, C.E. Neuzil, J.D. Bredehoeft, and S.E. Silliman, Transient laboratory method for determining the hydraulic properties of tight rocks – I. Theory, *Int. J. Rock Mech. Min. Sci. Geomech. Abstr.*, 18(5),245 – 252, 1981.

Jorgensen, D.G., *Using Geophysical Logs to Estimate Porosity, Water Resistivity and Intrinsic Permeability*, Report USGS-2321, U.S. Geological Survey, Washington, D.C., 1989.

Luffel, D.L. and J.B. Curtis, *Development of Laboratory and Petrophysical Techniques for Evaluating Shale Reservoirs*, Gas Research Institute, Houston, TX, 1996.

Ning, X., J. Fan, S.A. Holditch, and W.J. Lee, The measurement of matrix and fracture properties in naturally fractured cores, In *SPE Rocky Mountain Reg./Low Perm. Reserv. Symp.*, Denver, CO: Society of Petroleum Engineers, 1993.

Parra, J.O., Poroelastic model to relate seismic wave attenuation and dispersion to permeability anisotropy, *Geophysics*, 65(1), 202 – 210, 2000.

Profice, S., D. Lasseux, Y. Jannot, N. Jebara, and G. Hamon, Permeability, porosity and Klinkenberg coefficient determination on crushed porous media, In *Int. Symp. Soc. Core. Anal.,* number SCA2011-32, Austin, TX: The Society of Core Analysts, 2011.

Sondergeld, C.H., K.E. Nwsham, J.T. Comisky, M.C. Rice, and C.S. Rai, Petrophysical considerations in evaluating and producing shale gas resources, In *SPE Unconv. Gas Conf..*, Pittsburgh, PA: Society of Petroleum Engineers, 2010.

Yang, Y. and A.C. Aplin, Permeability and petrophysical properties of 30 natural mudstones, *J. Geophys. Res.,* 112, 2007.

FKF-TOUGH: A SOFTWARE PACKAGE FOR DATA ASSIMILATION IN TOUGH2 USING FAST KALMAN FILTER METHODS

A. Kokkinaki, J.Y. Li, H. Ghorbanidehno, E.F. Darve, P.K. Kitanidis

Stanford University
473 Via Ortega
Stanford, CA, 94403, U.S.A.
e-mail: amaliak@stanford.edu

ABSTRACT

In this work, we present fKF-TOUGH, a software package for stochastic Bayesian dynamic inversion encompassing a suite of fast Kalman Filter techniques recently developed at Stanford University. The software performs real-time estimation of dynamic variables, like CO_2 saturation, and their uncertainties, as well as characterization of heterogeneity, by combining TOUGH2 predictions with monitoring data of any type, in a statistically sound framework. Four different new algorithms are included in the fKF-TOUGH package, which have been specifically developed for systems with large number of unknowns, and have been designed to seamlessly integrate with the TOUGH2 family of codes. Two well-established data assimilation techniques are also included for comparison purposes. The software comes with comprehensive analysis and visualization tools developed in MATLAB®. We present the general software architecture, as well as some test cases to demonstrate the usage and capabilities of fKF-TOUGH.

INTRODUCTION

Data assimilation encompasses a wide range of techniques whose premise is the utilization of information as it becomes available in time, in order to improve the predictions of an uncertain physical model and to provide improved estimates of model parameters. The Kalman Filter (KF) was one of the first such data assimilation techniques. One example application of the KF is the use of various types of monitoring data collected through the course of a CCS project to characterize the properties of the geologic formation and to simultaneously track the position of the CO_2 plume in real time. Reliability in estimating the latter is crucial to ensure permanence of the injected CO_2 and/or to detect leakage to near-surface formations.

While the KF is ideally suited for this type of analysis and provides statistically optimal estimates for a given set of monitoring data, the computational cost of its textbook implementation is prohibitive for large-scale problems, with computations scaling with the number of unknowns cubed (Table 1). Methods that reduce the computational cost of the KF are necessary for real scale applications where the number of unknowns may exceed 10^4. The computational efficiency typically relies on some approximation of the original KF. Depending on the problem of interest, these approximations may have negligible impacts for all practical purposes, rendering the use of fast KF techniques a practical option for reliable data assimilation.

KALMAN FILTER THEORY

The KF is an algorithm that sequentially updates the predictions of a dynamic forward model that are uncertain (due to, e.g., unknown parameters or boundary conditions) using information from noisy measurements collected in time. Compared to standard (static) Bayesian inversion, the advantage of KF is that it can be used to estimate not only parameters (characterization mode), but also unknowns that are changing in time (monitoring mode). Measurements and unknowns (static and dynamic) are related through a state-space model, and are modeled as random variables with a certain probability distribution. The mean and covariance of the unknowns are estimated at each time where measurements are available through Bayesian updating theory. For a system with m unknowns, the estimation of the covariance is the most computationally expensive step, while also being the most critical for estimation accuracy. Most methods that accelerate the KF are based on approximating the covariance calculations.

OVERVIEW OF fKF-TOUGH

As part of our research on joint inversion in large-scale CCS projects and our collaboration with LBNL, we have developed a suite of fast Kalman Filter (fKF) methods and a software interface between fKF and several TOUGH2 modules. fKF-TOUGH can be used for real-time parameter and state estimation for any physical problem that can be modeled with the TOUGH codes. fKF-TOUGH is part of a larger software package being developed by our research group that integrates our fast Kalman filter methods with any general forward model, allowing the software to be used for a variety of data assimilation applications. In fKF-TOUGH, reduction in computational time and storage is achieved by exploiting the structure of high-dimensional dense matrices involved in these computations. This practically translates to fewer forward simulations per inversion, and allows for a larger number of unknowns and their uncertainties to be estimated. Our software involves five variants of the KF, each best suited for problems with different characteristics.

Table 1. Data assimilation methods in fKF-TOUGH.

Method	Characteristic	Cost
KF/Extended KF	Textbook	$O(m^3n)$
EnKF	Ensemble based	O(r)
HiKF	Random walk	O(n)
(n)CSKF	Smooth problem	O(m)
SpecKF	Few measurements	O(mn)
sCSKF	Parameter estimation	O(2mn)

SOFTWARE ARCHITECTURE

The core of the fKF-TOUGH software package has been developed in Matlab®. It has been designed such that it can be easily used as a black-box, where the user only needs to provide basic information about the physical problem in a simple text-based input file, run the program, and obtain the output in standardized format. TOUGH2 input files also need to be constructed by the user independently, so basic knowledge of TOUGH2 is assumed. Figure 1 shows the different components of the software:

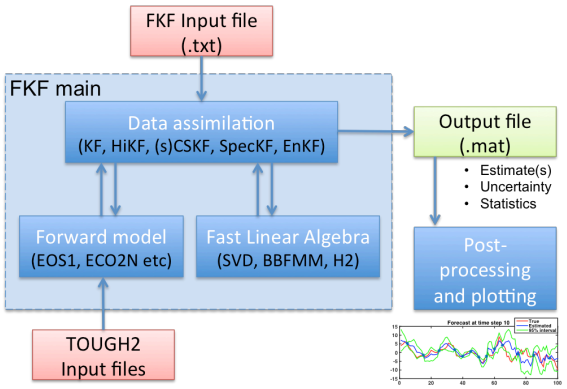

Figure 1. fKF-TOUGH system main architecture. Arrows indicate communication between the different modules.

Although the software can be used in a black-box fashion, the implementation of the fKF-TOUGH code follows principles of object oriented programming by using super-classes and classes, in order to increase modularity, and to allow for easy code extension and testing.

fKF modules

Each component of fKF-TOUGH has been developed as a separate module or class. Each module represents a set of techniques that can be used to do a similar action. For example, the fast linear algebra module consists of three different methods that can be used to perform matrix-matrix multiplications efficiently depending on the properties of the system and the input provided by the user.

Table 2. Module options in fKF-TOUGH.

Module	Function
KF Method	Table 1
Forward model	EOS1, ECO2N
Linear algebra	Low rank, H2, FMM
Jacobian eval	Matrix-free approach*

**The Jacobian module includes currently only the matrix-free option (Kitanidis and Lee, 2014)*

Data assimilation methods

fKF-TOUGH includes a total of five different data assimilation methods (Table 1). Each method is best suited for different problems, depending on the size of the problem, the type of variable being estimated, and the required output. The textbook version of the Kalman Filter is included. For testing purposes, the

performance of all other methods should be compared to the KF results, as the KF gives the statistically optimal estimates for a given problem and a given dataset.

Forward models

Depending on the physical problem of interest, our fast Kalman Filter algorithms can be combined with any forward model, provided that necessary input/output processing routines exist to transform the forward model output to the vector- and matrix-type data MATLAB format. For fKF-TOUGH, we have developed routines for processing TOUGH2 input and output files (SAVE, OUTPUT, FOFT and MESH files) to enable communication between the fKF code and TOUGH2. The I/O routines for TOUGH2 are part of the fKF-TOUGH package.

Plotting and post-processing

The output of fKF-TOUGH is provided in MATLAB form as matrices, vectors and structure type variables, and includes the estimated unknowns, and their uncertainties. Additional plotting and post processing routines are provided with fKF-TOUGH in order to visualize the output, and to evaluate the quality of the inversion, using various statistical metrics.

Suggested usage of fKF-TOUGH

The intended main usage is for TOUGH2 users who want to perform dynamic inversion for characterization and real time estimation of the system state in a black-box fashion, without specialized knowledge of Kalman Filtering. Such analysis can be used for formation characterization, as well as to optimize placement of wells and monitoring data collection when designing a monitoring network, as in a value of information type of analysis. Furthermore, since the KF code is open source, users can choose to use it to get more familiar with the KF and our fast KF algorithms and data assimilation in general. Lastly, users have the option to modify the code and/or extend it to include other data assimilation methods and other forward models.

Test cases

Tutorial type problems are included in the fKF-TOUGH package, in order to guide the user through the software's functions and capabilities. These test cases include linear and non-linear, 1-D and 2-D data assimilation problems, combined with different forward models. The use of simple forward models for the test cases helps the user get familiar with the KF codes, compare the various algorithms, and better understand the sensitivity of the results to the various parameters. Figure 2 shows such a comparison for test case 1, a linear 1-D data assimilation problem that was solved with two methods from the fKF-TOUGH2 package.

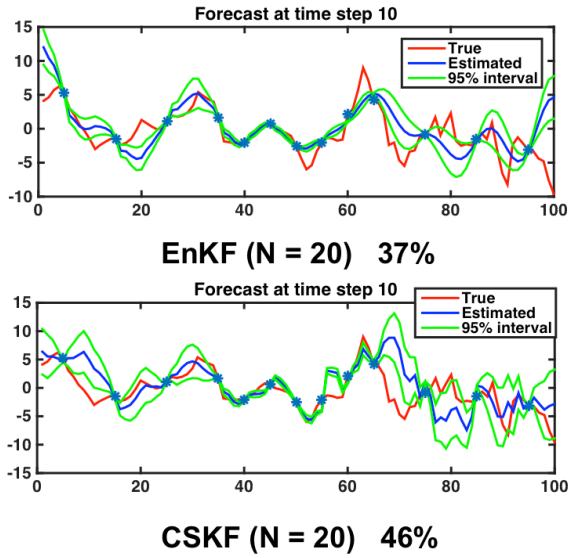

Figure 2. Comparison of EnKF and CSKF for test case 1.

EXAMPLE APPLICATIONS

Here, we briefly describe the results of our fKF-TOUGH algorithms for three different synthetic CCS applications, focusing on CO_2 tracking and formation characterization using datasets typically available.

Compressed State Kalman Filter (CSKF)

The compressed state Kalman Filter uses an efficient covariance compression scheme with a low rank approximation of the covariance matrix (Kitanidis, 2015). It gives best results for problems where the estimate varies smoothly, and its computational cost depends on how fast the eigenspectrum of the posterior covariance decays. It can be applied for both linear and non-linear problems. Figure 3 shows an example application for a strongly non-linear case of CO_2 monitoring (Li et al., 2015):

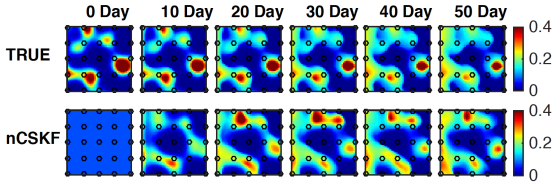

Figure 3.CCS application of CSKF (Li et al., 2015).

Spectral Kalman Filter (SpecKF)

The Spectral Kalman Filter is based on an approximation of the forward model and propagation of the cross-covariance instead of the covariance (Ghorbanidehno et al., 2015). It has good accuracy, as it does not approximate the covariance, it scales with the number of measurements, but gives only approximate uncertainty estimates.

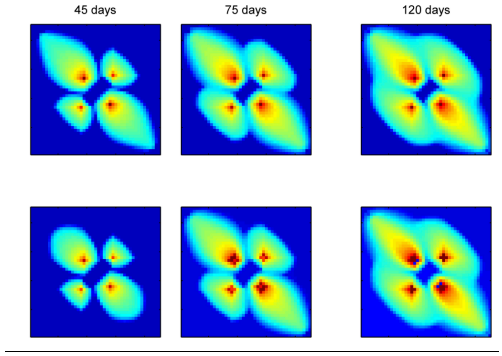

Figure 4. CCS application of SpecKF (Ghorbanidehno et al., 2015).

Smoothing based Compressed State Kalman Filter (sCSKF)

The sCSKF is a variant of CSKF with a modified algorithm with a one step ahead smoothing and is better suited for parameter estimation. The smoothing step improves non-linearity artifacts and prevents unphysical estimation, typically present in strongly non-linear problems. Figure 5 shows an example for CO_2 monitoring and formation characterization:

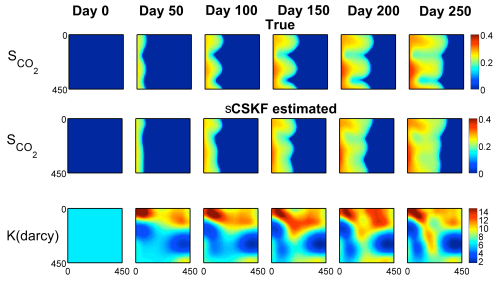

Figure 5. CCS application of sCSKF.

CONCLUSIONS

fKF-TOUGH2 is a software package with methods that can be used for reservoir/aquifer characterization, along with associated uncertainties at a reasonable computational cost, and to simultaneously update TOUGH2 predictions in real time. The package can be used with any TOUGH2 module, with no modifications of the TOUGH2 code. Data assimilation with the fKF-TOUGH can be performed sequentially, or in batches, depending on the availability of monitoring data. Usage of fKF-TOUGH can extend the scope of TOUGH2 applications to sophisticated monitoring data interpretation and informed monitoring design for a range of hydrogeologic applications.

ACKNOWLEDGMENTS

This material is based upon work supported by US Department of Energy, National Energy Technology Laboratory (DOE, NETL) under the award number DE-FE0009260: An Advanced Joint Inversion System for CO2 Storage Modeling with Large Data Sets for Characterization and Real-Time Monitoring, and also by the National Science Foundation Division of Mathematical Sciences under the award number: 1228275.

REFERENCES

Kitanidis, P. K., Compressed State Kalman Filter for large systems, Adv. in Water Resour., 76, 120-126, 2015.

Kitanidis, P. K., and J. Lee, Principal Component Geostatistical Approach for Large Dimensional Inverse Problems, Water Resour. Res., 50, 2015.

Li, J. Y., S. Ambikasaran, E. F. Darve and P K. Kitanidis, A Kalman filter powered by H2 matrices for quasi continuous data assimilation problems, Water Resour. Res., 50.

Li, J. Y., A. Kokkinaki, Ghorbanidehno, H., E. Darve, and P. K. Kitanidis, The non-linear compressed state Kalman Filter for efficient large scale reservoir monitoring. Adv. in Water Resour., 2015.

Ghorbanidehno, H., A. Kokkinaki, J. Y. Li, E. Darve, and P. K. Kitanidis, Real time data assimilation for large-scale systems: the Spectral Kalman Filter. Adv. in Water Resour., 2015.

FAST LARGE-SCALE INVERSION FOR DEEP AQUIFER CHARACTERIZATION

Jonghyun Harry Lee, Amalia Kokkinaki, Judith Yue Li and Peter K. Kitanidis

Stanford University
Y2E2 Bldg, 473 Via Ortega
Stanford, CA, 94306, USA
e-mail: jonghyun@stanford.edu

ABSTRACT

Characterization of geologic heterogeneity is crucial for reliable and cost-effective subsurface management operations, especially in problems that involve complex physics such as deep aquifer storage of carbon dioxide. With recent advances in computational power and sensor technology, large-scale aquifer characterization using various types of hydro-geophysical-biochemical measurements has been a promising approach to achieve high-resolution subsurface images. However, large-scale inversion with a large volume of measurements requires high, often prohibitive, computational costs associated with a number of large-scale coupled numerical simulation runs. As a result, traditional inversion methods have limited utility for such problems, e.g., applications with fine discretization on large domains (> ~ 100 m) and a large number of measurements to capture small-scale heterogeneity, like CO2 leakage detection.

We present an efficient inversion method for large-scale aquifer characterization. The domain we consider is a synthetic three dimensional deep saline aquifer intended for CO2 storage with relatively large number of unknown permeability grid blocks (~30,000). Transient pressure measurements from multiple pumping tests are used to delineate the heterogeneous permeability field and to quantify the corresponding estimation uncertainty. We use the Principal Component Geostatistical Approach (PCGA), which is a computationally efficient and scalable Jacobian-free geostatistical approach. PCGA can reduce the computational cost of the inversion significantly by using a low rank approximation of the high dimensional prior covariance matrix, effectively reducing the number of required TOUGH2 simulations by orders of magnitude. PCGA can also use forward simulators as a black-box, which facilitates a seamless and flexible integration with all TOUGH2 modules without intrusive code changes. In addition, the method can harness the parallel capabilities of TOUGH2-MP to efficiently scale to large-scale problems. We present results for a 3D synthetic aquifer using two pumping test configurations. Our results show that large-scale inversion at real field sites can become computationally feasible using our method, which shows a great potential for implementations in practice.

METHOD

In inverse modeling, a relationship between observations and unknowns is given by

$$\boldsymbol{y} = \boldsymbol{h}(\boldsymbol{s}) + \boldsymbol{v} \quad (1)$$

where $\boldsymbol{y}$ is the observation data such as pressure at monitoring wells, $\boldsymbol{h}$ is a forward model such as the TOUGH2 simulator, $\boldsymbol{s}$ is the unknown spatial field (e.g. permeability), and $\boldsymbol{v}$ is the error in the observation data $\boldsymbol{y}$ as well as the simulation model $\boldsymbol{h}$, usually modeled as Gaussian. To estimate the unknown $\boldsymbol{s}$ from the data and the forward model, the Bayesian geostatistical inverse approach (Kitanidis, 1995) is used in this study. In a Bayesian framework, the prior probability of $\boldsymbol{s}$ is assumed to be Gaussian with an unknown mean and a prior covariance matrix $\boldsymbol{Q}$. Then, the posterior probability density function (pdf) of $\boldsymbol{s}$ is computed through Bayes' theorem and the maximum a posteriori (MAP) estimate or most likely value of $\boldsymbol{s}$ is obtained by maximizing the posterior pdf (typically minimizing the negative log likelihood of the posterior pdf). The inverse problem becomes a nonlinear optimization problem that is commonly solved using an iterative Gauss-Newton method. However, the

geostatistical approach becomes computationally challenging for large-scale inversions because it requires computation of the derivative of the forward model, *i.e.*, Jacobian matrix $\boldsymbol{H}$ at a current estimate $\check{\mathbf{s}}$:

$$\boldsymbol{H} = \left.\frac{\partial \boldsymbol{h}}{\partial \boldsymbol{s}}\right|_{\boldsymbol{s}=\check{\boldsymbol{s}}} \quad (2)$$

which has computational costs proportional to the number of observations, even if the efficient adjoint-state method is used. Furthermore, the adjoint-state method often needs intrusive changes in the forward model code.

Overview of PCGA

To find the MAP estimate, the geostatistical approach requires Jacobian-covariance products such as $\boldsymbol{HQ}$. PCGA expedites the geostatistical inversion by avoiding the direct evaluation of the Jacobian matrix $\boldsymbol{H}$ utilizing a low-rank approximation of the prior covariance matrix $\boldsymbol{Q}$ and a finite difference approximation for Jacobian-covariance products. First, we assume that $\boldsymbol{Q}$ can be well-approximated as

$$\boldsymbol{Q} \approx \boldsymbol{Q}_K = \sum_{i=1}^{K} \boldsymbol{\zeta}_i \boldsymbol{\zeta}_i{}^T \quad (3)$$

where $\boldsymbol{Q}_K$ is a rank-K approximation of $\boldsymbol{Q}$ and ζ_i is i-th eigenvector multiplied by square root of i-th eigenvalue of $\boldsymbol{Q}$. A fast and accurate method to obtain Equation (3) for large-scale covariance matrices is explained in Lee and Kitanidis (2014). Then, the Jacobian-covariance product $\boldsymbol{HQ}$ can be approximated by:

$$\boldsymbol{HQ} = \boldsymbol{H}\left(\sum_{i}^{K} \boldsymbol{\zeta}_i \boldsymbol{\zeta}_i{}^T\right) = \sum_{i}^{K} (\boldsymbol{H}\boldsymbol{\zeta}_i)\, \boldsymbol{\zeta}_i^T \quad (4)$$

where $\boldsymbol{H}\boldsymbol{\zeta}_i$ is computed as

$$\boldsymbol{H}\boldsymbol{\zeta}_i \approx \frac{h(\boldsymbol{s} + \delta\boldsymbol{\zeta}_i) - h(\boldsymbol{s})}{\delta} \quad (5)$$

To evaluate equation (4), only "K" forward simulations are needed, which constitutes the main computational cost of the inverse solution at each iteration. By doing so, PCGA can reduce the number of numerical forward simulations by a factor of 10 or more, usually up to a few hundred simulation runs in total while in most practical situations, inverse solution is almost the same as those obtained from the conventional geostatistical approach as shown in Lee and Kitanidis (2014).

SYNTHETIC EXAMPLE

The domain we consider for heterogeneity characterization is a synthetic three dimensional, deep saline formation intended for CO2 storage. The sandstone formation is bounded by low permeability capstone from above and below, at depths of 1000 and 1020 m respectively. For the forward simulations, the size of the three dimensional domain used is 640 m x 640 m x 20 m (width x length x depth), with an active pumping network installed in the center of this domain, as shown in Figure 1. The network of five pumping wells includes one injection well at the center and four extraction wells (red wells in Figure 1). The discretization of the domain is fine close to the center (2 m x 2 m x 2 m), becomes coarser with distance from the center in the horizontal directions, and is constant in the vertical direction. This finer discretization compared to previous studies (e.g. Doughty and Pruess, 2004) allows the delineation of more details in the spatial heterogeneity of the soil properties and ensures more accurate numerical simulations. The total number of permeability grid blocks resulting from this discretization is 29,800.

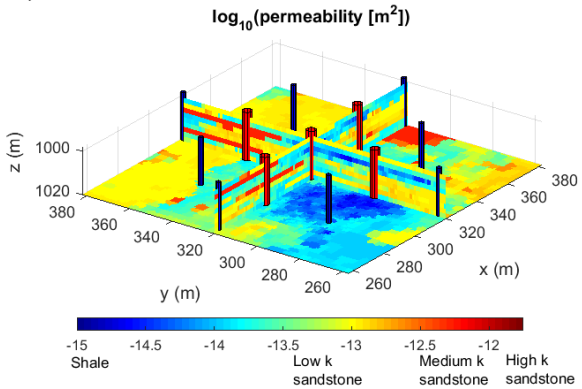

Figure 1. Synthetic true field; pumping (red) and monitoring (blue) wells

The synthetic true field is considered to have strong heterogeneity with high connectivity of large-scale features (channels) of four different soil types. This type of heterogeneity was generated using a transition probability based hydrofacies algorithm, TPROGS (Carle and Fogg, 1997). Within each soil type, small-scale heterogeneity is considered.

Pressure observations were generated using four dipole pumping tests between the center well and other four wells. For each pumping test, water was injected at 10 L/s at the center well and extracted at the same flow rate at an extraction well for 0.25 day. The monitoring network consists of a total of eight monitoring wells (blue wells in Figure 1), each of which has 10 multi-level monitoring ports. The distances between monitoring and pumping wells are relatively large, and have been chosen so as to resemble real-case scenarios where a limited number of monitoring wells is available. Transient pressure data from pumping tests were recorded and 11 pressure measurements were chosen at each monitoring port. Total 3,520 measurements were generated and Gaussian random error of 0.1 m was added to the data for the inversion, which is about 5 % of mean pressure changes. Parameters used in the forward simulation and data generation are summarized in Table 1.

Table 1. Problem setting

Parameter	Value
Domain (x,y,z)	640, 640, 20 (m)
# of grids (unknowns)	29800
# of injection wells	1 (center)
# of extraction wells	4
# of monitoring wells	8
Injection/extraction rates	3, 3 (L/s)
Simulation time	0.25 (day)
# of data (Case 1, 2)	880, 3520
Measurement error (std)	0.1 (m)

The three-dimensional domain and synthetic experiments were chosen such that they are similar to an existing CO2 storage application conducted at the Frio site (Daley et al., 2007). TOUGH2-MP with modules EOS1 was linked with a MATLAB-based PCGA code as a black-box simulator. Inversions were performed on a Linux workstation with Intel 12 core 3.4 GHz processors and 100 GB RAM. Each individual TOUGH2-MP simulation was executed on two CPU cores and six simulations were performed in parallel.

RESULTS

To show the efficiency and effectiveness of the proposed method, inversions with two different data sets are presented:

Case 1: one pumping test using the center well and the extraction well at x, y = 280, 320 m.

Case 2: four pumping tests using the center well and four extraction wells.

A total of K = 102 principal components were used. For both inversion tests, the best estimates were obtained in 3 iterations with total 321 and 1,274 TOUGH2-MP executions (~ 28 minutes and 2.3 hours) respectively. Case 2 was almost four times more expensive than Case 1 since simulations in Case 2 were repeated for four pumping tests. Inversion parameters are shown in Table 2.

Table 2. Inversion parameters

Parameter	Value
Covariance kernel	exponential
Prior variance	1 ($\log_{10}(m^2)^2$)
Correlation length (x,y,z)	100,100,10 (m)
# of principal components (K)	102
Total # of TOUGH2 runs	321 (Case 1)
	1274 (Case 2)
Inversion time (Case 1, 2)	0.48, 2.33 (hours)

Case 1: Inversion with one pumping test

The best estimates of the log permeability distribution are presented in Figure 2. It is shown that high permeability features between pumping wells and nearest monitoring wells are characterized relatively well. However, the entire field within the monitoring network was not identified clearly because of a limited number of data and relatively small pressure changes in the monitoring wells. Figure 3 (a) shows how closely the estimated field reproduces the data. Estimation uncertainty is presented in Figure 4 (a).

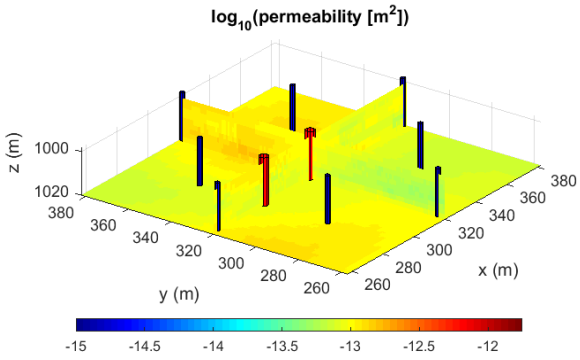

Figure 2. The best estimate for Case 1

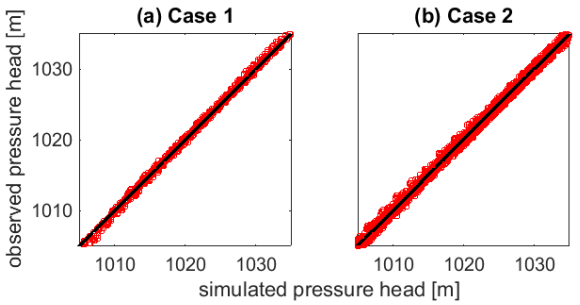

Figure 3. Data fitting; observed vs. simulated data

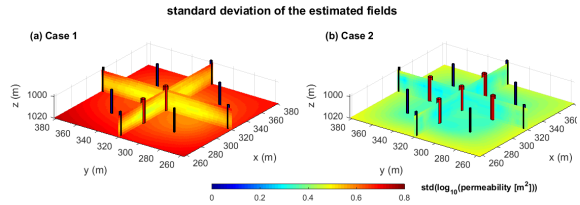

Figure 4. Estimation uncertainty

Case 2: Inversion with four pumping tests

Figure 5 shows the best estimate for Case 2. Since we used four pumping test data sets, large-scale features of the true field, especially high permeability zones, are identified better than Case 1. Still, the estimated field cannot identify low permeability channels and characterize small-scale variability. This finding is consistent with typical pressure data inversion as such data are not highly sensitive to permeability contrasts. Data fitting and estimation uncertainty are shown in Figures 3 (b) and 4 (b).

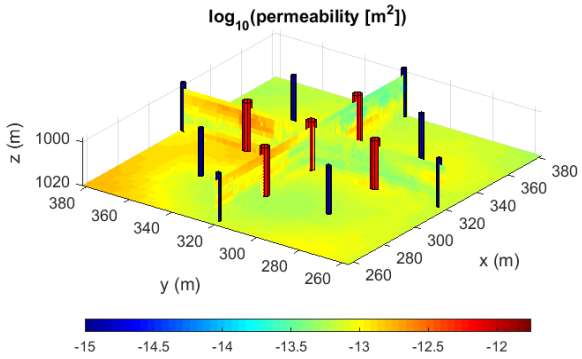

Figure 5. The best estimate for Case 2

CONCLUDING REMARKS

We implemented PCGA to perform pressure data inversions with multiple pumping tests and presented reasonable inversion results with affordable TOUGH2 runs. PCGA transforms an inverse problem with the computational cost associated with the number of observations into an approximately same problem with a constant number (~ total O(100)) of simulations, so that one would expect a great computational gain in solving large-scale inverse problems. In the examples presented, the estimated fields only captured dominant permeability features within the monitoring network as a result of the diffusive nature of pressure measurements and the scarce monitoring network. However, these results were obtained at a much smaller computational cost than traditional methods, allowing for the characterization of a large domain in less than a few hours. Additional data from tracer tests can be beneficial to identify connectivity features in the site without considerably increasing the computational costs. Joint inversions using pressure and temperature data will be conducted and presented at the TOUGH Symposium 2015.

ACKNOWLEDGMENT

The research was funded by the NSF ReNUWIt Engineering Research Center (www.renuwit.org; NSF EEC-1028968).

REFERENCES

Carle, S. F., and Fogg, G. E., Modeling spatial variability with one- and multi-dimensional Markov chains, *Mathematical Geology*, 28(7), 1997.

Daley, T., R. Solbau, J. Ajo-Franklin, and S. Benson, Continuous active-source seismic monitoring of injection in a brine aquifer, Geophysics, 72(5), A57–A61, 2007

Doughty, C. and K. Pruess., Modeling Supercritical Carbon Dioxide Injection in Heterogeneous Porous Media, *Vadose Zone J.*, 3(3), 837–847, 2004.

Kitanidis, P. K., Quasi-linear geostatistical theory for inversing, *Water Resour. Res.*, 31(10), 2411–2419, 1995.

Lee, J., and P. K. Kitanidis, Large-scale hydraulic tomography and joint inversion of head and tracer data using the Principal Component Geostatistical Approach (PCGA), *Water Resour. Res.*, 50(7), 5410–5427, 2014.

SMOOTHING-BASED COMPRESSED STATE KALMAN FILTER (sCSKF) FOR REAL-TIME DATA ASSIMILATION: APPLICATIONS IN CO_2 RESERVOIR MONITORING AND CHARACTERIZATION

Judith Yue Li, Amalia Kokkinaki, Eric F. Darve, Peter K. Kitanidis

Stanford University
Y2E2 Bldg, 473 Via Ortega
Stanford, CA, 94306, USA
e-mail: yuel@stanford.edu

ABSTRACT

Reservoir monitoring and forecasting are increasingly relying on a data-driven approach. Advances in monitoring techniques have made it possible to collect monitoring data from multiple sources, which are then assimilated into an uncertain numerical model in order to track a fluid in the subsurface in real-time and analyze the operational risk. This can be achieved with the aid of data processing algorithms like the Kalman filter (Kalman, 1960). However, the applicability of this real-time data assimilation approach is limited by the high computational cost of the traditional algorithm and the nonlinearity of the inverse problem.

We present a new Kalman filter variant that is computationally efficient for solving large-scale real-time data assimilation problems. The computational advantages are achieved by avoiding propagating the large covariance and Jacobian matrices directly, taking advantage of the fact that the information these matrices contain can be compressed efficiently using fast linear algebraic algorithms. The new filter, which we term the smoothing-based compressed state Kalman filter (sCSKF) is adapted from the Compressed State Kalman filter (Kitanidis, 2015, Li et al, 2015) for combined parameter and state estimation, such that it can be used both for characterization and fluid tracking. Improved accuracy in parameter estimation is achieved by adopting a one-step-ahead smoothing, which mitigates the unphysical updates resulting from the strong nonlinearity that often occurs when parameter estimation is desired.

We demonstrate the performance of the sCSKF using synthetic numerical CO_2 injection examples simulated with TOUGH2-ECO2N. In particular, we use measurements such as pressure, saturation and temperature to update the CO_2 distribution with time, and to simultaneously improve the estimate of the heterogeneous permeability field, which is initially assumed to be uniform. We investigate the impact of smoothing and covariance compression by comparing various filtering approaches. Overall, our method shows great potential for monitoring and characterizing the heterogeneity of realistic, large-scale systems with many unknowns, because of its computational efficiency. The developed interface between the new algorithm and TOUGH2 presents an integrated system that can be applied to ongoing projects to improve prior reservoir characterizations, monitor changes in the reservoir state and help better manage CCS projects.

OVERVIEW OF sCSKF

The sCSKF algorithm targets the real-time large-scale state-parameter estimation problem. Similar to the Kalman filter (KF), the current state is estimated recursively from the previous state given the newly obtained measurement. However, KF cannot be directly applied to large-scale reservoir monitoring due to the presence of strong nonlinearity and the formidable size of the problem. What sets the sCSKF apart from the conventional Kalman filter is that it is computationally feasible for large-scale problems due to an efficient covariance compression scheme and matrix-free Jacobian computation. Moreover, it adopts a one-step ahead smoothing to mitigate the nonlinearity introduces by parameter estimation.

One-step ahead smoothing

The conventional Kalman filter adopts a Bayesian recursion that consists of a prediction step followed by a measurement update step, which is often termed the P-path (Desbouvries et al., 2011). The measurement update is a linear correction. When Kalman filter is applied to a nonlinear problem, the linear correction often introduces unphysical updates to the state, an artifact from linearizing a strongly nonlinear objective function. An alternative recursion, namely the S-path, can be derived with a one-step-ahead smoothing followed by a prediction step (Desbouvries et al., 2011). The smoothing step is similar to the measurement update step except that the observation is used to update the previous state instead of the current state. For a linear problem, the two paths give equivalent filtering solution. However, the S-path gives more accurate estimates for nonlinear problems when the uncertain parameter in the dynamic model (such as permeability) causes strong bias in the forecast.

Covariance compression

For large-scale problems the computational cost for updating a large covariance matrix or explicitly computing Jacobian matrices becomes impractical. The information contained in the covariance matrix can be efficiently stored in a N-rank matrix,

$$\hat{\Sigma}_k = UC_kU^T$$

where $\hat{\Sigma}_k \in R^{m\times m}$ is the low-rank approximation of the covariance, $U \in R^{m\times N}$ is a preselected projection basis, and $C_k \in R^{N\times N}$ is the compressed covariance matrix. For most problems a high compression ratio m/N can be achieved, resulting in significant computational savings. Combined with a matrix-free approach the information in the Jacobian matrices can be extracted by only N evaluations of the forward model as opposed to m evaluations used in the traditional approach.

VALIDATION CASE

First, a state-parameter estimation problem based on air traffic control is presented to validate the sCSKF algorithm and to investigate the effect of one-step ahead smoothing. An airplane maneuvers at an unknown constant rate Ω. Radar measurements are acquired every Δt to monitor the location (x, y), velocity $(\dot{x}, \dot{y})$ as well as the turning rate Ω of the airplane. Both the dynamic and the measurement model are nonlinear. Extended Kalman filter (EKF), i.e., the nonlinear version of Kalman filter, and sCSKF with full rank (i.e, N=m) are used to correct the bias in the model prediction due to using an incorrect initial estimate of the turning rate Ω_0. The true turning rate is $3\ \mathrm{deg/s}$ and the variance is $1e-4$, and the total time step is $200s$.

$$RMSE(x) = \frac{1}{N_t}\sum_{i=1}^{N_t}\sqrt{(x-x_{true})^T(x-x_{true})}$$

Comparison with EKF

We compare three different scenarios with frequent observation ($\Delta t = 1$), sparse observation ($\Delta t = 10$) and a case with large error in the initial guess Ω_0 respectively. Table 1 shows the mean square error (RMSE) of the estimated turning rate and the location for each scenario. When measurements are assimilated very frequently (Case 1), sCSKF gives similar estimates compared to EKF. However, sCSKF gives better estimates when there is a large assimilation interval or a large initial variance in the turning rate, in which case a small error in the parameter will translate into a large error in the prediction. One-step-ahead smoothing conditions the parameter using future observation hence gives a better prediction with the improved parameter. The prediction serves as a reference point at which the objective function is linearized. In analogy to the iterative methods, by providing a reference point that is closer to the truth the nonlinearity in the optimization problem can be reduced.

Table 1. Comparison between EKF and sCSKF for air traffic control problem

	EKF	sCSKF
Case 1: Frequent observation ($\boldsymbol{\Delta t = 1}$)		
RMSE (location)	6.73m	6.73m
RMSE (turning rate)	3.19e-04	3.20e-04
Case 2: Sparse observation ($\boldsymbol{\Delta t = 10}$)		
RMSE (location)	10.20m	9.73m
RMSE (turning rate)	1.76e-04	1.60e-4
Case 3: Large variance ($5e-4$) in turning rate $\boldsymbol{\Omega_0}$		
RMSE (location)	15.00m	11.61m
RMSE (turning rate)	1.91e-04	0.74e-04

CO2 MONITORING EXAMPLE

The operation safety of CCS project can be ensured by monitoring potential CO_2 leakage in real-time. With the aid of a physical-based model and a smart data assimilation algorithm, monitoring data can be used to produce images of the reservoir state (e.g., pressure, saturation) and parameters (e.g., permeability) in real-time for reservoir management and risk analysis. Consider a synthetic CO_2 injection experiment featuring a $450m \times 450m$ horizontal reservoir defined on a $45 \times 45 \times 1$ grid shown in Figure 1. The domain has a no-flux boundary on the north and south boundary except at wells, 45 vertical injection wells with a constant CO_2 injection rate of 0.01 kg/s deployed on the left boundary, and 45 vertical extraction wells with a constant bottom hole pressure of 206 bar deployed on the right boundary. The true synthetic case is simulated with a permeability field shown in Figure 1 generated from a Gaussian distribution with a correlation length of 200m.

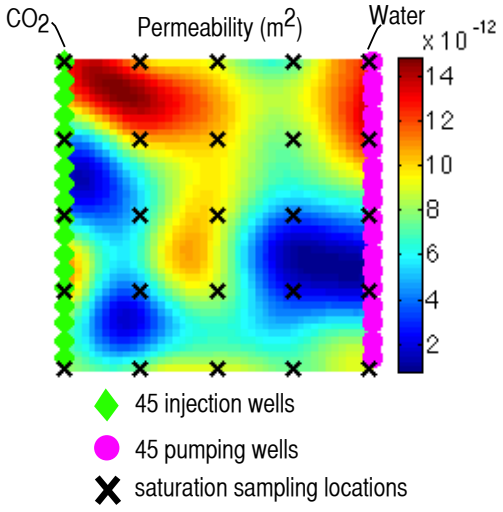

Figure 1. Experiment setting for the CO_2 reservoir monitoring case study.

Real-time state-parameter estimation

The quantities we are interested to estimate are the CO_2 saturation, pressure as well as the permeability every 50 days using pressure, flow rate and saturation measurements. The permeability field is initially assumed to be homogeneous, an assumption that is often made in practice given limited information. This state-parameter problem is characterized by a highly nonlinear dynamic governed by a multi-phase flow process. TOUGH2-MP with module ECO2N is used as the reservoir simulator to generate predictions of saturation and pressure given an initial condition. MATLAB scripts are used to automatically write and read input and output from TOUGH2 for data assimilation purpose. The sCSKF algorithm is implemented in MATLAB®. TOUGH2 text-based input/output is automatically transformed in MATLAB compatible format by scripts that we have developed as part of our FKF-TOUGH software package.

Through state augmentation, sCSKF can be used to solve this mid-size reservoir monitoring problem. The true and estimated saturation, pressure and permeability are shown in Figure 2. Beginning with a homogeneous permeability field, sCSKF manages to recover its spatial pattern accurately after assimilating pressure, flowrate and saturation data every 50 days for 250 days.

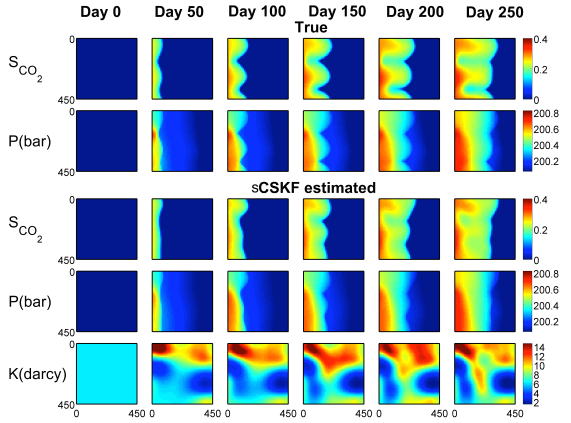

Figure 2. True and sCSKF-estimated CO_2 saturation (S_{co2}), pressure (P) and permeability (K) every 50 days.

Computational cost

The computational cost is significantly reduced by using covariance compression with 100 DCT bases for each state variable, resulting in a compression ratio of around 20 (m/N = 2025/100, where m is the number of unknowns and n is the number of measurements). It is expected that for a field size problem where m~1 million, the compression ratio will be much higher, potentially resulting in much more significant computational savings.

Table 2. Comparison of computational cost between EKF and sEKF for CO_2 monitoring problem

Per time step	EKF	sEKF
TOUGH2 calls	$3m \approx 4075$	$6N = 300$
Measurement update cost	$O(m^2)$	$O(m)$

Optimal rank selection

An important parameter in sCSKF is the rank N, the number of basis used in covariance compression. N provides robust control over the estimation error and the computational cost. When N is small, the computational cost is small while the estimation error is large, producing overly smoothed image (Figure 3). The estimation error decreases as N increases to around 100 in this case, where increasing N further will not improve the filter performance. For smooth problem, i.e., the eigenspectrum of the covariance matrix drops very fast, the rank N can be small, resulting in a large compression ratio and significant computational efficiency.

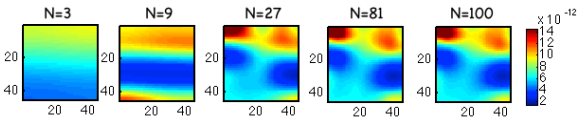

Figure 3. Permeability estimates using sCSKF with increasing rank N.

CONCLUDING REMARK

In this work, we present a Kalman filter variant sCSKF that is computationally efficient for real-time large-scale state-parameter estimation problem. The computational efficiency is achieved through covariance compression and a matrix-free approach that avoids computing Jacobian matrices directly. For smooth problems a large compression ratio can be reached, leading to significant computational savings. One-step-ahead smoothing reduces the nonlinearity of a state-parameter problem by processing information in advance. A better performance is observed for cases where a large assimilation interval is used or a large uncertainty in the parameter, indicating that a small improvement in the parameter estimates can have a huge effect on the forecast. This has significant implication in reservoir monitoring and forecasting, as the model parameter is highly uncertain due to limited information. By processing the information one step ahead, the linearization error in this inverse problem can be greatly reduced.

ACKNOWLEDGMENT

This material is based upon work supported by US Department of Energy, National Energy Technology Laboratory (DOE, NETL) under the award number DE-FE0009260: "An Advanced Joint Inversion System for CO2 Storage Modeling with Large Data Sets for Characterization and Real-Time Monitoring", and also by the "National Science Foundation" - Division of Mathematical Sciences -under the award number 1228275. The author would like to thank Dr. Quanlin Zhou and Noel Keen from the Lawrence Berkeley National Lab for the support on TOUGH2.

REFERENCES

Desbouvries, Francois, Yohan Petetin, and Boujemaa Ait-El-Fquih, Direct, prediction- and smoothing-based Kalman and particle filter algorithms, *Signal Processing,* 91 (8): 2064–77, 2011.

Li, J. Y., A. Kokkinaki, H. Ghorbanidehno, E. F. Darve, and P. K. Kitanidis, The nonlinear compressed state Kalman filter for efficient large-scale reserovir monitoring, *Water Resourc. Res.,* Under revision, 2015.

Kalman, R., A new approach to linear filtering and prediction problems, *Journal of Basic Engineering*, 82(1), 35-45, 1960.

Kitanidis, P. K., Compressed state Kalman filter for large systems, *Advances in Water Resources*, 76, 120-126, 2015.

BAYESIAN PARAMETER INVERSION WITH IMPLICIT SAMPLING FOR A VADOSE ZONE HYDROLOGICAL MODEL

Yaning Liu, George Shu Heng Pau, Stefan Finsterle

Lawrence Berkeley National Laboratory
1 Cyclotron Road
Berkeley, California, 94720, USA
e-mail: yaningliu@lbl.gov

ABSTRACT

We propose using an efficient importance sampling technique, referred to as implicit sampling (IS), for inverse modeling of a synthetic ponded infiltration experiment simulated with TOUGH2. IS generates samples in the high-probability region of the posterior distribution and ameliorates sample impoverishment. We show that IS provides an accurate Bayesian description of the parameterized permeability field at the pilot points. To further improve the efficiency of the inversion process, we discuss the implementation of a reduced order model (ROM) based on generalized polynomial chaos expansion (gPCE) for the forward model. The coefficients of the gPCE can be obtained using the sparse Bayesian learning technique to mitigate the "curse of dimensionality" of the PCE terms. However, our initial results indicate that the TOUGH2 model cannot be readily replaced by a ROM due to poor approximation properties of gPCE. In addition, direct use of implicit particles with a TOUGH2 model is in fact more computationally efficient for this 14-parameter problem after taking into account the computational cost of obtaining the training dataset needed by ROM due to the small number of particles needed to characterize the posterior distributions of the parameters

INTRODUCTION

Hydrological models are crucial to the understanding and description of water cycles. Hydrological model parameters, such as site-specific material properties and process-related parameters, as well as boundary conditions and site geometry play a major part in the model's capability of accurately representing the hydrological variables. The parameters can be large scale, highly uncertain and difficult to measure. Parameter inversion involves inferring the model parameter values based on sparse observations of some observables. A powerful tool to achieve this is the Bayesian probability theory, which relates the parameter posterior distribution conditioned on the observations to the product of the prior distribution and likelihood function. Samples are then generated from the resulting posterior density; they serve as a discrete representation of the posterior density. To this end, one resorts to Markov chain Monte Carlo (MCMC) methods that sample from complex probability densities by an acceptance-rejection approach. Evaluating the acceptance-rejection criteria in MCMC requires running the forward model, which can be extremely inefficient since the fraction of the rejected samples can be very large. In addition, the significant (high-probability) region of the posterior distribution can be small, so that few samples generated from MCMC are useful.

Particle filters are sequential Monte Carlo methods used in data assimilation to update the discrete representation (particles/samples with associated weights) of posteriors of the state variables serially as new observable data are available. The main drawback of particle filters is the weight collapse, where all particles except a few have negligible weights, causing the need to use many particles for a meaningful approximation of the posterior. As a remedy, the implicit particle filter (Morzfeld et al., 2012) finds and samples in the high probability region of the posterior by connecting the target particles with a reference distribution through a mapping of one's choice. The quality of the particles can therefore be greatly enhanced, as the proportion of the particles with non-negligible weights increases, and the overall number of particles needed is reduced. We implement the ideas of implicit particle filter in inverse modeling and

adopt the term "implicit sampling" (IS) henceforth.

Implicit sampling involves minimizing the negative logarithm of the posterior distribution, which necessitates repetitive calling of the forward model. In addition, the mapping from the reference samples to the target particles in IS may involve solving a nonlinear equation for each given sample, depending on the type of the mapping chosen, and thus constitutes another source that requires a large number of forward simulations. In view of this, we propose using a generalized polynomial chaos expansion (gPCE) (Xiu and Karniadakis, 2002) based reduced-order model (ROM) that serves as a potential surrogate for the forward model. The ROM is constructed with an initial set of forward simulations (training samples), and subsequently substitutes the forward model.

The focus of the construction of gPCE is to determine the coefficients of the expansion terms once the type of the polynomial basis and expansion order are selected. There is an abundant literature related to the construction of gPCE; however, the proposed methods suffer from some common difficulties. There is no *a priori* knowledge of the polynomial expansion order. Using a smaller order may not accurately represent the response surface, while using a larger order than necessary leads to more expansion terms. The increase in expansion terms is aggravated further by the "curse of dimensionality". The number of expansion terms can be prohibitively large, if the dimensionality of the stochastic space is large, even for a low expansion order. The consequence of the surge of expansion terms is two-fold. On one hand, the number of forward simulations to estimate the gPCE coefficients increases accordingly. On the other hand, the errors associated with the overall gPCE increases, as the coefficient of each expansion term is associated with an estimation error.

However, the gPCE coefficients can be sparse, i.e., they only contain a small portion of non-zeros. The sparsity is due to the following reasons: higher-order parameter interactions may not exist (Rabitz et al., 1999); components of the model are smooth and have higher-order smooth derivatives, leading to a fast decrease in the magnitude of the coefficients related to the polynomial bases involving the parameters of the components; and the components of the model are superpositions of only a sparse subset of all the polynomial bases up to a given order. In view of this, we follow Sargsyan et al. (2014) to treat the gPCE as a sparse Bayesian learning (SBL) problem (Tipping and Faul, 2003; Babacan et al., 2010), where the model outputs are characterized by a hierarchical form of Gaussian likelihood and prior. The sparsity is obtained by detecting and including only the non-zero gPCE coefficients one at a time by a greedy algorithm that iteratively selects the most contributing coefficients until a prescribed stopping criterion is reached. The initial set of coefficients is set to be empty, and an efficient algorithm to update the coefficient set, either by including a new one, updating the value of an existing one, or deleting an existing one, is described in Tipping and Faul (2003). It has been empirically demonstrated by Sargsyan et al. (2014) that good estimates of the gPCE coefficients can be achieved if the number of training samples (observations) is about five times that of non-zero coefficients. Therefore, both the number of forward model simulations to construct the ROM and the estimation errors associated with those zero terms can be greatly reduced, if the model is inherently sparse.

We demonstrate the efficiency of implicit sampling for a synthetic ponded infiltration experiment simulated with TOUGH2, as well as the use of ROM for potential greater efficiency. The goal of the inversion is to determine the permeability distribution of the vadose zone based on water content measurements.

In the following section, we will discuss the methodology used for the present work, including the ideas of implicit sampling, generalized polynomial chaos expansion, and sparse Bayesian learning. The main results and discussion are presented afterwards. We conclude the paper with possible improvements for future work.

METHODOLOGY

Implicit Sampling (IS)

Assume the k-dimensional observations $\boldsymbol{D}$ and d-dimensional input parameters $\boldsymbol{\theta}$ are related by the forward model $\boldsymbol{f}$ and random noises $\boldsymbol{\varepsilon}$:

$$\boldsymbol{D} = \boldsymbol{f}(\boldsymbol{\theta}) + \boldsymbol{\varepsilon}\,.$$

By Bayes' rule, the posterior distribution $p(\boldsymbol{\theta}|\boldsymbol{D})$ is proportional to the product of the prior distribution $p(\boldsymbol{\theta})$ and the likelihood $p(\boldsymbol{D}|\boldsymbol{\theta})$

$$p(\boldsymbol{\theta} \mid \boldsymbol{D}) \propto p(\boldsymbol{\theta}) p(\boldsymbol{D} \mid \boldsymbol{\theta})$$

The goal is to represent the posterior distribution $p(\boldsymbol{\theta}|\boldsymbol{D})$, which can be done in the important sampling framework by generating N weighted samples (particles), each with weight

$$w_i = \frac{p(\boldsymbol{\theta}_i) p(\boldsymbol{D} \mid \boldsymbol{\theta}_i)}{\pi(\boldsymbol{\theta}_i)}, i = 1,2,...,N ,$$

where $\pi(\theta)$ is the importance function, usually chosen as one that is convenient to sample from. Unlike MCMC, the samples in importance sampling are independent and thus can be embarrassingly parallelized. Nonetheless, the importance function must be chosen carefully, or else the sampling can be inefficient. In IS, an importance function is constructed so that it is large where the posterior distribution is large. This is realized by computing the maximizer of $p(\boldsymbol{\theta}|\boldsymbol{D})$, i.e., the maximum *a posteriori* (MAP). If the prior and likelihood are exponential functions (as they often are in applications), the MAP can be found by minimizing the function

$$F(\boldsymbol{\theta}) = -\log(p(\boldsymbol{\theta}) p(\boldsymbol{D} \mid \boldsymbol{\theta})) . \quad (1)$$

Once the minimization problem is solved, one generates samples in the neighborhood of the minimizer $\boldsymbol{\mu}$=argmin F as follows. A sequence of reference variables $\boldsymbol{\xi}_i$, i=1,2,…,N are first sampled from a reference probability density function (pdf) $g(\boldsymbol{\xi})$, and subsequently each target samples $\boldsymbol{\theta}_i$ are obtained by solving the equation

$$F(\boldsymbol{\theta}_i) - \phi = G(\boldsymbol{\xi}_i) - \gamma \quad (2)$$

where ϕ=min$_{\theta}F$, $G(\boldsymbol{\xi})$=-log($g(\boldsymbol{\xi})$) and γ=min$_{\xi}G$. The sample weights are

$$w_i \propto J(\boldsymbol{\theta}_i)$$

where J is the Jacobian of the bijective map $\boldsymbol{\xi} \to \boldsymbol{\theta}$. Note that the sequence of samples θ_i obtained by solving Eqn. (2) are in the neighborhood of the MAP $\boldsymbol{\mu}$, since the right-hand side of (2) is small if $\boldsymbol{\xi}_i$'s are sampled close to the minimizer of G. Thus, Eqn. (2) maps a likely $\boldsymbol{\xi}$ to a likely $\boldsymbol{\theta}$.

One strategy for solving (2), called "implicit sampling with linear maps", is inspired by the approximation of F by its second-order Taylor expansion around the MAP $\boldsymbol{\mu}$

$$F_0(\boldsymbol{\theta}) = \phi + \frac{1}{2}(\boldsymbol{\theta} - \boldsymbol{\mu})^T H(\boldsymbol{\theta} - \boldsymbol{\mu}) \quad (3)$$

where H is the Hessian matrix at $\boldsymbol{\mu}$. For an uncorrelated standard Gaussian reference variable, Eqn. (2) becomes

$$F(\boldsymbol{\theta}_i) - \phi = \frac{1}{2} \boldsymbol{\xi}_i^T \boldsymbol{\xi}_i \quad (4)$$

Equating (3) and (4), the mapping becomes

$$\boldsymbol{\theta}_i = \boldsymbol{\mu} + L^{-T} \boldsymbol{\xi}_i \quad (5)$$

Accounting for the approximation error of F, the weights are computed as

$$w_i \propto \exp(F_0(\theta) - F(\theta)) . \quad (6)$$

Generalized Polynomial Chaos Expansion (gPCE)

Polynomial chaos (PC) was originally developed to expand functions in terms of Hermite polynomial bases. Xiu and Karniadakis (2002) generalized the bases to the Askey family of orthogonal polynomials. The gPCE for a second-order random process $f(\boldsymbol{\theta})$ takes the form

$$f(\boldsymbol{\theta}) = \sum_{\boldsymbol{\alpha} \in \mathbb{N}^d} f_{\boldsymbol{\alpha}} \Phi_{\boldsymbol{\alpha}}(\boldsymbol{\theta}) \quad (7)$$

where $\boldsymbol{\theta}$ holds d-dimensional random parameters as before, $\boldsymbol{\alpha}$ holds d-dimensional integer index tuples $\boldsymbol{\alpha}$=(α_1, α_2, …, α_d), Φ_α are the multi-dimensional orthogonal polynomials whose individual one-dimensional components are of orders $\boldsymbol{\alpha}$, i.e., $\Phi_{\boldsymbol{\alpha}} = \phi_{\alpha_1} \phi_{\alpha_2} ... \phi_{\alpha_d}$, assuming the type of the polynomials ϕ for each dimension is the same, and $f_{\boldsymbol{\alpha}}$ are the PC coefficients corresponding to index $\boldsymbol{\alpha}$.

In the Askey family, for example, Legendre polynomials are used as the bases for uniform distributions, Hermite polynomials for Gaussian distributions, and Laguerre polynomials for Gamma distributions, to achieve the optimal convergence. In practice, the gPCE (7) is truncated to a finite number of terms, e.g., by specifying the total degree of the expansion, P_{pc}, such that the dimensionality of $\boldsymbol{\alpha}$, $|\boldsymbol{\alpha}|$=α_1+…+ α_d, is no larger than P_{pc}. As a result, the total number of expansion terms N_{pc} is

$$N_{PC} = \frac{(d + P_{PC})!}{d! P_{PC}!} \quad (8)$$

The gPCE coefficients f_α can be determined, in theory, by

$$f_{\boldsymbol{\alpha}} = \frac{\mathbb{E}\left[f(\boldsymbol{\theta})\Phi_{\boldsymbol{\alpha}}(\boldsymbol{\theta}) \right]}{\mathbb{E}\left[\Phi_{\boldsymbol{\alpha}}(\boldsymbol{\theta})\Phi_{\boldsymbol{\alpha}}(\boldsymbol{\theta}) \right]},$$

due to the orthogonality of the bases. We discuss utilizing the sparse Bayesian learning technique to determine the coefficients by taking the sparsity into account.

Sparse Bayesian Learning (SBL)

In the context of sparse Bayesian learning, one solves the regression problem for a quantity of interest

$$\hat{\boldsymbol{y}} = \boldsymbol{y} + \boldsymbol{\varepsilon} = \Phi \boldsymbol{w} + \boldsymbol{\varepsilon}, \tag{9}$$

where $\hat{\boldsymbol{y}} = (\hat{y}_1, \hat{y}_2, ..., \hat{y}_N)$ are N observations corresponding to N input parameters $\left\{ \boldsymbol{x}_i \right\}_{i=1}^{N}$, $\boldsymbol{\varepsilon}$ is the error vector, $\Phi = \left[\phi_1, \phi_2, ..., \phi_M \right]$ is the $N \times M$ design matrix, whose columns comprise the full set of M basis vectors, and $\boldsymbol{w}$ is the weight vector, which is sparsely non-zero. The goal is to find the values for $\boldsymbol{w}$.

The construction of gPCE can be easily cast as a SBL problem, where $\hat{\boldsymbol{y}}$ and $\boldsymbol{\varepsilon}$ are still the observation and error vectors, each row of Φ contains the N_{PC} multi-dimensional polynomial bases evaluated at the input parameters, and $\boldsymbol{w}$ is the vector of gPCE coefficients.

The errors $\boldsymbol{\varepsilon}$, in SBL, are conventionally modeled as independent Gaussian variables with zero means and variance σ^2. Hence, the Gaussian likelihood for the target $\hat{\boldsymbol{y}}$ is

$$p(\hat{\boldsymbol{y}} \mid \boldsymbol{w}, \sigma^2) = (2\pi)^{-N/2} \sigma^{-N} \exp\left(-\frac{\left\| \hat{\boldsymbol{y}} - \boldsymbol{y} \right\|^2}{2\sigma^2} \right).$$

The weights w is hierarchically modeled as a Gaussian prior with zero means and variances $\boldsymbol{\gamma} = (\gamma_1, \gamma_2, \ldots, \gamma_M)$:

$$p(\boldsymbol{w} \mid \boldsymbol{\gamma}) = (2\pi)^{-M/2} \prod_{m=1}^{M} \gamma_m \exp\left(-\frac{w_m^2}{2\gamma_m} \right).$$

Combining the likelihood and prior by Bayes' rule, the posterior distribution of $\boldsymbol{w}$ given $\boldsymbol{\gamma}$

$$p(\boldsymbol{w} \mid \hat{\boldsymbol{y}}, \boldsymbol{\alpha}, \sigma^2) = \frac{p(\hat{\boldsymbol{y}} \mid \boldsymbol{w}, \sigma^2) p(\boldsymbol{w} \mid \boldsymbol{\alpha})}{p(\hat{\boldsymbol{y}} \mid \boldsymbol{\alpha}, \sigma^2)}$$

can be shown Gaussian, i.e, $\boldsymbol{w} \sim \mathcal{N}(\boldsymbol{\mu}, \Sigma)$ where

$$\mu = \sigma^{-2} \Sigma \Phi^T \hat{y} \tag{10}$$

and

$$\Sigma = \left(\mathrm{diag}(\gamma_1^{-1}, ..., \gamma_M^{-1}) + \sigma^{-2} \Phi^T \Phi \right)^{-1} \tag{11}$$

The parameters $\gamma_1, \ldots, \gamma_M$ are found by maximizing the marginal likelihood

$$\begin{aligned} \mathcal{L}(\boldsymbol{\gamma}) &= \log p(\hat{\boldsymbol{y}} \mid \boldsymbol{\gamma}, \sigma^2) \\ &= -\frac{1}{2}\left(N \log 2\pi + \log |C| + \hat{\boldsymbol{y}} C^{-1} \hat{\boldsymbol{y}} \right) \end{aligned} \tag{12}$$

where $C = \sigma^2 I + \Phi \mathrm{diag}(\gamma_1, ..., \gamma_M) \Phi^T$.

The vector $\boldsymbol{\gamma}$ controls the sparsity of $\boldsymbol{w}$. If γ_i is zero, then the i-th weight w_i should be zero. Tipping and Faul (2003) provided an efficient algorithm to locate a single w_i that causes the largest increase in $\mathcal{L}(\boldsymbol{\alpha})$ in each iteration, take the corresponding action (add, update or delete), and derive a subset of $\boldsymbol{w}$ containing only the non-zero elements, until a prescribed stopping criterion is satisfied.

Translating the SBL theory to the computation of the gPCE coefficients, we can therefore obtain a ROM based on gPCE, which is a Gaussian process with mean

$$m(\boldsymbol{\theta}) = \sum_{|\boldsymbol{\alpha}| \le P_{PC}} \mu_{\boldsymbol{\alpha}} \Phi_{\boldsymbol{\alpha}}$$

and covariance

$$K(\boldsymbol{\theta}, \boldsymbol{\theta}') = \sum_{|\boldsymbol{\alpha}| \le P_{PC}, |\boldsymbol{\alpha}'| \le P_{PC}} \Phi_{\boldsymbol{\alpha}}(\boldsymbol{\theta}) \Sigma_{\boldsymbol{\alpha}, \boldsymbol{\alpha}'} \Phi_{\boldsymbol{\alpha}'}(\boldsymbol{\theta}'),$$

which can be used to estimate the error associated with the ROM.

RESULTS AND DISCUSSION

Problem Descriptions

The hydrological problem that we use to demonstrate our approach is based on a synthetic field experiment described in Finsterle and Kowalsky (2008). A pond releases water into a heterogeneous vadose zone with a water table at a depth of 3 m. The system is initially at a gravity-capillary equilibrium state. An infiltration rate is prescribed such that the water level in the pond is maintained at 2 cm for one day. Six monitoring boreholes are equipped with neutron probes to measure water content every two hours for

two days. In addition, the amount of water flowing out of the pond is measured at the same frequency. We model the process using Richards' equation as implemented in the integral finite-difference simulator TOUGH2 (Pruess et al., 1999). The discretized model is of size 4 m × 3 m with a uniform grid size of 0.05 m.

The goal of the field experiment is to determine the distribution of the permeability using the pilot-point method. Fourteen pilot points, for which the locations are shown in Figure **1**, serve as conditioning points for performing geostatistical simulations. We use a spherical semivariogram model with fixed parameters; the permeability field is determined by kriging. TOUGH2 expresses the permeability at a particular grid cell as

$$\kappa = \kappa_{ref} \times 10^{\kappa_m}$$

where κ_{ref} is a reference permeability value (10^{-13}), and κ_m is the permeability modifier on which the kriging is performed. Thus, the hydrologic inverse problem consists of determining the κ_m at the 14 pilot points.

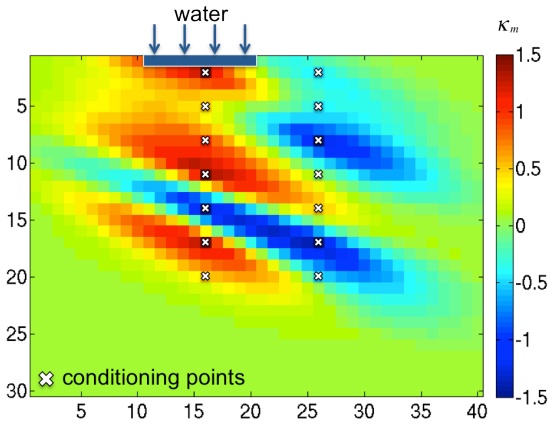

Figure 1. The true permeability field. The pilot points are marked with crosses.

To generate the measurement data used in this synthetic field experiment and avoid committing an "inverse crime", we do a forward run with $\boldsymbol{\theta}_{true}$ given in Table **1**. The true permeability field is shown in Figure **1**. In addition, we added a zero-mean Gaussian noise with a standard deviation of 0.005 for the amount of water flowing out of the pond, and 0.01 for the water content measurements. We prescribe a Gaussian prior with alternating 0.1 and -0.1 means, and a standard deviation of 1.0 for all parameters (Figure **2**).

The saturation profile associated with the true permeability values after two days is shown in Figure **3**.

Table 1. True permeability modifiers and the prior distributions at the 14 pilot points.

Pilot point #	true value	prior mean	prior std
1	1.5	0.1	1.0
2	0.5	-0.1	1.0
3	1.0	0.1	1.0
4	1.5	-0.1	1.0
5	-1.5	0.1	1.0
6	1.5	-0.1	1.0
7	0.5	0.1	1.0
8	-0.5	-0.1	1.0
9	-0.5	0.1	1.0
10	-1.5	-0.1	1.0
11	-0.001	0.1	1.0
12	0.5	-0.1	1.0
13	-1.5	0.1	1.0
14	-0.5	-0.1	1.0

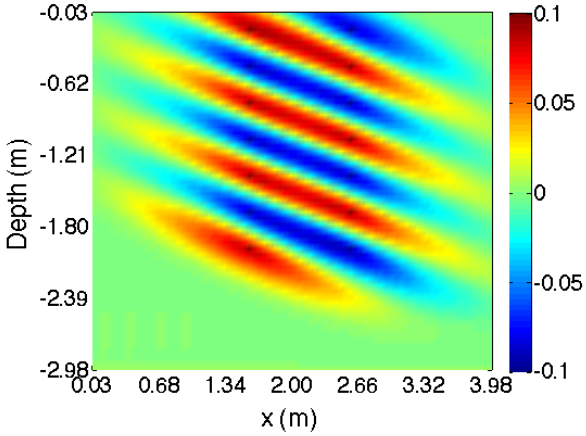

Figure 2. Permeability field corresponding to the mean of the prior distribution.

Reduced-order Model

We first determine whether we can accurately approximate the TOUGH2 model by gPCE ROMs (one for each observation). The ROMs are trained using 1200 training samples generated with Latin hypercube sampling in the parameter space $[-3, 3]^{14}$. The gPCE is expanded to the third order for each observation, leading to a total of 680 gPCE terms. Legendre polynomials are a natural choice for the bases, since the parameter space is finite. We validate

the ROMs for another set of randomly generated samples of size 400.

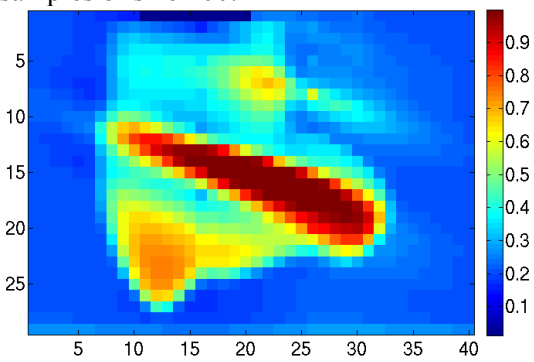

Figure 3. *Saturation profile at the end of day 2 for* $\kappa=\kappa_{true}$.

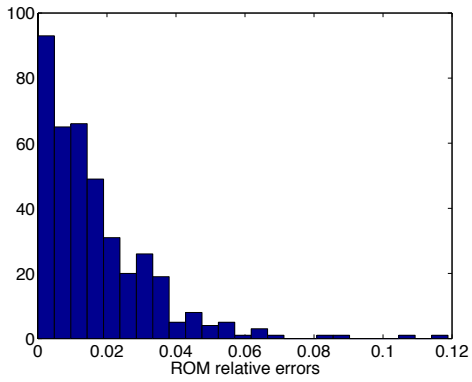

(a)

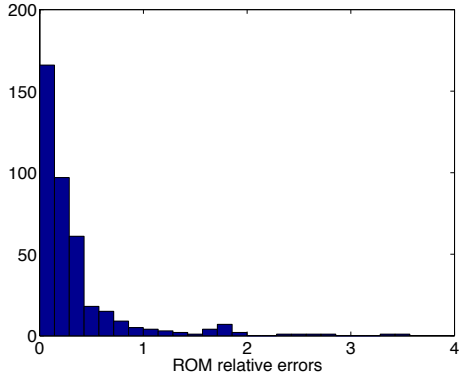

(b)

Figure 4. The histograms of the relative ROM errors compared with TOUGH2 simulations for (a) the 22nd observation for which the ROM has the smallest mean relative error (1.8%) and (b) the 42nd observation which has the largest mean relative ROM error (33.8%).

The 400 ROM predictions for each observation are compared against the corresponding TOUGH2-simulated 'true' values. The mean relative errors of the ROMs range from 1.8% to 33.8%. Figure **4**a shows the histogram of the 400 relative ROM errors for the observation with the smallest mean relative error (1.8%), and Figure **4**b shows that for the observation that is most poorly predicted by the ROM (33.8% mean error). The number of nonzero gPCE coefficients varies between 33 and 128 (out of a possible 680), which suggests that we can potentially train the ROM using ~650 samples, according to the rule of thumb given in Sargsyan et al. (2014).

The large errors in gPCE ROMs indicate that we cannot use gPCE ROMs as a surrogate for TOUGH2 model in the inverse modeling process. The poor performance is likely due to (1) nonsmooth properties of saturation, both in the temporal and spatial dimensions; and (2) priors that are too wide. We conclude that a naïve approach where we replace the TOUGH2 model by a ROM is unlikely to yield satisfactory results. Subsequent application of implicit sampling will use the TOUGH2 model directly.

Implicit Sampling with TOUGH2

Implicit sampling is performed for the synthetic field experiment using the full-order forward TOUGH2 model. The optimization problem of Eqn. (1) is solved by the Levenberg-Marquardt (LevMar) algorithm to obtain the MAP (

Table **2**). The linear map (5) is used to generate 200 particles from independent standard Gaussian variables. The LevMar optimization costs around 400 forward model simulations, and each particle costs one, resulting in a total of ~600 forward model simulations. However, the training for a ROM would be at least the same expensive, which constitutes another reason for not using ROMs for this application. To measure the degeneracy of the particles, we estimate the effective sample size by

$$\hat{N}_{eff} = \frac{1}{\sum_{i=1}^{N_s} (w_i)^2}$$

where N_s is the total number of particles. The larger the estimated effective sample size is, the less severely the sample quality degenerates. In this example, $\hat{N}_{eff}$=24. As a comparison, using sequential importance sampling (i.e., taking the prior distribution as the importance function π) only gives one sample whose weight is nonzero ($\hat{N}_{eff}$=1), which provides little help to characterize the posterior distribution.

Table 2. Maximum a posteriori and posterior mean for the permeability modifiers at pilot points, as well as their standard deviations.

Pilot point #	MAP	Posterior mean
1	1.48±0.02	1.47±0.02
2	0.52±0.01	0.522±0.007
3	0.997±0.007	0.997±0.007
4	1.488±0.006	1.489±0.006
5	-1.496±0.003	-1.495±0.004
6	1.504±0.009	1.503±0.008
7	0.482±0.009	0.484±0.008
8	-0.48±0.02	-0.47±0.02
9	-0.51±0.02	-0.50±0.02
10	-1.504±0.007	-1.502±0.009
11	-0.014±0.001	-0.015±0.001
12	0.518±0.004	0.517±0.006
13	-1.512±0.004	-1.512±0.004
14	-0.52±0.01	-0.52±0.01

The statistical moments of the posterior distribution can be approximated with the particles. The posterior mean $\boldsymbol{m}_{\text{post}}$ (shown in

Table **2**) is the weighted sample values:

$$\boldsymbol{m}_{post} = \sum_{i=1}^{N_s} w_i \boldsymbol{\theta}_i .$$

Higher-order moments can be computed similarly. The permeability field corresponding to the posterior mean of the pilot points is shown in Figure **5**.

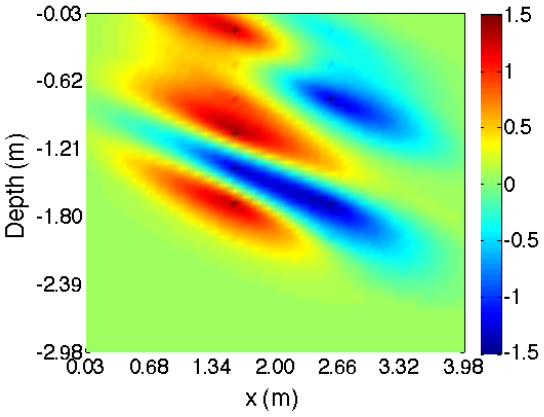

Figure 5. Permeability modifier field corresponding to the posterior mean.

The posterior means are all close to the MAP in this case. MAP doesn't provide a probabilistic characterization of the estimated permeability values at pilot points. As a remedy, one often measures the uncertainty of the MAP approximation using the inverse of the Hessian of the negative logarithm of the posterior, which is called linearization about the MAP point (LMAP). We compare in Figure 6 the Gaussian densities of LMAP and the posterior densities estimated from the implicit particles for four of the 14 pilot points. A resampling procedure (Arulampalam et al., 2002), aimed to eliminate particles with small weights and concentrate on particles with large weights, is performed before plotting the histograms. Obvious distinctions can be seen for the two types of densities.

CONCLUSIONS

In this paper, we performed implicit sampling for a synthetic field experiment to estimate the permeability values at pilot points based on observations of water content, and to further estimate the entire permeability field using geostatistical interpolation. The samples obtained from implicit sampling have better quality than those from other commonly used particle filtering methods, e.g., the sequential importance sampling, where sample impoverishment prevents effective and accurate descriptions of the posterior distributions. We discussed generalized polynomial chaos expansion, driven by a sparse Bayesian learning algorithm, as the reduced order model to approximate the TOUGH2 forward model. We concluded that our current implementation did not allow the resulting ROM to have sufficient accuracy to function as a surrogate for the TOUGH2 model.

ACKNOWLEDGMENT

This research was supported by the Director, Office of Science, of the U.S. Department of Energy under Contract No. DE-AC02-05CH11231.

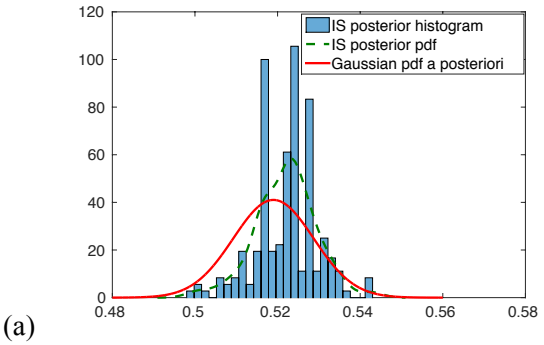

(a)

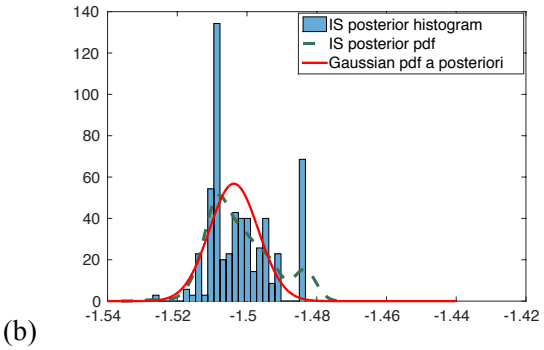

(b)

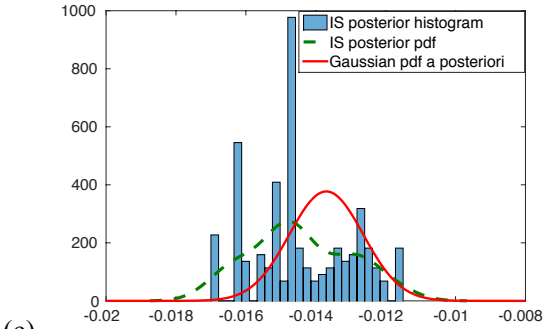

(c)

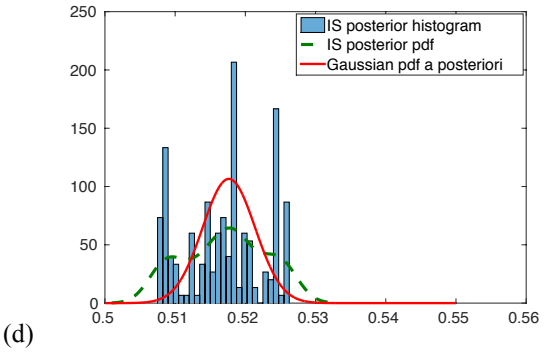

(d)

Figure 6. Comparison of the Gaussian density of LMAP (solid red) and the posterior density (dash green) estimated from the histogram (bins) of the implicit particles for (a) pilot point (pp) #2 (b) pp#10 (c) pp#11 and (d) pp#12. Distinctions can be found between the two densities.

REFERENCES

Arulampalam, M. S., S. Maskell, N. Gordon and T. Clapp (2002). A tutorial on particle filters for online nonlinear/non-Gaussian Bayesian tracking. *IEEE Transactions on Signal Processing* **50**(2): 174-188.

Babacan, S. D., R. Molina and A. K. Katsaggelos (2010). Bayesian Compressive Sensing Using Laplace Priors. *IEEE Transactions on Image Processing* **19**(1): 53-63.

Finsterle, S. and M. B. Kowalsky (2008). Joint hydrological-geophysical inversion for soil structure identification. *Vadose Zone Journal* **7**(1): 287-293.

Morzfeld, M., X. M. Tu, E. Atkins and A. J. Chorin (2012). A random map implementation of implicit filters. *Journal of Computational Physics* **231**(4): 2049-2066.

Pruess, K., G. Moridis and C. Oldenburg (1999). TOUGH2 user's guide, version 2.0, Rep. LBNL-43134, Lawrence Berkeley National Laboratory.

Rabitz, H., O. F. Alis, J. Shorter and K. Shim (1999). Efficient input-output model representations. *Computer Physics Communications* **117**(1-2): 11-20.

Sargsyan, K., C. Safta, H. N. Najm, B. J. Debusschere, D. Ricciuto and P. Thornton (2014). Dimensionality reduction for complex models via Bayesian compressive sensing. *International Journal for Uncertainty Quantification* **4**: 63-93.

Tipping, M. E. and A. C. Faul (2003). *Fast marginal likelihood maximisation for sparse Bayesian models*. The Ninth International Workshop on Artificial Intelligence and Statistics, Key West, FL.

Xiu, D. B. and G. E. Karniadakis (2002). The Wiener-Askey polynomial chaos for stochastic differential equations. *Siam Journal on Scientific Computing* **24**(2): 619-644.

GLOBAL SENSITIVITY AND DATA-WORTH ANALYSES IN iTOUGH2

Haruko Wainwright and Stefan Finsterle

Lawrence Berkeley National Laboratory
Earth Sciences Division
Berkeley, CA, 94720, USA
e-mail: hmwainwright@lbl.gov

ABSTRACT

We have implemented a global sensitivity analysis and a data-worth analysis module into iTOUGH2. In contrast to the derivative-based, local sensitivity method, global sensitivity analysis methods – such as the Morris and Sobol' methods – explore the parameter space so that they provide robust sensitivity measures in the presence of nonlinearity and interactions among parameters. The Morris one-at-a-time method is a computationally frugal method that changes one parameter at a time from randomly generated reference parameter sets, and computes the difference in outputs. The Sobol' method provides the variance-based sensitivity indices that quantify the relative contribution of each parameter to the uncertainty in outputs. A data-worth analysis complements a sensitivity analysis in the sense that it specifically identifies the contribution each (potential or existing) data point makes to the solution of an inverse problem and a subsequent predictive simulation. The data-worth analysis method described here makes use of the Jacobian matrix evaluated at a reference parameter or best-estimate parameter set after an inversion. In this study, we will demonstrate the effective use of sensitivity and data-worth analyses through two examples.

INTRODUCTION

iTOUGH2 (Finsterle, 2004) has been developed as an inverse modeling and parameter estimation (PE) tool for various modules of the non-isothermal multiphase flow and transport simulator TOUGH2 (e.g., Pruess et al., 2012). As analysis capabilities have been added, iTOUGH2 has become an integrated framework for hydrogeological modeling under uncertainty – from test design to site characterization to prediction – including parameter estimation (PE), uncertainty analysis (UA), and sensitivity analysis (SA). Moreover, all iTOUGH2 analysis tools can be applied to any text-based simulator through the use of the PEST interface (Finsterle and Zhang, 2011).

In general, a sensitivity analysis examines the relation between a parameter that is an input to the numerical model, and an observable variable that is an output of the numerical model. The input parameter can be a parameter to be estimated by inverse modeling, an uncertain parameter used in a predictive model, or an operational or design variable. Correspondingly, the output variable can be the observation at a calibration point or the value of an objective function, a predictive variable, or a cost function or other performance measure. It is therefore essential to clearly identify and report the objective of any sensitivity analysis for its results to be interpreted correctly, specifically when parameters are ranked according to their importance, or data points are valued according to their worth, where worth is a measure of how much the estimation or prediction uncertainty can be reduced by collecting a given data point or data set.

Depending on the modeling goals, sensitivity analyses are used to (1) identify which (uncertain) parameters have the greatest effect on model predictions and prediction uncertainties, and consequently (2) determine which properties need to be estimated with high accuracy. This allows one to (3) establish research priorities, and to (4) rank, screen, and thus reduce the number of parameters to be varied or estimated, lowering the computational burden of the subsequent parameter estimation and uncertainty analyses. Complementary to the measures of parameter influence, sensitivity indices may be used to (5) identify which observations are likely to contain useful

information about the parameters to be estimated (generally referred to as a value-of-information or data-worth analysis) (6) evaluate an observation's potential to reduce the uncertainty of the parameters in inverse modeling, or (7) evaluate an observation's potential to reduce prediction uncertainty through a more precise estimation of influential parameters.

In contrast to the derivative-based, local sensitivity method, global sensitivity analysis (GSA) methods, such as the Morris and Sobol' methods (Morris, 1991; Sobol', 2001; Saltelli et al., 2008), explore the parameter space so that they provide robust sensitivity measures in the presence of nonlinearity and interactions among parameters. The Morris one-at-a-time (OAT) method is a computationally frugal method that changes one parameter at a time from randomly generated reference parameter sets, and computes the difference in outputs. The Sobol' method provides the variance-based sensitivity indices that quantify the relative contribution of each parameter to the uncertainty in outputs.

A data-worth analysis complements a sensitivity analysis in the sense that it specifically identifies the contribution each (potential or existing) data point makes to the solution of an inverse problem and a subsequent predictive simulation. The basic idea behind the proposed approach is to examine how the addition of potential data (or removal of existing data) reduces (or increases) the uncertainty in select predictions made by a model that is to be calibrated against these data. Although this study uses prediction uncertainty as the ultimate criterion for evaluating data, the analysis could be pushed further to the level where monetary values are assigned to each data point or data set within a risk-cost-benefit decision framework.

METHODS

In this section, we introduce the three sensitivity methods and data-worth analysis implemented in iTOUGH2. Although more details of GSA are documented in Morris (1991), Sobol' (2001), Saltelli et al. (2008) and Wainwright et al. (2014), we include a short description of these methods for completeness.

We denote a set of parameters by $\mathbf{p} = [p_1, p_2, \ldots, p_n]$ and a set of model outputs $\mathbf{z} = [z_1, z_2, \ldots, z_m]$, which are a function of $\mathbf{p}$, i.e., $\mathbf{z} = f(\mathbf{p})$, where n is the number of parameters, m is the number of output variables of interest, and f represents any hydrological or other type of forward model.

Local Sensitivity Analysis

The local sensitivity coefficient is defined as a partial derivative, i.e., the change of an output variable caused by a unit change in each parameter from the reference value.

$$S_{ij} = \left.\frac{\partial z_i}{\partial p_j}\right|_{\mathbf{p}^*} \tag{1}$$

While there are several methods to calculate sensitivity coefficients, iTOUGH2 evaluates the derivative by changing each parameter i by a small increment δp_i from its reference value p_i^* and computes the difference of the output. If a first-order finite-difference method is used, the total number of forward simulations required to calculate n column vectors of length m, each holding the sensitivity coefficients of all outputs with respect to a parameter, is $(n+1)$, i.e., the reference-case simulation plus the n simulations. If centered finite differences are used, the number of simulations increases to $(2n+1)$.

Because the units of the partial derivatives are the units of the model output over the units of the parameter, they cannot be readily compared to each other if we are concerned with the sensitivity of different model outputs with respect to parameters of different types. We therefore introduce a scaled, dimensionless sensitivity index, which is defined as

$$\bar{S}_{ij} = S_{ij} \cdot \frac{\sigma_{p_j}}{\sigma_{z_i}} = \frac{\sigma_{p_j}}{\sigma_{z_i}} \cdot \left.\frac{\partial z_i}{\partial p_j}\right|_{\mathbf{p}^*} \tag{2}$$

where σ_p is the parameter-scaling factor, and σ_z is the output- or observation-scaling factor, also referred to as parameter variation or standard deviation, and observation standard deviation.

For example, σ_p is probably best thought of as the amount by which the parameter would be changed in a conventional sensitivity analysis, where the parameter is perturbed from its base-case value by an amount considered "reasonable" to examine its impact on the model

output. (If different perturbations would be chosen depending on whether the parameter is increased or decreased from its reference value, a parameter transformation is probably in order.) It can also be viewed as the standard deviation or range of the parameter that represents the parameter variability or its uncertainty. If scaled sensitivity coefficients are used as measures of relative parameter influence, σ_p reflects the leverage of this parameter's uncertainty on model predictions and thus indicates the potential need to obtain better estimates through independent measurements or inverse modeling. Accurately known parameters with a sufficiently low σ_p value are thus correctly identified as non-influential in the sense that they do not deserve our prime attention when designing an experiment. If sensitivity coefficients are used as rudimentary data-worth measures, σ_p reflects the target estimation uncertainty; the more accurately a parameter needs to be estimated, the comparatively less value does a certain data point with a given measurement uncertainty (σ_z) have when used as a calibration point in inverse modeling.

Morris Global Sensitivity Analysis

The Morris one-at-a-time (OAT) method is a global SA method developed by Morris (1991). It can be considered an extension of a local SA, since the Morris method randomly generates sets of reference values from the entire parameter range, and computes the difference of output caused by a fixed parameter change. The normalized parameter range is partitioned into (k–1) equally-sized intervals and a fixed normalized increment is calculated as $\Delta = k/\{2(k\text{-}1)\}$. A random reference point ξ is chosen from the set {0, 1/(k–1), 2/(k–1), …, 1-Δ}, and the increment Δ is added to each parameter in random order. The elementary effect (EE) for parameter p_i are calculated as:

$$EE_i = \left(\frac{1}{\sigma_z} \right) \frac{f(p_1^*, \ldots, p_i^* + \Delta_i, \ldots, p_n^*) - f(p_1^*, \ldots, p_n^*)}{\Delta_i} \quad (3)$$

where **p*** is the randomly selected parameter set, and σ_z is the output-scaling factor. Although the original sensitivity method proposed by Morris (1991) scales to EE values only by the parameter range, it is possible to scale EE by an output-weighting factor, as we discussed for the local sensitivity method.

By conducting simulations over multiple "paths" (i.e., multiple sets of reference parameter values and multiple, random orders of changing each parameter), an ensemble of EEs is obtained for each parameter. The number of required runs is $r(n+1)$, where r is the number of paths. Using the ensemble of EEs, we can compute three summary statistics: the mean of EE, the mean of absolute EEs (mean |EE|), and the standard deviation (SD) of EEs. The mean EE and mean |EE| can be regarded as a global sensitivity index, since they represent the average effect of each parameter over the parameter space. Wainwright et al. (2014) discussed that the sign (i.e., positive or negative) of mean EEs is useful for system understanding. The mean |EE| can be used to identify non-influential factors (Saltelli et al., 2008). The standard deviation of EE is used to identify nonlinear or interaction effects as well as to compute the standard error of the mean (SEM), i.e., SEM = SD/$r^{0.5}$ (Morris, 1991).

Results from a Morris analysis contain global sensitivity information even if only a small number of paths can be evaluated. This frugality makes the Morris method a very useful GSA tool also for computationally expensive high-fidelity models. Specifically, EE can be interpreted as the average parameter influence over the chosen parameter range, and the variability of the elementary effect provides insights into the model's degree of nonlinearity and parameter interaction. Moreover, the SEM value provides some indication of the accuracy of the estimated elementary effect.

Sobol' Global Sensitivity Analysis

While the local and Morris sensitivity methods are difference-based, the Sobol' method is variance-based. Here we define the random variable Z_j and the random vector $\mathbf{P} = [P_1, P_2, P_3, \ldots, P_n]$ for the system response and the parameters, respectively. The sampled response and parameters are z_j and p_i.

The Sobol' global sensitivity analysis evaluates two conditional variances as sensitivity indices. The first-order sensitivity index (referred to as the Sobol' index) is defined by S_{ij} =

$V[E[Z_j|P_i]]/V[Z_j]$, where $\mathbf{E}[\bullet]$ and $\mathbf{V}[\bullet]$ represent mean and variance, respectively. S_{ij} quantifies the first-order effect, i.e., the relative contribution of P_i to the uncertainty of Z_j. As it measures the variability of the output with respect to an individual parameter, it excludes the interaction effect with other parameters. The Sobol' index is used to identify influential parameters. The total sensitivity index is defined as $S_{tij} = 1 - V_{-i}[E[Z_j|P_{-i}]]/V[Z_j]$, where $\mathbf{E}[Z_j|P_{-i}]$ represents the mean of Z_j conditioned on all the parameters but P_i. S_{tij} accounts for the total effect of P_i including interaction effects, and is used to identify parameters with negligible effects and parameters that can be fixed. The interaction effect is the effect of each parameter depending on other parameters. We compute the sensitivity index S_i using an algorithm developed by Saltelli et al. (2003) and modified by Glen and Issacs (2012). The number of required runs is $r(n + 2)$, where r is the number of randomly generated parameter sets. Due to its high computational expense, it is important to account for the uncertainty in S_{ij} and S_{tij} caused by the number of simulations, and hence to compute the confidence interval of S_{ij} and S_{tij}. The uncertainties of S_{ij} and S_{tij} are computed in the same manner as in Wainwright et al. (2014).

Data-Worth Analysis

The data-worth analysis in iTOUGH2 consists of the following steps. First, we select parameters that potentially influence the prediction of interest, and also observable variables to be calculated by the model. We categorize observable variables into three groups: *actual (or existing) observations*, *potential observations*, and *predictions*. The potential observations are observations that could be collected for use in model calibration, should the data-worth analysis prove their value. Second, iTOUGH2 evaluates the sensitivity coefficients (Eq. 1) of all observations with respect to all parameters selected, and estimates the covariance matrix of the model parameters as well as the one of predictions. iTOUGH2 then removes (-) one actual calibration point (or one actual calibration data set), or adds (+) one potential observation point (or potential data set) and re-evaluates the parameter covariance matrix as well as prediction covariance matrix. Note that the prediction matrix is scaled by the acceptable prediction uncertainty.

In iTOUGH2, the data worth is defined as a measure of the relative increase in the prediction uncertainty caused by the removal of existing data, or the relative decrease in the prediction uncertainty caused by adding potential data. The data worth is therefore computed from the trace of the prediction covariance matrices.

Data worth depends not only on the reference parameter set, but also on the amount and quality of all the other data points presumed available for model calibration, including prior information. A data-worth analysis should thus be repeated for different reference parameter sets and different reference data sets with varying assumptions about the error structure of the residuals. In addition, the data-worth analysis method in iTOUGH2 makes use of the Jacobian matrix evaluated at a reference parameter point or the best-estimate parameter set after an inversion. It is therefore a local analysis that furthermore relies on the linearity and normality assumptions.

ILLUSTRATION

Sensitivity Analyses

To demonstrate the iTOUGH2-GSA module, we use the gas-pressure-pulse-decay experiment, which is Sample Problem No. 2 documented in *iTOUGH2 Sample Problems* (Finsterle, 2010). The experiments were conducted using a specially designed permeameter with small gas reservoirs. To conduct a test, the upstream reservoir is rapidly pressurized to a value about 300 kPa above the initial pressure of the system using nitrogen gas. Gas starts to flow through the dry sample, and the pressures in both the upstream and downstream reservoirs are monitored as they equilibrate with time. Among the three parts of the experiments, we use Part 1 (inversion of a single gas-pressure-pulse-decay experiment); see report *iTOUGH2 Sample Problems* and Finsterle and Persoff (2007)).

In porous media with very low permeability and porosity, gas mass flow F [kg s^{-1} m^{-2}] may be enhanced as a result of slip flow known as the Klinkenberg effect.

$$\mathbf{F} = -k\left(1 + \frac{b}{P_g}\right)\frac{\rho_g}{\mu_g}\nabla P_g \qquad (4)$$

Here, k is the absolute permeability, b is the Klinkenberg factor, ρ_g is the gas density, μ_g is the gas dynamic viscosity, and P_g is the gas pressure.

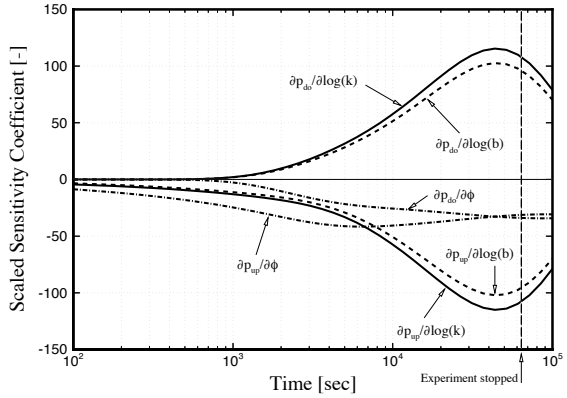

Figure 1: Local, scaled sensitivity coefficients as a function of time for upstream and downstream reservoir pressures observable during a gas-pressure-pulse-decay experiment.

Figure 1 shows the scaled local sensitivity coefficients of the upstream and downstream reservoir pressures with respect to three parameters as a function of time. The sensitivity coefficients with respect to porosity are negative because an increase in porosity leads to a decrease in pressure in both the upstream and downstream reservoirs. The porosity's influence increases with time and reaches a constant, when the pressure in the upstream and downstream reservoirs equilibrate. The steady-state pressures are thus sufficient to independently determine porosity. Conversely, upstream and downstream reservoir pressures have negative and positive sensitivity coefficients, respectively, with respect to permeability and the Klinkenberg factor, as in increase in gas mobility leads to a decrease/increase in the upstream/downstream reservoir pressure. Moreover, log(k) and log(b) have zero (or a small) influence at early times. The influences of these two parameters reaches their maxima when the reservoir pressures change most, and approach again zero as gas flow ceases near steady-state conditions.

Figure 3 shows the time evolution of the sensitivity indices from Morris and Sobol' methods for the downstream pressure. The number of simulations is 40 (r = 10, n = 3), and 5,000 (n = 3, r = 1,000) for the Morris and Sobol' methods, respectively. The confidence intervals are shown so that we can take into account the limited number of simulations. For the Morris method, the output scaling factor σ_z is 1000 Pa, which is the same value as used for the local sensitivity method.

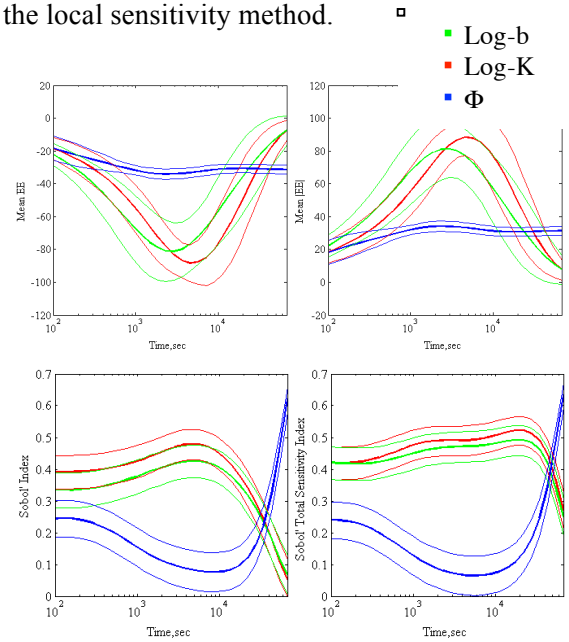

Figure 2: Time evolution of sensitivity index: (a) Mean EE, (b) Mean |EE| (c) Sobol' index, and (d) Sobol' total sensitivity index. The thin lines represent the 95% confidence intervals.

At each time point, we may define the importance ranking. Figure 3 shows that the important parameters change with time. The Mean-EE (Figure 3a) is always negative, which means that increasing any of these three parameters decreases the downstream pressure. In Figure 3b, Mean |EE| suggests that the permeability and Klinkenberg factors have a large impact around 10^3-10^4 seconds, while the porosity becomes more important after 5×10^4 seconds. Although the number of paths and number of simulations are not large (r = 10), the confidence intervals are separated well enough to confirm the relative importance (such as the importance of porosity in a later time). This is the same finding as obtained with the local sensitivity method, although with GSA, we can account for the nonlinearity and/or interaction effects, since we compute the average of the effects over the prescribed parameter range. Based on this result, we can capture the intervals

in which the three parameters are influential, and determine the experiment time that is large enough to estimate porosity.

In Figure 3c and d, the Sobol' indices provide the relative contribution of each parameter to the uncertainty of the output. For example, we may conclude that both the permeability and Klinkenberg factor account for approximately 40% of the pressure variance between 10^3 and 10^4 seconds, while the porosity accounts for only approximately 10%. Since the indices are normalized by the variance at each time step, the ranking of parameter importance is more easily recognized than Mean |EE|, although the effect of each parameter at different times cannot be compared.

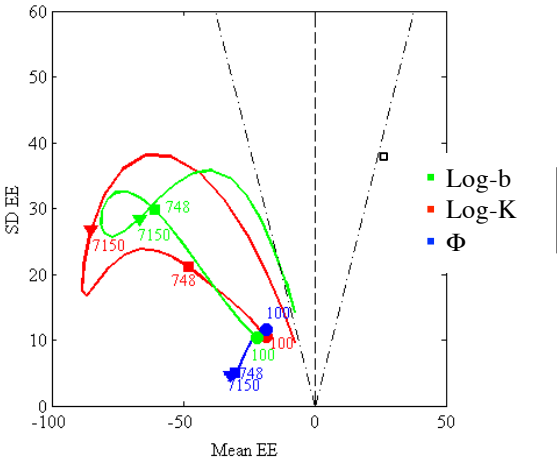

Figure 4: Mean EE vs. SD from the Morris method. The circle, square and triangle on each curve represent 100, 748 and 7150 seconds, respectively.

Figure shows a cross-plot between the mean and SD of EE, following Morris (1991). Each curve corresponds to the time evolution for a parameter's sensitivity index. The two black lines represent Mean EE = ±2SEM. Although the number of paths (r = 10) is small, all the parameters are below the black lines, indicating that their non-zero impact is statistically significant. All the parameters have a non-zero value of SD, indicating that they have nonlinearity and/or interaction effects. The ratio between the mean and SD of EE is larger for the permeability and Klinkenberg factor, which suggests the larger nonlinearity and/or interaction effects of these two parameters.

Figure 3 shows the difference between the Sobol' index and the total sensitivity index as a function of the Sobol' index, comparing the first-order effect and the interaction effects. The permeability and Klinkenberg factor have a particularly large difference relative to their Sobol' indices, suggesting that they have a large interaction effect compared to the first-order effect. Comparing Figure and Figure 3 allows us to separate interaction from nonlinearity effects, since Morris's SD of EE includes both, but the difference between the Sobol' index and total sensitivity index represent only the interaction effects. Although Eq. (4) suggests this flow process includes both nonlinearity and interactions, SD of EE of the permeability and Klinkenberg are caused mainly by the interaction effects.

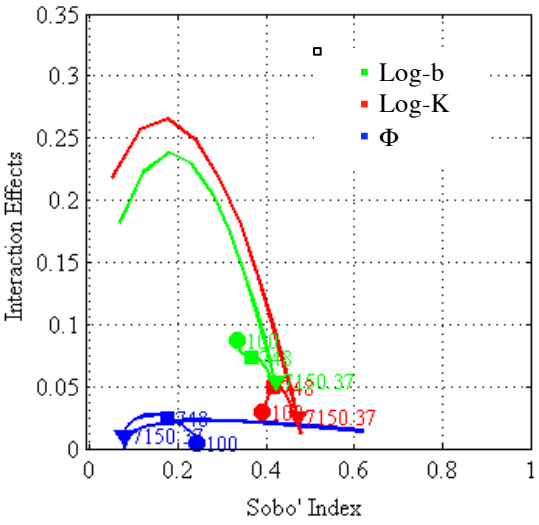

Figure 3: The interaction effect (the difference between the Sobol' index and the total sensitivity index) as a function of Sobol' index. The circle, square and triangle on each curve represent 100, 748.48 and 7150.37 seconds, respectively.

Data-Worth Analysis

The test case is based on a modified version of the five-spot geothermal injection/production problem described as Problem No. 4 in the *TOUGH2 User's Guide* (Pruess et al., 2012) as well as Problem No. 3 in *iTOUGH2 Sample Problems* (Finsterle, 2010). The problem considers a large well field with wells arranged in a five-spot configuration. For simplicity, the geothermal reservoir, which has a uniform initial temperature of 300°C and pressure of 85.93 bars, is represented by a single layer, discretized

into 36 primary elements. As a modification to the original formulation, the injected water is considered to contain a conservative tracer. The simulations are performed using the equation-of-state (EOS) module 1 (Pruess et al., 2012), which handles nonisothermal, two-phase flow of two water components.

For the data-worth analysis, we consider a scenario in which a model is to be developed for the prediction of two specific performance measures, namely (1) the enthalpy of the produced fluid mixture, and (2) the temperature in the center of the matrix near the edge of the reservoir; both measures are evaluated after 30 years of exploitation. They may be considered relevant to evaluate the field's long-term productivity and sustainability. Production enthalpy and reservoir temperature shall be predicted as accurately as possible using a model that is calibrated against data to be collected during the first five years of operation. A data-worth analysis is performed to examine which data set among an assembly of planned and potential data sets helps most to reach the objective of obtaining reliable long-term predictions of enthalpy and temperature, and which data set could be omitted without considerable loss of model predictability.

Seven potentially influential parameters are selected, with reference values: (1) $\log(k_X)$, (2) $\log(k_Y)$, (3) porosity of the fracture continuum, (4) residual liquid saturation of the fracture continuum, (5) thermal conductivity, (6) fracture spacing, and (7) initial reservoir temperature. Next, the five calibration data sets are defined, which are (1) the injection pressure, (2) the temperature of water flowing in a facture midway between the injection well and production well, (3) the temperature of the rock matrix (volume average of matrix continua), (4) the production enthalpy, and (5) the tracer concentration in the production well. Of these five data sets, only the injection pressure (Set 1) and production enthalpy (Set 4) are planned to be measured, i.e., they are expected to be existing data sets. These two data sets thus constitute the actual data available for model calibration. The other data sets are potential data sets. The two model outputs of interest are (1) the temperature in the middle of a matrix block, and (2) the production enthalpy.

In the data-worth analysis, the first analysis will consider the worth of colleting entire data sets, with prediction uncertainty as the criterion. In this particular example, the calibration and prediction phases are simulated using the same model; the calibration phase consists of the injection-production operation during the first five years, whereas the prediction phase consists of the subsequent 25 years of exploitation.

Table 1 shows the data-worth of each dataset. This analysis suggests that measuring enthalpy in the production well during the first five years of production is valuable; removing that data set would considerably increase the uncertainty with which reservoir temperature and future production enthalpy could be predicted. The high data worth of enthalpy is not surprising given that enthalpy is the same data type as the prediction of interest. Removing measurements of injection pressure is less detrimental.

Table 1. Data-worth analysis results

	Datasets	Category	DW
1	Injection press.	Existing	0.308
2	Fracture temp.	Potential	0.498
3	Rock temp.	Potential	0.325
4	Prod. enthalpy	Existing	0.884
5	Tracer conc.	Potential	0.558

Of the three potential data sets to be added to the reference data sets, measuring temperature along the likely flow path between the injector and producer as well as chloride concentrations appears to be most beneficial. This is likely because the arrival time of the cooling front and in particular tracer breakthrough data are the only data that contain useful information about porosity, which in turn affects production enthalpy.

The results of the data-worth analysis would be considerably different if the objective were to minimize the estimation uncertainty (i.e., the result of the calibration phase only), without considering the purpose for which the calibrated model will be used. In addition, the data-worth value would be different if the analysis were

performed for individual data points, because the degree of redundancy and reference data set are different.

CONCLUDING REMARKS

In addition to its inverse modeling capabilities, iTOUGH2 includes options for performing sensitivity and data-worth analyses, which improve system understanding and help design experiments and monitoring systems, so the data collected contain the information needed to calibrate the model.

A conventional, local sensitivity analysis can be performed as a pre-calibration task. However, sensitivity coefficients and composite sensitivity measures are also evaluated at the end of an inversion that uses a derivative-based minimization algorithm (specifically the Levenberg-Marquardt method).

Two global sensitivity analysis methods are implemented. The Morris one-at-a-time method can be considered an approach of great practical value, as it identifies influential parameters as well as the impact of nonlinearity and/or interaction effects with a limited number of simulation runs. In addition, by having confidence intervals of the indices, it is possible to compare the importance of parameters with a limited number of simulation runs. The Sobol' method yields a statistically more quantitative global sensitivity index in the context of UQ, at the expense of having to evaluate significantly more simulation runs. Similarity of the total sensitivity index and the Morris mean |EE| suggests that mean |EE| would be sufficient and could be used instead of the total sensitivity index, requiring fewer simulations. An advantage of the Sobol' method is that having two indices – Sobol' index and total sensitivity index – allows us to identify the presence and magnitude of interactions effects.

Finally, iTOUGH2 can be used to perform a data-worth analysis, which is based on local sensitivity analyses of a calibration and prediction model. It provides insights into the relative value of data points or entire data sets for the purpose of model calibration and related model predictions.

Sensitivity and data-worth analysis are essential tools for the development of more reliable and more defensible numerical models. They also help improve the design and analysis of laboratory experiments, field tests, and monitoring systems, making data collection more cost effective.

ACKNOWLEDGMENT

This work was supported, in part, by the TOUGH Development Grant and the U.S. Dept. of Energy under Contract No. DE-AC02-05CH11231.

REFERENCES

Finsterle, S., and P. Persoff, Determining permeability of tight rock samples using inverse modeling, *Water Resour. Res*., 33 (8), 1803–1811, 1997.

Finsterle, S., Multiphase inverse modeling: Review and iTOUGH2 applications, *Vadose Zone J*., 3: 747–762, 2004.

Finsterle, S., iTOUGH2 Sample Problems, Report LBNL-40042, Lawrence Berkeley National Laboratory, Berkeley, Calif., 2010.

Finsterle, S., and Y. Zhang, Solving iTOUGH2 simulation and optimization problems using the PEST protocol, *Environmental Modelling and Software*, 26, 959–968*,* 2011.

Glen, G. and K. Issacs, Estimating Sobol sensitivity indices using correlations, *Environ. Modelling Software*, 37, 157–166, 2012.

Morris, M.D., Factorial Sampling Plans for Preliminary Computational Experiments, *Technometrics*, 33(2), 161–174, 1991.

Pruess, K., C. Oldenburg, and G. Moridis, TOUGH2 User's Guide, Version 2.1, Report LBNL-43134, Lawrence Berkeley National Laboratory, Berkeley, Calif., 2012.

Saltelli, A., M. Ratto, T. Andres, F. Campolongo, J. Cariboni, D. Gatelli, M. Saisana, and S. Tarantola, *Global Sensitivity Analysis: The Primer*, John Wiley & Sons, West Sussex, England, 2008.

Sobol, I.M., Global sensitivity indices for nonlinear mathematical models and their Monte Carlo estimates, *Math. Comput. Simul.*, 55(1-3), 271–280, 2001.

Wainwright, H. M., S. Finsterle, Y. Jung, Q. Zhou, and J.T. Birkholzer, Making sense of global sensitivity analyses. *Computers & Geosciences*, 65, 84–94, 2014.

DETERMINING OPTIMAL MONITORING STRATEGIES FOR MANAGING RISKS OF CYCLIC STEAM INJECTION USING DATA-WORTH ANALYSIS

Yingqi Zhang, Laura Blanco-Martín, Christine Doughty,
Stefan Finsterle, Quanlin Zhou, and Curtis M. Oldenburg

Lawrence Berkeley National Laboratory, Earth Sciences Division, Berkeley, California
e-mail: yqzhang@lbl.gov

INTRODUCTION

The goal of cyclic steam injection in oil reservoirs is to heat up high-viscosity oil to increase its mobility for enhanced production. A typical single-well cycle consists of injection of steam, soaking for a period of time, and then production of oil. At some oil fields, repeated cycling induces considerable uplift for a short period, and compaction after several cycles, potentially leading to shear displacements that cause well failure and associated leakage of steam and/or oil upward to the ground surface. In this study, we carry out data-worth analysis to guide decision-making about monitoring strategies that address (1) potential well failure as a result of large shear displacement in the formation, and (2) potential steam/oil leakage at the ground surface. The nature and location(s) of flow pathways, and even the conceptual model for steam leakage, are highly uncertain and include the possibility that injected steam from different sources accumulates in shallower secondary reservoirs before eventually migrating up to the ground surface. The goal of this work is to identify monitoring approaches that ensure key observations are made to reduce uncertainty in the predictions of (1) key factors indicative of well failure, including pressure and temperature change, and ground surface displacement due to cyclic steam operation, and (2) the amount of steam/oil leakage at the ground surface.

We present the data-worth analysis (DWA) method as implemented in iTOUGH2 (Wainwright and Finsterle, 2015; Finsterle, 2015) for identifying key observations. Two numerical models are needed for predicting quantities of interest: one is a TOUGH-FLAC (Rutqvist *et al*., 2002) flow-geomechanics model for predictions related to potential well failure (Case 1); the other one is a TOUGH2 (Pruess *et al*., 2012) flow model for leakage prediction (Case 2). For the cyclic steam analysis, we will need to perform two separate DWAs for the two cases, as well as a combined DWA because the two analyses share some observations.

METHOD

A data-worth analysis aims at identifying the relative contribution that each data point makes to the solution of an inverse problem and the subsequent predictive simulation. The basic idea of DWA is to examine how the addition of potential monitoring data (or removal of existing data) reduces (or increases) the uncertainty in the selected predictions (Figure 1). A typical DWA contains two numerical models: a calibration model and a prediction model. The prediction model is used to predict quantities of interest; in our case, the prediction model is a coupled flow and geomechanical model for Case 1, and a flow model for Case 2. The predictions of interest are pressure and temperature changes, and ground-surface displacements for Case 1, and leakage flux of oil, steam and liquid water for Case 2 for a prediction period of three years. These predictions are sensitive to some of the model inputs, which may be unknown or uncertain. These influential inputs should also be inputs to another model – the calibration model. In our study, the calibration model is the same model as the prediction model, except its simulation period (referred to as calibration period) is an earlier period during which data are collected for model calibration. These observations can be either existing monitoring data or potential monitoring data. By calibrating the model against these observation data, the estimation uncertainty of the influential input parameters, and, consequently, the uncertainty in the predictions, can be reduced.

Calibration and prediction phases can be included in a single data-worth analysis; doing so has considerable advantages, because it automatically identifies data that contain information about those parameters that are most influential on the predictions of interest. The approach consists of the following steps:

(1) Define objectives based on the following questions: What are the predictions of interest? What is the appropriate prediction model? What is the acceptable uncertainty in the prediction?

(2) Determine uncertain parameters to model the predictions based on the following questions: What are the potential inputs to the prediction model? Which inputs are uncertain? If known a priori, what are the influential parameters (if not known, this will be analyzed in the sensitivity analysis)? What are the acceptable estimation uncertainties? Is there any prior information or knowledge about the parameter distribution?

(3) Define existing and potential observations based on the following questions: What are the existing monitoring data? What are the potential monitoring data? What model relates these existing and potential data to the uncertain parameters defined in the previous step? What are the spatial and temporal resolutions of these observations? With what accuracy can we measure these data?

(4) Develop calibration and prediction models.

(5) Evaluate uncertainties of estimated parameters and predicted model output based on the reference data set (existing data).

(6) Remove existing or add potential calibration data, and repeat uncertainty analysis of Step (5).

(7) Calculate a composite uncertainty-reduction measure (ω), which reflects data worth.

Data worth depends not only on the reference parameter set, but also on the amount and quality of all the other data points presumed available for model calibration. The data-worth analysis is thus repeated for different reference parameter sets and different reference data sets with varying assumptions about the error structure of the residuals. The approach is further described in Wainwright and Finsterle (2015) and Finsterle (2015).

The DWA implemented in iTOUGH2 has options to investigate

(1) the worth of adding potential data points/sets;

(2) the worth of removing data points/sets;

(3) data worth for reducing parameter uncertainty; and

(4) data worth for reducing prediction uncertainty;

The current implementation of DWA is a by-product of a local sensitivity analysis; therefore, it is based on linearity and normality assumptions. Multiple DWAs may need to be performed if the model is strongly nonlinear and/or the reference parameter set is highly uncertain.

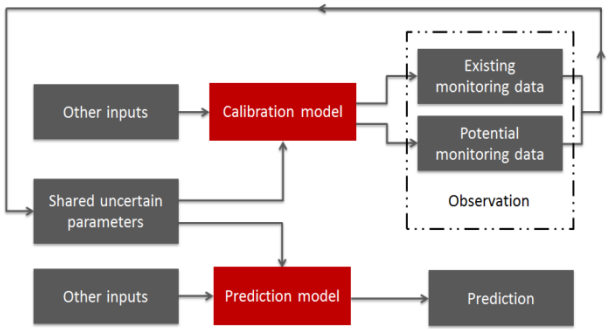

Figure 1. Illustration of how DWA examines reduction or increase in prediction uncertainty due to adding or removing observations.

SUMMARY

In this study we will demonstrate how to use DWA to determine monitoring strategies that will reduce prediction uncertainty. In addition, a DWA also informs us about what the influential parameters are in the prediction. We also demonstrate that results of a DWA are local, and the need to develop a global DWA approach, which will be a powerful tool in risk assessment.

ACKNOWLEDGMENT

Support for this work was provided, in part, by Lawrence Berkeley National Laboratory under Department of Energy Contract No. DE-AC02-05CH11231.

REFERENCES

Finsterle, S., Notes on sensitivity and data-worth analysis, *Water Resour. Res.*, 2015 (in review).

Pruess, K., C. Oldenburg, and G. Moridis, *TOUGH2 User's Guide, Version 2.0*, Report LBNL-43134 (revised), Lawrence Berkeley National Laboratory, Berkeley, Calif., 2012.

Rutqvist, J., Y.-S. Wu, C.-F. Tsang, G. Bodvarsson, A modeling approach for analysis of coupled multiphase fluid flow, heat transfer, and deformation in fractured porous rock, *International Journal of Rock Mechanics and Mining Sciences, 39*(4), 429–442, 2002.

Wainwright, H.M., and S. Finsterle, *Global Sensitivity and Data-Worth Analysis in iTOUGH2, User's Guide*, Report LBNL-TBD, Lawrence Berkeley National Laboratory, Berkeley, Calif., 2015.